

Final Report

Space Plasma Physics and Cosmic Rays

Principal Investigator:

Prof. Dr. David Ruffolo

August, 2019

Contract RTA5980003

Final Report

"Space Plasma Physics and Cosmic Rays"

The Research Team:

1. Prof. Dr. David Ruffolo (Mahidol U., MU)
2. Dr. Piyanate Chuychai (independent researcher, Chiang Rai)
3. Dr. rer. nat. Ronald Macatangay (National Astronomical Res. Inst. of Thailand, Chiang Mai)
4. Lect. Dr. Kittipat Malakit (Thammasat U.)
5. Asst. Prof. Dr. Warit Mitthumsiri (MU)
6. Lect. Dr. Waraporn Nuntiyakul (Chiang Mai U., CMU)
7. Asst. Prof. Dr. Tanin Nutaro (Ubon Rajathanee U.)
8. Lect. Dr. Peera Pongkitiwanichakul (Kasetsart U., KU)
9. Lect. Dr. Alejandro Sáiz (MU)
10. Dr. Achara Seripienlert (Dacon Inspection Services Co. Ltd., Rayong)
11. Lect. Dr. Andrew Snodin (King Mongkut's U. Tech. North Bangkok)
12. Lect. Dr. Wirin Sonsrettee (Panyapiwat Inst. Management)
13. Asst. Prof. Dr. Paisan Tooprakai (Chulalongkorn U.)
14. Asst. Prof. Dr. Suwicha Wannawichian (CMU)
15. Lect. Dr. Maneenate Wechakama (KU)
16. Lect. Dr. Petchara Pattarakijwanich (MU)
17. Miss Chanoknan Banglieng (MU)
18. Mr. Suttiwat Madlee (MU)
19. Mr. Pradiphat Muangha (MU)
20. Dr. Usanee Tortermpun (MU)

Supported by the Thailand Research Fund (TRF)

(The opinions presented here do not necessarily represent those of TRF)

Project Code: RTA5980003

Abstract and Executive Summary

Project Title: Space Plasma Physics and Cosmic Rays

Principal Investigator: Prof. Dr. David Ruffolo, Dept. of Physics, Faculty of Science, Mahidol University
E-mail address: david.ruf@mahidol.ac.th
Project Period: July 29, 2016 – July 28, 2019

The overall goals of this project were nine-fold: 1) to better understand turbulence and transport processes in space plasmas, such as the random walks of magnetic field lines and energetic particles; 2) to clarify patterning and intermittency in magnetic field line and energetic particle trajectories through space; 3) to study space plasma structures, including magnetic reconnection, dynamos, plasma bubbles, and the aurorae of Jupiter and Earth; 4) to study cosmic ray variations using neutron and muon detectors; 5) to determine the effects of radiation and related atmospheric phenomena; 6) to perform or prepare for cosmic ray studies using the Fermi-LAT satellite and other satellites; 7) to perform cosmic ray studies using air shower arrays; 8) to model possible observable effects of dark matter on cosmic rays; and 9) to model possible observable effects of dark matter on cosmic rays. We have worked on 91 lines of research and trained or involved 81 local participants. Output of the project includes 43 conference presentations and 21 articles for leading international journals (20 published and 1 submitted), with mean impact factor over 5, which have already accumulated 1590 reads and 80 citations.
Keywords: Cosmic rays, space physics, astrophysics, computer simulations, turbulence

ชื่อโครงการ: พลาสมาฟิสิกส์อวกาศและรังสีคอสมิก

ชื่อนักวิจัยหลัก: ศ.ดร.เดวิด รูฟโฟโล ภาควิชาฟิสิกส์ คณะวิทยาศาสตร์ มหาวิทยาลัยมหิดล
E-mail address: david.ruf@mahidol.ac.th
ระยะเวลาโครงการ: 29 กรกฎาคม 2559 - 28 กรกฎาคม 2562

วัตถุประสงค์ของโครงการนี้มี 9 ข้อ: 1) เพื่อเข้าใจความปั่นป่วนและกระบวนขนส่งในพลาสมาในอวกาศให้ดีขึ้น เช่นการเดินสุ่มของเส้นสนามแม่เหล็กและอนุภาคพลังงานสูง 2) เพื่อเข้าใจรูปแบบและอินเทอร์มิทเท็นซีในเส้นทางของเส้นสนามแม่เหล็กและอนุภาคพลังงานสูงในอวกาสให้ชัดเจนมากขึ้น 3) เพื่อศึกษาโครงสร้างพลาสมาในอวกาศ รวมทั้งการเชื่อมต่อใหม่ของเส้นสนามแม่เหล็ก ไดนาโม ฟองพลาสมา และแสงเหนือแสงใต้ของดาวพฤหัสบดีและโลก 4) เพื่อศึกษาการเปลี่ยนแปลงในรังสีคอสมิกโดยใช้เครื่องวัดนิวตรอนและมิวออน 5) เพื่อศึกษาผลกระทบของรังสีและปรากฏการณ์ที่เกี่ยวข้องในอวกาศ 6) เพื่อปฏิบัติหรือเตรียมสำหรับการศึกษารังสีคอสมิกโดยใช้ดาวเทียม Fermi-LAT และดาวเทียมอื่น 7) เพื่อปฏิบัติการศึกษารังสีคอสมิกโดยใช้ชุดเครื่องวัดชาวเวอร์ในอากาศ และ 9) เพื่อจำลองผลกระทบของสสารมืดต่อรังสีคอสมิกที่อาจสังเกตได้ เราได้ทำโครงการย่อยจำนวน 91 โครงการ และให้คนในประเทศไทยฝึกงานหรือให้มีส่วนร่วมในงานวิจัยจำนวน 81 คน ส่วนผลงานจากโครงการนี้ รวมถึงการเสนอที่ประชุม 43 เรื่อง และบทความสำหรับวารสารนานาชาติชั้นนำ 21 เรื่อง (ตีพิมพ์แล้ว 20 เรื่อง และส่งถึงวารสารแล้วอีก 1 เรื่อง) โดยมี impact factor เฉลี่ยเกิน 5 ซึ่งได้มีการอ่านแล้ว 1590 ครั้งและอ้างอิง 80 ครั้ง
คำหลัก: รังสีคอสมิก, ฟิสิกส์อวกาศ, ดาราศาสตร์, การจำลองด้วยดอมพิวเตอร์, ความปั่นป่วน

Some highlights of our research results are:

- Successful Monte Carlo modeling and analysis of the observed count rate and neutron leader fraction from time delay histograms from a ship-borne neutron monitor as a function of geomagnetic latitude, confirming that the leader fraction from a single neutron monitor station can indicate changes in the cosmic ray spectrum.
- New measurement of the cosmic-ray electron+positron spectrum over a very wide energy range using a single space instrument, which provides key information about cosmic ray transport in the Galaxy.
- New concepts of cosmic ray transport in the Galaxy.
- Calculated cosmic ray diffusion coefficients throughout the inner heliosphere in conjunction with a global solar wind simulation that includes magnetohydrodynamics and turbulence transport.
- Calculated ionization and biological radiation dosage in Earth's atmosphere (e.g., for airline passengers) as a function of altitude and time during the solar event of 2005 Jan 20.
- Developed new techniques to determine the hourly Galactic cosmic ray anisotropy using data from polar neutron monitors.
- Analyzed data from polar neutron monitors to determine the Galactic cosmic ray anisotropy during the Forbush decrease starting 2013 Apr 13, which agrees with our previous theoretical prediction of a cosmic ray flow due to guiding center drifts into one leg of a magnetic flux rope and out the other leg.
- The Princess Sirindhorn Neutron Monitor (PSNM) at Doi Inthanon has, for the first time, studied the effect of an entire sunspot cycle (of ~11 years) on the flux of Galactic cosmic rays, a process that provides remote sensing of the entire heliosphere. PSNM is the neutron monitor (NM) with the world's highest geomagnetic threshold energy. We discovered a new pattern of such "solar modulation" than was found NMs by sensitive to cosmic rays of lower energy.
- Discovery of a radio-quiet gamma-ray millisecond pulsar.
- Contributed to analysis of Galactic cosmic ray anisotropy in the Northern Hemisphere using data from ARGO-YBJ in China during 2008-2012.
- Analyzed data from a ship-borne 3-counter neutron monitor and 3 bare neutron counters during a latitude survey in 1995-1996, comparing the cosmic ray response of the bare counters to the neutron monitor.
- Analyzed data from another ship-borne latitude survey with 2 bare neutron counters of a different type. Comparing with direct satellite measurements of cosmic rays, we were able to determine the yield function of these counters, which were later deployed at the South Pole for spectral measurements of solar energetic particles.
- Constructed a new semi-leaded ship-borne neutron monitor, which conducted a latitude survey on a Chinese icebreaker ship during 2019 Feb-Mar.
- Contributed to an observing campaign using telescopes worldwide to study the disintegrating exoplanet K2-22b.
- Predicted the X-ray emission of e± pair haloes around active galaxies, which could possibly be detected by present-day X-ray observatories.
- Continued operation of the Princess Sirindhorn Neutron Monitor (PSNM) at the summit of Doi Inthanon, including improvements to the data acquisition.
- Organized semi-annual electronics training workshops and annual research meetings.
- Extensive outreach activities, including maintaining a Facebook page and a website, conducting a teaching lab as part of a required course, and taking on numerous research interns.

Contents

Research Activities 1

Research Output 5

Research impact 13

Other Activities 24

Attachments
1. Reprints of international journal articles
2. Abstracts of conference presentations and invited talks
3. List of the research team and students who received training as part of this project

RESEARCH ACTIVITIES

Output numbers refer to the list of output in the following section. Note that all output can be viewed in full in the Appendices.

1. **Turbulence and transport processes in space plasmas**
   Objective: To better understand turbulence and transport processes in space plasmas, such as the random walks of magnetic field lines and energetic particles.

1.1. **Lagrangian time correlations of increments in turbulence**
1.2. **Skewness and kurtosis of increments in space plasma turbulence measured by the MMS spacecraft**
1.3. **Fluctuations of the solar wind velocity and magnetic field** (Output 66)
1.4. **Modeling and spacecraft observations of energetic particle enhancements due to plasma structures in the solar wind**
1.5. **Simplified phase coherence index** (Output 51)
1.6. **Variations on Corrsin's hypothesis as an approximation to Lagrangian correlations**
1.7. **Conditions for quasilinear diffusion of the magnetic field line random walk in general turbulence**
1.8. **Random ballistic deceleration theory of magnetic field line separation**
1.9. **Magnetic field line random walk in stretched isotropic turbulence** (Output 49; 2 senior projects)
1.10. **Extrapolating model of magnetic field line spreading in isotropic turbulence with varying mean field** (Output 52)
1.11. **Particle diffusion coefficients in isotropic turbulence with no mean field** (Paper published; Output 2, 28)
1.12. **Fickian and non-Fickian diffusion of cosmic rays** (Paper published; Output 20)
1.13. **Simulation of spatial diffusion of particles in noisy RMHD turbulence**
1.14. **Simulation of spatial diffusion of particles in isotropic turbulence**
1.15. **Simulation of pitch angle diffusion of particles in noisy RMHD turbulence** (Output 61)
1.16. **Suppression of guiding center drifts by turbulence** (Output 50)
1.17. **Particle diffusion coefficients in a 3D model of the inner heliosphere** (Paper published; Output 5)
1.18. **Particle drift coefficients in a 3D model of the inner heliosphere**
1.19. **Magnetic field line diffusion and filamentation in a 3D model of the inner heliosphere**
1.20. **Effects of coherent magnetic structures on particle diffusion**
1.21. **Effect of reduced dimensionality of the magnetic field on particle transport**
1.22. **Relation between the perpendicular diffusion of particles and field line random walk in two-component magnetic turbulence**
1.23. **Transport equation for anisotropic distributions**
1.24. **Fluid description of cosmic ray transport**
1.25. **Connection between local and global diffusion of energetic charged particles**
1.26. **Equation of cosmic ray anisotropy evolution**

2. **Patterning and intermittency in magnetic field line and energetic particle trajectories through space plasmas**
   Objective: To clarify patterning and intermittency in magnetic field line and energetic particle trajectories through space.

2.1. **Cosmic rays in intermittent magnetic fields** (Paper published; Output 3)
2.2. **Relative distribution of cosmic rays and magnetic fields** (Paper published; Output 10)
2.3. **Simulation of dropouts of solar energetic particles in spherical geometry** (Output 24, 29)
2.4. **Analysis of observed dropouts of solar energetic particles near the Sun**
2.5. **Magnetic field line diffusion and filamentation in a 3D model of the inner heliosphere** (Output 48)
2.6. **Magnetic field line random walk at current sheets in magnetic loops in the solar corona** (Paper published; Output 6)

3. **Plasma structures**
   Objective: To study space plasma structures, including magnetic reconnection, dynamos, plasma bubbles, and the aurorae of Jupiter and Earth.

3.1. **Larmor electric field in asymmetric magnetic reconnection in the presence of a guide field** (Paper published; Output 7)
3.2. **Temperature dependence of the reconnection rate and outflow speed in collisionless reconnection: A scaling study**
3.3. **Reduction of magnetic reconnection outflow jets to sub-Alfvénic speeds** (Paper published; Output 18)
3.4. **Particle trajectories in asymmetric reconnecting magnetic fields** (Output 58)
3.5. **Magnetic reconnection at CME interfaces** (Output 53)
3.6. **Lattice Boltzmann model of plasmas**
3.7. **Electric field in laser-driven high-energy-density plasma**
3.8. **Nonlinear effects in a plasma dynamo**
3.9. **Simulation of current sheet instability** (Paper published; Output 11)
3.10. **Influence of magnetospheric plasma on the Jovian aurorae at magnetic footprints of the moons Io and Ganymede** (Paper published; Output 19, 47; M.Sc. thesis)
3.11. **Influence of magnetospheric dynamics on Jovian and terrestrial aurorae** (M.Sc. thesis)
3.12. **Intermittent turbulence in the ionosphere above Brazil** (Paper published; Output 15)
3.13. **Intermittent turbulence in the ionosphere above Thailand**

4. **Cosmic ray studies with neutron and muon detectors**
   Objective: To study cosmic ray variations using neutron and muon detectors.

4.1. **Princess Sirindhorn Neutron Monitor (PSNM) operation and improvements at Doi Inthanon, Thailand**
4.2. **Planning neutron monitor (NM) and muon detector operation and improvements at Mawson, Antarctica**
4.3. **Development of NM electronics with very low dead time**

4.4. **Measuring the effect of atmospheric water vapor on the PSNM count rate and leader fraction** (Output 55, 56)
4.5. **Measured and simulated leader fraction during a NM latitude survey** (Paper published; Output 1)
4.6. **Long-term variation of the PSNM leader fraction** (Output 30, 62)
4.7. **Environmental correction of the leader fraction from the South Pole NM** (Output 45)
4.8. **Measuring cross-tube time delay spectra of PSNM** (Output 31, 65)
4.9. **Exploring use of triggered information on absolute timing on multiple NM tubes** (Output 57; Senior project)
4.10. **Bare neutron counter and NM response to cosmic rays during a 1995 latitude survey** (Paper published; Output 16, 63)
4.11. **Analyzing bare neutron counter response during the 2009 all-time cosmic ray maximum** (Paper submitted; Output 22, 38, 46)
4.12. **Analyzing latitude survey NM tube ratios vs. cutoff rigidity**
4.13. **Ship-borne neutron monitor latitude survey between Antarctica and China in 2019** (Output 54)
4.14. **Simulating the effect of water in the ground surrounding the 18-tube NM and 3 bare neutron counter tubes at PSNM**
4.15. **Distinct pattern of solar modulation of Galactic cosmic rays above a high geomagnetic cutoff rigidity** (Paper published; Output 13, 27, 32)
4.16. **Search for spectral changes in Galactic cosmic rays during 27-day variations at Doi Inthanon** (Senior project)
4.17. **Disturbed solar diurnal anisotropy of Galactic cosmic rays in association with 27-day variations**
4.18. **Simulating the response of the NM and bare neutron counters at the South Pole**
4.19. **Analyzing data from the NM and bare neutron counters at the South Pole to explore environmental effects**
4.20. **Anisotropy of Galactic cosmic rays during solar-storm induced Forbush decreases** (Paper published; Output 9, 60, 64; Ph.D. thesis)
4.21. **Analysis of muon detector observations to determine Forbush decrease spectral cutoffs**
4.22. **Spectral changes of Forbush decreases between polar NMs and PSNM**
4.23. **Spectral changes in Galactic cosmic rays during Forbush decreases at Doi Inthanon** (Senior project)
4.24. **Short-term time correlations between NM data from McMurdo and Jang Bogo, Antarctica**
4.25. **Comparing gamma-ray and relativistic particle emission from the Sun on 2017 September 10** (Output 40, 41)
4.26. **Observation and modeling of relativistic solar particle distributions using the *Spaceship Earth* network** (Output 37)
4.27. **Using count rates at long and short dead time from Apatity to determine the spectral index of relativistic solar particles**

5. **Radiation and atmospheric phenomena**

Objective: To determine the effects of radiation and related atmospheric phenomena.

5.1. **Simulation of polar-region atmospheric ionization induced by the giant solar storm on 20 January 2005** (Paper published; Output 8, 39)

5.2. Comparing atmospheric ionization on 20 January 2005 with cloud data and setting limits on the cloud-cosmic ray relationship

5.3. Simulations of radiation shielding (Output 42, 43)

5.4. Sampling the air in Bangkok for cosmogenic ^{7}Be (Output 33)

6. Space-based cosmic ray studies

Objective: To perform or prepare for cosmic ray studies using the Fermi-LAT satellite and other satellites.

6.1. Pictures of Earth in Gamma Rays (Output 25, 59)

6.2. Einstein@Home discovers a radio-quiet gamma-ray millisecond pulsar (Paper published; Output 12)

6.3. Cosmic-ray electron+positron spectrum from 7 GeV to 2 TeV with the Fermi Large Area Telescope (Paper published; Output 4)

6.4. Design of a particle detector for a polar satellite

6.5. Theory of X-rays from electron-positron haloes from active galactic nuclei (Paper published; Output 21)

7. Cosmic ray studies with air shower arrays

Objective: To perform cosmic ray studies using air shower arrays.

7.1. Preparing to monitor GeV-range solar anisotropy using LHAASO in China

7.2. TeV-range cosmic ray sidereal anisotropy as measured by ARGO-YBJ in China (Paper published; Output 14)

7.3. Ground level enhancements due to solar storms in data from IceTop at the South Pole (Output 26, 34, 36; M.Sc. thesis)

7.4. Short-term increase in the Galactic cosmic ray flux at IceTop and the NM at the South Pole (Output 35)

7.5. IceTop rate fluctuations (Senior project)

8. Dark matter and cosmic rays

Objective: To model possible observable effects of dark matter on cosmic rays.

8.1. The origin of Galactic electrons and positrons

8.2. Search for dark matter annihilation signatures in Fermi-LAT spectra

9. Photometry and spectroscopy of transit events

Objective: To perform further observations of candidate transiting planets around other stars.

9.1. Photometric confirmation of exoplanet transits, including a disintegrating planet (Paper published; Output 17)

9.2. Spectroscopy of transits of EPIC225300403, with a candidate circumplanetary dusk disk

9.3. Spectroscopic vetting of TESS exoplanet candidates

RESEARCH OUTPUT

International journal articles. 2017 impact factor is shown in parentheses. Authors with Thai affiliations are indicated in bold type. An asterisk indicates the corresponding author. Numbers of reads and citations are from ResearchGate. **TOTAL: 1590 reads, 80 citations**.

Published

1. **P.-S. Mangeard, D. Ruffolo*, A. Sáiz, W. Nuntiyakul,** J. W. Bieber, J. Clem, P. Evenson, R. Pyle, M. L. Duldig, and J. E. Humble 2016, Dependence of the neutron monitor count rate and time delay distribution on the rigidity spectrum of primary cosmic rays, *J. Geophys. Res. Space Physics,* **121,** 11620 (2.752)

   Thai-US-Australian collaboration

   This work analyzed data from a ship-borne neutron monitor latitude survey to show that the leader fraction that we developed indeed provides information about the cosmic ray spectrum, representing a new capability in the 65-year history of neutron monitors. The work also presented a sea-level yield function for standard neutron monitors.

   165 reads, 12 citations
2. P. Subedi, **W. Sonsrettee,** P. Blasi, **D. Ruffolo,** W. H. Matthaeus*, D. Montgomery, P. Chuychai, P. Dmitruk, M. Wan, T. N. Parashar, and R. Chhiber 2017, Charged Particle Diffusion in Isotropic Random Magnetic Fields, *Astrophys. J.,* **837,** 140 (5.551)

   US-Thai-Italian-Argentinian-Chinese collaboration

   This work developed several new concepts of cosmic ray transport, which are relevant to transport in the Galaxy.

   110 reads, 5 citations
3. A. Shukurov, **A. P. Snodin,** A. Seta, P. J. Bushby, and T. S. Wood 2017, Cosmic Rays in Intermittent Fields, *Astrophys. J. Lett.,* **839,** L16 (6.634)

   UK-Thai collaboration

   114 reads, 3 citations
4. S. Abdollahi, et al. (including **W. Mitthumsiri**) 2017, Cosmic-ray electron-positron spectrum from 7 GeV to 2 TeV with the Fermi Large Area Telescope, *Phys. Rev. D,* **95,** 082007 (4.394)

   Multinational collaboration

   This presented an important measurement of the cosmic-ray electron+positron spectrum over a very wide energy range using a single instrument, and issue that is of fundamental interest and provides key information about cosmic ray transport in the Galaxy.

   91 reads, 42 citations
5. R. Chhiber, P. Subedi, A. V. Usmanov, W. H. Matthaeus*, **D. Ruffolo,** M. L. Goldstein, and T. N. Parashar, Cosmic Ray Diffusion Coefficients Throughout the Inner Heliosphere from Global Solar Wind Simulation, *Astrophys. J. Suppl.,* **230,** 21 (8.561)

US-Thai collaboration

This combined global plasma simulations of the solar wind, turbulence transport, and particle diffusion theory.

120 reads, 1 citation

6. A. F. Rappazzo*, W. H. Matthaeus, **D. Ruffolo,** M. Velli, and S. Servidio 2017, Coronal Heating Topology: The Interplay of Current Sheets and Magnetic Field Lines, *Astrophys. J.*, **844,** 87 (5.551)

   US-Thai-Italian collaboration

   61 reads, 2 citations

7. **S. Ek-In, K. Malakit*, D. Ruffolo,** M. A. Shay, and P. A. Cassak 2017, Effects of a Guide Field on the Larmor Electric Field and Upstream Electron Temperature Anisotropy in Collisionless Asymmetric Magnetic Reconnection, *Astrophys. J.*, **845,** 113 (5.551)

   Thai-US collaboration

   35 reads, 1 citation

8. **W. Mitthumsiri, A. Seripienlert, U. Tortermpun, P.-S. Mangeard, A. Sáiz, D. Ruffolo*, and R. Macatangay** 2017, Modeling polar-region atmospheric ionization induced by the giant solar storm on 20 January 2005, *J. Geophys. Res. Space Phys.,* **122,** 7946 (2.752)

   Thai collaboration

   This works toward addressing the question in Thai society of whether solar storms affect Earth's climate. While most research has focused on the effect of Galactic cosmic rays, we consider that the same physics should apply to solar energetic particles, which underwent a 50-fold increase in some parts of Antarctica. This work calculates the increase in atmospheric ionization, which can later be compared with the lack of new cloud formation at that time to possibly constrain mechanisms of cloud formation, and the possible radiation dosage that airline passengers could experience during a giant solar storm.

   78 reads

9. **U. Tortermpun, D. Ruffolo*,** and J. W. Bieber 2018, Galactic Cosmic Ray Anisotropy during the Forbush Decrease Starting 2013 April 13, *Astrophys. J. Lett.,* **852,** L26 (6.634)

   Thai-US collaboration

   72 reads, 1 citation

10. A. Seta*, A. Shukurov, T. S. Wood, P. J. Bushby, and **A. Snodin** 2018, Relative distribution of cosmic rays and magnetic fields, *Mon. Notices Royal Astron. Soc,* **473,** 4544 (5.194)

    UK-Thai collaboration

    79 reads, 5 citations

11. **P. Pongkitiwanichakul*,** K. D. Makwana, and **D. Ruffolo** 2018, Driving reconnection in sheared magnetic configurations with forced fluctuations, *Phys. Plasmas,* **45,** 022114 (1.941)

    Thai-Belgian collaboration

    25 reads, 1 citation

12. C. J. Clark, et al. (including **W. Mitthumsiri**) 2018, Einstein@Home discovers a radio-quiet gamma-ray millisecond pulsar, *Science Advances,* **4,** eaao7228 (11.51)

Multinational collaboration
134 reads, 3 citations

13. P.-S. Mangeard, J. Clem, P. Evenson, R. Pyle, **W. Mitthumsiri, D. Ruffolo*, A. Sáiz, and T. Nutaro** 2018, Distinct Pattern of Solar Modulation of Galactic Cosmic Rays above a High Geomagnetic Cutoff Rigidity, *Astrophys. J.,* **858,** 43 (5.551)

    US-Thai collaboration

    The Princess Sirindhorn Neutron Monitor (PSNM) at Doi Inthanon has, for the first time, studied the effect of an entire sunspot cycle (of ~11 years) on the flux of Galactic cosmic rays, a process that provides remote sensing of the entire heliosphere. PSNM is the neutron monitor (NM) with the world's highest geomagnetic threshold energy. We discovered a new pattern of such "solar modulation" than was found NMs by sensitive to cosmic rays of lower energy.

    87 reads, 1 citation

14. B. Bartoli, et al. (including **D. Ruffolo**) 2018, Galactic Cosmic Ray Anisotropy in the Northern Hemisphere from the ARGO-YBJ Experiment During 2008-2012, *Astrophys. J.,* **861,** 93 (5.551)

    Chinese-Italian-Thai collaboration
    60 reads, 1 citation

15. **A. C.-L. Chian,** J. R. Abalde*, R. A. Miranda, F. A. Borrotto, D. L. Hysell, E. L. Rempel, and **D. Ruffolo** 2018, Optical imaging of the spatiotemporal dynamics of ionospheric intermittent turbulence, *Sci. Rep.,* **8,** 10568 (4.122)

    Australian-Brazilian-Thai-Chilean-US collaboration
    149 reads, 1 citation

16. **W. Nuntiyakul, A. Sáiz*, D. Ruffolo, P.-S. Mangeard,** P. Evenson, J. W. Bieber, J. Clem, R. Pyle, M. L. Duldig, and J. E. Humble 2018, Bare Neutron Counter and Neutron Monitor Response to Cosmic Rays during a 1995 Latitude Survey, *J. Geophys. Res. Space Phys.,* **123,** 7181 (2.752)

    Thai-US-Australian collaboration
    131 reads

17. K. Colon, et al. (including **P. Pattarakijwanich, D. Ruffolo, S. Wannawichian**) 2018, A Large Ground-Based Observing Campaign of the Disintegrating Planet K2-22b, *Astronom. J.,* **156,** 227 (4.150)

    Multinational collaboration
    41 reads, 1 citation

18. C. C. Haggerty, M. A. Shay, A. Chasapis, T. D. Phan, J. F. Drake, **K. Malakit,** P. A. Cassak, and **R. Kieokaew** 2018, The Reduction of Magnetic Reconnection Outflow Jets to Sub-Alfvénic Speeds, *Phys. Plasmas,* **25,** 102120 (1.941)

    US-Thai collaboration
    20 reads

19. **S. Wannawichian* and A. Laphirattanakul**, Influence of plasma in the vicinity of Io on Brightness and Angular Extension of Io's Magnetic Footprint, *Chiang Mai Journal of Science,* **46,** 408 (0.437)

    Thai project

20. L. F. S. Rodrigues, **A. P. Snodin,** G. A. Sarson, and A. Shukurov, Fickian and non-Fickian diffusion of cosmic rays, accepted by *Mon. Not. R. Astron. Soc.,* **487,** 975 (5.194)

    UK-Thai collaboration

    12 reads

21. **A. Eungwanichayapant, W. Luangtip, W. Maithong, and D. Ruffolo,** X-rays from $e^{\pm}$ Pair Halos, accepted by *Astrophys. J.* (5.551)

    Thai collaboration

    6 reads

Submitted

22. J. W. Bieber, J. Clem, P. Evenson, A. Hallgren, J. Madsen, P.-S. Mangeard, **W. Nuntiyakul*,** R. Pyle, **D. Ruffolo, A. Sáiz,** and S. Tilav, Direct Determination of a Bare Neutron Counter Yield Function, submitted to *J. Geophys. Res. Space Phys.*

    US-Swedish-Thai collaboration

In Preparation

23. **Research Team on Space Plasma Physics and Cosmic Rays,** a popular book entitled "รังสีคอสมิก: ผจญภัยกับอนุภาคในอวกาศ"

Conference presentations. Presented by first author unless otherwise indicated. Authors working in Thailand are in bold type.

24. **D. J. Ruffolo, P. Tooprakai, A. Seripienlert, P. Chuychai, and** W. H. Matthaeus (presenter), Simulations of Lateral Transport and Dropout Structure of Energetic Particles from Impulsive Solar Flares (2016 Fall Meeting of the American Geophysical Union, San Francisco, December, 2016)
25. **S. Madlee, W. Mitthumsiri,** S. Digel, and **D. J. Ruffolo,** Gamma-ray Emission of the Earth's Upper Atmosphere in Geographical Coordinates with *Fermi*-LAT (2016 Fall Meeting of the American Geophysical Union, San Francisco, December, 2016)
26. P. A. Evenson, **P. Muangha, and D. J. Ruffolo,** GeV Solar Energetic Particle Observation and Search by IceTop from 2011 to 2016 (2016 Fall Meeting of the American Geophysical Union, San Francisco, December, 2016)
27. P.-S. Mangeard, J. Clem, P. Evenson, R. Pyle, **D. Ruffolo, A. Saiz, and T. Nutaro,** Cosmic ray modulation observed by the Princess Sirindhorn Neutron Monitor at high rigidity cutoff (2016 Fall Meeting of the American Geophysical Union, San Francisco, December, 2016)
28. P. Subedi, W. H. Matthaeus, **W. Sonsrettee, D. J. Ruffolo,** T. N. Parashar, P. Blasi, R. Chhiber, **P. Chuychai,** P. Dmitruk, M. Wan, and D. Montgomery, Charged Particle Diffusion in Isotropic

Random Magnetic Fields (2016 Fall Meeting of the American Geophysical Union, San Francisco, December, 2016)

29. **P. Tooprakai, D. Ruffolo** (presenter), **A. Seripienlert, P. Chuychai,** and W. H. Matthaeus, Simulations of Lateral Transport and Dropout Structure of Energetic Particles from Impulsive Solar Flares (International Cosmic Ray Conference 2017, Busan, South Korea, July, 2017)
30. **C. Banglieng, D. Ruffolo** (presenter), **A. Saiz,** P. Evenson, and **T. Nutaro,** Tracking cosmic-ray spectral variations with neutron monitor time-delay measurements at high cutoff rigidity during 2007-2017 (International Cosmic Ray Conference 2017, Busan, South Korea, July, 2017)
31. **A. Saiz, W. Mitthumsiri, D. Ruffolo,** P. Evenson, and **T. Nutaro,** Measurement of cross-counter leader fractions in an 18NM64: Detecting single and multiple atmospheric secondaries (International Cosmic Ray Conference 2017, Busan, South Korea, July, 2017)
32. P.-S. Mangeard, J. Clem, P. Evenson, R. Pyle, **W. Mitthumsiri, D. Ruffolo, A. Saiz, and T. Nutaro,** Cosmic Ray Modulation Observed by the Princess Sirindhorn Neutron Monitor at High Rigidity Cutoff (International Cosmic Ray Conference 2017, Busan, South Korea, July, 2017)
33. S. Suzuki, H. Sakurai, F. Tokanai, E. Inui, H. Shimizu, K. Masuda, **W. Mitthumsiri, D. Ruffolo, and R. Macatangay,** Observation of cosmogenic nuclide Be-7 concentrations in the air at Bangkok and trajectory analysis of global air-mass motion (International Cosmic Ray Conference 2017, Busan, South Korea, July, 2017)
34. The IceCube Collaboration (presented by P. Evenson), P.-S. Mangeard, **P. Muangha**, R. Pyle, **D. Ruffolo, and A. Sáiz,** GeV Solar Energetic Particle Observation and Search by IceTop from 2011 to 2016 (International Cosmic Ray Conference 2017, Busan, South Korea, July, 2017)
35. The IceCube Collaboration (presented by P. Evenson), P.-S. Mangeard, **P. Muangha**, R. Pyle, **D. Ruffolo, and A. Sáiz,** Impulsive Increase of Galactic Cosmic Ray Flux Observed by IceTop (International Cosmic Ray Conference 2017, Busan, South Korea, July, 2017)
36. **P. Muangha,** P. Evenson, P.-S. Mangeard, and the IceCube Collaboration, Ground Level Enhancements in Solar Energetic Particles Observed by IceTop during 2011 to 2016 (International Astronomical Union Symposium 335, Space Weather of the Heliosphere: Processes and Forecasts, Exeter, UK, July, 2017)
37. **D. Ruffolo,** Studies of cosmic rays using neutron monitors in Antarctica (4th SCAR Astronomy and Astrophysics from Antarctica Meeting, Chiang Mai, August, 2017)
38. **W. Nuntiyakul,** Analysis of Data from the 2009-10 Ship-Borne Bare Neutron Counter Latitude Survey (4th SCAR Astronomy and Astrophysics from Antarctica Meeting, Chiang Mai, August, 2017)

39. **W. Mitthumsiri,** Modeling polar-region atmospheric ionization induced by the giant solar storm on 20 January 2005 (4th SCAR Astronomy and Astrophysics from Antarctica Meeting, Chiang Mai, August, 2017)

40. G. Share, R. Murphy, P. Evenson, **D. Ruffolo, P. Pattarakijwanich,** and R. Pyle, Gamma-Ray and Neutron Monitor Observations of the 2017 September 10 Solar Eruptive Event (Solar Energetic Particles, Solar Modulation and Space Radiation: New Opportunities in the AMS Era #3, Washington, DC, April, 2018)

41. G. H. Share, R. J. Murphy, A. K. Tolbert, **P. Pattarakijwanich, D. J. Ruffolo,** P. A. Evenson, and R. Pyle, Gamma-Ray and Neutron Monitor Observations of the 2017 September 10 Solar Eruptive Event (Triennial Earth-Sun Summit, Leesburg, VA, May, 2018)

42. **C. Sriwunkum, T. Nutaro, and A. Saiz,** The comparative study of the radiation shielding of PbO–Li2O–B2O3 glass system by using FLUKA to XCOM and experimental data, *J. Phys: Conf. Ser.*, **1144**, 012135 (Siam Physics Congress, Phitsanulok, May, 2018)

43. **C. Mutuwong, T. Nutaro, and A. Saiz,** The comparative studies of gamma-ray shielding properties of the PbO–BaO–B 2 O 3 glass system by using FLUKA code to XCOM program and accessible experimental data, *J. Phys: Conf. Ser.*, **1144**, 012130 (Siam Physics Congress, Phitsanulok, May, 2018)

44. **C. Banglieng, D. Ruffolo**, **A. Sáiz,** P. Evenson, and **T. Nutaro,** Tracking cosmic-ray spectral variations with neutron monitor time-delay measurements (Siam Physics Congress, Phitsanulok, May, 2018)

45. **H. Janthaloet, C. Banglieng, D. Ruffolo**, **A. Sáiz, and P. Muangha,** Environmental Correction of Neutron Monitor Leader Fractions (Siam Physics Congress, Phitsanulok, May, 2018)

46. **W. Nuntiyakul,** J. Bieber, J. Clem, P. Evenson, T. Gaisser, A. Hallgren, J. Madsen, P.-S. Mangeard, R. Pyle, **D. Ruffolo, A. Sáiz,** S. Seunarine, S. Tilav, Solar Energetic Particle Spectra using Neutron Detectors at South Pole (POLAR 2018 Conference, Davos, Switzerland, June, 2018)

47. **S. Wannawichian,** J. T. Clarke, and J. D. Nichols, Angular Size of Io Magnetic Footprint's Main Alfvén Wing Spot: In Corresponding to Satellite's Locations (Magnetospheres of the Outer Planets Conference, Boulder, CO, USA, July, 2018)
48. **D. J. Ruffolo,** R. Chhiber (presenter), W H. Matthaeus, A. V. Usmanov, **P. Tooprakai, P. Chuychai,** and M. L. Goldstein, Field Line Trapping, Transport, and Random Walk in an Expanding Medium with Implications for SEP Transport (Oral presentation, 2018 Fall Meeting of the American Geophysical Union, Washington, DC, December, 2018)
49. **W. Sonsrettee, D. J. Ruffolo,** W. H. Matthaeus, **A. P. Snodin, P. Wongpan, P. Chuychai, P. Tooprakai,** S. Vyas, **J. Thueanmuenwai, S. Boonnum,** Magnetic Field Line Random Walk in

Arbitrarily Stretched Isotropic Turbulence (Oral presentation, 2018 Fall Meeting of the American Geophysical Union, Washington, DC, December, 2018)

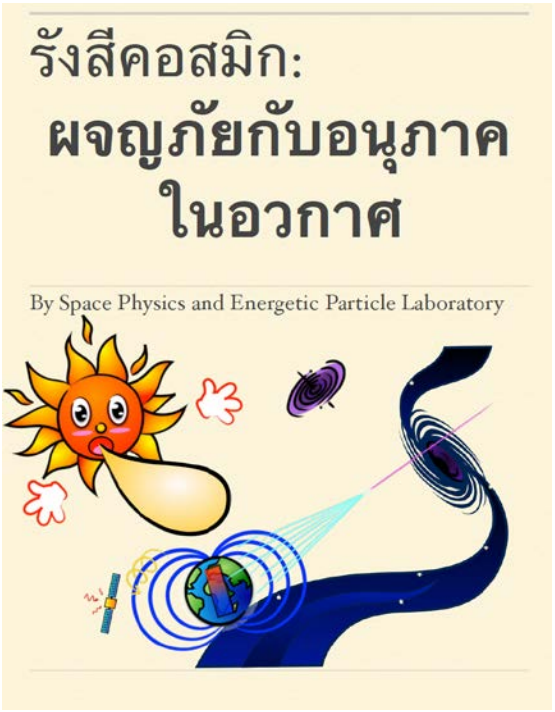
50. **P. Chuychai,** E. Engelbrecht, **D. J. Ruffolo,** Drift and Diffusion of Energetic Charged Particles in Nonaxisymmetric Two-Component Magnetic Turbulence with Nonuniform Large Scale Field (Poster presentation, 2018 Fall Meeting of the American Geophysical Union, Washington, DC, December, 2018)
51. **D. Ruffolo* and A. P. Snodin,** A simplified phase coherence index to characterize intermittent fluctuations (Siam Physics Congress, Hatyai, June, 2019)
52. **W. Sonsrettee*,** Empirical Model of Magnetic Field Line Spreading in Isotropic Turbulence with Zero Mean Field (Siam Physics Congress, Hatyai, June, 2019)
53. **P. Prapan*, K. Malakit, and D. Ruffolo,** A Data-Driven Simulation Study of Magnetic Reconnection at the Leading Edge of an Interplanetary Coronal Mass Ejection on 2005 January 21 (Siam Physics Congress, Hatyai, June, 2019)
54. **A. Pagwhan, W. Nuntiyakul*, and A. Sáiz,** Finding the response function of neutron monitors through FLUKA simulations: A case study of the Changvan neutron monitor (Siam Physics Congress, Hatyai, June, 2019)
55. **Y. Tangjai, W. Nuntiyakul*, D. Ruffolo, and C. Banglieng,** Water Vapor Correction to Cosmic Ray Flux Measurements with Neutron Counters at Doi Inthanon (Siam Physics Congress, Hatyai, June, 2019)
56. **C. Banglieng, P. Muangha, D. Ruffolo*, A. Sáiz, H. Janthaloet,** P. Evenson, T. Nutaro, P. Supnithi, and J. Budtho, Atmospheric water vapor correction to cosmic ray spectrum measurements from Princess Sirindhorn Neutron Monitor (Siam Physics Congress, Hatyai, June, 2019)
57. **H. Janthaloet, D. Ruffolo,** P.-S. Mangeard, and **A. Sáiz,** Can single secondary particles from cosmic rays explain the high counter multiplicity rate at the Princess Sirindhorn Neutron Monitor? (Siam Physics Congress, Hatyai, June, 2019)
58. **S. Ngamkhum* and K. Malakit,** Motion of charged particles around the region of magnetic reconnection: a test charge approach (Siam Physics Congress, Hatyai, June, 2019)
59. **S. Madlee, W. Mitthumsiri, D. Ruffolo,** S. Digel, and **W. Nuntiyakul,** Observations of the Earth's Gamma-ray Emission in Geographical Coordinates by *Fermi* LAT (Siam Physics Congress, Hatyai, June, 2019)
60. **G. Ihongo, D. Ruffolo, A. Sáiz, U. Tortermpun,** J. W. Bieber, and A. C.-L. Chian, Galactic Cosmic-Ray Anisotropy During Forbush Decreases: A Case Study of Six Forbush Decrease Events (Siam Physics Congress, Hatyai, June, 2019)
61. **C. Pleumpreedaporn and A. Snodin,** Pitch Angle Diffusion Coefficients in Test Particle Simulations and the Estimation of the Particle Parallel Mean Free Path (Siam Physics Congress, Hatyai, June, 2019)

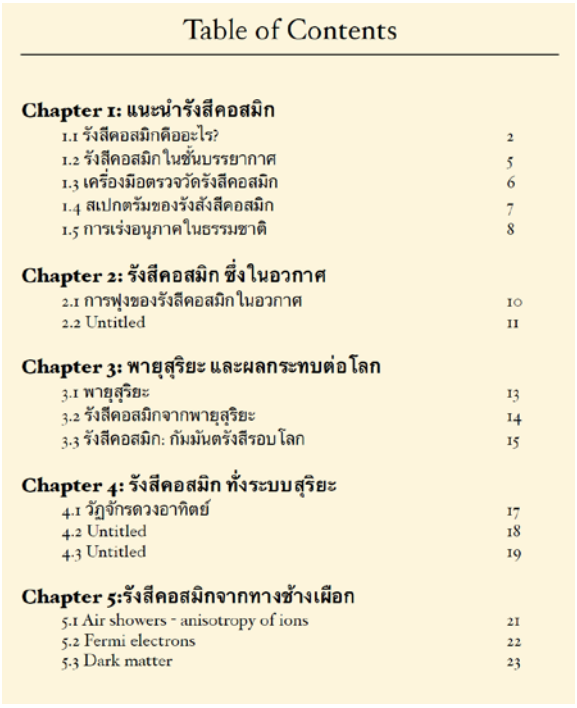
62. **C. Banglieng, H. Janthaloet, D. Ruffolo, A. Sáiz, W. Mitthumsiri,** P. Evenson, **T. Nutaro,** R. Pyle, S. Seunarine, and J. Madsen, Neutron monitor time–delay measurements to track cosmic ray spectral variation due to solar modulation at high and low cutoff rigidity (36th International Cosmic Ray Conference, Madison, WI, USA, July-August, 2019)
63. **W. Nuntiyakul, A. Sáiz, D. Ruffolo, P.-S. Mangeard,** P. Evenson, J. W. Bieber, J. Clem, R. Pyle, M. L. Duldig, and J. E. Humble, Bare neutron counter and neutron monitor response to cosmic rays during a 1995 latitude survey (36th International Cosmic Ray Conference, Madison, WI, USA, July-August, 2019)
64. **G. D. Ihongo, D. Ruffolo, A. Sáiz, U. Tortermpun,** J. W. Bieber, and A. C.-L. Chian, Galactic Cosmic-Ray Anisotropy During Forbush Decreases: Evidence for Diffusive Barriers and Large-Scale Flow (36th International Cosmic Ray Conference, Madison, WI, USA, July-August, 2019)
65. **A. Sáiz, W. Mitthumsiri, D. Ruffolo,** P. Evenson, and **T. Nutaro,** Detecting Single and Multiple Atmospheric Secondaries in an 18NM64 (36th International Cosmic Ray Conference, Madison, WI, USA, July-August, 2019)
66. **D. J. Ruffolo,** W. H. Matthaeus, C. DeForest, T. Parashar, M. L. Goldstein , D. A. Roberts, R. Chhiber, A. V. Usmanov, T. Dudok de Wit, R. Bandyopadhyay, A. Chasapis, B. Maruca, M. C. M. Velli, and J. C. Kasper, Flocculation, switchbacks, and loss of Alfvenicity: Indicators of shear-driven turbulence in the young solar wind? (2019 Fall Meeting of the American Geophysical Union, San Francisco, December, 2019)

RESEARCH IMPACT

1. Popular Thai-Language Book

We are drafting a Thai-language book entitled “รังสีคอสมิก: ผจญภัยกับอนุภาคในอวกาศ” (Cosmic Rays: Adventures of Particles in Space). The target group is teenagers or adults interested in science, with no particular background in physics. A draft of some pages is shown below. We will also express many of our research results in this book, in a manner that is accessible to a general audience.




Table of Contents

Chapter 1: แนะนำรังสีคอสมิก
1.1 รังสีคอสมิกคืออะไร? 2
1.2 รังสีคอสมิกในชั้นบรรยากาศ 5
1.3 เครื่องมือตรวจวัดรังสีคอสมิก 6
1.4 สเปกตรัมของรังสีคอสมิก 7
1.5 การเร่งอนุภาคในธรรมชาติ 8

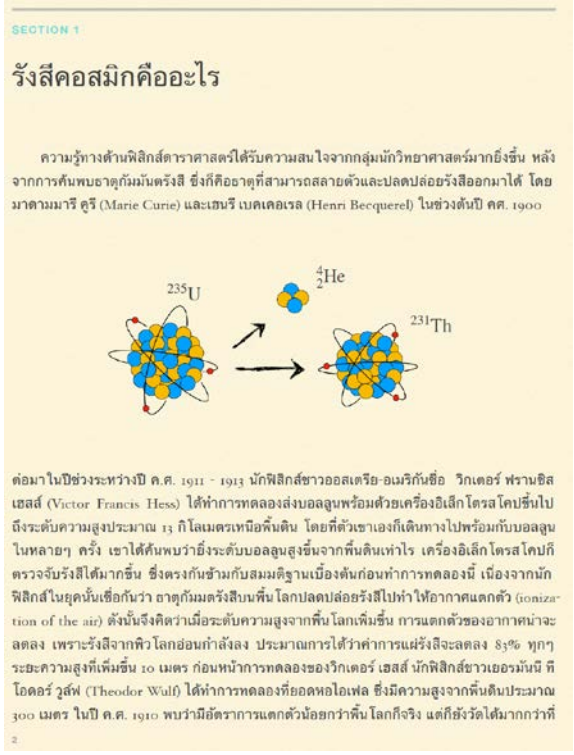
Chapter 2: รังสีคอสมิก ซึ่งในอวกาศ
2.1 การฟุ้งของรังสีคอสมิกในอวกาศ 10
2.2 Untitled 11

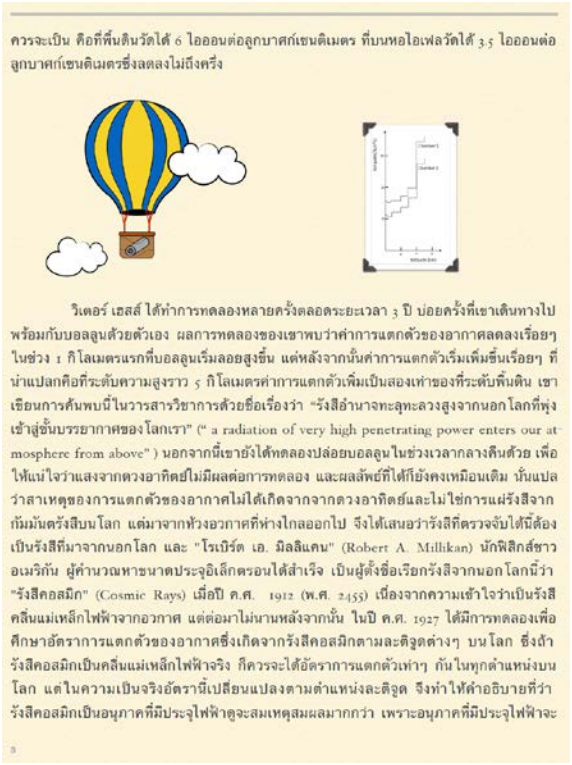
Chapter 3: พายุสุริยะ และผลกระทบต่อโลก
3.1 พายุสุริยะ 13
3.2 รังสีคอสมิกจากพายุสุริยะ 14
3.3 รังสีคอสมิก: กัมมันตรังสีรอบโลก 15

Chapter 4: รังสีคอสมิก ทั่งระบบสุริยะ
4.1 วัฏจักรดวงอาทิตย์ 17
4.2 Untitled 18
4.3 Untitled 19

Chapter 5:รังสีคอสมิกจากทางช้างเผือก
5.1 Air showers - anisotropy of ions 21
5.2 Fermi electrons 22
5.3 Dark matter 23







ควรจะเป็น คือที่พื้นดินวัดได้ 6 ไอออนต่อลูกบาศก์เซนติเมตร ที่บนหอไอเฟลวัดได้ 3.5 ไอออนต่อลูกบาศก์เซนติเมตรซึ่งลดลงไม่ถึงครึ่ง

วิเตอร์ เฮสส์ ได้ทำการทดลองหลายครั้งตลอดระยะเวลา 3 ปี บ่อยครั้งที่เขาเดินทางไปพร้อมกับบอลลูนด้วยตัวเอง ผลการทดลองของเขาพบว่าค่าการแตกตัวของอากาศลดลงเรื่อยๆ ในช่วง 1 กิโลเมตรแรกที่บอลลูนเริ่มลอยสูงขึ้น แต่หลังจากนั้นค่าการแตกตัวเริ่มเพิ่มขึ้นเรื่อยๆ ที่น่าแปลกคือที่ระดับความสูงราว 5 กิโลเมตรค่าการแตกตัวเพิ่มเป็นสองเท่าของที่ระดับพื้นดิน เขาเขียนการค้นพบนี้ในวารสารวิชาการด้วยชื่อเรื่องว่า "รังสีอำนาจทะลุทะลวงสูงจากนอกโลกที่พุ่งเข้าสู่ชั้นบรรยากาศของโลกเรา" (" a radiation of very high penetrating power enters our atmosphere from above") นอกจากนี้เขายังได้ทดลองปล่อยบอลลูนในช่วงเวลากลางคืนด้วย เพื่อให้แน่ใจว่าแสงจากดวงอาทิตย์ไม่มีผลต่อการทดลอง และผลลัพธ์ที่ได้ก็ยังคงเหมือนเดิม นั่นแปลว่าสาเหตุของการแตกตัวของอากาศไม่ได้เกิดจากจากดวงอาทิตย์และไม่ใช่การแผ่รังสีจากมันมันครั้งสิบนโลก แต่มาจากห้วงอวกาศที่ห่างไกลออกไป จึงได้เสนอว่ารังสีที่ตรวจจับได้นี้ต้องเป็นรังสีที่มาจากนอกโลก และ "โรเบิร์ต เอ. มิลลิแคน" (Robert A. Millikan) นักฟิสิกส์ชาวอเมริกัน ผู้คำนวณหาขนาดประจุอิเล็กตรอนได้สำเร็จ เป็นผู้ตั้งชื่อเรียกรังสีจากนอกโลกนี้ว่า "รังสีคอสมิก" (Cosmic Rays) เมื่อปี ค.ศ. 1912 (พ.ศ. 2455) เนื่องจากความเข้าใจว่าเป็นรังสีคล้ายแม่เหล็กไฟฟ้าจากอวกาศ แต่ต่อมาไม่นานหลังจากนั้น ในปี ค.ศ. 1927 ได้มีการทดลองเพื่อศึกษาอัตราการแตกตัวของอากาศซึ่งเกิดจากรังสีคอสมิกตามละติจูดต่างๆ บนโลก ซึ่งถ้ารังสีคอสมิกเป็นคลื่นแม่เหล็กไฟฟ้าจริง ก็ควรจะได้อัตราการแตกตัวเท่าๆ กันในทุกตำแหน่งบนโลก แต่ในความเป็นจริงอัตรานี้เปลี่ยนแปลงตามตำแหน่งละติจูด จึงทำให้คำอธิบายที่ว่ารังสีคอสมิกเป็นอนุภาคที่มีประจุไฟฟ้าดูจะสมเหตุสมผลมากกว่า เพราะอนุภาคที่มีประจุไฟฟ้าจะ



ได้รับอิทธิพลจากสนามแม่เหล็กของโลก ซึ่งมีค่าแตกต่างกันที่ละติจูดต่างๆ ซึ่งการค้นพบรังสีคอสมิกนี้ทำให้วิกเตอร์ เฮสส์ ได้รับรางวัลโนเบลสาขาฟิสิกส์ในปี ค.ศ. 1936 (พ.ศ. 2479)

ปี ค.ศ. 1949 นักฟิสิกส์นามอุโฆษ Enrico Fermi ก็ได้เสนอว่าซากหลงเหลือของการระเบิดซุปเปอร์โนวา (Supernova Remnant) สามารถประพฤติตัวเสมือนหนึ่งเป็นเครื่องเร่งอนุภาคก่อกำเนิดโปรตอนพลังงานสูงได้ เมื่อซากซุปเปอร์โนวาแผ่กระจายตัวออกเป็นรูปทรงกลมด้วยความเร็วสูง แรงของการแผ่กระจายจะไปดันอัตถุสุ่มแก๊สระหว่างดวงดาวทำให้มีคลื่นกระแทก (shock wave) เกิดขึ้นตรงผิวหน้าของทรงกลม และคลื่นกระแทกนี้ก็จะสร้างสนามแม่เหล็กของตัวเองขึ้นมา พอโปรตอนถูกกวาดหลุดเข้ามา (โปรตอนพวกนี้ก็ไม่ได้มาจากที่ไหนอื่นมันมาจากไฮโดรเจนเป็นองค์ประกอบหลักของแก๊สระหว่างดวงดาวนั่นเอง) พวกโปรตอนเหล่านั้นก็จะถูกกักอยู่ในสนามแม่เหล็กและโดนผลักไปข้างหน้าที่ข้างหลังที เด้งไปเด้งกลับเหมือนลูกปิงปอง พวกมันจึงสะสมความเร็วขึ้นเรื่อยๆ ตามเวลาที่มันถูกสนามแม่เหล็กของคลื่นกระแทกลากไป ในที่สุดความเร็วของโปรตอนก็จะมากพอจนเอาชนะหลุดออกมาจากสนามแม่เหล็กได้ (เร็วระดับเข้าใกล้ความเร็วแสง) นักวิทยาศาสตร์เชื่อว่านี่แหละคือโปรตอนพลังงานสูงที่อยู่ในรังสีคอสมิก

2. Communication to the Public by Mass Media

2.1. 2017 Outstanding Scientist Award

The Principal Investigator (PI) received the 2017 Outstanding Scientist Award during the course of this project. This was the first time in 30 years that a physicist received the award. There was extensive media coverage of this award. This allowed us to explain our research to the public. In addition, numerous speakers at these events, including the PI, explained the value of basic research and encouraged young Thais to pursue a career doing scientific research.



ถอดสูตรชีวิต..นักวิทย์ดีเด่น ปี 60
'ศ.พิเศษ ดร.เดวิด รูฟโฟโล'
เก่งระดับโลก..'ตกหลุมรักไทย!!'
ชีวิต
'คิด-วิเคราะห์' มากกว่า 'เดา'
" ต้องรู้สึกรู้จริง คาดเดาไม่ได้ "



2.2. Television Interviews

2.2.1. The PI was interviewed by Channel 3 Family (Channel 13) about a possible asteroid impact, solar storms, etc., August 5, 2016

2.2.2. The PI was interviewed by Channel 3 for the program "Chuai Kid Chuai Tam" about a new planetary system with 7 terrestrial planets, aired March 2-3, 2017

2.2.3. Kittipat Malakit and Maneenate Wechakama participated in a press conference at Thammasat University about a new planetary system with 7 terrestrial planets, March 10, 2017

2.2.4. The PI was interviewed by Channel 3 for the program "Chuai Kid Chuai Tam" about the total lunar eclipse, aired January 31, 2018

2.2.5. The PI, Warit Mittumsiri, Petchara Pattarakijwanich, and others organized a press conference at Mahidol University on the total lunar eclipse and new developments in astrophysics, January 31, 2018

2.2.6. All team members at Maihdol Univ. organized public viewing of total lunar eclipse at Mahidol Univ., January 31, 2018

2.2.6.1. TV interview for NBT, aired January 31, 2018

2.2.6.2. TV interview for Channel 3, aired February 1, 2018

2.2.7. The PI participated in a press conference about commemorations of the 150th anniversary of the Waghor total solar eclipse, on July 25, 2018

2.2.8. The PI was interviewed by Channel 3 for the program "Chuai Kid Chuai Tam" about another total lunar eclipse, aired July 27, 2018

2.2.9. The PI was interviewed by ThaiPBS about commemorations of the 150th anniversary of the Waghor total solar eclipse, on August 21, 2018

2.3. Other Events

2.3.1. Online video interview of the PI on Mahidol Channel about a new planetary system with 7 terrestrial planets, Feb. 28, 2017

2.3.2. Online podcast interview of the PI for WitCast, January 24, 2018

2.3.3. Radio interview of the PI about commemorations of the 150th anniversary of the Waghor total solar eclipse, on August 14-15, 2018

2.3.4. The PI was the key scientific organizer of a one-day set of lectures on solar eclipses, the Sun, and astrophysics, mostly for high school students, at Waghor, Prachuab Khiri Khan, in honor of the 150th anniversary of HM King Rama IV predicting and viewing a total solar eclipse there. The PI invited a retired NASA astronaut and former Associate Administrator to give two lectures over August 19 and 21, 2018. The PI also gave a lecture and invited three other prominent astrophysicists from Bangkok to speak at the event.

2.3.5. Online interview of the PI on Suthichai Live! (Facebook/suthichai.yoon) on September 8, 2018

2.3.6. Waraporn Nuntiyakul featured in a press conference at Chiang Mai University about the shipborne latitude survey cosmic ray detection project that she leads, on September 18, 2018. There were articles about this event in the Thai Rath, Daily News, Matichon, and Chiang Mai News newspapers.

3. Communication to the Public by Social Media

For some time we have already used a website, www.thaispaceweather.com, to share Thai-language information and also data from the Princess Sirindhorn Neutron Monitor at Doi Intanon. Now our group also has a Facebook page, "Thai Space Physics & Space Weather". In addition, one of our team members, has a Thai-language Facebook page for science, called "มณีมีเนิร์ด", which has 9,500 followers. Another team member, Waraporn Nuntiyakul, has an online blog about her cosmic ray studies and plans for Antarctic research.

4. Invited Lectures

The following were invited lectures in national or international conferences. In addition, we gave many more presentations at universities and schools.

4.1 D. J. Ruffolo, P. Tooprakai, A. Seripienlert, P. Chuychai, and W. H. Matthaeus (presenter), Simulations of Lateral Transport and Dropout Structure of Energetic Particles from Impulsive Solar Flares (2016 Fall Meeting of the American Geophysical Union, San Francisco, December, 2016). Note: David Ruffolo was invited to give this talk but was unable to attend, so he prepared the slides and the talk was delivered by William Matthaeus.

4.2 K. Malakit, Magnetic Reconnection (Lecturer, 3rd ASEAN School on Plasma and Nuclear Fusion, Bangkok, February, 2017)

4.3 D. Ruffolo, Simulations of Lateral Transport and Dropout Structure on Energetic Particles from Impulsive Solar Flares (Invited online lecture for Solar Probe Plus Theory Telecon, hosted by the Johns Hopkins University Applied Physics Laboratory, USA, February, 2017)

4.4 D. Ruffolo, Solar-Heliospheric Physics (Invited rapporteur talk to summarize 99 presentations about solar-heliospheric physics with cosmic rays, International Cosmic Ray Conference 2017, Busan, South Korea, July, 2017)

4.5 D. Ruffolo, Cosmic Rays (Honorable speaker to HRH Princess Sirindhorn and the 43rd Congress of Science and Technology in Thailand, Bangkok, October, 2017)

4.6 D. Ruffolo, Anisotropy of Cosmic Rays at ~10-100 GeV (Invited speaker, The International Conference on Science and Technology, Rajamangala University of Technology Thanyaburi, December, 2017)

4.7. D. Ruffolo, Anisotropy of Cosmic Rays at ~10-100 GeV (Invited speaker, 8th International Workshop on Cosmic Ray Detection at High Altitudes, Shianghai, China, December, 2017)

4.8. D. Ruffolo, Cosmic Electron and Positron Detection in Space (Invited speaker, 1st Thailand Space Exploration Fair, Bangkok, February, 2018)

4.9. D. Ruffolo, Field Line Random Walk and Energetic Particle Transport in Magnetic Turbulence (Invited speaker, 11th Latin American Conference on Space Geophysics, Buenos Aires, Argentina, April, 2018)

4.10. D. Ruffolo, Anisotropy of Cosmic Rays during the Forbush Decrease Starting 2013 April 13 (Invited speaker, 11th Latin American Conference on Space Geophysics, Buenos Aires, Argentina, April, 2018)

4.11. D. Ruffolo, Particle acceleration, diffusion, and shocks (Instructor for 4 lectures, CELFI Latin American School on Data Analysis and Simulations for Space Physics, Buenos Aires, Argentina, April, 2018)

4.12 D. Ruffolo, Monte Carlo simulations of energetic particle transport in space, in Earth's atmosphere, and in cosmic ray detectors (Plenary speaker, 22nd International Annual Symposium on Computational Science and Engineering, Bangkok, August, 2018)

4.13 D. Ruffolo, Acceleration or special activities for nurturing gifted minds (Plenary speaker, 15th Asia-Pacific Conference on Giftedness, Bangkok, August, 2018)

4.14 W. Nuntiyakul, Response Functions of Neutron Counters to Cosmic Rays from Latitude Survey Technique (Asian Forum for Polar Sciences, Xiamen, China, October, 2018)

4.15 D. Ruffolo, Studies of Cosmic Rays Using Neutron Monitors in Polar Regions (Invited Speaker, 44th Congress of Science and Technology in Thailand, Bangkok, October, 2018)

4.16 A. Sáiz, Cosmic ray and solar energetic particle flux and spectrum recorded by polar neutron monitors (Invited Speaker, 44th Congress of Science and Technology in Thailand, Bangkok, October, 2018)

4.17 W. Nuntiyakul, Latitude survey projects (Invited Speaker, 44th Congress of Science and Technology in Thailand, Bangkok, October, 2018)

4.18 K. Malakit, Plasmas in Space: An Introduction (5th ASEAN School on Plasma and Nuclear Fusion and SOKENDAI Winter School, Nakhon Pathom, January, 2019)

5. **Reviews:** We have made use of our expertise many times to serve as reviewers for international and national journals, for academic positions, etc.

6. **Development of Young Scientists**

In an attachment, we summarize the status of the 20 members of our research team, which aims to include all in Thailand who regularly perform research on Space Plasma Physics and Cosmic Rays. In addition, we have helped develop another 61 post-doctoral researchers, university students, and high school students, as detailed in the attached file.

7. **Collaboration within Thailand and Team Building Activities**

7.1. Within Thailand, the research team itself includes scientists who have worked at

Mahidol University
King Mongkut's University of Technology North Bangkok

Kasetsart University
Chandrakasem Rajabhat University
Chiang Mai University (CMU)
Thammasat University
Chulalongkorn University
Ubon Ratchathani University (UBU)
Panyapiwat Institute of Management
National Astronomical Research Institute of Thailand (NARIT)
Burapha University (BUU)

[Note that CMU, UBU, NARIT, and BUU are outside the Bangkok Metropolitan Region.] We have additional active collaboration with other institutions as follows:

King Mongkut's Institute of Technology Ladkrabang. Dr. Pornchai Supnithi has kindly let us use a dual-frequency GPS receiver to monitor atmospheric water vapor at PSNM on Doi Inthanon, and his Ph.D. students have helped to analyze those data.

Prince of Songkla University. Dr. Boonyarit Chatthong has Skyped into many of our weekly research meetings, and we have collaborated on a research project for his senior project student on particle diffusion in space plasmas with magnetic turbulence.

7.2. We have solidified this collaboration by means of numerous team building activities, many of which make use of support from the RTA grant, as follows:

7.2.1. We have two weekly meetings (one for Space Plasma Physics and the other for Cosmic Rays) that typically last 3 hours. Most of the collaboration members have frequently attended one (or both) of these meetings, either in person or by teleconference (from Chiang Mai, Chiang Rai, or Songkhla, and even from the US and Switzerland when members of our team were traveling for research or conferences). Outside the research meetings, most collaboration members also have frequent contact in person, by e-mail, or by Line. Therefore, such a researcher who needs advice can typically discuss their work with other team members within one week.

7.2.2. We have conducted an annual meeting in July called Thai Space Physics. Each time, the first scientific lecture was by a highlight speaker from the US, and oral talks were given by every team member except those who were traveling abroad and/or their students. This was very useful to provide scientific understanding of everyone's work.

7.2.3. Most of our research topics involve collaboration between multiple institutions in Thailand, which is an enriching experience for all concerned. We continued to develop new cooperative topics throughout the project.

7.2.4. In December, 2016, our team member Ronald Macatangay flew down from Chiang Mai, where he works at NARIT, to join with several researchers from Mahidol University (including a student) to visit Rajamangala University of Technology Thanyaburi and see their lightning detection system.

7.2.5. We began a new collaboration with Prince of Songkla University, for one of their students to perform senior project research with some guidance from the PI.

7.2.6. A team member, Suwicha Wannawichian, flew from Chiang Mai to Mahidol University in Bangkok in 2017 to give a seminar and discuss research under this project.

7.2.7. Two students from Chulalongkorn University worked on senior projects under the guidance of team member Warit Mitthumsiri at Mahidol University.

7.2.8. Several of our team members have been granted associate membership in the IceCube Collaboration, which allows us to potentially be co-authors of publications from our ongoing analyses of cosmic ray data from IceTop (the surface component of IceCube).

7.2.9. Another student from Prince of Songkla University performed a summer research project at Mahidol University under the supervision of the PI.

7.2.10. A student from Silpakorn University performed a summer research project in 2017 at Mahidol University under the supervision of the PI.

7.2.11. During September-November, 2017, Mahidol University supported a visit by Prof. Abraham Chian, who is affiliated with INPE & ITA in Brazil and the University of Adelaide in Australia. He gave 5 special lectures and 1 seminar, and we arranged several new collaborative projects with him and his collaborators in Brazil, Chile, and the US. One collaborative paper has already been published (Chian et al. 2018).

7.2.12. A new collaborative research project to analyze data from the MMS spacecraft to determine properties of turbulence was established with scientists in the US while the PI visited there in 2018. During the summer, we involved Thai undergraduate students from Mahidol Univ., Thammasat Univ., and Srinakarinwirot Univ.

7.2.13. Wirin Sonsrettee at Panyapiwat Inst. Man. helped supervise two senior projects of students at Chulalongkorn Univ., together with Paisan Tooprakai there.

7.2.14. An M.Sc. student from Mahidol Univ. is now working under the supervision of Kittipat Malakit at Thammasat Univ. to perform particle-in-cell (PIC) simulations of magnetic reconnection at the leading edge of a coronal mass ejection (CME), a project in collaboration Abraham Chian (Australia and Brazil) and Pablo Muñoz (Chile).

7.2.15. Two undergraduate students from Prince of Songkla Univ. worked with the PI to theoretically explore the phase coherence index during the summer of 2018.

7.2.16. In March, 2018, the PI traveled to Chiang Mai to explore collaboration with another research group at Chiang Mai Univ. and Japanese scientists to analyze data on plasma bubbles in Earth's ionosphere from an all-sky airglow camera in Chiang Mai.

7.2.17. An undergraduate student from Chiang Mai Univ. worked with the PI toward a vapor correction to PSNM data.

7.2.18. Team member Waraporn Nuntiyakul from Chiang Mai Univ. arranged support for an undergraduate student from Mahidol Univ. to join her in a visit to the US and supervised his Monte Carlo simulations regarding timing information from multiple PSNM counters.

7.2.19. An undergraduate student from Chiang Mai Univ. worked with Alejandro Sáiz at Mahidol Univ. to perform Monte Carlo simulations for a NM latitude survey.

7.2.20. Team member Suwicha Wannawichian of Chiang Mai Univ. hosted the NARIT COMputational Astrophysics and Cosmology (NARIT COMAC) Workshop 2018 during July 2-6, 2018 at Lotus Pangsuankaew Hotel in Chiang Mai. Some other team members from Bangkok and many other scientists attended this workshop.

7.2.21. An M.Sc. student from Chiang Mai Univ. visited team members at Mahidol Univ. for a week in January, 2019 to explore how to analyze muon detector data from Mawson, Antarctica as provided by our collaborator Marc Duldig in Australia.

7.2.22. Two undergraduate students from King Mongkut's Univ. of Tech. Thonburi worked with the PI to computationally explore the phase coherence index during the summer of 2019.

7.2.23. Two undergraduate students from Chiang Mai Univ. worked with the PI and Dr. Sáiz at Mahidol Univ. during the summer of 2019 to perform data analysis and Monte Carlo simulation regarding the Feb.-Mar. 2019 ship-borne neutron monitor survey from Antarctica to Shanghai.

8. International Collaboration

The research team maintains extensive contacts throughout the worldwide research community, including output with collaborators spanning six continents (not counting Antarctica, though we use data from cosmic ray detectors there), as follows:

North America

University of Delaware (USA). (Output 1-2, 5-7, 9, 13, 16, 18, 22, 24, 26-32, 34-36, 40-41, 44, 46, 48-49, 57, 60, 62-66) The Principal Investigator (PI) has made 17 extended (2-month) visits there since 1997, which are very important for the PI's continued scientific development. Several of us collaborate extensively with three different groups: 1) With Paul Evenson, John Clem, and Pierre-Simon Mangeard (who was a post-doc at Mahidol Univ. for 3 years, until recently) regarding neutron monitor data and Monte Carlo simulation of atmospheric secondary particles from cosmic rays, and their interactions in a detector. Paul typically visits Mahidol Univ. twice per year and more recently he visits Chiang Mai Univ. equally or more frequently. 2) With Bill Matthaeus and his research team regarding diffusion and patterning of magnetic field line and energetic particle trajectories, and evaluating turbulence properties from spacecraft data. 3) With Michael Shay, the Ph.D. advisor of Kittipat Malakit, regarding magnetic reconnection in space plasmas.

SLAC National Accelerator Laboratory (USA). (Output 4, 12, 25, 59) Warit Mitthumsiri collaborates with Elliott Bloom and Seth Digel on analyzing Fermi-LAT data, and his student Suttiwat Madlee has visited there.

NASA Goddard Space Flight Center (USA). (Output 5, 17, 48, 66) The PI collaborates with Melvyn Goldstein and Arcadi Usmanov. Petchara Pattarakijwanich and others in our team collaborated with Knicole Colón on an exoplanet study.

University of Wisconsin - River Falls (USA). (Output 22, 46, 62) Waraporn Nuntiyakul makes annual visits here to collaborate with two people: 1) Prof. James Madsen and 2) Dr. Surujhdeo Seunarine, regarding the IceCube Neutrino Observatory and neutron monitors, particularly for training and exchange of American and Thai undergraduate students.

University of California Los Angeles (USA). (Output 6, 66) The project head collaborated with Franco Rappazzo and Marco Velli on the field line random walk in magnetic loops in the solar corona and solar wind turbulence.

University of Maryland College Park (USA) (Output 40-41) Mahidol Univ. team members are collaborating with Gerry Share to compare neutron monitor data on solar energetic particles with data on solar gamma rays.

Harvard-Smithsonian Center for Astrophysics (USA). (Output 17) Petchara Pattarakijwanich and others in our team regularly collaborate with George Zhou on exoplanet studies, and an undergraduate student at Mahidol Univ. visited George Zhou during the summer of 2019.

Cornell University (USA). (Output 15) The PI has collaborated with David Hysell.

University of Chicago (USA). (Output 18) Several of us knew Colby Haggerty when he was a student of Michael Shay at U. Delaware, and Kittipat Malakit continues to collaborate with him after his move to U. Chicago.

West Virginia University (USA). (Output 18) Kittipat Malakit and the project head collaborate with Paul Cassak on magnetic reconnection.

Boston University (USA). (Output 47) Suwicha Wannawichian collaborates with Prof. John Clarke, on Jupiter's aurora using data from the Hubble Space Telescope

Princeton University (USA). Peera Pongkitiwanichakul and others in our team collaborate with Amitava Bhattacharjee, Will Fox, & Jaehong Park on high-energy-density plasma.

Massachusetts Institute of Technology (USA). Peera Pongkitiwanichakul collaborates with Dr. Nuno Gomes Loureiro on current sheet instability.

Los Alamos National Laboratory (USA). Peera Pongkitiwanichakul collaborates with Dr. Fan Guo on current sheet instability.

Europe

Newcastle University (UK). (Output 3, 10, 20) Andrew Snodin is collaborating with a number of people on various topics, e.g., (1) Kinematic and nonlinear dynamos (A. Shukurov, P. Bushby); (2) Subgrid modelling of cosmic rays (L. F. Rodrigues, G. Sarson, A. Shukurov, P. Bushby); and (3) Test particle simulations in dynamo generated fields (A. Seta, A. Shukurov, P. Bushby, T. Wood).

University of Leuven (Belgium). (Output 11) Peera Pongkitiwanichakul collaborates with Dr. Kirit Makwana on current sheet instability.

Osservatorio Astrofisico di Arcetri (Italy). (Output 2) The PI has collaborated with Prof. Pasquale Blasi on cosmic ray diffusion in our Galaxy.

University of Leicester (UK). (Output 47) Suwicha Wannawichian collaborates with Jonathan Nichols, on Jupiter's aurora using data from the Hubble Space Telescope and MHD modeling of Jupiter's magnetosphere

University of Bergen (Norway). Suwicha Wannawichian collaborates with Jone Peter Reistad, on Earth's aurora using observations from space.

Uppsala University (Sweden). Andrew Snodin is collaborating with Eniko Madarassy on modelling of Bose-Einstein condensates.

Universidad Autónoma de Madrid (Spain). Maneenate Wechakama collaborates with and visits Dr. Yago Ascarsibar on astroparticle physics and galaxy structure.

Leibniz-Insitut für Astrophysik Potsdam (Germany). Maneenate Wechakama collaborates with PD. Dr. Volker Müller on cosmology and Dr. Cecilia Scannapieco on numerical N-body simulation of galaxy formation. They have had exchange visits.

Australia

University of Tasmania (Australia). (Output 1, 16, 63) Various team members are collaborating with Profs. John Humble and Marc Duldig to analyze data from their American-Australian neutron monitor latitude survey, and at their suggestion we have submitted a proposal for the Thai team to operate Australian cosmic ray detectors in Antarctica with logistical from the Australian government. This has gotten our team involved with muon detector data for the first time, so we are actively discussing their analysis with Marc Duldig now.

University of Adelaide. (Output 15, 60, 64) The PI and Kittipat Malakit of our team have worked with Prof. Abraham Chian, especially when he visited our group during September-November, 2017, on various projects.

South America

Institute of Aeronautical Technology (ITA; Brazil). (Output 15, 60, 64) Prof. Abraham Chian is also affiliated here, and has arranged for us to collaborate with Dr. José Abalde and Dr. Erico Rempel on intermittent turbulence in the ionosphere.

University of Brasília (Brazil). (Output 15) The PI has also collaborated with Dr. Rodrigo Miranda on intermittent turbulence in the ionosphere, and they met in person at the COLAGE meeting in Argentina in 2018.

University of Buenos Aires (Argentina). (Output 2) When the PI visited this group at their invitation, he had collaborative discussions with Dr. Pablo Dmitruk and Dr. Pablo Mininni about performing computer simulations to determine properties of the turbulence.

Universidad de Concepción (Chile). (Output 15) The PI has also collaborated with Dr. Felix Borotto on intermittent turbulence in the ionosphere.

University of La Serena (Chile). Kittipat Malakit and the PI are collaborating with Dr. Pablo Muñoz on magnetic reconnection.

Asia

Institute of High Energy Physics (China). (Output 14) The PI collaborates with several people in the Particle Astrophysics section, led by Prof. Zhen Cao, to analyze data from the ARGO-YBJ air shower array and to prepare for the upcoming LHAASO air shower array.

Yamagata University (Japan). (Output 33) Prof. Hirohisa Sakurai visited our group at Mahidol Univ. and brought us air sampling equipment, which we have used in collaboration with him to measure ^{7}Be, an isotope produced by cosmic rays in the atmosphere, at Mahidol Univ. in Bangkok.

University of the Philippines. Ronald Macatangay collaborated with Dr. Gerry Bagtasa on numerical modeling and validation of lightning and thunderstorm activity.

Africa

Northwest University (South Africa). (Output 50) Until recently, we collaborated with the late Harm Moraal and his team, based on a joint experiment to operate their calibration neutron monitor at Doi Inthanon. We now collaborate with Eugene Engelbrecht on the diffusion of energetic particles in space.

9. Academic Impact

Among the 21 international journal articles that are already published, the maximum 2017 impact factor is 11.51 and the minimum are 1.941 and 0.437. **The mean impact factor of these articles is 4.870.**

According to ResearchGate, a social network for academic research, the international journal articles produced in this project have already received **1590 reads and 80 citations** from the worldwide community, indicating that our research output is rapidly making an academic impact.

OTHER ACTIVITIES

Other research grants received by team members

Thailand Research Fund (TRF)

- "Magnetospheric Plasma Controls over Jupiter's Auroral Emissions," 2 years from July, 2015 to June, 2017, TRF and Chiang Mai University, 600,000 baht. PI: Suwicha Wannawichian. Suwicha received salary support from that project and not from our RTA grant.
- "Study of Earth's γ-ray Emission with the Fermi Gamma-ray Space Telescope," 2 years from July, 2015 to June, 2017, 500,000 baht. PI: Warit Mitthumsiri. Warit received salary support from that project and not from our RTA grant.
- "Short-term variations of cosmic ray count rates with latitude, longitude, and time," 2 years from May, 2017 to April, 2019, 540,000 baht. PI: Waraporn Nuntiyakul. Since this grant started, Waraporn has received salary support from that project and not from our RTA grant.
- "Plasma Structures under Various Environments," 2 years from May, 2018 to April, 2020, 600,000 baht. PI: Peera Pongkitiwanichakul. Since this grant started, Peera has received salary support from that project and not from our RTA grant.
- "On the upstream plasma parameters that control magnetic reconnection," 2 years from May, 2018 to April, 2020, 600,000 baht. PI: Kittipat Malakit. Since this grant started, Kittipat has received salary support from that project and not from our RTA grant.

National Astronomical Research Institute of Thailand (NARIT)

- "Cosmic Rays, Atmospheric Ionization, and Clouds," 1 year from October, 2016 to September, 2017, for 356,000 baht, and renewed for 1 year from October, 2017 to September, 2018, for 302,600 baht. PI: David Ruffolo. NARIT invited our group to address society's concerns about whether the Sun plays a role in Earth's climate, mediated through solar effects on the Galactic cosmic ray flux. While there is some overlap in the science, that project and this one are largely complementary; the modest proposed budget will be spent mostly for the salaries of students and a young researcher. This does not include salary support for faculty members or funding for equipment.
- "Comparison of auroral phenomena on Earth and Jupiter," 1 year from October, 2016 to September, 2017, for 470,000 baht. PI: Suwicha Wannawichian. This does not include salary support for faculty members or funding for equipment. The grant mainly supports the salary and travel expenses for graduate students, who work as research assistants.
- "Study of influential factors on Jupiter's and Earth's auroral variability," 1 year from October, 2017 to September, 2018, for 399,500 baht. PI: Suwicha Wannawichian. That does not include salary support for faculty members or funding for equipment. The grant mainly supports the salary and travel expenses for graduate students, who work as research assistants.
- "Latitude Survey," 5 months from May 1, 2018 to September 30, 2018, for 100,000 baht. PI: Waraporn Nuntiyakul. That does not include salary support for faculty members or funding for equipment. The grant mainly supports hiring an electronics engineer.

- "Laying optimal foundation to Dark Matter science with Cherenkov Telescope Array (CTA)", 6 months from April, 2018 to September, 2018, for 400,000 baht. PI: Maneenate Wechakama. That does not include salary support for faculty members or funding for equipment. The grant mainly supports the travel expenses for researchers.
- "Earth's Radiation Environment," 1 year from October, 2018 to September, 2019, for 680,000 baht. PI: David Ruffolo. While there is some overlap in the science, that project and this one are largely complementary; the modest proposed budget will be spent mostly for the salaries of students and travel costs for NARIT administrators and staff as part of considering approval of further projects. This does not include salary support for faculty members or funding for equipment.
- "Exploring Cherenkov Telescope Array (CTA) Capability for Dark Matter Science", 1 year from October, 2018 to September, 2019, for 904,000 baht. PI: Maneenate Wechakama. That does not include salary support for faculty members or funding for equipment. The grant mainly supports a workshop, salary for a master student and the travel expenses for researchers.
- "Latitude survey to monitor cosmic rays along the voyage of an icebreaker ship between Shanghai, China to Zhongshan Station, Antarctica" ("การสำรวจตามแนวเส้นละติจูด เพื่อตรวจวัดรังสีคอสมิกตามแนวเส้นทางเดินเรือตัดน้ำแข็งจากเมืองเซี่ยงไฮ้ สาธารณรัฐประชาชนจีน ไปยังสถานี Zhongshan ทวีปแอนตาร์กติก"), 1 year from May 1, 2018 to April 30, 2019, for 1,100,000 baht. PI: Waraporn Nuntiyakul. That does not include salary support for faculty members or funding for equipment. The grant mainly supports travel for a conference, travel of an installation team from Chiang Mai University and the University of Delaware (USA) to Shanghai, hiring electricians and mechanical technicians, and transportation costs.

National Research Council of Thailand (NRCT)

- "Constraints on dark matter density profile in the Milky Way by synchrotron radiation and inverse Compton scattering," 1 year from October, 2017 to September, 2018, for 320,000 baht. PI: Maneenate Wechakama. That does not include salary support for faculty. The grant mainly supports equipment and the salary for graduate students, who work as research assistants.

Mahidol University

- "Investigating the Physics of High-Energy-Density Plasma by 3D Particle-in-Cell Simulations," 1 year from November, 2015 to October, 2016, from a Mahidol University Postdoctoral Fellowship, for 684,000 baht. PI: David Ruffolo. This supported our team member Peera Pongkitiwanichakul when he was a postdoctoral fellow at Mahidol University. He now works at Kasetsart University.
- "Galactic Cosmic Ray Anisotropy Associated with Forbush Decreases," 1 year from August, 2018 to July, 2019, from a Mahidol University Postdoctoral Fellowship, for 946,800 baht. PI: David Ruffolo. This supports a postdoctoral fellow from Nigeria, Dr. Grace Ihongo, to work at Mahidol Univ. with our group.

Chiang Mai University (CMU: University Income)

- "Latitude Survey Project," 1 year from June, 2018 to May 2019, for 300,000 baht. PI: Waraporn Nuntiyakul. That does not include salary support for faculty. The grant mainly supports hiring an electronics engineer and the transportation of two insulated containers from Japan to Chiang Mai.

US National Aeronautics and Space Administration (NASA)

- "Trapping, Transport and Dynamic Behavior of Magnetic Connectivity and Energetic Particles in the Inner Heliosphere: Implications for Solar Probe, Solar Orbiter and Heliospheric Prediction," NASA NNX15AB88G, 3 years from Nov. 1, 2014 to Oct. 31, 2017, for US $319,008. PI: William Matthaeus. This provides some support for David Ruffolo's annual research visits to U. Delaware, USA. It does not support any research performed in Thailand.

AGU PUBLICATIONS

JGR

Journal of Geophysical Research: Space Physics

RESEARCH ARTICLE

10.1002/2016JA023515

Dependence of the neutron monitor count rate and time delay distribution on the rigidity spectrum of primary cosmic rays

P.-S. Mangeard[1,2,3], D. Ruffolo[1], A. Sáiz[1], W. Nuntiyakul[1,4], J. W. Bieber[3], J. Clem[3], P. Evenson[3], R. Pyle[3], M. L. Duldig[5], and J. E. Humble[5]

[1]Department of Physics, Faculty of Science, Mahidol University, Bangkok, Thailand, [2]National Astronomical Research Institute of Thailand, Chiang Mai, Thailand, [3]Bartol Research Institute and Department of Physics and Astronomy, University of Delaware, Newark, Delaware, USA, [4]Faculty of Science, Chandrakasem Rajabhat University, Bangkok, Thailand, [5]School of Physical Sciences, University of Tasmania, Hobart, Tasmania, Australia

Key Points:
- For neutron monitor latitude surveys in 2000–2007 we analyzed the count rate and the leader fraction *L* from neutron time delay histograms
- We compared observations with Monte Carlo simulations of cosmic ray showers, including new yield functions for a sea-level neutron monitor
- The comparison confirms that observed changes in *L* reflect cosmic ray spectral variation with changing geomagnetic cutoff and sunspot cycle

Correspondence to:
D. Ruffolo,
david.ruf@mahidol.ac.th

Citation:
Mangeard, P.-S., D. Ruffolo, A. Sáiz, W. Nuntiyakul, J. W. Bieber, J. Clem, P. Evenson, R. Pyle, M. L. Duldig, and J. E. Humble (2016), Dependence of the neutron monitor count rate and time delay distribution on the rigidity spectrum of primary cosmic rays, *J. Geophys. Res. Space Physics*, *121*, 11,620–11,636, doi:10.1002/2016JA023515.

Received 24 SEP 2016
Accepted 16 NOV 2016
Accepted article online 22 NOV 2016
Published online 20 DEC 2016

©2016. American Geophysical Union. All Rights Reserved.

Abstract Neutron monitors are the premier instruments for precisely tracking time variations in the Galactic cosmic ray flux at GeV-range energies above the geomagnetic cutoff at the location of measurement. Recently, a new capability has been developed to record and analyze the neutron time delay distribution (related to neutron multiplicity) to infer variations in the cosmic ray spectrum as well. In particular, from time delay histograms we can determine the leader fraction *L*, defined as the fraction of neutrons that did not follow a previous neutron detection in the same tube from the same atmospheric secondary particle. Using data taken during 2000–2007 by a shipborne neutron monitor latitude survey, we observe a strong dependence of the count rate and *L* on the geomagnetic cutoff. We have modeled this dependence using Monte Carlo simulations of cosmic ray interactions in the atmosphere and in the neutron monitor. We present new yield functions for the count rate of a neutron monitor at sea level. The simulation results show a variation of *L* with geomagnetic cutoff as observed by the latitude survey, confirming that these changes in *L* can be attributed to changes in the cosmic ray spectrum arriving at Earth's atmosphere. We also observe a variation in *L* with time at a fixed cutoff, which reflects the evolution of the cosmic ray spectrum with the sunspot cycle, known as solar modulation.

1. Introduction

Neutron monitors (NMs) are ground-based detectors of secondary neutrons and other particles produced in atmospheric cascades from primary cosmic ray ions. NMs are sensitive to secondary particles that undergo nuclear interaction with a dense lead producer, inducing tertiary neutrons that are detected by proportional counters filled with BF_3 or ^{3}He gas. The count rate is the most widely used measurement from the NMs. Monitoring the count rate provides information about variations of the cosmic ray flux entering at the top of the atmosphere. Long-term variations (with the 11 year sunspot cycle and the 22 year solar magnetic cycle) and short-term variations (with the rotation period of the Sun or Earth and temporary Forbush decreases due to solar activity) have been intensively studied since the middle of the twentieth century with a worldwide NM network. The altitude and the geographic location of the detector affect the atmospheric structure and the geomagnetic field encountered by the primary particles. Combining the data from the different NMs requires a reliable characterization of the relationship, called the yield function, between the energy spectrum of the cosmic rays at the top of the atmosphere and the observed count rate. Data analysis as well as Monte Carlo simulations have often been used to provide estimates of the neutron monitor response function [*Clem and Dorman*, 2000; *Caballero-Lopez and Moraal*, 2012; *Mishev et al.*, 2013; *Nuntiyakul et al.*, 2014; *Maurin et al.*, 2015].

From 1994 to 2007, a shipborne neutron monitor with three BP-28 ($^{10}BF_3$) counter tubes which we call the mobile monitor (MM) was carried across a large range of geomagnetic cutoff rigidities to directly measure the response function and provided fruitful observations about the primary Galactic cosmic ray (GCR) spectrum [*Nuntiyakul et al.*, 2014]. Starting in 2000, thanks to special electronics, in addition to the count rate measurement, the MM was able to record histograms of the time delay between two consecutive counts in the same tube [*Bieber et al.*, 2004]. Such data are related to the multiplicity (number of counts per secondary particle) but provide additional information about variations in the cosmic ray spectrum [*Ruffolo et al.*, 2016]. So far, only a small portion of the latitude survey time delay data have been analyzed. From the multiple latitude

surveys, we now perform an analysis of the time delay histograms for varying geomagnetic cutoff rigidity by extracting a parameter introduced by *Ruffolo et al.* [2016], the leader fraction L, i.e., the fraction of counts that are not temporally associated with a previous count in the same neutron counter tube.

Section 2 presents analysis and results from the time delay histograms recorded during the latitude surveys of 2001–2007. In section 3, we detail a complete set of Monte Carlo simulations performed to model the count rate and the leader fraction L observed in the latitude survey data at varying cutoff rigidity. The comparison of observations with Monte Carlo results is discussed in sections 3.2 and 4.

2. Analysis of the Latitude Survey Data

The purpose of a latitude survey with a cosmic ray detector is to take data over a large range of cutoff rigidity in a short period of time. For each survey epoch, the derivative of the count rate as a function of cutoff rigidity, called the differential response function, is the NM yield function times the cosmic ray spectrum. Although the three-tube MM had a smaller size than most fixed NMs, there are clear advantages of using such an instrument to study the cosmic ray spectrum as opposed to using multiple fixed NM stations: (i) the single detector system requires no intercalibration; (ii) the geomagnetic field can be used as a continuous spectrometer; and (iii) a wide range of rigidity cutoffs can be covered, up to more than 16 GV. The only modern fixed station at such high cutoff, the Princess Sirindhorn Neutron Monitor station located in Thailand at a vertical cutoff of ~16.8 GV, began operating afterward, in August 2007.

The MM and its operation were described by *Nuntiyakul et al.* [2014], and so they are discussed only briefly in this article. The MM was composed of three proportional counter tubes of standard NM64 design [*Hatton and Carmichael*, 1964], in other words a 3NM64. The MM was installed inside an insulated container (called the TasVan) carried by one of the Polar Class icebreakers of the U.S. Coast Guard. As shown in Figure 1, a typical journey of the ship through the Pacific Ocean started from Seattle (USA) in November. The ship traveled to McMurdo Base in Antarctica during the austral summer and returned to Seattle in April. In the following, the "survey year" refers to the year in which the survey began.

2.1. Time Delay Distributions

For each of the three tubes, the electronics provided hourly time delay histograms with different time scales as presented in Figure 2. For more details about the experimental determination of the histograms, we refer to *Ruffolo et al.* [2016]; in particular, the present measurements used the 600 series electronics described there. The long time histogram presents an exponential tail representing the coincidence time delay distribution between two uncorrelated incoming secondary particles (SPs, mostly neutrons). The short time histogram, which is actually a zoom in the long time histogram, shows the nonexponential excess at short time delays that can be attributed to the time delays between neutrons produced in the same secondary particle interaction in the lead.

It has been shown by *Ruffolo et al.* [2016] that it is possible to extract a parameter from the time delay histograms, the leader fraction L, which is the statistically determined fraction of neutron counts that did not follow a related count due to the same primary cosmic ray. The L value is the inverse of the average multiplicity, i.e., the average number of counts produced by a secondary particle. Three methods can be used to estimate L from the time delays histograms [see *Ruffolo et al.*, 2016, section 3.1]. In the present work, we use the first method, in which L is determined by

$$L = \frac{1 - e^{-\alpha t_0}}{\alpha e^{\alpha t_d}} A \tag{1}$$

where α and A are the parameters from the long time histogram fitted to the function $\tilde{n}(t) = Ae^{-\alpha t}$, $t_0 = 142$ ms is the overflow time in the electronic system, and $t_d \sim 80$–90 μs is the electronic dead time in the circuit dedicated to the computation of the time delay histograms.

2.2. Data Selection

The full available data set was first cleaned using the redundancy of the three tubes and anomalous time periods were excluded as described in section 3 of *Nuntiyakul et al.* [2014]. As in that work, periods including Forbush decreases larger than 10% at the McMurdo NM were removed. In addition to this selection, we excluded from the analysis any period of time with at least one problematic neutron counter tube. The time delay distributions during survey year 2000 were recorded with an early version of the electronics. In order to

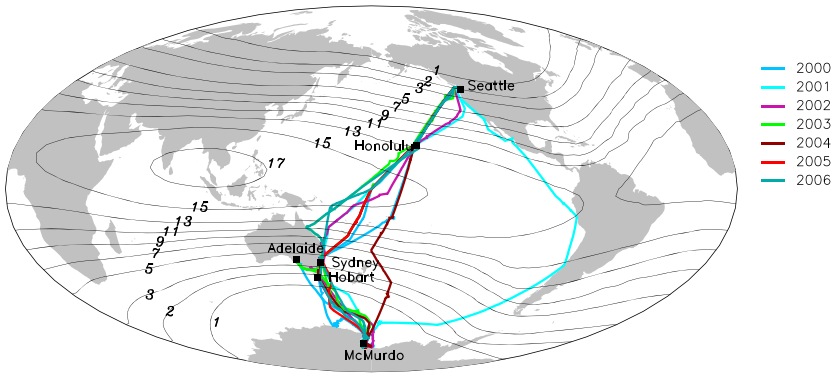


Figure 1. Tracks of the shipborne neutron monitor latitude surveys from 2000 to 2007, superimposed on contours of the vertical cutoff rigidity in GV. The year of a survey refers to the year in which it started.

avoid systematic effects from the firmware version, those data have also been excluded in the present analysis. Thus, only six surveys starting from 2001 have been used here.

The method described above requires sufficient statistics to properly fit a histogram and thus to extract the leader fraction from the time delay distribution. Due to the low count rate per tube at sea level, typically between 4 and 13 Hz, the histograms have been summed for every 3 h. We assume here that during a period of 3 h, the count rate as well as the rigidity cutoff are relatively constant. Then, for a given 3 h period at time t, the total leader fraction is computed as

$$L(t) = \sum_{i=1}^{3} f_i(t) L_i(t) \tag{2}$$

where $L_i(t)$ is the leader fraction of the ith tube as calculated from the time delay distribution and $f_i(t)$ is the contribution fraction of the ith tube to the total number of recorded time delays for the period t. Due to its central position in the 3NM64 configuration, the contribution of the middle tube, f_2, is larger than the individual contributions of the two edge tubes. Typical values were $f_1 \sim 0.32$, $f_2 \sim 0.36$, and $f_3 \sim 0.32$. Note that with this definition, L for the whole detector assesses the same information as each individual L_i, i.e., the ratio of the total number of leader counts by the total number of counts for the whole detector.

The geomagnetic rigidity cutoff R_c used in this analysis is the apparent cutoff presented by *Clem et al.* [1997], using the efficient calculation technique presented by *Bieber et al.* [1997]. For every location and time of data operations, nine incoming directions (the vertical one and eight directions with a zenith angle of 30°) are used to determine R_c. Thus, the anisotropy of the geomagnetic field and the east-west asymmetry at low latitude are taken into account.

2.3. Observational Results

For each of the six surveys, L is sorted per bin of R_c. Figure 3 presents the results. Each point shows the mean value of L for the corresponding bin, and the error bar corresponds to the standard error. For each survey year,

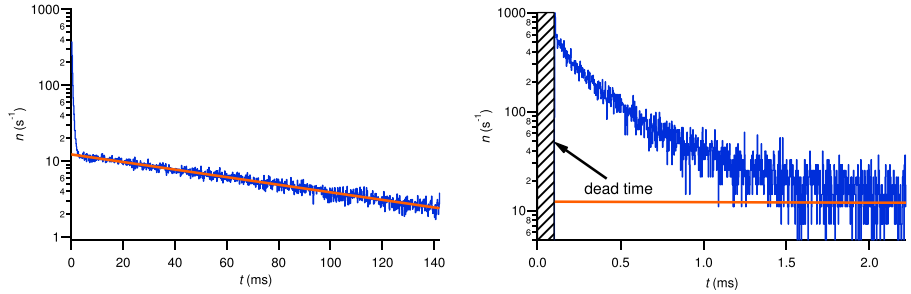


Figure 2. Distribution of the time delay between successive neutron counts at one counter tube recorded during one specific 3 h interval. (left) Long time delays show the exponential distribution typical of unrelated events, while (right) short time delays deviate substantially from the exponential function (red line). The electronic dead time is typically $t_d \sim 80 - 90\,\mu s$.

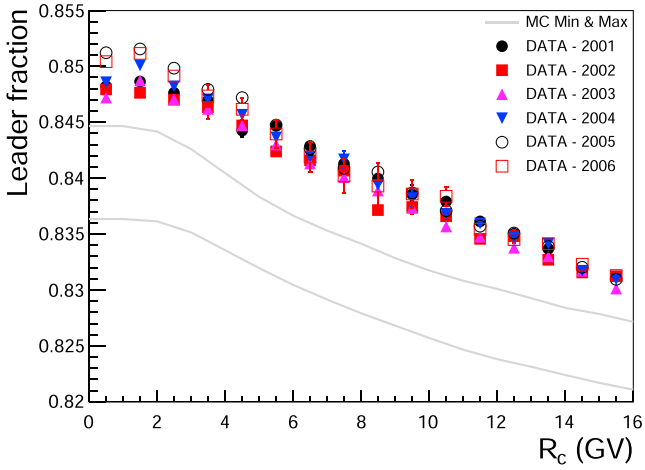


Figure 3. Dependence of the leader fraction L measured by the mobile neutron monitor on the apparent cutoff rigidity R_c for the six surveys operating with the same firmware, together with the range of Monte Carlo results for various cosmic ray spectra and atmospheric profiles. This confirms that the observed L is related to the rigidity spectrum of primary cosmic rays impinging on Earth's atmosphere. Note the overall dependence on time at a given R_c, which is clearest at low R_c, reflecting the variation of the cosmic ray spectrum with the sunspot cycle, known as solar modulation. Monte Carlo results reproduce those trends but slightly underestimate the absolute value of L.

a decrease from ~0.85 to ~0.83 is clearly visible when R_c increases within the available range. This observation confirms that L is related to the cosmic ray spectrum. The dependence of L on R_c is explained by the increased relative contribution of highly energetic primary particles (PPs) to the count rate at higher cutoff. A higher PP energy leads to a higher energy of the induced SPs and hence a higher multiplicity and lower leader fraction. Figure 3 also contains results from Monte Carlo simulations that will be discussed later in this paper.

The modulation due to changes in solar activity also impacts the value of L, as found by *Ruffolo et al.* [2016] for a fixed station. At low R_c, a variation up to ~0.004 is observed between the different surveys with a larger L for survey years 2005 and 2006, which correspond to a period of low solar activity, weaker solar modulation, and softer GCR spectra. Due to the lower modulation amplitude of the GCRs at high rigidity, this effect is smaller and cannot be clearly observed at high cutoff rigidity with the available data set.

The systematic decrease of L from the R_c range of 1 to 2 GV to the range of 0 to 1 GV could be related to a significant decrease of the atmospheric pressure near Antarctica, which is the location where the survey reached $R_c < 1$ GV. It is standard for NM count rates to be corrected for the effect of atmospheric pressure variations, which would otherwise dominate over cosmic ray flux variations. Similarly, the leader fraction at Doi Inthanon, Thailand, is corrected for a positive correlation with pressure variations [*Ruffolo et al.*, 2016]. However, in each case the pressure effect needs to be determined from a large data set with good statistics. In the present work, the statistics for L are insufficient to determine the pressure effect, so L has not been corrected for pressure variation. We can merely speculate that there could be a positive correlation between L and atmospheric pressure, as found at Doi Inthanon, because as the atmospheric depth seen by the primary particles is lower, the SP spectra are harder, and L decreases. This could account for the lower L value for R_c of 0 to 1 GV.

3. Monte Carlo Simulations

3.1. Methods

We performed Monte Carlo simulations using the software FLUKA 2011 [*Ferrari et al.*, 2005; *Bohlen et al.*, 2014] with the interaction model DPMJET-II.5 as recommended in the FLUKA manual. In this work we use the method presented in *Mangeard et al.* [2016], consisting of three stages: (i) interactions due to primary cosmic rays in the Earth's atmosphere are simulated and secondary particle fluxes are extracted at the altitude of the detector plus six meters, (ii) the sensitivity of the detector (including its surroundings) is determined for nine species of SPs, and (iii) both simulation outputs are combined to estimate the detector response to primary cosmic rays as well as the leader fraction.

3.1.1. Primary Cosmic Ray Spectrum

The simulated primary particles are protons (up to 1000 GeV) and alphas (up to 2000 GeV). Their distributions are assumed to be isotropic at the top of the Earth's atmosphere. Simulations are performed for different ranges of kinetic energies with the flux assumed to be uniform over kinetic energy within each range; the desired spectrum is implemented later by means of weighting. The transport through the atmosphere is determined without a geomagnetic field. Every SP produced by interactions in the atmosphere is linked to its PP. The SPs are selected postsimulation depending on the rigidity cutoff at the location of the detector.

Table 1. Characteristics of the Five Atmospheric Profiles

Name of Profile	McM	Hob	Sea4	Sea11	Hon
Location	McMurdo	Hobart	Seattle	Seattle	Honolulu
Latitude (deg)	77.86S	42.88S	47.59N	47.59N	21.3N
Longitude (deg)	166.65E	147.34E	122.34W	122.34W	157.87W
Period	Jan–Feb	Dec	Apr	Nov	Nov
R_c (GV)	0.1	1.71	1.73	1.73	12.6
Pressure P (mmHg)	745.3	756.8	760.4	763.8	761.5
Atmosphere depth D (g cm^{-2})	1013.0	1031.4	1035.8	1040.5	1039.8

The cosmic ray spectrum above the atmosphere is modeled postsimulation using weights according to the chosen model and solar activity. There is a systematic uncertainty from the choice of the local interstellar spectrum (LIS) of GCR protons. While the *Voyager 1* spacecraft has traveled beyond the heliopause, and its data [*Stone et al.*, 2013] can provide improved observational constraints on the LIS [*Bisschoff and Potgieter*, 2016; *Ghelfi et al.*, 2016], there are differing opinions as to whether Voyager 1 is directly measuring the LIS [e.g., *Scherer et al.*, 2011; *Zhang et al.*, 2015], and in this sense the LIS remains somewhat uncertain. To estimate the effect of the uncertain LIS, we employed a variety of LIS models for which the model dependence of the modulation parameter has been investigated by *Herbst et al.* [2010]. Effects from the GCR heliospheric modulation are determined with the widely used force field approximation of *Gleeson and Axford* [1968]. Despite some limitations exposed by *Caballero-Lopez and Moraal* [2004], the force field approximation allows a relatively good parameterization of the modulation with only one parameter (ϕ). This simplicity allows us to easily discuss the variations of the detector response with respect to the solar activity. The expression of the fluxes and of the modulation depends on the differentiating energy variable: the kinetic energy per nucleon T or the rigidity R. In the rest of this paper, this variable is indicated via a subscript. Let $\mathrm{LIS}_{T,i}$ be the LIS in terms of T, i.e., $\mathrm{d}N_i/\mathrm{d}T$, where N_i refers to the number of PP of type i (proton or alpha) per unit area, unit time, and unit solid angle at the edge of the heliosphere. The primary cosmic ray spectrum above the Earth's atmosphere can be expressed as a function of T and ϕ:

$$G_{T,i}(T,\phi) = \mathrm{LIS}_{T,i}(T+\Phi_i)\frac{T(T+2E_r)}{(T+\Phi_i)(T+\Phi_i+2E_r)}, \tag{3}$$

where $E_r = 938$ MeV/nucleon, $\Phi_i = (eZ_i/A_i)\phi$, and Z_i and A_i are the charge and the atomic number of the PP, respectively. If we express the flux in terms of R, the modulation relation becomes a function of R and ϕ:

$$G_{R,i}(R,\phi) = \frac{R^2}{(R+\phi)^2}\mathrm{LIS}_{R,i}(R+\phi). \tag{4}$$

Note here that ϕ can vary from a few hundred to more than a thousand MV during a solar cycle. As discussed by *Herbst et al.* [2010], the value of the modulation parameter ϕ actually depends significantly on the chosen LIS. *Herbst et al.* [2010] also determined linear relations between the modulation parameters for four different LISs with respect to the parameter ϕ_{US05} determined by *Usoskin et al.* [2005]. We use those relations for the parameter ϕ_{US11} (an updated version of ϕ_{US05} by *Usoskin et al.* [2011]). In this way, we tested five different LISs, each with an appropriate time-dependent modulation parameter derived from ϕ_{US11}. During the period of interest, ϕ_{US11} varied roughly from 350 to 1000 MV, so those two values are used in the simulation as boundaries for the solar activity during the latitude survey period (the peak $\phi_{\mathrm{US11}} > 1200$ MV in November 2003 occurred in the recovery period from a large Forbush decrease of 28 October 2003, which is removed from this analysis). In addition to those models, direct measurements of the proton and alpha spectra from the Payload for Antimatter Matter Exploration and Light-nuclei Astrophysics (PAMELA) satellite are also used. The proton spectrum combined data measured for the period of 13 November to 4 December 2006 [*Adriani et al.*, 2013] up to a break energy $E_{k,b} \sim 48.62$ GeV, and data from the period 2006–2008 [*Adriani et al.*, 2011] at higher energy, assuming a negligible solar modulation above $E_{k,b}$. We lowered the latter spectrum by 3.2% according to the footnote of *Adriani et al.* [2013]. The He spectrum comes only from the measurements of *Adriani et al.* [2011].

A significant fraction of the NM count rate is due to cosmic nuclei heavier than He impinging on the top of the atmosphere. Their contribution is simulated by applying the appropriate factor F_{hn} to the flux of alphas.

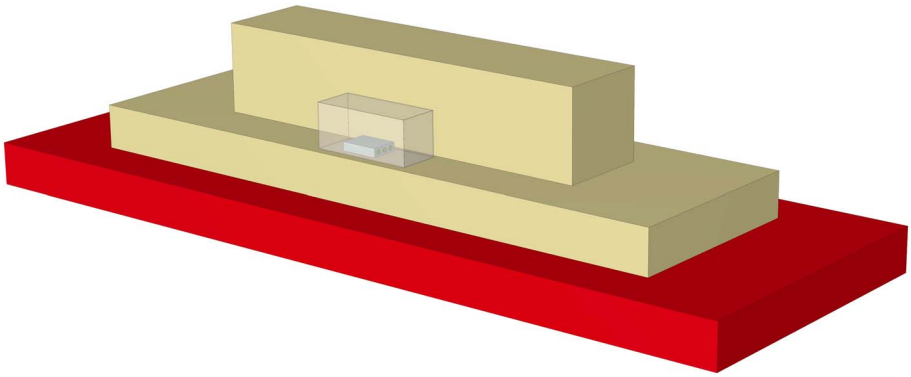


Figure 4. Model geometry for Monte Carlo simulation of the mobile neutron monitor in a shipping container on board a ship.

In the case of the LIS models, expressed in terms of kinetic energy per nucleon in *Herbst et al.* [2010], the overall ratio of nucleons in nuclei with $Z \geq 2$ (modeled as α particles) to protons is set to 0.3 following *Usoskin et al.* [2011]. In the case of the spectra from PAMELA for which the flux of alphas is measured, nuclei heavier than alphas at a given kinetic energy per nucleon are assumed to contribute a fraction $F = 0.354$ of the nucleons from cosmic rays heavier than protons, so we multiplied the PAMELA He spectrum in terms of kinetic energy per nucleon by the factor $F_{hn} = 1/(1 - F) = 1.548$ [*Caballero-Lopez and Moraal*, 2012].

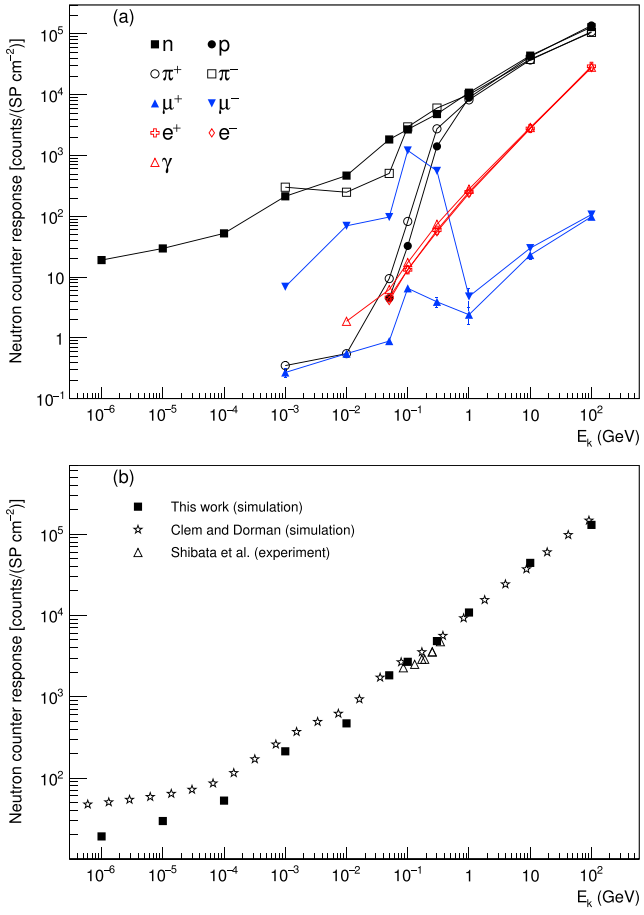


Figure 5. (a) Simulated response of the middle neutron counter tube as function of the secondary particle (SP) kinetic energy for various SP species at vertical incidence. (b) Comparison of the simulated neutron counter response to secondary neutrons from the present work and from *Clem and Dorman* [2000] along with experimental data from *Shibata et al.* [1997, 1999].

Table 2. Percentage Contributions of Various Cosmic Ray Shower Components to the MM Count Rates in Monte Carlo Simulations

Secondary Particle	Contribution (%)
$n, E_k < 10$ MeV	1.74(1)
n, 10 MeV $\leq E_k < 1$ GeV	79.6(5)
$n, E_k \geq 1$ GeV	8.1(1)
p	5.93(8)
μ^-	3.01(2)
μ^+	0.614(3)
γ	0.563(3)
e^-	0.153(1)
e^+	0.144(1)
π^-	0.128(8)
π^+	0.088(6)

3.1.2. Atmospheric Model

The atmospheric models we use represent typical profiles in temperature, pressure, and composition of the air with respect to altitude at the location of interest. The detailed calculation of the profiles used in this work is explained in the appendix of *Mangeard et al.* [2016]. The profiles combine information from the Global Data Assimilation System (https://ready.arl.noaa.gov/gdas1.php) at altitude up to ~26 km and the Naval Research Laboratory Mass Spectrometer, Incoherent Scatter Radar Extended model (NRLMSISE-00) [*Picone et al.*, 2002] at higher altitude. The simulation of the cascade development stops at an altitude of 6 m above the altitude of the detector. In the FLUKA simulation, the first 6 m over the detector are modeled by a fully absorbant (*blackhole*) material. Particles entering this layer are recorded as SPs along with their characteristics and those of their parent PP. Simulations of the cosmic ray interactions in the air were performed separately for five atmospheric models according to the typical journey of the ship: Seattle (Sea11) and Honolulu (Hon) in November, Hobart (Hob) in December, McMurdo (McM) in January and February, and Seattle (Sea4) in April. Their main characteristics are presented in Table 1. For each simulation, about 48 million (SP, PP) pairs were recorded.

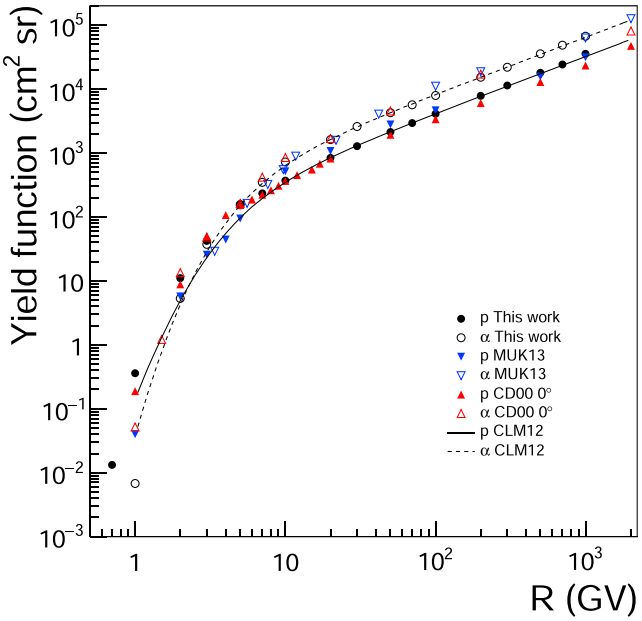


Figure 6. Simulated yield functions of the MM for primary cosmic ray p and α using the Sea4 atmospheric profile (P =760.4 mmHg and D =1035.8 g cm^{-2}) from the present work and previous results (scaled to three neutron counters) from *Mishev et al.* [2013] (MUK13) and from *Clem and Dorman* [2000] (CD00; vertical incidence only). The empirical yield functions from *Caballero-Lopez and Moraal* [2012] are presented for comparison.

Table 3. Proton Yield Functions of a Standard 3NM64 at Sea Level for Various Electronic Dead Times

		Counts Per Primary Flux (cm^2 sr)				
		Dead Time				
R (GV)	E_k/Nucleon (GeV)	0 s	20 μs	100 μs	1.2 ms	4 ms
0.5	0.1249	—	—	—	—	—
0.7	0.2324	1.34*e*−2	1.33*e*−2	1.30*e*−2	1.19*e*−2	1.18*e*−2
1	0.4331	3.65*e*−1	3.62*e*−1	3.52*e*−1	3.20*e*−1	3.18*e*−1
2	1.271	1.12*e*+1	1.10*e*+1	1.07*e*+1	9.60*e*+0	9.51*e*+0
3	2.205	4.26*e*+1	4.21*e*+1	4.06*e*+1	3.61*e*+1	3.57*e*+1
5	4.149	1.61*e*+2	1.59*e*+2	1.52*e*+2	1.33*e*+2	1.31*e*+2
7	6.125	2.38*e*+2	2.34*e*+2	2.24*e*+2	1.94*e*+2	1.91*e*+2
10	9.106	3.78*e*+2	3.72*e*+2	3.54*e*+2	3.05*e*+2	3.01*e*+2
20	19.08	8.59*e*+2	8.43*e*+2	7.99*e*+2	6.81*e*+2	6.71*e*+2
30	29.08	1.31*e*+3	1.28*e*+3	1.21*e*+3	1.03*e*+3	1.01*e*+3
50	49.07	2.18*e*+3	2.14*e*+3	2.01*e*+3	1.70*e*+3	1.67*e*+3
70	69.07	3.04*e*+3	2.97*e*+3	2.79*e*+3	2.34*e*+3	2.30*e*+3
100	99.07	4.23*e*+3	4.13*e*+3	3.87*e*+3	3.24*e*+3	3.19*e*+3
200	199.1	8.06*e*+3	7.83*e*+3	7.30*e*+3	6.06*e*+3	5.95*e*+3
300	299.1	1.18*e*+4	1.14*e*+4	1.06*e*+4	8.76*e*+3	8.59*e*+3
500	499.1	1.86*e*+4	1.80*e*+4	1.67*e*+4	1.38*e*+4	1.35*e*+4
700	699.1	2.53*e*+4	2.44*e*+4	2.26*e*+4	1.85*e*+4	1.81*e*+4
1000	999.1	3.73*e*+4	3.58*e*+4	3.30*e*+4	2.68*e*+4	2.62*e*+4

3.1.3. MM Response to Secondary Particles

The response of the MM to the SPs was estimated with a separate simulation. The geometry of the surroundings has been included inside the FLUKA geometry editor. The ship has been simulated as three hollow boxes (three decks) of stainless steel (thickness of 2 cm) as well as the shipping container as a smaller hollow box (thickness of 2.54 cm) as presented in Figure 4. The geometry reflects the actual placement of the shipping container on an upper deck to the side of the superstructure. The air composition is defined as that in the first layer of the atmospheric simulation, and the pressure chosen is the one from the McMurdo profile. As shown by *Clem and Dorman* [2000], the contribution of nonvertical SPs must be taken into account in the Monte Carlo simulation. Moreover, the position of the detector on board and the structure of the ship is not invariant with the incident azimuthal angle of the secondary particle. Following the method from *Mangeard et al.* [2016], many sets of simulations have been performed depending on the type of particle, the kinetic energy, and the incident direction with five zenith angles θ (0°, 15°, 30°, 50°, and 70°) and eight azimuthal angles φ (from 0° to 315°). The beam is centered and located at 6 m over the MM with a rectangular area of 100 m^2 for vertical incidence. The area is expanded depending on the incidence angle in order for the beam to cover the detector well [*Aiemsa-ad et al.*, 2015]. An electronic dead time of 28.4 μs has been used for the middle tube and 19.4 μs for the edge tubes, according to the experimentally determined dead times.

The determination of the leader fraction from the simulation results is simpler than the determination from the data for three reasons: (i) the absence of chance coincidences, (ii) the capability to identify each count with a specific simulated secondary particle, and (iii) the knowledge of the time of the boron disintegration. The dead time of the time delay electronics (known for each tube thanks to the time delay histograms) is then imposed. As reported in *Ruffolo et al.* [2016], the dead time in the time delay electronics is about ~62 μs larger than the dead time in the count rate electronics. A value of 90.4 μs is used for the middle tube and 81.4 μs for the edge tubes. The leader fraction is then determined as the ratio of the number of SPs giving at least one count to the total number of counts.

3.2. Monte Carlo Results

3.2.1. Count Rate as Related to Secondary Particles

Figure 5a presents the number of boron disintegrations (counts) in the middle counter tube of the 3NM64 per beam luminosity (SP cm^{-2}), i.e., the counter response, for beams of vertically incident SPs of various types. The response generally increases with increasing energy. Above 1 GeV, the detection efficiencies of hadronic,

Table 4. Alpha Particle Yield Functions of a Standard 3NM64 at Sea Level for Various Electronic Dead Times

		Counts Per Primary Flux (cm^2 sr)				
		Dead Time				
R (GV)	E_k/nucleon (GeV)	0 s	20 μs	100 μs	1.2 ms	4 ms
0.5	0.0327	—	—	—	—	—
0.7	0.0632	—	—	—	—	—
1	0.1249	6.80*e*−3	6.75*e*−3	6.59*e*−3	6.09*e*−3	6.05*e*−3
2	0.4331	5.37*e*+0	5.32*e*+0	5.17*e*+0	4.69*e*+0	4.65*e*+0
3	0.8311	3.76*e*+1	3.72*e*+1	3.60*e*+1	3.22*e*+1	3.19*e*+1
5	1.732	1.57*e*+2	1.56*e*+2	1.50*e*+2	1.32*e*+2	1.31*e*+2
7	2.685	3.54*e*+2	3.49*e*+2	3.35*e*+2	2.94*e*+2	2.90*e*+2
10	4.149	7.39*e*+2	7.29*e*+2	6.96*e*+2	6.04*e*+2	5.96*e*+2
20	9.106	1.66*e*+3	1.64*e*+3	1.56*e*+3	1.34*e*+3	1.32*e*+3
30	14.09	2.64*e*+3	2.59*e*+3	2.46*e*+3	2.10*e*+3	2.07*e*+3
50	24.08	4.35*e*+3	4.26*e*+3	4.04*e*+3	3.43*e*+3	3.38*e*+3
70	34.07	5.78*e*+3	5.67*e*+3	5.36*e*+3	4.55*e*+3	4.47*e*+3
100	49.07	8.15*e*+3	7.98*e*+3	7.52*e*+3	6.35*e*+3	6.25*e*+3
200	99.07	1.57*e*+4	1.53*e*+4	1.44*e*+4	1.21*e*+4	1.18*e*+4
300	149.1	2.28*e*+4	2.22*e*+4	2.08*e*+4	1.73*e*+4	1.70*e*+4
500	249.1	3.70*e*+4	3.59*e*+4	3.35*e*+4	2.78*e*+4	2.73*e*+4
700	349.1	5.03*e*+4	4.88*e*+4	4.54*e*+4	3.76*e*+4	3.68*e*+4
1000	499.1	7.01*e*+4	6.78*e*+4	6.29*e*+4	5.18*e*+4	5.07*e*+4

electromagnetic and muonic SPs are clearly separated. The hadronic SPs are the most efficient in producing counts. The response to protons and π^+ drops strongly below ~200 MeV, but the response to neutrons and π^- remains strong due to the greater possibility of binding with and disrupting a lead nucleus to produce neutrons that result in counts. The response to electromagnetic SPs increases by about 4 orders of magnitude from 10–100 MeV to 100 GeV but remains significantly lower than that of hadronic SPs. Note that the photonuclear resonance in the lead (~10–15 MeV) is not present in the plot and the simple line between 10 MeV and 50 MeV is not a proper estimation of the response to photons in the resonant energy range. We estimate that neglecting this resonance in the present work affects the count rate by ~1%. The response to μ^+ is about 3 orders of magnitude lower than that for neutrons. Above 1 GeV, the efficiency of μ^- is similar to that for μ^+, but below this energy, μ^- are much more efficient in producing counts. Due to its negative charge and small Bohr radius, a μ^- is likely to be bound to and absorbed by a lead nucleus that then deexcites by emitting neutrons that can enhance the count rate.

The contributions of the nine species of SPs to the total count rate are presented in Table 2. Percentages were determined using the atmosphere model "Sea4" at sea level for the case of PAMELA spectra and no geomagnetic cutoff. About 89.4% of the counts are produced by neutrons, mostly between 10 MeV and 1 GeV. However, about 10% of the count rate is due to the other SPs. Protons make the second largest contribution, 6%. Muons at sea level mostly have an energy between 1 and 100 GeV, where the detection efficiency is very low, so their contribution to the count rate remains low, ~3.6% (mostly μ^- with E_k<10 GeV). The electromagnetic component of the atmospheric shower at sea level is mainly at energies lower than 1 GeV, where the detector sensitivity is very low. Thus, the contributions of γ and $e^{\pm}$ to the count rate are minor. Despite the high sensitivity of the detector to pions, those SPs provide only a minor contribution to the total count rate due to their low fluxes at sea level. This is why the detector is called a *neutron monitor*.

We compared our simulation results with previous FLUKA work by *Clem and Dorman* [2000] and with experimental determination of efficiency of the NM64 by *Shibata et al.* [1997, 1999] (Figure 5b). The experimental results were obtained using neutron beams impacting about half of a 1NM64 detector. This includes more reflector than in our simulation of a 3NM64. All results were normalized to a 3NM64 middle tube response using the coefficients from *Mangeard et al.* [2016]. We observe a good agreement between the two simulations above 50 MeV where most of the counts come from. Differences at lower energy may be explained by different geometries and surroundings implemented in the simulations, and environmental details have

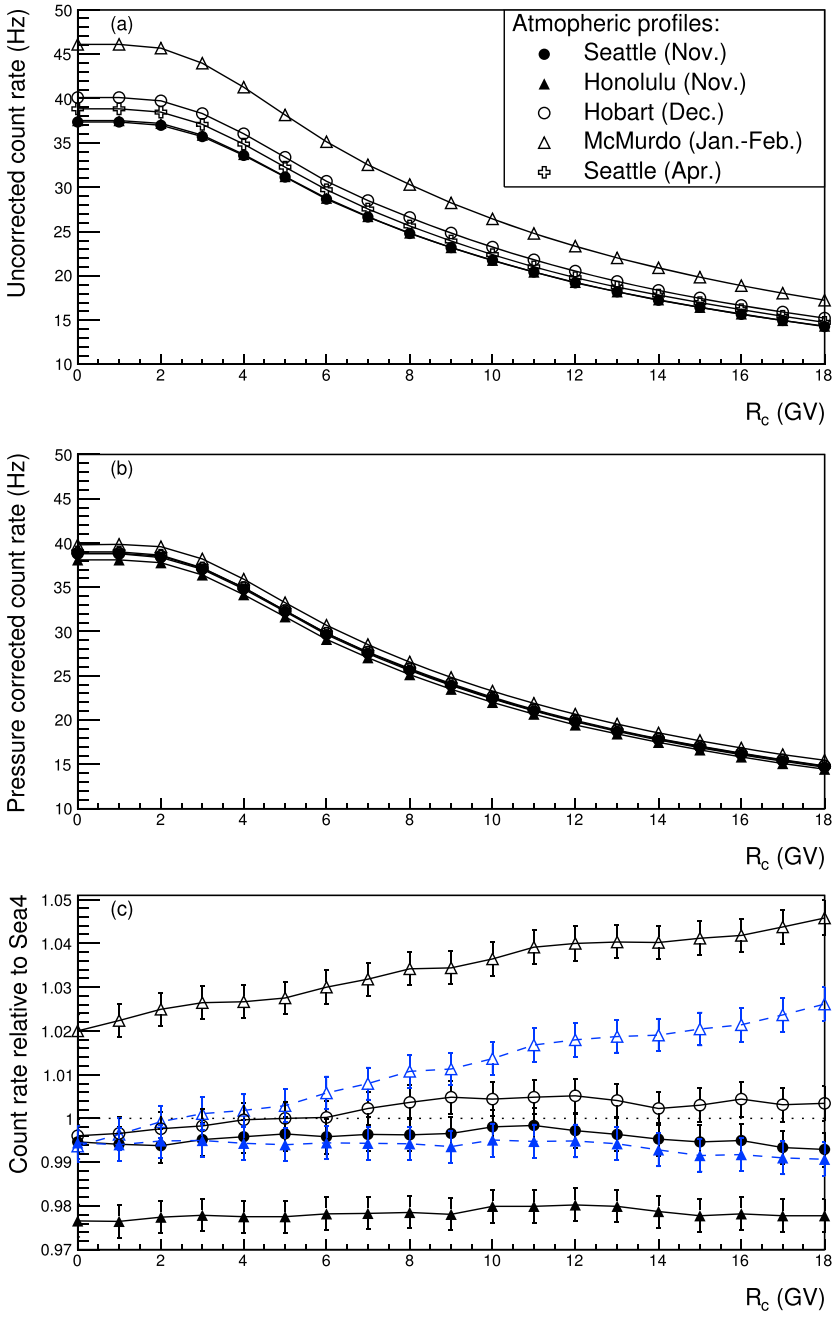


Figure 7. Dependence of the simulated count rate on the apparent cutoff rigidity R_c for the five atmospheric profiles. (a) Count rate as uncorrected for pressure. (b) Count rate corrected for pressure. (c) Black: Pressure corrected count rate relative to that for Seattle in April. Dashed blue: Relative count rate corrected using the effective pressure, for McM and Hon, which brings the relative count rates closer to unity.

significant effects on the neutron spectrum at this range of energy. Note, however, that such neutrons have little effect on the count rate (see Table 2). For this comparison, a dead time of 20 μs was used in all cases. To estimate the experimental response in terms of counts (SP $cm^{-2})^{-1}$, we multiplied the efficiency values from *Shibata et al.* [1997, 1999] by the area of a 1NM64 (48.5 × 226.5 cm^2). To take into account the difference between a 1NM64 counter tube and the middle tube of the simulated 3NM64, we multiplied the experimental 1NM64 efficiencies by a factor of 1.46 [*Shibata et al.*, 2001], because an additional ~46% of that

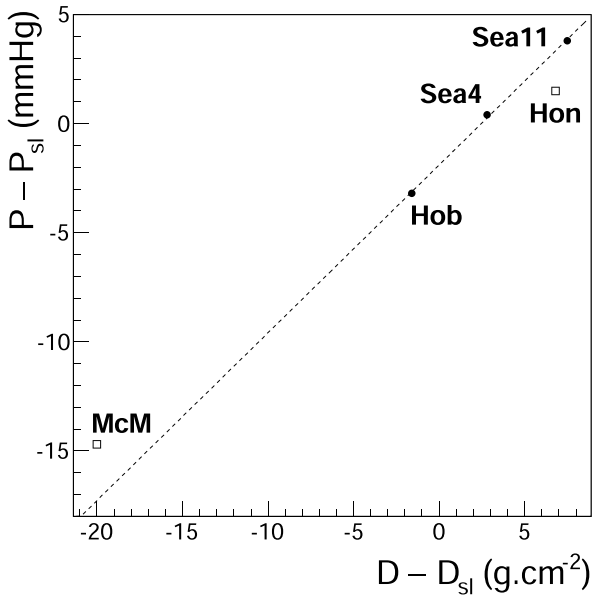


Figure 8. Deviation of the pressure P from the mean sea level pressure P_{sl} with respect to the deviation of the atmospheric depth D from the mean sea level atmospheric depth D_{sl} for the five atmospheric profiles. The relation for the profiles Hob, Sea4, and Sea11 (dots) can be fitted by a straight line of equation $y(x) = 0.77x - 1.9$ (dashed line). The points for the profiles McM and Hon (open squares) lie significantly away from the straight line. The fitted function is used to estimate effective pressures for McM and Hon.

count rate is expected in a middle tube due to neutrons impinging at the lead around neighboring tubes. Considering the differences in setup and uncertainties, the experimental results and simulations are in fairly good agreement.

3.2.2. Count Rate as Related to Primary Cosmic Rays

Our simulated yield functions for the profile Sea4 (760.4 mmHg; 1035.8 g cm^{-2}), calculated using monoenergetic and isotropic fluxes of protons and alphas, are presented by circles in Figure 6. The yield functions are expressed in counts per primary particle per cm^2 sr. The yield function values for protons and alphas are presented in Tables 3 and 4, respectively. Figure 6 also shows previous Monte Carlo simulation results for sea level by *Clem and Dorman* [2000] (vertical incidence only) and *Mishev et al.* [2013], as well as empirical yield functions that aim to explain latitude survey data by *Caballero-Lopez and Moraal* [2012]. We have corrected a printing error in the first five values of the alpha yield function in Table 1 of *Mishev et al.* [2013] (I. Usoskin, private communication, 2016). The previous Monte Carlo results were scaled from 6NM64 to 3NM64 configurations using the simulated normalization coefficients from *Mangeard et al.* [2016]. An electronic dead time of 20 μs is assumed. At high rigidity, the various yield functions are similar and the yield function for alphas is higher than that for protons by a factor of ∼2, roughly corresponding to the ratio of the total kinetic energy of an alpha and a proton at the same rigidity. In our results, the crossover at low rigidity between alpha and proton yield functions occurs at ∼5 GV, which is ∼3 GV higher than the value determined by *Clem and Dorman* [2000] and that reported in Figure 4 of *Caballero-Lopez and Moraal* [2012] and is compatible with the crossover of *Mishev et al.* [2013]. The proton yield function in our results below 100 GV is mostly similar to that of *Clem and Dorman* [2000] but seems to be significantly overestimated below 7 GV in comparison with *Caballero-Lopez and Moraal* [2012].

The systematic effect of the choice of the atmospheric profile as a function of the rigidity cutoff is shown in Figure 7, using PAMELA spectra of primary cosmic rays. Here and in other figures the error bars on Monte Carlo results indicate the statistical uncertainty. As expected the absolute difference of the count rate between the five profiles (Figure 7a) is dominated by the barometric effect. The simulated count rates were corrected to a mean sea level pressure P_{sl} =760 mmHg using

$$C_P = Ce^{\beta(P-P_{sl})}, \tag{5}$$

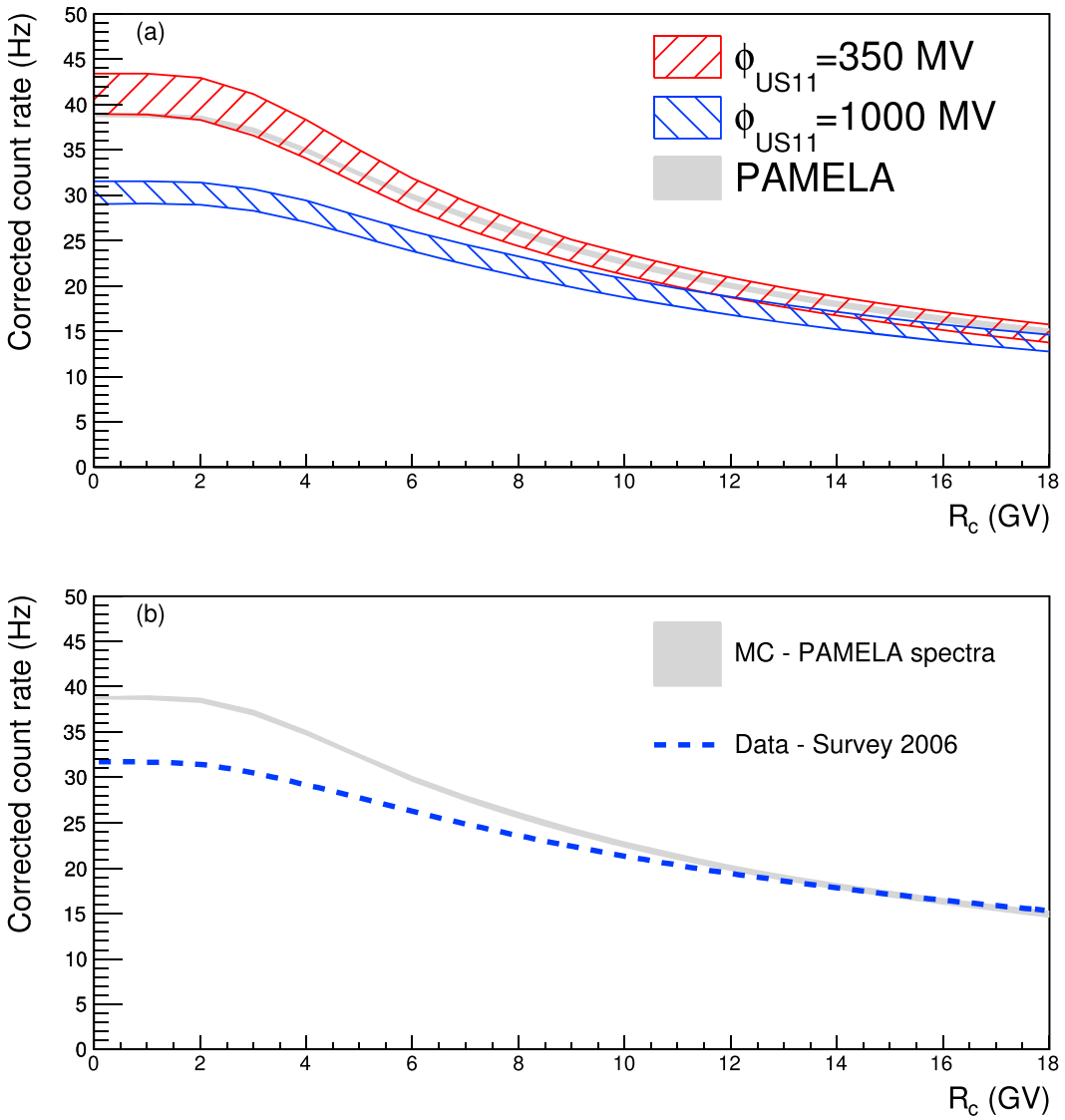


Figure 9. Dependence of the simulated pressure corrected count rates on the apparent cutoff rigidity R_c. (a) Several assumptions of local interstellar spectrum are presented, from *Herbst et al.* [2010], for two values of the solar modulation parameter ϕ_{US11} that bracket the range of values during the latitude survey period. The PAMELA spectra used here, for 2006, correspond to solar modulation at about 400 MV. (b) Comparison between the simulated response function for PAMELA spectra with the Dorman function from the 2006 latitude survey [*Nuntiyakul et al.*, 2014]. There is a substantial discrepancy from the data at $R_c \lesssim 6$ GV.

where P is the pressure, C the count rate, and C_P the count rate corrected for pressure variation. The pressure correction coefficient β, in units of percent per mmHg, was empirically determined by *Nuntiyakul et al.* [2014] and depends on the cutoff rigidity R_c (in GV):

$$\beta = 1.006 - 0.01534 R_c. \tag{6}$$

In other words, in order to correct the count rate, the variation of pressure is used here as a proxy of the variation of the atmospheric depth D with respect to a mean sea level atmospheric depth D_{sl} =1033 g cm^{-2}. The agreement between the two profiles at Seattle and the one at Hobart is ∼1% (Figure 7b). This shows the quality of the empirical correction for pressures close to P_{sl} and relatively similar profiles. For the other two profiles ("McM" and "Hon"), a remaining shift of ± ∼1 Hz can be observed after the pressure correction. Looking at McMurdo at $R_c = 0$ GV and at Honolulu at high R_c, i.e., in the real geomagnetic conditions, Figure 7c

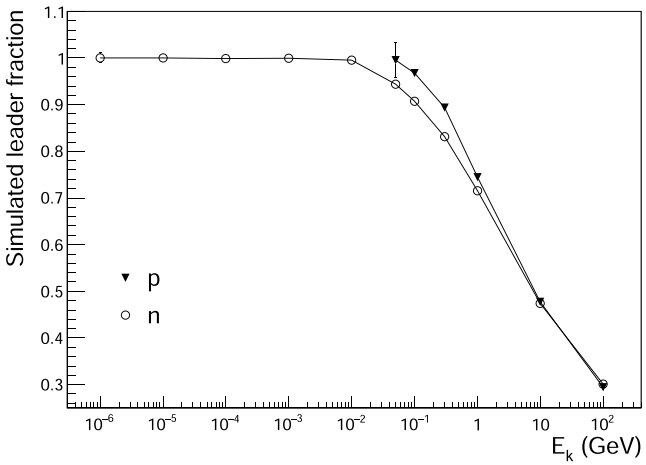


Figure 10. Simulated leader fraction of the middle neutron counter tube as a function of secondary proton or neutron kinetic energy at vertical incidence.

indicates that the pressure correction procedure of *Nuntiyakul et al.* [2014] can be expected to achieve the correction within about ±2%.

Much of the remaining difference of McM and Hon profiles relative to Sea4 is explained by the nonlinearity of the relation between the variation of P around P_{sl} and the variation of D around D_{sl} for the five simulated profiles. As one can see in Figure 8, the linearity holds well for the three profiles where the pressure correction gives good results ("Hob", Sea4, and "Sea11"). For McM and Hon, which are very different in terms of latitude, humidity, temperature, and vertical atmospheric structure, a different correction must be applied. In order to apply an appropriate correction, we determined, for each of those two profiles, an effective pressure P_{eff} such that

$$P_{eff} - P_{sl} = y\left(D - D_{sl}\right) \tag{7}$$

where $y(\Delta D)$ is the function of the straight line of Figure 8. We obtained $P_{eff,McM} = 742.3$ mmHg and $P_{eff,Hon} = 763.3$ mmHg. Figure 7c shows that the agreement after the final correction is around 1%. In the

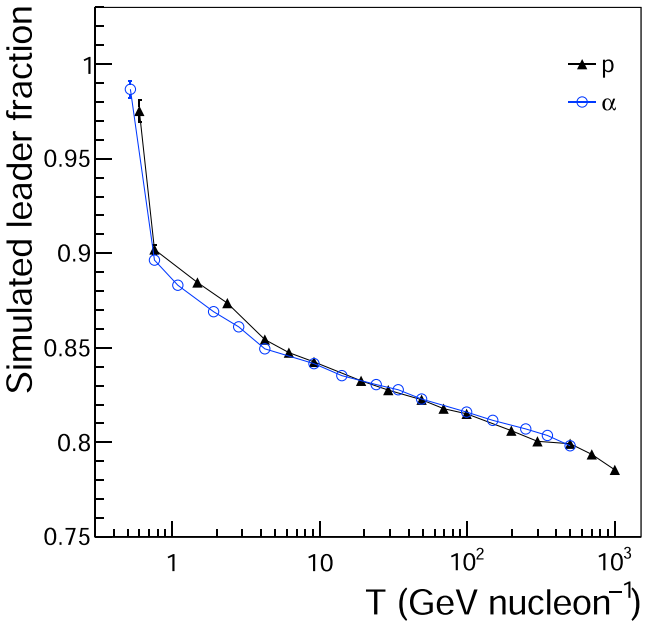


Figure 11. Simulated leader fraction for the MM as a function of kinetic energy per nucleon, T, of primary cosmic ray p and α using the atmospheric profile Sea4 ($P = 760.4$ mmHg; $D = 1035.8$ g cm^{-2}).

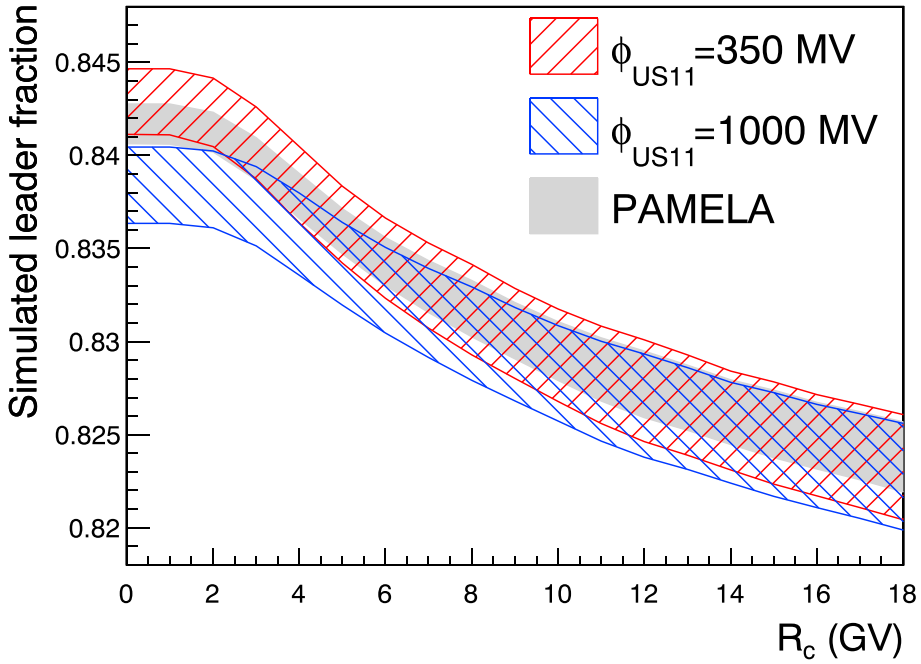


Figure 12. Monte Carlo results for the leader fraction as a function of the apparent cutoff rigidity R_c for five atmospheric profiles and five assumptions of the local interstellar spectrum from *Herbst et al.* [2010], for two values of the solar modulation intensity that bracket the range of values of ϕ_{US11} during the latitude survey period. In addition, we show the range of Monte Carlo results based on PAMELA spectra for 2006 corresponding to a solar modulation of about 400 MV.

case of McM, where the pressure is significantly different ($|P_{McM} - P_{sl}| \sim 15$ mmHg), the difference from Sea4 progressively increases to a level of 2–3% for $R_c > 12$ GV. This indicates that the correction is not sufficient at high-rigidity cutoff and at low atmospheric pressure. The lack of data with a large $|P - P_{sl}|$ at a location with a large R_c [see *Nuntiyakul*, 2014, Appendix B] probably contributes to this remaining shift.

The effects from the choice of LIS model were estimated. As we can see in Figure 9a, there are systematic variations due to the choice of model and more generally to the chosen primary cosmic ray spectrum. While the pressure effect is small and relatively constant with R_c, this LIS effect depends strongly on R_c as

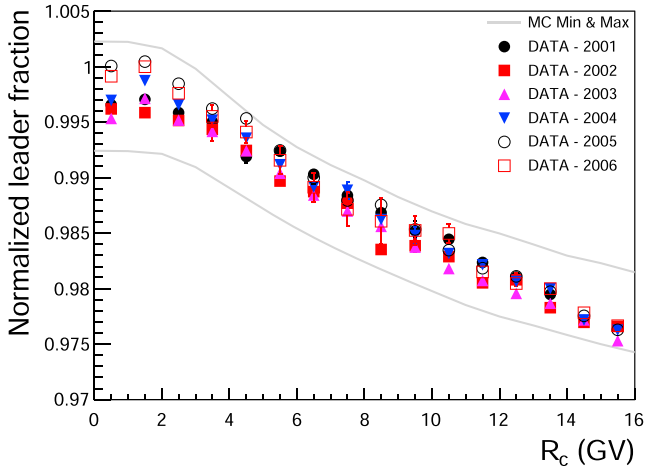


Figure 13. Dependence of the leader fraction L measured by the mobile neutron monitor on the apparent cutoff rigidity R_c for the six surveys operating with the same firmware, together with the range of Monte Carlo results for various cosmic ray spectra and atmospheric profiles. Observations were normalized relative to the leader fraction for the 1–2 GV cutoff rigidity bin for survey year 2006 (0.851). Simulation results are normalized to the calculated leader fraction at $R_c = 1$ GV using PAMELA spectra and the Sea11 atmosphere (0.843).

well as on the solar modulation. This finding is in agreement with previous work, which shows variations from 10 to 30% between different computed count rates [*Clem and Dorman*, 2000] and between different LIS models [*Herbst et al.*, 2010]. Taking into account the nonvertical primary particles at the top of the atmosphere does not reduce the yield function at low rigidities, and the simulated differential response function is still largely overestimated under 10 GV (Figure 9b) in comparison with latitude survey data. Finally, the difference of response to primary cosmic rays between the middle tube and the edge tubes is noticeable in our simulated results where the edge-to-middle tube count rate ratio decreases from about 0.894 at $R_c = 0$ GV to 0.892 at $R_c = 16$ GV, for PAMELA spectra.

3.2.3. Leader Fraction as Related to Secondary Particles

Figure 10 presents the variation of the leader fraction in the middle tube with kinetic energy for SP protons and neutrons with vertical incidence angle, using the measured dead time of 90.4 μs for time delay data; note that the dead time for the count rate is much shorter at 28.4 μs. As expected, the more energetic hadronic SPs undergo interactions (typically in the producer) with greater multiplicity (lower L). The leader fraction for hadronic SPs is highly dependent on the SP energy and decreases from $L \approx 1$ at 1 MeV to $L < 0.5$ at 10 GeV. Neutrons with energy lower than 1 MeV typically produce at most only one count; the corresponding leader fraction is consequently about 1. As was found for the count rate, the asymmetric surroundings have significant effects on L, depending on the incidence angle. For instance, in the middle tube for a beam of 100 MeV neutrons, the azimuthal dependence (~1%) of the leader fraction at nonzero zenith angle is associated with the ship's structure due to attenuation of the high-energy portion of the neutron beam along with production of less energetic neutrons as the beam passes though the metal structure. The same effect, upon passage through the atmosphere, explains an overall increase in L at high zenith angle.

3.2.4. Leader Fraction as Related to Primary Cosmic Rays

The leader fraction has been also calculated using monoenergetic and isotropic fluxes of primary cosmic ray protons and alphas. Figure 11 shows a decrease of L with the kinetic energy per nucleon of the simulated primary particle. Above 10 GeV, protons and alphas of the same energy per nucleon give the same L value. It can be interpreted that the secondary particle spectrum (at sea level) is similar for both types of primaries for the same energy per nucleon.

The leader fraction, L_{MC}, was determined from simulation results as a function of the cutoff rigidity for realistic models of the primary cosmic ray spectrum. For each of two solar modulation parameters, $\phi_{US11} = 350$ and 1000 MV, which bracket the range of values during the latitude surveys, Figure 12 shows the ranges of L_{MC} values for the 25 combinations of 5 LIS + force field models and the 5 atmospheric profiles. The range of results using PAMELA spectra for five atmospheric profiles is also shown. Note that no pressure correction is applied to the leader fraction. L_{MC} decreases by ~0.02 as the apparent rigidity cutoff increases from 0 to 18 GV. The solar modulation is stronger at low rigidity, where the ranges of L_{MC} values for $\phi_{US11} = 350$ and 1000 MV are separated. At large R_c, for a given ϕ_{US11} deviations between results for different LIS models and for atmospheric profiles are larger than at low R_c. The overlap of the bands shows that the variation with the solar modulation is smaller at large R_c. Figures 3 and 13 show that the Monte Carlo results can explain the observed changes in L, both with respect to the cutoff rigidity R_c and with respect to the solar modulation, with a nearly constant shift in the absolute value. This confirms that changes in L can be used as an indicator of the spectral variation of the primary cosmic ray flux at the top of the atmosphere.

4. Discussion

In this work, we further explore the use of the leader fraction L determined from neutron monitor time delay histograms to indicate changes in the primary cosmic ray spectrum. Our analysis of multiple latitude surveys (from 2001 to 2006) provides the first measurements of the variation of a neutron monitor leader fraction L with geomagnetic cutoff rigidity and with solar modulation. To confirm that the observed changes in L indeed indicate changes in the cosmic ray spectrum, we developed a Monte Carlo simulation of the mobile neutron monitor. We determined the sea-level yield functions for the MM count rate as well as expected variations in the count rate and L.

Our results show an absolute count rate agreement within 22% between our Monte Carlo results and latitude survey observations from *Nuntiyakul et al.* [2014] with a better agreement, <5%, at large cutoff rigidity. Note that to account for overall changes in the MM count rate for some (but not all) surveys, presumably due to different placement and surroundings of the MM on the ship from year to year, *Nuntiyakul et al.* [2014] nor-

malized the MM count rate in those surveys based on the count rate ratio of the MM to the NM at McMurdo, Antarctica while the ship was near McMurdo, with changes up to 4.7%. This shows that the varying placement of the MM on the ship affected the observed count rate by up to 4.7%, implying an uncertainty on the Monte Carlo estimation of the count rate. In any case, our Monte Carlo results overestimate the count rate at low cutoff rigidity by more than this uncertainty.

If the count rate is normalized to 1 at $R_c = 0$ GV, the normalized count rate at a given R_c represents the fractional contribution of primary cosmic rays at $R > R_c$ to the total count rate at all P. Our simulated results predict the contribution to the count rate of the primary cosmic rays at $R_c > 17$ GV to be about 40.2%, compared with about 50.2% in the observation. Comparing to the Figure 4 of *Mishev et al.* [2013] that gathers several previous results for an equivalent solar modulation, our values are in agreement with previous results of simulation using the GEANT4 simulation package [*Agostinelli et al.*, 2003] by *Debrunner et al.* [1982], *Flückiger et al.* [2008] and *Matthiä et al.* [2009]. We obtain a better agreement with the observation than the previous FLUKA simulation results by *Clem and Dorman* [2000], which predict a much lower contribution (<35%) from primary particles with $R_c > 17$ GV. We do not achieve a relative agreement with normalized latitude survey data as good as in *Mishev et al.* [2013] and *Gil et al.* [2015], which use GEANT4 with PLANETOCOSMICS [*Desorgher et al.*, 2005]. This may be due to the change of the hadronic interaction model used by FLUKA from DPMJET at $T > 5$ GeV nucleon^{-1} to the Relativistic Quantum Molecular Dynamics (RQMD) model at lower T. The transition energy is within our energy range of interest. Improvements in the FLUKA atmospheric shower development calculation are needed to achieve a better agreement between the observed and simulated count rates for the primary particles with a rigidity lower than 10 GV. At $R_c > 12$ GV, we note that absolute (unnormalized) agreement between our simulated and observed count rates is very good (<5%).

We studied the systematic effect from the choice of atmospheric profile. The count rate can be corrected for pressure and atmospheric depth differences. After correction, the agreement between the count rates using the five atmospheric profiles is at the level of ∼1%. We studied the systematic effect of the choice of the cosmic ray spectrum at the top of the atmosphere. In particular, we employed five existing models of the local interstellar spectrum (LIS) together with the force field model for a previously tabulated solar modulation parameter as a function of time, adjusted as appropriate for each model [*Herbst et al.*, 2010]. We also used the spectrum observed by PAMELA during 2006 (for details see section 3.1.1). The difference between Monte Carlo results for different LIS models represents the dominant uncertainty in Monte Carlo estimation of both the count rate and the leader fraction.

There is a shift of about 1% in the absolute value of L between data and Monte Carlo simulation (Figure 3). This could be explained by an incomplete simulation of the detection process within the detector (e.g., all boron disintegrations are counted in the simulation). The simple geometry for simulation of the ship may also impact the SP interactions in the surroundings of the MM and modify the energy distributions of the SPs that produce counts.

The observed variations of L with changing cutoff rigidity and solar modulation are consistent with our Monte Carlo simulation results, confirming that L can be used as an indicator of cosmic ray variation.

Acknowledgments
This work was partially supported by the postdoctoral research sponsorship of Mahidol University; the Thailand Research Fund award RTA5980003; the United States National Science Foundation awards PLR-1245939, PLR-1341562, and their predecessors; and the Australian Antarctic Division. We thank the officers and crew of the USCG icebreakers Polar Star and Polar Sea for their assistance in conducting the surveys. We also thank Leonard Shulman, James Roth, and Keith Bolton for their technical assistance in preparing and maintaining the TasVan and enclosed mobile monitor; Suttiwat Madlee for visualization assistance; and Andrew Snodin for setting up and maintaining the computing cluster on which our simulations were performed. The data displayed in the figures are available upon request to the corresponding author.

References

Adriani, O., et al. (2011), PAMELA measurements of cosmic-ray proton and helium spectra, *Science*, *332*, 69–72, doi:10.1126/science.1199172.

Adriani, O., et al. (2013), Time dependence of the proton flux measured by PAMELA during the 2006 July–2009 December solar minimum, *Astrophys. J.*, *765*, 91, doi:10.1088/0004-637X/765/2/91.

Agostinelli, S., et al. (2003), Geant4—A simulation toolkit, *Nucl Instr. Meth. Phys. Res. A*, *506*, 250–303.

Aiemsa-ad, N., et al. (2015), Measurement and simulation of neutron monitor count rate dependence on surrounding structure, *J. Geophys. Res. Space Physics*, *120*, 5253–5265, doi:10.1002/2015JA021249.

Bieber, J. W., J. Clem, and P. Evenson (1997), Efficient computation of apparent cutoffs, in *25th International Cosmic Ray Conference*, vol. 2, pp. 389–392, World Scientific, Durban, South Africa.

Bieber, J. W., J. M. Clem, M. L. Duldig, P. A. Evenson, J. E. Humble, and R. Pyle (2004), Latitude survey observations of neutron monitor multiplicity, *J. Geophys. Res.*, *109*, A12106, doi:10.1029/2004JA010493.

Bisschoff, D., and M. S. Potgieter (2016), New local interstellar spectra for protons, helium and carbon derived from PAMELA and Voyager 1 observations, *Astrophys. Space Sci.*, *361*, 48, doi:10.1007/s10509-015-2633-8.

Bohlen, T. T., F. Cerutti, M. P. W. Chin, A. Fassò, A. Ferrari, P. G. Ortega, A. Mairani, P. R. Sala, G. Smirnov, and V. Vlachoudis (2014), The FLUKA code: Developments and challenges for high energy and medical applications, *Nuclear Data Sheets*, *120*, 211–214.

Caballero-Lopez, R. A., and H. Moraal (2004), Limitations of the force field equations to describe cosmic ray modulation, *J. Geophys. Res.*, *109*, A01101, doi:10.1029/2003JA010098.

Caballero-Lopez, R. A., and H. Moraal (2012), Cosmic-ray yield and response functions in the atmosphere, *J. Geophys. Res.*, *117*, A12103, doi:10.1029/2012JA011794.
Clem, J., J. W. Bieber, P. Evenson, D. Hall, J. E. Humble, and M. Dulding (1997), Contribution of obliquely incident particles to neutron monitor counting rate, *J. Geophys. Res.*, *102*, A12, doi:10.1029/97JA02366.
Clem, J., and L. Dorman (2000), Neutron monitor response functions, *Space Sci. Rev.*, *93*, 335, doi:10.1023/A:1026508915269.
Debrunner, H., E. Flückiger, and J. Lockwood (1982), Specific yield function S(P) for a neutron monitor at sea level, paper presented at 8th Europ. Cosmic Ray Symposium, Rome.
Desorgher, L., E. O. Flückiger, M. Gurtner, M. R. Moser, and R. Bütikofer (2005), Atmocosmics: A geant 4 code for computing the interaction of cosmic rays with the Earth's atmosphere, *Int. J. Modern Phys. A*, *20*, 6802–6804, doi:10.1142/S0217751X05030132.
Ferrari, A., P. R. Sala, A. Fassò, and J. Ranft (2005), FLUKA: A multi-particle transport code. CERN, Geneva, CERN-2005-10, INFN/TC_05/11, SLAC-R-773.
Flückiger, E. O., M. R. Moser, B. Pirard, R. Bütikofer, and L. Desorgher (2008), A parameterized neutron monitor yield function for space weather applications, in *30th International Cosmic Ray Conference*, vol. 1, pp. 289–292, Universidad Nacional Autónoma de México, Mexico City, Mexico.
Ghelfi, A., F. Barao, L. Derome, and D. Maurin (2016), Non-parametric determination of H and He interstellar fluxes from cosmic-ray data, *Astron. Astrophys.*, *591*, A94, doi:10.1051/0004-6361/201527852.
Gil, A., I. G. Usoskin, G. A. Kovaltsov, A. L. Mishev, C. Corti, and V. Bindi (2015), Can we properly model the neutron monitor count rate?, *J. Geophys. Res. Space Phys.*, *120*, 7172–7178, doi:10.1002/2015JA021654.
Gleeson, L. J., and W. I. Axford (1968), Solar modulation of Galactic cosmic rays, *Astrophys. J.*, *154*, 1011–1026.
Hatton, C. J., and H. Carmichael (1964), Experimental investigation of the NM-64 neutron monitor, *Can. J. Phys.*, *42*, 2443–2472.
Herbst, K., A. Kopp, B. Heber, F. Steinhilber, H. Fichtner, K. Scherer, and D. Matthiä (2010), On the importance of the local interstellar spectrum for the solar modulation parameter, *J. Geophys. Res.*, *115*, D00I20, doi:10.1029/2009JD012557.
Mangeard, P.-S., D. Ruffolo, A. Sáiz, S. Madlee, and T. Nutaro (2016), Monte Carlo simulation of the neutron monitor yield function, *J. Geophys. Res. Space Physics*, *121*, 7435–7448, doi:10.1002/2016JA022638.
Matthiä, D., B. Heber, G. Reitz, M. Meier, L. Sihver, T. Berger, and K. Herbst (2009), Temporal and spatial evolution of the solar energetic particle event on 20 January 2005 and resulting radiation doses in aviation, *J. Geophys. Res.*, *114*, A08104, doi:10.1029/2009JA014125.
Maurin, D., A. Cheminet, L. Derome, A. Ghelfi, and G. Hubert (2015), Neutron monitors and muon detectors for solar modulation studies: Interstellar flux, yield function, and assessment of critical parameters in count rate calculations, *Adv. Space Res.*, *55*, 363–389, doi:10.1016/j.asr.2014.06.021.
Mishev, A. L., I. G. Usoskin, and G. A. Kovaltsov (2013), Neutron monitor yield function: New improved computations, *J. Geophys. Res. Space Physics*, *118*, 2783–2788, doi:10.1002/jgra.50325.
Nuntiyakul, W. (2014), Analysis of data from a calibration neutron monitor at Doi Inthanon and a ship-borne neutron monitor, PhD Thesis, Mahidol Univ., Bangkok.
Nuntiyakul, W., P. Evenson, D. Ruffolo, A. Sáiz, J. W. Bieber, J. Clem, R. Pyle, M. L. Duldig, and J. E. Humble (2014), Latitude survey investigation of Galactic cosmic ray solar modulation during 1994–2007, *Astrophys. J.*, *795*, 11, doi:10.1088/0004-637X/795/1/11.
Picone, J. M., A. E. Hedin, D. P. Drob, and A. C. Aikin (2002), NRLMSISE-00 empirical model of the atmosphere: Statistical comparisons and scientific issues, *J. Geophys. Res.*, *107*(A12), 1468, doi:10.1029/2002JA009430.
Ruffolo, D., et al. (2016), Monitoring short-term cosmic ray spectral variations using neutron monitor time delay measurements, *Astrophys. J.*, *817*, 38, doi:10.3847/0004-637X/817/1/38.
Scherer, K., H. Fichtner, R. D. Strauss, S. E. S. Ferreira, M. S. Potgieter, and H.-J. Fahr (2011), On cosmic ray modulation beyond the heliopause: Where is the modulation boundary?, *Astrophys. J.*, *735*, 128, doi:10.1088/0004-637X/735/2/128.
Shibata, S., et al. (1997), Calibration of neutron monitor using an accelerator, in *Proceedings of the 25th International Cosmic Ray Conference*, vol. 1, Durban, South Africa.
Shibata, S., et al. (1999), Calibration of neutron monitor using accelerator neutron beam, in *Proceedings of the 26th International Cosmic Ray Conference*, vol. 7, p. 313, International Union of Pure and Applied Physics (IUPAP), Salt Lake City, Utah.
Shibata, S., et al. (2001), Detection efficiency of a neutron monitor calibrated by an accelerator neutron beam, *Nucl. Inst. Meth. Phys. Res.*, *A463*, 316–320, doi:10.1016/S0168-9002(01)00280-7.
Stone, E. C., A. C. Cummings, F. B. McDonald, B. C. Heikkila, N. Lal, and W. R. Webber (2013), Voyager 1 observes low-energy galactic cosmic rays in a region depleted of heliospheric ions, *Science*, *341*, 150–153, doi:10.1126/science.1236408.
Usoskin, I. G., K. Alanko-Huotari, G. A. Kovaltsov, and K. Mursula (2005), Heliospheric modulation of cosmic rays: Monthly reconstruction for 1951–2004, *J. Geophys. Res.*, *110*, A12108, doi:10.1029/2005JA011250.
Usoskin, I. G., A. Bazilevskaya, and G. A. Kovaltsov (2011), Solar modulation parameter for cosmic rays since 1936 reconstructed from ground-based neutron monitors and ionization chambers, *J. Geophys. Res.*, *116*, A02104, doi:10.1029/2010JA016105.
Zhang, M., X. Luo, and N. Pogorelov (2015), Where is the cosmic-ray modulation boundary of the heliosphere?, *Phys. Plasmas*, *22*, 91501, doi:10.1063/1.4928945.

The Astrophysical Journal, 837:140 (10pp), 2017 March 10 https://doi.org/10.3847/1538-4357/aa603a
© 2017. The American Astronomical Society. All rights reserved.

Charged Particle Diffusion in Isotropic Random Magnetic Fields

P. Subedi[1], W. Sonsrettee[2], P. Blasi[3,4], D. Ruffolo[5], W. H. Matthaeus[1], D. Montgomery[6], P. Chuychai[1], P. Dmitruk[7], M. Wan[8], T. N. Parashar[1], and R. Chhiber[1]

[1] Department of Physics and Astronomy, University of Delaware, Newark, Delaware 19716, USA
[2] Faculty of Engineering and Technology, Panyapiwat Institute of Management, Nonthaburi 11120, Thailand
[3] INAF/Osservatorio Astrofisico di Arcetri, Largo E. Fermi, 5—I-50125 Firenze, Italy
[4] Gran Sasso Science Institute (INFN), Viale F. Crispi, 7, I-67100 L'Aquila, Italy
[5] Department of Physics, Faculty of Science, Mahidol University, Bangkok 10400, Thailand
[6] Department of Physics and Astronomy, Dartmouth College, Hanover, NH 03755, USA
[7] Departamento de Física Facultad de Ciencias Exactas y Naturales, Universidad de Buenos Aires Ciudad Universitaria, 1428 Buenos Aires, Argentina
[8] Department of Mechanics and Aerospace Engineering, Southern University of Science and Technology, Shenzhen, Guangdong 518055, China
Received 2016 December 29; revised 2017 February 9; accepted 2017 February 10; published 2017 March 13

Abstract

The investigation of the diffusive transport of charged particles in a turbulent magnetic field remains a subject of considerable interest. Research has most frequently concentrated on determining the diffusion coefficient in the presence of a mean magnetic field. Here we consider the diffusion of charged particles in fully three-dimensional isotropic turbulent magnetic fields with no mean field, which may be pertinent to many astrophysical situations. We identify different ranges of particle energy depending upon the ratio of Larmor radius to the characteristic outer length scale of turbulence. Two different theoretical models are proposed to calculate the diffusion coefficient, each applicable to a distinct range of particle energies. The theoretical results are compared to those from computer simulations, showing good agreement.

Key words: astroparticle physics – cosmic rays – diffusion – magnetic fields – scattering – turbulence

1. Introduction

Transport of charged particles in many astrophysical systems is governed by a highly turbulent magnetic field, which leads to the diffusion of charged particles in space. Some of the most notable ideas in the study of diffusion of charged particles in magnetic turbulence are quasilinear theory (Jokipii 1966), field line random walk theory (FLRW; e.g., Jokipii & Parker 1968), and nonlinear guiding center theory (Matthaeus et al. 2003). These theories focus on calculating the diffusion of charged particles in directions parallel and perpendicular to a constant mean magnetic field $\boldsymbol{B}_0$, under the influence of a fluctuating magnetic field $\boldsymbol{b}(\boldsymbol{x})$ that depends on position $\boldsymbol{x}$ but not on time. A considerable modification to these theories is required when the fluctuations are isotropic with a zero (or very small) mean field. Such modification turns out to be of the highest importance when describing the transport of cosmic rays (CRs) in the Galaxy, as well as for the modeling of diffusive CR acceleration in astrophysical sources. Here we consider the problem of magnetostatic scattering with $\boldsymbol{B}_0 = 0$, and for fluctuations $\boldsymbol{b}$ that are statistically isotropic, in terms of both polarization and spectral distribution.

The propagation of CRs in the Galaxy is usually modeled as diffusive in a turbulent magnetic field where the rms fluctuations of strength δb are of the same order of magnitude as the large-scale field B_0 (e.g., Jansson & Farrar 2012), $\delta b/B_0 \sim 1$, although it is not clear whether this condition is fulfilled both in the disk and the halo of the Galaxy. On the other hand, supernova shocks, usually invoked to be the main sites of acceleration of Galactic CRs (Blasi 2013), are observed to possess intense turbulent magnetic fields, where the large-scale field, if any, only affects the development of the fast growing instabilities that lead to the existence of intense turbulent fields (Caprioli 2015). At the shock itself, the field is probably well modeled as isotropic with a negligible mean field.

There have been some studies of diffusion of charged particles in magnetic turbulence without a mean field (e.g., Casse et al. 2002; Parizot 2004; de Marco et al. 2007; Plotnikov et al. 2011; Snodin et al. 2016), but a clear theory covering all ranges of particle energies is still lacking. In particular, the simulations carried out by de Marco et al. (2007) clearly showed that, in the limit $\delta b/B_0 \gg 1$, the diffusion coefficient of particles with a Larmor radius much smaller than the energy containing scale of the turbulent field closely resembles the one naively estimated from quasilinear theory, which is a rather curious result since such theory applies to the opposite limit. When the field is purely turbulent, the combination of particle diffusion and random walk of magnetic field lines is expected to play a crucial role. Diffusion of magnetic field lines in isotropic turbulence with a zero mean field was examined by Sonsrettee et al. (2015), and that paper is in some ways an antecedent of the present work. We note that the high-energy theory described below was originally presented by David Montgomery.[9]

The transport of charged particles in interplanetary space and the interstellar medium, including in regions of particle acceleration, is highly influenced by the presence of turbulent magnetic fields and their spectral distribution. The nature of particle transport in these fields also depends on particle energy. In general, higher energy particles, with a gyroradius larger than the correlation length of the magnetic field, will sample many uncorrelated field lines within one gyration. Lower energy particles with a gyroradius much smaller than the magnetic field correlation length, on the other hand, will see a relatively coherent large-scale field, and their transport will be

[9] Presentations at the Santa Fe Workshop, 2004 October 5, and APS-Division of Plasma Physics Mini-Conference, 2004 November 15.

heavily affected by resonances with local magnetic fluctuations.

In this paper, we classify the diffusive behavior of charged particles into three different regimes based on the ratio of the Larmor radius R_L of the charged particle to the characteristic outer length scale of turbulence l_c: a high-energy region with $R_L/l_c \gg 1$, an intermediate-energy region with $R_L/l_c \sim 1$, and the low-energy region with $R_L/l_c \ll 1$. Corresponding to the two extreme inequalities, we will develop two corresponding theoretical approaches for particle diffusion in the extreme energy ranges. First, in the high-energy limit, the path of the particle experiences only small deviations from its initial trajectory due to small angle scattering on magnetic field irregularities. In this case, velocity diffusion is achieved when the magnetic fluctuations probed by the particles become uncorrelated. At the opposite extreme, particles with a very small gyroradius will gyrate about the local field produced by the large-scale fluctuations while experiencing perturbations, the most effective of which will be at scales comparable to the gyroradius. This leads to resonant interactions and a random walk of the particle pitch angle. The particle guiding center will eventually reverse direction and parallel spatial diffusion is achieved. The range of validity of both the high-energy and the low-energy asymptotic theories will be extended by building in additional decorrelation effects in the relevant Lagrangian correlation functions, thereby providing an accurate description of the particle mean-free paths also in the intermediate range of energies.

The paper is organized as follows. In Section 2, we write down the fundamental equations describing the diffusive motion of the particles in velocity (or momentum) space. In Section 3, we specialize the theory to the high-energy regime. In Section 4, we show that a nonlinear theory can be developed that reproduces the high-energy behavior of the diffusion coefficient (Section 3) for $R_L/l_c \gg 1$ while also describing the results of numerical simulations down to $R_L/l_c \approx 0.5$. Finally, in Section 5, we describe our formulation of a low-energy theory that, while accounting for particle-wave resonances, also keeps a memory of perpendicular decorrelation, thereby describing simulation results for $R_L/l_c \lesssim 0.5$. A detailed comparison of our theoretically calculated spatial diffusion coefficients with the results of numerical simulations is discussed in Section 6. We summarize in Section 7. Three Appendices are included. The first derives the relationship between velocity diffusion and real space diffusion for isotropic turbulence. The second estimates the angular deflection of a field line over scales in the inertial range and justifies neglecting such deflection in the low-energy theory. The third compares the numerical simulation results with the theories developed in this work when applied to interplanetary parameters.

2. Velocity Space Diffusion and Spatial Diffusion

Since the turbulence is isotropic, and the the particle speed $|\boldsymbol{v}|$ is constant in the absence of electric fields, the velocity space diffusion tensor is expected to have an isotropic form (Batchelor 1953),

$$D_{ij}(v) = (\delta_{ij} - \hat{v}_i\hat{v}_j)D_v, \tag{1}$$

which implies that

$$D_v = \frac{1}{2}Tr\,[D_{ij}(v)]. \tag{2}$$

The distribution function of test particles obeys the Fokker–Planck equation in velocity space, which when spatial gradients are present can be written as

$$\frac{\partial f}{\partial t} + \boldsymbol{v}\cdot\nabla f = \frac{\partial}{\partial v_i}D_{ij}\frac{\partial f}{\partial v_j}. \tag{3}$$

Plugging in the isotropic form of the velocity space diffusion (Equation (1)) into Equation (3), we get

$$\frac{\partial f}{\partial t} + \boldsymbol{v}\cdot\nabla f = D_v\nabla_\perp^2 f, \tag{4}$$

where $\nabla_\perp^2$ stands for that part of the velocity space Laplacian in spherical co-ordinates that involves no radial derivatives.

To make a connection with spatial diffusion, we construct a multiple timescale solution of Equation (4), by breaking down time and spatial scales into fast (τ, ξ) and slow variables (T, X). We seek a solution with $f = f^{(0)} + \epsilon f^{(1)} + \epsilon^2 f^{(2)} + \ldots$ where $\epsilon \ll 1$. The qth order distribution function can be expanded in the spherical harmonics as

$$f^{(q)} = \sum_{l,m} C_{lm}^{(q)}(\boldsymbol{x}, v, t)Y_{lm}(\theta, \phi). \tag{5}$$

The details of the multiple timescale solution are given in Appendix A, where a relationship between the velocity space diffusion coefficient D_v and spatial diffusion coefficient κ is obtained for isotropic turbulence:

$$\kappa = \kappa_{xx} = \kappa_{yy} = \kappa_{zz} = \frac{v^4}{6D_v}. \tag{6}$$

The mean-free path (λ) in terms of the diffusion coefficient is simply

$$\lambda = \frac{3\kappa}{v}. \tag{7}$$

Particle statistics may be related to the spatial diffusion coefficient by the Taylor–Green–Kubo (TGK) formula (Taylor 1922; Green 1951; Kubo 1957):

$$\kappa_{xx} \equiv \lim_{t\to\infty}\frac{\langle\Delta x^2\rangle}{2t} = \int_0^\infty dt\,\langle v_x(0)v_x(t)\rangle. \tag{8}$$

This formula, with v_x interpreted as the guiding center velocity in the x-direction, was used to calculate the diffusion coefficient in theories that have a mean magnetic field, e.g., BAM theory (Bieber & Matthaeus 1997), the original NLGC theory (Matthaeus et al. 2003), etc.

The velocity space diffusion coefficient can also be written in a TGK formulation as

$$D_{ij}(v) = \int_0^\infty dt\left\langle \frac{dv_i}{dt}\bigg|_0 \frac{dv_j}{dt}\bigg|_t \right\rangle. \tag{9}$$

To calculate the rate of change of velocity in Equation (9), we use the Newton–Lorentz equation of motion

$$\frac{d\boldsymbol{v}}{dt} = \frac{q}{m\gamma c}(\boldsymbol{v}\times\mathbf{b}) = \alpha(\boldsymbol{v}\times\mathbf{b}), \tag{10}$$

where q and m are the particle charge and mass, respectively, γ is the Lorentz factor, c is the speed of light, $\boldsymbol{b}$ is the magnetic fluctuation field and we define $\alpha = q/(m\gamma c)$. Apply the Newton–Lorentz equation in Equation (9) to find

$$D_{ij}(v) = \alpha^2 \int_0^\infty dt \;\; \epsilon_{i\alpha\beta}\epsilon_{j\gamma\eta}\langle v_\alpha(0)v_\gamma(t)b_\beta(0)b_\eta[\boldsymbol{x}(t)]\rangle. \tag{11}$$

Assuming that the particle velocity and magnetic field are uncorrelated (as would be the case, e.g., for an isotropic particle distribution) and that the turbulence is statistically homogeneous, one finds

$$D_{ij}(v) = \alpha^2\epsilon_{i\alpha\beta}\epsilon_{j\gamma\eta}\int_0^\infty dt\,\langle v_\alpha(0)v_\gamma(t)\rangle\langle b_\beta(0)b_\eta[\boldsymbol{x}(t)]\rangle. \tag{12}$$

Equation (1) is used to simplify Equation (12). The high-energy theory and nonlinear theory differ in the treatment of the correlation tensors in Equation (12) (more details are in Sections 3 and 4). Section 5 contains a theoretical description of diffusive transport for low-energy particles.

3. High-energy Theory

The high-energy theory developed in this section is applicable when $R_L/l_c \gg 1$. In this regime, when the particles traverse a distance equivalent to the correlation length of the magnetic field, they experience only minor deflections from their original path.

The appropriate simplifying assumptions in this case are that the displacement follows a straight line $\boldsymbol{x}(t) = \boldsymbol{v}t$, and, that the velocity autocorrelation is simply $\langle v_\alpha(0)v_\gamma(t)\rangle = v_\alpha v_\gamma$. Using these, Equation (12) can be written as

$$D_{ij}(v) = \alpha^2\epsilon_{i\alpha\beta}\epsilon_{j\gamma\eta}v_\alpha v_\gamma\int_0^\infty dt\;\;\langle b_\beta(0)b_\eta(\boldsymbol{x}(t) = \boldsymbol{v}t)\rangle. \tag{13}$$

In view of Equation (2), computing the trace of Equation (13) gives an expression for the high-energy velocity space diffusion coefficient,

$$D_v = \frac{\alpha^2 v\delta b^2 l_c}{3}, \tag{14}$$

where δb is the rms magnetic field and the correlation length is

$$l_c = \frac{v\int_0^\infty dt\,\langle b_i(0)b_i(vt,0,0)\rangle}{\delta b^2}. \tag{15}$$

Notice that D_v is independent of the spectrum of turbulence because most of the energy is near the scale $\sim l_c$ where the effective magnetic field magnitude is δb. Plugging D_v in Equation (6), in terms of gyrofrequency $\Omega_0 = \alpha\delta b$, the spatial diffusion coefficient is then

$$\kappa_{xx} = \kappa_{yy} = \kappa_{zz} = \frac{v^3}{2\Omega_0^2 l_c}. \tag{16}$$

This result is not entirely new to the astrophysics community (see, e.g., Aloisio & Berezinsky 2004), though we give a more formal derivation. An intuitive derivation of Equation (16) proceeds as follows. Suppose that most of the power in the magnetic field spectrum is on a spatial scale l_c, which is much smaller than the Larmor radius of particles. Then one can think of a very large but otherwise arbitrary distance l_d as being tiled with cells of size l_c. In each cell, when $R_L \gg l_c$, one has a deflection of the order $l_c/R_L \ll 1$. The average angle of deflection when there are n scatterings satisfies

$$\langle\theta^2\rangle = n\left(\frac{l_c}{R_L}\right)^2, \tag{17}$$

where $n = l_d/l_c$. Now, the average deflection angle is of the order of unity when

$$l_d = \frac{R_L^2}{l_c}. \tag{18}$$

At that point the distance is also $l_d \sim vt$ (because the displacement from the unperturbed trajectory is small), and the diffusion coefficient is

$$\kappa = \frac{l_d^2}{2t} = \frac{l_d v}{2} = \frac{R_L^2 v}{2l_c} = \frac{v^3}{2\Omega_0^2 l_c}, \tag{19}$$

which is identical to Equation (16).

4. Nonlinear Extended High-energy Theory

For rigidity decreasing toward unity from large values, the assumption above that the unperturbed particle trajectory is a straight line with constant velocity becomes less accurate. Instead, we assume that the velocity autocorrelation is exponential with a characteristic decorrelation time τ,

$$\langle v_\alpha v_\gamma(t)\rangle = (v^2/3)\delta_{\alpha\gamma}e^{-t/\tau}. \tag{20}$$

However, making use of the TGK formula, Equation (8), one sees that the spatial diffusion coefficient κ_{xx} is related to the timescale τ by

$$\kappa_{xx} = \frac{1}{3}v^2\tau. \tag{21}$$

That is, from Equation (6)

$$\tau = \frac{v^2}{2D_v}. \tag{22}$$

Then, using Equations (2), (12), and (20) one finds that

$$D_v = \frac{1}{2}Tr\,[D_{ij}(v)] = \alpha^2\int_0^\infty dt\frac{v^2}{3}e^{-t/\tau}\,\langle b_i(0)b_i[\boldsymbol{x}(t)]\rangle, \tag{23}$$

where there is an implied summation over i. The closure for the Lagrangian correlation in this equation should now be reconsidered. In particular, we question the approximation of a straight-line unperturbed trajectory $\boldsymbol{x}(t) = \boldsymbol{v}t$ that was previously used in the high-energy theory. To allow for the effect of perturbations of this trajectory, $\boldsymbol{x}(t)$ may be treated as a random variable. Following the familiar procedure used in other nonlinear diffusion theories (e.g., Matthaeus et al. 2003), Corrsin's independence hypothesis (Corrsin 1959) is used to write the magnetic correlation in terms of the power spectrum in Fourier space to obtain

$$\langle b_i(0)b_i[\boldsymbol{x}(t)]\rangle = \int d\boldsymbol{k}P_{ii}(\boldsymbol{k})\langle e^{i\boldsymbol{k}\cdot\boldsymbol{x}(t)}\rangle. \tag{24}$$

In order to evaluate the characteristic functional $\langle e^{i\boldsymbol{k}\cdot\boldsymbol{x}(t)}\rangle$, we now use the approximation of a Gaussian distribution of displacements, along with the random ballistic decorrelation (RBD) approximation (Ruffolo et al. 2012). The latter was first introduced in describing the magnetic field line random walk by Ghilea et al. (2011). Here, the result is

$$\langle e^{i\boldsymbol{k}\cdot\boldsymbol{x}(t)}\rangle = \langle e^{ik\mu vt}\rangle_\mu = \frac{1}{2}\int_{-1}^{1} d\mu\, e^{ik\mu vt} = \frac{\sin(kvt)}{kvt}. \quad (25)$$

The random ballistic model is justified since the particles undergo ballistic motion at earlier times before they reach the asymptotic diffusive regime.

With τ given by Equation (22), substituting Equation (25) into Equation (24) and then into Equation (23) gives

$$D_v = \alpha^2 \frac{v^2}{3}\int dk E(k)\int_0^\infty dt \frac{\sin(kvt)}{kvt} e^{-2tD_v/v^2}, \quad (26)$$

where $E(k) = 4\pi k^2 P_{ii}(\boldsymbol{k})$ is the omnidirectional energy spectrum. If we take the limit $\tau = v^2/(2D_v) \to \infty$ in Equation (26), Equation (14) is recovered, which is the high-energy limit. Hence, the nonlinear theory allows departures from the high-energy limit, but also recovers the exact form of the high-energy limit as τ becomes large. More generally, Equation (26) is an implicit equation for D_v and Equation (6) gives the spatial diffusion coefficient. It is worth pointing out that another standard approximation would be to treat the trajectories of the particles as having a diffusive distribution (DD) for the purpose of calculating the Lagrangian magnetic correlation function (Matthaeus et al. 2003; Bieber et al. 2004; Shalchi 2006, 2010). In that case, the ensemble average on the left-hand side of Equation (25) would then be $\langle e^{i\boldsymbol{k}\cdot\boldsymbol{x}(t)}\rangle = e^{-k^2\kappa_{xx}t}$. This alternative approach, however, fails to predict the high-energy behavior of the particles where the particles are ballistic for a long time before undergoing multiple deflections to reach the diffusive limit. For the intermediate range DD converges with the RBD model.

5. Low-energy Quasilinear Theory

Low-energy particles ($R_L/l_c \ll 1$) behave entirely differently because they experience a local mean magnetic field due to large-scale fluctuations. These small gyroradius particles typically scatter before moving far enough for the local mean field to average to zero. In such circumstances, there are two dominant effects that are expected to contribute to transport and diffusion: FLRW and a kind of resonant wave particle scattering in which the local field acts as a mean field that organizes the particle gyro-motion.

In the presence of FLRW alone, particles would follow magnetic field lines and achieve spatial diffusion as the magnetic field lines diffuse in space. Decorrelation of the particle trajectories due to this mechanism (Jokipii & Parker 1968; Hauff et al. 2010) gives rise to an energy-independent mean-free path. This would not explain the results of our numerical simulations, as discussed below. One may, however, estimate from a simple Kolmogorov turbulence theory the degree to which the field lines bend for distances shorter than a correlation scale, as is done in Appendix B. The conclusion is that the angular deflection of the mean field seen by a particle in moving over a scale l is small provided that l/l_c is small, i.e., the scale l lies deep in the inertial range. This conclusion is also empirically supported, in that the numerical results (Figure 2) show that at low energy the particle mean-free path is smaller than the correlation length of the magnetic field. For lower energy the local mean field, due to the large-scale parts of the spectrum, becomes increasingly coherent.

Making the assumption that the local mean field remains well defined for a long enough distance, we may examine whether the resonant scattering of particles on fluctuations with wavenumbers around the inverse of the Larmor radius (Jokipii 1966; Fisk et al. 1974) provides effective scattering, in the regime in which turbulence is weak compared to a locally evaluated large-scale mean magnetic field. Of course if the small-scale power is suppressed, then one recovers the FLRW result (see also Karimabadi et al. 1992; Mace et al. 2012).

In the presence of a guide field, the original quasilinear theory (Jokipii 1966) represents the standard tool for calculating resonant pitch-angle diffusion coefficients of particles. It is successful in predicting the resonant scattering of the particles in the case of a slab fluctuation field (wave vectors parallel to the mean field) but may require some modification in other fluctuation geometries (e.g., Qin et al. 2002). Nonlinear theories are also useful in attaining better agreement with the results of numerical simulations of particle propagation (Dupree 1966, 1967; Owens 1974; Matthaeus et al. 2003; Shalchi et al. 2004; Shalchi 2006).

In the present case of isotropic turbulence, with no guide field, the assumptions of QLT can no longer be applied, though we are encouraged to proceed based on the above reasoning concerning the local mean field. To be specific, it is useful to first put forward a physical explanation of the approach we propose to describe the low-energy regime: if the power spectrum of magnetic fluctuations is such that most power is on scales of the order of $\sim l_c$, then particles with Larmor radius much smaller than l_c move following a roughly ordered magnetic field line at least until a distance of $\sim l_c$ has been covered. On such scales, the propagation is diffusive in the direction of the local magnetic field, though particles suffer little motion in the direction perpendicular to that of the local field. Let us refer to this parallel diffusion coefficient as $\kappa_\parallel$, though the physical meaning of this quantity should be kept in mind. The effective velocity of particles in the direction of the local field is $v_p \simeq \kappa_\parallel/l_c$. When particles move over many times the coherence scale l_c, their transport in the directions perpendicular to the original local field becomes evident (due to isotropic turbulence) and one can estimate the global diffusion coefficient as

$$\kappa(p) = \frac{1}{3}L_c v_p \simeq \frac{1}{3}L_c\frac{\kappa_\parallel}{L_c} \simeq \frac{1}{3}\kappa_\parallel. \quad (27)$$

In other words, provided the propagation is diffusive on small scales, the global diffusion coefficient on large scales proceeds with a similar diffusion coefficient to that calculated using the local magnetic field as an effective local guide field. The problem is now reduced to calculating the diffusion coefficient experienced by particles along the local magnetic field. This can be done by using a close analogy to the case of QLT.

The parallel spatial diffusion coefficient $\kappa_\parallel$, is calculated using a well-known relationship between $\kappa_\parallel$ and the pitch-angle diffusion coefficient $D_{\mu\mu}$ (Jokipii 1966; Hasselmann &

Wibberenz 1970; Earl 1974),

$$\kappa_{\parallel} = \frac{v^2}{8}\int_{-1}^{1} d\mu\, \frac{(1-\mu^2)^2}{D_{\mu\mu}}. \quad (28)$$

The diffusion coefficient along a fixed direction (e.g., the x-direction) is given by

$$\kappa_{xx} = \kappa_{\parallel}\cos^2\theta + \kappa_{\perp}\sin^2\theta, \quad (29)$$

where θ is the angle between the magnetic field direction and the x-axis. Since the particles are expected to travel parallel to the local mean field and undergo resonant pitch-angle scattering, which eventually causes a random walk in the parallel direction with little average perpendicular motion, we neglect $\kappa_{\perp}$ in Equation (29) and average over all directions to obtain

$$\kappa_{xx} = \kappa_{yy} = \kappa_{zz} = \kappa_{\parallel}/3, \quad (30)$$

consistent with Equation (27).

Using the TGK formula, the pitch-angle diffusion coefficient is given by

$$D_{\mu\mu}(\mu) = \int_0^{\infty} dt\, \langle \dot{\mu}\dot{\mu}'\rangle, \quad (31)$$

where μ is the pitch angle at time $t = 0$ and μ' is the pitch angle at a later time t. Particles are assumed to follow a local field line. The initial direction of the field line can be assumed without loss of generality to be the z-direction and using $v_z = \mu v$, we get

$$D_{\mu\mu}(\mu) = \frac{1}{v^2}\int_0^{\infty} dt\, \langle \dot{v}_z\dot{v}_z'\rangle.$$

Using Equation (10), one can write

$$D_{\mu\mu}(\mu) = \frac{\alpha^2}{v^2}\int_0^{\infty} dt\, [\langle v_x v_x' b_y b_y'\rangle + \langle v_y v_y' b_x b_x'\rangle - \langle v_x v_y' b_y b_x'\rangle - \langle v_y v_x' b_x b_y'\rangle]. \quad (32)$$

The Cartesian x and y components of the velocities are given by

$$v_x = v_{\perp}\sin\phi_0 \quad v_y = v_{\perp}\cos\phi_0$$
$$v_x' = v_{\perp}\sin(\Omega t + \phi_0) \quad v_y' = v_{\perp}\cos(\Omega t + \phi_0), \quad (33)$$

where $v_{\perp} = v\sqrt{1-\mu^2}$ is the perpendicular component of the velocity, Ω is the local gyrofrequency, and ϕ_0 is the initial gyrophase of the particle motion. Assuming the product $b_i b_j'$ is independent of ϕ_0, assuming axi-symmetry of magnetic fluctuations along the local mean field ($\langle b_x b_x'\rangle = \langle b_y b_y'\rangle$ and $\langle b_x b_y'\rangle = \langle b_y b_x'\rangle$), using elementary identities and after averaging over the initial gyrophase ϕ_0, Equation (32) reduces to

$$D_{\mu\mu}(\mu) = \frac{\alpha^2 v_{\perp}^2}{v^2}\left[\int_0^{\infty} dt\, \cos(\Omega t)\langle b_y b_y'\rangle\right]. \quad (34)$$

The Lagrangian two-time correlation function $\langle b_y b_y'\rangle = \langle b_y(0,0) b_y(\boldsymbol{x}(t), t)\rangle$ is greatly simplified using the QLT-like assumption that the particles locally follow straight magnetic field lines in the z-direction with constant pitch angle, so that $z = v\mu t$. Using Corrsin's hypothesis (Corrsin 1959), which is exact for slab fluctuations that vary only along z, the Fourier transform of the correlation function $\langle b_y b_y'\rangle$ in terms of the power spectrum $P_{yy}(\boldsymbol{k})$ becomes

$$\langle b_y b_y'\rangle = \int\int\int dk_x dk_y dk_z P_{yy}(\boldsymbol{k}) e^{ik_z v\mu t}\langle e^{ik_x x} e^{ik_y y}\rangle. \quad (35)$$

In the following two subsections, we proceed to evaluate Equation (35) by adopting different approximations for the characteristic functional $\langle e^{ik_x x} e^{ik_y y}\rangle$ that describes the statistics of the local random perpendicular displacements $x(t)$ and $y(t)$.

5.1. Standard QLT Approach

When the perpendicular displacements $x(t)$, $y(t)$ are very small, we may adopt the approximation $\langle e^{ik_x x} e^{ik_y y}\rangle \approx 1$. This can be viewed as an approximation that the particle is at its guiding center, or that the fluctuations b_x and b_y are independent of x and y. This approximation is implemented in standard QLT, and is exact in one-dimensional slab geometry (Jokipii 1966). Using this in Equation (35), one finds

$$\langle b_y b_y'\rangle = \int dk_z \left[\int\int dk_x dk_y P_{yy}(\boldsymbol{k})\right] e^{ik_z v\mu t}. \quad (36)$$

In the usual way, we define $E_y(k_z) = \int\int P_{yy}(\boldsymbol{k}) dk_x dk_y$ as a one-dimensional reduced transverse spectrum function. Substituting Equation (36) in Equation (34), and carrying out the time integral yields a Dirac delta function that defines the resonance. Then, the integral over the parallel wave number (k_z) gives

$$D_{\mu\mu} = \frac{\pi\alpha^2(1-\mu^2)}{v}\left[\frac{E_y\left(k_z = \frac{\Omega}{v|\mu|}\right)}{|\mu|}\right], \quad (37)$$

which is the standard QLT result.

One modification applicable to isotropic turbulence that we would like to discuss in detail is related to the μ dependence of $D_{\mu\mu}$ in Equation (37). It is well known that quasilinear theory does not provide correct pitch-angle diffusion coefficients for pitch angles close to 90° ($\mu \approx 0$) where nonlinear effects are important (Bieber et al. 1988; Tautz et al. 2008; Shalchi 2009, p. 362). This problem was discovered in the years after quasilinear theory had been proposed (Kaiser et al. 1978; Owens 1974; Goldstein 1976). The strict quasilinear calculation using Equation (37) (for typical spectra of turbulence) has $D_{\mu\mu} \to 0$ as $\mu \to 0$, which is applicable in slab turbulence (Qin & Shalchi 2009) where nonlinear effects are weak. In most other geometries, however, for any realistic finite amplitude fluctuations, nonlinear orbit effects (Karimabadi et al. 1992) allow particles to scatter more easily through the neighborhood of $\mu = 0$ than would be expected from QLT calculations (see also Qin & Shalchi 2009). Our numerical results also indicate that the quasilinear theory for isotropic turbulence as derived using Equations (28), (30), and (37) gives mean-free paths much larger than those obtained from a numerical simulation, since the parallel diffusion coefficient is unrealistically amplified by $D_{\mu\mu}$ near zero in the denominator.

To account for such nonlinear effects, we consider an ansatz that the pitch-angle dependence of $D_{\mu\mu}$ is of the form $D_{\mu\mu} \propto 1-\mu^2$ and set $|\mu| = 1$ inside the square bracket of Equation (37) so that $D_{\mu\mu}$ has a finite nonzero value at $\mu = 0$. Before implementing this, we checked our numerical simulation results for the pitch-angle distribution. For $D_{\mu\mu} \propto 1-\mu^2$ (isotropic scattering), the eigenfunctions of the diffusion

operator are Legendre polynomials, and at late times when the pitch-angle distribution is nearly isotropic, the distribution should be dominated by the most slowly evolving eigenfunctions, $P_0 = 1$ and $P_1 = \mu$, yielding a nearly linear pitch-angle distribution. We indeed found this in our simulation data. Thus we implemented the ansatz, which is more appropriate for our case of isotropic turbulence with $B_0 = 0$ than for a perturbative situation with $b \ll B_0$, where nonlinear effects are weak. The ansatz is also justified a posteriori in Section 6, where the theoretical predictions now provide a much better fit to the numerical results.

With this physically motivated modification, the simplified pitch-angle diffusion coefficient can be written as

$$D_{\mu\mu} = \frac{\pi\alpha^2(1-\mu^2)}{v} E_z\left(k_z = \frac{\Omega}{v}\right). \tag{38}$$

If we assume that the local mean field is constant throughout the system with magnitude $B_{\rm local}$, then in Kolmogorov turbulence $E_z \sim k_z^{-5/3}$ and (from Equation (10)) $\alpha = \Omega/B_{\rm local}$ with $\Omega = v/R_L$, it is straightforward to show that the substitution of Equation (38) into (28) gives $\kappa \sim v l_c (R_L/l_c)^{1/3}$ and the mean-free path (Equation (7)) scales as $\lambda \sim l_c (R_L/l_c)^{1/3}$.

A further correction that we apply here is related to the variability of the magnetic field strength in an isotropic random field. In the realization of turbulence used here, the components of the magnetic field have a Gaussian distribution (this is also usually a reasonable approximation for fully developed turbulence). Therefore, the gyrofrequency $\Omega = qb/(\gamma mc) = \alpha b$ and Larmor radius $R_L = \gamma mvc/(qb) = v/(\alpha b)$ vary in space as the magnetic field strength b changes. In fact, b is likely to undergo major changes during the parallel scattering process described by $\kappa_{||}$. It is fairly simple to show that b has a Maxwellian distribution given by

$$\mathcal{F}(b)db = 3^{3/2}\sqrt{\frac{2}{\pi}}\frac{b^2}{\delta b^3} e^{-\frac{3b^2}{2\delta b^2}} db, \tag{39}$$

where δb is the root-mean-square field strength. With the above Maxwellian distribution, we use Equation (38) to compute the average $\overline{D_{\mu\mu}(\mu)}$ over the local field b before substitution in Equation (28) to obtain

$$\kappa_{||} = \frac{v^2}{8}\int_{-1}^{1} d\mu \frac{(1-\mu^2)^2}{\overline{D_{\mu\mu}}}. \tag{40}$$

Equation (30) gives the spatial diffusion coefficient along a particular axis. The mean-free path scaling of $\lambda \sim l_c (R_L/l_c)^{1/3}$ is also maintained.

5.2. Extended Low-energy Theory

As an extension to the above quasilinear approach, we now take into account the perpendicular displacements that enter into consideration in Equation (35). Assuming a Gaussian distribution of the perpendicular displacements x and y implies that

$$\langle e^{ik_x x} e^{ik_y y}\rangle = e^{-\frac{1}{2}[\langle x^2\rangle k_x^2 + \langle y^2\rangle k_y^2]}. \tag{41}$$

Since we are assuming locally an unperturbed orbit about a well-defined local mean magnetic field, it is clear that $\langle x^2\rangle = \langle y^2\rangle \sim R_L^2$. In particular, for pitch-angle θ and gyrophase ϕ,

$$x = R_L \sin\theta\cos\phi, \quad y = R_L \sin\theta \sin\phi. \tag{42}$$

After omnidirectional averaging of x^2 and y^2 over θ and ϕ, Equation (41) can be written as

$$\langle e^{ik_x x} e^{ik_y y}\rangle = e^{-k_\perp^2 R_L^2/6}, \tag{43}$$

where $k_\perp^2 = k_x^2 + k_y^2$. This statistical description of the perpendicular displacement is consistent with our earlier assumption that $b_i b_j'$ is independent of the initial gyrophase. Using Equation (34) along with Equations (35) and (43), one finds

$$D_{\mu\mu}(\mu) = \frac{2\pi^2\alpha^2(1-\mu^2)}{v} \times \int_0^\infty k_\perp dk_\perp \left[\frac{P_{yy}\left(k_\perp, k_z = \frac{\Omega}{v|\mu|}\right)}{|\mu|}\right] e^{-k_\perp^2 R_L^2/6}. \tag{44}$$

According to the arguments used in Section 5.1, we take into account the presence of nonlinear orbit effects near a 90° pitch angle and modify the pitch-angle dependence so that $D_{\mu\mu} \sim (1-\mu^2)$ and set $|\mu| = 1$ inside the square bracket of Equation (44). For the extended case, the pitch-angle diffusion coefficient is now given by

$$D_{\mu\mu}(\mu) = \frac{2\pi^2\alpha^2(1-\mu^2)}{v} \times \int_0^\infty k_\perp dk_\perp P_{yy}\left(k_\perp, k_z = \frac{\Omega}{v}\right) e^{-k_\perp^2 R_L^2/6}. \tag{45}$$

Note that when the exponential term is set to unity (e.g., for $R_L \to 0$), this reduces to Equation (38). As described in Section 5.1, we average Equation (45) over a Maxwellian distribution of the magnetic field magnitude b before substitution in Equation (28) to obtain our final result for the spatial diffusion coefficient.

The exponential term can be seen as another modification to the original quasilinear theory appropriate for the pitch-angle diffusion of low-energy particles in isotropic turbulence. Hence, we use this extended low-energy theory in the following Section 6 to compare with numerical simulation results.

6. Comparison with the Numerical Simulation

In this section, we present results of numerical simulations of charged particle propagation in synthetic magnetostatic turbulence with a specified spectrum. The numerical results are compared to the theoretical formulations described above.

The numerical simulations make use of a homogeneous and isotropic magnetic fluctuation field, generated on a spatial grid with a specified energy spectrum. Trajectories of 2000 particles are obtained by numerical solution of the Newton–Lorentz equation, using a fifth-order Runge–Kutta method with adaptive time-stepping. To satisfy the magnetostatic assumption, the velocity v of the particles is chosen so that $v \gg v_A$, where v_A is the Alfvén speed. The electric field is ignored because it is of the order of $v_A B/c$, where B is the magnetic field and c is the speed of light.

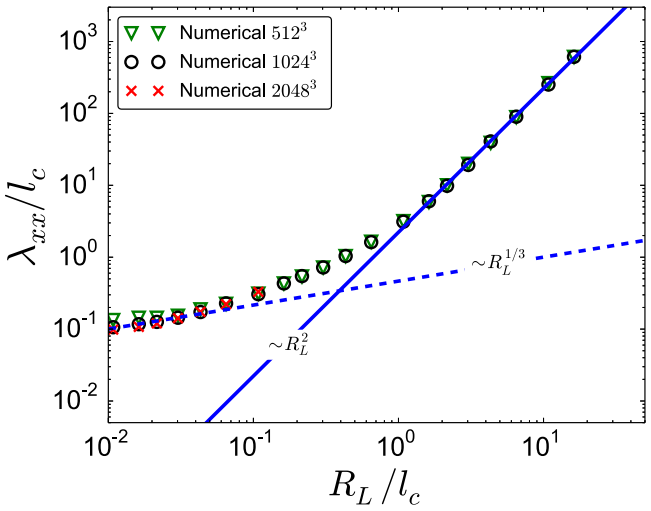


Figure 1. Mean-free path of protons as a function of R_L/l_c (gyroradius divided by correlation scale). The solid line is the high-energy scaling $\lambda_{xx} \sim R_L^2$ and the dashed line is the low-energy scaling $\lambda_{xx} \sim R_L^{1/3}$. The inverted triangles are the results of the 512^3 numerical simulation, circles are those of the 1024^3 simulation, and the crosses are the results of the 2048^3 numerical simulation.

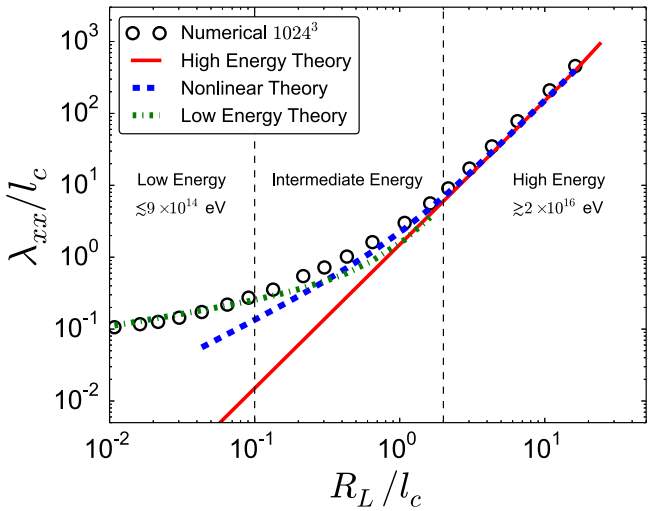


Figure 2. Theoretical vs. numerical results for cosmic rays in isotropic turbulence with a zero mean field, showing good agreement. The circles represent the numerical results, the solid line represents the high-energy theory, the dashed line is the nonlinear theory and the dotted–dashed line is the theoretical estimate for low energies. The energy ranges are shown for cosmic rays in our Galaxy.

The random magnetic field realization is generated in a periodic box as described by Sonsrettee et al. (2015). The functional form of the omnidirectional spectrum used in the numerical simulation is given by

$$E(k) = C\lambda_c \frac{(k\lambda_c)^4}{[1 + (k\lambda_c)^2]^{17/6}},$$

with a normalization constant C, which is used to control the magnetic field strength b. The parameter λ_c is the bendover scale, which is of the same order as the correlation length. This form of $E(k)$ is chosen so that $E(k) \propto k^4$ for low k to be consistent with strict homogeneity (Batchelor 1969), and $E(k) \propto k^{-5/3}$ for high k to represent Kolmogorov scaling in an inertial range of turbulence. We have chosen the Kolmogorov spectrum which is often employed in scattering theory (Harari et al. 2002; Parizot 2004), but emphasize that the theoretical approach can be applied to any reasonable spectrum.

The diffusion coefficient is calculated from the asymptotic rate of increase of the mean square displacement of the particles

$$\kappa_{xx} = \lim_{t\to\infty} \frac{\langle \Delta x^2 \rangle}{2\Delta t}. \quad (46)$$

The results of the numerical simulations are shown in Figure 1. The general asymptotic trends for the mean-free path at low energies ($R_L \ll l_c$) and high energies ($R_L \gg l_c$) are easy to identify. In the low-energy regime, the mean-free path scales as $\lambda_{xx} \propto R_L^{1/3}$, while in the high-energy regime $\lambda_{xx} \propto R_L^2$, and these scalings are valid whether the particles are relativistic or non-relativistic. As discussed above, this high-energy scaling is obtained irrespective of the power spectrum, provided most power is concentrated on scales around $\sim l_c$. These results confirm previous functional forms proposed by Aloisio & Berezinsky (2004) and Parizot (2004) and the numerical results of Casse et al. (2002), de Marco et al. (2007), and Snodin et al. (2016). Observations of isotopic composition (Obermeier et al. 2012; Aguilar et al. 2016) also support a scaling of $\lambda_{xx} \propto R_L^{1/3}$ at $R_L \ll l_c$.

The resonant nature of particle scattering in the low-energy regime makes the numerical simulation rather challenging, in that the resulting mean-free path is sensetive to the resolution in real space, which is equivalent to the number of independent degrees of freedom in k-space used to represent the magnetic power spectrum (see also Snodin et al. 2016). In Figure 1, we show the results of our simulations for 512^3, 1024^3, and 2048^3 real space grid points, from which it is possible to see that the lower resolution (512^3) case does not correctly match the scaling of the mean-free path with Larmor radius. This is because the 512^3 simulation does not numerically resolve the resonant scales corresponding to the Larmor radius of the particles. On the other hand, no appreciable difference can be seen in the two higher resolution cases with 1024^3 and 2048^3 simulations. Hence, we will use the 1024^3 realization for a subsequent discussion of the results.

The mean-free path calculated using the theoretical framework developed above is compared to the results of simulations in Figure 2. These results may be considered as representative of propagation of very-high-energy CR protons in the Galactic magnetic field (Ruzmaikin et al. 1988) with a correlation length of $l_c = 10\,\mathrm{pc}$ and a root-mean-square magnetic field of $\delta b = 0.1\,\mathrm{nT}$. The Larmor radius of the particles equals the correlation length of the magnetic field fluctuations at energy $E \sim 9 \times 10^{15}\,\mathrm{eV}$, somewhat above the knee in the all-particle spectrum of Galactic CRs. However, we note that when plotted this way, as mean-free path versus Larmor radius, with both quantities normalized to the correlation scale of the turbulence, the actual curves are identical for any energy range. In Appendix C, we provide a short account of the results of our analysis when applied to non-relativistic and moderately relativistic particles in isotropic turbulence that has parameters akin to heliospheric parameters.

7. Discussion and Conclusions

The spatial diffusion of charged particles in the presence of turbulent magnetic fields is significant in describing the

transport of charged particles in the interplanetary, interstellar, and intergalactic media. Most of the standard descriptions of diffusion involve the existence of a non-negligible ordered field. In this paper, we considered the case of a vanishingly small background ordered magnetic field and studied the diffusive transport of charged particles in isotropic magnetic field (magnetostatic) turbulence. The turbulent Galactic magnetic field, where the mean magnetic field is of the order of fluctuations, is found to have reversals in the field orientation implying the existence of regions with negligible regular fields (Minter & Spangler 1996). Similarly the extragalactic voids might have negligible regular fields (Kronberg 1994; Blasi et al. 1999). In the highly turbulent plasma near supernova shocks that are actively accelerating CRs (Blasi 2013) there may be regions in which the fluctuations might be so large that the present fully isotropic model is applicable. The isotropic assumption is also relevant in other highly disturbed and turbulent plasmas, such as planetary wakes (Gombosi et al. 1979).

Naturally, in the Galactic system, the turbulent magnetic field is not the only complication that appears in a realistic scenario of CR transport. The complex composition of background plasma and the presence of neutral hydrogen atoms that suppress the propagation of waves through ion-neutral damping are examples of factors that could influence the charged particle propagation. Including these complexities in our theoretical calculations is beyond the scope of the current paper. Here we have developed a systematic derivation of charged particle diffusion in the presence of an isotropic turbulent magnetic field and tested its validity using a Monte-Carlo simulation of particles in a synthetically generated turbulent magnetic field. In fact, we would like to point out that incorporating the several factors mentioned above will probably require MHD, hybrid, or PIC simulations that provide a self-consistent picture of the development of the CR transport phenomenon (e.g., Reville et al. 2008; Caprioli & Spitkovsky 2014).

The transport of charged particles in a magnetic field is conceptually simple, requiring mostly the integration of particle trajectories using the Lorentz force (Equation (10)). The detailed treatment is complex, influenced by several parameters like the particle energy, correlation length of turbulence, the geometry of fluctuations, the presence of a dissipation range, and the magnetic Reynolds number. In particular, the study of transport of particles in isotropic magnetic field turbulence is found to be complicated by the different conditions seen by charged particles at high, low, and intermediate energies as defined. Here the controlling parameter is the rigidity, or the ratio of Larmor radius (R_L) to the turbulence correlation length (l_c). When the ratio R_L/l_c is much smaller than one, we refer to the low-energy limit, when it is greater than one, this is the high-energy limit and in between low and high energy lies the intermediate-energy region. We have devised two different theoretical models in an attempt to understand the transport processes in these three regions. Rather than just using parametric and scaling arguments, we provide systematic and thorough theoretical constructs to describe the diffusive transport of particles in each range of energy.

The paths of the higher energy particles are almost straight up to the correlation length of the magnetic field, where the particles undergo only a slight change from the original trajectory. In contrast, the lower energy particles are almost strictly tied to their initial field lines and are pitch-angle scattered due to resonance with small-scale irregularities of the field line. The intermediate-energy particles have a more complicated nonlinear diffusion that connects the two extremes.

The theoretical ideas presented here have been tested against results of detailed numerical experiments using Monte-Carlo simulations of particle propagation in stochastic magnetic fields. The magnetic field constructed for numerical purposes has three-dimensional isotropic fluctuations with a standard Kolmogorov spectrum and no mean field. Diffusion coefficients are calculated using the microscopic displacements of particles along the trajectory. The diffusion coefficients obtained using our numerical simulation are compared to theoretical predictions yielding very good agreement.

Referring again to Figure 2, we can see that both the asymptotic low- and high-energy limits are fitted well by our theoretical approach. The high-energy theory fails in the intermediate- and low-energy regime because the particle velocity changes over a shorter period of time, contrary to the high-energy assumption. The extended low-energy theory compares well with the numerical data even in the intermediate-energy regime when $R_L/l_c \lesssim 0.5$. However, it fails when $R_L/l_c \gtrsim 0.5$ as a consequence of the fact that the effective guide field becomes ill-defined. The nonlinear theory best describes the scattering of the intermediate-energy particles in the range of $R_L/l_c \gtrsim 0.5$. The two extended theories give equal results at $R_L/l_c \approx 0.3$ where they each differ from the numerical results by about 30%.

In summary, we have devised theoretical descriptions of charged particles in isotropic turbulence with no mean field that are applicable to distinct ranges of particle energies. Different reasoning enters in the various ranges of rigidity R_L/l_c. Properly normalized, the results apply equally well to relativistic and non-relativistic particle transport, provided that the random magnetic field is isotropic with zero mean.

This research is supported in part by the NSF Solar Terrestrial Program Grant AGS-1063439 and SHINE grant AGS-1156094, the NASA Heliophysics Grand Challenge Research Theory & Modeling Program, NNX14AI63G, the MMS Theory and Modeling project, the Solar Probe Plus project, POR Calabria FSE-2007/2013, EU Turboplasmas project, and by grant RTA5980003 from the Thailand Research Fund. M.W. acknowledges the support from the National Natural Science Foundation of China (NSFC Grant No. 11672123).

Appendix A
Relation between Diffusion Coefficients in Velocity Space and Position Space

We proceed using spatial and temporal variables divided into slow variables X and T, and fast variables ξ and τ, respectively. The slow and the fast variables can be written in terms of a small parameter ϵ as

$$T = \epsilon^2 t, \quad X = \epsilon x$$
$$\tau = t, \quad \xi = x\,.$$

The motivation for different time ordering when compared to the spatial ordering comes from the fact that, if we let ϵ be the ratio of scattering length scale to the transport length scale, then from the spatial diffusion equation a simple dimensional

analysis shows that the ratio of scattering timescale to the transport timescale should be of the order of ϵ^2 (see, e.g., Frisch 1995).

The derivatives can then be written as

$$\frac{\partial}{\partial t} = \frac{\partial}{\partial \tau} + \epsilon^2 \frac{\partial}{\partial T},$$
$$\nabla_x = \nabla_\xi + \epsilon \nabla_X.$$

Considering Equation (3) (Fokker–Plank equation), we seek a solution for the distribution function f with

$$f = f^{(0)} + \epsilon f^{(1)} + \epsilon^2 f^{(2)} + ..., \quad (47)$$

where each order of f can be expanded in terms of the spherical harmonics $Y_{lm}(\theta, \phi)$ (Equation (5)), which satisfy

$$v^2 \nabla_\perp^2 Y_{lm}(\theta, \phi) = [-l(l+1)] Y_{lm}(\theta, \phi). \quad (48)$$

The expansion in Equation (47) is inserted into Equation (4). With the help of Equations (5) and (48), we get separate equations for each of the different orders of f.

The $O(\epsilon^0)$ terms give

$$\frac{\partial f^{(0)}}{\partial \tau} + \boldsymbol{v} \cdot \nabla_\xi f^{(0)} = D_v \nabla_\perp^2 f^{(0)}. \quad (49)$$

Now we introduce an operator $\langle \cdots \rangle$, which is the spacetime average over the fast variables. Since all variables will be assumed to have finite variations in time and space, the averaging operator gives a zero result when operating on any quantity that may be written as a derivative with respect to fast variables. This is also known as the solvability condition so that we have a closed form of equations. Also, let $\langle f^{(q)} \rangle = F^{(q)}$.

Equation (49) averaged over the fast variables gives

$$D_v \nabla_\perp^2 F^{(0)} = 0, \quad (50)$$

which implies that $F^{(0)}$ is isotropic in $\boldsymbol{v}$.

Averaged over the fast variables, the $O(\epsilon^1)$ term is

$$\boldsymbol{v} \cdot \nabla_X F^{(0)} = D_v \nabla_\perp^2 F^{(1)}. \quad (51)$$

Without loss of generality, we may pick the direction of the gradient to be the z-direction. The left-hand side of Equation (51) has a projection only onto the Y_{10} term of the spherical harmonics. The right-hand side must also have a projection onto the Y_{10} term. With the help of Equations (5) and (48) in Equation (51), one finds

$$\boldsymbol{v} \cdot \nabla_X F^{(0)} = -2 \frac{D_v}{v^2} F^{(1)} \Rightarrow F^{(1)} = \frac{-v^2}{2D_v} \boldsymbol{v} \cdot \nabla_X F^{(0)}. \quad (52)$$

When averaged over the fast variables, the $O(\epsilon^2)$ term gives

$$\frac{\partial F^{(0)}}{\partial T} + \boldsymbol{v} \cdot \nabla_X F^{(1)} = D_v \nabla_\perp^2 F^{(2)}. \quad (53)$$

Substituting the relation between $F^{(1)}$ and $F^{(0)}$ from Equation (52) into Equation (53), one gets

$$\frac{\partial F^{(0)}}{\partial T} - \frac{v^2}{2D_v} (v_i v_j \nabla_{X_i} \nabla_{X_j}) F^{(0)} = D_v \nabla_\perp^2 F^{(2)}, \quad (54)$$

where a repeated index indicates summation. To study the diffusion of the bulk distribution, we consider the average over all directions. From Equation (48), we see that the right-hand side of Equation (54) averages to zero. Using

$$[v_i v_j]_{\text{direction averaged}} = \frac{v^2}{3} \delta_{ij}, \quad (55)$$

we then obtain

$$\frac{\partial F^{(0)}}{\partial T} = \frac{v^4}{6D_v} \nabla_X^2 F^{(0)}. \quad (56)$$

This is a diffusion equation in configuration space with diffusion coefficient

$$\kappa = \frac{v^4}{6D_v}.$$

Appendix B
Angular Deflection of a Magnetic Field Line Over an Inertial Range of Turbulence

We examine the angular deflection of a field line over a separation l from the perspective of turbulence theory. The magnetic field vector and its associated field lines experience a change of direction due to the turbulence. If we initially start with no transverse component, then the transverse component at a separation l in the inertial range of turbulence can be estimated approximately for an ensemble of field lines by Kolmogorov's law.

Let $S_2^t(l)$ be the second-order transverse structure function with separation l. Kolmogorov's 2/3 law states that

$$S_2^t(l) = \delta b_l^2 = \langle [b_t(\boldsymbol{x}) - b_t(\boldsymbol{x} + l)]^2 \rangle \propto l^{2/3}.$$

If $S_2^t(l_c)$ is the second-order transverse structure function at a separation of a correlation length l_c, then one finds

$$\frac{\delta b_l^2}{\delta b_c^2} = \left(\frac{l}{l_c} \right)^{2/3}.$$

Initially, there is no transverse component and if approximately 2/3 of the energy is present in the transverse component at the correlation length, then

$$\delta b_l^2 \approx \frac{2}{3} \delta b^2 \left(\frac{l}{l_c} \right)^{2/3},$$

and

$$\frac{\delta b_l}{|\delta b|} \approx 0.8 \left(\frac{l}{l_c} \right)^{1/3}.$$

If θ is the angular deflection at the mean-free path of a particle λ, then

$$\sin\theta = \frac{\delta b_l}{|\delta b|} \approx 0.8 \left(\frac{\lambda}{l_c} \right)^{1/3}.$$

For $R_L/l_c = 0.01$, which is relevant for a low energy that is numerically attainable, our numerical results give $\lambda = 0.1\, l_c$, implying $\theta \approx 20^0$. At lower particle energy, the relevant angular deflection is still smaller. We neglect this deflection in the low-energy quasilinear theory presented in Section 5.

Appendix C
Non-relativistic Example

To provide a broader context, in Figure 3, we evaluate the theory for the case of non-relativistic particles or moderately

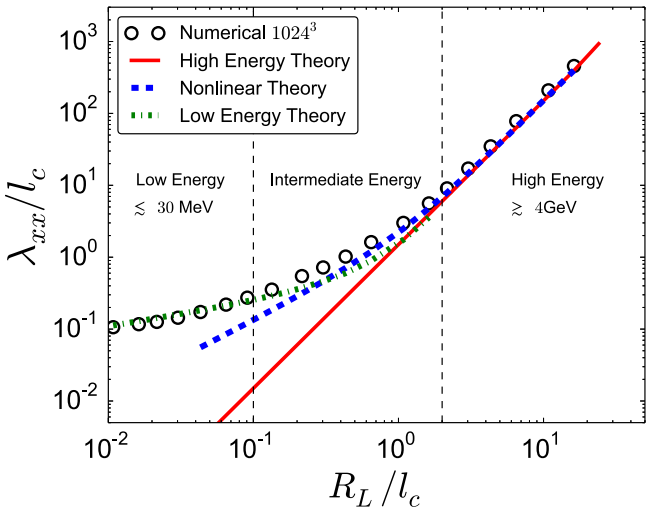


Figure 3. Theoretical vs. numerical results for non-relativistic or moderately relativistic charged particles in isotropic turbulence with zero mean field for parameters as listed in Appendix C. The circles represent the numerical results, the solid line represents the high-energy theory, the dashed line is the nonlinear theory and the dotted–dashed line is the theoretical estimate for low energies. The energy ranges are shown for protons and magnetic field parameters for interplanetary turbulence. The results also apply to any non-relativistic particles of a given R_L/l_c.

relativistic particles. For convenience, we adopt parameters that closely resemble interplanetary space in our solar system, except that here no mean magnetic field is included. For this example, the particles are non-relativistic at low energies with $R_L/l_c < 1$, but become moderately relativistic at higher energies. The correlation length is chosen to be $l_c = 0.01$ au and the root-mean-square magnetic field to be 5 nT (Burlaga et al. 2013). Then $R_L = l_c$ at 1.5 GeV. The theoretical mean-free paths depend only on rigidity, and the test particle simulation is in close agreement whether the particles are relativistic or non-relativistic.

It is well known that the interplanetary turbulent magnetic field is represented by an anisotropic spectral model in which the fluctuations are of the same order of magnitude as the mean field. Numerous realistic studies have also been performed and compared with observational results in the past (e.g., Tautz & Shalchi 2013), so our study with isotropic turbulence and no background field should be interpreted as simply a test case.

References

Aguilar, M., Ali Cavasonza, L., Ambrosi, G., et al. 2016, PhRvL, 117, 231102
Aloisio, R., & Berezinsky, V. 2004, ApJ, 612, 900
Batchelor, G. K. 1953, The Theory of Homogeneous Turbulence (Cambridge: Cambridge Univ. Press)
Batchelor, G. K. 1969, PhFl, 12, II233
Bieber, J. W., & Matthaeus, W. H. 1997, ApJ, 485, 655
Bieber, J. W., Matthaeus, W. H., Shalchi, A., & Qin, G. 2004, GeoRL, 31, L10805
Bieber, J. W., Smith, C. W., & Matthaeus, W. H. 1988, ApJ, 334, 470
Blasi, P. 2013, A&ARv, 21, 70
Blasi, P., Burles, S., & Olinto, A. V. 1999, ApJL, 514, L79
Burlaga, L., Ness, N., & Stone, E. 2013, Sci, 341, 147
Caprioli, D. 2015, arXiv:1510.07042
Caprioli, D., & Spitkovsky, A. 2014, ApJ, 794, 47
Casse, F., Lemoine, M., & Pelletier, G. 2002, PhRvD, 65, 023002
Corrsin, S. 1959, in Advances in Geophysics, Atmospheric Diffusion and Air Pollution, Vol. 6, ed. F. Frenkel & P. Sheppard (New York: Academic), 161
de Marco, D., Blasi, P., & Stanev, T. 2007, JCAP, 2007, 027
Dupree, T. H. 1966, PhFl, 9, 1773
Dupree, T. H. 1967, PhFl, 10, 1049
Earl, J. A. 1974, ApJ, 193, 231
Fisk, L. A., Goldstein, M. L., Klimas, A. J., & Sandri, G. 1974, ApJ, 190, 417
Frisch, U. 1995, Turbulence. The Legacy of A. N. Kolmogorov (Cambridge: Cambridge Univ. Press)
Ghilea, M. C., Ruffolo, D., Chuychai, P., et al. 2011, ApJ, 741, 16
Goldstein, M. L. 1976, ApJ, 204, 900
Gombosi, T., Cravens, T. E., Nagy, A. F., Brace, L. H., & Owens, A. J. 1979, GeoRL, 6, 349
Green, M. S. 1951, JChPh, 19, 1036
Harari, D., Mollerach, S., & Roulet, E. 2002, JHEP, 7, 006
Hasselmann, K., & Wibberenz, G. 1970, ApJ, 162, 1049
Hauff, T., Jenko, F., Shalchi, A., & Schlickeiser, R. 2010, ApJ, 711, 997
Jansson, R., & Farrar, G. R. 2012, ApJ, 757, 14
Jokipii, J. R. 1966, ApJ, 146, 480
Jokipii, J. R., & Parker, E. N. 1968, PhRvL, 21, 44
Kaiser, T. B., Birmingham, T. J., & Jones, F. C. 1978, PhFl, 21, 361
Karimabadi, H., Krauss-Varban, D., & Terasawa, T. 1992, JGR, 97, 13
Kronberg, P. P. 1994, RPPh, 57, 325
Kubo, R. 1957, JPSJ, 12, 570
Mace, R. L., Dalena, S., & Matthaeus, W. H. 2012, PhPl, 19, 032309
Matthaeus, W. H., Qin, G., Bieber, J. W., & Zank, G. P. 2003, ApJL, 590, L53
Minter, A. H., & Spangler, S. R. 1996, ApJ, 458, 194
Obermeier, A., Boyle, P., Hörandel, J., & Müller, D. 2012, ApJ, 752, 69
Owens, A. J. 1974, ApJ, 191, 235
Parizot, E. 2004, NuPhS, 136, 169
Plotnikov, I., Pelletier, G., & Lemoine, M. 2011, A&A, 532, A68
Qin, G., Matthaeus, W. H., & Bieber, J. W. 2002, GeoRL, 29, 7
Qin, G., & Shalchi, A. , 2009, ApJ, 707, 61
Reville, B., O'Sullivan, S., Duffy, P., & Kirk, J. G. 2008, MNRAS, 386, 509
Ruffolo, D., Pianpanit, T., Matthaeus, W. H., & Chuychai, P. 2012, ApJL, 747, L34
Ruzmaikin, A. A., Sokoloff, D., & Shukurov, A. M. 1998, Magnetic Fields of Galaxies (Berlin: Springer)
Shalchi, A. 2006, A&A, 453, L43
Shalchi, A. 2009, Nonlinear Cosmic Ray Diffusion Theories (Berlin: Springer)
Shalchi, A. 2010, ApJL, 720, L127
Shalchi, A., Bieber, J. W., Matthaeus, W. H., & Qin, G. 2004, ApJ, 616, 617
Snodin, A. P., Shukurov, A., Sarson, G. R., Bushby, P. J., & Rodrigues, L. F. S. 2016, MNRAS, 457, 3975
Sonsrettee, W., Subedi, P., Ruffolo, D., et al. 2015, ApJ, 798, 59
Tautz, R. C., & Shalchi, A. 2013, JGRA, 118, 642
Tautz, R. C., Shalchi, A., & Schlickeiser, R. 2008, ApJL, 685, L165
Taylor, G. I. 1922, Proc. London Math. Soc, 20, 196

The Astrophysical Journal Letters, 839:L16 (5pp), 2017 April 10 https://doi.org/10.3847/2041-8213/aa6aa6
© 2017. The American Astronomical Society. All rights reserved.

Cosmic Rays in Intermittent Magnetic Fields

Anvar Shukurov[1], Andrew P. Snodin[2], Amit Seta[1], Paul J. Bushby[1], and Toby S. Wood[1]
[1] School of Mathematics and Statistics, Newcastle University, Newcastle Upon Tyne NE1 7RU, UK; a.seta1@ncl.ac.uk, amitseta90@gmail.com
[2] Department of Mathematics, Faculty of Applied Science, King Mongkut's University of Technology North Bangkok, Bangkok 10800, Thailand
Received 2017 February 8; revised 2017 March 12; accepted 2017 March 31; published 2017 April 12

Abstract

The propagation of cosmic rays in turbulent magnetic fields is a diffusive process driven by the scattering of the charged particles by random magnetic fluctuations. Such fields are usually highly intermittent, consisting of intense magnetic filaments and ribbons surrounded by weaker, unstructured fluctuations. Studies of cosmic-ray propagation have largely overlooked intermittency, instead adopting Gaussian random magnetic fields. Using test particle simulations, we calculate cosmic-ray diffusivity in intermittent, dynamo-generated magnetic fields. The results are compared with those obtained from non-intermittent magnetic fields having identical power spectra. The presence of magnetic intermittency significantly enhances cosmic-ray diffusion over a wide range of particle energies. We demonstrate that the results can be interpreted in terms of a correlated random walk.

Key words: cosmic rays – diffusion – dynamo – magnetic fields

1. Introduction

Cosmic rays are charged relativistic particles (mostly protons) scattered, as they propagate, by random magnetic fields (Berezinskii et al. 1990). Over sufficiently long time and length scales, their propagation is diffusive (Cesarsky 1980). Assuming an interstellar magnetic field of strength 5 μG, the Larmor radius $r_{\rm L}$ of a cosmic-ray proton of energy 5 GeV is of the order of 10^{12} cm, much smaller than the correlation length of interstellar MHD turbulence ($\sim 10^{20}$ cm). Thus, cosmic rays closely follow field lines (for a significant time), and so the geometry and statistical properties of magnetic fields control their propagation. The dominant contribution to particle scattering is from magnetic irregularities at a scale comparable to $r_{\rm L}$. In this Letter, we mostly discuss cosmic rays that propagate diffusively.

With some exceptions that are discussed below (see also Alouani-Bibi & le Roux 2014; Pucci et al. 2016), studies of cosmic-ray propagation employ random magnetic fields with Gaussian statistics that are completely described by the two-point correlation function or the power spectrum (e.g., Michalek & Ostrowski 1997; Giacalone & Jokipii 1999; Casse et al. 2002; Candia & Roulet 2004; Parizot 2004; DeMarco et al. 2007; Globus et al. 2008; Plotnikov et al. 2011; Harari et al. 2014; Snodin et al. 2016; Subedi et al. 2017). However, the interstellar and intergalactic magnetic fields have a more complicated structure. The fluctuation (small-scale) dynamo (Zeldovich et al. 1990; Wilkin et al. 2007) and random shock waves (Bykov & Toptygin 1987) produce highly intermittent, strongly non-Gaussian, essentially three-dimensional magnetic fields with random magnetic filaments and ribbons surrounded by weaker fluctuations. Filamentary and planar structures in the interstellar medium, consistent with the notion of spatial intermittency, have been detected in the radio (Section 5.2 in Haverkorn & Spangler 2013) and submillimeter (Zaroubi et al. 2015) ranges as well as in the neutral hydrogen distribution (Heiles & Troland 2005). In such a magnetic field, the propagation of charged particles is controlled not only by its power spectrum, but also by the size and separation of the magnetic structures. The influence of such a complex magnetic field upon cosmic-ray propagation is poorly understood. Existing theories, using the quasilinear approach (Jokipii 1966; Berezinskii et al. 1990; Schlickeiser 2002), or its nonlinear extensions and alternative ideas (e.g., Vlad et al. 1998; Yan & Lazarian 2002; Matthaeus et al. 2003; Shalchi 2009), do not consider intermittency, or use the Corrsin hypothesis (Corrsin 1959), which assumes Gaussian statistics for the magnetic field. Recent test particle simulations used magnetic fields obtained from simulations of MHD turbulence (e.g., Dmitruk et al. 2004; Reville et al. 2008; Beresnyak et al. 2011; Lynn et al. 2012; Weidl et al. 2015; Cohet & Marcowith 2016) (see also Roh et al. 2016). These models are free from the assumption of Gaussian statistics, but they do not consider any effects of magnetic structures even if those were present. There have been no systematic attempts to examine the significance of realistic, physically realizable magnetic intermittency in 3D; this is our goal here. In intermittent magnetic fields, particle trapping can be important even in 3D. We note that the Kubo number, often used to delineate different transport regimes, depends only on second-order correlations and is therefore insensitive to intermittency.

We use test particle simulations (Giacalone & Jokipii 1999; Casse et al. 2002; Desiati & Zweibel 2014; Snodin et al. 2016), integrating the equation of motion for a large number of particles in a statistically isotropic, prescribed magnetic field, in the regime where cosmic-ray pressure is too low to excite significant MHD waves. The magnetic field is obtained as a solution of the induction equation with a prescribed velocity field that drives the fluctuation dynamo. This produces a realistic, intermittent magnetic field. The degree of intermittency depends on the magnetic Reynolds number $R_{\rm m}$. As $R_{\rm m}$ increases, the magnetic structures occupy a smaller proportion of the volume. The intermittency introduces two distinct particle propagation regimes, one within a magnetic structure and another between them. Cosmic-ray particles are strongly scattered by the magnetic structures and move relatively freely between them. By comparing particle diffusion in an intermittent field with that in a magnetic field lacking structure, but with an identical power spectrum, we demonstrate that intermittency can significantly enhance diffusion, and so diffusion cannot be described in terms of the power spectrum alone.

2. Magnetic Field Produced by Dynamo Action

We generate intermittent, statistically isotropic, fully three-dimensional random magnetic fields $\boldsymbol{b}$ by solving the induction equation with a prescribed velocity field $\boldsymbol{u}$:

$$\frac{\partial \boldsymbol{b}}{\partial t} = \nabla \times (\boldsymbol{u} \times \boldsymbol{b}) + R_{\rm m}^{-1}\nabla^2 \boldsymbol{b}, \qquad \nabla \cdot \boldsymbol{b} = 0, \qquad (1)$$

with periodic boundary conditions in a cubic domain of width $L = 2\pi$ and 256^3 or 512^3 mesh points. Equation (1) is written in a dimensionless form, expressing length in the units of the flow scale l_0 and time in the units of l_0/u_0, where u_0 is the rms flow speed. Here, $R_{\rm m} = l_0 u_0/\eta$ is the magnetic Reynolds number[3] and η is the magnetic diffusivity, assumed to be constant. In a generic, three-dimensional, random flow, dynamo action occurs (i.e., the mean magnetic energy density grows exponentially with t) provided $R_{\rm m} > R_{\rm m,c}$, where $R_{\rm m,c}$ is the critical magnetic Reynolds number (Zeldovich et al. 1990). Depending on the nature of the velocity field, typically $R_{\rm m,c} \simeq 10$–100, and the magnetic field decays for $R_{\rm m} < R_{\rm m,c}$ (Brandenburg & Subramanian 2005). As $R_{\rm m} \to \infty$, the magnetic structures produced by the dynamo become progressively more filamentary in nature, with the thickness of each filament of the order of $d = l_0 R_{\rm m}^{-1/2}$ and a characteristic filament length (radius of curvature) of the order of l_0 (Zeldovich et al. 1990; Wilkin et al. 2007). The magnetic field used in our simulations is an eigenfunction obtained by renormalizing the exponentially growing solution of Equation (1) to have a constant rms field strength b_0. We expect the magnetic structure of the corresponding nonlinear dynamo to be similar to that of the marginal eigenfunction obtained at $R_{\rm m} \approx R_{\rm m,c}$ (Subramanian 1999). However, we consider a wider range of $R_{\rm m}$ to explore the effects of a variable degree of intermittency: it increases with $R_{\rm m}$. To isolate robust features of cosmic-ray propagation independent of the particular form of intermittent magnetic field, we use two types of incompressible flow to drive the dynamo, both chaotic, but one of a single scale and the other multi-scale with a controlled power spectrum. The first flow (Willis 2012), henceforth referred to as flow W, is stationary:

$$\boldsymbol{u}(\boldsymbol{x}) = (2/\sqrt{3})(\sin y \cos z,\ \sin z \cos x,\ \sin x \cos y). \qquad (2)$$

It is a very efficient dynamo with $R_{\rm m,c} \approx 11$, producing regularly spaced magnetic structures in the form of ellipsoids of identical size that become thinner as $R_{\rm m}$ increases and whose positions are determined solely by the flow geometry (so are independent of $R_{\rm m}$). The second flow (KS) is time-dependent and multi-scale; it was employed for dynamo simulations (Wilkin et al. 2007) and as a Lagrangian model of turbulence (Fung et al. 1992):

$$\boldsymbol{u}(\boldsymbol{x}, t) = \sum_{n=0}^{N-1} (\boldsymbol{C}_n \cos\phi_n + \boldsymbol{D}_n \sin\phi_n), \qquad (3)$$

where $\phi_n = \boldsymbol{k}_n \cdot \boldsymbol{x} + \omega_n t$, with $\boldsymbol{k}_n$ a randomly oriented wave vector (of magnitude k_n) and ω_n a frequency specified below. The random vectors, $\boldsymbol{C}_n$ and $\boldsymbol{D}_n$, are chosen to be orthogonal to $\boldsymbol{k}_n$ to ensure $\nabla \cdot \boldsymbol{u} = 0$. We select $N = 40$ distinct wave vectors, with magnitudes between $k_0 = 2\pi/L$ and $k_{N-1} \approx 8k_0$, so that the flow is periodic with the outer scale $l_0 = L$. The amplitudes of $\boldsymbol{C}_n$ and $\boldsymbol{D}_n$ are selected to produce an energy spectrum $E(k) \propto k^{-5/3}$ with $\int_{k_0}^{k_{N-1}} E(k)dk = u_0^2/2$. We take $\omega_n = [k_n^3 E(k_n)]^{1/2}$, which introduces a scale-dependent time variation. The dynamo in this flow has $R_{\rm m,c} \approx 1000$ (Wilkin et al. 2007). The flow produces transient magnetic structures, consisting of filaments of various sizes, as illustrated in the leftmost panel of Figure 1.

To identify the effects of magnetic intermittency on cosmic-ray diffusion, we also consider random magnetic fields where the structures have been destroyed but the magnetic energy spectrum remains unchanged (Snodin et al. 2013). This is achieved by taking the spatial Fourier transform of $\boldsymbol{b}(\boldsymbol{x})$ from Equation (1) and then multiplying each complex Fourier mode by $\exp[i\psi(\boldsymbol{k})]$, with $\psi(\boldsymbol{k})$ a random phase selected independently for each $\boldsymbol{k}$. The inverse Fourier transform of the result produces a magnetic field with an unchanged spectrum but with little remaining structure, as demonstrated in the second from left panel of Figure 1. As shown in the second from right panel of Figure 1, the probability density functions (PDFs) of the field components for the intermittent fields produced by each flow (W and KS) have long, heavy tails, while the phase randomization produces nearly Gaussian random fields. Another aspect of this difference is also illustrated in the rightmost panel of Figure 1 where the fractional volume occupied by magnetic structures with $b/b_0 > \nu$ is shown as a function of ν: an intermittent magnetic field has more strong, localized structures with $\nu \gtrsim 1.4$ than a Gaussian field with an identical power spectrum.

To explore the effects of a mean magnetic field, we also consider particle propagation in a magnetic field given by $\boldsymbol{B} = \boldsymbol{b} + \boldsymbol{B}_0$, where $\boldsymbol{B}_0$ is an imposed uniform magnetic field. In such cases, the rms magnetic field $\tilde{b}_0$ quoted below includes the mean part, $\tilde{b}_0^2 = B_0^2 + b_0^2$.

3. Cosmic-ray Propagation

Using magnetic field realizations generated from Equation (1), or the corresponding randomized magnetic fields, we obtain an ensemble of cosmic-ray trajectories ($\geqslant$1000 in number) by solving numerically the dimensionless equation of motion for the particle trajectories $\boldsymbol{x}(t)$,

$$\ddot{\boldsymbol{x}} = \alpha \dot{\boldsymbol{x}} \times \boldsymbol{B}(\boldsymbol{x}), \qquad (4)$$

with $\alpha = q l_0 \tilde{b}_0/(\gamma m c v_0)$, q the particle charge, m its rest mass, $\tilde{b}_0$ the total rms field strength, γ the Lorentz factor, v_0 the particle speed, and c the speed of light. As in most cosmic-ray propagation models (Berezinskii et al. 1990; Schlickeiser 2002; Shalchi 2009), we neglect electric fields in Equation (4): they are negligible at the scales of interest ($\simeq$1 kpc in galaxies and $\simeq$10 kpc in galaxy clusters). Hence, the particle speed v_0 remains constant. Each particle is given a random initial position and propagation direction, but the same initial speed. The *characteristic* dimensionless Larmor radius, based on the rms magnetic field strength, is $r_{\rm L}/l_0 = \alpha^{-1}$; we use this ratio to characterize the particle properties. When $B_0 = 0$, we calculate the isotropic diffusion coefficient $\kappa = \lim_{t\to\infty} \langle |\Delta \boldsymbol{x}(t)|^2 \rangle/(6t)$, where $\Delta \boldsymbol{x}(t)$ is the particle displacement, and the angular brackets denote averaging over particle displacements. In the

[3] Some authors define $R_{\rm m}$ in terms of the wavenumber k_0, resulting in $R_{\rm m}$ values a factor of 2π smaller.

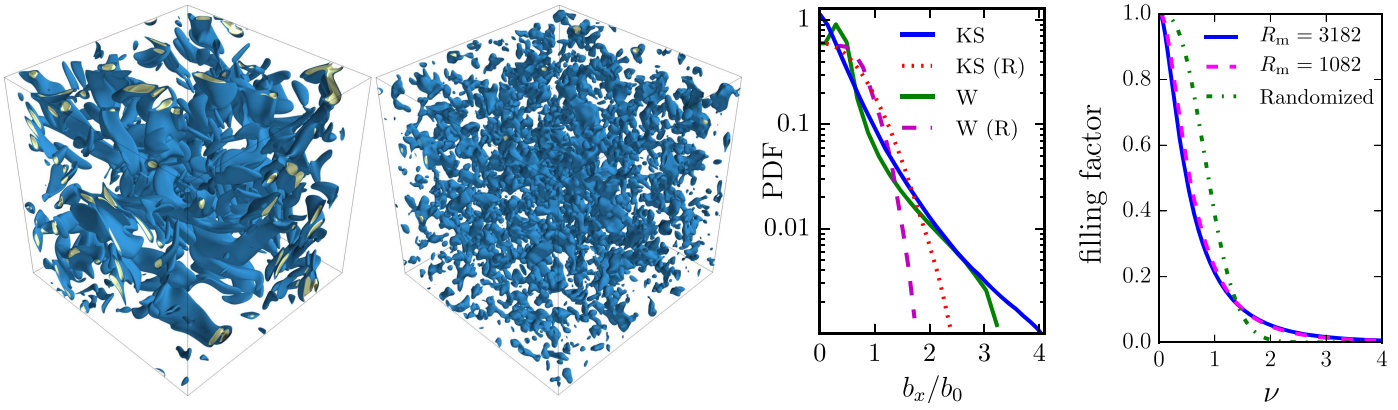


Figure 1. Isosurfaces of magnetic field strength $b^2/b_0^2 = 2.5$ (blue) and $b^2/b_0^2 = 5$ (yellow) with b_0 the rms magnetic field, for magnetic field generated by the KS flow (3) at $R_m = 1082$ (left) and for the same magnetic field after Fourier phase randomization as described in the text (second from left). Magnetic field generated by the W flow (2) is similarly affected (not shown). The second from right panel shows the PDFs of a magnetic field component b_x for the original (KS, W: solid) and randomized (KS (R), W (R): dashed) magnetic fields obtained with both velocity fields (only $b_x > 0$ is shown as the PDFs are essentially symmetric about $b_x = 0$). The randomized fields have almost perfectly Gaussian statistics, whereas magnetic intermittency leads to heavy tails. The panel on the right shows the fractional volume within magnetic structures where $b \geqslant \nu b_0$, with b_0 the rms field strength, as a function of ν for the intermittent magnetic field produced by the flow (3) (solid for $R_m = 3182$ and dashed for $R_m = 1082$) and its Gaussian counterpart (dashed–dotted for $R_m = 3142$ and 1082) obtained by Fourier phase randomization; the filling factor of the randomized fields is independent of R_m.

presence of a mean magnetic field directed along the z-axis, we introduce similarly defined parallel and perpendicular diffusion coefficients, which are given by $\kappa_\parallel = \lim_{t\to\infty}\langle \Delta z(t)^2\rangle/(2t)$ and $\kappa_\perp = \lim_{t\to\infty}\langle[\Delta x(t)^2 + \Delta y(t)^2]\rangle/(4t)$.

4. Cosmic-ray Diffusivity

Figure 2(a) shows the dependence of the cosmic-ray diffusion coefficient on r_L/l_0 (proportional to the particle energy) for $B_0 = 0$. For $r_L/l_0 \gg 1$, we recover the asymptotic scaling $\kappa \propto r_L^2$ (high energy limit) in agreement with earlier results (Parker 1965; Aloisio & Berezinsky 2004; Parizot 2004; DeMarco et al. 2007; Globus et al. 2008; Beresnyak et al. 2011; Plotnikov et al. 2011; Harari et al. 2014; Snodin et al. 2016; Subedi et al. 2017). At lower energies, the dependence of κ on particle energy is weaker and is sensitive to magnetic structure. Magnetic intermittency is expected to be important at those energies where

$$r_L/l_0 \lesssim 1, \tag{5}$$

and the dependence $\kappa(r_L/l_0)$ in Figure 2(a) indeed deviates from the asymptotic form in this range. The role of magnetic intermittency is demonstrated in Figure 2(b), showing the ratio of the diffusivity κ calculated with a dynamo-generated magnetic field to that in the corresponding randomized field, κ_R ($B_0 = 0$ in panels (a) and (b)). At high energies (large r_L/l_0), $\kappa/\kappa_R \simeq 1$, suggesting that the magnetic structures play an insignificant role. However, κ/κ_R increases rapidly up to more than 2.5 at lower energies: magnetic structures enhance diffusion when inequality (5) is satisfied. We find that the ratio κ/κ_R at fixed r_L/l_0 increases with R_m for a given flow. At high values of r_L/l_0, the diffusivity still depends on R_m via changes in the magnetic correlation length (Figure 2(a)), but not via the R_m-dependent intermittency, as suggested by Figure 2(b), where κ/κ_R tends to unity as r_L/l_0 increases. One might expect a change in the diffusivity behavior at $r_L/l_0 \approx R_m^{-1/2}$, associated with the thickness of magnetic filaments, and this may explain the variation in slope of κ at low r_L/l_0 in

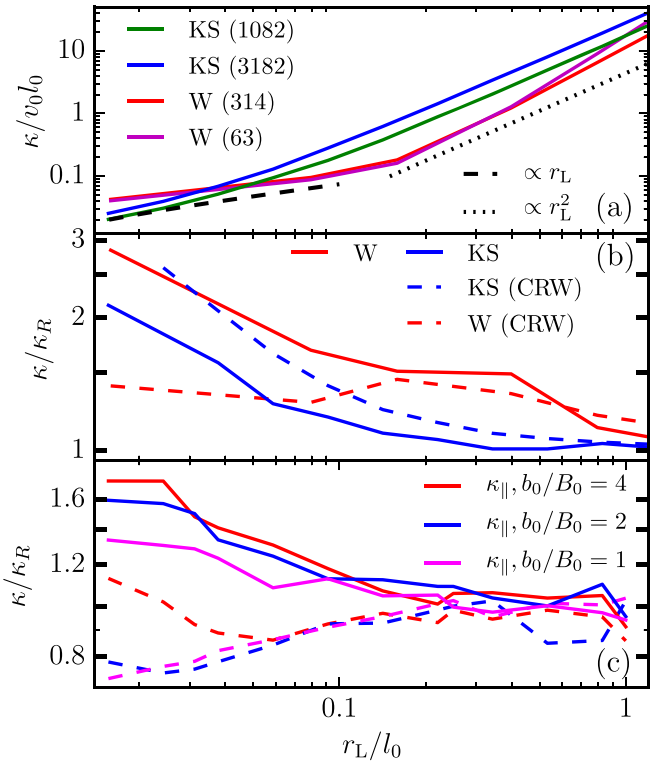


Figure 2. (a) Cosmic-ray diffusion coefficient for the W flow (2) (red, magenta) and the KS flow (3) (blue, green) as a function of r_L/l_0 for the values of R_m given in parenthesis in the legend. The dotted–dashed line shows the scaling $\kappa \propto r_L^2$ and $\kappa \propto r_L$, respectively. (b) The ratio of diffusion coefficients from intermittent, κ, and randomized, κ_R, magnetic fields for the two flows (solid lines, KS with $R_m = 3182$, W with $R_m = 314$). The dashed lines of the same color show the corresponding CRW model, Equation (7). (c) As in (b), but in the presence of a mean magnetic field B_0, of the relative strength specified in the legend, for the KS flow with $R_m = 3182$; $\kappa_\parallel$ and $\kappa_\perp$ are shown as solid and dashed lines, respectively.

Figure 2(a) (or the ratios in Figure 2(b)). However, at present, the role of this scale is unclear.

Figure 2(c) illustrates the effects of the mean magnetic field, presenting the ratio of the parallel and perpendicular

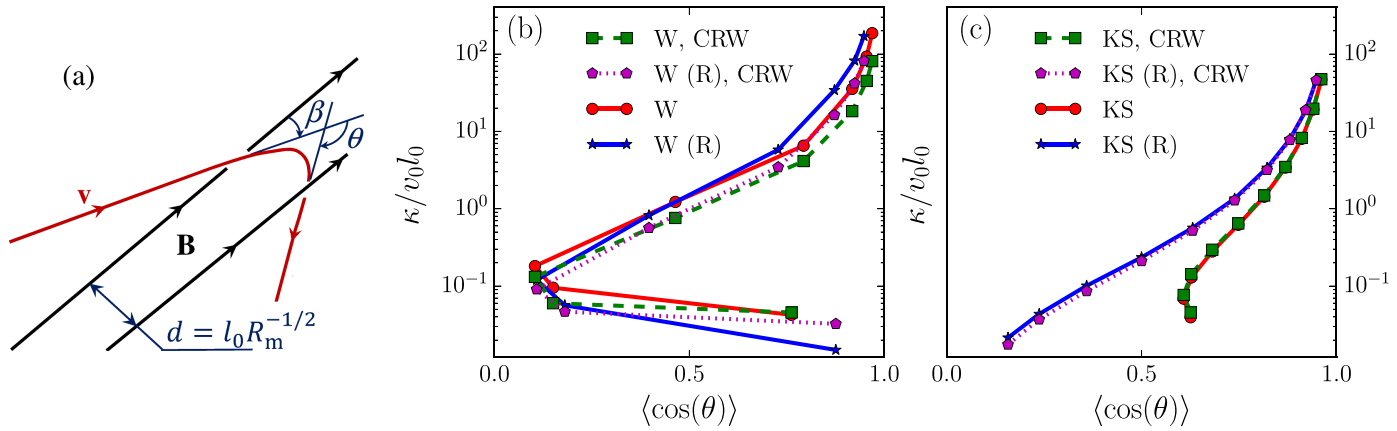


Figure 3. (a) A charged particle with the pitch angle β is deflected by an angle θ in a magnetic structure of a thickness d, thus introducing correlation into the random particle trajectory. The dependence of the diffusivity in simulations on $\langle\cos\theta\rangle$ in the W flow and the randomized (R) magnetic field is shown in (b) (solid lines). The corresponding CRW approximations (Equation (7)) are shown with broken lines. (c) As in (b), but for the KS flow. These results are obtained for $B_0 = 0$.

diffusivities in the intermittent and Gaussian magnetic fields. A mean magnetic field somewhat reduces the effect of intermittency, but does not eliminate it even for $b_0/B_0 = 1$. Magnetic intermittency enhances $\kappa_\parallel$ (i.e., $\kappa_\parallel > (\kappa_\parallel)_R$) at all but the highest energies, but $\kappa_\perp < (\kappa_\perp)_R$ at lower energies for $b_0/B_0 = 2$ and $b_0/B_0 = 1$. The effects of the mean field will be discussed in detail elsewhere.

5. Cosmic-ray Propagation as a Correlated Random Walk (CRW)

The Brownian motion is a widely used model for diffusive processes. This is the simplest type of random walk where each step is made in a direction independent of the previous direction. In a continuum limit, it leads to the diffusion equation. However, a charged particle moves differently. As illustrated in Figure 3(a), the direction of its motion after deflection by a magnetic structure is correlated with the previous direction. The deflection angle θ is related to r_L, the angle between the velocity and magnetic field, β, and the magnetic structure width d:

$$\theta \simeq d/(r_L \sin\beta). \tag{6}$$

This is a correlated random walk (CRW) (Gillis 1955), a first-order Markov chain (since the correlation does not extend beyond two consecutive steps). For a symmetric probability distribution of θ, the CRW diffusivity depends on $\langle\cos\theta\rangle$, where angular brackets denote the ensemble average. The mean-square displacement in the CRW was obtained in 2D (Kareiva & Shigesada 1983) and implies the following 3D diffusivity (Equation (3.3.7) in Chen & Renshaw 1992):

$$\kappa = \frac{\langle l^2\rangle}{6\tau} + \frac{\langle l\rangle^2}{3\tau}\frac{\langle\cos\theta\rangle}{1-\langle\cos\theta\rangle}, \tag{7}$$

with $\tau = \langle l\rangle/v$, v the particle speed, and l the step length. To calculate $\langle\cos\theta\rangle$, we assume that the pitch angle β is uniformly distributed between 0 and π. Defining $a = d/r_L \simeq l_0 R_m^{-1/2}/r_L$, it can be shown that

$$\begin{aligned}\langle\cos\theta\rangle &= \pi^{-1}\int_0^\pi \cos(a/\sin\beta)\,\mathrm{d}\beta \\ &= 1 - \tfrac{1}{2}\pi a\,[J_0(a)\mathcal{H}_{-1}(a) - J_{-1}(a)\mathcal{H}_0(a)],\end{aligned} \tag{8}$$

where $J_n(x)$ and $\mathcal{H}_n(x)$ are the Bessel and Struve functions (2.5.8.6 in Prudnikov et al. 1991). Finite length of the magnetic structures can be accounted for, but this represents a small correction and the integral cannot be taken analytically.

To derive $\langle\cos\theta\rangle$ in the simulations, the particle trajectories were sampled at a rate that is comparable to the local Larmor time; the sampling frequency does not affect the results much (cf. Codling & Hill 2005; Rosser et al. 2013). $\langle\cos\theta\rangle$ computed using Equation (8) and the same obtained from the simulations show reasonable qualitative agreement if we adopt $d = l_0 R_m^{-1/2}$ for the flow (2) and d as the thickness of the magnetic structures calculated using the Minkowski functionals (Wilkin et al. 2007) for the flow (3).

Figures 3(b) and (c) show the variation of κ with $\langle\cos\theta\rangle$, where κ is obtained numerically for both the intermittent and randomized magnetic fields, and in each case, the corresponding κ predicted from Equation (7) is also shown. For τ in Equation (7), we have used r_L/v_0, where r_L is the local Larmor radius. The agreement is remarkably good for the flow (2) and excellent for the less regular magnetic field resulting from the flow (3). This confirms directly that the cosmic-ray propagation is a CRW with the diffusivity given by Equation (7). This applies to *both* intermittent and Gaussian random magnetic fields (see also Figure 2(b)). We note that the first term in Equation (7) dominates at large r_L.

6. Conclusions

We have demonstrated that cosmic-ray propagation in random magnetic fields is affected by magnetic intermittency in the range of energies (5), or

$$\frac{E}{1\ \mathrm{GeV}} \lesssim 10^9 \frac{l_0}{1\ \mathrm{kpc}}\frac{B}{1\ \mu\mathrm{G}}.$$

In the interstellar medium, $l_0 \simeq 100$ pc and $B \simeq 10\ \mu$G, and for ultra-relativistic protons, this energy range is $E \lesssim 10^9$ GeV. In galaxy clusters, $l_0 \simeq 10$ kpc, $B \simeq 2\ \mu$G, and $E \lesssim 10^{10}$ GeV.

Assuming $R_{m,\mathrm{eff}} = R_{m,c} = 100$ in the interstellar medium, we might expect some effect at $r_L/l_0 = 0.1$, which would correspond to 10^8 GeV protons using the above values. Such an effect might produce a knee or spectral break in the cosmic-ray energy spectrum near this energy. The influence of magnetic intermittency extends to below this energy (the effect of

intermittency on cosmic-ray diffusivity increases as energy decreases), but further investigation is needed to quantify this. Finally, we note that magnetic intermittency may also affect ultrahigh-energy cosmic rays that propagate non-diffusively and that their propagation can also be interpreted as a CRW.

We are grateful to J. Rachen, A. van Vliet, and L. F. S. Rodrigues for useful discussions. This work was supported by the Thailand Research Fund (RTA5980003), the Leverhulme Trust (RPG-2014-427), and STFC (ST/N000900/1, Project 2).

References

Aloisio, R., & Berezinsky, V. 2004, ApJ, 612, 900
Alouani-Bibi, F., & le Roux, J. A. 2014, ApJ, 781, 93
Beresnyak, A., Yan, H., & Lazarian, A. 2011, ApJ, 728, 60
Berezinskii, V. S., Bulanov, S. V., Dogiel, V. A., & Ptuskin, V. S. 1990, Astrophysics of Cosmic Rays (Amsterdam: North-Holland)
Brandenburg, A., & Subramanian, K. 2005, PhR, 417, 1
Bykov, A. M., & Toptygin, I. N. 1987, Ap&SS, 138, 341
Candia, J., & Roulet, E. 2004, JCAP, 10, 7
Casse, F., Lemoine, M., & Pelletier, G. 2002, PhRvD, 65, 023002
Cesarsky, C. J. 1980, ARA&A, 18, 289
Chen, A., & Renshaw, E. 1992, J. Appl. Probab., 29, 792
Codling, E., & Hill, N. 2005, J. Theor. Biol., 233, 573
Cohet, R., & Marcowith, A. 2016, A&A, 588, A73
Corrsin, S. 1959, AdGeo, 6, 161
DeMarco, D., Blasi, P., & Stanev, T. 2007, JCAP, 6, 027
Desiati, P., & Zweibel, E. G. 2014, ApJ, 791, 51
Dmitruk, P., Matthaeus, W. H., & Seenu, N. 2004, ApJ, 617, 667
Fung, J. C. H., Hunt, J. C. R., Malik, N. A., & Perkins, R. J. 1992, JFM, 236, 281
Giacalone, J., & Jokipii, J. R. 1999, ApJ, 520, 204
Gillis, J. 1955, PCPS, 51, 639
Globus, N., Allard, D., & Parizot, E. 2008, A&A, 479, 97
Harari, D., Mollerach, S., & Roulet, E. 2014, PhRvD, 89, 123001
Haverkorn, M., & Spangler, S. R. 2013, SSRv, 178, 483
Heiles, C., & Troland, T. H. 2005, ApJ, 624, 773
Jokipii, J. R. 1966, ApJ, 146, 480
Kareiva, P. M., & Shigesada, N. 1983, Oecologia, 56, 234
Lynn, J. W., Parrish, I. J., Quataert, E., & Chandran, B. D. G. 2012, ApJ, 758, 78
Matthaeus, W. H., Qin, G., Bieber, J. W., & Zank, G. P. 2003, ApJL, 590, L53
Michalek, G., & Ostrowski, M. 1997, A&A, 326, 793
Parizot, E. 2004, NuPhS, 136, 169
Parker, E. N. 1965, P&SS, 13, 9
Plotnikov, I., Pelletier, G., & Lemoine, M. 2011, A&A, 532, A68
Prudnikov, A. P., Brychkov, Y. A., & Marichev, O. I. 1991, Integrals and Series: Elementary Functions, Vol. 1 (New York: Gordon & Breach)
Pucci, F., Malara, F., Perri, S., et al. 2016, MNRAS, 459, 3395
Reville, B., O'Sullivan, S., Duffy, P., & Kirk, J. G. 2008, MNRAS, 386, 509
Roh, S., Inutsuka, S.-i., & Inoue, T. 2016, APh, 73, 1
Rosser, G., Fletcher, A. G., Maini, P. K., & Baker, R. E. 2013, J. R. Soc. Interface, 10, 20130273
Schlickeiser, R. 2002, Cosmic Ray Astrophysics (Berlin: Springer)
Shalchi, A. 2009, Nonlinear Cosmic Ray Diffusion Theories (Berlin: Springer)
Snodin, A. P., Ruffolo, D., Oughton, S., Servidio, S., & Matthaeus, W. H. 2013, ApJ, 779, 56
Snodin, A. P., Shukurov, A., Sarson, G. R., Bushby, P. J., & Rodrigues, L. F. S. 2016, MNRAS, 457, 3975
Subedi, P., Sonsrettee., W., Blasi, P., et al. 2017, ApJ, 837, 140
Subramanian, K. 1999, PhRvL, 83, 2957
Vlad, M., Spineanu, F., Misguich, J. H., & Balescu, R. 1998, PhRvE, 58, 7359
Weidl, M. S., Jenko, F., Teaca, B., & Schlickeiser, R. 2015, ApJ, 811, 8
Wilkin, S. L., Barenghi, C. F., & Shukurov, A. 2007, PhRvL, 99, 134501
Willis, A. P. 2012, PhRvL, 109, 251101
Yan, H., & Lazarian, A. 2002, PhRvL, 89, 281102
Zaroubi, S., Jelić, V., de Bruyn, A. G., et al. 2015, MNRAS, 454, L46
Zeldovich, Ya. B., Ruzmaikin, A. A., & Sokoloff, D. D. 1990, The Almighty Chance (Singapore: World Scientific)

Cosmic-ray electron-positron spectrum from 7 GeV to 2 TeV with the Fermi Large Area Telescope

S. Abdollahi,[1] M. Ackermann,[2] M. Ajello,[3] W. B. Atwood,[4] L. Baldini,[5] G. Barbiellini,[6,7] D. Bastieri,[8,9] R. Bellazzini,[10] E. D. Bloom,[11] R. Bonino,[12,13,*] T. J. Brandt,[14] J. Bregeon,[15] P. Bruel,[16,†] R. Buehler,[2] R. A. Cameron,[17] R. Caputo,[4] M. Caragiulo,[18,19] D. Castro,[14] E. Cavazzuti,[20] C. Cecchi,[21,22] A. Chekhtman,[23] S. Ciprini,[20,21] J. Cohen-Tanugi,[15] F. Costanza,[19] A. Cuoco,[24,12] S. Cutini,[20,21] F. D'Ammando,[25,26] F. de Palma,[19,27] R. Desiante,[12,28] S. W. Digel,[17] N. Di Lalla,[10] M. Di Mauro,[17] L. Di Venere,[18,19] P. S. Drell,[17] A. Drlica-Wagner,[29] C. Favuzzi,[18,19] W. B. Focke,[17] S. Funk,[30] P. Fusco,[18,19] F. Gargano,[19] D. Gasparrini,[20,21] N. Giglietto,[18,19] F. Giordano,[18,19] M. Giroletti,[25] D. Green,[31,14] L. Guillemot,[32,33] S. Guiriec,[14,34] A. K. Harding,[14] T. Jogler,[35] G. Jóhannesson,[36] T. Kamae,[37] M. Kuss,[10] G. La Mura,[38] L. Latronico,[12] F. Longo,[6,7] F. Loparco,[18,19] P. Lubrano,[21] S. Maldera,[12] D. Malyshev,[30] A. Manfreda,[5,‡] M. N. Mazziotta,[19] P. F. Michelson,[17] N. Mirabal,[14,34] W. Mitthumsiri,[39] T. Mizuno,[40] A. A. Moiseev,[41,31] M. E. Monzani,[17] A. Morselli,[42] I. V. Moskalenko,[17] M. Negro,[12,13] E. Nuss,[15] E. Orlando,[17] D. Paneque,[43] J. S. Perkins,[14] M. Pesce-Rollins,[10] F. Piron,[15] G. Pivato,[10] T. A. Porter,[17] G. Principe,[30] S. Rainò,[18,19] R. Rando,[8,38] M. Razzano,[10,44] A. Reimer,[45,17] O. Reimer,[45,17] C. Sgrò,[10] D. Simone,[19] E. J. Siskind,[46] F. Spada,[10] G. Spandre,[10] P. Spinelli,[18,19] H. Tajima,[47,17] J. B. Thayer,[17] L. Tibaldo,[48] D. F. Torres,[49,50] E. Troja,[14,31] M. Wood,[17] A. Worley,[51] G. Zaharijas,[52,53] and S. Zimmer[54]

(The Fermi-LAT Collaboration)

[1]*Department of Physical Sciences, Hiroshima University, Higashi-Hiroshima, Hiroshima 739-8526, Japan*
[2]*Deutsches Elektronen Synchrotron DESY, D-15738 Zeuthen, Germany*
[3]*Department of Physics and Astronomy, Clemson University, Kinard Lab of Physics, Clemson, South Carolina 29634-0978, USA*
[4]*Santa Cruz Institute for Particle Physics, Department of Physics and Department of Astronomy and Astrophysics, University of California at Santa Cruz, Santa Cruz, California 95064, USA*
[5]*Università di Pisa and Istituto Nazionale di Fisica Nucleare, Sezione di Pisa I-56127 Pisa, Italy*
[6]*Istituto Nazionale di Fisica Nucleare, Sezione di Trieste, I-34127 Trieste, Italy*
[7]*Dipartimento di Fisica, Università di Trieste, I-34127 Trieste, Italy*
[8]*Istituto Nazionale di Fisica Nucleare, Sezione di Padova, I-35131 Padova, Italy*
[9]*Dipartimento di Fisica e Astronomia "G. Galilei," Università di Padova, I-35131 Padova, Italy*
[10]*Istituto Nazionale di Fisica Nucleare, Sezione di Pisa, I-56127 Pisa, Italy*
[11]*W. W. Hansen Experimental Physics Laboratory, Kavli Institute for Particle Astrophysics and Cosmology, Department of Physics and SLAC National Accelerator Laboratory, Stanford University, Stanford, California 94305, USA*
[12]*Istituto Nazionale di Fisica Nucleare, Sezione di Torino, I-10125 Torino, Italy*
[13]*Dipartimento di Fisica, Università degli Studi di Torino, I-10125 Torino, Italy*
[14]*NASA Goddard Space Flight Center, Greenbelt, Maryland 20771, USA*
[15]*Laboratoire Univers et Particules de Montpellier, Université Montpellier, CNRS/IN2P3, F-34095 Montpellier, France*
[16]*Laboratoire Leprince-Ringuet, École polytechnique, CNRS/IN2P3, F-91128 Palaiseau, France*
[17]*W. W. Hansen Experimental Physics Laboratory, Kavli Institute for Particle Astrophysics and Cosmology, Department of Physics and SLAC National Accelerator Laboratory, Stanford University, Stanford, California 94305, USA*
[18]*Dipartimento di Fisica "M. Merlin" dell'Università e del Politecnico di Bari, I-70126 Bari, Italy*
[19]*Istituto Nazionale di Fisica Nucleare, Sezione di Bari, I-70126 Bari, Italy*
[20]*Agenzia Spaziale Italiana (ASI) Science Data Center, I-00133 Roma, Italy*
[21]*Istituto Nazionale di Fisica Nucleare, Sezione di Perugia, I-06123 Perugia, Italy*
[22]*Dipartimento di Fisica, Università degli Studi di Perugia, I-06123 Perugia, Italy*
[23]*College of Science, George Mason University, Fairfax, VA 22030, resident at Naval Research Laboratory, Washington, District of Columbia 20375, USA*
[24]*RWTH Aachen University, Institute for Theoretical Particle Physics and Cosmology, (TTK), D-52056 Aachen, Germany*
[25]*INAF Istituto di Radioastronomia, I-40129 Bologna, Italy*
[26]*Dipartimento di Astronomia, Università di Bologna, I-40127 Bologna, Italy*
[27]*Università Telematica Pegaso, Piazza Trieste e Trento, 48, I-80132 Napoli, Italy*
[28]*Università di Udine, I-33100 Udine, Italy*
[29]*Center for Particle Astrophysics, Fermi National Accelerator Laboratory, Batavia, Illinois 60510, USA*
[30]*Erlangen Centre for Astroparticle Physics, D-91058 Erlangen, Germany*

 © 2017 American Physical Society

[31]*Department of Physics and Department of Astronomy, University of Maryland, College Park, Maryland 20742, USA*
[32]*Laboratoire de Physique et Chimie de l'Environnement et de l'Espace - Université d'Orléans / CNRS, F-45071 Orléans Cedex 02, France*
[33]*Station de radioastronomie de Nançay, Observatoire de Paris, CNRS/INSU, F-18330 Nançay, France*
[34]*NASA Postdoctoral Program Fellow, USA*
[35]*Friedrich-Alexander-Universität, Erlangen-Nürnberg, Schlossplatz 4, 91054 Erlangen, Germany*
[36]*Science Institute, University of Iceland, IS-107 Reykjavik, Iceland*
[37]*Department of Physics, Graduate School of Science, University of Tokyo, 7-3-1 Hongo, Bunkyo-ku, Tokyo 113-0033, Japan*
[38]*Dipartimento di Fisica e Astronomia "G. Galilei", Università di Padova, I-35131 Padova, Italy*
[39]*Department of Physics, Faculty of Science, Mahidol University, Bangkok 10400, Thailand*
[40]*Hiroshima Astrophysical Science Center, Hiroshima University, Higashi-Hiroshima, Hiroshima 739-8526, Japan*
[41]*Center for Research and Exploration in Space Science and Technology (CRESST) and NASA Goddard Space Flight Center, Greenbelt, Maryland 20771, USA*
[42]*Istituto Nazionale di Fisica Nucleare, Sezione di Roma "Tor Vergata," I-00133 Roma, Italy*
[43]*Max-Planck-Institut für Physik, D-80805 München, Germany*
[44]*Funded by contract FIRB-2012-RBFR12PM1F from the Italian Ministry of Education, University and Research (MIUR)*
[45]*Institut für Astro- und Teilchenphysik and Institut für Theoretische Physik, Leopold-Franzens-Universität Innsbruck, A-6020 Innsbruck, Austria*
[46]*NYCB Real-Time Computing Inc., Lattingtown, New York 11560-1025, USA*
[47]*Solar-Terrestrial Environment Laboratory, Nagoya University, Nagoya 464-8601, Japan*
[48]*Max-Planck-Institut für Kernphysik, D-69029 Heidelberg, Germany*
[49]*Institute of Space Sciences (IEEC-CSIC), Campus UAB, E-08193 Barcelona, Spain*
[50]*Institució Catalana de Recerca i Estudis Avançats (ICREA), Barcelona E-08010, Spain*
[51]*Department of Physics and Astronomy, University of Denver, Denver, Colorado 80208, USA*
[52]*Istituto Nazionale di Fisica Nucleare, Sezione di Trieste, and Università di Trieste, I-34127 Trieste, Italy*
[53]*Laboratory for Astroparticle Physics, University of Nova Gorica, Vipavska 13, SI-5000 Nova Gorica, Slovenia*
[54]*University of Geneva, Department of Nuclear and Particle Physics, 24 quai Ernest-Ansermet, CH-1211 Geneva 4, Switzerland*

(Received 21 September 2016; revised manuscript received 28 March 2017; published 21 April 2017)

We present a measurement of the cosmic-ray electron + positron spectrum between 7 GeV and 2 TeV performed with almost seven years of data collected with the *Fermi* Large Area Telescope. We find that the spectrum is well fit by a broken power law with a break energy at about 50 GeV. Above 50 GeV, the spectrum is well described by a single power law with a spectral index of 3.07 ± 0.02 (stat + syst) ± 0.04(energy measurement). An exponential cutoff lower than 1.8 TeV is excluded at 95% CL.

DOI: 10.1103/PhysRevD.95.082007

I. INTRODUCTION

While propagating throughout the Galaxy, high-energy cosmic-ray electrons and positrons (CRE) rapidly lose energy by interacting with the interstellar radiation field through inverse Compton scattering and by synchrotron emission on the Galactic magnetic field. Their diffusion distance is several hundred parsecs at 1 TeV, much shorter than the radial scale of the Galaxy [1]. Therefore, the shape of the CRE spectrum from ~100 GeV up to several TeV (as well as the positron fraction [2–4] and CRE anisotropy [5]) can provide evidence for local CRE sources of astrophysical (supernova remnants and pulsar wind nebulae [6–11]) or exotic (dark matter [12–14]) nature.

Recent measurements by AMS-02 [15] and *Fermi* [16] have shown that the CRE spectrum can be fit with a single power law up to ~1 TeV, with an index of 3.170 ± 0.008 and 3.08 ± 0.05, respectively. The H.E.S.S. [17,18] measurements gave the first indication of a cutoff at ~2 TeV. These results can be interpreted as local CRE sources with a spectral cutoff at about this energy [19].

The *Fermi* Large Area Telescope (LAT) [20], while designed to detect gamma rays, is able to collect and identify CREs with a large acceptance by combining

*rbonino@to.infn.it
†Philippe.Bruel@llr.in2p3.fr
‡alberto.manfreda@pi.infn.it

information from its three subsystems, a silicon-strip detector based tracker-converter (TKR), an imaging calorimeter (CAL) consisting of eight layers of CsI crystals and an anticoincidence detector (ACD) constructed from tiles of plastic scintillator surrounding the TKR and CAL.

Extending the CRE energy measurement beyond 1 TeV with the LAT is challenging because, at such high energy, only ∼35% of the shower is on average contained in the CAL and a significant fraction of the CAL crystals along the shower axis are saturated (crystal saturation occurs when more than ∼70 GeV is deposited in one crystal, which occurs for CREs above ∼600 GeV). Thanks to the new Pass 8 event analysis [21], with improved track and shower reconstruction as well as improved multivariate methods for background suppression, we can achieve a level of background contamination smaller than 25% and an energy resolution (defined as the half-width of the 68% containment range) better than 20% up to 2 TeV.

In this article, we present an updated measurement of the CRE spectrum, using almost seven years of LAT Pass 8 data up to 2 TeV, performing the first direct measurement above 1 TeV. A search for anisotropies, using the same data and event selection, and a theoretical interpretation of the CRE spectrum are presented in separate publications [22] [23].

The paper is structured as follows: the event selection is introduced in Sec. II and further detailed in the two following sections. The energy measurement and the study of systematic uncertainties are described in Secs. V and VI, respectively, while the results are presented and discussed in Sec. VII.

II. EVENT SELECTION

The LAT on-board gamma filter is designed to reject charged particles, but it accepts all events with a deposited energy in the CAL larger than 20 GeV. As in the previous LAT CRE measurement [16], we performed two independent analyses: the high-energy (HE) analysis above 42 GeV and the low-energy (LE) analysis between 7 and 70 GeV. The former selects events passing the on-board gamma filter, whereas for the latter we use an unbiased sample of all trigger types, prescaled on-board by a factor of 250. In both analyses, we first apply a set of simple cuts before performing a multivariate analysis in order to reduce as much as possible the residual proton contamination.

We use LAT Pass 8 data collected between August 4, 2008, and June 24, 2015, requiring that the rocking angle of the LAT from the zenith is less than 51 degrees. The overall live time for this data set is 4.68 years. We select events within 60 degrees from the LAT boresight in order to eliminate potential contamination from photons produced in cosmic-ray induced air showers in Earth's atmosphere. The so-called photon Earth limb is located at 113 degrees from the zenith.

We require events with a well reconstructed track, whose path lengths through the CAL are larger than 8 radiation lengths. The event energy is estimated by fitting the shower profile in the CAL. We reject badly reconstructed events by requiring that the $\chi^2/\text{n.d.f.}$ of the shower profile fit is less than 20. In order to remove alphas and heavier ions we use the path-length-corrected signal in the ACD and the TKR time over threshold which provide charge-deposition information. Both variables are sensitive to the ionization signal which is proportional to Z^2. Applying a cut in the plane spanned by these two variables around the $Z = 1$ group reduces contamination of alphas and ions to less than a few per mil with respect to protons. This cut also reduces the residual contribution from celestial photons below 1% of the CRE flux. The LE selection requires more than 2 GeV deposited in the CAL.

For both the HE and the LE analyses, these cuts (hereafter referred to as "precuts") are combined with further selections based on multivariate classification analyses. We use the multivariate analysis toolkit TMVA [24] to train boosted decision trees (BDT) with simulated data sets. After training, each BDT provides a variable p_{BDT} between -1 and $+1$, corresponding to most protonlike and most electronlike events, respectively. Since the p_{BDT} distribution for electrons peaks very sharply at 1, we use $P_{\text{CRE}} = \log_{10}(1 - p_{\text{BDT}})$ as the CRE estimator. For each energy bin of the analyses, we fit the distribution of P_{CRE} with two templates corresponding to simulated electrons and background, respectively. After choosing the cut on P_{CRE} that selects the CRE candidates, we use the result of the template fit to estimate and subtract the number of residual background events. The HE and LE multivariate analyses are described in the two following sections.

The simulated data sets that are used to train the BDTs were generated with the standard LAT Monte Carlo (MC) suite [20], a detailed simulation of the passage of particles through the LAT based on the GEANT4 package [25]. Independent simulated data sets were produced to perform data/MC comparisons, model the CRE acceptance and estimate the residual background contamination. Above 42 GeV, the residual background after precuts due to nonproton particles is negligible compared to that due to protons, so the Monte Carlo background sample used in the HE analysis is the output of a pure proton simulation, from 4 GeV to 20 TeV. For the LE analysis, the background MC sample used for the training is a simulation of cosmic rays of both primary and secondary origin in low Earth orbit and Earth limb photons [26].

III. HIGH-ENERGY ANALYSIS

To account for the rapid changes in event topology in the LAT between several GeV and several TeV, we define eight bins in measured energy (equally spaced in $\log_{10} E$ between 31.6 GeV and 3.16 TeV) and train a BDT for each bin. All BDTs are trained with the same set of variables among the hundreds computed during the LAT event reconstruction. These variables were proven to be the most efficient ones in

discriminating between electrons and protons thanks to an optimization procedure using only MC data sets.

These discriminating variables characterize the shower trajectory and topology using information from the CAL and TKR subsystems. We use TKR-only information, such as the average time over threshold and the number of hits in the three sections of the TKR, as well as CAL-only information, such as estimates of the shower transverse size, the crystal-based χ^2 of the shower profile fit, and the ratio of the energies deposited in the first and second CAL layers. We also use TKR-CAL information like the ratio of the number of TKR hits to the energy deposited in the first two CAL layers and the distance of closest approach of the CAL cluster centroid to the track.

A. Data/MC agreement

The agreement between data and simulation for P_{CRE} is critical to the analysis: it ensures the goodness of the template fit, from which the background contamination is estimated, and it drives the precision of the selection efficiency predicted by the simulation. As this agreement depends on the data/MC agreement of the individual variables used as input to the BDTs, we performed a systematic comparison of their distributions measured in data and predicted by the simulation for electrons at various energies (eight bins in $\log_{10} E$ between 31.6 GeV and 3.16 TeV) and incidence angles (five bins in $\cos\theta$ between 0.5 and 1, where θ is the angle between the event direction and the LAT boresight).

We found that the widths of the distributions are in good agreement (within 15%), but, for some variables, the position of the peak is shifted. From the differences of peak positions between data and MC, we derived additive corrections that we parametrized as functions of energy and incidence angle, to ensure good data/MC agreement. We refer to these corrections as the individual variables calibration (IVC) corrections. Rather than applying them to the simulation, we apply them to data. Both solutions are equivalent with respect to BDT efficiency (because the IVC corrections are simple shifts) but the latter is more computationally convenient as it does not require retraining the BDTs.

Figure 1 shows the energy dependence of the peak positions for two variables, the transverse size of the shower and the crystal-based χ^2 of the shower profile fit, for data and MC. Although the data/MC discrepancy for the transverse size of the shower could be solved by rescaling the energy, it is not the case for the crystal-based χ^2 of the shower profile fit. As a consequence, these disagreements are not an indication of a problem in energy measurement. We believe that they are the consequence of imperfections in the instrument simulation.

The effect of the IVC corrections is clearly visible in Fig. 2 for the transverse size of the shower, which is one of the variables with the largest data/MC discrepancy.

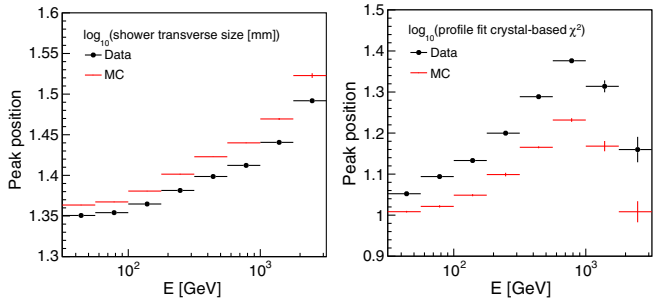


FIG. 1. Energy dependence of the peak position of the distribution of two variables: the logarithm of the transverse size of the shower (left) and the logarithm of the crystal based χ^2 of the shower profile fit (right). The black and red points correspond to data and simulation, respectively.

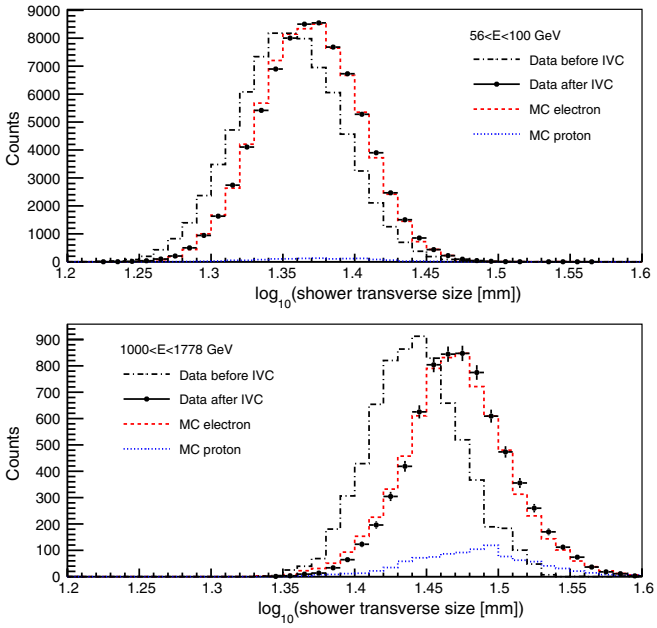


FIG. 2. The logarithm of the shower transverse size before (*black lines*) and after (*black circles*) IVC correction for events between 56 and 100 GeV (top) and between 1 and 1.78 TeV (bottom). The contribution from residual background (blue) has been subtracted from the data distributions. The red histograms correspond to the electron simulation.

The general trend is that, before correction, the shifts increase with energy and can be as large as the distribution RMS. After correction, the residual differences between peak positions are less than 10% of the distribution RMS; we take them into account when estimating the systematic uncertainties, as described in Sec. VI.

B. Template fit

For each energy bin, we construct the MC electron and proton distributions of P_{CRE} and use them as templates: we fit the P_{CRE} distribution of the data with the sum of two MC

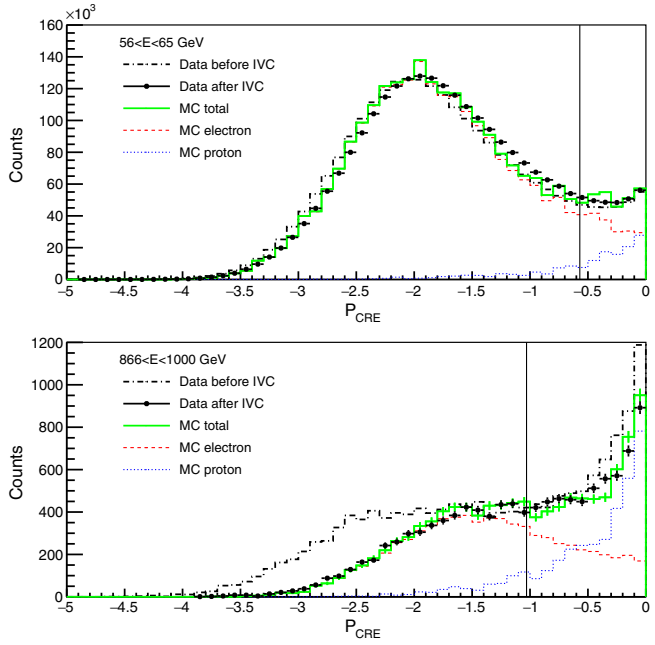


FIG. 3. The result of the template fit in two energy bins [56, 65 GeV] (top) and [866, 1000 GeV] (bottom). For both energy bins, the fit is performed over the interval [−5, 0] and the x-axis range is chosen to focus on the electron peak region. The data P_{CRE} distribution is shown before (black lines) and after (black circles) IVC corrections. The green histograms correspond to the sum of the electron (red) and proton (blue) templates. The vertical line show for each energy bin the position of the selection cut $P_{\mathrm{CRE}} < P_{\mathrm{cut}}$.

templates whose normalizations are the two parameters of the fit.

Ideally, we would perform the fit over the whole range of P_{CRE}. Unfortunately, the data/MC agreement after IVC corrections is not good enough in the "pure" proton range, i.e., for P_{CRE} above ∼0. This is simply due to the fact that the initial data/MC disagreement of individual variables is not always the same for electrons and protons. The IVC corrections, which are optimized for electrons, cannot ensure a good data/MC agreement for protons. As a result, the peak of the proton P_{CRE} distribution ($P_{\mathrm{CRE}} \gtrsim 0$) is not well reproduced by the simulation.

To mitigate the effect of the data/MC discrepancy near the proton peak we restrict the template fit to an interval $P_{\mathrm{CRE}} < P_{\mathrm{max}}$. To find the optimal value of P_{max} we looked at how the χ^2 of the template fit depends on it. We performed a scan starting at $P_{\mathrm{max}} = -1$, which is well outside the proton peak, but still above the predicted position of the maximum of the signal distribution, and then progressively increasing it. We found that the χ^2/n.d.f. remains flat until the fit interval starts to comprise a significant part of the proton peak and we chose P_{max} for which the χ^2 has doubled compared to its initial plateau. Because the data/MC disagreement is larger at high energy, the chosen value of P_{max} decreases with energy, as can be seen in Fig. 5.

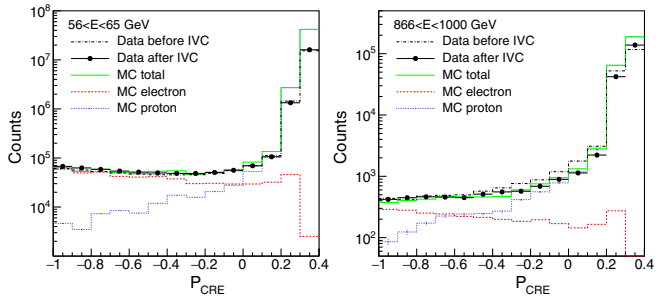


FIG. 4. The result of the template fit in two energy bins [56, 65 GeV] (left) and [866, 1000 GeV] (right). For both energy bins, the fit is performed over the interval [-5,0] and the x-axis range is chosen to focus on the proton peak region. The data P_{CRE} distribution is shown before (black lines) and after (black circles) IVC corrections. The green histograms correspond to the sum of the electron (red) and proton (blue) templates.

Figures 3 and 4 show the result of the template fit in two energy bins. One can see that the IVC corrections improve the data/MC agreement for the electron peak but not for the proton peak.

It is to be noted that the data/MC disagreement for the proton peak of the P_{CRE} distribution is not an issue for the CRE analysis: the residual background contamination corresponds to protons whose showers appear very much like electromagnetic showers. So, by construction, the IVC corrections are valid for these events and we expect the tail of the proton P_{CRE} distribution in the signal region to be well reproduced by the simulation.

C. High-energy selection

We define our selection by looking, in each energy bin, for the cut on P_{CRE} which minimizes the flux uncertainty, taking into account all systematics (discussed in Sec. VI). The minimum is not very pronounced, especially above 100 GeV. We choose to apply a slightly harder cut between 300 GeV and 2 TeV, in order to facilitate the IVC corrections, whose precision benefits from a low residual background contamination. Figure 5 shows the P_{CRE} selection cut and its efficiency as a function of energy.

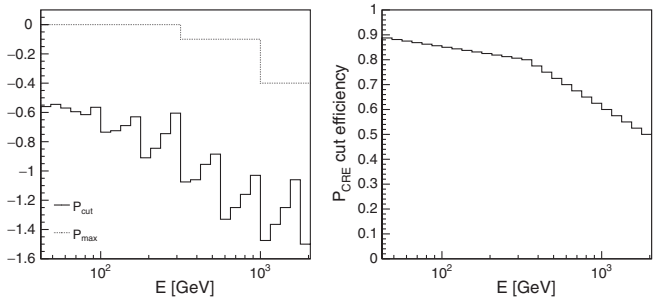


FIG. 5. Left: P_{CRE} selection cut (solid) and P_{max}, the upper end of the template fit interval (dotted), as a function of energy. Right: efficiency of the P_{CRE} selection cut as a function of energy.

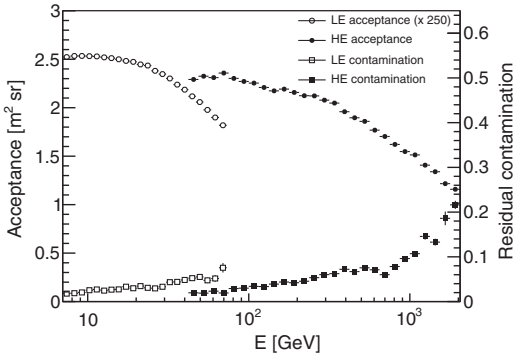


FIG. 6. Acceptance and residual background contamination as a function of energy. The displayed LE acceptance is multiplied by 250 (as if there were no prescale factor due to the on-board filter).

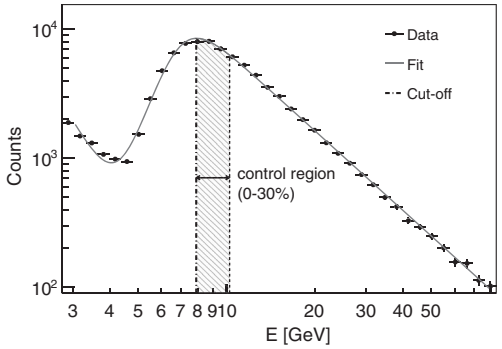


FIG. 7. Fit of the count spectrum for the McIlwain L bin [1.44, 1.49]. The control region, used in the estimation of the systematic uncertainties, corresponds to the interval $[E_c, 1.3E_c]$, where E_c is the measured energy cutoff.

The steps seen every four bins in the selection cut correspond to the transitions between the different P_{CRE} estimators at the boundaries of the BDT $\log_{10} E$ bins. The P_{CRE} selection cut is well below P_{max}.

The acceptance and the residual background contamination (defined as the ratio of the number of residual background events to the total number of events) for the HE selection are shown in Fig. 6. The fact that the acceptance decreases with energy, while the residual contamination increases, highlights the increasing difficulty of the background rejection with energy. Because the IVC corrections procedure requires enough statistics and at the same time a low background contamination, we stop the HE analysis when the residual contamination reaches 20%, which occurs at 2 TeV.

IV. LOW-ENERGY ANALYSIS

The LE selection is based on the same multivariate analysis approach as used for the HE selection. Because the energy range of the LE selection is much smaller than the HE one, we trained only one BDT, with a set of variables optimized for the LE energy range. Since the LE analysis stops at 70 GeV, there is no need to apply the IVC corrections.

The cut on P_{CRE} as a function of energy is set so that the cut efficiency for electrons is ∼90% from 7 GeV to 20 GeV and decreases to ∼65% at 70 GeV. The residual background contamination is estimated by the same template fitting technique used in the HE analysis. The acceptance and the residual background contamination for the LE selection are shown in Fig. 6.

Below ∼20 GeV, the flux of CREs observed by the LAT is strongly influenced by the shielding effect of the magnetic field of the Earth. At a given geomagnetic position and direction with respect to zenith, Galactic charged particles can reach the detector only if they are above a certain rigidity. The dependence of the rigidity cutoff on location can be conveniently parametrized by the McIlwain L parameter [27]. Geographic coordinates with the same McIlwain L parameter are magnetically equivalent from the standpoint of incoming charged particles. The orbit of *Fermi* spans an interval of McIlwain L of 0.98–1.73, corresponding to vertical rigidity cutoff values from ∼6 GeV to ∼14 GeV. Therefore, measuring the CRE spectrum at a given energy E requires selecting data collected in a McIlwain L interval in which the rigidity cutoff is smaller than E.

In order to parametrize the relation between the rigidity cutoff and McIlwain L, we fit the count spectrum in 15 McIlwain L bins with $f(E) = c_s E^{-\gamma_s} + c_p E^{-\gamma_p} / (1 + (E/E_0)^{-\alpha})$. The first term in $f(E)$ corresponds to secondary CREs while the second term in $f(E)$ corresponds to primary CREs,[1] which are suppressed below the energy E_0. An example of this fit is shown in Fig. 7. We use the position of the maximum of the second term as a measure of the local value of the energy cutoff E_c averaged over the instrument acceptance.

We map the dependence of the energy cutoff on the McIlwain L parameter with the empirical relation $E_c = -14.91 + 67.25/\mathrm{L} - 75.71/\mathrm{L}^2 + 39.44/\mathrm{L}^3$. For each energy bin of the CRE spectrum, we use this relation to find the McIlwain L value $\mathrm{L_{min}}$ corresponding to the lower boundary of the energy bin and select data collected in regions with $\mathrm{L} > \mathrm{L_{min}}$. The corresponding fraction of live time spent by the LAT in the selected regions is ∼1.25% in the lowest energy bin (from 7 to 7.8 GeV) and becomes ∼100% above ∼18.2 GeV (see Fig. 8).

Even above the nominal rigidity cutoff a fraction of electrons and positrons is prevented from reaching the detector by the magnetic shadow of the Earth. In order to estimate this fraction of undetected CREs, we use the particle trajectory tracing code (hereafter "tracer") developed by

[1]In this section, we refer to primary CREs as electrons of Galactic origin, and to secondary CREs as splash and reentrant electrons produced in the interactions of primaries in the Earth's atmosphere.

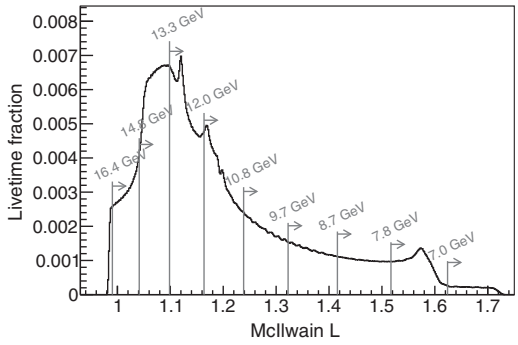


FIG. 8. Normalized distribution of the instrument live time in different McIlwain L bins for the data sample. Grey lines show the McIlwain L cut in each energy bin (with numbers indicating the lower edge of the bin).

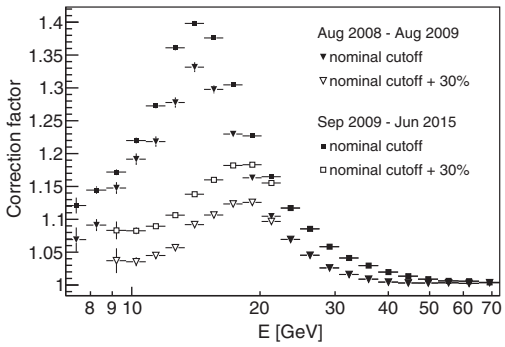


FIG. 9. LE correction factors for the first year of the mission (triangles) and for the following years (squares). Full markers correspond to the nominal energy cutoff, while the empty markers correspond to a cutoff 30% higher. Both are almost identical above 22 GeV.

Smart and Shea [27] and the 2010 model of the Earth's magnetic field from the International Geomagnetic Reference Field (IGRF) [28], as we did in [29]. For efficiency's sake, the tracer computes the trajectories of test particles in the reverse direction, starting from the spacecraft. The test particles (electrons and positrons) are generated according to a power law with an index of 3.2 using the abundance ratios measured by AMS-02 for electrons and positrons [4].

We consider test particles with trajectories reaching 20 Earth radii to have escaped the geomagnetic field, thus corresponding to CREs actually observed by the instrument, while trajectories intersecting the Earth's atmosphere correspond to lost particles. For a given McIlwain L selection, we use the tracer output to estimate the fraction of the latter.

The effect of the geomagnetic field on the loss of primaries is enhanced by a combination of the wide angular aperture of the LAT and its periodic rocking motion with respect to the local zenith, with the result that the edge of the field of view is often very close to the Earth. Because of the rocking angle dependence, we derived correction factors separately for the first year of the mission (rocking angle of 35°) and for the following years (rocking angle of 50°). These correction factors are shown in Fig. 9, as well as the correction factors that we obtain when considering energy cutoffs 30% higher. When estimating the systematic uncertainty for the LE analysis, we vary the energy cutoff choice between E_c and $1.3E_c$. For each energy cutoff, we derive the corresponding McIlwain L selection and tracer correction and compute the CRE flux. The CRE fluxes that we obtain are within 3% of the nominal flux despite the large variation of the tracer correction.

V. ENERGY MEASUREMENT

As for the previous versions of the LAT event analysis Passes 6 and 7, the Pass 8 energy reconstruction above ~5 GeV is performed by fitting the longitudinal shower profile, using the 8 CAL layer energies. The fit parameters are the energy and two parameters that describe the shape of the profile: the shape parameter α and the position of the shower maximum $T_{\max}$. Further details on the profile fit can be found in Appendix A.

Pass 8 improves the energy reconstruction and extends the energy range up to at least 2 TeV. Figure 10 shows that the energy resolution (defined as the half-width of the 68% containment range) ranges from 4% at 10 GeV to 8% at 800 GeV. Above 800 GeV the energy reconstruction is more difficult because of both low shower containment and crystal saturation. As a result the energy resolution increases more rapidly up to 17% at 2 TeV.

Compared to the previous CRE LAT analysis [16], the energy resolution is significantly improved: at 1 TeV the 68% and 95% containment half-widths were 14% and 34%, respectively. With Pass 8 they are 10% and 25%, while the gain in acceptance is 50%.

In order to define a subclass of events with a better energy resolution, which is used in Sec. VII to test the sensitivity of

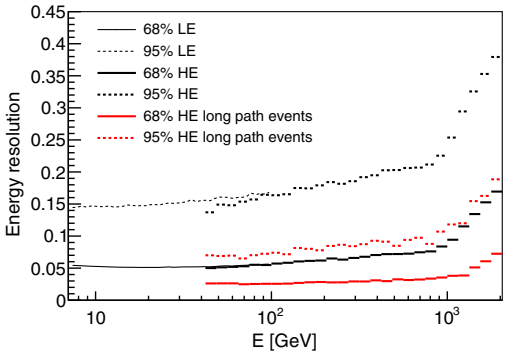


FIG. 10. Energy resolution for various selections: all events (black), events with more than 12 radiation lengths in the CAL (red). Solid (dotted) lines correspond to the 68% (95%) containment halfwidth. Thin and thick lines correspond to the LE and the HE analysis, respectively.

the spectrum to energy resolution, we select events with a CAL path-length greater than 12 X_0. It corresponds to ∼15% of the whole data set. The average CAL path-length of this long-path-events selection is 13.3 X_0 and the energy resolution is 4% at 1 TeV and 8% at 2 TeV.

Because the CAL is only 8.6 X_0 long on-axis, the showers of electrons in the energy range of our analysis are not fully contained. The shower leakage is corrected for by the energy reconstruction. Therefore we have to consider two independent sources of systematic uncertainties for the measured energy. The first one is the uncertainty of the absolute energy scale and the second one is the uncertainty induced by the energy reconstruction. The estimation of these uncertainties is described below.

The geomagnetic cutoff in the CRE spectrum at about 10 GeV provides a spectral feature that allows an absolute calibration of the LAT energy scale. At this energy, the leakage from the CAL is ∼20% and the shower maximum lies in the middle of the CAL. As a consequence, the shower profile fit allows a precise energy reconstruction and the systematic uncertainty on the energy reconstruction at 10 GeV is negligible.

A previous measurement of the geomagnetic cutoff was used to check the LAT energy scale based on one year of LAT data [29]. The same analysis, using almost seven years of Pass 8 data, is reported in Appendix B. We find that the ratio of the measured to expected geomagnetic cutoff is $1.033 \pm 0.004(\text{stat}) \pm 0.020(\text{syst})$. As a result, we decrease the event energies in data by −3.3% in both the LE and HE analyses and conclude that the systematic uncertainty on the absolute energy scale is 2%.

Above 10 GeV the shower leakage increases linearly with $\log_{10} E$ and the shower maximum gets closer to the end of the CAL. Therefore we expect that a potential systematic bias on the energy reconstruction would increase with the energy as well. For each event, the rear leakage corresponds to the extrapolation of the shower profile beyond the total amount of radiation lengths seen by the shower. The precision of this extrapolation depends on the precision we have on the parameters of the fit that drive the shower shape. In order to assess this precision, we compare the distributions of α and $T_{\max}$ in data and in the simulation, as shown in Fig. 11 for events between 1 and 1.78 TeV. We find that the data/MC differences as a function of energy for α and $T_{\max}$ are, respectively, within $\pm\delta_\alpha(E)$ and $\pm\delta_T(E)$, with $\delta_\alpha(E) = 0.05\log_{10}(E/[10\,\text{GeV}])$ and $\delta_T(E) = 0.1\log_{10}(E/[10\,\text{GeV}])$.

We estimate the uncertainty due to shower leakage by varying α and $T_{\max}$ within $\pm\delta_\alpha(E)$ and $\pm\delta_T(E)$, renormalizing the modified profile so that it matches the last layer energy and computing the maximum leakage variation. We find that it varies linearly with $\log_{10} E$ and that the resulting variation of the total reconstructed energy varies linearly with $\log_{10} E$ as $\delta E_{\text{rec}}(E) = 0.025\log_{10}(E/[10\,\text{GeV}])$, which is 5% at 1 TeV. We have checked that saturation does not contribute significantly to this systematic uncertainty, as explained in Appendix A.

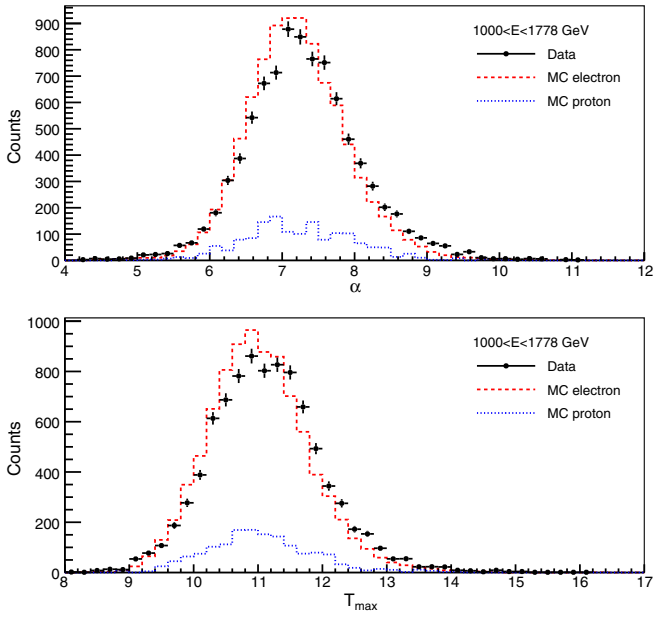


FIG. 11. The shower profile parameters α (top) and $T_{\max}$ (bottom) for events between 1 and 1.78 TeV. The contribution from residual background (blue) has been subtracted from the data distributions. The red histograms correspond to the electron simulation.

VI. SYSTEMATIC UNCERTAINTIES

For the HE analysis, we consider four sources of systematic uncertainty. The first three (acceptance, contamination, IVC) relate to the event selection, while the last one is the uncertainty of the energy measurement.

The uncertainty on the acceptance is estimated in each energy bin by measuring the sensitivity of the measured CRE flux to the choice of the cut on P_{CRE} by varying P_{cut} in a range corresponding to a variation in efficiency of ±20% around the nominal efficiency (under the requirement that $P_{\text{cut}} < P_{\max}$). The flux variation, which we attribute to a remaining data/MC disagreement, is found to be less than 2% up to ∼500 GeV, increasing to 6% at 2 TeV.

The number of residual background events is estimated by fitting simulated background templates to the data. In order to take into account the uncertainty of the GEANT4 prediction of the fraction of protons mimicking electromagnetic showers, we assume a 20% uncertainty on the number of background events after the selection cut [30–32]. Due to the small residual background contamination, this uncertainty leads to a change in the number of signal events of less than 2% up to 1 TeV, increasing to 7% at 2 TeV.

For each input variable to the BDT, the IVC corrections are derived from the difference between the peak position of the data and MC distributions. After IVC corrections, there are still some small residual differences. We derive two alternative sets of IVC corrections in which each correction is displaced by plus or minus the maximum of the residual differences at any energy and inclination angle.

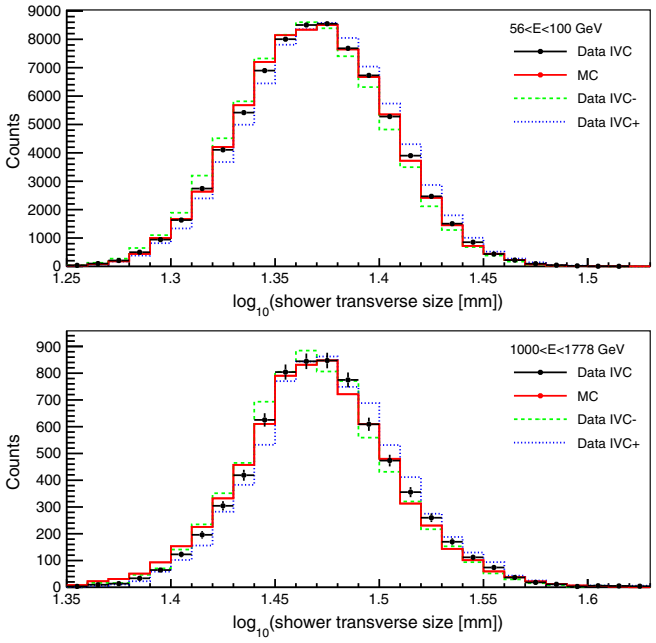


FIG. 12. The logarithm of the shower transverse size after the nominal IVC correction (black) and after moving the correction factors by plus or minus the maximum data/MC residual differences (blue and green) for events between 56 and 100 GeV (top) and between 1 and 1.78 TeV (bottom). The contribution from residual background has been subtracted from the data distributions. The red histograms correspond to the electron simulation.

Figure 12 compares the distributions of the transverse size of the shower obtained with these two sets of corrections to the nominal one and the prediction of the simulation. The variation of the number of signal events compared to the nominal IVC corrections increases from 2% at 42 GeV to 10% at 1 TeV, reaching 14% at 2 TeV.

Regarding the systematic uncertainty on the energy measurement, there are two independent sources of uncertainty as presented in Sec. V. The first one is the systematic uncertainty on the absolute energy scale, which does not depend on energy and is 2%. The second one is the systematic uncertainty on the energy reconstruction and varies linearly with $\log_{10} E$ from 0% at 10 GeV to 5% at 1 TeV.

In order to account for the energy dependent part of the energy measurement systematic uncertainty, we change the energies of all flight-data events according to some conservative scenarios that depend on the spectral hypothesis we test and repeat the whole analysis. Compared to this uncertainty, the constant 2% uncertainty on the absolute energy scale is subdominant and is not considered when fitting the CRE spectrum.

When fitting the CRE spectrum in the HE analysis energy range, we add in quadrature the acceptance uncertainty to the statistical uncertainty and we treat the sum of the contamination and the IVC corrections uncertainties as nuisance parameters, as described in Appendix C. When displaying the spectrum, the statistical and systematic uncertainties (except the one on the energy measurement) are added in quadrature.

For the LE analysis, we consider the acceptance and contamination systematic uncertainties, as well as the changes induced in the spectrum by changing the McIlwain L selection. The sum of these uncertainties is $\lesssim$4% and is added in quadrature to the statistical uncertainty.

VII. RESULTS AND DISCUSSION

For both the LE and HE analyses, we fit the CRE count spectrum by forward folding the input flux using the detector response matrix (DRM) in order to take into account the detector energy resolution. The results are shown in Figs. 13 and 15. Tables with fluxes as well as event numbers can be found in Appendix D. The bin-by-bin fluxes are obtained by performing a fit with the DRM in each bin separately with a single power law with a fixed 3.1 spectral index. We note that the LE and HE spectra match very well over the overlapping range $42 < E < 70$ GeV.

The dashed lines illustrate the systematic uncertainty on the energy reconstruction and correspond to the central values of the LAT flux for two scenarios in which the energy is changed by a factor that varies linearly in $\log_{10} E$ between 0% at 10 GeV and $\pm$5% at 1 TeV. We emphasize that these lines do not take into account the statistical uncertainty nor the systematic uncertainties unrelated to the energy measurement.

We also derive the HE spectrum using the subclass of events with a path length in the CAL greater than 12 X_0 introduced in Sec. V. This spectrum is systematically lower

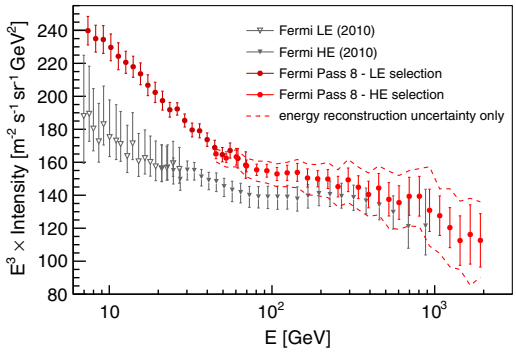


FIG. 13. CRE spectrum between 7 GeV and 2 TeV measured by the LAT and the previous LAT measurement [16]. All error bars represent the quadratic sum of statistical and systematic uncertainties (except the one on the energy measurement). The LAT flux is multiplied by the cube of the representative energy in each bin, computed following Eq. (6) of [33] with an E^{-3} spectrum. The area between the dashed lines corresponds to the uncertainty band due to the LAT energy reconstruction uncertainty only. The 2% systematic uncertainty on the energy scale is not indicated.

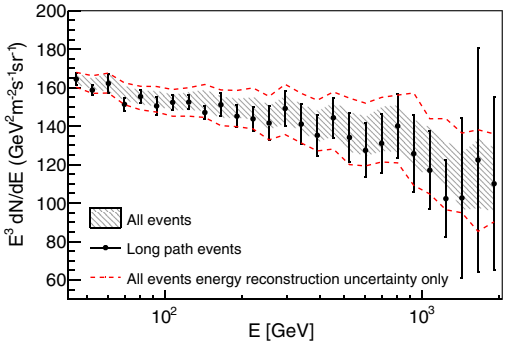


FIG. 14. CRE spectrum between 42 GeV and 2 TeV measured with all events (grey band) and with long-path events (black points). In both cases, the statistical and systematic uncertainties (except for the energy measurement) are added in quadrature. The area between the dashed lines corresponds to the uncertainty band due to the LAT energy reconstruction uncertainty only of the all-event selection.

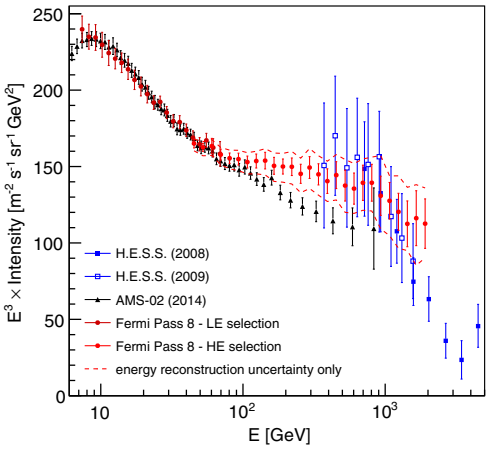


FIG. 15. CRE spectrum between 7 GeV and 2 TeV measured by the LAT along with other recent measurements by AMS-02 [15] and H.E.S.S. [17,18]. All error bars represent the quadratic sum of statistical and systematic uncertainties (except the one on the energy measurement). The LAT flux is multiplied by the cube of the representative energy in each bin, computed following Eq. (6) of [33] with an E^{-3} spectrum. The area between the dashed lines corresponds to the uncertainty band due to the LAT energy measurement uncertainty only. The 2% systematic uncertainty on the energy scale is not indicated.

than but compatible with the all-events spectrum, as can be seen in Fig. 14. Although the energy resolution for the long-path selection is much better, the systematic uncertainties (except the one on the energy measurement) are similar to the ones of the all-events spectrum up to 200 GeV and larger above. Regarding the systematic uncertainty on the energy measurement, the long-path selection spectrum is halfway between the nominal spectrum and the spectrum corresponding to an energy correction of -5% at 1 TeV. It is compatible with the systematic uncertainty on the energy measurement of the long-path selection which is 2.5% at 1 TeV. We conclude that the long-path selection does not allow a more precise measurement of the CRE spectrum but it tends to favor a scenario in which the energy correction is negative rather than positive.

Below 100 GeV, the new LAT measurement differs from the previous one by 10%–30%, as can be seen in Fig. 13. A large part of this difference below 30 GeV is due to the lack of correction in the previous analysis for the loss of CREs above the geomagnetic energy cutoff. After applying this correction, the remaining difference is 10–15% and is due to imperfections in the simulation that was used in the previous analysis (remnants of electronic signals from out-of-time particles were not simulated [34]).

The CRE spectrum between 7 and 42 GeV is well fitted by a power law with a spectral index 3.21 ± 0.02. The low χ^2 (2.25 for 15 degrees of freedom) means that the systematic uncertainties are too large to detect the deviation from a power law due to the magnetic field of the heliosphere. This is strengthened by the fact that fitting between 15 and 42 GeV changes the spectral index by only 0.005. We therefore do not take into account the heliospheric effects in the following fits.

As can be seen in Fig. 15, when not taking into account the uncertainty on the energy reconstruction, the LAT CRE spectrum is above the AMS-02 one for energies larger than ~70 GeV and suggests the presence of a break in the spectrum. Fitting the spectrum between 7 GeV and 2 TeV with a single power law yields $\chi^2 = 64.6$ for 36 degrees of freedom, corresponding to a probability of 2.4×10^{-3}. As expected, a broken power-law fit yields a much lower $\chi^2 = 19.2$ for 34 degrees of freedom. The break energy is 53 ± 8 GeV and the spectral indices below and above the break are 3.21 ± 0.02 and 3.07 ± 0.02, respectively.

In order to estimate the influence of the energy measurement systematic uncertainty on the detection of a break, we consider the event-energy rescaling scenario that would be responsible for such a break, among the scenarios allowed by the systematic uncertainty on the energy reconstruction. In this scenario, the energy is unchanged up to 50 GeV and then decreases linearly with $\log_{10} E$ to −5% at 1 TeV. The single power-law fit then yields a $\chi^2 = 49.9$ for 36 degrees of freedom, corresponding to a 6% probability.

This relatively low probability suggests that the broken power-law hypothesis would be preferred. The broken power-law fit, performed with the same scenario, yields indeed a lower $\chi^2 = 28.9$ for 34 degrees of freedom, a break energy of 47 ± 6 GeV and spectral indices below and above the break of 3.21 ± 0.02 and 3.11 ± 0.02, respectively. The χ^2 difference is 21 for two less degrees of freedom. The broken power-law hypothesis is thus preferred at the 4σ level. We note that in all the fits, some of the systematic uncertainties are treated using the nuisance parameter approach. Therefore the χ^2 and corresponding probabilities depend slightly on the number of nuisance

parameters but the level of significance of the break does not change.

AMS-02 estimated the lower limit above which the flux is described by a single power law and found 30.2 GeV [15], reporting a spectral index above this energy of $3.170 \pm 0.008(\text{stat} + \text{syst}) \pm 0.008(\text{energy measurement})$. Performing a single power-law fit of the LAT spectrum above the same energy with the energy modification scenario introduced above, we find a spectral index of 3.125 ± 0.020, with a χ^2 of 28.9 for 22 degrees of freedom, corresponding to a 14% probability. Comparing this result to the lower AMS-02 value allowed by the systematic uncertainty on the energy scale, we find that the difference between the Fermi and AMS-02 spectral indices above 30.2 GeV is 0.037 ± 0.022. The difference is at the level of 1.7σ. This could indicate that systematic uncertainties on the energy measurement in one or both of the results are slightly larger than estimated.

At higher energies, H.E.S.S. reported in [17] that, leaving its energy scale factor free, the H.E.S.S. data above 600 GeV combined with earlier data were well reproduced by an exponentially cutoff power law with an index of 3.05 ± 0.02 and a cutoff at 2.1 ± 0.3 TeV. The LAT CRE spectrum above 50 GeV, as indicated by the previous broken power-law fits, is compatible with a single power law with a spectral index of $3.07 \pm 0.02(\text{stat} + \text{syst}) \pm 0.04(\text{energy measurement})$. Fitting the count spectrum above 50 GeV with an exponentially cutoff power law $E^{-\gamma} e^{-E/E_c}$ does not yield statistically significant evidence for a cutoff (a χ^2 difference of 1 for 1 less degree of freedom) and we exclude $E_c < 2.1$ TeV at 95% CL. Assuming a scenario in which the energy is changed by 0% at 50 GeV to −5% at 1 TeV, we exclude $E_c < 1.8$ TeV at 95% CL.

Regarding the agreement between the H.E.S.S. and LAT spectra, we note that, as can be seen in Fig. 15, the energy measurement scenario corresponding to the lower dashed line yields a LAT CRE spectrum that connects to H.E.S.S. data around 1 TeV. With this scenario, the LAT spectral index is ∼3.11, relatively steeper than 3.05, as reported by H.E.S.S. As a result, a LAT and H.E.S.S. combined fit would lead to a cutoff larger than ∼2.1 TeV, well above the LAT lower limit of 1.8 TeV.

The precision of the LAT measurement is limited primarily by the energy dependent systematic uncertainty on the energy measurement, due to the low containment of CRE induced showers in the LAT calorimeter that worsens with energy. A possible way to mitigate this issue would be to use CRE events with an incidence angle greater than 60 degrees. The showers of these events are much more contained in the LAT instrument and the systematic uncertainty on the energy reconstruction would thus be reduced. Unfortunately, the drawback of this approach is that the track information of such events is scarce or inaccurate, which strongly hampers background rejection. We have started to investigate this approach but assessing the improvement that it can lead to is beyond the scope of this paper.

If this approach proves to be successful, its results, along with updated measurements of AMS-02 and H.E.S.S. and the first results of DAMPE [35] and CALET [36], would certainly help in detecting and characterizing precisely the features of the CRE spectrum between 10 GeV and several TeVs.

ACKNOWLEDGMENTS

The *Fermi*-LAT Collaboration acknowledges support for LAT development, operation and data analysis from NASA and DOE (United States), CEA/Irfu and IN2P3/CNRS (France), ASI and INFN (Italy), MEXT, KEK, and JAXA (Japan), and the K. A. Wallenberg Foundation, the Swedish Research Council and the National Space Board (Sweden). Science analysis support in the operations phase from INAF (Italy) and CNES (France) is also gratefully acknowledged. We would like to thank the INFN GRID Data Centers of Pisa, Trieste and CNAF-Bologna, the DOE SLAC National Accelerator Laboratory Computing Division, and the CNRS/IN2P3 Computing Center (CC-IN2P3—Lyon/Villeurbanne) in partnership with CEA/DSM/Irfu for their strong support in performing the massive simulations necessary for this work. W. Mitthumsiri is partially supported by the Thailand Research Fund (Grants No. TRG5880173 and No. RTA5980003).

APPENDIX A: ENERGY RECONSTRUCTION

The LAT energy reconstruction above ∼5 GeV is performed by fitting the shower profile, using the eight CAL layer energies. We use the following representation of the longitudinal shower profile [37],

$$\frac{dE(t)}{dt} = E \times \mathcal{P}(\alpha, \beta, t) = E \times \frac{(\beta t)^{\alpha-1} \beta e^{-\beta t}}{\Gamma(\alpha)}, \qquad \text{(A1)}$$

where t is the longitudinal shower depth in units of radiation length, α the shape parameter, and β the scaling parameter. The profile shape $\mathcal{P}$ is such that $\int \mathcal{P}(\alpha, \beta, t) dt = 1$ and its maximum for given values of α and β is reached at $T_{\max} = (\alpha - 1)/\beta$. The profile fit has three parameters (the energy and two shape parameters) and 5 degrees of freedom.

We use a model of the longitudinal profile (mean and standard deviation of the shape parameters) and a model of the average radial profile of electromagnetic showers in CsI. Both models describe the variation of the longitudinal and radial profiles with energy and were derived using dedicated GEANT4 simulations from 1 GeV to 3 TeV.

The profile fit fully takes into account the geometry of the LAT calorimeter (especially the gaps between modules) in order to predict the energy deposited in the layers

and crystals for any given shower profile. The energy deposition prediction is performed on an event-by-event basis, by going forward along the event axis (measured with the tracker) in steps of 1.85 mm ($0.1X_0$). At each step, we compute the fraction of energy deposited in each crystal, taking into account the shower longitudinal and radial profiles and the calorimeter geometry.

The fraction of energy deposited in the crystals as a function of distance along the event axis is translated into a fraction of deposited energy as a function of radiation length, which is used in the profile fit to compute the layer energies that are compared to the measured ones. It is to be noted that the longitudinal profile is free to fluctuate in the fit according to the model of the longitudinal profile derived with GEANT4. This is done by adding to the χ^2 a gaussian prior for each of the shape parameters, with mean and standard deviation as given by the model of the longitudinal profile. More information can be found in [38].

Pass 8 introduces several improvements to the energy reconstruction:

(i) the upper end of the energy range over which the shower longitudinal and radial models have been computed has been increased from 150 GeV to 3 TeV;
(ii) the widening of the radial profile in the gaps between modules has been modeled;
(iii) in the Pass 6/7 version of the profile fit, layers with at least one saturated crystal were discarded. In Pass 8, only the saturated crystals are discarded: for each layer, the energy that is considered in the fit is the sum of the energy of the nonsaturated crystals.

The last point must be taken into account when estimating the systematic uncertainty on the energy reconstruction presented in Sec. V. The energy deposited in the saturated crystals is missed and this additional leakage amounts on average to 10% at 1 TeV, increasing to 25% at 2 TeV. Saturation occurs for crystals in the core of the shower. Therefore, the predicted energy for the layers with saturated crystals depends on the radial profile model that we use.

In order to quantify the dependence of the energy reconstrution on the radial profile model, we scale it by ±20%. As expected, scaling the radial profile changes the χ^2 of the fit but we find that this variation occurs only above ~800 GeV, that is to say when crystal saturation is important. Below ~800 GeV, the χ^2 is unchanged. The comparison of the $\log_{10}\chi^2$ between data and MC shows that the data/MC difference increases linearly with $\log_{10} E$, from 0 at 10 GeV to 0.13 at 1 TeV, without any sharp variation around 800 GeV. Quantitatively, the variation of this data/MC difference between 800 GeV and 1 TeV is less than 0.05, which would correspond to a 5% scaling of the radial profile. We therefore conclude that the radial profile model we use is correct within 5%. When scaling the radial profile within 5%, we find that the reconstructed energy variation is smaller than $0.1\delta E_{\rm rec}(E)$ and conclude that saturation does not significantly contribute to the systematic uncertainty on the energy reconstruction.

APPENDIX B: MEASUREMENT OF THE ABSOLUTE ENERGY SCALE AT ~10 GeV

The geomagnetic cutoff in the CRE spectrum provides a spectral feature that allows an absolute calibration of the LAT energy scale. A previous measurement of the geomagnetic cutoff was used to calibrate the LAT energy scale based on one year of LAT data [29]. We performed the same analysis, using almost seven years of Pass 8 data, in six McIlwain L intervals. We used the LE CRE estimator with a cut ensuring a constant 2% residual background contamination. The $P_{\rm CRE}$ cut efficiency for electrons is ~30% below 5 GeV, rising to 90% at 10 GeV. In order to check the sensitivity of the measurements to the selection, we also used a selection ensuring a constant 5% residual background contamination, which corresponds to an efficiency of 70% below 5 GeV, rising to 95% at 10 GeV.

After background subtraction, we are left with primary and secondary electrons. In order to measure the fraction of secondaries, we fit the CRE azimuthal distribution with the sum of two templates: for primary CREs, we use the one predicted by the tracer and, for secondary electrons, we use the one observed in data well below the rigidity cutoff (when the primary fraction is lower than 0.5%). Figure 16

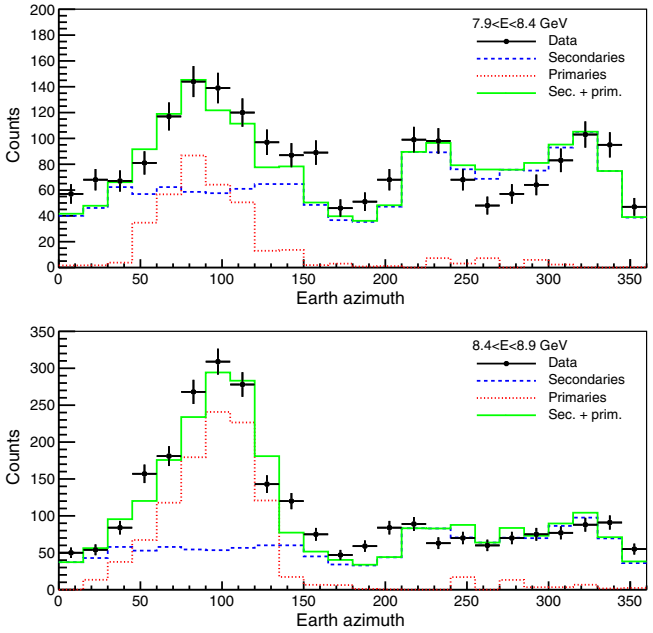


FIG. 16. Examples of the template fit of the azimuthal distribution for McIlwain L in [1.0, 1.1]: events between 7.9 and 8.4 GeV (top) and between 8.4 and 8.9 GeV (bottom). The black, red, blue and green histograms correspond to data, the secondary template, the primary template, and the sum of the secondary and primary templates. North and East correspond to 0 and 90°, respectively.

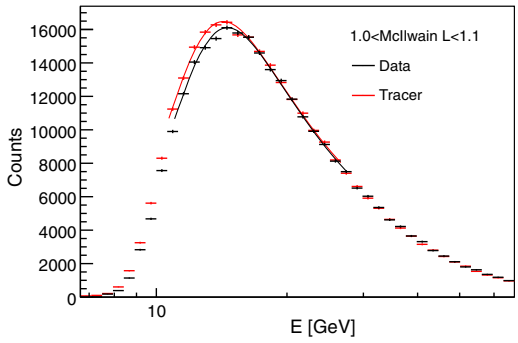


FIG. 17. Measured count spectrum (black) of primary CREs after removal of secondary electrons for the McIlwain L interval [1.0, 1.1], and the count spectrum predicted by the tracer. The latter is normalized so that its integral above 20 GeV is the same as in the data.

shows two examples of such fits for McIlwain L in [1.0, 1.1]. They correspond to two adjacent energy bins below the geomagnetic cutoff, in which the primary fraction increases from 20% to 45%.

For each McIlwain L interval, we fit for the contribution of secondaries as a function of energy and subtract it to obtain the count spectrum of primary CRE. We fit the count spectrum with $E^{-\gamma_p}/(1+(E/E_c)^{-\alpha})$, where E_c is the cutoff and γ_p is the spectral index above E_c. We modify the tracer input spectrum according to solar modulation, using the force field approximation with a solar modulation parameter ϕ set to an average value for the 2008–2015 period of 500 MV. Figure 17 shows the result of the fit for the McIlwain L interval [1.0, 1.1]. We then compare the values of E_c obtained in the data and predicted by the tracer to check the LAT absolute energy scale.

The $E_c^{\rm data}/E_c^{\rm tracer}$ ratios in the six McIlwain L intervals are in agreement, as shown in Fig. 18, and the average ratio is 1.033 ± 0.004. We varied the parameters of the analysis (event selection, energy interval used to derive the template of secondaries and spectral index of the tracer spectrum) and found that the average ratio did not vary by more than 0.3%. Using the IGRF 1995 model changed the result by less than 0.1%. We performed this analysis in various time periods and the ratio was constant within less than 1%. We also changed the solar modulation parameter ϕ to 0 and 1000 MV and the ratio changed by 0.5%. We thus estimate the systematic uncertainty of the ratio measurement to be 2%. The previous LAT measurement of the absolute energy scale found an average ratio of $1.025 \pm 0.005(\text{stat}) \pm 0.025(\text{syst})$, which is compatible with the new result.

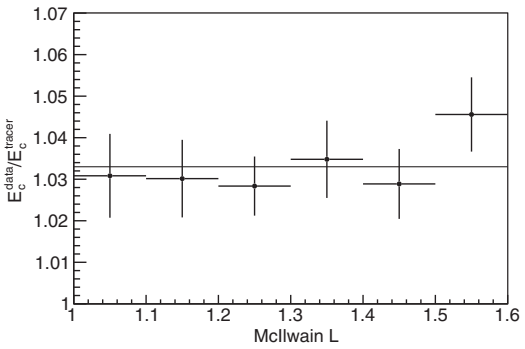


FIG. 18. The $E_c^{\rm data}/E_c^{\rm tracer}$ ratio as a function of McIlwain L. The horizontal line corresponds to the average ratio.

APPENDIX C: SYSTEMATIC UNCERTAINTIES AS NUISANCE PARAMETERS

The potential systematic bias in the CRE flux measurement induced by the systematic uncertainties on background subtraction and the IVC corrections can be modeled as a sequence of unknown correction factors. They correspond to nuisance parameters that are derived in the fit of the CRE spectrum when we test different parameterizations for the CRE spectrum.

We define $\mathcal{S}(E)$ as the quadratic sum of the contamination and IVC corrections systematic uncertainties (discussed in Sec. VI) as a function of energy. We choose $\mathcal{N}$ reference energies $\mathcal{E}_j$, logarithmically spaced between 42 GeV and 2 TeV, in order to define $s(E;\mathbf{w})$, a piecewise function, linear in $\log_{10} E$, defined by its values w_j at $\mathcal{E}_j$. The set of w_j are the nuisance parameters. The correction factor for the predicted number of counts in the analysis energy bin i is $1+s(E_i;\mathbf{w})\mathcal{S}(E_i)$ and the χ^2 function for the spectral fit is given by

$$\chi^2 = \sum_{i=1}^{n}\left(\frac{N_i - [1+s(E_i;\mathbf{w})\mathcal{S}(E_i)]\mu_i(\boldsymbol{\theta})}{\delta N_i}\right)^2 + \sum_{j=1}^{\mathcal{N}} w_j^2, \tag{C1}$$

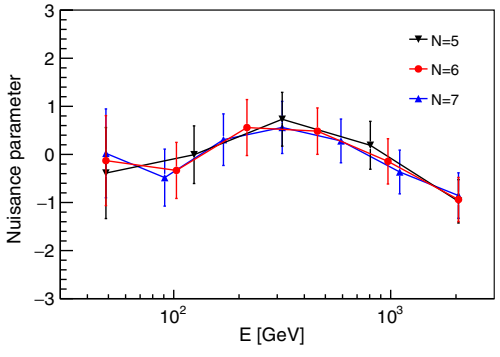


FIG. 19. Nuisance parameters found by the fit of the CRE spectrum between 50 GeV and 2 TeV for various numbers of reference energies: $\mathcal{N}=5$ (black), 6 (red), and 7 (blue).

where $\boldsymbol{\theta}$ are the free parameters of the CRE spectral model, n is the number of energy bins of the analysis, N_i is the number of counts measured in bin i, μ_i is the predicted number of counts after convolution with the DRM and δN_i is the quadratic sum of the statistical and acceptance uncertainties. The second term of the χ^2 function corresponds to a Gaussian prior on the amplitude of the nuisance parameters.

The choice of the number of nuisance parameters $\mathcal{N}$ cannot be inferred from first principles. Between the contamination and the IVC corrections systematic uncertainties, the latter dominates. Because we build eight BDTs, the importance of the BDT input variables can change from bin to bin. As a consequence, a change of the IVC correction for one observable can have a significantly different impact even on two adjacent BDT energy bins.

Ignoring any correlation between BDT energy bins would lead to the choice $\mathcal{N} = 8$. But the importance of the input variables depends on the variation of the event topology with energy, which is not expected to change abruptly at the BDT energy boundaries. And this argument also applies for the contamination uncertainty. In order to take into account the BDT bin-to-bin correlation, we chose $\mathcal{N} = 6$. We checked that the fit results do not change significantly with $\mathcal{N} = 5$ or 7.

When fitting the CRE spectrum between 50 GeV and 2 TeV with a single power law and $\mathcal{N} = 6$, we find $\chi^2 = 15.5$ for 18 degrees of freedom. The nuisance parameters values found by the fitting procedure are shown in Fig. 19, as well as those found with $\mathcal{N} = 5$ and 7. In all three cases, the nuisance parameters are within ± 1 and the spectral index is 3.07 ± 0.02.

When fitting with an exponentially cutoff power law $E^{-\gamma} e^{-E/E_c}$, the 95% CL lower limit on the energy cutoff for $\mathcal{N} = 5$, 6 and 7 is 2.18, 2.13, and 2.19, respectively.

APPENDIX D: TABLES

Tables I and II give the number of events, the residual background contamination, and the CRE flux in each energy bin for the LE and HE analyses, respectively. These tables are available in machine-readable format at https://www-glast.stanford.edu/pub_data/1144.

TABLE I. Number of events after background subtraction (without correction for the loss of CREs above the geomagnetic energy cutoff), residual background contamination and flux J_E, with its statistical and systematic errors, for the LE selection.

Energy (GeV)	Counts	Contamination	J_E (GeV^{-1} s^{-1} m^{-2} sr^{-1})
7.0–7.8	8231	0.02	$5.93\times (1 \pm 0.016 \pm 0.032) \times 10^{-01}$
7.8–8.7	35912	0.02	$4.18\times (1 \pm 0.008 \pm 0.034) \times 10^{-01}$
8.7–9.7	51417	0.02	$3.02\times (1 \pm 0.007 \pm 0.035) \times 10^{-01}$
9.7–10.8	60019	0.03	$2.15\times (1 \pm 0.007 \pm 0.035) \times 10^{-01}$
10.8–12.0	66545	0.03	$1.53\times (1 \pm 0.007 \pm 0.036) \times 10^{-01}$
12.0–13.3	74725	0.02	$1.09\times (1 \pm 0.007 \pm 0.030) \times 10^{-01}$
13.3–14.8	84090	0.03	$7.90\times (1 \pm 0.007 \pm 0.029) \times 10^{-02}$
14.8–16.4	89109	0.03	$5.67\times (1 \pm 0.007 \pm 0.030) \times 10^{-02}$
16.4–18.2	81203	0.03	$4.02\times (1 \pm 0.007 \pm 0.030) \times 10^{-02}$
18.2–20.2	68111	0.03	$2.88\times (1 \pm 0.008 \pm 0.029) \times 10^{-02}$
20.2–22.4	56832	0.03	$2.06\times (1 \pm 0.008 \pm 0.028) \times 10^{-02}$
22.4–24.8	46535	0.03	$1.47\times (1 \pm 0.009 \pm 0.022) \times 10^{-02}$
24.8–27.6	38267	0.03	$1.07\times (1 \pm 0.010 \pm 0.017) \times 10^{-02}$
27.6–30.7	30449	0.03	$7.54\times (1 \pm 0.011 \pm 0.018) \times 10^{-03}$
30.7–34.1	23408	0.04	$5.33\times (1 \pm 0.013 \pm 0.020) \times 10^{-03}$
34.1–37.9	18867	0.04	$3.87\times (1 \pm 0.014 \pm 0.019) \times 10^{-03}$
37.9–42.2	14718	0.05	$2.72\times (1 \pm 0.016 \pm 0.017) \times 10^{-03}$
42.2–47.0	11186	0.05	$1.92\times (1 \pm 0.019 \pm 0.018) \times 10^{-03}$
47.0–52.3	8618	0.06	$1.35\times (1 \pm 0.021 \pm 0.015) \times 10^{-03}$
52.3–58.5	6942	0.05	$9.89\times (1 \pm 0.023 \pm 0.015) \times 10^{-04}$
58.5–65.3	5165	0.05	$6.89\times (1 \pm 0.027 \pm 0.024) \times 10^{-04}$
65.3–73.0	3891	0.08	$4.82\times (1 \pm 0.034 \pm 0.038) \times 10^{-04}$

TABLE II. Number of events after background subtraction, residual background contamination and flux J_E, with its statistical and systematic errors (the acceptance uncertainty and the sum of the contamination and IVC correction uncertainties are shown separately), for the HE selection.

Energy (GeV)	Counts	Contamination	J_E (GeV^{-1} s^{-1} m^{-2} sr^{-1})
42.2–48.7	3948132	0.02	$1.78\times (1 \pm 0.001 \pm 0.012 \pm 0.013) \times 10^{-03}$
48.7–56.2	2945632	0.02	$1.14\times (1 \pm 0.001 \pm 0.008 \pm 0.014) \times 10^{-03}$
56.2–64.9	2189648	0.02	$7.42\times (1 \pm 0.002 \pm 0.027 \pm 0.016) \times 10^{-04}$
64.9–75.0	1609640	0.02	$4.66\times (1 \pm 0.001 \pm 0.016 \pm 0.017) \times 10^{-04}$
75.0–86.6	1161424	0.03	$2.98\times (1 \pm 0.002 \pm 0.009 \pm 0.020) \times 10^{-04}$
86.6–100.0	865855	0.03	$1.93\times (1 \pm 0.002 \pm 0.012 \pm 0.022) \times 10^{-04}$
100.0–115.5	629884	0.03	$1.24\times (1 \pm 0.002 \pm 0.012 \pm 0.023) \times 10^{-04}$
115.5–133.4	466148	0.03	$8.06\times (1 \pm 0.002 \pm 0.016 \pm 0.025) \times 10^{-05}$
133.4–154.0	343066	0.04	$5.24\times (1 \pm 0.002 \pm 0.021 \pm 0.029) \times 10^{-05}$
154.0–177.8	253798	0.04	$3.33\times (1 \pm 0.003 \pm 0.013 \pm 0.034) \times 10^{-05}$
177.8–205.4	187997	0.04	$2.16\times (1 \pm 0.003 \pm 0.015 \pm 0.029) \times 10^{-05}$
205.4–237.1	138234	0.05	$1.40\times (1 \pm 0.003 \pm 0.020 \pm 0.032) \times 10^{-05}$
237.1–273.8	101444	0.05	$8.80\times (1 \pm 0.004 \pm 0.016 \pm 0.040) \times 10^{-06}$
273.8–316.2	75547	0.06	$5.88\times (1 \pm 0.005 \pm 0.014 \pm 0.045) \times 10^{-06}$
316.2–365.2	54462	0.06	$3.70\times (1 \pm 0.005 \pm 0.018 \pm 0.044) \times 10^{-06}$
365.2–421.7	37883	0.07	$2.33\times (1 \pm 0.006 \pm 0.019 \pm 0.054) \times 10^{-06}$
421.7–487.0	28142	0.07	$1.56\times (1 \pm 0.007 \pm 0.007 \pm 0.060) \times 10^{-06}$
487.0–562.3	19641	0.08	$9.62\times (1 \pm 0.008 \pm 0.016 \pm 0.071) \times 10^{-07}$
562.3–649.4	14000	0.07	$6.16\times (1 \pm 0.009 \pm 0.033 \pm 0.067) \times 10^{-07}$
649.4–749.9	10240	0.06	$4.11\times (1 \pm 0.010 \pm 0.042 \pm 0.070) \times 10^{-07}$
749.9–866.0	7338	0.08	$2.67\times (1 \pm 0.012 \pm 0.024 \pm 0.082) \times 10^{-07}$
866.0–1000.0	4938	0.10	$1.63\times (1 \pm 0.015 \pm 0.024 \pm 0.094) \times 10^{-07}$
1000.0–1154.8	3406	0.11	$1.03\times (1 \pm 0.018 \pm 0.028 \pm 0.088) \times 10^{-07}$
1154.8–1333.5	2249	0.15	$6.31\times (1 \pm 0.023 \pm 0.016 \pm 0.097) \times 10^{-08}$
1333.5–1539.9	1491	0.13	$3.83\times (1 \pm 0.027 \pm 0.075 \pm 0.107) \times 10^{-08}$
1539.9–1778.3	1086	0.19	$2.57\times (1 \pm 0.036 \pm 0.047 \pm 0.143) \times 10^{-08}$
1778.3–2053.5	737	0.22	$1.62\times (1 \pm 0.039 \pm 0.077 \pm 0.115) \times 10^{-08}$

[1] J. Nishimura, M. Fujii, and T. Taira, *International Cosmic Ray Conference* 1, 488 (1979).
[2] O. Adriani *et al.*, Nature (London) **458**, 607 (2009).
[3] M. Ackermann *et al.* (Fermi-LAT Collaboration), Phys. Rev. Lett. **108**, 011103 (2012).
[4] L. Accardo *et al.* (AMS Collaboration), Phys. Rev. Lett. **113**, 121101 (2014).
[5] M. Ackermann *et al.* (Fermi-LAT Collaboration), Phys. Rev. D **82**, 092003 (2010).
[6] C. S. Shen, Astrophys. J. **162**, L181 (1970).
[7] J. Nishimura, M. Fujii, T. Taira, E. Aizu, H. Hiraiwa, T. Kobayashi, K. Niu, I. Ohta, R. L. Golden, and T. A. Koss, Astrophys. J. **238**, 394 (1980).
[8] J. Nishimura, T. Kobayashi, Y. Komori, and K. Yoshida, Adv. Space Res. **19**, 767 (1997).
[9] F. A. Aharonian, A. M. Atoyan, and H. J. Voelk, Astron. Astrophys. **294**, L41 (1995).
[10] T. Kobayashi, Y. Komori, K. Yoshida, and J. Nishimura, Astrophys. J. **601**, 340 (2004).
[11] P. Blasi, Phys. Rev. Lett. **103**, 051104 (2009).
[12] I. Cholis, L. Goodenough, D. Hooper, M. Simet, and N. Weiner, Phys. Rev. D **80**, 123511 (2009).
[13] M. Cirelli, M. Kadastik, M. Raidal, and A. Strumia, Nucl. Phys. **B813**, 1 (2009); **B873**, 530 (2013).
[14] L. Bergstrom, J. Edsjo, and G. Zaharijas, Phys. Rev. Lett. **103**, 031103 (2009).
[15] M. Aguilar *et al.* (AMS Collaboration), Phys. Rev. Lett. **113**, 221102 (2014).
[16] M. Ackermann *et al.* (Fermi-LAT Collaboration), Phys. Rev. D **82**, 092004 (2010).
[17] F. Aharonian *et al.* (H.E.S.S. Collaboration), Phys. Rev. Lett. **101**, 261104 (2008).
[18] F. Aharonian *et al.* (H.E.S.S. Collaboration), Astron. Astrophys. **508**, 561 (2009).
[19] M. Di Mauro, F. Donato, N. Fornengo, R. Lineros, and A. Vittino, J. Cosmol. Astropart. Phys. 04 (2014) 006.
[20] W. B. Atwood *et al.* (Fermi-LAT Collaboration), Astrophys. J. **697**, 1071 (2009).
[21] W. Atwood *et al.* (Fermi-LAT Collaboration), arXiv: 1303.3514.

[22] S. Abdollahi *et al.* (Fermi-LAT Collaboration), Phys. Rev. Lett. **118**, 091103 (2017).
[23] M. Di Mauro *et al.* (Fermi-LAT Collaboration), arXiv: 1703.00460.
[24] A. Hocker *et al.*, *Proc. Sci.*, ACAT2007 (2007) 040 [arXiv: physics/0703039].
[25] S. Agostinelli *et al.* (Geant4 Collaboration), Nucl. Instrum. Methods Phys. Res., Sect. A **506**, 250 (2003).
[26] T. Mizuno, T. Kamae, G. Godfrey, T. Handa, D. J. Thompson, D. Lauben, Y. Fukazawa, and M. Ozaki, Astrophys. J. **614**, 1113 (2004).
[27] D. F. Smart and M. A. Shea, Adv. Space Res. **36**, 2012 (2005).
[28] C. C. Finlay *et al.*, Geophys. J. Int. **183**, 1216 (2010).
[29] M. Ackermann *et al.* (Fermi-LAT Collaboration), Astropart. Phys. **35**, 346 (2012).
[30] J. Yarba, J. Phys. Conf. Ser. **396**, 022060 (2012).
[31] A. Dotti (Geant4 Hadronic Working Group, Electromagnetic Working Group Collaboration), in *Proceedings, International Conference on Calorimetry for the High Energy Frontier (CHEF 2013)* (2013), p. 247.
[32] B. Bilki *et al.* (CALICE Collaboration), J. Instrum. **10**, P04014 (2015).
[33] G. D. Lafferty and T. R. Wyatt, Nucl. Instrum. Methods Phys. Res., Sect. A **355**, 541 (1995).
[34] M. Ackermann *et al.* (Fermi-LAT Collaboration), Astrophys. J. Suppl. Ser. **203**, 4 (2012).
[35] F. Gargano (DAMPE Collaboration), in *25th European Cosmic Ray Symposium (ECRS 2016) Turin, Italy, 2016* (2017) arXiv:1701.05046.
[36] P. S. Marrocchesi (CALET Collaboration), J. Phys. Conf. Ser. **718**, 052023 (2016).
[37] E. Longo and I. Sestili, Nucl. Instrum. Methods **128**, 283 (1975), **135**, 587 (1976).
[38] P. Bruel, J. Phys. Conf. Ser. **404**, 012033 (2012).

The Astrophysical Journal Supplement Series, 230:21 (15pp), 2017 June https://doi.org/10.3847/1538-4365/aa74d2
© 2017. The American Astronomical Society. All rights reserved.

Cosmic-Ray Diffusion Coefficients throughout the Inner Heliosphere from a Global Solar Wind Simulation

R. Chhiber[1], P. Subedi[1], A. V. Usmanov[1,2], W. H. Matthaeus[1], D. Ruffolo[3], M. L. Goldstein[2], and T. N. Parashar[1]
[1] Bartol Research Institute and Department of Physics and Astronomy, University of Delaware, Newark, DE 19716, USA
[2] NASA Goddard Space Flight Center, Greenbelt, MD 20771, USA
[3] Department of Physics, Faculty of Science, Mahidol University, Bangkok 10400, Thailand
Received 2017 March 29; revised 2017 May 11; accepted 2017 May 21; published 2017 June 16

Abstract

We use a three-dimensional magnetohydrodynamic simulation of the solar wind to calculate cosmic-ray diffusion coefficients throughout the inner heliosphere ($2\ R_{\odot} - 3$ au). The simulation resolves large-scale solar wind flow, which is coupled to small-scale fluctuations through a turbulence model. Simulation results specify background solar wind fields and turbulence parameters, which are used to compute diffusion coefficients and study their behavior in the inner heliosphere. The parallel mean free path (mfp) is evaluated using quasi-linear theory, while the perpendicular mfp is determined from nonlinear guiding center theory with the random ballistic interpretation. Several runs examine varying turbulent energy and different solar source dipole tilts. We find that for most of the inner heliosphere, the radial mfp is dominated by diffusion parallel to the mean magnetic field; the parallel mfp remains at least an order of magnitude larger than the perpendicular mfp, except in the heliospheric current sheet, where the perpendicular mfp may be a few times larger than the parallel mfp. In the ecliptic region, the perpendicular mfp may influence the radial mfp at heliocentric distances larger than 1.5 au; our estimations of the parallel mfp in the ecliptic region at 1 au agree well with the Palmer "consensus" range of 0.08–0.3 au. Solar activity increases perpendicular diffusion and reduces parallel diffusion. The parallel mfp mostly varies with rigidity (P) as $P^{.33}$, and the perpendicular mfp is weakly dependent on P. The mfps are weakly influenced by the choice of long-wavelength power spectra.

Key words: cosmic rays – diffusion – methods: numerical – solar wind – turbulence

Supporting material: tar.gz file

1. Introduction

The interaction of energetic particles with the solar wind is a topic of wide interest in space physics and astrophysics. Several varieties of charged particles populate the heliosphere, including energetic particles originating at the Sun (solar energetic particles or SEPs) and galactic cosmic rays (GCRs) that enter the heliosphere uniformly and nearly isotropically from the outside (Kunow et al. 1991). These cosmic rays (CRs) are strongly guided and scattered by the solar wind and the turbulent fluctuations that are transported with it (Parker 1956, 1964; Jokipii 1966). As such, the study of the origin and transport of CRs is an important problem in heliospheric physics, with implications ranging from space weather and exploration to fundamental space plasma physics (Jokipii 1971; Fisk 1979; Kunow et al. 1991). The effects of these energetic particles on the health of astronauts (Parker 2005) and the safety of electronic components in spacecraft (Tylka et al. 1997) are an immediate concern. In addition, the accuracy with which we can understand CR propagation also provides a testbed for energetic particle transport in numerous space and astrophysical applications (Kulsrud & Pearce 1969; Dröge 2003). The solar wind provides us with an opportunity to observe, at close range, the behavior of energetic particles in random, turbulent magnetic fields (Bruno & Carbone 2013). Such fields are ubiquitous in astrophysical systems (Candia & Roulet 2004), and the insights we glean from studies of CRs in the heliosphere can potentially find application elsewhere in the universe. Finally, observations of CRs can also serve as probes into solar activity and solar wind structure, as CR variations are seen to be correlated with solar and geomagnetic activity (Snyder et al. 1963).

Theories of the modulation of CRs in the heliosphere attempt to explain the observed temporal and spatial variation in the CR spectra (Fisk 1979; Potgieter 2013), and for that purpose, require knowledge of the CR diffusion tensor. In fact, one of the key challenges in solving the Parker CR transport equation (Parker 1965) is the inadequate knowledge of the spatial, temporal, and rigidity dependence of the components of the diffusion tensor. In turn, the specification of this tensor through the heliosphere requires an understanding of two topics. First, a theoretical understanding of the diffusion process itself is needed, which would lead to predictions of the structure of the diffusion tensor itself. Equally important is the knowledge of the large-scale flows and electromagnetic field in the plasma, and the distribution of the background solar wind turbulence in which the particles are scattered. The present approach permits three-dimensional (3D), and (in principle) time-varying, calculation of all three of these properties (diffusion tensor, large-scale flow, large-scale electromagnetic field) to be computed in a single model.

The formal structure of the diffusion tensor involves diagonal components corresponding to diffusion parallel and perpendicular to the interplanetary magnetic field (IMF), as well as off-diagonal components describing perpendicular drifts (e.g., Moraal 1976; Minnie et al. 2007). Although quasi-linear theory (Jokipii 1966) extended to include time-dependent and nonlinear corrections (Goldstein 1976; Bieber et al. 1994; Dröge 2003) provides a relatively good accounting of parallel diffusion, theories of perpendicular diffusion have

faced the challenge of accounting for nonlinear effects such as the transfer of particles across field lines, backscatter from parallel diffusion, and field-line random walk (FLRW; Jokipii 1966; Giacalone & Jokipii 1999). The nonlinear guiding center (NLGC) theory (Matthaeus et al. 2003; see also Shalchi 2009) accounts for the above and is further improved by the random ballistic interpretation of Ruffolo et al. (2012a). In the current work, we focus on the parallel and perpendicular diffusion coefficients; the drift motion could be a topic for future work.

Since turbulent fluctuations are responsible for scattering CRs, the diffusion theories mentioned above typically involve turbulence parameters such as the energy of the random magnetic fluctuations and correlation scales. In the solar wind, low-frequency turbulence evolves via nonlinear cascade, while also being transported and modified by the large-scale radially expanding solar wind. At all but the smallest scales, these processes are well described by magnetohydrodynamic (MHD) models (Marsch & Tu 1989; Zhou & Matthaeus 1990). Over the years, turbulence models have incorporated simplifying assumptions relevant to the solar wind, yielding increased tractability of the governing equations (Zank et al. 1996; Matthaeus et al. 1999b). The increased sophistication of the models and improvements in computational power have led to numerical simulations yielding good agreement with *Voyager, Ulysses, Helios*, and *WIND* observations (Breech et al. 2008; Usmanov et al. 2011). These turbulence models have also been used to study the propagation of coronal mass ejections (CMEs) (Wiengarten et al. 2015). Extensions to the Breech et al. (2008) model have been developed (Oughton et al. 2011; Zank et al. 2012, 2017) and applied to the inhomogeneous solar wind (Shiota et al. 2017).

Our strategy for evaluating the CR diffusion coefficients through the inner heliosphere consists of two steps: first, specification of the relevant turbulence parameters based on a global solar wind model, and second, evaluation of the CR diffusion coefficients using the specified heliographic distribution of turbulence. For the first step, we deduce turbulence parameters from a global, 3D MHD simulation of the solar wind (Usmanov et al. 2014).

The spatial resolution that can be realistically achieved in such simulations cannot resolve the small-scale fluctuations that cause the scattering of CRs. For instance, the spatial resolution of our simulation, at 1 au, can be estimated to be roughly 0.03 au. However, the mean free path (mfp), at 1 au, for scattering perpendicular to the mean magnetic field has been estimated to be as low as 0.001 au (Zhang et al. 2009; Pei et al. 2010), and the correlation scale of the turbulence has been estimated to be around 0.007 au (Matthaeus et al. 2005; Bruno & Carbone 2013). This is where our turbulence model for the "subresolution" physics comes in. Our simulation explicitly resolves the large-scale, mean solar wind bulk flow, which is coupled to small-scale inhomogeneities by means of an MHD-Reynolds-averaged Navier–Stokes (RANS; see, e.g., McComb 1990) model for random fluctuations. The simulation has been well tested and has reasonable agreement with many spacecraft observations of large-scale solar wind fields, turbulence parameters (energy, cross helicity, and correlation scale), and the temperature for varying heliocentric distances, and where feasible, varying heliolatititudes (Usmanov et al. 2011, 2012, 2016). In a recent "applied" work, the simulation was used to study the collisional age of the solar wind plasma (Chhiber et al. 2016), and we view the present work as a continuation of such application-oriented studies.

Once the turbulence parameters are specified through the model heliosphere, for the second step of our calculation, we use, as a starting point, fairly standard, well-tested formalisms for the parallel and perpendicular diffusion coefficients: quasi-linear theory (Jokipii 1966; Bieber et al. 1995; Zank et al. 1998) to compute the parallel component of the diffusion tensor, and the random ballistic decorrelation (RBD) interpretation of NLGC theory (Matthaeus et al. 2003; Ruffolo et al. 2012a) for the perpendicular diffusion.

Previous studies of the heliographic dependence of the CR diffusion coefficients include work based on both WKB models for Alfvén waves (Völk et al. 1974; Morfill & Voelk 1979) and models for strong turbulence (Bieber et al. 1995; Zank et al. 1998; Pei et al. 2010). The present work builds on these studies but also makes some significant departures, motivated and enabled by recent advances in diffusion theory and the sophistication of solar wind simulations. The major points of departure from previous works are listed below.

1. We use a fully 3D global simulation of the solar wind that provides us with a reliable and self-consistent model heliosphere. Previous work has used one-dimensional (1D) radial evolution models with spherical symmetry, with shear-driving effects included through a model (Zank et al. 1998; Pei et al. 2010). Thus, while examining the latitudinal dependence of the diffusion tensor, these studies implicitly assume that they are far from regions with significant latitudinal gradients. In contrast, three-dimensionality improves the physical authenticity of the simulation by explicitly including shear-driving effects on the flow across latitudes, and leads to improved data visualization through two-dimensional (2D) contour plots. A similar 3D approach has been recently used in Guo & Florinski (2016) to study the propagation of GCRs from 0.3 au to the termination shock.

2. The computation of the CR diffusion tensor requires specification of the background solar wind speed and the underlying large-scale heliospheric magnetic field. Previous works (Bieber et al. 1995; Zank et al. 1998; Pei et al. 2010) used a radially constant solar wind speed with some latitudinal variation and a Parker-spiral type magnetic field model. However, the use of a prescribed model for the background fields has been found inadequate (Reinecke et al. 1997), and instead we use the large-scale resolved flow from our MHD-RANS simulation. This provides a complete specification of the background large-scale fields, with spatial variation that has been found to agree well with observations (Usmanov et al. 2014).

3. We examine the diffusion coefficients at radial distances between 2 $R_\odot$ and 3 au, where $R_\odot$ denotes a solar radius. We are not aware of any other similar study that has probed regions this close to the Sun, which are of prime interest for SEP propagation, space weather, and for upcoming spacecraft missions, including the *Parker Solar Probe*. Resolving this entire domain (2 $R_\odot$ − 3 au) in one simulation is a challenge, as modeling approximations that are appropriate very close to the Sun may not be valid at larger heliocentric distances. Furthermore, the timescales associated with the different domains are disparate (Hundhausen 1972; Tu & Marsch 1995; Bruno & Carbone 2013). We use an approach where the computational domain is split into three regions: inner (1–20 $R_\odot$), intermediate (20–45 $R_\odot$), and outer (45 $R_\odot$ − 3 au). The inner and intermediate regions employ a

WKB Alfvén wave model, and the outer region solves a full turbulence transport model, with the inner boundary conditions for each region being provided by the preceding one (Usmanov et al. 2014).

4. A magnetic dipole with its tilt (relative to the solar rotation axis) varying through the solar activity cycle is a first and rough approximation for the solar magnetic field (Babcock 1961). We examine the effect of changing the tilt of the source solar dipole by using simulations with a dipole untilted with respect to the solar rotation axis, and a dipole with 30° tilt, in contrast to previous works employing axisymmetric solar wind parameters (Zank et al. 1998; Pei et al. 2010). The tilt of the solar dipole and the warping of the heliospheric current sheet (Smith 2001) indicate high levels of solar activity (Heber & Potgieter 2006), which is a factor of interest since CR intensity is anticorrelated with solar activity levels (Forbush 1954; Fisk 1979). We note here that previous works that examined the effect of solar activity on CR-intensity variation (Jokipii & Kota 1995) did not include turbulence modeling, and here we examine how varying turbulence levels influence the diffusion coefficients.

5. The perpendicular diffusion coefficient has been previously evaluated using the "BAM" model (Bieber & Matthaeus 1997) by Zank et al. (1998), and using the NLGC theory (Matthaeus et al. 2003) by Pei et al. (2010) and Zank et al. (2004). Recently, the NLGC theory has been reinterpreted by Ruffolo et al. (2012a), and their RBD theory yields significantly improved agreement with numerical experiments for magnetic fluctuation amplitudes comparable to the large-scale magnetic field. This makes it very well suited for application to the solar wind, where the IMF includes a strong fluctuating component (Belcher et al. 1969; Marsch 1991), and we use the RBD theory to derive a new expression for the perpendicular diffusion coefficient.

6. With the above improvements, the present approach departs significantly from both SEP studies (e.g., Zhang et al. 2009) and GCR modulation studies (e.g., Engelbrecht & Burger 2013) that have used relatively simplified assumptions in one or more of the above categories, such as semiempirical diffusion coefficients and simple scalings with magnetic field magnitude.

The outline of this paper is as follows. We describe the form of the CR diffusion tensor in Section 2, and briefly discuss the turbulence model and the simulation in Section 3. Section 4 presents the heliographic distribution of the diffusion coefficients. In the Appendix, we briefly describe how other types of diffusion coefficients might be estimated using similar approaches.

2. Cosmic-Ray Diffusion Tensor

The CR diffusion tensor, κ_{ij}, describes the scattering of CRs by random fluctuations in the IMF. It may be expressed as (Parker 1965; Jokipii & Parker 1970)

$$\kappa_{ij} = \kappa_\perp \delta_{ij} + \frac{B_i B_j}{B^2}(\kappa_\parallel - \kappa_\perp) + \epsilon_{ijk}\kappa_A \frac{B_k}{B}, \quad (1)$$

where $\boldsymbol{B}$ is the mean IMF, δ_{ij} is the Kronecker delta, and ϵ_{ijk} is the Levi-Civita symbol. This work presents calculations of $\kappa_\parallel$ and $\kappa_\perp$, which are the diagonal components of the diffusion tensor parallel and perpendicular, respectively, to the mean IMF.

The present work does not calculate κ_A, which can describe particle drifts under the influence of large-scale gradients and curvature in the IMF. Our results are directly relevant to the outward propagation of SEPs, for which $\kappa_\parallel$ and $\kappa_\perp$ are needed to describe how the SEP distribution spreads in the parallel and perpendicular directions, whereas over the short timescale of the SEP outflow the drifts may mainly shift the lateral distribution over a small angle. The lateral distribution of particle injection is often unknown, and the effects of drifts are often ignored, though Marsh et al. (2013) argue that they should be considered. Both diffusion and drifts are considered to be important to the modulation of GCR with the solar cycle and the small gradients in GCR density (Moraal 1976; Jokipii & Thomas 1981), though these processes take place over a wider region than considered in the present work ($r \leqslant 3$ au).

We shall also examine the radial diffusion coefficient

$$\kappa_{rr} \equiv \kappa_\parallel \cos^2\Psi + \kappa_\perp \sin^2\Psi, \quad (2)$$

which is of particular relevance to models of solar modulation of CRs. Here, Ψ is the "winding" angle between the IMF and the radial direction. Following previous works, we define mfps, $\lambda_{\parallel,\perp}$, that are equivalent to the diffusion tensor through

$$\lambda_{\parallel,\perp} \equiv 3\kappa_{\parallel,\perp}/v, \quad (3)$$

where v is the particle speed.

We note that in the present work, we use the large-scale flow from our simulation to specify B and Ψ as spatially varying fields through the 3D heliosphere. This is in contrast to previous studies (Bieber et al. 1995; Zank et al. 1998; Pei et al. 2010), where B and Ψ were specified through a Parker-type model and a radially constant solar wind speed (to compute Ψ). However, the features of the IMF have a major influence on CR transport, and a Parker-type field is an oversimplification, particularly at high heliolatitudes (see Heber & Potgieter 2006 for an overview of suggested modifications to the Parker field). Moreover, the use of a priori prescribed background fields in modulation studies has been held responsible for restricting the diffusion tensor to values that preclude agreement of models with observations (Reinecke et al. 1997), and the present work makes a significant improvement in this regard.

2.1. Parallel Mean Free Path

In determining the parallel mfp, the turbulence "geometry", i.e., the distribution of energy over parallel and perpendicular wave vectors, is a controlling factor. Observations (Bieber et al. 1994) show that a pure "slab" model of heliospheric turbulence (Jokipii 1966) underestimates the parallel mfp. In the slab model, the magnetic fluctuations are polarized perpendicular to the mean field and their wave vectors are parallel to the mean field. Bieber et al. (1994) find that a composite model with a dominant 2D part (fluctuations and their wave vectors both perpendicular to the mean field) and a minor slab part provides a better approximate parametrization of the turbulence and an improved description of the observed mfps. Furthermore, theoretical studies and observations (Matthaeus et al. 1990; Zank & Matthaeus 1992, 1993; Bieber et al. 1996; Ghosh & Goldstein 1997) suggest that around 80% of magnetic fluctuation energy in the inertial range should reside in the 2D component, with the rest in the slab component.

In the following, we take the z-component along the mean field. Considering parallel diffusion first, we note that in quasi-linear theory the 2D fluctuations are effectively invisible to CRs resonating with the turbulence, and the scattering by slab

fluctuations (assumed to be axisymmetric) is described by the parallel mfp (Zank et al. 1998):

$$\lambda_{\parallel} = 6.2742 \frac{B^{5/3}}{\langle b_s^2 \rangle} \left(\frac{P}{c} \right)^{1/3} \lambda_s^{2/3} \times \left[1 + \frac{7A/9}{(1/3 + q)(q + 7/3)} \right], \quad (4)$$

where

$$A = (1 + s^2)^{5/6} - 1, \quad (5)$$

$$q = \frac{5s^2/3}{1 + s^2 - (1 + s^2)^{1/6}}, \quad (6)$$

$$s = 0.746834 \frac{R_L}{\lambda_s}, \quad (7)$$

and a model 1D Kolmogorov spectrum is assumed, with a power spectrum of the form $\tilde{P}(k_{\parallel}) \propto (1 + k_{\parallel}\lambda_s)^{-5/6}$. Here, c is the speed of light, $R_L = P/Bc$ the particle Larmor radius, $\langle b_s^2 \rangle$ the variance of the slab geometry fluctuation, $P \equiv \tilde{p}c/Ze$ the particle rigidity ($\tilde{p}$ and Ze are the particle momentum and charge, respectively), $k_{\parallel}$ the wave vector parallel to the mean field, and λ_s the correlation length for slab turbulence. Equation (4) is valid at rigidities ranging from from 10 MV to 10 GV (Zank et al. 1998). At larger heliocentric distances, the fractional term in braces becomes significant due to high-rigidity particles resonating with fluctuations in the energy-containing range instead of the inertial range. This is discussed further below in the context of rigidity dependence of the mfps (Section 4.4).

2.2. Perpendicular Mean Free Path

Perpendicular diffusion is often not considered as important as parallel diffusion in energetic particle studies, because it is usually inferred that $\lambda_{\perp} \ll \lambda_{\parallel}$ (Palmer 1982). However, Dwyer et al. (1997) found that for strong particle enhancements related to corotating interaction regions, $\lambda_{\perp}/\lambda_{\parallel}$ rose to $\sim$1 in the fast solar wind stream arriving after the stream interface. Using data from the *Ulysses* spacecraft during the SEP event of 2000 July 14, Zhang et al. (2003) inferred $\lambda_{\perp}/\lambda_{\parallel} \approx 0.25$. Our 3D model inner heliosphere provides an opportunity to examine the domains where perpendicular diffusion can be comparable with parallel diffusion.

Quasi-linear theory (Jokipii 1966) provides a physically appealing description of perpendicular diffusion in terms of the diffusive spread of magnetic field lines, with the gyrocenters of charged particles following the field lines. Other approaches have considered the relationship between $\kappa_{\perp}$ and $\kappa_{\parallel}$ (Axford 1965; Gleeson 1969) and applied the Taylor–Green–Kubo formulation (BAM; Bieber & Matthaeus 1997) to the problem. However, the FLRW approach (Jokipii 1966) overestimates the strength of the diffusion, while BAM predicts diffusion that is weaker than that observed in numerical experiments (Giacalone & Jokipii 1999; Mace et al. 2000). The NLGC theory (Matthaeus et al. 2003) accounts for both the random walk of the field lines and the influence of parallel scattering, and shows good agreement with both observations (Bieber et al. 2004) and simulations, with the NLGC results bracketed by the FLRW and BAM results (Matthaeus et al. 2003).

A recent work (Ruffolo et al. 2012a) has reinterpreted NLGC by replacing the diffusion of gyrocenter trajectories with RBD, where the guiding center motion is approximated as ballistic (i.e., with constant velocity) between scattering events. The RBD-modified theory agrees with numerical simulations over a wider range of fluctuation amplitudes than the original NLGC, specifically for fluctuations comparable in size to the large-scale field. This makes it particularly suited for application to the solar wind (Belcher et al. 1969; Marsch 1991). Other improvements to NLGC have also been developed (see, e.g., Shalchi 2009).

The phenomenon of "backtracking" due to parallel scattering causes a particle to reverse its motion along the field line, thus retracing its steps over a certain time span. This leads to a negative v_x correlation (v_x being a component of the particle's velocity perpendicular to the mean field), which results in a reduction in the running perpendicular diffusion coefficient. With this backtracking correction, RBD yields the following perpendicular diffusion coefficient (Ruffolo et al. 2012a):

$$\kappa_{\perp} = \frac{a^2 v^2}{6B^2} \sqrt{\frac{\pi}{2}} \int_0^{\infty} \frac{S_2(k_{\perp}) \mathrm{Erfc}(\alpha) 2\pi k_{\perp} dk_{\perp}}{k_{\perp} \sqrt{\langle \tilde{v}_x^2 \rangle}}, \quad (8)$$

where $a^2 = 1/3$, v is the particle speed, $\tilde{v}_x$ is the x-component of the guiding center velocity, S_2 is the 2D axisymmetric turbulent fluctuation spectrum, Erfc is the complementary error function, and $k_{\perp}$ is the component of the wave vector perpendicular to the mean magnetic field. We also have

$$\alpha = \frac{v^2}{3\kappa_{\parallel} k_{\perp} \sqrt{2 \langle \tilde{v}_x^2 \rangle}} \quad (9)$$

and

$$\langle \tilde{v}_x^2 \rangle = \frac{a^2 v^2 b^2}{6B^2}, \quad (10)$$

where b^2 is the combined variance of the 2D and slab magnetic fluctuations: $b^2 = \langle b_2^2 \rangle + \langle b_s^2 \rangle$. Note that in Equation (8), the slab turbulence spectrum does not appear. This is because we follow the suggestion by Shalchi (2006) that the direct contribution of the slab component to perpendicular transport is subdiffusive and therefore the slab term should not contribute to Equation (8). This hypothesis has been supported by simulations (Ruffolo et al. 2012a, 2012b) and accordingly has been adopted in the present work as well. Slab fluctuations can, however, still influence $\kappa_{\perp}$ through $\kappa_{\parallel}$, which appears in Equation (9) for α, and $\langle \tilde{v}_x^2 \rangle$.

The 2D power spectrum may be expressed as a power law (Matthaeus et al. 2007):

$$S_2(k_{\perp} \leqslant 1/\lambda_2) = C_2 \langle b_2^2 \rangle \lambda_2^2 (\lambda_2 k_{\perp})^p, \quad (11)$$

$$S_2(k_{\perp} > 1/\lambda_2) = C_2 \langle b_2^2 \rangle \lambda_2^2 (\lambda_2 k_{\perp})^{-\nu - 1}, \quad (12)$$

where λ_2 is the 2D correlation scale, C_2 is a normalization constant, $\langle b_2^2 \rangle$ is the variance of the 2D turbulent fluctuations, and p is a power index that takes on integral values that correspond to different power spectra. We assume a Kolmogorov spectrum in the inertial range by taking $\nu = 5/3$. From the requirement that

$\langle b_2^2 \rangle = 2\pi \int_0^\infty S_2(k) k \; dk$, we get

$$C_2 = \frac{(\nu - 1)(p + 2)}{2\pi (p + \nu + 1)}. \tag{13}$$

Note that the inertial range ($k_\perp > 1/\lambda_2$) behavior is described by a conventional power law, and p only determines the long-wavelength properties of the spectrum. The spectral behavior of interplanetary magnetic fluctuations at long wavelengths is not well determined from single point measurements (Matthaeus et al. 2016), and there are ambiguities surrounding the question of whether the observed structures are spatial or temporal in origin. The observations of "$1/f$" noise at low frequencies also complicate matters (Matthaeus & Goldstein 1986). All values of $p \geqslant -1$ yield power spectra that give rise to a finite energy, but these spectra may be differentiated based on the characteristic length scales associated with them. In addition to the standard correlation scale (Batchelor 1953), there is a distinct scale, called the ultrascale, which is of importance in applications of 2D turbulence (Matthaeus et al. 2007 and references therein). The ultrascale is so named because it is generally larger than the correlation scale, and it may be interpreted as a typical size of an "island" of 2D turbulence (Matthaeus et al. 1999a) and as the perpendicular coherence length of the FLRW (Ruffolo et al. 2004).

We consider the following cases (Matthaeus et al. 2007): $p = -1$ (infinite correlation scale and an infinite ultrascale), $p = 0$ (finite correlation scale but an infinite ultrascale), and $p \geqslant 1$ (finite ultrascale and finite correlation scale). The case $p = 2$ is of special interest since it corresponds to homogeneous turbulence. Each of the above possibilities is realizable as each yields a finite energy. However, unlike the correlation scale, the values taken by the ultrascale in space and astrophysical plasmas are not well known, and there is a paucity of established methods to measure it (see Matthaeus et al. 2007 for a proposed technique). Therefore, it is of interest to examine the dependence of the diffusion coefficients on p. If there is a marked differentiation between the mfps computed for different cases, then observations of the mfps may be used to infer constraints on the ultrascales prevailing in the heliospheric plasma.

To finally obtain an expression for the perpendicular mfp, we use Equations (11) and (12) in Equation (8) and set $\nu = 5/3$ to get

$$\begin{aligned}\lambda_\perp = \mathscr{F}_1 \Bigg\{ & \frac{\lambda_2^{-2/3}}{5\mathscr{F}_2^{5/3}\sqrt{\pi}} [3\sqrt{\pi}\mathscr{F}_2^{5/3}\lambda_2^{5/3}\mathrm{Erfc}(\mathscr{F}_2\lambda_2) \\ & + \Gamma\left(\frac{1}{3}\right) - 3\Gamma\left(\frac{4}{3}, \mathscr{F}_2^2\lambda_2^2\right)\Bigg] \\ & + \delta_{p,-1}\lambda_2 \Bigg[\mathscr{F}_2\lambda_2 \frac{2}{\sqrt{\pi}\,{}_2} F_2\left(\frac{1}{2}, \frac{1}{2}; \frac{3}{2}, \frac{3}{2}; -\mathscr{F}_2^2\lambda_2^2\right) \\ & - 0.981755 - \log(\mathscr{F}_2\lambda_2)] \\ & + (1 - \delta_{p,-1}) \frac{\lambda_2}{p+1} [\mathrm{Erfc}(\mathscr{F}_2\lambda_2) \\ & - \frac{\mathscr{F}_2\lambda_2}{\sqrt{\pi}} E_{\frac{p}{2}+1}(\mathscr{F}_2^2\lambda_2^2)\Bigg]\Bigg\},\end{aligned} \tag{14}$$

where

$$\mathscr{F}_1 = \sqrt{\pi^3} C_2 \frac{\nu \langle b_2^2 \rangle a^2}{B^2 \sqrt{2\langle \tilde{v}_x^2 \rangle}}, \tag{15}$$

and

$$\mathscr{F}_2 = \frac{\nu}{\lambda_\parallel \sqrt{2\langle \tilde{v}_x^2 \rangle}}. \tag{16}$$

In Equation (14), Erf is the error function, Γ is the gamma function, ${}_2F_2$ is a hypergeometric function, $E_{\frac{p}{2}+1}$ is the generalized exponential integral function, and the Kronecker delta function is used as a switch between the four values of p. C_2 depends on the value of p, as can be seen from Equation (13). Note that in the corresponding NLGC result (Pei et al. 2010), an implicit method is required to obtain $\lambda_\perp$, in contrast to the RBD result, which is an explicit solution for $\lambda_\perp$.

3. Solar Wind Model

Equations (4) and (14) require specification of the large-scale IMF, and the magnetic fluctuation energies and correlation lengths for both slab and 2D turbulence. For this purpose, we use a Reynolds-averaged Navier–Stokes approach, based on the Reynolds decomposition (e.g., McComb 1990) of a physical field, $\tilde{\boldsymbol{a}}$, into a mean and a fluctuating component:

$$\tilde{\boldsymbol{a}} = \boldsymbol{a} + \boldsymbol{a}', \tag{17}$$

where $\boldsymbol{a} = \langle \tilde{\boldsymbol{a}} \rangle$ is an ensemble average, associated with the large scales of motion and $\boldsymbol{a}'$ is a fluctuating component, here assumed to be small scale. By construction, $\langle \boldsymbol{a}' \rangle = 0$. Application of this decomposition to the MHD equations, along with a series of approximations appropriate to the solar wind, leads us to a set of mean-flow equations that are coupled to the small-scale fluctuations via another set of equations for the statistical descriptors of turbulence. For the details of the procedure for handling the fluctuations, we refer the reader to Breech et al. (2008).

In this study, we use the solar wind model described in detail by Usmanov et al. (2014). It is a global, fully 3D MHD model that accounts for the effects of fluctuations in the heating and acceleration of the solar wind flow. The computational domain, which in the present study extends from the coronal base to 3 au, is split into three regions: inner (1–20 $R_\odot$), intermediate (20–45 $R_\odot$), and outer (45 $R_\odot$ − 3 au). In the inner region, steady-state solutions of one-fluid, polytropic ($\gamma = 1.08$) solar wind equations with WKB Alfvén waves are obtained by time relaxation starting from an initial state composed of a Parker-type flow in a dipole magnetic field (Usmanov et al. 2000; Usmanov & Goldstein 2003). Two-fluid steady-state equations for protons and electrons with Hollweg's electron heat flux and WKB Alfvén waves are solved in the intermediate region by forward integration along the radius r (Pizzo 1978, 1982; Usmanov 1993). The boundary conditions for the intermediate region are extracted from the inner region solution. In the outer region, we solve three-fluid (thermal protons, electrons, and pickup protons) Reynolds-averaged solar wind equations simultaneously with transport equations for turbulence energy, cross helicity, and correlation length. Steady-state solutions in the outer region are obtained by time relaxation, using an

eddy-viscosity approximation for the Reynolds stress tensor and turbulent electric field, with boundary conditions provided by solutions in the intermediate region (Usmanov et al. 2014). The use of steady-state simulations is justified here since ambient solar wind conditions change on timescales that are long compared to the time energetic particles spend in the inner heliosphere.

In our calculations, we have used the same input parameters at the coronal base as in Usmanov et al. (2014): the driving amplitude of Alfvén waves is set to 35 km s^{-1}, the initial density is 0.4×10^8 cm^{-3}, and the initial plasma temperature is 1.8×10^6 K. The magnetic field magnitude is assigned as the field strength of the source magnetic dipole on the poles. This parameter is set to 16 G to match the magnitude of the heliospheric magnetic field observed by *Ulysses*. The computations are carried out on a composite spherical grid (Usmanov 1996; Usmanov et al. 2012) using the Central Weighted Essentially Non-Oscillatory (CWENO) spatially third-order reconstruction algorithm of Kurganov & Levy (2000). The spatial CWENO discretization is combined with the Strong Stability-Preserving Runge–Kutta scheme of Gottlieb et al. (2001) for time integration and the method of Powell (1994) for maintaining the $\nabla \cdot \boldsymbol{B} = 0$ condition.

For our purposes here, we extract from the outer region simulation ($45\,R_\odot - 3$ au) the mean magnetic field $\boldsymbol{B}$, the fluctuation energy Z^2 (defined below), and the correlation length for the turbulence λ. Here,

$$Z^2 = \langle v'^2 + b'^2 \rangle \tag{18}$$

is twice the turbulent energy per unit mass, defined in terms of the velocity and magnetic field fluctuations, $\boldsymbol{v}'$ and $\boldsymbol{B}'$, respectively. The amplitude of magnetic fluctuations has been normalized to Alfvén units using $\boldsymbol{b}' = \boldsymbol{B}'(4\pi\rho)^{-1/2}$, where ρ is the mass density. To extend our calculation closer to the Sun, we use data from the inner (1–$20\,R_\odot$) and intermediate (20–$45\,R_\odot$) regions, where the simulation does not have a turbulence model for Z^2 and λ. Here we use the the WKB Alfvén wave energy density (Usmanov et al. 2000), $\mathcal{E}$, as a proxy for the turbulent fluctuation energy via $Z^2 = 2\mathcal{E}/\rho$. To get an approximation for the correlation scale in these regions, we use the hypothesis from Hollweg (1986) that the correlation length varies as the distance between magnetic field lines, which in turn depends on the field strength (Spruit 1981), so that $\lambda \propto B^{-1/2}$. We set the constant of proportionality such that the λ at the boundaries of the intermediate and outer regions matches. We are currently working on refinements of the model that will modify the region in which turbulence modeling is included, so that this region will extend closer to the Sun.

To proceed with the calculation of the mfps, some assumptions must be made in order to relate the correlation scale of our turbulence model (λ) to the slab and 2D correlation scales in Equations (4) and (14), respectively. First, we note that the turbulent fluctuations in our model are primarily transverse to the mean magnetic field (Breech et al. 2008), and thus identify the correlation scale of 2D turbulence to be equal to the correlation scale of our turbulence model, so that $\lambda_2 = \lambda$. Observational studies (Osman & Horbury 2007; Weygand et al. 2009, 2011) indicate that the slab correlation scale is about a factor of two larger than the 2D correlation scale, and accordingly, we assume $\lambda_s = 2\lambda_2$. In our approximate treatment, we assume in effect that the magnetic and velocity correlation functions are structurally similar (Zank et al. 1996), so that the magnetic correlation length is found to be equal to the single correlation scale that we follow dynamically. In the inner heliosphere where the cross helicity is large, it becomes advantageous to employ a two-correlation length theory (Matthaeus et al. 1994; Wan et al. 2012; Zank et al. 2012, 2017), as has been implemented, e.g., by Adhikari et al. (2015).

To approximate the energy in slab and 2D magnetic fluctuations, we first convert Z^2 to B'^2 using Equation (18):

$$\langle B'^2 \rangle = \frac{Z^2}{r_A + 1} 4\pi\rho, \tag{19}$$

where $r_A = \langle v'^2 \rangle / \langle b'^2 \rangle$ is the Alfvén ratio. An accurate dynamical model for r_A is desirable, but must include complications such as non-local effects (e.g., Grappin et al. 1983; Matthaeus et al. 1994; Hossain et al. 1995). At present, we maintain a simpler approach, and take r_A to have a value of 1 in the inner and intermediate regions (1–$45\,R_\odot$), and a value of $1/2$ for heliocentric distances larger than $45\,R_\odot$. These values are motivated by spacecraft observations (Tu & Marsch 1995), but we recognize that attempts have been made to treat r_A dynamically (Grappin et al. 1983; Marsch & Tu 1989; Tu & Marsch 1990; Matthaeus et al. 1994; Yokoi & Hamba 2007; Zank et al. 2012). See especially the comparison with observations by Adhikari et al. (2015) and Zank et al. (2017).

Next, recalling the assumption that the magnetic fluctuations have a dominant 2D component with a small slab contribution, and following observations (Matthaeus et al. 1990; Bieber et al. 1994) that find the ratio of the 2D and slab energies to be 80% to 20%, we use

$$\frac{\langle b_s^2 \rangle}{\langle b_2^2 \rangle} = \frac{20}{80} = 0.25 \tag{20}$$

to compute the slab and 2D fluctuation energies from Equation (19) and $\langle b_2^2 \rangle + \langle b_s^2 \rangle = \langle B'^2 \rangle$. In recent works by Hunana & Zank (2010) and Zank et al. (2017), refinements to this simplified perspective on the breakdown of the slab and 2D fluctuation energies are discussed. In particular, Zank et al. (2017) solve separate equations for the slab and 2D energies with a simplified IMF and background solar wind flow. They find that the evolution of the two components is markedly different in the outer heliosphere (beyond ~3 au), where driving by pickup ions leads to an increase in the slab component's energy, while the energy of the 2D component continues to decrease with heliocentric distance. Their results show, however, that the radial evolution of slab and 2D energies is not too dissimilar below 3 au. Similar results are presented by Oughton et al. (2011) using their two-component model. Therefore, for the purposes of our present work, where we focus on the inner heliosphere, our simple decomposition of $\langle B'^2 \rangle$ into slab and 2D components, using the constant ratio expressed in Equation (20), seems appropriate. Studies of CR diffusion in the outer heliosphere would undoubtedly benefit from using a two-component turbulence transport model. A detailed assessment of different transport equations for turbulence is beyond the scope of this work.

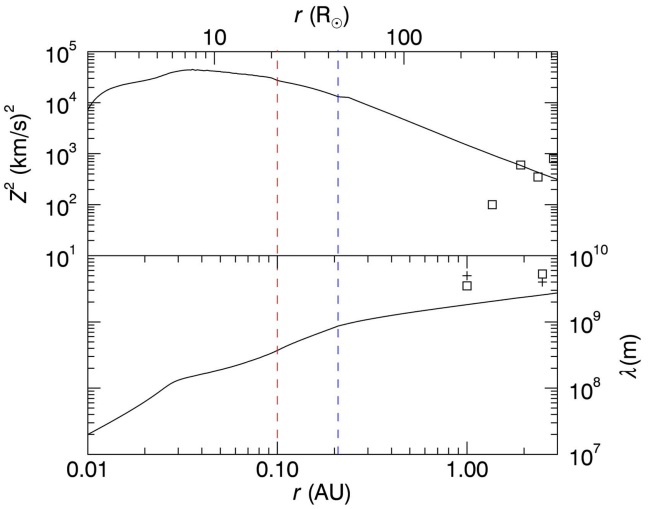


Figure 1. Model results near the ecliptic plane, for a run with an untilted solar dipole, are compared with observational data from *Voyager* 2, *Helios*, and the NSSDC Omnitape. The Z^2 data are from Zank et al. (1996), and the λ data are from Smith et al. (2001). The solid lines are from our simulations. The different symbols represent different methods of calculation. The dashed vertical lines represent the boundaries of the different simulation regions, with red marking the inner−intermediate region boundary at 20 $R_\odot$, and blue marking the intermediate−outer region boundary at 45 $R_\odot$, respectively. Note that the observations are for various times in the solar cycle, and are shown here for general context only.

4. Results

4.1. Solar Wind Model Results

We begin our presentation of the results with a discussion of the core fields from the simulation—B, λ, and Z^2—which are the ingredients that go into our calculation of the diffusion coefficients. Figure 1 shows the radial evolution of the turbulence energy and the turbulence correlation scale from our model and simulation with an untilted dipole source. The data are for a 7° heliolatitude, which we take to be the broadly defined ecliptic region. Also shown are observational results from *Voyager* 2, *Helios*, and the National Space Science Data Center (NSSDC) Omnitape data set, indicating reasonable agreement with the simulation results. The observational data for Z^2 and λ are from Zank et al. (1996) and Smith et al. (2001), respectively. Note that the observations are for various times in the solar cycle, and are shown here for general context only. The dashed vertical lines in Figure 1 represent the boundaries of the different simulation regions, with red marking the inner −intermediate region boundary at 20 $R_\odot$, and blue marking the intermediate−outer region boundary at 45 $R_\odot$, respectively. Note that we present results for $r > 2\,R_\odot$ (r is the radial distance measured from the solar center), even though the inner boundary of the inner region simulation is at 1 $R_\odot$. The parallel mfp acquires extremely large values (>10 au) in the region very close to the solar surface, due to the large values of B prevailing there. These large values of $\lambda_\parallel$ are not of physical relevance and present problems for visualization, and we therefore restrict our results to $r > 2\,R_\odot$.

Figure 2 shows the distribution in the meridional plane of the three ingredients—B, Z^2, and λ—for a simulation with an untilted source dipole. The figures on the left are from the inner and intermediate regions (2–45 $R_\odot$), and the ones on the right are from the outer region (0.21–3 au). For a detailed discussion

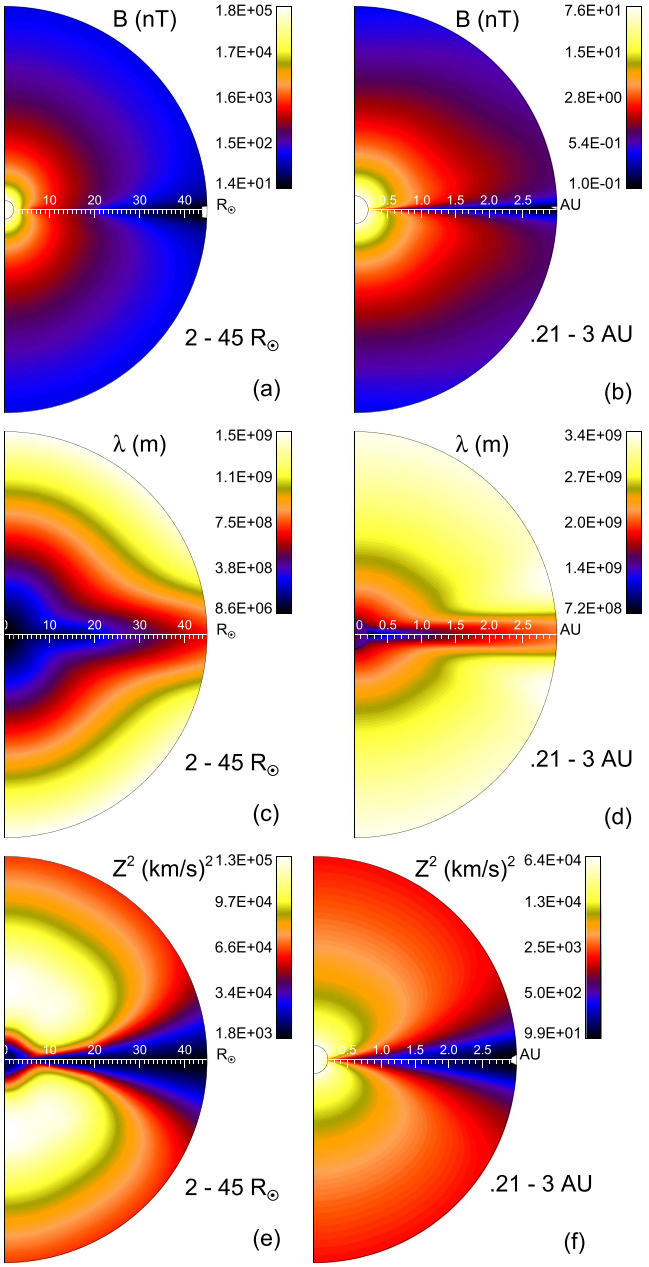


Figure 2. Contour plots of the heliospheric magnetic field (B), the turbulence correlation scale (λ), and the turbulence energy (Z^2) in the meridional plane for an untilted solar dipole. The figures on the left cover 2–45 $R_\odot$, and the ones on the right cover 0.21–3 au (45–645 $R_\odot$).

of these simulation results, we refer the reader to Usmanov et al. (2000, 2014). We note here that the magnetic field results agree well with *Ulysses* observations (see Figure 8 of Usmanov et al. 2014), with the field vanishing at the heliospheric current sheet (HCS) at 0° heliolatitude. The turbulence correlation scale increases with heliocentric distance, as is well known from observations (Tu & Marsch 1995). The turbulence energy increases when moving from the ecliptic plane toward higher heliolatitudes because of shear interactions between slow (low latitude) and fast (high latitude) wind (see, e.g., Breech et al. 2008). In the following subsections, we will discuss how these distributions influence the behavior of the diffusion length scales.

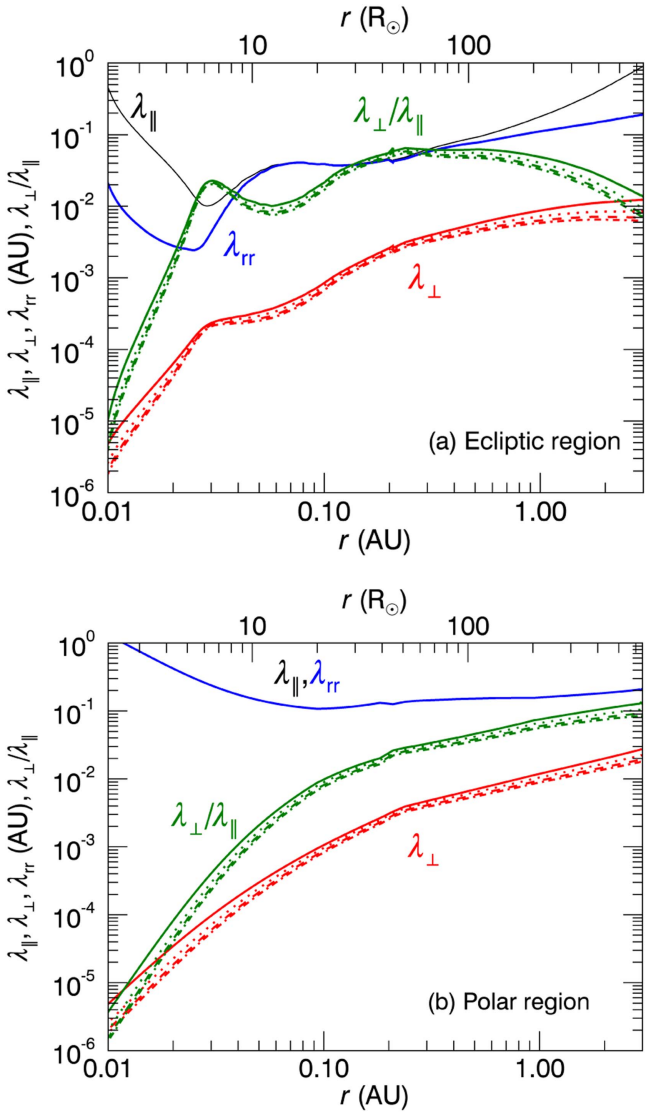


Figure 3. Radial dependence of the parallel (black), perpendicular (red), and radial (blue) mfps (a) near the ecliptic plane (7° heliolatitude) and (b) near the pole (86° heliolatitude). Also shown is $\lambda_\perp/\lambda_\parallel$ (green). The solid lines are for $p = -1$, the dotted lines for $p = 0$, the dashed lines for $p = 1$, and the dashed −dotted lines for $p = 2$. Proton rigidity is 445 MV (100 MeV kinetic energy). Note that the curves for $\lambda_\parallel$ and λ_{rr} coincide in (b).

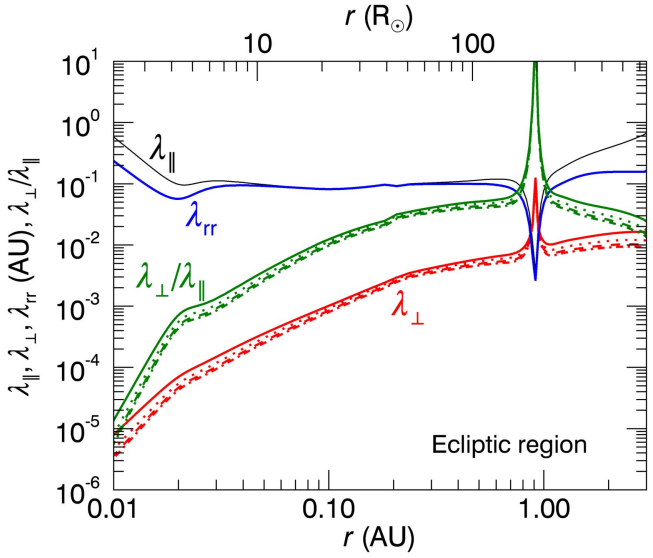


Figure 4. Radial dependence of the parallel (black), perpendicular (red), and radial (blue) mfps near the ecliptic plane (7° heliolatitude), with a solar dipole having a 30° tilt. For our particular choice of azimuthal angle (26°), an HCS crossing occurs at 0.8 au. Also shown is $\lambda_\perp/\lambda_\parallel$ (green). The solid lines are for $p = -1$, the dotted lines for $p = 0$, the dashed lines for $p = 1$, and the dashed −dotted lines for $p = 2$. Proton rigidity is 445 MV (100 MeV kinetic energy).

4.2. Radial Evolution of Mean Free Paths

In Figure 3, we show the radial evolution of the parallel, perpendicular, and radial mfps (black, red, and blue lines, respectively) in the ecliptic region (Figure 3(a)) and near the solar rotation axis (86° heliolatitude, Figure 3(b)) for an untilted source dipole. Also shown is the ratio of the perpendicular mfp to the parallel mfp (green lines). The solid, dotted, dashed, and dashed−dotted lines correspond to $p = -1$, 0, 1, and 2, respectively, and the mfps are computed for protons with rigidity equal to 445 MV, corresponding to a kinetic energy of 100 MeV. Here we would like to remind the reader that our turbulence parameters (Z^2 and λ) in the region 1–45 $R_\odot$ are not from the turbulence model, but are calculated using the approximations detailed in Section 3. As such, these results represent a preliminary attempt at mapping the diffusion length scales in a region that will soon be investigated by upcoming spacecraft missions such as the *Parker Solar Probe*.

Near the ecliptic plane (Figure 3(a)), as one moves outward from the solar surface, the increasing strength of the turbulence energy (see Figure 1) leads to a sharp decrease in $\lambda_\parallel$ in the region 2–5 $R_\odot$, with the rapidly decreasing IMF reinforcing this behavior. In this region, $\lambda_\parallel \propto r^{-3.46}$, and there is a corresponding increase in $\lambda_\perp$ ($\propto r^{3.55}$ for $p = -1$ and $\propto r^{4.34}$ for $p = 2$). Since the IMF has a significant meridional component here, the large winding angle (Ψ) between the radial direction and the IMF leads to $\lambda_\perp$ having an influence on the radial mfp (see Equation (2)), with $\lambda_{rr} \propto r^{-1.97}$. From 0.03 to 3 au, $\lambda_\parallel$ mostly increases as $r^{0.82}$, and $\lambda_\perp$ as $r^{0.79}$. From 0.1 to 3 au, Ψ is once again large because of the increased azimuthal component of the IMF, and $\lambda_\perp$ reduces the radial mfp, with $\lambda_{rr} \propto r^{0.53}$. Observational studies for $r < 3$ au have found $\lambda_{rr} \propto r^b$ with b ranging from 0.4 to 0.7 (Beeck et al. 1987). Note that the radial mfp depends on the value of p (through $\lambda_\perp$), but the λ_{rr} curves for different p coincide.

Moving on to the radial evolution of the mfps in the polar region, Figure 3(b) shows that the radial mfp is completely dominated by $\lambda_\parallel$. This is because the IMF is near radial at the poles, with a very small winding angle. At the poles, $\lambda_{rr} \propto r^{-1.1}$ until 0.1 au, after which it remains nearly constant, with identical behavior exhibited by $\lambda_\parallel$. From 2 $R_\odot$ − 0.2 au, $\lambda_\perp \propto r^{2.10}$ for $p = -1$ and $\lambda_\perp \propto r^{2.34}$ for $p = 2$. From 0.2 to 3 au, $\lambda_\perp \propto r^{0.78}$ for $p = -1$ and $\lambda_\perp \propto r^{0.69}$ for $p = 2$.

Figure 4 shows the effect of a source dipole with a 30° tilt when one encounters the HCS at around 1 au: $\lambda_\parallel$ goes through a sudden dip of almost two orders of magnitude, while $\lambda_\perp$ has a corresponding increase of around an order of magnitude. (The radius where the HCS crosses our chosen heliolatitude of 7° depends on our choice of the azimuthal angle for which we plot results as a function of radius.) The vanishing mean magnetic field and non-vanishing turbulence amplitude at the HCS explain this behavior, which will be further illustrated in the next subsection discussing the 2D variation of the mfps in the meridional plane. We note from Figures 3 and 4 that the ratio

$\lambda_\perp/\lambda_\parallel$ stays between 0.1 and 0.01 for most of the inner heliosphere, but it exceeds unity at the HCS. Keeping in mind that the current sheet is a singular region in our simulation, in its vicinity the fields do possess physically realizable values. Therefore, we may stress the fact that similarly large values of $\lambda_\perp/\lambda_\parallel$ have been observed (Dwyer et al. 1997; Zhang et al. 2003). We will come across these domains of significant perpendicular diffusion once again in the meridional plane contours in Section 4.5, below.

In the results presented so far the choice of the long-wavelength spectral index p does not significantly alter the mfps, with $\lambda_\perp$ for $p = -1$ generally not more than a factor of two larger than $\lambda_\perp$ for $p = 2$. Referring to the discussion in Section 2.2, this result indicates a rather weak dependence of the mfps on the ultrascale (via different p values). The exception appears very close to the solar surface ($2\,R_\odot$) in Figure 3, where the perpendicular mfp for the $p = -1$ case is several times larger than that for the $p = 2$ case. This behavior may be probed further in simulations with improved coronal turbulence models that are more reliable at such small heliocentric distances. In the following results, unless specified otherwise, we will choose $p = 2$, which corresponds to homogeneous turbulence.

In Figure 5, we examine the effect of varying the turbulence energy amplitude at the inner boundary ($45\,R_\odot$) of the outer region of the simulation, again for 100 MeV protons. Such variation may arise due to solar activity. The solid lines represent a standard Z^2 specified at the inner boundary, and the dashed and dotted lines represent simulations performed with double and half this standard value specified at the inner boundary, respectively. In the ecliptic region (7° heliolatitude), Figure 5(a) indicates, as expected, that an increasing turbulence level leads to a decrease in $\lambda_\parallel$ (and consequently λ_{rr}). The stronger turbulence increases $\lambda_\perp$ in proportion to Z, and therefore increases the extent to which particles may diffusively penetrate the heliosphere. Comparing Figures 5(a) and (b), it is interesting to note that in the ecliptic region, varying turbulence at the inner boundary leads to an effect on $\lambda_\parallel$ that becomes less pronounced with radial distance. This is not the case in the polar regions with fast wind, however, where the turbulence is less "aged" compared with low latitudes (Matthaeus et al. 1998). Stream interactions near the ecliptic plane reduce the turbulence at a faster rate compared to the rate in the polar regions far from such shearing interactions.

We end this subsection by comparing our solutions in the ecliptic plane with "consensus" constraints on observations (Palmer 1982; Bieber et al. 1994). Based on information compiled from several sources, the Palmer consensus finds that for particles in the rigidity range 0.5–5000 MV, $\lambda_\parallel = 0.08$–0.3 au. We note here that the values for the mfps obtained by fitting observational data may depend on the model used; Reames (1999) reviews some such results and suggests a higher parallel mfp of ~1 au. Our $\lambda_\parallel$ for a 100 MeV proton at 1 au varies from 0.29 to 0.40 au, and fits the consensus range well. Our solutions are smaller than the values from Breech et al. (2008) and Pei et al. (2010), which we list in Table 1, along with our results. Here, cases 1, 2, and 3 refer to the standard, doubled, and halved turbulence levels, as described above. Note that unlike our calculation of $\lambda_\parallel$, the calculations from Breech et al. (2008) and Pei et al. (2010) depend on the value of p.

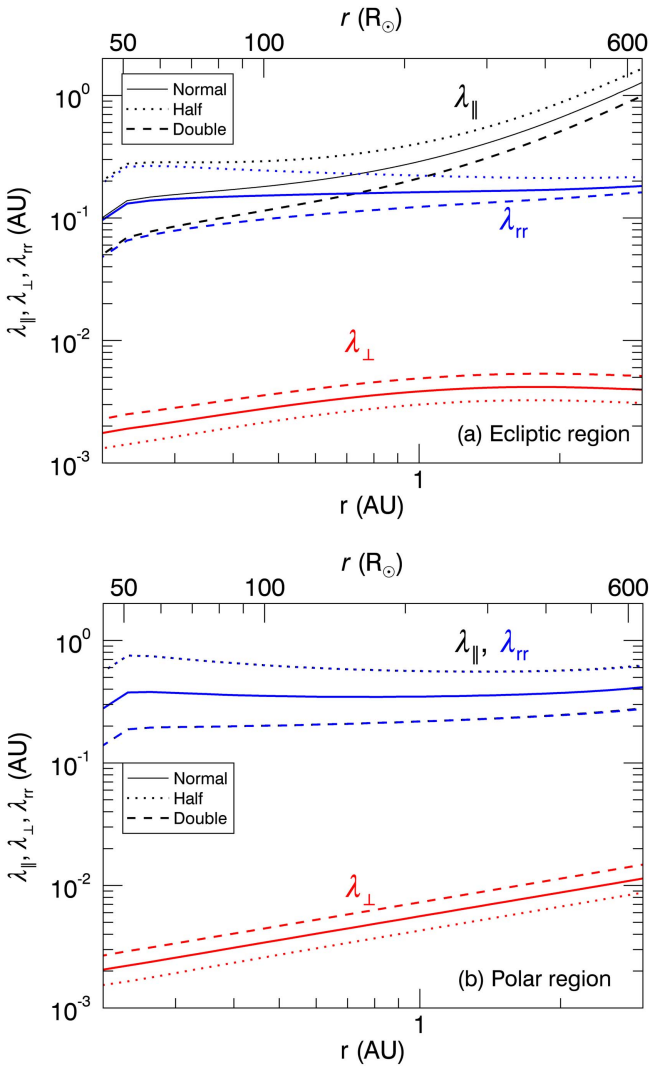


Figure 5. Radial dependence of the parallel (black), perpendicular (red), and radial (blue) mfps (a) near the ecliptic plane (7° heliolatitude) and (b) in the polar region (86°), for varying turbulence amplitudes, with $p = 2$. The dashed and dotted lines represent simulations with the turbulence energy (Z^2) at the inner boundary of the outer region ($45\,R_\odot$) doubled and halved, respectively, relative to a standard level. See text for more details. Note that the curves for $\lambda_\parallel$ and λ_{rr} coincide in (b).

Table 1
Parallel mfps in au for 100 MeV Protons in the Ecliptic Region at 1 au

p	B1	B2	B3	P1	P2	Case 1	Case 2	Case 3
−1	2.92	6.86	1.64	0.92	0.47	0.29	0.21	0.40
0	2.33	5.49	1.31	0.74	0.38			
1	2.14	5.03	1.20	0.68	0.35			
2	2.04	4.80	1.15	0.64	0.33			

Note. B1, B2, and B3 are from Breech et al. (2008); P1 and P2 are from Pei et al. (2010); cases 1–3 are our solutions for varying turbulence levels. Note that our calculation of $\lambda_\parallel$ is independent of p.

Our improved agreement with the Palmer consensus range may be attributed to two improvements in modeling. (1) Here, B is a spatially varying field computed dynamically from a self-consistent 3D model, in contrast to the Parker-type model used in Breech et al. (2008) and Pei et al. (2010). (2) The effect of shear interactions is computed self-consistently in our

turbulence model (Usmanov et al. 2014), unlike in Breech et al. (2008) and Pei et al. (2010), where a shear-driving parameter is employed.

4.3. Latitudinal Evolution of Mean Free Paths

Figure 6 shows the variation of mfps with latitude at different heliocentric distances for an untilted solar dipole. We see from Figure 6(a) that, in general, $\lambda_\parallel$ (solid lines) increases by almost an order of magnitude as one leaves the solar equatorial plane and moves to higher latitudes, and assumes a near constant value as one approaches the polar regions. The opposite behavior is seen for $\lambda_\perp$ (dashed lines), which decreases on moving away from the equatorial plane. This is a combined result of the increase in the IMF strength and the correlation scale of the turbulence (λ) while moving away from the solar equatorial plane (i.e., away from the HCS), and the increase in the turbulence energy due to shear interactions between slow and fast solar winds. We note that very close to the Sun (4 $R_\odot$, black line), $\lambda_\parallel$ first decreases with latitude as one leaves the equatorial plane, then increases at higher latitudes, to values larger even than those seen at larger heliocentric distances. This behavior is because of the IMF increasing monotonically with latitude, close to the Sun. At larger distances, the IMF plateaus with increasing latitude, and from 1 au onwards it decreases in the polar regions (See Figure 2). Thus, particles experience less scattering in polar regions close to the Sun. This also explains the latitudinal variation of $\lambda_\perp$ at 4 $R_\odot$.

Figure 6(b) shows the increase in λ_{rr} as one moves toward the polar regions, and illustrates once again the fact that while λ_{rr} is affected by $\lambda_\perp$ very close to the Sun at low latitudes, near the polar regions it follows the trend set by $\lambda_\parallel$. Figure 6(c) shows that the ratio of $\lambda_\perp$ to $\lambda_\parallel$ decreases as one leaves the solar equatorial plane (i.e., away from the HCS), with the perpendicular mfp staying one to two orders of magnitude below the parallel mfp, except very close to the Sun (4 $R_\odot$, black line), where it becomes three orders of magnitude smaller because of the low turbulence levels in that region. We will examine the latitudinal dependence of the mfps once again in meridional plane figures in Section 4.5, below.

4.4. Rigidity Dependence of Mean Free Paths

In Figure 7, we plot the rigidity (P) dependence of mfps for protons at different radial distances in the ecliptic and polar regions. Below 1 au, $\lambda_\parallel \propto P^{0.33}$ for all rigidities considered here (10–10^4 MV). Above 1 au, there is a steepening of the slope for rigidities larger than 10^3 MV. As noted in Section 2.1, this is due to high-energy particles resonating with turbulent fluctuations in the energy-containing range instead of the inertial range. As the IMF (B) decreases with heliocentric distance, a high-rigidity particle's Larmor radius ($R_L = P/Bc$) may become resonant with the correlation scale of the turbulence (λ_s). When $R_L/\lambda_s \gg 1$, the expression in braces in Equation (4) scales with rigidity as $P^{5/3}$, and we have $\lambda_\parallel \propto P^2$ instead of $\lambda_\parallel \propto P^{1/3}$. Indeed, for rigidities $\sim 10^4$ MV we find that $\lambda_\parallel \propto P^{1.2}$ at 1 au and $\lambda_\parallel \propto P^{1.8}$ at 3 au (see also the discussion on the effect of pickup ion-driven turbulence on high-rigidity particles in the outer heliosphere in Zank et al. 1998). Our results agree well with the observations shown in Bieber et al. (1994), with power indices ranging from 0.2 to

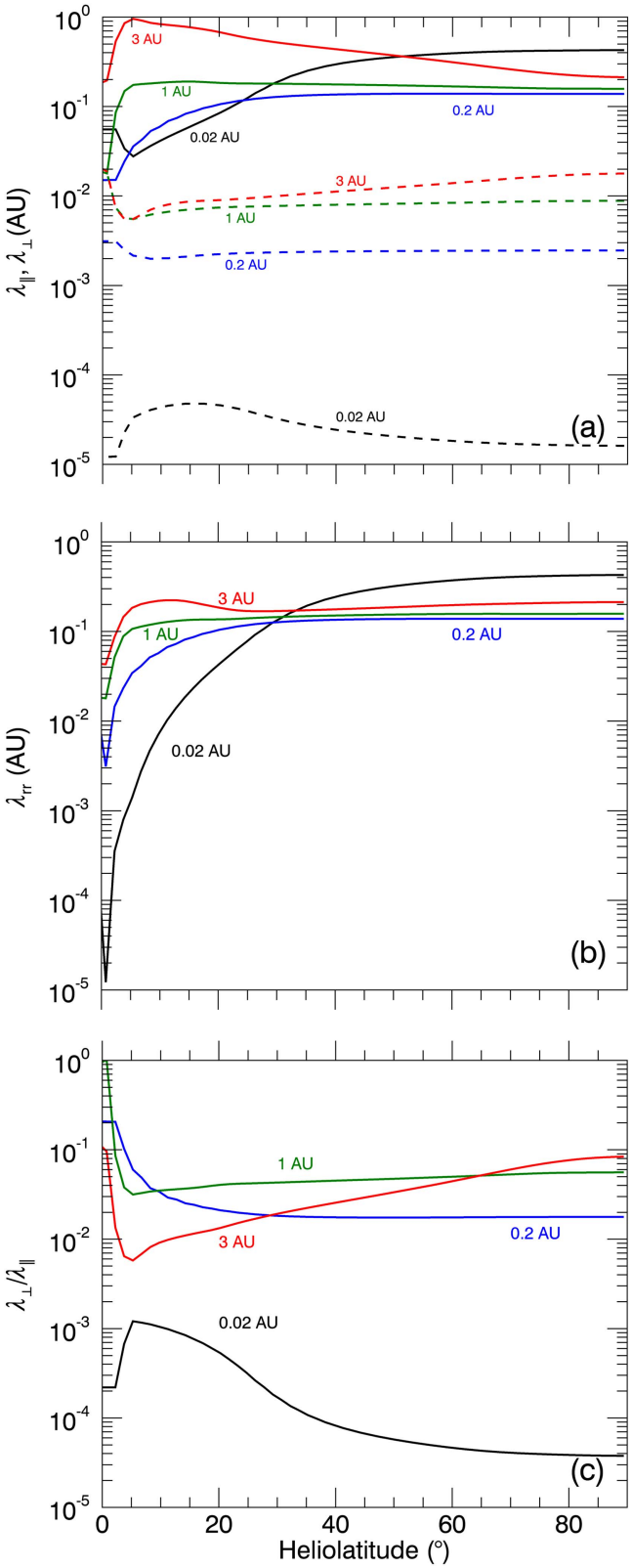


Figure 6. Top panel (a) shows the latitudinal dependence of parallel (solid lines) and perpendicular (dashed lines) mfps. Middle (b) and bottom (c) panels show the latitudinal variation of λ_{rr} and $\lambda_\perp/\lambda_\parallel$, respectively. All panels are for an untilted solar dipole and $p = 2$. Black, blue, green, and red lines represent radial distances of 0.02, 0.2, 1, and 3 au (4, 45, 215, and 645 $R_\odot$), respectively. Proton rigidity is 445 MV (100 MeV kinetic energy).

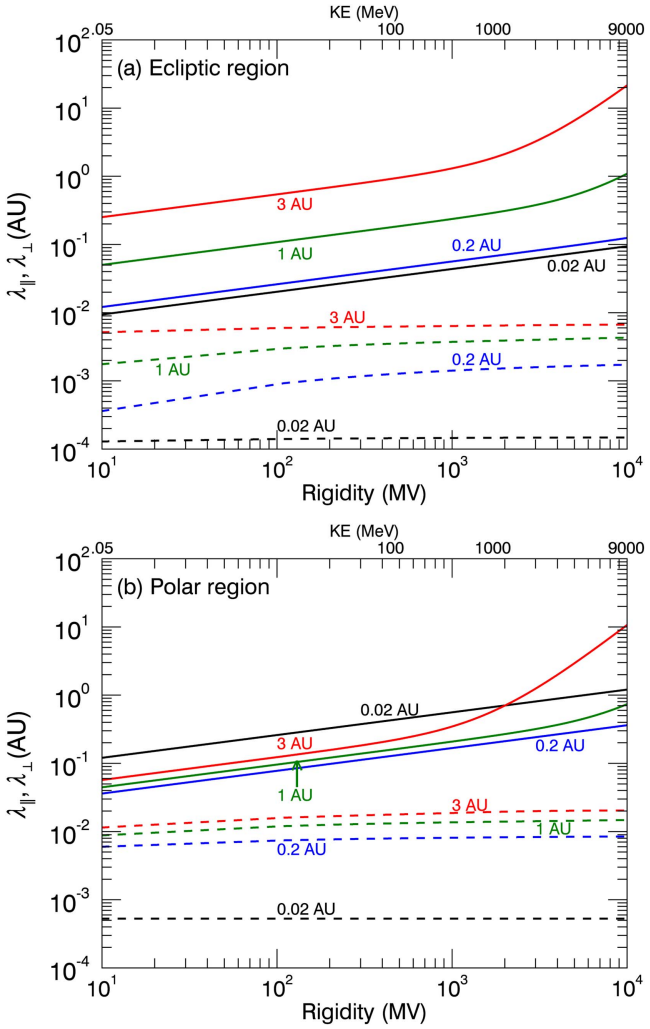


Figure 7. Rigidity dependence of $\lambda_\parallel$ (solid line) and $\lambda_\perp$ (dashed line) (a) near the ecliptic plane (7° heliolatitude) and (b) in the polar regions (86° heliolatitude), for an untilted solar dipole and $p = 2$. Black, blue, green, and red lines represent radial distances of 0.02, 0.2, 1, and 3 au (4, 45, 215, and 645 $R_\odot$), respectively.

0.56 for a number of solar events where rigidity ranges from 10 to 10^3 MV. Our results also agree with the theoretical and numerical findings in Bieber et al. (1994) and Pei et al. (2010).

In general, $\lambda_\perp$ shows lower variation with rigidity. In the polar regions, $\lambda_\perp$ stays nearly constant with rigidity. This behavior is consistent with the finding of Bieber et al. (2004) that NLGC predicts a very weak rigidity dependence, and they note that this is supported by observations for rigidities between 10^2 and 10^4 MV. Note that the rigidity profiles of $\lambda_\parallel$ and $\lambda_\perp$ that we derive from simulation results and diffusion theories are quite different from some that have been employed in the literature to model solar modulation of GCRs (e.g., see Figure 12 of Vos & Potgieter 2015).

4.5. Meridional Plane Contours

In this section, we describe the variation of $\lambda_\parallel$, $\lambda_\perp$, λ_{rr}, and $\lambda_\perp/\lambda_\parallel$ in meridional planes for 100 MeV protons, complementing results of the previous sections. Figure 8 shows the results from a simulation with a source magnetic dipole that is untilted with respect to the solar rotation axis. It is clear that at the HCS, with its vanishing magnetic field, perpendicular diffusion is comparable to parallel diffusion in most of the inner heliosphere, with $\lambda_\perp$ and $\lambda_\parallel$ both around 0.01 au. In the broader ecliptic plane, however, $\lambda_\parallel$ remains one to two orders of magnitude above $\lambda_\perp$, varying from 0.01 to almost 1 au within a radial distance of 10 $R_\odot$ to 3 au, while $\lambda_\perp$ increases from ∼0.0001 to 0.01 au. As noted in the 1D plots, very close to the Sun, $\lambda_\parallel$ experiences a dramatic increase to a value of 1 au due to the weak turbulence and strong magnetic field prevailing there.

We also see that at radial distances of 1.5–3 au, $\lambda_\parallel$ is a few times larger at lower latitudes, compared to values in polar regions. This is because the IMF decreases and the turbulence energy increases with latitude at these radial distances, leading to a reduction in parallel diffusion in the polar regions and a corresponding increase in perpendicular diffusion. This can also be seen in Figure 8(h) showing contours of $\lambda_\perp/\lambda_\parallel$, which increases by nearly one order of magnitude from low latitudes to the poles. The radial mfp increases uniformly with heliocentric distance at lower latitudes, but is dominated by $\lambda_\parallel$ in polar regions, because of the small winding angle between the IMF and the radial direction here. This leads to λ_{rr} acquiring a nearly constant value of around 0.2 au in polar regions beyond 2 au.

Figure 9 shows contour plots for mfps in the meridional plane at an azimuthal angle equal to 26°, for a simulation with a source magnetic dipole that is tilted by 30° with respect to the solar rotation axis. In this case, solar rotation produces an asymmetrical magnetic field structure, which has a striking effect on the diffusion parameters, with the displacement of the current sheet from the ecliptic plane modifying their distribution at low latitudes. Note that the blob-like structures in Figures 9(f) and (h) arise due to grid points coinciding with the HCS. The rapid decrease in the magnitude of the IMF near the HCS leads to the formation of the blob contours around grid points where B vanishes. This effect is not seen in Figure 8 for the untilted dipole case, where the HCS lies at 0° heliolatitude, where no grid points are present, by construction.

As noted previously in Section 4.2, observations indicate that the ratio $\lambda_\perp/\lambda_\parallel$ may approach, and even exceed, unity. In our simulation, this happens in the HCS. The basic features described above for the untilted dipole are still present in this case, but are now organized with respect to the tilted HCS. During periods when solar activity levels are high, the warped current sheet is spread out across a larger portion of the heliosphere (Figure 9) compared with the low activity case (untilted dipole, Figure 8), and the HCS is thus more likely to influence CRs.

5. Conclusions and Discussion

We have presented a detailed analysis of the diffusion coefficients for CR transport in the inner heliosphere. The purpose is to use a well-tested, fully 3D global simulation of the solar wind, with turbulence modeling, to obtain the heliospheric distribution of the large-scale heliospheric magnetic field, the energy in the turbulent fluctuations, and the correlation scale of the turbulence. This distribution has been coupled with a quasi-linear theory for parallel diffusion and the recent RBD interpretation of the nonlinear guiding center theory for perpendicular diffusion. The present work extends previous studies on the heliospheric diffusion of CRs by Bieber et al. (1995), Zank et al. (1998), and Pei et al. (2010), but has a stronger focus on the inner heliosphere, with the inner

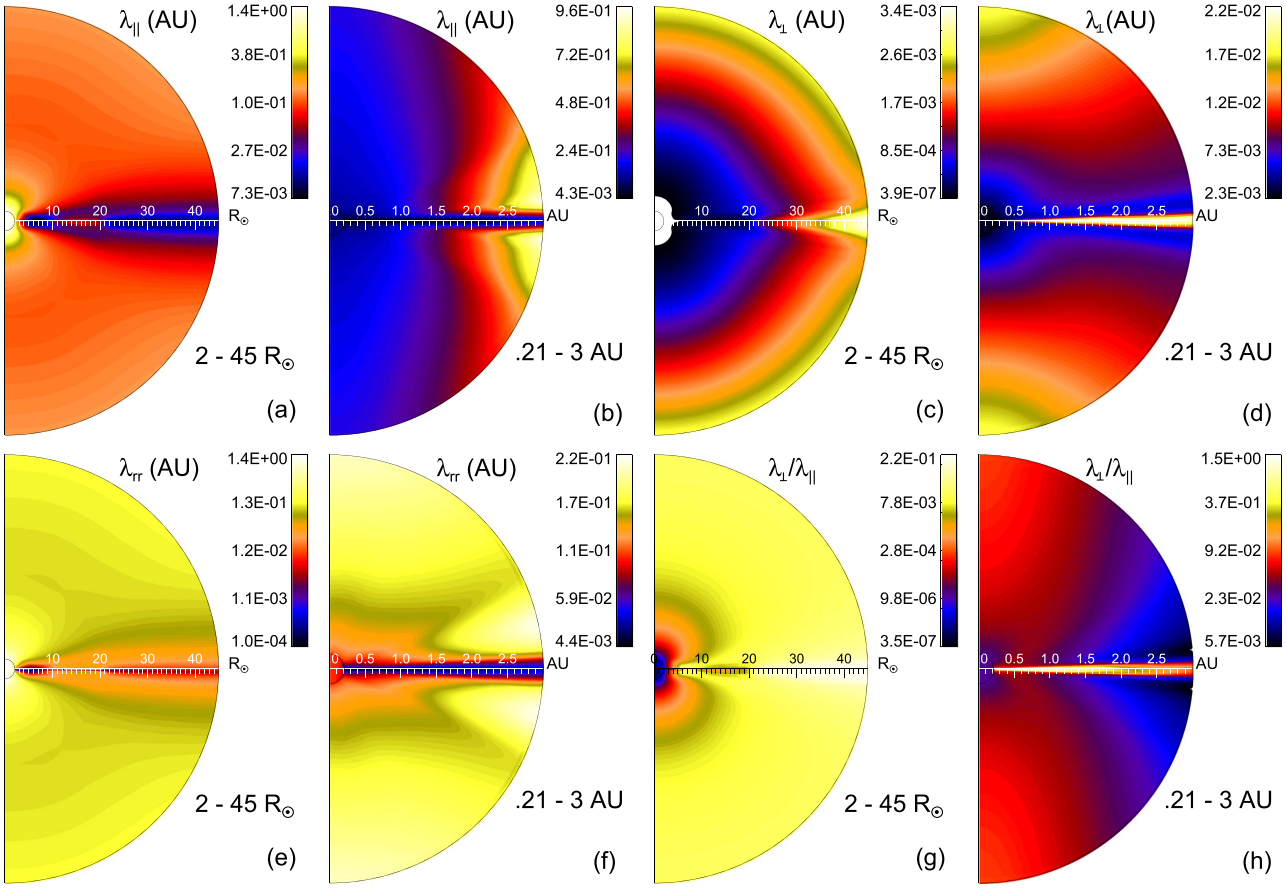


Figure 8. Contour plots in the meridional plane of mfps, with a solar dipole that is untilted with respect to the solar rotation axis. The inner and intermediate regions (2–45 $R_\odot$) and the outer region (0.21–3 au, or 45–645 $R_\odot$) are shown separately. Proton rigidity is 445 MV (100 MeV kinetic energy) and $p = 2$.

boundary of our simulations at 1 $R_\odot$. Recent complementary work (Guo & Florinski 2016) carries out similar computations of diffusion coefficients for the outer heliosphere.

We find that at the HCS $\lambda_\perp$ can be greater than $\lambda_\parallel$, but $\lambda_\parallel$ is usually one to two orders of magnitude larger through most of the inner heliosphere. Very close to the Sun (2 $R_\odot$), the strong IMF leads to a large value of $\lambda_\parallel$ ($\sim$0.5 au), which initially decreases for several solar radii before increasing with radial distance at low to intermediate latitudes, and becomes nearly constant at the polar regions. $\lambda_\perp$ increases with heliocentric distance throughout the inner heliosphere, and is larger in the polar regions compared to low latitudes. λ_{rr} is dominated by $\lambda_\parallel$ through most of the inner heliosphere. However, $\lambda_\perp$ does affect λ_{rr} in parts of the near-ecliptic region. Our estimations of $\lambda_\parallel$ near the ecliptic plane at 1 au show good agreement with the Palmer consensus range of 0.08–0.3 au.

At heliocentric distances below 1 au, we find that the parallel mfp varies with rigidity as $P^{0.33}$ for all rigidities considered here (10–10^4 MV). Above 1 au, highly energetic particles begin to resonate with turbulent fluctuations in the energy-containing scales, and the rigidity dependence of $\lambda_\parallel$ steepens. The perpendicular mfp is weakly dependent on rigidity. Our results on the rigidity dependence of mfps are consistent with observations.

The mfps are found to be weakly dependent on the type of power spectrum used to represent the large-scale fluctuations. This suggests that any attempts to use spacecraft observations of mfps to infer constraints on the ultrascale would be challenging. The effects of solar activity (via a tilted solar dipole and variations of turbulence levels) are also studied, with increased activity leading to stronger perpendicular diffusion and weaker parallel diffusion.

The model we have adopted for turbulence transport has been thoroughly studied and tested (Breech et al. 2008). More elaborate models, with more transport equations (and more free parameters), are available (Zank et al. 2012). In particular, these models include extensions such as dynamically variable residual energy, separate transport equations for slab and 2D fluctuations, and as many as three distinct dynamically evolving correlation lengths (Oughton et al. 2011; Zank et al. 2017). For the present, we forgo the associated additional complication and rely on the present model's ability to account very well for a variety of observations (Usmanov et al. 2011, 2012, 2014).

We also remark that the turbulent fluctuations we follow dynamically are the quasi-two-dimensional fluctuations that we assume are energetically dominant. A variety of studies (Matthaeus et al. 1990; Zank & Matthaeus 1993; Bieber et al. 1994, 1996) are consistent with dominance by quasi-2D turbulence in solar wind turbulence. In the present approach, we assumed that the quasi-slab component of the fluctuations, which represent perhaps 20% of the total fluctuation energy, are a constant fraction of the turbulence energy. Useful extensions that adopt somewhat different approaches have been presented by Oughton et al. (2011) and Zank et al. (2017), with the common goal of independently transporting both 2D and slab-like fluctuations. As noted above, these models find that the radial evolution of 2D and slab fluctuation energies is

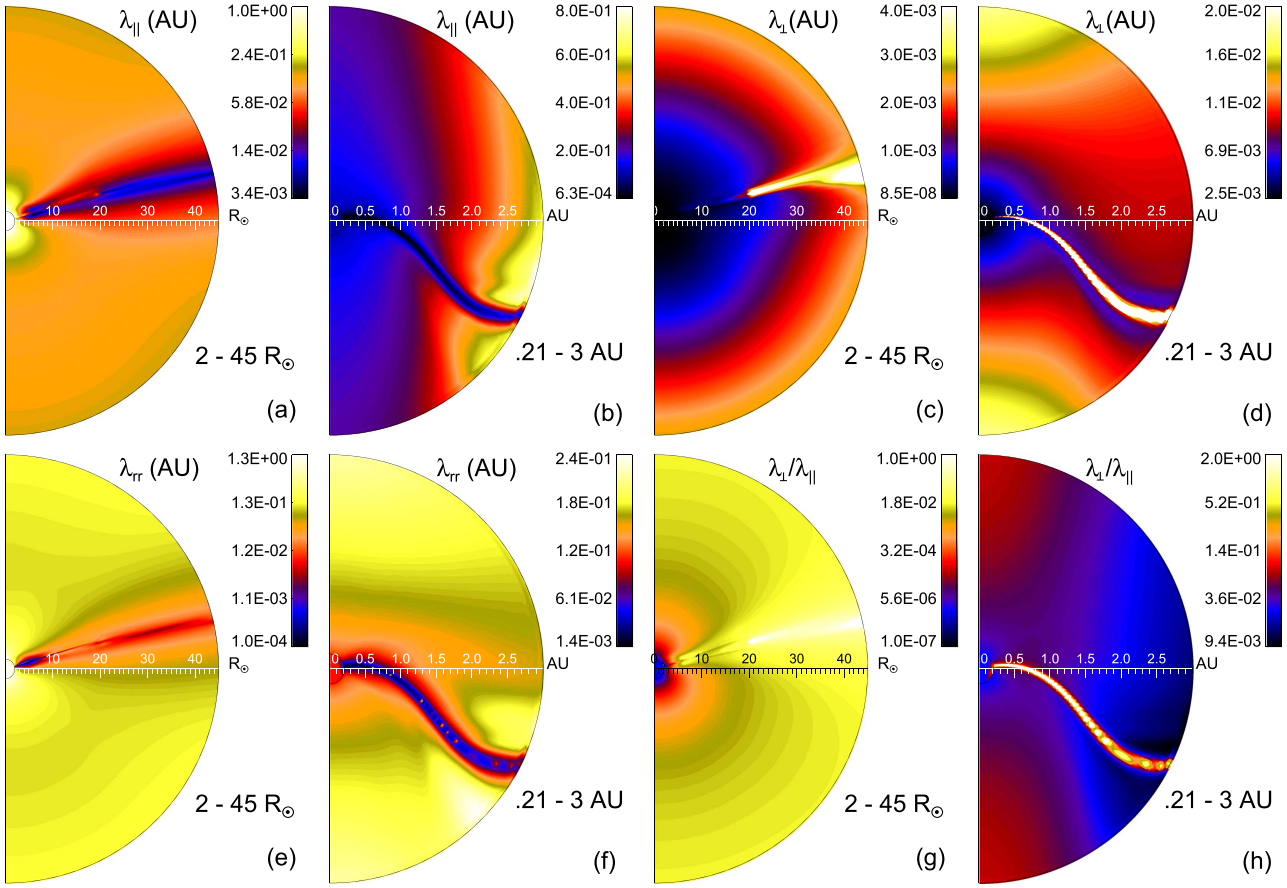


Figure 9. Contour plots of mfps in the meridional plane with azimuthal angle of 26°, with a solar dipole tilted 30° with respect to the solar rotation axis. The inner and intermediate regions (2–45 $R_\odot$) and the outer region (0.21–3 au, or 45–645 $R_\odot$) are shown separately. Proton rigidity is 445 MV (100 MeV kinetic energy) and $p = 2$.

not too dissimilar in the inner heliosphere, and therefore our decomposition of the total turbulence energy into slab and 2D components using a constant ratio appears reasonable. These models also show that in the outer heliosphere (above 3–4 au), the energy in the slab fluctuations increases with heliocentric distance due to driving by pickup ions, while the 2D fluctuation energy continues to decrease. As such, studies of CR diffusion in the outer heliosphere would undoubtedly benefit from using a two-component turbulence transport model.

Such models have been implemented (Wiengarten et al. 2016; Shiota et al. 2017), with many differences relative to the present model. For example, the Shiota et al. (2017) model has a more elaborate transport formalism, as described above, but neglects the impact of turbulence on the background flow and relies on ad hoc shear terms instead of fully coupling to the large-scale solar wind solutions. In contrast, we employ a dynamic eddy-viscosity model (Usmanov et al. 2014) to achieve this coupling. Clearly, no model at present is a complete treatment, and there are advantages and trade-offs in various approaches. We hope to advance our own model with additional refinements in the near future.

We anticipate that 3D calculations of CR diffusion coefficients in the way we have demonstrated here, employing large-scale solar wind solutions with turbulence transport and turbulence modeling, will become increasingly important for realistic energetic particle transport calculations in the future. We also note that related types of diffusion coefficients, such as drag or self-diffusion, may be similarly estimated using adaptations of the above approach, as described briefly in the Appendix. Studies of phenomena such as shock ensembles and super-events (Mueller-Mellin et al. 1986; Kunow et al. 1991), where several shocks merge to influence energetic particle transport at widely separated locations, would benefit enormously from such 3D studies in model heliospheres. Our findings of domains where $\lambda_\perp/\lambda_\parallel \geqslant 1$ may be used to further study the effects of significant perpendicular diffusion, which has been seen to reduce the SEP flux and make it more uniform (Zhang et al. 2009). Additional development at the MHD level will be needed to utilize this kind of tool for explaining observed SEP events associated with transient phenomena such as flares, CMEs, and interplanetary shocks (Ruffolo et al. 2006; Agueda & Lario 2016; Dröge et al. 2016). In the present paper, we have not undertaken specific calculations employing the diffusion coefficients we obtained using a global model; this is deferred to future work. We anticipate that this approach will be useful in understanding *Parker Solar Probe* observations of energetic particles near the Sun.

As we have now demonstrated that such an approach can provide detailed 3D information concerning both MHD transport and particle mfps, it becomes clear that what will be needed are improved methods for driving this kind of model with more sophisticated and detailed solar observations. Meanwhile, we are continuing to improve our MHD modeling by building a coronal module that includes a full turbulence

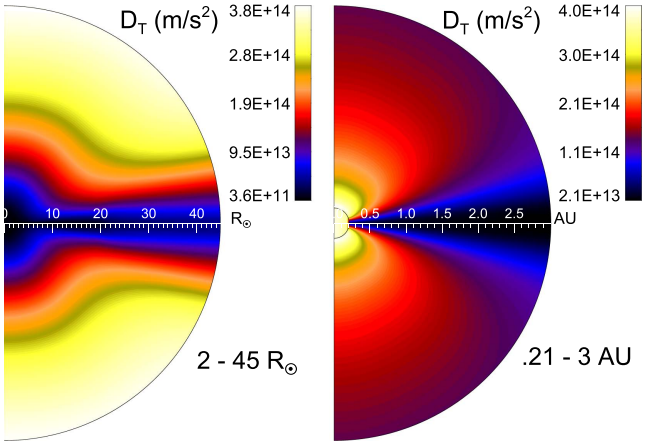


Figure 10. Turbulent drag coefficient computed from a simulation with a solar dipole that is untilted with respect to the solar rotation axis. The inner and intermediate regions (2–45 $R_\odot$) and the outer region (0.21–3 au, or 45–645 $R_\odot$) are shown separately.

transport model and by further developing the eddy-viscosity approach (Usmanov et al. 2014). Future work could also investigate the influence of drifts on CR modulation. To facilitate the use of the present data from this model for particle transport calculations relevant to the current generation of energetic particle and space weather studies, we are uploading as Supplementary Material 3D data sets of the diffusion coefficients that were described here. Separate data sets are available for untilted and tilted solar dipoles.

This research is partially supported by NASA grant NNX14AI63G (Heliophysics Grand Challenges Research), NASA LWS grants NNX15AB88G and NNX13AR42G, and the *Parker Solar Probe* mission through the ISOIS project and SWRI subcontract D99031L, and the Thailand Research Fund (grant RTA5980003). The authors would like to thank the anonymous referee for their thorough reading of the manuscript and useful suggestions for its improvement.

Appendix

Here we present an estimation of a general turbulent diffusion coefficient that is based on Taylor's formulation of the problem (Taylor 1922). The diffusion coefficient for the passive transport of any quantity in a turbulent neutral fluid may be approximated by (Choudhuri 1998)

$$D_T \approx \frac{1}{3}\langle v^2\rangle \tau_{\rm cor}, \tag{21}$$

where $\langle v^2\rangle$ is the mean square turbulent velocity and $\tau_{\rm cor}$ is the correlation time of the turbulence. By assuming $\langle v^2\rangle \sim Z^2$ and defining the turbulence correlation length $\lambda \sim Z\tau_{\rm cor}$, we rewrite the above equation as

$$D_T \propto Z\lambda. \tag{22}$$

Note that any standard diffusion coefficient, drag coefficient, eddy viscosity, or other similar quantity can be expressed in a form similar to Equation (22), i.e., as a product of a characteristic velocity and a length scale (see, for example, Tennekes & Lumley 1972).

In Figure 10, we show contour plots for D_T in the meridional plane, computed from a simulation with a solar dipole that is untilted with respect to the solar rotation axis. We may interpret D_T as a turbulent drag coefficient, which is of relevance to the propagation of CMEs in the solar wind. At high heliolatitudes, the drag coefficient increases from the solar surface to 0.5 au, and then gradually decreases. Notably, at heliocentric distances smaller than 0.5 au, D_T increases by an order of magnitude in moving from the ecliptic to polar regions. This implies that a CME would be "channelled" to lower latitudes as it propagates through the inner heliosphere. Applications involving these more general approximations to diffusion processes may also be enabled by the approach described in the present paper.

References

Adhikari, L., Zank, G. P., Bruno, R., et al. 2015, ApJ, 805, 63
Agueda, N., & Lario, D. 2016, ApJ, 829, 131
Axford, W. I. 1965, P&SS, 13, 115
Babcock, H. W. 1961, ApJ, 133, 572
Batchelor, G. K. 1953, The Theory of Homogeneous Turbulence (Cambridge: Cambridge Univ. Press)
Beeck, J., Mason, G. M., Hamilton, D. C., et al. 1987, ApJ, 322, 1052
Belcher, J. W., Davis, L., Jr., & Smith, E. J. 1969, JGR, 74, 2302
Bieber, J. W., Burger, R. A., & Matthaeus, W. H. 1995, Proc. ICRC (Rome), 24, 694
Bieber, J. W., & Matthaeus, W. H. 1997, ApJ, 485, 655
Bieber, J. W., Matthaeus, W. H., Shalchi, A., & Qin, G. 2004, GeoRL, 31, L10805
Bieber, J. W., Matthaeus, W. H., Smith, C. W., et al. 1994, ApJ, 420, 294
Bieber, J. W., Wanner, W., & Matthaeus, W. H. 1996, JGR, 101, 2511
Breech, B., Matthaeus, W. H., Minnie, J., et al. 2008, JGRA, 113, A08105
Bruno, R., & Carbone, V. 2013, LRSP, 10, 2
Candia, J., & Roulet, E. 2004, JCAP, 2004, 007
Chhiber, R., Usmanov, A., Matthaeus, W., & Goldstein, M. 2016, ApJ, 821, 34
Choudhuri, A. R. 1998, The Physics of Fluids and Plasmas: An Introduction for Astrophysicists (Cambridge: Cambridge Univ. Press)
Dröge, W. 2003, ApJ, 589, 1027
Dröge, W., Kartavykh, Y. Y., Dresing, N., & Klassen, A. 2016, ApJ, 826, 134
Dwyer, J. R., Mason, G. M., Mazur, J. E., et al. 1997, ApJL, 490, L115
Engelbrecht, N. E., & Burger, R. A. 2013, ApJ, 779, 158
Fisk, L. A. 1979, in Solar System Plasma Physics, Vol. 1, ed. E. N. Parker, C. F. Kennel, & L. J. Lanzerotti (Amsterdam: North Holland Publishing Co.), 177
Forbush, S. E. 1954, JGR, 59, 525
Ghosh, S., & Goldstein, M. L. 1997, JPlPh, 57, 129
Giacalone, J., & Jokipii, J. R. 1999, ApJ, 520, 204
Gleeson, L. J. 1969, P&SS, 17, 31
Goldstein, M. L. 1976, ApJ, 204, 900
Gottlieb, S., Shu, C.-W., & Tadmor, E. 2001, SIAMR, 43, 89
Grappin, R., Leorat, J., & Pouquet, A. 1983, A&A, 126, 51
Guo, X., & Florinski, V. 2016, ApJ, 826, 65
Heber, B., & Potgieter, M. S. 2006, SSRv, 127, 117
Hollweg, J. V. 1986, JGR, 91, 4111
Hossain, M., Gray, P. C., Pontius, D. H., Jr., Matthaeus, W. H., & Oughton, S. 1995, PhFl, 7, 2886
Hunana, P., & Zank, G. P. 2010, ApJ, 718, 148
Hundhausen, A. J. 1972, Coronal Expansion and Solar Wind, XII (Berlin, New York: Springer)
Jokipii, J. R. 1966, ApJ, 146, 480
Jokipii, J. R. 1971, RvGSP, 9, 27
Jokipii, J. R., & Kota, J. 1995, SSRv, 72, 379
Jokipii, J. R., & Parker, E. N. 1970, ApJ, 160, 735
Jokipii, J. R., & Thomas, B. 1981, ApJ, 243, 1115
Kulsrud, R., & Pearce, W. P. 1969, ApJ, 156, 445
Kunow, H., Wibberenz, G., Green, G., Müller-Mellin, R., & Kallenrode, M.-B. 1991, in Physics of the Inner Heliosphere II, ed. R. Schwenn & E. Marsch (Berlin: Springer), 243
Kurganov, A., & Levy, D. 2000, SIAM J. Sci. Comput., 22, 1461
Mace, R. L., Matthaeus, W. H., & Bieber, J. W. 2000, ApJ, 538, 192
Marsch, E. 1991, in Physics of the Inner Heliosphere II, ed. R. Schwenn & E. Marsch (Berlin: Springer), 159
Marsch, E., & Tu, C.-Y. 1989, JPlPh, 41, 479
Marsh, M. S., Dalla, S., Kelly, J., & Laitinen, T. 2013, ApJ, 774, 4
Matthaeus, W. H., Bieber, J. W., Ruffolo, D., Chuychai, P., & Minnie, J. 2007, ApJ, 667, 956

Matthaeus, W. H., Dasso, S., Weygand, J. M., et al. 2005, PhRvL, 95, 231101
Matthaeus, W. H., & Goldstein, M. L. 1986, PhRvL, 57, 495
Matthaeus, W. H., Goldstein, M. L., & Roberts, D. A. 1990, JGR, 95, 20673
Matthaeus, W. H., Oughton, S., Pontius, D. H., Jr., & Zhou, Y. 1994, JGR, 99, 19
Matthaeus, W. H., Qin, G., Bieber, J. W., & Zank, G. P. 2003, ApJL, 590, L53
Matthaeus, W. H., Smith, C. W., & Bieber, J. W. 1999a, in AIP Conf. Proc. 382, Solar Wind Nine, ed. S. R. Habbal et al. (Melville, NY: AIP), 511
Matthaeus, W. H., Smith, C. W., & Oughton, S. 1998, JGR, 103, 6495
Matthaeus, W. H., Weygand, J. M., & Dasso, S. 2016, PhRvL, 116, 245101
Matthaeus, W. H., Zank, G. P., Smith, C. W., & Oughton, S. 1999b, PhRvL, 82, 3444
McComb, W. D. 1990, The Physics of Fluid Turbulence (Oxford: Oxford Univ. Press)
Minnie, J., Bieber, J. W., Matthaeus, W. H., & Burger, R. A. 2007, ApJ, 670, 1149
Moraal, H. 1976, SSRv, 19, 845
Morfill, G. E., & Voelk, H. J. 1979, JGR, 84, 4446
Mueller-Mellin, R., Roehrs, K., & Wibberenz, G. 1986, ASSL, 123, 349
Osman, K. T., & Horbury, T. S. 2007, ApJL, 654, L103
Oughton, S., Matthaeus, W. H., Smith, C. W., Breech, B., & Isenberg, P. A. 2011, JGRA, 116, A08105
Palmer, I. D. 1982, RvGSP, 20, 335
Parker, E. N. 1956, PhRv, 103, 1518
Parker, E. N. 1964, JGR, 69, 1755
Parker, E. N. 1965, P&SS, 13, 9
Parker, E. N. 2005, SpWea, 3, s08004
Pei, C., Bieber, J. W., Breech, B., et al. 2010, JGRA, 115, A03103
Pizzo, V. 1978, JGR, 83, 5563
Pizzo, V. J. 1982, JGR, 87, 4374
Potgieter, M. S. 2013, LRSP, 10, 3
Powell, K. G. 1994, An Approximate Riemann Solver for Magnetohydrodynamics, (that Works in More Than One Dimension), Tech. Rep. No. 94-24 (Hampton, VA: Institute for Computer Applications in Science and Engineering)
Reames, D. V. 1999, SSRv, 90, 413
Reinecke, J. P. L., Steenberg, C. D., Moraal, H., & McDonald, F. B. 1997, AdSpR, 19, 901
Ruffolo, D., Matthaeus, W. H., & Chuychai, P. 2004, ApJ, 614, 420
Ruffolo, D., Pianpanit, T., Matthaeus, W. H., & Chuychai, P. 2012a, ApJL, 747, L34
Ruffolo, D., Tooprakai, P., Rujiwarodom, M., et al. 2006, ApJ, 639, 1186
Ruffolo, D. J., Pianpanit, T., Chuychai, P., Matthaeus, W. H., & Qin, G. 2012b, in AGU Fall Meeting Abstracts, SH21A-2188
Shalchi, A. 2006, A&A, 453, L43
Shalchi, A. 2009, Nonlinear Cosmic Ray Diffusion Theories, Vol. 362 (Berlin: Springer)
Shiota, D., Zank, G. P., Adhikari, L., et al. 2017, ApJ, 837, 75
Smith, C. W., Matthaeus, W. H., Zank, G. P., et al. 2001, JGR, 106, 8253
Smith, E. J. 2001, JGR, 106, 15819
Snyder, C. W., Neugebauer, M., & Rao, U. R. 1963, JGR, 68, 6361
Spruit, H. C. 1981, NASSP, 450, 385
Taylor, G. I. 1922, Proceedings of the London Mathematical Society, s2-20, 196
Tennekes, H., & Lumley, J. L. 1972, A First Course in Turbulence (Cambridge, MA: MIT Press)
Tu, C.-Y., & Marsch, E. 1990, JPlPh, 44, 103
Tu, C.-Y., & Marsch, E. 1995, SSRv, 73, 1
Tylka, A. J., Adams, J. H., Boberg, P. R., et al. 1997, ITNS, 44, 2150
Usmanov, A. V. 1993, SoPh, 146, 377
Usmanov, A. V. 1996, in AIP Conf. Ser. 382, 8th International Solar Wind Conference,, ed. D. Winterhalter et al., 141
Usmanov, A. V., & Goldstein, M. L. 2003, JGRA, 108, 1354
Usmanov, A. V., Goldstein, M. L., Besser, B. P., & Fritzer, J. M. 2000, JGR, 105, 12675
Usmanov, A. V., Goldstein, M. L., & Matthaeus, W. H. 2012, ApJ, 754, 40
Usmanov, A. V., Goldstein, M. L., & Matthaeus, W. H. 2014, ApJ, 788, 43
Usmanov, A. V., Goldstein, M. L., & Matthaeus, W. H. 2016, ApJ, 820, 17
Usmanov, A. V., Matthaeus, W. H., Breech, B. A., & Goldstein, M. L. 2011, ApJ, 727, 84
Völk, H. J., Morfill, G., Alpers, W., & Lee, M. A. 1974, Ap&SS, 26, 403
Vos, E. E., & Potgieter, M. S. 2015, ApJ, 815, 119
Wan, M., Oughton, S., Servidio, S., & Matthaeus, W. H. 2012, JFM, 697, 296
Weygand, J. M., Matthaeus, W. H., Dasso, S., et al. 2009, JGRA, 114, A07213
Weygand, J. M., Matthaeus, W. H., Dasso, S., & Kivelson, M. G. 2011, JGRA, 116, A08102
Wiengarten, T., Fichtner, H., Kleimann, J., & Kissmann, R. 2015, ApJ, 805, 155
Wiengarten, T., Oughton, S., Engelbrecht, N. E., et al. 2016, ApJ, 833, 17
Yokoi, N., & Hamba, F. 2007, PhPl, 14, 112904
Zank, G. P., Adhikari, L., Hunana, P., et al. 2017, ApJ, 835, 147
Zank, G. P., Dosch, A., Hunana, P., et al. 2012, ApJ, 745, 35
Zank, G. P., Li, G., Florinski, V., et al. 2004, JGRA, 109, A04107
Zank, G. P., & Matthaeus, W. H. 1992, JGR, 97, 17189
Zank, G. P., & Matthaeus, W. H. 1993, PhFl, 5, 257
Zank, G. P., Matthaeus, W. H., Bieber, J. W., & Moraal, H. 1998, JGR, 103, 2085
Zank, G. P., Matthaeus, W. H., & Smith, C. W. 1996, JGR, 101, 17093
Zhang, M., Jokipii, J. R., & McKibben, R. B. 2003, ApJ, 595, 493
Zhang, M., Qin, G., & Rassoul, H. 2009, ApJ, 692, 109
Zhou, Y., & Matthaeus, W. H. 1990, JGR, 95, 10291

The Astrophysical Journal, 844:87 (8pp), 2017 July 20 https://doi.org/10.3847/1538-4357/aa79f2
© 2017. The American Astronomical Society. All rights reserved.

Coronal Heating Topology: The Interplay of Current Sheets and Magnetic Field Lines

A. F. Rappazzo[1], W. H. Matthaeus[2], D. Ruffolo[3], M. Velli[1], and S. Servidio[4]
[1] Department of Earth, Planetary, and Space Sciences, UCLA, Los Angeles, CA 90095, USA; rappazzo@ucla.edu
[2] Bartol Research Institute, Department of Physics and Astronomy, University of Delaware, Newark, DE 19716, USA
[3] Department of Physics, Faculty of Science, Mahidol University, Bangkok 10400, Thailand
[4] Dipartimento di Fisica, Università della Calabria, Cosenza I-87036, Italy
Received 2017 March 28; revised 2017 June 12; accepted 2017 June 13; published 2017 July 25

Abstract

The magnetic topology and field line random walk (FLRW) properties of a nanoflare-heated and magnetically confined corona are investigated in the reduced magnetohydrodynamic regime. Field lines originating from current sheets form coherent structures, called current sheet connected (CSC) regions, which extend around them. CSC FLRW is strongly anisotropic, with preferential diffusion along the current sheets' in-plane length. CSC FLRW properties remain similar to those of the entire ensemble but exhibit enhanced mean square displacements and separations due to the stronger magnetic field intensities in CSC regions. The implications for particle acceleration and heat transport in the solar corona and wind, and for solar moss formation are discussed.

Key words: magnetohydrodynamics (MHD) – solar wind – Sun: activity – Sun: corona – Sun: magnetic fields – turbulence

Supporting material: animation

1. Introduction

The stochastic properties of magnetic fluctuations in turbulent plasmas are reflected in the stochastic character of magnetic field lines, giving rise to field line random walk (FLRW, Jokipii & Parker 1968; Jokipii 1973; Matthaeus et al. 1995) that strongly affects the propagation and cross-field transport of energetic particles. Additionally, the intense electric fields associated to turbulent coherent structures, such as current sheets (and the related in- and outflows), strongly contribute to particle acceleration (Swann 1933; Drake et al. 2005; Dalena et al. 2014).

Because particles are energized and plasma is heated in current sheets, the topology of field lines that originate from them determines how these accelerated particles and heat are transported. Furthermore, in strong magnetic fields, where particle diffusion perpendicular to field lines is small and thermal conduction is highly anisotropic (essentially parallel), heat and particles are in first approximation transported along field lines. It is therefore key to understand the interplay between current sheets and magnetic field lines.

It has become increasingly clear that the effective heating and particle acceleration occur at scales of the order of the ion (proton) inertial length d_i (Sonnerup 1979; Mozer et al. 2002; Runov et al. 2006; Phan et al. 2007; Xiao et al. 2007; Wu et al. 2011; Liu et al. 2014), that in the solar corona, for an ion density $n_i \sim 10^8\,\mathrm{cm}^{-3}$, is $d_i = c/\omega_{pi} \sim 23$ m ($\omega_{pi} = \sqrt{4\pi n_i e^2/m_i}$ is the proton plasma frequency, c is the speed of light, e is the electron charge, and m_i is the proton mass). For typical hot coronal loops with temperatures $T \sim 10^6$ K and magnetic field intensities $B \sim 50$ G, the ion gyroradius is much smaller than d_i (reaching d_i only in the higher β regions typical of the solar wind).

In situ measurements in Earth's magnetotail (Runov et al. 2005, 2006) and magnetosheath (Retinò et al. 2007), and laboratory experiments (Matthaeus et al. 2005; Yamada et al. 2006) show that current sheet thickness is generally somewhat larger than the ion inertial length, with activity increasing for thinner current sheets as their width approaches d_i.

Additionally, PIC simulations of fully developed turbulence have shown that clustering of current sheet thickness occurs at scales of $\sim d_i$, with substructures down to the electron inertial length d_e (Karimabadi et al. 2013). These are the natural scales at which kinetic effects will convert the energy coming from large scales into the different species' thermal and non-thermal energies.

Note that these findings are also consistent with the recent understanding that thin current sheets are strongly unstable under the plasmoid instability (Bulanov et al. 1978; Biskamp 1986; Loureiro et al. 2007; Lapenta 2008; Bhattacharjee et al. 2009), with growth rates reaching fast "ideal" Alfvén values ($\gamma\tau_A \sim 1$) for sufficiently small thicknesses (Pucci & Velli 2014; Landi et al. 2015; Tenerani et al. 2015). Including the Hall effect the instability becomes explosive as the current sheet thickness approaches d_i (Pucci et al. 2017).

Although the aforementioned studies include at most a weak guide magnetic field, the formation of current sheets with the exponentially thinning widths have been observed in fully nonlinear 2D and 3D MHD simulations (Sulem et al. 1983; Frisch et al. 2003; Krstulovic et al. 2011; Brachet et al. 2013), and line-tied simulations with a strong guide field and vanishing initial velocity (Rappazzo & Parker 2013). Although kinetic simulations with a strong guide field are still computationally challenging, we expect that the overall phenomenology and current sheet structure is not substantially modified in the strong guide field case of interest to the solar corona and inner heliosphere. We then consider the gyroradii of bulk ions and electrons to be generally smaller than the current sheet thickness, and the initial stage of their acceleration is thus strongly affected by the field line topology.

FLRW in turbulent fields is a topic of intense research (Jokipii & Kota 1989; Zimbardo et al. 2000; Beresnyak 2013; Snodin et al. 2013), but little attention has been dedicated to the effects of spatial intermittency and coherent structures (Pucci et al. 2016). However, the plasma thermodynamical properties

are strongly affected by the topology of field lines originating in current sheets, both in the corona and solar wind. For instance, the thermodynamics and high-energy radiative emission of coronal loops are determined by the temporal and spatial properties of energy dissipation along the field lines (Klimchuk 2006; Reale 2014). Additionally, energetic particles and heat transport toward the transition region at coronal loop footpoints give rise to a reticulated spongy pattern in X-rays and EUV, so-called *moss*, that could be explained by the complex trajectories of energetic particles in a stochastic magnetic field (Kittinaradorn et al. 2009).

Here we investigate the magnetic field line's random walk in a nanoflare-heated and magnetically confined corona to advance our understanding of transport of heat and energetic particles in stochastic magnetic fields, its relationship with coherent structures, and discuss its impact on coronal and solar wind dynamics.

2. Model

Our model coronal loops are "straightened-out" in a Cartesian elongated box with axial length L (along the z-direction) and an orthogonal square cross-section of size ℓ(x–y planes), with aspect ratio $L/\ell = 10$. The system, with uniform density ρ_0, is threaded by a strong axial magnetic field $\boldsymbol{B}_0 = B_0\hat{\boldsymbol{e}}_z$, and its dynamics are well described by the reduced magnetohydrodynamic equations (Kadomtsev & Pogutse 1974; Strauss 1976; Montgomery 1982; Zank & Matthaeus 1992), valid in the limit of a large loop aspect ratio ($\epsilon = \ell/L \ll 1$) and of a small ratio of orthogonal to axial magnetic field ($b/B_0 \leqslant \epsilon$). The velocity ($\boldsymbol{u}$) and fluctuating magnetic field ($\boldsymbol{b}$) have only components perpendicular to the axial direction z, and, indicating their potentials with φ and ψ, they can be written as $\boldsymbol{u} = \nabla\varphi \times \hat{\boldsymbol{e}}_z$ and $\boldsymbol{b} = \nabla\psi \times \hat{\boldsymbol{e}}_z$, with the current density $j = -\nabla^2\psi$, and vorticity $\omega = -\nabla^2\varphi$. In non-dimensional form, they are given by

$$\partial_t\psi = [\varphi, \psi] + B_0\partial_z\varphi + \eta\nabla^2\psi, \tag{1}$$

$$\partial_t\omega = [j, \psi] - [\omega, \varphi] + B_0\partial_z j + \nu\nabla^2\omega, \tag{2}$$

where the magnetic field has been expressed as an Alfvén velocity (i.e., $b \to b/\sqrt{4\pi\rho_0}$), and then all velocities normalized to $u^* = 1$ km s^{-1} (the photospheric granulation velocity rms). The Poisson bracket is defined as, e.g., $[\varphi, \psi] = \partial_x\varphi\partial_y\psi - \partial_y\varphi\partial_x\psi = -\boldsymbol{u}\cdot\nabla\psi$, and the Laplacian operator has only orthogonal components. Lengths are normalized to the orthogonal box length, thus $\ell = 1$ and $L = 10$. Normalized resistivity and viscosity coefficients are set equal to $\eta = \nu = 1/R$, where the Reynolds number $R = 800$, numerical resolution $2048^2 \times 512$, and the guide field intensity $B_0 = 10^3$. As in previous simulations, field lines are line-tied to the top and bottom plates $z = 0$, 10 where they are shuffled by a prescribed photospheric granulation-mimicking velocity constant in time with length scale $\sim 1/4$ (Rappazzo et al. 2008), while in x–y planes periodic boundary conditions are implemented. In the x–y planes, a pseudo-spectral scheme with periodic boundary conditions is implemented, time is advanced with a third-order Runge–Kutta and an adaptive time step. More details on the model and numerical code can be found in Rappazzo et al. (2007, 2008).

The numerical integration of Equations (1)–(2) cannot implement enough grid points to attain a realistic description of the internal structure of current sheets (that would additionally require the inclusion of the Hall term, or the integration of a kinetic model, that in turn could not properly describe the large-scale dynamics). Nevertheless, while a good representation of the small-scale structure is very important for the acceleration of particles (and we have developed a hierarchical multi-scale model to this effect in Dalena et al. 2014), since FLRW is affected mostly by the large-scale components of the magnetic field, its properties should not depend critically on the small-scale structure of the current sheets, and an MHD model represents a good starting point. For these reasons, we adopt an empirical approach, selecting the value of resistivity for essentially numerical reasons, but subsequently associating the resulting dissipative scale with the ion inertial length.

3. Results

Our simulations start with the guide field B_0 (directed along z) and no magnetic or velocity fluctuations in the computational box. The imposed large-scale velocity at the boundaries $z = 0$, and L twists the field lines and, once the twist exceeds a small critical threshold, the orthogonal magnetic field line tension is no longer balanced. Thus, as proposed by Parker (1972, 1994), the magnetic field $\boldsymbol{b}$ transitions to non-equilibrium (Rappazzo & Parker 2013; Rappazzo 2015), bringing about turbulent dynamics that transfers energy toward the small scales where it is dissipated in nanoflares (Parker 1988). Line-tying keeps the velocity field in the computational box smaller than the magnetic field (far from equipartition). Nevertheless, a cascade with preferential energy transfer in the x–y planes orthogonal to B_0 and a broadband power-law magnetic energy spectrum develop, but the enhanced field line stiffness introduced by line-tying gives rise to steeper magnetic energy spectra $E_M(k_\perp) \propto k_\perp^{-\alpha}$ with $\alpha \in [5/3, 3]$, with the steepest spectra corresponding to stronger guide fields B_0 (Einaudi et al. 1996; Dmitruk & Gómez 1997; Dmitruk et al. 1998; Dmitruk & Gómez 1999; Dmitruk et al. 2003; Rappazzo et al. 2007, 2008; Rappazzo & Velli 2011). In the simulations considered here, $\alpha \sim 3$.

The magnetic field structure is characterized by approximately field-aligned current sheets. Although the overall physical conditions are markedly different between the line-tied and fully periodic reduced MHD, we hypothesize that the FLRW properties of field lines traced from current sheets are qualitatively the same, since in both cases current sheets are field aligned (e.g., Dmitruk et al. 2005) and their axial extension must be linked to the parallel correlation length. Clearly, the current sheet extension in the axial direction can change depending on the particular type of forcing, but our conclusions on FLRW and diffusion properties may be tentatively extended to the fully periodic case, as discussed in our conclusions, Section 4.

3.1. Field Line Diffusion from a Single Point

Since in reduced MHD the z-component (B_0) of the magnetic field is constant, the magnetic field line equation can be written as

$$\frac{d\boldsymbol{x}}{dz}(z) = \frac{1}{B_0}\boldsymbol{b}(\boldsymbol{x}(z), z) \quad \to \quad \frac{d}{dz}\boldsymbol{x}^2 = \frac{2}{B_0}\,\boldsymbol{x}\cdot\boldsymbol{b}, \tag{3}$$

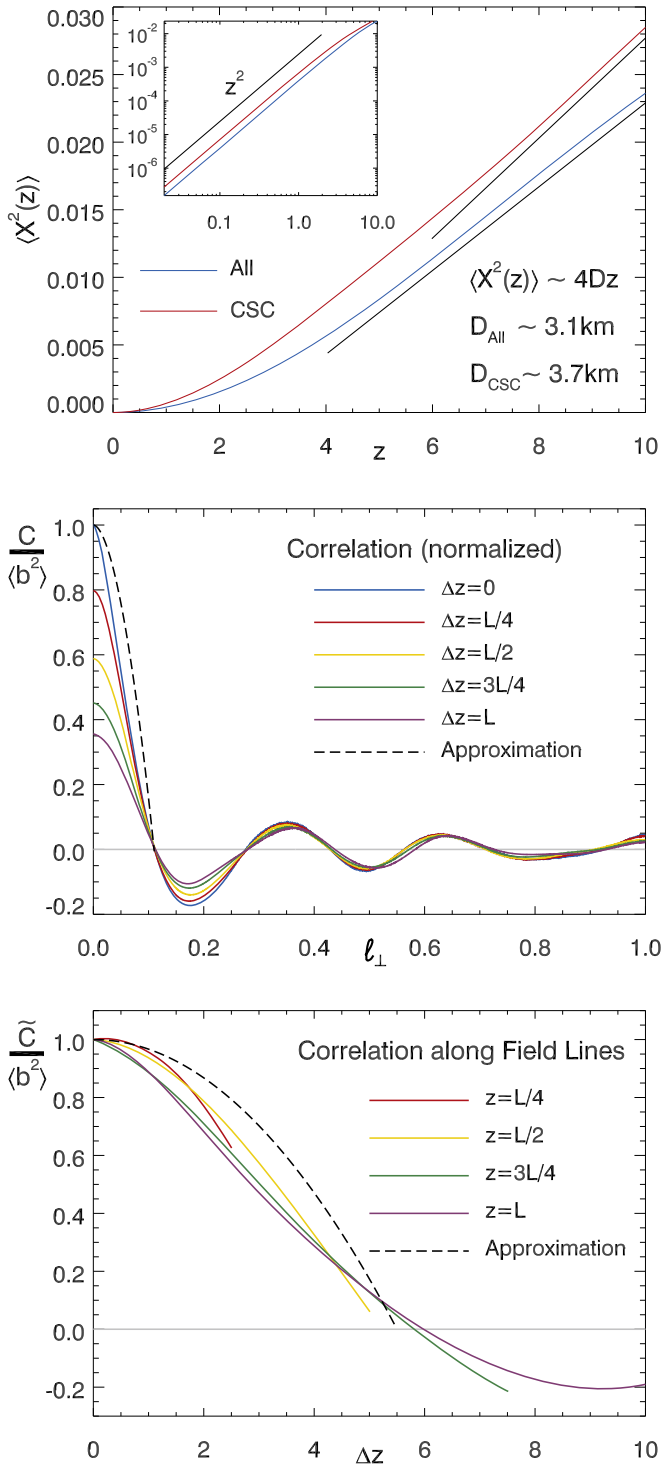


Figure 1. Top: mean square displacement averaged over all field lines and within the CSC region. Middle: magnetic field correlation function (Equation (6)) normalized with the mean square intensity $\langle b^2 \rangle$. The parallel correlation length is larger than the box size $\lambda_\parallel > L$, while $\lambda_\perp \sim 0.11$. The approximated correlation computed in Equation (11) is shown as a dashed line. Bottom: Lagrangian correlation function computed along field lines (see Equation (7)) as a function of Δz for different z-values. The approximated expression from Equation (12) is shown as a dashed line.

where $\boldsymbol{x} = (x, y)$ indicates the orthogonal coordinates. The mean square displacement $\langle \boldsymbol{X}^2(z) \rangle = \langle [\boldsymbol{x}(z) - \boldsymbol{x}_0]^2 \rangle = \langle \boldsymbol{x}^2(z) \rangle - \boldsymbol{x}_0^2$, where $\langle \ldots \rangle$ indicates the ensemble average, is shown in Figure 1 (top panel). After an initial ballistic stage with $\langle \boldsymbol{X}^2 \rangle \propto z^2$, it subsequently exhibits diffusion with $\langle \boldsymbol{X}^2 \rangle = 4Dz$. To understand this behavior, from Equation (3,) we can write

$$\frac{d}{dz}\langle \boldsymbol{x}^2(z) \rangle = \frac{2}{B_0^2} \int_0^z dz' \, \langle \boldsymbol{b}(\boldsymbol{x}(z'), z') \cdot \boldsymbol{b}(\boldsymbol{x}(z), z) \rangle. \quad (4)$$

Although the position vectors $\boldsymbol{x}(z)$ are random functions determined by the trajectory, the integrand in Equation (4) is linked to the magnetic field two-point correlation function:

$$C(\boldsymbol{x}_1, z_1, \boldsymbol{x}_2, z_2) = \langle \boldsymbol{b}(\boldsymbol{x}_1, z_1) \cdot \boldsymbol{b}(\boldsymbol{x}_2, z_2) \rangle. \quad (5)$$

For homogeneity and isotropy, this depends only on the relative parallel and orthogonal distances of the two points, i.e., indicating with $\boldsymbol{\ell}_\perp = \boldsymbol{x}_2 - \boldsymbol{x}_1$, and $\Delta z = z_2 - z_1$:

$$C(\ell_\perp, |\Delta z|) = \langle \boldsymbol{b}(\boldsymbol{0}, 0) \cdot \boldsymbol{b}(\boldsymbol{\ell}_\perp, \Delta z) \rangle, \quad (6)$$

independent of the origination point (as long as both points are within the z-span). As shown in Figure 1 (center), the correlation decreases at larger $\ell_\perp$ and z. However, while it vanishes in the perpendicular direction at the correlation length $\lambda_\perp \sim 0.11$, it does not vanish in the parallel direction (for $\ell_\perp = 0$). Namely, the parallel correlation length $\lambda_\parallel$ is larger than the box size L, i.e., the turbulent field has a strong 2D component. Clearly, this is due to the low frequency of photospheric motions. Indeed, for typical hot loops, the field line footpoints are shuffled slowly compared to the fast Alfvén crossing timescale at which the induced magnetic field twist propagates along the loop axis.

The correlation in Equation (4) is Lagrangian, i.e., it is computed along the field lines:

$$\widetilde{C}(z, \Delta z) = \langle \boldsymbol{b}(\boldsymbol{x}(z - \Delta z), z - \Delta z) \cdot \boldsymbol{b}(\boldsymbol{x}(z), z) \rangle, \quad (7)$$

with $0 \leqslant \Delta z \leqslant z$, and it is shown in Figure 1 (bottom panel). Introducing the change of variable $\Delta z = z - z'$, we can then write

$$\frac{d}{dz}\langle \boldsymbol{x}^2(z) \rangle = \frac{2}{B_0^2} \int_0^z d\Delta z \, \widetilde{C}(z, \Delta z). \quad (8)$$

Since the mean square displacement between two points along a field line at a parallel distance Δz is to a good approximation given by $\langle \boldsymbol{X}^2(\Delta z) \rangle$, the two correlations are then approximately linked by

$$\widetilde{C}(\Delta z) \sim C(\langle \boldsymbol{X}^2(\Delta z) \rangle^{1/2}, \Delta z). \quad (9)$$

Additionally, the correlation function is connected to the second-order structure function as $C(0, 0) - C(\ell_\perp, 0) = \langle \delta b_{\ell_\perp}^2 \rangle / 2$ (e.g., see Biskamp 2003), that in turn, for values of $\ell_\perp$ in the inertial range is linked to the magnetic energy spectrum by $E_{\ell_\perp} \propto \ell_\perp \delta b_{\ell_\perp}^2$, consequently,

$$E_{\ell_\perp} \propto \ell_\perp^\alpha \longrightarrow \delta b_{\ell_\perp}^2 \propto \ell_\perp^{\alpha - 1}, \quad (10)$$

with $\alpha \in [5/3, 3]$ for our boundary forced coronal loop model (Dmitruk et al. 2003; Rappazzo et al. 2007, 2008). Therefore, extending the power-law behavior beyond the inertial range for all $\ell_\perp \leqslant \lambda_\perp$, and taking into account that the correlation vanishes at $\lambda_\perp$, we can approximate the magnetic correlation

function with

$$\frac{C(\ell_\perp, 0)}{\langle b^2\rangle} \sim \begin{cases} 1 - \left(\dfrac{\ell_\perp}{\lambda_\perp}\right)^{\alpha-1} & \text{for } \ell_\perp \leqslant \lambda_\perp, \\ 0 & \text{for } \ell_\perp \geqslant \lambda_\perp, \end{cases} \tag{11}$$

with the exponent ranging from $2/3$ for $\alpha = 5/3$ up to 2 for $\alpha = 3$. This function is plotted in Figure 1 (middle) for $\alpha = 3$. Here we neglect the parallel variation of C when used in Equation (9) because $\langle \boldsymbol{X}^2(\Delta z)\rangle$ increases monotonically with Δz, and as shown in Figure 1 (middle) the curves then tend to overlap quickly, becoming approximately independent of Δz.

The behavior of the mean square displacement $\langle \boldsymbol{X}^2(z)\rangle$ can then be readily understood from the correlation function $C(\ell_\perp, \Delta z)$ (Figure 1). For small values of z, the integral in Equation (8) can be Taylor-expanded, and since $C(0, 0) = \langle b^2\rangle$, to the first order, we obtain $\langle \boldsymbol{X}^2(z)\rangle \approx z^2\langle b^2\rangle/B_0^2$. On the other hand, as soon as $\langle \boldsymbol{X}^2(z)\rangle^{1/2} \gtrsim \lambda_\perp$ exceeds the orthogonal correlation length $\lambda_\perp \sim 0.11$, the integral in Equation (8) remains approximately constant, because the largest contribution comes from $\ell_\perp < \lambda_\perp$, hence $\langle \boldsymbol{X}^2(z)\rangle \sim 4Dz$ diffuses linearly. The transition from the ballistic to the diffusive stage occurs for $\langle \boldsymbol{X}^2(z)\rangle \sim z^2\langle b^2\rangle/B_0^2 \sim \lambda_\perp^2$, i.e., for $z_D \sim \lambda_\perp B_0/\langle b^2\rangle^{1/2}$. In our case, since $\lambda_\perp \sim 0.11$, $B_0 = 10^3$, and $\langle b^2\rangle^{1/2} \sim 20$, the transition occurs at $z_D \approx 5.5$, as confirmed in Figure 1 (top).

We can estimate the diffusion coefficient D by using in Equation (9) the approximation for the mean square displacement outlined in the previous paragraph (i.e., $\langle \boldsymbol{X}^2(\Delta z)\rangle \approx \Delta z^2\langle b^2\rangle/B_0^2$ for $z \leqslant z_D$). The Lagrangian correlation along the field lines can then be approximated from Equations (9) and (11) with

$$\frac{\widetilde{C}(\Delta z)}{\langle b^2\rangle} = \begin{cases} 1 - \left(\dfrac{\Delta z}{z_D}\right)^{\alpha-1} & \text{for } \Delta z \leqslant z_D, \\ 0 & \text{for } \Delta z \geqslant z_D. \end{cases} \tag{12}$$

Substituting in Equation (8), and integrating it to obtain $\langle \boldsymbol{X}^2(z)\rangle$, the diffusion coefficient D is then given by

$$D \sim \frac{\alpha - 1}{2\alpha}\,\lambda_\perp \frac{\langle b^2\rangle^{1/2}}{B_0}, \tag{13}$$

a functional form characteristic of Bohm diffusion (Ghilea et al. 2011), with the coefficient $(\alpha - 1)/2\alpha$ ranging in the narrow interval $[1/5, 1/3]$ as $\alpha \in [5/3, 3]$. Since $\langle b^2\rangle^{1/2} \sim 20$, $B_0 = 10^3$, $\lambda_\perp \sim 0.11$, and $\alpha \sim 3$, we obtain $D \sim 7.3 \times 10^{-4}$, corresponding to $D \sim 2.9$ km in conventional units, compatible with $D \sim 3.1$ km computed from our simulation (Figure 1, top panel). The approximated Lagrangian correlation function $\widetilde{C}(\Delta z)$ (Equation (12)) with $\alpha = 3$ and $z_D \sim 5.5$ is shown in Figure 1 (bottom panel).

3.2. Current Sheet Connected Regions

The current density j is intermittently distributed in space, as is typical of turbulent systems. Its probability density function (pdf), shown in Figure 2, is not Gaussian and exhibits typical large tails where the current is strong, corresponding to current sheets in physical space. The noticeable skewness in Figure 2 results from the use of a single snapshot, and it is a fluctuation

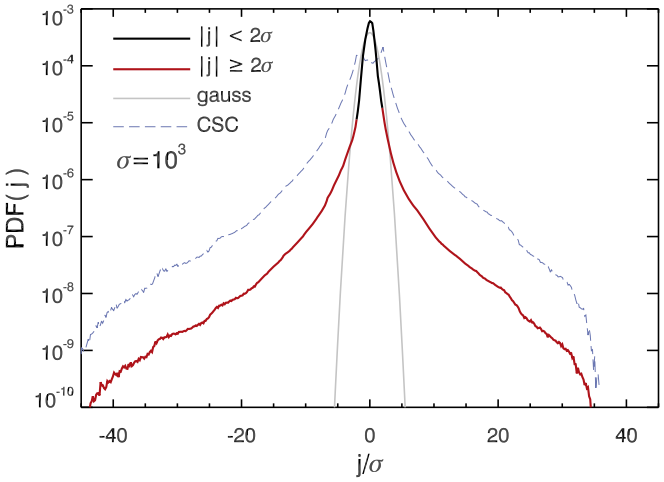


Figure 2. Probability density function (pdf) of current density. Current sheets are defined as the spatial regions, where $|j| \geqslant 2\sigma$, with $\sigma = \langle j^2\rangle^{1/2}$. For reference, we also plot the Gaussian distribution with the same standard deviation σ, and the pdf of j computed in the CSC region (dashed line).

that vanishes when averaging over several snapshots, i.e., the time-averaged distribution is symmetric.

We define as current sheets all those spatial regions where the current is larger than two standard deviations $|j| \geqslant 2\sigma$, with $\sigma = \langle j^2\rangle^{1/2}$, shown in yellow for the representative planes $z = 0$, $L/2$ and L in Figure 3.

The relationship between magnetic field topology and current sheets is then investigated by tracing field lines originating in current sheets. Specifically, field lines are traced from all the grid points where $|j| \geqslant 2\sigma$ in nine equispaced x–y planes (from $z = 0$ up to $z = L$, separated by $L/8$). For grid points that are not at the boundaries $z = 0$ or $z = L$ the respective field lines are traced both forward and backward with respect to the z-direction. We trace a total of 1,107,242 field lines, extending from the bottom to the top plate, and their intersection with the selected plane is shown as a black dot in Figure 3. Clearly, field lines are also present in the yellow regions, both those traced from there plus others originating from current sheets in different planes.

Current sheets are elongated in the guide field direction z, and the field lines traced from them form similarly shaped coherent structures, which we indicate as current sheet connected (CSC) regions. Although current sheets in reduced MHD have a complex structure with a cross-shear magnetic field component and mostly external X-points (Zhdankin et al. 2013; Wan et al. 2014), noticeably, the presence of a strong magnetic shear in correspondence of current sheets makes the FLRW strongly anisotropic, with field lines diffusing preferably along the in-plane sheet length and very little across it (Figure 3). Since diffusion increases with distance, its effects are most apparent in planes $z = 0$ and L.

The coherence and strong anisotropy of the CSC regions are in stark contrast with the homogeneity of the stochastic properties typically associated with FLRW, and their well-know tendency to fragment flux tubes (Matthaeus et al. 1995; Rappazzo et al. 2012; Servidio et al. 2014). Nevertheless, the mean square displacement $\langle \boldsymbol{X}^2(z)\rangle$ of the CSC field lines has properties similar to those of the entire ensemble, as shown in Figure 1 (top). The higher value of the diffusion coefficient $D_{\rm CSC}/D_{\rm All} \sim 1.2$ is due to the higher magnetic field intensity in

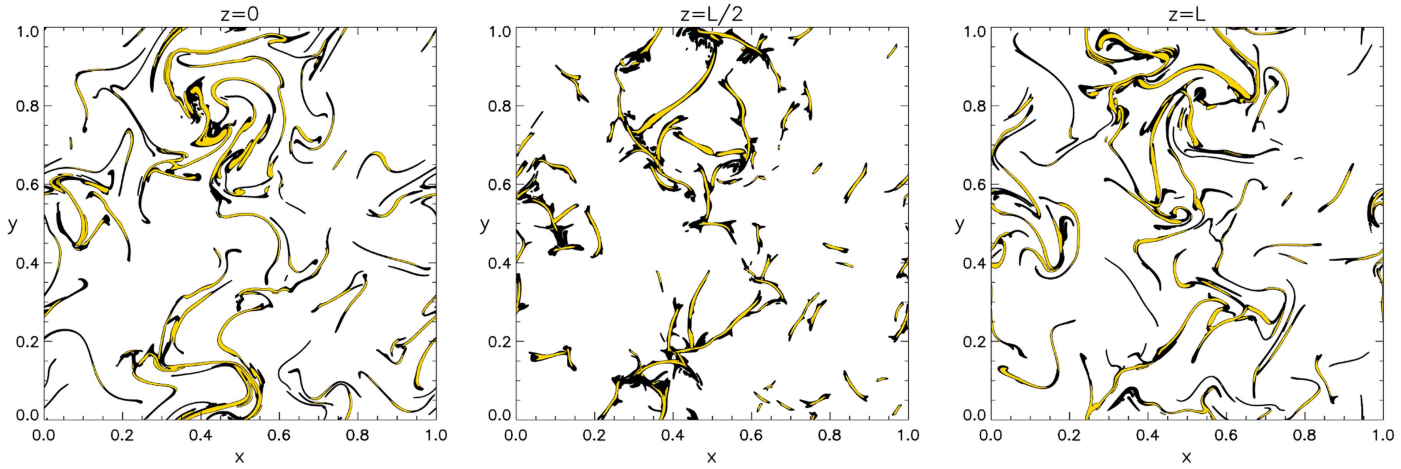


Figure 3. Current sheets (defined as those locations where $|j| \geqslant 2\langle j^2\rangle^{1/2}$) are shown in yellow in the left, middle, and right plates ($z = 0$, L/2, and L, with axial length L = 10). The locations where the field lines traced from current sheets in other planes cross the present plane outside the current sheet are drawn as black dots. Together both regions form the current sheet connected (CSC) region.

(An animation of this figure is available.)

the CSC region as $\langle b^2\rangle_{\rm CSC}^{1/2}/\langle b^2\rangle_{\rm All}^{1/2} \sim 1.2$ in agreement with Equation (13).

3.3. Pair Separation

To further understand the magnetic topology, we consider the separation of field line pairs. From Equation (3), their orthogonal separation in the x–y plane $\boldsymbol{\xi}(z) = \boldsymbol{x}_2(z) - \boldsymbol{x}_1(z)$, given the initial separation $\boldsymbol{\xi}(0) = \boldsymbol{\xi}_0$, is determined as a function of z by

$$\frac{d\boldsymbol{\xi}}{dz}(z) = \frac{1}{B_0}[\boldsymbol{b}(\boldsymbol{x}_2(z), z) - \boldsymbol{b}(\boldsymbol{x}_1(z), z)]. \tag{14}$$

Similarly to the single field line case, we obtain

$$\frac{d\langle\boldsymbol{\xi}^2(z)\rangle}{dz} = \frac{2}{B_0^2}\int_0^z dz'\langle[\boldsymbol{b}(\boldsymbol{x}_2(z'), z') - \boldsymbol{b}(\boldsymbol{x}_1(z'), z')] \cdot [\boldsymbol{b}(\boldsymbol{x}_2(z), z) - \boldsymbol{b}(\boldsymbol{x}_1(z), z)]\rangle, \tag{15}$$

which, following Ruffolo et al. (2004), can be written as

$$\frac{d}{dz}\langle\boldsymbol{\xi}^2(z)\rangle = \frac{4}{B_0^2}(I_{11} - I_{12}), \quad \text{where} \tag{16}$$

$$I_{11} = \int_0^z dz'\langle\boldsymbol{b}(\boldsymbol{x}_1(z'), z') \cdot \boldsymbol{b}(\boldsymbol{x}_1(z), z)\rangle, \tag{17}$$

$$I_{12} = \int_0^z dz'\langle\boldsymbol{b}(\boldsymbol{x}_1(z'), z') \cdot \boldsymbol{b}(\boldsymbol{x}_2(z), z)\rangle. \tag{18}$$

I_{11} is the same as the integral in Equation (4) because it refers to single field lines, therefore we already understand its behavior. However, I_{12} differs as it considers a pair.

As indicated by Batchelor (1950) for the hydrodynamic case, for sufficiently small z, the mean square separation will grow quadratically with z (see inset in Figure 4, left panel) and it will be proportional to the second-order structure function. Indeed, from Equation (16), Taylor-expanding Equations (17)–(18) in z, and since $C(0, 0) - C(\boldsymbol{\xi}_0, 0) = \langle\delta b_{\xi_0}^2\rangle/2$, we obtain

$$\frac{d}{dz}\langle\boldsymbol{\xi}^2(z)\rangle = 2z\,\frac{\langle\delta b_{\xi_0}^2\rangle}{B_0^2}, \text{ hence} \tag{19}$$

$$\langle\boldsymbol{\xi}^2(z)\rangle - \boldsymbol{\xi}_0^2 = z^2\,\frac{\langle\delta b_{\xi_0}^2\rangle}{B_0^2}, \tag{20}$$

where, as usual, $\xi_0 = |\boldsymbol{\xi}_0|$. Additionally, we can now approximate the second-order structure function as in Equation (11) with $\langle\delta b_{\xi_0}^2\rangle \sim 2\langle b^2\rangle(\xi_0/\lambda_\perp)^{\alpha-1}$ for $\xi_0 \leqslant \lambda_\perp$ and $\langle\delta b_{\xi_0}^2\rangle \sim 2\langle b^2\rangle$ for $\xi_0 \geqslant \lambda_\perp$, with the scaling relation being more accurate for values of ξ_0 in the inertial range. We can then write

$$\langle\boldsymbol{\xi}^2(z)\rangle - \boldsymbol{\xi}_0^2 \approx \begin{cases} \dfrac{2}{\lambda_\perp^{\alpha-1}}\dfrac{\langle b^2\rangle}{B_0^2}\,z^2\,\xi_0^{\alpha-1}, & \text{for } \xi_0 \leqslant \lambda_\perp \\ 2\dfrac{\langle b^2\rangle}{B_0^2}\,z^2, & \text{for } \xi_0 \geqslant \lambda_\perp \end{cases}, \tag{21}$$

with $\alpha \in [5/3, 3]$.

We plot $(\langle\boldsymbol{\xi}^2(z)\rangle - \boldsymbol{\xi}_0^2)/z^2$ in Figure 4 (right panel) as a function of ξ_0 for 11 values of $z \in [0, 2]$ separated by 0.2, almost perfectly overlapping and showing that, in the inertial range ($\xi_0 \lesssim 0.1$), it scales approximately as ξ_0^2, compatible with $\alpha \sim 3$ in our simulations, and saturates correctly to $\sim 2\langle b^2\rangle/B_0^2 \sim 8 \times 10^{-4}$ with our parameters ($\langle b^2\rangle \sim 400$, $B_0 = 10^3$, $\lambda_\perp \sim 0.11$). The small departure from ξ_0^2 in the inertial range shown in Figure 4 occurs because the second-order structure function $\langle\delta b_{\xi_0}^2/2\rangle = C(0, 0) - C(\xi_0, 0)$ considers zero separation in z and is calculated in the bottom boundary plane $z = 0$ (since the coefficients in the Taylor expansion in z of Equations (17)–(18) are calculated for $z = 0$). Indeed the 2D magnetic energy spectrum averaged over the whole box $E_{\ell_\perp} \propto \ell_\perp \delta b_{\ell_\perp} \sim \ell_\perp^3$, corresponding to $\delta b_{\ell_\perp} \sim \ell_\perp^2$, and the same behavior is observed for the spectra in all z-planes, except those in proximity of the boundaries $z = 0$ and L, where

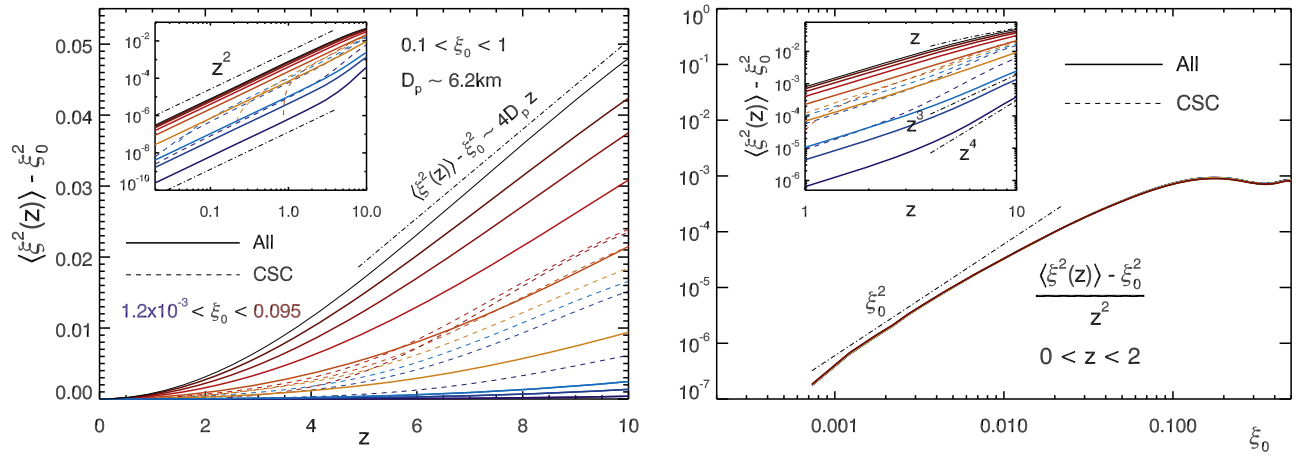


Figure 4. Left: the mean square separation of field line pairs is plotted against axial distance z for different initial separations ξ_0 (continuous lines consider the whole field line ensemble). Each red continuous line represents a bin of initial separation 0.01 wide centered at $\xi_0 = 0.015, 0.035, .., 0.095$. Since all curves with $0.1 < \xi_0 < 1$ overlap, we draw their average with a black continuous line. The three blue continuous lines represents bins with grid resolution width $dx = 1/2048$, centered at $\xi_0 = 2.5$, 6.5, and 10.5 dx corresponding to $\xi_0 = 1.2$, 3.2, and 5.2×10^{-3}. Insets in both panels show logarithmic plots of mean square separations, the right inset is a magnification of the left one showing the development of superdiffusion. Dashed lines show CSC field line separations with red and blue lines centered at the same bins as the corresponding curves for the all ensemble, and with bin width dx. The red line at $\xi_0 = 0.095$ is not drawn for the CSC case due to low statistics. Right: $(\langle\xi^2(z)\rangle - \xi_0^2)/z^2$ is plotted against ξ_0 for different values of $z \in [0, 2]$ showing that it scales approximately as ξ_0^2 in the inertial range.

line-tying boundary conditions are applied. At these boundaries, the velocity field is prescribed and therefore the dynamics does not follow the same equations as in the interior, with the effect of slightly modifying the magnetic energy spectrum for the planes in their close proximity. Nevertheless the scaling for the separation remains very close to a $\propto \xi_0^2$ scaling, departing strongly in the inertial range from $\xi_0^{2/3}$ expected for a standard Kolmogorov spectrum with $\alpha = 5/3$ (Batchelor 1950; Bourgoin et al. 2006). Therefore, the ratio of mean square separations for field lines with relatively larger initial separations $\xi_0' > \xi_0$ are increasingly bigger for steeper spectral indices, indeed from Equation (21) the ratio of their separations in the ballistic range ($\propto z^2$) grows like $(\xi_0'/\xi_0)^{\alpha-1}$.

In general, as $\xi_0 \to 0$ the two field lines tend to the same field line, i.e., $\boldsymbol{x}_2(z) \to \boldsymbol{x}_1(z)$, consequently $I_{12} \to I_{11}$, and the mean square separation vanishes in this limit. On the other hand, the mean square separation in I_{12}, i.e., $\xi_{12}(z', z) = \langle[\boldsymbol{x}_2(z') - \boldsymbol{x}_1(z)]^2\rangle^{1/2}$ is always larger than ξ_0. For initial separations larger than $\lambda_\perp$, the correlation is small $\forall z \in [0, L]$ so that $I_{12} \approx 0$. In this case, the diffusion coefficient for pair separation is double that of single field line diffusion, i.e., $\langle\boldsymbol{\xi}^2(z)\rangle - \boldsymbol{\xi}_0^2 = 4D_p z$ with $D_p = 2D$, as shown in Figure 4 (left panel) for $0.1 < \xi_0 < 1$ by the continuous black line (we average these curves since they overlap). For any $\xi_0 < \lambda_\perp$, there is always a critical height $z_D(\xi_0)$ above which the mean separation between the two field lines in I_{12} is larger than $\lambda_\perp$. Hence, the increasingly larger negative contribution of the I_{12} term to mean square pair separation will display diffusion at progressively lower heights, with a smaller total diffusion coefficients $D \leqslant D_p \leqslant 2D$, as shown in Figure 4 by the red lines, that consider five bins with $\xi_0 \in [0.015, 0.095]$ with $\Delta\xi_0 = 0.02$. Clearly, for sufficiently small initial separations, field lines will not be able to display diffusion because our system is bounded in the axial direction $z$to maximum length L and separation cannot grow up to the perpendicular correlation length, as shown well by the blue continuous lines in Figure 4.

A ballistic stage $\propto z^2$ is always present initially for $z \lesssim 3$, as shown in Figure 4 (insets), but field lines with initial separation within the dissipative range ($\xi_0 \lesssim 10\,dx$, where $dx = 1/nx = 1/2048$ is the numerical grid step size) exhibit subsequently a Richardson-like superdiffusive stage (Beresnyak 2013; Eyink et al. 2013; Servidio et al. 2016) with a mean square separation up to $\propto z^4$ (blue continuous lines in Figure 4, with, respectively, $\xi_0 = 2.5$, 6.5, and $10.5\,dx$), while for larger separations they transition to the diffusive regime.

Even though FLRW in CSC regions is strongly anisotropic, CSC field line pair separations (shown in Figure 4 with dashed lines) exhibit similar properties to the whole ensemble (shown with continuous lines, the color code is the same for both line types). Their statistics are degraded for larger ξ_0 because in CSC regions the number of field line couples diminishes at larger separations so that the averages do not saturate yet to their ensemble value. This can be seen in the left inset, where the red dashed curves become negative, because the relation $\langle\boldsymbol{\xi}^2(z)\rangle - \boldsymbol{\xi}_0^2 = \langle(\boldsymbol{\xi}(z) - \boldsymbol{\xi}_0)^2\rangle \geqslant 0$ is valid only for a sufficiently high number of field lines, when $\langle\boldsymbol{\xi}(z)\rangle = \boldsymbol{\xi}_0$.

The main difference between CSC pair separations and the whole ensemble is that for the same initial separation ξ_0, the CSC field lines exhibit higher separations. Similarly to mean square displacement (Figure 1, top panel) the higher values are due to the greater magnetic field intensity in CSC regions ($\langle b^2\rangle_{\rm CSC}/\langle b^2\rangle \sim 1.5$), and indeed the separation in the ballistic range is proportional to $\langle b^2\rangle$ (Equation (21)). Notice that the coefficient in Equation (21) also includes the perpendicular correlation length $\lambda_\perp$ that is not readily computable in the non-Cartesian CSC region, but, from the data, we can estimate that the separation for field lines with the same initial separation is about 10 times larger in CSC regions than for the whole ensemble. As mentioned previously, the statistics are degraded for CSC field lines with larger initial separations. Therefore, while the larger separations for CSC field lines is very well demonstrated for smaller initial separations (blue dashed lines, and first red dashed line), we cannot yet fully verify this conclusion for larger initial separations because the averages

have not yet saturated to their ensemble values (this point will be further investigated in upcoming work).

4. Conclusions and Discussion

To gain insight into particle acceleration and heat transport in coronal loops, solar wind, and more in general for plasmas in the reduced MHD regime, we have investigated the magnetic topology of field lines originating from current sheets. We have found that they form coherent structures, dubbed CSC regions, similarly to the current sheets they originate from. Field lines in these regions perform highly anisotropic FLRW, with diffusion occurring preferentially along the current sheet in-plane length. Nevertheless, FLRW and diffusion coefficients have similar properties for CSC field lines and the whole ensemble, with larger displacement and separations occurring in CSC regions where the magnetic field intensity is higher.

This emerging picture has strong implications for particle acceleration and heat transport, particularly in the low corona, where all protons and electrons with temperatures below 10^6 K have gyroradii smaller than the current sheet thickness. It indeed implies that, in coronal loops, particle and heat are transported almost exclusively within the CSC region, a small volume of plasma around current sheets with a small filling factor, while most of the volume is topologically disconnected from current sheets and the associated flow of particles and heat.

This picture is fully consistent with observations (Warren et al. 2008; Klimchuk 2009; Ugarte-Urra et al. 2009; Schmelz et al. 2010) and recent thermodynamical 3D simulations (Dahlburg et al. 2012, 2016) strongly suggesting that coronal loops cannot be modeled with single isothermal flux tubes, because their radiative properties can only be explained by the presence of both hot and cold plasmas at observational sub-resolution scales (multi-temperature loops). Also, the complex topology in CSC regions, with enhanced magnetic field line displacements and separations, points to a complex stochastic nature for the heating function along the field lines.

Additionally, the structure of the CSC regions in the top and bottom plates $z = 0$ and L is consistent with that of so-called moss, the spongy reticulated pattern in X-rays and EUV formed at the coronal base of hot loops, confirming that the FLRW can play a strong role in the formation of these structures as was recently proposed (Kittinaradorn et al. 2009).

The reduced MHD FLRW properties and topology strongly support the results of recent test-particle simulations (Dalena et al. 2014) with initial gyroradii smaller than current sheet widths propagated in similar magnetic fields to those discussed here. Particles are at first strongly accelerated along the z-direction in current sheets by the strong electric field associated with the current, until they pitch-angle scatter, thus increasing their gyroradii. Subsequently, as long as the gyroradius is smaller than the orthogonal correlation length, those that remain close to the CSC region are accelerated by a (non-magnetic moment conserving) betatron-like mechanism due to the inhomogeneous $\boldsymbol{u} \times B_0\hat{\boldsymbol{z}}$ electric field associated with outflows in current sheets.

For parameters typical of hot solar coronal loops we have found that the parallel correlation length is longer than the loop length, and our results consider this specific case. Nevertheless, they may also apply to the unbounded (e.g., periodic) case, which we plan to investigate thoroughly in upcoming work. In general, we expect the current sheet length along z to be strongly correlated with the magnetic field parallel correlation length $\lambda_\parallel$. Therefore, we expect that CSC regions connected to any such current sheet of length $\sim\lambda_\parallel$ to have a similar structure to those found here around the current sheet. However, as field lines are traced further away at distances larger than $\lambda_\parallel$, we expect the CSC region to fragment and the associated FLRW to lose anisotropy and acquire more homogeneous properties, i.e., the CSC field lines will at that point connect and diffuse isotropically throughout the volume (hence mostly in regions with low currents).

Therefore, in unbounded systems, we expect heat and accelerated particles to be initially confined to CSC regions around current sheets (of length $\sim\lambda_\parallel$), but further away heat and particles would distribute more uniformly throughout the plasma. This picture is strongly consistent with recent analyses of solar wind data (Osman et al. 2012), where temperature is found to peak in regions with high magnetic field gradients, while it rapidly descends to approach the ambient solar wind temperature as the distance from those regions increases.

Resources supporting this work were provided by the NASA High-End Computing (HEC) Program through the NASA Advanced Supercomputing (NAS) Division at the Ames Research Center. This work was partially supported by NASA through Grand Challenge Research grant NNX15AB88G, Living with a Star grant NNX14AI63G, as well as the Solar Probe Plus Observatory Scientist grant, and by the Thailand Research Fund (grant RTA5980003).

References

Batchelor, G. K. 1950, QJRMS, 76, 133
Beresnyak, A. 2013, ApJL, 767, L39
Bhattacharjee, A., Huang, Y.-M., Yang, H., & Rogers, B. 2009, PhPl, 16, 112102
Biskamp, D. 1986, PhFl, 29, 1520
Biskamp, D. 2003, Magnetohydrodynamic Turbulence (Cambridge: Cambridge Univ. Press)
Bourgoin, M., Ouellette, N. T., Xu, H., Berg, J., & Bodenschatz, E. 2006, Sci, 311, 835
Brachet, M. E., Bustamante, M. D., Krstulovic, G., et al. 2013, PhRvE, 87, 013110
Bulanov, S. V., Syrovatskii, S. I., & Sakai, J. 1978, ZhPmR, 28, 193
Dahlburg, R. B., Einaudi, G., Rappazzo, A. F., & Velli, M. 2012, A&A, 544, L20
Dahlburg, R. B., Einaudi, G., Taylor, B. D., et al. 2016, ApJ, 817, 47
Dalena, S., Rappazzo, A. F., Dmitruk, P., Greco, A., & Matthaeus, W. H. 2014, ApJ, 783, 143
Dmitruk, P., & Gómez, D. O. 1997, ApJL, 484, L83
Dmitruk, P., & Gómez, D. O. 1999, ApJL, 527, L63
Dmitruk, P., Gómez, D. O., & DeLuca, E. E. 1998, ApJ, 505, 974
Dmitruk, P., Gómez, D. O., & Matthaeus, W. H. 2003, PhPl, 10, 3584
Dmitruk, P., Matthaeus, W. H., & Oughton, S. 2005, PhPl, 12, 112304
Drake, J. F., Shay, M. A., Thongthai, W., & Swisdak, M. 2005, PhRvL, 94, 095001
Einaudi, G., Velli, M., Politano, H., & Pouquet, A. 1996, ApJL, 457, L113
Eyink, G., Vishniac, E., Lalescu, C., et al. 2013, Natur, 497, 466
Frisch, U., Matsumoto, T., & Bec, J. 2003, JSP, 113, 761
Ghilea, M. C., Ruffolo, D., Chuychai, P., et al. 2011, ApJ, 741, 16
Jokipii, J. R. 1973, ApJ, 183, 1029
Jokipii, J. R., & Kota, J. 1989, GeoRL, 16, 1
Jokipii, J. R., & Parker, E. N. 1968, PhRvL, 21, 44
Kadomtsev, B. B., & Pogutse, O. P. 1974, JETP, 38, 283
Karimabadi, H., Roytershteyn, V., Wan, M., et al. 2013, PhPl, 20, 012303
Kittinaradorn, R., Ruffolo, D., & Matthaeus, W. H. 2009, ApJL, 702, L138
Klimchuk, J. A. 2006, SoPh, 234, 41
Klimchuk, J. A. 2009, in ASP Conf. Ser. 415, The Second Hinode Science Meeting: Beyond Discovery-Toward Understanding, ed. B. Lites et al. (San Francisco, CA: ASP), 221
Krstulovic, G., Brachet, M.-E., & Pouquet, A. 2011, PhRvE, 84, 016410

Landi, S., Del Zanna, L., Papini, E., Pucci, F., & Velli, M. 2015, ApJ, 806, 131
Lapenta, G. 2008, PhRvL, 100, 235001
Liu, Y. H., Kistler, L. M., Mouikis, C. G., Roytershteyn, V., & Karimabadi, H. 2014, GeoRL, 41, 4819
Loureiro, N. F., Schekochihin, A. A., & Cowley, S. C. 2007, PhPl, 14, 100703
Matthaeus, W. H., Cothran, C. D., Landreman, M., & Brown, M. R. 2005, GeoRL, 32, L23104
Matthaeus, W. H., Gray, P. C., Pontius, J. D. H., & Bieber, J. W. 1995, PhRvL, 75, 2136
Montgomery, D. 1982, PhST, 2, 83
Mozer, F. S., Bale, S. D., & Phan, T. D. 2002, PhRvL, 89, 015002
Osman, K. T., Matthaeus, W. H., Wan, M., & Rappazzo, A. F. 2012, PhRvL, 108, 261102
Parker, E. N. 1972, ApJ, 174, 499
Parker, E. N. 1988, ApJ, 330, 474
Parker, E. N. 1994, Spontaneous Current Sheets in Magnetic Fields (New York: Oxford Univ. Press)
Phan, T. D., Drake, J. F., Shay, M. A., Mozer, F. S., & Eastwood, J. P. 2007, PhRvL, 99, 255002
Pucci, F., Malara, F., Perri, S., et al. 2016, MNRAS, 459, 3395
Pucci, F., & Velli, M. 2014, ApJL, 780, L19
Pucci, F., Velli, M., & Tenerani, A. 2017, arXiv:1704.08793
Rappazzo, A. F. 2015, ApJ, 815, 8
Rappazzo, A. F., Matthaeus, W. H., Ruffolo, D., Servidio, S., & Velli, M. 2012, ApJL, 758, L14
Rappazzo, A. F., & Parker, E. N. 2013, ApJL, 773, L2
Rappazzo, A. F., & Velli, M. 2011, PhRvE, 83, 065401
Rappazzo, A. F., Velli, M., Einaudi, G., & Dahlburg, R. B. 2007, ApJL, 657, L47
Rappazzo, A. F., Velli, M., Einaudi, G., & Dahlburg, R. B. 2008, ApJ, 677, 1348
Reale, F. 2014, LRSP, 11, 4
Retinò, A., Sundkvist, D., Vaivads, A., et al. 2007, NatPh, 3, 236
Ruffolo, D., Matthaeus, W. H., & Chuychai, P. 2004, ApJ, 614, 420
Runov, A., Nakamura, R., & Baumjohann, W. 2006, AdSpR, 38, 85
Runov, A., Sergeev, V. A., Baumjohann, W., et al. 2005, AnGeo, 23, 1391
Runov, A., Sergeev, V. A., Nakamura, R., et al. 2006, AnGeo, 24, 247
Schmelz, J. T., Saar, S. H., Nasraoui, K., et al. 2010, ApJ, 723, 1180
Servidio, S., Haynes, C. T., Matthaeus, W. H., et al. 2016, PhRvL, 117, 095101
Servidio, S., Matthaeus, W. H., Wan, M., et al. 2014, ApJ, 785, 56
Snodin, A. P., Ruffolo, D., Oughton, S., Servidio, S., & Matthaeus, W. H. 2013, ApJ, 779, 56
Sonnerup, B. U. Ö 1979, in Magnetic Field Reconnection, ed. L. J. Lanzerotti, C. F. Kennel, & E. N. Parker (Vol. 3; Amsterdam: North-Holland Publishing Co.), 45
Strauss, H. R. 1976, PhFl, 19, 134
Sulem, C., Sulem, P.-L., & Frisch, H. 1983, JCoPh, 50, 138
Swann, W. F. 1933, PhRv, 43, 217
Tenerani, A., Rappazzo, A. F., Velli, M., & Pucci, F. 2015, ApJ, 801, 145
Ugarte-Urra, I., Warren, H. P., & Brooks, D. H. 2009, ApJ, 695, 642
Wan, M., Rappazzo, A. F., Matthaeus, W. H., Servidio, S., & Oughton, S. 2014, ApJ, 797, 63
Warren, H. P., Ugarte-Urra, I., Doschek, G. A., Brooks, D. H., & Williams, D. R. 2008, ApJL, 686, L131
Wu, P., Shay, M. A., Phan, T. D., Oieroset, M., & Oka, M. 2011, PhPl, 18, 111204
Xiao, C. J., Pu, Z. Y., Wang, X. G., et al. 2007, GeoRL, 34, 1101
Yamada, M., Ren, Y., Ji, H., et al. 2006, PhPl, 13, 052119
Zank, G. P., & Matthaeus, W. H. 1992, JPlPh, 48, 85
Zhdankin, V., Uzdensky, D. A., Perez, J. C., & Boldyrev, S. 2013, ApJ, 771, 124
Zimbardo, G., Veltri, P., & Pommois, P. 2000, PhRvE, 61, 1940

The Astrophysical Journal, 845:113 (11pp), 2017 August 20 https://doi.org/10.3847/1538-4357/aa7f2c
© 2017. The American Astronomical Society. All rights reserved.

Effects of a Guide Field on the Larmor Electric Field and Upstream Electron Temperature Anisotropy in Collisionless Asymmetric Magnetic Reconnection

Surapat Ek-In[1], Kittipat Malakit[2,1], David Ruffolo[1], Michael A. Shay[3], and Paul A. Cassak[4]
[1] Department of Physics, Faculty of Science, Mahidol University, Bangkok, Thailand
[2] Department of Physics, Faculty of Science and Techonology, Thammasat University, Pathum Thani, Thailand; kmalakit@gmail.com
[3] Department of Physics and Astronomy, University of Delaware, Newark, DE, USA
[4] Department of Physics and Astronomy, West Virginia University, Morgantown, WV, USA
Received 2017 April 11; revised 2017 June 11; accepted 2017 July 5; published 2017 August 17

Abstract

We perform the first study of the properties of the Larmor electric field (LEF) in collisionless asymmetric magnetic reconnection in the presence of an out-of-plane (guide) magnetic field for different sets of representative upstream parameters at Earth's dayside magnetopause with an ion temperature greater than the electron temperature (the ion-to-electron temperature ratio fixed at 2) using two-dimensional particle-in-cell simulations. We show that the LEF does persist in the presence of a guide field. We study how the LEF thickness and strength change as a function of guide field and the magnetospheric temperature and reconnecting magnetic field strength. We find that the thickness of the LEF structure decreases, while its magnitude increases when a guide field is added to the reconnecting magnetic field. The added guide field makes the Larmor radius smaller, so the scaling with the magnetospheric ion Larmor radius is similar to that reported for the case without a guide field. Note, however, that the physics causing the LEF is not well understood, so future work in other parameter regimes is needed to fully predict the LEF for arbitrary conditions. We also find that a previously reported upstream electron temperature anisotropy arises in the vicinity of the LEF region both with and without a guide field. We argue that the generation of the anisotropy is linked to the existence of the LEF. The LEF can be used in combination with the electron temperature anisotropy as a signature to effectively identify dayside reconnection sites in observations.

Key words: magnetic reconnection – methods: numerical – plasmas – solar–terrestrial relations

1. Introduction

Magnetic reconnection is an important plasma process that converts the energy stored in magnetic fields into heat and kinetic energy. It plays a crucial role in many magnetized plasma systems, such as governing the dynamics of Earth's magnetospheric plasma system and rearranging the coronal magnetic field configuration and releasing energy in the form of solar and stellar flares and coronal mass ejections. Reconnection occurs in a diffusion region in which the plasma is no longer ideal. Understanding the physics of the diffusion region of collisionless reconnection, containing both an ion diffusion region and a smaller electron diffusion region, is therefore a key to understanding reconnection as a whole. The physics of the diffusion region, especially the electron diffusion region, is considered sufficiently important that the *Magnetospheric Multiscale* (*MMS*) mission (Burch et al. 2015) is mainly dedicated to studying it in the Earth's magnetosphere.

An issue for high-resolution instruments such as those on the *MMS* is that they can produce data at a rate that exceeds the available downlink capacity. Therefore, only promising time intervals are selected for full downlink (Burch & Drake 2009; Burch et al. 2015). To aid the real-time selection process, signatures for the diffusion region and its surroundings are crucial.

Based on a particle-in-cell (PIC) simulation study of anti-parallel asymmetric reconnection, a new in-plane electric field structure called the Larmor electric field (LEF) was identified (Malakit et al. 2013). The LEF is adjacent to the in-plane "Hall electric field" structure dominated by the $\boldsymbol{J} \times \boldsymbol{B}/(n_e ec)$ term in the generalized Ohm's law, where n_e is the electron density, e is the proton charge, $\boldsymbol{J}$ is the current density and $\boldsymbol{B}$ is the magnetic field. Note that in this manuscript, by "Hall electric field," we mean the very strong sunward-pointing electric field during asymmetric magnetic reconnection at the Earth's magnetopause (André et al. 2004; Vaivads et al. 2004; Mozer et al. 2008; Tanaka et al. 2008). At the magnetopause, this electric field is located in the area of strong out-of-plane current on the magnetospheric side of the x-line. In contrast, the LEF points away from the X-line, or Earthward, and is farther into the magnetosphere than the Hall electric field. It was proposed that the LEF could possibly be used as a signature for the region immediately upstream on the magnetospheric side of the ion diffusion region of dayside reconnection (Malakit et al. 2013). Its presence at a dayside reconnection site has been reported using *Polar* observations by Koga et al. (2014).

Currently, the mechanism of LEF generation is not completely understood. Malakit et al. (2013) argued that the electric field appears to "hold back" hot magnetospheric ions as they cross the stagnation point. This implies that magnetospheric ions play a role in governing the width and the magnitude of the LEF, which was consistent with the PIC simulations for the parameter range studied. Alternately, Shay et al. (2016) and Phan et al. (2016) recently showed using simulation and observation that the inflowing magnetosheath ions can overshoot the diffusion region and enter the magnetosphere. Their bulk flow through the magnetospheric reconnecting field produces a drift out of the reconnection plane, contributing an electric field to the LEF through the ion convection term. Magnetosheath ions penetrating into the magnetosphere and drifting out of the plane near a reconnection site were recently reported in THEMIS observations (Phan et al. 2016). Thus, there remain open questions about the physical cause of the LEF for arbitrary upstream conditions;

Table 1
Upstream Parameters and Key Results of the Simulations in this Study

Run	$B_{\mathrm{rec},1}$	$B_{\mathrm{rec},2}$	n_1	n_2	B_g	$T_{e,1}$	$T_{i,1}$	$T_{e,2}$	$T_{i,2}$	m_i/m_e	$\delta_{E,\mathrm{Larmor}}$	E_{Larmor}	$\delta_{e,\mathrm{Anisotropy}}$
1*A*	1.0	2.0	1.0	0.1	0.0	0.67	1.33	1.67	3.33	25	3.5	1.15	4.0
1*A**	1.0	2.0	1.0	0.1	0.0	0.67	1.33	1.67	3.33	100	4.0	1.15	4.0
1*B*	1.0	2.0	1.0	0.1	0.5	0.67	1.33	1.67	3.33	25	4.0	1.08	3.0
1*C*	1.0	2.0	1.0	0.1	1.0	0.67	1.33	1.67	3.33	25	3.0	1.33	3.0
1*D*	1.0	2.0	1.0	0.1	2.0	0.67	1.33	1.67	3.33	25	2.0	2.33	2.0
2*A*	1.0	1.5	1.0	0.1	0.0	0.67	1.33	4.59	9.16	25	5.0	1.52	4.0
2*B*	1.0	1.5	1.0	0.1	0.5	0.67	1.33	4.59	9.16	25	5.0	1.47	4.0
2*C*	1.0	1.5	1.0	0.1	1.0	0.67	1.33	4.59	9.16	25	4.5	1.92	3.0
2*D*	1.0	1.5	1.0	0.1	2.0	0.67	1.33	4.59	9.16	25	2.5	2.43	2.0
3*A*	1.0	1.0	1.0	0.1	0.0	0.67	1.33	6.67	13.33	25	8.0	1.16	7.5
3*B*	1.0	1.0	1.0	0.1	0.5	0.67	1.33	6.67	13.33	25	7.5	1.39	5.0
3*C*	1.0	1.0	1.0	0.1	1.0	0.67	1.33	6.67	13.33	25	5.0	2.33	2.5
3*D*	1.0	1.0	1.0	0.1	2.0	0.67	1.33	6.67	13.33	25	3.0	3.20	1.5

both mechanisms can likely be active for various upstream conditions.

Malakit et al. (2013) varied the reconnecting magnetic field strengths, magnetospheric density, and magnetospheric temperature, but treated only anti-parallel reconnection and held the upstream ion-to-electron temperature T_i/T_e fixed at 2, so it only treated a limited region of parameter space. At the dayside magnetopause, reconnection is not always anti-parallel (Paschmann et al. 1986; Scurry et al. 1994; Phan et al. 1996; Burch & Phan 2016; Cassak & Fuselier 2016; Eriksson et al. 2016a, 2016b). Therefore, it is important to understand how the LEF is affected when there is a guide field, i.e., a magnetic field parallel to the X-line and perpendicular to the reconnection plane. Whether the LEF persists and whether it can still be a useful signature when there is a guide field has not yet been determined.

We perform an initial parametric study of the effect of a guide field on reconnection, retaining the assumption that $T_i/T_e = 2$ except where otherwise noted. We show in this study that the LEF structure can still exist in the presence of a guide field. By examining how the width of the LEF varies with upstream parameters, we find that the width of the LEF is linked to the ion Larmor radius. Moreover, the stronger the guide field and smaller the ion Larmor radius, the more localized the LEF structure and the stronger the LEF magnitude. We further find that the electron temperature anisotropy and associated parallel electric field in the upstream region, discussed by Egedal et al. (2011), is present in a similar region as the LEF both with and without a guide field. We argue that this parallel electric field is related to the physics of the LEF, being generated partly by ion pressure gradients and partly by ion inertia terms from magnetosheath ions crossing to the magnetosphere. We conclude that the LEF and electron temperature anisotropy can be used in combination as a stronger signature for dayside reconnection than using the LEF alone.

The simulation setup is discussed in Section 2. Section 3 shows that the LEF exists with a guide field and investigates its scaling on upstream parameters. The coincidence of the LEF and electron temperature anisotropy is discussed in Section 4. Some new insights on the physical mechanism causing the existence of the LEF are discussed in Section 5, including simulations with T_i/T_e different than 2 that underscore the importance of studying the LEF in other parameter regimes. Section 6 has a brief conclusion.

2. Simulation

We use the PIC code P3D (Zeiler et al. 2002) to perform simulations in 2.5 dimensions of collisionless asymmetric reconnection with sets of inflow parameters representing dayside reconnection and with different guide field strengths and magnetosphere-to-magnetosheath reconnecting magnetic field strength ratios. The guide field is modeled as uniform throughout the simulation region.

In the simulations, magnetic field strengths and particle number densities are normalized to arbitrary values B_0 and n_0, respectively. Lengths are normalized to the ion inertial length $d_{i0} = c/\omega_{pi}$ at the reference density. Time is normalized to the ion cyclotron time $\Omega_{ci0}^{-1} = (eB_0/m_ic)^{-1}$. Speeds are normalized to the Alfvén speed $c_{A0} = B_0/(4\pi m_i n_0)^{1/2}$. Electric fields and temperatures are normalized to $E_0 = c_{A0}B_0/c$ and $T_0 = m_i c_{A0}^2/k_{\mathrm{B}}$, respectively.

Each simulation is performed in a periodic domain of size $L_x \times L_y = 204.8 \times 102.4$. The grid size $\Delta x = \Delta y$ is 0.05. The time step Δt is 0.005. The number of particles per grid cell, *ppg*, which represents the normalized particle density n_0, is 200. The ion to electron mass ratio m_i/m_e is 25 except where noted. The speed of light c is 15. The initial conditions represent two current sheets. A small perturbation in the magnetic field is used to initiate the reconnection. Before analyzing the results, the simulations are allowed to evolve until they reach a quasi-steady state, in which the reconnection rate is nearly constant. See Malakit et al. (2010) for more details on the simulation procedures.

We use three sets of upstream parameters in our simulations. For all three sets, the ratio of the density from the two inflow sides n_2/n_1 is 0.1, where the 1 and 2 subscripts denote the magnetosheath and magnetospheric sides, respectively. However, the in-plane upstream magnetic field ratio $B_{\mathrm{rec},2}/B_{\mathrm{rec},1}$ is varied as 1.0, 1.5, or 2.0, with the stronger field on the same side as the lower density. These asymmetries in the density and magnetic field reasonably represent the typical range of dayside magnetospheric reconnection parameters (Phan & Paschmann 1996; Mozer et al. 2008; Tanaka et al. 2008). For each set, the magnitude of the guide field is varied as 0.0, 0.5, 1.0, or 2.0. We fix $T_i/T_e = 2$ on both sides since $T_i > T_e$ for magnetopause applications. The initial upstream parameters on side 1 and 2—magnetic field, density, ion temperature, and electron temperature—and key results are shown in Table 1.

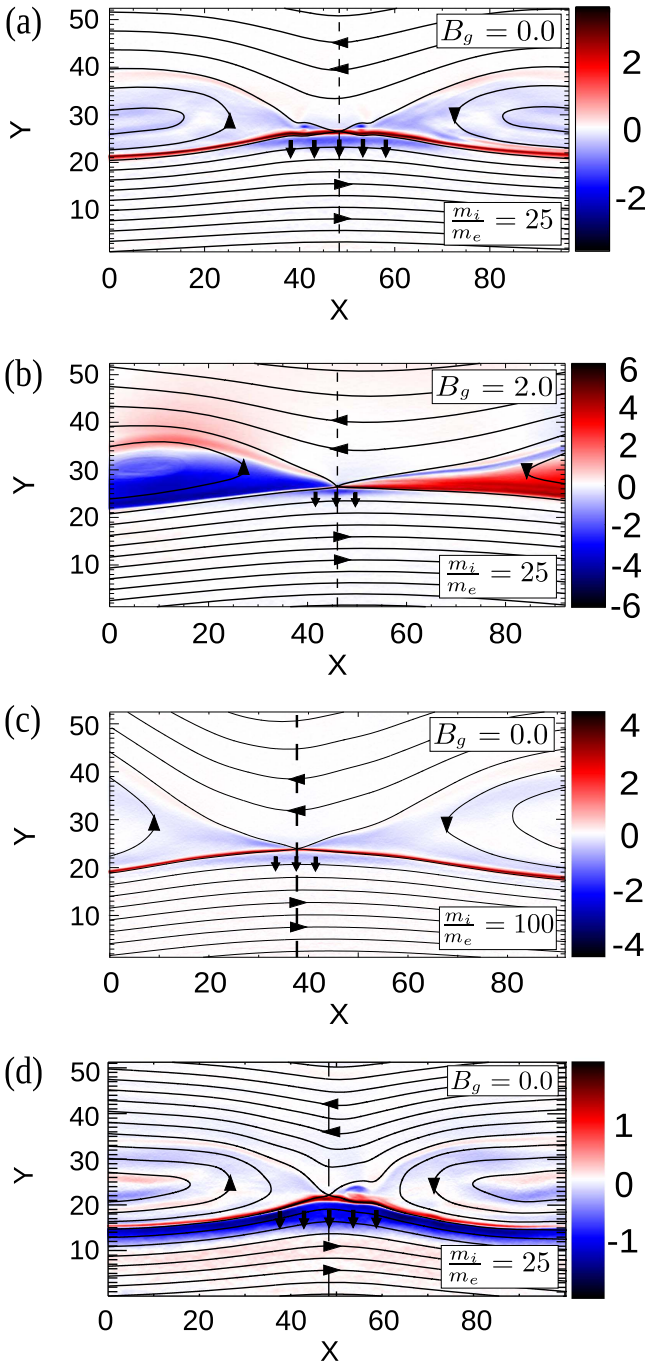


Figure 1. Two-dimensional plots of the electric field in the vertical direction E_y for the cases of (a) zero guide field (Run 1A), (b) non-zero guide field $B_g = 2.0$ (Run 1D), and (c) zero guide field with a different mass ratio $m_i/m_e = 100$ (Run 1A*). Note that (a)–(c) share the same set of upstream parameters ($B_{\rm rec,1} = 1$, $B_{\rm rec,2} = 2$, $n_1 = 1$, $n_2 = 0.1$) that can be considered typical for magnetopause reconnection. (d) is also a case of zero guide field, but with another set of typical magnetopause reconnection parameters ($B_{\rm rec,1} = 1$, $B_{\rm rec,2} = 1$, $n_1 = 1$, $n_2 = 0.1$) (Run 3A). The blue region below the X-line represents the LEF region with arrows pointing downward to indicate the LEF direction. The black lines represent magnetic field lines with arrow heads indicating the magnetic field direction. The dashed line shows a vertical cut through the X-line. (The data for all three different sets of parameter values ($B_{\rm rec,1}$, $B_{\rm rec,2}$, n_1, n_2) and four different guide field values B_g are provided in the Appendix.)

3. Larmor Electric Field and its Guide Field Dependence

We first demonstrate that the LEF exists in the presence of a guide field. Figures 1(a) and (b) show the in-plane electric field E_y in Run 1A and 1D, respectively. The only difference between these simulations is that the latter has a guide field of 2, while the former is anti-parallel. For the case with no guide field, the Hall electric field structure is the red region close to the magnetospheric separatrix in panel (a), and the LEF is the blue region with arrows pointing down below the X-line. Panel (b) reveals that there is an analogous downward-pointing in-plane electric field in the guide field case, denoted by the arrows. Therefore, the simulations confirm the LEF structure is still present but more localized in systems with a guide field.

We now determine how properties of the LEF depend on upstream parameters in the presence of a guide field. Two key properties of the LEF are its thickness $\delta_{E,\rm Larmor}$ and its magnitude $E_{\rm Larmor}$ (Malakit et al. 2013). Consider Figure 2, which shows 1D cuts along the vertical dashed line through the X-lines in Figure 1, to see how the LEF thickness $\delta_{E,\rm Larmor}$ and the LEF magnitude $E_{\rm Larmor}$ are measured. On the magnetospheric side (left side) of the X-line, there is a bipolar structure of the Hall electric field (positive) and the LEF (negative). The magnitude $E_{\rm Larmor}$ is measured from the peak value of the LEF indicated by the horizontal dashed line. The thickness $\delta_{E,\rm Larmor}$ is measured as the distance between the two vertical dotted lines. The dotted line on the right, located where E_y switches signs, marks the border between the Hall and the LEF structure. The dotted line on the left, located where E_y becomes zero again, marks the other end of the LEF structure.

We find that the structure of the LEF is modified in the presence of a guide field and that the degree of modification depends on the strength of the guide field. When there is a non-zero guide field, the LEF becomes more localized. We can see that in comparisons between Figure 1(a) for zero guide field and 1(b) for a guide field of 2. The LEF structure (the blue area below the X-line) spans a smaller area compared with its counterpart in Figure 1(a). Thus, we expect the LEF would be more difficult to detect with satellites as the guide field increases. At the same time, the LEF, if observed, ensures closer proximity to the X-line and the ion diffusion region.

While the thickness of the LEF structure becomes smaller when the guide field strength increases, the magnitude of the LEF does the opposite: the stronger the guide field, the larger the magnitude of the LEF. Comparing Figure 2(a), where there is no guide field (Run 1A), to Figure 2(b), where there is a guide field of 2 (Run 1D), one observes the increase in magnitude of $E_{\rm Larmor}$ (the negative peak of E_y) from about 1.2 to 2.3 as well as the decrease in the thickness of the LEF $\delta_{E,\rm Larmor}$ from about 3.5 to 2.

To study the factors affecting the width and strength of the LEF, in Figure 3 we plot $\delta_{E,\rm Larmor}$ and $E_{\rm Larmor}$ versus the upstream parameters that are changed in this study: $B_{\rm rec,2}$, B_g, and $T_{i,2}$. Note that although $T_{e,2}$ is varied to maintain pressure balance, the LEF is a kinetic ion effect so there is not expected to be any intrinsic dependence on electron dynamics. We measure the LEF thickness $\delta_{E,\rm Larmor}$ and the LEF magnitude $E_{\rm Larmor}$ with three sets of upstream parameters representing typical dayside magnetopause reconnection and with four different values of guide field for each set as shown in Table 1. Figure 3 shows these quantities for the new simulation results (the solid symbols) as well as the results from Malakit et al. (2013) (the open symbols), which is a zero guide field study, plotted as a function of the initial upstream parameter of interest. For all four of the varying parameters there is significant spread in the data, but some general behaviors are

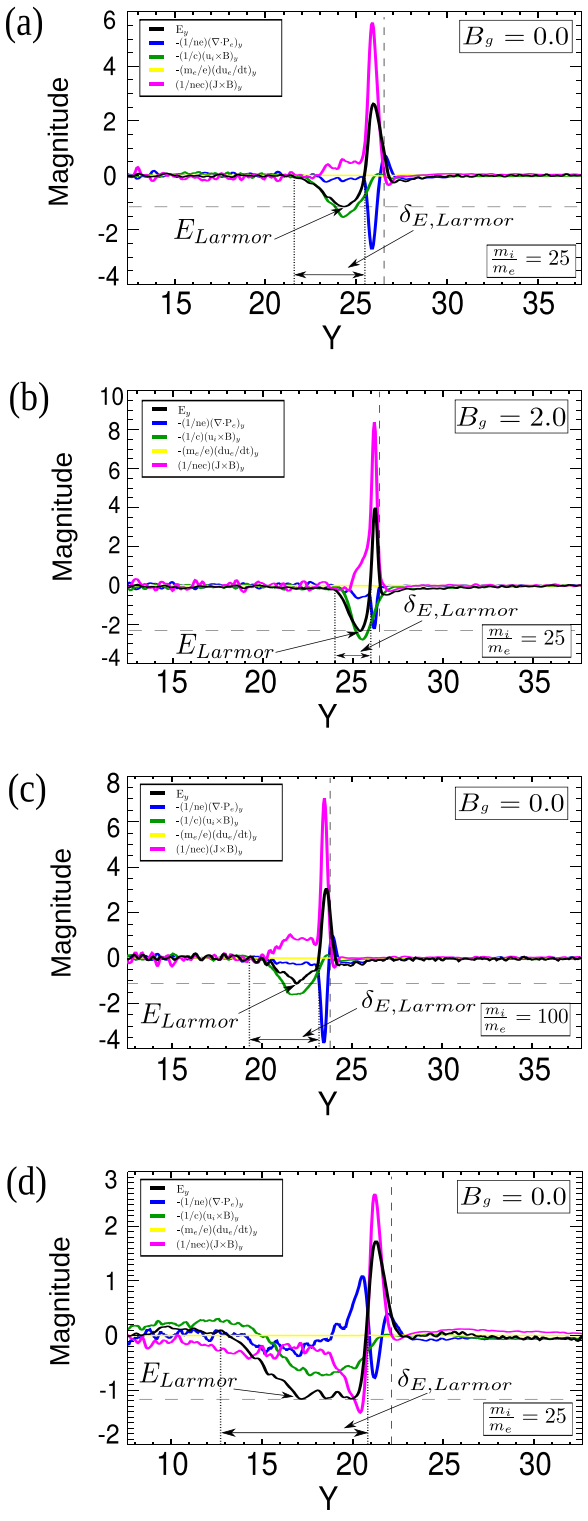


Figure 2. Vertical cut of E_y through the X-line as shown by the dashed line in Figure 1, for the same four simulations. In each plot, the vertical dashed line is provided to show the y position of the X-line for reference. The two vertical dotted lines mark the boundaries of the LEF structure. The distance between the two lines represents the thickness of the LEF structure $\delta_{E,\mathrm{Larmor}}$. The horizontal dashed line marks the magnitude of the LEF E_{Larmor}. The contributions from different terms in the generalized Ohm's law are shown in different colors as indicated in the box on the upper left of each plot. (The data for all three different sets of parameter values ($B_{\mathrm{rec},1}$, $B_{\mathrm{rec},2}$, n_1, n_2) and four different guide field values B_g are provided in the Appendix.)

evident. First, an increasing guide field (Figures 3(b) and (f)) tends to decrease the width of the LEF while increasing its magnitude; a similar behavior is evident in Figures 3(c) and (g) for the total magnetospheric field. Finally, an increase in magnetospheric ion temperature (Figure 3(e)) tends to increase the width of the LEF.

The particular mechanism or mechanisms generating the LEF are not fully understood as to whether it is there to prevent magnetospheric ions from flooding into the diffusion region due to their finite Larmor radius (Malakit et al. 2013) or whether it is a natural consequence of finite Larmor radius of magnetosheath ions penetrating into the magnetosphere (Phan et al. 2016; Shay et al. 2016). It seems clear, however, that the Larmor radius of ions is playing an important role, which is consistent with the trends shown in Figure 3. Consider the scaling of the ion Larmor radius,

$$\rho_i \sim \frac{c\sqrt{m_i k_{\mathrm{B}} T_i}}{eB}, \tag{1}$$

where k_{B} is the Boltzmann constant and B is the total magnetic field magnitude,

$$B = \sqrt{B_{\mathrm{rec}}^2 + B_g^2}, \tag{2}$$

where B_{rec} is the in-plane reconnecting magnetic field. The introduction of a guide field in addition to the existing in-plane reconnecting magnetic field makes the total magnetic field stronger and consequently makes the ion Larmor radius smaller, while an increase in temperature makes the ion Larmor radius larger.

As both magnetospheric and magnetosheath ions have been implicated in the physics of the LEF, we explore the LEF scaling using both magnetosheath (side 1) and magnetospheric (side 2) ion temperatures. We define $\rho_{i,2}$ as the Larmor radius using asymptotic magnetospheric ion temperature and magnetic field; $\rho_{i,1*}$ is calculated using the asymptotic sheath ion temperature but using the magnetospheric magnetic field. The dependence of $\rho_{i,2}$ and $\rho_{i,1*}$ on $\delta_{E,\mathrm{Larmor}}$ are shown in Figures 4(a) and (b), respectively. There is a general trend of increasing $\delta_{E,\mathrm{Larmor}}$ for increasing $\rho_{i,2}$ and $\rho_{i,1*}$. While $\delta_{E,\mathrm{Larmor}}$ and $\rho_{i,2}$ correlated reasonably well for the simulations performed in the present study, the fit for $\rho_{i,sh*}$ is less clear; there is a striking spread of $\delta_{E,\mathrm{Larmor}}$ points for $\rho_{i,1*} \approx 1.15$ for the simulations without a guide field that suggest the two quantities are not linearly related.

Given that the results for $\delta_{E,\mathrm{Larmor}}$ with a guide field are consistent with the expression tested in Malakit et al. (2013), we also compare the magnitude of the LEF versus the Malakit et al. (2013) prediction for the magnitude of the LEF given by

$$E_{\mathrm{Larmor}} \sim \frac{k_{\mathrm{B}} T_{i,2}}{e\rho_{i,2}}, \tag{3}$$

where $T_{i,2}$ is the magnetospheric asymptotic ion temperature. As before, $\rho_{i,2}$ includes both the asymptotic reconnecting and guide magnetic fields. If this expression remains valid, the introduction of a guide field into the system would result in a larger E_{Larmor}. The results of comparing the measured E_{Larmor} for the simulations in the present study with Equation (3) are shown in Figure 4(c). The two quantities agree quite well. The

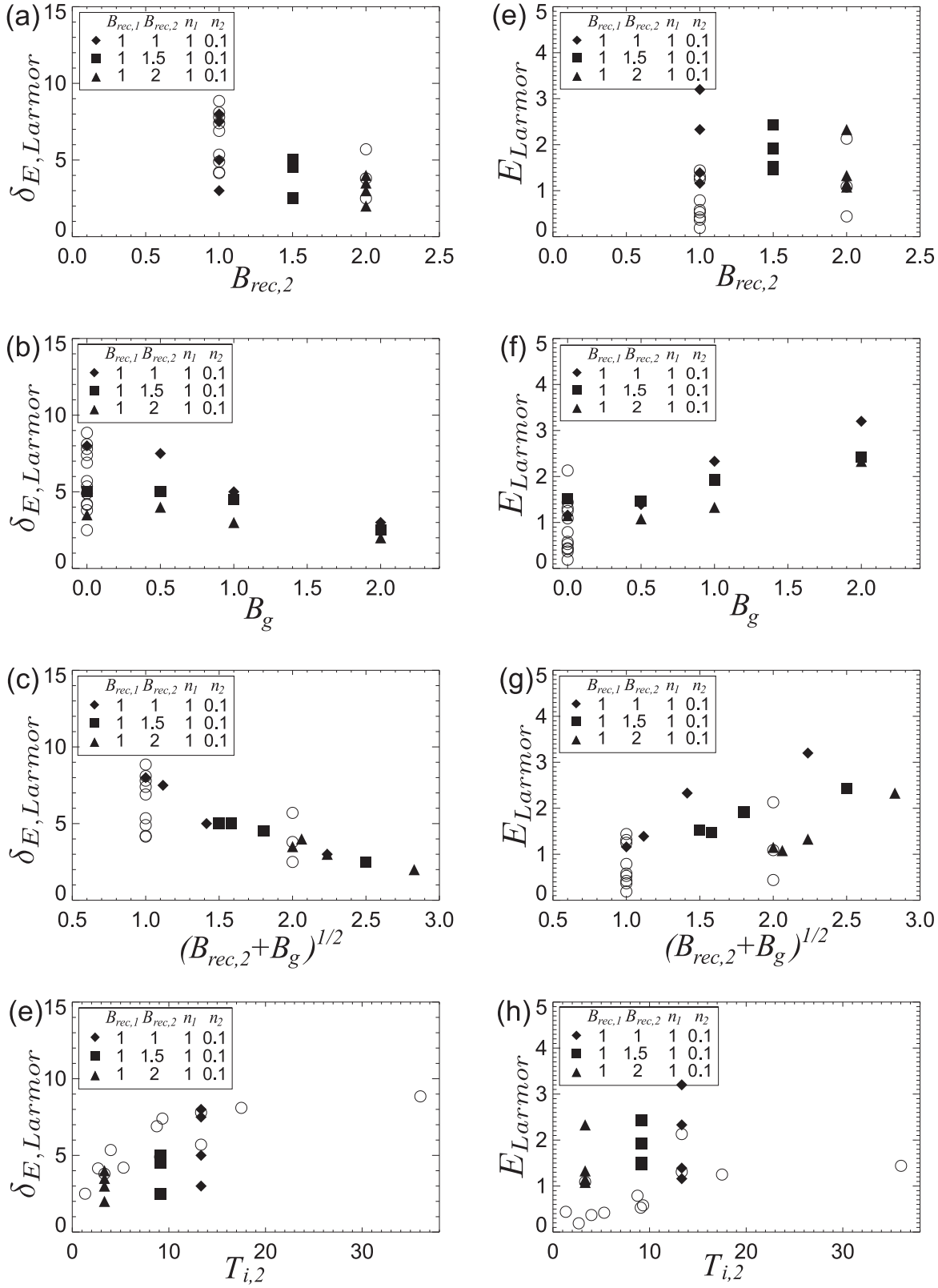


Figure 3. Effect of inflow conditions on the LEF properties: (a)–(d) the thickness of the LEF $\delta_{E,\mathrm{Larmor}}$ and (e)–(h) magnitude of the LEF E_{Larmor}. Variation with (a), (e) magnetospheric reconnecting field $B_{\mathrm{rec},2}$; (b), (e) guide field B_g; (c), (f) total magnetospheric field $\sqrt{B_{\mathrm{rec},2}^2 + B_g^2}$; and (d), (h) magnetospheric ion temperature $T_{i,2}$. Because the introduction of a guide field can lead to secondary island formation (Drake et al. 2006), the data presented here are selected from either the upper or lower X-line that is less affected by secondary islands. The data from runs in this study are shown in solid symbols while the data of runs from the zero-guide-field study (Malakit et al. 2013) are plotted with open circles. The ion temperature and the magnetic field used for calculating the scaling estimates are the asymptotic values on the magnetospheric side.

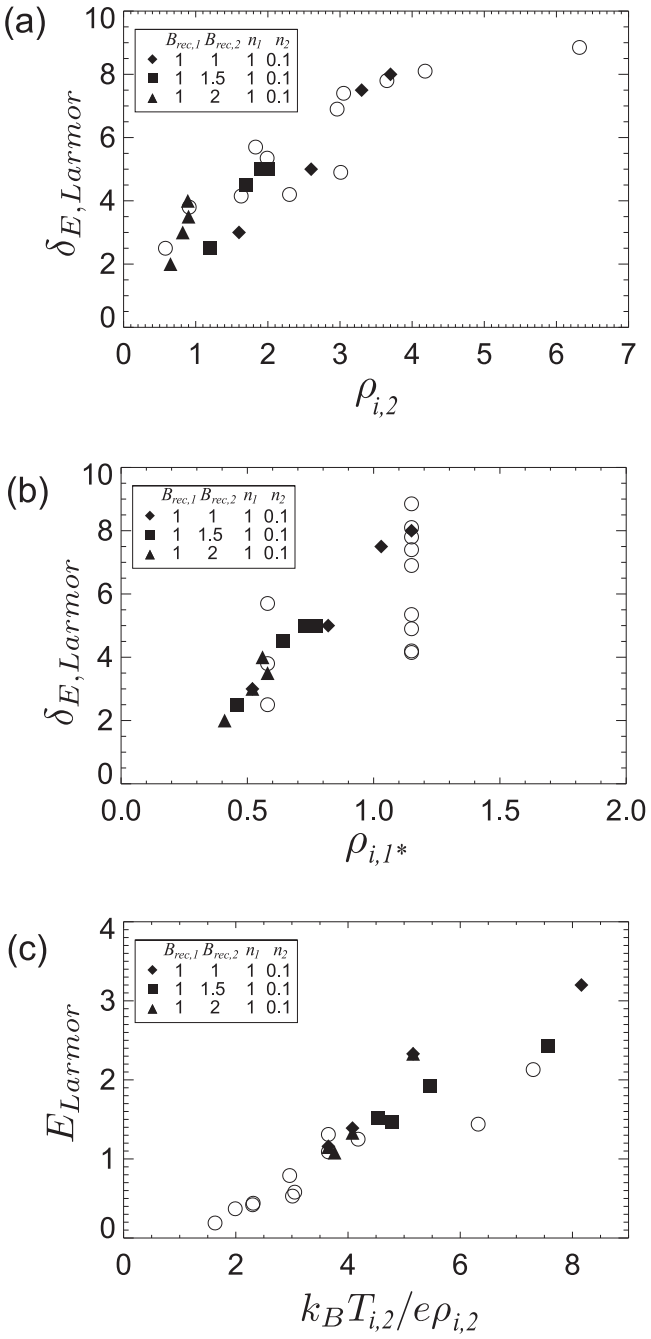


Figure 4. Thickness of the LEF structure $\delta_{E,\mathrm{Larmor}}$ vs. (a) asymptotic magnetospheric ion Larmor radius $\rho_{i,2}$ and (b) Larmor radius based on asymptotic magnetosheath ion temperature and magnetospheric total magnetic field $\rho_{i,1*}$. (c) The magnitude of the LEF vs. the Malakit et al. (2013) prediction generalized to include a guide field. The notation is the same as in Figure 3.

comparison shows that for the parameter space explored in this study, Equation (3) from (Malakit et al. 2013) can be generalized to the guide field case.

Apart from affecting the LEF, the introduction of a guide field also affects E_y in the outflow as well. This E_y in the outflow region is caused by the bulk flow in the x-direction and the guide field in the z-direction. With a strong guide field, this newly created E_y can exceed the Hall electric field expected in the case of no guide field as seen on the left of the magnetospheric separatrix in Figure 1(b). With such electric field structures, looking at E_y alone might not be sufficient to tell whether one is actually in the immediate upstream region of dayside reconnection. However, the following section discusses another structure that can be used in combination with the LEF to help locate the ion diffusion region.

4. Electron Temperature Anisotropy and its Guide Field Dependence

An electron temperature anisotropy also appears in the upstream region on the magnetospheric side of the diffusion region, as identified by Egedal et al. (2011, 2013). This is shown in Figure 5(a) in a plot of the electron temperature anisotropy, defined as $T_{e,\parallel}/T_{e,\perp} - 1$. Red indicates a positive electron temperature parallel anisotropy. This region below the X-line spans a similar (but not exactly the same) area as the blue region below the X-line in Figure 1(a), which is the region of the LEF, as pointed out by Shay et al. (2016). The electron temperature anisotropy requires a parallel electric field (Figures 6(a) and (d)), as identified by Egedal et al. (2011, 2013).

We argue that the physics of ion finite Larmor radius in the LEF region is related to the cause of the parallel electric field. To have the parallel electric field, we need a charge buildup. This can be partially due to the magnetospheric ions that cross the stagnation point and then cause a charge buildup as suggested by the scaling relation for the LEF magnitude Equation (3). In addition, as only magnetosheath ions, not the electrons, can overshoot into the LEF region on the magnetospheric side, these can contribute to a positive charge in the overshoot region. In strongly asymmetric systems, such as those that are typical of the dayside magnetopause, the magnetosheath is significantly more dense than the magnetosphere. It is therefore more likely that the magnetosheath ions are responsible for creating a charge imbalance. This charge imbalance then produces the parallel electric field that pulls magnetospheric electrons into the LEF region to help achieve charge neutrality (Shay et al. 2016). At the same time, this same electric field accelerates the ions toward the downstream region (Figure 6(d)), resulting in the flow of ions parallel to the field toward the outflow directions in the LEF region before the ions cross the separatrix (Figure 6(b)). Such ion outflow overshoot has been observed by spacecraft (Phan et al. 2016). Besides causing a charge imbalance, when the magnetosheath ions overshoot into the region, they change the ion temperature in the region as well (Figure 6(c)). Following a thread of field line as indicated by the curved dashed line in Figure 6(c), we can see that a part of the field line is immersed with varying degree in the region of modified ion temperature. The field line is most immersed at the center and less immersed to the left and right. This leads to a non-zero ion pressure gradient parallel to the magnetic field (Figure 6(d)) and, consequently, partially contributes to the parallel electric field in the LEF region. The combination of the parallel ion acceleration and the parallel ion pressure gradient results in the total parallel electric field (Figure 6(d)) that causes counter-streaming motion of the electrons and the enhanced electron parallel temperature.

Because the generation of the electron temperature anisotropy structure is linked to the LEF structure, which is insensitive to the electron mass, the location of the electron temperature anisotropy structure is insensitive to the electron mass as well. This is confirmed by comparing Figures 5(a) and 7(a), which display the anisotropy for the case of $m_i/m_e = 25$, with Figures 5(c) and 7(c), which display the anisotropy for the

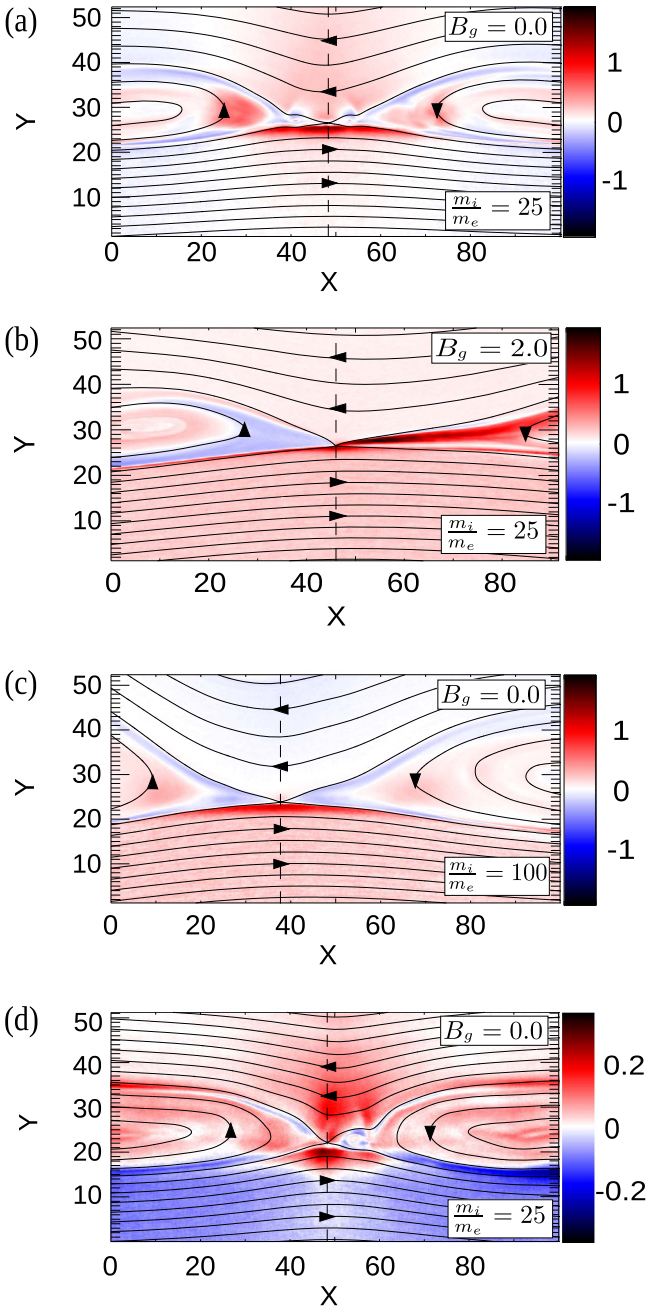


Figure 5. Two-dimensional plot of electron temperature anisotropy $T_{e,\parallel}/T_{e,\perp} - 1$ for the same four simulations shown in Figure 1. The red region below the X-line is the region of high $T_{e,\parallel}$, which is similar to the region where the LEF is present (Figure 1(a)). We note that there is also anisotropy that occurs weakly and uniformly in the upstream regions. This is very likely not physical, but rather numerical. (The data for all three different sets of parameter values ($B_{\rm rec,1}$, $B_{\rm rec,2}$, n_1, n_2) and four different guide field values B_g are provided in the Appendix.)

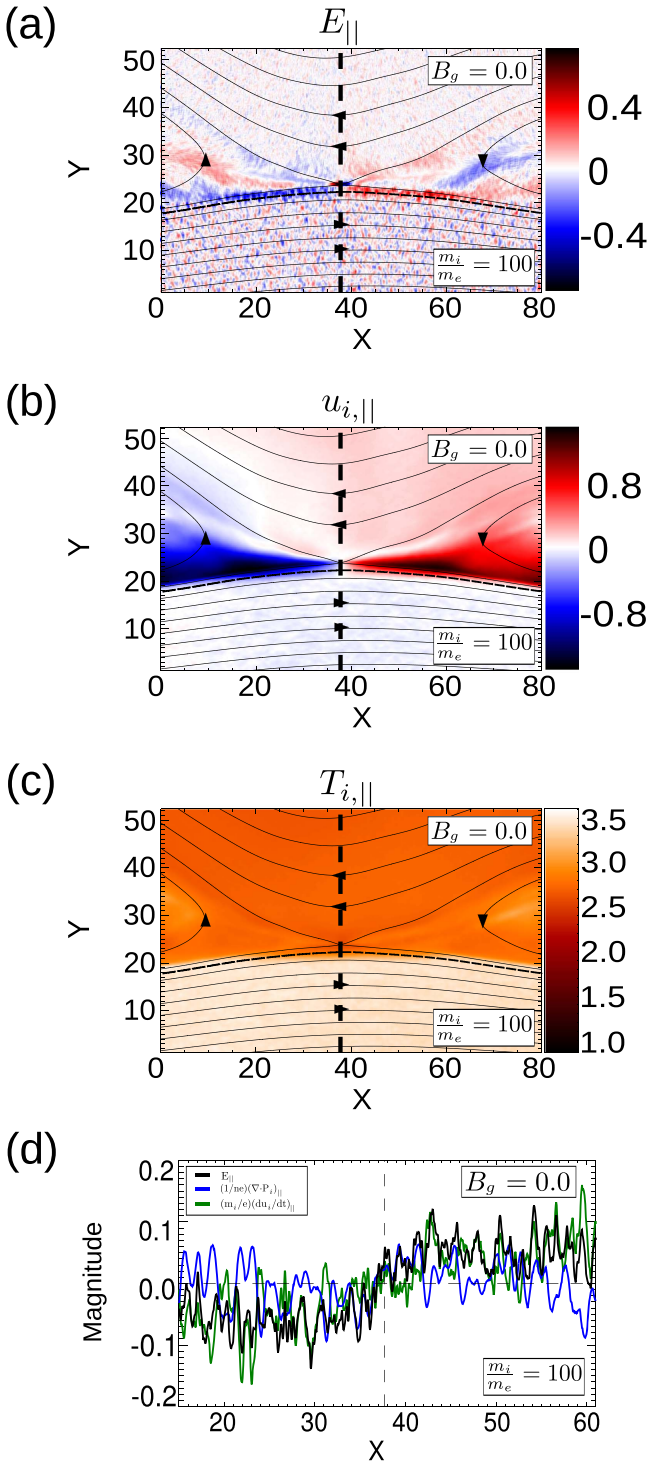


Figure 6. (a) Two-dimensional plot of parallel electric field $E_\parallel$ for the cases of zero guide field with a mass ratio $m_i/m_e = 100$ and the upstream parameters ($B_{\rm rec,1} = 1$, $B_{\rm rec,2} = 2$, $n_1 = 1$, $n_2 = 0.1$) that can be considered characteristic of magnetopause reconnection (Run 1A*). (b) 2D plot of parallel ion flow $u_{i,\parallel}$ (c) 2D plot of parallel ion temperature $T_{i,\parallel}$ (d) 1D cuts of $E_\parallel$ (black), $(m_i/e)(d\boldsymbol{u}_{i,\parallel}/dt)$ (blue), and $(1/ne)(\nabla \cdot \boldsymbol{P}_i)_\parallel$ (green) along the magnetic field line indicated by the curved dashed line in (a). The vertical dashed line is provided to show the x position of the X-line for reference. The arrows in (a), (b), and (c) indicate the direction of the magnetic field.

case of $m_i/m_e = 100$. There are no significant changes with its overlaps with the LEF structure.

We now compare the thickness of the electron temperature anisotropy structure $\delta_{e,\rm aniso}$ with the thickness of the LEF structure. We measure $\delta_{e,\rm aniso}$ as shown in Figure 7. Figure 8 shows that these two physical structures have similar thicknesses for various sets of upstream parameters. We also point out that this continues to be the case when there is a guide field.

Using both the LEF and the electron temperature anisotropy in combination as a signature for reconnection is more effective than using the LEF or the anisotropy alone. The LEF structure

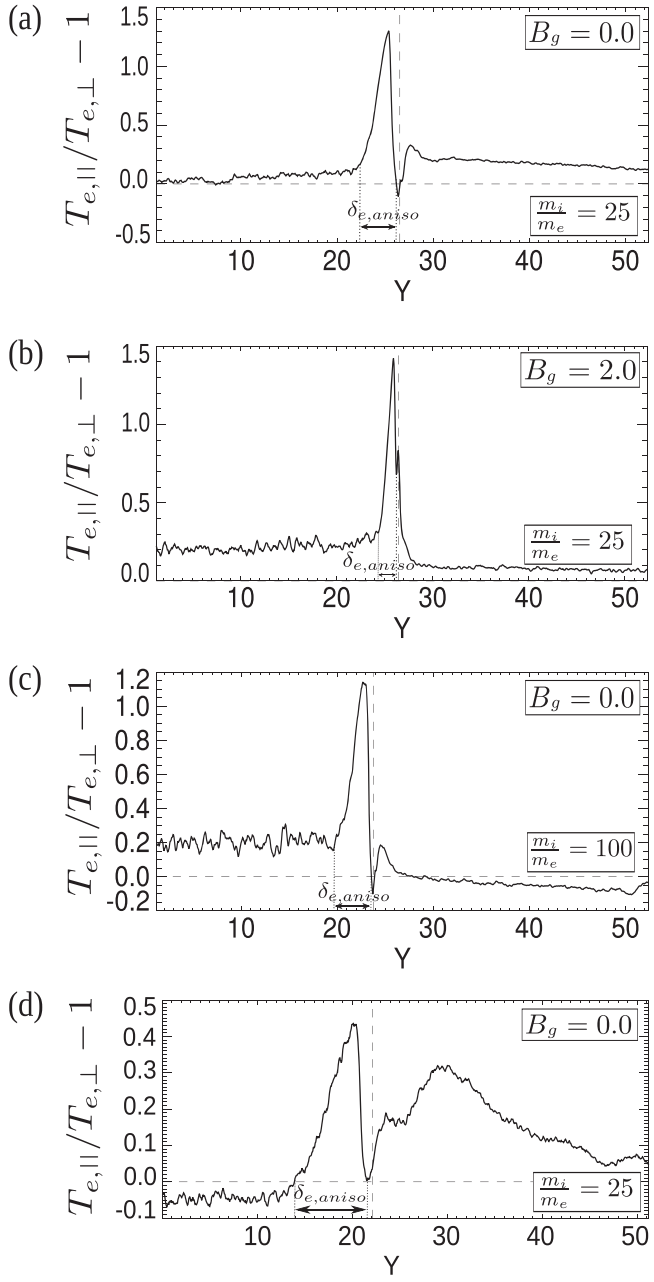


Figure 7. Vertical 1D cut of electron temperature anisotropy $T_{e,\parallel}/T_{e,\perp} - 1$ through the X-line along the dashed lines in Figure 5. The vertical dashed line is provided to show the y position of the X-line for reference. The two vertical dotted lines mark the boundaries of the electron temperature anisotropy region, and the distance between them represents the thickness of the electron temperature anisotropy structure $\delta_{e,\mathrm{aniso}}$. (The data for all three different sets of parameter values ($B_{\mathrm{rec},1}$, $B_{\mathrm{rec},2}$, n_1, n_2) and four different guide field values B_g are provided in the Appendix.)

can sometimes extend far away from the reconnection area (Figure 1(d)). However, the electron temperature anisotropy, with a similar thickness to the LEF's, does not extend to the sides as far, being more confined to the immediate upstream region (Figure 5(d)). Furthermore, as discussed at the end of Section 3, in the case of a strong guide field, the generation of E_y in the downstream region and the suppression of the Hall electric field structure might lead to a misinterpretation of where a satellite locates a diffusion region if we only look for the LEF (Figure 1(b)). Looking at the anisotropy in conjunction with the LEF, the confusion can be eliminated. Figure 5(b)

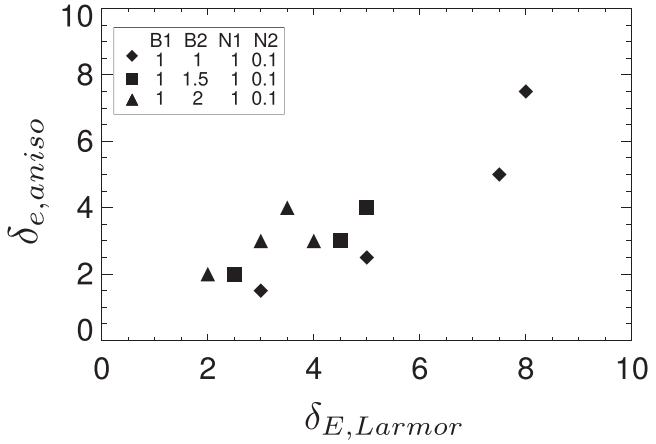


Figure 8. Thickness of the electron temperature anisotropy region $\delta_{e,\mathrm{aniso}}$ vs. the thickness of the LEF region $\delta_{E,\mathrm{Larmor}}$ for various simulations with and without a guide field. Because an introduction of a guide field into the system can lead to secondary island formation, the data presented here are selected from either the upper or lower X-line that is not or less affected by secondary islands. The direct relationship under a variety of conditions indicates that the electron temperature anisotropy and the LEF are physically related and can be used jointly as a stronger marker of proximity of the diffusion region.

shows that in the vicinity of the magnetospheric separatrix left of the X-line, the anisotropy sharply switches signs making the boundary between the immediate upstream and the downstream clear, eliminating the ambiguity caused by looking at E_y alone. Using the anisotropy alone might cause the same boundary problem on the right of the X-line. The E_y signature has a sharp boundary between the immediate upstream and the immediate downstream regions.

5. Discussion on the Larmor Electric Field Mechanism

We emphasize that a general understanding of the mechanism of LEF generation remains elusive. Malakit et al. (2013) argued that magnetospheric ions govern the width and the magnitude of the LEF. However, that model does not capture the involvement of the magnetosheath ions in the generation of the LEF. Shay et al. (2016) and Phan et al. (2016) argued that magnetosheath ions overshoot into the LEF region in the magnetosphere, drift out of plane, and produce a convective electric field that contributes to the LEF. The ion convection term does dominate the LEF in some of the simulations of the present study (such as Run 1A, Run 1D, and Run 1A*; see Figures 2(a)–(c), respectively). However, in the simulation where reconnection is asymmetric only in density (Run 3A), the ion convection term, the Hall term, and the electron pressure gradient term all significantly contribute (Figure 2(d)). This is consistent with the results in Phan et al. (2016), which show that the LEF region is broader than the region where the ion overshoot occurs, suggesting that the ion overshoot is not the sole contributor to the LEF. Furthermore, the penetration of magnetosheath ions into the magnetosphere alone is not adequate to explain the results in Malakit et al. (2013), in which the LEF properties depend on magnetospheric plasma parameters while the magnetosheath plasma parameters are kept unchanged. Therefore, the origin of the LEF likely involves more than one mechanism and depends strongly on the upstream parameters.

We further note that all of the simulations presented thus far in this study and in Malakit et al. (2013) have been performed with $T_i/T_e = 2$ since $T_i > T_e$ is typical at Earth's dayside

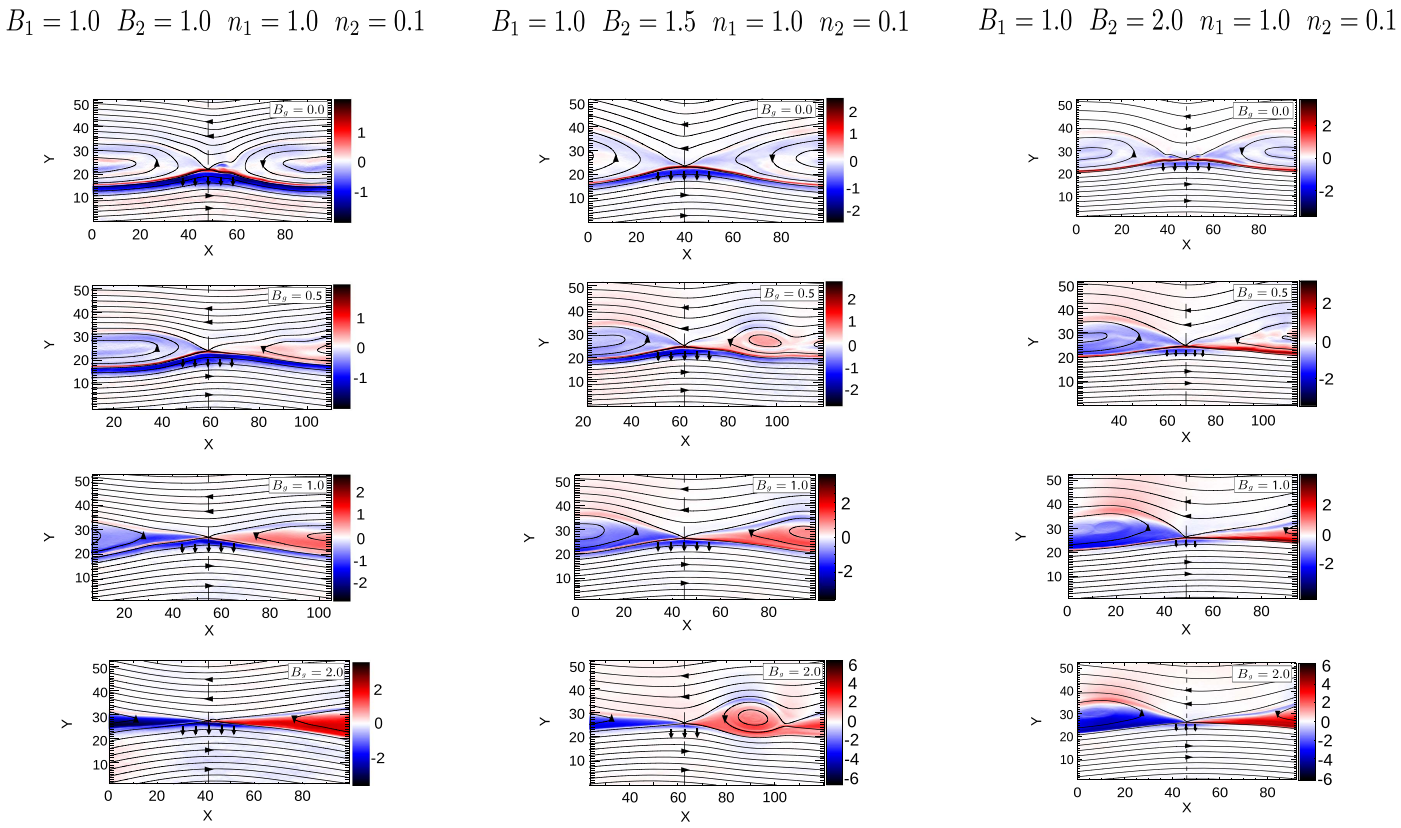


Figure 9. Similar to Figure 1 in the main article. Two-dimensional plots of the electric field in the vertical direction E_y. The blue region below the X-line represents the LEF with arrows pointing downward to indicate the LEF direction. The black lines represent magnetic field lines with arrow heads indicating the magnetic field direction. The dashed line shows a vertical cut through the X-line.

magnetopause. Therefore, key insights of the physics of the LEF will likely be obtained by going beyond this restricted parameter regime. Interestingly, we have preliminary simulation results in the case of $T_i/T_e < 1$ showing that and the scaling relations proposed by Malakit et al. (2013) do not apply in this limit. Thus, future work is needed to determine the roles of the magnetosheath and magnetospheric ions for general asymmetric upstream conditions. Nevertheless, for cases where $T_i > T_e$ such as the dayside magnetopause, the scaling relations are expected to be applicable.

6. Conclusion

We explored the effects of a guide field on the LEF in collisionless asymmetric reconnection using fully kinetic PIC simulations. We demonstrated that the LEF persists in guide field asymmetric reconnection. We analyzed how the LEF varies with changing inflow conditions and have shown that its width and magnitude are strongly linked to the ion Larmor radius; the stronger the guide field, the smaller the Larmor radius, thus the more localized and stronger the LEF. While there are uncertainties regarding the causal agent or agents of the LEF, for the simulation parameter space explored here the scaling estimates of the width and magnitude of the LEF from Malakit et al. (2013) can be generalized successfully for the guide field case. The only modification necessary is that the Larmor radius is determined using the total magnetic field (reconnection and guide).

We also found that in the LEF region, there exists an electron temperature anisotropy, both with and without a guide field. The electron anisotropy is caused by the parallel electric field, which we argue is generated by both an ion pressure gradient and an inertial ion acceleration due to magnetosheath ions crossing the diffusion region into the magnetospheric side; this leads to a rough co-location of the LEF and the electron temperature anisotropy. Using the electron temperature anisotropy and the LEF together as a signature increases the potential of locating the magnetospheric surrounding of the ion diffusion region for dayside reconnection, which can be useful for *MMS* and other satellites.

We thank T. D. Phan and M. Fujimoto for helpful discussions regarding the physics of the Larmor electric field. This research was supported by the Sri Trung Thong scholarship (S.E.) and postdoctoral research sponsorship (K.M.) of Mahidol University, NSF grants AGS-1219382 (MAS) and AGS-0953463 (PAC), NASA grants NNX08A083G—*MMS* IDS, NNX13AD72G (MAS), NNX16AF75G, and NNX16AG76G (PAC), and Thailand Research Fund grant BRG 5880009 (D.R.) and RTA 5980003 (D.R. and K.M.). Simulations were performed at the National Center for Atmospheric Research Computational and Information System Laboratory (NCAR-CISL). The data used in this study are available upon request to the corresponding author.

Appendix

This Appendix provides provides 4 figures similar to Figures 1, 2, 5, and 7 in the main article, but now including plots for all the different upstream densities, in-plane magnetic field strengths, and guide field values used in our simulations.

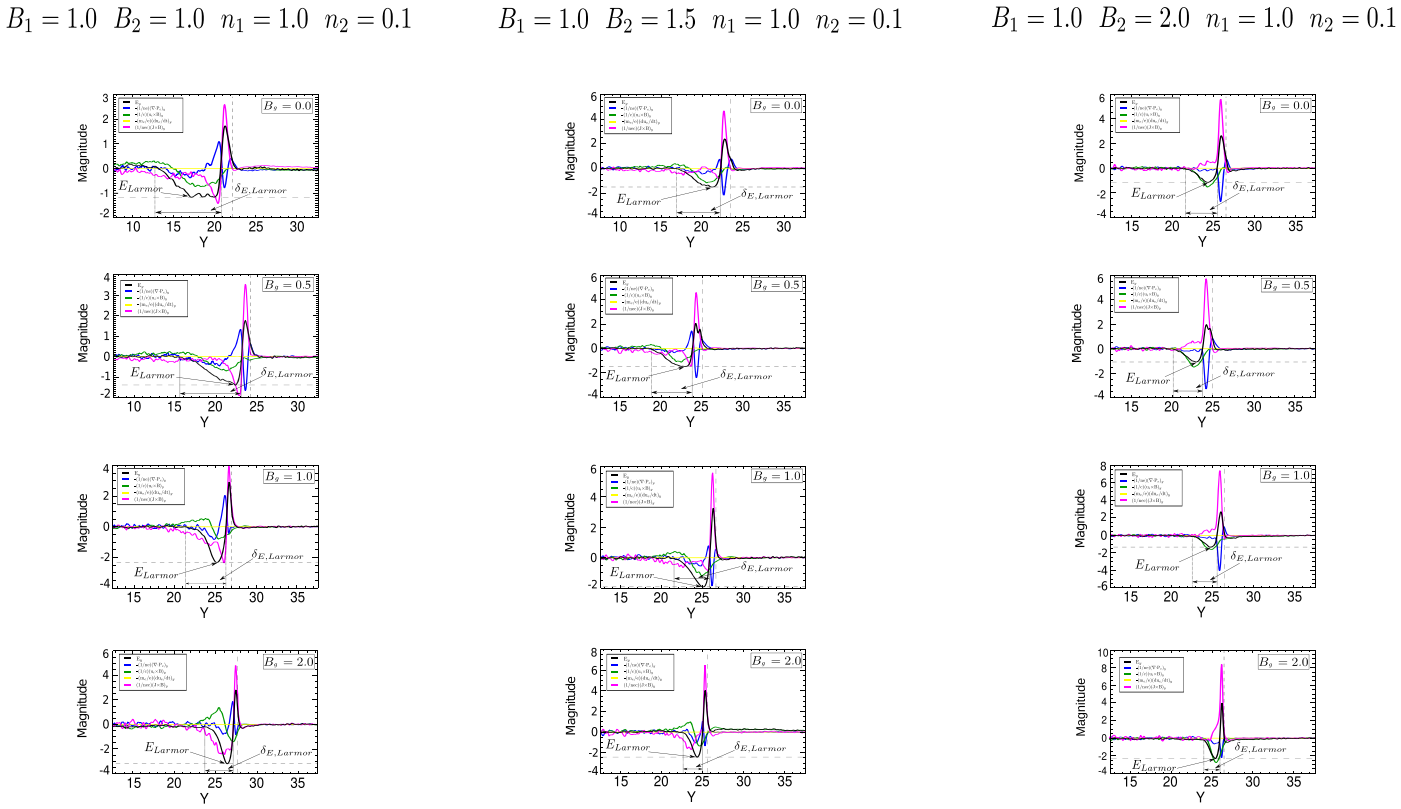


Figure 10. Similar to Figure 2 in the main article. Vertical cut of E_y through the X-line as shown by the dashed line in Figure 1. In each plot, the vertical dashed line is provided to show the y position of the X-line for reference. The two vertical dotted lines mark the boundaries of the LEF structure. The distance between the two lines represents the thickness of the LEF structure $\delta_{E,\mathrm{Larmor}}$. The horizontal dashed line marks the magnitude of the LEF E_{Larmor}. The contributions from different terms in the generalized Ohm's law are shown in different colors as indicated in the box on the upper left of each plot.

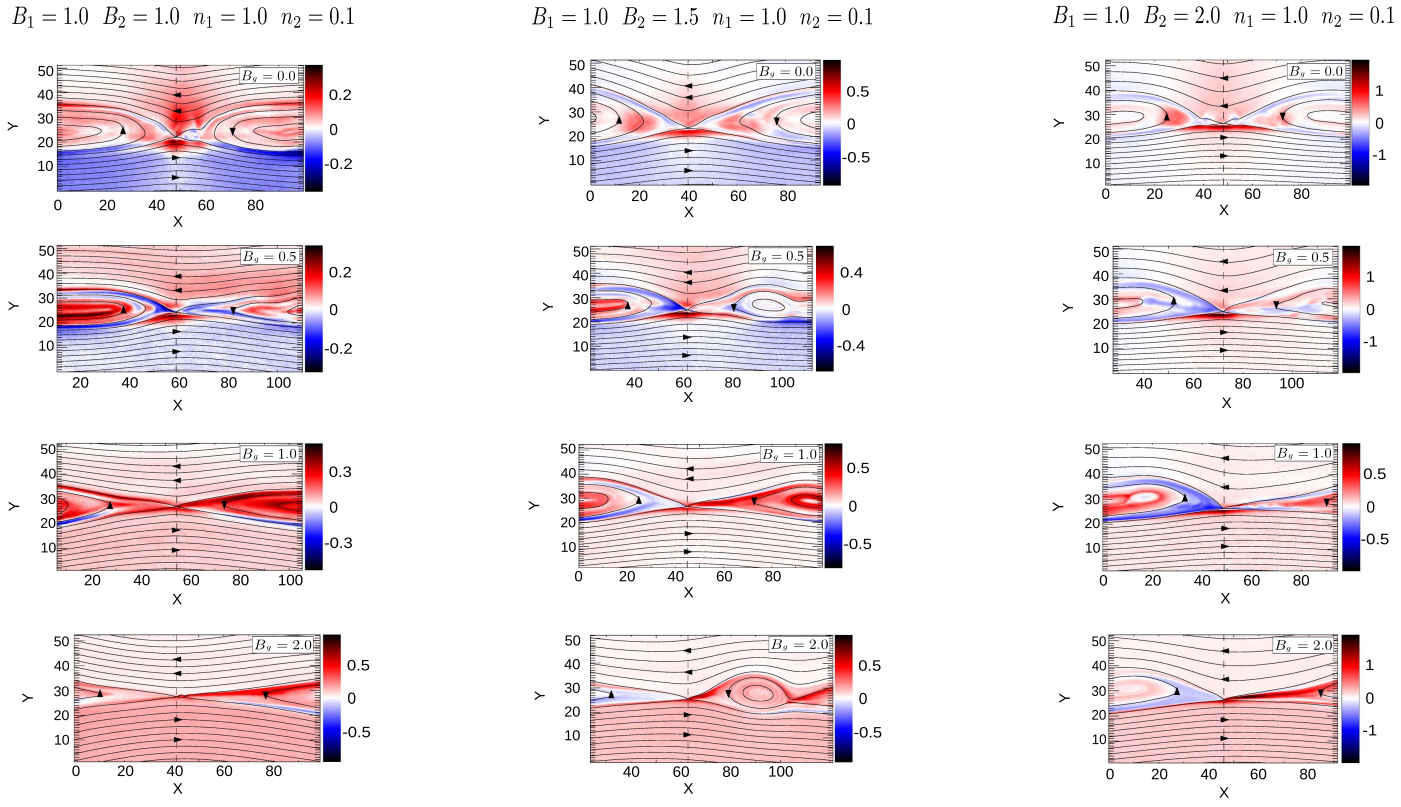


Figure 11. Similar to Figure 5 in the main article. Two-dimensional plot of electron temperature anisotropy $T_{e,\parallel}/T_{e,\perp} - 1$. The red region below the X-line is the region of high $T_{e,\parallel}$, which is similar to the region where the LEF is present (the blue region below the X-line in Figure 1). The black lines represent magnetic field lines with arrow heads indicating the magnetic field direction. The dashed line shows a vertical cut through the X-line.

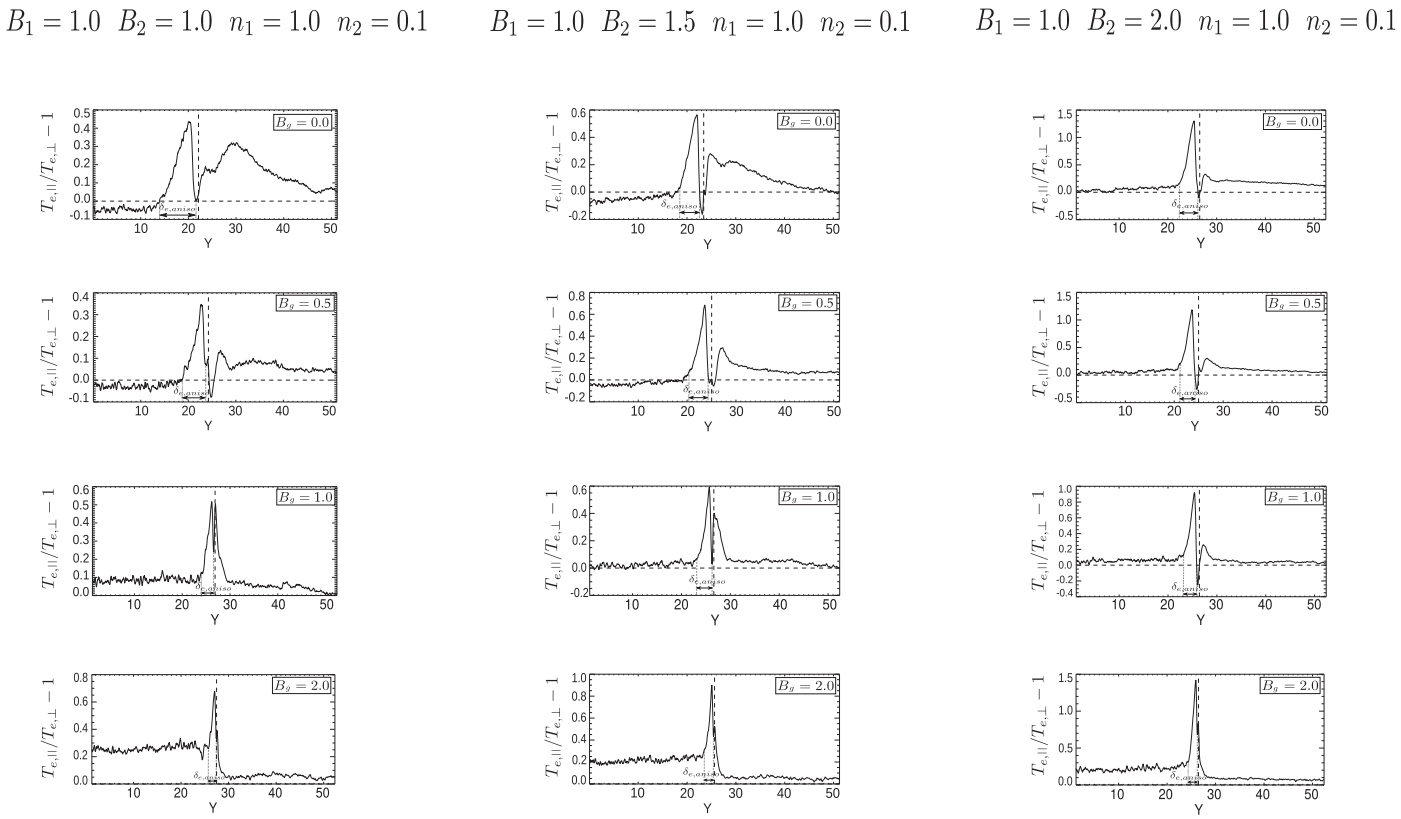


Figure 12. Similar to Figure 7 in the main article. Vertical 1D cut of electron temperature anisotropy through the X-line along the dashed line in Figure 3. In each plot, the vertical dashed line is provided to show the y position of the X-line for reference. The two vertical dotted lines mark the boundaries of the electron temperature anisotropy region, and the distance between them represents the thickness of the electron temperature anisotropy structure $\delta_{e,\mathrm{aniso}}$.

All of our asymmetric reconnection simulations have been performed using the P3D code, a fully kinetic PIC code. The boundaries are periodic in all directions. The initial condition is a double asymmetric current sheet with a small magnetic perturbation to initiate reconnection. Each simulation is allowed to evolve until the reconnection has reached a steady state. Since there is a guide field in our simulations, current sheets are prone to secondary island formation (Drake et al. 2006). We therefore select one X-line from either the upper or lower X-line that is less affected by secondary islands to analyze. Plots of the normal electric field E_y and the electron temperature anisotropy of the selected X-line from all of our simulations are reported in Figures 9–12.

In each figure, the plots are divided into three columns. At the top of each column, there is information about the in-plane magnetic field strengths (B) and number densities (n) of plasma from side "1" (plasma above the X-line in Figures 1 and 3; plasma on the right of the X-line in Figures 2 and 4) and side "2" (plasma below the X-line in Figures 1 and 3; plasma on the left of the X-line in Figures 2 and 4). For each set of B_1, B_2, n_1, n_2, the guide field B_g is varied from 0.0, 0.5, 1.0, and 2.0 as indicated in the box on the upper right of each plot.

In Figures 11 and 12, where the electron temperature anisotropy is shown, we note that there is also anisotropy that occurs weakly and uniformly in the upstream regions. This is very likely not physical but rather numerical.

ORCID iDs

Surapat Ek-In https://orcid.org/0000-0002-2232-6760
Kittipat Malakit https://orcid.org/0000-0002-0915-5979
David Ruffolo https://orcid.org/0000-0003-3414-9666
Michael A. Shay https://orcid.org/0000-0003-1861-4767
Paul A. Cassak https://orcid.org/0000-0002-5938-1050

References

André, M., Vaivads, A., Buchert, S. C., Fazakerley, A. N., & Lahiff, A. 2004, GeoRL, 31, L03803
Burch, J. L., & Drake, J. F. 2009, AmSci, 97, 392
Burch, J. L., Moore, T. E., Torbert, R. B., & Giles, B. L. 2015, SSRv, 199, 5
Burch, J. L., & Phan, T. D. 2016, GeoRL, 43, 8327
Cassak, P. A., & Fuselier, S. A. 2016, in Magnetic Reconnection: Concepts and Applications, ed. W. D. Gonzalez & E. N. Parker (Berlin: Springer), 213
Drake, J. F., Swisdak, M., Schoeffler, K. M., Rogers, B. N., & Kobayashi, S. 2006, GeoRL, 33, L13105
Egedal, J., Le, A., & Daughton, W. 2013, PhPl, 20, 061201
Egedal, J., Le, A., Pritchett, P. L., & Daughton, W. 2011, PhPl, 18, 102901
Eriksson, S., Lavraud, B., Wilder, F. D., et al. 2016a, GeoRL, 43, 5606
Eriksson, S., Wilder, F. D., Ergun, R. E., et al. 2016b, PhRvL, 117, 015001
Koga, D., Gonzalez, W. D., Mozer, F. S., Silveira, M. V. D., & Cardoso, F. R. 2014, PhPl, 21, 100701
Malakit, K., Shay, M. A., Cassak, P. A., & Bard, C. 2010, JGR, 115, A10223
Malakit, K., Shay, M. A., Cassak, P. A., & Ruffolo, D. J. 2013, PhRvL, 111, 135001
Mozer, F. S., Pritchett, P. L., Bonnell, J., Sundkvist, D., & Chang, M. T. 2008, JGRA, 113, A00C03
Paschmann, G., Baumjohann, W., Sckopke, N., Papamastorakis, I., & Carlson, C. W. 1986, JGR, 91, 11099
Phan, T. D., & Paschmann, G. 1996, JGR, 101, 7801
Phan, T.-D., Paschmann, G., & Sonnerup, B. U. Ö 1996, JGR, 101, 7817
Phan, T. D., Shay, M. A., Haggerty, C. C., et al. 2016, GeoRL, 43, 8844
Scurry, L., Russell, C. T., & Gosling, J. T. 1994, JGR, 99, 14815
Shay, M. A., Phan, T. D., Haggerty, C. C., et al. 2016, GeoRL, 43, 4145
Tanaka, K. G., Retinò, A., Asano, Y., et al. 2008, AnGeo, 26, 2471
Vaivads, A., Khotyaintsev, Y., André, M., et al. 2004, PhRvL, 93, 105001
Zeiler, A., Biskamp, D., Drake, J. F., et al. 2002, JGRA, 107, 1230

AGU PUBLICATIONS

JGR

Journal of Geophysical Research: Space Physics

RESEARCH ARTICLE

10.1002/2017JA024125

Key Points:
- We model polar region tropospheric ionization and radiation dosage from the 20 January 2005 solar storm in 1 min steps during 6:50-8:00 UT
- Our methods, based on neutron monitor data, account for the time-dependent relativistic solar ion spectrum and anisotropy
- The most severe radiation dose an airplane passenger could have been exposed to during this event is ~0.75 mSv

Supporting Information:
- Supporting Information S1
- Figure S1
- Movie S1
- Movie S2

Correspondence to:
D. Ruffolo,
david.ruf@mahidol.ac.th

Citation:
Mitthumsiri, W., A. Seripienlert, U. Tortermpun, P.-S. Mangeard, A. Sáiz, D. Ruffolo, and R. Macatangay (2017), Modeling polar region atmospheric ionization induced by the giant solar storm on 20 January 2005, *J. Geophys. Res. Space Physics*, *122*, 7946–7955, doi:10.1002/2017JA024125.

Received 14 MAR 2017
Accepted 28 JUL 2017
Accepted article online 2 AUG 2017
Published online 26 AUG 2017

©2017. American Geophysical Union. All Rights Reserved.

Modeling polar region atmospheric ionization induced by the giant solar storm on 20 January 2005

W. Mitthumsiri[1], A. Seripienlert[2,3,4], U. Tortermpun[1,3], P.-S. Mangeard[1,3,5], A. Sáiz[1], D. Ruffolo[1], and R. Macatangay[3]

[1]Department of Physics, Faculty of Science, Mahidol University, Bangkok, Thailand, [2]Division of Physics, Faculty of Science and Technology, Rajamangala University of Technology Thanyaburi, Pathum Thani, Thailand, [3]National Astronomical Research Institute of Thailand, Chiang Mai, Thailand, [4]Now at Dacon Inspection Services Co., Ltd., Rayong, Thailand, [5]Now at Department of Physics and Astronomy, University of Delaware, Newark, Delaware, USA

Abstract Ionization in Earth's troposphere is mainly due to Galactic cosmic rays. Occasionally, solar storms produce intense relativistic ion beams that significantly increase such ionization. One of the largest recorded solar radiation storms, on 20 January 2005, resulted in up to 55-fold increases in the count rates of ground-based particle detectors in polar regions. We use McMurdo and Inuvik neutron monitor data to estimate accurate time profiles of ion energy spectra above the atmosphere at each location. Using data-driven atmospheric models, we perform Monte Carlo simulations of particle-air interactions and calculate atmospheric ionization and potential biological dosage versus altitude and time for each location. We found that if airplane passengers had traversed the south polar region, they could have been exposed to the typical annual cosmic radiation dosage at sea level within 1 h. These techniques can help evaluate possible influences of solar activity on atmospheric properties.

1. Introduction

There is a variety of "space weather" effects on human activity due to high-speed solar wind streams and solar storms, including those associated with solar energetic particles (SEPs). While humans at Earth are usually well protected by Earth's magnetic field and atmosphere, there are occasional solar storms that produce SEPs of sufficient energy and intensity to shower in the atmosphere and significantly enhance the flux of ionizing radiation above the background level due to Galactic cosmic rays (GCRs), for which the flux decreases less rapidly with energy. Higher in the atmosphere, the less energetic SEPs have a relatively stronger contribution to the ionizing radiation. Even at ground level, neutron monitors (NMs), as the ground-based detectors that are most sensitive to relatively low energy cosmic rays (CRs), can sometimes detect SEPs. Such events of solar origin are known as ground level enhancements (GLEs).

Potential space weather hazards for air travelers and aircraft electronics are closely related to atmospheric ionization, as both are due to ionizing radiation from atmospheric showers. Historically, the first GLE was discovered by Forbush in February 1942 [*Forbush*, 1946]. Later, enhanced atmospheric ionization at altitudes above 30 km was observed during the giant GLE of 23 February 1956 [*Dorman*, 1963, 2004]. Modern measurements of atmospheric ionization [e.g., *Bazilevskaya et al.*, 2008] can provide a reality check on calculations. Furthermore, atmospheric ionization is important to the formation and development of condensation nuclei for aerosols [*Mironova et al.*, 2012]. Some simulation studies suggest significant contributions from GCRs to the atmospheric chemical composition in the stratosphere and troposphere, especially near the polar regions, by enhancing the production of NO_x and HO_x [e.g., *Calisto et al.*, 2011]. Hypothetically, these molecules have measurable impacts on the amount of ozone which consequently affects the tropospheric temperature and wind flow. Thus, the present study aims to estimate the distribution of ionization and radiation dosage in the lower atmosphere (up to 25 km) as expected from a large GLE to provide more information about the connections between CRs and the various phenomena mentioned above.

The giant GLE of 20 January 2005 was the strongest event in the past 60 years, and relativistic solar particle fluxes were well measured by polar NMs, including the *Spaceship Earth* network [*Bieber et al.*, 2013]. The CR flux

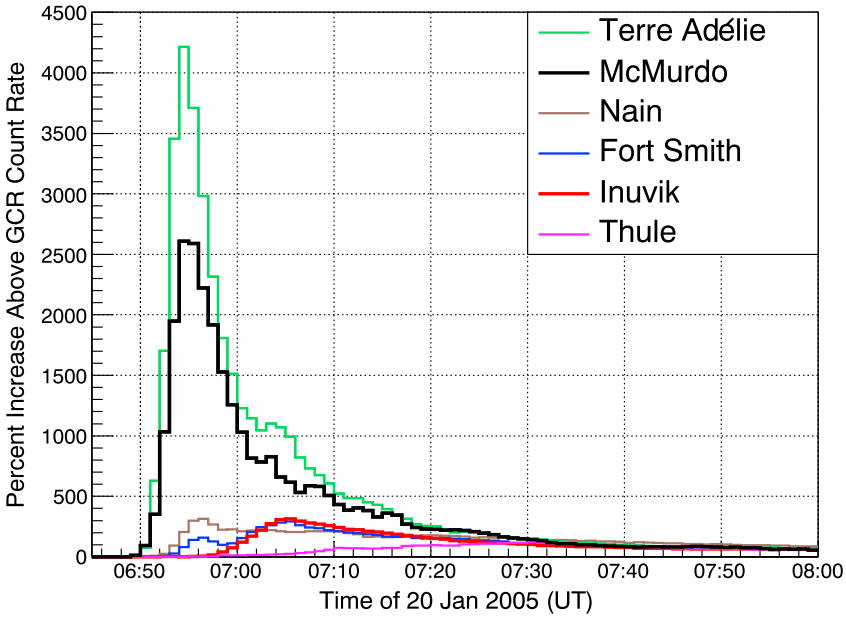


Figure 1. One minute averaged percent increases of count rates, above the background rate produced by Galactic cosmic rays (GCRs), from six polar region neutron monitor (NM) stations due to the giant solar radiation storm on 20 January 2005 (replotted from *Bieber et al.* [2013]). McMurdo and Inuvik data are emphasized in this work.

as measured by the high-altitude South Pole NM increased by ≈5500%. Fortunately, such high increases occurred only at or near Antarctica, with no commercial air travel; this event highlights the potential effects on polar air flights when such increases occur over the north polar region in the future. With such a large increase in particle fluxes, this event provides a good example case for estimating atmospheric ionization [*Mishev et al.*, 2012] and radiation dosage [*Bütikofer and Flückiger*, 2011; *Mishev*, 2014; *Mishev et al.*, 2015]. Here we make direct use of accurate measurements by NMs of the time-dependent particle flux at different locations, combined with detailed Monte Carlo simulations based on the estimated atmospheric structure at those locations and times, to precisely estimate atmospheric ionization and radiation dosage due to relativistic solar particles as a function of altitude and time.

2. Methods

2.1. Neutron Monitor Data

When CRs strike the upper atmosphere, showers of secondary particles, including neutrons, are produced and can be detected by NMs on the ground. An important advantage of NMs is a high detection rate, allowing precise measurement of secondary neutron count variation in a relatively short (e.g., 1 min) time interval. We can use the NM count rate data to obtain information about the CR spectrum at the top of the atmosphere as a function of time. This is discussed in detail in section 2.2.

For a given location on Earth, only CRs above a certain rigidity (momentum per charge) can penetrate the Earth's magnetic field to interact with the atmosphere. This geomagnetic cutoff rigidity varies from ≈17 GV in and near Thailand to ≤0.01 GV near the geomagnetic poles, where there is an atmospheric cutoff of ∼1 GV for CR showers to register counts in ground-based NMs. Therefore, NM stations at different locations are sensitive to different rigidity ranges of the CR spectrum. SEPs, predominantly relativistic protons and alpha particles, can have a rigidity up to ∼10 GV and may arrive to Earth mostly near the polar regions, resulting in increases of NM count rates above the background GCR count rates. On 20 January 2005 starting from 6:50 UT, a major GLE was observed near the polar regions. Satellite instruments also clearly registered this event with enormous increases of particle fluxes and significant changes of spectral parameters. Percent increases of selected polar region NM count rates of this GLE are shown in Figure 1.

Near the start of this GLE, as shown in Figure 1, there was a very strong anisotropy in the solar particle flux, with a ratio of flux arriving near the South Pole to that near the North Pole of over 1000:1 at 6:54 UT, and the anisotropy became much weaker in the later (decay) phase of the event [*Bieber et al.*, 2013]. At times of strong

anisotropy, remote satellite data may not provide accurate particle fluxes above specific locations of interest. We therefore use NM count rate data, specifically from low-cutoff stations at McMurdo (77.9°S 166.6°E, in Antarctica) and Inuvik (68.4°N 133.7°W, in Canada), to calculate the time-dependent CR spectra above the atmosphere at those locations. As shown in Figure 1, NM data from Terre Adélie and Thule during this GLE event could represent two opposite ends of the extreme cases, while data from McMurdo and Inuvik are good base-case scenarios for the south and north polar regions, enabling us to compare our results against those from other studies more consistently. Furthermore, an important motivation to study the location at Inuvik station is the dense air traffic in that region, for relevance to the actual health effects on airline passengers.

2.2. Estimations of GCR and SEP Spectra

GCR Spectra. The solar cycle effects known as solar modulation can affect GCRs up to ~30 GV and are known to follow a cycle of about 11–12 years. We use the parameterization of the local GCR proton spectrum from *Usoskin et al.* [2011a], taking into account the solar modulation effect for this specific event by putting in the force field potential $\phi = 1188$ MV as estimated for 20 January 2005 [*Usoskin et al.*, 2011b]. As recommended by *Usoskin et al.* [2011a], we model the contribution of ions with $Z \geq 2$, which we call "heavy ions," as if they were alpha particles with a flux of number of nucleons equal to 30% of the proton flux. Our trajectory simulations using the 11th generation International Geomagnetic Reference Field and the method of *Lin et al.* [1995] indicate that during times of interest, the vertical geomagnetic cutoff rigidity was below about 10 MV, a rigidity range where particles generate negligible ionization below 25 km in altitude. Therefore, we do not implement a geomagnetic cutoff at McMurdo or Inuvik. For the timescale of a few hours in this study, it is sufficient to approximate that the GCR fluxes are constant in time and isotropic.

SEP Spectra. The SEP spectra of this GLE are more complicated to model. The SEP-induced ionization of the lower atmosphere is dominated by GeV range particles, so we stress an accurate representation of the time dependence of SEP spectra in this high-energy range. The time variation of the GeV range SEP flux is measured precisely at NM stations, and as described earlier we estimate the SEP fluxes at McMurdo, Antarctica, and Inuvik, Canada, based on the near-sea level NM count rates there.

We use NM count rates only to estimate the time-dependent amplitudes of the SEP spectra; the spectral shapes are as estimated below. To justify the use of local NM count rates to determine the time-dependent amplitudes of the SEP spectra at each location, we note that our calculation of the median kinetic energy of primary cosmic rays, in terms of their contribution to either atmospheric ionization or radiation dosage at 12 km altitude above either McMurdo or Inuvik, ranges between 0.8 and 1.4 GeV, in comparison with the median kinetic energy of protons contributing to the NM count rate of 1.40 GeV [*Bieber et al.*, 2013]. Furthermore, because of magnetic mirroring along the converging magnetic field lines near Earth's poles, a wide range of particle arrival directions at a given rigidity maps to a narrow range of asymptotic directions in space. For example, we calculate that for the median rigidity for either NM station, arrival directions at zenith angle 30°, i.e., over a circle of diameter 60°, map into asymptotic directions over an oval of diameter ~3°. Thus, the primary cosmic ray directions contributing to the NM count rate are very similar to those contributing to atmospheric ionization and radiation dosage at aircraft altitude.

Regarding the SEP spectral shape, the rigidity spectral index of SEPs during the GLE of 20 January 2005 was measured minute by minute using the count rate ratio of bare neutron counters to the NM at the South Pole [*Bieber et al.*, 2013]. These two detector systems have different energy sensitivity so their ratio can be used to roughly estimate the spectral index [*Bieber and Evenson*, 1991]. This method has been used to study the spectral index of various GLEs [*Bieber et al.*, 2002; *Sáiz et al.*, 2008] and gave very similar results to an independent method based on data for many NMs [*Cramp et al.*, 1997] for the GLE of 22 October 1989 [*Ruffolo et al.*, 2006]. Because the SEP spectral index reported by *Bieber et al.* [2013] for 20 January 2005 was measured with 1 min resolution over the narrow rigidity range of ~1 to 5 GV as sampled by polar NMs, it is the most relevant determination of the spectral index for the present study. (That work also contains a summary of widely varying estimates of the spectral index for that event, for different or broader ranges of rigidity and coarser time resolution.) *Bieber et al.* [2013] found that the apparent spectral index γ over that rigidity range was ~3 at the the onset at 0649 UT but rapidly increased (softened) to nearly 5 by 0653 UT. The spectrum was initially hard because the most energetic particles arrived first, but it quickly softened due to velocity dispersion. There was another dip to a lower (harder) spectral index at 0655 UT due to a second dispersive injection peak. Afterward, the spectrum gradually became softer to approach a steady state with $\gamma = 5.0$. An attractive physical interpretation is that the acceleration of particles near the Sun, of short duration, produced an SEP distribution with a spectral index of 5.0 over this rigidity interval and that the apparent spectral index as

observed at Earth was lower (harder) immediately after each injection because many lower energy particles had not arrived yet. This interpretation is supported by Figure 4 of *Bieber et al.* [2013], which compares the spectrum at a polar NM with the proton spectrum measured by the GOES spacecraft at lower energies, and shows that the GOES spectrum was initially much lower than the NM spectral trend and then caught up to it at later times. (Note that *Mewaldt et al.* [2005] consider that the GOES proton data channels above 200 MeV are difficult to reconcile with a smooth extrapolation of the spectra observed below 100 MeV and therefore do not make use of such data; if such data are removed from Figure 4 of *Bieber et al.* [2013], the data are indeed easier to understand in terms of velocity dispersion.)

To model this dispersive onset, we implement a simple time-varying cutoff at low energy; recall that our estimates of ionization and radiation dosage below an altitude of 25 km are most sensitive to GeV range particles. The time-dependent p and He energy spectra are described by a power law in rigidity with the constant spectral index of 5.0 and a low-energy cutoff T_c

$$\frac{\mathrm{d}N}{\mathrm{d}}R = I_0(t)\left(\frac{R_0}{R(T)}\right)^5 \exp\left(\frac{T_c}{T_c(t)-T}\right) \text{ for } T > T_c(t), \tag{1}$$

where N is particle intensity (number of particles per unit area, per unit time, and per unit solid angle), T is kinetic energy per nucleon, R is rigidity, and t is time. Here I_0 is the spectral amplitude, which depends on the (arbitrary) choice of reference rigidity, R_0.

With the spectral shape determined in this way, the remainder of this subsection describes how we use the precisely measured NM count rate at each station during each 1 min interval to infer the *amplitude* I_0 of the proton and heavy ion spectra for that minute.

In order to extract the SEP spectra from NM count rates, we use results from an analysis of data from a latitude survey [*Nuntiyakul et al.*, 2014], which was performed by carrying an NM on a ship across a wide range of geographical locations with widely varying geomagnetic cutoff rigidity between October 2004 and April 2005. This provides a measured combined response function of sea level NMs to all GCR particle types around January 2005 as a function of rigidity.

Next, we employ the local GCR proton and heavy ion (with He + heavy ions modeled as additional He) spectral models from *Usoskin et al.* [2011a] as previously described. Using the average solar modulation potential during the period of interest (ϕ = 636.3 MV between October 2004 and April 2005; see http://cosmicrays.oulu.fi/phi/Phi_mon.txt) along with the parameterized ratio of He to p yield functions at varying rigidity from *Caballero-Lopez and Moraal* [2012], we obtain the NM yield functions for p and He separately, for which the values are shown in Table S1 in the supporting information and a comparison with some other yield functions in the literature is shown in Figure S1 in the supporting information. Our yield functions based on latitude survey data can then be used to calculate the SEP p and heavy ion spectra above McMurdo and Inuvik NM stations from the measured percentage increases of NM count rates (over the GCR background) under these assumptions.

1. The yield functions for the shipborne NM in the latitude survey [*Nuntiyakul et al.*, 2014] are used for the McMurdo and Inuvik NM, which is reasonable given that they use the same NM64 design and were all near-sea level. Differences in pressure and atmospheric properties at different locations affect the yield functions at the level of a few percent and are negligible compared to other uncertainties.
2. The low-energy cutoff of the spectra $T_c(t)$ decreases with time, depending on the arrival of particles with different velocities traversing a distance of 1.029 AU along the mean interplanetary magnetic field following the Archimedean spiral for the measured solar wind speed of about 800 km s^{-1} starting from injection at ≈2 solar radii. Particles with $T > 1$ GeV nucleon^{-1} started to arrive at 6:50 UT (see top left panel of Figure 4 in *Bieber et al.* [2013]). This simple form of the low-energy cutoff is derived for an instantaneous injection of particles at the distance of 0.01 AU from the solar center. Given that the low-energy cutoff very rapidly decreases to below 100 MeV, as can be seen in the supporting information, and particles at such low energies have very little effect on the ionization and dosage below 25 km, we consider these approximations to be justified and to have very little effect on the results.
3. The SEP He/p ratio for this event is 0.044 at 1.4 GeV/n, which is obtained from fitting the highest-energy data sets for He (20–60 MeV/n) and p (20–400 MeV/n) fluence spectra in *Mewaldt* [2006] and extrapolating

the fits to 1.4 GeV/n, the SEP proton median energy for polar NM observations during this event. The extrapolation is needed because only GeV range SEPs contribute significantly to the atmospheric ionization below ~25 km altitude. It is even more challenging to quantify the GeV range SEP heavy ion composition, so we assume the same relative fractional contribution of ions with $Z > 2$ as for GCR (~50% of He). This gives the (heavy ion)/p ratio of 0.066 at 1.4 GeV/n, the number used in this study. This ratio is likely time and location dependent, but due to the lack of measured GeV data, it is impossible to precisely model it. We therefore assume that the ratio is constant in time and is the same for both McMurdo and Inuvik. By analyzing measurements at lower energies, we estimate the uncertainty of this ratio in the GeV range to be ~20% and observe that varying this ratio by ±20% results in roughly ∓5% changes in the calculated ionization, indicating a small impact from the uncertainty of this ratio.

We have checked the validity of our calculated NM yield functions due to GCR protons and heavy ions as follows. We compute that, at McMurdo and Inuvik, ~40% of NM counts are produced by ions heavier than protons, which is reasonable compared to other estimations from the literature, such as 33% by *Caballero-Lopez and Moraal* [2012] (sea level, 1.0 GV rigidity cutoff) and 51% by *Maurin et al.* [2015] (at 10 GV). Note that this fraction depends on numerous factors such as atmospheric depth, cutoff rigidity, and solar modulation. We also tested using simulation-based NM yield functions at sea level for p and He from *Mangeard et al.* [2016b], which are significantly higher than ours between 1 and 10 GV (see Figure S1 in the supporting information). We then obtain a lower SEP spectral amplitude and understandably obtain ionization rates that are lower than the results shown here by ~35%. Those authors pointed out that FLUKA simulations such as theirs overestimate the yield function below 7 GV when compared with other estimates, and the SEP flux is concentrated at such lower rigidities, so we instead use our yield functions based on latitude survey data and claim ~35% uncertainty in the resulting ionization due to the choice of NM yield functions.

2.3. Monte Carlo Simulations of Atmospheric Ionization

Realistic models of Earth's atmosphere for McMurdo and Inuvik are created with meteorological data from the Global Data Assimilation System (GDAS; see https://www.ready.noaa.gov/gdas1.php) below ~25 km altitude and from NRLMSISE [*Picone et al.*, 2002] above that. The GDAS database provides average atmospheric properties (e.g., humidity, density, pressure, and temperature) from actual measurements between 6:00 and 12:00 UT, while the NRLMSISE model is averaged monthly. Our atmospheric models are composed of 0.25 km thick layers from the altitude of each NM up to ~70 km. More details can be found in Appendix A of *Mangeard et al.* [2016a]. As noted in section 2.2, the primary cosmic ray directions contributing to the NM count rate are very similar to those contributing to atmospheric ionization and radiation dosage at aircraft altitudes and that range of directions is quite narrow [see *Bieber et al.*, 2013, Figure 2], so we neglect effects of differences in the SEP flux over that narrow range.

We use the FLUKA 2011 package [*Ferrari et al.*, 2005; *Böhlen et al.*, 2014] to perform the simulations of atmospheric ionization. GCR and SEP particles with energy spectra described in section 2.2 are simulated to interact with the modeled atmosphere. For both GCRs and SEPs, we apply no geomagnetic rigidity cutoff at either McMurdo or Inuvik. The exact value does not significantly affect the result because showers from low-energy particles have a negligible effect on atmospheric ionization at altitudes of interest (below 25 km). In 1 min time steps during 6:50–8:00 UT, the energy deposited in each atmospheric layer is recorded and converted into an ionization rate using the average ionization potential of air of 35 eV [*Porter et al.*, 1976], a value that was also used by *Mishev et al.* [2012]. The radiation equivalent dose for each layer is also recorded using FLUKA's "DOSE-EQ" default option which provides particle fluences convoluted with conversion factors for different types of particles. The ambient dose equivalent conversion data are from the International Commission on Radiological Protection [*ICRP*, 1996]. Therefore, we obtain the ionization and equivalent dose rate as a function of altitude at any given time between 6:50 and 8:00 UT. We show results up to only 25 km altitude because of the uncertainties in the determination of lower energy CR fluxes which strongly affect the calculations at high altitude but have negligible effects below 25 km.

Atmospheric ionization and radiation dosage from this specific event have been studied by *Mishev et al.* [2012, 2015] and at higher altitudes by *von Savigny et al.* [2007], using space-based CR spectral data and a different simulation method for various geographical locations. The present analysis is complementary to previous studies because it is based on detailed temporal measurements from NMs at specific locations, to precisely specify the time evolution of atmospheric ionization and radiation dosage as a function of altitude.

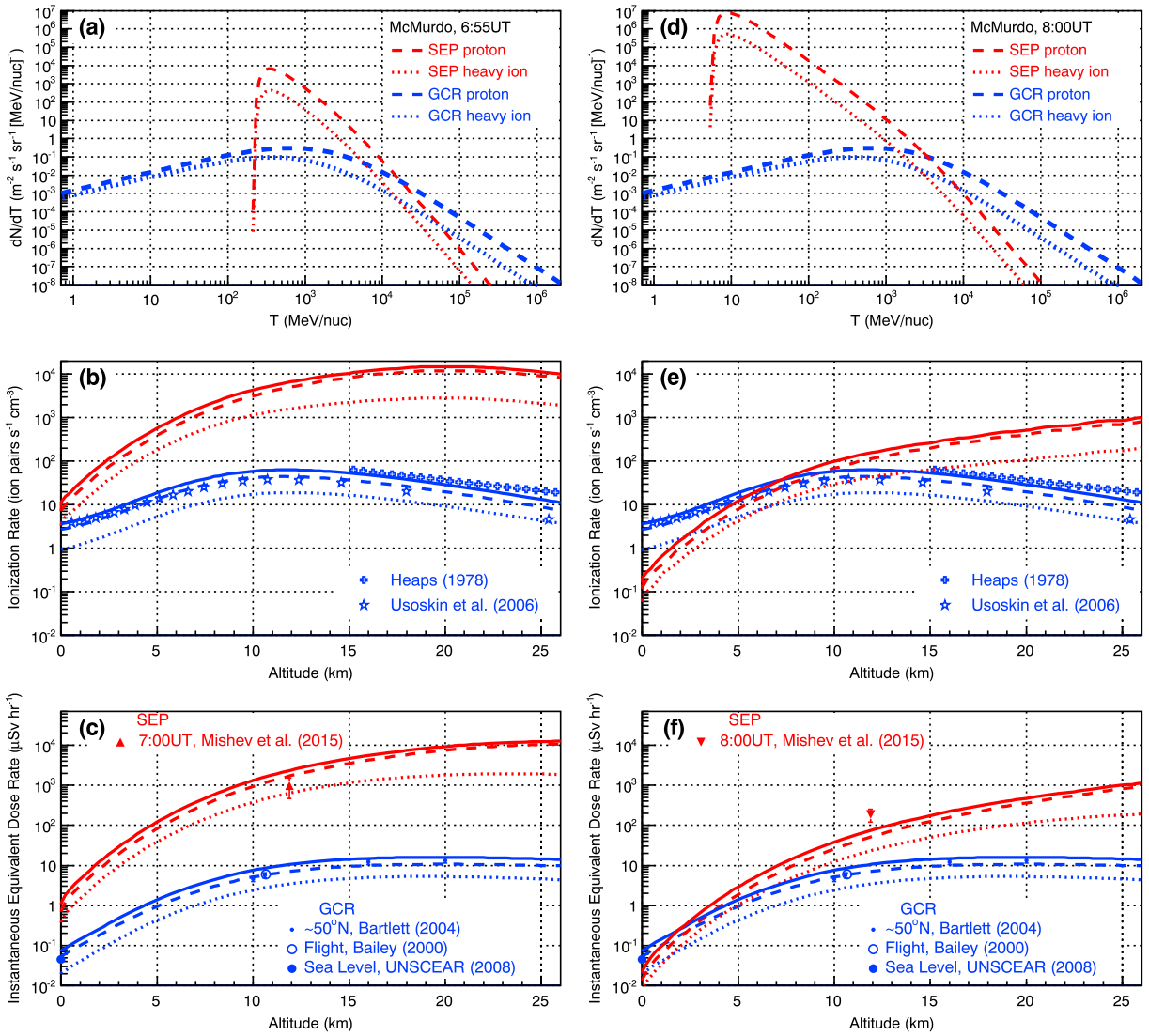


Figure 2. (a, d) Modeled cosmic ray spectra used as inputs to simulate the (b, e) atmospheric ionization production rate and (c, f) instantaneous equivalent dose rate above McMurdo (Antarctica) NM station at the peak time of the GLE of 20 January 2005 (Figures 2a–2c) and a time during the decay phase (Figures 2d–2f). Here the blue and red lines or symbols are associated with GCRs and solar energetic particles (SEPs), respectively. An animation of these graphs as a function of time throughout the event is included in the supporting information.

3. Results and Discussion

Results from simulations for selected times are shown in Figure 2 for McMurdo and Figure 3 for Inuvik. Results for all times are included in the supporting information. Figures 2a–2c and 3a–3c are at the (local) GLE peak time, while Figures 2d–2f and 3d–3f are during the GLE decay phase. The peak times of the SEP fluxes above McMurdo and Inuvik are different: 6:55 UT at McMurdo and 7:06 UT at Inuvik. Estimated SEP and GCR spectra are shown in Figures 2a and 2d and 3a and 3d. Our estimated SEP flux is comparable to that of GCRs near ~10 GeV nucleon^{-1} during the peak of the NM count rate at each location. Our inferred SEP proton flux around ~600 MeV at 6:55 UT above McMurdo is similar to that measured by the Geostationary Orbit Environment Satellite (GOES) [see, e.g., *Matthiä et al.*, 2009, Figure 7] considering the instrumental energy bin and extreme anisotropy for this event.

Results of atmospheric ionization production rates are shown in Figures 2b and 2e and 3b and 3e. We first consider the total ionization rate at about 12 km above sea level, which is a typical altitude for commercial aircraft. Near the peak time, the ionization rate from SEPs at McMurdo is greater than that from GCRs by ~2 orders of magnitude, whereas at Inuvik, the ionization rate from SEPs is greater than that from GCRs by an order

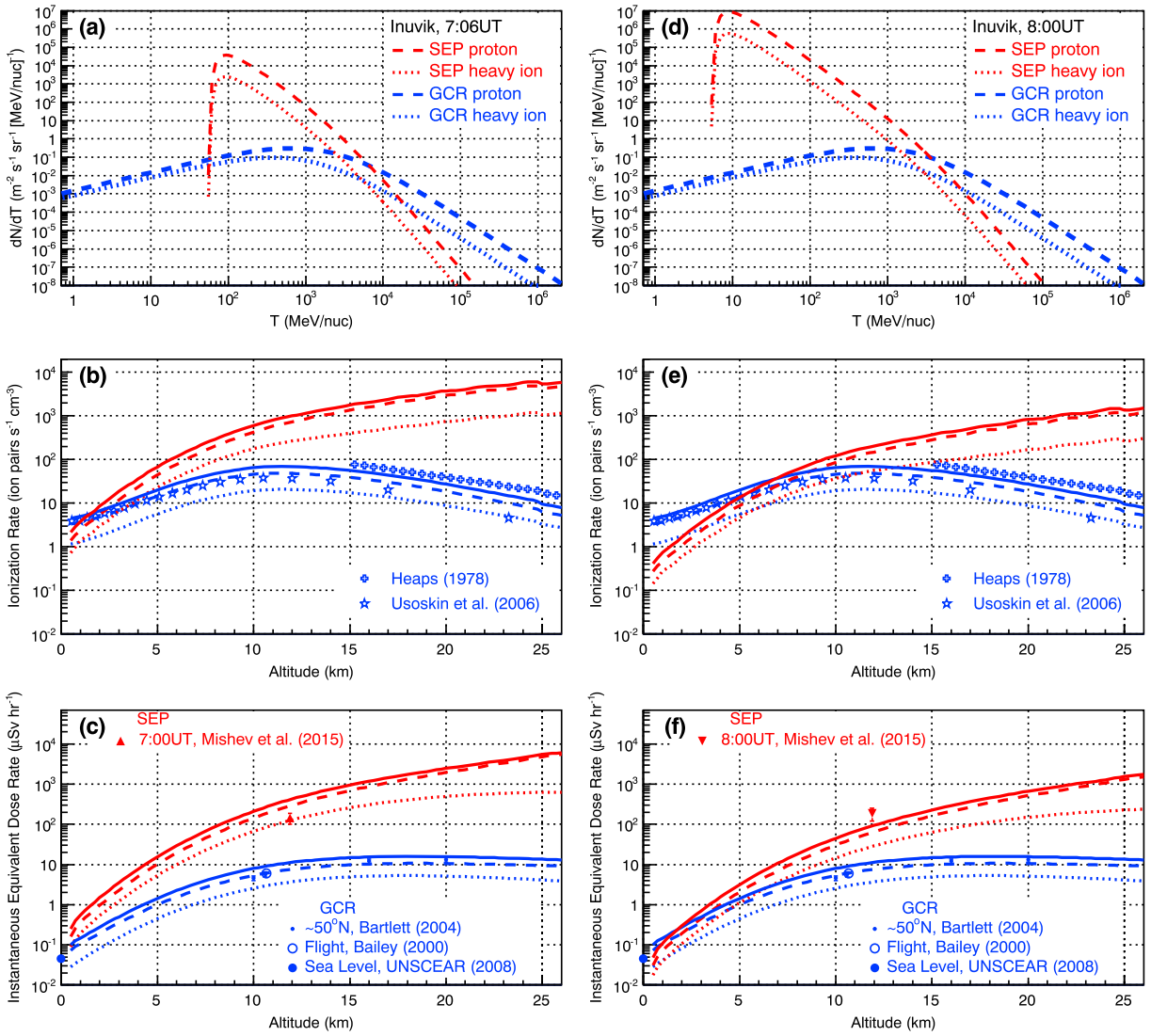


Figure 3. Same as Figure 2 but for the Inuvik (Canada) NM station. Fortunately for air travelers, the relativistic solar particle fluxes were much lower in the north polar region, where commercial air flights are more frequent, compared with the south polar region. An animation of these graphs as a function of time throughout the event is included in the supporting information.

of magnitude. During the decay phase of the GLE, the ionization rate from SEPs is roughly a factor of 3 higher than that from GCRs at both McMurdo and Inuvik.

Near the peak time of this GLE, at sea level, the ionization rate from SEPs was about a factor of 2 over that from GCRs at McMurdo, while the ionization rate from SEPs at Inuvik was only ~25% of that from GCRs. During the decay phase of the GLE, the ionization rate from SEPs was negligible at both locations near the ground. At above ~10 km, ionization rates from SEPs are higher than those from GCRs for all times between 6:50 and 8:00 UT considered at both locations. This is because most charged SEPs have lower energies than most GCRs, and they cannot penetrate the atmosphere to low altitudes, tending to ionize the air only at higher altitudes.

Before comparing with some previous results, we note some potential sources of uncertainty. *Mishev and Velinov* [2014] report very good agreement between data from balloon-borne measurements and FLUKA simulation results for GCR-induced ionization. Nevertheless, this does not guarantee such accuracy for SEP-induced ionization. Their study reveals an effect of the choice of the hadron interaction generator on the order of 15% for GCR-induced ionization. A similar spread among the GCR-induced radiation dose rates from different models was reported by *Bütikofer et al.* [2009]; however, they found a much wider variation of up to 48% among estimates for SEP-induced radiation, when changing only the interaction model. Such an

effect of the hadronic interaction generator may be the largest source of uncertainty in our results. As noted earlier, the conversion from NM observations to the time-dependent SEP amplitude requires the use of yield functions, and we estimate that to cause an uncertainty of ~35% in our results. In section 2.2, we noted that our estimated 20% uncertainty in the SEP heavy/*p* ratio should lead to only a 5% uncertainty in the results. Combining these uncertainties in quadrature, we estimate a total uncertainty of ~60% in our results.

We now compare our simulation results for the atmospheric ionization to those from previous analyses. The parameterization of GCR-induced ion-pair production rates from balloon measurements at solar maximum by *Heaps* [1978] and calculations using the CR-induced ionization model by *Usoskin and Kovaltsov* [2006] with our GCR *p* and He spectra are shown by cross and star symbols, respectively, in Figures 2b and 2e and 3b and 3e. Our simulated ionization rate due to GCRs has a profile shape that is consistent with results from both analyses. The magnitude is lower than that of *Heaps* [1978] by ≈20% at above 15 km and greater than that of *Usoskin and Kovaltsov* [2006] by ≈10% at a few kilometers above the ground. These small differences are not unreasonable since there are many caveats in the comparison, such as differences in geomagnetic location, solar modulation, and atmospheric properties. Furthermore, our calculations and the simulated ionization yield functions by *Usoskin and Kovaltsov* [2006] consider only GCRs and neglect other ionization sources such as ultraviolet radiation from the Sun, which may be important at above ~20 km [see *Calisto et al.*, 2011, Figure 1]. This could partly explain the discrepancies with the empirical data based on observations of all ionization sources by *Heaps* [1978]; the present calculations for GCRs are closer to results by *Heaps* [1978] than are the calculations by *Usoskin and Kovaltsov* [2006]. Our simulated ion pair production rates are also qualitatively consistent with other previous studies [see, e.g., *Bazilevskaya et al.*, 2008, Figure 2; *Mishev et al.*, 2012].

Our calculated instantaneous equivalent dose rates at different altitudes are shown in Figures 2c and 2f and 3c and 3f, in which the measured average GCR-generated dose rate received by air crews at typical airplane altitude [*Bailey*, 2000; *Bartlett*, 2004] and at sea level is also shown for comparison. Our simulation results are somewhat higher than the measurements, with improved agreement at higher altitude. The triangles represent calculations of the combined GCR and SEP contribution on 20 January 2005 from *Mishev et al.* [2015] for the north and south polar regions: The upward triangle is for the time at 7:00 UT, and the downward triangle is for 8:00 UT. Comparisons with *Mishev et al.* [2015] are more clearly illustrated in Figure 4. Results from our simulations in Figures 2c and 3c suggest that during the peak of this GLE at ~12 km altitude, the instantaneous radiation dose rate increased by a factor of ~300 above the average GCR rate at McMurdo and by a factor of ~40 at Inuvik.

Time variations of our total (GCR + SEP) ionization and equivalent dose rates at 11.7 km altitude, the value considered by *Mishev et al.* [2015], are shown in Figures 4a and b4. Our simulated equivalent dose rates at McMurdo and Inuvik are consistent with the results by *Mishev et al.* [2015] at 7:00 UT and 8:00 UT at the same altitude as shown in Figure 4b and are qualitatively consistent with Figure 4 in *Bütikofer et al.* [2009].

The world average annual background radiation exposure for humans is ~2.4 mSv, in which ~0.4 mSv is from CRs [*United Nations Scientific Committee on the Effects of Atomic Radiation*, 2008]. The suggested annual limit of radiation exposure for the public is 1 mSv above the background, though a higher dose could be allowed if the 5 year average dose does not exceed 1 mSv/yr [*ICRP*, 2007]. From Movies S1d and S2d in the supporting information, we estimate that an airplane passenger spending ~1 h at 12 km altitude above McMurdo or Inuvik during this GLE would have received ≈0.5 mSv or ≈0.2 mSv additional radiation exposure, respectively, due to the SEPs. Since the NM count rate at Terre Adélie is ≈1.5 times of that at McMurdo (see Figure 1), the most extreme additional radiation dose due to this GLE event could be at least ≈0.75 mSv. These amounts are similar to the average dosage from GCRs during an entire year at ground level and are still within the suggested annual limit of 1 mSv above the background.

For the strongest GLE ever recorded in February 1956, the maximum percent increase of the atmospheric neutron count rate is estimated to be ~9000% near the polar regions [*Duggal*, 1979; *Bieber et al.*, 2013], which is ~4 times the maximum count rate at McMurdo during the January 2005 event and lasted for about 5 h. If we assume that the time profiles of the percent increase for both events near the peak time are similar, a simple scaling of our results would place the radiation dosage received by airplane passengers near the poles during this enormous February 1956 event at around a few millisievert per hour. Passengers spending ~5 h near the polar regions could have been exposed to a dosage which greatly exceeded the suggested annual limit just from this event alone. Even if the accumulated radiation exposure at airplane altitude for either the

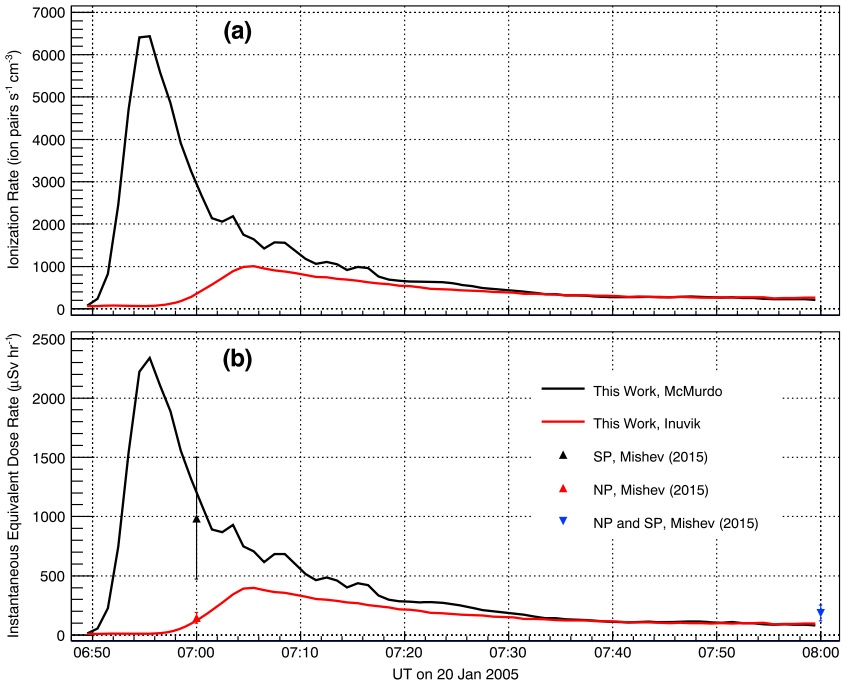


Figure 4. (a) Simulated total (GCR + SEP) ionization and (b) equivalent dose rates in 1 min time steps at 11.7 km above sea level. Results by *Mishev et al.* [2015] at the same altitude for south polar (SP) and north polar (NP) regions are shown for comparison.

2005 or 1956 GLE event does not exceed the suggested annual or 5 year average limit, receiving an enormous amount of radiation in a very short period of time may pose dangerous health effects, which need to be further studied.

Acknowledgments
This research project is supported by Mahidol University, the Thailand Research Fund (grants TRG5880173, BRG5580001, BRG5880009, and RTA5980003 and Royal Golden Jubilee fellowship PHD/0136/2552) and the National Astronomical Research Institute of Thailand (NARIT). P.-S.M. was partially supported under the postdoctoral research sponsorship of Mahidol University. We thank John Bieber for useful discussions, Andrew Snodin for his assistance with cluster computing, and Waraporn Nuntiyakul for providing valuable latitude survey data. For data from the McMurdo and Inuvik neutron monitors, we thank the Bartol Research Institute neutron monitor program, which is supported by the U.S. National Science Foundation via awards PLR-1341562 and PLR-1245939 and their predecessors. The data displayed in the figures are available upon request from the corresponding author.

References

Bailey, S. (2000), Air crew radiation exposure—An overview, *Nuclear News*, *32*, 32–40.
Bartlett, D. T. (2004), Radiation protection aspects of the cosmic radiation exposure of aircraft crew, *Radiat. Prot. Dosim.*, *109*(4), 349–355.
Bazilevskaya, G. A., et al. (2008), Cosmic ray induced ion production in the atmosphere, *Space Sci. Rev.*, *137*, 149–173, doi:10.1007/s11214-008-9339-y.
Bieber, J. W., and P. Evenson (1991), Determination of energy spectra for the large solar particle events of 1989, in *Proceedings of the 22nd International Cosmic Ray Conference*, vol. 3, pp. 129–132, The Inst. for Adv. Studies, Dublin.
Bieber, J. W., et al. (2002), Energetic particle observations during the 2000 July 14 solar event, *Astrophys. J.*, *567*, 622–634.
Bieber, J. W., J. Clem, P. Evenson, R. Pyle, A. Sáiz, and D. Ruffolo (2013), Giant ground level enhancement of relativistic solar protons on 2005 January 20. I. Spaceship Earth observations, *Astrophys. J.*, *771*, 92, doi:10.1088/0004-637X/771/2/92.
Böhlen, T. T., et al. (2014), The FLUKA code: Developments and challenges for high energy and medical applications, *Nuclear Data Sheets*, *120*, 211–214.
Bütikofer, R., E. O. Flückiger, B. Pirard, and L. Desorgher (2009), Effective radiation dose for selected intercontinental flights during the GLEs on 20 January 2005 and 13 December 2006, in *Proc. 21st European Cosmic Ray Symposium*, pp. 158–163, Inst. Exp. Phys. Slovak Acad. Sci., Košice, Slovakia.
Bütikofer, R., and E. O. Flückiger (2011), Radiation doses along selected flight profiles during two extreme solar cosmic ray events, *Astrophys. Space Sci. Trans.*, *7*, 105–109, doi:10.5194/astra-7-105-2011.
Caballero-Lopez, R. A., and H. Moraal (2012), Cosmic-ray yield and response functions in the atmosphere, *J. Geophys. Res.*, *117*, A12103, doi:10.1029/2012JA017794.
Calisto, M., I. Usoskin, E. Rozanov, and T. Peter (2011), Influence of Galactic Cosmic Rays on atmospheric composition and dynamics, *Atmos. Chem. Phys.*, *11*, 4547–4556, doi:10.5194/acp-11-4547-2011.
Cramp, J., et al. (1997), The October 22, 1989, solar cosmic ray enhancement: An analysis of the anisotropy and spectral characteristics, *J. Geophys. Res.*, *102*, 24,237–24,248, doi:10.1029/97JA01947.
Dorman, L. I. (1963), Geophysical and astrophysical aspects of cosmic rays, in *Progress in Elementary Particle and Cosmic Ray Physics*, vol. 7, edited by J. G. Wilson and S. A. Wouthuysen, pp. 1–324, North-Holland, Amsterdam.
Dorman, L. I. (2004), *Cosmic Rays in the Earth's Atmosphere and Underground*, Kluwer, Dordrecht, Netherlands.
Duggal, S. P. (1979), Relativistic solar cosmic rays, *Rev. Geophys.*, *17*(5), 1021–1058.
Ferrari, A., P. R. Sala, A. Fassò, and J. Ranft, (2005), FLUKA: A multi-particle transport code, *Tech. Rep. CERN-2005-10, INFN/TC_05/11, SLAC-R-773*, European Organization for Nuclear Research, Geneva, Switzerland.
Forbush, S. E. (1946), Three unusual cosmic-ray increases possibly due to charged particles from the Sun, *Phys. Rev.*, *70*, 771–772.
Heaps, M. G. (1978), Parametrization of the cosmic ray ion-pair production rate above 18 km, *Planet. Space Sci.*, *26*, 513–517.
ICRP (1996), *Conversion Coefficients for Use in Radiological Protection Against External Radiation*, ICRP Publ. 74, *Ann. ICRP, 26*(3-4).
ICRP (2007), *The 2007 Recommendations of the International Commission on Radiological Protection*, ICRP Publ. 103, *Ann. ICRP, 37*(2-4).

Lin, Z., J. W. Bieber, and P. Evenson (1995), Electron trajectories in a model magnetosphere: Simulation and observation under active conditions, *J. Geophys. Res.*, *100*(A12), 23,543–23,549, doi:10.1029/95JA02696.

Mangeard, P.-S., D. Ruffolo, A. Sáiz, S. Madlee, and T. Nutaro (2016a), Monte Carlo simulation of the neutron monitor yield function, *J. Geophys. Res. Space Physics*, *121*, 7435–7448, doi:10.1002/2016JA022638.

Mangeard, P.-S., et al. (2016b), Dependence of the neutron monitor count rate and time delay distribution on the rigidity spectrum of primary cosmic rays, *J. Geophys. Res. Space Physics*, *121*, 620–636, doi:10.1002/2016JA023515.

Matthiä, D., et al. (2009), Temporal and spatial evolution of the solar energetic particle event on 20 January 2005 and resulting radiation doses in aviation, *J. Geophys. Res.*, *114*, A08104, doi:10.1029/2009JA014125.

Maurin, D., A. Cheminet, L. Derome, A. Ghelfi, and G. Hubert (2015), Neutron monitors and muon detectors for solar modulation studies: Interstellar flux, yield function, and assessment of critical parameters in count rate calculations, *Adv. Space Res.*, *55*, 363–389.

Mewaldt, R. A., et al. (2005), Proton, helium, and electron spectra during the large solar particle events of October–November 2003, *J. Geophys. Res.*, *110*, A09S18, doi:10.1029/2005JA011038.

Mewaldt, R. A. (2006), Solar energetic particle composition, energy spectra, and space weather, *Space Sci. Rev.*, *124*, 303–316.

Mironova, I. A., I. G. Usoskin, G. A. Kovaltsov, and S. V. Petelina (2012), Possible effect of extreme solar energetic particle event of 20 January 2005 on polar stratospheric aerosols: Direct observational evidence, *Atmos. Chem. Phys.*, *12*, 769–778.

Mishev, A. L. (2014), Computation of radiation environment during ground level enhancements 65, 69 and 70 at equatorial region and flight altitudes, *Adv. Space Res.*, *54*, 528–535.

Mishev, A. L., and P. I. Y. Velinov (2014), Influence of hadron and atmospheric models on computation of cosmic ray ionization in the atmosphere—Extension to heavy nuclei, *J. Atmos. Sol. Terr. Phys.*, *120*, 111–120.

Mishev, A. L., P. I. Y. Velinov, L. Mateev, and Y. Tassev (2012), Ionization effect of nuclei with solar and galactic origin in the Earth atmosphere during GLE 69 on 20 January 2005, *J. Atmos. Sol. Terr. Phys.*, *89*, 1–7.

Mishev, A. L., F. Adibpour, I. G. Usoskin, and E. Felsberger (2015), Computation of dose rate at flight altitudes during ground level enhancements no. 69, 70 and 71, *Adv. Space Res.*, *55*, 354–362.

Nuntiyakul, W., et al. (2014), Latitude survey investigation of Galactic cosmic ray solar modulation during 1994–2007, *Astrophys. J.*, *795*, 11, doi:10.1088/0004-637X/795/1/11.

Picone, J. M., A. E. Hedin, D. P. Drob, and A. C. Aikin (2002), NRLMSISE-00 empirical model of the atmosphere: Statistical comparisons and scientific issues, *J. Geophys. Res.*, *107*(A12), 1468, doi:10.1029/2002JA009430.

Porter, H. S., C. H. Jackman, and A. E. S. Green (1976), Efficiencies for production of atomic nitrogen and oxygen by relativistic proton impact in air, *J. Chem. Phys.*, *65*(1), 154, doi:10.1063/1.432812.

Ruffolo, D., et al. (2006), Relativistic solar protons on 1989 October 22: Injection and transport along both legs of a closed interplanetary magnetic loop, *Astrophys. J.*, *639*, 1186–1205.

Sáiz, A., D. Ruffolo, J. W. Bieber, P. Evenson, and R. Pyle (2008), Anisotropy signatures of solar energetic particle transport in a closed interplanetary magnetic loop, *Astrophys. J.*, *672*, 650–658.

United Nations Scientific Committee on the Effects of Atomic Radiation (2008), *Sources and Effects of Ionizing Radiation*, vol. 4, United Nations, New York.

Usoskin, I. G., and G. A. Kovaltsov (2006), Cosmic ray induced ionization in the atmosphere: Full modeling and practical applications, *J. Geophys. Res.*, *111*, D21206, doi:10.1029/2006JD007150.

Usoskin, I. G., G. A. Bazilevskaya, and G. A. Kovaltsov (2011a), Solar modulation parameter for cosmic rays since 1936 reconstructed from ground-based neutron monitors and ionization, *J. Geophys. Res.*, *116*, A02104, doi:10.1029/2010JA016105.

Usoskin, I. G., G. A. Kovaltsov, I. A. Mironova, A. J. Tylka, and W. F. Dietrich (2011b), Ionization effect of solar particle GLE events in low and middle atmosphere, *Atmos. Chem. Phys.*, *11*, 1979–1988.

von Savigny, C., M. Sinnhuber, H. Bovensmann, J. P. Burrows, M.-B. Kallenrode, and M. Schwartz (2007), On the disappearance of noctilucent clouds during the January 2005 solar proton events, *Geophys. Res. Lett.*, *34*, L02805, doi:10.1029/2006GL028106.

The Astrophysical Journal Letters, 852:L26 (6pp), 2018 January 10 https://doi.org/10.3847/2041-8213/aaa407
© 2018. The American Astronomical Society. All rights reserved.

Galactic Cosmic-Ray Anistropy During the Forbush Decrease Starting 2013 April 13

U. Tortermpun[1], D. Ruffolo[1], and J. W. Bieber[2]
[1] Department of Physics, Faculty of Science, Mahidol University, Bangkok 10400, Thailand; usanee.tor@gmail.com, david.ruf@mahidol.ac.th
[2] Bartol Research Institute, Department of Physics and Astronomy, University of Delaware, Newark, DE 19716, USA; jwbieber@bartol.udel.edu
Received 2017 November 1; revised 2017 December 22; accepted 2017 December 26; published 2018 January 9

Abstract

The flux of Galactic cosmic rays (GCRs) can undergo a Forbush decrease (FD) during the passage of a shock, sheath region, or magnetic flux rope associated with a coronal mass ejection (CME). Cosmic-ray observations during FDs can provide information complementary to in situ observations of the local plasma and magnetic field, because cosmic-ray distributions allow remote sensing of distant conditions. Here we develop techniques to determine the GCR anisotropy before and during an FD using data from the worldwide network of neutron monitors, for a case study of the FD starting on 2013 April 13. We find that at times with strong magnetic fluctuations and strong cosmic-ray scattering, there were spikes of high perpendicular anisotropy and weak parallel anisotropy. In contrast, within the CME flux rope there was a strong parallel anisotropy in the direction predicted from a theory of drift motions into one leg of the magnetic flux rope and out the other, confirming that the anisotropy can remotely sense a large-scale flow of GCRs through a magnetic flux structure.

Key words: cosmic rays – Sun: coronal mass ejections (CMEs) – turbulence

1. Introduction

Variations in the distribution of Galactic cosmic rays (GCRs) can provide useful information on the properties of the solar wind plasma and interplanetary magnetic field (IMF) that complement in situ measurements. These energetic charged particles from outside the solar system gyrate around a local magnetic field and undergo scattering from magnetic fluctuations with a mean-free path of $\gtrsim$0.1 au (Chhiber et al. 2017), and can reflect or drift due to magnetic structures. Therefore, they can provide remote sensing of magnetic structures and turbulent fluctuations over such distances (Bieber & Evenson 1998).

Some of the most interesting structures in the solar wind are caused by coronal mass ejections (CMEs). The ejecta often include a magnetic flux rope with strong and smoothly structured magnetic fields and special plasma properties compared with the ambient solar wind (see Richardson & Cane 1993, and references therein), including lower turbulence levels and weak pitch-angle scattering of particles (Burlaga et al. 1981; Tranquille et al. 1987). Thus inside a CME flux rope, GCRs can provide particularly effective remote information. A CME frequently drives a shock in front, with a sheath region between the shock and CME, where magnetic fluctuations from the upstream solar wind have been compressed and further fluctuations have been excited. The arrival of such shocks at Earth can mark the start of geomagnetic storms and various space weather effects of practical importance.

The GCR flux has long been known to decrease along with geomagnetic storms (Forbush 1937), e.g., in association with the arrival of a CME and/or interplanetary shock. Such a decrease is known as a Forbush decrease (FD). The anisotropy of GCRs has also been investigated (see Cane 2000, and references therein). For example, the anisotropy perpendicular to the large-scale magnetic field, as observed by the Global Muon Detector Network, has been interpreted as a gradient anisotropy and used to infer GCR gradients and the properties of magnetic flux ropes (Kuwabara et al. 2004, 2009). A CME flux rope typically has a clear boundary separating external field lines from the internal field lines that form closed loops connecting back to the Sun at both ends (Vandas et al. 1996). Hence the field line random walk across the flux rope boundary is suppressed, as is the perpendicular diffusion of particles, and indeed when a CME passes Earth, it is generally found to contain the lowest GCR flux of the FD (Cane 2000). Therefore, Krittinatham & Ruffolo (2009) considered that particles mostly enter or exit the loop by guiding center drifts. Each flux rope leg should have a roughly conical shape, and the GCR drift is inward along the leg where the field line winding is counterclockwise (CCW, viewing from the wide part of the cone) and outward along the other leg with clockwise (CW) winding. They predicted that this should lead to a unidirectional anisotropy of GCRs parallel to the magnetic field during an FD.

With this motivation, in the present work, we have developed techniques to analyze the GCR anisotropy using neutron monitors (NMs) in the worldwide network. For polar NMs, the FD is dominated by cosmic-ray protons of $\sim$10 GeV (which for $B = 5$ nT as typical in the solar wind at Earth orbit have a gyroradius of $\sim$0.04 au), whereas for muon detectors the characteristic energy is $\sim$30 GeV (with gyroradius of $\sim$0.13 au; Leerungnavarat et al. 2003). Thus the different detectors can probe different interplanetary structures and transport processes. We were also motivated to look for the unidirectional parallel anisotropy proposed by Krittinatham & Ruffolo (2009). As a case study, we have examined a strong FD starting on 2013 April 13, for which NM profiles clearly exhibited strong diurnal variations, indicating a strong anisotropy for which we could develop our techniques. This FD is associated with a CME observed at the Sun on 2013 April 11 (Lario et al. 2014; Vemareddy & Zhang 2014), and the CME flux rope structure as it passed Earth has been determined (Vemareddy & Mishra 2015; Vemareddy et al. 2016).

2. Data Analysis

2.1. Data

To accurately determine the three-dimensional anisotropy before and during the FD, we used data from 19 NM stations

Table 1
Sources of Neutron Monitor Data

NM Location	Geographic Latitude (deg)	Geographic Longitude (deg)	Cutoff Rigidity P_c (GV)	Median Rigidity P_m (GV)
Thule, Greenland	76.60	−68.80	0.00	17.2
Fort Smith, Canada	60.02	−111.93	0.00	17.2
Peawanuck, Canada	54.98	−85.44	0.00	17.2
Barentsburg, Russia	78.68	14.22	0.00	17.2
McMurdo, Antarctica	−77.95	166.60	0.00	17.2
Nain, Canada	56.55	61.68	0.01	17.2
South Pole, Antarctica	−90.00	0.00	0.09	17.2
Inuvik, Canada	68.35	−133.72	0.18	17.2
Mawson, Antarctica	−67.60	62.88	0.22	17.2
Cape Schmidt, Russia	68.92	−179.47	0.45	17.2
Tixie Bay, Russia	71.60	128.90	0.48	17.2
Norilsk, Russia	69.26	88.05	0.58	17.2
Apatity, Russia	67.55	33.33	0.65	17.2
Oulu, Finland	65.02	25.50	0.81	17.2
Sanae, Antarctica	−70.30	−2.35	1.06	17.3
Newark, USA	39.70	−75.70	1.97	17.4
Kiel, Germany	54.30	10.10	2.29	22.9
Moscow, Russia	−34.42	19.22	4.90	27.4
Doi Inthanon, Thailand	18.59	98.49	16.80	35.5

with good statistics and no major data gaps during mid-April of 2013, covering a wide distribution in latitude and longitude. Table 1 lists these NM stations and their geographic locations, along with our calculation using the techniques of Lin et al. (1995) of the effective vertical geomagnetic cutoff rigidity (P_c) and mean rigidity (P_m) of detected GCR ions, where rigidity is $P = pc/q$ for particles of momentum p and charge q, with c as the speed of light. Note that there is also an atmospheric cutoff of ∼1 GV, which we impose via the NM differential response function. The NM data were obtained from the Neutron Monitor Database,[3] which also has more details about the stations.

Figure 1 shows hourly count rates of nine selected NM stations during 2013 April 13–18. Each NM count rate indicates the GCR flux from a certain set of asymptotic viewing directions at rigidities above P_c, where a station code and P_c in units of GV are indicated to the right of each trace. The vertical axis is a relative logarithmic axis with different NM station rates offset for clarity; one minor tick corresponds to a 2.3% change. (We do not compare count rates on a finer timescale because of statistical fluctuations.) For each station, a horizontal solid line indicates the mean count rate during a fixed pre-FD reference period (2013 April 12). The FD is evident as a decrease in the count rate of each station, and the details of the decrease depend on the viewing direction and P_c, with a weaker decrease for higher P_c.

The vertical dashed lines in Figure 1 indicate approximate times at Earth passage of an interplanetary shock (S, blue line), the most intense magnetic fluctuations before and after the CME ejecta (B1 and B2, orange lines), and the leading and trailing edges of the CME ejecta (R1 and R2, purple lines). Times of S, R1, and R2 were 22:50 UT on April 13, 17:35 UT on April 14, and 19:20 UT on April 15, respectively, based on data from the *Wind* spacecraft (Vemareddy & Mishra 2015). We determined the times of B1 and B2 as 05:24 UT on April 14 and 20:44 UT on April 15, from local maxima in magnetic fluctuations as reported by the *Advanced Composition Explorer*

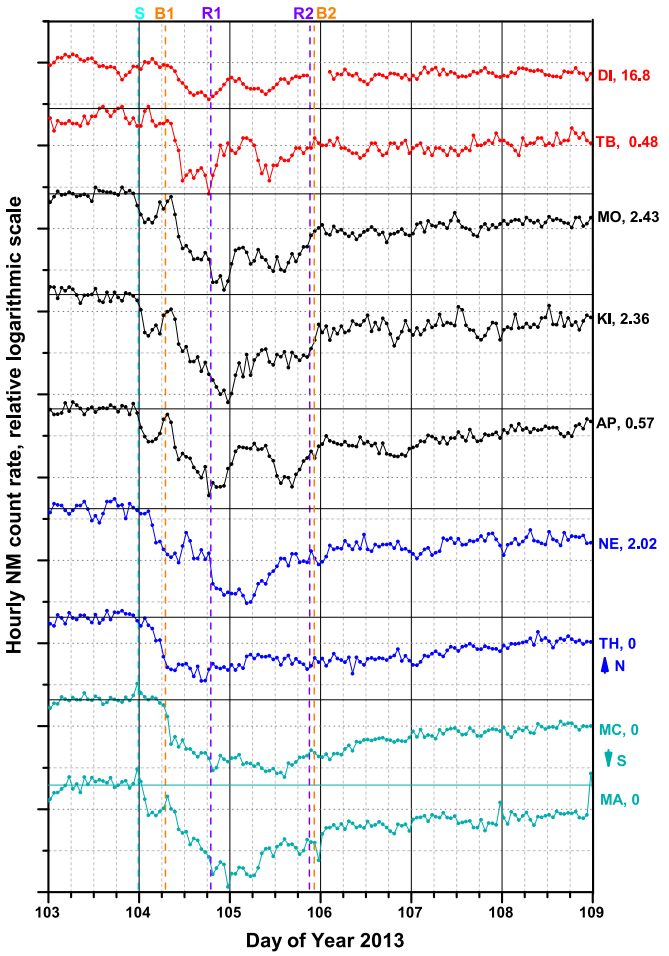


Figure 1. Hourly count rates from selected NM stations before and during a Forbush decrease, on 2013 April 13–18. Each station's count rate indicates the cosmic-ray flux from a set of asymptotic viewing directions, above the local cutoff rigidity. Notation at the right of the plot indicates the station code (first letters of two words in station name, or first two letters of a one-word name) and geomagnetic cutoff rigidity in GV. Arrows at the right indicate that asymptotic directions at Thule (TH) are mostly northward and those at McMurdo (MC) are mostly southward. Grouping of stations, indicated by color of traces, is based on asymptotic directions. Vertical dashed lines indicate approximate times at Earth passage of shock (blue), start and end of CME ejecta (purple), and peaks in magnetic fluctuations (orange).

(*ACE*) spacecraft. Both *Wind* and *ACE* were near the Sun–Earth L1 Lagrange point, located 0.01 au Sunward of Earth, so for convenience of comparison, all five times are indicated one hour later on our plots of NM data, to roughly account for the solar wind travel time from L1 to Earth (greater accuracy is not needed for the comparison with hourly NM data). The NM data in Figure 1 are grouped according to similar viewing directions, for stations in Asia (red), Europe (black), North America (dark blue), and Antarctica (light blue).

We also used Level 2 data from the *ACE* spacecraft[4] for the root-mean-squared magnetic fluctuation ($\Delta B_{\rm rms}$), and the magnitude (B) and geocentric solar-ecliptic (GSE) z-component (B_z) of the IMF. For the solar wind speed ($|V_{\rm sw}|$), we used data from the *Wind* spacecraft.[5]

[3] http://www.nmdb.eu

[4] http://www.srl.caltech.edu/ACE/ASC/

[5] https://wind.nasa.gov/data_sources.php

2.2. Determination of First-order Anisotropy

Our goal is to provide an independent determination of the three-dimensional first-order anisotropy for each hour during a period before and during the FD. Initially, we normalized each count rate to the pre-FD reference period, estimated a fractional decrease $D(t)$ (explained shortly) for polar NM stations for each hour, and performed a least squares fit to all count rates for that hour, with fit parameters as the anisotropy components along GSE coordinates with x toward the Sun and z along ecliptic north. However, the results were not physically reasonable. In particular, during quiescent times before and after the FD, when count rates exhibited a steady diurnal anisotropy indicative of a small and steady anisotropy, the fit results included a strong and spurious equatorial anisotropy rotating with the Earth.

We identified two reasons for this: (1) When comparing with a fixed reference time before the FD, the count rate at a given station may not decrease according to the trend expected from other stations. Previous work comparing different NM count rates found systematic deviations from the expected ratio over timescales of a few days, including during FDs (see Figure 1 of Ruffolo et al. 2016). In our initial fitting technique, any such mismatch is fit in the same way as an anisotropy feature, and such mismatches will rotate with Earth. (2) In the distribution of NM asymptotic directions, polar directions in geographic (GEO) coordinates are under-represented. This makes it difficult for the fit to distinguish between a fixed north–south anisotropy and a rotating equatorial anisotropy.

Our new procedure successfully avoids such effects. We first consider a pair of NM stations (Thule and McMurdo) selected to have asymptotic directions near Earth's poles and similar equatorial components, so their difference indicates the GEO z-component of anisotropy. Then we fit data from all stations to determine the two-dimensional equatorial anisotropy.

Following the usual usage in ground-based cosmic-ray studies, we define the direction of an anisotropy vector as the look direction for which we see the highest cosmic-ray flux (which is opposite the flow direction in space). Then the first-order cosmic-ray anisotropy in Earth's reference frame is $\boldsymbol{\xi} = \boldsymbol{\delta} + \boldsymbol{\chi}$, where $\boldsymbol{\delta}$ is the first-order anisotropy in the solar wind frame, $\boldsymbol{\chi}(P) = -\gamma(P)\boldsymbol{u}/v$ is the Compton-Getting anisotropy (Compton & Getting 1935; Forman 1970), and $\boldsymbol{u}$ is the solar wind velocity relative to the observer. Here $\gamma(P) \equiv d(\log f)/d(\log p)$ and v is the particle speed, both of which depend on the rigidity P. Also, p is the particle momentum and f is the phase space density. We evaluate $\gamma(P)$ from $f \propto \Phi/(vp^2)$, where Φ is the differential rigidity spectrum of cosmic-ray protons from Aguilar et al. (2015). Because of its rigidity dependence, we have included the Compton-Getting effect before integrating over rigidity. We have insufficient data to constrain the rigidity dependence of $\boldsymbol{\delta}$, and other than Doi Inthanon, all NMs in our fit have similar mean rigidities, so we include components of $\boldsymbol{\delta}$ as rigidity-independent parameters determined by the data.

In general, we model the count rate of NM station n at a given time (hour) t using

$$A_n(t) \equiv \sum_{l=0}^{8} w_l \int_{P_{\mathrm{min},n}}^{P_{\max}} \left(-\frac{dN(P_c)}{dP_c}\bigg|_P \right) T_{n,l}(P) \frac{P}{D(t)+P} \times \{1 + [\delta_x(t) + \chi_x(t,P)] n_{n,x}(t,P) + [\delta_y(t) + \chi_y(t,P)] n_{n,y}(t,P) + [\delta_z(t) + \chi_z(t,P)] n_{n,z}(t,P)\} dP. \quad (1)$$

To account for different arrival directions, we sum over nine directions, labeled $l = 0$–8, with a weight w_l that is $1/2$ for the vertical direction and $1/16$ for eight directions at zenith angle 30° with azimuthal angles equally spaced from 22°.5 to 337°.5 (Bieber et al. 1997). Also, $N(P_c)$ represents the count rate (integral response function) of an NM as a function of the cutoff (threshold) rigidity P_c. Thus its negative derivative is the differential response function. For $N(P_c)$, we use the Dorman function fit to latitude survey data of Nuntiyakul et al. (2014) for survey year 2004–2005, for which the modulation of GCRs at polar NMs due to solar activity was similar to that during 2013 (see their Figure 1). The transmission function is $T_{n,l}(P) = 1$ when our trajectory tracing indicates that cosmic rays can arrive at this t, P, and l, and is 0 otherwise. We use $P/[D(t) + P]$, for P in units of GV, as a simple non-negative model of the rigidity-dependent fractional change in GCR flux due to an FD (a function that is poorly known). This form, for which the GCR flux $\propto P^{-1}$ at $P \gg 1$ GV, is motivated by reports that FDs observed at different P_c have a maximum decrease with a power law $\propto P_c^{-\gamma}$ for $\gamma = 0.4$–1.2 (Cane 2000). Our analysis mostly includes polar NM stations with a constant atmospheric cutoff at ∼1 GV so this form does not strongly affect the results. Finally, the expression in braces accounts for the first-order anisotropy, using $\boldsymbol{n}_n$ as the unit vector along the asymptotic direction in space for which a cosmic ray of a given rigidity can pass through Earth's magnetic field to arrive at station n at a given time and arrival direction, which is calculated using the techniques of Lin et al. (1995). For computational convenience, the integration is performed between station-dependent limits where the integrand is non-negligible.

Then, for reasons described above, we evaluate $\delta_z(t)$ in GEO coordinates, i.e., the north–south anisotropy, using the normalized count rates at Thule, $T(t)$, and McMurdo, $M(t)$:

$$\frac{T(t) - M(t)}{2\mathcal{P}(t)} = \frac{\sum_{l=0}^{8} w_l \int_{1\ \mathrm{GV}}^{P_{\max}} \left(-\frac{dN(P_c)}{dP_c}\Big|_P \right) \frac{P}{D(t)+P} [\delta_z(t) + \chi_z(t,P)][n_{T,z}(t,P) - n_{M,z}(t,P)] dP}{2\sum_{l=0}^{8} w_l \int_{1\ \mathrm{GV}}^{P_{\max}} \left(-\frac{dN(P_c)}{dP_c}\Big|_P \right) \frac{P}{D(t)+P} dP}. \quad (2)$$

Here $\mathcal{P}(t)$ refers to the average count rate of 13 polar stations (the first 13 listed in Table 1), which is taken to average over asymptotic directions. For these stations, the geomagnetic cutoff rigidity P_c is well below the atmospheric cutoff at ∼1 GV, so we start the integration there and the transmission function is taken to be $T_{n,l}(P) = 1$. Then Equation (2) allows us to algebraically determine $\delta_z(t)$ from the Thule and McMurdo NM data.

When determining the equatorial GEO anisotropy (the x- and y-components), to avoid fitting a count rate mismatch unrelated

to anisotropy as mentioned above, we compare a normalized hourly NM count rate C_n from station n at time t with a "daily average" rate that is designed to average over the daily wave and is defined as

$$C_{n,da}(t) = \frac{1}{2}\left[C_n + \frac{C_n^- + C_n^+}{2} - \frac{1}{4}\left(\frac{C_n^{--} + C_n^{++}}{2} - C_n\right)\right], \quad (3)$$

where C_n^{--}, C_n^-, C_n^+, and C_n^{++} represent the count rates of the same NM station at times $t - 24$ hr, $t - 12$ hr, $t + 12$ hr, and $t + 24$ hr. This formula is based on a model that $C_n(t)$ varies as a second-order polynomial (parabola) plus a daily sinusoidal wave due to Earth's rotation and equatorial GCR anisotropy (the effect of poleward anisotropy is included in the polynomial). With that assumption, $C_{n,da}$ is the normalized count rate due to the parabolic trend with no effect of equatorial anisotropy.

Then for a given time (hour) t, we simultaneously fit $C_n(t)/C_{n,da}(t)$ for all stations to determine the GEO anisotropy components δ_x and δ_y. Our fit equation at each hour is

$$\frac{C_n(t)}{C_{n,da}(t)} = \frac{A_n(t)}{B_n(t)}, \quad (4)$$

where $A_n(t)$ is given by Equation (1), and $B_n(t)$ models the daily average over equatorial directions by removing the equatorial anisotropy terms from $A_n(t)$:

$$B_n(t) \equiv \sum_{l=0}^{8} w_l \int_{P_{\min,n}}^{P_{\max}} \left(-\frac{dN(P_c)}{dP_c}\bigg|_P\right) T_{n,l}(P) \frac{P}{D(t) + P} \times \{1 + [\delta_z(t) + \chi_z(t, P)] n_{n,z}(t, P)\} dP. \quad (5)$$

Figure 2 displays our results for the components of $\boldsymbol{\delta}$ in GSE coordinates. From this figure, we can see the level of fluctuation in the components of $\boldsymbol{\delta}$, including that during quiescent times in the first half of day of year (DOY) 103 and the second half of DOY 108.

3. Results and Discussion

There are various effects that could contribute to $\boldsymbol{\delta}$, including the following. (1) Parallel diffusive anisotropy. In addition to the general inflow of GCRs from the outer heliosphere, the GCR flux decrease has been attributed to inhibited parallel diffusion, e.g., a diffusive barrier at the shock (e.g., Wibberenz et al. 1998). Precursory anisotropy before an FD (e.g., Nagashima et al. 1992; Fushishita et al. 2010) can exhibit unusual pitch-angle distributions attributed to parallel scattering effects (Ruffolo 1999; Leerungnavarat et al. 2003). (2) Parallel flow, as proposed by Krittinatham & Ruffolo (2009), within a CME flux rope. (3) Perpendicular diffusive anisotropy, due to cosmic-ray scattering and diffusion perpendicular to the large-scale magnetic field (Shalchi 2010; Ruffolo et al. 2012). In particular, Cane et al. (1995) proposed that GCRs enter a closed CME flux rope via perpendicular diffusion. (4) Perpendicular guiding center drifts (Kadokura & Nishida 1986). (5) Gradient anisotropy due to particle gyration, with the magnitude given by the gyroradius times fractional particle density gradient, also perpendicular to the large-scale field (Kuwabara et al. 2004, 2009). To determine which effects explain the first-order anisotropy in the solar wind frame for this FD, we resolve $\boldsymbol{\delta}$ into components perpendicular and parallel to the magnetic field. The magnitudes of these components, $\delta_\perp$ and $\delta_\parallel$, respectively, are shown in Figure 3 in comparison with IMF and solar wind parameters.

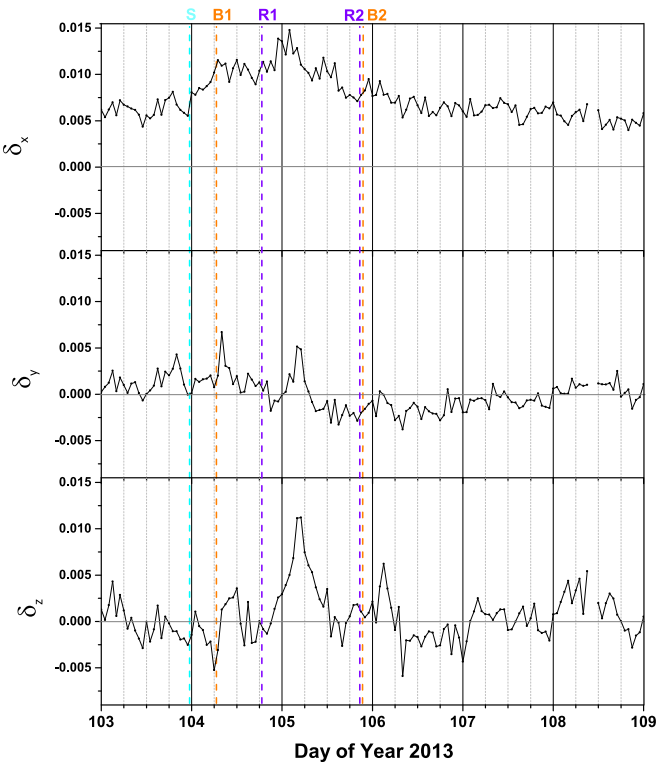


Figure 2. Cosmic-ray first-order anisotropy in the solar wind frame during 2013 April 13–18 as derived from 19 NM count rates. Vertical dashed lines indicate event times at Earth as in Figure 1.

First, note that $\delta_\perp$ was stronger before time S (shock arrival) and after B2 (trailing edge of CME). In fact, during those times $\boldsymbol{\delta}$ was mostly antisunward and did not reverse with the various magnetic reversals. This conflicts with perpendicular drift or gradient anisotropy, which should reverse when $\boldsymbol{B}$ reverses, and favors diffusive anisotropy. Further support for a diffusive origin of $\delta_\perp$ comes from the general decrease in $\delta_\perp$ between S and R2, when B was much stronger and diffusion should be weaker. Exceptions were times of relatively strong fluctuation $\Delta B_{\rm rms}$ near S, B1, and B2, with local spikes of strong $\delta_\perp$. Theories of the perpendicular diffusion coefficient (Shalchi 2010; Ruffolo et al. 2012) predict that it increases with increasing $\Delta B_{\rm rms}/B$, so these spikes again support a diffusive origin of $\delta_\perp$.

Because the gradient anisotropy is proportional to the particle gyroradius, it may play a greater role at higher rigidity than used in the present analysis. For example, the NM station at Doi Inthanon has the world's highest vertical cutoff rigidity ($\approx$17 GV), and enhanced trains of diurnal anisotropy were attributed to gradient anisotropy (Yeeram et al. 2014). For much higher median rigidity, the Global Muon Detector Network reported analyses interpreting perpendicular anisotropy during FDs as due to gradient anisotropy (Kuwabara et al. 2004, 2009). In contrast, here we find that at the lower median rigidity for typical NMs, the perpendicular anisotropy during this FD can be attributed to diffusive effects.

Turning to $\delta_\parallel$, Figure 3 shows that stronger magnetic fluctuations are associated with lower $\delta_\parallel$, as in the sheath region between S and R1, and inside the CME where fluctuations were very weak, $\delta_\parallel$ was quite strong. This is consistent with theoretical expectations that strong fluctuations

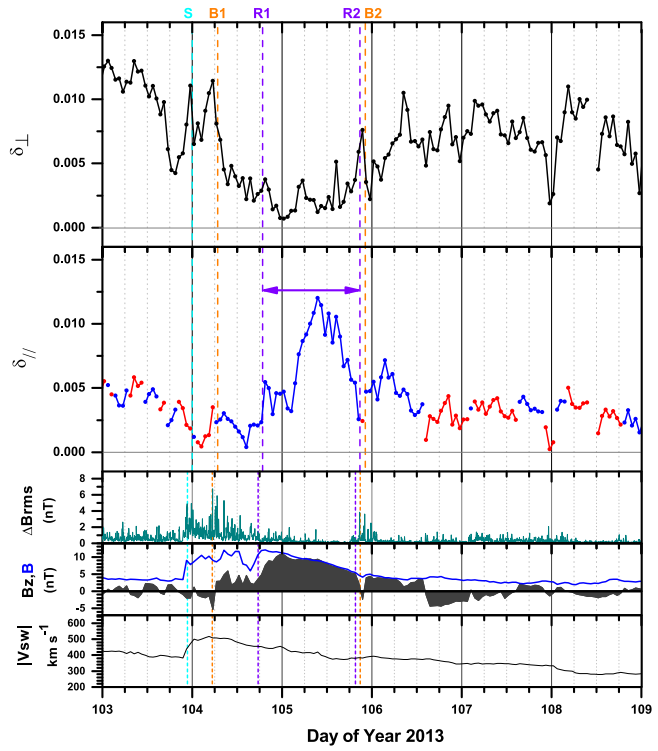


Figure 3. Cosmic-ray first-order anisotropy magnitude in the solar wind frame perpendicular ($\delta_\perp$) and parallel ($\delta_\parallel$) to the interplanetary magnetic field (IMF) during 2013 April 13–18 as derived from 19 NM count rates, as well as the rms magnetic fluctuation ($\Delta B_{\rm rms}$) from *ACE*/MAG, the IMF magnitude (B) and GSE z-component (B_z) from *ACE*/MAG, and the solar wind speed ($|V_{\rm sw}|$) from *Wind*/SWE. Vertical dashed lines in the two upper panels indicate event times at Earth as in Figure 1; those in the three lower panels indicate event times at *Wind* (at the L1 point). For $\delta_\parallel$, the color indicates a higher GCR flux when viewing along $\boldsymbol{B}$ (blue) or along $-\boldsymbol{B}$ (red). Times of strong IMF fluctuation (blue and orange dashed lines) correspond to spikes of high $\delta_\perp$ and to low $\delta_\parallel$, as expected from transport theory, indicating that anisotropy during these times was dominated by scattering and diffusion. During the period when CME ejecta passed Earth, indicated by a purple arrow, there was a strong field-aligned anisotropy, with higher GCR flux when viewing to ecliptic north, matching the prediction of Krittinatham & Ruffolo (2009).

lead to strong cosmic-ray scattering and a low parallel diffusion coefficient, and is consistent with the idea that a GCR flux decrease after the shock (in the sheath region) is due to a parallel diffusive barrier (Wibberenz et al. 1998). The $\delta_\parallel$ trace in Figure 3 indicates a higher GCR flux when viewing along $\boldsymbol{B}$ (blue) or $-\boldsymbol{B}$ (red). The color changes with almost every reversal of B_z, which is consistent with standard parallel scattering and flow processes that do not depend on the sign of $\boldsymbol{B}$. Inside the CME, there was a strong GCR enhancement when viewing toward ecliptic north.

According to the geometry inferred by Vemareddy & Mishra (2015) from observations of the CME flux rope that passed Earth on 2013 April 14–15 (see Figure 4), the flux rope was oriented with one leg north of the ecliptic plane and the other to the south, with CCW winding along the northern leg and CW winding along the southern leg. Thus the theory of Krittinatham & Ruffolo (2009) predicts that guiding center drifts lead to cosmic-ray inflow along the northern leg and outflow along the southern leg, leading to a parallel anisotropy at Earth with GCR flow from the north (Figure 4), which is consistent with our present observations. This agreement

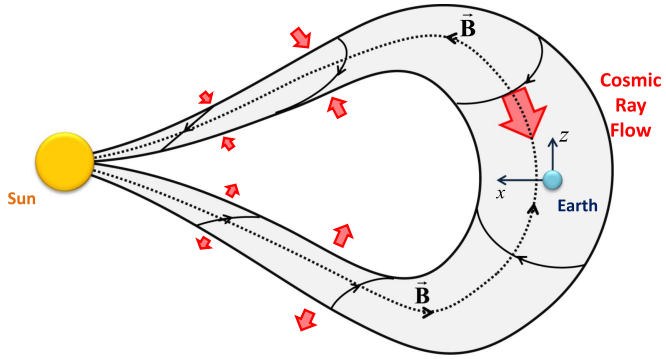


Figure 4. Illustration of the CME flux rope configuration at the time of Earth passage on 2013 April 14–15, following Vemareddy & Mishra (2015), indicating GSE x- and z-coordinates, and the prediction of Krittinatham & Ruffolo (2009) as applied to this event, in which cosmic rays enter the flux rope along the CCW (northern) leg and exit along the CW (southern) leg, leading to a unidirectional flow anisotropy from the north. The observed parallel anisotropy shown in Figure 3 confirms this prediction, supporting the model that cosmic rays enter and exit a Sun-connected flux rope due to guiding center drifts.

supports the idea that GCR flows across the boundary of a closed CME flux rope are mainly due to guiding center drifts.

Note that this information from remote sensing about the large-scale drift motion of GCRs into and out of the CME flux rope is not available by other means, and it addresses the larger issue of how a closed magnetic flux rope, newly ejected by a CME, is accessed by the external GCR population and how the FD recovers.

In summary, we have developed techniques to examine the GeV-range cosmic-ray anisotropy during an FD by fitting data from numerous NM stations worldwide, for an example case of the FD starting 2013 April 13. In contrast with the interpretation of observations at higher rigidity, we demonstrate that perpendicular anisotropy features can be attributed to diffusive effects. Outside the CME flux rope, the parallel anisotropy can be attributed to diffusive effects, which is consistent with the diffusive barrier concept for the sheath-region GCR decrease. Inside the closed flux rope where magnetic fluctuations and cosmic-ray scattering are very weak, we observe a strong unidirectional parallel flow as predicted by a model in which GCRs drift into the flux rope along one leg and out along the other, with the anisotropy providing remote sensing of those processes.

This research was supported by Royal Golden Jubilee Fellowship PHD/0112/2551 and grant RTA5980003 from the Thailand Research Fund. U.T. and D.R. thank the University of Delaware for their hospitality during the formative stages of this work. We thank the Neutron Monitor Database and operators of all NM stations who freely provided their data. We also thank the *ACE* MAG instrument team and the *ACE* Science Center for providing the *ACE* data, and the *Wind* SWE instrument team for providing the *Wind* data.

ORCID iDs

U. Tortermpun https://orcid.org/0000-0003-3703-4389
D. Ruffolo https://orcid.org/0000-0003-3414-9666

References

Aguilar, M., Aisa, D., Alpat, B., et al. 2015, PhRvL, 114, 171103
Bieber, J. W., Clem, J., & Evenson, P. 1997, Proc. ICRC (Durban), 2, 389
Bieber, J. W., & Evenson, P. 1998, GeoRL, 25, 2955

Burlaga, L. F., Hundhausen, A. J., & Zhao, X.-P. 1981, JGR, 86, 8893
Cane, H. V. 2000, SSRv, 93, 55
Cane, H. V., Richardson, I. G., & Wibberenz, G. 1995, Proc. ICRC (Rome), 4, 377
Chhiber, R., Subedi, P., Usmanov, A. V., et al. 2017, ApJS, 230, 21
Compton, A. H., & Getting, I. A. 1935, PhRv, 47, 817
Forbush, S. E. 1937, PhRv, 51, 1108
Forman, M. A. 1970, P&SS, 18, 25
Fushishita, A., Kuwabara, T., Kato, C., et al. 2010, ApJ, 715, 1239
Kadokura, A., & Nishida, A. 1986, JGR, 91, 13
Krittinatham, W., & Ruffolo, D. 2009, ApJ, 704, 831
Kuwabara, T., Bieber, J. W., Evenson, P., et al. 2009, JGR, 114 A05109
Kuwabara, T., Munakata, K., Yasue, S., et al. 2004, GeoRL, 31, L19803
Lario, D., Raouafi, N. E., Kwon, R.-Y., et al. 2014, ApJ, 797, 8
Leerungnavarat, K., Ruffolo, D., & Bieber, J. W. 2003, ApJ, 593, 587
Lin, Z., Bieber, J. W., & Evenson, P. 1995, JGR, 100, 23543
Nagashima, K., Fujimoto, K., Sakakibara, S., Morishita, I., & Tatsuoka, R. 1992, P&SS, 40, 1109
Nuntiyakul, W., Evenson, P., Ruffolo, D., et al. 2014, ApJ, 795, 11
Richardson, I. G., & Cane, H. V. 1993, JGR, 98, 15295
Ruffolo, D. 1999, ApJ, 515, 787
Ruffolo, D., Pianpanit, T., Matthaeus, W. H., & Chuychai, P. 2012, ApJL, 747, L34
Ruffolo, D., Sáiz, A., Mangeard, P.-S., et al. 2016, ApJ, 817, 38
Shalchi, A. 2010, ApJL, 720, L127
Tranquille, C., Sanderson, T. R., Marsden, R. G., Wenzel, K.-P., & Smith, E. J. 1987, JGR, 92, 6
Vandas, M., Fischer, S., Dryer, M., Smith, Z., & Detman, T. 1996, JGR, 101, 2505
Vemareddy, P., & Mishra, W. 2015, ApJ, 814, 59
Vemareddy, P., Möstl, C., Amerstorfer, T., et al. 2016, ApJ, 828, 12
Vemareddy, P., & Zhang, J. 2014, ApJ, 797, 80
Wibberenz, G., le Roux, J. A., Potgieter, M. S., & Bieber, J. W. 1998, SSRv, 83, 309
Yeeram, T., Ruffolo, D., Sáiz, A., Kamyan, N., & Nutaro, T. 2014, ApJ, 784, 136

Monthly Notices of the ROYAL ASTRONOMICAL SOCIETY

MNRAS **473,** 4544–4557 (2018) doi:10.1093/mnras/stx2606
Advance Access publication 2017 October 9

Relative distribution of cosmic rays and magnetic fields

Amit Seta,[1]★ Anvar Shukurov,[1] Toby S. Wood,[1] Paul J. Bushby[1] and Andrew P. Snodin[2]

[1]*School of Mathematics, Statistics and Physics, Newcastle University, Newcastle Upon Tyne, NE1 7RU, UK*
[2]*Department of Mathematics, Faculty of Applied Science, King Mongkut's University of Technology North Bangkok, Bangkok 10800, Thailand*

Accepted 2017 October 4. Received 2017 September 28; in original form 2017 August 9

ABSTRACT

Synchrotron radiation from cosmic rays is a key observational probe of the galactic magnetic field. Interpreting synchrotron emission data requires knowledge of the cosmic ray number density, which is often assumed to be in energy equipartition (or otherwise tightly correlated) with the magnetic field energy. However, there is no compelling observational or theoretical reason to expect such a tight correlation to hold across all scales. We use test particle simulations, tracing the propagation of charged particles (protons) through a random magnetic field, to study the cosmic ray distribution at scales comparable to the correlation scale of the turbulent flow in the interstellar medium ($\simeq$100 pc in spiral galaxies). In these simulations, we find that there is no spatial correlation between the cosmic ray number density and the magnetic field energy density. In fact, their distributions are approximately statistically independent. We find that low-energy cosmic rays can become trapped between magnetic mirrors, whose location depends more on the structure of the field lines than on the field strength.

Key words: dynamo – MHD – scattering – cosmic rays – ISM: magnetic fields – radio continuum: ISM.

1 INTRODUCTION

Synchrotron emission is the main source of information about the non-thermal components of the interstellar and intergalactic medium (ISM and IGM). Its interpretation depends crucially on the relative distribution of magnetic fields and cosmic ray electrons. Cosmic rays tend to gyrate around magnetic field lines, so it is natural to expect some correlation between the cosmic ray and magnetic energy densities. On sufficiently long length- and time-scales, the cosmic ray distribution may achieve energy equipartition (Burbidge 1956), or pressure balance, with the magnetic field (see review by Beck & Krause 2005). Although the assumption of a tight, point-wise correlation between cosmic rays and magnetic fields across a wide range of scales lacks a compelling justification, it is often used in interpretations of synchrotron observations, regardless of the spatial resolution. Most of the energy of cosmic rays is carried by protons and heavier particles, therefore, such interpretations rely on an additional assumption that relativistic electrons are distributed similarly to the heavier cosmic ray particles.

The diffusivity of 5 GeV cosmic rays in a 5 μG magnetic field is believed to be about 10^{28}–10^{29} cm^2 s^{-1}, implying a diffusion length of the order of 1 kpc over the time-scale of cosmic ray confinement in galaxies, 10^6 yr (Berezinskii et al. 1990). This suggests that the cosmic ray distribution will be significantly more uniform than that of the interstellar magnetic field, which varies strongly on scales smaller than 0.1 kpc (Ruzmaikin, Sokoloff & Shukurov 1989; Beck et al. 1996). However, cosmic rays are more tightly confined to field lines where the field is strongest, and so we might still expect some positive correlation between cosmic ray density and magnetic energy on small scales. On the other hand, overall pressure balance can, equally plausibly, lead to local anticorrelation between cosmic ray and magnetic energy densities (Beck et al. 2003). Indeed, from a comparison of the observed and modelled magnitude of the fluctuations in synchrotron intensity in the Milky Way and nearby spiral galaxies, Stepanov et al. (2014) suggested that cosmic ray electrons and interstellar magnetic fields are slightly anticorrelated at scales $\lesssim$100 pc.

Large-scale simulations of cosmic ray propagation in the advection–diffusion approximation rely on various (often crude) parametrizations of the diffusion tensor and its dependence on the magnetic field. Using a fluid description of cosmic rays in non-linear dynamo simulations, assuming anisotropic (but constant) diffusion coefficients, Snodin et al. (2006) found no correlation between magnetic field and cosmic ray energy densities. Such simulations may be appropriate at scales exceeding the diffusion length (of the order of 1 kpc), but not at the smaller scales that are relevant in this study. For a typical cosmic ray proton, with energy 1–10 GeV, in a 5 μG magnetic field, the Larmor radius is about 10^{-6}–10^{-5} pc, which is much smaller than the correlation length of a magnetic field (50–100 pc) or the diffusion length of cosmic rays (which is of the order of 1 kpc). Thus, the small-scale structure of the magnetic field will

★ E-mail: a.seta1@ncl.ac.uk

© 2017 The Authors
Published by Oxford University Press on behalf of the Royal Astronomical Society

Downloaded from https://academic.oup.com/mnras/article-abstract/473/4/4544/4411829
by Library - Faculty of Medicine Ramathibodi Hospital user
on 27 June 2018

be particularly important for the propagation of cosmic rays in this energy range.

In this paper, we use test particle simulations to explore, in detail, the spatial distribution of cosmic ray particles propagating in a random magnetic field. Whereas previous test particle simulations have been mostly concerned with the calculation of the cosmic ray diffusion coefficient, we primarily consider the spatial distribution of cosmic rays and its relation to the magnetic field. Our model is kinematic, i.e. we only consider the effect of the magnetic field on the cosmic rays and neglect any effects of cosmic ray pressure on the gas flow and hence on the magnetic field. In Section 2, we describe the numerical model for random magnetic fields, and in Section 3 we present our model for simulating cosmic ray propagation. Our results on cosmic ray density and its relation to the magnetic field are presented in Section 4. We conclude in Section 5 and suggest further avenues for study.

2 IMPLEMENTATION OF RANDOM MAGNETIC FIELDS

The propagation of cosmic rays is sensitive to rather subtle details of the magnetic field in which they move. The spectrum provides a complete statistical description of a Gaussian random magnetic field, so it must also determine the corresponding cosmic ray diffusivity for a given energy of particle. The propagation of cosmic rays in an isotropic Gaussian random magnetic field (for which the probability distribution function of each vector component is Gaussian) has been the subject of many studies (Berezinskii et al. 1990; Michalek & Ostrowski 1997; Giacalone & Jokipii 1999; Casse, Lemoine & Pelletier 2002; Schlickeiser 2002; Candia & Roulet 2004; Parizot 2004; DeMarco, Blasi & Stanev 2007; Globus, Allard & Parizot 2008; Shalchi 2009; Plotnikov, Pelletier & Lemoine 2011; Harari, Mollerach & Roulet 2014; Snodin et al. 2016; Subedi et al. 2017). However, radio (Gaensler et al. 2011; Haverkorn & Spangler 2013), submillimeter (Zaroubi et al. 2015) and neutral hydrogen (Heiles & Troland 2005; Kalberla & Kerp 2016) observations suggest that the magnetic field in the ISM is strongly non-Gaussian, spatially intermittent and filamentary. Such an intermittent field is also expected theoretically, as a result of turbulent dynamo action (Wilkin, Barenghi & Shukurov 2007) and random shock compression (Bykov & Toptygin 1985, 1987; Bykov 1988). The magnetic field generated by dynamo action in galaxy clusters is also likely to be intermittent (Ruzmaikin, Sokoloff & Shukurov 1989; Subramanian, Shukurov & Haugen 2006). The presence of magnetic intermittency can significantly affect the propagation of cosmic rays (Shukurov et al. 2017). In non-Gaussian fields, the separation and size of magnetic structures may play an important role (Shukurov et al. 2017), especially for low-energy particles. In this section, we describe the magnetic fields that are used in our analysis of cosmic ray propagation. A discussion of the structure of a small-scale interstellar magnetic field can be found in Appendix A. Throughout the text, the small-scale or fluctuating field is represented by $\boldsymbol{b}$, the large-scale (or mean) field by $\boldsymbol{B_0}$ and the total field by $\boldsymbol{B} = \boldsymbol{b} + \boldsymbol{B_0}$.

2.1 Magnetic fields generated by a random flow

For our numerical study, we use a random magnetic field produced by kinematic fluctuation (small-scale) dynamo action. Using a triply periodic cubic box of length L, with 512^3 grid points, we solve the induction equation

$$\frac{\partial \boldsymbol{b}}{\partial t} = \nabla \times (\boldsymbol{u} \times \boldsymbol{b}) + \eta \nabla^2 \boldsymbol{b}, \tag{1}$$

where $\boldsymbol{u}(\boldsymbol{x}, t)$ is a prescribed velocity field and η is the magnetic diffusivity, which we take to be constant. To ensure $\nabla \cdot \boldsymbol{b} = 0$, we numerically solve for the corresponding magnetic vector potential. We define the magnetic Reynolds number to be $R_\mathrm{m} = l_0 u_0/\eta$, where l_0 is the outer scale of the turbulent velocity flow and u_0 is the root-mean-square (rms) velocity. Dynamo action occurs, i.e. the magnetic field grows exponentially, if R_m exceeds a critical magnetic Reynolds number, $R_{\mathrm{m,\,c}}$, whose value depends on the velocity field.

We construct the velocity field, $\boldsymbol{u}$, by superposing Fourier modes with a range of wavenumbers, k, and a chosen energy spectrum $E(k)$, using the same prescription as Fung et al. (1992) and Wilkin et al. (2007):

$$\boldsymbol{u}(\boldsymbol{x}, t) = \sum_{n=0}^{N-1} \left[\boldsymbol{C}_n(\boldsymbol{k}_n) \cos\phi_n + \boldsymbol{D}_n(\boldsymbol{k}_n) \sin\phi_n\right], \tag{2}$$

where $\phi_n = \boldsymbol{k}_n \cdot \boldsymbol{x} + \omega_n t$, $\boldsymbol{k}_n$ is a randomly oriented wavevector of magnitude k_n, and $\omega_n = [k_n^3 E(k_n)]^{1/2}$ is the frequency at that scale. The vectors $\boldsymbol{C}_n(\boldsymbol{k}_n)$ and $\boldsymbol{D}_n(\boldsymbol{k}_n)$ have random directions in the plane perpendicular to $\boldsymbol{k}_n$, so that the flow is incompressible ($\nabla \cdot \boldsymbol{u} = 0$). Their magnitudes determine the power spectrum $E(k)$, and are chosen such that $E(k) \propto k^{-5/3}$ and the rms velocity is u_0. We chose $N = 40$ with $\boldsymbol{k}_n$ such that the flow is periodic, and with distinct k_n between $2\pi/L$ and $8\pi/L$, where $L = 2\pi$ is the width of our domain which is also equal to the outer scale, l_0, of the velocity flow. This flow acts as a dynamo if $R_\mathrm{m} > R_{\mathrm{m,\,c}} \simeq 1000$, and produces a spatially intermittent magnetic field, as can be seen in the left-hand panel of Figs 1 and 2.

The presence of structures in the magnetic field affects the propagation of cosmic rays, especially for low-energy particles. For such particles, intermittency enhances cosmic ray diffusion (Shukurov et al. 2017). Here, we are interested in exploring the correlation between the magnetic field and cosmic rays. The intermittent nature of this dynamo-generated magnetic field provides an excellent test case for this study since there are localized regions of strong magnetic field.

We also consider a Gaussian random magnetic field having the same power spectrum $M_b(k)$ as the intermittent magnetic field. Such a Gaussian random field is obtained as follows: First, a spatial Fourier transform of the intermittent magnetic field is taken and then each complex mode is multiplied with a random phase. Then taking an inverse Fourier transform gives a Gaussian randomized magnetic field with an unchanged $M_b(k)$, but where coherent structures have been destroyed (chapter 7 in Biskamp 2003; Snodin et al. 2013; Shukurov et al. 2017). The structural difference between intermittent and Gaussian random magnetic fields is illustrated in Fig. 1 that shows the magnetic fields in a 2D cut through the middle of the numerical domain, with colours showing the third component. Fig. 2 shows the filamentary structure of the intermittent magnetic field (at b^2/b_rms^2 of the order ten). The probability distribution function of a single component of both the intermittent and randomized fields is shown in Fig. 3. The intermittent field has long heavy tails, whereas the randomized field has a Gaussian probability distribution.

2.2 Large-scale magnetic field

The ISM contains both fluctuating (small-scale) and mean (large-scale) magnetic fields (chapter 5 in Klein & Fletcher 2015; Beck

Downloaded from https://academic.oup.com/mnras/article-abstract/473/4/4544/4411829
by Library - Faculty of Medicine Ramathibodi Hospital user
on 27 June 2018

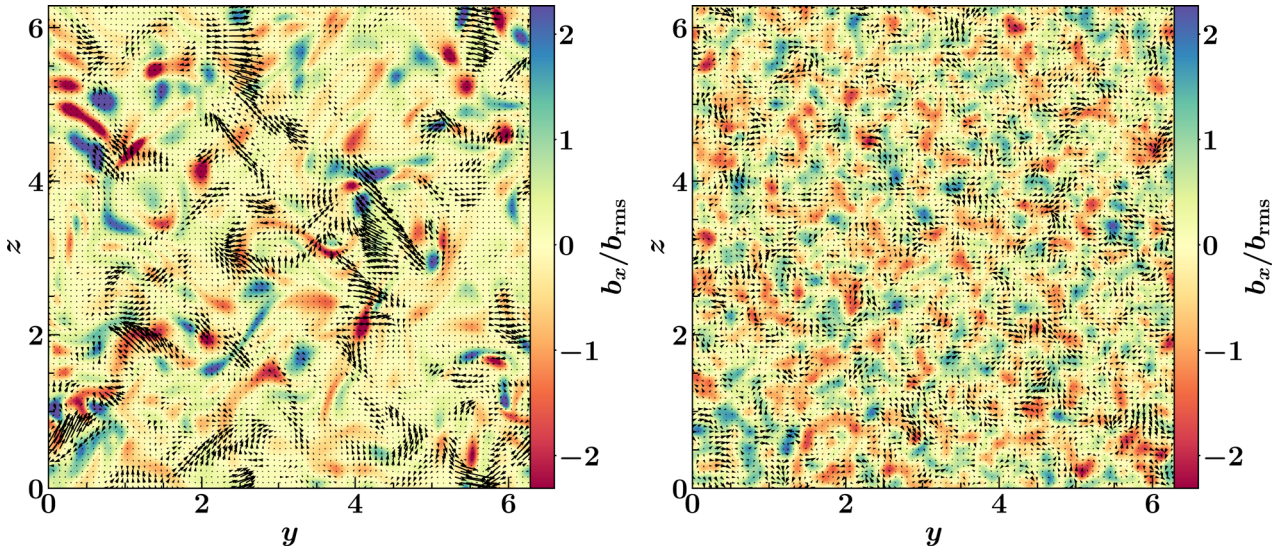


Figure 1. A 2D cut in the yz-plane through the middle of the domain with vectors for ($b_y/\,b_{\rm rms}$, $b_z/\,b_{\rm rms}$) and colours showing the magnitude of $b_x/\,b_{\rm rms}$ for intermittent (left) and randomized (right) magnetic fields. For an intermittent magnetic field, the colours are saturated for both positive and negative values to match the scale of the randomized field (see the x-axis of Fig. 3 for the actual difference in numbers). The intermittent magnetic field is more ordered and stronger in the filaments whereas the randomized field lacks such structures.

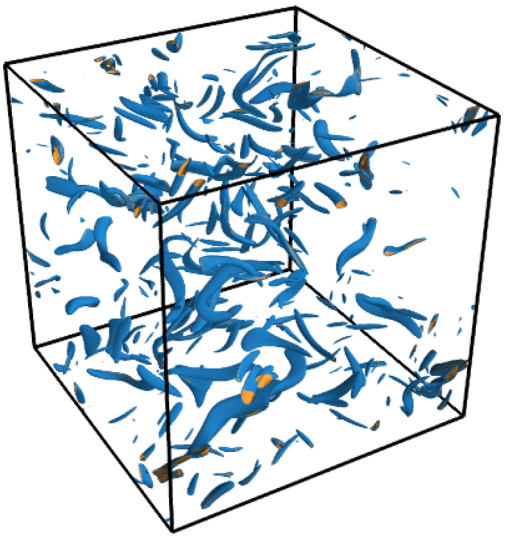


Figure 2. The figure shows isosurfaces of $b^2/\,b^2_{\rm rms} = 12$ (blue) and $b^2/\,b^2_{\rm rms} = 15$ (yellow) for the dynamo-generated magnetic field at $R_{\rm m} = 3182$. It is intermittent, showing long filaments with large gaps between filaments.

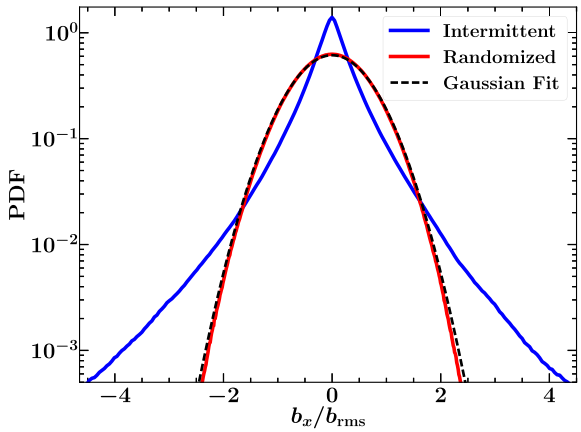


Figure 3. The figure shows PDFs of $b_x/\,b_{\rm rms}$ for intermittent (blue) and randomized (red) magnetic fields. Both have a zero mean but the intermittent magnetic field has long tails whereas the randomized field (obtained by Fourier phase randomization) has a Gaussian PDF (dashed).

et al. 1996; Beck 2016). The large-scale component is correlated over several kpc whereas the small-scale component has a correlation length less than the correlation scale of turbulence ($\lesssim$0.1 kpc). The small-scale and the large-scale components of the magnetic field contain comparable energies. By comparing large-scale magnetic field models (with resolution of $\sim$75 pc) of a spiral galaxy with observations, Moss et al. (2007) found that a spatially uniform distribution of cosmic rays was better at matching the observations than an equipartition assumption between cosmic rays and a large-scale magnetic field. This suggests that the cosmic rays may not be correlated with a large-scale magnetic field.

To explore the effects of a large-scale magnetic field on the propagation of cosmic rays, we add a uniform mean field directed along the x-axis to the random magnetic field as described in Section 2.1. We consider several values for the ratio of the mean field B_0 to the random field, $b_{\rm rms}$, up to $B_0/\,b_{\rm rms} = 3$.

3 COSMIC RAY PROPAGATION

The propagation of cosmic rays in random magnetic fields is largely determined by the ratio between the Larmor radius $r_{\rm L}$ of the particle gyration and the length-scale l_b of magnetic field variations, e.g. its correlation length. The Larmor radius and Larmor frequency of a relativistic particle of rest mass m and charge q, travelling at a speed v in a magnetic field of strength B, are given by

$$r_{\rm L} = \frac{\gamma m c v}{q B} \qquad \text{and} \qquad \omega_0 = \frac{v}{r_{\rm L}}, \tag{3}$$

respectively, where $\gamma = (1 - v^2/c^2)^{-1/2}$ is the Lorentz factor and c is the speed of light in a vacuum. The correlation length l_b of an

Downloaded from https://academic.oup.com/mnras/article-abstract/473/4/4544/4411829
by Library - Faculty of Medicine Ramathibodi Hospital user
on 27 June 2018

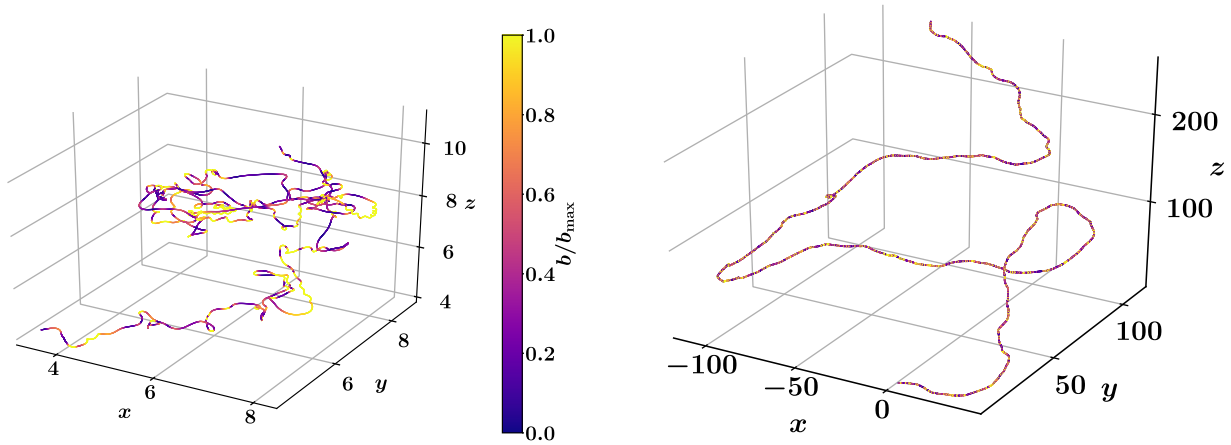


Figure 4. Single particle trajectories for $r_L/l_0 = 0.011$ (left-hand panel) and 0.318 (right-hand panel) in the intermittent magnetic field of the left-hand panel of Figs 1 and 2. Colours show the strength of the magnetic field along the trajectory normalized to its maximum value along the part of trajectory shown. For $r_L/l_0 = 0.011$, the particle path is more tangled than for $r_L/l_0 = 0.318$ where the particle motion is almost ballistic between rare scattering events.

isotropic random field with a power spectrum $M_b(k)$ is defined as (Monin & Yaglom 1971)

$$l_b = \frac{\pi}{2} \frac{\int_0^\infty k^{-1} M_b(k)\,\mathrm{d}k}{\int_0^\infty M_b(k)\,\mathrm{d}k}. \tag{4}$$

The correlation length of a magnetic field produced by the fluctuation dynamo action is significantly smaller than l_0, at least in the kinematic stage where l_b/l_0 is of the order $R_\mathrm{m}^{-1/2}$ (Kazantsev 1967; Zeldovich, Ruzmaikin & Sokoloff 1990; Schekochihin et al. 2004; Brandenburg & Subramanian 2005). For $R_\mathrm{m} = 3182$, we have $l_b/l_0 \approx 0.0244$.

3.1 Test particle simulations of cosmic rays

We consider relativistic charged particles propagating in a static magnetic field, $\boldsymbol{B}(\boldsymbol{x})$. The trajectory of each particle satisfies

$$\frac{\mathrm{d}^2\boldsymbol{r}}{\mathrm{d}t^2} = \frac{v_0}{r_\mathrm{L}} \frac{\mathrm{d}\boldsymbol{r}}{\mathrm{d}t} \times \frac{\boldsymbol{B}}{B_\mathrm{rms}}, \tag{5}$$

where $\boldsymbol{r}$ is the particle's position, v_0 is its speed, $\boldsymbol{B}/B_\mathrm{rms}$ is the total magnetic field normalized to its rms value B_rms and r_L is the Larmor radius (defined with respect to B_rms). The time-scale over which interstellar magnetic fields change significantly is of the order of the eddy turnover time in interstellar turbulence, 10^7 yr (Beck et al. 1996). This time-scale is longer than the (diffusive) confinement time of cosmic rays in galaxies, which is of the order of 10^6 yr (Berezinskii et al. 1990). It is therefore customary to neglect any time dependence of the magnetic field in equation (5) and, correspondingly, neglect any electric fields (e.g. Giacalone & Jokipii 1999; Casse et al. 2002). This means that the speed of each particle remains constant. This is equivalent to neglecting particle acceleration, a process physically distinct from diffusive particle propagation (which is the focus of this article) which is due to scattering of cosmic ray particles by magnetic inhomogeneities. Since we consider a static magnetic field, the diffusive reacceleration (Strong, Moskalenko & Ptuskin 2007; Grenier, Black & Strong 2015), which is due to moving magnetic inhomogeneities, is also neglected.

We solve equation (5) numerically for an ensemble of cosmic ray particles (specifically, 8192), all of the same speed v_0, but giving each a random initial position and velocity direction. The initial conditions are chosen randomly, and are uniformly distributed over all positions and directions, but do not very uniformly fill the magnetic field cube, due to there only being a finite number of particles. For a given energy of particle, we find the smallest Larmor time ($2\pi/\omega_0$) based on the maximum magnetic field in the domain and then fix the time-step as 0.001 times the smallest Larmor time, to ensure that we carefully resolve all particle gyrations. We also check that the energy is conserved (as far as is permitted by the numerical scheme) throughout the total propagation time T. For a given magnetic field configuration, the nature of the trajectories depends only on the parameter r_L/l_0, which is indicative of the particle energy, as illustrated in Fig. 4. By construction, the static magnetic field through which the particle propagates is periodic in all three directions, with a period $L = 2\pi$. Even though the magnetic field is periodic, the particle trajectories are not: they enter and leave the domain at different points. There is an important distinction between the Eulerian frame of the computational domain and the Lagrangian frame moving with each particle. Whilst the magnetic field is periodic in the Eulerian sense, there is no periodicity in the magnetic field along each particle trajectory (however, many times the particle enters and leaves the domain).

A high-energy particle, with $r_\mathrm{L} \gg l_b$, is typically deflected by only a small angle of the order l_b/r_L over a distance l_b and its trajectory is, therefore, rather insensitive to the structural properties of the magnetic field at scales smaller than r_L. By the central limit theorem, the statistical properties of an ensemble of cosmic ray particles become Gaussian after a large number of such deflections. Particles of smaller energies, $r_\mathrm{L} \lesssim l_b$, are more sensitive to the fine structure of the magnetic field, and it is not obvious how the spatial distribution of such cosmic rays will be related to the magnetic energy density, especially given that their diffusion tensor is sensitive to magnetic intermittency (Shukurov et al. 2017). In particular, the distribution of cosmic rays may be intermittent in a spatially intermittent magnetic field. Fig. 4 shows the trajectories of particles of low and high energy (left- and right-hand panels, respectively). The latter move faster (note the different axis scales in the two panels) and, at the scale of the left-hand panel, the trajectory of the higher energy particles is nearly straight almost everywhere.

Downloaded from https://academic.oup.com/mnras/article-abstract/473/4/4544/4411829
by Library - Faculty of Medicine Ramathibodi Hospital user
on 27 June 2018

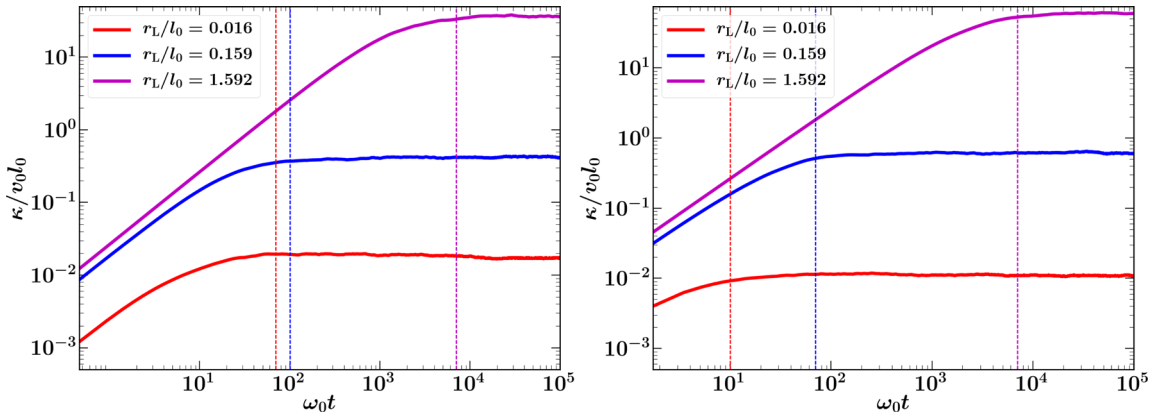


Figure 5. Normalized cosmic ray diffusivity $\kappa/v_0 l_0$ as a function of normalized time $\omega_0 t$ for $r_L/l_0 = 0.016, 0.159, 1.592$ for the intermittent (left) and randomized (right) magnetic fields shown in Fig. 1. Here, $\omega_0 = v_0/r_L$ is the Larmor frequency based on B_{rms}. The dashed lines of the corresponding colours show the time t_d after which the propagation becomes diffusive: $\kappa(t) \approx \kappa$ at $t > t_d$. For low-energy particles ($r_L \leq l_b$), the diffusivity in the intermittent magnetic field is larger than in the randomized (Gaussian) field of an identical power spectrum.

The random nature of the magnetic field makes the particle propagation diffusive at sufficiently large spatial and temporal scales. Without a mean field, the propagation is isotropic. We therefore calculate the isotropic diffusion coefficient as the limit of the finite-time diffusivity $\kappa(t)$,

$$\kappa = \lim_{t\to\infty} \kappa(t), \qquad \kappa(t) = \frac{1}{6t}\langle|\boldsymbol{r}(t) - \boldsymbol{r}(0)|^2\rangle, \tag{6}$$

where the angular brackets denote averaging over the ensemble of particles. Fig. 5 shows $\kappa(t)$ for the two magnetic fields shown in Fig. 1, one intermittent and the other statistically Gaussian, and for several values of r_L/l_0. In each case, there is an initial phase of ballistic particle motion, in which $\kappa(t)$ is approximately linear in t, followed by a diffusive phase where $\kappa(t)$ settles to its asymptotic value. The start of the diffusive phase, t_d, is the time when the slope of $\kappa(t)$ becomes small, $\mathrm{d}\kappa/\mathrm{d}(\omega_0 t) \simeq 10^{-6}$; this time is indicated by a vertical dashed line in Fig. 5.

To obtain the number density of cosmic rays, n_{cr}, from the test particle simulations, we calculate the coordinates of each particle modulo $L = 2\pi$, i.e. relative to the periodic magnetic field. Next, we divide the periodic domain into 512^3 cubes and count the number of particles within each cube. The size of the cubes was chosen to match the spatial resolution of the magnetic field, which was obtained from a dynamo simulation on a 512^3 grid, but we have checked that the results are not very sensitive to the exact size of the cubes. The result is the instantaneous number density of the particles $\tilde{n}(\boldsymbol{x}, t)$. We then average the density of particles within each cube over a sufficiently long period, T ($\gg t_d$), to obtain the cosmic ray density $n_{cr}(\boldsymbol{x}) = (T - t_d)^{-1}\int_{t_d}^{T} \tilde{n}(\boldsymbol{x}, t')\,\mathrm{d}t'$. We have checked that the results are not dependent on the sampling time ($\mathrm{d}t'$) as long as it is smaller than a few times the Larmor time ($2\pi/\omega_0$). But for a lower sampling rate, the simulation has to be averaged over a longer total time (higher T) to collect sufficient statistics. We note that different energies were simulated over different periods T to obtain roughly the same $\langle n_{cr}(\boldsymbol{x})\rangle$ for all energies.

3.2 Magnetic field at the Larmor scale

Cosmic ray particles are especially sensitive to magnetic fluctuations at a scale comparable to their Larmor radius. As described by Kulsrud (2005), when a cosmic ray particle encounters such a magnetic fluctuation, its pitch angle θ, defined via

$$\mu \equiv \cos\theta = \frac{\boldsymbol{v}\cdot\boldsymbol{B}}{|\boldsymbol{v}||\boldsymbol{B}|}, \qquad \boldsymbol{v} = \frac{\mathrm{d}\boldsymbol{r}}{\mathrm{d}t}, \tag{7}$$

changes by

$$\delta\theta = -\pi\frac{\delta B}{B}\cos\chi, \tag{8}$$

where $\delta B/B$ is the ratio of the fluctuation amplitude at the Larmor scale to the local mean magnetic field (i.e. the field averaged over a scale significantly larger than r_L), and χ is the relative phase between the cosmic ray velocity vector and the wavevector of the magnetic fluctuation with which the particle interacts.

Magnetic fluctuations at the Larmor scale can be a part of a magnetic energy spectrum that extends from larger scales or be excited by cosmic rays themselves via the streaming instability (Kulsrud & Pearce 1969; Wentzel 1974; Kulsrud 2005). The latter are usually referred to as 'self-generated waves'. The scattering due to magnetic fluctuations at the Larmor scale is referred to as pitch angle scattering (PAS), and Desiati & Zweibel (2014) stress its importance for cosmic ray diffusion. The magnitude of the magnetic fluctuations that are associated with PAS due to self-generated waves is estimated in Appendix B as $\delta B/B \simeq 10^{-2}$ in the hot interstellar gas.

The spectrum of hydromagnetic turbulence in the ISM extends to very small scales. Schekochihin et al. (2009) suggest that the spectrum of kinetic Alfvén waves is truncated by dissipation at scales as small as the thermal electron Larmor radius, which is approximately 3×10^6 cm in the warm ionized ISM. This scale is much smaller than the Larmor radius of the relativistic particles of cosmic rays. However, the spectrum of Alfvén wave turbulence is rather steep: $k^{-5/3}$ at larger scales (above 1 pc – Brandenburg & Subramanian 2005) where the gas is collisional and, at smaller scales, $k_\parallel^{-2}$ for the perturbations parallel to the magnetic field (which matter for the cosmic ray scattering – Farmer & Goldreich 2004). For such steep spectra, the relative magnitude of the magnetic fluctuations at the Larmor radius of a 5 GeV particle is of the order of $\delta B/B \simeq 10^{-4}$, which is negligible in comparison with the self-generated waves.

Within our model, the magnetic field is imposed and the streaming instability cannot occur. We therefore parametrize the cosmic ray

Downloaded from https://academic.oup.com/mnras/article-abstract/473/4/4544/4411829
by Library - Faculty of Medicine Ramathibodi Hospital user
on 27 June 2018

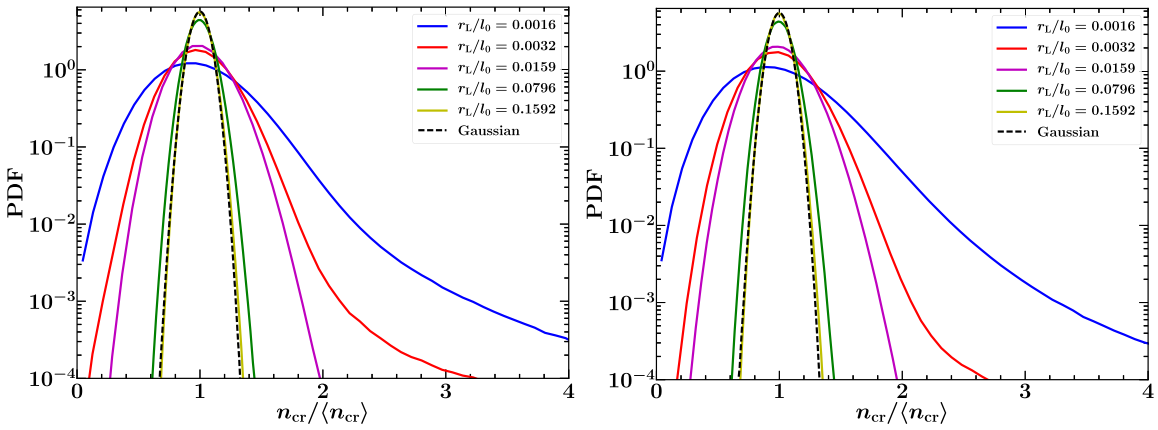


Figure 6. PDF of the relative number density of cosmic ray particles, $n_{\rm cr}/\langle n_{\rm cr}\rangle$, for various $r_{\rm L}/l_0$ in intermittent (left-hand panel) and randomized (Gaussian) magnetic fields (right-hand panel), with no mean field and no PAS. Long tails are a signature of intermittent structures in the cosmic ray distribution. For high-energy particles, the distribution is nearly Gaussian (with width increasing as energy decreases) in both intermittent and Gaussian magnetic fields, but below a certain energy ($r_{\rm L} \lesssim l_b$) long tails develop. A black dashed line shows the PDF of a random variable drawn from a Gaussian distribution with a unit mean value and a standard deviation of 0.07.

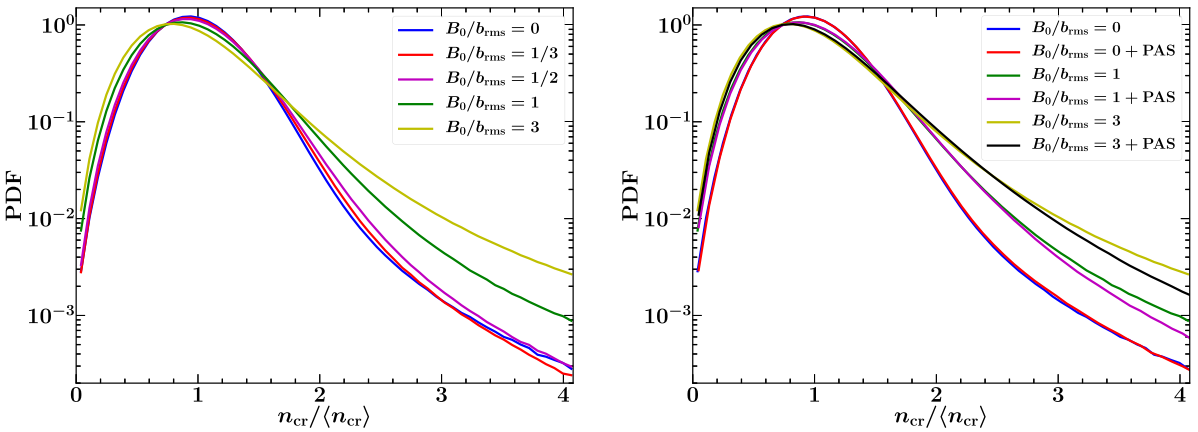


Figure 7. PDF of $n_{\rm cr}/\langle n_{\rm cr}\rangle$ for $r_{\rm L}/l_0 = 0.0016$ in the intermittent field of Fig. 2 with an imposed mean field of various magnitudes B_0 (left-hand panel) and with the PAS further included (right-hand panel). Intermittency in the cosmic ray distribution increases as the mean field becomes stronger, especially for $B_0/\,b_{\rm rms} \geq 1$, manifested in heavier tails at larger $n_{\rm cr}/\langle n_{\rm cr}\rangle$. The PAS enhances diffusion and thus decreases the level of intermittency.

scattering by self-generated waves. This is done by rotating the velocity vector of each particle every Larmor time ($2\pi/\omega_0$) by an angle given by equation (8), with $\delta B/B = 10^{-2}$ and χ uniformly distributed between 0 and 2π. Throughout the text, this is referred to as PAS.

4 RESULTS

Fig. 6 shows the probability density function (PDF) of the particle number density $n_{\rm cr}$ obtained in intermittent and randomized (Gaussian) magnetic fields. For cosmic rays of relatively high energy ($r_{\rm L}/l_b > 1$ or $r_{\rm L}/l_0 > 0.0244$), the number density $n_{\rm cr}$ is very nearly uniform in space, and its PDF is Gaussian. At lower energies, the PDF has a long, heavy tail, which signifies the presence of spatially localized structures in the cosmic ray distribution. It is remarkable that the distribution of cosmic rays is intermittent in both intermittent and Gaussian magnetic fields. The PDF of $n_{\rm cr}$ on including mean magnetic fields of various strength, with (right-hand panel) and without (left-hand panel) particle PAS, is shown in Fig. 7. Here too, for low energies the cosmic ray number density distribution has a long tail.

4.1 Spatial intermittency of cosmic rays

Cosmic rays fill all the volume available. However, the distribution for low-energy cosmic rays (especially for $r_{\rm L}/l_0 = 0.0016$ or $r_{\rm L}/l_b \simeq 0.06$) is not homogeneous. Random magnetic fields produce cosmic ray distributions where a significant fraction of the volume is occupied by strong particle concentrations. The PDFs of $n_{\rm cr}$ shown in Fig. 6 have a Gaussian core and a heavy tail, a manifestation of the spatial intermittency. The core contains most of the particles and has $n_{\rm cr}$ close to its mean value. The tail represents rare but intense small-scale spatial structures. Fig. 8 shows the number density of cosmic rays, obtained as described in Section 3.1, in the intermittent magnetic field shown in the left-hand panel of Figs 1 and 2. The distribution is inhomogeneous and evidently sensitive to the magnetic field structure. The distribution of cosmic rays is affected by both the mean magnetic field and PAS. As shown in Fig. 7, the mean magnetic field enhances the intermittency in the cosmic ray distribution, whereas PAS reduces it. Fig. 9 illustrates how the shape and number of structures in the cosmic ray distribution are affected. With a mean field, the structures are more numerous and many extend along the mean field direction, aligned with the x-axis in the example shown. This effect becomes significant when

Downloaded from https://academic.oup.com/mnras/article-abstract/473/4/4544/4411829
by Library - Faculty of Medicine Ramathibodi Hospital user
on 27 June 2018

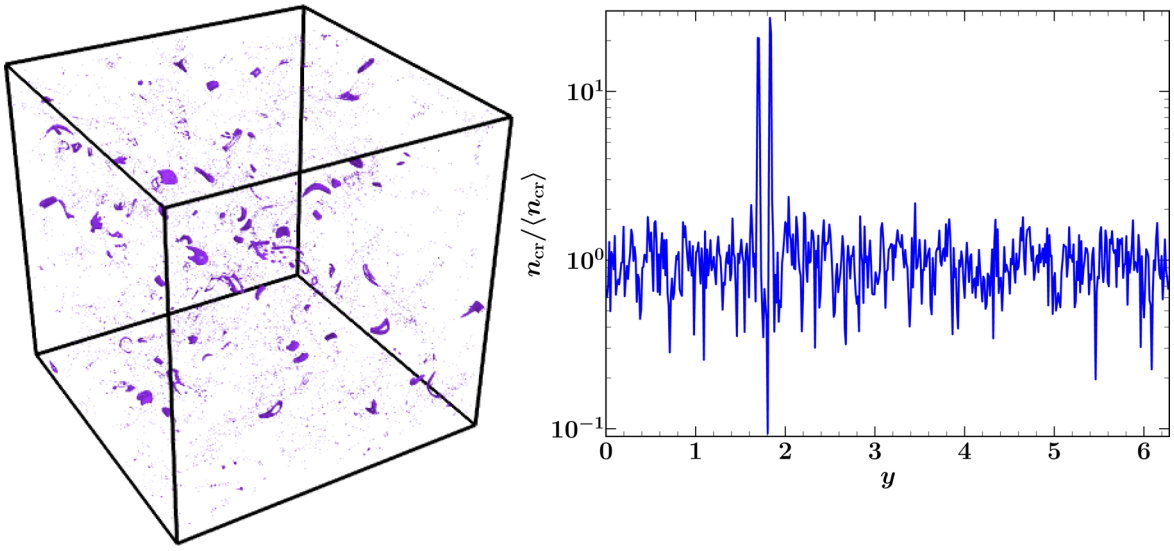


Figure 8. Isosurfaces of the number density of cosmic rays at $n_{cr}/\langle n_{cr}\rangle = 3.5$ for $r_L/l_0 = 0.0016$ in an intermittent magnetic field showing a highly inhomogeneous distribution (left-hand panel). The right-hand panel shows the variation of the relative number density of the particles along the straight line $(x, z) = (\pi, 3.97)$, characterized by rare, strong maxima against a weakly fluctuating background.

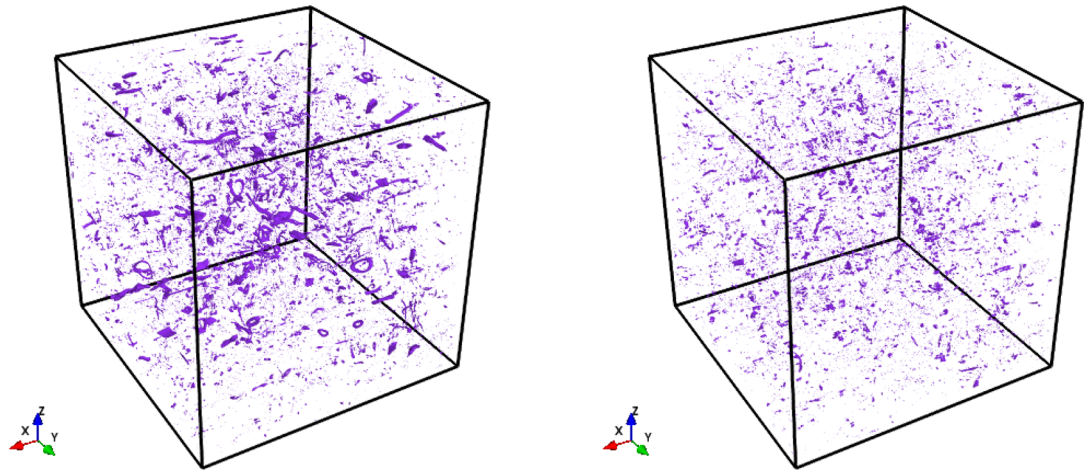


Figure 9. Isosurfaces of the number density of cosmic rays at $n_{cr}/\langle n_{cr}\rangle = 3.5$ for $r_L/l_0 = 0.0016$ in an intermittent magnetic field with an imposed mean field of a strength $B_0/\,b_{rms} = 1$ aligned with the x-axis (left-hand panel) and with PAS further added (right-hand panel).

Table 1. Representative selection of simulations, summarizing the effects of particle energy, magnetic field structure and PAS. All quantities are defined in the text.

Model	r_L/l_0	$\boldsymbol{b}$	$B_0/\,b_{rms}$	PAS	f
A	0.0016	Intermittent	0	no	0.81
B	0.0016	Intermittent	1	no	0.68
C	0.0016	Intermittent	1	yes	0.84
D	0.0016	Randomized	0	no	0.96
E	0.1592	Intermittent	0	no	0.99

$B_0/\,b_{rms} \geq 1$. On the other hand, PAS enhances cosmic ray diffusion and, consequently, reduces their intermittency, as shown in the right-hand panel of Fig. 9. The degree of intermittency can be measured in terms of the parameter $f = \langle n_{cr}\rangle^2/\langle n_{cr}^2\rangle$ (see Table 1). For high-energy particles, $r_L/l_0 = 0.1592$ or $r_L/l_b \simeq 6.52$, and f is close to unity, indicating a homogeneous particle distribution. This feature of the cosmic ray distribution is further detailed in Fig. 10

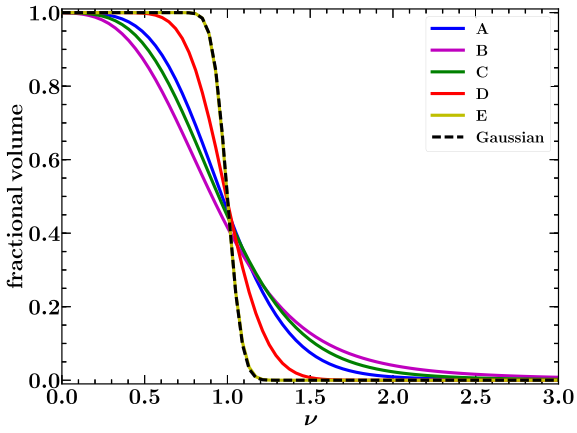


Figure 10. The fractional volume of cosmic ray structures with $n_{cr}/\langle n_{cr}\rangle \geq \nu$ for Models A–E of Table 1. A black dashed line shows the fractional volume for a random variable drawn from a Gaussian distribution with a unit mean value and a standard deviation of 0.07.

Downloaded from https://academic.oup.com/mnras/article-abstract/473/4/4544/4411829
by Library - Faculty of Medicine Ramathibodi Hospital user
on 27 June 2018

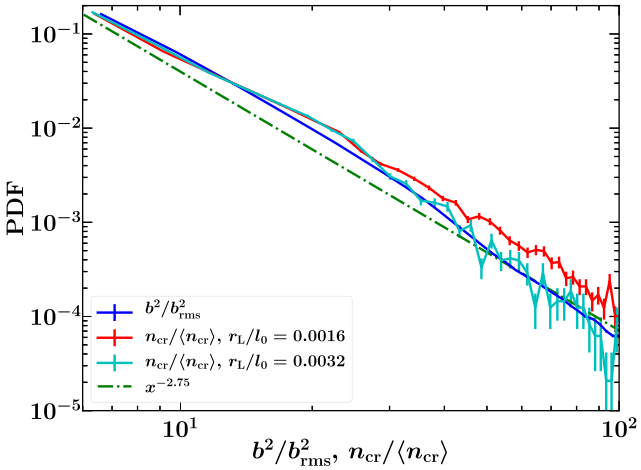


Figure 11. PDF of intermittent magnetic field energy density normalized to its rms value, $b^2/b^2_{\rm rms}$, and the number density of cosmic rays normalized to its mean, $n_{\rm cr}/\langle n_{\rm cr}\rangle$, for $r_{\rm L}/l_0 = 0.0016$, 0.0032. All three of them have power-law tails and the same exponent. Statistical errors are considerable at probability densities below about $\lesssim 5 \times 10^{-5}$.

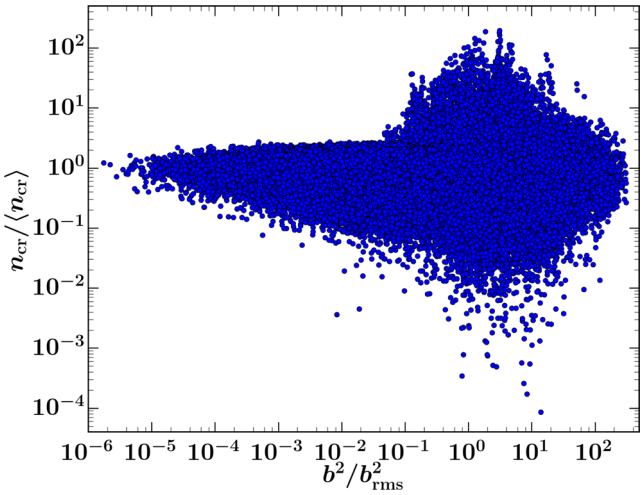


Figure 12. The scatter plot of cosmic ray number density, $n_{\rm cr}/\langle n_{\rm cr}\rangle$, and magnetic energy density, $b^2/b^2_{\rm rms}$, in an intermittent magnetic field for $r_{\rm L}/l_0 = 0.0016$.

where we show the dependence of the fractional volume of a region where $n_{\rm cr}/\langle n_{\rm cr}\rangle \geq \nu$ on ν for the configurations of Table 1. Particles of sufficiently high energy, $r_{\rm L}/l_b \gg 1$, are not sensitive to the fine structure of the magnetic field and the probability distribution of their number density is Gaussian. The dependence of the fractional volume, shown in Fig. 10, on the presence of the mean magnetic field and its change due to PAS confirms that the spatially intermittency increases on including a mean field and decreases on including PAS. Fig. 11 shows the PDF of magnetic field energy density and cosmic ray distribution for the tail region (values higher than the mean for each of the distributions). Both distributions are power laws and the exponent for the magnetic field roughly matches that for the cosmic ray number density. The cosmic ray distribution for low-energy particles is intermittent with heavy power-law tails.

4.2 Statistical relation between magnetic field and cosmic rays

The simplest measure of a relation between cosmic rays and a magnetic field is their cross-correlation coefficient,

$$C(n_{\rm cr}, B^2) = \frac{\overline{n_{\rm cr} B^2} - \overline{n}_{\rm cr}\overline{B^2}}{\sigma_{n_{\rm cr}}\sigma_{B^2}}, \qquad (9)$$

where the overbar denotes an average over the whole domain and σ is the standard deviation of the quantity specified in the subscript. The value of C ranges from $C = 1$ for a perfect correlation to $C = -1$ for a perfect anticorrelation. In all cases considered, we find that the two distributions are uncorrelated, $C \approx 0$. This is true even for the lowest energy cosmic rays considered ($r_{\rm L}/l_0 = 0.0016$), despite the fact that they are closely confined to magnetic lines. The correlation does not emerge even when the cosmic ray density and magnetic field are smoothed to a coarser spatial grid. To confirm that this behaviour is not an artefact of the initial conditions used for the cosmic ray particles, we have also performed a simulation with their initial positions in the regions of the strongest magnetic field shown in Fig. 2. The value of C in this case is very close to unity initially but vanishes quickly, within the time $t_{\rm d}$.

Fig. 12 shows the scatter plot of the cosmic ray number density and magnetic field energy density, whose form confirms that the two variables are uncorrelated. We also confirm that cosmic rays and magnetic field distributions are statistically independent. As demonstrated in Appendix C (where more details can be found), the joint probability distribution function of cosmic rays and magnetic field distributions, $p(n_{\rm cr}, b^2)$, can be factorized as follows:

$$p(n_{\rm cr}, b) \approx (1.6 + 9.9{\rm e}^{-10.5 b^2/b^2_{\rm rms}}){\rm e}^{-(n_{\rm cr}/\langle n_{\rm cr}\rangle - 1)^2/0.18}, \qquad (10)$$

for the intermittent magnetic field and

$$p(n_{\rm cr}, b) \approx 0.5(b^2/b^2_{\rm rms})^{-1}{\rm e}^{-0.3\ln(b^2/b^2_{\rm rms})^2}{\rm e}^{-(n_{\rm cr}/\langle n_{\rm cr}\rangle - 0.9)^2/0.32}, \qquad (11)$$

for the randomized (Gaussian) magnetic field. In both cases, the joint PDF is separable which illustrates that the cosmic rays and magnetic field distributions are independent in the diffusive regime of the cosmic rays.

4.3 Random magnetic traps

Since $n_{\rm cr}$ is not correlated with the magnetic field strength, the regions of high cosmic ray density must instead be caused by some geometrical property of the magnetic field lines. In fact, we find that these regions occur where cosmic rays become trapped between two magnetic mirrors, i.e. positions where magnetic lines converge. As shown in Fig. 13, if a magnetic flux tube is pinched at both ends, then particles are repeatedly reflected between the two ends, creating a 'magnetic trap'. Because the field lines must be reasonably smooth in order to form a trap, the regions of high cosmic ray density are typically smaller than the magnetic correlation length, l_b. The cosine of the particle's pitch angle, μ, defined in equation (7), is shown in the right-hand panel of Fig. 13 as a function of position and magnetic field strength. This quantity reverses sign along the trajectory whenever the particle is reflected at an end of the magnetic trap. This happens where the magnetic field is relatively strong. Magnetic trapping is associated with the conservation of $v_\perp^2/B$, an adiabatic invariant (Jackson 1998), where $v_\perp = v\sin\theta$ is the particle speed perpendicular to the local magnetic field. We have verified that $v_\perp^2/B =$ constant with relative accuracy of the order of 10^{-5} along the trajectories of the trapped particles.

We estimate the enhancement of cosmic ray number density due to magnetic traps as follows. Consider a magnetic trap of a length l

Downloaded from https://academic.oup.com/mnras/article-abstract/473/4/4544/4411829
by Library - Faculty of Medicine Ramathibodi Hospital user
on 27 June 2018

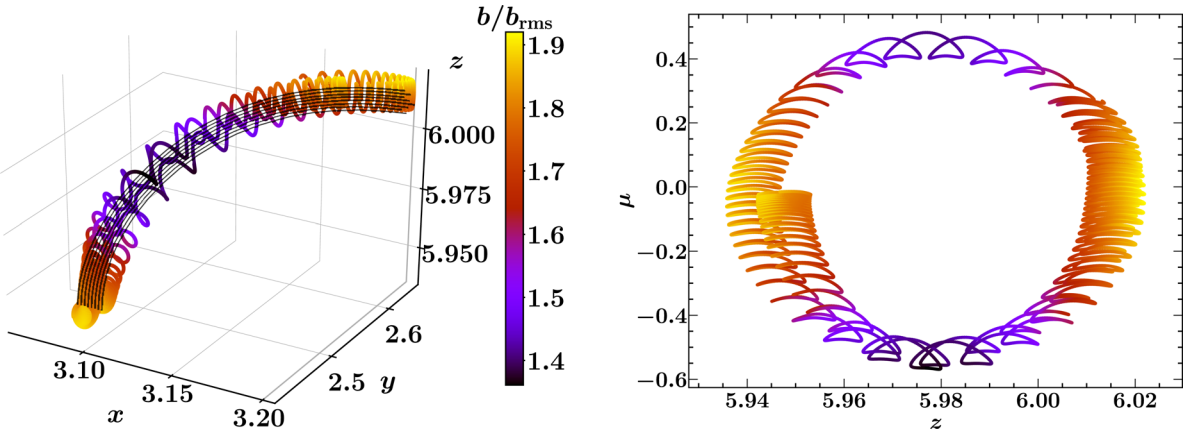


Figure 13. The left-hand panel shows a particle trajectory with magnetic field strength along the trajectory shown with colour. The dark grey lines show magnetic field lines near the trajectory. The particle moves forward and backward between two magnetic mirrors. The right-hand panel shows the angle between the particle velocity vector and the z-axis with magnetic field strength colour coded. The particle turns around (μ changes sign) at the magnetic mirrors, regions where the magnetic field is stronger.

in a magnetic flux tube of a radius d. For an ensemble of particles within the trap, the expected trapping time τ is $d^2/\kappa_\perp$, where $\kappa_\perp$ is the local transverse diffusivity of cosmic rays. Defining N to be the number of times that a particle travels along the trap before leaving it, we expect $N \sim \tau v/l$. The resulting number density of particles within the trap is given by $n_0 = N\overline{n}_{\rm cr}$ with $\overline{n}_{\rm cr}$ the mean number density of cosmic rays. The number density of the particles within the trap is as follows:

$$n_0 \simeq \frac{vd^2}{l\kappa_\perp}\overline{n}_{\rm cr}. \tag{12}$$

According to this order of magnitude estimate, we therefore expect that the number of trapped particles will depend inversely upon the local cosmic ray diffusivity as well as upon the size and number of traps.

A mean magnetic field introduces a specific direction which particles follow and so increases the probability for a magnetic trap to occur, as shown in the left-hand panel of Fig. 9. On the other hand, the PAS due to self-generated waves decreases the level of intermittency in the cosmic ray number density, as shown in the right-hand panel of Fig. 9, because it facilitates the transverse diffusion. When the distribution on the right-hand panel of Fig. 9 is smoothed over a coarser scale, it does not correlate with the distribution on the left-hand panel of Fig. 9. This further illustrates that the PAS not only reduces the length of trapping region but also changes the propagation of particles significantly.

It is important to note that the spatial intermittency of cosmic rays does not require the intermittent structure of the random magnetic field. Even in the randomized magnetic field, which has almost perfect Gaussian statistics and is free of intermittency, magnetic traps occur and lead to a spatial intermittency of cosmic rays.

5 CONCLUSIONS AND DISCUSSION

Using test particle simulations of cosmic ray propagation, we have demonstrated that the spatial distribution of cosmic rays is not correlated with magnetic field strength on spatial scales that are less than (or comparable to) the outer scale, l_0, of a random flow that produces a magnetic field. This implies that the local equipartition between cosmic ray and magnetic field energy densities does not occur on these scales. In fact, we find that cosmic ray number density and magnetic field are approximately statistically independent.

At high energies, $r_{\rm L} > l_b$ with l_b the correlation length of the magnetic field, the cosmic ray distribution is uniform. At low energies, $r_{\rm L} < l_b$, the spatial distribution of cosmic rays is intermittent in both Gaussian and non-Gaussian (spatially intermittent) magnetic fields. This occurs because of the presence of magnetic traps in random magnetic fields where the local magnetic field has a specific structure but is not necessarily strong. As a result, the cosmic ray number density is not directly related to the local magnetic field strength.

The trapping and the ensuing intermittency in the cosmic ray distribution are enhanced by a mean magnetic field and reduced by the PAS of cosmic ray particles or any other additional diffusion. The number density of cosmic ray particles within the traps depends on the size of the trap and the transverse diffusivity of cosmic rays with respect to the local magnetic field. Statistical properties of the traps (such as their rate of occurrence, size, etc.) are controlled by subtle properties of the random magnetic field; it appears that finding them is a non-trivial probabilistic problem.

For cosmic rays to become trapped, their Larmor radius must be smaller than the correlation length of the magnetic field, i.e. $r_{\rm L} \leq l_b$. In spiral galaxies, where $l_b \lesssim 100\,{\rm pc}$, the proton energy in a 5 μG field with $r_{\rm L} = 100\,{\rm pc}$ is 10^8 GeV. Thus, the trapping of cosmic rays described above should be effective and efficient for galactic cosmic rays. In galaxy clusters, with $l_b \lesssim 10\,{\rm kpc}$ and $b \simeq 1\,\mu{\rm G}$, protons of energy up to 10^9 GeV can be trapped and thus exhibit spatial intermittency. This particle trapping can effectively confine higher energy particles for which other confinement mechanisms (scattering by self-generated waves, magnetic field structure and field line random walk) are not very active (Chandran 2000).

The lack of correlation between cosmic rays and magnetic field in galaxies at small scales (below a few kiloparsecs) is suggested by analyses of the radio–far-infrared correlation (Hoernes, Berkhuijsen & Xu 1998; Berkhuijsen, Beck & Tabatabaei 2013; Basu & Roy 2013). Here, we have presented a physical reason for that. Energy equipartition (or pressure balance) between cosmic rays and a magnetic field may yet hold at scales much larger than the driving scale of turbulence, $l_0 \simeq 100\,{\rm pc}$ in spiral galaxies and 10 kpc in galaxy clusters.

The assumption of energy equipartition between cosmic rays and magnetic fields, and related assumptions of their pressure balance or minimum energy are routinely used in interpretations of synchrotron observations (Beck & Krause 2005; Arbutina et al. 2012; Beck 2016, and references therein). Apart from assuming that the

Downloaded from https://academic.oup.com/mnras/article-abstract/473/4/4544/4411829
by Library - Faculty of Medicine Ramathibodi Hospital user
on 27 June 2018

cosmic ray energy density, dominated by protons, is related to the local magnetic energy density, these interpretations also rely on a fixed ratio of the number densities of cosmic ray electrons and protons and presume that the electrons and protons are identically distributed in space. We have shown that local, small-scale energy equipartition between cosmic rays and random magnetic field does not occur. The spatial distribution of cosmic ray energy is sensitive to the geometry of magnetic field rather than its strength. However, the distribution of cosmic ray electrons responsible for synchrotron emission must be modelled separately with allowance for their synchrotron and inverse-Compton energy losses. We expect that the distribution of cosmic ray electrons would differ significantly from that of protons, plausibly exhibiting stronger intermittency since the electrons would spend more time in magnetic traps as they lose their energy. This would mean that equipartition-type estimates are even less reliable when applied to the local energy densities. It cannot be excluded, however, that the spatial distributions of cosmic ray and magnetic field energy densities are related at larger scales of the order of kiloparsec, comparable to the diffusion length of cosmic ray particles over their confinement time. We shall discuss elsewhere this version of the equipartition arguments.

The intermittency in the distribution of cosmic ray particles discussed above is a robust feature of their propagation in a random magnetic field that emerges in both Gaussian and non-Gaussian magnetic fields. This extreme small-scale inhomogeneity may affect interactions of cosmic rays with interstellar gas (Grenier et al. 2015, and references therein), including spallation reactions and ionization, e.g. producing strong local variations in the ionization rate. The γ-ray emissivity can also be affected by the trapping of cosmic rays particles in random magnetic traps. Quantifying the effect of cosmic ray intermittency on these and other observables (such as spectra) will require energy losses to be included in the model, which we aim to do in the future. The effects of intermittency in the cosmic ray distribution may be numerous and require a careful, systematic study.

Test particle simulations are constrained by the need to resolve the Larmor radius and period of the particle gyration. For this reason, it is not practical to model those particles of energies of the order of GeV which contribute most to the energy density of cosmic rays if the magnetic field structure is to be resolved in full. For example, the Larmor radius of a 5 GeV proton in a 5 μG ISM magnetic field is 10^8 times smaller than 100 pc, the typical scale of the magnetic field. Our conclusions are based on an extrapolation of the results obtained for particles of effectively much larger energies. Then modelling of cosmic ray propagation at lower energies requires a fluid model based on a variant of the diffusion–advection equation but with the diffusion tensor that allows for the non-trivial structure of the magnetic field. Such modelling is beyond the scope of this paper but remains our high priority.

ACKNOWLEDGEMENTS

We are grateful to Ellen Zweibel, Prateek Sharma and Pasquale Blasi for useful discussions. We thank the anonymous referee for her/his helpful suggestions and comments. This work was supported by the STFC (ST/N000900/1, Project 2), the Leverhulme Trust (RPG-2014-427) and the Thailand Research Fund (RTA5980003).

REFERENCES

Arbutina B., Urošević D., Andjelić M. M., Pavlović M. Z., Vukotić B., 2012, ApJ, 746, 79
Basu A., Roy S., 2013, MNRAS, 433, 1675
Beck R., 2016, A&AR, 24, 4
Beck R., Krause M., 2005, Astron. Nachr., 326, 414
Beck R., Brandenburg A., Moss D., Shukurov A., Sokoloff D., 1996, ARA&A, 34, 155
Beck R., Shukurov A., Sokoloff D., Wielebinski R., 2003, A&A, 411, 99
Berezinskii V. S., Bulanov S. V., Dogiel V. A., Ptuskin V. S., 1990, Astrophysics of Cosmic Rays. North-Holland, Amsterdam
Berkhuijsen E. M., Beck R., Tabatabaei F. S., 2013, MNRAS, 435, 1598
Biskamp D., 2003, Magnetohydrodynamic Turbulence. Cambridge Univ. Press, Cambridge
Brandenburg A., Subramanian K., 2005, Phys. Rep., 417, 1
Burbidge G. R., 1956, ApJ, 124, 416
Bykov A. M., 1988, Sov. Astron. Lett., 14, 60
Bykov A. M., Toptygin I. N., 1985, Sov. Astron. Lett., 11, 75
Bykov A. M., Toptygin I. N., 1987, Ap&SS, 138, 341
Candia J., Roulet E., 2004, J. Cosmology Astropart. Phys., 10, 7
Casse F., Lemoine M., Pelletier G., 2002, Phys. Rev. D, 65, 023002
Cesarsky C. J., Kulsrud R. M., 1981, in Setti G., Spada G., Wolfendale A. W., eds, Proc. IAU Symp. 94, Origin of Cosmic Rays. D. Reidel, Dordrecht, p. 251
Chamandy L., Shukurov A., Subramanian K., Stoker K., 2014, MNRAS, 443, 1867
Chandran B. D. G., 2000, ApJ, 529, 513
DeMarco D., Blasi P., Stanev T., 2007, J. Cosmology Astropart. Phys., 6, 027
Desiati P., Zweibel E. G., 2014, ApJ, 791, 51
Evirgen C. C., Gent F. A., Shukurov A., Fletcher A., Bushby P., 2017, MNRAS, 464, L105
Farmer A. J., Goldreich P., 2004, ApJ, 604, 671
Federrath C., Roman-Duval J., Klessen R. S., Schmidt W., Mac Low M.-M., 2010, A&A, 512, A81
Felice G. M., Kulsrud R. M., 2001, ApJ, 553, 198
Fung J. C. H., Hunt J. C. R., Malik N. A., Perkins R. J., 1992, J. Fluid Mech., 236, 281
Gaensler B. M. et al., 2011, Nature, 478, 214
Giacalone J., Jokipii J. R., 1999, ApJ, 520, 204
Globus N., Allard D., Parizot E., 2008, A&A, 479, 97
Grenier I. A., Black J. H., Strong A. W., 2015, ARA&A, 53, 199
Harari D., Mollerach S., Roulet E., 2014, Phys. Rev. D, 89, 123001
Haverkorn M., Spangler S. R., 2013, Space Sci. Rev., 178, 483
Heiles C., Troland T. H., 2005, ApJ, 624, 773
Hoernes P., Berkhuijsen E. M., Xu C., 1998, A&A, 334, 57
Jackson J. D., 1998, Classical Electrodynamics, 3rd edn. Wiley, New York
Kalberla P. M. W., Kerp J., 2016, A&A, 595, A37
Kazantsev A. P., 1967, Zh. Eksp. Teor. Fiz., 53, 1807
Klein U., Fletcher A., 2015, Galactic and Intergalactic Magnetic Fields. Springer Praxis Books, Springer International Publishing, Heidelberg, Germany
Kulsrud R. M., 2005, Plasma Physics for Astrophysics. Princeton Univ. Press, Princeton
Kulsrud R., Pearce W. P., 1969, ApJ, 156, 445
Michalek G., Ostrowski M., 1997, A&A, 326, 793
Moffatt H. K., 1978, Magnetic Field Generation in Electrically Conducting Fluids. Cambridge Univ. Press, Cambridge
Monin A. S., Yaglom A. M., 1971, Statistical Fluid Mechanics. MIT Press, Cambridge, Massachusetts, USA
Moss D., Snodin A. P., Englmaier P., Shukurov A., Beck R., Sokoloff D. D., 2007, A&A, 465, 157
Parizot E., 2004, Nucl. Phys. B, 136, 169
Plotnikov I., Pelletier G., Lemoine M., 2011, A&A, 532, A68
Ruzmaikin A., Sokoloff D., Shukurov A., 1989, MNRAS, 241, 1
Schekochihin A. A., Cowley S. C., Taylor S. F., Maron J. L., McWilliams J. C., 2004, ApJ, 612, 276
Schekochihin A. A., Cowley S. C., Dorland W., Hammett G. W., Howes G. G., Quataert E., Tatsuno T., 2009, ApJS, 182, 310
Schlickeiser R., 2002, Cosmic Ray Astrophysics. Springer, Berlin

Downloaded from https://academic.oup.com/mnras/article-abstract/473/4/4544/4411829
by Library - Faculty of Medicine Ramathibodi Hospital user
on 27 June 2018

Shalchi A., 2009, Nonlinear Cosmic Ray Diffusion Theories. Vol. 362, Springer, Berlin
Shukurov A., Snodin A. P., Seta A., Bushby P. J., Wood T. S., 2017, ApJ, 839, L16
Snodin A. P., Brandenburg A., Mee A. J., Shukurov A., 2006, MNRAS, 373, 643
Snodin A. P., Ruffolo D., Oughton S., Servidio S., Matthaeus W. H., 2013, ApJ, 779, 56
Snodin A. P., Shukurov A., Sarson G. R., Bushby P. J., Rodrigues L. F. S., 2016, MNRAS, 457, 3975
Stepanov R., Shukurov A., Fletcher A., Beck R., La Porta L., Tabatabaei F., 2014, MNRAS, 437, 2201
Strong A. W., Moskalenko I. V., Ptuskin V. S., 2007, Annu. Rev. Nucl. Part. Sci., 57, 285
Subedi P. et al., 2017, ApJ, 837, 140
Subramanian K., 1999, Phys. Rev. Lett., 83, 2957
Subramanian K., Shukurov A., Haugen N. E. L., 2006, MNRAS, 366, 1437
Wentzel D. G., 1974, ARA&A, 12, 71
Wilkin S. L., Barenghi C. F., Shukurov A., 2007, Phys. Rev. Lett., 99, 134501
Zaroubi S. et al., 2015, MNRAS, 454, L46
Zeldovich Ya. B., Ruzmaikin A. A., Sokoloff D. D., 1990, The Almighty Chance. World Scientific, Singapore
Zelenyi L. M., Bykov A. M., Uvarov Y. A., Artemyev A. V., 2015, J. Plasma. Phys., 81, 395810401

APPENDIX A: FINE STRUCTURE OF INTERSTELLAR MAGNETIC FIELDS

Several mechanisms produce the random magnetic fields in the ISM. Tangling of the large-scale magnetic field by turbulent flows produces a volume-filling random field whose statistical properties are controlled by the turbulence. This magnetic field is a by-product of the large-scale (mean-field) dynamo action. If the turbulent velocity has Gaussian statistical properties, the resulting random magnetic field is also a Gaussian random field. Random motions can also generate a random magnetic field directly through the small-scale (fluctuation) dynamo action. The resulting magnetic field is spatially intermittent (magnetic field concentrated in filaments and ribbons) and has strongly non-Gaussian statistical properties (Zeldovich et al. 1990; Schekochihin et al. 2004; Brandenburg & Subramanian 2005; Wilkin et al. 2007). Another similarly structured contribution is produced by compression in random shock fronts driven by supernova explosions (Bykov & Toptygin 1985; Federrath et al. 2010). The result of such compression is a complex random magnetic field represented by both Gaussian and non-Gaussian parts that scatter cosmic rays differently (Zelenyi et al. 2015; Shukurov et al. 2017). In this section, we estimate the contribution of each of the above mechanisms to the small-scale interstellar magnetic fields. For clarity, we denote $\boldsymbol{b}_1$, $\boldsymbol{b}_2$ and $\boldsymbol{b}_3$ the random magnetic fields produced by tangling of the mean field, by the fluctuation dynamo action and by shock compression, respectively.

The tangling of a large-scale magnetic field $\boldsymbol{B_0}$ by a random flow $\boldsymbol{u}$ can be described by the induction equation, equation (1), with magnetic diffusion neglected over the time-scales of interest, $\partial \boldsymbol{b}_1/\partial t \approx \nabla \times (\boldsymbol{u} \times \boldsymbol{B_0})$ (e.g. Moffatt 1978). By the order of magnitude, $b_1 \simeq uB_0\tau/l$, where τ and l are the relevant time and length-scales, respectively. Assuming that τ is equal to the eddy turnover time, l/u, we obtain $b_1 \simeq B_0$. This part of the random magnetic field is present wherever $B_0 \neq 0$, i.e. presumably at all positions. The strength of the interstellar large-scale magnetic field is controlled by the global properties of ISM, such as the velocity shear rate due to differential rotation, the Rossby number and the magnetic helicity flux (see Chamandy et al. 2014, for a compilation of useful results for non-linear mean-field dynamos). Observations suggest $B_0 \simeq 1$–$5\,\mu$G, varying between galaxies and between various locations within a given galaxy (Beck 2016). Thus, $b_1 \simeq 1$–$5\,\mu$G.

Magnetic structures produced by the small-scale dynamo due to a turbulent flow, with the kinetic energy spectrum $E \propto k^{-s}$ (where k is the wavenumber), produce magnetic structures of length l_0 which have a typical width of $l_0 R_{\rm m}^{-1/2}$ and thickness $l_0 R_{\rm m}^{-2/(1+s)}$ (Wilkin et al. 2007). The magnetic correlation length-scale l_b, discussed in Section 3 ($l_b/l_0 \simeq 0.02$ in our simulations of the kinematic dynamo), lies between the three characteristic scales. Wilkin et al. (2007) find that $l_b/l_0 \simeq R_{\rm m}^{-0.4}$. Subramanian (1999) suggests that the statistically steady (saturated) state of the dynamo corresponds to the effective value of the magnetic Reynolds number $R_{\rm m} \simeq R_{\rm m,\,c}$, where $R_{\rm m,\,c} \simeq 10^2$–$10^3$ is the critical magnetic Reynolds number for the dynamo action. Then $l_b/l_0 \simeq R_{\rm m,c}^{-0.4} \simeq 0.2$–$0.05$. Given that the magnetic field strength within such structures is close to energy equipartition with the turbulent energy, the rms magnetic field strength (averaged over a volume l_0^3, or larger) follows as $b_2 \simeq (l_b/l_0)^{3/2}\, B_{\rm eq} \simeq R_{\rm m,c}^{-0.6}\, B_{\rm eq} \simeq (0.02$–$0.06)\, B_{\rm eq}$ with $B_{\rm eq} = (4\pi\rho u_0^2)^{1/2} \simeq 5\,\mu$G. Numerical simulations suggest that the fluctuation dynamo produces a stronger rms magnetic field, $b_2 \simeq 0.3\, B_{\rm eq}$ (Brandenburg & Subramanian 2005) in a saturated state of a non-linear dynamo. This implies that random magnetic fields outside the filaments and ribbons contribute significantly to the magnetic energy density.

Another contribution to non-Gaussian magnetic fields in the ISM is due to shocks. Primary and secondary shock fronts produced by supernova explosions and strong stellar winds can be described as pervasive shock-wave turbulence in the ISM (Bykov & Toptygin 1987). The typical separation between random shocks in the warm ISM is 10^{16}–10^{17} cm (Bykov 1988). The magnetic field associated with shock-wave turbulence has a spectrum close to k^{-2} and is intermittent at scales smaller than the separation of the shock fronts. It is reasonable to expect that the energy density of these random magnetic fields is of the same order of magnitude as the kinetic energy of turbulence, $b_3 \simeq B_{\rm eq}$.

Overall, the small-scale magnetic field in the ISM is a combination of both the non-Gaussian (due to fluctuation dynamo and shocks) and Gaussian (due to tangling of mean field) components of comparable energy density. Thus, we consider both the intermittent and randomized fields for our study of cosmic ray propagation.

The magnetic field structure is likely to be different in different phases of the ISM. The warm, partially ionized gas occupies a large fraction of the galactic disc volume and hosts both the large-scale and small-scale dynamos. The gas has a scaleheight larger than the disc thickness and flows up to fill the hot galactic corona. Numerical simulations of the multiphase ISM driven by supernovae suggest that the large-scale magnetic field is stronger in the warm phase whereas random fields are present in all the phases of the ISM (Evirgen et al. 2017). Also, scattering of cosmic rays due to self-generated waves depends on the wave damping mechanisms, which differs in different phases of ISM (Cesarsky & Kulsrud 1981; Felice & Kulsrud 2001). The damping is strongest in the cold phase and is weakest in the hot phase (leading to efficient PAS of cosmic rays). So, the structure of the magnetic field and the self-generated waves would vary depending on the phase of the ISM.

APPENDIX B: MAGNITUDE OF MAGNETIC FLUCTUATIONS AT THE LARMOR SCALE DUE TO SELF-GENERATED WAVES

When the velocity of cosmic rays is greater than the local Alfvén speed, the streaming instability excites Alfvén waves of a wavelength comparable to the particles' Larmor radius (Kulsrud &

Downloaded from https://academic.oup.com/mnras/article-abstract/473/4/4544/4411829
by Library - Faculty of Medicine Ramathibodi Hospital user
on 27 June 2018

Pearce 1969; Wentzel 1974). Cosmic rays (originally propagating at speeds very close to the speed of light) are slowed down by PAS till they move around with the local Alfvén speed. We assume that the cosmic rays, moving initially with the speed of light, transfer all of their momentum to Alfvén waves (no damping processes are assumed). Using conservation of momentum, we can then estimate the maximum possible amplitude (i.e. δB) of these waves.

The initial momentum of cosmic rays is

$$p = n_{\rm cr} m v \simeq n_{\rm cr} m c \simeq \epsilon_{\rm cr}/c\,, \tag{B1}$$

where $n_{\rm cr}$ is the number density of cosmic ray particles, m is the proton mass, v is the particle speed (taken to be close to c, the speed of light) and $\epsilon_{\rm cr}$ is the energy density of cosmic rays. When all the momentum has been transferred to Alfvén waves, the bulk speed of the ensemble of cosmic ray particles reduces to the Alfvén speed. Momentum conservation then implies that

$$p = \frac{\delta B^2}{8\pi}\frac{1}{V_{\rm A}} + n_{\rm cr} m V_{\rm A}\,, \tag{B2}$$

where δB is the amplitude of the Alfvén waves generated by the streaming instability and $V_{\rm A}$ is the local Alfvén speed. Combining equations (B1) and (B2), we obtain, for $V_{\rm A} \ll c$,

$$\epsilon_{\rm cr} \simeq \frac{\delta B^2}{8\pi}\frac{c}{V_{\rm A}}\,. \tag{B3}$$

Assuming that the energy density of cosmic rays is comparable to the energy density of the magnetic field at larger scales, $\epsilon_{\rm cr} \simeq B^2/(8\pi)$, it follows that

$$\frac{\delta B}{B} \simeq \left(\frac{V_{\rm A}}{c}\right)^{1/2}\,. \tag{B4}$$

The PAS is most efficient in the hot phase of the ISM (Kulsrud & Pearce 1969; Cesarsky & Kulsrud 1981; Kulsrud 2005), where $B \simeq 5\mu$G and $n \simeq 10^{-3}{\rm cm}^{-3}$ for the thermal gas number density, the Alfvén speed is of the order of $10^7\,{\rm cm\,s}^{-1}$. Equation (B4) then yields $\delta B/B \simeq 10^{-2}$. Since the damping of Alfvén waves (Kulsrud & Pearce 1969; Kulsrud 2005) is neglected, this is an upper estimate.

A similar estimate can be obtained without a direct appeal to the energy equipartition between the magnetic fields at a larger scale and cosmic rays. Farmer & Goldreich (2004), using properties of MHD turbulence, obtain $\delta B/B \simeq (r_{\rm L}/l_0)^{1/4}$, where $r_{\rm L}$ is the Larmor radius of the particle and l_0 is the outer scale of turbulence ($\sim$100 pc for the ISM). For a 5 GeV proton in a 5 μG magnetic field, the Larmor radius of the particle is 10^{12} cm. Thus, at that scale $\delta B/B \simeq (10^{12}/10^{18})^{1/4} \simeq 10^{-2}$, which agrees with our estimate in the previous paragraph.

APPENDIX C: STATISTICAL INDEPENDENCE OF COSMIC RAY AND MAGNETIC FIELD DISTRIBUTIONS

The distributions of cosmic rays and magnetic field energy density are uncorrelated (as discussed in Section 4.2) and we check for their statistical independence, i.e. whether $p(n_{\rm cr}, b^2)$, the joint probability distribution function of two components is equal to $p(n_{\rm cr})p(b^2)$, the product of the probability distribution function of each component. This is tested especially for the core region where $n_{\rm cr}$ is close to its mean value. The upper left panels of Figs C1 and C2 show the joint probability densities of magnetic field strength and cosmic ray number densities in the intermittent and Gaussian (randomized) magnetic fields, respectively. We use the Kolmogorov–Smirnov (KS) test to check whether the two distributions are independent. We perform a KS test on marginal probability distributions, $p(b|n_{\rm cr})$ and $p(n_{\rm cr}|b)$, to check whether each of them are drawn from the same distribution. This is measured by the D statistics of the test, which is the absolute maximum distance between the cumulative distribution function of the two samples. A value of D smaller than 0.087 represents 95 per cent confidence that the two samples are drawn from the same distribution. For this, we consider two samples from the marginal probability distribution $p(b|n_{\rm cr})$ with consecutive $n_{\rm cr}$ (cuts along consecutive values of y-axis of the upper left panel of Fig. C1). We performed the KS test for all such pairs and found the mean value of D to be $\simeq$0.062. A similar calculation for $p(n_{\rm cr}|b)$ gives $\simeq$0.072. The mean D values for Gaussian (randomized) magnetic fields are $\simeq$0.054 for $p(n_{\rm cr}|b)$ and $\simeq$0.114 for $p(b|n_{\rm cr})$. The small D values suggest that the cosmic ray number density and magnetic field distributions are independent of each other and the joint probability $p(n_{\rm cr}, b^2)$ can be factorized into $p(n_{\rm cr})$ and $p(b^2)$. We find the functional dependence of $p(n_{\rm cr})$ on $n_{\rm cr}$ and $p(b^2)$ on b^2 as follows. Cuts through the joint PDF in the intermittent magnetic field, shown in the upper right panel of Fig. C1, are well fitted with a Gaussian which, remarkably, has neither the mean value nor the standard deviation dependent on b. The dependence of the maximum value of the conditional PDF $p_n(n_{\rm cr}|b^2)$ on b^2 is shown in the lower left panel of Fig. C1 together with its fit with an exponential function. Thus, the joint PDF of $n_{\rm cr}$ and b has the form

$$p(n_{\rm cr}, b) \approx (1.6 + 9.9{\rm e}^{-10.5 b^2/b_{\rm rms}^2}){\rm e}^{-(n_{\rm cr}/\langle n_{\rm cr}\rangle - 1)^2/0.18} \tag{C1}$$

for $0 \le b^2/b_{\rm rms}^2 \le 0.3$ and $0.25 \le n_{\rm cr}/\langle n_{\rm cr}\rangle \le 1.75$. The relative accuracy of the fitted parameters is better than 5 per cent. This is confirmed by the 2D histogram of the measured and fitted values of $p(n_{\rm cr}, b)$ shown in the lower left panel of Fig. C1: for a perfect fit, the points would be all on the bisector of the quadrant angle. The scatter about that line, shown dashed (blue), provides a measure of the accuracy of the fit. A very small number of points systematically deviate from the main dependence, yet lying on a straight line as well. The joint PDF is thus factorizable, emphasizing that both the distributions are independent.

Similar analysis for $p(n_{\rm cr}, b)$ in the randomized (Gaussian) magnetic field is illustrated in Fig. C2. As in the intermittent magnetic field, the joint PDF is roughly factorizable, and thus $n_{\rm cr}$ and b are statistically independent. The form of the conditional PDF of magnetic field strength is a lognormal distribution,

$$p(b|n_{\rm cr}) \approx 0.5(b^2/b_{\rm rms}^2)^{-1}{\rm e}^{-0.3\ln(b^2/b_{\rm rms}^2)^2} \tag{C2}$$

for $0 \le b^2/b_{\rm rms}^2 \le 3$. We find that

$$p(n_{\rm cr}, b) \approx 0.5(b^2/b_{\rm rms}^2)^{-1}{\rm e}^{-0.3\ln(b^2/b_{\rm rms}^2)^2}{\rm e}^{-(n_{\rm cr}/\langle n_{\rm cr}\rangle - 0.9)^2/0.32}\,. \tag{C3}$$

The 2D histogram of the measured and fitted values is shown [with the dashed (blue) line for the perfect match] in the lower right panel of Fig. C2.

To summarize, the distributions of cosmic ray number density and magnetic field strength are statistically independent in the diffusive regime of the cosmic rays. In the intermittent magnetic field, the joint PDF of $n_{\rm cr}$ and b is well approximated by a Gaussian in $n_{\rm cr}$ and a modified Gaussian in b. In a randomized (Gaussian) field, the joint PDF is approximated by a Gaussian in $n_{\rm cr}$ and a lognormal distribution in b^2. The two variables remain statistically independent for cosmic rays of other energies too. The exact parameters of the joint PDF are likely to depend on details of the magnetic field structure and the energy of the particle.

Downloaded from https://academic.oup.com/mnras/article-abstract/473/4/4544/4411829
by Library - Faculty of Medicine Ramathibodi Hospital user
on 27 June 2018

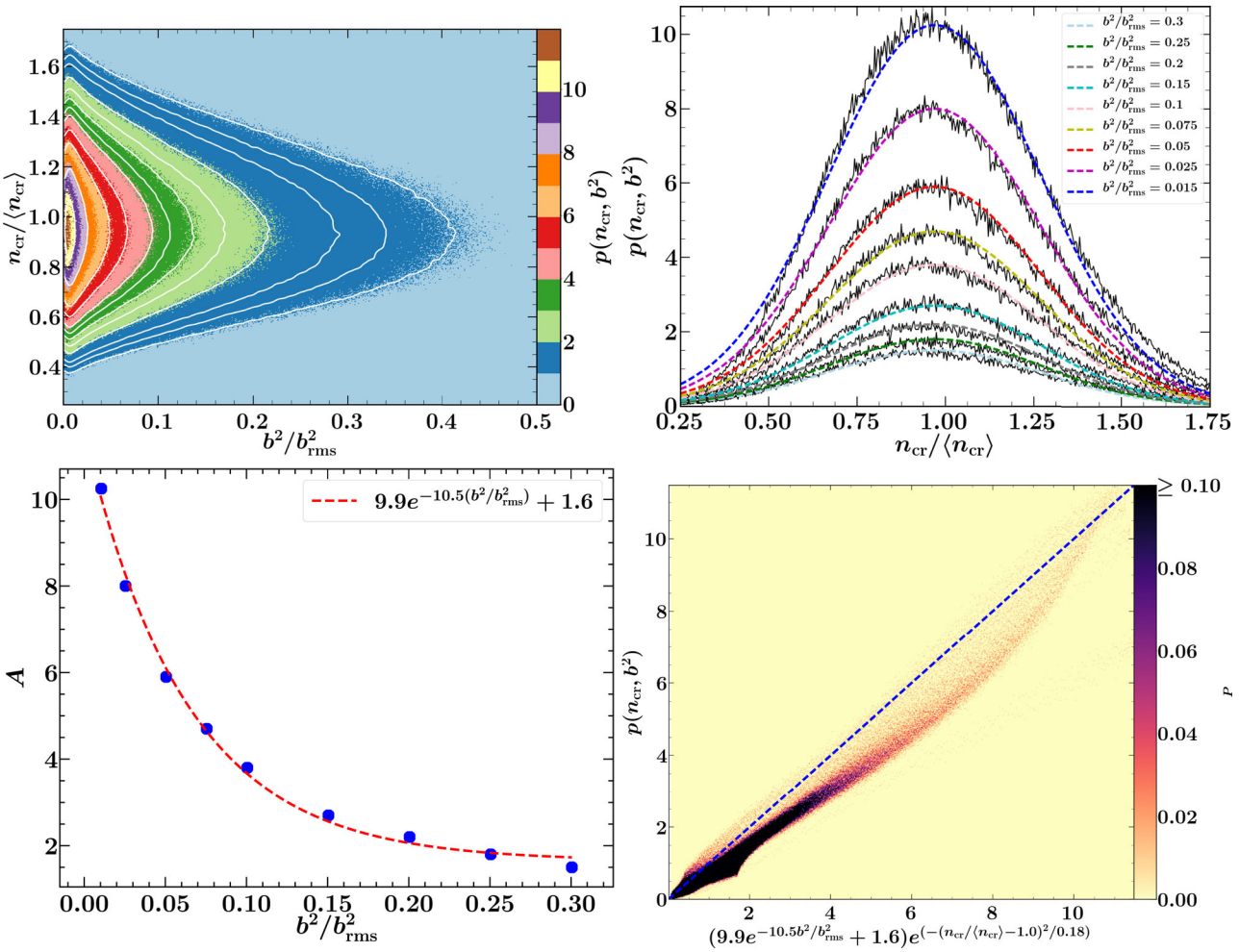


Figure C1. The joint PDF $p(n_{\rm cr}, b^2)$ of $b^2/\,b^2_{\rm rms}$ and $n_{\rm cr}/\langle n_{\rm cr}\rangle$ in the intermittent magnetic field for $0 \leq b^2/\,b^2_{\rm rms} \leq 0.5$ and $0.25 \leq n_{\rm cr}/\langle n_{\rm cr}\rangle \leq 1.75$ (upper left panel). The joint PDF $p(n_{\rm cr}, b^2)$ as a function of $n_{\rm cr}/\langle n_{\rm cr}\rangle$ alone for various fixed values of $b^2/\,b^2_{\rm rms}$ is shown in the upper right panel together with least-square fits of the form $p(n_{\rm cr}, b^2) = A(b^2)\mathrm{e}^{-(n_{\rm cr}-1.0)^2/0.18}$ (smooth dashed curves). The lower left panel presents A as a function of $b^2/\,b^2_{\rm rms}$ fitted with an exponential (red, dashed). The lower right panel shows the 2D histogram of the computed and fitted values of $p(n_{\rm cr}, b^2)$, with a linear fit (dashed, blue).

Downloaded from https://academic.oup.com/mnras/article-abstract/473/4/4544/4411829
by Library - Faculty of Medicine Ramathibodi Hospital user
on 27 June 2018

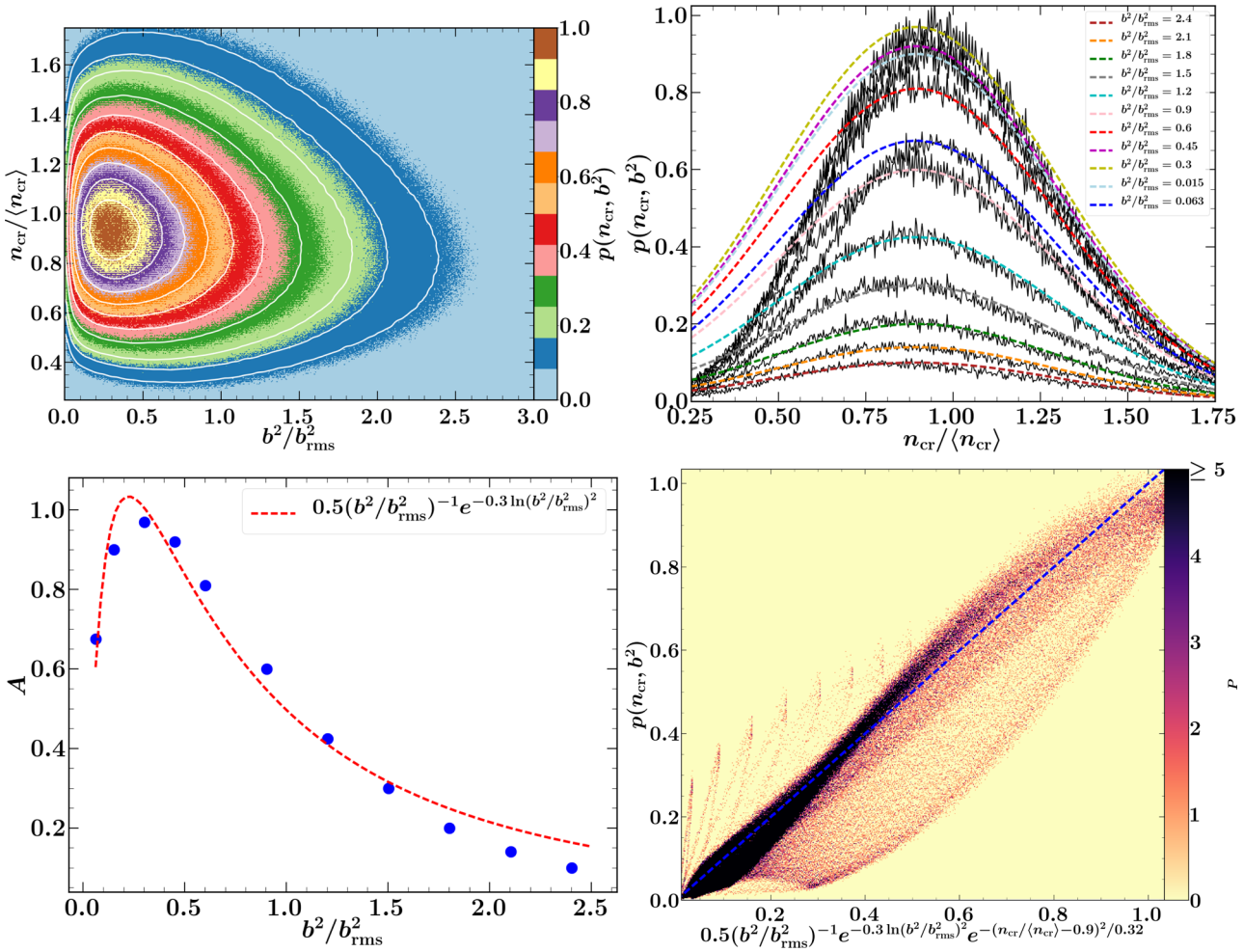


Figure C2. As in Fig. C1 but for the randomized (Gaussian) magnetic field for $0 \leq b^2/b^2_{\rm rms} \leq 3.0$ and $0.25 \leq n_{\rm cr}/\langle n_{\rm cr}\rangle \leq 1.75$ and the lower right panel shows the 2D histogram with blue dashed line as $y = x$ (the bisector of the angle between the axes).

This paper has been typeset from a TEX/LATEX file prepared by the author.

Downloaded from https://academic.oup.com/mnras/article-abstract/473/4/4544/4411829
by Library - Faculty of Medicine Ramathibodi Hospital user
on 27 June 2018

Driving reconnection in sheared magnetic configurations with forced fluctuations

Peera Pongkitiwanichakul, Kirit D. Makwana, and David Ruffolo

Citation: Physics of Plasmas **25**, 022114 (2018);
View online: https://doi.org/10.1063/1.5014026
View Table of Contents: http://aip.scitation.org/toc/php/25/2
Published by the American Institute of Physics



Driving reconnection in sheared magnetic configurations with forced fluctuations

Peera Pongkitiwanichakul,[1,2,a)] Kirit D. Makwana,[3] and David Ruffolo[1]
[1]*Department of Physics, Faculty of Science, Mahidol University, Bangkok 10400, Thailand*
[2]*Department of Physics, Faculty of Science, Kasetsart University, Bangkok 10900, Thailand*
[3]*Centre for Mathematical Plasma Astrophysics, Department of Mathematics, KU Leuven, Celestijnenlaan 200B, 3001 Heverlee, Belgium*

(Received 14 November 2017; accepted 24 January 2018; published online 15 February 2018)

We investigate reconnection of magnetic field lines in sheared magnetic field configurations due to fluctuations driven by random forcing by means of numerical simulations. The simulations are performed with an incompressible, pseudo-spectral magnetohydrodynamics code in 2D where we take thick, resistively decaying, current-sheet like sheared magnetic configurations which do not reconnect spontaneously. We describe and test the forcing that is introduced in the momentum equation to drive fluctuations. It is found that the forcing does not change the rate of decay; however, it adds and removes energy faster in the presence of the magnetic shear structure compared to when it has decayed away. We observe that such a forcing can induce magnetic reconnection due to field line wandering leading to the formation of magnetic islands and O-points. These reconnecting field lines spread out as the current sheet decays with time. A semi-empirical formula is derived which reasonably explains the formation and spread of O-points. We find that reconnection spreads faster with stronger forcing and longer correlation time of forcing, while the wavenumber of forcing does not have a significant effect. When the field line wandering becomes large enough, the neighboring current sheets with opposite polarity start interacting, and then the magnetic field is rapidly annihilated. This work is useful to understand how forced fluctuations can drive reconnection in large scale current structures in space and astrophysical plasmas that are not susceptible to reconnection. *Published by AIP Publishing.* https://doi.org/10.1063/1.5014026

I. INTRODUCTION

In dynamic plasmas, energy conversion between the magnetic field and plasma flow occurs continuously everywhere. The magnitude and direction of the conversion depend greatly on the magnetic structures of the plasma itself. If there is plenty of free energy in the magnetic field, plasma flow could be triggered by an instability and cause the field to be rearranged. In this case, the energy conversion is mostly from magnetic energy to kinetic energy. Magnetic reconnection is often associated with such a conversion.[1] Reconnection processes are ubiquitous in dynamic plasmas, ranging from sawtooth oscillations in tokamaks,[2] to reconnection in solar flares,[3] reconnection in Earth's magnetosphere,[4] reconnection in astrophysical objects like pulsars and active galactic nuclei,[5] etc. The rate of magnetic reconnection has been a major topic of research for several decades. For resistive magnetohydrodynamics (MHD) at the high Lundquist number (ratio of magnetic field diffusion time to Alfven wave crossing time) of solar plasma, the theory of steady-state reconnection by Sweet and Parker[6,7] predicted a rate of reconnection that was too slow to explain the energy release rate in solar flares. Petschek proposed setting up an X-point-like reconnection geometry, with shocks supporting the X-point structure, allowing faster reconnection at high Lundquist numbers.[8] However, numerical simulations showed that the Petschek X-point structure is not maintained in the nonlinear state at high Lundquist numbers, going back to a Sweet-Parker geometry and reconnection rate. Since then, several studies have shown that reconnection is faster with the inclusion of Hall physics and kinetic physics.[9] In these models, the Hall physics separates the electron and ion dynamics at length scales smaller than the ion skin depth. At these length scales, the electron dynamics are governed by whistler waves, which make the reconnection rate independent of the strength of dissipation.

The presence of turbulence has also been shown to increase the rate of reconnection within the framework of resistive MHD.[10,11] In these models, the diffusion region size and geometry, and thus the reconnection rate, are controlled by the magnetic field line wandering produced by turbulence. This again makes the reconnection rate independent of the specific dissipation mechanism. However, the reconnection rate in nature is not always fast. Reconnection events in several of the above-mentioned systems show a slow build-up of magnetic energy followed by a sudden onset of reconnection and energy release.[12,13] This is known as the "trigger" problem.[14] At high Lundquist numbers, it has been found that Sweet-Parker current sheets are unstable to the tearing instability, which breaks up the sheet into a chain of plasmoids.[15,16] As a Sweet-Parker current sheet is slowly evolving (with the aspect ratio of its length to thickness increasing), at some stage, it will become unstable to the tearing instability,[17] leading to disruption of the current sheet. This is a possible mechanism for explaining the onset

a)Electronic mail: fscipepo@ku.ac.th

of fast reconnection in nature. Current sheet disruption is also a possible explanation for the onset of substorms in the Earth's space weather system.[18]

Just as turbulence can affect the rate of reconnection, turbulence can also play a role in the onset of reconnection. Studies have been done where broadband fluctuations are added as an initial value to a periodic sheet pinch, and this leads to rapid magnetic reconnection.[19,20] Laminar initial perturbations have also been added to multiple current sheets which are unstable to the tearing mode. For perturbation wavelengths longer than twice the current sheet separation, there is a complete reconfiguration of the magnetic field and a large fraction of magnetic energy is converted into kinetic energy.[21] This is also related to the so-called "Taylor" problem in which magnetic reconnection is forced in a tearing-stable current sheet by small-amplitude boundary perturbations.[22]

In nature, we often find large current sheet structures (or more generally sheared magnetic field structures) which are stable. The current sheets that have been observed in the solar corona are very large-scale,[23] much thicker than the thin Harris sheet setup used in the Geospace Environmental Modeling (GEM) challenge for simulations to study reconnection[9] in a kinetic regime. Therefore, it is important to study how reconnection can be initiated in thick current sheets, which is an open question,[24,25] and to study the effect of driven fluctuations. These fluctuations can be driven by various sources in the real world, like turbulence, or photospheric motion in the case of the solar corona, or a variety of plasma waves that are ubiquitous in many systems. In this work, we consider such stable sheared magnetic field configurations and perturb them with driven fluctuations. We study the energy dynamics of this process and the characteristics of the reconnection that occurs. In Sec. II, we describe our code and numerical setup. We then put our code to the test with the tearing mode instability in Sec. II B. Here, we also show that the sheared magnetic field setup is stable to reconnection and test the forcing we have introduced. In Sec. III, we show results from driving fluctuations in our initial setup. We calculate the energy injection and energy dissipation. We show that O-points form in this system indicating the occurrence of reconnection. We find that the O-points spread out as the sheared magnetic field decays. In Sec. IV, we derive a semi-empirical formula to describe this spread of O-points due to field line wandering and show that it gives a reasonable description of the phenomena. We study how this field line wandering depends on the parameters of the driving. The discussion and conclusions are given in Sec. V.

II. NUMERICAL SETUP

A. Code description

We solve the set of incompressible MHD equations

$$\frac{\partial \boldsymbol{u}}{\partial t} = -\boldsymbol{u}\cdot\nabla\boldsymbol{u} + \boldsymbol{B}\cdot\nabla\boldsymbol{B} + S^{-1}\nabla^2\boldsymbol{u} + \boldsymbol{F}_u \tag{1}$$

and

$$\frac{\partial \boldsymbol{B}}{\partial t} = \nabla\times(\boldsymbol{u}\times\boldsymbol{B}) + S^{-1}\nabla^2\boldsymbol{B}, \tag{2}$$

where $\boldsymbol{u}$ is the flow velocity normalized by $v_A = B_0/\sqrt{4\pi\rho}$, $\boldsymbol{B}$ is the magnetic field normalized by B_0, and η is the resistivity. The plasma density ρ is constant, and B_0 is the maximum value of the initial background field. Therefore, v_A is the initial Alfvén velocity calculated where the background magnetic field is the strongest. The force per mass $\boldsymbol{F}_u$ is normalized by v_A^2/L_0, where L_0 is a reference length scale related to the simulation box size. Here, we define the Lundquist number as $S = L_0 v_A/\eta$ and set the magnetic Prandtl number, the ratio of viscosity to resistivity, to unity. We use L_0/v_A as the unit of time τ_A and L_0 as that of distance. This is a simplified version of MHD equations after using $\nabla\cdot\boldsymbol{B} = 0$ and $\nabla\cdot\boldsymbol{u} = 0$. These two equations are solved within a 2D periodic domain. The forcing in Eq. (1) is of the following form:

$$\boldsymbol{F}_u = \sum_{|k|=k_1}^{k_2} \boldsymbol{F}_{\boldsymbol{k}} \exp(i\boldsymbol{k}\cdot\boldsymbol{x}). \tag{3}$$

To satisfy incompressibility, we set $\boldsymbol{F}_k = \boldsymbol{D}_k - (\boldsymbol{D}_k\cdot\boldsymbol{k})\boldsymbol{k}/k^2$, where vector $\boldsymbol{D}_k$ is a randomly generated vector. The direction of $\boldsymbol{D}_k$ is purely random but the magnitude of $\boldsymbol{D}_k$ is randomly assigned from a uniform distribution from 0 to A_0, where A_0 is used to control the strength of the force. The force is also time-dependent since $\boldsymbol{D}_k$ changes with time in the following way. We fix one number n_s between 0 and 1, and then at every fixed time step Δt, we randomly pick another number n_r from 0 to 1. If $n_r < n_s$, we change $\boldsymbol{D}_k$. By this method, the average changing time (or correlation time of $\boldsymbol{D}_k$) is

$$\tau_F = \Delta t/n_s. \tag{4}$$

The initial magnetic field is chosen to have a shear in the vertical z direction (the horizontal direction is x). If the field is stable, the field can only decay due to resistivity. There are two initial forms of the magnetic field used in this work. One is an array of four current sheets with alternating polarity

$$B_x = B_0\left[1 + \sum_{i=-1}^{2}(-1)^i \tanh\frac{z - z_i}{\lambda}\right] \tag{5}$$

and

$$B_y = B_0\left[\sum_{i=-1}^{2}(-1)^i \operatorname{sech}\frac{z - z_i}{\lambda}\right], \tag{6}$$

where i is an integer and

$$z_i = \frac{(1+2i)L_0}{4}. \tag{7}$$

We call this the sheet form, and λ sets the sheet thickness. An individual sheet in this setup is force-free by itself. However, since we have a periodic pseudo-spectral code, we set up this form of array of sheets. We simulate the two current sheets with z_i between 0 and L_0, providing the main

structure of the magnetic field, with the simulation box in the z direction going from 0 to L_0. However, if there are only these two terms, i.e., $i=0$ and $i=1$, in Eqs. (5) and (6), then small discontinuities of B_y and $\partial B_x/\partial z$ occur at the periodic boundary between $z=0$ and $z=L_0$. Therefore, the two extra sheets are included to moderate these discontinuities at the boundaries. A perfectly periodic system would ideally have an infinite number of sheets. However, since we only consider the values of z in the box from 0 to L_0, the contribution from the sheets with distant z_i is small and we can keep only a few terms that have z_i inside or close to the box.

The other form of the magnetic field is composed of a simpler, sinusoidal profile of the magnetic field compared to a current sheet, as follows:

$$B_x = B_0 \cos\left(\frac{2\pi z}{L_0}\right) \tag{8}$$

and

$$B_y = B_0 \sin\left(\frac{2\pi z}{L_0}\right). \tag{9}$$

We call this form the sinusoidal form. We use a fully de-aliased 2 D pseudo spectral algorithm to perform the spatial discretization on a Cartesian grid. A description of the numerical scheme can be found in Cattaneo and Emonet 2003.[26] Many of the simulations were performed on the XSEDE Stampede machine at TACC.[27]

B. Test of the tearing mode and forcing

The tearing mode instability is one of the most important instabilities of a current sheet.[28] It turns an unstable sheared magnetic structure into a stable structure of greater width. For the current sheet setup of Eqs. (5) and (6), the condition for the tearing instability is

$$\Delta' = \frac{2}{k}\left(\frac{1}{\lambda^2} - k_x^2\right), \tag{10}$$

where Δ' must be positive for the instability and k_x is the wavenumber of the perturbation in the x direction.[29] In a simulation box, if all the possible wavenumbers k_x are larger than $1/\lambda$, then the tearing mode is stable and cannot occur. However, even in a large enough box which allows the instability, the current sheet decays on a time-scale which can interfere with the growth of the tearing mode. Therefore, to benchmark the tearing mode in our simulations with Eq. (10), we also add one extra term $-S^{-1}\nabla^2\boldsymbol{B}_0$ to the induction equation [Eq. (2)] to maintain the initial magnetic field $\boldsymbol{B}_0$ and prevent the current sheet from decaying.

We then test our code for the instability condition Eq. (10). We use a current with half width $\lambda = 0.05L_0$. The resistivity is $\eta = 5\times10^{-5}L_0 v_A$ and the box length $L_z = L_0$. We vary the smallest k_x in the simulation by varying the length L_x of the box in the x direction. The resolution for these simulations is 2048^2 grid points. According to Eq. (10) for $\lambda = 0.05L_0$, the tearing mode will be unstable for $k_x < 20/L_0$, i.e., $L_x > (\pi/10)L_0$. We seed the initial state with random noise of fluctuations at all wavelengths with very little amplitude in order to test instability. Naturally, the most unstable mode starts to grow and dominates. In Fig. 1, we show the growth of the averaged B_z^2 in the simulation box, associated with the growth of the tearing island. We can clearly see that as predicted, the tearing mode grows for $L_x > (\pi/10)L_0$ but not for $L_x = 0.3L_0$.

Figure 2 shows the results from the simulation with $L_x = L_0$. Here, we see that the tearing mode causes B_z^2 to rise and reach the saturation point once a steady state is reached. The total B^2 does not change much due to the instability. Figure 2 also shows the initial current density and the current density during the steady phase (after $1500\tau_A$). We see that the sheet deforms as the tearing mode islands form and grow. The sheets stay at this steady state as long as we keep the extra term $-S^{-1}\nabla^2\boldsymbol{B}_0$ in Eq. (2).

Taking the reference length $L_0 = L_0$, these simulations were performed at $S = 2\times10^4$. However, for lower $S = 250$, B_z^2 grows only for $L_x \geq 1$, which is far above the theoretical instability threshold. This might be because of the existence of viscosity in the simulations, which is not accounted for in the analysis of Eq. (10). We take the magnetic Prandtl number to be unity. Therefore at low S, the viscosity is large and can have a significant effect on the velocity field, in addition to the Lorentz force. It has been calculated[30,31] that viscosity tends to reduce the growth rate of the tearing mode, especially when close to the instability threshold. This could be the reason that at low Lundquist numbers, we do not see the growth of the tearing mode unless we are significantly above the instability threshold. This effect is enhanced in the case of shorter length L_x, when the growth rate is weaker. We may reduce only viscosity to make our setup for simulations match the assumption behind the theory of the tearing mode, but the viscosity must still be high enough so the solution of the simulation is resolved. This rules out the exact solution for zero viscosity as used for deriving the condition in Eq. (10).

We also vary the Lundquist number parameter by changing the resistivity η while keeping a fixed box size of $L_x = L_0$. We find the growth rate of the tearing mode by keeping the extra term $-S^{-1}\nabla^2\boldsymbol{B}_0$ in the induction equation. Figure 3 shows the variation of the growth rate with S. It is seen that as Lundquist number increases, the growth rate

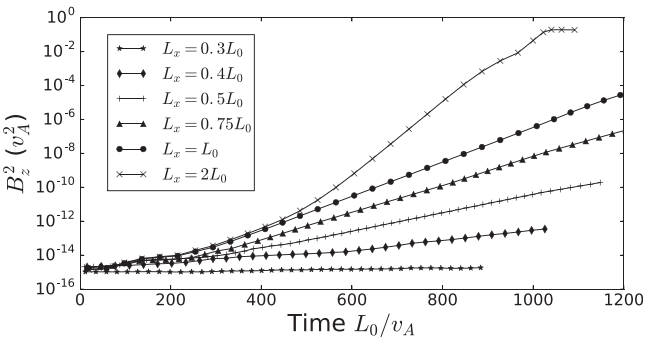


FIG. 1. The averaged values of B_z^2 from various simulations are plotted versus time. Most cases exhibit exponential growth due to the tearing mode instability.

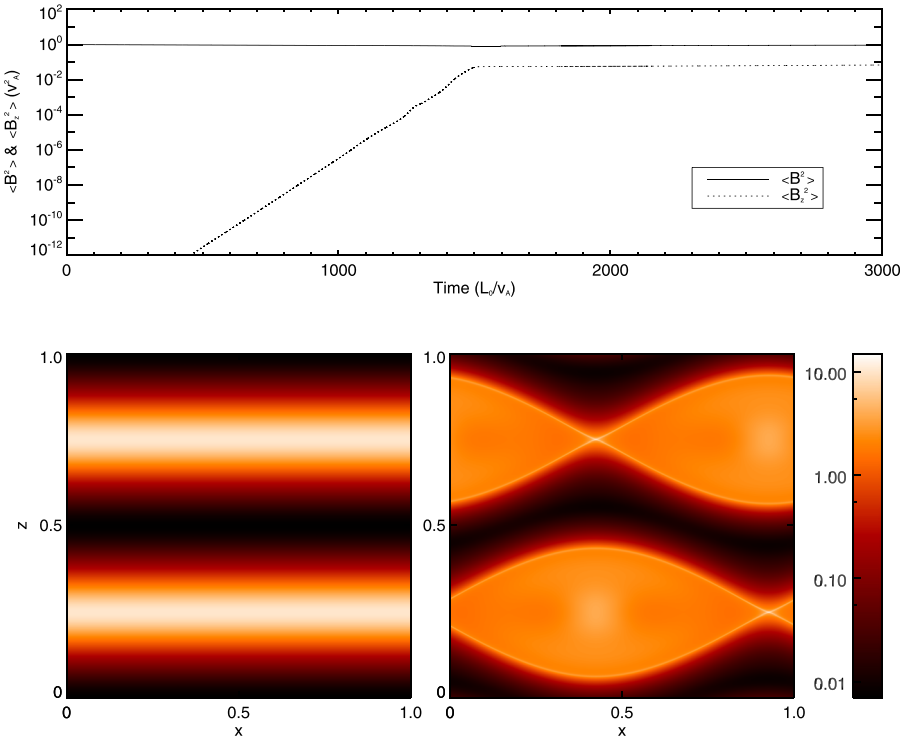


FIG. 2. Top panel shows the growth of the B_z^2 field due to island growth and its saturation. The total B^2 is not affected much. The bottom left panel shows the current density initially, while the bottom right panel shows the state of current density in the saturated state. The sheets are deformed into magnetic islands with strong current sheets located between two islands. The current sheets become much shorter once a steady state is reached.

goes as $\sim S^{-3/5}$, as found in previous work.[30] This trend is indicated by the dashed line in Fig. 3.

In the above tests for tearing mode, we had the extra term $-S^{-1}\nabla^2\boldsymbol{B}_0$ in the induction equation to maintain the sheets against dissipation for testing the instability condition. However, in nature, dissipation will be present, although at realistic Lundquist numbers, it will be very weak. Nevertheless, the tearing mode instability requires the resistivity but it must also act against the dissipation at the same time. Now, we exclude the extra term, $-S^{-1}\nabla^2\boldsymbol{B}_0$, and solve only our original set of MHD equations with all same parameters from the previous simulation. This is also done because it is easier to interpret the following results without having this extra artificial term. We use L_x equal to L_0, $2L_0$, and $4L_0$ with $S = 10^4$. The simulations with $L_x = 2L_0$ and $L_x = 4L_0$ show sheets being deformed by the tearing mode even when the sheets are decaying due to resistivity. However, the sheets from the simulation with $L_x = L_0$ remain close to the original sheets. The tearing mode grows initially, but its growth soon stops as the current sheet has decayed away significantly. The main factor behind this could be that the growth rate is too low to overcome the dissipation rate at small scales. The dissipation makes the current sheets become thicker. Once the thickness of the current sheet λ grows past the critical thickness for the instability, the tearing mode no longer grows. In the simulations we present below, we take this setting of $L_x = L_0$, so that the current sheet decays smoothly without reconnection happening due to the tearing instability. On top of this, we apply driven fluctuations and study the characteristics of the resulting reconnection. We also test our forcing term by using it in a purely hydrodynamic 2 D simulation. In this case, we force at small wavenumbers and recover the well known inverse cascade of energy as shown in Fig. 4. The forcing is at k from $368\pi/L_0$ to $384\pi/L_0$. The spectrum is calculated at a time when the solution has reached its steady state.

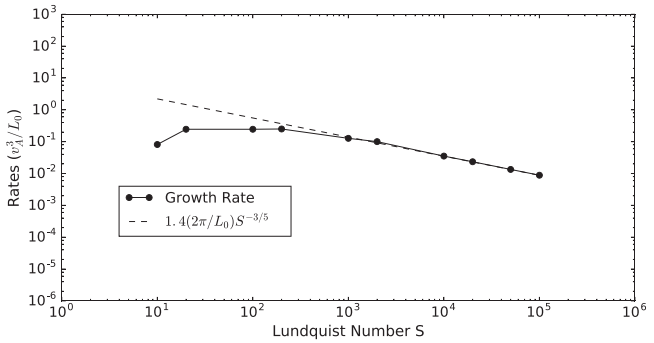


FIG. 3. Growth rate of the most unstable tearing mode as a function of Lundquist number, shown by blue dots. The dashed red line shows a reference slope of $S^{-3/5}$.

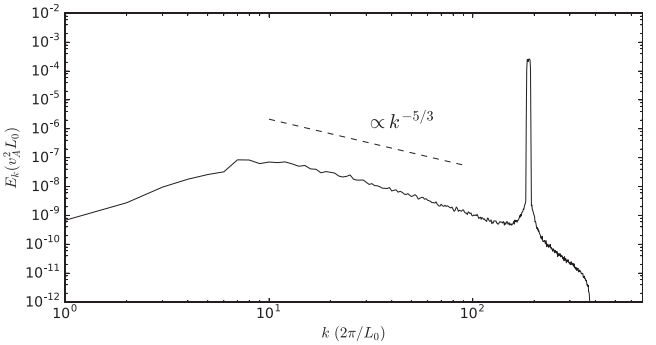


FIG. 4. Inverse cascade of energy in 2D hydrodynamic simulation. The energy cascades from high wavenumbers to low wavenumbers causing the spectral index of $-5/3$ in the inertial range.

TABLE I. List of simulations with perturbation. We vary the forcing amplitude A_0, the range of forcing wavenumbers $k_1 - k_2$, and the correlation time τ_F.

ID	$A_0 L_0/v_A^2$	$kL_0/(2\pi)$	τ_F/τ_A
1	2×10^{-2}	3–4	1
2	2×10^{-2}	6.5–7.5	1
3	2×10^{-2}	3–4	10
4	6×10^{-2}	3–4	1
5	10^{-2}	3–4	1
6	2×10^{-2}	3–4	100
7	2×10^{-2}	13.5–14.5	100

III. RECONNECTION DUE TO DRIVEN FLUCTUATIONS

A. In a current sheet system

In this section, we start with the initial magnetic field configuration of the sheet form. We include fluctuations in the system while the stable sheets decay freely due to resistivity. The perturbation is added by placing a force [Eq. (3)] in the momentum equation. The force is set to provide perturbations, with the energy of the magnetic fluctuations driven by the forcing around one order of magnitude lower than the energy of the initial equilibrium magnetic field. Different forcing parameters are utilized. We run simulations with parameters shown in Table I. The form of force is shown in Sec. II. Figure 5 shows the time evolution of the average kinetic energy u^2, the average magnetic energy B^2, and J^2 as functions of time from the simulation run 1. Initially, the energy in the velocity fluctuations is one order of magnitude smaller than the magnetic field energy. From the figure, we separate the process into two phases. In the first phase, up to $t/\tau_A \approx 13\,000$, the magnetic energy drops steadily as the magnetic structure decays. We find that the rate of magnetic energy decay is not affected by the presence of these driven fluctuations, compared to the decay of the magnetic energy without any driven fluctuations. These simulations are also computationally expensive due to the long time it takes for the decay process, going over 10^4 Alfvén times. The average energy level of the driven fluctuations remains steady. However, once the kinetic energy of fluctuations becomes comparable to the magnetic energy, the magnetic structure is rapidly destroyed with a much greater decay rate. After $t/\tau_A \approx 13\,000$, the magnetic energy drops rapidly over the time scale of around tens of τ_A. As the net magnetic flux in this periodic domain is nearly zero, the magnetic field is completely destroyed and the plasma is not magnetized after this. Simultaneously, all the energy goes into kinetic energy, which rapidly rises and saturates.

Figure 6 shows the rate of energy injection, the viscous dissipation rate, and the Ohmic heating rate. The energy injection rate (per mass) is simply given by

$$\gamma_{inj} = \sum_{\boldsymbol{k}} \boldsymbol{F_k} \cdot \boldsymbol{u_k^*}, \tag{11}$$

where the force is as in Eq. (3) and $\boldsymbol{u_k}$ is the Fourier amplitude of the velocity $\boldsymbol{u}$. In the first phase, the viscous dissipation rate remains nearly steady at around 10^{-3}, while the Ohmic heating rate continues to rise slowly until the end of the phase. Even with higher energy input rate into the flow during this phase, the energy in the flow is lower in this phase than in the later phase (Fig. 5). At the end of the first phase at around $t/\tau_A \approx 13\,000$, the Ohmic dissipation rate becomes comparable to the energy injection rate. Then, the magnetic field rapidly drops, as does the Ohmic dissipation. In this second phase, the energy injection rate also drops, but the viscous dissipation rate drops further. This is like driving an unmagnetized fluid. Therefore, the kinetic energy rises in the second phase. We conclude that both energy injection and viscous dissipation are stronger in the presence of a background magnetic field, compared to when there is no magnetic field present.

Figure 7 contains a set of figures showing J^2 at different times in the simulation ID 1 with the current sheet setup. At the initial time, we can see the two current sheets with straight magnetic field lines in the x direction. The out-of-plane magnetic field component B_y is ignored while plotting the field lines. At time $t = 3.6\tau_A$, the sheets start to deform due the driven fluctuations. The vector potential ψ is calculated using the in-plane magnetic field (B_x, B_z) such that $\partial\psi/\partial x = B_z$ and $\partial\psi/\partial z = -B_x$. This potential ψ gives the location of O-points in the field which are identified as the extrema in ψ in some region of space. The samples of O-points are represented by the white circles in Fig. 7. These samples are the points that have the absolute value of ψ greater than ψ from its neighborhood of the radius of $0.03L_0$. These O-points represent the formation of closed field lines, indicating magnetic reconnection and a change in topology. Zooming in one can see closed field lines around several of

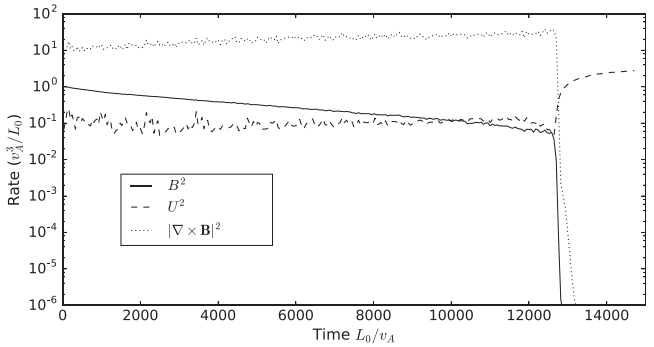


FIG. 5. The average values of u^2, B^2, and J^2 as functions of time for a current sheet system with driven fluctuations (run 1).

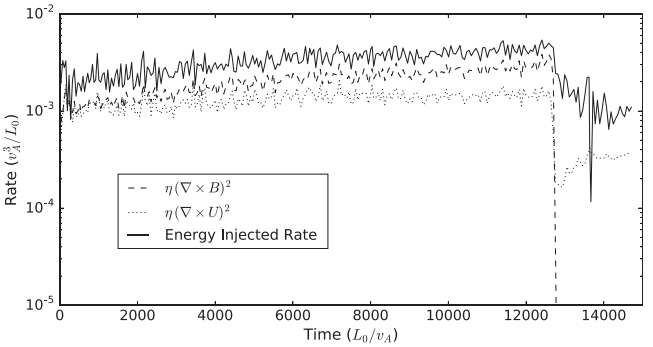


FIG. 6. The rate of energy input, the Ohmic dissipation rate $(\eta(\nabla\times\boldsymbol{B})^2)$, and the viscous heating rate $(\eta(\nabla\times\boldsymbol{U})^2)$ from simulation run 1.

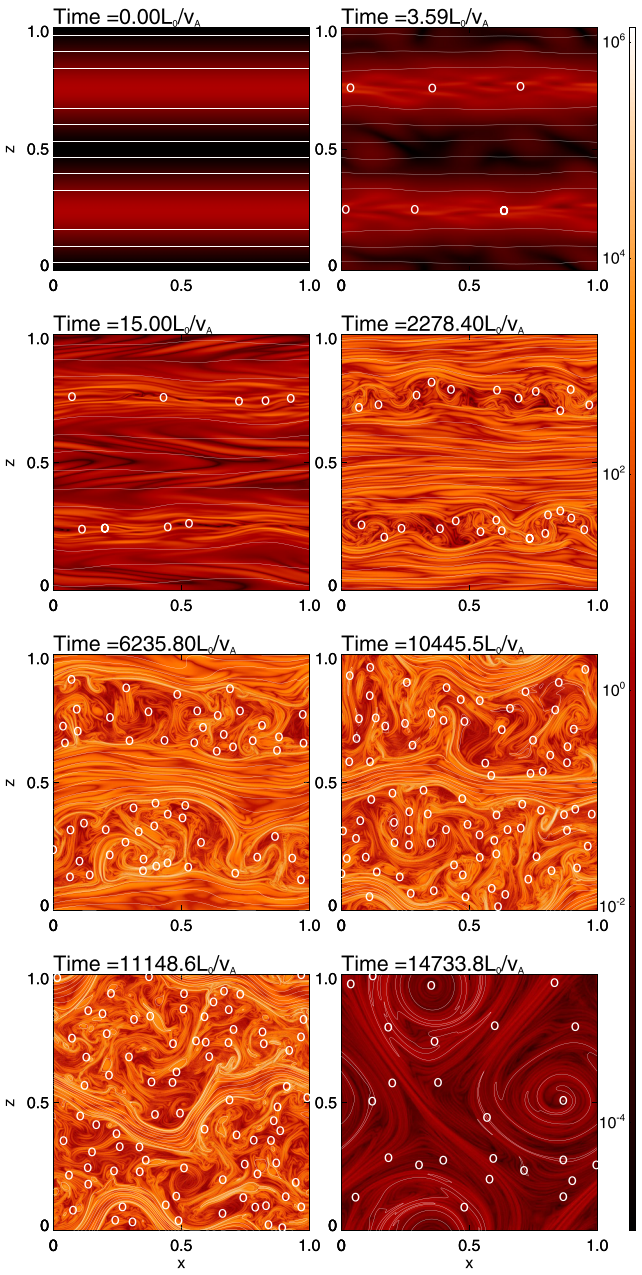


FIG. 7. This figure shows a series of color images of squared current density at different times in the simulation. All figures use the same logarithmic color axis. The white lines represent a sample of magnetic field lines. The white dots represent the O-points of the magnetic field.

these O-points. We see the formation of a few O-points around the center of the two current sheets at time $t = 3.6\tau_A$. The field lines are starting to bend at this time and thinner current sheets start to appear. As time progresses, the number of O-points increases and they also start to migrate further away from the mid-plane of the two current sheets. The strength of the current density also becomes localized, with thinner but stronger current sheets.

At time $t = 15\tau_A$, we can still see the original current sheets but develop a fine scale structure compared to outside the current sheet. At $t = 2300\tau_A$, the structure of the original current sheets has been totally destroyed, and at their locations, we see many small-scale vortices and sheet-like structures. The region between the two current sheets seems quieter with more laminar magnetic field lines. As time advances, this quiet region between the two current sheets shrinks, while the turbulent region around the current sheets widens. This process continues for times $t = 6200\tau_A$ and $t = 10\,400\tau_A$. We see that the identified O-points closely track the expansion of the chaotic region around the current sheets and are a good proxy for determining the region where the fluctuations are driving reconnection. Until $t = 10\,400\tau_A$, we can still distinguish regions that expanded from the original current sheets and the quiet regions between them. At $t = 11\,100\tau_A$, the O-points from the two distinct sheets have come very close to each other. The quiet regions in between have almost shrink away. It is difficult to say, which O-point originates from which current sheet in the region close to $z = 0.5L_0$. This is just before the time when the magnetic field disrupts and the magnetic energy rapidly drops (between $12\,000\tau_A$ and $13\,000\tau_A$ as seen in Fig. 5). This indicates that when the field lines from one current sheet start interfering with the field lines from the other current sheet under the influence of these fluctuations, then the magnetic field is rapidly destroyed. This would not happen in the absence of driven fluctuations. After the disruption event, the current density is very low as seen at time $t = 14\,700\tau_A$. There are a few O-points, which are randomly spread out and noisy due to the very weak magnetic field. We observe large vortices formed in this mostly hydrodynamic plasma.

B. In a sinusoidal field system

In previous simulations, we used the sheet form of the initial magnetic field [Eqs. (5) and (6)]. The initial current sheets can be decomposed into a Fourier series. The high wavenumber components of this series will decay faster due to dissipation, leaving only the low wavenumber components. To test how important the modes with high wavenumber are, we then set the initial magnetic field to only contain the modes with the smallest wavenumber. This is the sinusoidal form of the initial magnetic field [Eqs. (8) and (9)]. We run the simulation by using parameters for Run ID 1 from Table I with this new initial sinusoidal magnetic field. As shown in Figs. 5–7 for the current sheet form, for this case also, we compute the energy evolution, the energy dissipation, and the energy injection rate, as well as the form of current density and the formation of O-points. We find almost exactly the same results as for the current sheet setup. Thus, we conclude that the initial high-wavenumber Fourier modes do not change the dynamics of the sheets significantly.

From this simulation with the simple initial field, we also compare the total dissipation rates at the early phase and the later phase. We only are interested in a dissipation rate that does not take the decaying initial field into account. Therefore, we subtract the rate of decay of the large scale initial magnetic field from the total dissipation rate. This rate is purely from the tiny current sheets and viscosity. At the early phase, the average dissipation rate is $3.5 \times 10^{-3} v_A^2/\tau_A$. At later phases, the average dissipation rate is purely from the momentum equation and it is around $5 \times 10^{-4} v_A^2/\tau_A$. We can see that the dissipation rate or the heating rate is stronger

in the presence of the decaying magnetic field. With a higher dissipation rate, the energy input rate at the early phase is also greater than the rate at the later phase. The total energy input rate is $3.4 \times 10^{-3} v_A^2/\tau_A$ at the early phase and is $1.0 \times 10^{-3} v_A^2/\tau_A$ at the later phase. Thus, the forcing can put more energy into the system with the decaying magnetic structure.

IV. SEMI-EMPIRICAL FORMULA FOR SPREAD OF RECONNECTION

We observed that driving fluctuations in a sheared magnetic structure lead to formation of O-points which indicates reconnection of the magnetic field lines. It appears that the fluctuations lead to field line wandering so that they reconnect and change their connectivity. Now, we derive an expression to describe the formation and spread of reconnection by the driven fluctuations in thick current sheets. Let us consider a sheared background magnetic field in the x direction

$$B_x = \frac{B_0 z}{\lambda}. \tag{12}$$

This can be thought of as a zeroth order approximation of the $B_x = B_0 \tanh(z/\lambda)$ field near the current sheet [Eq. (5)]. We are making this field reconnect by driving sinusoidal perturbations of the form

$$B_z = \tilde{B} \sin(k_x x). \tag{13}$$

Figure 8 shows a cartoon of how this perturbation is making the background field reconnect. As shown in the figure, we expect field lines to bend and reconnect because of the superposition of the added B_z fluctuations. Let us

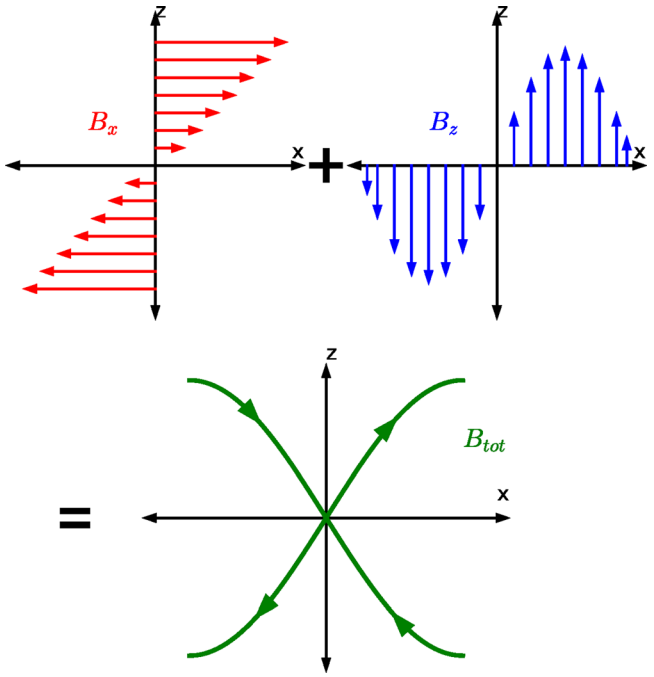


FIG. 8. Adding the B_x and B_z fields together, we expect the field lines to look as shown in the third figure with green lines. This indicates reconnection of field lines, with the origin becoming an X-point, or a meeting place for field lines from above and from below.

calculate the trajectory of these field lines. If the trajectory is defined by the locus of points (x, z), then this locus of points satisfies the equation

$$\frac{dz}{dx} = \frac{B_z}{B_x} = \frac{\tilde{B}}{B_0}\frac{\lambda}{z}\sin k_x x. \tag{14}$$

Integrating this equation gives

$$\frac{z^2}{2} = -\frac{\tilde{B}}{B_0}\frac{\lambda}{k_x}\cos(k_x x) + \text{constant}. \tag{15}$$

These bent field lines will create O-points and X-points in the field as shown in Fig. 8. Let us consider a set of field lines which form an X-point at the origin. The trajectory which passes through origin $(x, z) = (0, 0)$ will be

$$\frac{z^2}{2} = \frac{\tilde{B}}{B_0}\frac{\lambda}{k_x}(1 - \cos(k_x x)). \tag{16}$$

This gives us an upper limit on how far the reconnecting field line trajectories will spread. Thus, the r.m.s. value of the spread of these reconnecting field lines will be

$$z_{\text{r.m.s.}} \sim \sqrt{2\frac{\tilde{B}}{B_0}\frac{\lambda}{k_x}}. \tag{17}$$

The O-points will track this wandering of field lines. Please note that all the quantities on the right-hand-side change with time. According to this formula, the spread of O-points will depend on the amplitude of fluctuations $\tilde{B}$, the gradient length scale λ of the current density, and the wavenumber of forcing k_x. We calculate Eq. (17) semi-empirically from the simulations. We take the wavenumber of forcing k_x to be the average of the limiting wavenumbers k_1 and k_2 in Eq. (3). We measure the forcing amplitude $\tilde{B}$ directly from the simulation, as it changes with time. The current density gradient length scale λ is set initially by the initial condition, but it changes as the current sheet relaxes. Therefore, this gradient is also measured instantaneously inside the simulation by setting

$$\frac{B_0}{\lambda} \sim \left\langle \frac{\partial B_x}{\partial z} \right\rangle. \tag{18}$$

The spread of the reconnected field lines is estimated by taking the r.m.s. distance of the O-points from the center of the current sheet, thereby giving an estimate of the observed $z_{\text{r.m.s.}}$. We compare these two quantities from all runs to check whether this simple picture is correct.

Figure 9 compares z calculated from Eq. (17) to the z observed by looking at the spread of reconnected field lines. We analyze runs 1, 4, and 5 which vary the forcing amplitude A_0. The prediction of the semi-empirical formula shows that it follows the spread of O-points reasonably well. The formula gives an upper bound on how much the O-points will spread, as they are contained within the reconnected field lines. As the forcing amplitude increases, the level of fluctuation $\tilde{B}$ also rises and the O-points spread faster.

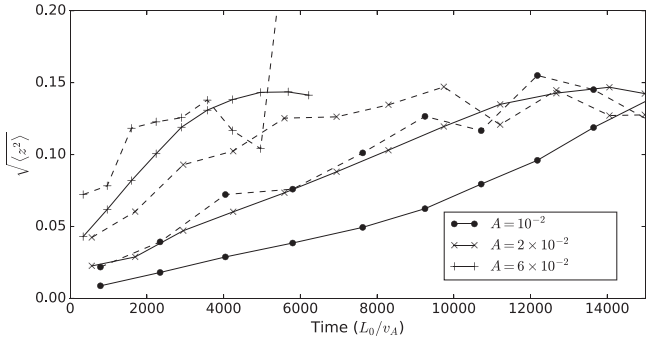


FIG. 9. Solid lines are from the observations and dashed lines are from the semi-empirical formula [Eq. (17)]. The different traces are for varying the forcing amplitude A_0 (runs 1, 4, and 5).

Figure 10 shows the comparison of the formula with the observed spreading of O-points for the simulations with a varying correlation time. Again we find that the formula reasonably captures the behavior of the field line wandering. As the correlation time increases from τ_A to $10\tau_A$, the O-points spread faster. This is because as the correlation time increases, the force persists for a longer time allowing for stronger deformation. However, increasing the correlation time from $10\tau_A$ to $100\tau_A$ does not change the behavior of field line wandering much, as shown by both the formula as well as simulation. Therefore, there is a limit to how much the force can bend the field lines, as probably non-linear effects start to play a role at strong field line bending.

Figure 11 shows the results for simulations with different forcing wavenumbers. The k_f is the average wavenumber of forcing, corresponding to the average of k_1 and k_2. For run 1 with $\langle k_f \rangle = 7\pi/L_0$, the semi-empirical formula correctly tracks the spread of O-points and gives an approximate upper bound to it. However, for runs 2 and 7 which have forcing at larger wavenumbers, the formula underestimates the spread of O-points. As the wavenumber of forcing is increased, the formula predicts that the field line wandering should decrease. This can be understood as the fact that a perturbation with longer wavelength will bend the field line for a longer distance, bending the field line more. However, this is not observed in the spread of O-points. Going from $k_f = 7\pi/L_0$ to $k_f = 14\pi/L_0$, there is no change in the spread of O-points and there is a slight increase in going up to $k_f = 28\pi/L_0$. It appears changing the wavenumber of forcing

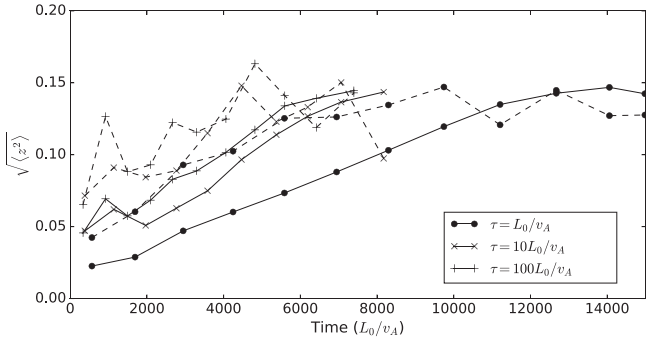


FIG. 10. Solid lines are from the observations and dashed lines are from the semi-empirical formula [Eq. (17)]. The different traces are for varying the correlation time of forcing τ_F (runs 1, 3, and 6).

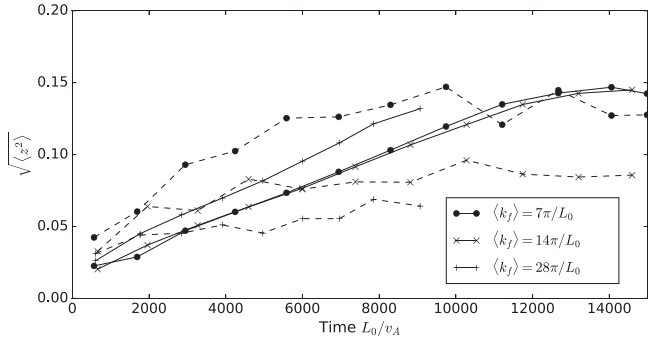


FIG. 11. Solid lines are from the observations and dashed lines are from the semi-empirical formula [Eq. (17)]. The different traces are for varying the forcing wavenumber range (k_1, k_2) (runs 1, 2, and 7).

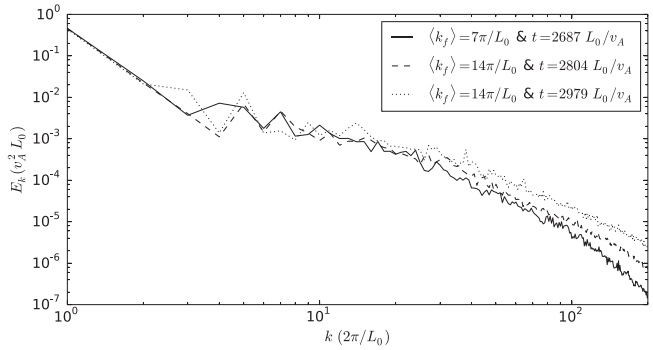


FIG. 12. The magnetic energy wavenumber spectrum at similar times (when $B^2 = B_0^2/2$) for runs 1, 2, and 7.

does not have a strong effect on the field line wandering. This could be because the nonlinear interaction transfers energy to a variety of different wavenumbers irrespective of the starting fluctuations. We compare the magnetic energy wavenumber spectra in these three simulations at similar times in Fig. 12. The spectra are picked at the time when $B^2 = B_0^2/2$, which is a similar time in all 3 cases. In addition to these spectra, Figure 13 shows the kinetic energy wavenumber spectra from the same set of simulations. The spectra have peaks near the forcing wavenumbers and initial power laws with spectral indices consistent with $-5/3$, followed by steepening at higher wavenumbers. Although the forcing wavenumbers are quite distinct in these three simulations, by a time of around $2500\tau_A$, the magnetic energy wavenumber spectra are similar, with nonlinear excitation of a wide range

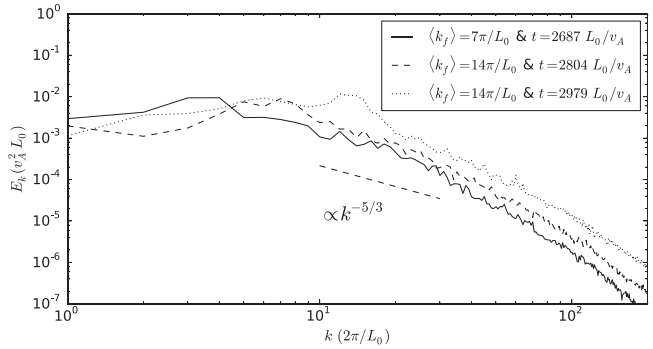


FIG. 13. The kinetic energy wavenumber spectrum at similar times (when $B^2 = B_0^2/2$) for runs 1, 2, and 7.

of wavenumbers in the system. Therefore, the change in driving wavenumbers does not seem to affect the simulation much.

Common across all the simulation results in Figs. 9–11, we find that the spread of field lines steadily rises till the spread of O-points $\sqrt{\langle z^2 \rangle}$ reaches around 0.14. This is the r.m.s. value of the z-distance of a set of uniformly distributed, randomly placed O-points in the simulation domain. This is because the z-distance of an O-point is calculated from its nearest current sheet and the current sheets are $0.5L_0$ apart. Therefore, the O-points will be uniformly distributed within a distance of 0 and $0.25L_0$, and their r.m.s. distance would be $\sqrt{\langle z^2 \rangle} = (\int_0^{0.25} 4z^2 \mathrm{d}z)^{1/2}$, where 4 is the probability of a uniform distribution between 0 and $0.25L_0$. This value is close to $0.14L_0$. In other words, when $\sqrt{\langle z^2 \rangle}$ reaches $0.14L_0$, it is not possible to identify which current sheet the O-point belongs to and that field lines are intermingling freely among the different current sheets. As a result of this, the magnetic field structure rapidly breaks down. We find that at the time when the spread of magnetic field line reaches this critical value, then the magnetic energy drops rapidly. Table II shows two characteristic times in the simulations. One is the field annihilation time τ_R when the magnetic energy drops below $10^{-4}B_0^2$. The other one is the time τ_H when $z_{\mathrm{r.m.s.}}$ reaches $0.14L_0$. The value of τ_H is assumed to be the intersection between the line $y = 0.14L_0$ and the curve of $y = z_{\mathrm{r.m.s.}}(t)$. From the plots of $z_{\mathrm{r.m.s.}}(t)$, we found that $z_{\mathrm{r.m.s.}}(t)$ is highly fluctuating but has a linear relation with time on average when $z_{\mathrm{r.m.s.}}(t)$ approaches $0.14L_0$ from below. So, we use this linear relationship to predict the time t_H at when $z_{\mathrm{r.m.s.}}(t)$ reaches $0.14L_0$ on average. Both τ_R and τ_H are similar in all simulations and they show that the spreading of O points is related with the destruction of magnetic structures. If the velocity fluctuation is stronger (higher A_0), then τ_R is shorter because the flow can deform the magnetic field more easily. The longer τ_F also provides a similar effect by maintaining the flow with high amplitude.

V. CONCLUSION AND DISCUSSION

We have run simulations to investigate how driven fluctuations modify thick, stable, and sheared magnetic field configurations. Before the investigation, we have tested our code to show that the tearing mode instability occurs under the appropriate conditions. We notice that the analytic expression for tearing mode instability we use is based on the assumption of no viscosity. However, with finite viscosity, in order to keep the solution resolved, we are able to benchmark our simulations with the instability condition only when one extra term is added into the induction equation to keep the sheets from dissipating away due to resistivity at the low Lundquist numbers reachable in simulations. This term is non-physical in the incompressible fluid framework since the only term to drive the magnetic field is $\nabla \times (\boldsymbol{v} \times \boldsymbol{B})$ in the induction equation and there is no velocity $\boldsymbol{v}$ to maintain such a force-free field.

TABLE II. The sheet destruction time τ_R and the approximate time τ_H for $z_{\mathrm{r.m.s.}}$ to reach 0.14.

ID	τ_R/τ_A	τ_H/τ_A
1	12 724	∼12 000
2	13 525	∼12 000
3	8297	∼7000
4	5336	∼3500
5	15 953	∼15000
6	7232	∼6000
7	11 606	∼9500

We then increase the Lundquist number S to the maximum possible for a given resolution and let the sheets decay freely (without that extra term). For our simulations, even if our starting equilibrium is weakly tearing unstable, still the tearing mode is not able to grow due to the faster decay of our equilibrium. In such a setup where reconnection normally does not occur, we then drive fluctuations on the equilibrium field. At the beginning, the perturbation cannot alter the shape of the sheets much because of the strong magnetic field. As the magnetic field decays, the effect of the perturbation increases and its area expands. While the net current density decreases, small current sheets are created with much stronger current density. These can be the sites where reconnection occurs.[32,33] After running for a long time while the initial magnetic field decays and its energy becomes comparable to the fluctuation energy, there is a rapid drop in the magnetic energy. During the whole process in all simulations, there is no signature of tearing mode of the initially stable sheet at the large scale under strong perturbation. We find that the energy injection rate, the energy dissipation rate, and the energy transfer rate from kinetic to magnetic energy are higher in the first phase when the initial magnetic field exists, compared to the later phase when it is destroyed. However, in the first phase, the injection rate is well matched by the dissipation rate, whereas in the second phase, the energy rises as the energy input is higher than the energy dissipation. This tells us that driven fluctuations can inject and dissipate more energy in the presence of a background magnetic structure than in a hydrodynamic plasma. We find very similar results even when we initialize our simulations with a simpler sinusoidal magnetic field structure rather than a sharp hyperbolic profile, implying that this is a general process occurring in any general sheared magnetic field structure.

The driven fluctuations cause the magnetic field lines to bend and reconnect. As a result, O-points are formed. We detect the formation of these O-points. A simple expression can be derived to describe this bending and spreading of field lines. The field line bending increases with stronger fluctuations and with smaller wavenumbers. We compare the predictions of this semi-empirical formula with the observed spread of O-points in our simulations and find that it does reasonably well in tracking the spread of O-points and provides an approximate upper limit on their distance from the current sheet center. It does not work well for larger wavenumbers due to the nonlinear interactions and energy transfer between the various wavenumbers. We also find that the reconnecting field lines spread faster with a longer correlation time of the fluctuations, but only up to a certain limit, beyond which they do not spread faster. This could again be

because of nonlinear effects not taken into account in this model. We confirm that once the wandering field lines from current sheets of opposite polarity start interacting, then the sheets are rapidly annihilated and magnetic energy drops explosively.

We can easily find sheared magnetic fields in nature, for example, in flux ropes. However, it is difficult to find and observe thin current sheets that readily reconnect in a steady environment. Therefore, it is a problem to explain how reconnection occurs, or is initiated in such systems. In this work, the perturbation is not weak but we can always pick a stronger initial magnetic field and the mechanism should be similar to what occurs in the first phase. This study thus also implies that even weak or moderately driven fluctuations can drive reconnection in such magnetic field configurations, while the level of reconnection depends on the strength of our plasma flow. Such fluctuations can drastically alter the energy dynamics of these systems. In the solar corona, shearing of the magnetic field occurs frequently. On top of this, there are numerous sources that can drive fluctuations, ranging from explosive events like flares to wave drivers like footpoint motions. These can interact with the sheared field and drive reconnection in such regions. We find that this process will intimately depend on the driving amplitude, and its wavelength and correlation time. The reconnection probability will improve with stronger driving, longer wavelengths, and longer correlation times. However, this study is limited to 2D simulations where the freedom of field lines is restricted. This picture might change in 3D where field lines have more freedom and can behave differently. In 3D, once the reconnection is allowed all over space, we expect that the magnetic energy should be maintained by balancing the turbulent dynamo generation with resistive dissipation. The magnetic energy should be similar to the energy in the eddies at the dissipation scale. We expect the magnetic energy to drop from the level of energy of the driving eddies to the energy of the eddies at the viscous scale after the disruption. We can also expect the disruption of the current sheets to be slower.

ACKNOWLEDGMENTS

P.P. would like to thank the Mahidol University Postdoctoral Fellowship Program for their support. K.M. was supported by the Interuniversity Attraction Poles Programme (initiated by the Belgian Science Policy Office, No. IAP P7/08 CHARM) and by the KU Leuven GOA/2015–014. P.P. and D.R. were also supported by Grant No. RTA5980003 from the Thailand Research Fund. This work used the Extreme Science and Engineering Discovery Environment (XSEDE) Stampede at the Texas Advanced Computing Center (TACC) through allocation TG-PHY170003. The authors would like to acknowledge useful discussions with Professor Nuno Loureiro and Dr. Fan Guo.

[1]E. G. Zweibel and M. Yamada, Annu. Rev. Astron. Astrophys. **47**, 291 (2009).
[2]S. van Goeler, W. Stodiek, and N. Sauthoff, Phys. Rev. Lett. **33**, 1201 (1974).
[3]K. Shibata and T. Magara, Living Rev. Sol. Phys. **8**, 6 (2011).
[4]T. Pulkkinen, Living Rev. Sol. Phys. **4**, 1 (2007).
[5]D. Kagan, L. Sironi, B. Cerutti, and D. Giannios, Space Sci. Rev. **191**, 545 (2015).
[6]P. A. Sweet, *Electromagnetic Phenomena in Cosmical Physics*, 6th ed., edited by B. Lehnert (Cambridge University Press, London, 1958), pp. 1231–1234.
[7]E. N. Parker, J. Geophys. Res. **62**, 509, https://doi.org/10.1029/JZ062i004p00509 (1957).
[8]H. E. Petschek, in *AAS-NASA Symposium on the Physics of Solar Flares*, edited by. W. N. Hess (NASA SP-50, Washington, DC, 1964), pp. 4239–4254.
[9]J. Birn, J. F. Drake, M. A. Shay, B. N. Rogers, R. E. Denton, M. Hesse, M. Kuznetsova, Z. W. Ma, A. Bhattacharjee, A. Otto, and P. L. Pritchett, J. Geophys. Res.: Space Phys. **106**(A3), 3715–3719, https://doi.org/10.1029/1999JA900449 (2001).
[10]A. Lazarian and E. T. Vishniac, Astrophys. J. **517**, 700 (1999).
[11]G. Kowal, A. Lazarian, E. T. Vishniac, and K. Otmianowska-Mazur, Astrophys. J. **700**, 63 (2009).
[12]A. Bhattacharjee, Annu. Rev. Astron. Astrophys. **42**, 365 (2004).
[13]P. Pongkitiwanichakul, F. Cattaneo, S. Boldyrev, J. Mason, and J. C. Perez, Mon. Not. R. Astron. Soc. **454**(2), 1503 (2015).
[14]E. G. Zweibel and M. Yamada, "Perspectives on magnetic reconnection," Proc. Math. Phys. Eng. Sci. **472**, 20160479 (2016).
[15]N. F. Loureiro, S. C. Cowley, W. D. Dorland, M. G. Haines, and A. A. Schekochihin, Phys. Rev. Lett. **95**, 235003 (2005).
[16]N. F. Loureiro, A. A. Schekochihin, and S. C. Cowley, Phys. Plasmas **14**, 100703 (2007).
[17]D. A. Uzdensky and N. F. Loureiro, Phys. Rev. Lett. **116**, 105003 (2016).
[18]R. E. Lopez, Adv. Space Res. **25**(7/8), 1667 (2000).
[19]W. H. Matthaeus and S. L. Lamkin, Phys. Fluids **28**, 303 (1985).
[20]W. H. Matthaeus and S. L. Lamkin, Phys. Fluids **29**, 2513 (1986).
[21]M. Yan, A. Otto, D. Muzzell, and L. C. Lee, J. Geophys. Res. **99**(A5), 8657, https://doi.org/10.1029/94JA00301 (1994).
[22]T. S. Hahm and R. M. Kulsrud, Phys. Fluids **28**, 2412 (1985).
[23]A. Bemporad, G. Poletto, S. T. Suess, Y.-K. Ko, N. A. Schwadron, H. A. Elliott, and J. C. Raymond, Astrophys. J. **638**, 1110–1128 (2006).
[24]P. F. Chen, Living Rev. Sol. Phys. **8**, 1 (2011).
[25]Y. Fan, "MHD equilibria and triggers for prominence eruption," in *Solar Prominences, Astrophysics Space Science Library*, Vol. 415, edited by J.-C. Vial and O. Engvold (Springer, 2015), p. 297.
[26]F. Cattaneo and T. Emonet, Astrophys. J. **588**, 1183 (2003).
[27]J. Towns, T. Cockerill, M. Dahan, I. Foster, K. Gaither, A. Grimshaw, V. Hazlewood, S. Lathrop, D. Lifka, G. D. Peterson, R. Roskies, J. R. Scott, and N. Wilkins-Diehr, "XSEDE: Accelerating scientific discovery," Comput. Sci. Eng. **16**(5), 62–74 (2014).
[28]H. P. Furth, J. Killeen, and M. N. Rosenbluth, Phys. Fluids **6**, 459–484 (1963).
[29]M. Velli and A. W. Hood, Sol. Phys. **119**, 107–124 (1989).
[30]F. Porcelli, Phys. Fluids **30**, 1734 (1987).
[31]B. Coppi, J. M. Greene, and J. L. Johnson, Nucl. Fusion **6**, 101 (1966).
[32]K. D. Makwana, V. Zhdankin, H. Li, W. Daughton, and F. Cattaneo, Phys. Plasmas **22**, 042902 (2015).
[33]K. Makwana, H. Li, F. Guo, and X. Li, J. Phys: Confer. Series **837**(1), 012004 (2017).

ASTRONOMY

Einstein@Home discovers a radio-quiet gamma-ray millisecond pulsar

Colin J. Clark,[1,2,3]* Holger J. Pletsch,[1,2] Jason Wu,[4] Lucas Guillemot,[4,5,6] Matthew Kerr,[7] Tyrel J. Johnson,[8†] Fernando Camilo,[9] David Salvetti,[10] Bruce Allen,[1,2,11] David Anderson,[12] Carsten Aulbert,[1,2] Christian Beer,[1,2] Oliver Bock,[1,2] Andres Cuéllar,[1,2] Heinz-Bernd Eggenstein,[1,2,13] Henning Fehrmann,[1,2] Michael Kramer,[3,4] Shawn A. Kwang,[11] Bernd Machenschalk,[1,2] Lars Nieder,[1,2] Markus Ackermann,[14] Marco Ajello,[15] Luca Baldini,[16] Jean Ballet,[17] Guido Barbiellini,[18,19] Denis Bastieri,[20,21] Ronaldo Bellazzini,[22] Elisabetta Bissaldi,[23,24] Roger D. Blandford,[25] Elliott D. Bloom,[25] Raffaella Bonino,[26,27] Eugenio Bottacini,[25] Terri J. Brandt,[28] Johan Bregeon,[29] Philippe Bruel,[30] Rolf Buehler,[14] Toby H. Burnett,[31] Sara Buson,[28†] Rob A. Cameron,[25] Regina Caputo,[32] Patrizia A. Caraveo,[10] Elisabetta Cavazzuti,[33] Claudia Cecchi,[34,35] Eric Charles,[25] Alexandre Chekhtman,[8‡] Stefano Ciprini,[34,36] Lynn R. Cominsky,[37] Denise Costantin,[21] Sara Cutini,[34,36] Filippo D'Ammando,[38,39] Andrea De Luca,[10,40] Rachele Desiante,[26,41] Leonardo Di Venere,[23,24] Mattia Di Mauro,[25] Niccolò Di Lalla,[16] Seth W. Digel,[25] Cecilia Favuzzi,[23,24] Elizabeth C. Ferrara,[28,42] Anna Franckowiak,[14] Yasushi Fukazawa,[43] Stefan Funk,[44] Piergiorgio Fusco,[23,24] Fabio Gargano,[24] Dario Gasparrini,[34,36] Nico Giglietto,[23,24] Francesco Giordano,[23,24] Marcello Giroletti,[38] Germán A. Gomez-Vargas,[45,46] David Green,[28,47] Isabelle A. Grenier,[17] Sylvain Guiriec,[28,48] Alice K. Harding,[28] John W. Hewitt,[49] Deirdre Horan,[30] Guðlaugur Jóhannesson,[50,51] Shiki Kensei,[43] Michael Kuss,[22] Giovanni La Mura,[21] Stefan Larsson,[52,53] Luca Latronico,[26] Jian Li,[54] Francesco Longo,[18,19] Francesco Loparco,[23,24] Michael N. Lovellette,[7] Pasquale Lubrano,[34] Jeffrey D. Magill,[47] Simone Maldera,[26] Alberto Manfreda,[16] Mario N. Mazziotta,[24] Julie E. McEnery,[28,47] Peter F. Michelson,[25] Nestor Mirabal,[28†] Warit Mitthumsiri,[55] Tsunefumi Mizuno,[56] Maria Elena Monzani,[25] Aldo Morselli,[46] Igor V. Moskalenko,[25] Eric Nuss,[29] Takashi Ohsugi,[56] Nicola Omodei,[25] Monica Orienti,[38] Elena Orlando,[25] Michele Palatiello,[18,19] Vaidehi S. Paliya,[15] Francesco de Palma,[24,57] David Paneque,[58] Jeremy S. Perkins,[28] Massimo Persic,[18,59] Melissa Pesce-Rollins,[22] Troy A. Porter,[25] Giacomo Principe,[44] Silvia Rainò,[23,24] Riccardo Rando,[20,21] Paul S. Ray,[7] Massimiliano Razzano,[22] Anita Reimer,[25,60] Olaf Reimer,[25,60] Roger W. Romani,[25] Pablo M. Saz Parkinson,[61,62,63] Carmelo Sgrò,[22] Eric J. Siskind,[64] David A. Smith,[65] Francesca Spada,[22] Gloria Spandre,[22] Paolo Spinelli,[23,24] Jana B. Thayer,[25] David J. Thompson,[28] Diego F. Torres,[54,66] Eleonora Troja,[28,47] Giacomo Vianello,[25] Kent Wood,[67‡] Matthew Wood[25]

Copyright © 2018 The Authors, some rights reserved; exclusive licensee American Association for the Advancement of Science. No claim to original U.S. Government Works. Distributed under a Creative Commons Attribution NonCommercial License 4.0 (CC BY-NC).

Millisecond pulsars (MSPs) are old neutron stars that spin hundreds of times per second and appear to pulsate as their emission beams cross our line of sight. To date, radio pulsations have been detected from all rotation-powered MSPs. In an attempt to discover radio-quiet gamma-ray MSPs, we used the aggregated power from the computers of tens of thousands of volunteers participating in the Einstein@Home distributed computing project to search for pulsations from unidentified gamma-ray sources in Fermi Large Area Telescope data. This survey discovered two isolated MSPs, one of which is the only known rotation-powered MSP to remain undetected in radio observations. These gamma-ray MSPs were discovered in completely blind searches without prior constraints from other observations, raising hopes for detecting MSPs from a predicted Galactic bulge population.

INTRODUCTION

Since its launch in 2008, the Large Area Telescope (LAT) on board the Fermi Gamma-ray Space Telescope (*1*) has detected pulsations from more than 200 gamma ray–emitting rotation-powered pulsars (see http://tinyurl.com/fermipulsars). Nearly half of these are millisecond pulsars (MSPs), old neutron stars thought to have been spun up by accreting matter from a companion star (*2*, *3*), reaching fast rotation rates of hundreds of revolutions per second (*4*). The first gamma-ray MSPs were found shortly after Fermi's launch by folding gamma-ray photon arrival times using rotational ephemerides from concurrent radio telescope observations (*5*). Dedicated radio searches targeting unidentified LAT sources (*6*) have also led to the discovery of more than 80 new MSPs.

However, radio pulsations from many gamma-ray pulsars are not detectable from Earth because of their low intrinsic luminosity or their radio beams not intersecting our line of sight. These radio-quiet pulsars can only be found by directly searching for pulsations at unknown frequencies in gamma-ray data. These "blind" searches in LAT data (*7*, *8*) have discovered 57 young pulsars, 53 of which are radio quiet (*9*–*11*). However, the blind search detection of gamma-ray MSPs is challenging. Only one gamma-ray MSP (*12*), also detected later in radio (*13*), has been found in previous blind searches, and this was only possible with additional positional and orbital constraints from optical and x-ray observations (*14*). With this exception, all rotationally powered MSPs have been discovered through their radio pulsations, limiting knowledge of the

Downloaded from http://advances.sciencemag.org/ on April 8, 2018

population of MSPs to nearby bright pulsars with radio emission beamed toward Earth (*15*).

Thus, in contrast to the large number of radio-quiet young pulsars seen by the LAT, no radio-quiet gamma-ray MSP has been found. Some disparity between the numbers observed in each of these two groups is expected; MSPs have wider radio beams that are visible from a larger range of viewing angles, making radio-quiet MSPs less common (*16*). However, the apparent absence of this source class so far is more likely to be due to the inherent difficulty of detecting the signal from an MSP at an unknown location. At higher pulsation frequencies, higher precision is required for the position-dependent "barycentering" corrections applied to photon arrival times to account for the Doppler shift due to Fermi's motion through the solar system. The localization region of a typical unidentified gamma-ray source, limited by the LAT's angular resolution to a few arc minutes (*17*), is far larger than the arc second precision required to detect gamma-ray pulsations from MSPs. Hundreds of thousands of sky locations covering the source localization region must therefore be searched, incurring a large computational cost.

In a recent study (*18*), we improved gamma-ray pulsar blind search methods to reduce their computational cost and increase their sensitivity. These methods are based on an efficient "semicoherent" first stage, in which only photons arriving within a short time of one another (within a "lag window") are combined coherently. More sensitive, but more computationally expensive, follow-up stages are then used to pick out and refine weak candidate signals. The efficient search-grid spacings derived from our study (*18*) allowed us to use a longer lag window and, hence, achieve higher sensitivity than was possible in previous surveys.

Using these techniques, we performed a survey (*10*) on the distributed volunteer computing system Einstein@Home (*19*) to search for pulsations from 152 pulsar-like unidentified sources (which have curved spectra and low flux variability) from the Fermi-LAT Third Source Catalog (3FGL) (*17*). The survey searched 5.5 years of improved "Pass 8" Fermi-LAT data (*20*). We searched the full gamma-ray source localization region for each source and over a range of spin frequencies and spin-down rates broad enough to cover all known young pulsars and MSPs. This search volume for each source was split into hundreds of thousands of smaller regions, each of which could be searched by a typical personal computer within a few hours. These are then distributed among the computers of tens of thousands of volunteers located across the globe, which run the search when otherwise idle. Using more than 10,000 years of volunteered central processing unit (CPU) time, this gamma-ray pulsar survey has discovered 17 young pulsars (*10*, *11*).

RESULTS

Among the sources searched by the Einstein@Home survey were two of the three unassociated 3FGL sources with the highest detection significance, 3FGL J1035.7−6720 and 3FGL J1744.1−7619 (*18*). Both of these have high Galactic latitudes and pulsar-like spectra, marking them as promising MSP candidates (*21*). These sources were searched

[1]Albert-Einstein-Institut, Max-Planck-Institut für Gravitationsphysik, D-30167 Hannover, Germany. [2]Leibniz Universität Hannover, D-30167 Hannover, Germany. [3]Jodrell Bank Centre for Astrophysics, School of Physics and Astronomy, University of Manchester, Manchester M13 9PL, UK. [4]Max-Planck-Institut für Radioastronomie, Auf dem Hügel 69, D-53121 Bonn, Germany. [5]Laboratoire de Physique et Chimie de l'Environnement et de l'Espace–Université d'Orléans/CNRS, F-45071 Orléans Cedex 02, France. [6]Station de radioastronomie de Nançay, Observatoire de Paris, CNRS/INSU, F-18330 Nançay, France. [7]Space Science Division, Naval Research Laboratory, Washington, DC 20375–5352, USA. [8]College of Science, George Mason University, Fairfax, VA 22030, USA. [9]Square Kilometre Array South Africa, Pinelands 7405, South Africa. [10]Istituto Nazionale di Astrofisica (INAF)–Istituto di Astrofisica Spaziale e Fisica Cosmica Milano, via E. Bassini 15, I-20133 Milano, Italy. [11]Department of Physics, University of Wisconsin-Milwaukee, P.O. Box 413, Milwaukee, WI 53201, USA. [12]Space Sciences Laboratory, University of California at Berkeley, Berkeley, CA 94720, USA. [13]Albert-Einstein-Institut, Max-Planck-Institut für Gravitationsphysik, D-14476 Potsam-Golm, Germany. [14]Deutsches Elektronen Synchrotron (DESY), D-15738 Zeuthen, Germany. [15]Department of Physics and Astronomy, Clemson University, Kinard Laboratory of Physics, Clemson, SC 29634–0978, USA. [16]Università di Pisa and Istituto Nazionale di Fisica Nucleare, Sezione di Pisa I-56127 Pisa, Italy. [17]Laboratoire AIM, CEA-IRFU/CNRS/Université Paris Diderot, Service d'Astrophysique, CEA Saclay, F-91191 Gif sur Yvette, France. [18]Istituto Nazionale di Fisica Nucleare, Sezione di Trieste, I-34127 Trieste, Italy. [19]Dipartimento di Fisica, Università di Trieste, I-34127 Trieste, Italy. [20]Istituto Nazionale di Fisica Nucleare, Sezione di Padova, I-35131 Padova, Italy. [21]Dipartimento di Fisica e Astronomia "G. Galilei," Università di Padova, I-35131 Padova, Italy. [22]Istituto Nazionale di Fisica Nucleare, Sezione di Pisa, I-56127 Pisa, Italy. [23]Dipartimento di Fisica "M. Merlin" dell'Università e del Politecnico di Bari, I-70126 Bari, Italy. [24]Istituto Nazionale di Fisica Nucleare, Sezione di Bari, I-70126 Bari, Italy. [25]W. W. Hansen Experimental Physics Laboratory, Kavli Institute for Particle Astrophysics and Cosmology, Department of Physics and SLAC National Accelerator Laboratory, Stanford University, Stanford, CA 94305, USA. [26]Istituto Nazionale di Fisica Nucleare, Sezione di Torino, I-10125 Torino, Italy. [27]Dipartimento di Fisica, Università degli Studi di Torino, I-10125 Torino, Italy. [28]NASA Goddard Space Flight Center, Greenbelt, MD 20771, USA. [29]Laboratoire Univers et Particules de Montpellier, Université Montpellier, CNRS/IN2P3, F-34095 Montpellier, France. [30]Laboratoire Leprince-Ringuet, École polytechnique, CNRS/IN2P3, F-91128 Palaiseau, France. [31]Department of Physics, University of Washington, Seattle, WA 98195–1560, USA. [32]Center for Research and Exploration in Space Science and Technology (CRESST) and NASA Goddard Space Flight Center, Greenbelt, MD 20771, USA. [33]Italian Space Agency, Via del Politecnico snc, 00133 Roma, Italy. [34]Istituto Nazionale di Fisica Nucleare, Sezione di Perugia, I-06123 Perugia, Italy. [35]Dipartimento di Fisica, Università degli Studi di Perugia, I-06123 Perugia, Italy. [36]Space Science Data Center–Agenzia Spaziale Italiana, Via del Politecnico snc, I-00133, Roma, Italy. [37]Department of Physics and Astronomy, Sonoma State University, Rohnert Park, CA 94928–3609, USA. [38]INAF Istituto di Radioastronomia, I-40129 Bologna, Italy. [39]Dipartimento di Astronomia, Università di Bologna, I-40127 Bologna, Italy. [40]Istituto Universitario di Studi Superiori (IUSS), I-27100 Pavia, Italy. [41]Università di Udine, I-33100 Udine, Italy. [42]Center for Research and Exploration in Space Sciences and Technology II, University of Maryland, College Park, MD 20742, USA. [43]Department of Physical Sciences, Hiroshima University, Higashi-Hiroshima, Hiroshima 739-8526, Japan. [44]Friedrich-Alexander-Universität Erlangen-Nürnberg, Erlangen Centre for Astroparticle Physics, Erwin-Rommel-Strasse 1, 91058 Erlangen, Germany. [45]Instituto de Astrofísica, Facultad de Física, Pontificia Universidad Católica de Chile, Casilla 306, Santiago 22, Chile. [46]Istituto Nazionale di Fisica Nucleare, Sezione di Roma "Tor Vergata," I-00133 Roma, Italy. [47]Department of Physics and Department of Astronomy, University of Maryland, College Park, MD 20742, USA. [48]Department of Physics, The George Washington University, 725 21st Street, NW, Washington, DC 20052, USA. [49]Department of Physics, University of North Florida, 1 UNF Drive, Jacksonville, FL 32224, USA. [50]Science Institute, University of Iceland, IS-107 Reykjavik, Iceland. [51]NORDITA, Roslagstullsbacken 23, 106 91 Stockholm, Sweden. [52]Department of Physics, KTH Royal Institute of Technology, AlbaNova, SE-106 91 Stockholm, Sweden. [53]The Oskar Klein Centre for Cosmoparticle Physics, AlbaNova, SE-106 91 Stockholm, Sweden. [54]Institute of Space Sciences (IEEC-CSIC), Campus UAB, Carrer de Magrans s/n, E-08193 Barcelona, Spain. [55]Department of Physics, Faculty of Science, Mahidol University, Bangkok 10400, Thailand. [56]Hiroshima Astrophysical Science Center, Hiroshima University, Higashi-Hiroshima, Hiroshima 739-8526, Japan. [57]Università Telematica Pegaso, Piazza Trieste e Trento, 48, I-80132 Napoli, Italy. [58]Max-Planck-Institut für Physik, D-80805 München, Germany. [59]Osservatorio Astronomico di Trieste, Istituto Nazionale di Astrofisica, I-34143 Trieste, Italy. [60]Institut für Astro- und Teilchenphysik and Institut für Theoretische Physik, Leopold-Franzens-Universität Innsbruck, A-6020 Innsbruck, Austria. [61]Santa Cruz Institute for Particle Physics, Department of Physics and Department of Astronomy and Astrophysics, University of California at Santa Cruz, Santa Cruz, CA 95064, USA. [62]Department of Physics, The University of Hong Kong, Pokfulam Road, Hong Kong, China. [63]Laboratory for Space Research, The University of Hong Kong, Hong Kong, China. [64]NYCB Real-Time Computing Inc., Lattingtown, NY 11560–1025, USA. [65]Centre d'Études Nucléaires de Bordeaux Gradignan, IN2P3/CNRS, Université Bordeaux 1, BP120, F-33175 Gradignan Cedex, France. [66]Institució Catalana de Recerca i Estudis Avançats (ICREA), E-08010 Barcelona, Spain. [67]Praxis Inc., Alexandria, VA 22303, USA.
*Corresponding author. Email: colin.clark-2@manchester.ac.uk
†NASA Postdoctoral Program Fellow, USA.
‡Resident at Naval Research Laboratory, Washington, DC 20375, USA.

Downloaded from http://advances.sciencemag.org/ on April 8, 2018

9 and 10 times, respectively, in a survey of unidentified Fermi-LAT sources performed with the Parkes radio telescope (*6*), but no pulsations were detected. Previous blind gamma-ray searches of these sources, including an earlier Einstein@Home survey (*22*) using less data and a shorter lag window, were also unsuccessful.

The latest Einstein@Home survey revealed gamma-ray pulsations from these sources, at frequencies of $\nu = 348$ Hz and $\nu = 213$ Hz, identifying them as isolated MSPs now known as PSR J1035–6720 and PSR J1744–7619. The gamma-ray pulsations had H test [a significance test for pulsations in unbinned event data (*23*)] values of $H = 389$ and $H = 494$, corresponding to single-trial false-alarm probabilities of $< 5 \times 10^{-68}$ and $< 4 \times 10^{-86}$, respectively. For comparison, Einstein@Home can perform fewer than 10^{20} independent trials in 1 year.

Following their discoveries, we refined the rotational and astrometric parameters of each pulsar by timing their gamma-ray pulsations. The resulting estimates and uncertainties on their timing and spectral parameters are given in Table 1, and the resulting integrated pulse profiles are shown in Fig. 1.

These MSPs remained undetected in more sensitive analyses of the earlier Parkes survey data (*6*), using the now-known pulsation periods. However, a weak signal [with average flux density $S_{1400} \approx 40$ μJy (microjanskys) at a radio frequency of 1400 MHz] was detected from PSR J1035–6720 in four follow-up Parkes searches. Its estimated distance derived from its dispersion measure ($\mathrm{DM} = 84.16 \pm 0.22$ pc cm^{-3}) is $d \approx 1.46$ kpc or $d \approx 2.24$ kpc, according to the YMW16 (*24*) and NE2001 (*25*) Galactic electron-density models, respectively. PSR J1035–6720 therefore has a pseudo-luminosity of $L_{1400} = S_{1400}d^2 \sim 0.085$ to 0.20 mJy (millijanskys) kpc^2. This is less luminous than the majority of known radio MSPs with measured pseudo-luminosities in the Australia Telescope National Facility (ATNF) Catalogue (*26*), as shown in Fig. 2.

In contrast, PSR J1744–7619 has remained undetected in two dedicated 3-hour follow-up searches on 19 March 2017 and 10 April 2017. These give an upper limit of ~ 23 μJy on its radio flux density, below the 30 μJy threshold used by Abdo *et al.* (*9*) to classify gamma-ray pulsars as radio quiet. This threshold is chosen to represent a limiting sensitivity for pulsar surveys; a new generation of radio telescopes will be needed to discover new Galactic field pulsars with flux densities below this level (*27*).

In the absence of a dispersion measurement, the distance to PSR J1744–7619 is hard to constrain. A weak upper limit of $d \sim 1$ kpc can be obtained by assuming that its loss in rotational energy as it spins down is converted entirely into the observed gamma-ray emission. This distance limit implies a maximum $L_{1400} \approx 0.023$ mJy kpc^2. Only two known MSPs have lower reliably measured pseudo-luminosities (*28*, *29*). Even if the lack of detection in these follow-up searches was due to temporary interstellar scintillation, the upper limit from the multiple shorter observations from the previous survey suggests a maximum $L_{1400} \approx 0.15$ mJy kpc^2, weaker than 90% of radio MSPs. PSR J1744–7619 therefore has (at least) an unusually low radio luminosity.

The fields of PSRs J1035–6720 and J1744–7619 were observed in x-rays by XMM-Newton as part of a complementary effort to discover radio-quiet MSPs by searching for possible x-ray counterparts to unidentified LAT sources (*21*). Positionally coincident x-ray counterparts were detected for both pulsars. Their gamma-ray–to–x-ray flux ratios ($F_\gamma/F_X \approx 700$ and 1100, respectively) are consistent with those of other known isolated gamma-ray MSPs (*30*). The gamma-ray spectral properties of these pulsars are also consistent with those of the

Table 1. Measured and derived properties of the newly discovered MSPs. For timing parameters, we report the mean values from a Monte Carlo timing analysis and 1σ uncertainties on the final digits in parentheses. The first set of uncertainties on spectral parameters is statistical and the second set estimates the effects of systematic uncertainties in the LAT's effective collecting area and the Galactic diffuse emission model. Timing parameters are in barycentric dynamical time (TDB) units. The spin-down power of PSR J1035–6720 has been corrected for the Doppler shift induced by its proper motion; only an upper limit is given for PSR J1744–7619, because this correction cannot be applied as a result of its uncertain distance. mas, milli–arc second.

Parameter	PSR J1035–6720	PSR J1744–7619
Timing parameters		
Reference time (MJD)	55716	
Data span (MJD)	54682–57828	
Right ascension (R.A.) (J2000.0), α (hh:mm:ss)	10:35:27.478(1)	17:44:00.488(2)
Declination (Decl.) (J2000.0), δ (dd:mm:ss)	−67:20:12.692(6)	−76:19:14.710(9)
Proper motion in R.A., $\mu_\alpha \cos\delta$ (mas year^{-1})	−12(3)	−21(3)
Proper motion in Decl. μ_δ (mas year^{-1})	1(3)	−7(3)
Spin frequency, ν (Hz)	348.18864014054 (8)	213.33223675351 (5)
Spin-down rate, $-\dot{\nu}$ (10^{-15} Hz s^{-1})	5.633(1)	0.4405(8)
Second frequency derivative, $\lvert\ddot{\nu}\rvert$ (10^{-25} Hz s^{-2})	< 1.1	< 0.7
Spin period, P (ms)	2.8720063916972(7)	4.687524094895(1)
Period derivative, $\dot{P}$ (10^{-20} s s^{-1})	4.647(1)	0.968(2)
Derived parameters		
Galactic longitude, l (°)	290.37	317.11
Galactic latitude, b (°)	−7.84	−22.46
Spin-down power, $\dot{E}$ (10^{33} erg s^{-1})	75.0	< 3.7
Characteristic age, τ_c (10^9 years)	1.0	7.7
Surface magnetic field, B_S (10^8 G)	3.7	2.2
Light-cylinder magnetic field, B_{LC} (10^5 G)	1.4	0.2
Phase-averaged gamma-ray spectral parameters above 100 MeV		
Test statistic, TS	1839.2	2492.2
Photon index, Γ	1.46 ± 0.07 ± 0.09	1.07 ± 0.10 ± 0.02
Cutoff energy, E_c (GeV)	2.76 ± 0.26 ± 0.36	1.82 ± 0.19 ± 0.01
Photon flux (10^{-9} cm^{-2} s^{-1})	24.4 ± 1.7 ± 1.5	19.2 ± 1.5 ± 1.0
Energy flux, F_γ (10^{-12} erg cm^{-2} s^{-1})	21.5 ± 0.8 ± 1.1	20.8 ± 0.8 ± 1.1
Off-pulse spectral parameters above 100 MeV		
Test statistic, TS	7.4	33.8
TS of exponential cutoff, TS_{cut}	—	8.3
Photon index, Γ	—	1.35 ± 0.70 ± 0.09
Cutoff energy, E_c (GeV)	—	1.06 ± 0.76 ± 0.13
Photon flux (10^{-9} cm^{-2} s^{-1})	—	1.9 ± 0.9 ± 0.1
Energy flux, F_γ (10^{-12} erg cm^{-2} s^{-1})	—	1.2 ± 0.3 ± 0.1

Downloaded from http://advances.sciencemag.org/ on April 8, 2018

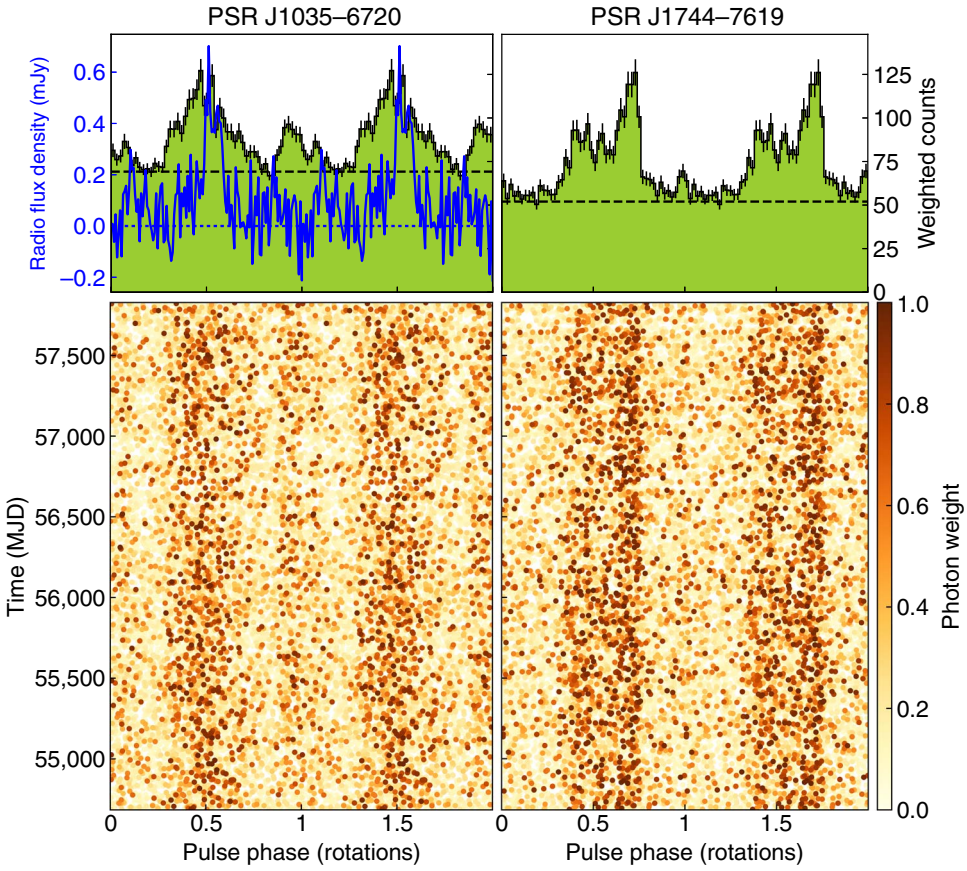


Fig. 1. Pulsed signals from the two newly discovered MSPs. Rotational phases of individual gamma-ray photons (**bottom**) and integrated pulse profiles (**top**) of the newly detected MSPs. Each photon has been assigned a weight, determined by its energy and arrival direction, representing the probability of it having come from the gamma-ray source in question. These weights are indicated by the color bar. In the top panels, the black dashed line shows the estimated background level, derived from the photon weights as in study of Abdo *et al.* (*9*). For PSR J1035–6720, the blue line shows the radio profile as measured by the Parkes radio telescope at 1400 MHz, averaged over four observations after subtracting an estimated baseline (dotted line). Two identical rotations are shown for clarity. MJD, Modified Julian Date.

MSPs studied in the Second Fermi-LAT Catalog of Gamma-ray Pulsars (*9*). Their x-ray and gamma-ray spectra therefore give us no reason to suspect that these radio-faint MSPs belong to another class of objects different from that of other gamma-ray emitting MSPs.

One explanation for their weak radio pulsations could therefore be that their radio beams either clip our line of sight or, in the case of PSR J1744–7619, do not cross it at all. To investigate this scenario, we modeled the gamma-ray emission geometries by fitting simulated pulse profiles to the observed gamma-ray photon phases, using the fitting technique and models described in the study of Johnson *et al.* (*31*) and references therein. We considered three emission models: an outer gap (OG) model, a two-pole caustic (TPC) model, and a pair-starved polar cap (PSPC) model.

For PSR J1035–6720, only the PSPC model is consistent with the detection of radio pulsations. This model predicts that the gamma-ray pulse should lead the radio pulse, an unusual characteristic shared by only six other MSPs studied by Johnson *et al.* (*31*). The observed lag between the radio and gamma-ray pulses, shown in Fig. 1, is consistent with this prediction. However, the uncertainty of DM leads to an additional uncertainty of the arrival phase of the radio pulse of 0.15 rotations, larger than the observed lag between the two pulses. Because of this phase uncertainty and the faintness of the radio pulse, we have not attempted a joint fit of the radio and gamma-ray data.

The best-fitting models (TPC and PSPC) for PSR J1744–7619 have our line of sight cutting across the predicted radio emission cone and not merely clipping it. The lack of radio emission from PSR J1744–7619 is therefore not easily explained by small offsets of a few degrees from the best-fitting geometry. The best-fitting TPC model for this pulsar is further supported by a spectral analysis of off-pulse flux from PSR J1744–7619, which revealed likely magnetospheric unpulsed emission. Therefore, either the nondetection of radio pulsations is due to an extremely low intrinsic radio luminosity or it is at odds with the best-fitting emission models. More elaborate pulsar emission models, including emission from the current sheet (*32*, *33*), may be required to address this tension.

DISCUSSION

At least 12 high-confidence pulsar-like 3FGL sources at high Galactic latitudes have been identified but have remained undetected in repeated radio pulsation searches. Several convincing MSP candidates have also been highlighted by Saz Parkinson *et al.* (*21*). The most natural explanation for these sources is that they are either radio-quiet MSPs or MSPs in eclipsing binary systems, which are also difficult to detect in radio searches. Our results demonstrate that blind gamma-ray pulsation searches of LAT data are now able to find isolated MSPs

Downloaded from http://advances.sciencemag.org/ on April 8, 2018

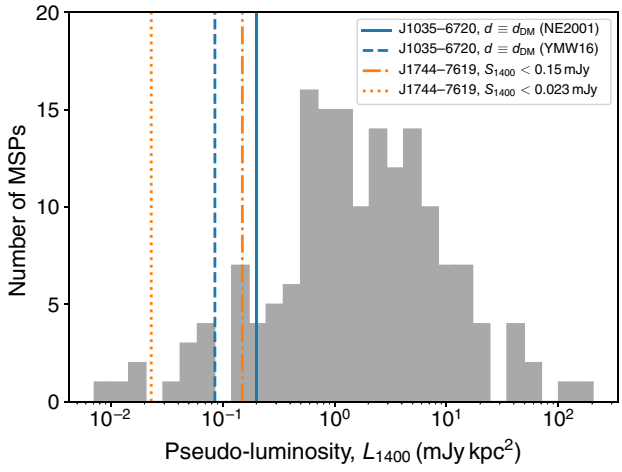


Fig. 2. Pseudo-luminosities ($L_{1400} = S_{1400}\, d^2$) of known MSPs (including both Galactic field MSPs and those found in globular clusters) with flux density and distance measurements in the ATNF Catalogue (*26*), version 1.57. The measured pseudo-luminosities of PSR J1035−6720 according to the NE2001 and YMW16 Galactic dispersion models are shown by solid and dashed vertical lines, respectively. The dotted and dashed-dotted vertical lines show the upper limits on the pseudo-luminosity of PSR J1744−7619, assuming a maximum distance of 1 kpc, from two dedicated follow-up radio observations and (a conservative estimate) from the 10 shorter observations of Camilo *et al.* (*6*), respectively.

among these sources without requiring any additional constraints from multiwavelength observations and therefore provide an entirely new method through which to investigate the Galactic MSP population.

In particular, blind gamma-ray searches may partially address the severe biases in the observed radio MSP luminosity distribution because of the difficulty of detecting faint MSPs (*15*). A sizeable sample of gamma ray–selected MSPs would also provide an unbiased estimate of the relative numbers of radio-loud and radio-quiet gamma-ray MSPs, constraining the ratio of the radio and gamma-ray beam solid angles, an important discriminator for pulsar emission models (*16*, *34*). These models suggest that a large fraction of gamma-ray MSPs could be radio quiet; the contrast with the present situation of just three gamma ray–selected MSPs compared to almost 100 radio-loud gamma-ray MSPs illustrates both the technical barrier faced by blind searches for gamma-ray MSPs until now and their large discovery potential.

Furthermore, the rotational stability and low flux variability of MSPs mean that their recoverable signals will accumulate steadily over time. Blind gamma-ray searches will therefore become sensitive to fainter and more distant MSPs as the Fermi mission continues. The rotation rates of MSPs are also unaffected by glitches or timing noise, which often interrupt the signals from young pulsars. We may therefore expect future blind gamma-ray searches to find a larger proportion of MSPs compared to previous surveys, whose discoveries have been dominated by young pulsars.

The ability to detect radio-quiet MSPs in blind gamma-ray searches is also an important tool for the search for gamma-ray emission from dark matter. A number of unidentified LAT sources at high Galactic latitudes have curved spectra that are consistent with the annihilation of a candidate for dark matter in ultra-faint dwarf spheroidal galaxies or dark matter subhalos (*35*, *36*). However, these sources are perhaps more likely to be MSPs, whose spectra are similar. If these sources continue to remain undetected at other wavelengths, then blind gamma-ray searches are necessary to confirm or rule out at least an isolated, radio-quiet MSP explanation. The observed GeV (billion electron volts) excess toward the Galactic center (*37*), another possible dark matter annihilation signal, is also consistent with an unresolved population of thousands of MSPs in the Galactic bulge (*38*–*40*). No more than a handful of these are expected to be detected with current radio telescopes because of the large distance to the bulge and the strong scattering in that region of the Galaxy (*40*). This latter issue does not affect gamma-ray pulsations, meaning that gamma-ray searches perhaps have the highest potential to uncover the brightest members of this population.

MATERIALS AND METHODS

LAT data preparation

The data in which the two MSPs were first detected covered approximately 5.5 years of LAT observations between 4 August 2008 and 6 April 2014. They were produced using preliminary internal versions of the Pass 8 instrument response functions (IRFs) and background models. Using gtselect, which is part of the Fermi Science Tools (http://fermi.gsfc.nasa.gov/ssc/data/analysis/software/), we selected SOURCE-class photons, within an 8° region of interest (ROI) around the positions of the corresponding 3FGL sources, with energies > 100 MeV and zenith angles < 100°. We excluded photons recorded when the LAT's rocking angle was > 52° and when the LAT was not operating in normal science mode.

A photon-weighting scheme developed by Kerr (*41*) greatly increases the sensitivity when searching for gamma-ray pulsations by weighting the contribution of each photon to a detection statistic according to the probability of it having been emitted by the target source, derived from its reconstructed energy and arrival direction. To assign these weights, we first carried out a spectral analysis of the target sources. The initial source model consisted of all sources in the 3FGL catalog within 13° of the target source and Galactic diffuse emission and isotropic diffuse background models. With this source model, we performed a binned maximum likelihood analysis using the pointlike package (*42*). The spectrum of the target source was modeled with an exponentially cutoff power law (PL) with pre-factor N_0, spectral index Γ, and cutoff energy E_c

$$\frac{dN}{dE} = N_0 \left(\frac{E}{1\ \mathrm{GeV}}\right)^{-\Gamma} \exp\left(-\left(\frac{E}{E_c}\right)\right) \quad (1)$$

The spectral parameters of the target and all sources within 5° were free to vary in the fit, as were the normalizations of the background models. From the results of this spectral fitting, probability weights were calculated for each photon using gtsrcprob.

After discovering the pulsars, we refined their spin parameters (see the "Pulsar parameter estimation" section) using extended data sets, which included LAT photons recorded from 4 August 2008 to 16 March 2017. These data consisted of publicly available Pass 8 R2 SOURCE-class photons, processed with the P8R2_SOURCE_V6 IRFs. When producing the extended data sets, we extended the size of the ROI to 15° and reduced the zenith angle cutoff to < 90°. To produce a source model for use with gtsrcprob, another binned spectral analysis was performed using gtlike, including sources within 20° of the pulsars, and with the latest gll_iem_v06.fits map cube (*43*) and iso_P8R2_SOURCE_V6_v06.txt template (http://fermi.gsfc.nasa.gov/ssc/data/access/lat/BackgroundModels.html) used to model the diffuse

Downloaded from http://advances.sciencemag.org/ on April 8, 2018

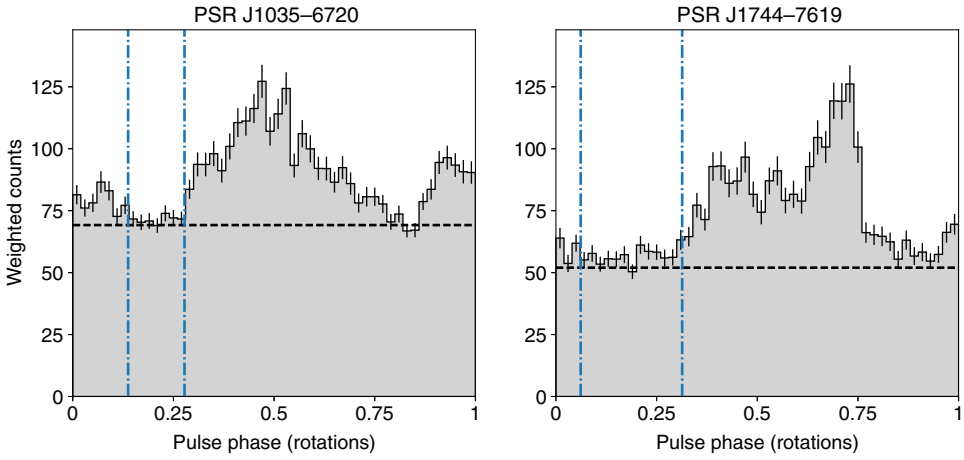


Fig. 3. Pulse profiles of the two new gamma-ray MSPs, showing the phase definitions of the off-pulse regions (blue dashed-dotted lines) used to search for unpulsed gamma-ray emission. The estimated background levels are shown by the black dashed lines. No significant off-pulse emission was detected from PSR J1035–6720. Off-pulse emission was detected with a significance of ~ 5σ from PSR J1744–7619.

emission. The source positions were fixed at the preliminary timing positions of the pulsars.

The estimates of the spectral parameters contain systematic uncertainties due to our choice of IRFs and diffuse background models. To estimate these systematic uncertainties, we performed the same spectral analysis with rescaled effective areas (http://fermi.gsfc.nasa.gov/ssc/data/analysis/scitools/Aeff_Systematics.html) and with the normalization of the Galactic diffuse emission rescaled to ± 6 % of the best-fit value.

The results of this spectral analysis for both pulsars are summarized in Table 1. The spectral properties (Γ and E_c) of PSRs J1035–6720 and J1744–7619 are similar to those of the MSP population seen in the Second Fermi-LAT Catalog of Gamma-ray Pulsars (*9*).

LAT off-pulse analysis

The integrated pulse profile for PSR J1744–7619 includes unpulsed emission at all phases above the estimated background level. We performed a spectral analysis of this "off-pulse" emission to determine whether this is likely to be magnetospheric emission or contamination from a nearby source. We performed a similar analysis to search for unpulsed emission from PSR J1035–6720.

We defined off-pulse regions for the two pulsars using the Bayesian block decomposition method described by Scargle *et al.* (*44*). The definitions of the off-pulse regions are shown in Fig. 3. We first computed residual test statistic maps (TS = 2 Δ log *L*, where Δ log *L* is the difference in log-likelihood between models with and without a putative source) with gamma-ray photons coming solely from the off-pulse region to look for putative sources around the pulsar position. No significant off-pulse emission was detected from PSR J1035–6720. This could be due to the low photon statistics in the defined off-pulse region; because the duty cycle for PSR J1035–6720 is close to 100%, a phase interval covering only ~14% of a rotation was selected for the analysis. Off-pulse emission at the position of PSR J1744–7619 was detected with TS = 33.8. Under the null hypothesis, the TS is approximately χ^2 distributed with three degrees of freedom (from the normalization, spectral index, and cutoff that are free in this test). This TS therefore corresponds to a significance of ~ 5.0 σ. We computed the TS value with both PL and exponentially cutoff PL (PLEC) models to test for curvature of the gamma-ray spectrum. The off-pulse emission from PSR J1744–7619 shows marginal evidence of a cutoff, with $TS_{cut} = TS_{PLEC} - TS_{PL} = 8.3$ and one degree of freedom, corresponding to a significance of ~ 2.6σ. The positional consistency between the off-pulse source and the pulsar and the hint of a spectral cutoff suggest a magnetospheric origin for the unpulsed emission (*9*).

Pulsar parameter estimation

After discovering the pulsars, we performed dedicated timing analyses using the extended data sets described above. To speed up our parameter estimation procedures, we applied a photon probability weight cutoff to remove the lowest-weighted photons. The cutoff values for each pulsar were chosen such that only 1% of the pulsation signal-to-noise ratio would be lost by this but around 90% of the lowest-weight photons would be removed. The analyses followed the timing procedure described by Clark *et al.* (*10*), with photon arrival times being corrected to the solar system barycenter using the JPL DE405 solar system ephemeris.

Starting with the signal parameters detected by the search (sky position, rotational frequency, and spin-down rate), we "phase-folded" the photon arrival times. We then fit template pulse profiles by minimizing the Bayesian information criterion (BIC) (*45*), the sum of the negative log-likelihood and a penalty factor proportional to the number of model parameters that prevents overfitting. We then varied the signal parameters using a parallelized affine-invariant Monte Carlo sampling algorithm (*46*, *47*) to maximize the likelihood given our template pulse profile. This process continued iteratively until the likelihood stopped increasing: After each Monte Carlo step, we refolded the data with the most likely set of signal parameters, constructed a new template pulse profile, and repeated the Monte Carlo sampling.

We then added additional parameters to our phase model one by one, performed a further Monte Carlo step, and kept the new parameter in our model if its inclusion led to a decrease in the BIC. By this criterion, we were unable to measure a second frequency derivative or parallax from either pulsar. The inclusion of proper motion in our timing models led to a moderate decrease in the BIC (ΔBIC = −7.8) for PSR J1035–6720 and a significant decrease (ΔBIC = −40.6) for PSR J1744–7619.

Because we measured proper motion from each pulsar, a portion of the observed spin-down rate for each must be caused by the Doppler shift introduced by their velocity gaining an increasing radial component (*9*, *48*), known as the Shklovskii effect. Correcting the observed

Downloaded from http://advances.sciencemag.org/ on April 8, 2018

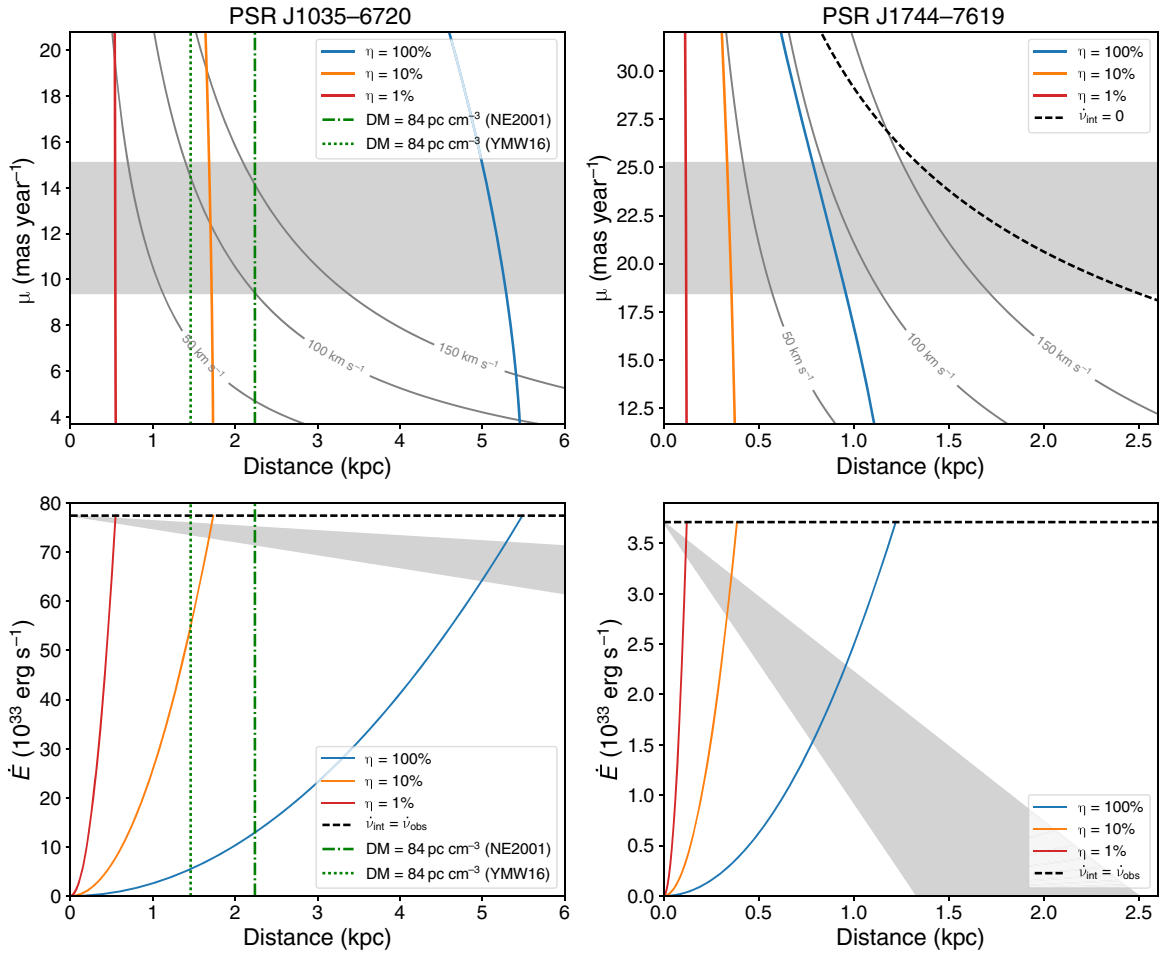


Fig. 4. Distance and spin-down constraints for the two new MSPs obtained from their gamma-ray flux, radio dispersion measure, and timing measurements of their proper motion. (**Top**) constraints on MSP distances, as in figure 11 of the work by Abdo *et al.* (*9*). Assuming certain gamma-ray efficiencies, constraints on the pulsar distance are inferred from the gamma-ray flux and spin-down power, after correcting the observed $\dot{\nu}$ for the Shklovskii effect due to the measured proper motion (1σ range given by the gray shaded region). The physically realistic region is to the left of the 100% efficiency line ($L_\gamma = \dot{E}$), although higher apparent efficiencies are possible, depending on the beam correction factor. Contours of constant transverse velocity are shown in gray. For PSR J1035–6720, the green dotted and dashed-dotted vertical lines show the DM distance according to the YMW16 and NE2001 models, respectively. For PSR J1744–7619, the $\dot{\nu}_{INT} = 0$ line shows the required distance for the observed spin down to be purely due to the Shklovskii effect, giving a hard upper limit. (**Bottom**) Spin-down powers after correcting $\dot{\nu}$ for the Shklovskii effect. The shaded region shows the allowed range for $\dot{E}$ at each distance, given the observed proper motion. The solid curves show $\dot{E}$ as a function of distance at fixed gamma-ray efficiencies. The dashed line shows the maximum $\dot{E}$, that is, if there was no proper motion.

spin-down rates ($\dot{\nu}_{OBS}$) of the pulsars for the Doppler-induced apparent spin-down ($\dot{\nu}_{SHK}$) due to their proper motion to retrieve their intrinsic spin-down rate ($\dot{\nu}_{INT}$) requires knowledge of their distances, which are uncertain without additional dispersion or parallax measurements. However, we can use the observed gamma-ray fluxes (F_γ) and proper motions (μ), and assume certain gamma-ray efficiencies (η), to retrieve constraints on the distances (d) by solving

$$\dot{\nu}_{OBS} = \dot{\nu}_{INT} + \dot{\nu}_{SHK} = -\frac{F_\gamma f_\Omega d^2}{\eta \pi I \nu} - \frac{\mu^2 \nu d}{c} \quad (2)$$

Figure 4 shows the results of this, assuming a canonical moment of inertia $I = 10^{45}$ g cm^2, a gamma-ray beam correction factor of $f_\Omega = 1$ (*49*), and a realistic range of gamma-ray efficiencies $0.01 < \eta < 1$ (converting loss of rotational energy into gamma-ray emission) (*9*). From the inferred distances, we can retrieve Shklovskii-corrected spin-down powers ($\dot{E}$) via $\dot{E} = F_\gamma 4\pi f_\Omega d^2/\eta$. These ranges are shown in the lower panels of Fig. 4.

From its DM distance, the gamma-ray efficiency of PSR J1035–6720 is around 7% (YMW16 model) to 17% (NE2001 model). For PSR J1744–7619, the Shklovskii effect can account for up to 65% of the apparent spin-down rate of PSR J1744–7619. The observed gamma-ray flux constrains the distance to PSR J1744–7619 to be less than ~1 kpc, assuming $\eta = 1$ and $f_\Omega = 1$.

If the gamma-ray efficiency of PSR J1744–7619 is high, then its spin-down power could be as low as 1.5×10^{33} erg s^{-1}, which would make this one of the least energetic gamma-ray MSPs and close to the empirical gamma-ray "death line," that is, the minimum spin-down power an MSP must have to emit gamma rays (*50*).

An additional comparison can be made between the transverse velocities of known isolated MSPs and the transverse velocities given by the proper motion measurements and distance constraints described above. Lines of constant transverse velocity are shown in Fig. 4 to illustrate this. The mean (median) transverse velocity of isolated MSPs (outside of globular clusters) in the ATNF Catalogue is 84 (59) km s^{-1}. For PSR J1035–6720, the DM distances correspond to transverse velocities of

Downloaded from http://advances.sciencemag.org/ on April 8, 2018

84 ± 20 km s^{-1} (YMW16) and 130 ± 30 km s^{-1} (NE2001). For PSR J1744–7619, assuming 100% gamma-ray efficiency leads to a transverse velocity of around 90 km s^{-1}, suggesting that the 1-kpc distance limit derived above is likely to be realistic for this pulsar. However, larger distances (for example, due to a lower beam correction factor) cannot be excluded on the basis of the resulting transverse velocity alone.

Radio observations

The radio pulsar survey performed by Camilo *et al.* (*6*) targeted 56 unidentified Fermi-LAT sources with the Parkes radio telescope and detected 11 MSPs, 10 of which were new discoveries. As part of this survey, we observed the LAT sources now known to be associated with the two MSPs multiple times between 2009 and 2012, at a center frequency of 1390 MHz using an analog filter-bank system. The total power from the central beam of the Parkes multibeam receiver (full width at half maximum = 14′), filtered through 512 frequency channels spanning a bandwidth of 256 MHz, was sampled every 125 μs and recorded for off-line analysis.

Typical integration times were around 1 hour, although they ranged between 41 and 136 min for these two sources [see table 1 of Abdo *et al.* (*7*)]. The LAT source associated with PSR J1035–6720 was observed a total of nine times, at a typical offset from the actual pulsar position of 4.3′. This reduced the sensitivity of those observations to 80% of the maximum (on axis) sensitivity. The LAT source associated with PSR J1744–7619 was observed 10 times at a typical offset of 1′, with no material impact on the sensitivity.

The data were analyzed using standard pulsar search techniques implemented in PRESTO (*51*). Before the new gamma-ray pulsars were known, the data were searched as described by Camilo *et al.* (*6*), considering possible DMs up to approximately twice the maximum DM predicted by the NE2001 model (*25*) for the corresponding line of sight [about 500 pc cm^{-3} for PSR J1035–6720 and 200 pc cm^{-3} for PSR J1744–7619; table 1 of Abdo *et al.* (*7*)]. Subsequently, we reanalyzed the data sets using the timing ephemerides obtained from gamma-ray data, folding the radio data while searching only in DM. None of the observations yielded significant radio pulsations.

The nominal threshold for these searches depends on the putative radio duty cycle of these pulsars and their DM. For an assumed duty cycle of 25% and DM < 50 pc cm^{-3}, an indicative 1.4-GHz flux density threshold for PSR J1035–6720 is about 0.25 mJy normalized to a 1-hour integration. For PSR J1744–7619, the equivalent figure is approximately 0.15 mJy.

Some of the MSPs discovered by Camilo *et al.* (*6*) were not detected in all their search observations. This can be caused by a combination of orbital acceleration, eclipses, or interstellar scintillation. The first two effects are not relevant for the two new isolated MSPs. Depending on the distance of the new MSPs, especially if they are nearby objects, interstellar scintillation could very much modulate any putative radio flux density recorded by our Parkes observing system. In extreme cases, such as PSR J1514–4946 (*6*), this can lead to radio-loud MSPs being discoverable for less than one-third of the time. However, we know of no established isolated radio-loud MSP in the Galactic disk that is undetectable as much as 90% of the time.

Following the discoveries of the pulsars, we performed five long observations toward PSR J1035–6270 with the Parkes radio telescope. All observations were performed at a center frequency of 1369 MHz and sampled voltages were processed online with a digital polyphase filter bank into 2048 channels across a bandwidth of 256 MHz, for an effective sampling time of 4 μs. The filter-bank outputs were detected and folded online into 256-bin profiles using the known spin ephemeris. Before each observation, we observed a pulsed noise diode to facilitate polarization and flux density (via archival observation of the radio galaxy Hydra A) calibration. The first four observations used the wideband "H-OH" receiver, whereas the latter used the center pixel of the "multibeam" receiver; for consistency, we report results only from the first four observations.

We searched the first observation over a range of DMs and found a promising signal with a signal-to-noise ratio of ~ 10 and a duty cycle of about 10% at a DM of 84.2 pc cm^{-3}. The signal appears at the same DM and pulse phase in the observations on 24 August 2016 and, particularly, 26 September 2016, confirming the detection. Using a Gaussian template, we maximized the likelihood for the data from 09 June 2016, 24 August 2016, and 26 September 2016 to estimate an optimal DM of 84.16 ± 0.22 pc cm^{-3}. With this template and DM, we measured the average flux density in each observation. The results are summarized in Table 2. (The pulsed emission in the observation on 07 August 2016 is too weak to be detected independently, but with knowledge of the phase and profile shape, the flux density can be estimated.)

For PSR J1744–7619, we performed two long observations using an identical observational setup and the multibeam system. We performed a similar search over DM (up to 800 pc cm^{-3}) and found no pulsed emission. Restricting consideration to DM < 200 pc cm^{-3}, we smoothed the fully averaged profile at each trial DM with a top hat of width 12.5% and recorded the maximum flux density. The results depend modestly on the baseline subtraction method used, and taking the average of two methods gives 95% confidence flux density upper limits of 0.031 and 0.032 mJy, respectively, for the two observations and 0.023 mJy for their coadded sum.

Combined with our estimated distance upper limit of $d < 1$ kpc, we found an upper limit on the pseudo-luminosity of PSR J1744–7619 of $L_{1400} < 0.023$ mJy kpc^2. Only two known MSPs with both reliable flux density measurements and DM-independent distance estimates have lower pseudo-luminosities, PSR J1400–1431 with $L_{1400} = 0.01$ mJy kpc^2 (*28*) and PSR J2322–2650 with $L_{1400} = 0.008$ mJy kpc^2 (*29*). Of the 164 remaining MSPs in the ATNF Catalogue with reported flux density measurements and distance estimates (including those inferred from DM measurements), only two have apparent pseudo-luminosities below that of PSR J1744–7619. For one of these, PSR J0922–52, the reported flux density is only a lower bound because of an unknown pointing offset in its discovery observation (*52*). For the other, PSR J1745–0952, the YMW16 distance estimate (0.23 kpc) strongly disagrees with that from NE2001

Table 2. Summary of dedicated follow-up radio observations with the Parkes radio telescope.

Target	Date	Duration (min)	Receiver	S_{1400} (mJy)
PSR J1035–6720	09 June 2016	188	H-OH	0.052 ± 0.0064
	07 August 2016	164	H-OH	0.023 ± 0.0064
	24 August 2016	169	H-OH	0.039 ± 0.0061
	26 September 2016	232	H-OH	0.045 ± 0.005
	19 March 2017	180	Multibeam	—
PSR J1744–7619	19 March 2017	180	Multibeam	< 0.031
	10 April 2017	163	Multibeam	< 0.032

Downloaded from http://advances.sciencemag.org/ on April 8, 2018

(1.8 kpc). This pulsar lies toward the Galactic Loop I bubble, within which the YMW16 distance for the closest pulsar with an independently estimated distance (PSR J1744−1134, angular separation $\Delta\theta = 1.7°$ from PSR J1745−0952) was seen to be underestimated by a factor of 2.6 [parallax distance $d = 0.395$ kpc and DM distance $d_{DM} = 0.148$ kpc; (*24*)]. In combination with the extremely low apparent pseudo-luminosity, this suggests that the DM distance estimate is unreliable in this case.

X-ray observations

The fields of PSRs J1035−6720 and J1744−7619 were observed by XMM-Newton for 25 ks (obsids 692830101 and 692830201) with the aim of detecting x-ray counterparts to possible radio-quiet MSPs in unidentified LAT sources (*21*). These gamma-ray sources were selected before the pulsation discoveries, because their gamma-ray properties indicated a probable pulsar nature.

Plausible x-ray counterparts for both pulsars were detected with a significance greater than 10σ at locations consistent with the newly discovered pulsars' timing positions. Their x-ray unabsorbed flux in the 0.3- to 10-keV energy range is $3.06^{+0.96}_{-0.50} \times 10^{-14}$ erg cm^{-2} s^{-1} for PSR J1035−6720 and $1.92^{+0.59}_{-0.39} \times 10^{-14}$ erg cm^{-2} s^{-1} for PSR J1744−7619. See table 11 of Saz Parkinson *et al.* (*21*) for additional information. We computed the probability that the association between the x-ray source and the MSP is due to a chance coincidence using $P = 1 - \exp(\pi\rho r^2)$, where r is the matching radius (in our case, the x-ray source error radius) and ρ is the density of x-ray objects in the XMM−Newton EPIC (European Photon Imaging Camera) field, regardless of their flux. We estimated $P \sim 1.3 \times 10^{-4}$ for PSR J1035−6720 ($r = 2''$ and $\rho \sim 0.038$ arc min^{-2}) and $P \sim 1.4 \times 10^{-4}$ for PSR J1744−7619 ($r = 1.9''$ and $\rho \sim 0.046$ arc min^{-2}), which make a chance positional coincidence unlikely. In addition, the gamma-ray–to–x-ray flux ratios of the two likely x-ray counterparts (~700 and ~1100) were consistent with an MSP nature (*30*), confirming their associations with PSRs J1035−6720 and J1744−7619.

Gamma-ray pulse profile modeling

To model the gamma-ray emission geometry of the MSPs, we fit simulated pulse profiles to the observed photon phases, using the fitting technique described by Johnson *et al.* (*31*). We considered three emission models: an OG model, a TPC model, and a PSPC model. These are also described in the study of Johnson *et al.* (*31*) and references therein, and briefly summarized here. In the first two models, particle acceleration takes place in narrow "gaps" in the magnetosphere, where the plasma charge density deviates from the force-free configuration. In both models, these gaps border the last-closed magnetic field lines. In the OG model, the lower bound of the gap is defined by the "null-charge surface," where the plasma charge density changes sign. In the TPC model, the gap begins at the pulsar surface and extends to the light cylinder. The PSPC model is valid for low-$\dot{E}$ pulsars, where pair creation may be insufficient to reach the force-free configuration, allowing for particle acceleration throughout the regions of open field lines. We assumed a hollow-cone model (*16*) for the radio beams.

We used simulated rotation periods of 2.5 and 4.5 ms, respectively, and a simulated period derivative of 1×10^{-20} s s^{-1} for both. Instead of a Poisson likelihood, we used a χ^2 statistic to fit the weighted-counts light curves, using 60 bins for both MSPs, with background levels and uncertainties calculated as in the study of Abdo *et al.* (*9*). The best-fit parameters (the angle between spin axis and magnetic dipole, α; the angle between the spin axis and the line-of-sight, ζ; and the estimated beam correction factor, f_Ω) for each model are given in Table 3, with 95% confidence-level uncertainties estimated as described by Johnson *et al.* (*31*). The best-fitting light curves from all models for each pulsar are shown in Fig. 5. It should be noted that, as pointed out by Pierbattista *et al.* (*53*), fitting only the gamma-ray light curves with these toy models can lead to systematic biases in the best-fit parameters of ~ 10°. We also note that no model considered here successfully reproduces the broad double-peaked pulse profile of PSR J1035−6720.

Table 3. Best-fit parameters from gamma-ray pulse profile modeling. For each pulsar, we report the best-fitting magnetic inclination angles (α), viewing angles (ζ), and beam correction factors (f_Ω), according to the OG, TPC, and PSPC models.

Parameter	PSR J1035−6720			PSR J1744−7619		
Model	OG	TPC	PSPC	OG	TPC	PSPC
−ln(L)	84.5	78.9	72.0	84.6	58.1	72.7
α (deg)	9^{+1}_{-2}	7^{+2}_{-1}	51^{+4}_{-3}	67^{+2}_{-2}	62^{+1}_{-2}	62^{+5}_{-1}
ζ (deg)	75^{+1}_{-1}	70^{+1}_{-1}	78^{+3}_{-3}	32^{+2}_{-2}	44^{+3}_{-3}	74^{+5}_{-3}
f_Ω	$0.22^{+0.25}_{-0.04}$	$0.62^{+0.08}_{-0.11}$	$0.98^{+0.12}_{-0.04}$	$0.94^{+0.05}_{-0.10}$	$0.89^{+0.03}_{-0.09}$	$1.14^{+0.15}_{-0.09}$

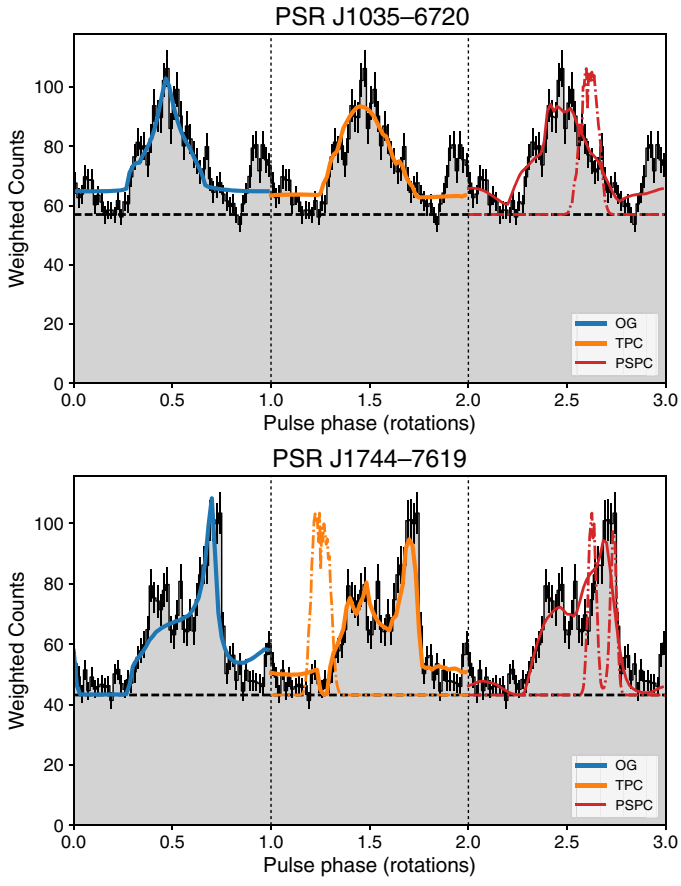


Fig. 5. Gamma-ray pulse profiles of the newly detected MSPs. The overlaying curves are the best-fitting pulse profiles predicted by fits to OG, TPC, and PSPC gamma-ray emission models. The black dashed line is the estimated background level, derived from the photon weights as in the study of Abdo *et al.* (*9*). Predicted radio pulse profiles (with arbitrary baseline and normalization) are shown by dashed-dotted lines. The three models are shown in separate rotations for clarity.

Downloaded from http://advances.sciencemag.org/ on April 8, 2018

The PSPC model for PSR J1035−6720 predicted a phase offset between the gamma-ray and radio pulses that was reasonably consistent with that observed. However, the uncertainty in DM led to an additional uncertainty in the radio pulse phase of 0.15 rotations, precluding a joint fit of the radio and gamma-ray pulse profiles as is normally possible for other gamma-ray MSPs.

For the models that did not predict radio emission (TPC and OG for PSR J1035−6720 and OG for PSR J1744−7619), the lines of sight barely missed the edges of the emission cones at 300 MHz, suggesting that these MSPs might appear brighter at even lower frequencies.

REFERENCES AND NOTES

1. W. B. Atwood, A. A. Abdo, M. Ackermann, W. Althouse, B. Anderson, M. Axelsson, L. Baldini, J. Ballet, D. L. Band, G. Barbiellini, J. Bartelt, D. Bastieri, B. M. Baughman, K. Bechtol, D. Bédérède, F. Bellardi, R. Bellazzini, B. Berenji, G. F. Bignami, D. Bisello, E. Bissaldi, R. D. Blandford, E. D. Bloom, J. R. Bogart, E. Bonamente, J. Bonnell, A. W. Borgland, A. Bouvier, J. Bregeon, A. Brez, M. Brigida, P. Bruel, T. H. Burnett, G. Busetto, G. A. Caliandro, R. A. Cameron, P. A. Caraveo, S. Carius, P. Carlson, J. M. Casandjian, E. Cavazzuti, M. Ceccanti, C. Cecchi, E. Charles, A. Chekhtman, C. C. Cheung, J. Chiang, R. Chipaux, A. N. Cillis, S. Ciprini, R. Claus, J. Cohen-Tanugi, S. Condamoor, J. Conrad, R. Corbet, L. Corucci, L. Costamante, S. Cutini, D. S. Davis, D. Decotigny, M. DeKlotz, C. D. Dermer, A. de Angelis, S. W. Digel, E. do Couto e Silva, P. S. Drell, R. Dubois, D. Dumora, Y. Edmonds, D. Fabiani, C. Farnier, C. Favuzzi, D. L. Flath, P. Fleury, W. B. Focke, S. Funk, P. Fusco, F. Gargano, D. Gasparrini, N. Gehrels, F.-X. Gentit, S. Germani, B. Giebels, N. Giglietto, P. Giommi, F. Giordano, T. Glanzman, G. Godfrey, I. A. Grenier, M.-H. Grondin, J. E. Grove, L. Guillemot, S. Guiriec, G. Haller, A. K. Harding, P. A. Hart, E. Hays, S. E. Healey, M. Hirayama, L. Hjalmarsdotter, R. Horn, R. E. Hughes, G. Jóhannesson, G. Johansson, A. S. Johnson, R. P. Johnson, T. J. Johnson, W. N. Johnson, T. Kamae, H. Katagiri, J. Kataoka, A. Kavelaars, N. Kawai, H. Kelly, M. Kerr, W. Klamra, J. Knödlseder, M. L. Kocian, N. Komin, F. Kuehn, M. Kuss, D. Landriu, L. Latronico, B. Lee, S.-H. Lee, M. Lemoine-Goumard, A. M. Lionetto, F. Longo, F. Loparco, B. Lott, M. N. Lovellette, P. Lubrano, G. M. Madejski, A. Makeev, B. Marangelli, M. M. Massai, M. N. Mazziotta, J. E. McEnery, N. Menon, C. Meurer, P. F. Michelson, M. Minuti, N. Mirizzi, W. Mitthumsiri, T. Mizuno, A. A. Moiseev, C. Monte, M. E. Monzani, E. Moretti, A. Morselli, I. V. Moskalenko, S. Murgia, T. Nakamori, S. Nishino, P. L. Nolan, J. P. Norris, E. Nuss, M. Ohno, T. Ohsugi, N. Omodei, E. Orlando, J. F. Ormes, A. Paccagnella, D. Paneque, J. H. Panetta, D. Parent, M. Pearce, M. Pepe, A. Perazzo, M. Pesce-Rollins, P. Picozza, L. Pieri, M. Pinchera, F. Piron, T. A. Porter, L. Poupard, S. Rainò, R. Rando, E. Rapposelli, M. Razzano, A. Reimer, O. Reimer, T. Reposeur, L. C. Reyes, S. Ritz, L. S. Rochester, A. Y. Rodriguez, R. W. Romani, M. Roth, J. J. Russell, F. Ryde, S. Sabatini, H. F.-W. Sadrozinski, D. Sanchez, A. Sander, L. Sapozhnikov, P. M. Saz Parkinson, J. D. Scargle, T. L. Schalk, G. Scolieri, C. Sgrò, G. H. Share, M. Shaw, T. Shimokawabe, C. Shrader, A. Sierpowska-Bartosik, E. J. Siskind, D. A. Smith, P. D. Smith, G. Spandre, P. Spinelli, J.-L. Starck, T. E. Stephens, M. S. Strickman, A. W. Strong, D. J. Suson, H. Tajima, H. Takahashi, T. Takahashi, T. Tanaka, A. Tenze, S. Tether, J. B. Thayer, J. G. Thayer, D. J. Thompson, L. Tibaldo, O. Tibolla, D. F. Torres, G. Tosti, A. Tramacere, M. Turri, T. L. Usher, N. Vilchez, V. Vitale, P. Wang, K. Watters, B. L. Winer, K. S. Wood, T. Ylinen, M. Ziegler, The Large Area Telescope on the Fermi Gamma-ray Space Telescope mission. *Astrophys. J.* **697**, 1071 (2009).
2. M. A. Alpar, A. F. Cheng, M. A. Ruderman, J. Shaham, A new class of radio pulsars. *Nature* **300**, 728–730 (1982).
3. D. Bhattacharya, E. P. J. van den Heuvel, Formation and evolution of binary and millisecond radio pulsars. *Phys. Rep.* **203**, 1–124 (1991).
4. J. W. T. Hessels, S. M. Ransom, I. H. Stairs, P. C. C. Freire, V. M. Kaspi, F. Camilo, A radio pulsar spinning at 716 Hz. *Science* **311**, 1901–1904 (2006).
5. A. A. Abdo, M. Ackermann, M. Ajello, W. B. Atwood, M. Axelsson, L. Baldini, J. Ballet, G. Barbiellini, M. G. Baring, D. Bastieri, B. M. Baughman, K. Bechtol, R. Bellazzini, B. Berenji, G. F. Bignami, R. D. Blandford, E. D. Bloom, E. Bonamente, A. W. Borgland, J. Bregeon, A. Brez, M. Brigida, P. Bruel, T. H. Burnett, G. A. Caliandro, R. A. Cameron, F. Camilo, P. A. Caraveo, P. Carlson, J. M. Casandjian, C. Cecchi, Ö. Çelik, E. Charles, A. Chekhtman, C. C. Cheung, J. Chiang, S. Ciprini, R. Claus, I. Cognard, J. Cohen-Tanugi, L. R. Cominsky, J. Conrad, R. Corbet, S. Cutini, C. D. Dermer, G. Desvignes, A. de Angelis, A. de Luca, F. de Palma, S. W. Digel, M. Dormody, E. do Couto e Silva, P. S. Drell, R. Dubois, D. Dumora, Y. Edmonds, C. Farnier, C. Favuzzi, S. J. Fegan, W. B. Focke, M. Frailis, P. C. C. Freire, Y. Fukazawa, S. Funk, P. Fusco, F. Gargano, D. Gasparrini, N. Gehrels, S. Germani, B. Giebels, N. Giglietto, P. Giordano, T. Glanzman, G. Godfrey, I. A. Grenier, M. H. Grondin, J. E. Grove, L. Guillemot, S. Guiriec, Y. Hanabata, A. K. Harding, M. Hayashida, E. Hays, G. Hobbs, R. E. Hughes, G. Jóhannesson, A. S. Johnson, R. P. Johnson, T. J. Johnson, W. N. Johnson, S. Johnston, T. Kamae, H. Katagiri, J. Kataoka, N. Kawai, M. Kerr, J. Knödlseder, M. L. Kocian, M. Kramer, M. Kuss, J. Lande, L. Latronico, M. Lemoine-Goumard, F. Longo, F. Loparco, B. Lott, M. N. Lovellette, P. Lubrano, G. M. Madejski, A. Makeev, R. N. Manchester, M. Marelli, M. N. Mazziotta, W. McConville, J. E. McEnery, M. A. McLaughlin, C. Meurer, P. F. Michelson, W. Mitthumsiri, T. Mizuno, A. A. Moiseev, C. Monte, M. E. Monzani, A. Morselli, I. V. Moskalenko, S. Murgia, P. L. Nolan, J. P. Norris, E. Nuss, T. Ohsugi, N. Omodei, E. Orlando, J. F. Ormes, D. Paneque, J. H. Panetta, D. Parent, V. Pelassa, M. Pepe, M. Pesce-Rollins, F. Piron, T. A. Porter, S. Rainò, R. Rando, S. M. Ransom, P. S. Ray, M. Razzano, N. Rea, A. Reimer, O. Reimer, T. Reposeur, S. Ritz, L. S. Rochester, A. Y. Rodriguez, R. W. Romani, M. Roth, F. Ryde, H. F. W. Sadrozinski, D. Sanchez, A. Sander, P. M. Saz Parkinson, J. D. Scargle, T. L. Schalk, C. Sgrò, E. J. Siskind, D. A. Smith, P. D. Smith, G. Spandre, P. Spinelli, B. W. Stappers, J. L. Starck, E. Striani, M. S. Strickman, D. J. Suson, H. Tajima, H. Takahashi, T. Tanaka, J. B. Thayer, J. G. Thayer, G. Theureau, D. J. Thompson, S. E. Thorsett, L. Tibaldo, D. F. Torres, G. Tosti, A. Tramacere, Y. Uchiyama, T. L. Usher, A. Van Etten, V. Vasileiou, C. Venter, N. Vilchez, V. Vitale, A. P. Waite, E. Wallace, P. Wang, K. Watters, N. Webb, P. Weltevrede, B. L. Winer, K. S. Wood, T. Ylinen, M. Ziegler, A population of gamma-ray millisecond pulsars seen with the Fermi Large Area Telescope. *Science* **325**, 848–852 (2009).
6. F. Camilo, M. Kerr, P. S. Ray, S. M. Ransom, J. Sarkissian, H. T. Cromartie, S. Johnston, J. E. Reynolds, M. T. Wolff, P. C. C. Freire, B. Bhattacharyya, E. C. Ferrara, M. Keith, P. F. Michelson, P. M. Saz Parkinson, K. S. Wood, Parkes radio searches of *Fermi* gamma-ray sources and millisecond pulsar discoveries. *Astrophys. J.* **810**, 85 (2015).
7. A. A. Abdo, M. Ackermann, M. Ajello, B. Anderson, W. B. Atwood, M. Axelsson, L. Baldini, J. Ballet, G. Barbiellini, M. G. Baring, D. Bastieri, B. M. Baughman, K. Bechtol, R. Bellazzini, B. Berenji, G. F. Bignami, R. D. Blandford, E. D. Bloom, E. Bonamente, A. W. Borgland, J. Bregeon, A. Brez, M. Brigida, P. Bruel, T. H. Burnett, G. A. Caliandro, R. A. Cameron, P. A. Caraveo, J. M. Casandjian, C. Cecchi, Ö. Çelik, A. Chekhtman, C. C. Cheung, J. Chiang, S. Ciprini, R. Claus, J. Cohen-Tanugi, J. Conrad, S. Cutini, C. D. Dermer, A. de Angelis, A. de Luca, F. de Palma, S. W. Digel, M. Dormody, E. do Couto e Silva, P. S. Drell, R. Dubois, D. Dumora, C. Farnier, C. Favuzzi, S. J. Fegan, Y. Fukazawa, S. Funk, P. Fusco, F. Gargano, D. Gasparrini, N. Gehrels, S. Germani, B. Giebels, N. Giglietto, P. Giommi, F. Giordano, T. Glanzman, G. Godfrey, I. A. Grenier, M.-H. Grondin, J. E. Grove, L. Guillemot, S. Guiriec, C. Gwon, Y. Hanabata, A. K. Harding, M. Hayashida, E. Hays, R. E. Hughes, G. Jóhannesson, R. P. Johnson, T. J. Johnson, W. N. Johnson, T. Kamae, H. Katagiri, J. Kataoka, N. Kawai, M. Kerr, J. Knödlseder, M. L. Kocian, M. Kuss, J. Lande, L. Latronico, M. Lemoine-Goumard, F. Longo, F. Loparco, B. Lott, M. N. Lovellette, P. Lubrano, G. M. Madejski, A. Makeev, M. Marelli, M. N. Mazziotta, W. McConville, J. E. McEnery, C. Meurer, P. F. Michelson, W. Mitthumsiri, T. Mizuno, C. Monte, M. E. Monzani, A. Morselli, I. V. Moskalenko, S. Murgia, P. L. Nolan, J. P. Norris, E. Nuss, T. Ohsugi, N. Omodei, E. Orlando, J. F. Ormes, D. Paneque, D. Parent, V. Pelassa, M. Pepe, M. Pesce-Rollins, M. Pierbattista, F. Piron, T. A. Porter, J. R. Primack, S. Rainò, R. Rando, P. S. Ray, M. Razzano, N. Rea, A. Reimer, O. Reimer, T. Reposeur, S. Ritz, L. S. Rochester, A. Y. Rodriguez, R. W. Romani, F. Ryde, H. F.-W. Sadrozinski, D. Sanchez, A. Sander, P. M. Saz Parkinson, J. D. Scargle, C. Sgrò, E. J. Siskind, D. A. Smith, P. D. Smith, G. Spandre, P. Spinelli, J.-L. Starck, M. S. Strickman, D. J. Suson, H. Tajima, H. Takahashi, T. Takahashi, T. Tanaka, J. G. Thayer, D. J. Thompson, L. Tibaldo, O. Tibolla, D. F. Torres, G. Tosti, A. Tramacere, Y. Uchiyama, T. L. Usher, A. Van Etten, V. Vasileiou, N. Vilchez, V. Vitale, A. P. Waite, P. Wang, K. Watters, B. L. Winer, M. T. Wolff, K. S. Wood, T. Ylinen, M. Ziegler, Detection of 16 gamma-ray pulsars through blind frequency searches using the Fermi LAT. *Science* **325**, 840–844 (2009).
8. H. J. Pletsch, L. Guillemot, B. Allen, M. Kramer, C. Aulbert, H. Fehrmann, P. S. Ray, E. D. Barr, A. Belfiore, F. Camilo, P. A. Caraveo, Ö. Çelik, D. J. Champion, M. Dormody, R. P. Eatough, E. C. Ferrara, P. C. C. Freire, J. W. T. Hessels, M. Keith, M. Kerr, A. de Luca, A. G. Lyne, M. Marelli, M. A. McLaughlin, D. Parent, S. M. Ransom, M. Razzano, W. Reich, P. M. Saz Parkinson, B. W. Stappers, M. T. Wolff, Discovery of nine gamma-ray pulsars in *Fermi* Large Area Telescope data using a new blind search method. *Astrophys. J.* **744**, 105 (2012).
9. A. A. Abdo, M. Ajello, A. Allafort, L. Baldini, J. Ballet, G. Barbiellini, M. G. Baring, D. Bastieri, A. Belfiore, R. Bellazzini, B. Bhattacharyya, E. Bissaldi, E. D. Bloom, E. Bonamente, E. Bottacini, T. J. Brandt, J. Bregeon, M. Brigida, P. Bruel, R. Buehler, M. Burgay, T. H. Burnett, G. Busetto, S. Buson, G. A. Caliandro, R. A. Cameron, F. Camilo, P. A. Caraveo, J. M. Casandjian, C. Cecchi, Ö. Çelik, E. Charles, S. Chaty, R. C. G. Chaves, A. Chekhtman, A. W. Chen, J. Chiang, G. Chiaro, S. Ciprini, R. Claus, I. Cognard, J. Cohen-Tanugi, L. R. Cominsky, J. Conrad, S. Cutini, F. D'Ammando, A. de Angelis, M. E. DeCesar, A. De Luca, P. R. den Hartog, F. de Palma, C. D. Dermer, G. Desvignes, S. W. Digel, L. Di Venere, P. S. Drell, A. Drlica-Wagner, R. Dubois, D. Dumora, C. M. Espinoza, L. Falletti, C. Favuzzi, E. C. Ferrara, W. B. Focke, A. Franckowiak, P. C. C. Freire, S. Funk, P. Fusco, F. Gargano, D. Gasparrini, S. Germani, N. Giglietto, P. Giommi, F. Giordano, M. Giroletti, T. Glanzman, G. Godfrey, E. V. Gotthelf, I. A. Grenier, M.-H. Grondin, J. E. Grove, L. Guillemot, S. Guiriec, D. Hadasch, Y. Hanabata, A. K. Harding, M. Hayashida, E. Hays, J. Hessels, J. Hewitt, A. B. Hill, D. Horan, X. Hou, R. E. Hughes, M. S. Jackson, G. H. Janssen, T. Jogler, G. Jóhannesson, R. P. Johnson, A. S. Johnson, T. J. Johnson, W. N. Johnson, S. Johnston, T. Kamae, J. Kataoka, M. Keith, M. Kerr, J. Knödlseder, M. Kramer, M. Kuss, J. Lande, S. Larsson, L. Latronico, M. Lemoine-Goumard, F. Longo, F. Loparco, M. N. Lovellette, P. Lubrano, A. G. Lyne, R. N. Manchester, M. Marelli, F. Massaro, M. Mayer, M. N. Mazziotta, J. E. McEnery, M. A. McLaughlin, J. Mehault, P. F. Michelson, R. P. Mignani, W. Mitthumsiri, T. Mizuno, A. A. Moiseev, M. E. Monzani, A. Morselli, I. V. Moskalenko, S. Murgia, T. Nakamori,

Downloaded from http://advances.sciencemag.org/ on April 8, 2018

R. Nemmen, E. Nuss, M. Ohno, T. Ohsugi, M. Orienti, E. Orlando, J. F. Ormes, D. Paneque, J. H. Panetta, D. Parent, J. S. Perkins, M. Pesce-Rollins, M. Pierbattista, F. Piron, G. Pivato, H. J. Pletsch, T. A. Porter, A. Possenti, S. Rainò, R. Rando, S. M. Ransom, P. S. Ray, M. Razzano, N. Rea, A. Reimer, O. Reimer, N. Renault, T. Reposeur, S. Ritz, R. W. Romani, M. Roth, R. Rousseau, J. Roy, J. Ruan, A. Sartori, P. M. Saz Parkinson, J. D. Scargle, A. Schulz, C. Sgrò, R. Shannon, E. J. Siskind, D. A. Smith, G. Spandre, P. Spinelli, B. W. Stappers, A. W. Strong, D. J. Suson, H. Takahashi, J. G. Thayer, J. B. Thayer, G. Theureau, D. J. Thompson, S. E. Thorsett, L. Tibaldo, O. Tibolla, M. Tinivella, D. F. Torres, G. Tosti, E. Troja, Y. Uchiyama, T. L. Usher, J. Vandenbroucke, V. Vasileiou, C. Venter, G. Vianello, V. Vitale, N. Wang, P. Weltevrede, B. L. Winer, M. T. Wolff, D. L. Wood, K. S. Wood, M. Wood, Z. Yang, The second *Fermi* Large Area Telescope catalog of gamma-ray pulsars. *Astrophys. J. Suppl. Ser.* **208**, 17 (2013).

10. C. J. Clark, J. Wu, H. J. Pletsch, L. Guillemot, B. Allen, C. Aulbert, C. Beer, O. Bock, A. Cuéllar, H. B. Eggenstein, H. Fehrmann, M. Kramer, B. Machenschalk, L. Nieder, The Einstein@Home gamma-ray pulsar survey. I. Search methods, sensitivity, and discovery of new young gamma-ray pulsars. *Astrophys. J.* **834**, 106 (2017).
11. C. J. Clark, "A Blind-search Survey for Gamma-ray Pulsars," thesis, Leibniz Universität Hannover (2017).
12. H. J. Pletsch, L. Guillemot, H. Fehrmann, B. Allen, M. Kramer, C. Aulbert, M. Ackermann, M. Ajello, A. de Angelis, W. B. Atwood, L. Baldini, J. Ballet, G. Barbiellini, D. Bastieri, K. Bechtol, R. Bellazzini, A. W. Borgland, E. Bottacini, T. J. Brandt, J. Bregeon, M. Brigida, P. Bruel, R. Buehler, S. Buson, G. A. Caliandro, R. A. Cameron, P. A. Caraveo, J. M. Casandjian, C. Cecchi, Ö. Çelik, E. Charles, R. C. G. Chaves, C. C. Cheung, J. Chiang, S. Ciprini, R. Claus, J. Cohen-Tanugi, J. Conrad, S. Cutini, F. D'Ammando, C. D. Dermer, S. W. Digel, P. S. Drell, A. Drlica-Wagner, R. Dubois, D. Dumora, C. Favuzzi, E. C. Ferrara, A. Franckowiak, Y. Fukazawa, P. Fusco, F. Gargano, N. Gehrels, S. Germani, N. Giglietto, F. Giordano, M. Giroletti, G. Godfrey, I. A. Grenier, M.-H. Grondin, J. E. Grove, S. Guiriec, D. Hadasch, Y. Hanabata, A. K. Harding, P. R. den Hartog, M. Hayashida, E. Hays, A. B. Hill, X. Hou, R. E. Hughes, G. Jóhannesson, M. S. Jackson, T. Jogler, A. S. Johnson, W. N. Johnson, J. Kataoka, M. Kerr, J. Knödlseder, M. Kuss, J. Lande, S. Larsson, L. Latronico, M. Lemoine-Goumard, F. Longo, F. Loparco, M. N. Lovellette, P. Lubrano, F. Massaro, M. Mayer, M. N. Mazziotta, J. E. McEnery, J. Mehault, P. F. Michelson, W. Mitthumsiri, T. Mizuno, M. E. Monzani, A. Morselli, I. V. Moskalenko, S. Murgia, T. Nakamori, R. Nemmen, E. Nuss, M. Ohno, T. Ohsugi, N. Omodei, M. Orienti, E. Orlando, F. de Palma, D. Paneque, J. S. Perkins, F. Piron, G. Pivato, T. A. Porter, S. Rainò, R. Rando, P. S. Ray, M. Razzano, A. Reimer, O. Reimer, T. Reposeur, S. Ritz, R. W. Romani, C. Romoli, D. A. Sanchez, P. M. Saz Parkinson, A. Schulz, C. Sgrò, E. do Couto e Silva, E. J. Siskind, D. A. Smith, G. Spandre, P. Spinelli, D. J. Suson, H. Takahashi, T. Tanaka, J. B. Thayer, J. G. Thayer, D. J. Thompson, L. Tibaldo, M. Tinivella, E. Troja, T. L. Usher, J. Vandenbroucke, V. Vasileiou, G. Vianello, V. Vitale, A. P. Waite, B. L. Winer, K. S. Wood, M. Wood, Z. Yang, S. Zimmer, Binary millisecond pulsar discovery via gamma-ray pulsations. *Science* **338**, 1314–1317 (2012).
13. P. S. Ray, S. M. Ransom, C. C. Cheung, M. Giroletti, I. Cognard, F. Camilo, B. Bhattacharyya, J. Roy, R. W. Romani, E. C. Ferrara, L. Guillemot, S. Johnston, M. Keith, M. Kerr, M. Kramer, H. J. Pletsch, P. M. Saz Parkinson, K. S. Wood, Radio detection of the *Fermi*-LAT blind search millisecond pulsar J1311–3430. *Astrophys. J.* **763**, L13 (2013).
14. R. W. Romani, 2FGL J1311.7–3429 joins the black widow club. *Astrophys. J.* **754**, L25 (2012).
15. D. R. Lorimer, Binary and millisecond pulsars. *Living Rev. Relativ.* **11**, 8 (2008).
16. S. A. Story, P. L. Gonthier, A. K. Harding, Population synthesis of radio and γ-ray millisecond pulsars from the galactic disk. *Astrophys. J.* **671**, 713 (2007).
17. F. Acero, M. Ackermann, M. Ajello, A. Albert, W. B. Atwood, M. Axelsson, L. Baldini, J. Ballet, G. Barbiellini, D. Bastieri, A. Belfiore, R. Bellazzini, E. Bissaldi, R. D. Blandford, E. D. Bloom, J. R. Bogart, R. Bonino, E. Bottacini, J. Bregeon, R. J. Britto, P. Bruel, R. Buehler, T. H. Burnett, S. Buson, G. A. Caliandro, R. A. Cameron, R. Caputo, M. Caragiulo, P. A. Caraveo, J. M. Casandjian, E. Cavazzuti, E. Charles, R. C. G. Chaves, A. Chekhtman, C. C. Cheung, J. Chiang, G. Chiaro, S. Ciprini, R. Claus, J. Cohen-Tanugi, L. R. Cominsky, J. Conrad, S. Cutini, F. D'Ammando, A. de Angelis, M. DeKlotz, F. de Palma, R. Desiante, S. W. Digel, L. Di Venere, P. S. Drell, R. Dubois, D. Dumora, C. Favuzzi, S. J. Fegan, E. C. Ferrara, J. Finke, A. Franckowiak, Y. Fukazawa, S. Funk, P. Fusco, F. Gargano, D. Gasparrini, B. Giebels, N. Giglietto, P. Giommi, F. Giordano, M. Giroletti, T. Glanzman, G. Godfrey, I. A. Grenier, M.-H. Grondin, J. E. Grove, L. Guillemot, S. Guiriec, D. Hadasch, A. K. Harding, E. Hays, J. W. Hewitt, A. B. Hill, D. Horan, G. Iafrate, T. Jogler, G. Jóhannesson, R. P. Johnson, A. S. Johnson, T. J. Johnson, W. N. Johnson, T. Kamae, J. Kataoka, J. Katsuta, M. Kuss, G. La Mura, D. Landriu, S. Larsson, L. Latronico, M. Lemoine-Goumard, J. Li, L. Li, F. Longo, F. Loparco, B. Lott, M. N. Lovellette, P. Lubrano, G. M. Madejski, F. Massaro, M. Mayer, M. N. Mazziotta, J. E. McEnery, P. F. Michelson, N. Mirabal, T. Mizuno, A. A. Moiseev, M. Mongelli, M. E. Monzani, A. Morselli, I. V. Moskalenko, S. Murgia, E. Nuss, M. Ohno, T. Ohsugi, N. Omodei, M. Orienti, E. Orlando, J. F. Ormes, D. Paneque, J. H. Panetta, J. S. Perkins, M. Pesce-Rollins, F. Piron, G. Pivato, T. A. Porter, J. L. Racusin, R. Rando, M. Razzano, S. Razzaque, A. Reimer, O. Reimer, T. Reposeur, L. S. Rochester, R. W. Romani, D. Salvetti, M. Sánchez-Conde, P. M. Saz Parkinson, A. Schulz, E. J. Siskind, D. A. Smith, F. Spada, G. Spandre, P. Spinelli, T. E. Stephens, A. W. Strong, D. J. Suson, H. Takahashi, T. Takahashi, Y. Tanaka, J. G. Thayer, J. B. Thayer, D. J. Thompson, L. Tibaldo, O. Tibolla, D. F. Torres, E. Torresi, G. Tosti, E. Troja, B. Van Klaveren, G. Vianello, B. L. Winer, K. S. Wood, M. Wood, S. Zimmer, *Fermi* Large Area Telescope third source catalog. *Astrophys. J. Suppl. Ser.* **218**, 23 (2015).
18. H. J. Pletsch, C. J. Clark, Optimized blind gamma-ray pulsar searches at fixed computing budget. *Astrophys. J.* **795**, 75 (2014).
19. B. Knispel, B. Allen, J. M. Cordes, J. S. Deneva, D. Anderson, C. Aulbert, N. D. R. Bhat, O. Bock, S. Bogdanov, A. Brazier, F. Camilo, D. J. Champion, S. Chatterjee, F. Crawford, P. B. Demorest, H. Fehrmann, P. C. C. Freire, M. E. Gonzalez, D. Hammer, J. W. T. Hessels, F. A. Jenet, L. Kasian, V. M. Kaspi, M. Kramer, P. Lazarus, J. van Leeuwen, D. R. Lorimer, A. G. Lyne, B. Machenschalk, M. A. McLaughlin, C. Messenger, D. J. Nice, M. A. Papa, H. J. Pletsch, R. Prix, S. M. Ransom, X. Siemens, I. H. Stairs, B. W. Stappers, K. Stovall, A. Venkataraman, Pulsar discovery by global volunteer computing. *Science* **329**, 1305 (2010).
20. W. Atwood, A. Albert, L. Baldini, M. Tinivella, J. Bregeon, M. Pesce-Rollins, C. Sgrò, P. Bruel, E. Charles, A. Drlica-Wagner, A. Franckowiak, T. Jogler, L. Rochester, T. Usher, M. Wood, J. Cohen-Tanugi, S. Zimmer, Pass 8: Toward the Full Realization of the Fermi-LAT Scientific Potential, in *Proceedings of the 4th Fermi Symposium*, T. J. Brandt, N. Omodei, C. Wilson-Hodge, Eds., eConf C121028 (2012), arXiv:1303.3514.
21. P. M. Saz Parkinson, H. Xu, P. L. H. Yu, D. Salvetti, M. Marelli, A. D. Falcone, Classification and ranking of *Fermi* LAT gamma-ray sources from the 3FGL catalog using machine learning techniques. *Astrophys. J.* **820**, 8 (2016).
22. H. J. Pletsch, L. Guillemot, B. Allen, D. Anderson, C. Aulbert, O. Bock, D. J. Champion, H. B. Eggenstein, H. Fehrmann, D. Hammer, R. Karuppusamy, M. Keith, M. Kramer, B. Machenschalk, C. Ng, M. A. Papa, P. S. Ray, X. Siemens, Einstein@Home discovery of four young gamma-ray pulsars in *Fermi* LAT data. *Astrophys. J.* **779**, L11 (2013).
23. O. C. De Jager, J. W. H. Swanepoel, B. C. Raubenheimer, A powerful test for weak periodic signals with unknown light curve shape in sparse data. *Astron. Astrophys.* **221**, 180–190 (1989).
24. J. M. Yao, R. N. Manchester, N. Wang, A new electron-density model for estimation of pulsar and FRB distances. *Astrophys. J.* **835**, 29 (2017).
25. J. M. Cordes, T. J. W. Lazio, NE2001.I. A new model for the galactic distribution of free electrons and its fluctuations. arXiv:astro-ph/0207156 (2002).
26. R. N. Manchester, G. B. Hobbs, A. Teoh, M. Hobbs, The Australia Telescope National Facility Catalogue. *Astron. J.* **129**, 1993 (2005).
27. M. Kramer, B. Stappers, Pulsar Science with the SKA, in *Advancing Astrophysics with the Square Kilometre Array (AASKA14)* (Proceedings of Science, Trieste, 2014), p. 36.
28. J. K. Swiggum, D. L. Kaplan, M. A. McLaughlin, D. R. Lorimer, S. Bogdanov, P. S. Ray, R. Lynch, P. Gentile, R. Rosen, S. A. Heatherly, B. N. Barlow, R. J. Hegedus, A. Vasquez Soto, P. Clancy, V. I. Kondratiev, K. Stovall, A. Istrate, B. Penprase, E. C. Bellm, A multiwavelength study of nearby millisecond pulsar PSR J1400−1431: Improved astrometry and an optical detection of its cool white dwarf companion. *Astrophys. J.* **847**, 25 (2017).
29. R. Spiewak, M. Bailes, E. D. Barr, N. D. R. Bhat, M. Burgay, A. D. Cameron, D. J. Champion, C. M. L. Flynn, A. Jameson, S. Johnston, M. J. Keith, M. Kramer, S. R. Kulkarni, L. Levin, A. G. Lyne, V. Morello, C. Ng, A. Possenti, V. Ravi, B. W. Stappers, W. van Straten, C. Tiburzi, PSR J2322−2650—A low-luminosity millisecond pulsar with a planetary-mass companion. *Mon. Not. R. Astron. Soc.* **475**, 469–477 (2018).
30. M. Marelli, A. De Luca, P. A. Caraveo, A multiwavelength study on the high-energy behavior of the *Fermi*/LAT pulsars. *Astrophys. J.* **733**, 82 (2011).
31. T. J. Johnson, C. Venter, A. K. Harding, L. Guillemot, D. A. Smith, M. Kramer, Ö. Çelik, P. R. den Hartog, E. C. Ferrara, X. Hou, J. Lande, P. S. Ray, Constraints on the emission geometries and spin evolution of gamma-ray millisecond pulsars. *Astrophys. J. Suppl. Ser.* **213**, 6 (2014).
32. C. Kalapotharakos, A. K. Harding, D. Kazanas, Gamma-ray emission in dissipative pulsar magnetospheres: From theory to *Fermi* observations. *Astrophys. J.* **793**, 97 (2014).
33. B. Cerutti, A. A. Philippov, A. Spitkovsky, Modelling high-energy pulsar light curves from first principles. *Mon. Not. R. Astron. Soc.* **457**, 2401–2414 (2016).
34. J. Takata, Y. Wang, K. S. Cheng, Population study for γ-ray pulsars with the outer gap model—II. Millisecond pulsars. *Mon. Not. R. Astron. Soc.* **414**, 2173–2185 (2011).
35. N. Mirabal, E. Charles, E. C. Ferrara, P. L. Gonthier, A. K. Harding, M. A. Sánchez-Conde, D. J. Thompson, 3FGL demographics outside the galactic plane using supervised machine learning: Pulsar and dark matter subhalo interpretations. *Astrophys. J.* **825**, 69 (2016).
36. M. Ackermann, A. Albert, B. Anderson, W. B. Atwood, L. Baldini, G. Barbiellini, D. Bastieri, K. Bechtol, R. Bellazzini, E. Bissaldi, R. D. Blandford, E. D. Bloom, R. Bonino, E. Bottacini, T. J. Brandt, J. Bregeon, P. Bruel, R. Buehler, G. A. Caliandro, R. A. Cameron, R. Caputo, M. Caragiulo, P. A. Caraveo, C. Cecchi, E. Charles, A. Chekhtman, J. Chiang, G. Chiaro, S. Ciprini, R. Claus, J. Cohen-Tanugi, J. Conrad, A. Cuoco, S. Cutini, F. D'Ammando, A. de Angelis, F. de Palma, R. Desiante, S. W. Digel, L. Di Venere, P. S. Drell, A. Drlica-Wagner, R. Essig, C. Favuzzi, S. J. Fegan, E. C. Ferrara, W. B. Focke, A. Franckowiak, Y. Fukazawa, S. Funk, P. Fusco, F. Gargano, D. Gasparrini, N. Giglietto, F. Giordano, M. Giroletti, T. Glanzman, G. Godfrey, G. A. Gomez-Vargas, I. A. Grenier, S. Guiriec, M. Gustafsson, E. Hays, J. W. Hewitt, D. Horan, T. Jogler, G. Jóhannesson, M. Kuss, S. Larsson, L. Latronico, J. Li, L. Li, M. Llena Garde, F. Longo, F. Loparco, P. Lubrano, D. Malyshev, M. Mayer, M. N. Mazziotta, J. E. McEnery, M. Meyer, P. F. Michelson, T. Mizuno, A. A. Moiseev, M. E. Monzani, A. Morselli, S. Murgia, E. Nuss, T. Ohsugi, M. Orienti, E. Orlando, J. F. Ormes, D. Paneque, J. S. Perkins, M. Pesce-Rollins, F. Piron, G. Pivato, T. A. Porter, S. Rainò, R. Rando, M. Razzano, A. Reimer, O. Reimer, S. Ritz,

Downloaded from http://advances.sciencemag.org/ on April 8, 2018

M. Sánchez-Conde, A. Schulz, N. Sehgal, C. Sgrò, E. J. Siskind, F. Spada, G. Spandre, P. Spinelli, L. Strigari, H. Tajima, H. Takahashi, J. B. Thayer, L. Tibaldo, D. F. Torres, E. Troja, G. Vianello, M. Werner, B. L. Winer, K. S. Wood, M. Wood, G. Zaharijas, S. Zimmer; Fermi-LAT Collaboration, Searching for dark matter annihilation from Milky Way dwarf spheroidal galaxies with six years of Fermi Large Area Telescope data. *Phys. Rev. Lett.* **115**, 231301 (2015).

37. M. Ackermann, M. Ajello, A. Albert, W. B. Atwood, L. Baldini, J. Ballet, G. Barbiellini, D. Bastieri, R. Bellazzini, E. Bissaldi, R. D. Blandford, E. D. Bloom, R. Bonino, E. Bottacini, T. J. Brandt, J. Bregeon, P. Bruel, R. Buehler, T. H. Burnett, R. A. Cameron, R. Caputo, M. Caragiulo, P. A. Caraveo, E. Cavazzuti, C. Cecchi, E. Charles, A. Chekhtman, J. Chiang, A. Chiappo, G. Chiaro, S. Ciprini, J. Conrad, F. Costanza, A. Cuoco, S. Cutini, F. D'Ammando, F. de Palma, R. Desiante, S. W. Digel, N. Di Lalla, M. Di Mauro, L. Di Venere, P. S. Drell, C. Favuzzi, S. J. Fegan, E. C. Ferrara, W. B. Focke, A. Franckowiak, Y. Fukazawa, S. Funk, P. Fusco, F. Gargano, D. Gasparrini, N. Giglietto, F. Giordano, M. Giroletti, T. Glanzman, G. A. Gomez-Vargas, D. Green, I. A. Grenier, J. E. Grove, L. Guillemot, S. Guiriec, M. Gustafsson, A. K. Harding, E. Hays, J. W. Hewitt, D. Horan, T. Jogler, A. S. Johnson, T. Kamae, D. Kocevski, M. Kuss, G. La Mura, S. Larsson, L. Latronico, J. Li, F. Longo, F. Loparco, M. N. Lovellette, P. Lubrano, J. D. Magill, S. Maldera, D. Malyshev, A. Manfreda, P. Martin, M. N. Mazziotta, P. F. Michelson, N. Mirabal, W. Mitthumsiri, T. Mizuno, A. A. Moiseev, M. E. Monzani, A. Morselli, M. Negro, E. Nuss, T. Ohsugi, M. Orienti, E. Orlando, J. F. Ormes, D. Paneque, J. S. Perkins, M. Persic, M. Pesce-Rollins, F. Piron, G. Principe, S. Rainò, R. Rando, M. Razzano, S. Razzaque, A. Reimer, O. Reimer, M. Sánchez-Conde, C. Sgrò, D. Simone, E. J. Siskind, F. Spada, G. Spandre, P. Spinelli, D. J. Suson, H. Tajima, K. Tanaka, J. B. Thayer, L. Tibaldo, D. F. Torres, E. Troja, Y. Uchiyama, G. Vianello, K. S. Wood, M. Wood, G. Zaharijas, S. Zimmer, The *Fermi* Galactic center GeV excess and implications for dark matter. *Astrophys. J.* **840**, 43 (2017).
38. R. Bartels, S. Krishnamurthy, C. Weniger, Strong support for the millisecond pulsar origin of the galactic center GeV excess. *Phys. Rev. Lett.* **116**, 051102 (2016).
39. S. K. Lee, M. Lisanti, B. R. Safdi, T. R. Slatyer, W. Xue, Evidence for unresolved γ-ray point sources in the inner galaxy. *Phys. Rev. Lett.* **116**, 051103 (2016).
40. F. Calore, M. Di Mauro, F. Donato, J. W. T. Hessels, C. Weniger, Radio detection prospects for a bulge population of millisecond pulsars as suggested by Fermi-LAT observations of the inner galaxy. *Astrophys. J.* **827**, 143 (2016).
41. M. Kerr, Improving sensitivity to weak pulsations with photon probability weighting. *Astrophys. J.* **732**, 38 (2011).
42. M. Kerr, "Likelihood methods for the detection and characterization of gamma-ray pulsars with the Fermi Large Area Telescope," thesis, University of Washington (2010).
43. F. Acero, M. Ackermann, M. Ajello, A. Albert, L. Baldini, J. Ballet, G. Barbiellini, D. Bastieri, R. Bellazzini, E. Bissaldi, E. D. Bloom, R. Bonino, E. Bottacini, T. J. Brandt, J. Bregeon, P. Bruel, R. Buehler, S. Buson, G. A. Caliandro, R. A. Cameron, M. Caragiulo, P. A. Caraveo, J. M. Casandjian, E. Cavazzuti, C. Cecchi, E. Charles, A. Chekhtman, J. Chiang, G. Chiaro, S. Ciprini, R. Claus, J. Cohen-Tanugi, J. Conrad, A. Cuoco, S. Cutini, F. D'Ammando, A. de Angelis, F. de Palma, R. Desiante, S. W. Digel, L. Di Venere, P. S. Drell, C. Favuzzi, S. J. Fegan, E. C. Ferrara, W. B. Focke, A. Franckowiak, S. Funk, P. Fusco, F. Gargano, D. Gasparrini, N. Giglietto, F. Giordano, M. Giroletti, T. Glanzman, G. Godfrey, I. A. Grenier, S. Guiriec, D. Hadasch, A. K. Harding, K. Hayashi, E. Hays, J. W. Hewitt, A. B. Hill, D. Horan, X. Hou, T. Jogler, G. Jóhannesson, T. Kamae, M. Kuss, D. Landriu, S. Larsson, L. Latronico, J. Li, L. Li, F. Longo, F. Loparco, M. N. Lovellette, P. Lubrano, S. Maldera, D. Malyshev, A. Manfreda, P. Martin, M. Mayer, M. N. Mazziotta, J. E. McEnery, P. F. Michelson, N. Mirabal, T. Mizuno, M. E. Monzani, A. Morselli, E. Nuss, T. Ohsugi, N. Omodei, M. Orienti, E. Orlando, J. F. Ormes, D. Paneque, M. Pesce-Rollins, F. Piron, G. Pivato, S. Rainò, R. Rando, M. Razzano, S. Razzaque, A. Reimer, O. Reimer, Q. Remy, N. Renault, M. Sánchez-Conde, M. Schaal, A. Schulz, C. Sgrò, E. J. Siskind, F. Spada, G. Spandre, P. Spinelli, A. W. Strong, D. J. Suson, H. Tajima, H. Takahashi, J. B. Thayer, D. J. Thompson, L. Tibaldo, M. Tinivella, D. F. Torres, G. Tosti, E. Troja, G. Vianello, M. Werner, K. S. Wood, M. Wood, G. Zaharijas, S. Zimmer, Development of the model of galactic interstellar emission for standard point-source analysis of *Fermi* large area telescope data. *Astron. Astrophys. Suppl. Ser.* **223**, 26 (2016).
44. J. D. Scargle, J. P. Norris, B. Jackson, J. Chiang, Studies in astronomical time series analysis. VI. Bayesian block representations. *Astrophys. J.* **764**, 167 (2013).
45. G. Schwarz, Estimating the dimension of a model. *Ann. Stat.* **6**, 461–464 (1978).
46. D. Foreman-Mackey, D. W. Hogg, D. Lang, J. Goodman, emcee: The MCMC Hammer. *Publ. Astron. Soc. Pac.* **125**, 306 (2013).
47. J. Goodman, J. Weare, Ensemble samplers with affine invariance. *Comm. App. Math. Comp. Sci.* **5**, 65–80 (2010).
48. I. S. Shklovskii, Possible causes of the secular increase in pulsar periods. *Soviet Astron.* **13**, 562 (1970).
49. K. P. Watters, R. W. Romani, P. Weltevrede, S. Johnston, An atlas for interpreting γ-ray pulsar light curves. *Astrophys. J.* **695**, 1289 (2009).
50. L. Guillemot, D. A. Smith, H. Laffon, G. H. Janssen, I. Cognard, G. Theureau, G. Desvignes, E. C. Ferrara, P. S. Ray, The gamma-ray millisecond pulsar deathline, revisited—New velocity and distance measurements. *Astron. Astrophys.* **587**, A109 (2016).
51. S. M. Ransom, "New search techniques for binary pulsars," thesis, Harvard University (2001).
52. M. B. Mickaliger, D. R. Lorimer, J. Boyles, M. A. McLaughlin, A. Collins, L. Hough, N. Tehrani, C. Tenney, A. Liska, J. Swiggum, Discovery of five new pulsars in archival data. *Astrophys. J.* **759**, 127 (2012).
53. M. Pierbattista, A. K. Harding, I. A. Grenier, T. J. Johnson, P. A. Caraveo, M. Kerr, P. L. Gonthier, Light-curve modelling constraints on the obliquities and aspect angles of the young *Fermi* pulsars. *Astron. Astrophys.* **575**, A3 (2015).

Acknowledgments: We are grateful to the thousands of volunteers who have supported Einstein@Home. We also thank those volunteers whose computers discovered the new MSPs: PSR J1035–6720: "WSyS"; K. Kovacs, of Seattle, WA, USA, and the ATLAS Cluster, AEI, Hannover, Germany; PSR J1744–7619: D. Hoberer, of Gainesville, TX, USA, and the ATLAS Cluster, AEI, Hannover, Germany; I. Yakushin of Chicago, IL, USA, and the LIGO Laboratory, USA; and K. Pickstone of Oldham, UK. **Funding:** This work was supported by the Max-Planck-Gesellschaft, the Deutsche Forschungsgemeinschaft through an Emmy Noether Research Grant [no. PL 710/1-1 (H.J.P.)], and NSF award 1104902. C.J.C. acknowledges support from the European Research Council under the European Union's Horizon 2020 research and innovation programme (grant agreement no. 715051; Spiders). W.M. was partially supported by the Thailand Research Fund (grants TRG5880173 and RTA5980003). M.R. was funded by the Italian Ministry of Education, University and Research (contract no. FIRB-2012-RBFR12PM1F). Work at the Naval Research Laboratory is supported by NASA. The Parkes Observatory is part of the Australia Telescope, funded by the Commonwealth of Australia for operation as a National Facility managed by the Commonwealth Scientific and Industrial Research Organisation (CSIRO). The *Fermi* LAT Collaboration acknowledges generous ongoing support from a number of agencies and institutes that have supported both the development and the operation of the LAT, as well as scientific data analysis. These include the National Aeronautics and Space Administration and the Department of Energy in the United States, the Commissariat à l'Energie Atomique and the Centre National de la Recherche Scientifique/Institut National de Physique Nucléaire et de Physique des Particules in France; the Agenzia Spaziale Italiana and the Istituto Nazionale di Fisica Nucleare in Italy, the Ministry of Education, Culture, Sports, Science and Technology (MEXT), High Energy Accelerator Research Organization (KEK), and Japan Aerospace Exploration Agency (JAXA) in Japan; and the K. A. Wallenberg Foundation, the Swedish Research Council, and the Swedish National Space Board in Sweden. Additional support for science analysis during the operations phase is gratefully acknowledged from the Istituto Nazionale di Astrofisica in Italy and the Centre National d'Études Spatiales in France. This work performed in part under DOE Contract DE-AC02-76SF00515. **Author contributions:** C.J.C., H.J.P., J.W., and L.G. designed and implemented the Einstein@Home gamma-ray pulsar searches. M. Kerr performed follow-up searches with the Parkes radio telescope. T.J.J. carried out the gamma-ray pulse profile modeling. F.C. reanalyzed archival Parkes observations. D.S. performed analyses of x-ray observations. The manuscript was written by the aforementioned authors. The remaining authors contributed to the development and operation of the Einstein@Home project, to the design and operation of the Fermi LAT and analysis of its observations, or to the Fermi Pulsar Search Consortium. **Competing interests:** The authors declare that they have no competing interests. **Data and materials availability:** Fermi-LAT data are available from the Fermi Science Support Center (http://fermi.gsfc.nasa.gov/ssc). XMM-Newton data are available from the XMM-Newton Science Archive (http://nxsa.esac.esa.int). Parkes radio telescope data recorded for this paper will be made available from the CSIRO Data Access Portal (https://data.csiro.au/) 18 months after the observation dates and are available upon request before that. All data needed to evaluate the conclusions in the paper are present in the paper and/or the Supplementary Materials. Additional data related to this paper may be requested from the authors.

Submitted 18 August 2017
Accepted 24 January 2018
Published 28 February 2018
10.1126/sciadv.aao7228

Citation: C. J. Clark, H. J. Pletsch, J. Wu, L. Guillemot, M. Kerr, T. J. Johnson, F. Camilo, D. Salvetti, B. Allen, D. Anderson, C. Aulbert, C. Beer, O. Bock, A. Cuéllar, H.-B. Eggenstein, H. Fehrmann, M. Kramer, S. A. Kwang, B. Machenschalk, L. Nieder, M. Ackermann, M. Ajello, L. Baldini, J. Ballet, G. Barbiellini, D. Bastieri, R. Bellazzini, E. Bissaldi, R. D. Blandford, E. D. Bloom, R. Bonino, E. Bottacini, T. J. Brandt, J. Bregeon, P. Bruel, R. Buehler, T. H. Burnett, S. Buson, R. A. Cameron, R. Caputo, P. A. Caraveo, E. Cavazzuti, C. Cecchi, E. Charles, A. Chekhtman, S. Ciprini, L. R. Cominsky, D. Costantin, S. Cutini, F. D'Ammando, A. De Luca, R. Desiante, L. Di Venere, M. Di Mauro, N. Di Lalla, S. W. Digel, C. Favuzzi, E. C. Ferrara, A. Franckowiak, Y. Fukazawa, S. Funk, P. Fusco, F. Gargano, D. Gasparrini, N. Giglietto, F. Giordano, M. Giroletti, G. A. Gomez-Vargas, D. Green, I. A. Grenier, S. Guiriec, A. K. Harding, J. W. Hewitt, D. Horan, G. Jóhannesson, S. Kensei, M. Kuss, G. La Mura, S. Larsson, L. Latronico, J. Li, F. Longo, F. Loparco, M. N. Lovellette, P. Lubrano, J. D. Magill, S. Maldera, A. Manfreda, M. N. Mazziotta, J. E. McEnery, P. F. Michelson, N. Mirabal, W. Mitthumsiri, T. Mizuno, M. E. Monzani, A. Morselli, I. V. Moskalenko, E. Nuss, T. Ohsugi, N. Omodei, M. Orienti, E. Orlando, M. Palatiello, V. S. Paliya, F. de Palma, D. Paneque, J. S. Perkins, M. Persic, M. Pesce-Rollins, T. A. Porter, G. Principe, S. Rainò, R. Rando, P. S. Ray, M. Razzano, A. Reimer, O. Reimer, R. W. Romani, P. M. Saz Parkinson, C. Sgrò, E. J. Siskind, D. A. Smith, F. Spada, G. Spandre, P. Spinelli, J. B. Thayer, D. J. Thompson, D. F. Torres, E. Troja, G. Vianello, K. Wood, M. Wood, Einstein@Home discovers a radio-quiet gamma-ray millisecond pulsar. *Sci. Adv.* **4**, eaao7228 (2018).

Downloaded from http://advances.sciencemag.org/ on April 8, 2018

ScienceAdvances

Einstein@Home discovers a radio-quiet gamma-ray millisecond pulsar

Colin J. Clark, Holger J. Pletsch, Jason Wu, Lucas Guillemot, Matthew Kerr, Tyrel J. Johnson, Fernando Camilo, David Salvetti, Bruce Allen, David Anderson, Carsten Aulbert, Christian Beer, Oliver Bock, Andres Cuéllar, Heinz-Bernd Eggenstein, Henning Fehrmann, Michael Kramer, Shawn A. Kwang, Bernd Machenschalk, Lars Nieder, Markus Ackermann, Marco Ajello, Luca Baldini, Jean Ballet, Guido Barbiellini, Denis Bastieri, Ronaldo Bellazzini, Elisabetta Bissaldi, Roger D. Blandford, Elliott D. Bloom, Raffaella Bonino, Eugenio Bottacini, Terri J. Brandt, Johan Bregeon, Philippe Bruel, Rolf Buehler, Toby H. Burnett, Sara Buson, Rob A. Cameron, Regina Caputo, Patrizia A. Caraveo, Elisabetta Cavazzuti, Claudia Cecchi, Eric Charles, Alexandre Chekhtman, Stefano Ciprini, Lynn R. Cominsky, Denise Costantin, Sara Cutini, Filippo D'Ammando, Andrea De Luca, Rachele Desiante, Leonardo Di Venere, Mattia Di Mauro, Niccolò Di Lalla, Seth W. Digel, Cecilia Favuzzi, Elizabeth C. Ferrara, Anna Franckowiak, Yasushi Fukazawa, Stefan Funk, Piergiorgio Fusco, Fabio Gargano, Dario Gasparrini, Nico Giglietto, Francesco Giordano, Marcello Giroletti, Germán A. Gomez-Vargas, David Green, Isabelle A. Grenier, Sylvain Guiriec, Alice K. Harding, John W. Hewitt, Deirdre Horan, Guðlaugur Jóhannesson, Shiki Kensei, Michael Kuss, Giovanni La Mura, Stefan Larsson, Luca Latronico, Jian Li, Francesco Longo, Francesco Loparco, Michael N. Lovellette, Pasquale Lubrano, Jeffrey D. Magill, Simone Maldera, Alberto Manfreda, Mario N. Mazziotta, Julie E. McEnery, Peter F. Michelson, Nestor Mirabal, Warit Mitthumsiri, Tsunefumi Mizuno, Maria Elena Monzani, Aldo Morselli, Igor V. Moskalenko, Eric Nuss, Takashi Ohsugi, Nicola Omodei, Monica Orienti, Elena Orlando, Michele Palatiello, Vaidehi S. Paliya, Francesco de Palma, David Paneque, Jeremy S. Perkins, Massimo Persic, Melissa Pesce-Rollins, Troy A. Porter, Giacomo Principe, Silvia Rainò, Riccardo Rando, Paul S. Ray, Massimiliano Razzano, Anita Reimer, Olaf Reimer, Roger W. Romani, Pablo M. Saz Parkinson, Carmelo Sgrò, Eric J. Siskind, David A. Smith, Francesca Spada, Gloria Spandre, Paolo Spinelli, Jana B. Thayer, David J. Thompson, Diego F. Torres, Eleonora Troja, Giacomo Vianello, Kent Wood and Matthew Wood

Sci Adv **4** (2), eaao7228.
DOI: 10.1126/sciadv.aao7228

ARTICLE TOOLS http://advances.sciencemag.org/content/4/2/eaao7228

REFERENCES This article cites 47 articles, 5 of which you can access for free
http://advances.sciencemag.org/content/4/2/eaao7228#BIBL

PERMISSIONS http://www.sciencemag.org/help/reprints-and-permissions

Use of this article is subject to the Terms of Service

Science Advances (ISSN 2375-2548) is published by the American Association for the Advancement of Science, 1200 New York Avenue NW, Washington, DC 20005. 2017 © The Authors, some rights reserved; exclusive licensee American Association for the Advancement of Science. No claim to original U.S. Government Works. The title *Science Advances* is a registered trademark of AAAS.

Downloaded from http://advances.sciencemag.org/ on April 8, 2018

The Astrophysical Journal, 858:43 (12pp), 2018 May 1 https://doi.org/10.3847/1538-4357/aabd3c
© 2018. The American Astronomical Society. All rights reserved.

Distinct Pattern of Solar Modulation of Galactic Cosmic Rays above a High Geomagnetic Cutoff Rigidity

Pierre-Simon Mangeard[1], John Clem[1], Paul Evenson[1], Roger Pyle[2], Warit Mitthumsiri[3], David Ruffolo[3], Alejandro Sáiz[3], and Tanin Nutaro[4]
[1] Bartol Research Institute and Department of Physics and Astronomy, University of Delaware, Newark, DE 19716, USA
[2] Pyle Consulting Group, Inc., St. Charles, IL 60174, USA
[3] Department of Physics, Faculty of Science, Mahidol University, Bangkok 10400, Thailand; david.ruf@mahidol.ac.th
[4] Department of Physics, Faculty of Science, Ubon Ratchathani University, Ubon Ratchathani 34190, Thailand
Received 2018 March 23; revised 2018 April 5; accepted 2018 April 8; published 2018 May 3

Abstract

Solar modulation refers to Galactic cosmic-ray variations with the ∼11 yr sunspot cycle and ∼22 yr solar magnetic cycle and is relevant to the space radiation environment and effects on Earth's atmosphere. Its complicated dependence on solar and heliospheric conditions is only roughly understood and has been empirically modeled in terms of a single modulation parameter. Most analyses of solar modulation use neutron monitor (NM) data from locations with relatively low geomagnetic cutoff rigidity, i.e., the threshold for cosmic rays to penetrate Earth's magnetic field. The Princess Sirindhorn Neutron Monitor at Doi Inthanon, Thailand, has the world's highest cutoff rigidity (≈17 GV) where observations span a complete solar modulation cycle (since late 2007). The pattern of solar modulation at Doi Inthanon during 2011–2014 was qualitatively very different from that at a low geomagnetic cutoff and is not well described by the same modulation parameter. At other times, NM count rates from Doi Inthanon and McMurdo, Antarctica (cutoff ∼1 GV), were linearly correlated and confirm the observation from latitude surveys in the previous solar cycle that the slope of the correlation changes with solar magnetic polarity. Low solar magnetic tilt angles (<40° at negative polarity) were well correlated with variations at both NM stations, as predicted by drift models. At a higher tilt angle, the Doi Inthanon count rate is well correlated with the interplanetary magnetic field, which is consistent with an increase in diffusion at high rigidity short-circuiting the effects of drifts and the heliospheric current sheet.

Key words: cosmic rays – solar–terrestrial relations – Sun: activity – Sun: magnetic fields

1. Introduction

While Galactic cosmic rays (GCRs) originate outside the heliosphere, the time variation of the flux traversing the solar wind to arrive at or near Earth is produced by solar and heliospheric effects. As a result, the GCR flux below ∼50 GeV varies throughout the sunspot (solar activity) cycle of ∼11 yr (Forbush 1954) and the solar magnetic cycle of ∼22 yr (Jokipii & Thomas 1981), a process known as solar modulation. The GCR flux is highest at sunspot minimum and lowest at sunspot maximum. This process affects the space radiation environment and ionization in Earth's atmosphere (Bazilevskaya et al. 2008). Observations of solar modulation also provide important and arguably unique information about the global properties of the heliosphere, because GCRs reach Earth after traveling over a great range of distance, heliolatitude, and heliolongitude. Their transport is affected by the interplanetary magnetic field (IMF), magnetic turbulence, and solar wind speed over a large heliospheric volume.

Direct measurements of cosmic rays have the advantage of determining the particle species and energy and hold great promise for the future. To date, energy-dependent spectra or abundance ratios at GeV-range energies have been reported for discrete epochs by using balloon-borne instruments, e.g., Clem & Evenson (2009) for electrons and positrons and Abe et al. (2016) for protons and alphas; by the *PAMELA* spacecraft for protons over four epochs during 2006–2009 (Adriani et al. 2013) and alphas over 2006–2008 (Adriani et al. 2011); and by the AMS-02 instrument on the *International Space Station* over 2011–2013 for protons (Aguilar et al. 2015a) and alphas (Aguilar et al. 2015b).

Spectral variations of GCRs have also been tracked over discrete epochs by repeated latitude surveys using a neutron monitor (NM) on a ship. An NM can have a collecting area of tens of m^2 and can achieve much greater statistical accuracy over a much shorter time duration by detecting atmospheric showers from cosmic-ray ions. While the primary cosmic-ray species and energy are no longer directly measured, ground-based detectors have a minimum threshold in rigidity, $P = pc/q$, where p is the particle momentum, c is the speed of light, and q is the particle charge. The rigidity threshold is either a geomagnetic cutoff rigidity, P_c, which varies from near zero in polar regions to ∼17 GV in parts of Southeast and South Asia, or an atmospheric cutoff (which for an NM is at ∼1 GV) corresponding to the energy needed to generate secondary shower particles that can be detected at ground level (Mangeard et al. 2016a, 2016b). Therefore, the negative rate of change of the NM count rate with cutoff rigidity, as the ship travels, is proportional to a cosmic-ray spectrum at that rigidity, and minute changes in the spectrum can be determined by comparing results from successive latitude surveys. From a recent sequence of 13 consecutive latitude surveys during 1994–2007, Nuntiyakul et al. (2014) confirmed a crossover between spectra before and after the 2000 reversal in solar magnetic polarity. Furthermore, they reported that in years other than 2000, there were linear trends between the shipborne NM count rate at each cutoff rigidity and the fixed NM count rate at McMurdo, Antarctica, at low cutoff, with a change of slope upon the magnetic polarity reversal.

Continuous, high-precision measurements of the solar modulation of GCRs available from fixed NM stations are the subject of the present work. Each NM count rate is an integral measurement above a rather sharp cutoff rigidity, as described above, and the sensitivity (count rate per primary cosmic-ray flux) as a function of rigidity, known as the "yield function," can be estimated by Monte Carlo simulation of particle interactions in the atmosphere and the detector (e.g., Mishev et al. 2013; Mangeard et al. 2016a, 2016b) or inferred from latitude survey and direct spectral measurements (Caballero-Lopez & Moraal 2012; Mitthumsiri et al. 2017). At low cutoff rigidity, there have been continuous measurements of solar modulation for six solar cycles (Simpson 2000; Oh et al. 2013).

These detailed time series have defied simple explanation. One popular model is the spherically symmetric force-field model, in which cosmic-ray spectra at Earth are characterized by a single modulation parameter, ϕ (Gleeson & Axford 1968; Caballero-Lopez & Moraal 2004). This parameter approximates the change in rigidity due to adiabatic deceleration after a GCR diffuses inward from an outer modulation boundary to the location of interest, assuming a near balance between the inward diffusive flux and the outward convective flux due to the solar wind. Based on NM observations at low cutoff rigidity, empirical modulation parameters have been tabulated as a function of time (Ghelfi et al. 2017b; Usoskin et al. 2017). Because of its simplicity, the force-field model remains popular for estimating cosmic-ray spectra as a function of solar modulation. Recent works (Corti et al. 2016; Gieseler et al. 2017) proposed modification of the force-field model by adding a second modulation parameter that leads to a rigidity-dependent solar modulation. While remaining relatively simple with only two parameters, these models give a better estimate of the solar modulation at low rigidities that are only marginally accessible with the NM network. In addition, there are observed effects of the solar magnetic polarity, commonly expressed as "$A > 0$" when the solar magnetic field is predominantly outward in the northern hemisphere and inward in the southern hemisphere and "$A < 0$" for the reverse polarity. Guiding center drifts of the charged cosmic rays in the IMF (Levy 1976; Jokipii et al. 1977) were proposed as a mechanism to explain changes in the time profiles of NM count rates upon a solar magnetic polarity reversal (Jokipii & Thomas 1981). Another proposed mechanism involves the effect of magnetic helicity on GCR diffusion (Bieber & Burger 1990). Both effects should depend on the product qA, and charge-sign-dependent modulation has been observed (Garcia-Munoz et al. 1986; Clem et al. 2000; Asaoka et al. 2002; Clem & Evenson 2009; Adriani et al. 2016), but charge sign and energy dependences are not yet fully resolved.

So far, most reported analyses of solar modulation based on NM time series were for a relatively low cutoff rigidity; there are not many long-term time series of NM data at $P_c > 12$ GV, as shown in Figure 1. Here we express P_c using the apparent cutoff rigidity, which takes obliquely incident GCRs into account (Clem et al. 1997) and has been calculated by weighting effective cutoffs calculated for nine arrival directions (Bieber et al. 1997). The effective cutoff is determined using the International Geomagnetic Reference Field (IGRF-12) and the methods of Lin et al. (1995). The apparent cutoff, P_c, changes as a function of time due to secular changes in Earth's magnetic field. For NM stations worldwide with $P_c > 9.5$ GV, Figure 1 shows the time periods and P_c values for which data are available, e.g., at the World Data Center for Cosmic Rays[5] or the Neutron Monitor Database[6] (NMDB). Vertical lines indicate approximate times of solar magnetic polarity reversal, which occurs near sunspot maxima. The NMs are sensitive to relativistic GCR ions with a positive charge, so Figure 1 also indicates time periods when positive magnetic polarity $A > 0$ resulted in qA-positive solar modulation and $A < 0$ resulted in qA-negative solar modulation. There are few NM stations at high P_c with data that span a solar cycle.

Among these, only the Princess Sirindhorn Neutron Monitor (PSNM) at Doi Inthanon, Thailand, had $P_c > 17$ GV, and indeed, it has the highest cutoff of any monitor currently in operation. After the start of full operation in 2007 December, the count rate rose to a maximum in 2009 (near sunspot minimum), fell to a minimum in 2014–2015 (near sunspot maximum), and then returned to its original count rate, thus spanning a full cycle. This time period also included a solar magnetic polarity reversal from $A < 0$ to $A > 0$.

In this work, we show that the solar modulation of GCRs as observed at Doi Inthanon from 2007 December to 2017 January exhibited a qualitatively distinct pattern from that observed at low cutoff rigidity. We also demonstrate that a force-field model using an empirical modulation parameter $\phi(t)$ as determined from low cutoff NM data provides a poor description of the time profile measured at Doi Inthanon. In other words, the spectral effects of solar modulation over roughly 1–17 GV are too complex to be well described by a single modulation parameter. We compare the Doi Inthanon NM count rate profile with low-P_c data from McMurdo, as well as the sunspot number, tilt angle of the heliospheric current sheet (HCS), solar wind speed, and IMF, and we identify different patterns of solar modulation during periods of low and high tilt angle.

2. PSNM Data and Water Vapor Correction

We focus on data from the PSNM at the summit of Doi Inthanon, Thailand's highest mountain, with geographic coordinates 18°.59 N, 98°.49 E and altitude 2560 m. The PSNM has taken data since 2007 August, and since 2007 December 9 it has operated with a complete set of 18 BP-28 ($^{10}BF_3$) neutron-sensitive proportional counter tubes with the standard NM64 configuration (18NM64). The 18 tubes are arranged in a single row to reduce edge effects. Further details are available from Ruffolo et al. (2016). At this altitude, the count rate is about 2.2 million counts hr^{-1}, providing a statistical accuracy better than 0.1% in hourly rates. The present study considers monthly or Carrington (solar) rotation (CarRot) averages (with truly negligible statistical uncertainty) from 2007 December 9 to 2017 January 7. At the end of that period, the apparent cutoff rigidity was 17.3 GV, and the effective vertical cutoff rigidity was 16.7 GV. Our calculated response function implies a median primary GCR rigidity of 35 GV and a 10th–90th percentile range of 18–155 GV (Ruffolo et al. 2016).

According to standard practice, PSNM data have been corrected for variations in atmospheric pressure, so the pressure-corrected count rate is $C_{\rm Pcorr}(t) = C(t)\exp[\beta(p - p_0)]$, where $C(t)$ is the measured count rate, $\beta = 0.641\%$ hPa^{-1} is the

[5] http://cidas.isee.nagoya-u.ac.jp/WDCCR
[6] http://nmdb.eu

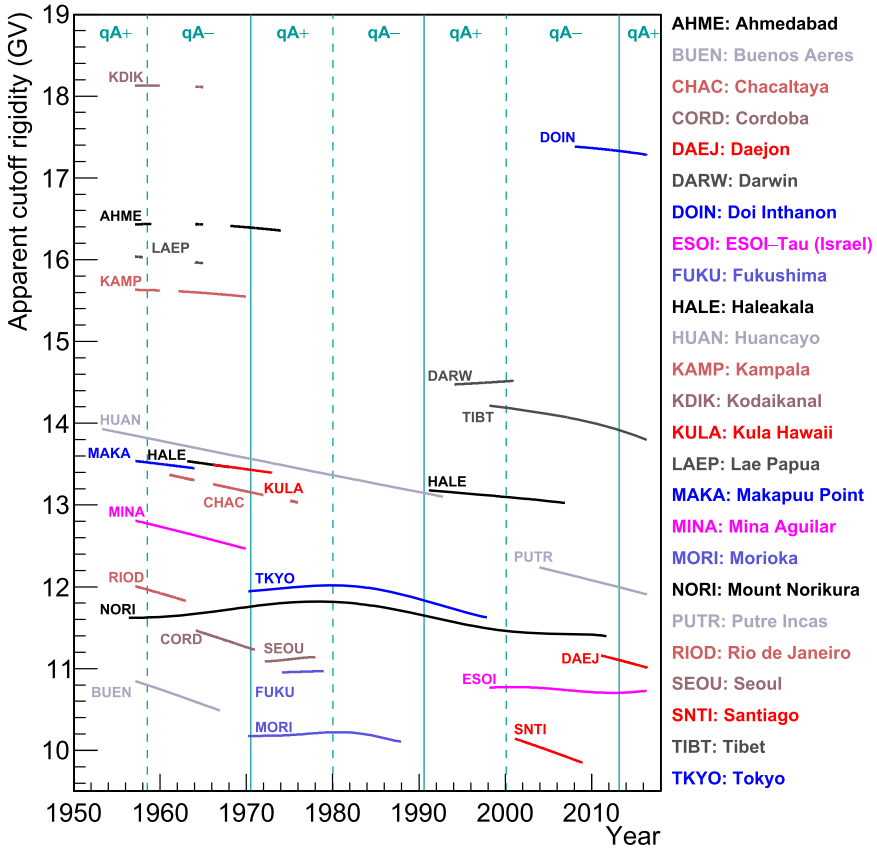


Figure 1. Time periods and apparent cutoff rigidities above 9.5 GV for which NM data are available. Reversals in solar magnetic polarity near sunspot maxima are indicated by vertical lines. Since NMs are sensitive to relativistic GCR ions, positive magnetic polarity $A > 0$ results in qA-positive solar modulation, and $A < 0$ results in qA-negative solar modulation. Among the few time series spanning a solar cycle, the NM data from Doi Inthanon have the highest apparent cutoff rigidity (over 17 GV) and are the focus of this study.

pressure coefficient determined from the data, and $p_0 = 750.6$ hPa is a reference pressure. Furthermore, Ruffolo et al. (2016) showed that the leader fraction L (inverse of mean multiplicity) derived from the neutron time delay distributions at Doi Inthanon is related not only to the atmospheric pressure but also to the surface water vapor pressure E_w. Because of the significantly different meteorological and environmental conditions during the dry and rainy seasons at this tropical location, for which the E_w values between ~1 and 15 hPa serve as a proxy, this effect is characterized by a yearly wave in L. Now considering the pressure-corrected count rate (see their Figure 5(a)), a hint of a yearly wave is again visible, though with a much smaller amplitude. Hence, in the present work, we have investigated the effect of surface water vapor on the PSNM count rate.

Following Ruffolo et al. (2016), we used data at 6 hr time intervals from the Global Atmospheric Data Assimilation[7] to calculate E_w values for a pressure of 750 hPa (close to the mean pressure at the Doi Inthanon NM) at neighboring 1° grid points and interpolate to the location of Doi Inthanon. Figure 2 shows the pressure-corrected PSNM count rate C_{Pcorr} for each 6 hr interval from 2007 December 9 to 2017 January 28 plotted as a function of E_w. There is a small but noticeable trend of decreasing count rate with increasing E_w, which is more apparent when considering the mean count rate in each 1 hPa interval of E_w (solid circles in Figure 2). While the fitting function used previously for the leader fraction by Ruffolo et al. (2016) was nonlinear in E_w, in this case, the mean count rate is well modeled as a linear function of E_w. We therefore determine a pressure- and water vapor–corrected count rate C_{PWcorr} by dividing out the best-fit linear trend,

$$C_{PWcorr}(t) = C_{Pcorr}(t)\frac{1 - aE_{w,0}}{1 - aE_w(t)}, \quad (1)$$

where the correction coefficient from the linear fit is $a = (2.05 \pm 0.19) \times 10^{-4}$ hPa^{-1} and the reference value $E_{w,0} = 6.3$ hPa as in Ruffolo et al. (2016). We estimate the peak-to-peak annual wave in C_{Pcorr} as the change when E_w varies from 1 to 15 hPa, which is 0.3%. The PSNM has observed a total peak-to-peak solar modulation of about 3%, so this correction is nonnegligible. In the remainder of this work, we only use C_{PWcorr}, the pressure- and water vapor–corrected count rate.

3. Solar Modulation Observed by PSNM

3.1. Overview

Figures 3(a) and (b) present the count rates averaged over CarRots from the PSNM at Doi Inthanon and the McMurdo NM, respectively. The data reported in this work cover the period from 2007 December 9 (start of full operation at Doi Inthanon) to 2017 January 7 (closure of the McMurdo NM station). Both count rates have been corrected for pressure variation, and the Doi Inthanon count rate has also been corrected for water vapor variation as described in the previous section. Note that for clarity of presentation, the two count rates are shown on very different scales; the peak-to-peak solar

[7] See http://ready.arl.noaa.gov/gdas1.php.

modulation at Doi Inthanon was ≈3%, whereas that at McMurdo was ≈15%. It is a well-known property of solar modulation that it is weaker at higher rigidity, and indeed, it may be negligible at $\gtrsim$50 GeV.

In addition to the long-term process of solar modulation, the GCR flux undergoes Forbush decreases, which are temporary decreases due to the passage by Earth of a coronal mass ejection (CME) or other structures (Forbush 1937). A Forbush decrease typically involves a flux decrease over hours or days followed by a recovery over some days. When we average NM count rates over CarRots, the time profile of a Forbush decrease is not visible, yet the average count rate can be affected by the event. To check whether our understanding of the global heliospheric process of solar modulation is affected by the local effects of CME passage, which may have a different influence on the GCR spectrum, we show the NM count rates when time periods with a strong Forbush decrease are either included (light blue points) or excluded (black points). Here a strong Forbush decrease is defined as an event with a McMurdo count rate decrease of >5%. Actually, for most months, there were no effects of strong Forbush decreases (i.e., the light blue and black points coincide), and none of the qualitative conclusions of our study depend on whether they are included or excluded. In subsequent sections, we exclude the times with strong Forbush decreases. Indeed, it is fascinating that even with strong Forbush decreases excluded, both NM count rates show numerous short-term modulation features that last only 1–2 CarRots. We speculate that these may be associated with CME-related structures that do not directly pass the Earth, yet as they propagate outward, they can affect solar modulation, e.g., by forming merged interaction regions or global merged interaction regions (Burlaga et al. 1983). These short-term features are stronger and more frequent during times of strong solar activity, supporting the idea that they are related to CMEs. Note also that these short-term variations affected the GCR spectrum near sunspot maximum at high rigidity (at Doi Inthanon) more strongly than solar modulation.

From late 2007, the two NM count rates increased until reaching a maximum in late 2009. This GCR maximum followed a very low minimum in the mean total sunspot number (shown in Figure 3(c)), as reported by WDC-SILSO, Royal Observatory of Belgium, Brussels,[8] with some delay, as expected for solar effects to propagate throughout the heliosphere. Indeed, this time period witnessed the highest GCR flux in over 60 yr, since continuous NM measurements have been available (McDonald et al. 2010; Mewaldt et al. 2010; Oh et al. 2013). After the GCR maximum, both NM count rates initially decreased rather rapidly, until 2010 April. From 2007 December to 2010 April, the count rate variations at Doi Inthanon and McMurdo were well correlated.

Figure 3 also shows time series of the HCS tilt angle, solar wind speed, and IMF strength. These quantities could have causal effects on solar modulation, and detailed comparisons of their variations with NM count rate variations will be shown in later sections. For now, we discuss broad-brush comparisons for different time periods. At the time of the GCR maximum in 2009, all three quantities were near their minimum values. However, the IMF strength was nearly constant during the preceding period when the two NM count rates rose to their maxima, whereas the tilt and solar wind speed were

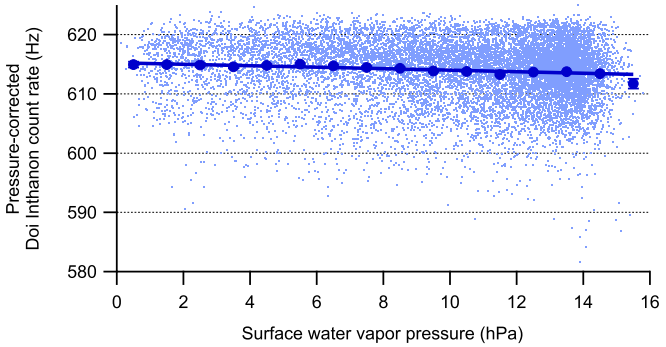


Figure 2. Scatter plot of the pressure-corrected NM count rate at Doi Inthanon as a function of surface water vapor pressure E_w for each 6 hr interval from 2007 December 9 to 2017 January 28, along with the mean count-rate values for 1 hPa intervals in E_w (solid circles). The linear fit to those mean values (solid line) was used for water vapor correction of the count rate.

anticorrelated with NM count rates during the GCR flux increase and initial decrease.

Then, starting in mid-2010, as the sunspot number and tilt angle generally increased, distinct patterns developed in the two NM count rates. Aside from the temporary decreases of 1–2 CarRots, as mentioned earlier, the McMurdo count rate (at low cutoff rigidity) generally decreased until early 2015, whereas the Doi Inthanon count rate (at high cutoff rigidity) remained relatively stable up to mid-2014. We call this the "plateau" period for Doi Inthanon. Then, in late 2014, the Doi Inthanon count rate underwent a sharp decrease to near its minimum value. Doi Inthanon observed a cosmic-ray maximum a few CarRots later than McMurdo and a cosmic-ray minimum a few CarRots earlier, so the total time from maximum to minimum was several months shorter.

Starting in 2015, both the Doi Inthanon and McMurdo count rates generally increased along with the general decline in the sunspot number, tilt angle, and IMF. In contrast, the solar wind speed was nearly constant (with significant fluctuations) and did not serve as a good predictor of solar modulation. During this period, the count rate variations at Doi Inthanon and McMurdo were again well correlated.

It is important to note that the Sun's polar magnetic fields underwent polarity reversals during 2012–2014, during the Doi Inthanon plateau period, which was also a time of high sunspot number and high tilt angle, i.e., conditions near solar maximum. Figure 3(d) shows the solar polar field strengths as measured by the Wilcox Solar Observatory (WSO).[9] The 20 nHz low-pass-filtered values are used here. Both north (Bn; red) and south (Bs; blue) polar magnetic field observations are presented, as well as their average Ba = (Bn − Bs)/2 (black). The zero crossing of the average value in 2013 March (black vertical line) is a useful indicator of the overall solar magnetic polarity reversal from $A < 0$ to $A > 0$. In any case, the complete sequence of polarity reversals lasted for about 2 yr, with three reversals near the North Pole from 2012 June to 2014 September and a single reversal near the South Pole in 2013 July.

Note that this 4 yr plateau started about 2 yr before the sequence of polarity reversals at the solar poles as observed by WSO (Figure 3(d)) and lasted until the end of the sequence. Thus, we see that this plateau period is not determined by the

[8] See http://sidc.be/silso/home.

[9] See http://wso.stanford.edu/Polar.html.

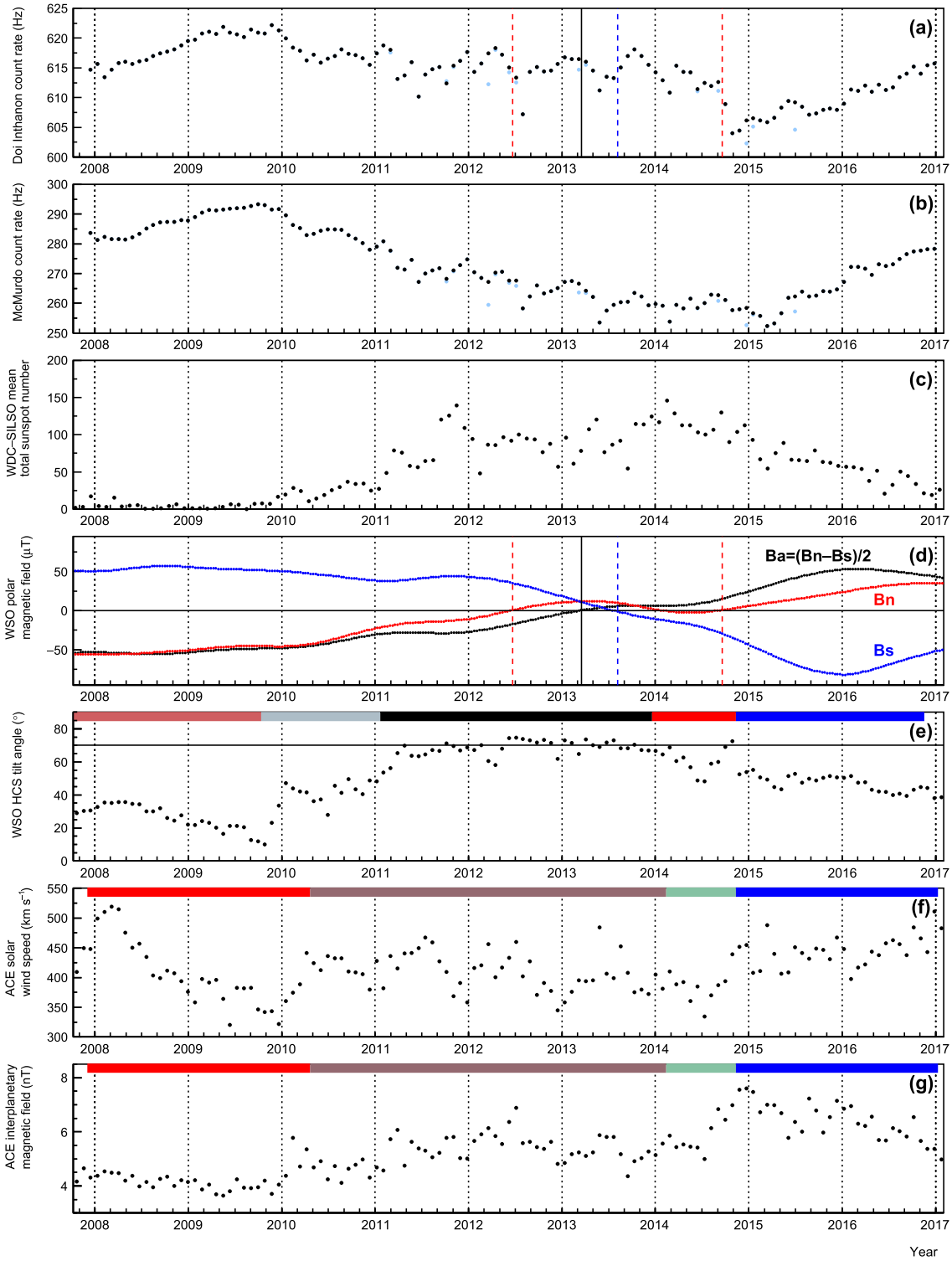


Figure 3. Time series from late 2007 to early 2017 of (a) the pressure- and water vapor–corrected NM count rate at Doi Inthanon, averaged over CarRots; (b) the pressure-corrected NM count rate at McMurdo, averaged over CarRots; (c) the WDC-SILSO monthly mean total sunspot number; (d) the WSO solar polar magnetic fields (traces explained in the text); (e) the WSO HCS tilt angle, averaged over CarRots; (f) the *ACE*/SWEPAM solar wind speed, averaged over CarRots; and (g) the *ACE*/MAG IMF strength, averaged over CarRots. In (a) and (b), fluxes before and after removing periods of strong Forbush decreases are shown by light blue and black points, respectively. Vertical lines in panels (a) and (d) indicate the first and last zero crossings of Bn (red) and the zero crossings of Bs (blue) and Ba (black). The horizontal line in panel (e) indicates a tilt angle of 70°; values above this line should be considered as lower limits. The color code over panel (e) indicates time periods of distinct tilt angle levels or trends, as used in Figure 6, while another color code over panels (f) and (g) indicates time periods of distinct levels or trends in interplanetary parameters, as used in Figures 4, 7, and 8. A key point is that during the years 2011–2014, corresponding to very high tilt angles, the NMs at Doi Inthanon (at high cutoff) and McMurdo (at low cutoff) exhibited distinct patterns of solar modulation, whereas before and after that time (for lower tilt angles), the two NM count-rate variations were well correlated.

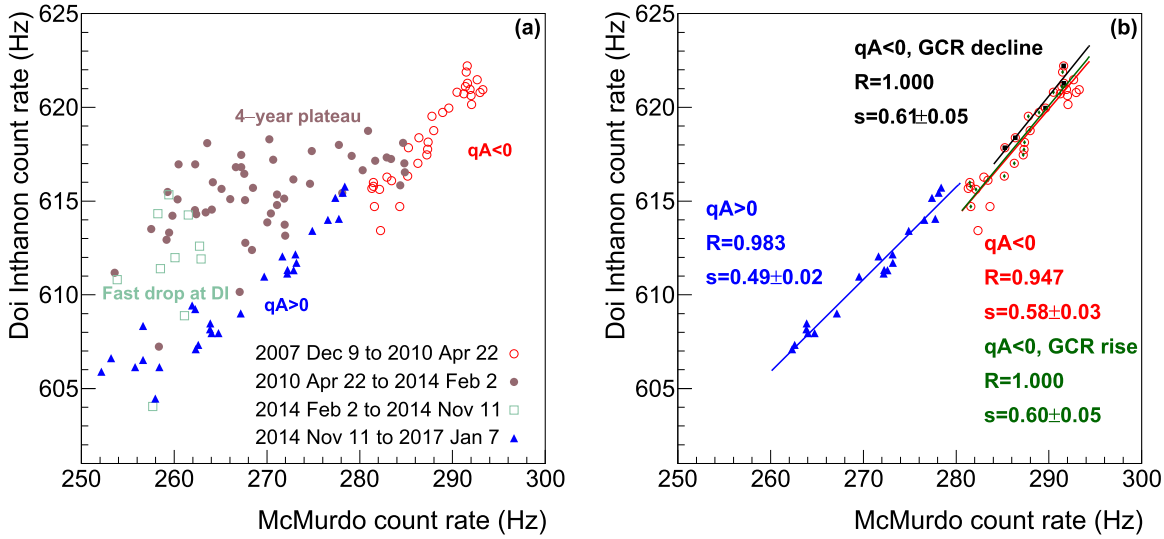


Figure 4. (a) Scatter plot of NM count rates at Doi Inthanon (high cutoff rigidity) and McMurdo (low cutoff rigidity) from 2007 December to 2017 January. (b) Same plot but restricted to the earliest and latest time periods, for low solar activity and an HCS tilt angle $\lesssim$50°; at such times, the two stations' count rates have a linear relationship, and the slope depends on solar magnetic polarity as found by Nuntiyakul et al. (2014). For a higher tilt angle, from mid-2010 to late 2014, there is no longer a linear relationship, as Doi Inthanon has a pattern of solar modulation distinct from that observed at low cutoff.

solar polarity reversal alone. The plateau period corresponds more closely to the period of very high tilt angle.

3.2. Comparison of PSNM Data with Other NM Data

There have been previous comparisons of the count rates of fixed NMs located at different rigidity cutoffs in order to study solar modulation over long periods. Its detailed evolution over previous solar cycles was analyzed by Popielawska & Simpson (1991) and Popielawska (1992, 1995) with NM data from Climax (~3 GV) and Huancayo (~13 GV) and from Kiel (~2.3 GV) and Tsumeb (~9.3 GV). Here we compare PSNM data from Doi Inthanon with NM data from McMurdo and examine how well a modulation parameter inferred from other NM data can be used to describe solar modulation as observed by the PSNM at high cutoff rigidity.

3.2.1. Comparison with McMurdo NM

Variations of the count rate at an apparent rigidity cutoff of ≈17.3 GV, as observed at Doi Inthanon, show interesting behavior with respect to variations observed at McMurdo with an atmospheric cutoff at ~1 GV. The basic features were described in Section 3.1; here we compare the Doi Inthanon and McMurdo NM count rates in more detail. Figure 4(a) presents the scatter plot of the count rates (in Hz) at Doi Inthanon and McMurdo from the start of PSNM operations to the end of operations at McMurdo. Each marker is an average value per CarRot, and the marker color corresponds to the time period as indicated in Figures 3(f) and (g), i.e., from 2007 December to 2010 April, while the Doi Inthanon and McMurdo count rates were well correlated (red open circles); during the Doi Inthanon plateau (brown filled circles); during the fast drop at Doi Inthanon (green open squares); and during the GCR rise (blue filled triangles), when the two count rates were again well correlated.

Note that for clarity of presentation, the Doi Inthanon scale is again expanded relative to the McMurdo scale, with the full scale of solar modulation at Doi Inthanon corresponding to a much smaller percentage increase than that at McMurdo. As a result, the temporary decreases during 1–2 CarRots, as noted earlier, have a strong relative impact on modulation at Doi Inthanon and cause a large vertical scatter in the graph during the 4 yr plateau period. As previously mentioned, the 4 yr plateau is followed by a transition period with a very fast drop in the count rate at Doi Inthanon. This decrease represents roughly half of the amplitude of the modulation observed during the full solar cycle at Doi Inthanon. In fact, a similar percentage decrease is present in the observations at McMurdo during the same time period, but that represents a smaller portion of the full modulation there.

During times of low tilt angle, the count rates at Doi Inthanon and McMurdo were linearly related. Figure 4(b) shows the linear trends between the count rates for such periods, i.e., from 2007 December 9 to 2010 April 22 for $qA < 0$ (red circles) and from 2015 July 14 to 2017 January 7 for $qA > 0$ (blue triangles). When $qA < 0$, the value of the slope was the same (within the uncertainties) during the GCR rise (green diamonds) and decline (black squares). After the period of high tilt angle near solar maximum, during which no clear correlation between the count rates was observed, the linear trend returned after the last large Forbush decrease, now with $qA < 0$. However, the slope of Doi Inthanon versus McMurdo count rate variations was lower when $qA > 0$ (slope ≈0.5) than when $qA < 0$ (slope ≈0.6). This confirms the linear trends between count rates at different cutoff rigidity, as observed from latitude surveys during the previous solar cycle and polarity reversal (Nuntiyakul et al. 2014), except for the year 2000 near solar maximum. The change in slope with solar magnetic polarity reversal, as reported here, is in the same direction as found in that work.[10]

[10] Due to a misunderstanding of the units, the McMurdo NM count rates reported by Nuntiyakul et al. (2014) should all be multiplied by 5/3, and the regression coefficients of the shipborne monitor versus the McMurdo NM count rate should all be multiplied by 3/5. The qualitative conclusions of that work remain unchanged. Note also that it is difficult to compare absolute values of the slope from that work with those in the present work because the count rates depend on the number of counter tubes, altitude, tube configuration, dead time, and surrounding structure (Mangeard et al. 2016b).

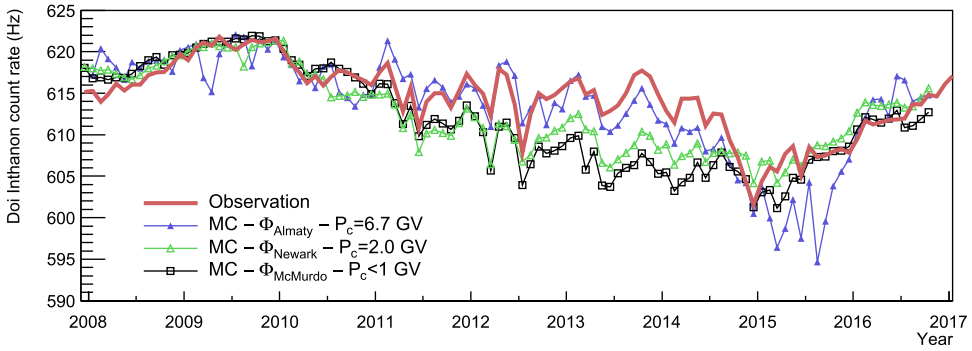


Figure 5. Comparison of the measured NM count rate at Doi Inthanon (thick red line) with simulated count rates for Doi Inthanon as estimated using yield functions from Monte Carlo simulation (Mangeard et al. 2016b) and a model GCR spectrum based on the LIS from Ghelfi et al. (2016, 2017a) and the force-field approximation. This approximation used solar modulation parameters estimated from NMs at different rigidity cutoffs, i.e., Almaty (blue line), Newark (green line), and McMurdo (black line), according to the method presented by Ghelfi et al. (2017b). The simulated count rates were normalized to that of the PSNM at the cosmic-ray maximum (2009 December). During times of high tilt angle, the solar modulation parameter time series based on NMs at low cutoff provide a poor description of solar modulation at Doi Inthanon at high cutoff, indicating that a model with a single empirical modulation parameter does not accurately describe solar modulation over a wide rigidity range.

3.2.2. Inadequacy of Modulation Parameter Derived from Low Cutoff NM Data

Recently, Ghelfi et al. (2017b) provided time series of empirical solar modulation parameters Φ_{NM} derived using data from a single NM.[11] They based their calculations on (i) the nonparametric proton and helium local interstellar spectra (LIS) determined from recent direct measurements with high statistics from balloon experiments (BESS, BESS-Polar) and spacecraft data (*PAMELA*, AMS-02; Ghelfi et al. 2016, 2017a), (ii) the force-field model of solar modulation (Gleeson & Axford 1968), and (iii) NM data from the station of interest. Time series of Φ_{NM} up to 2016 October were tabulated for various NMs located at different geomagnetic cutoffs.

Here we use such time series of Φ_{NM} to infer the GCR spectrum at Earth and yield functions for the PSNM based on Monte Carlo simulation results to generate simulated count rates for Doi Inthanon, which we then compare with the measured PSNM count rate (Figure 5). We employ monthly time series of Φ_{NM} from three NMs: McMurdo (Antarctica; $P_c \sim 1$ GV), Newark (USA; $P_c = 2.0$ GV), and Almaty (Kazakhstan; $P_c = 6.7$ GV). Note that some anomalous variations for Almaty in 2015 are not understood and not correlated with variations for other NM stations. For each of these three stations, we derive the time series of the spectra of protons and helium nuclei at the top of the atmosphere (based on the work of Ghelfi et al. 2016, 2017a, 2017b). We then apply the simulated yield functions from Mangeard et al. (2016b) to determine the count rates expected for the PSNM. We aim to examine the accuracy of a force-field model that uses a single empirical modulation parameter to describe solar modulation of the GCR spectrum over a wide rigidity range, given that models such as this are widely used in the community.

The comparison of the simulated count rates (thin lines) with the PSNM observations at Doi Inthanon (thick red line) is presented in Figure 5. The simulated count rates were normalized to that of the PSNM at solar minimum (2009 December). We see that that solar modulation of the PSNM count rate, i.e., the variation over the solar activity cycle, is poorly described by the force-field model that used a modulation parameter based on McMurdo data. This is consistent with our observation of a different pattern of solar modulation at McMurdo and Doi Inthanon. Interestingly, the simulated PSNM count rates based on modulation parameters for Newark and Almaty, which are located at intermediate geomagnetic cutoffs, are usually bracketed by the simulated PSNM count rate based on McMurdo data (black line) and the actually observed PSNM count rate (except during the time period in 2015 with anomalous Almaty count rates). Thus, the accuracy of the force-field model systematically increases when the modulation parameter is based on NM data with cutoff rigidity closer to the value of interest. In particular, we can infer that solar modulation at Almaty, at $P_c = 6.7$ GV, is qualitatively (physically) more similar to that at Doi Inthanon than is solar modulation at low cutoff rigidity. Note also that the time lag in the modulation during the period of high solar activity increases with the cutoff. Finally, the main conclusion is that a force-field model with a single solar modulation parameter cannot reproduce the observations made at multiple rigidity cutoffs (~1–17 GV) over a full solar cycle.

3.3. Comparison with Heliospheric Measurements

In this section, we compare measurements of heliospheric parameters (HCS tilt angle, solar wind speed, and IMF) with NM count rates at Doi Inthanon and McMurdo, where all quantities are averaged over CarRots. Tables 1–3 show the correlation coefficient between each parameter and NM count rate as recorded after a delay time of 0–3 CarRots, in order to allow for the possibility that a heliospheric parameter value as measured near the Sun or Earth will propagate outward with the solar wind and then affect solar modulation as indicated by the NM count rates. Correlation coefficients are shown for all data and for four to five shorter time periods (color-coded in Figure 3) corresponding to phases of solar modulation in which there could be different relationships between the data. When considering the tilt angle, we found very different behaviors depending on the value of the tilt angle, so the time periods shown in Table 1 are used for the tilt angle data, which are compared with the NM data after the appropriate delay, to the extent that NM data were available from both Doi Inthanon and McMurdo. For the solar wind speed and magnetic field, the comparison depends on the values of the NM count rates, so the time periods shown in

[11] See http://lpsc.in2p3.fr/crdb.

Table 1
Correlation Coefficient between HCS Tilt Angle and NM Count Rates

		Doi Inthanon NM				McMurdo NM			
		Tilt-to-NM Delay (CarRots)				Tilt-to-NM Delay (CarRots)			
Period	Polarity	0	1	2	3	0	1	2	3
All		−0.42	−0.45	−0.47	−0.46	**−0.78**	**−0.81**	**−0.83**	**−0.84**
Start to 2009 Oct 13	$A < 0$	**−0.91**	**−0.87**	**−0.84**	**−0.79**	**−0.93**	**−0.92**	**−0.86**	**−0.79**
2009 Oct 13 to 2011 Jan 1	$A < 0$	−0.55	−0.62	**−0.70**	−0.66	−0.68	**−0.75**	**−0.81**	**−0.73**
2011 Jan 1 to 2013 Dec 19	$A < 0 \rightarrow A > 0$	−0.42	−0.26	−0.05	−0.19	−0.55	−0.51	−0.50	−0.34
2013 Dec 19 to 2014 Nov 11	$A > 0$	−0.45	−0.39	−0.29	−0.00	−0.33	−0.50	**−0.73**	−0.58
2014 Nov 11 to End	$A > 0$	**−0.73**	**−0.75**	**−0.77**	**−0.78**	−0.65	−0.67	**−0.71**	**−0.74**

Table 2
Correlation Coefficient between Solar Wind Speed (SWS) and NM Count Rates

		Doi Inthanon NM				McMurdo NM			
		SWS-to-NM Delay (CarRots)				SWS-to-NM Delay (CarRots)			
Period	Polarity	0	1	2	3	0	1	2	3
All		−0.41	−0.36	−0.28	−0.19	−0.10	−0.08	−0.05	0.00
2007 Dec 9 to 2010 Apr 22	$A < 0$	**−0.88**	**−0.82**	**−0.71**	−0.67	**−0.88**	**−0.81**	**−0.73**	−0.65
2010 Apr 22 to 2014 Feb 2	$A < 0 \rightarrow A > 0$	−0.25	−0.27	−0.20	−0.05	0.14	0.15	0.15	0.17
2014 Feb 2 to 2014 Nov 11	$A > 0$	−0.64	0.11	0.24	0.56	−0.56	−0.41	−0.67	−0.13
2014 Nov 11 to 2017 Jan 7	$A > 0$	0.31	0.25	0.46	0.51	0.43	0.26	0.40	0.42

Table 3
Correlation Coefficient between IMF and NM Count Rates

		Doi Inthanon NM				McMurdo NM			
		IMF-to-NM Delay (CarRots)				IMF-to-NM Delay (CarRots)			
Period	Polarity	0	1	2	3	0	1	2	3
All		**−0.85**	**−0.84**	**−0.78**	**−0.75**	**−0.75**	**−0.74**	**−0.71**	−0.68
2007 Dec 9 to 2010 Apr 22	$A < 0$	−0.48	−0.54	−0.53	−0.65	−0.51	−0.60	−0.63	−0.66
2010 Apr 22 to 2014 Feb 2	$A < 0 \rightarrow A > 0$	−0.55	−0.57	−0.26	−0.15	−0.56	−0.55	−0.46	−0.33
2014 Feb 2 to 2014 Nov 11	$A > 0$	**−0.78**	−0.54	−0.45	−0.37	0.02	−0.10	−0.15	−0.14
2014 Nov 11 to 2017 Jan 7	$A > 0$	−0.69	−0.58	−0.38	−0.27	−0.61	−0.53	−0.45	−0.37

Tables 2–3 are used for the NM count rate data, which are compared with the solar wind speed and IMF data at an earlier time to give the appropriate delay. In all tables, particularly strong correlations (of absolute value 0.70 or greater) are indicated in bold type. For each parameter, an optimal delay time is identified, which is used when comparing with NM count rates in Figures 6–8.

3.3.1. HCS Tilt Angle

The "classic" average tilt angle (Hoeksema 1995) computed from WSO observations[12] is shown in Figure 3(e), which gives information about the HCS near the Sun only. Its correlation with the inclination of the HCS further in the heliosphere is expected to be better during or near solar minimum. Near solar maximum, the fast variation of conditions near the Sun makes it difficult to directly extrapolate from the tilt angle to the HCS properties at a long distance from the Sun. Furthermore, the tilt angle data are accompanied by a notice that values above 70° (indicated by a horizontal line in Figure 3(e) and vertical lines in Figure 6) should be considered as lower limits, so near solar maximum, the tilt angle is not well measured.

Table 1 presents the correlation coefficients between the count rates at Doi Inthanon and McMurdo and the tilt angle for five time periods based on the value of the tilt angle and the solar activity and for four delays, 0–3 CarRots. A delay time of 2 CarRots provides the greatest number of strong (>70%) correlation coefficients with the NM data during various time periods. Figure 6 presents the correlations between the count rates (average per CarRot) at Doi Inthanon and McMurdo with the tilt angle after the optimal delay of 2 CarRots was applied to the count rates. Note that the time periods indicated in the legend refer to times of NM data to simplify the comparison with other figures.

During the initial period of low solar activity with a tilt angle below 50° at negative solar magnetic polarity ($A < 0$), Figure 6 shows that both NM count rates were strongly anticorrelated with the tilt angle, either during the GCR rise (open red circles) or GCR decline (solid gray circles). For McMurdo, the trends during the $A < 0$ GCR rise and decline at such low tilt angles are similar, and it could be said that the tilt angle is an excellent predictor of the McMurdo count rate,

[12] See http://wso.stanford.edu/Tilts.html.

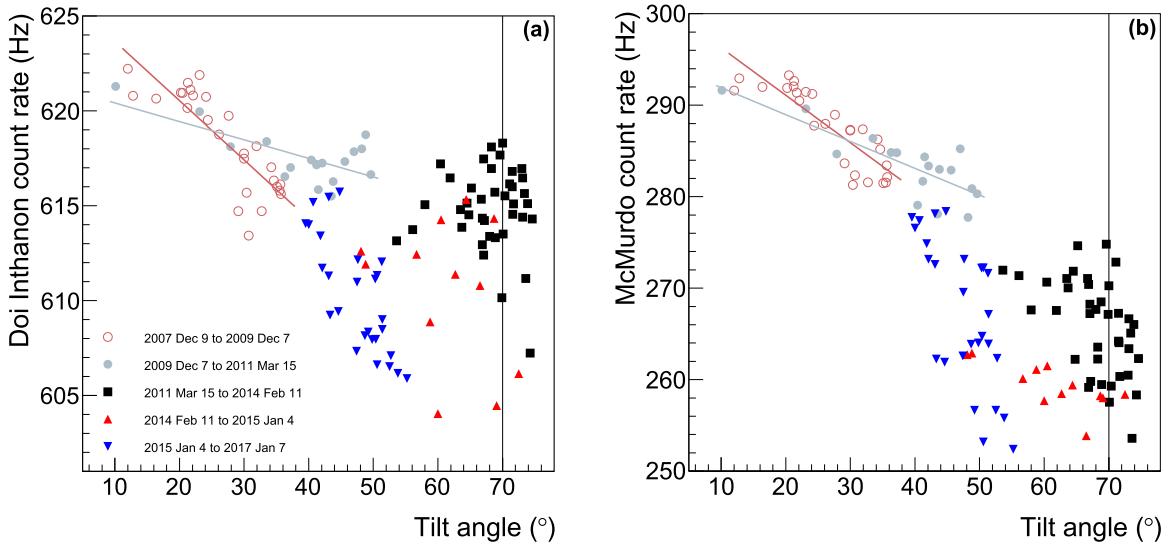


Figure 6. Scatter plots of the CarRot-averaged count rates at (a) Doi Inthanon and (b) McMurdo with the WSO HCS tilt angle. NM count rates were compared with the tilt angle from 2 CarRots earlier to maximize the correlation factors; the dates indicated in (a) refer to the dates of NM data.

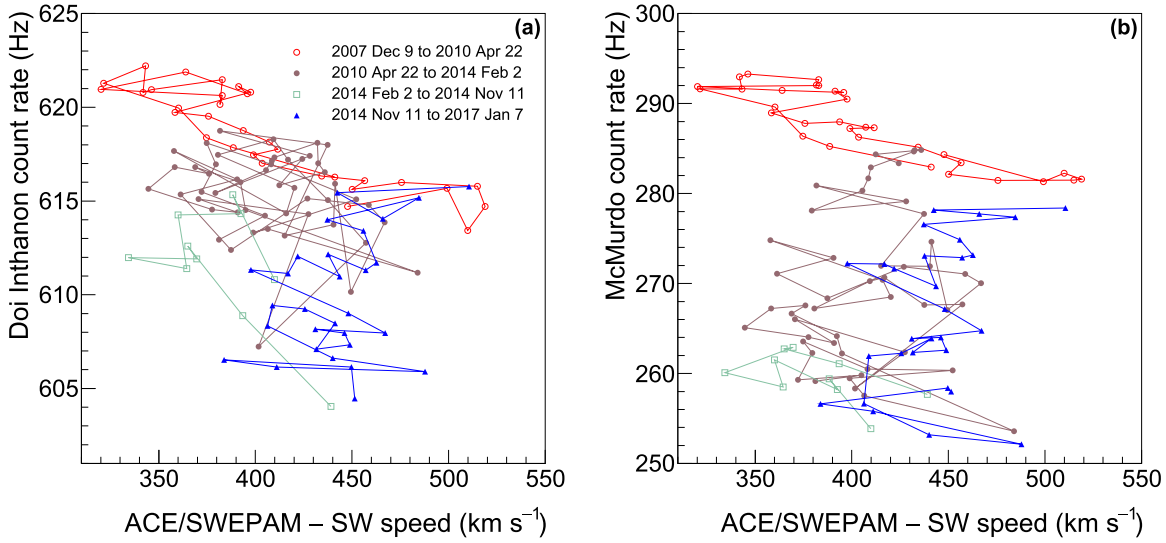


Figure 7. Scatter plots of the CarRot-averaged count rates at (a) Doi Inthanon and (b) McMurdo with the contemporaneous *ACE*/SWEPAM solar wind speed, averaged over CarRots.

as expected from drift models (Jokipii & Thomas 1981; Strauss et al. 2012). Then, at a tilt angle $>50°$ and during the period of solar polarity reversals (black squares), the McMurdo count rate was suddenly lower, and at $>60°$, the count rate is apparently uncorrelated with the measured tilt angle. After the period of polarity reversals, during 2014 February to 2015 January (red triangles), the McMurdo count rate recovered only slightly with decreasing tilt angle, and it recovered much more rapidly in the final time period (blue triangles).

While the pattern for Doi Inthanon was similar at low solar activity, the pattern changed in mid-2010 at the start of the "plateau" count rate, as the tilt angle exceeded 40°. During the third and fourth time periods, there was little or no correlation between the tilt angle and the Doi Inthanon count rate. During the final period, when the tilt angle was below ∼50°, the Doi Inthanon count rate increased rapidly while the tilt angle was decreasing, as seen for McMurdo.

3.3.2. Solar Wind Speed

Next, we consider the solar wind speed, as measured by the Solar Wind Electron, Proton, and Alpha Monitor[13] (SWEPAM) on the *Advanced Composition Explorer* (*ACE*) spacecraft (located at the L1 Lagrange point) as the second heliospheric measurement that we compared to the count rates at Doi Inthanon and McMurdo. The optimal delay is zero, for which the overall correlation factor between the count rates and the solar wind is −0.41 and −0.10 for Doi Inthanon and McMurdo, respectively (see Table 2), indicating a poor correlation over the course of the solar modulation cycle.

Figures 7(a) and (b) present scatter plots between the solar wind speed and the count rates (averaged per CarRot) at Doi Inthanon and McMurdo, respectively, which confirm the poor overall correlation. However, during the initial period of low solar activity and negative solar polarity, there was a strong

[13] See http://www.srl.caltech.edu/ACE/ASC/level2/swepam_l2desc.html.

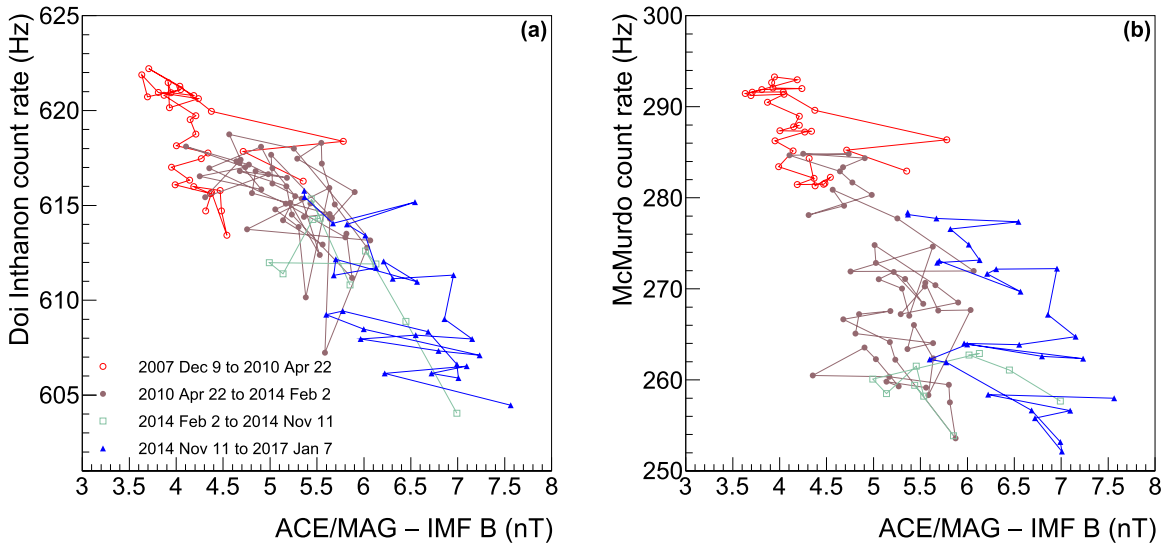


Figure 8. Scatter plots of the CarRot-averaged count rates at (a) Doi Inthanon and (b) McMurdo with the contemporaneous *ACE*/MAG IMF, averaged over CarRots.

anticorrelation for both stations, with a correlation coefficient of −0.88 for both NM stations. During the period of high solar activity, as well as the last period of low solar activity at positive solar magnetic polarity, the correlation with the solar wind speed at Earth was quite weak. This suggests that the underlying physics of the solar modulation during these time periods was not related to the local solar wind speed at Earth.

3.3.3. IMF

Finally, we consider the IMF, here defined as the mean magnitude of the magnetic field as measured by the Magnetic Field Experiment[14] (MAG) on the *ACE* spacecraft, in comparison with NM count rates. The optimal delay time is zero, for which the overall correlation coefficient between the count rates and the solar wind is −0.85 and −0.74 for Doi Inthanon and McMurdo, respectively (see Table 3). Figure 3(f) presents the time series of the IMF during the period of interest of this work. Figures 8(a) and (b) present scatter plots between the IMF and the count rates (averaged per CarRot) at Doi Inthanon and McMurdo, respectively.

The McMurdo NM count rate, at low cutoff rigidity, has a strong overall anticorrelation with the IMF, but each individual time period has a substantially weaker correlation, and during the third time period (2014 February–November) there was virtually no correlation at all. Thus, the IMF serves to roughly indicate times of weak or strong solar modulation (i.e., low or high solar activity) but does not correlate well with the details of solar modulation as observed by a polar NM at low cutoff rigidity.

In contrast, the Doi Inthanon NM count rate, at high cutoff rigidity, has a very strong overall anticorrelation with the IMF that is also quite strong during the third period (2014 February–November). Among the heliospheric parameters we have considered, the IMF clearly has the best predictive power for the Doi Inthanon count rate, approximately following a common linear trend for all time periods of solar modulation. An exception is that during the first period, corresponding to $A < 0$ solar magnetic polarity and low tilt angle, when the tilt angle has a tighter correlation with the Doi Inthanon count rate. During the second period, there was a nearly constant IMF and a corresponding plateau in the Doi Inthanon count rate, both of which were punctuated by short-term (1–2 CarRot) modulation events. Thus, the somewhat lower correlation coefficient during this time period does not indicate that the IMF fails to explain the Doi Inthanon count rate, because the nearly constant IMF is consistent with the 4 yr plateau in the count rate. For this solar modulation cycle, the IMF is clearly a key determinant of the high cutoff count rate.

[14] See http://www.srl.caltech.edu/ACE/ASC/level2/mag_l2desc.html.

4. Discussion

We have examined the first set of continuous NM data of the time-varying cosmic-ray flux at cutoff rigidity >16 GV over a cycle of solar modulation. We compared these data from Doi Inthanon from 2007 December 9 until 2017 January 7 with data over the same time period from McMurdo with an atmospheric cutoff rigidity of ∼1 GV. During times when the HCS tilt angle was $\lesssim$50°, corresponding to periods of lower solar activity, the Doi Inthanon and McMurdo count rates were linearly related (see Figure 4). However, at other times, they exhibited distinct patterns of solar modulation, which we attribute to a difference in the dominant physical mechanism.

For latitude survey data from 1994 to 2007, either before or after survey year 2000 with maximum solar activity, Nuntiyakul et al. (2014) concluded that at a given cutoff rigidity, the mobile monitor count rate as a function of time was linearly correlated with the count rate at McMurdo. The slope of the linear relation was higher during the time period of $A < 0$ solar magnetic polarity. Our present results comparing the fixed NM data from Doi Inthanon and McMurdo are qualitatively consistent with the latitude survey results. (Note that PSNM data can be used to measure the slope of the linear relation much more precisely for continuous measurements with 18 NM counters at high altitude compared with three NM counters on a ship that only occasionally reached that cutoff rigidity.) One difference is that the time period of the present work includes a 4 yr period of high solar activity, from 2010 April to 2014 November, when the Doi Inthanon and McMurdo NM count rates were not well correlated, which roughly corresponds to a period of HCS tilt angle $\gtrsim$50°. In contrast, the time period of those latitude surveys included such

a high tilt angle only during about 1999–2000 (McDonald et al. 2010), which is consistent with their need to exclude only survey year 2000 from their periods with linear relationships between NM count rates. In summary, the present study, as well as those of Nuntiyakul et al. (2014) and Popielawska (1992), paints a consistent picture that NM count rates at different cutoff rigidities are linearly related under conditions of low solar activity, with a slope that depends on the solar magnetic polarity.

Based on our finding of different patterns of solar modulation at low and high cutoff rigidity for over 4 yr at high solar activity and high HCS tilt angle, from 2010 April to 2014 November, it is perhaps unsurprising that a simple force-field model of solar modulation, with a single modulation parameter inferred from low cutoff NM data as commonly used to model solar effects on the GCR spectrum, fails to accurately describe solar modulation above a high cutoff rigidity ($\gtrsim$17 GV). From Figure 5, we see that when using an empirical modulation parameter as a function of time based on data from low cutoff rigidity ($\sim$1 GV), the predicted solar modulation in the NM count rate (relative to the count rate maximum) from a force-field model was typically a factor of two greater than the modulation observed at Doi Inthanon during that 4 yr period. This indicates that a force-field model based on a single modulation parameter can fail to even approximately describe changes in the GCR spectrum during times of high solar activity and high tilt angle. On the other hand, during periods of low tilt angle, this force-field model performs reasonably well in simultaneously matching NM variations at low and high cutoff rigidity (keeping in mind that the traces in Figure 5 are all normalized at the solar minimum conditions of 2009 December), given an empirical modulation parameter based on data from one NM station. Apparently, the assumptions of the force-field model, such as spherical symmetry, a quasi-steady state, and a diffusion coefficient that increases linearly with rigidity, work reasonably well during relatively quiet solar conditions and are able to reproduce observed count-rate variations relative to the relevant solar minimum count rate. Note, however, that the effects of solar magnetic polarity on the GCR ion spectrum (Moraal et al. 1989; Nuntiyakul et al. 2014) are not included in the force-field model.

We have also examined the effects of three heliospheric parameters, the HCS tilt angle, solar wind speed, and IMF, on the Doi Inthanon and McMurdo NM rates. The tilt angle refers to the global tilt of the HCS near the Sun and thus might be expected to be relevant to the heliosphere as a whole. Furthermore, *Ulysses* observations have indicated that the radial magnetic flux $|B_r|r^2$ is independent of location in the inner heliosphere at a given time (Smith & Balogh 1995), so the IMF at any one point (e.g., near Earth) is indicative of the global IMF throughout much of the heliosphere. In contrast, the solar wind speed near Earth, even when averaged over CarRots, is a more local indicator of conditions near the solar equatorial plane. We find a weaker correlation between the local solar wind speed and solar modulation of NM count rates, which is consistent with the common view that solar modulation mainly reflects global conditions in the heliosphere.

Tables 1–3 show the correlation coefficient of each parameter as compared with each NM count rate as measured after a delay time of 0–3 CarRots, and the optimal comparisons are plotted in Figures 6–8. The Doi Inthanon count rate has a strong overall anticorrelation with the magnetic field (with no delay), with an overall linear trend. The IMF is also the parameter that best correlates with the Doi Inthanon count for individual time periods, except during the initial period of low solar activity and $A < 0$ solar magnetic polarity, when the tilt angle (with 2 CarRot delay) provides a better correlation. During the GCR rise with $A > 0$ polarity in the final period (2014 November–2017 January), the correlation coefficients for the IMF and tilt angle are similar, but the slope of the GCR rise with decreasing tilt angle is so strong that the tilt angle has little predictive power during that time period. For the McMurdo count rate, the HCS tilt angle has a strong anticorrelation with the McMurdo count rate (especially after a delay of 2 CarRots) and is clearly better correlated than the other heliospheric parameters. However, the relation is not linear and exhibits hysteresis, as the McMurdo count rate follows a different track as a function of tilt angle after the solar magnetic polarity reversal.

The high NM count rates near solar minimum coincide with a very low value of the tilt angle, $\sim$10°–20°, in agreement with the calculation of Webber et al. (1990). Their model, which includes the effects of guiding center drifts and a wavy neutral sheet, describes a dependence of the solar modulation on the tilt angle during negative ($A < 0$) solar polarity. For this polarity, drift models generally predict that positively charged particles (including GCR ions) enter the inner solar system by drifting along the wavy path following the HCS current sheet (Jokipii & Thomas 1981; Strauss et al. 2012). Thus, a small tilt angle implies a shorter path length and less scattering on the way to Earth, with a lower modulation effect and higher count rate in comparison to that at large tilt angle. Our observations confirm that at low tilt angle and negative solar polarity, the drift of the cosmic-ray particles in the IMF seems to affect NM count rates up to a cutoff rigidity of about 17 GV.

At high tilt angle, the Doi Inthanon count rate is poorly correlated with the tilt angle. On the other hand, there is a strong overall anticorrelation between the magnetic field strength and the Doi Inthanon count rate with a single linear trend for the entire solar modulation cycle. An inverse correlation between the IMF and the count rate of an NM at low cutoff (Mount Wellington) was previously observed and described in Cane et al. (1999). They also reported a loss of correlation in 1969, 1980, and 1990 near the periods of solar polarity reversal. For Doi Inthanon, at high cutoff rigidity, we observe that the IMF still has useful predictive power even near the periods of polarity reversal. In particular, the 4 yr plateau in the Doi Inthanon count rate from mid-2010 to mid-2014 (which is not observed in the McMurdo count rate) corresponded to a period in which the IMF fluctuated over a moderate value of about 4–6 nT with little or no long-term time variation. Then, shortly after the IMF began to increase rapidly in the latter half of 2014, rising from about 5 to 8 nT, the Doi Inthanon count rate underwent a sharp drop over about 2 months (2014 September–October) that accounted for about half of the total solar modulation over this cycle at Doi Inthanon. These results strongly suggest a causal link between changes in the IMF and the NM count rate at high cutoff rigidity, which is not observed at low cutoff.

We propose the following physical explanation of this distinct pattern of solar modulation of GCRs at high cutoff rigidity. Changes in the magnetic field strength over the solar cycle should result in changes in the GCR diffusion coefficient throughout the heliosphere, and GCRs of high rigidity should

have a much higher diffusion coefficient (Chhiber et al. 2017). As noted above, the usual expectation of the effect of guiding center drifts on GCR ions during $A < 0$ solar magnetic polarity is that they should follow a convoluted path as they drift inward along the HCS, with a path length that depends on the tilt angle. Our interpretation of the distinct pattern of solar modulation at Doi Inthanon is that GCRs of high rigidity can have a very large diffusion coefficient and can "short-circuit" the drift process along the wavy current sheet, providing a shorter path length and access to the inner heliosphere that depends mostly on the diffusion coefficient, and hence the IMF. This view is supported by Strauss et al. (2012), in particular the simulation results in their Figure 12, in which a higher diffusion coefficient is seen to short-circuit the very long path along a highly tilted current sheet, implying that modulation is insensitive to the exact value of a large tilt angle, as found in our observations. Then, the result shown in Figure 5, that a force-field model with a modulation parameter derived from low cutoff NM data is unable to explain high cutoff solar modulation near solar maximum, can be attributed to the very different trajectories and physical processes experienced by cosmic rays above a high cutoff rigidity. This different type of heliospheric propagation of GCRs with high rigidity and large diffusion coefficients can give rise to the distinct pattern of solar modulation that we observe at tilt angles $\gtrsim 50^\circ$ above a high cutoff rigidity ($\sim$17 GV).

This work was partially supported by the Thailand Research Fund award RTA5980003 and the US National Science Foundation awards PLR-1245939, PLR-1341562, and their predecessors. We acknowledge the NMDB database, founded under the European Union's FP7 program (contract No. 213007), and the PIs of individual NMs for providing data. We thank David Maurin for useful discussions.

ORCID iDs

Pierre-Simon Mangeard https://orcid.org/0000-0003-4865-6968
Paul Evenson https://orcid.org/0000-0001-7929-810X
David Ruffolo https://orcid.org/0000-0003-3414-9666
Alejandro Sáiz https://orcid.org/0000-0001-7771-4341

References

Abe, K., Fuke, H., Haino, S., et al. 2016, ApJ, 822, 16
Adriani, O., Barbarino, G. C., Bazilevskaya, G. A., et al. 2011, Sci, 332, 69
Adriani, O., Barbarino, G. C., Bazilevskaya, G. A., et al. 2013, ApJ, 765, 91
Adriani, O., Barbarino, G. C., Bazilevskaya, G. A., et al. 2016, PhRvL, 116, 241105
Aguilar, M., Aisa, D., Alpat, B., et al. 2015a, PhRvL, 114, 171103
Aguilar, M., Aisa, D., Alpat, B., et al. 2015b, PhRvL, 115, 211101
Asaoka, Y., Shikaze, Y., Abe, K., et al. 2002, PhRvL, 88, 051101
Bazilevskaya, G. A., Usoskin, I. G., Flückiger, E. O., et al. 2008, SSRv, 137, 149
Bieber, J. W., & Burger, R. A. 1990, ApJ, 348, 597
Bieber, J. W., Clem, J., & Evenson, P. 1997, Proc. ICRC (Durban), 2, 389
Burlaga, L. F., Schwenn, R., & Rosenbauer, H. 1983, GeoRL, 10, 413
Caballero-Lopez, R. A., & Moraal, H. 2004, JGRA, 109, A01101
Caballero-Lopez, R. A., & Moraal, H. 2012, JGRA, 117, A12103
Cane, H. V., Wibberenz, G., Richardson, I. G., & von Rosenvinge, T. T. 1999, GeoRL, 26, 565
Chhiber, R., Subedi, P., Usmanov, A. V., et al. 2017, ApJS, 230, 21
Clem, J., & Evenson, P. 2009, JGRA, 114, A10108
Clem, J. M., Bieber, J. W., Evenson, P., et al. 1997, JGR, 102, 26919
Clem, J. M., Evenson, P., Huber, D., et al. 2000, JGR, 105, 23099
Corti, C., Bindi, V., Consolandi, C., & Whitman, K. 2016, ApJ, 829, 8
Forbush, S. E. 1937, PhRv, 51, 1108
Forbush, S. E. 1954, JGR, 59, 525
Garcia-Munoz, M., Meyer, P., Pyle, K. R., Simpson, J. A., & Evenson, P. 1986, JGR, 91, 2858
Ghelfi, A., Barao, F., Derome, L., & Maurin, D. 2016, A&A, 591, A94
Ghelfi, A., Barao, F., Derome, L., & Maurin, D. 2017a, A&A, 605, C2
Ghelfi, A., Maurin, D., Cheminet, A., et al. 2017b, AdSpR, 60, 833
Gieseler, J., Heber, B., & Herbst, K. 2017, JGRA, 122, 10964
Gleeson, L. J., & Axford, W. I. 1968, ApJ, 154, 1011
Hoeksema, J. T. 1995, SSRv, 72, 137
Jokipii, J. R., Levy, E. H., & Hubbard, W. B. 1977, ApJ, 213, 861
Jokipii, J. R., & Thomas, B. 1981, ApJ, 243, 1115
Levy, E. H. 1976, JGR, 81, 2082
Lin, Z., Bieber, J. W., & Evenson, P. 1995, JGR, 100, 23543
Mangeard, P.-S., Ruffolo, D., Sáiz, A., et al. 2016a, JGRA, 121, 11620
Mangeard, P.-S., Ruffolo, D., Sáiz, A., Madlee, S., & Nutaro, T. 2016b, JGRA, 121, 7435
McDonald, F. B., Webber, W. R., & Reames, D. V. 2010, GeoRL, 37, L18101
Mewaldt, R. A., Davis, A. J., Lave, K. A., et al. 2010, ApJL, 723, L1
Mishev, A. L., Usoskin, I. G., & Kovaltsov, G. A. 2013, JGRA, 118, 2783
Mitthumsiri, W., Seripienlert, A., Tortermpun, U., et al. 2017, JGRA, 122, 7946
Moraal, H., Potgieter, M. S., Stoker, P. H., & van der Walt, A. J. 1989, JGR, 94, 1459
Nuntiyakul, W., Evenson, P., Ruffolo, D., et al. 2014, ApJ, 795, 11
Oh, S., Bieber, J. W., Evenson, P., et al. 2013, JGRA, 118, 5431
Popielawska, B. 1992, P&SS, 40, 811
Popielawska, B. 1995, JGR, 100, 5883
Popielawska, B., & Simpson, J. A. 1991, Proc. ICRC (Dublin), 3, 660
Ruffolo, D., Sáiz, A., Mangeard, P.-S., et al. 2016, ApJ, 817, 38
Simpson, J. A. 2000, SSRv, 93, 11
Smith, E. J., & Balogh, A. 1995, GeoRL, 22, 3317
Strauss, R. D., Potgeiter, M. S., Büsching, I., & Kopp, A. 2012, ApSS, 339, 223
Usoskin, I. G., Gil, A., Kovaltsov, G. A., Mishev, A. L., & Mikhailov, V. V. 2017, JGRA, 122, 3875
Webber, W. R., Potgieter, M. S., & Burger, R. A. 1990, ApJ, 349, 634

ResearchGate

See discussions, stats, and author profiles for this publication at: https://www.researchgate.net/publication/326283318

Galactic Cosmic-Ray Anisotropy in the Northern Hemisphere from the ARGO-YBJ Experiment during 2008–2012

Article *in* The Astrophysical Journal · July 2018

DOI: 10.3847/1538-4357/aac6cc

CITATIONS
0

READS
2

72 authors, including:



Bruno Bartoli
University of Naples Federico II
135 PUBLICATIONS **1,779** CITATIONS
SEE PROFILE



Paolo Bernardini
Università del Salento
299 PUBLICATIONS **5,955** CITATIONS
SEE PROFILE



Xiao-Hui Bi
Nankai University
160 PUBLICATIONS **1,899** CITATIONS
SEE PROFILE



Zheng Cao
Vanderbilt University
233 PUBLICATIONS **3,811** CITATIONS
SEE PROFILE

Some of the authors of this publication are also working on these related projects:

ARGO-YBJ View project

Lithium-sulfur batteries View project

All content following this page was uploaded by Huihai He on 13 July 2018.

The user has requested enhancement of the downloaded file.

The Astrophysical Journal, 861:93 (7pp), 2018 July 10 https://doi.org/10.3847/1538-4357/aac6cc
© 2018. The American Astronomical Society. All rights reserved.

Galactic Cosmic-Ray Anisotropy in the Northern Hemisphere from the ARGO-YBJ Experiment during 2008–2012

B. Bartoli[1,2], P. Bernardini[3,4], X. J. Bi[5,6], Z. Cao[5,6], S. Catalanotti[1,2], S. Z. Chen[5], T. L. Chen[7], S. W. Cui[8], B. Z. Dai[9], A. D'Amone[3,4], Danzengluobu[7], I. De Mitri[4,23], B. D'Ettorre Piazzoli[1,10], T. Di Girolamo[1,2], G. Di Sciascio[10], C. F. Feng[11], Z. Y. Feng[12], W. Gao[5,6], Q. B. Gou[5], Y. Q. Guo[5], H. H. He[5,6], Haibing Hu[7], Hongbo Hu[5], M. Iacovacci[1,2], R. Iuppa[13,14], H. Y. Jia[11], Labaciren[7], H. J. Li[7], C. Liu[5], J. Liu[9], M. Y. Liu[7], H. Lu[5], L. L. Ma[5], X. H. Ma[5], G. Mancarella[3,4], S. M. Mari[15,16], G. Marsella[3,4], S. Mastroianni[2], P. Montini[17], C. C. Ning[7], L. Perrone[3,4], P. Pistilli[15,16], D. Ruffolo[24], P. Salvini[18], R. Santonico[9,19], P. R. Shen[5], X. D. Sheng[5], F. Shi[5], A. Surdo[4], Y. H. Tan[5], P. Vallania[20,21], S. Vernetto[20,21], C. Vigorito[21,22], H. Wang[5], C. Y. Wu[5], H. R. Wu[5], L. Xue[11], Q. Y. Yang[9], X. C. Yang[9], Z. G. Yao[5], A. F. Yuan[7], M. Zha[5], H. M. Zhang[5], L. Zhang[9], X. Y. Zhang[11], Y. Zhang[5], J. Zhao[5], Zhaxiciren[7], Zhaxisangzhu[7], X. X. Zhou[12], F. R. Zhu[12], and Q. Q. Zhu[5]
(The ARGO-YBJ Collaboration)

[1] Dipartimento di Fisica dell'Universitá di Napoli "Federico II," Complesso Universitario di Monte Sant'Angelo, via Cinthia, I-80126 Napoli, Italy
[2] Istituto Nazionale di Fisica Nucleare, Sezione di Napoli, Complesso Universitario di Monte Sant'Angelo, via Cinthia, I-80126 Napoli, Italy
[3] Dipartimento Matematica e Fisica "Ennio De Giorgi," Universitá del Salento, via per Arnesano, I-73100 Lecce, Italy
[4] Istituto Nazionale di Fisica Nucleare, Sezione di Lecce, via per Arnesano, I-73100 Lecce, Italy
[5] Key Laboratory of Particle Astrophysics, Institute of High Energy Physics, Chinese Academy of Sciences, P.O. Box 918, 100049 Beijing, People's Republic of China; chensz@ihep.ac.cn, gaowei@ihep.ac.cn, hhh@ihep.ac.cn
[6] School of Physical Sciences, University of Chinese Academy of Sciences, 100049 Beijing, People's Republic of China
[7] Tibet University, 850000 Lhasa, Xizang, People's Republic of China
[8] Hebei Normal University, 050024 Shijiazhuang Hebei, People's Republic of China
[9] Yunnan University, 2 North Cuihu Road, 650091 Kunming, Yunnan, People's Republic of China
[10] Istituto Nazionale di Fisica Nucleare, Sezione di Roma Tor Vergata, via della Ricerca Scientifica 1, I-00133 Roma, Italy
[11] Shandong University, 250100 Jinan, Shandong, People's Republic of China
[12] Southwest Jiaotong University, 610031 Chengdu, Sichuan, People's Republic of China
[13] Dipartimento di Fisica dell'Universitá di Trento, via Sommarive 14, I-38123 Povo, Italy
[14] Trento Institute for Fundamental Physics and Applications, via Sommarive 14, I-38123 Povo, Italy
[15] Dipartimento di Fisica dell'Universitá "Roma Tre," via della Vasca Navale 84, I-00146 Roma, Italy
[16] Istituto Nazionale di Fisica Nucleare, Sezione di Roma Tre, via della Vasca Navale 84, I-00146 Roma, Italy
[17] Dipartimento di Fisica dell'Universitá di Roma "La Sapienza" and INFN Sezione di Roma, piazzale Aldo Moro 2, I-00185 Roma, Italy
[18] Istituto Nazionale di Fisica Nucleare, Sezione di Pavia, via Bassi 6, I-27100 Pavia, Italy
[19] Dipartimento di Fisica dell'Universit'á di Roma "Tor Vergata," via della Ricerca Scientifica 1, I-00133 Roma, Italy
[20] Osservatorio Astrofisico di Torino dell'Istituto Nazionale di Astrofisica, via P. Giuria 1, I-10125 Torino, Italy
[21] Istituto Nazionale di Fisica Nucleare, Sezione di Torino, via P. Giuria 1, I-10125 Torino, Italy
[22] Dipartimento di Fisica dell'Universitá di Torino, via P. Giuria 1, I-10125 Torino, Italy
[23] Gran Sasso Science Institute (GSSI), Via M. Iacobucci 2, I-67100 L'Aquila, Italy
[24] Department of Physics, Faculty of Science, Mahidol University, Bangkok 10400, Thailand
Received 2018 April 13; revised 2018 May 11; accepted 2018 May 17; published 2018 July 9

Abstract

This paper reports on the observation of the sidereal large-scale anisotropy of cosmic rays using data collected by the ARGO-YBJ experiment over 5 years (2008–2012). This analysis extends previous work limited to the period from 2008 January to 2009 December, near the minimum of solar activity between cycles 23 and 24. With the new data sample, the period of solar cycle 24 from near minimum to maximum is investigated. A new method is used to improve the energy reconstruction, allowing us to cover a much wider energy range, from 4 to 520 TeV. Below 100 TeV, the anisotropy is dominated by two wide regions, the so-called "tail-in" and "loss-cone" features. At higher energies, a dramatic change of the morphology is confirmed. The yearly time dependence of the anisotropy is investigated. Finally, no noticeable variation of cosmic-ray anisotropy with solar activity is observed for a median energy of 7 TeV.

Key words: astroparticle physics – cosmic rays

1. Introduction

In the past decades, the sidereal directional variation of the Galactic cosmic-ray intensity, which we refer to as the anisotropy, was observed by many detectors across a wide energy range from 60 GeV to 8 EeV. The morphology of anisotropy and the corresponding amplitude are energy dependent. The anisotropy implies important information about the magnetic structure of the heliosphere, the local interstellar space surrounding the heliosphere, and large portions of the Galaxy through which cosmic rays propagate to the Earth. The study of anisotropy can shed new light on the origin and propagation of cosmic rays.

Below 100 TeV, two large-scale features recognized as "tail-in" and "loss-cone" features in two-dimensional (2D) maps are observed with very high significance both in the northern hemisphere (Amenomori et al. 2006; Bartoli et al. 2015a) and in the southern hemisphere (Aartsen et al. 2016). According to the ARGO-YBJ observations at energies from 1 to 30 TeV, the amplitude of anisotropy increases with energy, reaching a maximum at around 10 TeV, while the angular phase is approximately stable (Bartoli et al. 2015a). Different models

have been proposed to explain the origin of the anisotropy, concerning different aspects of cosmic-ray physics, from the sources of cosmic rays to the propagation to the Earth. Some models consider the anisotropy due to the spatial distribution of cosmic-ray sources, as the presence of a nearby strong source (Erlykin & Wolfendale 2006; Liu et al. 2017). Other interpretations concern the structure of the Galactic (Qu et al. 2012), local interstellar (Schwadron et al. 2014), and interplanetary magnetic fields (Nagashima et al. 1998). Besides the large-scale anisotropy (LSA), some works focusing on medium scale anisotropy were also reported by Milagro (Abdo et al. 2008) and ARGO-YBJ (Bartoli et al. 2013b).

No variations with time are expected if the LSA is produced by a nearby source or due to the interstellar magnetic field, while a significant heliospheric influence would show time variation in association with the 11 year solar cycle. Several long term experiments allow time-dependent studies of the LSA; however, contradictory results were obtained. In the northern hemisphere, Milagro reported a steady increase in the amplitude of the "loss-cone" at 6 TeV over a 7 year time period (2000–2007) as the solar activity varied from near maximum to minimum (Abdo et al. 2009). If this observation is true, it will be a challenge to find a consistent explanation of the observed anisotropy and the corresponding time evolution. However, no significant time variations were observed by Tibet ASγ at 4.4, 6.2, and 11 TeV over a period that overlapped with the Milagro observation time, from 1999 to 2008 (Amenomori et al. 2012). In the southern hemisphere, no time dependence was observed by IceCube at energies above 13 TeV over a 6 year time period (2009–2015) as the solar activity varied from near minimum to maximum (Aartsen et al. 2016).

As the energy increases above 100 TeV, a major change in the morphology of the anisotropy is observed by several experiments. For such high energy cosmic rays, the influence of the magnetic field within the heliosphere on the cosmic-ray anisotropy is expected to be negligible. Therefore, the morphology should be time independent. The EAS-TOP collaboration reported a detection of a new anisotropy pattern at 370 TeV with a limited significance (Aglietta et al. 2009) for the first time. Around 400 TeV, IceCube found that the structure of the anisotropy is mostly characterized by a wide relative deficit at a R.A. of 30°–120° (Abbasi et al. 2012). With the accumulation of 6 years of data, the IceCube collaboration found that the change in the morphology starts from about 100 TeV and the amplitude of the deficit increases with energy up to at least 5 PeV (Aartsen et al. 2016). Recently, the Tibet ASγ collaboration improved their analysis with detecting LSA at 300 TeV, which is in close agreement with IceCube's results (Amenomori et al. 2017). The study of LSA at energies above 100 TeV is helpful to understand the origin and propagation of Galactic cosmic rays. The observed phase of the excess region includes the direction of the Galactic center (Aartsen et al. 2016; Amenomori et al. 2017), perhaps indicating the dominant source(s) of the cosmic rays (Guo et al. 2013a, 2013b). It is worth noting that the Auger collaboration have observed LSA at an energy above 8 EeV (Aab et al. 2017). The morphology is different from that at 100 TeV–5 PeV. The direction of the anisotropy indicates an extragalactic origin for these ultrahigh energy particles.

Based on the first 2 years of data (2008 and 2009), the ARGO-YBJ collaboration reported an energy dependence of the LSA at energies from 1 to 30 TeV (Bartoli et al. 2015a). In this paper, we present a new analysis with 5 years of data of the ARGO-YBJ experiment collected from 2008 to 2012. During this period, the solar activity varied from near minimum to maximum. Therefore, the time dependence of the anisotropy is analyzed to address the contradiction between Milagro and Tibet ASγ data. Here, we also adopt an improved energy estimation to extend the maximum energy to above 100 TeV, for which few results have been reported.

2. Data and Analysis Methods

2.1. The ARGO-YBJ Experiment and Data

The ARGO-YBJ experiment, located at the Yangbajing Cosmic Ray Laboratory (Tibet, China, 30.11 N, 90.53 E, altitude of 4300 m a.s.l.), is mainly devoted to γ-ray astronomy (Bartoli et al. 2013a, 2014, 2016) and cosmic-ray physics (Bartoli et al. 2012, 2015b). The detector consists of a carpet ($\sim 74 \times 78\ m^2$) of resistive plate chambers (RPCs) with ~93% of active area, surrounded by a partially instrumented area (~20%) up to $\sim 100 \times 110\ m^2$. Each RPC is read out via 80 strips (6.75 cm × 61.8 cm), logically organized in 10 pads (55.6 cm × 61.8 cm). The pad is the basic unit for timing and trigger purposes. Each pad can count the number of particles, up to 8. More details of the detector and its performance can be found in Aielli et al. (2006, 2009). The ARGO-YBJ experiment in its final configuration started taking data in 2007 November and stopped in 2013 January. The ARGO-YBJ detector is operated by requiring the coincidence of at least 20 fired pads within 420 ns on the central carpet detector. The trigger rate is 3.5 kHz with a dead time of 4%. Through the whole operation period, the average duty-cycle is higher than 86%. The data collected from 2008 January to 2012 December are used in this analysis.

According to the data selection used in the analysis carried out in Bartoli et al. (2015a), only the data collected in days with average temperature inside the ARGO Hall $\langle T_{\rm in} \rangle > 10^{\circ}$ C are used. This selection removed 35, 78, 130, and 87 days of data during the years 2008, 2010, 2011, and 2012, respectively.

2.2. Energy Reconstruction and Data Selection

The cosmic-ray energy has been estimated by a Monte Carlo simulation. Five groups of dominant component elements, H, He, CNO, Mg–Si, and Fe, are generated according to Gaisser et al. (2013). The interaction of cosmic rays in the atmosphere is simulated by CORSIKA code v.7.4005 (Heck et al. 1998), with the hadronic interaction model GHEISHA at lower energy and QGSJET-II at higher energy. About 4×10^{10} events are sampled with zenith angle distributed from 0° to 60° and energy distributed from 10 GeV to 10 PeV. The detector response is simulated with the G4argo code (Guo et al. 2010) based on GEANT-4.

Generally, the primary energy of an event is positively correlated with the number of fired detectors. The number of fired pads was solely adopted to infer the primary energy in our previous analysis (Bartoli et al. 2013b, 2015a). In fact, for events with the same number of fired strips (or pads), the true primary energy $E_{\rm true}$ is also related to the incident zenith angle. In this analysis, the primary energy is first reconstructed based on the number of fired strips $N_{\rm str}$. The left panel of Figure 1 shows the average relation between $N_{\rm str}$ and $E_{\rm true}$. The

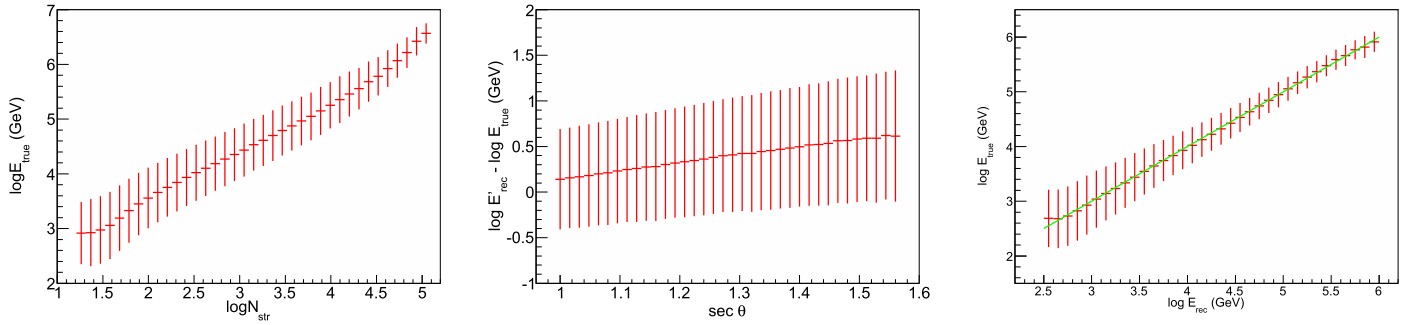


Figure 1. Energy reconstruction of the ARGO-YBJ events. Left: the primary energy of the cosmic ray ($E_{\rm true}$) as a function of the number of fired strips $N_{\rm str}$. Middle: the difference between $E'_{\rm rec}$ and $E_{\rm true}$ as a function of the secant of the zenith angle θ. Right: the relation between the reconstructed energy and primary energy. The green line indicates a linear function $y = a + bx$. The error bars along the x-axis indicate the width of each bin and those along the y-axis indicate the rms of the parameter distribution.

reconstructed energy at this step is denoted as $E'_{\rm rec}$. Second, the reconstructed energy is further corrected based on the zenith angle. The middle panel of Figure 1 shows the difference between $E'_{\rm rec}$ and $E_{\rm true}$ as a function of zenith angle. The final reconstructed energy is denoted as $E_{\rm rec}$. The right panel of Figure 1 shows the relation between $E_{\rm true}$ and $E_{\rm rec}$, which is a good linear relation.

For the analysis presented in this paper, events are selected according to the following cuts: (1) more than 20 fired strips in the central carpet ($N_{\rm str} \geqslant 20$), (2) zenith angle less than 50°, (3) core location less than 100 m from the carpet center, and (4) reconstructed energy $E_{\rm rec} \geqslant 10^{3.5}$ GeV. Finally, about 3.03×10^{10} events survived. The median energy is about 7 TeV.

2.3. Analysis Methods

The same analysis methods as those used in Bartoli et al. (2015a) are adopted in this work. The background map is estimated via the equi-zenith angle method based on an iterative procedure. More details about this approach can be found elsewhere (Amenomori et al. 2005a; Li et al. 2012). This method can reduce the influence of instrumental and environmental variations. With this approach, the 2D LSA anisotropy can be determined. The 2D sky in celestial coordinates is divided into a grid of $2^\circ \times 2^\circ$ pixels. The relative intensity in the (i, j)th pixel is defined as

$$I_{i,j} = \frac{N_{i,j}}{B_{i,j}}, \quad (1)$$

where $N_{i,j}$ is the number of detected events, and $B_{i,j}$ is the estimate of isotropic background events. Due to the Earth's rotation, a ground-based array such as ARGO-YBJ is sensitive to the anisotropy in R.A. The exposure at different decl. bands has been estimated with good precision enough to measure the cosmic-ray energy spectrum. However, a better accuracy is likely needed to measure a dipolar signal along the decl. Thus this analysis is sensitive to anisotropy in R.A. and the changes in relative intensity across decl. belts.

To estimate the amplitude and phase of the anisotropy, a one-dimensional (1D) anisotropy is calculated as the profile of relative intensity in R.A. The 1D profile of the anisotropy is fitted by a first-order harmonic function in the form of:

$$I = 1 + A\cos(\alpha - \phi), \quad (2)$$

where A is the amplitude of the anisotropy and ϕ is the corresponding phase.

3. Results

3.1. Time Dependence of the Sidereal Anisotropy

Figure 2 shows the yearly relative intensity of the LSA from 2008 to 2012. The 2D maps are smoothed with an angular radius of 15°. The median energy is about 7 TeV. The "tail-in" and "loss-cone" structures are distinct in the map and almost stable in these years. To check the yearly variation of the anisotropy, the penultimate panel of Figure 2 shows 1D profiles of the sidereal anisotropy for the five years. The bin size for the 1D profile is 20° in the direction of R.A. No substantial or significant variation of the LSA is detected over five years for our total sample with a median energy of 7 TeV. The anti-sidereal anisotropy, shown in the bottom panel of Figure 2, should not have a physical origin but rather could arise due to an interaction between a solar diurnal anisotropy and an annual variation. Such an interaction could also contaminate the sidereal anisotropy. The bottom panel shows a very weak anti-sidereal anisotropy, which therefore implies very little contamination of the sidereal anisotropy by such an interaction.

The Milagro collaboration reported a steady increase in the amplitude of the "loss-cone" at 6 TeV from 2000 July to 2007 July, corresponding to the period from maximum to near minimum of solar cycle 23 (Abdo et al. 2009). However, the Tibet ASγ collaboration reported a stable anisotropy from 1999 November to 2008 December (Amenomori et al. 2012). Located at the northern hemisphere, ARGO-YBJ covers about the same sky region as Milagro and Tibet ASγ. The energy range of this ARGO-YBJ sample is also very similar to those of Milagro and Tibet ASγ. The operation period from 2008 to 2012 covers the period of solar cycle from minimum to near maximum. Therefore, ARGO-YBJ is a very suitable detector to address the conflict between those Milagro and Tibet ASγ results.

Table 1 shows the "loss-cone" amplitude observed by ARGO-YBJ along with the statistical and systematic errors. The "loss-cone" amplitude is defined as the difference between the relative intensity at the minimum of a best-fit second-order harmonic function and unity. The statistical error is calculated simply by propagating the statistical errors of the parameters in the fit function. The systematic errors are estimated by the fitted amplitude in anti-sidereal time (the last panel of Figure 2).

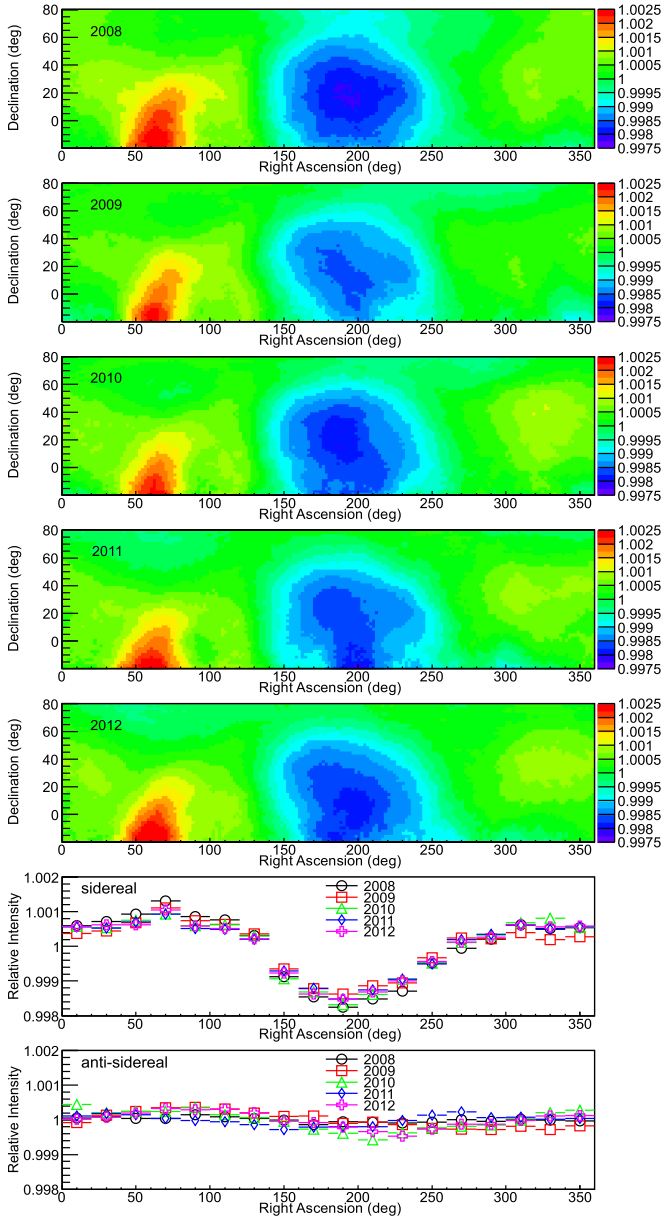


Figure 2. Relative intensity of LSA from 2008 to 2012, including all energies. The maps are smoothed with 15° angular radius. The bottom two panels show the 1D profile of sidereal and anti-sidereal anisotropy, respectively, from 2008 to 2012.

Table 1
Yearly Loss-cone Amplitude along with Statistical and Systematic Errors for Our Total Sample with a Median Energy of 7 TeV

Year	Loss-cone Amplitude (%)	Stat. Error (%)	Syst. Error (%)
2008	0.172	0.00175	0.0076
2009	0.137	0.00168	0.0300
2010	0.158	0.00192	0.0376
2011	0.142	0.00208	0.0160
2012	0.149	0.00194	0.0279

Figure 3 shows the yearly "loss-cone" amplitude observed by ARGO-YBJ during the five years. The error bars represent the sum of statistical and systematic errors. The "loss-cone" amplitude is constant within errors. No significant time dependence is observed by ARGO-YBJ during the five years

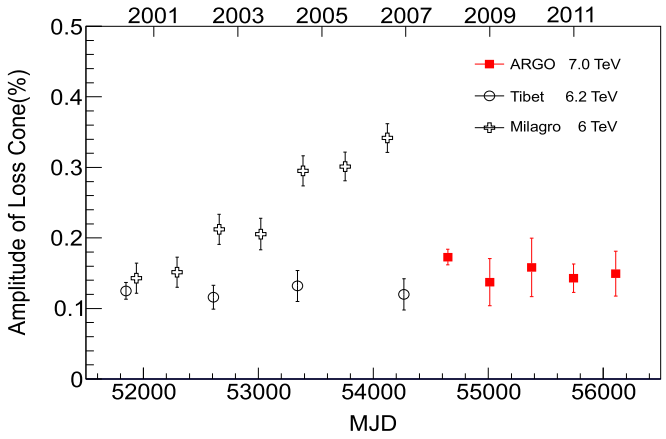


Figure 3. Temporal variation of "loss-cone" amplitude of ARGO-YBJ data from 2008 January to 2012 December. The error bars represent the sum of systematic and statistical errors. The results of Milagro (Abdo et al. 2009) and Tibet ASγ (Amenomori et al. 2012) are also presented here for comparison.

Table 2
Energy Bin, Median Energy, Number of Events, and Amplitude and Phase of the LSA Dipole Component

$\log E_{\rm rec}$ (GeV)	E_m (TeV)	N ($\times 10^8$)	A ($\times 10^{-4}$)	ϕ (deg)
3.50–3.75	4.0	145.0	9.54 ± 0.12	24.7 ± 0.7
3.75–4.00	7.1	77.4	11.92 ± 0.16	29.9 ± 0.8
4.00–4.25	12	41.7	11.71 ± 0.22	24.0 ± 1.1
4.25–4.50	22	21.4	11.17 ± 0.31	22.3 ± 1.6
4.50–4.75	39	10.1	8.19 ± 0.45	358.9 ± 3.1
4.75–5.00	71	4.4	4.23 ± 0.67	347.0 ± 9.1
5.00–5.50	160	2.6	7.81 ± 0.88	251.1 ± 6.5
$\geqslant$5.50	520	0.4	9.10 ± 2.29	279.2 ± 14.5

from 2008 to 2012. For comparison, the results of Milagro and Tibet ASγ are also shown in Figure 3. Obviously, the ARGO-YBJ result is mostly consistent with the same constant value as the Tibet ASγ experiment.

3.2. Energy Dependence of the Sidereal Anisotropy

To study the energy dependence of the LSA, events are divided into eight samples according to the reconstructed energy $E_{\rm rec}$ as listed in Table 2. The median energies (E_m) of the primary true energies for the eight intervals are 4.0, 7.1, 12, 22, 39, 71, 160, and 520 TeV, respectively. It is important to emphasize that the maximum energy, 520 TeV, is much higher than that in our previous analysis, 30 TeV. The energy range presented in this work partly overlaps with that of IceCube (Aartsen et al. 2016) and Tibet ASγ (Amenomori et al. 2017). The number of events (N) in each interval is also listed in Table 2. It is about 1.5×10^{10} in the first energy interval and gradually decreases to be 4×10^7 in the last interval.

Figure 4 shows the 2D map of the relative intensity of the LSA for each energy interval. The maps are smoothed with an angular radius of 30°. The "tail-in" and "loss-cone" features are significant at energies from 4 to 22 TeV. At energies from 39 to 71 TeV, the "tail-in" and "loss-cone" features gradually fade away. At the same time, a new excess feature around the R.A. of 250°–300° gradually appears, replacing the structure of the "loss-cone." At energies above 160 TeV, the "tail-in" and "loss-cone" features completely disappear, and the map is dominated by a new pattern with an excess around the R.A. of 200°–310° and a deficit around 0°–100°. These characteristics

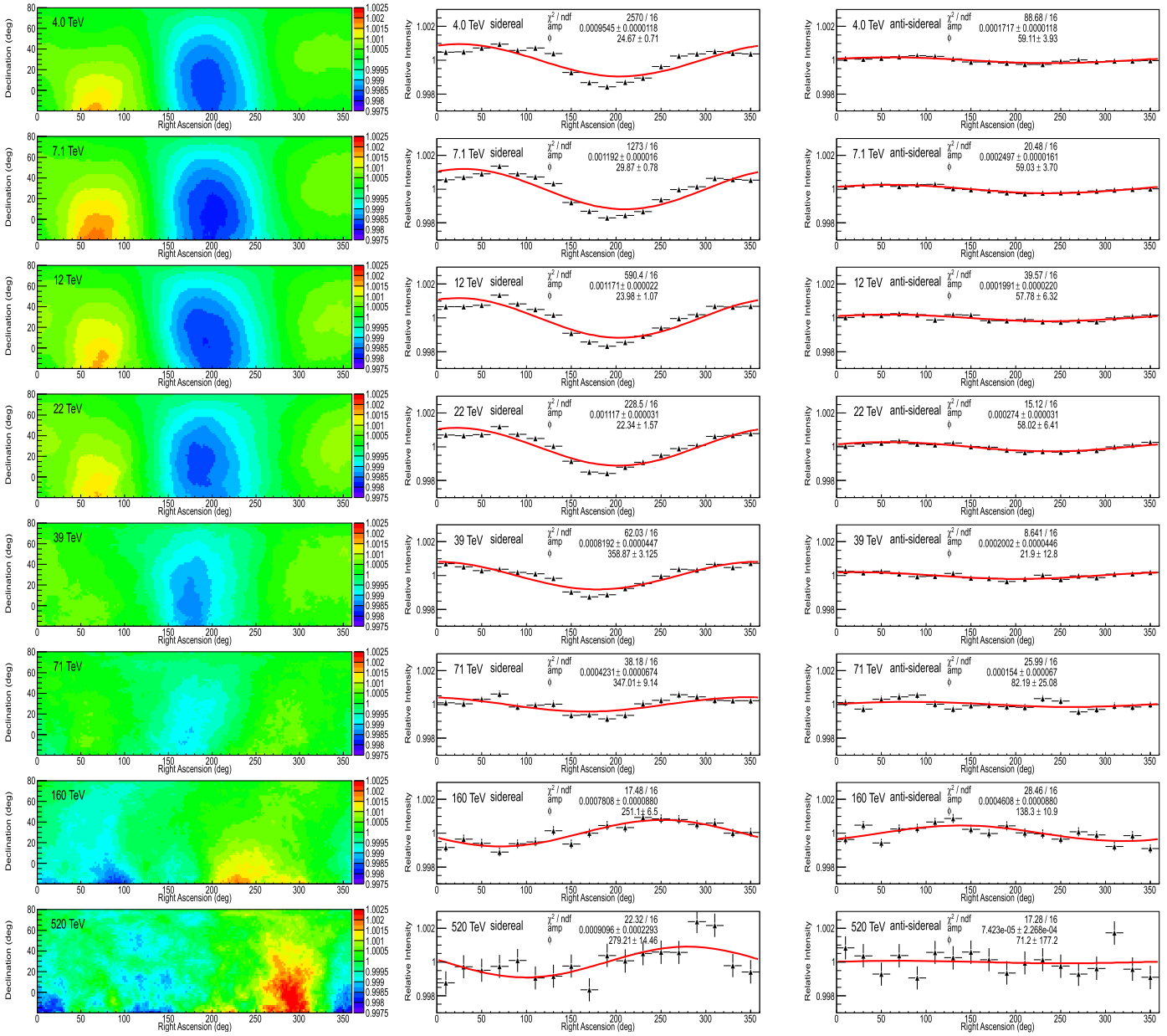


Figure 4. The 2D maps of relative intensity of LSA (left panels) and 1D projections on R.A. (middle panels) for eight energy bins (top to bottom: median energy at 4.0, 7.1, 12, 22, 39, 71, 160, and 520 TeV). Each 2D plot is smoothed with a 30° angular radius. The median energy of each data sample is labeled at the left. The right panels show the 1D profiles of the anti-sidereal results.

are consistent with those observed by the Tibet experiment (Amenomori et al. 2017) in the Northern Hemisphere.

To quantitatively estimate the evolution of the LSA, Equation (2) presented in Section 2.3 is used to fit the 1D profiles shown in Figure 4 (middle panels). The chi-square values indicate that, mainly at low energies, the cosmic-ray anisotropy is not well described by a pure dipole, but a simple dipole fit is commonly used to estimate its amplitude and phase. The fitted parameters, i.e., the amplitudes and phases, as a function of energy are shown in Figure 5 and also listed in Table 2. The error bars of the amplitude contain the statistical errors and the systematic errors exhibited by the anti-sidereal 1D profiles of Figure 4 (right panels). As shown, the amplitudes are energy dependent with a maximum around 7 TeV, above which the amplitude begins to decrease with the phase gradually shifting. At energies above 100 TeV, a sudden change of the phase is observed and the amplitude also begins to increase. According to the fitting parameters shown in Figure 4, the significance of non-zero amplitude is 8.8σ and 4.0σ at energies of 160 TeV and 520 TeV, respectively, implying that the obtained LSA features are significant. The phases at 160 TeV and 520 TeV are $\alpha = 251.^{\circ}1 \pm 6.^{\circ}5$ and $\alpha = 279.^{\circ}2 \pm 14.^{\circ}5$, respectively, which are consistent with Tibet ASγ (Amenomori et al. 2017) and IceCube (Aartsen et al. 2016). The direction of the new excess is very close to the direction of the Galactic center ($268.^{\circ}4$ R.A.), hinting that this region is the dominant origin of the cosmic rays. For comparison, the results reported by other detectors are also shown in Figure 5. The results obtained in this work generally agree with others.

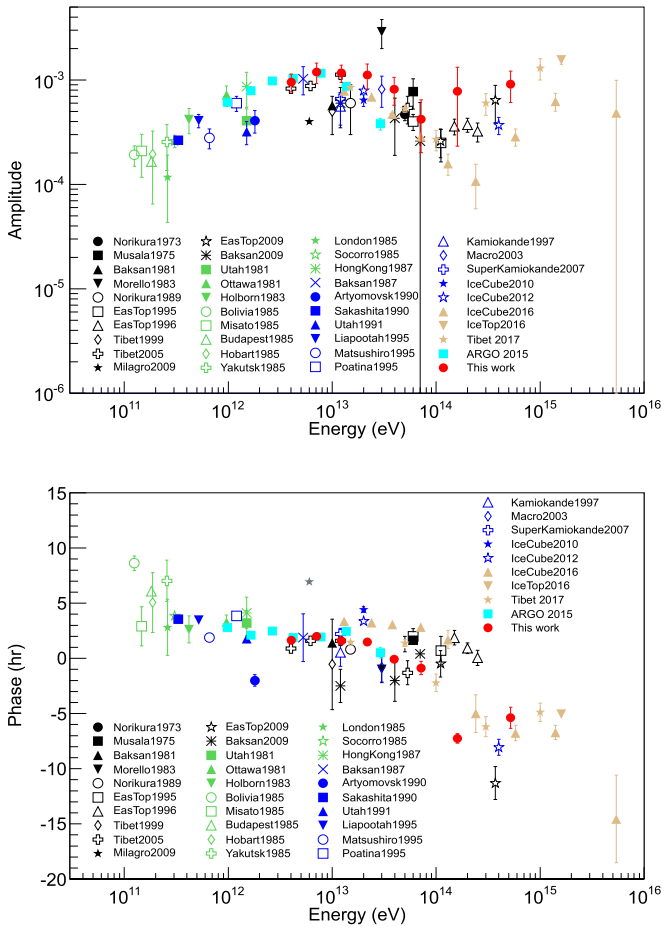


Figure 5. The amplitude (top panel) and phase (bottom panel) of the first harmonic of the sidereal anisotropy as a function of the cosmic-ray energy measured by ARGO-YBJ and other experiments (for details and references see Sakakibara et al. 1973; Gombosi et al. 1975; Alexeenko et al. 1981; Cutler et al. 1981; Lagage & Cesarsky 1983; Morello et al. 1983; Thambyahpillai 1983; Nagashima et al. 1985; Swinson & Nagashima 1985; Andreyev et al. 1987; Lee & Ng 1987; Nagashima et al. 1989; Kuznetsov 1990; Ueno et al. 1990; Cutler & Groom 1991; Aglietta et al. 1995, 1996; Fenton et al. 1995; Mori et al. 1995; Munakata et al. 1997, 1999; Ambrosio et al. 2003; Amenomori et al. 2005b, 2017; Guillian et al. 2007; Abdo et al. 2008, 2009; Aglietta et al. 2009; Alekseenko et al. 2009; Abbasi et al. 2010, 2012; Bartoli et al. 2015a; Aartsen et al. 2016).

3.3. The Anti-sidereal Anisotropy

Imitating the sidereal and solar time frames, a spurious time frame with 364.242 cycles a year is defined as the anti-sidereal time frame (Farley & Storey 1954). It is expected to have no physical signal. Therefore, the anti-sidereal anisotropy is usually used to estimate the systematic error of the sidereal anisotropy. In this work, we also analyze the anti-sidereal anisotropy using the same data used for Sections 3.1 and 3.2. The 1D profiles of the anti-sidereal anisotropy are shown in Figures 2 and 4, respectively, which are used to indicate the systematic error in this work. The maximum systematic error for the yearly sidereal anisotropy shown in Figure 2 is about 0.03%, which is much smaller than the LSA amplitude in sidereal time. The systematic errors from 4.0 to 71 TeV as well as at 520 TeV are also much smaller than the LSA amplitude in sidereal time. At 160 TeV, the systematic error, about 0.04%, seems larger than at other energies, while it is still smaller than the observed sidereal anisotropy. The observed results for the anti-sidereal frequency support the reliability of the observed sidereal anisotropy presented in this work.

4. Discussion and Summary

In this analysis, only events with reconstructed energy above 3 TeV are used. During five years, no significant time dependence of the anisotropy is detected. However, this result does not exclude the possibility of time-dependent variation of the anisotropy at lower energy. According to the estimation of Zhang et al. (2014), the magnetic field within the heliosphere has minor influence on anisotropy above 4 TeV, and the influence will be visible at energies below 1 TeV. According to Figure 1, ARGO-YBJ can also reach the sub-TeV energy band. A study of the behavior of the anisotropy at energies below 3 TeV is deferred to a future publication.

This paper reports on the measurement of the large-scale cosmic-ray anisotropy by the ARGO-YBJ experiment with data collected from 2008 January to 2012 December. This analysis extends a previous report limited to the period from 2008 January to 2009 December, near the minimum of solar activity between cycles 23 and 24. In contrast with a previous report by the Milagro experiment, no significant time dependence of the anisotropy is detected for a median energy of 7 TeV during 5 years, when the solar activity changed from near minimum to maximum of solar cycle 24. With an improved energy reconstruction procedure, we extended the energy range investigated by ARGO-YBJ up to 520 TeV. A dramatic change of the morphology, consistent with the observations reported by IceCube in the southern hemisphere and Tibet ASγ in the northern hemisphere, is clearly observed starting from about 50 TeV. The dipole at 160 TeV and 520 TeV is aligned (at $\alpha = 251.^{\circ}1 \pm 6.^{\circ}5$ and $\alpha = 279.^{\circ}2 \pm 14.^{\circ}5$, respectively) near the direction of the Galactic center (268.°4 R.A.), suggesting this region as a possible source of cosmic rays.

This work is supported in China by the National Natural Science Foundation of China (NSFC) under the grant Nos. 11575203, 11375052, 11635011, and 11761141001, the Chinese Ministry of Science and Technology, the Chinese Academy of Sciences (CAS), the Key Laboratory of Particle Astrophysics, Institute of High Energy Physics (IHEP), in Italy by the Istituto Nazionale di Fisica Nucleare (INFN), and in Thailand by grant RTA5980003 from the Thailand Research Fund. We also acknowledge essential support from W. Y. Chen, G. Yang, X. F. Yuan, C. Y. Zhao, R. Assiro, B. Biondo, S. Bricola, F. Budano, A. Corvaglia, B. D'Aquino, R. Esposi to, A. Innocente, A. Mangano, E. Pastori, C. Pinto, E. Reali, F. Taurino, and A. Zerbini in the installation, debugging, and maintenance of the detector.

ORCID iDs

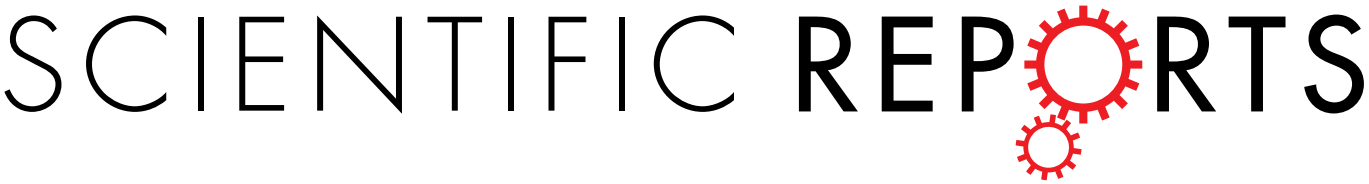
S. Z. Chen https://orcid.org/0000-0003-0703-1275
S. W. Cui https://orcid.org/0000-0002-0183-2410
W. Gao https://orcid.org/0000-0003-0656-8572
D. Ruffolo https://orcid.org/0000-0003-3414-9666

References

Aab, A., Abreu, P., Aglietta, M., et al. 2017, Sci, 357, 1266
Aartsen, M. G., Abraham, K., Ackermann, M., et al. 2016, ApJ, 826, 220
Abbasi, R., Abdou, Y., Abu-Zayyad, T., et al. 2010, ApJL, 718, L194
Abbasi, R., Abdou, Y., Abu-Zayyad, T., et al. 2012, ApJ, 746, 33
Abdo, A. A., Allen, B. T., Aune, T., et al. 2008, PhRvL, 101, 221101

Abdo, A. A., Allen, B. T., Aune, T., et al. 2009, ApJ, 698, 2121
Aglietta, M., Alessandro, B., Antonioli, P., et al. 1995, Proc. ICRC (Rome), 24, 800
Aglietta, M., Alessandro, B., Antonioli, P., et al. 1996, ApJ, 470, 501
Aglietta, M., Alekseenko, V. V., Alessandro, B., et al. 2009, ApJL, 692, L130
Aielli, G., Assiro, R., Bacci, C., et al. 2006, NIMPA, 562, 92
Aielli, G., Bacci, C., Bartoli, B., et al. 2009, NIMPA, 608, 246
Alekseenko, V. V., Cherniaev, A. B., Djappuev, D. D., et al. 2009, NuPhB, 196, 179
Alexeenko, V. V., Chudakov, E. A., Gulieva, N. E., & Sborshikov, G. V. 1981, Proc. ICRC (Paris), 17, 146
Ambrosio, M., Antolini, R., Baldini, A., et al. 2003, PhRvD, 67, 042002
Amenomori, M., Ayabe, S., Chen, D., et al. 2005a, ApJ, 633, 1005
Amenomori, M., Ayabe, S., Chen, D., et al. 2005b, ApJL, 626, L32
Amenomori, M., Ayabe, S., Bi, X. J., et al. 2006, Sci, 314, 439
Amenomori, M., Bi, X. J., Chen, D., et al. 2012, APh, 36, 237
Amenomori, M., Bi, X. J., Chen, D., et al. 2017, ApJ, 836, 153
Andreyev, Y. M., Chudakov, A. E., Kozyarivsky, V. A., et al. 1987, Proc. ICRC (Moscow), 20, 22
Bartoli, B., Bernardini, P., Bi, X. J., et al. 2012, PhRvD, 85, 092005
Bartoli, B., Bernardini, P., Bi, X. J., et al. 2013a, ApJ, 779, 27
Bartoli, B., Bernardini, P., Bi, X. J., et al. 2013b, PhRvD, 88, 082001
Bartoli, B., Bernardini, P., Bi, X. J., et al. 2014, ApJ, 790, 152
Bartoli, B., Bernardini, P., Bi, X. J., et al. 2015a, ApJ, 809, 90
Bartoli, B., Bernardini, P., Bi, X. J., et al. 2015b, PhRvD, 92, 092005
Bartoli, B., Bernardini, P., Bi, X. J., et al. 2016, ApJS, 222, 6
Cutler, D. J., Bergeson, H. E., Davies, J. F., & Groom, D. E. 1981, ApJ, 248, 1166
Cutler, D. J., & Groom, D. E. 1991, ApJ, 376, 322
Erlykin, A. D., & Wolfendale, A. W. 2006, APh, 25, 183
Farley, F. J. M., & Storey, J. R. 1954, PPSA, 67, 996
Fenton, K. B., Fenton, A. G., & Humble, J. E. 1995, Proc. ICRC (Rome), 24, 63
Gaisser, T. K., Stanev, T., & Tilav, S. 2013, FrPhy, 8, 748
Gombosi, T., Kota, J., Somogyi, A. J., et al. 1975, Proc. ICRC (Munich), 14, 586
Guillian, G., Hosaka, J., Ishihara, K., et al. 2007, PhRvD, 75, 062003
Guo, Y. Q., Zhang, X. Y., Zhang, J. L., et al. 2010, ChPhC, 34, 555
Guo, Y. Q., Feng, Z. Y., Yuan, Q., Liu, C., & Hu, H. B. 2013a, NJPh, 15, 013053
Guo, Y. Q., Yuan, Q., Liu, C., & Li, A. F. 2013b, JPhG, 40, 065201
Heck, D., Knapp, J., Capdevielle, J. N., Schatz, G., & Thouw, T. 1998, CORSIKA: A Monto Carlo Code to Simulate Extensive Air Showers (Karlsruhe: Forschungszentrum Karlsruhe)
Kuznetsov, A. V. 1990, Proc. ICRC (Adelaide), 21, 372
Lagage, P. O., & Cesarsky, C. J. 1983, A&A, 125, 249
Lee, Y. W., & Ng, L. K. 1987, Proc. ICRC (Moscow), 20, 18
Li, T. L., Liu, M. Y., Cui, S. W., & Hou, Z. T. 2012, APh, 39–40, 144
Liu, W., Bi, X. J., Lin, S. J., Wang, B. B., & Yin, P. F. 2017, PhRvD, 96, 023006
Morello, C., Navarra, G., & Vernetto, S. 1983, Proc. ICRC (Bangalore), 18, 127
Mori, S., Yasue, S., Munakata, K., et al. 1995, Proc. ICRC (Rome), 24, 648
Munakata, K., Hara, T., Yasue, S., et al. 1999, AdSpR, 23, 611
Munakata, K., Kiuchi, T., Yasue, S., et al. 1997, PhRvD, 56, 23
Nagashima, K., Fujimoto, K., & Jacklyn, R. M. 1998, JGR, 103, 17429
Nagashima, K., Fujimoto, K., Sakakibara, S., et al. 1989, NCimC, 12, 695
Nagashima, K., Sakakibara, S., Fenton, A. G., & Humble, J. E. 1985, P&SS, 33, 395
Qu, X. B., Zhang, Y., Xue, L., Liu, C., & Hu, H. B. 2012, ApJL, 750, 17
Sakakibara, S., Ueno, H., Fujimoto, K., Kondo, I., & Nagashima, K. 1973, Proc. ICRC (Denver), 13, 1058
Schwadron, N. A., Adams, F. C., Christian, E. R., et al. 2014, Sci, 343, 988
Swinson, D. B., & Nagashima, K. 1985, P&SS, 33, 1069
Thambyaphillai, T. 1983, Proc. ICRC (Bangalore), 18, 383
Ueno, H., Fujii, Z., Yamada, T., et al. 1990, Proc. ICRC (Adelaide), 21, 361
Zhang, M., Zuo, P. B., & Pogorelov, N. 2014, ApJ, 790, 5

View publication stats



OPEN

Multi-spectral optical imaging of the spatiotemporal dynamics of ionospheric intermittent turbulence

Received: 29 December 2017
Accepted: 20 June 2018
Published online: 12 July 2018

Abraham C.-L. Chian[1,2,3,4], José R. Abalde[2], Rodrigo A. Miranda[5], Felix A. Borotto[6], David L. Hysell[7], Erico L. Rempel[2,3] & David Ruffolo[4]

Equatorial plasma depletions have significant impact on radio wave propagation in the upper atmosphere, causing rapid fluctuations in the power of radio signals used in telecommunication and GPS navigation, thus playing a crucial role in space weather impacts. Complex structuring and self-organization of equatorial plasma depletions involving bifurcation, connection, disconnection and reconnection are the signatures of nonlinear evolution of interchange instability and secondary instabilities, responsible for the generation of coherent structures and turbulence in the ionosphere. The aims of this paper are three-fold: (1) to report the first optical imaging of reconnection of equatorial plasma depletions in the South Atlantic Magnetic Anomaly, (2) to investigate the optical imaging of equatorial ionospheric intermittent turbulence, and (3) to compare nonlinear characteristics of optical imaging of equatorial plasma depletions for two different altitudes at same times. We show that the degree of spatiotemporal complexity of ionospheric intermittent turbulence can be quantified by nonlinear studies of optical images, confirming the duality of amplitude-phase synchronization in multiscale interactions. By decomposing the analyses into North-South and East-West directions we show that the degree of non-Gaussianity, intermittency and multifractality is stronger in the North-South direction, confirming the anisotropic nature of the interchange instability. In particular, by using simultaneous observation of multi-spectral all-sky emissions from two different heights we show that the degree of non-Gaussianity and intermittency in the bottomside F-region ionosphere is stronger than the peak F-region ionosphere. Our results are confirmed by two sets of observations on the nights of 28 September 2002 and 9 November 2002.

Nonlinear dynamics of equatorial plasma depletions

Equatorial plasma depletions (EPDs) related to density irregularities often occur in the nighttime ionosphere at low- and mid-latitudes. The first observation of EPDs was reported by Booker and Wells[1] in 1938 when they discovered spread-F in the ionogram of backscattered signals of an ionosonde in Huancayo, Peru. Booker[2] developed a theory of ionospheric turbulence to explain EPDs responsible for the scintillation of radio waves from stars. EPDs are produced by the generalized Rayleigh-Taylor instability, or more generally, interchange instability, which evolves nonlinearly to form EPDs along Earth's magnetic flux tubes[3]. Farley *et al.*[4] used the incoherent scatter observations of EPDs from the 50 MHz Jicamarca radar to constrain the theories for the origin of EPDs, and suggested that gradients of density and drift velocity might be possible sources of instability. Woodman and La Hoz[5] suggested that the rising EPDs are the source of radar echoes detected by Farley *et al.*[4]. Recent satellite observations and numerical simulations indicated that small-scale magnetic field variations in the nighttime ionosphere can originate from EPDs[6]. The structures of EPDs are anisotropic as a result of the large divergence between ionospheric conductivities parallel and perpendicular to the geomagnetic field. If we consider the

[1]School of Mathematical Sciences, University of Adelaide, Adelaide, SA, 5005, Australia. [2]Institute of Aeronautical Technology (ITA), São José dos Campos, SP, 12228-900, Brazil. [3]National Institute for Space Research (INPE), P.O. Box 515, São José dos Campos, SP, 12227-010, Brazil. [4]Department of Physics, Faculty of Science, Mahidol University, Bangkok, 10400, Thailand. [5]UnB-Gama Campus, and Plasma Physics Laboratory, Institute of Physics, University of Brasília (UnB), Brasília DF, 70910-900, Brazil. [6]Departamento de Física, Facultad de Ciencias Físicas y Matemáticas, Universidad de Concepción, Concepción, Chile. [7]Department of Earth and Atmospheric Sciences, Cornell University, Ithaca, New York, 14850, USA. Correspondence and requests for materials should be addressed to A.C.-L.C. (email: abraham.chian@gmail.com)

North-South (N-S) dimension to be a proxy for magnetic apex height, then it is evident why the structures of EPDs should be anisotropic. Due to the interchange instability, the EPD structures are stretched in the vertical (N-S) direction as flows are mainly along that direction.

The dynamical evolution of ionospheric EPDs leads to complex structuring and self-organization of depleted density structures such as bifurcation, connection, disconnection, and reconnection. Bifurcation of EPDs creates Y-shaped EPDs which have been observed by radars[7,8], airglow images[9], satellites[10], and numerical simulations[11,12]. The equatorial ionosphere can be subject to an interchange instability after sunset which generates gradients in the background plasma density. This primary instability often leads to the formation of large-scale EPDs that can rise to high altitudes in the topside F-region. Associated with these large-scale EPDs are small-scale secondary instabilities that can develop on the walls of EPDs[8,10]. A linear eigenmode analysis of secondary instabilities forming on an ascending circular EPD indicates that a single mode could not give rise to bifurcation, whereas a superposition of two modes with comparable and opposite amplitudes would; bifurcation in radar plumes occurs when the linear growth rate of secondary instabilities is greatest[8]. Numerical simulations of Huba and Joyce[11] showed that the initial bifurcation of EPDs can be triggered by a Rayleigh-Taylor instability when the top of the EPD flattens at the head as it rises through the ionosphere, which can undergo multiple bifurcations in the F-region.

Disconnection (or pinching) of EPDs occurs when the rising regions of a depleted density structure disconnect from the lower regions in their ascent, which has also been observed by radars[7,8], satellites[7,13], airglow images[14,15], and numerical simulations[12]. Laakso *et al.*[13] showed that a downward motion of the plasma within the EPDs can occur if the background westward zonal electric field and upward vertical neutral wind in the equatorial ionosphere are sufficiently strong. A simultaneous occurrence of the updrafting and downdrafting plasma flows in a single EPD structure may cause the disconnection of the lower part of the EPD from its upper part. Hysell[8] showed that an EPD can narrow to the point where disconnection occurs by diffusive dissipation if a small electric field normal to the background density gradient with the proper sign is present.

Reconnection (or merging) of EPDs has been observed by airglow images[15–17], numerical simulations[11,16,18], and satellites[18,19]. Merging can occur in three different ways: (i) several highly tilted EPDs from adjacent areas form a reconnected EPD structure consisting of several strings[18]; (ii) reconnection of a branch of an EPD arising from secondary instabilities with an adjacent EPD;[16] (iii) reconnection of a slowing leading EPD, due to the reduction of its zonal drift speed, with another trailing EPD[15]. Broad plasma depletions are wide and deep decreases of plasma density whose longitudinal width is over several hundred kilometres, associated with plasma density reductions of large magnitude, which have been observed by satellites[19], numerical simulations[18], incoherent scatter radars[20], radio-tomography images[21], and airglow images[15]. Broad plasma depletions can be formed either by the merging of EPDs[15,18,19] or ionospheric uplift[20].

Multi-spectral optical imaging of double EPD reconnection in the South Atlantic Magnetic Anomaly on 28 September 2002

In optical images of airglow emissions, EPDs are observed as dark bands due to a decrease in emission intensity[3,9]. Fig. 1a,c shows near simultaneous all-sky images of OI 630.0 nm (21:48:08 LT) and OI 777.4 nm emissions (21:46:04 LT) observed on the night of 28 September 2002, indicating the field of view to 90° zenith angle of the multi-spectral all-sky (180°) imager located in Brazópolis (22.5°S, 45.6°W; dip latitude 17.5°S; altitude 1860 m), Brazil[14,22,23]. Top and right correspond to the north (N) and east (E), respectively. The back-illuminated charge-coupled device (CCD) (1024 × 1024 pixels) with high quantum efficiency of about 80% in the visible region was used for imaging. The raw images from the CCD camera were calibrated using the known star field to determine the pixel scale size and orientation of image data. The OI 630.0 nm and OI 777.4 nm emissions arise from the dissociative recombination of O_2^+ ions and radiative recombination of O^+ ions, respectively. Both emissions show large-scale EPDs aligned along the geomagnetic field lines, with a westward declination of about 20°, and with spatial resolution of the order of kilometers. The all-sky images are obtained with interference filters for the two emission lines, with a narrow bandwidth of only 2 nm to minimize the effects of viewing an optically thin target that adds effects at different altitudes. For filters with this narrow band, we mainly detect the emission lines of interest and the underlying continuum has not been removed. The peak OI 630.0 nm emission is from the bottomside F-region at an altitude ~280 km, while the peak OI 777.4 nm emission is from the peak F-region at an altitude ~330 km. These two F-region heights, each with a vertical width of about 50 km, are the source regions of the majority of the respective emissions.

Note that the raw images in Fig. 1a,c are distorted, curved, and compressed at the edges (low elevation angles) and inflated near the center or zenith (high elevation angles) due to the effect of the fish-eye lens. For any quantitative analysis, it is necessary to apply the linearization method to remove this effect[24,25]. Hence, we transform the box areas of raw images in Fig. 1a,c to linearized images of 500 × 500 km^2 (Fig. 1b) and 750 × 750 km^2 (Fig. 1d), respectively, with uniformly spaced geographic grids at an assumed emission altitude of 280 km (330 km) for the OI 630.0 nm (777.4 nm) emissions. The coordinates in Fig. 1b,d are given in latitude, longitude, and magnetic apex height projected to the magnetic equatorial plane[15,26–28].

During the period of optical imaging on 28 September 2002, the geomagnetic activity was quiet. According to the IUGG (International Union of Geodesy and Geophysic) and NASA/OMNI data sets, the solar and geomagnetic indices were: the daily planetary index ΣKp (24-h sum of three-hourly index Kp) was 10-, the daily Ap index was 5, and the daily F10.7 solar flux index was 149.1. On the nights with no occurrence of EPDs, the ionospheric plasma density profile obtained by ionosounding was homogeneous, displaying a positive gradient with altitude in the bottomside F-region. On the night of 28 September 2002 when EPDs appeared on all-sky images, the ionospheric plasma density profile became inhomogeneous due to the presence of plasma density irregularities associated with spread-F[23].

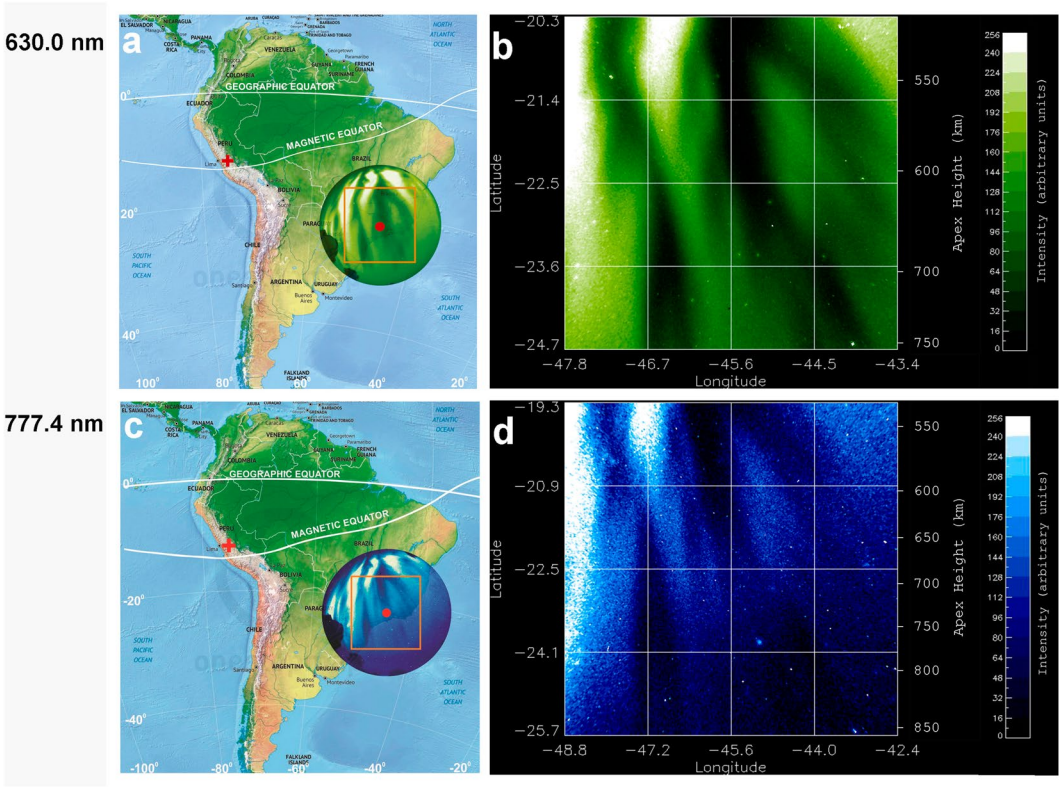


Figure 1. Multi-spectral optical imaging of equatorial plasma depletions on 28 September 2002. Map showing the projected circular field of view of the multi-spectral all-sky imager in the South Atlantic Magnetic Anomaly for: (**a**) the OI 630.0 nm emission peaked at an altitude ~280 km (bottomside F-region) and (**c**) the OI 777.4 nm emission peaked at an altitude ~330 km (peak F-region), observed on 28 September 2002 from Brazópolis, Brazil (marked by a red point). The orange boxes mark the areas of images to be investigated by quantitative analysis; the corresponding linearized grid images are divided into 16 cells covering an area of (**b**) $500 \times 500\,km^2$ and (**d**) $750 \times 750\,km^2$, respectively, indicated in latitude, longitude and magnetic apex height. The site of the first observation of equatorial plasma depletions by Booker and Wells in 1938 in Huancayo, Peru is marked by a red cross. The times of images in (**a**,**b**) (21:48:08 LT) and (**c**,**d**) (21:46:04 LT) correspond to Figs 2i and 4c and Figs 3i and 4f, respectively. The videos for this event can be found in Supplementary Videos S1 and S2. (**a**,**c** are modified from the Map of South America by onestopmap.com).

An overview of optical imaging of the OI 630.0 nm and 777.4 nm emission on 28 September 2002 is given in Figs 2 and 3, which display a time sequence of 12 linearized images. To facilitate the visualization of EPD interactions the images in Figs 2 and 3 cover areas of $1500 \times 1500\,km^2$ and $1530 \times 1530\,km^2$, respectively, larger than the areas of Fig. 1b,d. These images exhibit the dynamical processes of multiple bifurcations, connection, disconnection, and reconnection of EPDs as classified in Table 1. In Figs 4 and 5 we describe in detail the first EPD reconnection event observed in the South Atlantic Magnetic Anomaly based on selected images of Figs 2 and 3.

A complex region of multiple EPDs is identified inside the ellipses of Fig. 4, where we can observe the dynamical phenomena of complex structuring and self-organization of the ionosphere by following the temporal evolution of three EPD structures: A, B and C. In Fig. 4a,d, A, B and C are connected at the two bifurcation sites indicated by two arrows. In Fig. 4b,e, C is disconnected[14] from B at the disconnection site indicated by an arrow, while A remains connected to B. In Fig. 4c,f, C is reconnected to A at the reconnection site indicated by an arrow to form a merged elongated structure, the base of which is also connected to B. Table 1 and Fig. 4 show that the large-scale dynamics of EPD structures are similar at the two different altitudes at the same times. Another overview of optical imaging of this EPD reconnection event for smaller areas at the central regions of images similar to Fig. 1b,d, suitable for quantitative analysis, is given in Supplementary Fig. S1.

In addition to the aforementioned first EPD reconnection event, we have detected a second EPD reconnection event in the images of Figs 2 and 3, involving the interaction of three EPD structures denoted by X, Y and Z. Figure 5 covers the same regions of complex EPD interactions as Fig. 4 and provides the details of the second EPD reconnection event in the regions encircled by the ellipses. In Fig. 5a,d, Y and Z are connected forming an elongated EPD structure Y-Z, but X is not connected to Y-Z within the field-of-view of the all-sky imager; the arrow marks the site of EPD bifurcation. In Fig. 5b,e, Z becomes disconnected from Y at the disconnection site marked by an arrow. In Fig. 5c,f, X is reconnected to Z at the reconnection site marked by an arrow to form an elongated EPD structure X-Z. It is worth pointing out that the two EPD reconnection events shown in Figs 4c–f and 5c–f occur at same times in the same region of the ionosphere. Hence, we call this event "double EPD reconnection". It is likely that multiple EPD reconnections are a common phenomenon in the evolution of Rayleigh-Taylor instability.

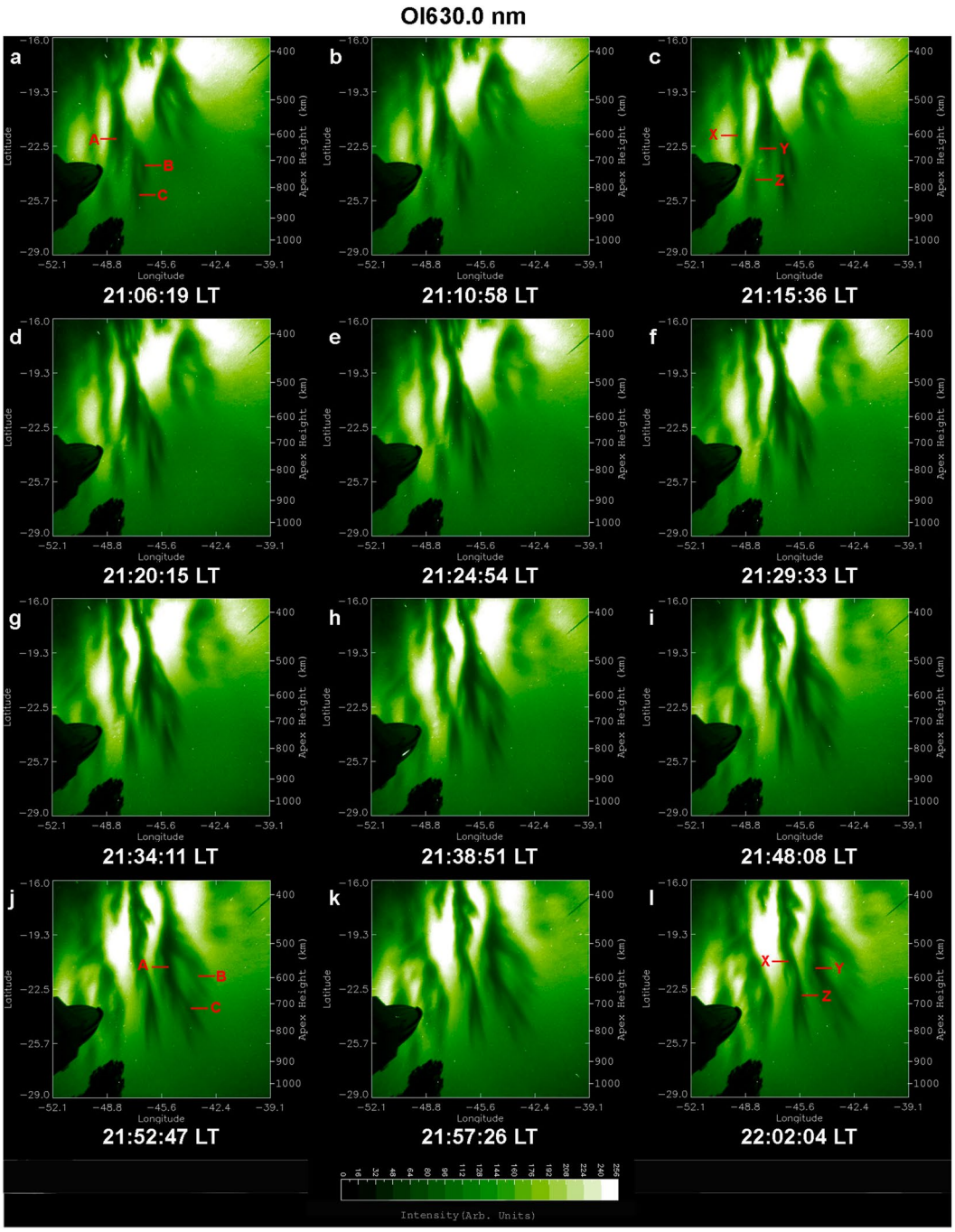


Figure 2. Overview of time sequence of all-sky images of the OI 630.0 nm emission observed on 28 September 2002. Each image has been linearized and projected to the magnetic equatorial plane onto an area of $1500 \times 1500\,km^2$ with uniformly spaced geographic grids at an assumed airglow emission height of 280 km. (A, B, C) denote EPD structures involved in the first EPD reconnection event to be described in detail in Fig. 4. The characterization of EPD dynamics for the first EPD reconnection event in terms of (A, B, C) for the images is given in Table 1. (X, Y, Z) denote EPD structures involved in the second EPD reconnection event to be described in detail in Fig. 5.

The three-dimensional numerical simulation of Huba *et al.*[16] showed the development of multiple EPDs from initial perturbations near the equator and their ascension to high altitudes. Bifurcation and complex structuring involving the merger of two EPD structures were seen in this simulation. The detailed discussion of electrostatic reconnection of EPDs depicted in Figs 1 to 3 of Huba *et al.*[16] is useful to interpret the two EPD reconnections we reported in Fig. 4c,f and in Fig. 5c,f. According to Huba *et al.*[16], the EPD reconnection is a result of the connection of the electrostatic potential of an EPD with the electrostatic potential of an adjacent EPD which allows plasma flow from one EPD to another EPD through high-speed channels. This proposed reconnection mechanism provides a plausible physical interpretation for the occurrence of our observed EPD reconnections via the action of the electrostatic potential.

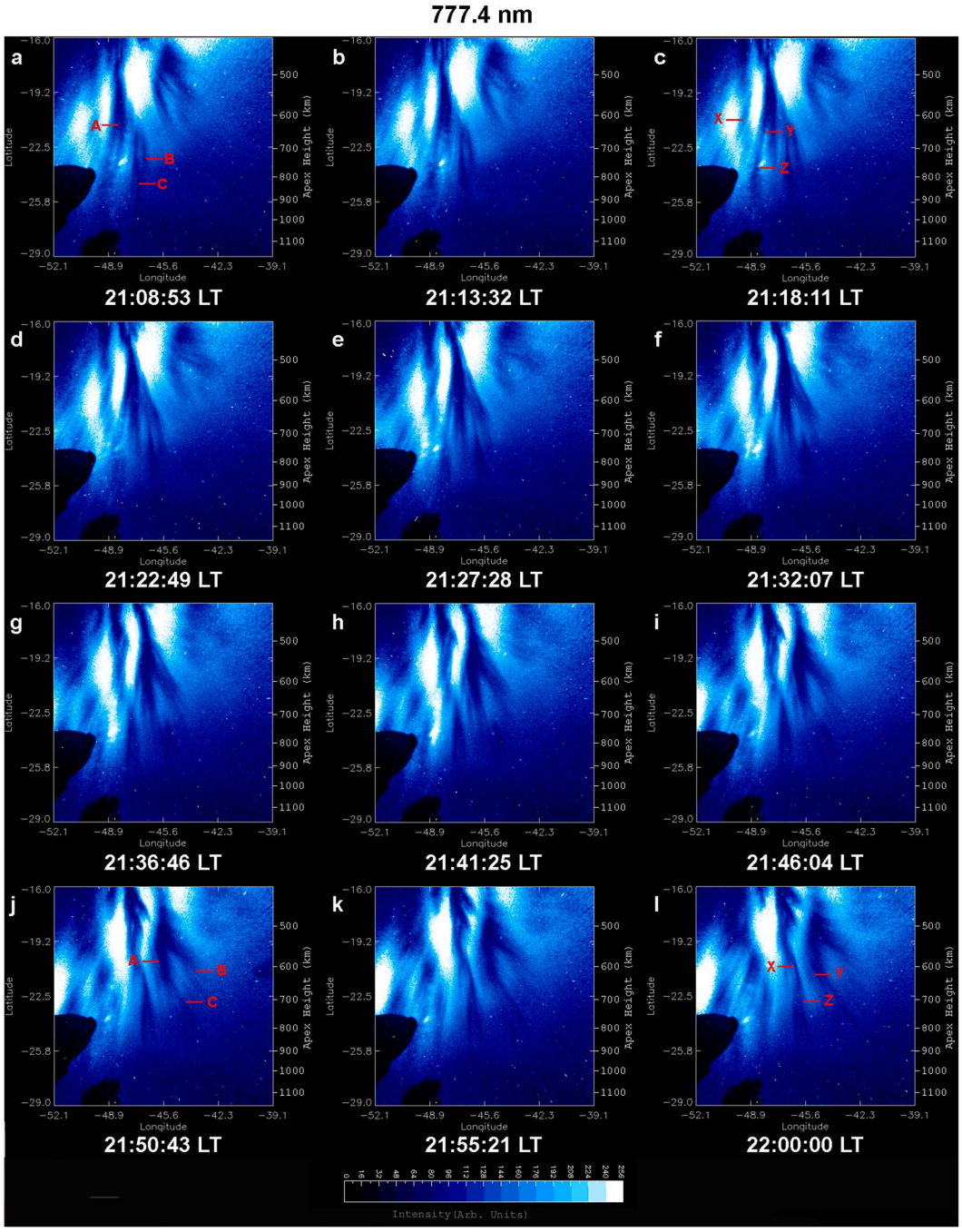


Figure 3. Overview of time sequence of all-sky images of the OI 777.4 nm emission observed on 28 September 2002. Each image has been linearized and projected to the magnetic equatorial plane onto an area of $1530 \times 1530\,km^2$ with uniformly spaced geographic grids at an assumed airglow emission height of 330 km. (A, B, C) denote EPD structures involved in the first EPD reconnection event to be described in detail in Fig. 4. The characterization of EPD dynamics for the first EPD reconnection event in terms of (A, B, C) for the images is given in Table 1. (X, Y, Z) denote EPD structures involved in the second EPD reconnection event to be described in detail in Fig. 5.

The first optical observation of EPD reconnection was reported by Huba *et al.*[16] using an airglow imager of OI 630.0 nm emission in Tahiti on 5 July 2015. Initially two EPD structures were distinct and separated. Later, one EPD bifurcated and moved towards the other EPD until two structures merged at an altitude of around 550 km. Three different types of EPD reconnection processes were observed by Narayanan *et al.*[15] using OI 630 nm imagers from Panhala, India, on 6 January 2008 and on 3 and 5 February 2008, and from Gandanki, India, on 23 March 2009, involving: (i) reconnection of various highly tilted EPDs from adjacent areas to form a merged structure; (ii) reconnection of a branch of an EPD resulting from secondary instabilities with a neighbouring EPD; (iii) reconnection of a slowing leading EPD, due to the reduction of its zonal drift speed, with another trailing EPD.

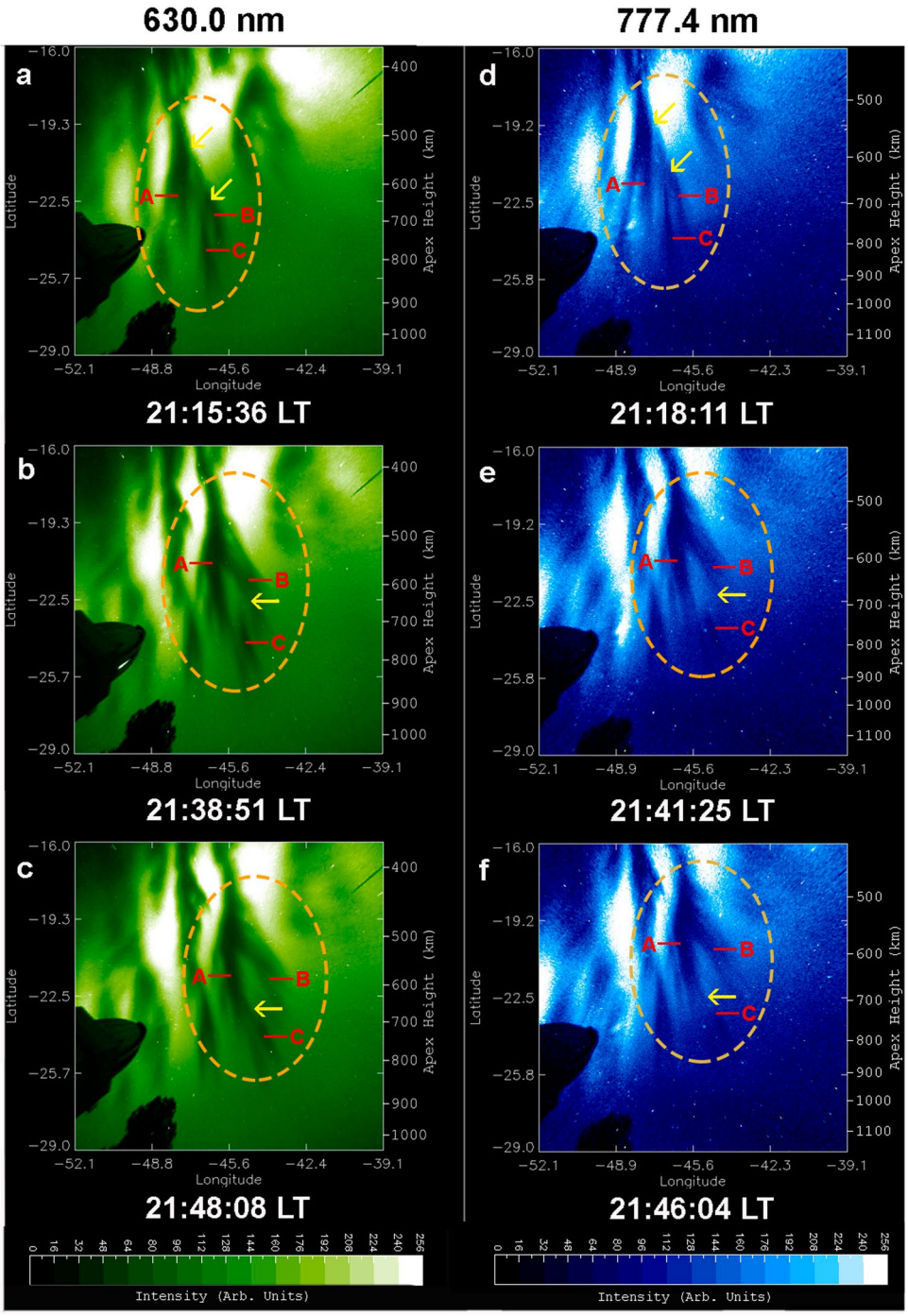


Figure 4. First EPD reconnection event on 28 September 2002. All-sky images of the OI 630.0 nm (left column) and OI 777.4 nm (right column) emissions observed on 28 September 2002. (A, B, C) denote EPD structures involved in the first EPD reconnection event. (**a**,**d**) A-B-C connected, the two arrows indicate the sites of bifurcation and connection of A and B-C and of B and C. (**b**,**e**) C disconnected from A-B, the arrow indicates the site of disconnection. (**c**,**f**) A-B-C reconnected, the arrow indicates the site of reconnection. The ellipses encircle the regions of dynamical interaction of EPD structures (A, B, C). The two Supplementary Videos provide a clearer view of EPD interactions.

EPD reconnection was observed by Xiong *et al.*[17] using an OI 630.0 nm imager from Fuke, China, on the night of 23–24 September 2014. Initially, Xiong *et al.*[17] observed bifurcation at a higher-latitude region of EPDs, and then at lower latitudes; the subbranches of EPD generated through bifurcations merge with each other to form a complicated mesh of plasma depletion regions. All previous observations of EPD reconnections were performed only by the OI 630.0 nm emission. The present paper is the first to report simultaneous multi-spectral observations of EPD reconnections at two heights. Since our observations and the observations of Huba *et al.*[16] were

OI 630.0 nm (in Local Time)		OI 777.4 nm (in Local Time)	
21:06:19	A-B-C connected	21:08:53	A-B-C connected
21:10:58	A-B-C connected	21:13:32	A-B-C connected
21:15:36	A-B-C connected	21:18:11	A-B-C connected
21:20:15	A-B-C connected	21:22:49	A-B-C connected
21:24:54	A-B-C connected	21:27:28	A-B-C connected
21:29:33	A-B-C connected	21:32:07	A-B-C connected
21:34:11	C disconnected from A-B	21:36:46	C disconnected from A-B
21:38:51	C disconnected from A-B	21:41:25	C disconnected from A-B
21:48:08	A-B-C reconnected	21:46:04	A-B-C reconnected
21:52:47	A-B-C reconnected	21:50:43	A-B-C reconnected
21:57:26	A-B-C reconnected	21:55:21	A-B-C reconnected
22:02:04	A-B-C reconnected	22:00:00	A-B-C reconnected

Table 1. Time sequence of EPD dynamics for the first EPD reconnection event on 28 September 2002.

carried out in the Southern Hemisphere, the EPDs first form at the top of the images and then ascend to higher magnetic apex heights toward the bottom of the images. In contrast, in the observations of Narayanan *et al.*[15] and Xiong *et al.*[17] carried out in the Northern Hemisphere, the EPDs first form at the bottom of the images and rise to higher magnetic apex heights toward the top of the images. Our multi-spectral observations confirm the occurrence of EPD bifurcation reported by Huba *et al.*[16], Narayanan *et al.*[15] and Xiong *et al.*[17]; as well as the occurrence of EPD disconnection seen in Fig. 3 of Narayanan *et al.*[15] and Fig. 5 of Xiong *et al.*[17]. Both of our EPD reconnections shown in Figs 4 and 5 correspond to the third type of EPD reconnection process seen in Fig. 3 of Narayanan *et al.*[15] and Fig. 5 of Xiong *et al.*[17] involving first the disconnection of an EPD due to the change of its zonal drift speed, and its subsequent reconnection with an adjacent EPD to form an elongated structure.

Nonlinear analysis of ionospheric intermittent turbulence on 28 September 2002

The rich dynamics of EPDs discussed in the previous section is the manifestation of nonlinear spatiotemporal evolution of primary and secondary instabilities of EPDs, leading to the formation of coherent structures and intermittent turbulence in the equatorial ionosphere. In this section, we show that nonlinear analysis of optical images of EPDs is capable of providing quantitative information of ionospheric intermittent turbulence.

Figure 6a,d shows the azimuthal average of the spatial power spectral density (PSD) of the emission intensity of OI 630.0 nm and OI 777.4 nm computed for the linearized images of Fig. 1b,d at 21:48:08 LT and 21:46:04 LT, respectively. Note that Fig. 1b,d is the same as Fig. S1c,f and its time is the same as Figs 2i, 3i, 4c,f and 5c,f. The straight line indicates the inertial subrange with k ~0.02 to 0.1 km^{-1} (i.e., for spatial scales r~300 to 60 km) as estimated by the compensated PSD method[29–31], with a spectral index of −2.3 (−1.5). The validity of power spectra can be verified by computing the following relation between the power spectrum $P(k)$ and the variance σ^2 in the spatial domain, adapted from the corresponding relation in the temporal domain[32]

$$\int_{-\infty}^{\infty} P(k)dk = \sigma^2, \tag{1}$$

where $P(k)$ is given by Fig. 6a,d; the variance is normalized by the square of the mean emission intensity of the respective linearized image. For comparison, we also compute the normalized variance directly from the emission intensity I of the linearized images given by Fig. 1b,d. For the OI 630.0 nm emission, the normalized variance computed from both methods is 0.377. For the OI 777.4 nm emission, the normalized variance computed from the PSD is 0.407 and from the emission intensity is 0.409.

Figure 6b,c shows the probability density functions (PDFs) as a function of the normalized increment of the emission intensity $\Delta I = (\delta I - <\delta I>)/\sigma_I$, where δI denotes two-point differences of the emission intensity I for a given spatial scale r; the angular brackets denote the mean value of δI, and σ_I denotes the standard deviation of δI for two spatial scales, r~300 km and 60 km, respectively, of the emission intensity in the North-South (N-S, black) and East-West (E-W, red) directions of Fig. 1b superposed by a Gaussian PDF (dotted line). Figure 6e,f shows similar plots for the two spatial scales based on Fig. 1d. Note that the PDFs are closer to Gaussian distributions at large spatial scales, but become highly non-Gaussian at small spatial scales. At small spatial scales the shape of the PDF becomes leptokurtic, displaying fat tails in Fig. 6c,f, which are the signatures of nonlinear coherent (intermittent) structures responsible for large-amplitude fluctuations in the ionospheric turbulence. Figure 6c,f shows that the degree of intermittency and non-Gaussianity in the N-S direction is stronger than the E-W direction.

The intermittent and non-Gaussian nature of the ionospheric turbulence can be quantified by computing the kurtosis and/or phase coherence index[29,31]. Kurtosis is a measure of amplitude synchronization in multiscale interactions, given by the normalized fourth-order moment

$$K(r) = \frac{1}{n}\sum_{i=1}^{n}\left(\frac{\delta I_i - \langle \delta I_i \rangle}{\sigma_I}\right)^4 - 3, \tag{2}$$

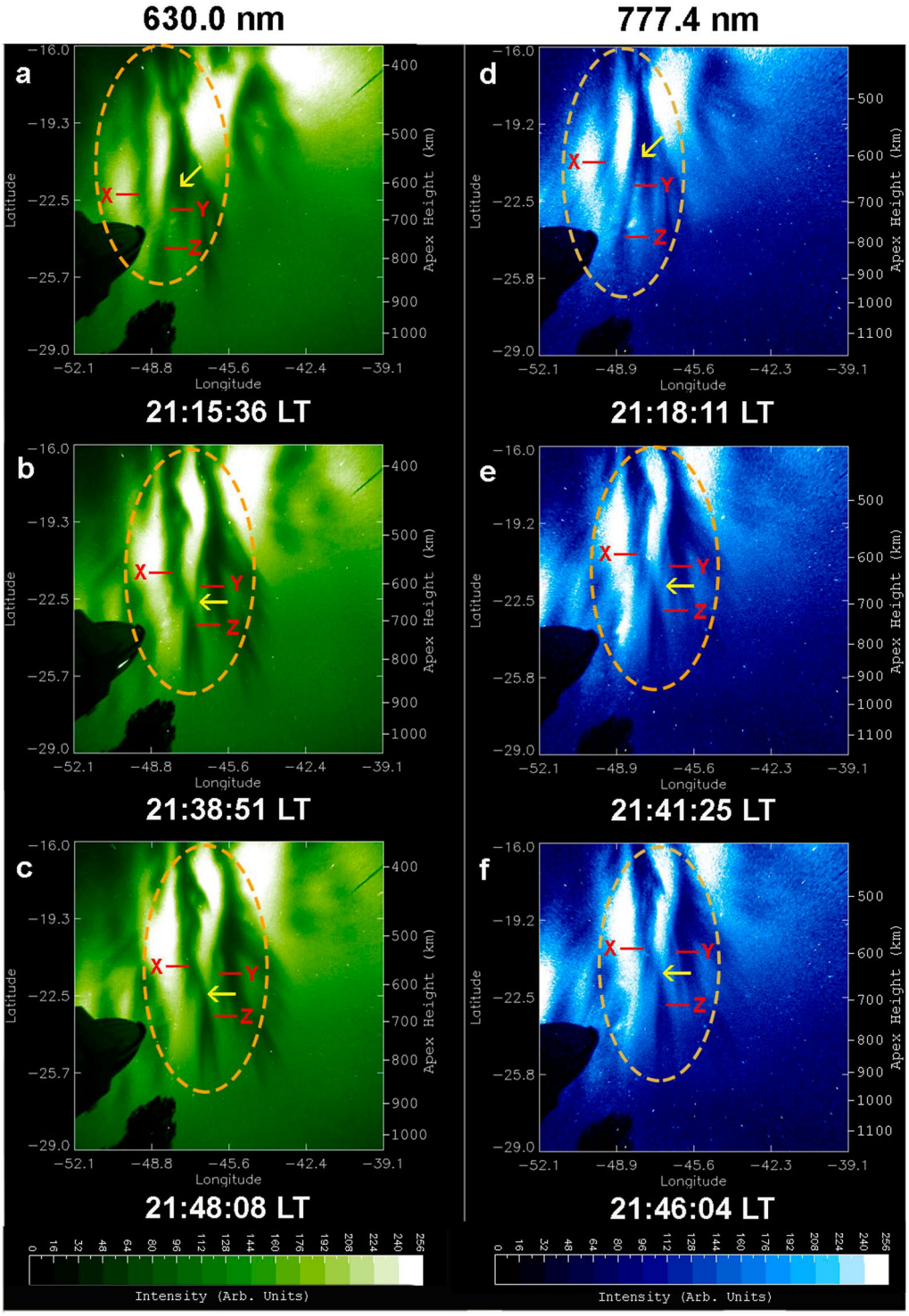


Figure 5. Second EPD reconnection event on 28 September 2002. All-sky images of the OI 630.0 nm (left column) and OI 777.4 nm (right column) emissions observed on 28 September 2002. (X, Y, Z) denote EPD structures involved in the second EPD reconnection event. (**a**,**d**) Y-Z connected, the arrow indicates the site of an EPD bifurcation. (**b**,**e**) Z disconnected from Y, the arrow indicates the site of disconnection. (**c**,**f**) X-Z reconnected, the arrow indicates the site of reconnection. The ellipses encircle the regions of dynamical interaction of EPD structures (X, Y, Z). The two Supplementary Videos provide a clearer view of EPD interactions.

where δI_i denotes two-point differences of the emission intensity I for a given spatial scale r; the angular brackets denote the mean values of δI_i, and σ_I denotes the standard deviation of δI_i. The variation of K as a function of r in the N-S (black) and E-W (red) directions for the images of Fig. 1b,d is plotted in Fig. 7a,d. For Gaussian

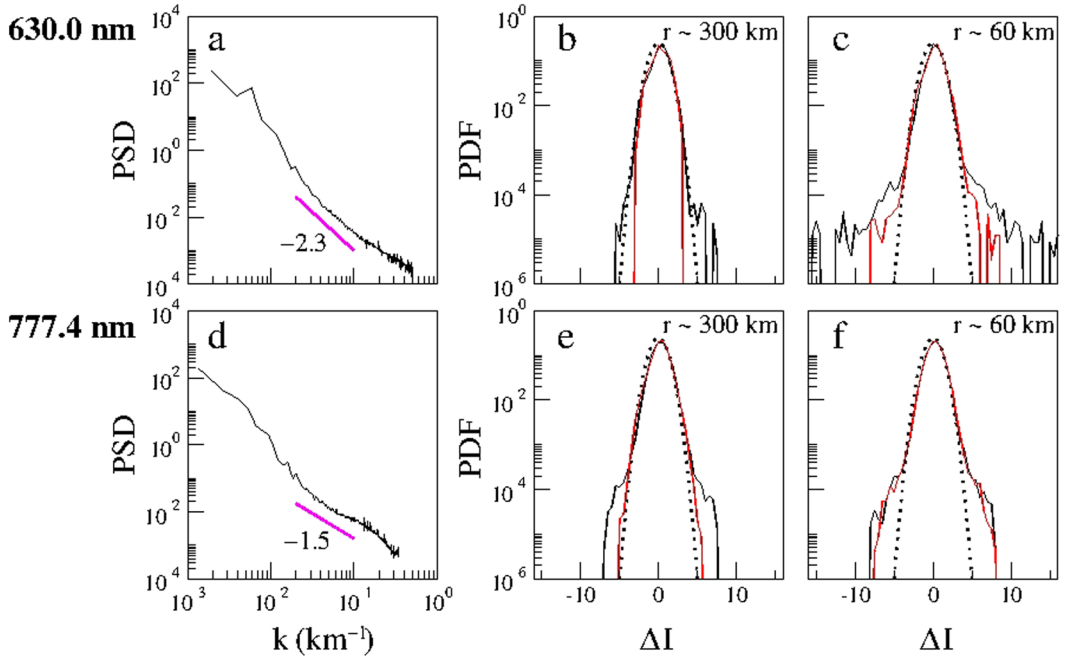


Figure 6. Power spectral density and probability density function of equatorial plasma depletions on 28 September 2002. Power spectral density (PSD) of the emission intensity I as a function of the wavenumber k of the: (**a**) OI 630.0 nm emission at 21:48:08 LT of Fig. 1b; (**d**) OI 777.4 nm emission at 21:46:04 LT of Fig. 1d. The straight line indicates the inertial subrange and the corresponding spectral index is given in (**a**,**d**). Probability density function (PDF) as a function of the normalized two-point differences of the emission intensity (ΔI) in the North-South direction (black) and East-West (red) direction of the: (**b**,**c**) OI 630.0-nm emission; (**e**,**f**) OI 777.4-nm emission for two spatial scales, $r \sim 300$ km and 60 km, superposed by a Gaussian PDF (dotted line).

fluctuations $K = 0$ for all scales, whereas for non-Gaussian or intermittent fluctuations $K > 0$. Figure 7a,d shows that K increases as the scale decreases, demonstrating that the ionospheric turbulence is intermittent and non-Gaussian over a broad range of spatial scales. In particular, they show that the degree of intermittency and non-Gaussianity in the N-S direction is stronger than the E-W direction. The difference between the two directions at the bottomside F-region is greater than the peak F-region.

Phase synchronization in multiscale interactions can be quantified by computing the phase coherence index[29]

$$C_\phi(r) = \frac{S_{PRS}(r) - S_{ORG}(r)}{S_{PRS}(r) - S_{PCS}(r)}, \tag{3}$$

where

$$S_j(r) = \sum_{i=1}^{n} |\delta I_i|, \tag{4}$$

with $j = ORG, PRS, PCS$. This index measures the degree of phase coherence in an original data set (*ORG*) by comparing it with two surrogate data sets constructed from the original data set: a phase-randomized surrogate (*PRS*) in which the phases of the Fourier modes are set fully random, and a phase-correlated surrogate (*PCS*) in which the phases of the Fourier modes are set fully equal. The power spectra of three data sets *ORG*, *PRS* and *PCS* are kept the same, but their phase spectra are different. $C_\phi(r) = 0$ implies that the phases of the fluctuations of the original data set are completely random, whereas $C_\phi(r) = 1$ implies that the phases are fully correlated. Figure 7b,e shows the variation of C_ϕ as a function of r in the N-S (black) and E-W (red) directions for the image of Fig. 1b,d. The behaviour of C_ϕ in Fig. 7b,e follows that of kurtosis in Fig. 7a,d, which is a demonstration of the duality of amplitude-phase synchronization[33] in multiscale interactions in ionospheric intermittent turbulence. Note that we have removed the pixels with saturated values of the emission intensity from the linearized images before computing kurtosis and $C_\phi(r)$.

The multifractal nature of ionospheric intermittent turbulence can be determined by computing the scaling exponent $\zeta(p)$ of the pth-order structure function. We apply the extended self-similarity technique[29,31] to refine the calculation of the scaling exponent for the inertial subrange k ~0.02 to 0.1 km^{-1}, so that the pth-order structure function $S_p(r) \sim [S_3(r)]^{\zeta(p)}$. Figure 7c,f shows $\zeta(p)$ decomposed in N-S (black) and E-W (red) directions for the images of Fig. 1b,d, respectively. The dashed line denotes the Kolmogorov K41 self-similarity scaling, $\zeta(p) = p/3$. The computed scaling exponents show significant departures from self-similarity at higher moments, proving the multifractal nature of ionospheric intermittent turbulence as well as a higher degree of multifractality

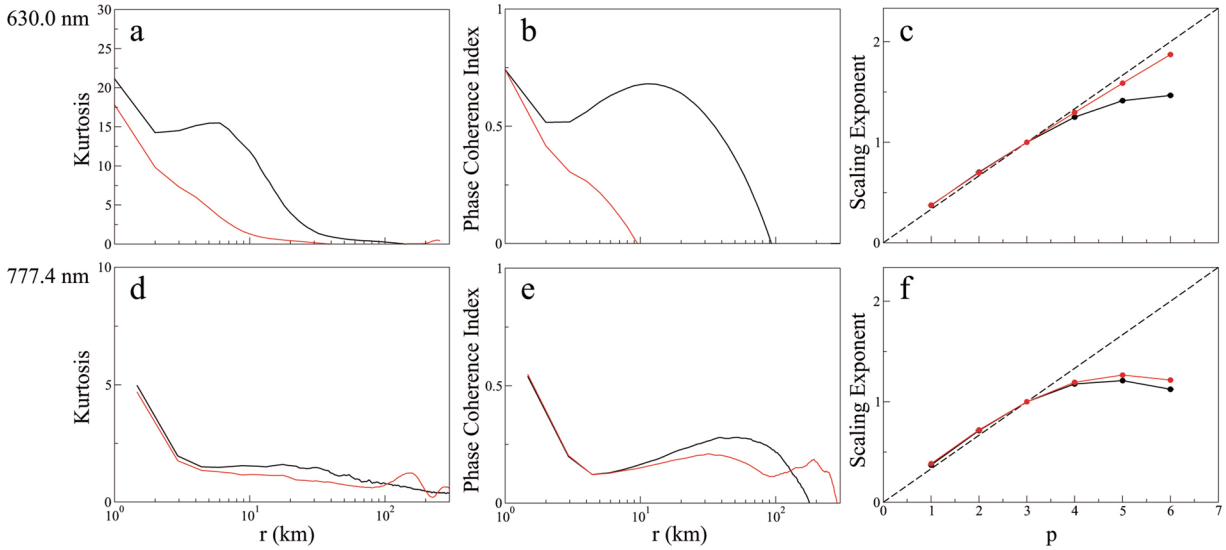


Figure 7. Nonlinear analysis of ionospheric intermittent turbulence on 28 September 2002. Kurtosis and phase coherence index as a function of the spatial scale r, and scaling exponents $\zeta(p)$ of the pth-order structure function for two-point differences of the emission intensity (δI) in the North-South direction (black) and East-West (red) direction of the: (**a**,**b**,**c**) OI 630.0 nm emission at 21:48:08 LT of Fig. 1b; (**d**,**e**,**f**) OI 777.4 nm emission at 21:46:04 LT of Fig. 1d. The Kolmogorov K41 self-similar scaling is indicated by a dashed line in (**c**,**f**).

in the N-S direction compared with the E-W direction over these scales, especially for the bottomside F-region. As shown by Fig. 6c,f, the origin of multifractality is the small-scale intermittent events in the fat-tail PDFs. These large-amplitude coherent structures embedded in ionospheric intermittent turbulence are driven by amplitude-phase synchronization related to multiscale interactions that lead to large-amplitude energy bursts[33,34]. A view of the multifractal behavior of this event for a time sequence of images before and after the EPD reconnection is given in Supplementary Figs S1 and S2.

Next we apply the aforementioned tools to distinguish the nature of ionospheric turbulence, after the onset of EPD reconnection, using simultaneous multi-spectral optical imaging at two different heights by comparing for the sake of clarity in Fig. 8 the total power spectral density, and the probability density function for the spatial scale 60 km, kurtosis and phase coherent index of the N-S emission intensity of OI 630.0 nm (21:48:08 LT) and OI 777.4 nm (21:46:04 LT) emissions taken from Figs 6 and 7. It follows from Fig. 8 that the power spectral density of the bottomside F-region is steeper than the peak F-region as seen in Fig. 6, and the degree of non-Gaussianity (PDF) and intermittency (kurtosis and phase coherence index) in the bottomside F-region is stronger than the peak F-region, in agreement with previous rocket and satellite studies that showed very different features of ionospheric turbulence in the bottomside and topside F-regions[35–37]. Note that it is not straightforward to make a quantitative comparison of the scaling exponents of Fig. 7c,f because the ionospheric turbulence in the bottomside (peak) F-region is not (is) Kolmogorov-like.

Nonlinear analysis of ionospheric intermittent turbulence on 9 November 2002

In order to demonstrate the consistency with our results of 28 September 2002, we carried out nonlinear analysis of multi-spectral images taken by the all-sky imager at the same site and at same times on the night of 9 November 2002. The geomagnetic activity on this day was quiet with the daily planetary index ΣKp of 10+, the daily Ap index of 6, and the daily solar flux index F10.7 of 185.5. Figure 9a,c shows the raw images of OI 630.0 nm (21:11:57 LT) and OI 777.4 nm (21:14:31 LT) emissions, respectively, on 9 November 2002. Figure 9b,d shows the corresponding linearized images covering an area of $500 \times 500\,km^2$ and $750 \times 750\,km^2$, respectively. For consistency of statistics, the dimensions of the areas in Fig. 9b,d are the same as Fig. 1b,d. We applied the same nonlinear analysis of Fig. 8 to the images of Fig. 9b,d. Figure 10 shows the total power spectral density and the probability density function for the spatial scale 60 km, and the kurtosis and phase coherence index of the N-S emission intensity of OI 630.0 nm and OI 777.4 nm emissions. Evidently, Fig. 10 shows that the slope of power spectral density in the bottomside F-region ionosphere is steeper than in the peak F-region ionosphere, and the degree of PDF non-Gaussianity and intermittency (kurtosis and phase coherence index) in the bottomside F-region ionosphere is stronger than in the peak F-region ionosphere, which confirms the results of Fig. 8. Hence, our results for 28 September 2002 are robust and in agreement with the results of 9 November 2002. The value of the normalized variance computed by Eq. (1) for the power spectrum of Fig. 10a for OI 630.0 nm (OI 777.4 nm) emission is 0.341 (0.180), very close to the value of 0.342 (0.181) obtained by computing the normalized variance of the emission intensity of the linearized images of Fig. 9b,d.

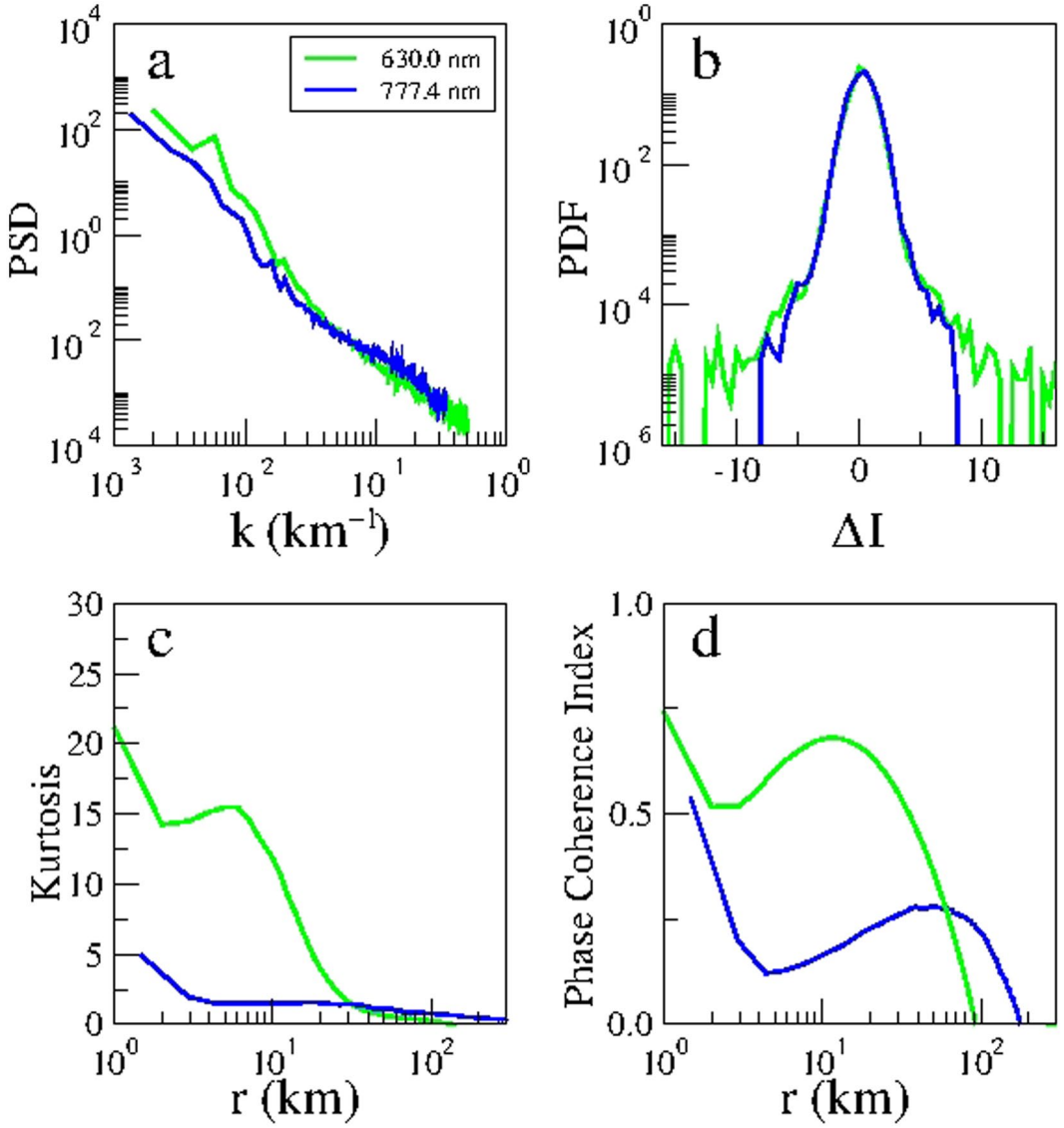


Figure 8. Nonlinear analysis of simultaneous optical imaging of the bottomside (OI 630.0 nm emission) and peak (OI 777.4 nm emission) F-region ionosphere on 28 September 2002: (**a**) Total power spectral density (PSD) as a function of the wavenumber k. (**b**) Probability density function (PDF) as a function of the normalized two-point differences of the emissions intensity (ΔI) for the spatial scale $r = 60$ km. (**c**) kurtosis and (**d**) phase coherence index as a function of the spatial scale r for two-point differences of the emission intensity (δI) in the North-South direction of the OI 630.0 nm (21:48:08 LT, green) and OI 777.4 nm (21:46:04 LT, blue) emissions.

Discussion and Conclusions

Coherent structures and intermittent turbulence are well-known in the atmosphere[38], solar wind[29–31], and auroral ionosphere[39]. In this paper, we investigated the first optical imaging of intermittent turbulence in the equatorial ionosphere. In the atmosphere, kinematic coherent structures such as vortices (eddies) dominate the atmospheric intermittent turbulence. In the solar wind, magnetic coherent structures such as current sheets and magnetic flux ropes dominate the interplanetary intermittent turbulence. Coherent structures and turbulence in the bottomside and topside F-region ionosphere have been observed previously by rockets, satellites, radars, and numerical simulations. The measured power spectral densities of EPDs display various power-law spectral indices that signal a degree of self-similar scale invariance over a range of scale sizes[35]. In contrast to the well-developed Kolmogorov turbulence in the topside equatorial F-region where an inertial subrange with a spectral slope −5/3 has been observed by satellites[36,37], the bottomside EPDs do not seem to be the product of Kolmogorov turbulence but rather seem to involve coherent steepened structures such as shocks and solitary waves[35]. This is consistent with the computed power spectral densities of Fig. 6a,d, which show that the spectral index is −2.3 in the bottomside F-region and −1.5 (i.e., close to the Kolmogorov spectral index −5/3) in the peak F-region.

Nonlinear steepened waves such as shocks, solitons and vortices are ubiquitous in turbulent plasmas[31,34,40]. Nonlinear coherent structures such as shocks and solitary waves, resulting from nonlinear steepening of waveforms, in the equatorial ionosphere have been studied by a number of papers. McClure and Hanson[41] reported the

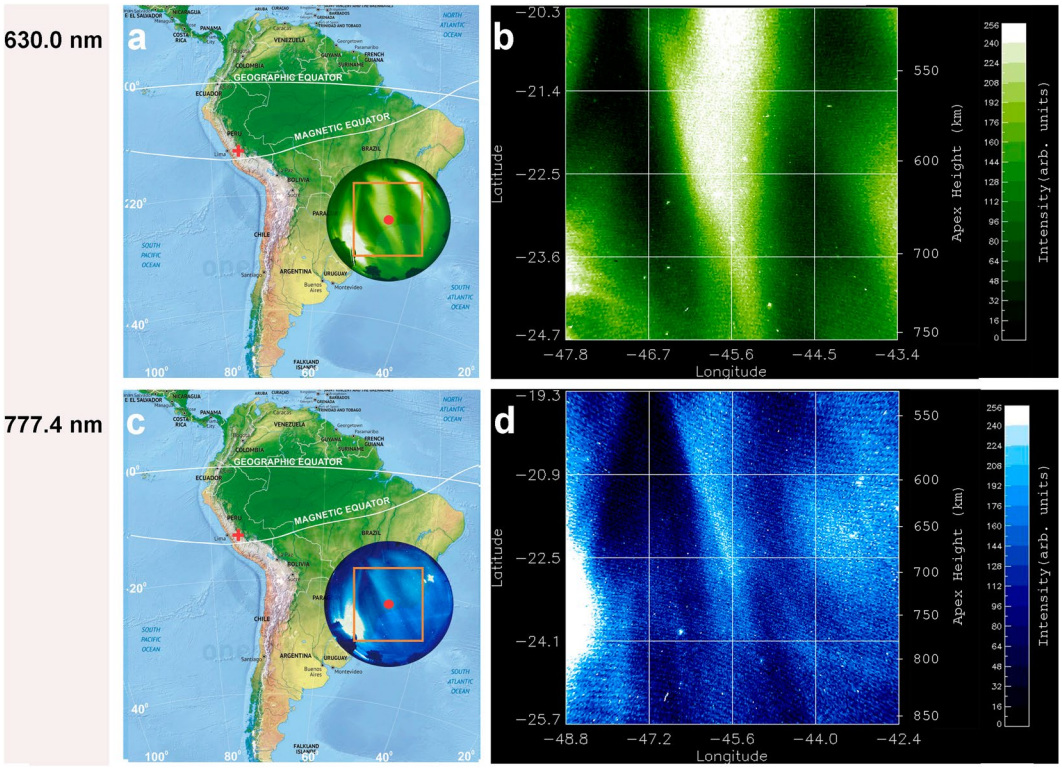


Figure 9. Multi-spectral optical imaging of equatorial plasma depletions on 9 November 2002. Map of the multi-spectral all-sky imaging on 9 November 2002 (similar to Fig. 1). The time of images in Fig. 9a,b is 21:11:57 LT, and in Fig. 9c,d is 21:14:31 LT. (Fig. 9a,c is modified from the Map of South America by onestopmap.com).

detection by the OGO-6 satellite over Brazil of large-amplitude density irregularities related to EPDs with amplitudes comparable to the largest auroral density irregularities. A theoretical analysis of Chaturvedi and Ossakow[42] shows that nonlinear evolution of the collisional Rayleigh-Taylor instability in the equatorial ionosphere can evolve to steepened structures with a power-law spectrum. Costa and Kelley[43] showed that the Rayleigh-Taylor instability that initiates in the bottomside equatorial F-region can nonlinearly develop very sharp gradients leading to the formation of steepened structures responsible for the power-law spectra observed by a rocket experiment in Natal, Brazil. Shock waves were observed by numerical simulation[44] of the generalized Rayleigh-Taylor instability at the bottomside and topside F-region equatorial ionosphere, confirmed by rocket and satellite *in situ* data[45]. Hysell *et al.*[46,47] proposed a model of plasma steepening, evolving from plasma advection that occurs on the vertical leading edges of plasma depletion wedges, to interpret shock waves detected in the equatorial ionosphere by rockets launched from Kwajalein Atoll. Jahn and Labelle[48] measured shocklike structures characterized by the density waveforms at the bottomside and topside F-region of the equatorial ionosphere in a rocket experiment in Alcântara, Brazil. Hysell and Kelley[49] and Hysell[35] obtained analytical and numerical solutions of solitary waves for a one-dimensional model of steepened structures which bear a striking resemblance to kilometer-scale waves associated with EPDs observed by the AE-E satellite in the bottomside layers of the equatorial ionosphere. At intermediate-scale sizes, multiscale interactions are acting as energy is transferred from the vertical steepened structures to the horizontal kilometer-scale waves to small-scale waves and then diffusively dissipated[35]. Berthelier *et al.*[50] reported observations of equatorial plasma waves that indicate the excitation of lower-hybrid solitary structures induced by lightning and the simultaneous occurrence of ion heating in large-scale EPDs that form at night during disturbed geomagnetic conditions. Numerical simulations of Huba and Joyce[11] showed that during the bifurcation process of EPDs, small-scale structures can interact and merge to form large-scale structures. In addition, numerical simulations of Yokoyama *et al.*[12] showed that bifurcation, pinching and merging can lead to the formation of turbulent density structures inside EPDs. The steeper slope of power spectral density, the thicker fat-tail in the probability density function, and the higher degrees of kurtosis and phase coherent indices of the bottomside F-region compared to the peak F-region, seen in Figs 8 and 10, are the manifestations of aforementioned nonlinear coherent structures in the bottomside F-region equatorial ionosphere.

The morphology of the airglow images in Figs 1–5 shows that the EPDs are highly anisotropic. In fact, the decomposition of nonlinear analyses into N-S and E-W directions confirms that the degree of complexity (intermittency, non-Gaussianity, multifractality) at these scales is stronger in the N-S direction compared to the E-W direction, especially at the bottomside F-region. Note, however, that the airglow imagery is ambiguous, and the N-S variations conflate meridional and apex-height variations. Nevertheless, when we find that N-S variations have a longer characteristic scale it implies that both meridional and apex-height variations have a longer scale than longitudinal (E-W) variations. Furthermore, airglow is a representation of plasma density passed through

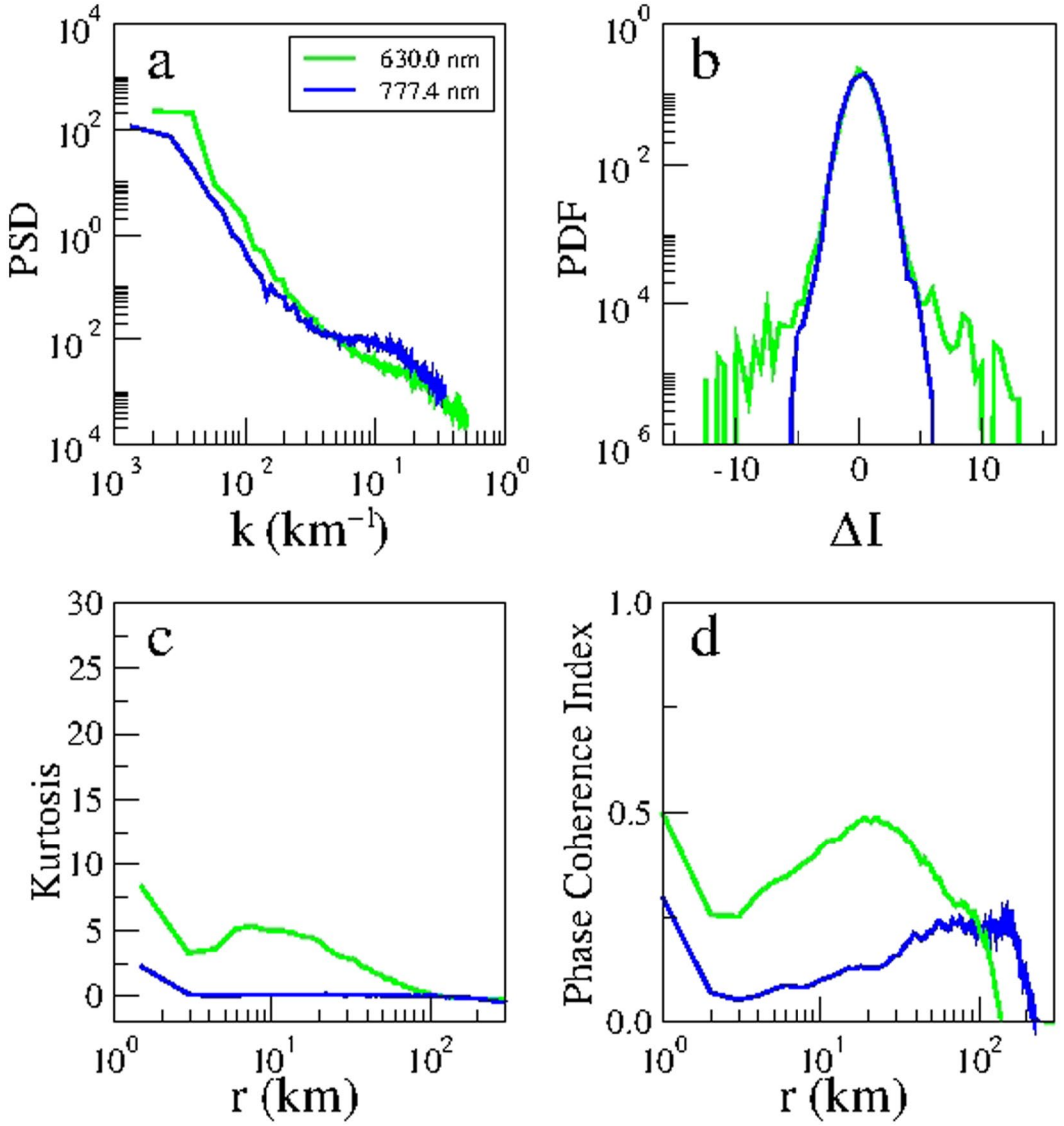


Figure 10. Nonlinear analysis of simultaneous optical imaging of the bottomside (OI 630.0 nm emission) and peak (OI 777.4 nm emission) F-region ionosphere on 9 November 2002: (**a**) Total power spectral density (PSD) as a function of the wavenumber k. (**b**) Probability density function (PDF) as a function of the normalized two-point differences of the emission intensity (ΔI) for the spatial scale $r = 60$ km. (**c**) kurtosis and (**d**) phase coherence index as a function of the spatial scale r for two-point differences of the emission intensity (δI) in the N-S direction of the OI 630.0 nm (21:11:57 LT, green) and OI 777.4 nm (21:14:31 LT, blue) emissions.

a complicated instrument function that acts like an averaging kernel. Some of the structures we see are an artefact of the imaging process and would not be present, for example, in radar images or *in-situ* rocket and satellite measurements. Finally, whereas magnetic field lines are equipotentials, they are not isodensity curves, and the field-aligned mapping of EPDs is very imperfect. Hence, it is difficult to relate airglow intensity to plasma state variables and therefore difficult to draw precise quantitative conclusions.

In conclusion, we reported multi-spectral all-sky observations of equatorial plasma depletions in Brazópolis, Brazil, on the nights of 28 September 2002 and 9 November 2002. Our optical observations at two different altitudes at same times provide new insights on the nonlinear dynamics of EPDs. So far the studies of EPD turbulence were mostly based on analyses of power spectra and waveforms, without quantifying the degree of intermittency or multifractality which are essential for understanding the EPD dynamics and structures. By applying the nonlinear techniques of kurtosis and phase-coherence index, we quantified the degree of amplitude-phase synchronization as a function of spatial scale which demonstrated that the amplitude-phase synchronization due to multiscale interactions is responsible for generating coherent structures and intermittent turbulence in the equatorial ionosphere. By computing the scaling exponents for higher moments of the emission intensity, we quantified the degree of multifractality and proved the multifractal nature of equatorial plasma depletions. Our new nonlinear tools showed that the degree of intermittency and non-Gaussianity at the bottomside F-region ionosphere is higher than at the peak F-region ionosphere, due to a higher rate of occurrence of nonlinear coherent

structures such as steepened kilometer-scale waves. Our results are consistent for observations on two different dates. In particular, we showed for the first time that optical imaging using all-sky imagers can be readily used to characterize the nonlinear spatiotemporal dynamics of equatorial plasma depletions, which can be used in conjunction with radars, rockets, satellites and numerical simulations for future studies of the equatorial ionosphere turbulence.

References

1. Booker, H. G. & Wells, H. W. Scattering of radio waves by the F-region of the ionosphere. *J. Geophys. Res.* **43**, 249–256 (1938).
2. Booker, H. G. Turbulence in the ionosphere with applications to meteor-trails, radio-star scintillation, auroral radar echoes, and other phenomena. *J. Geophys. Res.* **61**, 673–705 (1956).
3. Kelley, M. C., Makela, J. J., de La Beaujardière, O. & Retterer, J. Convective ionospheric storms: a review. *Rev. Geophys.* **49**, RG2003 (2011).
4. Farley, D. T., Balsley, B. B., Woodman, R. F. & McClure, J. P. Equatorial spread F: Implications of VHF radar observations. *J. Geophys. Res.* **75**(34), 7199–7216 (1970).
5. Woodman, R. F. & La Hoz, C. Radar observations of F region equatorial irregularities. *J. Geophys. Res.* **81**(31), 5447–5466 (1976).
6. Yokoyama, T. & Stolle, C. Low and midlatitude ionospheric plasma density irregularities and their effects on geomagnetic field. *Space Sci. Rev.* **206**, 495–519 (2017).
7. Tsunoda, R. T., Livingston, R. C., McClure, J. P. & Hanson, W. B. Equatorial plasma bubbles: vertically elongated wedges from the bottomside F layer. *J. Geophys. Res.* **87**(A11), 9171–9180 (1982).
8. Hysell, D. L. Imaging coherent backscatter radar studies of equatorial spread F. *J. Atm. Solar-Terr. Phys.* **61**, 701–716 (1999).
9. Makela, J. J. A review of imaging low-latitude ionospheric irregularity processes. *J. Atm. Solar-Terr. Phys.* **68**, 1441–1458 (2006).
10. Aggson, T. L., Laasko, H., Maynard, N. C. & Pfaff, R. F. *In situ* observations of bifurcations of equatorial bubbles. *J. Geophys. Res.* **101**(A3), 5125–5132 (1996).
11. Huba, J. D. & Joyce, G. Equatorial spread F modeling: Multiple bifurcated structures, secondary instabilities, large density 'bite-outs' and supersonic flows. *Geophys. Res. Lett.* **34**, L07105 (2007).
12. Yokoyama, T., Shinagawa, H. & Jin, H. Nonlinear growth, bifurcation and pinching of equatorial plasma bubble simulated by three-dimensional high-resolution bubble model. *J. Geophys. Res. Space Phys.* **119**, 10474–10482 (2014).
13. Laakso, H., Aggson, T. L. & Pfaff, R. F. Downdrafting plasma flow in equatorial bubbles. *J. Geophys. Res.* **99**(A6), 11507–11515 (1994).
14. Sahai, Y., J. R., Abalde, J. R., Fagundes, P. R. Pillat, V. G. & Bittencourt, J. A. First observations of detached equatorial ionospheric plasma depletions using OI 630.0 nm and OI 777.4 nm emissions nightglow imaging. *Geophys. Res. Lett.* **33**, L11104 (2006).
15. Narayanan, V. L., Gurubaran, S. & Shiokawa, K. Direct observational evidence for the merging of equatorial plasma bubbles. *J. Geophys. Res. Space Phys.* **121**, 7923–7931 (2016).
16. Huba, J. D., Wu, T.-W. & Makela, J. J. Electrostatic reconnection in the ionosphere. *Geophys. Res. Lett.* **42**, 1626–1631 (2015).
17. Xiong, C., Xu, J., Wu, K. & Yuan, W. Longitudinal thin structure of equatorial plasma depletions coincidently observed by Swarm constellation and all-sky imager. *J. Geophys. Res.* **123**, 1–10 (2018).
18. Huang, C.-S. *et al*. Observations and simulations of formation of broad plasma depletions through merging process. *J. Geophys. Res.* **117**, A02314 (2012).
19. Huang, C.-S. *et al*. Evolution of equatorial ionospheric plasma bubbles and formation of broad plasma depletions measured by the C/NOFS satellite during deep solar minimum. *J. Geophys. Res.* **116**, A03309 (2011).
20. Kil, H. *et al*. Broad plasma depletions detected in the bottomside of the equatorial F region. Simultaneous ROCSAT-1 and JULIA observations. *J. Geophys. Res. Space Phys.* **119**, 5978–5984 (2014).
21. Hei, M. A. *et al*. Radio-tomographic images of postmidnight equatorial plasma depletions. *Geophys. Res. Lett.* **41**, 13–19 (2014).
22. Abalde, J. R., Fagundes, P. R., Bittencourt, J. A. & Sahai, Y. Observations of equatorial F region plasma bubbles using simultaneous OI 777.4 nm and OI 630.0 nm imaging: New results. *J. Geophys. Res.* **106**(A12), 30331–30336 (2001).
23. Abalde, J. R. *et al*. Day-to-day variability in the development of plasma bubbles associated with geomagnetic disturbances. *J. Geophys. Res.* **114**, A04304 (2009).
24. Garcia, F. J., Taylor, M. J. & Kelley, M. C. Two-dimensional spectral analysis of mesospheric airglow image data. *Appl. Opt.* **36**(29), 7374–7385 (1997).
25. Abalde, J. R. *et al*. Height-resolved ionospheric drifts at low latitudes from simultaneous OI 777.4 nm and OI 630.0 nm imaging observations. *J. Geophys. Res.* **109**, A11308 (2004).
26. Makela, J. J., Kelley, M. C. & Nicolls, M. J. Optical observations of the development of secondary instabilities on the eastern wall of an equatorial plasma bubble. *J. Geophys. Res.* **111**, A09311 (2006).
27. Sobral, J. H. A. *et al*. Ionospheric zonal velocities at conjugate points over Brazil during the COPEX campaign: Experimental observations and theoretical validations. *J. Geophys. Res.* **114**, A04309 (2009).
28. Chapagain, N. P. *et al*. Equatorial plasma bubble zonal velocity using 630.0 nm airglow observations and plasma drift modeling over Ascension Island. *J. Geophys. Res.* **117**, A06316 (2012).
29. Chian, A. C.-L. & Miranda, R. A. Cluster and ACE observations of phase synchronization in intermittent magnetic field turbulence: a comparative study of shocked and unshocked solar wind. *Ann. Geophys.* **27**, 1789–1801 (2009).
30. Chian, A. C.-L. & Muñoz, P. R. Detection of current sheets and magnetic reconnections at the turbulent leading edge of an interplanetary coronal mass ejection. *Astrophys. J. Lett.* **733**, L34 (2011).
31. Chian, A. C.-L. *et al*. Genesis of interplanetary intermittent turbulence: A case study of rope-rope magnetic reconnection. *Astrophys. J.* **832**, 179 (2016).
32. Negrea, C. & Zabotin, N. A. Mean spectral characteristics of acoustic gravity waves in the thermosphere-ionosphere determined from Dynasonde data. *Radio Sci.* **51**, 213–222 (2016).
33. Chian, A. C.-L., Miranda, R. A., Rempel, E. L., Saiki, Y. & Yamada, M. Amplitude-phase synchronization at the onset of permanent spatiotemporal chaos. *Phys. Rev. Lett.* **104**, 254102 (2010).
34. He, K. F. & Chian, A. C.-L. On-off collective imperfect phase synchronization and bursts in wave energy in a turbulent state. *Phys. Rev. Lett.* **91**, 034102 (2003).
35. Hysell, D. L. An overview and synthesis of plasma irregularities in equatorial spread F. *J. Atm. Solar-Terr. Phys.* **62**, 1037–1056 (2000).
36. Shume, E. B. & Hysell, D. L. Spectral analysis of plasma drift measurements from the AE-E satellite: Evidence of an inertial subrange in equatorial spread F. *J. Atmos. Sol. Terr. Phys.* **66**, 57–65 (2004).
37. Rodrigues, F. S. *et al*. C/NOFS observations of intermediate and transitional scale-size equatorial spread F irregularities. *Geophys. Res. Lett.* **36**, L00C05 (2009).
38. Zeff, B. W. *et al*. Measuring intense rotation and dissipation in turbulent flows. *Nature* **42**, 146–149 (2003).
39. Spicher, A., Miloch, W. J., Clausen, L. B. N. & Moen, J. I. Plasma turbulence and coherent structures in the polar cap observed by the ICI-2 sounding rocket. *J. Geophys. Res. Space Phys.* **120,** 10959–10978 (2015).
40. Chian, A. C.-L. & Clemmow, P. C. Nonlinear, periodic waves in a cold plasma: a quantitative analysis. *J. Plasma Phys.* **14**, 505–527 (1975).

41. McClure, J. P. & Hanson, W. B. A catalog of ionospheric region irregulary behavior based on Ogo 6 retarding potential analyzer data. *J. Geophys. Res.* **78**(31), 7431–7440 (1973).
42. Chaturvedi, P. K. & Ossakow, S. L. Nonlinear theory of the collisional Rayleigh-Taylor instability in equatorial spread F. *Geophys. Res. Lett.* **4**(12), 558–560 (1977).
43. Costa, E. & Kelley, M. C. On the role of steepened structures and drift waves in equatorial spread F. *J. Geophys. REs.* **83**(A9), 4359–4364 (1978).
44. Zargham, S. & Seyler, C. E. Collisional interchange instability 1. Numerical simulations of intermediate-scale irregularities *J. Geophys. Res.* **92**(A9), 10073–10087 (1987).
45. Kelley, M. C., Seyler, C. E. & Zargham, S. Collisional interchange instability 2. A comparison of the numerical simulations with the *in situ* experimental data. *J. Geophys. Res.* **92**(A9), 10089–10094 (1987).
46. Hysell, D. L. *et al*. Steepened structures in equatorial spread F 1. *New observations. J. Geophys. Res.* **99**(A5), 8827–8840 (1994).
47. Hysell, D. L., Seyler, C. E. & Kelley, M. C. Steepened structures in equatorial spread F 2. Theory. *J. Geophys. Res.* **99**(A5), 8841–8850 (1994).
48. Jahn, J. M. & LaBelle, J. Rocket measurements of high-altitude spread F irregularities at the magnetic dip equator. *J. Geophys. Res.* **103**(A10), 23427–23441 (1998).
49. Hysell, D. L. & Kelley, M. C. Decaying equatorial F region plasma depletions. *J. Geophys. Res.* **102**(A9), 20007–20017 (1997).
50. Berthelier, J.-J. *et al*. Lightning-induced plasma turbulence and ion heating in equatorial ionospheric depletions. *Nature Geo.* **1**, 101–105 (2008).

Acknowledgements

This paper is dedicated to Drs H. G. Booker, P. C. Clemmow and D. T. Farley for their pioneer work on ionosphere and plasmas. A.C.L.C. is grateful to Drs. Farley (Cornell) and Clemmow (Cambridge) for supervision of undergraduate and doctoral studies. Dr. Booker supervised doctoral thesis of Drs Clemmow and Farley. A.C.L.C. thanks Mahidol University for a visiting professor fellowship. We acknowledge the financial support of CAPES (88881.068051/2014-01, 88887-138078/2017-00), CNPq (305540/2014-9, 305374/2012-5, 473805/2006-5), FAPESP (2013/26258-4, 2009/15769-2, 1998/09892-0), FAPDF (0193.000984/2015), and the Thailand Research Fund (RTA5980003). We thank the National Laboratory of Astrophysics (LNA/CNPq) for the opportunity to operate the all-sky imager, L.E.C.A. Schiavo for technical assistance with figures and videos, and the three reviewers for their valuable comments.

Author Contributions

A.C.L.C. drafted the manuscript. J.R.A. installed the all-sky imager and collected the data. R.A.M. and F.A.B. analysed the data. All authors contributed to the discussion of the results and the preparation of the manuscript.

Additional Information

Supplementary information accompanies this paper at https://doi.org/10.1038/s41598-018-28780-5.

Competing Interests: The authors declare no competing interests.

Publisher's note: Springer Nature remains neutral with regard to jurisdictional claims in published maps and institutional affiliations.

Open Access This article is licensed under a Creative Commons Attribution 4.0 International License, which permits use, sharing, adaptation, distribution and reproduction in any medium or format, as long as you give appropriate credit to the original author(s) and the source, provide a link to the Creative Commons license, and indicate if changes were made. The images or other third party material in this article are included in the article's Creative Commons license, unless indicated otherwise in a credit line to the material. If material is not included in the article's Creative Commons license and your intended use is not permitted by statutory regulation or exceeds the permitted use, you will need to obtain permission directly from the copyright holder. To view a copy of this license, visit http://creativecommons.org/licenses/by/4.0/.

© The Author(s) 2018

Journal of Geophysical Research: Space Physics

RESEARCH ARTICLE
10.1029/2017JA025135

Bare Neutron Counter and Neutron Monitor Response to Cosmic Rays During a 1995 Latitude Survey

W. Nuntiyakul[1,2], A. Sáiz[2,3], D. Ruffolo[2,3], P.-S. Mangeard[4,5], P. Evenson[5], J. W. Bieber[5], J. Clem[5], R. Pyle[6], M. L. Duldig[7], and J. E. Humble[7]

[1]Department of Physics and Materials Science, Faculty of Science, Chiang Mai University, Chiang Mai, Thailand, [2]Thailand Center of Excellence in Physics, CHE, Ministry of Education, Bangkok, Thailand, [3]Department of Physics, Faculty of Science, Mahidol University, Bangkok, Thailand, [4]National Astronomical Research Institute of Thailand (NARIT), Chiang Mai, Thailand, [5]Bartol Research Institute, Department of Physics and Astronomy, University of Delaware, Newark, DE, USA, [6]Pyle Consulting Group, Inc., St. Charles, IL, USA, [7]School of Natural Sciences, University of Tasmania, Hobart, Tasmania, Australia

Abstract Neutron monitors of standard design (IGY or NM64) are employed worldwide to study variations in the flux of galactic cosmic rays and solar energetic particles in the GeV range. The design minimizes detector response to neutrons below ~10 MeV produced by cosmic ray interactions in the ambient medium. Increasingly, however, such neutrons are of interest as a means of obtaining spectral information on cosmic rays, for studies of soil moisture, and for nuclear threat detection. Bare neutron counters, a type of lead-free neutron monitor, can detect such neutrons, but comparatively little work has been done to characterize the dependence of their count rate on cutoff rigidity. We analyze data from three bare neutron counters operated on a ship together with a three-tube NM64 monitor from November 1995 to March 1996 over a wide range of magnetic latitude, that is, a latitude survey. The bare counter design used foamed-in-place polyurethane insulation to keep the temperature uniform and to some extent moderate high-energy neutrons. When the ship was near land, the bare/NM64 count rate ratio was dramatically higher. Considering only data from open sea, the bare and NM64 pressure coefficients are not significantly different. We determine the response function of these bare counters, which is weighted to Galactic cosmic rays of lower energy than the NM64. This measurement of the response function may improve determination of the spectral index of solar energetic particles and Galactic cosmic rays from a comparison of bare and NM64 count rates.

Key Points:
- Bare neutron counters and NM64 monitors operated on a ship over a wide range of magnetic latitudes
- Measured bare counter and NM64 response functions are weighted to different Galactic cosmic ray energies
- Bare counter to NM64 count rate ratio relates to spectrum of cosmic rays or solar particles

Supporting Information:
- Supporting Information S1

Correspondence to:
A. Sáiz,
alejandro.sai@mahidol.ac.th

Citation:
Nuntiyakul, W., Sáiz, A., Ruffolo, D., Mangeard, P.-S., Evenson, P., Bieber, J. W., et al. (2018). Bare neutron counter and neutron monitor response to cosmic rays during a 1995 latitude survey. *Journal of Geophysical Research: Space Physics*, *123*, 7181–7195. https://doi.org/10.1029/2017JA025135

Received 18 DEC 2017
Accepted 10 AUG 2018
Accepted article online 20 AUG 2018
Published online 8 SEP 2018

©2018. American Geophysical Union. All Rights Reserved.

1. Introduction

Neutron monitors are ground-level detectors of cosmic-ray-induced atmospheric secondary particles that respond mostly to secondary neutrons (Simpson, 1948). Neutron monitors of the standard IGY and NM64 designs are optimized so that their count rates provide a precise and reliable measurement of the GeV-range cosmic-ray flux (Hatton & Carmichael, 1964). In particular, a neutron monitor at a given location is most sensitive to cosmic rays within a range in rigidity (momentum per charge, expressed in GV) somewhat above the local geomagnetic cutoff, which varies from near 0 GV at Earth's polar regions to ~17 GV at some parts of the geomagnetic equator, and above the atmospheric cutoff of $\gtrsim$1 GV needed to generate atmospheric secondary particles that can be recorded at ground level (see the response functions determined by Nuntiyakul et al., 2014). A standard neutron monitor includes a *producer*, typically ~5–30 tons of lead, in which atmospheric secondary particles of $\geq$10 MeV have a high probability of interacting to produce multiple MeV-range neutrons that can be detected in gas-filled proportional counters containing ^{10}B or ^{3}He. A standard neutron monitor is also surrounded by a *reflector* comprising several centimeters of paraffin or polyethylene, which aims to contain the neutrons produced in the lead as well as minimize the detector response to secondary neutrons of $\leq$10 MeV, which are mainly produced by cosmic ray interactions in surrounding materials at ground level and thus are sensitive to changes in the local environment. Also important is the *moderator*, consisting typically of a thinner layer of the same material as the reflector placed between the lead producer and each gas-filled counter, which helps slow down the neutrons in order to be detected efficiently. Standard neutron monitors are operated at more than 40 locations worldwide, taking advantage of the varying geomagnetic cutoff, and are widely used to monitor Earth's radiation environment due to relativistic solar energetic

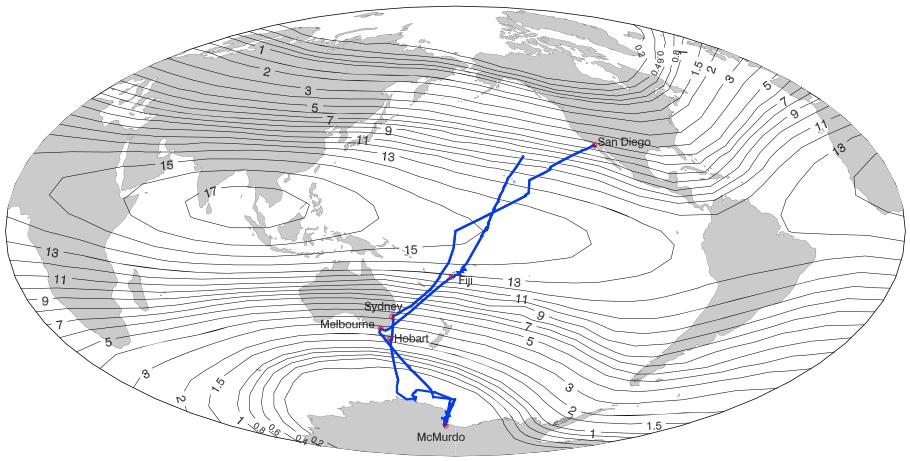


Figure 1. Track of the USCGC Polar Star for the 1995–1996 survey, superimposed on contours of vertical cutoff rigidity. Numbers give vertical cutoff rigidity in GV. This survey carried a standard neutron monitor (3NM64) and three bare neutron detectors, permitting a direct comparison of their response to primary cosmic rays.

particles and galactic cosmic rays and their variations associated with solar activity, and for applications concerning space weather and space radiation.

Such observations can be complemented by measurements using bare neutron counters that lack the reflector and lead producer of standard neutron monitors, making them also sensitive to atmospheric neutrons of $\leq$10 MeV. Such detectors are widely used to detect soil moisture (Zreda et al., 2008), for nuclear threat detection (Kouzes et al., 2008), and to obtain spectral information on solar energetic particles.

From a fixed location, a standard neutron monitor (NM64) count rate alone cannot be used to measure the energy spectrum of cosmic rays. However, since a bare counter (BC) has a different energy response from an NM64, operating them together provides some knowledge of the spectrum (e.g., Bieber & Evenson, 1991; Bieber et al., 2013) while avoiding the systematic errors of comparing count rates from different locations (Figure 2 of Ruffolo et al., 2016). The accuracy of this method requires knowing how the energy responses of the different types of detector are related.

In this work we focus on developing optimal methods for extracting the response function of three BCs that were operated aboard the U.S. Coast Guard icebreaker *Polar Star* along the route illustrated in Figure 1. This voyage was one of a series of latitude surveys in which the magnetic field of the Earth was used as a spectrometer to explore the time dependence of the spectrum of cosmic rays striking the atmosphere (Nuntiyakul et al., 2014). All of these surveys carried a NM64 neutron monitor with three counter tubes, that is, a 3NM64, and in addition the survey from San Diego, USA, to McMurdo, Antarctica, and back during a voyage of ~4 months from 6 November 1995 to 20 March 1996 carried three bare detectors. To our knowledge, there have been two previously published bare surveys: the 1976 survey (Stoker et al., 1980) did not extend to polar latitudes, and the 1996 survey (Dorman et al., 2000; Villoresi et al., 2000) was conducted with unmoderated bare detectors. Therefore, direct comparison of results is difficult.

2. Methodology

2.1. Latitude Surveys and Response Functions

The count rate $N(t)$ of a ground based detector resulting from the impact of cosmic rays at the top of the atmosphere is described by

$$N(\Theta,\Phi,h,t) = \int_0^\infty \left[\sum_i J_i(P,t)\, Y_i(P,h)\right] T(P,\Theta,\Phi,t)\, \mathrm{d}P, \tag{1}$$

where J_i is the Galactic cosmic ray spectrum for primary cosmic rays of particle type i near Earth expressed as a function of rigidity (P) and time (t). The primary cosmic rays are approximately 90% protons (in particle number) while 9% are alpha particles (helium nuclei) and 1% are the nuclei of heavier elements; their fluxes near Earth include variations with the 22-year solar magnetic and 11-year solar activity cycles as the result of

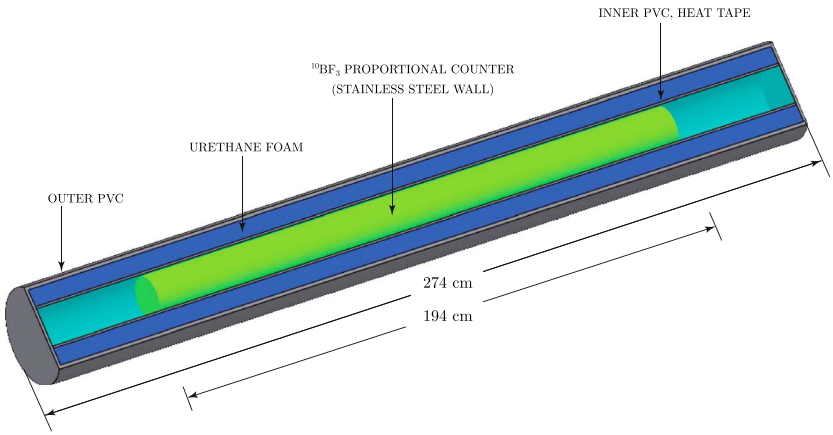


Figure 2. Rendered sketch of the "bare" neutron counter configuration used in this work. Each BP-28 neutron-sensitive proportional counter was operated inside a 20-cm-diameter PVC pipe covered with heat tape and thermally insulated by foamed-in-place polyurethane inside a larger, 30 cm diameter PVC pipe. Three such bare counters and a three-counter neutron monitor were operated along the survey route shown in Figure 1.

interactions with the solar wind and magnetic fields in interplanetary space. (Here we neglect the cosmic ray anisotropy, which is usually $\lesssim 1\%$.) The yield function Y_i for primary particles of type i, a function of rigidity (P) and atmospheric depth (h), is the actual relationship between the cosmic ray flux at the top of atmosphere and the observed count rate from the detectors. The transmission function T_i describes the transmission through the magnetosphere of the Earth. It is a function of particle rigidity (P), latitude (Θ) and longitude (Φ) of the detector location, and time (t).

At a given latitude and longitude, the effective cutoff rigidity for transmission through Earth's magnetic field depends on the arrival direction of each primary cosmic ray described by the local zenith and azimuthal angles. However T_i can be approximated by a step function at a single cutoff rigidity P_c, that we call the *apparent cutoff rigidity*. With the assumption that the transmission is a step function, the count rate relation becomes

$$N(P_c, h, t) = \int_{P_c}^{\infty} \sum_i J_i(P, t)\, Y_i(P, h)\, \mathrm{d}P. \tag{2}$$

The apparent cutoff used in this work considers both vertically incident particles and obliquely incident particles (Clem et al., 1997); this is calculated individually at 1-hr intervals at the actual position of the ship with a time-dependent model of the magnetic field according to an *efficient* method (Bieber et al., 1997). We use a particle propagation code from the Bartol Research Institute (Lin et al., 1995) together with an accurate model of the terrestrial magnetic field including any field disturbance present as indicated by the K_p index value at the time. K_p quantifies variations of the horizontal component of the magnetic field of the Earth as an integer in the range 0–9, that is, a lower number indicates quiet conditions and a higher number indicates a stronger geomagnetic storm (Thomsen, 2004).

The differential response function (DRF) is defined as the negative of the derivative of the count rate as a function of cutoff rigidity. The most common type of analysis for measuring a response function is the Dorman et al. (1969) analysis, in which corrections are first applied to the data points, then a parameterized function of apparent geomagnetic cutoff rigidity, termed a *Dorman function*, is fitted to the data:

$$N(P_c) = N_0 \left(1 - \mathrm{e}^{-\alpha P_c^{-\kappa}}\right), \tag{3}$$

where N_0, α, and κ are unphysical parameters that provide a good representation of the integral response function N, which can be analytically differentiated to determine the DRF:

$$N(P_c) = \int_{P_c}^{\infty} \mathrm{DRF}\,(P)\, \mathrm{d}P, \tag{4}$$

$$\mathrm{DRF}\,(P) = N_0 \alpha P^{-\kappa-1} \kappa\, \mathrm{e}^{-\alpha P^{-\kappa}}. \tag{5}$$

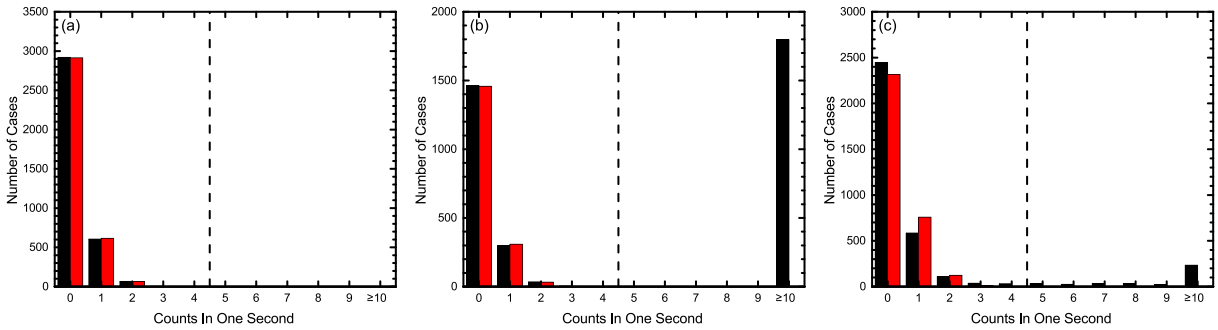


Figure 3. Examples of 1-s count distributions (black) and Poisson distributions based on the rates of 0–4 counts (red), each for 1 hr from one bare counter. (a) This measured distribution closely matches a Poisson distribution. (b) Here many seconds had multiple counts, but the distribution of 0–4 counts closely matches a Poisson distribution. (c) Ambiguous data. In all cases only the data to the left of the dashed line were used in further analysis.

From equations (2) and (4), we can express the DRF as the summed product of $J_i(P, t)$ and $Y_i(P, h)$:

$$\text{DRF}\,(P) = -\left[\frac{dN}{dP_c}\right]_P = \sum_i J_i(P, t)\, Y_i(P, h). \tag{6}$$

2.2. Instrumentation

The 1995 latitude survey employed two types of neutron detectors, three bare neutron detectors and a 3NM64 neutron monitor. The three BCs were installed exposed on an upper deck of the ship, whereas the 3NM64 was installed in an insulated shipping container (called the "TasVan"). Nuntiyakul et al. (2014) provide a detailed description of the TasVan and the series of latitude surveys. In summary, the detectors are Chalk River BP-28 proportional counter cylinders filled with boron trifluoride gas (enriched in the isotope ^{10}B). The boron nuclei react with neutrons and undergo nuclear fission. The reaction products (^{4}He and ^{7}Li) ionize the gas and eventually produce electrical pulses on a central anode wire maintained at ground, while a cylindrical outer cathode is at a potential of about −2,800 V.

Unlike for an NM64, there is no standard design for a bare neutron counter. The detectors discussed in the present work were prototypes for a system that was intended for outdoor deployment at the South Pole. The design used 2-lb density (2 lb/ft^3 ∼ 32 kg/m^3) foamed-in-place polyurethane insulation for thermal control between an inner, 8" thin-wall PVC pipe (outer diameter 219 mm, thickness 4.75 mm) and an outer, 12" schedule-40 PVC pipe (outer diameter 324 mm, thickness 10.3 mm), which also served as a moderator for high-energy secondary neutrons. The standard polyethylene moderator on a BP-28 was not used. A rendered drawing of the detector is shown in Figure 2.

3. Data Reduction

3.1. Overview

Throughout this work all the dates during the survey will be referred to as "day of the year of 1995" (DOY1995). The 12th generation International Geomagnetic Reference Field (IGRF12) and the 1989 revision of the Tsyganenko (1987) model were used for calculating the cutoff rigidity. Numerical results for the 3NM64 in the present work differ slightly from those presented by Nuntiyakul et al. (2014) for three main reasons: (1) data intervals were selected such that they had good data in both the BCs and the 3NM64 whereas the earlier study only considered the 3NM64; (2) no corrections for short term modulation based on the McMurdo count rate were applied in this work; and (3) no normalization of the data to the McMurdo count rate was performed in this work.

3.2. Initial Processing

The most serious problem encountered in the data was mutual interference of the instrument with communications equipment on the ship. This equipment was used only when at sea, so any attempt at debugging the problems during port calls was not possible. However, a relatively simple realization enabled the extraction of a useful data set. Our data were recorded with one second time resolution together with clinometer readings to allow for possible corrections due to the varying orientation of the ship in rough seas. Looking closely at the 1-s data, we found that the noise was often quite "bursty" with seemingly unaffected seconds interspersed with seconds recording hundreds of counts.

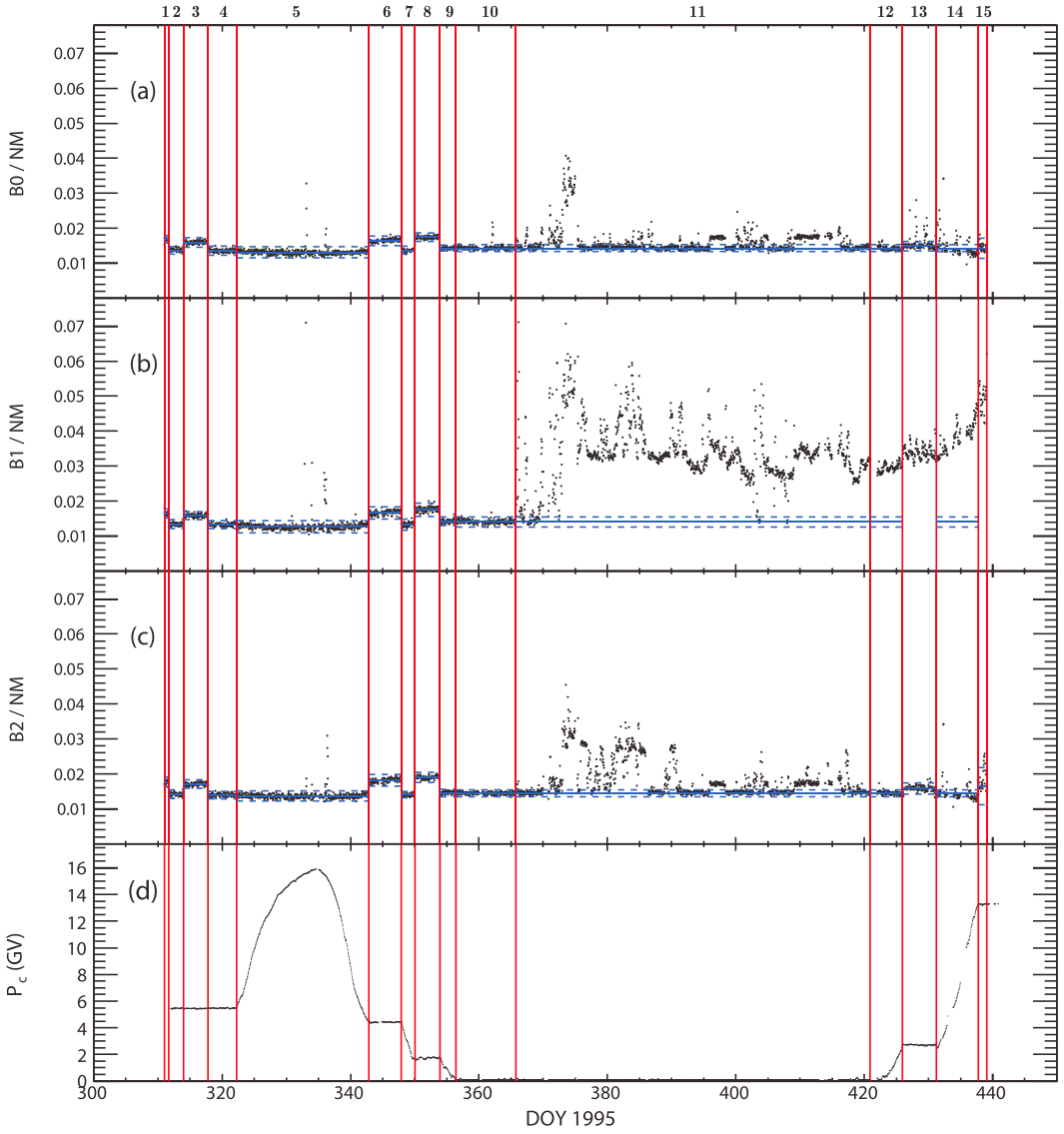


Figure 4. Summary of hourly averaged data as a function of time. (a)–(c) Ratios of individual bare detector count rates to 3NM64 count rate. Red vertical lines define 15 time periods used in the analysis. In each time period, the horizontal blue solid line shows the reference value $\langle B_i/\mathrm{NM}\rangle$ and blue dashed lines illustrate the $\pm 3\sigma$ interval around the reference. (d) Apparent geomagnetic cutoff rigidity P_c.

We therefore made histograms of the 1-s readings for each tube for each hour of the survey, with typical examples shown in Figure 3. The observed distribution of counts is shown in black whereas the red shows the Poisson distribution expected based on the average rate over the first five channels. Figure 3a shows an hour with essentially no noise—typical of all of the time spent in port when the investigators had access to the equipment. In this case all of the individual measurements fall nicely on the distribution. Figure 3b shows a case where there is a clean Poisson component plus a clearly separated noise component. In Figure 3c the separation fails, for reasons that we have been unable to establish. We investigated automatically extracting data from noisy hours based on a quantitative test for deviations from a Poisson distribution in the first five channels but no clear method emerged. Instead, we prepared our basic data set with 1-hr resolution by taking averages over the first five channels (those left of the dashed lines) independent of the quality of fit to a Poisson distribution. We deferred rejecting bad hours to a later stage of analysis.

The data set thus obtained is plotted in Figure 4. In this figure we show hourly averages of BC count rates divided by NM count rates (where NM means the summed count rate of the three counters in the 3NM64), without any further correction. On this plotting scale the small variations in the ratios due to cutoff variation

Table 1
Reference BC to NM Count Rate Ratios

Period	Start DOY	Environment	$\langle B_0/\mathrm{NM}\rangle \pm \sigma$	$\langle B_1/\mathrm{NM}\rangle \pm \sigma$	$\langle B_2/\mathrm{NM}\rangle \pm \sigma$
TP1	311.000	San Diego	0.0169 ± 0.0003	0.0165 ± 0.0004	0.0177 ± 0.0005
TP2	311.667	Naval maneuvers	0.0137 ± 0.0004	0.0134 ± 0.0004	0.0142 ± 0.0004
TP3	314.000	San Diego	0.0159 ± 0.0004	0.0159 ± 0.0004	0.0171 ± 0.0004
TP4	317.833	Naval maneuvers	0.0136 ± 0.0004	0.0133 ± 0.0004	0.0139 ± 0.0003
TP5	322.250	Open sea	0.0131 ± 0.0005	0.0127 ± 0.0006	0.0137 ± 0.0005
TP6	342.875	Sydney	0.0164 ± 0.0005	0.0166 ± 0.0006	0.0181 ± 0.0005
TP7	347.917	Open sea	0.0137 ± 0.0004	0.0133 ± 0.0005	0.0140 ± 0.0003
TP8	350.042	Hobart	0.0174 ± 0.0004	0.0176 ± 0.0006	0.0190 ± 0.0005
TP9	353.917	Open sea	0.0143 ± 0.0003	0.0143 ± 0.0004	0.0145 ± 0.0004
TP10	356.375	Open sea	0.0143 ± 0.0003	0.0141 ± 0.0005	0.0145 ± 0.0003
TP11[a]	365.792	Mixed	0.0143 ± 0.0003	0.0141 ± 0.0005	0.0145 ± 0.0003
TP12[a]	420.917	Open sea	0.0143 ± 0.0003	0.0141 ± 0.0005	0.0145 ± 0.0003
TP13	425.917	Melbourne	0.0149 ± 0.0004	—	0.0158 ± 0.0006
TP14[a]	431.208	Open sea	0.0143 ± 0.0003	0.0141 ± 0.0005	0.0145 ± 0.0003
TP15	437.792	Fiji	0.0142 ± 0.0010	—	0.0166 ± 0.0018

[a]Using reference values measured for TP10.

are not readily visible. We term the count rates of the three BCs as B_0 for the left BC, B_1 for the center BC, and B_2 for the right BC. The reference values are explained in the following section. The figure also shows the calculated apparent cutoff rigidity as a function of time.

The shown data set, which includes the correction for instrumental interference explained above, still contains many clear outliers with a count rate enhanced beyond 3σ above the reference value, especially for the center BC after DOY 370. For those outlier hours with high hourly average count rates, the counts-per-second distributions show no recognizable noise component or signatures of double pulsing, so we conjecture that some change in the surroundings may have caused the neutron flux to be enhanced (possibly materials stored in the space immediately under the detectors). In any case, only data within $\pm 3\sigma$ of the reference value are selected for further analysis, as specified below.

Table 2
Reference BC to BC Count Rate Ratios

Period	Start DOY	Status	$\langle B_0/B_1\rangle \pm \sigma$	$\langle B_1/B_2\rangle \pm \sigma$	$\langle B_2/B_0\rangle \pm \sigma$
TP1	311.000	San Diego	1.015 ± 0.03	0.933 ± 0.04	1.053 ± 0.04
TP2	311.667	Naval maneuvers	1.032 ± 0.04	0.939 ± 0.03	1.033 ± 0.03
TP3	314.000	San Diego	1.001 ± 0.03	0.926 ± 0.03	1.075 ± 0.04
TP4	317.833	Naval maneuvers	1.028 ± 0.04	0.947 ± 0.03	1.030 ± 0.04
TP5	322.250	Open sea	1.034 ± 0.06	0.927 ± 0.05	1.045 ± 0.05
TP6	342.875	Sydney	0.987 ± 0.04	0.916 ± 0.03	1.106 ± 0.04
TP7	347.917	Open sea	1.027 ± 0.05	0.957 ± 0.04	1.026 ± 0.04
TP8	350.042	Hobart	0.991 ± 0.04	0.926 ± 0.04	1.090 ± 0.03
TP9	353.917	Open sea	1.008 ± 0.04	0.975 ± 0.03	1.018 ± 0.03
TP10	356.375	Open sea	1.018 ± 0.03	0.976 ± 0.04	1.013 ± 0.03
TP11[a]	365.792	Mixed	1.018 ± 0.03	0.976 ± 0.04	1.013 ± 0.03
TP12[a]	420.917	Open sea	1.018 ± 0.03	0.976 ± 0.04	1.013 ± 0.03
TP13	425.917	Melbourne	—	—	—
TP14[a]	431.208	Open sea	1.018 ± 0.03	0.976 ± 0.04	1.013 ± 0.03
TP15	437.792	Fiji	—	—	—

[a]Using reference values measured for TP10.

Table 3
Pressure Coefficient of BC to NM Count Rate Ratios for Fixed Stations

Location	Epoch	Altitude (m)	P_c (GV)	b (10^{-4} mmHg^{-1})	BC rate[a](s^{-1})	NM rate[a](s^{-1})	Ratio
Doi Inthanon	2007–2013	2560	17.4	3.30 ± 0.49	6.0	34.0	0.176
Newark	2015–2016	40	2.3	9.13 ± 0.06	2.7	12.0	0.225
McMurdo	2016	48	< 0.1	2.16 ± 0.09	3.2	16.7	0.192
South Pole, BF_3	1990–2004	2820	< 0.1	4.10 ± 0.16	15.0	87.0	0.172
South Pole, ^{3}He	2005–2016	2820	< 0.1	2.94 ± 0.07	12.5	103.0	0.121

[a]Average rates per tube.

3.3. Data Cleaning Based on Neutron Monitor Count Rate

The selection of usable data (data *cleaning*) and the adjustment of bad or missing individual counter data (data *correction*) are performed based on BC-to-NM ratios (B_i/NM) and BC-to-BC ratios (B_i/B_j).

We start by choosing appropriate time periods during the 1995 survey year for which data were taken in a relatively stable environment. The 15 time periods used (TP1 to TP15) are indicated in Tables 1 and 2, and shown in Figure 4. Data cleaning is then applied separately for each time period. This division into time intervals is based on the locations near which the ship passed, that is, San Diego, Sydney, Hobart, McMurdo, Melbourne, and Fiji, as well as on apparent step-like changes in the ratio values elsewhere.

For each time period we generated histograms of the hourly B_i/NM values to characterize and remove outliers. Figures 4a–4c illustrate the individual B_i/NM ratios as a function of time. The red vertical lines show the division in time periods. The blue solid horizontal lines illustrate the B_i/NM *reference values* $\langle B_0/\mathrm{NM}\rangle$, $\langle B_1/\mathrm{NM}\rangle$, and $\langle B_2/\mathrm{NM}\rangle$. In most cases, these were defined as the mean of a Gaussian fit to the ratio histogram for each time period. For three time periods, namely TP11, TP12, and TP14, we used the reference calculated during TP10 because it was noticed that the noise was too high for the center BC (B_1). Using the TP10 ratio reference for those three problematic time periods, we avoided bias in the data that could induce further analysis errors. For the $\langle B_1/\mathrm{NM}\rangle$ ratio reference, during TP13 and TP15 data were also noisy but no appropriate reference based on another time period with similar environment could be identified, so those intervals have no reference available. The blue horizontal dashed lines illustrate plus and minus three standard deviations from the reference for each time period, also based on the Gaussian fit. The $\langle B_i/\mathrm{NM}\rangle$ ratio reference values and their standard deviations σ for the 15 time periods are also shown in Table 1. B_i/NM data points lying outside the range defined by 3 standard deviations (i.e., $\pm 3\sigma$) from the reference were considered to indicate bad data and the count rate B_i was then corrected (if possible) as explained in the next section or removed before subsequent analysis.

3.4. Data Correction Based on BC Ratios

The rough and changing conditions on board the ships caused the response of individual BCs to occasionally change, become noisy, or even stop completely. In order to correct for these effects during the surveys, we used the inherent redundancy of the three bare detectors.

The histograms of individual BC ratio values (B_0/B_1, B_1/B_2, and B_2/B_0) were plotted for each time period (except for periods with no appropriate reference for the B_i/NM ratio, as mentioned above). For TP1–TP10, reference values were calculated for these BC ratios based on a fit to a Gaussian, but for TP11, TP12, and TP14 we used the BC ratio reference of TP10 instead. For TP13 and TP15, the BC ratios were not used because the center tube had bad counts during the whole time period and there was no other appropriate reference.

The BC ratio references $\langle B_0/B_1\rangle$, $\langle B_1/B_2\rangle$, and $\langle B_2/B_0\rangle$ and their standard deviations for the 15 time periods are shown in Table 2. We defined the range of three standard deviations ($\pm 3\sigma$) from the reference values $\langle B_i/B_j\rangle$ to select good data points (count rates B_i and B_j that needed no further correction) or identify count rates that needed to be corrected. The reference values for the BC ratios were then used to correct those count rates, using the same method as explained in Nuntiyakul et al. (2014). The count rates of the three bare tubes for each hour (B_1, B_2, and B_3) were corrected if the BC ratio data were outside the 3σ range and there was a valid BC ratio reference for calculating the missing data. We calculated a corrected count rate from the actual count rate of the properly operating detectors. If only one tube was ignored, we calculated the corrected count rate based on the measurement in the other two tubes and the ratio reference values. If two tubes were

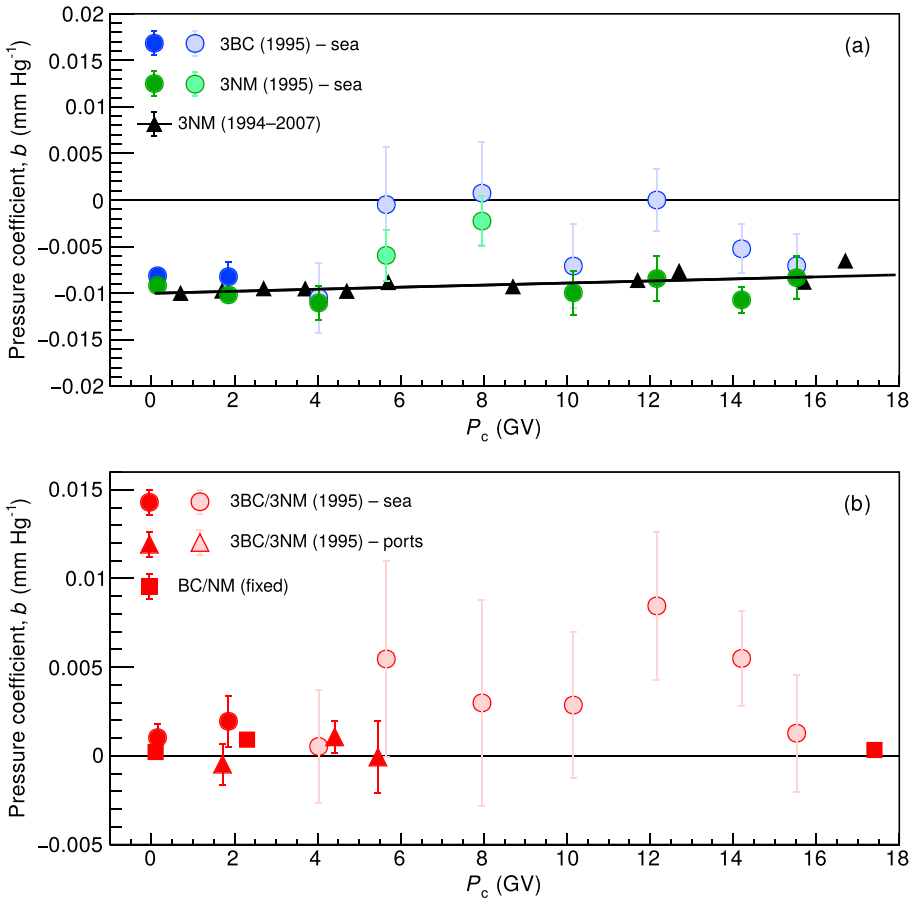


Figure 5. Pressure coefficient *b* (defined in text) as a function of apparent geomagnetic cutoff rigidity P_c. (a) Black triangles and heavy line: 3NM64 from 13 years of summed data (Nuntiyakul et al., 2014). Green circles: 3NM64 from 1995 data. Blue circles: three bare counters (3BC) from 1995 data. (b) Red circles: 3BC/3NM64 ratio in 1995, open sea. Red triangles: 3BC/3NM64 ratio in 1995, near land. Red squares: Fixed locations. Pastel shaded points are less accurate, with standard errors of *b* larger than 0.0025 $mmHg^{-1}$.

removed, we similarly used the remaining tube to determine the corrected count rates. If none of the tubes were operating properly, that hour was considered a data gap.

3.5. Barometric Pressure Correction

Although Stoker and Raubenheimer (1985) report that there is no difference between the barometric pressure correction coefficient for BCs and NM64, they have been measured to be different for the neutron monitor at Doi Inthanon, Thailand (Muangha, 2013). The first entry in Table 3 gives the result of that analysis. As the correction for variation in barometric pressure is critical to proper interpretation of the data, we carefully investigated this with the data from the 1995 survey.

We define a pressure coefficient (*b*) as the slope of a linear fit to the logarithm of counting rate as a function of barometric pressure. To control for short term variations, we extract this by calculating the deviation of the hourly average of each quantity from the overall average for that day.

We determined *b* separately for the 3NM64 and the BCs, with the data divided into bins of apparent cutoff rigidity. The width of each bin was determined by the number of data points available. Results of this analysis are shown in Figure 5a, along with the more statistically accurate determinations based on 13 years of data in Nuntiyakul et al. (2014). We also calculated pressure coefficients for the ratios of the summed count rate of the three BCs (3BC) to that of the 3NM64. Since there is no evidence for a major difference in coefficients from the survey data alone, in the present analysis we have corrected both 3BC and 3NM64 with the well-determined coefficient from the 13-year data set for the 3NM64.

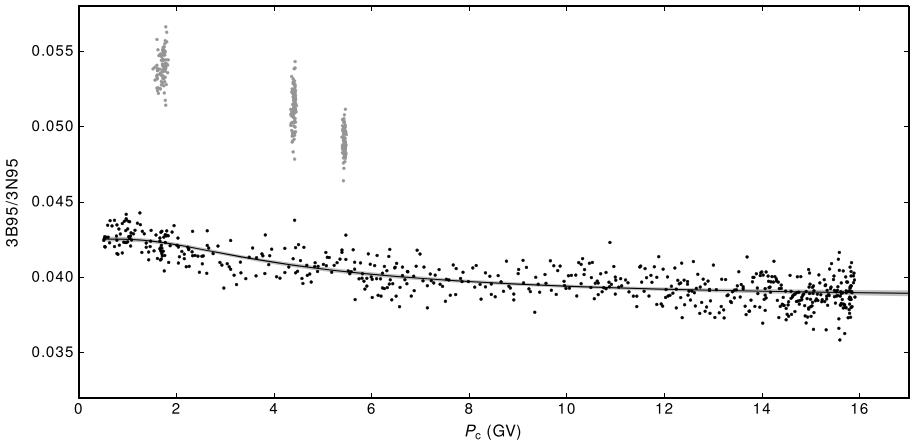


Figure 6. BC/NM ratio in 1995 as a function of apparent geomagnetic cutoff rigidity P_c. Black dots: ship in open sea. Gray dots: port calls at Hobart (P_c = 1.71 GV), Sydney (P_c = 4.41 GV), and San Diego (P_c = 5.45 GV). Line: ratio of Dorman functions shown in Figures 7a and 7b. Each dot represents a 1-hr data point.

We also extracted coefficients from historical data for two different land-based BC configurations and the 3 × 1NM64 neutron monitor at South Pole and for BCs and an 18NM64 at Doi Inthanon, Thailand. In addition, we set up BCs at Newark, Delaware (three spare BP-28 counters) and McMurdo (one BP-28 removed from the NM64) to investigate this issue. Results are plotted in Figure 5b and given in detail in Table 3, along with various parameters characterizing the stations. Here *b* refers to the pressure coefficient of the ratio of the BC and NM64 count rates per tube, which corresponds to the difference in pressure coefficients of the two types of neutron detectors. All of the land-based installations show small positive coefficients. The value at Newark is significantly larger than those at South Pole, McMurdo, and Doi Inthanon. The building construction (masonry with slate roof) at Newark is different from the light construction at the other stations. In general, there is no specific pattern with altitude or cutoff; rather the data provide an additional caution regarding the environmental sensitivity of bare detectors. In other words, the observed pressure coefficient of the shipborne BC to NM64 count rate ratio is consistent with zero, given the uncertainties.

3.6. Temperature Correction

We investigated the need for a temperature correction. The BCs were in a different location from the three neutron monitors and neither had very good temperature control. We know from Evenson et al. (2005) that temperature correction coefficients are different for NM64s operated with $^{10}BF_3$ and ^3He detectors. Therefore we looked for temperature effects by searching for correlations of the measured ratios with differences in the measured tube temperatures. Within the statistical accuracy permitted by the data, we could not find any. Therefore we did not attempt a temperature correction for the present study.

3.7. Port Effects

The extreme sensitivity of bare detectors to the environment is clearly illustrated in Figure 6, which shows the ratio of the BC to NM count rate after all of the corrections discussed above have been applied. Substantial increases in the ratio occur whenever the ship is in port, as was also found by Villoresi et al. (2000). This can be explained by a higher density of albedo neutrons near solid ground compared with open water, and the fact that neutron detectors lacking a reflector (such as the BCs) are much more sensitive to these environmental neutrons than the standard NM64. We therefore classified the data carefully so as to be certain that the results we report are representative of the open ocean. Times "near port" were defined to be when the ship was close to port and "ocean" times were when the ship was away from land. This consideration was used when establishing the 15 time periods as shown in Figure 4 divided by red vertical lines. As noted above, the BC/NM ratio was high near ports but lower when the ship was at sea. For example, around San Diego (P_c = 5.45 GV, TP1 and TP3) the ship moved to near port twice, once at Sydney (P_c = 4.41 GV, TP6), and once at Hobart (P_c = 1.71 GV, TP8). Data from port calls near McMurdo (two steps in TP11), Melbourne (TP13), and Fiji (TP15) are not included in our analysis, according to the procedure described in section 3.4, because they had no ratio reference to clean the data.

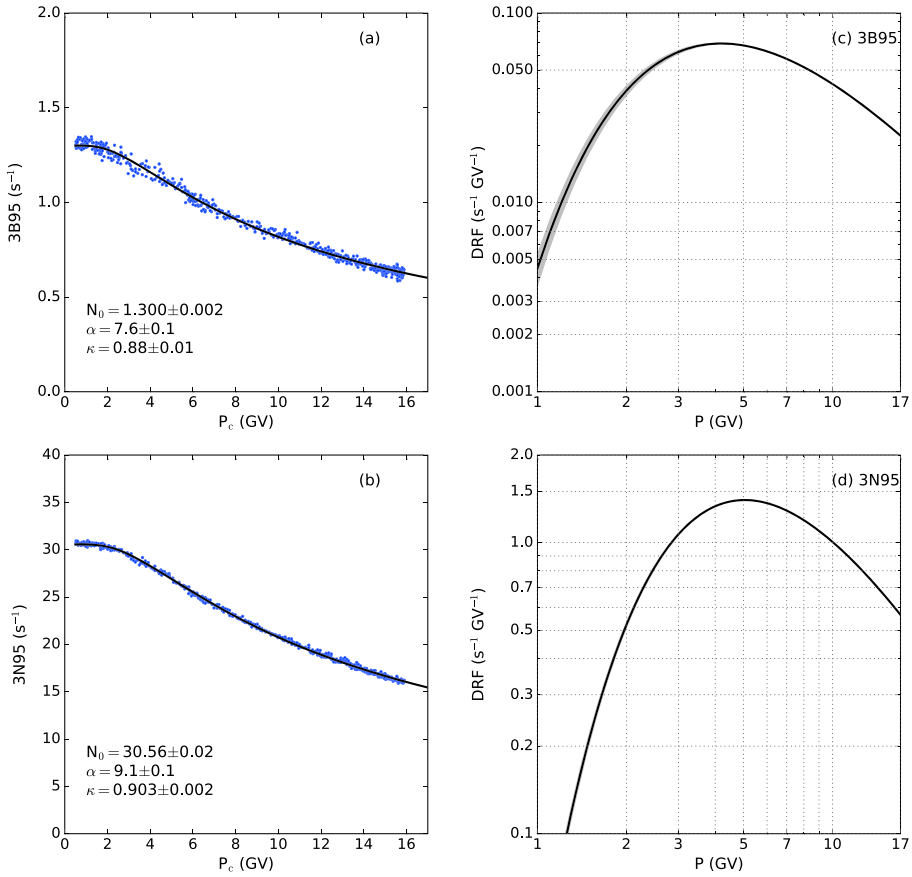


Figure 7. Dorman function fits to (a) bare and (b) neutron monitor data separately; (c) and (d) show the resulting differential response functions (DRFs).

4. Discussion

4.1. 1995 Survey

To quantify the dependence shown in Figure 6 we performed a fit to a Dorman function (Dorman et al., 1969) to the data for 3BC and 3NM64 separately. To do the fit we minimize the least squares function using the Levenburg-Marquardt algorithm and provide estimates for the statistical errors in the determination of the parameters from the scatter of the data points about the resulting fit. The results of the fits are shown in Figure 7. In this case, as in subsequent ones, we show the best fit as a solid line and the (two sigma) range of possible fits as a shaded area. In many cases the shaded area cannot be distinguished from the solid line. The parameters of these fits, along with other Dorman fit parameters discussed later, are summarized in Table 4. This Table also defines the nomenclature used in further discussions of these fits. The present analysis of the 3NM64 count rate from the 1995 survey differs from that of Nuntiyakul et al. (2014) for the same survey in that the present data are restricted to time periods with usable BC data, without correction for short-term cosmic ray variations and without a normalization factor of 1.015 to account for the 3NM64 location on the ship relative to other survey years.

DRFs, as well as the fit parameters, depend on the physical size of the detectors. To compare the inherent response of the 3BC and 3NM64, some normalization is necessary. Various normalizations are proposed in the literature, but for our purposes we adopt a rather simple one, namely, setting the parameter N_0 to one. This corresponds to normalizing the counting rate of a detector to 1.0 at zero cutoff. With this normalization we compare our DRF for the BCs to that for monitors in Figure 8. As expected, the response of the BCs is significantly greater than that of the monitors at low rigidity.

4.2. Comparison with 1976 and 1996 Surveys

Figure 9 compares our results with various interpretations of the data from the 1976 survey (Stoker et al., 1980) and the 1996 survey (Dorman et al., 2000). The 1995 and 1976 surveys were performed under remarkably sim-

Table 4
Dorman Function Fit Parameters

Configuration	Analysis	Survey year	Tag	N_0 (s^{-1})[a]	α	κ
3NM64	This Work	1995	3N95	30.56(2)	9.1(1)	0.903(2)
3NM64	Nuntiyakul et al. (2014)	1995	—	30.9	9.05	0.899
3BC	This Work	1995	3B95	1.300(2)	7.6(1)	0.88(1)
1BC	Stoker (1985) (A)	1976	1B76A	157.68[b]	7.32	0.898
1BC	Stoker (1985) (B)	1976	1B76B	157.68[b]	7.85	0.940
1BC	This Work	1976	1B76C	197.9(9)[b]	8.7(3)	0.93(1)
1NM64-N1	This Work	1976	1N76A	189.6(5)[b]	9.2(2)	0.926(9)
1NM64-N2	This Work	1976	1N76B	192.0(7)[b]	9.4(3)	0.94(1)
1NM64-N1	Caballero-Lopez and Moraal (2012)	1976	1N76C	8.6806	8.953	0.916
1NM64-N1	Stoker (1985)	1976	1N76D	151.67[b]	8.41	0.894
2BC	Dorman et al. (2000)	1996	2B96	—	9.694(37)	0.9954(38)
3NM64	Dorman et al. (2000)	1996	3N96	—	10.275(23)	0.9615(21)

[a]Figure in parenthesis is the 1σ uncertainty on the last decimal. Uncertainties were not provided for the previously published values. [b]Scaled units (not s^{-1}).

ilar solar modulation conditions. The solar modulation parameters calculated from Usoskin et al. (2017) were ~514 and ~518 MV, respectively, for the 1976 survey and 1995 survey. Averaged over the survey, the McMurdo neutron monitor count rates were within 2% of each other, and both surveys took place in epochs of positive solar magnetic polarity. Therefore, we compare the results directly, without any adjustment for changed modulation. Figure 9a illustrates leaded neutron monitor DRFs. (The 3NM64 DRF for 1995 from Nuntiyakul et al. (2014) is not shown here because it is indistinguishable from the one determined in this paper.) Two different designs of leaded monitors were used in 1976, denoted N1 and N2 in Table 4. We show four interpretations of the 1976 data. The first two result from applying our Dorman fit procedure to the summary data for N1 and N2 in Table 4 of Potgieter et al. (1980). We also show interpretations by Caballero-Lopez and Moraal (2012) and from the caption of Figure 1 of Stoker (1985). Because of various normalizations of the data the values of the parameter N_0 cannot be compared directly. The DRF for the 1996 survey uses the preferred Dorman functions from Dorman et al. (2000). We assume here that we can compare directly the DRF without solar modulation correction. Indeed, the 1996 survey was realized from December 1996 to March 1997 with an average solar modulation of 504 MV (calculated from updated parameters from Usoskin et al., 2017). This is very similar to the above-mentioned values for the 1976 and 1995 surveys.

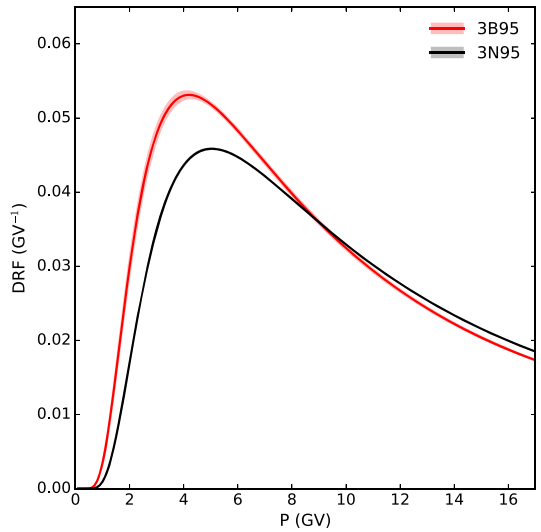


Figure 8. Comparison of the normalized differential response functions (bare neutron detectors and standard 3NM64) for the 1995 latitude survey.

The different interpretations of the 1976 NM64 data are all rather consistent, but all show a slightly higher response at low rigidity than the 1995 data. There is no evidence that this difference might be due to different primary spectra but it is possible that it represents a difference due to the use of 1NM64 detectors (of two slightly different designs) in the 1976 survey whereas the 1995 survey used a 3NM64. It is well known that the "outer" detectors in a multi-detector NM64 show a significantly lower count rate than the inner ones as they are, in effect, surrounded by less lead (Mangeard, Ruffolo, Sáiz & Madlee et al., 2016). In our survey, the average end-to-center ratio was 0.891. Based on a simple fit, it decreased by 0.002 from 0 to 16 GV cutoff, a result different from zero by slightly more that one standard deviation. We were able to reprocess simulations from a recent paper by Mangeard, Ruffolo, Sáiz and Nuntiyakul et al. (2016) to make a specific prediction of these quantities. The end-to-center ratio is reproduced to within 1%, with a predicted decline of 0.0032. We therefore think it is at least plausible that the 1NM64 may have slightly "softer" response function than a 3NM64. This is of interest to us in a practical sense, since the installation at South Pole is in fact three 1NM64 units, individually insulated and heated, but mounted on a common platform. We are currently running more detailed simulations to investigate the effect of this configuration at South Pole.

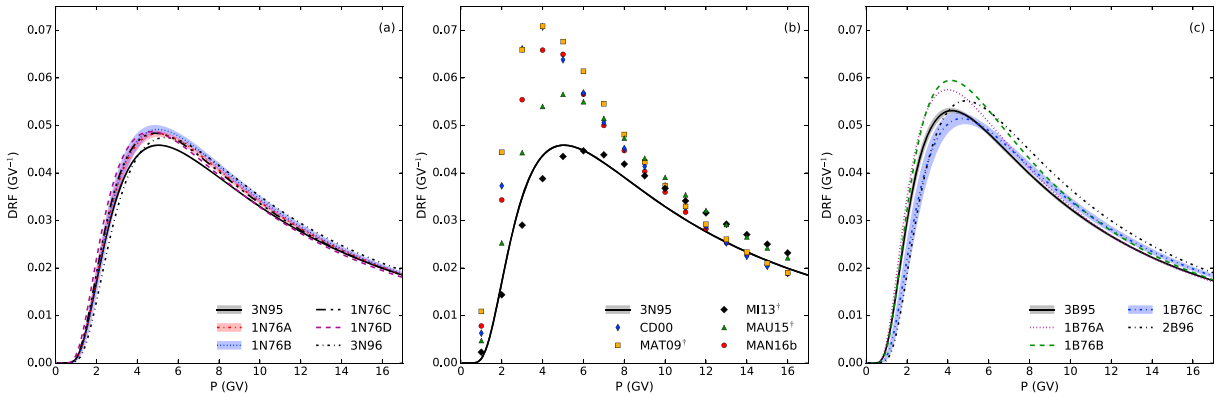


Figure 9. (a) Comparison of leaded neutron monitor response functions determined on latitude surveys. (b) Calculated response functions compared with the 1995 survey result. See text for details of this calculation. (c) Comparison of bare neutron detector response functions. Nomenclature for different surveys is defined in Table 4.

Figure 9b compares the observed normalized DRF of the 3NM64 of 1995 latitude survey with several calculations using recent computed models of "yield functions" (count rates as a function of rigidity and type of the primary particle at the top of the atmosphere). We used the model of Galactic cosmic ray spectra based on the local interstellar spectra (LIS) of proton and helium as proposed by Ghelfi et al. (2016), Ghelfi and Barao et al. (2017) and the force-field model of solar modulation from Gleeson and Axford (1968). For the period of the survey, the modulation parameter corresponding to this LIS was determined using the method presented in Ghelfi and Maurin et al. (2017) and was about 580 MV (the value was extracted from the database http://lpsc.in2p3.fr/crdb). Note that this is preferred for this purpose but it is different from the Usoskin et al. (2017) parameters used elsewhere in this paper. The nomenclature for the five simulated yield functions used in this work is as follows: CD00 from Clem and Dorman (2000), MAT09 from Matthiä et al. (2009), MI13 from Mishev et al. (2013), MAU15 from Maurin et al. (2015), and MAN16b from Mangeard, Ruffolo, Sáiz and Nuntiyakul et al. (2016). For MAT09 and MI13, the parametrizations of Maurin et al. (2015) were used (marked with a dagger in the Figure's legend). The differences between simulations are clearly visible with an overall agreement within 50%. Below 10 GV, MI13 provides a better estimate of the normalized DRF than the other models. Above 10 GV, the simulated results CD00, MAT09, and MAN16b provide a better estimate. More details about comparison between simulated yields can be found in Maurin et al. (2015) and Caballero-Lopez (2016).

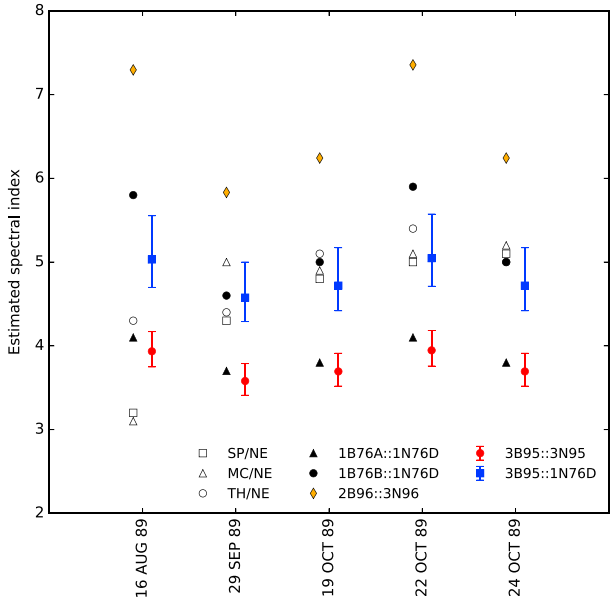


Figure 10. Comparison of estimated spectral indexes for GLEs of 1989. Black markers are taken unchanged from Bieber and Evenson (1991). Estimated spectral indices calculated in this article are shown in colored markers with error bars. Nomenclature for different surveys is defined in Table 4. More details are available in the text.

Figure 9(c) compares determinations of the BC response. Our result for 1995 agrees reasonably well with our analysis of the raw data for 1976 tabulated by Potgieter et al. (1980). What is rather surprising is the difference from the interpretation of Stoker (1985), where the "A" and "B" analyses were presented as an envelope of all possible fits to the data. At present, we have no specific comment on this apparent discrepancy. However as we have used the Stoker (1985) "B" results extensively in our previous work to use the BC/NM count rate ratio at South Pole to infer the spectral index of relativistic solar particles (Bieber & Evenson, 1991; Bieber et al., 2002, 2013; Sáiz et al., 2008), we have examined the extent to which this difference might influence our previous conclusions. Figure 10 is based on Figure 1 of Bieber and Evenson (1991), which compared spectral indices determined from NM64s at different P_c with the same events analyzed using the monitors and bare counters at South Pole alone. In this analysis, based on ratios of count rate increases, the implicit assumption is that the entire DRF scales with altitude with the same barometer coefficient—in other words, the entire altitude dependence may be expressed as a variation in N_0.

In Figure 10 the black symbols are taken directly from Bieber and Evenson (1991), where the open symbols are derived from station ratios (SP: South Pole, MC: McMurdo, TH: Thule, and NE: Newark) and the closed symbols from BC/NM ratios. The conclusion of that paper was that the "Stoker B"

interpretation of the BC/NM ratio at South Pole provided a better consistency with fixed station ratios, which was supported by comparison with the results of Cramp et al. (1997) as reported by Ruffolo et al. (2006). Applying this approach to the present work results in the red points. Here the error bars are constructed from the extremes allowed by the one sigma errors on the Dorman parameters discussed earlier. The result is similar to the "Stoker A" analysis, but like that analysis is not consistent with the station ratio determination. On the other hand, keeping in mind that the South Pole installation is actually three 1NM64 units we also show the result (blue symbols) obtained with the 1995 bare survey and the 1976 1NM64 result. Here the agreement with the station ratios is as good as that obtained with the "Stoker B" analysis.

In Figures 9 and 10 we also show the results from applying the Dorman et al. (2000) response functions, which are significantly different, presumably because the bare detectors in that work had no moderators.

5. Conclusions

We report an analysis of data taken using three bare neutron counters with a novel design and a standard three-counter neutron monitor (3NM64) on board the U.S. Coast Guard icebreaker *Polar Star* from 6 November 1995 to 20 March 1996, over a route from San Diego, USA, to McMurdo Base, Antarctica, and back to the northern Pacific Ocean. This latitude survey sampled geomagnetic cutoffs over $0 < P_c < 15$ GV, allowing a determination of the BC and 3NM64 response functions over that range. Various techniques were used to clean and correct the data. The pressure correction coefficient as a function of P_c was previously determined for this ship-borne 3NM64 (using data from 13 latitude surveys over 1994–2007), and here we investigated whether the BC count rate requires a different pressure coefficient. We concluded that the statistics available for these BCs are insufficient to determine whether the pressure coefficients are different, and therefore we used the same coefficient. The temperatures of both detector systems were controlled to some extent and we did not find a significant temperature effect on the count rates. The BC response was strongly affected by proximity to any port along the route, and such time periods were excluded when determining the response functions.

The only directly comparable latitude survey with bare neutron counters (of a different design, but with moderators) was performed in 1976 (Potgieter et al., 1980; Stoker et al., 1980), a time when solar modulation conditions were very similar to those in 1995. The neutron monitor response functions were similar, with small differences that might be attributed to the use of different pressure coefficients or the different detector design (1NM64 in 1976 versus 3NM64 in 1995). We will further investigate this effect for interpretation of data from the South Pole NM, which actually consists of three independent 1NM64 units. The BC response function for 1995 is similar to what we derive from the raw data from 1976 using the same analysis techniques but is substantially outside the allowed range according to Stoker (1985). One of the extremes of that range has been successfully used to determine the spectral index of relativistic solar particles from BC and NM data at South Pole during ground level enhancements. When applied in simplest form the results from the present work do not directly give such good agreement.

It must however be noted that the counting rates for the typically steep solar particle spectra at the high altitude of South Pole are determined in large part by response functions (or more properly the underlying yield functions) in a rigidity range below the atmospheric cutoff at sea level. Thus, the use of data from sea level surveys in this range is an extrapolation.

As the spectrum gets steeper the sensitivity to the choice of fit parameters also increases. In Figure 10 the formal errors on the spectral index for the apparently better choice of the parameters (blue points) are much larger than the formal errors on the less favored choice of parameters (red points) that would imply a flatter spectrum. In fact, the interpretation of the "Stoker A" and "Stoker B" as defining the range of variation in the spectral index allowed by uncertainties in the measured response is essentially confirmed. The BC to monitor comparison indeed gives a rather precise measurement of the spectral index, and in particular the variation of the spectral index within a given event (Ruffolo et al., 2006), but the actual value of the spectral index cannot be determined from latitude survey data alone.

In work in progress, we will follow up on this issue by analyzing data from a third latitude survey with BCs (of yet another design, but now installed at South Pole) conducted in 2009. We are investigating these various aspects of the analysis with Monte Carlo simulations, also currently in progress.

Acknowledgments
This study is supported in part by the Thailand Research Fund via grant RTA5980003 and Research Grant for New Scholar MRG6080086; by the U.S. National Science Foundation via awards PLR-1341562, PLR-1245939, and their predecessors; and by the Australian Antarctic Division. We thank the officers and crew of the USCG icebreaker Polar Star for their assistance in conducting the survey. We also thank Leonard Shulman, James Roth, and Keith Bolton for their technical assistance in preparing and maintaining the TasVan. W. N. would like to thank the Faculty of Science, Chandrakasem Rajabhat University, Bangkok, Thailand, for their support. The data displayed in the figures are available as supporting information.

References

Bieber, J. W., Clem, J., & Evenson, P. (1997). Efficient computation of apparent cutoffs. In *Proceedings of the 25th International Cosmic Ray Conference*, *2* (pp. 389–392). Transvaal, South Africa: Potchefstroom University.

Bieber, J. W., Clem, J., Evenson, P., Pyle, R., Sáiz, A., & Ruffolo, D. (2013). Giant ground level enhancement of relativistic solar protons on 2005 January 20. I. Spaceship Earth Observations. *Astrophysical Journal*, *771*, 92. https://doi.org/10.1088/0004-637X/771/2/92

Bieber, J. W., Dröge, W., Evenson, P., Pyle, R., Ruffolo, D., Pinsook, U., et al. (2002). Energetic particle observations during the 2000 July 14 solar event. *Astrophysical Journal*, *567*, 622–634. https://doi.org/10.1086/338246

Bieber, J. W., & Evenson, P. (1991). Determination of energy spectra for the large solar particle events of 1989. In *Proceedings of the 22nd International Cosmic Ray Conference* (Vol. 3, pp. 129–132). Dublin, Ireland.

Caballero-Lopez, R. A. (2016). An estimation of the yield and response functions for the mini neutron monitor. *Journal of Geophysical Research: Space Physics*, *121*, 7461–7469. https://doi.org/10.1002/2016JA022690

Caballero-Lopez, R. A., & Moraal, H. (2012). Cosmic-ray yield and response functions in the atmosphere. *Journal of Geophysical Research: Space Physics*, *117*, A12103. https://doi.org/10.1029/2012JA017794

Clem, J. M., Bieber, J. W., Evenson, P., Hall, D., Humble, J. E., & Duldig, M. (1997). Contribution of obliquely incident particles to neutron monitor counting rate. *Journal of Geophysical Research*, *102*, 26,919–26,926. https://doi.org/10.1029/97JA02366

Clem, J. M., & Dorman, L. I. (2000). Neutron monitor response functions. *Space Science Reviews*, *93*, 335–359. https://doi.org/10.1023/A:1026508915269

Cramp, J. L., Duldig, M. L., Flückiger, E. O., Humble, J. E., Shea, M. A., & Smart, D. F. (1997). The October 22, 1989, solar cosmic ray enhancement: An analysis of the anisotropy and spectral characteristics. *Journal of Geophysical Research*, *102*, 24,237–24,248. https://doi.org/10.1029/97JA01947

Dorman, L. I., Fedchenko, S. G., Granitsky, L. V., & Rishe, G. A. (1969). Coupling and barometer coefficients for measurements of cosmic ray variations at altitudes of 260–400 mb. In *Proceedings of the 11th International Conference on Cosmic Rays* (Vol. 2, pp. 233–236). Budapest.

Dorman, L. I., Villoresi, G., Iucci, N., Parisi, M., Tyasto, M. I., Danilova, O. A., & Ptitsyna, N. G. (2000). Cosmic ray survey to Antarctica and coupling functions for neutron component near solar minimum (1996–1997): 3. Geomagnetic effects and coupling functions. *Journal of Geophysical Research: Space Physics*, *105*, 21,047–21,056. https://doi.org/10.1029/2000JA900051

Evenson, P., Bieber, J. W., Clem, J., & Pyle, R. (2005). Neutron monitor temperature coefficients: Measurements for BF_3 and ^{3}He counter tubes. In *Proceedings 29th International Cosmic Ray Conference* (Vol. 2, pp. 485–488). Pune, India.

Ghelfi, A., Barao, F., Derome, L., & Maurin, D. (2016). Non-parametric determination of H and He interstellar fluxes from cosmic-ray data. *Astronomy and Astrophysics*, *591*, A94. https://doi.org/10.1051/0004-6361/201527852

Ghelfi, A., Barao, F., Derome, L., & Maurin, D. (2017). Non-parametric determination of H and He interstellar fluxes from cosmic-ray data (Corrigendum). *Astronomy and Astrophysics*, *605*, C2. https://doi.org/10.1051/0004-6361/201527852e

Ghelfi, A., Maurin, D., Cheminet, A., Derome, L., Hubert, G., & Melot, F. (2017). Neutron monitors and muon detectors for solar modulation studies: 2. ϕ time series. *Advances in Space Research*, *60*, 833–847. https://doi.org/10.1016/j.asr.2016.06.027

Gleeson, L. J., & Axford, W. I. (1968). Solar modulation of galactic cosmic rays. *Astrophysical Journal*, *154*, 1011–1026. https://doi.org/10.1086/149822

Hatton, C. J., & Carmichael, H. (1964). Experimental investigation of the NM-64 neutron monitor. *Canadian Journal of Physics*, *42*, 2443–2472. https://doi.org/10.1139/p64-222

Kouzes, R. T., Siciliano, E. R., Ely, J. H., Keller, P. E., & McConn, R. J. (2008). Passive neutron detection for interdiction of nuclear material at borders. *Nuclear Instruments and Methods in Physics Research Section A: Accelerators, Spectrometers, Detectors and Associated Equipment*, *584*, 383–400. https://doi.org/10.1016/j.nima.2007.10.026

Lin, Z., Bieber, J. W., & Evenson, P. (1995). Electron trajectories in a model magnetosphere: Simulation and observation under active conditions. *Journal of Geophysical Research*, *100*, 23,543–23,549. https://doi.org/10.1029/95JA02696

Mangeard, P.-S., Ruffolo, D., Sáiz, A., Madlee, S., & Nutaro, T. (2016). Monte Carlo simulation of the neutron monitor yield function. *Journal of Geophysical Research: Space Physics*, *121*, 7435–7448. https://doi.org/10.1002/2016JA022638

Mangeard, P.-S., Ruffolo, D., Sáiz, A., Nuntiyakul, W., Bieber, J. W., Clem, J., et al. (2016). Dependence of the neutron monitor count rate and time delay distribution on the rigidity spectrum of primary cosmic rays. *Journal of Geophysical Research: Space Physics*, *121*, 11,620–11,636. https://doi.org/10.1002/2016JA023515

Matthiä, D., Heber, B., Reitz, G., Meier, M., Sihver, L., Berger, T., & Herbst, K. (2009). Temporal and spatial evolution of the solar energetic particle event on 20 January 2005 and resulting radiation doses in aviation. *Journal of Geophysical Research*, *114*, A08104. https://doi.org/10.1029/2009JA014125

Maurin, D., Cheminet, A., Derome, L., Ghelfi, A., & Hubert, G. (2015). Neutron monitors and muon detectors for solar modulation studies: Interstellar flux, yield function, and assessment of critical parameters in count rate calculations. *Advances in Space Research*, *55*, 363–389. https://doi.org/10.1016/j.asr.2014.06.021

Mishev, A. L., Usoskin, I. G., & Kovaltsov, G. A. (2013). Neutron monitor yield function: New improved computations. *Journal of Geophysical Research: Space Physics*, *118*, 2783–2788. https://doi.org/10.1002/jgra.50325

Muangha, P. (2013). *Observation of Cosmic Ray Apectral Variation Using Bare Counters at Doi Inthanon with Princess Sirindhorn Neutron Monitor, Unpublished Undergraduate Senior Project*. Bangkok, Thailand: Mahidol University.

Nuntiyakul, W., Evenson, P., Ruffolo, D., Sáiz, A., Bieber, J. W., Clem, J., et al. (2014). Latitude survey investigation of Galactic cosmic ray solar modulation during 1994–2007. *Astrophysical Journal*, *795*, 11. https://doi.org/10.1088/0004-637X/795/1/11

Potgieter, M. S., Raubenheimer, B. C., Stoker, P. H., & van der Walt, A. J. (1980). Modulation of cosmic rays during solar minimum. Part 2. Cosmic ray latitude distribution at sea-level during 1976. *South African Journal of Physics*, *3*(3–4), 77–89.

Ruffolo, D., Sáiz, A., Mangeard, P.-S., Kamyan, N., Muangha, P., Nutaro, T., et al. (2016). Monitoring short-term cosmic-ray spectral variations using neutron monitor time-delay measurements. *Astrophysical Journal*, *817*(38). https://doi.org/10.3847/0004-637X/817/1/38

Ruffolo, D., Tooprakai, P., Rujiwarodom, M., Khumlumlert, T., Wechakama, M., Bieber, J. W., et al. (2006). Relativistic solar protons on 1989 October 22: Injection and transport along both legs of a closed interplanetary magnetic loop. *Astrophysical Journal*, *639*, 1186–1205. https://doi.org/10.1086/499419

Sáiz, A., Ruffolo, D., Bieber, J. W., Evenson, P., & Pyle, R. (2008). Anisotropy signatures of solar energetic particle transport in a closed interplanetary magnetic loop. *Astrophysical Journal*, *672*, 650–658. https://doi.org/10.1086/523663

Simpson, J. A. Jr. (1948). The latitude dependence of neutron densities in the atmosphere as a function of altitude. *Physical Review*, *73*, 1389–1391. https://doi.org/10.1103/PhysRev.73.1389

Stoker, P. H. (1985). Spectra of solar proton ground level events using neutron monitor and neutron moderated detector recordings. In *Proceedings 19th International Cosmic Ray Conference* (Vol. 4, pp. 114–117).

Stoker, P. H., & Raubenheimer, B. C. (1985). The neutron moderated detector and groundbased cosmic ray modulation studies. In *Proceedings 19th International Cosmic Ray Conference* (Vol. 5, pp. 502–505).

Stoker, P. H., van der Walt, A. J., & Potgieter, M. S. (1980). Modulation of cosmic rays during solar minimum. Part 1. Cosmic ray intensity survey at sea-level during 1976: Experimental details. *South African Journal of Physics*, *3*, 73–76.

Thomsen, M. F. (2004). Why K_p is such a good measure of magnetospheric convection. *Space Weather*, *2*, S11004. https://doi.org/10.1029/2004SW000089

Tsyganenko, N. A. (1987). Global quantitative models of the geomagnetic field in the cislunar magnetosphere for different disturbance levels. *Planetary and Space Science*, *35*, 1347–1358. https://doi.org/10.1016/0032-0633(87)90046-8

Usoskin, I. G., Gil, A., Kovaltsov, G. A., Mishev, A. L., & Mikhailov, V. V. (2017). Heliospheric modulation of cosmic rays during the neutron monitor era: Calibration using PAMELA data for 2006–2010. *Journal of Geophysical Research: Space Physics*, *122*, 3875–3887. https://doi.org/10.1002/2016JA023819

Villoresi, G., Dorman, L. I., Iucci, N., & Ptitsyna, N. G. (2000). Cosmic ray survey to Antarctica and coupling functions for neutron component near solar minimum (1996–1997): 1. Methodology and data quality assurance. *Journal of Geophysical Research*, *105*, 21,025–21,034. https://doi.org/10.1029/2000JA900048

Zreda, M., Desilets, D., Ferré, T. P. A., & Scott, R. L. (2008). Measuring soil moisture content non-invasively at intermediate spatial scale using cosmic-ray neutrons. *Geophysical Research Letters*, *35*, L21402. https://doi.org/10.1029/2008GL035655

The Astronomical Journal, 156:227 (11pp), 2018 November https://doi.org/10.3847/1538-3881/aae31b
© 2018. The American Astronomical Society. All rights reserved.

A Large Ground-based Observing Campaign of the Disintegrating Planet K2-22b

Knicole D. Colón[1], George Zhou[2], Avi Shporer[3], Karen A. Collins[2], Allyson Bieryla[2], Néstor Espinoza[4,5,6], Felipe Murgas[7,8], Petchara Pattarakijwanich[9], Supachai Awiphan[10], James D. Armstrong[11], Jeremy Bailey[12,13], Geert Barentsen[14,15], Daniel Bayliss[16], Anurak Chakpor[10], William D. Cochran[17], Vikram S. Dhillon[7,18], Keith Horne[19], Michael Ireland[20], Lucyna Kedziora-Chudczer[12,13], John F. Kielkopf[21], Siramas Komonjinda[22,23], David W. Latham[2], Tom. R. Marsh[16], David E. Mkrtichian[10], Enric Pallé[7,8], David Ruffolo[9], Ramotholo Sefako[24], Chris G. Tinney[12,13], Suwicha Wannawichian[22], and Suraphong Yuma[9]

[1] NASA Goddard Space Flight Center, Exoplanets and Stellar Astrophysics Laboratory (Code 667), Greenbelt, MD 20771, USA
[2] Harvard-Smithsonian Center for Astrophysics, Cambridge, MA 02138, USA
[3] Massachusetts Institute of Technology, Cambridge, MA 02139, USA
[4] Max-Planck-Institut für Astronomie, Königstuhl 17, D-69117 Heidelberg, Germany
[5] Instituto de Astrofísica, Facultad de Física, Pontificia Universidad Católica de Chile, Av. Vicuña Mackenna 4860, 782-0436 Macul, Santiago, Chile
[6] Millennium Institute of Astrophysics (MAS), Av. Vicuña Mackenna 4860, 782-0436 Macul, Santiago, Chile
[7] Instituto de Astrofísica de Canarias (IAC), E-38205 La Laguna, Tenerife, Spain
[8] Departamento de Astrofísica, Universidad de La Laguna (ULL), E-38205 La Laguna, Tenerife, Spain
[9] Department of Physics, Faculty of Science, Mahidol University, Bangkok 10400, Thailand
[10] National Astronomical Research Institute of Thailand, 260 Moo 4, Donkaew, Mae Rim, Chiang Mai, 50180, Thailand
[11] Institute for Astronomy, University of Hawaii, 34 Ohia Ku St., Pukalani, Maui, HI 96768, USA
[12] School of Physics, University of New South Wales, Sydney, NSW 2052, Australia
[13] Australian Centre for Astrobiology, University of New South Wales, Sydney, NSW 2052, Australia
[14] NASA Ames Research Center, M/S 244-30, Moffett Field, CA 94035, USA
[15] Bay Area Environmental Research Institute, 625 2nd St. Ste 209, Petaluma, CA 94952, USA
[16] Department of Physics, University of Warwick, Coventry CV4 7AL, UK
[17] McDonald Observatory and Department of Astronomy, The University of Texas at Austin, Austin, TX 78712, USA
[18] Department of Physics and Astronomy, University of Sheffield, Sheffield, S3 7RH, UK
[19] SUPA Physics and Astronomy, University of St Andrews, North Haugh, St Andrews KY16 9SS, UK
[20] Research School of Astronomy & Astrophysics, Australian National University, Canberra, ACT 2611, Australia
[21] Department of Physics and Astronomy, University of Louisville, Louisville, KY 40292, USA
[22] Department of Physics and Materials Science, Faculty of Science, Chiang Mai University, 239 Huay Kaew Road, Chiang Mai, 50200, Thailand
[23] Research Center in Physics and Astronomy, Faculty of Science, Chiang Mai University, 239 Huay Kaew Road, Chiang Mai, 50200, Thailand
[24] South African Astronomical Observatory, P.O. Box 9, Observatory, Cape Town 7935, South Africa
Received 2018 April 9; revised 2018 September 14; accepted 2018 September 18; published 2018 October 26

Abstract

We present 45 ground-based photometric observations of the K2-22 system collected between 2016 December and 2017 May, which we use to investigate the evolution of the transit of the disintegrating planet K2-22b. Last observed in early 2015, in these new observations we recover the transit at multiple epochs and measure a typical depth of <1.5%. We find that the distribution of our measured transit depths is comparable to the range of depths measured in observations from 2014 and 2015. These new observations also support ongoing variability in the K2-22b transit shape and time, although the overall shallowness of the transit makes a detailed analysis of these transit parameters difficult. We find no strong evidence of wavelength-dependent transit depths for epochs where we have simultaneous coverage at multiple wavelengths, although our stacked Las Cumbres Observatory data collected over days-to-months timescales are suggestive of a deeper transit at blue wavelengths. We encourage continued high-precision photometric and spectroscopic monitoring of this system in order to further constrain the evolution timescale and to aid comparative studies with the other few known disintegrating planets.

Key words: planets and satellites: detection – planets and satellites: individual (K2-22 b) – techniques: photometric

Supporting material: machine-readable tables

1. Introduction

Exoplanet surveys have yielded many surprises over the years. The discovery of "disintegrating" exoplanets was one such surprise. These are planets that appear to have tails of dusty material that produce asymmetric transit shapes. At present, there are only three such planets known around main-sequence stars: KIC 12557548b (Rappaport et al. 2012), KOI-2700b (Rappaport et al. 2014), and K2-22b (Sanchis-Ojeda et al. 2015). The first two were discovered in NASA's *Kepler* prime mission, while the latter was discovered in Campaign 1 of NASA's K2 mission (Howell et al. 2014). Given that *Kepler* and K2 have observed a combined total of several hundred thousand stars, this suggests that such objects are either intrinsically rare or have a short enough survival lifetime that we are lucky to catch any in the act of disintegrating (van Lieshout & Rappaport 2017).

Because such objects are rare, the systems named above have been under intense study so as to better understand their formation and evolution. In particular, observations over long timescales can be used to determine the rate at which the transit depth evolves over time. In addition, multi-wavelength observations can provide constraints on the properties of the grains that are present in the dust tails. For example, several such studies have been done for WD 1145+017 (Vanderburg et al. 2015; Vanderburg & Rappaport 2018), which is a white dwarf star that has disintegrating planetesimals in orbit around

it and is perhaps the most well-studied "disintegrating" system to date (e.g., Alonso et al. 2016; Gänsicke et al. 2016; Zhou et al. 2016; Croll et al. 2017; Hallakoun et al. 2017; Redfield et al. 2017; Vanderburg & Rappaport 2018; Xu et al. 2018). However, because this system consists of debris orbiting a post-main-sequence star, it is arguably in a different class than the other three disintegrating planets known.

The planetary companion KIC 12557548b, which orbits a highly spotted K-dwarf star with a period of ∼16 hr, displays variable transit depths ranging from <0.2% to 1.3% within *Kepler* data obtained between 2009 and 2013 (e.g., Rappaport et al. 2012). It was later observed in 2013 and 2014 to have weaker transits overall than seen in the *Kepler* data (e.g., Schlawin et al. 2016). Studies have found evidence for a correlation between the variability of the transit depth and the stellar rotation period (∼23 days; Kawahara et al. 2013; Croll et al. 2015). These studies suggest that either the activity corresponding to enhanced ultraviolet and/or X-ray radiation in turn causes increased mass-loss and therefore increased variability in the transit depth, or the apparent changes in transit depth occur as a dust tail passes over star spots. In addition, while simultaneous *Kepler* and near-infrared observations of KIC 12557548b revealed no significant difference in transit depth with wavelength (Croll et al. 2014), evidence for a color dependence of the transit depth between g' and z' was later found by Bochinski et al. (2015). These observations provide an estimate on the grain size within the dust tail of 0.25–1 μm in radius.

Similar to KIC 12557548b, the planetary object KOI-2700b orbits an active mid-K star with a period of ∼22 hr (Rappaport et al. 2014). However, the transit depth is measured to be <0.04% on average in the *Kepler* data, much shallower than measured for KIC 12557548b. Due to the shallowness of the transit, any transit-to-transit variability in the *Kepler* data is difficult to study. Still, the transit depth was shown to be monotonically decreasing over the four-year timescale of the *Kepler* observations (Rappaport et al. 2014). Unfortunately, further follow-up observations of this system are inherently difficult given the shallow transit.

The planet K2-22b orbits an M-dwarf with a period of just ∼9 hr (Sanchis-Ojeda et al. 2015), much shorter than the two aforementioned disintegrating planets. The star itself exhibits photometric variability at the 1% level with a rotation period of 15 days. Sanchis-Ojeda et al. (2015) presented the analysis of the K2 observations that were obtained between 2014 May and August and 15 ground-based follow-up light curves obtained between 2015 January and March. From these data, Sanchis-Ojeda et al. (2015) measured rapidly variable transit depths for K2-22b ranging from ∼0% to 1.3%, comparable to KIC 12557548b. A wavelength-dependent transit light curve shape was also measured during one particularly deep transit, supporting dust scattering during the transit. Another significant difference between K2-22b and both KIC 12557548b and KOI-2700b is that K2-22b appears to have both a leading and trailing dust tail, rather than just a trailing one.

Given that the K2-22 system is unique among the few disintegrating planets known, we undertook a new observing campaign to further investigate the nature of this system. Here, we present 45 new ground-based light curves of the K2-22 system obtained between 2016 December and 2017 May, 31 of which cover complete transit windows as predicted based on the ephemeris from Sanchis-Ojeda et al. (2015). In Section 2, we describe these observations, which were obtained with telescopes ranging in size from 0.5 to 10.4 m and spanning optical to near-infrared wavelengths. In Section 3, we present our analysis and modeling of the light curves, and we describe and discuss our findings in Sections 4 and 5.

2. Observations and Data Analysis

In the following sections, we describe the observations of K2-22 performed with nine different facilities located around the world. The time-series photometry from each observatory is presented in Figure 1 and Table 1, and a summary of the observations is given in Table 2.

2.1. Anglo-Australian Telescope (AAT)

Near-infrared light curves of K2-22 were obtained using the IRIS2 camera on the 3.9 m AAT (Tinney et al. 2004), located at Siding Spring Observatory (SSO) in Australia. IRIS2 is a 1K × 1K camera utilizing a HAWAII-1 HgCdTe detector, read out over four quadrants in the double-read mode, achieving a field of view of 7.′7 × 7.′7, at a pixel scale of 0.″4486 pixel^{-1}.

Observations were obtained on UT 2017 March 15 (transit epoch = 2669) and UT 2017 March 16 (transit epoch = 2671) with IRIS2 in the *Ks* band, at 30 s exposure time. These observations were scheduled to accompany simultaneous optical photometry from the LCO 1 m telescope at SSO. The IRIS2 observing procedure and photometric reductions largely follow that described in Zhou et al. (2014). Dark exposures were subtracted from the data frames, and flat-field division was performed with the aid of on-sky offset frames taken before and after the time-series observations. To ensure the target star remained on the same pixel throughout the time-series observations, we made use of an off-axis guider, as well as manual adjustments to the telescope pointing via real-time plate solutions from the science frames. Plate solving and final aperture photometric extraction were performed with the FITSH package (Pál 2012). Relative photometry was performed with a set of four reference stars in the field.

2.2. Fred Lawrence Whipple Observatory (FLWO)

We used KeplerCam on the 1.2 m telescope at the FLWO on Mt. Hopkins, Arizona to observe 5 transit windows of K2-22b. KeplerCam has a single 4 K × 4 K Fairchild CCD486 with a 0.″366 pixel^{-1} and a field of view of 23.′1 × 23.′1. The observations were made on UT 2017 March 8 (transit epoch = 2650), UT 2017 March 9 (transit epoch = 2652), UT 2017 April 16 (transit epoch = 2752), UT 2017 April 21 (transit epoch = 2765) and UT 2017 May 22 (transit epoch = 2846). All observations were obtained in an SDSS *i* filter with a 120 s exposure time. Images were reduced using standard IDL routines as outlined in Carter et al. (2011). AstroImageJ (Collins et al. 2017) was used to perform aperture photometry on the processed images. We used an aperture radius of 8 pixels, corresponding to a 2.″93 radius.

2.3. Gao Mei Gu Observatory (GAO)

We observed three transits of K2-22 on three consecutive nights from UT 2017 March 15 to UT 2017 March 17 (transit epochs = 2669, 2672, 2674) using the 0.7 m Thai Robotic Telescope—Gao Mei Gu Observatory (TRT-GAO), in Lijiang, China, with an Andor iKon-L 936 2 K × 2 K CCD camera with a scale of 0.″613 pixel^{-1}. The observations were

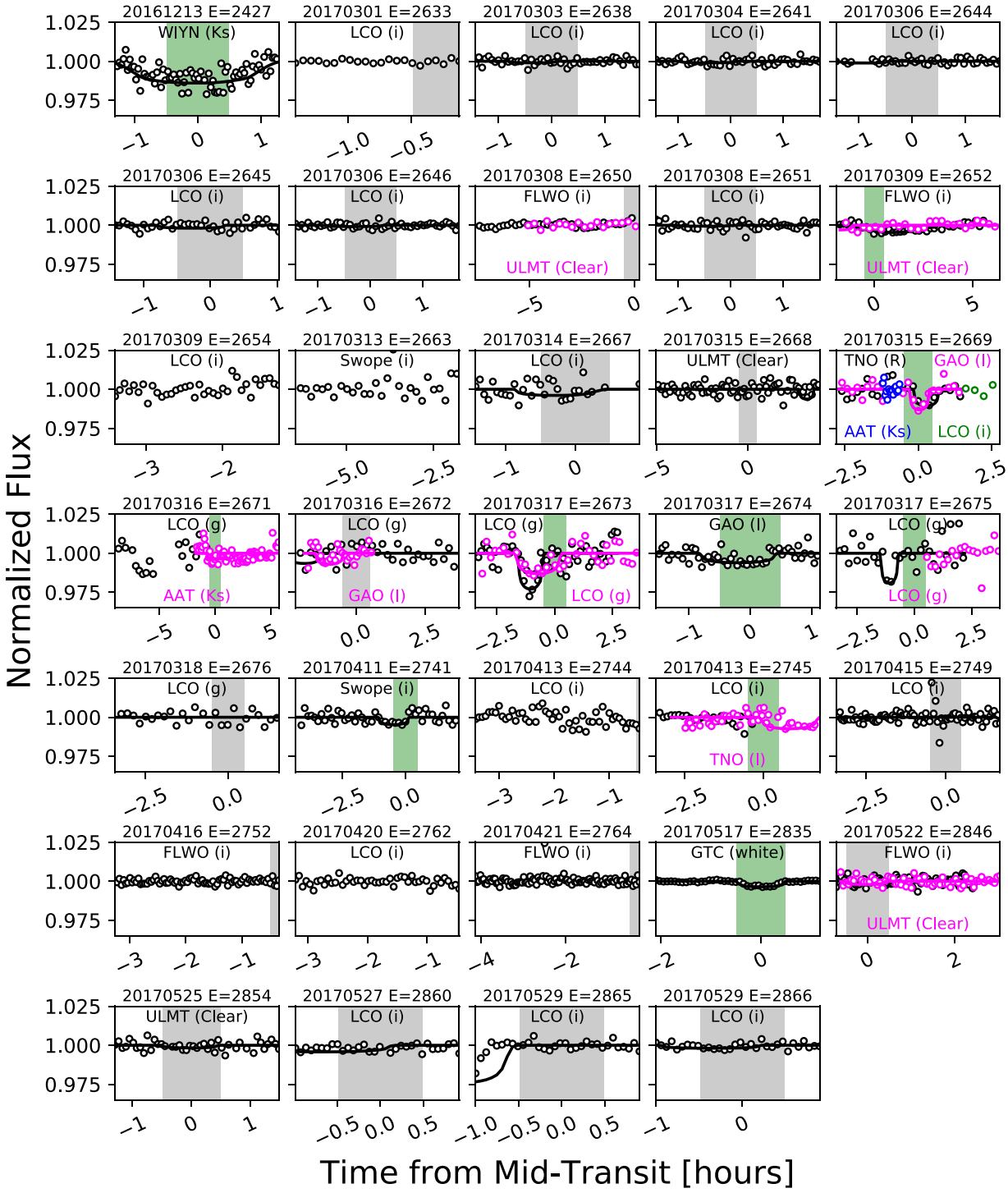


Figure 1. Ground-based photometric follow-up light curves of K2-22 (open circles). Each panel lists the facility and filter used to collect the data as well as the start date of the observations (UT) and the transit epoch, relative to the transit ephemeris from Sanchis-Ojeda et al. (2015). To aid visual comparisons between different light curves, all panels have the same vertical axis, and some light curves have been binned for clarity. As shown in some panels, data from different observatories covered the same epoch and are plotted in different colors. The green or gray shaded regions in some panels mark the transit windows of K2-22b based on the ephemeris and duration (48 minutes) from Sanchis-Ojeda et al. (2015). The panels with shaded green regions specifically highlight epochs where we were able to robustly measure a transit depth (see Table 2). Solid lines are the models that were fitted to the light curves that spanned a complete transit window (see Section 3 for details). The data in the second to last panel on the bottom show a significant trend at the beginning of the observations, which is likely not astrophysical and adversely affected the best-fitting model (see Section 4 for details).

performed through a Cousins-I filter with 60 s exposures. The total science images on each night are 250 (UT 2017 March 15), 140 (UT 2017 March 16) and 150 (UT 2017 March 17). The calibration was carried out using the IRAF tasks along with astrometric calibration using Astrometry.net (Lang et al. 2010). The aperture photometry was carried out using SExtractor (Bertin & Arnouts 1996) with an adaptive scaled aperture based on the seeing in an individual image. The final apertures used were between 4 and 5 pixels equivalent to 2.″45–3.″07 (Bertin & Arnouts 1996).

Table 1
Time-series Photometry of K2-22

Observatory	Filter	BJD	Relative Flux	Relative Flux Error
WIYN	Ks	2457735.942395	0.999131	0.009729
WIYN	Ks	2457735.942858	0.998627	0.009729
WIYN	Ks	2457735.943321	0.991867	0.009729
WIYN	Ks	2457735.943773	1.004635	0.009729
WIYN	Ks	2457735.944236	0.993868	0.009729
…	…	…	…	…

(This table is available in its entirety in machine-readable form.)

2.4. Gran Telescopio Canarias (GTC)

We were awarded Director's Discretionary Time to use the OSIRIS instrument (Cepa et al. 2000) mounted on the 10.4 m GTC to observe 1 transit of K2-22b (PI: E. Pallé). The data were obtained on UT 2017 May 17 (transit epoch = 2835) using OSIRIS long-slit spectroscopy mode with the R1000R grism (spectral coverage of 510–1000 nm), 2 × 2 binning mode (0.″254 pixel^{-1}), readout speed of 200 kHz, gain of 0.95 e$^-$/ADU, and readout noise of 4.5 e$^-$. A custom built long slit with a width of 12″ was used to obtain spectra of K2-22 and one reference star. The exposure time was set to 250 s and the total observing time was 3.3 hr (airmass varied from 1.12 to 1.97). A total of 45 science images was acquired during the run. Images were reduced using standard procedures (bias and flat calibration), and the spectral extraction of K2-22 and the reference star was done using an aperture of 40 binned pixels (10.″2) in width. For more details on the GTC data reduction procedure, we refer the reader to Section 7 of Sanchis-Ojeda et al. (2015).

2.5. Las Cumbres Observatory (LCO)

We collected 24 light curves of K2-22 between UT 2017 March 1 and UT 2017 May 29 in either the Sloan *g* or Sloan *i* band from multiple 1 m telescopes in the LCO network (Brown et al. 2013). The corresponding transit epochs and site of each observation are given in Table 2, where CTIO refers to Cerro Tololo Inter-American Observatory in Chile, McDonald refers to McDonald Observatory in Texas, SAAO refers to South African Astronomical Observatory in Sutherland, South Africa, and SSO refers to Siding Spring Observatory near Coonabarabran, New South Wales, Australia. The 1 m LCO telescopes each have a 4 K × 4 K Sinistro detector with a 26′ × 26′ field of view and a pixel scale of 0.″39 pixel^{-1}. Calibrated data were downloaded from the LCO archive and then analyzed to extract the photometry following a similar procedure as described in the following section.

2.6. The Swope Telescope

We collected two light curves of K2-22 on UT 2017 March 13 (transit epoch = 2663) and UT 2017 April 11 (transit epoch = 2741) using the E2V 4 K × 4 K CCD at the 40 inch Swope telescope at Las Campanas Observatory. Observations were acquired in both cases with the SDSS *i* filter but with different exposure times. Due to the closeness of the target to the Moon on the March 13 observations, the exposure times were set at 70 s. This allowed us to achieve photometry at the ∼2% level only, due to the local sky brightness. The observations spanned almost 5 hr, covering a significant portion of the orbit of K2-22b. On April 11, the Moon did not interfere with our observations and thus the exposure times were set to 110 s, which allowed us to reach photometry at the 0.5% level per point over 6.5 hr, covering a significant fraction of the orbit of K2-22b. The data were reduced using a standard photometric pipeline which makes use mainly of tools from the Astropy package (Astropy Collaboration et al. 2013), and performs bias, dark and flat-field corrections, along with astrometric identification of stars in the field using Astrometry.net (Lang et al. 2010) and subsequent extraction of photometry for all the stars in the field. Differential photometry for K2-22 was produced by using an ensemble of 10 comparison stars over a 10 pixel radius, which implies a radius of 4.″35 as the pixel scale is 0.″435 pixel^{-1}.

2.7. Thai National Observatory (TNO)

At TNO, in Chiang Mai, Thailand, we conducted photometric observations of K2-22b on the 0.5 m Thai Robotic Telescope—Thai National Observatory (TRT-TNO) and the 2.4 m Thai National Telescope (TNT) on UT 2017 March 15 (transit epoch = 2669) and UT 2017 April 13 (transit epoch = 2745), respectively.

A transit observation was conducted with the TRT-TNO through a Cousins-R filter using an Andor iKon-L 936 2 K × 2 K CCD camera attached to the 0.5 m Schmidt–Cassegrain Telescope. The field-of-view of each image is 23.′4 × 23.′4. The observation was conducted using 60 s exposure time and 250 science images were obtained. The calibration and photometry were performed using the same routine as TRT-GAO observations.

For the TNT observations, the target was observed with ULTRASPEC (Dhillon et al. 2014) in the *i*-band. ULTRASPEC is a high-speed camera using a frame-transfer electron-multiplying CCD (EMCCD). The target was observed in full-frame mode, with a field-of-view of 7.′7 × 7.′7 and a pixel scale of 0.″45 pixel^{-1}. The exposure time was 42.78 s, with a dead time of 15 ms between each frame. More than 400 science images were obtained, but only the first 221 images are used in our analysis as latter images were affected by clouds. Plate matching and aperture photometric extraction were performed using the FITSH package (Pál 2012). Relative photometry utilized a largely similar set of reference stars as the LCO observations (barring differences due to the different field of view). Light curves were extracted over six different apertures and background annulus radii to optimize the point-to-point photometric scatter.

2.8. University of Louisville Manner Telescope (ULMT)

We observed five complete transit windows of K2-22b on UT 2017 March 08 (transit epoch = 2650), UT 2017 March 09 (transit epoch = 2652), UT 2017 March 15 (transit epoch = 2668), UT 2017 May 22 (transit epoch = 2846), and UT 2017 May 25 (transit epoch = 2854) using the ULMT located at the Mt. Lemmon summit of Steward Observatory, AZ. The observations employed a 0.6 m *f*/8 RC Optical Systems Ritchey–Chrétien telescope and an SBIG STX-16803 CCD with a 4K × 4K array of 9 μm pixels, yielding a 26.′6 × 26.′6 field of view and 0.″39 pixel^{-1} image scale. All observations were conducted using 200 s exposure times and no filter. Conditions were clear except for some thin clouds during the observations on

Table 2
Summary and Results of Photometric Observations of K2-22

Start Date (UT)	Transit Epoch	Facility	Aperture (m)	Filter	Phase Coverage	N_{points}	Cadence (min)	σ_{median} (%)	R_p/R_* (measured)	R_p/R_* (corrected)
2016 Dec 13	2427	WIYN	3.5	*Ks*	−0.144 to +0.140	232	0.67	0.973	0.1142 ± 0.0342	⋯
2017 May 01	2633	LCO/SAAO	1.0	*i*	−0.154 to −0.0135	22	3.67	0.225	⋯	⋯
2017 May 03	2638	LCO/SAAO	1.0	*i*	−0.156 to +0.180	51	3.68	0.214	<0.0426	<0.0438
2017 May 04	2641	LCO/SAAO	1.0	*i*	−0.156 to +0.186	52	3.69	0.231	<0.0495	<0.0509
2017 May 06	2644	LCO/SAAO	1.0	*i*	−0.155 to +0.180	44	3.66	0.276	<0.0434	<0.0448
2017 May 06	2645	LCO/SSO	1.0	*i*	−0.156 to +0.112	41	3.67	0.406	<0.0552	<0.0568
2017 May 06	2646	LCO/SAAO	1.0	*i*	−0.156 to +0.186	52	3.67	0.270	<0.0366	<0.0376
2017 May 08	2650	FLWO	1.2	*i*	−0.827 to −0.00465	198	2.30	0.192	⋯	⋯
2017 May 08	2650	ULMT	0.6	*Clear*	−0.587 to +0.0261	94	3.54	0.298	⋯	⋯
2017 May 08	2651	LCO/SAAO	1.0	*i*	−0.156 to +0.186	52	3.69	0.269	<0.0364	<0.0375
2017 May 09	2652	FLWO	1.2	*i*	−0.211 to +0.612	198	2.30	0.225	0.0762 ± 0.0139	0.0784
2017 May 09	2652	ULMT	0.6	*Clear*	−0.189 to +0.695	135	3.54	0.425	<0.0588	<0.0612
2017 May 09	2654	LCO/SAAO	1.0	*i*	−0.373 to −0.138	36	3.69	0.414	⋯	⋯
2017 May 13	2663	Swope	1.0	*i*	−0.708 to −0.191	143	2.00	1.75	⋯	⋯
2017 May 14	2667	LCO/SAAO	1.0	*i*	−0.156 to +0.0999	30	3.69	0.339	<0.0849	<0.0875
2017 May 15	2668	ULMT	0.6	*Clear*	−0.551 to +0.430	146	3.54	0.491	<0.1287	<0.1340
2017 May 15	2669	TRT-TNO	0.5	*R*	−0.307 to +0.174	250	1.04	1.13	0.0929 ± 0.0184	0.0943
2017 May 15	2669	TRT-GAO	0.7	*I*	−0.304 to +0.169	250	1.04	1.06	0.1035 ± 0.0147	0.1084
2017 May 15	2669	AAT	3.9	*Ks*	−0.136 to −0.0637	160	0.19	0.473	⋯	⋯
2017 May 15	2669	LCO/SAAO	1.0	*i*	+0.144 to +0.305	24	3.67	1.28	⋯	⋯
2017 May 16	2671	LCO/McDonald	1.0	*g*	−0.975 to −0.0629	104	3.70	1.44	⋯	⋯
2017 May 16	2671	AAT	3.9	*Ks*	−0.186 to +0.624	3022	0.10	1.56	0.0572 ± 0.0122	0.0615
2017 May 16	2672	LCO/SAAO	1.0	*g*	−0.238 to +0.406	97	3.69	1.10	<0.1001	<0.1026
2017 May 16	2672	TRT-GAO	0.7	*I*	−0.203 to +0.0680	140	1.04	0.880	<0.09776	<0.1025
2017 May 17	2673	LCO/CTIO	1.0	*g*	−0.372 to +0.296	101	3.67	1.22	0.1362 ± 0.0422	0.1396
2017 May 17	2673	LCO/McDonald	1.0	*g*	−0.361 to +0.401	114	3.70	1.08	0.1031 ± 0.0188	0.1056
2017 May 17	2674	TRT-GAO	0.7	*I*	−0.167 to +0.123	150	1.04	0.647	0.0700 ± 0.0120	0.0733
2017 May 17	2675	LCO/SAAO	1.0	*g*	−0.373 to +0.238	92	3.69	1.26	0.1243 ± 0.0576	0.1274
2017 May 18	2675	LCO/CTIO	1.0	*g*	+0.0391 to +0.407	56	3.67	0.801	⋯	⋯
2017 May 18	2676	LCO/McDonald	1.0	*g*	−0.372 to +0.168	80	3.70	1.05	<0.0952	<0.0975
2017 Apr 11	2741	Swope	1.0	*i*	−0.477 to +0.233	145	2.66	0.473	0.0619 ± 0.0224	0.0637
2017 Apr 13	2744	LCO/CTIO	1.0	*i*	−0.376 to −0.0480	50	3.67	0.531	⋯	⋯
2017 Apr 13	2745	LCO/SSO	1.0	*i*	−0.375 to −0.0385	51	3.69	0.388	⋯	⋯
2017 Apr 13	2745	TNT-TNO	2.4	*i*	−0.321 to +0.197	221	0.72	0.345	0.0779 ± 0.0168	0.0802
2017 Apr 15	2749	LCO/CTIO	1.0	*i*	−0.376 to +0.185	85	3.67	0.337	<0.0676	<0.0695
2017 Apr 16	2752	FLWO	1.2	*i*	−0.356 to −0.0368	78	2.27	0.190	⋯	⋯
2017 Apr 20	2762	LCO/CTIO	1.0	*i*	−0.351 to −0.0504	46	3.67	0.284	⋯	⋯
2017 Apr 21	2765	FLWO	1.2	*i*	−0.451 to −0.0278	103	2.28	0.173	⋯	⋯
2017 May 17	2835	GTC	10.4	510–1000 nm	−0.229 to +0.128	44	4.56	0.044	0.0536 ± 0.0057	0.0558
2017 May 22	2846	FLWO	1.2	*i*	−0.0780 to +0.267	84	2.28	0.166	<0.0473	<0.0487
2017 May 22	2846	ULMT	0.6	*Clear*	−0.0665 to +0.331	61	3.54	0.266	<0.0618	<0.0644
2017 May 25	2854	ULMT	0.6	*Clear*	−0.141 to +0.162	43	3.54	0.292	<0.0507	<0.0528
2017 May 27	2860	LCO/SSO	1.0	*i*	−0.108 to +0.100	32	3.69	0.373	<0.0769	<0.0791
2017 May 29	2865	LCO/SSO	1.0	*i*	−0.109 to +0.0985	32	3.67	0.327	<0.1793	<0.1846
2017 May 29	2866	LCO/SAAO	1.0	*i*	−0.110 to +0.0983	32	3.69	0.307	<0.0526	<0.0542

Note. The transit epoch is relative to the transit ephemeris given in Sanchis-Ojeda et al. (2015). The cadence is defined as the median time between data points.

(This table is available in machine-readable form.)

UT 2017 March 09 and UT 2017 March 15, which caused higher scatter in the light curves.

We used AstroImageJ (Collins et al. 2017) to perform bias, dark, and flat-field corrections, and to perform fixed radius circular aperture photometry on the final processed images. We used aperture radii of 10 pixels (3.″9) and a comparison ensemble of four or more stars to produce differential target star light curves.

2.9. Wisconsin-Indiana-Yale-NOAO Observatory (WIYN)

We observed one complete transit window of K2-22b on UT 2016 December 13 (transit epoch = 2427) using the WIYN[25] High-Resolution Infrared Camera (WHIRC) installed on the 3.5 m WIYN telescope at Kitt Peak National Observatory in Arizona. WHIRC is a Raytheon Virgo HgCdTe detector with a 2048 × 2048 array, a pixel scale of 0.″1 pixel^{-1}, and a 3.′4 × 3.′3 field of view. The *Ks*-band observations began about one hour before the expected transit and ended approximately one hour after the end of the expected transit, when morning twilight began. Some clouds were present during the observations.

The first step in processing the WHIRC data involved using the *wprep* IRAF script available on the WHIRC instrument website[26] to trim the images and perform a linearity correction. We then corrected the images against darks, masked bad pixels, removed the pupil ghost using an image generated by dividing *Ks* and *J* flats, and performed flat-fielding. We used AstroImageJ (Collins et al. 2017) to perform circular aperture photometry on the final processed images, using an aperture radius of 13 pixels (1.″3) and one comparison star to produce a light curve.

3. Analysis

3.1. Light Curve Modeling

To better understand the distribution of transit depths in our data and our detection limits, we performed a transit light curve fit using the Mandel & Agol (2002) model to all 31 data sets that covered most of the expected transit window (as per the ephemeris from Sanchis-Ojeda et al. 2015). The following constraints were imposed on the fits: the transit duration[27] was required to be <2 hr, the planet-star radius ratio (R_p/R_*) to be <1, and the mid-transit time should be within 1 hr of the predicted transit time. To account for long-term trends in the baseline of a light curve, we also allowed for a quadratic trend to be fitted simultaneous to the transit fit. The resulting values measured for R_p/R_* are given in Table 2. If no uncertainty in R_p/R_* is provided in the table, then the value for R_p/R_* is the 1σ upper limit. If no value for R_p/R_* is given at all, then that particular light curve did not cover a complete transit window of K2-22b. Figure 1 shows the detrended data and best-fitting models to the 31 light curves that fit our criteria.

[25] The WIYN Observatory is a joint facility of the University of Wisconsin-Madison, Indiana University, the National Optical Astronomy Observatory and the University of Missouri.

[26] https://www.noao.edu/kpno/manuals/whirc/WHIRC.html

[27] The transit duration previously measured from K2 and ground-based data is 48 ± 3 minutes (Sanchis-Ojeda et al. 2015).

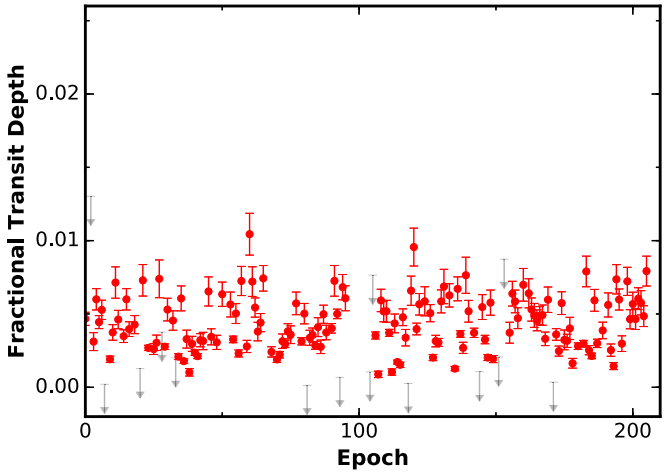


Figure 2. Fractional transit depth as a function of epoch for K2-22b measured from K2 Campaign 1 data collected between 2014 May and August. The epoch is relative to the ephemeris and orbital period from Sanchis-Ojeda et al. (2015): 2456811.1208 BJD and 9.145872 hr. Red points and error bars are detections of the transit, while gray markers with downward facing arrows are upper limits. The vertical axis is the same scale as in Figure 3 to aid visual comparison between the measured K2 and follow-up transit depths.

3.2. Impact of the Nearby Neighbor

As identified in Sanchis-Ojeda et al. (2015), K2-22 has a faint nearby companion located ∼2″ away. The angular proximity of this neighboring star means that in most of our photometry, the flux from the target and the neighbor are blended. To mitigate the effects of the neighboring star, we follow Ciardi et al. (2015) to calculate the true planet radius (and therefore the true planet-star radius ratio): $R_p(\text{true})/R_p(\text{observed}) = \sqrt{F_{\text{total}}/F_1}$, where F_1 is the flux of K2-22 as it is the star that is being transited and F_{total} is the combined flux of the primary and neighbor star. We used magnitudes provided in Table 3 of Sanchis-Ojeda et al. (2015) for K2-22 and its neighbor to compute F_1 and F_{total} for the relevant bandpasses where we measured either a detection or upper limit of the transit of K2-22b. We provide the corrected planet-star radius ratios in Table 2.

Given the proximity of the neighbor, there is some probability that it is the source of the transit signal rather than K2-22. However, Sanchis-Ojeda et al. (2015) argue why K2-22 is the most likely transit host rather than the neighbor. Furthermore, the WIYN observations presented here resolved K2-22 from the neighbor and provided a tentative detection of the K2-22b transit. More importantly, the neighbor did not display an obvious deep transit during the WIYN observations, which is additional evidence it is not the source of the transit signal.

4. Results

4.1. Long-term Monitoring of the Transit Depth

To determine how our measured transit depths compare to previous observations, we returned to the K2 Campaign 1 discovery data collected between 2014 May and August and followed the procedure outlined in Section 3 to measure the depths of transits in that long-cadence data (where each measurement has an integration time of 30 minutes). Depths were measured for transits that had at least two points in-transit, and the results are shown in Figure 2 as a function of epoch.

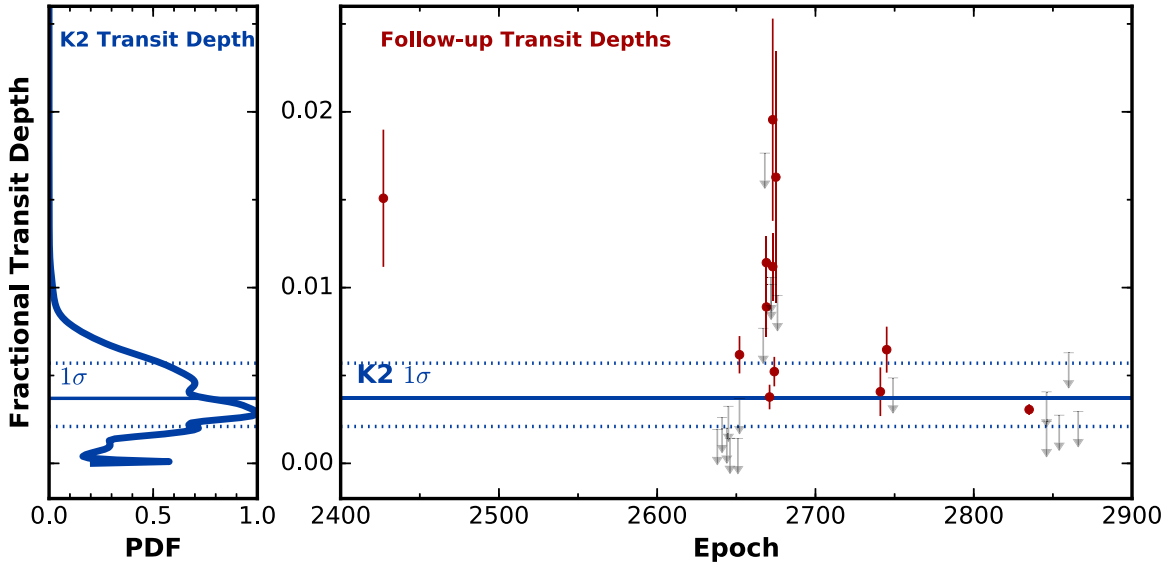


Figure 3. Left: probability Distribution Function of the transit depths measured from K2 Campaign 1 data (Figure 2). The horizontal solid line marks the median transit depth measured from K2, while the horizontal dotted lines indicate the 1σ distribution of the measured depths. Right: measured transit depth from our follow-up photometry of K2-22b as a function of epoch. As in Figure 2, the epoch is relative to the ephemeris and orbital period from Sanchis-Ojeda et al. (2015) and red points and error bars are detections of the transit, while gray markers with downward facing arrows are upper limits. The transit depths have been corrected for the flux contribution from the companion star. The transit depths we measure in our follow-up data are consistent with those measured from K2 data, within the uncertainties.

The detected K2 transits have depths ranging from 0.21 to 0.57% (the 1σ distribution) with a median depth of 0.37%.

In Figure 3, we show the measured transit depth (or upper limit on the transit depth) as a function of epoch from our ground-based follow-up campaign, along with the Probability Distribution Function (PDF) of the transit depths measured from K2 data. Due to the overall shallowness of the transit, we detected the transit in just ∼one-third of the 31 complete transit windows observed. We still find that our measured depths are consistent with what K2 detected, within the uncertainties.

Our most robust detection was obtained from the GTC, with a measured transit depth of ∼0.3% (Figure 1). To test whether we should have recovered a transit of this depth in our other individual data sets, we injected the GTC signal into the other light curves we collected. The resulting Box-fitting Least Squares (BLS; Kovács et al. 2002) spectrum is shown in Figure 4. When performing the BLS search on our data, we searched for transits with $q_{\rm min} = 0.02$, $q_{\rm max} = 0.15$, and orbital periods between 0 and 10 days, where q is the transit duration/orbital period. Figure 4 illustrates that if the transit of K2-22b had a consistent depth of ∼0.3%, we would have recovered it in the other individual observations. This suggests that the transit depth of K2-22b was changing over the course of our campaign. Figure 3 further supports this: for example, an initial detection of the K2-22b transit was made in 2016 December followed by a cluster of non-detections (upper limits) in early 2017 March (epoch 2638), and then beginning in 2017 mid-March (epoch 2669) we had several positive detections of the transit. Several of the light curves where we had a non-detection had sufficiently high photometric precision that we should have recovered a ∼0.3% transit. Therefore, we conclude that over the course of our observing campaign, the transit depth was indeed changing and was at times deeper and at other times shallower than the highest-precision event obtained by the GTC on 2017 May 17 (Figure 1).

Comparing the high-precision transits observed with the GTC in 2015 and in 2017 (Figure 5) also reveals that the 2017

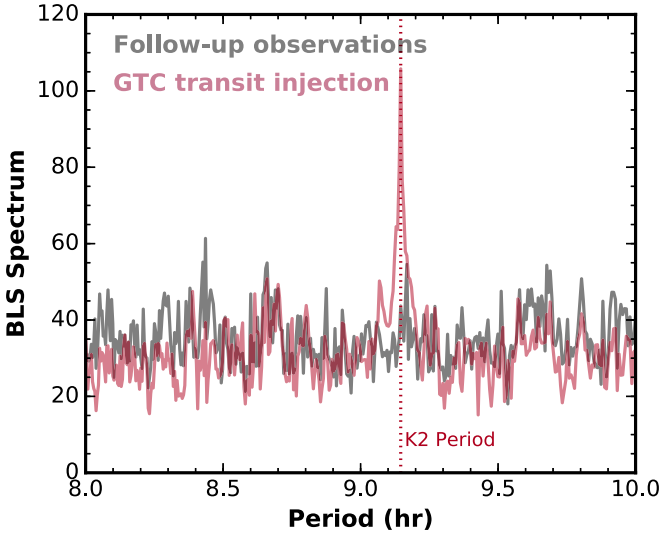


Figure 4. BLS spectrum of the light curves presented in Figure 1. The gray curve shows that no clear periodicity is seen in our data at the period of K2-22b (marked with the vertical dashed line). The red curve shows that a periodic signal is recovered at the period of K2-22b when injecting a transit with the same depth as the GTC-measured transit into our other data.

transit is shallower than previously measured in 2015, however, the 2017 observations are still consistent with depths measured from K2 overall. This instead suggests that the 2015 transits may have been observed at a time of relatively higher activity (e.g., enhanced ultraviolet and/or X-ray radiation) that led to increased mass-loss and deeper transits than typically seen by K2.

One additional note of interest is that the GTC transit observed in 2017 appears to have occurred exactly when predicted and to be more symmetric than the previously observed transits from the GTC. The other light curves presented in Figure 1 have poorer individual photometric precision than the GTC, so we are unable to perform a robust investigation of any changes in the transit shape or ephemeris

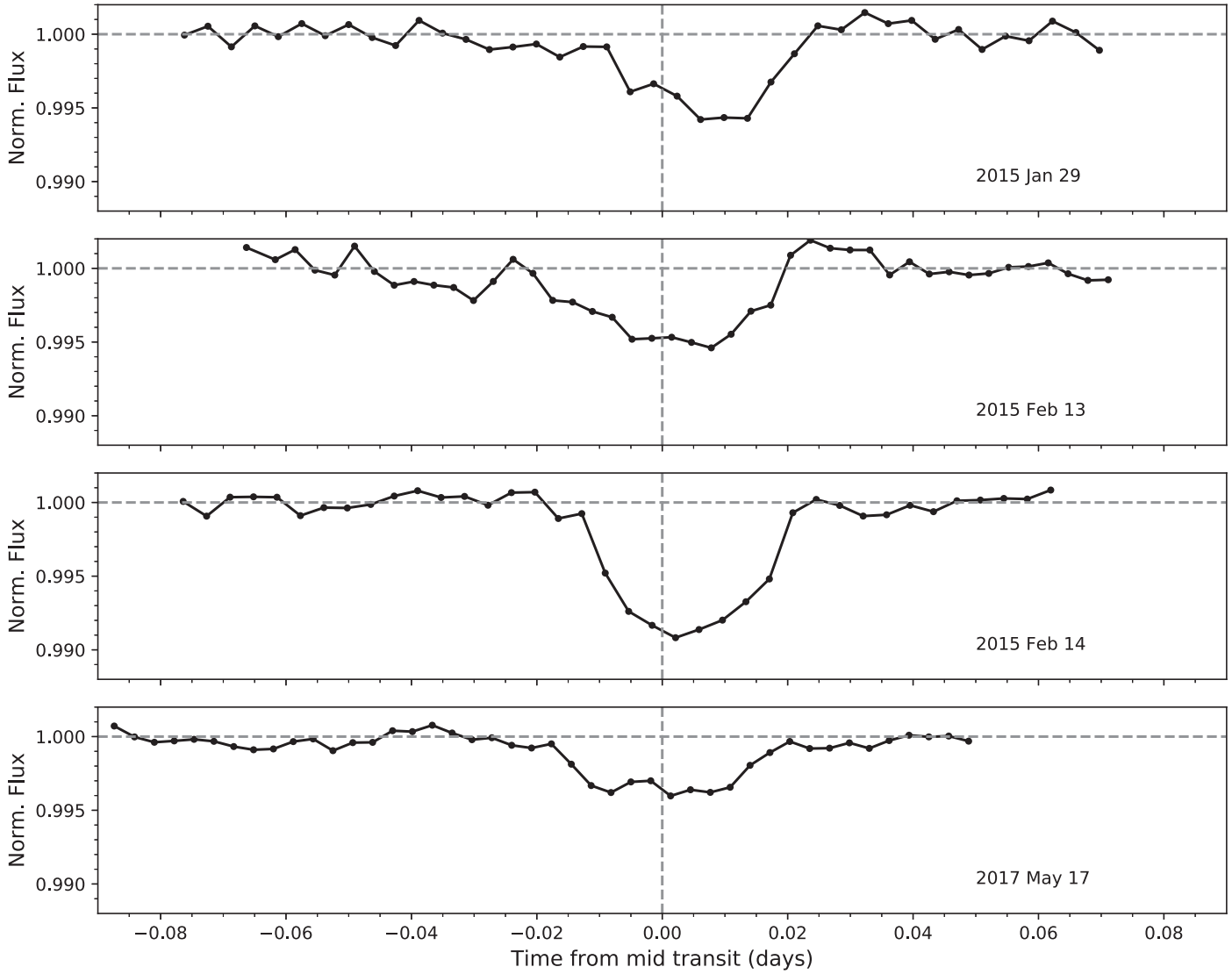


Figure 5. White light curves of K2-22b from the GTC. The top three panels show data from 2015 (transit epoch = 634, 673, 676, respectively), originally presented in Sanchis-Ojeda et al. (2015). The bottom panel shows the data from 2017 (transit epoch = 2835), and it is clear that this transit is shallower than previously recorded. However, this latest transit remarkably takes place right at the predicted time, and it also appears to be more symmetric than previous transits.

over each epoch. While some appear to have longer durations than expected and/or occur outside the predicted transit window, due to the relatively poor photometric precision in those cases we do not claim that those deviations in transit duration or time are significant.

Because we have 24 light curves from LCO in total (17 in Sloan *i* band and 7 in Sloan *g* band), we explored whether stacking the phased light curves would provide a clear detection of the K2-22b transit. Figure 6 shows the stacked light curves from LCO in both bands, where the photometric error bars are defined as the standard deviation of the binned light curve outside of the expected transit window. Interestingly, while we do not see an obvious transit in the *i* band data, the *g* band data reveal a potential ∼0.3% transit occurring slightly earlier than predicted. We note the *g* band data were collected between UT 2017 March 16–18 between transit epochs 2671 and 2676, while the *i* band data were collected over several months between UT 2017 March 1 and May 29. Since the *g* band data were collected over a relatively short timescale, this suggests the *g* band detection is robust, although these data have notably poorer photometric precision than the *i* band data. The *g* band depth is also consistent with what we measured from the high-precision GTC light curve collected two months later on UT 2017 May 17. However, given the significant scatter in the *g* band data, we cannot definitively conclude that an early transit of K2-22b was detected in the stacked light curves.

In addition, there are a few individual measurements that may be anomalous and therefore affecting our interpretation of the data. The first detection in 2016 December (with WIYN; see Figure 1) is highly dependent on detrending. If we assume the transit is longer than expected, then the curvature seen in the light curve could be indicative of a transit as we present here. On the other hand, if we assume the transit has the expected duration of ∼48 minutes, then detrending the data results in a null detection of a transit and reduces the apparent slope in the transit depth over time. The uncertainty in the transit duration and depth for the WIYN data likely stems from the fact that we only had one suitable comparison star in the field of view. LCO observations at epoch 2865 (Figure 1) also show a significant trend at the beginning of the light curve, but as the data acquired at the subsequent epoch do not show any

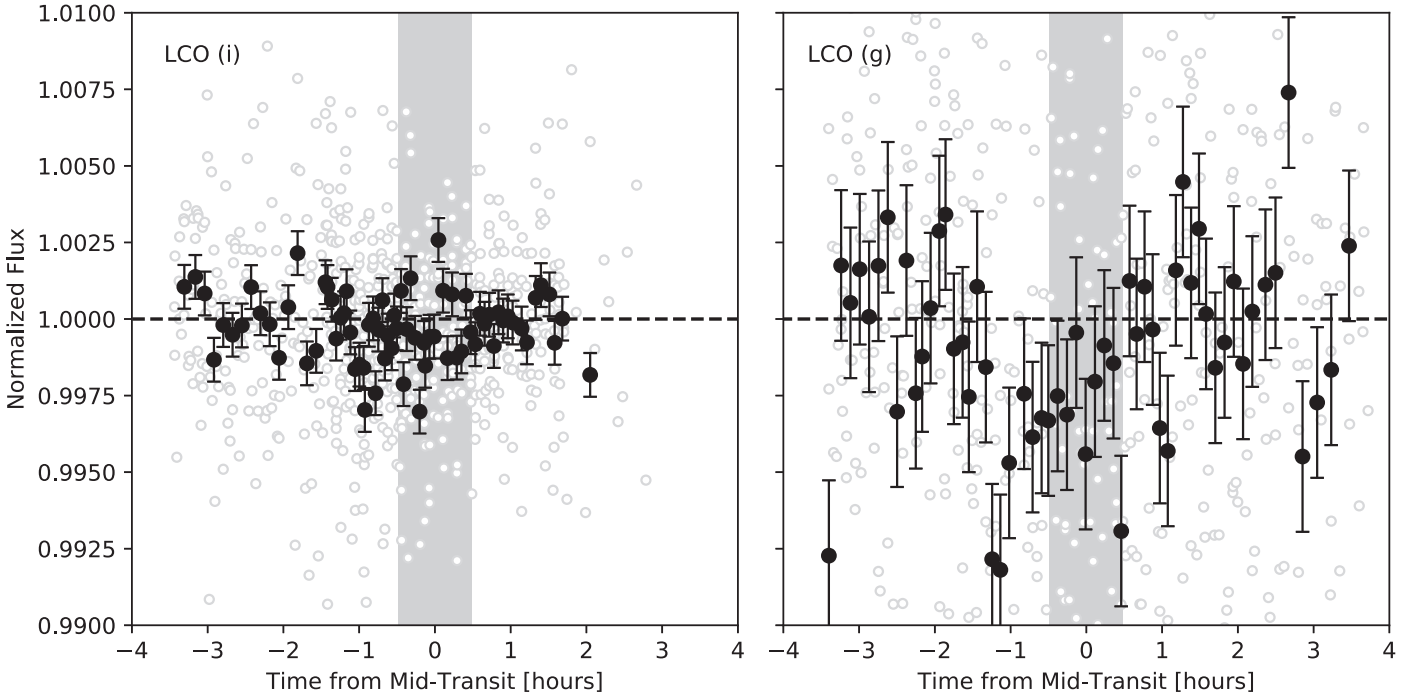


Figure 6. Stacked and phased light curves from LCO in the Sloan *i* band (left) and *g* band (right). In total, 17 *i* band light curves were stacked in the left panel and 7 *g* band light curves were stacked in the right panel. The full data sets are shown in light gray open circles, while binned light curves are shown as blacked filled circles. The dark gray shaded region indicates the predicted time and duration of the transit of K2-22b, and the horizontal dashed line marks where the normalized flux = 1 to guide the eye. All *g* band data were obtained between UT 2017 March 16–18 over five transit epochs (2671–2676), while the *i* band data were collected between UT 2017 March 1 and May 29. The LCO *i* band data do not show an obvious transit. While the LCO *g* band data display evidence of a ∼0.3% transit that occurs slightly earlier than predicted, it has significantly larger photometric error bars than the *i* band data.

anomalous trend, we believe this is not astrophysical and instead some type of instrumental artifact. The best-fitting model is correspondingly a poor fit given this anomalous light curve feature.

4.2. Search for Wavelength-dependent Transit Light Curve Shape

The few epochs where we have multi-wavelength coverage over a complete transit window (i.e., epochs 2652, 2669, 2672, 2846 in Figure 1) do not reveal any significant color dependence. While the *R* and *I* band data at epoch 2669 are suggestive of a depth difference, we do not have the photometric precision to make a robust claim.

Figure 6 shows the stacked light curves from LCO in Sloan *i* and *g* bands, and there we see that the *g* band data are suggestive of a ∼0.3% transit. On the other hand, we see no clear evidence for a transit in the *i* band data. That we find evidence of a chromatic transit that is deeper at bluer wavelengths is consistent with what has been observed for, e.g., KIC 12557548b (Bochinski et al. 2015) and KIC 8462852 (Boyajian et al. 2018; Deeg et al. 2018) (see Section 5 for further discussion of these other systems). The caveat is that we are comparing stacked light curves collected over several days to months, and the *g* band data have poorer photometric precision than the *i* band data. We therefore cannot make any definitive claims about the chromaticity based on the LCO data and instead conclude that the LCO data are *suggestive* of a deeper transit at blue wavelengths.

We also analyzed the spectroscopic data collected from the GTC, where in Figure 7 we present the GTC data split into blue and red wavelengths and also in three different color bands. During this one transit, no significant color dependence in the depth is measured. We note that of the three transits observed previously with the GTC, only one displayed a color-dependent depth (with a deeper transit seen at blue wavelengths than red), and that was the deepest transit measured on UT 2015 February 4 as shown in Figure 5 and Sanchis-Ojeda et al. (2015). Ridden-Harper et al. (2018) recently demonstrated that the transit depth of disintegrating rocky planets is wavelength-independent for optically thick tails. The single wavelength-dependent transit observed for K2-22b to date could therefore be a sign of an optically thin tail at that particular epoch.

5. Discussion

We have presented 45 new ground-based light curves of the K2-22 system collected in 2016 December and between 2017 March and May. These light curves span 34 individual transit epochs of K2-22, and we were able to measure a transit depth for 12 of these epochs. We find that the measured transit depths of K2-22b over this period are variable at a level that is consistent with the range of transit depths measured by the K2 mission between 2014 May and August as well as with the ground-based campaign conducted between 2015 January and March. We particularly find evidence for ongoing variability when comparing the high-precision GTC data obtained in 2015 with our 2017 data (Figure 5). We also find evidence of transit-like variability outside of the predicted transit windows that were determined based on the ephemeris from Sanchis-Ojeda et al. (2015), but the photometric precision of our data limits us from performing a detailed investigation. Given that our highest quality data set from the GTC produced a transit that occurred at the expected time and has a duration consistent with Sanchis-Ojeda et al. (2015), it is somewhat surprising to see transit-like features occurring outside of the predicted windows

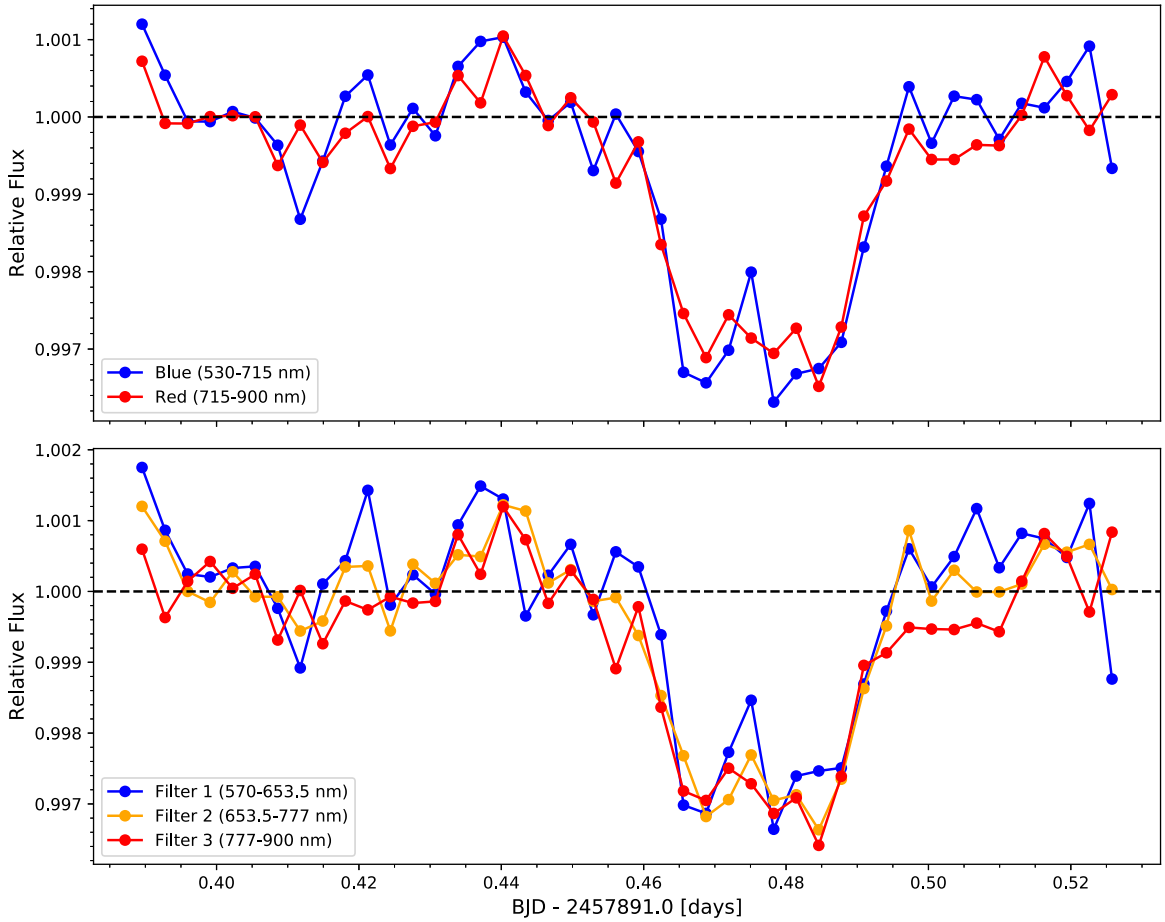


Figure 7. GTC observations of K2-22 from UT 2017 May 17 (transit epoch = 2835) split among blue and red wavelengths (top panel) and among three color bands (bottom panel). No significant variations in the color of the transit are detected in either case.

or lasting longer than expected. Still, our photometric monitoring campaign suggests that this disintegrating planet may potentially be outgassing at sporadic intervals since some of the transits of K2-22b that we robustly detect occur either earlier or later than predicted (Figure 1).

At the epochs where we have multi-wavelength coverage during the transit windows, we find no significant color dependence of the transit light curve shape (Figure 7). This lack of a color dependence is largely consistent with Sanchis-Ojeda et al. (2015). However, the one color-dependent transit observed for K2-22b in 2015 is reminiscent of studies of KIC 12557548b, where Bochinski et al. (2015) find evidence of deeper transits at shorter wavelengths, and of the famously dimming star KIC 8462852, where recently Bodman et al. (2018a), Boyajian et al. (2018), and Deeg et al. (2018) observed clear chromaticity during a dimming event. While the dimmings that occur around KIC 8462852 are more than likely due to a different phenomenon (e.g., exocomets; Bodman & Quillen 2016; Boyajian et al. 2016) than a disintegrating planet, that dimming was also observed to be deeper at blue than at red wavelengths (Bodman et al. 2018a; Boyajian et al. 2018; Deeg et al. 2018). Bodman et al. (2018a) and Boyajian et al. (2018) specifically find that the chromaticity is consistent with occultation of the star by optically thin dust of the order $\ll 1$ μm in size on average. Deeg et al. (2018) also attribute the color dependence to absorption by dust with particles sizes of $\sim$0.0015–0.15 μm, and they support the argument that occultation by dusty material is what causes the dimming events in that star. To strengthen the evidence for transient occurrences of dust tails and potentially even determine whether the constituents of its dust tail are similar in size to those found in KIC 12557548b's dust tail or perhaps those seen around KIC 8462852, continued monitoring of K2-22b at multiple wavelengths is warranted. Since the only color-dependent transit detected so far was also observed during one of the deepest transits of K2-22b seen to date (third panel of Figure 5 in this paper and Figure 12 in Sanchis-Ojeda et al. 2015), it would be interesting to determine with future observations whether extra material being blown off the planet is what causes both a deep and color-dependent transit.

A comprehensive overview and comparison of the three known disintegrating planets around main-sequence stars was provided in van Lieshout & Rappaport (2017), and the data presented here further supports the fact that all disintegrating planets seem to display variable transit depths on all timescales observed, from transit to transit to several years. A continuous observing campaign by a facility capable of high-precision photometry, such as NASA's *Spitzer Space Telescope*, may help elucidate both the frequency at which the K2-22 system varies outside the primary transit window and how quickly the transit depth itself varies. However, *Spitzer* is currently expected to only operate through the end of 2019 November. NASA's *Transiting Exoplanet Survey Satellite* (*TESS*; Ricker et al. 2015; Huang et al. 2018) successfully began science operations in July 2018 and could also nominally collect additional long-baseline photometry of this system. One caveat

is that the orientation of the *TESS* field of view on the sky during its 2-year prime mission is such that it covers the ecliptic poles in full to overlap with the continuous viewing zone of NASA's *James Webb Space Telescope* (*JWST*) and largely avoids the ecliptic plane. K2-22, being in the ecliptic plane, is therefore not within the visibility window of the prime *TESS* mission. An extended mission for *TESS* in the 2020s with strategic pointings could provide the opportunity to acquire additional long-baseline time-series observations of this unique system. In the meantime, ESA's CHaracterising ExOPlanet Satellite (CHEOPS; Broeg et al. 2013) is also expected to launch by the end of 2018 and will perform photometric follow-up of known exoplanets, potentially including K2-22.

Bodman et al. (2018b) recently highlighted the unique opportunity to study the composition of K2-22b via *JWST* transmission spectroscopy of the planet's tail. Given the intrinsic rarity of disintegrating rocky planets like K2-22b and that the launch of *JWST* is in the near future (2021), now is the optimal time to prepare for such follow-up observations via additional characterization efforts with currently operating facilities.

This work has made use of observations from the LCOGT network. Based in part on observations made with the Gran Telescopio Canarias (GTC), installed in the Spanish Observatorio del Roque de los Muchachos of the Instituto de Astrofísica de Canarias, in the island of La Palma. This work has made use of data obtained at the Thai National Observatory on Doi Inthanon, operated by NARIT. This research was supported by the grant RTA5980003 from the Thailand Research Fund. Based in part on observations at Kitt Peak National Observatory, National Optical Astronomy Observatory (NOAO Prop. ID: 2016B-0196; PI: K. D. Colón), which is operated by the Association of Universities for Research in Astronomy (AURA) under a cooperative agreement with the National Science Foundation. Some data presented herein were obtained at the WIYN Observatory from telescope time allocated to NN-EXPLORE through the scientific partnership of the National Aeronautics and Space Administration, the National Science Foundation, and the National Optical Astronomy Observatory. KH acknowledges support from STFC grant ST/M001296/1. IRAF is distributed by the National Optical Astronomy Observatory, which is operated by the Association of Universities for Research in Astronomy (AURA) under a cooperative agreement with the National Science Foundation.

Facilities: LCOGT, WIYN (WHIRC).

Software: AstroImageJ (Collins et al. 2017), Astrometry.net (Lang et al. 2010), Astropy (Astropy Collaboration et al. 2013), IDL (Landsman 1993), SExtractor (Bertin & Arnouts 1996), FITSH (Pál 2012), IRAF (Tody 1986, 1993).

ORCID iDs

Knicole D. Colón https://orcid.org/0000-0001-8020-7121
George Zhou https://orcid.org/0000-0002-4891-3517
Avi Shporer https://orcid.org/0000-0002-1836-3120
Karen A. Collins https://orcid.org/0000-0001-6588-9574
Allyson Bieryla https://orcid.org/0000-0001-6637-5401
Petchara Pattarakijwanich https://orcid.org/0000-0001-8451-5316
Daniel Bayliss https://orcid.org/0000-0001-6023-1335
William D. Cochran https://orcid.org/0000-0001-9662-3496
Keith Horne https://orcid.org/0000-0003-1728-0304
Michael Ireland https://orcid.org/0000-0002-6194-043X
Lucyna Kedziora-Chudczer https://orcid.org/0000-0001-7212-0835
David W. Latham https://orcid.org/0000-0001-9911-7388
Tom. R. Marsh https://orcid.org/0000-0002-2498-7589
David Ruffolo https://orcid.org/0000-0003-3414-9666
Chris G. Tinney https://orcid.org/0000-0002-7595-0970
Suraphong Yuma https://orcid.org/0000-0002-0269-0135

References

Alonso, R., Rappaport, S., Deeg, H. J., & Palle, E. 2016, A&A, 589, L6
Astropy Collaboration, Robitaille, T. P., Tollerud, E. J., et al. 2013, A&A, 558, A33
Bertin, E., & Arnouts, S. 1996, A&AS, 117, 393
Bochinski, J. J., Haswell, C. A., Marsh, T. R., Dhillon, V. S., & Littlefair, S. P. 2015, ApJL, 800, L21
Bodman, E., Wright, J., Boyajian, T., & Ellis, T. 2018a, arXiv:1806.08842
Bodman, E. H. L., & Quillen, A. 2016, ApJL, 819, L34
Bodman, E. H. L., Wright, J. T., Desch, S. J., & Lisse, C. M. 2018b, arXiv:1808.07043
Boyajian, T. S., Alonso, R., Ammerman, A., et al. 2018, ApJL, 853, L8
Boyajian, T. S., LaCourse, D. M., Rappaport, S. A., et al. 2016, MNRAS, 457, 3988
Broeg, C., Fortier, A., Ehrenreich, D., et al. 2013, European Physical Journal Web of Conferences, 47, 03005
Brown, T. M., Baliber, N., Bianco, F. B., et al. 2013, PASP, 125, 1031
Carter, J. A., Winn, J. N., Holman, M. J., et al. 2011, ApJ, 730, 82
Cepa, J., Aguiar, M., Escalera, V. G., et al. 2000, Proc. SPIE, 4008, 623
Ciardi, D. R., Beichman, C. A., Horch, E. P., & Howell, S. B. 2015, ApJ, 805, 16
Collins, K. A., Kielkopf, J. F., Stassun, K. G., & Hessman, F. V. 2017, AJ, 153, 77
Croll, B., Dalba, P. A., Vanderburg, A., et al. 2017, ApJ, 836, 82
Croll, B., Rappaport, S., DeVore, J., et al. 2014, ApJ, 786, 100
Croll, B., Rappaport, S., & Levine, A. M. 2015, MNRAS, 449, 1408
Deeg, H. J., Alonso, R., Nespral, D., & Boyajian, T. S. 2018, A&A, 610, L12
Dhillon, V. S., Marsh, T. R., Atkinson, D. C., et al. 2014, MNRAS, 444, 4009
Gänsicke, B. T., Aungwerojwit, A., Marsh, T. R., et al. 2016, ApJL, 818, L7
Hallakoun, N., Xu, S., Maoz, D., et al. 2017, MNRAS, 469, 3213
Howell, S. B., Sobeck, C., Haas, M., et al. 2014, PASP, 126, 398
Huang, C. X., Shporer, A., Dragomir, D., et al. 2018, arXiv:1807.11129
Kawahara, H., Hirano, T., Kurosaki, K., Ito, Y., & Ikoma, M. 2013, ApJL, 776, L6
Kovács, G., Zucker, S., & Mazeh, T. 2002, A&A, 391, 369
Landsman, W. B. 1993, in ASP Conf. Ser. 52, Astronomical Data Analysis Software and Systems II, ed. R. J. Hanisch, R. J. V. Brissenden, & J. Barnes (San Francisco, CA: ASP), 246
Lang, D., Hogg, D. W., Mierle, K., Blanton, M., & Roweis, S. 2010, AJ, 139, 1782
Mandel, K., & Agol, E. 2002, ApJL, 580, L171
Pál, A. 2012, MNRAS, 421, 1825
Rappaport, S., Barclay, T., DeVore, J., et al. 2014, ApJ, 784, 40
Rappaport, S., Levine, A., Chiang, E., et al. 2012, ApJ, 752, 1
Redfield, S., Farihi, J., Cauley, P. W., et al. 2017, ApJ, 839, 42
Ricker, G. R., Winn, J. N., Vanderspek, R., et al. 2015, JATIS, 1, 014003
Ridden-Harper, A. R., Keller, C. U., Min, M., van Lieshout, R., & Snellen, I. A. G. 2018, arXiv:1807.07973
Sanchis-Ojeda, R., Rappaport, S., Pallè, E., et al. 2015, ApJ, 812, 112
Schlawin, E., Herter, T., Zhao, M., Teske, J. K., & Chen, H. 2016, ApJ, 826, 156
Tinney, C. G., Ryder, S. D., Ellis, S. C., et al. 2004, Proc. SPIE, 5492, 998
Tody, D. 1986, Proc. SPIE, 627, 733
Tody, D. 1993, in ASP Conf. Ser. 52, Astronomical Data Analysis Software and Systems II, ed. R. J. Hanisch, R. J. V. Brissenden, & J. Barnes (San Francisco, CA: ASP), 173
Vanderburg, A., Johnson, J. A., Rappaport, S., et al. 2015, Natur, 526, 546
Vanderburg, A., & Rappaport, S. A. 2018, arXiv:1804.01997
van Lieshout, R., & Rappaport, S. 2017, arXiv:1708.00633
Xu, S., Rappaport, S., van Lieshout, R., et al. 2018, MNRAS, 474, 4795
Zhou, G., Bayliss, D. D. R., Kedziora-Chudczer, L., et al. 2014, MNRAS, 445, 2746
Zhou, G., Kedziora-Chudczer, L., Bailey, J., et al. 2016, MNRAS, 463, 4422

The reduction of magnetic reconnection outflow jets to sub-Alfvénic speeds

Colby C. Haggerty, Michael A. Shay, Alexandros Chasapis, Tai D. Phan, James F. Drake, Kittipat Malakit, Paul A. Cassak, and Rungployphan Kieokaew

Citation: Physics of Plasmas **25**, 102120 (2018); doi: 10.1063/1.5050530
View online: https://doi.org/10.1063/1.5050530
View Table of Contents: http://aip.scitation.org/toc/php/25/10
Published by the American Institute of Physics

Articles you may be interested in

Turbulent heating due to magnetic reconnection
Physics of Plasmas **25**, 012304 (2018); 10.1063/1.4993423

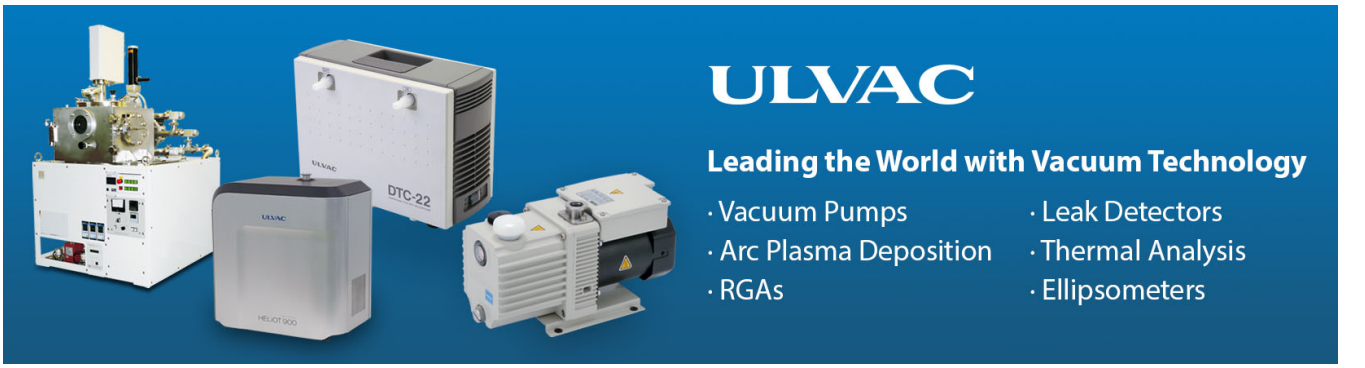
On the effect of parallel shear flow on the plasmoid instability
Physics of Plasmas **25**, 102117 (2018); 10.1063/1.5061818

Magnetohydrodynamic waves and the Kelvin-Helmholtz instability at the boundary of plasma mediums
Physics of Plasmas **25**, 102119 (2018); 10.1063/1.5048913

Strongly localized magnetic reconnection by the super-Alfvénic shear flow
Physics of Plasmas **25**, 080701 (2018); 10.1063/1.5042539

Theory of critical balance in plasma turbulence
Physics of Plasmas **25**, 092301 (2018); 10.1063/1.5041754

Eulerian variational formulations and momentum conservation laws for kinetic plasma systems
Physics of Plasmas **25**, 102506 (2018); 10.1063/1.5031155



The reduction of magnetic reconnection outflow jets to sub-Alfvénic speeds

Colby C. Haggerty,[1,2,a)] Michael A. Shay,[2] Alexandros Chasapis,[2] Tai D. Phan,[3] James F. Drake,[4] Kittipat Malakit,[5] Paul A. Cassak,[6] and Rungployphan Kieokaew[7]
[1]*Department of Astronomy and Astrophysics, University of Chicago, Chicago, Illinois 60637, USA*
[2]*Department of Physics and Astronomy, Bartol Research Institute, University of Delaware, Newark, Delaware 19716, USA*
[3]*Space Sciences Laboratory, University of California, Berkeley, California 94720, USA*
[4]*Institute for Research in Electronics and Applied Physics, University of Maryland, College Park, Maryland 20742, USA*
[5]*Department of Physics, Faculty of Science and Technology, Thammasat University, Pathum Thani 12120, Thailand*
[6]*Department of Physics and Astronomy, West Virginia University, Morgantown, West Virginia 26506, USA*
[7]*CGAFD, Mathematics, CEMPS, University of Exeter, Exeter EX4 4QF, United Kingdom*

(Received 31 July 2018; accepted 8 October 2018; published online 31 October 2018)

The outflow velocity of jets produced by collisionless magnetic reconnection is shown to be reduced by the ion exhaust temperature in fully kinetic particle in cell simulations and *in situ* satellite observations. We derive a scaling relationship for the outflow velocity based on the upstream Alfvén speed and the parallel ion exhaust temperature, which is verified in kinetic simulations and observations. The outflow speed reduction is shown to be due to the firehose instability criterion, and so, for large enough guide fields, this effect is suppressed and the outflow speed reaches the upstream Alfvén speed based on the reconnecting component of the magnetic field. *Published by AIP Publishing*. https://doi.org/10.1063/1.5050530

I. INTRODUCTION

Magnetic reconnection is a plasma process that efficiently releases energy stored in magnetic fields and generates fast plasma jets.[1] Reconnection occurs at thin current sheets where the direction of the magnetic field changes over a small spatial scale. During reconnection, the frozen-in condition of magnetohydrodynamics is broken and field lines effectively "break" and cross connect, creating stretched field lines, which relax via the tension force. This contraction of the field line generates bulk plasma outflow away from the location where this breaking occurred (called the x-line) with a speed expected to reach the Alfvén speed based on the inflowing plasma parameters and the changing component of the magnetic field.[2]

Outflow jets are one of the most recognizable features of reconnection. They have been repeatedly observed in simulations and laboratory and satellite observations (e.g., Paschmann *et al.*,[3] Sonnerup,[4] Sato and Hayashi,[5] Birn and Hones,[6] and Stenzel *et al.*[7]). Observational events typically require a jet detection to be classified as reconnection. However, in both simulations and observations, the magnitude of the outflow speed is often found to be significantly less than the Alfvén speed (e.g., Paschmann *et al.*,[8] Phan *et al.*,[9] Gosling *et al.*,[10] Liu *et al.*,[11] and Haggerty *et al.*[12]). A significant amount of the converted magnetic energy is transferred into the outflow jets,[13–18] and the magnitude of the jet velocities has important consequences for many different collisionless plasma systems where reconnection occurs (e.g., dipolarization fronts,[19,20] in thermal[12,21] and non-thermal particle energization,[22,23] and potentially many others). The ability to predict the effects of reconnection on any plasma system requires the accurate prediction of outflow jets, and this work offers a simple scaling prediction consistent with observations and simulations and is thus a critical step in a predictive description of magnetic reconnection.

In this work, we show that the firehose instability criterion being reached in the exhaust[11,24] reduces the outflow velocity in nearly anti-parallel reconnection events and derive a prediction for the reduction. A relationship is derived by matching the anisotropic Rankine-Hugoniot conditions across the edge of the reconnection exhaust boundary. The prediction is tested using 81 particle-in-cell (PIC) reconnection simulations and 14 previously published observational events and is found to agree remarkably well. Finally, we discuss the implications of this result, and its importance to understanding how released magnetic energy is partitioned during reconnection.

II. SIMULATIONS AND OBSERVATIONS

To study why the outflow velocity is less than the Alfvén speed, we examine 81 reconnection simulations [56 where the two reconnecting field lines are separated by more than 135° (nearly anti-parallel) and 25 where they are separated by some smaller angle (in this work <135°) (guide field)] preformed using the kinetic-PIC code P3D Zeiler *et al.*[25] In the simulations, magnetic field strengths and particle number densities are normalized to arbitrary characteristic values B_0 and n_0, respectively. Lengths are normalized to the ion inertial length $d_{i0} = c/\omega_{pi0}$ at the reference density n_0. Time is normalized to the ion cyclotron time $\Omega_{ci0}^{-1} = (eB_0/m_i c)^{-1}$. Speeds are normalized to the Alfvén speed $c_{A0} = \sqrt{B_0^2/(4\pi m_i n_0)}$. Electric fields and temperatures are normalized to $E_0 = c_{A0}B_0/c$ and

a)Electronic mail: CHaggerty@UChicago.edu

$T_0 = m_i c_{A0}^2$, respectively. The coordinate system is in "simulation coordinates," meaning that the reconnection outflows are along $\hat{x}$ and the inflows are along $\hat{y}$.

Simulations are performed in a periodic domain with size and grid scale varied based on simulation and inflow parameters. The reconnection simulation parameters are described in detail in two previous publications[12,17] A range of reconnection magnetic fields B_r, upstream densities n_{up}, and upstream ion and electron temperatures $T_{i,up}$ and $T_{e,up}$ are used. The parameters for the simulations are shown in the supplementary material.

In each simulation, we take a trapezoidal region from 5 to 20 d_i downstream of the x-line bounded by the exhaust boundary in order to calculate the average parallel ion exhaust temperature. The outflow velocity is taken as the asymptotic $E \times B$ velocity at the midplane sufficiently far downstream of the x-line. Further details about the calculation of these values are detailed in the work of Haggerty *et al.*[12]

Along with simulations, we also examine 14 previously published observed reconnection events.[10,26–33] These events were measured in several different plasma systems, including the solar wind, the magnetosheath, and the magnetotail.

In Figs. 1(a) and 1(b), the asymptotic $E \times B$ outflow velocity is plotted against the upstream Alfvén speed based on the reconnecting magnetic field c_{Ar} with a dashed black line corresponding to a slope of 1 for the simulations and observations, respectively. For the guide field cases (green circles), there is good agreement between the outflow velocity and the upstream Alfvén speed based on the reconnecting magnetic field. However, for every nearly anti-parallel simulation and observation (red white and blue triangles) irrespective of the initial conditions, the outflow velocity is less than the Alfvén speed. The difference between the outflow and the Alfvén speed also varies dramatically between different events. There are numerous cases where the outflow is almost as large as Alfvén speed, and there are also many events where the outflow is an order of magnitude smaller than the Alfvén speed. It is clear that in the absence of a guide field, the outflow velocity can be significantly reduced.

The reduction of the outflow velocity is linked in some way to the upstream ion beta β_i based on the reconnecting component of the upstream magnetic field indicated by the triangle's color in Fig. 1(a). As β_i goes to zero (blue triangles), the outflow approaches the Alfvén speed, and as β_i becomes larger (red triangles), the outflow velocity is reduced. This suggests that the ion upstream thermal velocity relative to the upstream Alfvén speed reduces the outflow. This is explored in Sec. III where we have analyzed the effects of the firehose instability in reconnection exhausts. In Sec. III, a theory for this relationship is derived.

III. THEORY

Using double adiabatic theory[34] for a parallel propagating shear Alfvén wave, the dispersion relationship can be shown to be $\omega^2 = \frac{k^2}{m_i n}\left(\frac{B^2}{4\pi} + P_\perp - P_\parallel\right)$ where $P_\parallel$ and $P_\perp$ are the sum of the ion and electron thermal pressures parallel and perpendicular to the local magnetic field line.[35] For an isotropic system, the relationship becomes $\omega = c_A k$ with the phase velocity equal to the Alfvén speed. There is clearly a

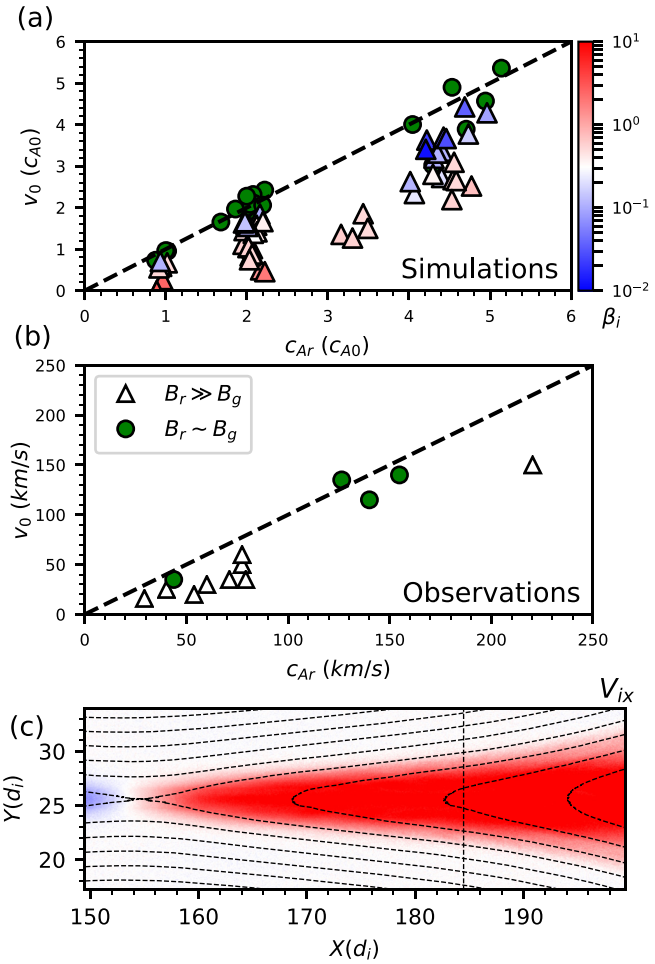


FIG. 1. (a) and (b) The asymptotic $E \times B$ outflow velocity v_0 against the upstream Alfvén speed based on the reconnecting magnetic field c_{Ar} for 81 different PIC simulations (a) and 14 previously published observational events (b). The green circles correspond to simulations with a guide field comparable to the reconnecting field, and the blue/white/red triangles correspond to nearly anti-parallel reconnection events. (c) 2D color plot of the ion outflow velocity v_{ix} for an example simulation with contours of the magnetic field plotted in black dashed lines. The vertical dashed black line shows where the cut is taken for Fig. 2(a). This is simulation 693 in the table in the supplementary material.

regime where the right side is negative, and the wave is unstable. This occurs when $P_\parallel > \frac{B^2}{4\pi} + P_\perp$ or equivalently when ϵ defined as $\epsilon = 1 + 4\pi(P_\perp - P_\parallel)/B^2 < 0$ and is referred to as the firehose instability. Conceptually, this instability can be interpreted as an effective centrifugal force from particles traveling along curved magnetic field lines due to $P_\parallel$ that beats the tension force trying to straighten out the field line. When $\epsilon \to 0$, the pressure force is completely counter-balancing the tension in the magnetic field line, and the field line cannot accelerate the plasma.

Previous work has accounted for anisotropic pressures and has shown that the tangential flow across a rotational discontinuity (RD) is given by

$$\mathbf{v}_{t2} - \mathbf{v}_{t1} = \sqrt{\frac{n_1 \epsilon_1}{4\pi m_i}}\left(\frac{\mathbf{B}_{t1}}{n_1} - \frac{\mathbf{B}_{t2}}{n_2}\right). \quad (1)$$

This prescription can be applied to the boundary of a reconnection exhaust to give a prediction for the outflow

velocity.[4,36] This is done by taking the "1" location to be upstream of the reconnection exhaust, and the "2" location where the reconnecting magnetic field goes to zero, as well as taking the tangential direction parallel to the outflow and the normal along the inflow direction. Assuming that the upstream pressure is isotropic, the outflow is predicted to be the upstream Alfvén speed based on the reconnecting component of the magnetic field, $v_0 = \frac{B_r}{\sqrt{4\pi m_i n_u}} = c_{Ar}$. In Figs. 1(a) and 1(b), it is clear that for both simulations and observations with a guide field (denoted by green circles), the outflow agrees with this prediction. However, for nearly anti-parallel events, there is significant deviation from what theory predicts.

This effect can be seen even more clearly in Figs. 2(a) and 2(b), which show cuts of the ion outflow velocity normalized to the upstream Alfvén speed (solid blue line), the ion firehose parameter (solid black line), and the prediction (red dashed line) plotted along the inflow direction $30d_{i0}$ downstream of the x-line for an anti-parallel and guide field simulation, a and b, respectively. For both the guide field and anti-parallel case, there is a deviation between the ion outflow and the RD prediction along the edge of the exhaust associated with an electron return current required that generates the hall magnetic field structure;[37,38] however, farther into the exhaust outflow velocity agrees well with the ion outflow in the guide field simulation but not in the anti-parallel case. In the guide field case, the jet speed continues to increase towards the center of the exhaust, reaching the upstream Alfvén speed at the midplane. In the anti-parallel cut, precisely at the region where $\epsilon \to 0$, the outflow velocity stops increasing and flattens off to a value significantly less than 1. This suggests that the firehose instability is potentially responsible for limiting the outflow velocity.

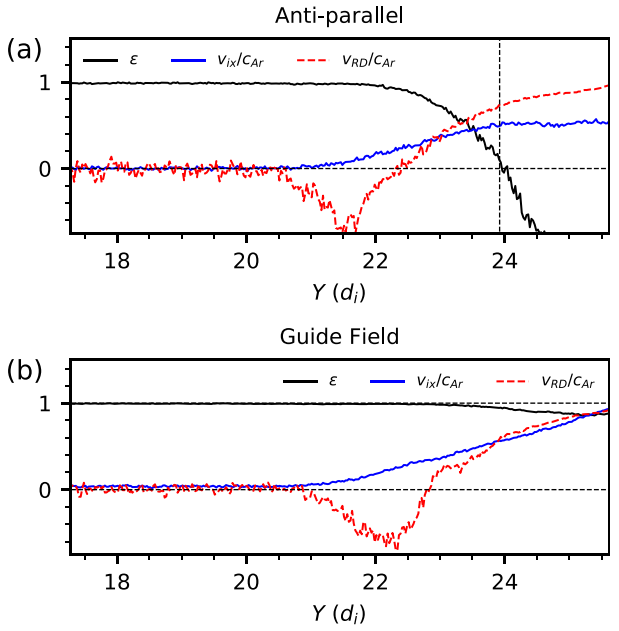


FIG. 2. (a) A cut of the ion firehose parameter ϵ (solid black line), ion outflow velocity normalized to the upstream Alfvén speed v_{ix}/c_{Ar} (solid blue line), and the out flow predicted by Eq. (1) normalized to the upstream Alfvén speed along the x direction for an anti-parallel [(a) simulation 693] and guide field [(b) simulation 708] simulation. Each cut is taken $30d_i$ downstream of the x-line, as is demonstrated in Fig. 1(c) for simulation 693.

To derive a prediction for the scaling of the outflow velocity, we analyze the anisotropic Rankine-Hugoniot jump conditions across the reconnection exhaust boundary layer.[36] Note that the exhaust boundary is different from the separatrix which is the topological boundary defined by the field line passing through the x-point; the exhaust boundary is a line quasi-parallel to, but contained within, the separatrix which separates the hot, fast flowing exhaust plasma and the cooler, slowly inward convecting plasma [diagrammed in Fig. 3(a)]. The jump conditions are[11,24,36]

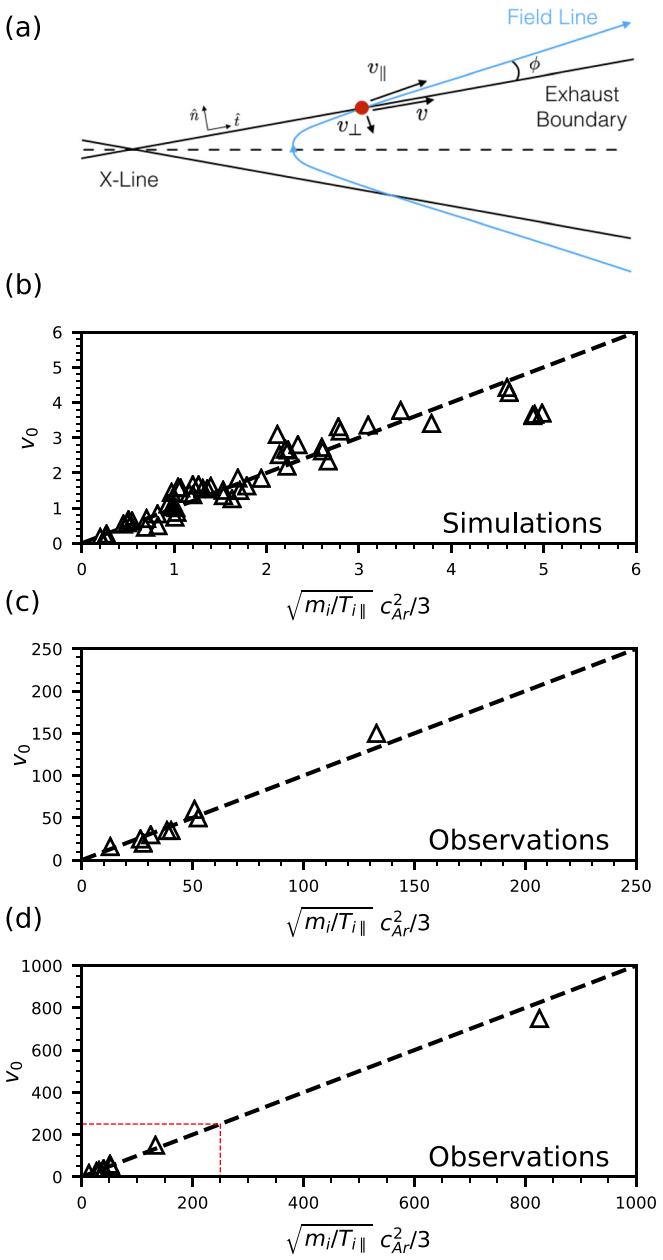


FIG. 3. (a) Diagram of an accelerated ion's (red circle) motion relative to the exhaust boundary (black line) and the magnetic field (blue curve). (b)–(d) The asymptotic $E \times B$ outflow velocity versus the outflow prediction described in Eq. (12) for PIC simulations (b) and for observations (c) and (d) for nearly anti-parallel events. Panel (d) is the same as (c), but it includes a magnetotail event with an outflow velocity so large that it obscures the data from the other events. The red dashed box shows the limits of panel (c) for comparison.

$$[B_n]_d^u = 0, \tag{2}$$

$$[nv_n]_d^u = 0, \tag{3}$$

$$\left[m_i n v_n \boldsymbol{v}_t - \epsilon \frac{B_n \boldsymbol{B}_t}{4\pi}\right]_d^u = 0, \tag{4}$$

where $[\ldots]_d^u$ represent the difference between the upstream and downstream of the exhaust boundary and the subscripts n and t correspond to the directions normal and tangential to the exhaust boundary, respectively, shown in Fig. 3(a). By comparing at a point upstream of the reconnection and the location where ϵ goes to zero in the exhaust, we find from Eqs. (2) and (4) that the outflow velocity (which at this location $v_0 \approx v_{td}$) satisfies the relationship

$$(nv_n)_d v_0 = (nv_n v_t)_u - \epsilon_u \frac{B_n B_{tu}}{4\pi m_i}. \tag{5}$$

This equation can be further simplified by noting that the upstream inflowing velocity v_{nu} and the upstream flow tangential to the exhaust boundary v_{tu} are both very small quantities compared to either the outflow velocity or the upstream Alfvén speed. The first term of the right hand side of Eq. (5) can, therefore, be ignored and the outflow velocity becomes

$$v_0 = -\epsilon_u \frac{B_n B_{tu}}{4\pi m_i n_u v_{nu}}, \tag{6}$$

where we have used $n_d v_{nd} = n_u v_{nu}$ from Eq. (3).

Figure 3(a) shows a schematic of a magnetic field line threading through the exhaust boundary layer at a small angle ϕ. The magnetic field and bulk flow can then be rewritten in terms of this angle

$$B_{tu} = B\cos\phi \approx B_r, \tag{7}$$

$$B_n = B\sin\phi \approx B_r\phi, \tag{8}$$

$$v_{nu} = -v_{E\times B}\cos\phi \approx -v_{E\times B}, \tag{9}$$

where $v_{E\times B}$ is the $E\times B$ velocity of the inflowing plasma. Substituting Eqs. (7)–(9) into Eq. (6), we find

$$v_0 = \epsilon_u c_{Ar}^2 \frac{\phi}{v_{E\times B}}. \tag{10}$$

In Fig. 3(a), we show a diagram of ion population (denoted by the red circle) that has been accelerated by the Fermi mechanism and is now traveling out of the exhaust along a field line. In the magnetic field coordinate system, the ion is traveling with a parallel and perpendicular velocity ($v_\parallel$ and $v_\perp$ respectively). This population of ions entered the reconnection exhaust closer to the x-line and is now traveling away from the midplane on the upper half of the exhaust. These ions mix with the inflowing plasma and form the density enhancement associated with the exhaust boundary layer. Since these ions make up this boundary, the population's relative motion should be parallel to the boundary. This implies that $\phi \approx \tan\phi = v_\perp/v_\parallel$. Using the $E\times B$ velocity for the perpendicular velocity and substituting this into Eq. (10), we find that the outflow velocity should be $v_0 = \epsilon_u c_{Ar}^2/v_\parallel$ where $v_\parallel$ is the parallel velocity component of the ions flowing away from the midplane at the leading edge of the exhaust boundary.

It is not clear exactly what value $v_\parallel$ should have. In the limit where the inflowing ion thermal velocity is much larger than the Alfvén speed, only half of the inflowing population would enter the exhaust (the half with a parallel velocity pointing towards the midplane) and then $v_\parallel \sim \sqrt{T_i/m_i}$. In this limit as the upstream ion temperature increases, the outflow velocity becomes much smaller than the Alfvén speed. In the limit of cold inflowing ions, if we neglect the effect of the potential associated with electron trapping,[12,39,40] the parallel velocity is simply $v_\parallel = 2v_0$. Using this, the outflow velocity should be $v_0 = c_A/\sqrt{2}$. This can be interpreted as an upper bound for the outflow velocity in anti-parallel reconnection. Using this prediction for the outflow with the ion heating predicted by Eq. (8) in the work of Drake *et al.*,[13] the total ion heating is $\Delta T_i = .167 m_i c_A^2$ which is within 20% of the reported heating identified in observations and simulations.[12,41] The behavior in both of these limits and the physical interpretation of this velocity suggests that $v_\parallel \propto \sqrt{T_{i\parallel}/m_i}$, where $T_{i\parallel}$ is the parallel ion temperature in the exhaust. Note that this temperature is the parallel ion exhaust temperature and, thus, includes both the initial upstream temperature and the additional temperature generated during reconnection. Furthermore, in the cold upstream, potential free limit $T_{i\parallel} \sim \Delta T_{i\parallel} = v_\parallel^2$, and in the hot upstream limit $T_{i\parallel} \sim T_{i,up} \sim v_\parallel^2$. From this, we find

$$v_0 \propto \epsilon_u \frac{c_{Ar}^2}{\sqrt{T_{i\parallel}/m_i}}. \tag{11}$$

This scaling prediction agrees with what is found in Fig. 1(a). When the reconnecting plasma's ion beta is small, $T_{i\parallel} \sim \Delta T_{i\parallel} \sim m_i v_0^2$, so using this in Eq. (11) implies $v_0 \sim c_{Ar}$, which is in agreement with the blue triangles lying on a line with the same slope. When the plasma has a larger initial ion beta, $T_{i\parallel} \sim T_{i\mathrm{up}}$ and so Eq. (11) becomes $v_0 \propto c_{Ar}/\sqrt{\beta_i}$, which agrees with Fig. 1(a) as well.

Because $T_{i\parallel}$ includes the ion heating generated during reconnection and the heating is linked to the outflow velocity,[12,13] this relationship does not uniquely determine the outflow velocity. To explicitly link the upstream ion temperature and the outflow would require incorporating a prediction for the ion heating which ultimately depends not only on the outflow but also the electron temperature/heating and the associated parallel potential, which is beyond the scope of this work. Equation (11), however, provides an important link between temperature and exhaust velocity which can be tested experimentally and numerically. It may ultimately form the basis of a complete predictive theory for both outflow velocities and heating. This is an important outstanding problem in reconnection and plasma physics and should be addressed in the future.

To test Eq. (11), we examine nearly anti-parallel simulations and observations shown in Figs. 1(a) and 1(b). In Fig. 3, the outflow velocity measured in nearly anti-parallel simulations (b) and observations (c and d) is plotted against the

formula given in Eq. (11) using 1/3 as the proportionality constant. The agreement between the theory and measured outflow velocity is remarkable. Both simulation and observation data points now lie along a single line with the same empirical factor of 1/3 for both, whereas before the inclusion of the ion temperature term events would have a range of different velocities for the same prediction [i.e., the spread in y in Fig. 1(a)].

In Fig. 3(d), the same data are shown as in Fig. 3(c) with an extra observational event. This event occurred in Earth's magnetotail and was studied extensively by Hietala *et al.*[31] The magnitude of the upstream Alfvén speed in this event is so large that it dwarfs all the other events. The red dashed lines show the limits of Fig. 3(c) to emphasize this point. In this event, the outflow velocity was significantly reduced from the Alfvén speed by as much as 400 km/s; its speed is consistent with the theory presented here. Putting in the empirical multiplicative factor of 1/3 gives an accurate prediction for the outflow velocity v_0 in nearly anti-parallel symmetric magnetic reconnection

$$v_0 = \frac{\epsilon_u}{3}\frac{c_{Ar}^2}{\sqrt{T_{i\|}/m_i}}. \tag{12}$$

In the presence of a sufficiency strong guide field, the outflow velocity agrees with the Hudson[36] prediction for a rotational discontinuity. The outflow velocity reaching the Alfvén speed in guide field reconnection is consistent with the physics leading to Eq. (11). In the presence of a strong guide field, the firehose instability is suppressed in the reconnection exhaust, leaving the reconnected field lines' tension force intact.

Finally, we estimate the strength of the guide field required to transition from firehose unstable to stable. The firehose instability will be suppressed when the guide field in the exhaust is large enough to keep $\epsilon \geq 0$. Neglecting the reconnecting component of the magnetic field in the exhaust and compressional effects in the exhaust, this translates to $\frac{B_g^2}{8\pi n} \geq \Delta T_{i\|} - \Delta T_{i\perp}$. The difference in heating can be estimated from observations and simulations where the total ion heating is found to be $(\Delta T_{i\|} + 2\Delta T_{i\perp})/3 \sim 0.125\frac{B_r^2}{4\pi n}$ and $\Delta T_{i\|} \approx 2\Delta T_{i\perp}$.[12,18] This can be rearranged as $\Delta T_{i\|} - \Delta T_{i\perp} \approx 0.094 m_i c_{Ar}^2$. Substituting in the difference in heating, we find that firehose instability should be approximately suppressed for $B_g \approx 0.43 B_r$ which corresponds to an approximate shear angle of 135°. This value is consistent with the transition found in simulations and serves as a natural value to separate nearly anti-parallel and guide field reconnection.

IV. DISCUSSION AND CONCLUSION

We have shown in simulations and observations that there is a systematic reduction of the outflow velocity in nearly anti-parallel magnetic reconnection events. The reduction of the outflow velocity is correlated with the ion temperature and is shown to be due to the firehose instability in the exhaust. The outflow velocity is shown to be well predicted by $v_0 = c_{Ar}^2/\left(3\sqrt{T_{i\|}/m_i}\right)$. It is also shown that for events with a sufficiently strong guide field (with strength comparable to the reconnecting magnetic field) that the outflow velocity reaches the Alfvén speed. The clear agreement between the theory proposed in this paper with the simulations and observations strengthens the claim that the firehose instability in reconnection exhausts is responsible for the reduction of the outflow velocity.

This result has significant implications for an important open question about the nature of collisionless magnetic reconnection: What is the partition of converted magnetic energy? The bulk outflow contains a significant fraction of the released magnetic energy[14,16,17,42] and so if the outflow velocity is reduced and the total magnetic energy released remains the same, then more energy will be released into other degrees of freedom. Therefore, the relationship between exhaust ion temperature and outflow velocity described here is an important step towards a predictive model of the partition of reconnection energy.

SUPPLEMENTARY MATERIAL

See supplementary material for the initial parameters of the 81 different PIC simulations used in this study, where m_i/m_e is the artificial ion to electron mass ratio, B_r is the magnitude of the reconnection component of the upstream magnetic field, B_g is the upstream component of the magnetic field normal to the current sheet and the outflow direction called the guide field, n_{in} is the initial upstream density, T_e and T_i are the initial electron and ion temperature, respectively, and β_r is the total plasma beta based on the reconnecting component of the magnetic field.

ACKNOWLEDGMENTS

This research was supported by NSF under Grant Nos. AGS-1460130 and AGS-1460037 as well as NASA under Grant Nos. NNX08A083G (MMS IDS), NNX14AC39G (MMS Theory and Modeling team), NNX15AW58G, NNX16AF75G, NNX16AG76G, and NNX17AI25G, and Thailand Research Fund under Grant No. RTA5980003. Simulations and analysis were performed at the National Center for Atmospheric Research Computational and Information Systems Laboratory (NCAR-CISL) and at the National Energy Research Scientific Computing Center (NERSC). Rungployphan Kieokaew acknowledges financial support from the Faculty of Science at Mahidol University on short-term research overseas to visit Bartol Research Institute.

[1]E. Priest and T. Forbes, *Magnetic Reconnection, MHD Theory and Applications* (Cambridge University Press, New York, NY, 2000).
[2]E. N. Parker, J. Geophys. Res. **62**, 509, https://doi.org/10.1029/JZ062i004p00509 (1957).
[3]G. Paschmann, I. Papamastorakis, N. Sckopke, G. Haerendel, B. U. O. Sonnerup, S. J. Bame, J. R. Asbridge, J. T. Gosling, C. T. Russel, and R. C. Elphic, Nature **282**, 243 (1979).
[4]B. U. Sonnerup, J. Geophys. Res. **86**, 10049, https://doi.org/10.1029/JA086iA12p10049 (1981).
[5]T. Sato and T. Hayashi, Phys. Fluids **22**, 1189 (1979).
[6]J. Birn and J. E. W. Hones, J. Geophys. Res. **86**, 6802, https://doi.org/10.1029/JA086iA08p06802 (1981).
[7]R. L. Stenzel, W. Gekelman, and N. Wild, J. Geophys. Res. **87**, 111, https://doi.org/10.1029/JA087iA01p00111 (1982).

[8]G. Paschmann, W. Baumjohann, N. Sckopke, I. Papamastorakis, and C. W. Carlson, J. Geophys. Res. **91**, 11099, https://doi.org/10.1029/JA091iA10p11099 (1986).
[9]T.-D. Phan, G. Paschmann, and B. U. Sonnerup, J. Geophys. Res. **101**, 7817, https://doi.org/10.1029/95JA03751 (1996).
[10]J. T. Gosling, S. Eriksson, T. D. Phan, D. E. Larson, R. M. Skoug, and D. J. McComas, Geophys. Res. Lett. **34**, L06102 https://doi.org/10.1029/2006GL029033 (2007).
[11]Y.-H. Liu, J. F. Drake, and M. Swisdak, Phys. Plasmas **19**, 22110 (2012).
[12]C. C. Haggerty, M. A. Shay, J. F. Drake, T. D. Phan, and C. T. McHugh, Geophys. Res. Lett. **42**, 9657, https://doi.org/10.1002/2015GL065961 (2015).
[13]J. F. Drake, M. Swisdak, T. D. Phan, P. A. Cassak, M. A. Shay, S. T. Lepri, R. P. Lin, E. Quataert, and T. H. Zurbuchen, J. Geophys. Res. **114**, A05111, https://doi.org/10.1029/2008JA013701 (2009).
[14]J. P. Eastwood, T. D. Phan, J. F. Drake, M. A. Shay, A. L. Borg, B. Lavraud, and M. G. G. T. Taylor, Phys. Rev. Lett. **110**, 225001 (2013).
[15]G. Lapenta, M. Goldman, D. Newman, S. Markidis, and A. Divin, Phys. Plasmas **21**, 055702 (2014).
[16]M. Yamada, J. Yoo, J. Jara-Almonte, H. Ji, R. M. Kulsrud, and C. E. Myers, Nat. Commun. **5**, 4774 (2014).
[17]M. A. Shay, C. C. Haggerty, T. D. Phan, J. F. Drake, P. A. Cassak, P. Wu, M. Oieroset, M. Swisdak, and K. Malakit, Phys. Plasmas **21**, 122902 (2014).
[18]T. D. Phan, M. A. Shay, J. T. Gosling, M. Fujimoto, J. F. Drake, G. Paschmann, M. Oieroset, J. P. Eastwood, and V. Angelopoulos, Geophys. Res. Lett. **40**, 4475, https://doi.org/10.1002/grl.50917 (2013).
[19]H. S. Fu, J. B. Cao, Y. V. Khotyaintsev, M. I. Sitnov, A. Runov, S. Y. Fu, M. Hamrin, M. André, A. Retinò, Y. D. Ma, H. Y. Lu, X. H. Wei, and S. Y. Huang, Geophys. Res. Lett. **40**, 6023, https://doi.org/10.1002/2013GL058620 (2013).
[20]P. L. Pritchett, Earth, Planets Space **67**, 103 (2015).
[21]J. F. Drake, M. Swisdak, K. M. Schoeffler, B. N. Rogers, and S. Kobayashi, Geophys. Res. Lett. **33**, L13105, https://doi.org/10.1029/2006GL025957 (2006).
[22]J. T. Dahlin, J. F. Drake, and M. Swisdak, Phys. Plasmas **21**, 92304 (2014).
[23]J. T. Dahlin, J. F. Drake, and M. Swisdak, Phys. Plasmas **22**, 100704 (2015).
[24]Y.-H. Liu, J. F. Drake, and M. Swisdak, Phys. Plasmas **18**, 92102 (2011).
[25]A. Zeiler, D. Biskamp, J. F. Drake, B. N. Rogers, M. A. Shay, and M. Scholer, J. Geophys. Res. **107**, 1230, https://doi.org/10.1029/2001JA000287 (2002).
[26]J. T. Gosling, R. M. Skoug, D. J. McComas, and C. W. Smith, Geophys. Res. Lett. **110**, A01107, https://doi.org/10.1029/2004JA010809 (2005).
[27]J. T. Gosling, S. Eriksson, R. M. Skoug, D. J. McComas, and R. J. Forsyth, Astrophys. J. **644**, 613 (2006).
[28]M. S. Davis, T. D. Phan, J. T. Gosling, and R. M. Skoug, Geophys. Res. Lett. **33**, L19102, https://doi.org/10.1029/2006GL026735 (2006).
[29]T. D. Phan, G. Paschmann, C. Twitty, F. S. Mozer, J. T. Gosling, J. P. Eastwood, M. Øieroset, H. Rème, and E. A. Lucek, Geophys. Res. Lett. **34**, L14104, https://doi.org/10.1029/2007GL030343 (2007).
[30]T. D. Phan, J. T. Gosling, and M. S. Davis, Geophys. Res. Lett. **36**, L09108, https://doi.org/10.1029/2009GL037713 (2009).
[31]H. Hietala, J. F. Drake, T. D. Phan, J. P. Eastwood, and J. P. McFadden, Geophys. Res. Lett. **42**, 7239, https://doi.org/10.1002/2015GL065168 (2015).
[32]M. Øieroset, T. D. Phan, C. Haggerty, M. A. Shay, J. P. Eastwood, D. J. Gershman, J. F. Drake, M. Fujimoto, R. E. Ergun, F. S. Mozer, M. Oka, R. B. Torbert, J. L. Burch, S. Wang, L. J. Chen, M. Swisdak, C. Pollock, J. C. Dorelli, S. A. Fuselier, B. Lavraud, B. L. Giles, T. E. Moore, Y. Saito, L. A. Avanov, W. Paterson, R. J. Strangeway, C. T. Russell, Y. Khotyaintsev, P. A. Lindqvist, and K. Malakit, Geophys. Res. Lett. **43**, 5536, https://doi.org/10.1002/2016GL069166 (2016).
[33]M. Øieroset, T. Phan, M. Shay, C. Haggerty, M. Fujimoto, V. Angelopoulos, J. Eastwood, and F. Mozer, Geophys. Res. Lett. **44**, 7598, https://doi.org/10.1002/2017GL074196 (2017).
[34]G. F. Chew, M. L. Goldberger, and F. E. Low, Proc. R. Soc. A **236**, 112 (1956).
[35]E. N. Parker, Phys. Rev. **109**, 1874 (1958).
[36]P. D. Hudson, Planet. Space Sci. **18**, 1611 (1970).
[37]M. A. Shay, J. F. Drake, B. N. Rogers, and R. E. Denton, J. Geophys. Res. **106**, 3759, https://doi.org/10.1029/1999JA001007 (2001).
[38]R. Mistry, J. Eastwood, C. Haggerty, M. Shay, T. Phan, H. Hietala, and P. Cassak, Phys. Rev. Lett. **117**, 185102 (2016).
[39]A. Le, J. Egedal, W. Daughton, W. Fox, and N. Katz, Phys. Rev. Lett. **102**, 85001 (2009).
[40]J. Egedal, W. Fox, N. Katz, M. Porkolab, M. ØIeroset, R. P. Lin, W. Daughton, and J. F. Drake, J. Geophys. Res. (Space Phys.) **113**, A12207, https://doi.org/10.1029/2008JA013520 (2008).
[41]T. D. Phan, J. F. Drake, M. A. Shay, J. T. Gosling, G. Paschmann, J. P. Eastwood, M. Oieroset, M. Fujimoto, and V. Angelopoulos, Geophys. Res. Lett. **41**, 7002, https://doi.org/10.1002/2014GL061547 (2014).
[42]J. Birn, J. E. Borovsky, M. Hesse, and K. Schindler, Phys. Plasmas **17**, 052108 (2010).

Chiang Mai J. Sci. 2019; 46(2) : 408-416
http://epg.science.cmu.ac.th/ejournal/
Contributed Paper

Influence of Plasma in the Vicinity of Io on Brightness and Angular Extension of Io's Magnetic Footprint

Suwicha Wannawichian* [a,b] and Arthit Laphirattanakul [a]

[a] Department of Physics and Materials Science, Faculty of Science, Chiang Mai University, Chiang Mai 50200, Thailand.

[b] National Astronomical Research Institute of Thailand (NARIT), Chiang Mai 50200, Thailand.

*Author for correspondence; e-mail: suwicha.w@cmu.ac.th

Received: 5 January 2018
Revised: 11 September 2018
Accepted: 12 September 2018

ABSTRACT

In Jupiter's auroral region, a spot-like emission feature, called the auroral magnetic footprint, is the result of a magnetic disturbance near the extended atmosphere of Io. The magnetic footprint is direct evidence of the interaction between the atmosphere of slow-orbiting Io and the rapidly-corotating magnetic field and magnetospheric plasma of Jupiter. The result of the magnetic disturbance is that a significant amount of current is carried from the interaction region towards Jupiter's ionosphere. Accordingly the precipitating electrons result in the auroral emission. Far ultraviolet (FUV) images of Jupiter's auroral region were used to study this phenomenon. In 2007, using the Advanced Camera for Surveys (ACS) instrument on the Hubble Space Telescope (HST), the observation of Io's magnetic footprint provided the opportunity for a detailed study of the correlation between the spot's brightness and its angular size. With a strong correlation (>0.7) between the brightness and the angular size, these two physical properties were clearly related during March and June, 2007, several weeks after major volcanic eruptions on Io were observed. These results suggest a connection between the plasma supply from Io, due to the volcanic activities on Io and the satellite's auroral magnetic footprint morphology.

Keywords: Jupiter, Io, planets and satellites: aurorae

1. INTRODUCTION

The electrodynamic interaction between Jupiter's magnetospheric plasma and Io's atmospheric particles takes place in the vicinity of Io (see review by Kivelson et al., 2004) [1]. The interaction corresponds to the fast corotation velocity of the magnetospheric plasma (74 km/s) and the much slower particles in Io's extended atmosphere, which move within the inertial frame of Io's orbit velocity (17 km/s). The differential velocity causes the collision between the magnetospheric plasma and the moon's atmosphere. As a result, the Alfvenic disturbance is created at the upstream of the interaction region and travels along Jupiter's magnetic field lines, escaping from

the satellite towards Jupiter's ionosphere. The newly ionized charged particles in the interaction region near Io are picked up and accelerated. In this process, some of the electrons are accelerated along the magnetic field and into Jupiter's atmosphere. These precipitating electrons excite atmospheric H_2 molecules and release the energy in the Lyman and Werner bands [2]. The emission, which is directly connected to the interaction region, is called the Main Alfven Wing spot (MAW). On the other hand, the reflection of the Alfvèn wave in Jupiter's plasma torus could cause the secondary spot called the Reflected Alfvèn wing spot (RAW). During the acceleration of electrons towards Jupiter's ionosphere, the reflection of electrons towards the auroral region in the opposite hemisphere could create the Trans-hemispheric Electron Beam spot (TEB). The last feature is tail emission, which connects to the location downstream from interaction region at Io [3-5]. The MAW spot will be referred to as *Io's magnetic footprint* emission, which is the main focus in this study, as shown in Figure 1. In Figure 1, at Io's system III longitude of 135.6 degrees, where there is minimal effect of reflected Alfven wave toward Jupiter's northern hemisphere, the magnetic footprint appears as one emission spot. The appearance of multiple spots of Io's magnetic footprint strongly corresponds to Io's location in plasma torus [6].

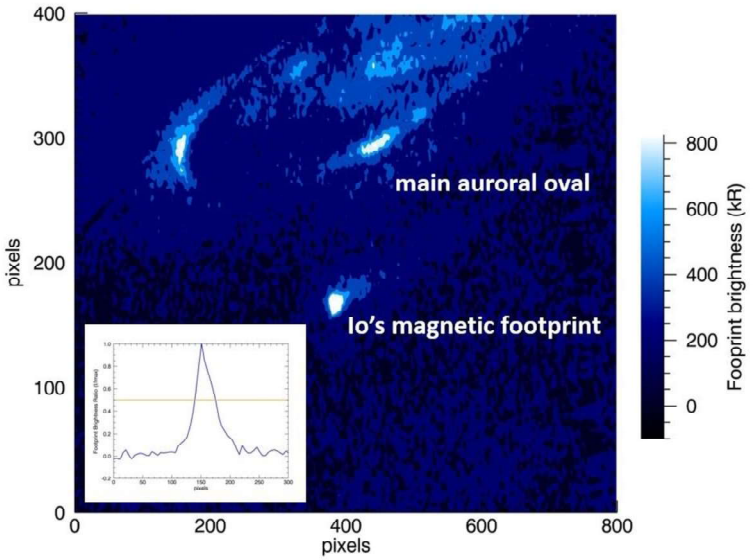


Figure 1. This FUV image of Jupiter's northern auroral region was taken in March 2, 2007 at universal time 07:12:29 by an ACS instrument onboard the HST. Io's magnetic footprint is clearly seen at a lower latitude from the main oval emission. The image was taken when Io was located at a system III longitude of 135.6 degrees. The left inset image is the magnified version of brightness distribution of Io's magnetic footprint. The displayed pixel size appears twice the actual size of the image. Along with the peak emission of Io's magnetic footprint, the angular extension of the footprint was analyzed as an equivalent scale to the full width at half maximum (FWHM) of the emission. In this work, the FWHM cuts were made according to the size of major axis of the MAW footprint emission, while we considered the footprint extending along an elliptical path.

Io's magnetic footprint is evidence of the strong electrodynamics interaction between Jupiter's magnetic field and the satellite's extended atmosphere. The neutral atmospheric particles mostly originate from the atomic and molecular components of SO_2 ejected from the active volcanoes of Io. These neutral particles become ionized via collisional and charge exchange processes with the magnetospheric plasma as well as through photoionization due to the solar radiation in Io's upper atmosphere [7].

The interaction is thought to take place far from Io's surface, at ~ 1.5 Io radii (R_{Io}) [8, 9]. With the conservation of magnetic flux, the interaction region of Io can be mapped to the size of Io's magnetic footprint of ~100 km. This scale length is approximately equivalent to 1-2 pixels detectable by FUV imaging instruments onboard the Hubble Space Telescope (HST). An earlier study of Jupiter's far ultraviolet (FUV) imaging by the Faint Object Camera onboard HST was presented by Prange et al. (1996) [10]. The size of Io's magnetic footprint was found to be approximately 5° at half-maximum elongation in longitude. With FUV auroral imaging by HST Wild Planetary Camera 2 (WFPC2), Clarke et al. (1996) [11] found that, while the magnetic flux mapped to Io's diameter projecting to distance of 200 km at Jupiter's ionosphere, the full width at half maximum of the footprint was in fact between 1000-2000 km. The more detail study of the main spot's size, by Space Telescope Imaging Spectrograph (STIS) and Advanced Camera for Surveys (ACS) instruments on HST, revealed that the footprint's size varies between approximately 400 - 8000 km, or 1-14° on the planet, which is suggested to depend on the size of interaction region at Io [12]. Moreover this detail study of Io's magnetic footprint in three dimensions showed complex variation trends of the footprint's width and length. A previous study [13] revealed a study of the angular sizes of Io's magnetic footprints, when the satellite was at different locations in Jupiter's magnetosphere. During the 1997-1999 observation era of HST, the footprint's angular sizes appeared to be most extended when Io was near the center of the plasma torus (approximately 110° system III longitude).

With approximately a 10° tilt between the magnetic axis and rotation axis, the central density of Jupiter magnetospheric plasma, or plasma torus, inclined ~7° from the orbital plane of Io, which is illustrated in Figure 2. As a result, the brightness of Io's magnetic footprint was found to be tightly connected to the location of Io [14]. Previously, with WFPC2 instrument onboard HST, the systematic variation in system III longitude of Io's footprint emission was presented [15]. Brightness distribution, peak emission, and the appearance of multiple spots were found to connect with Io's system III longitude and latitude from the plasma torus plane [6]. In addition, based on STIS/HST observations during 1997-2001, the systematic variation of Io's magnetic footprint brightness was found to strongly connect with Io's location in System III longitude, which is an indication of Io's position in the plasma torus [16]. The confirmation of this systematic variation was presented by the longitudinal modulation of Io's auroral footprint brightness based on ten-year observation of HST [17]. Along with the location of Io in the plasma torus, the study of Io's magnetic footprint from 1997 to 2009 showed that the magnetic field asymmetry influences the variation of Io's magnetic footprint brightness as well [18].

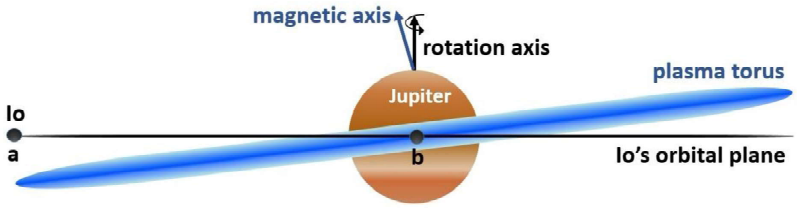


Figure 2. Under the influence of the tilted magnetic axis at approximately 10° from the rotation axis [13], Io experiences a dramatic change of plasma density in the vicinity of the satellite. During the course of orbiting Jupiter, Io is periodically located far from the center of the plasma torus (a), especially when Io is located at approximately 20° and 190° System III longitude. On the other hand, Io can also be embedded in the center of the plasma torus (b), when located at approximately 110° and 270° System III longitude [14]. The above sketch is not to actual scale.

In this study, the variation of angular extension from another observation era by the HST in 2007 is presented. In addition, a direct comparison between the angular size and the brightness of Io's magnetic footprint will reveal the influence of satellite location in the plasma torus on electrodynamic interactions at Io.

2. OBSERVATION AND DATA ANALYSIS

During the observational campaign of the Hubble Space Telescope (HST) in 2007, FUV images of Jupiter's auroral region were taken. All images were reduced under the pipeline routine developed at Boston University [14]. HST's two instruments; the Advanced Camera for Surveys (ACS) and the Solar Blind Channel (SBC), were employed for imaging with two filters: 115LP and 125LP. Filter 115LP is sensitive to wavelengths greater than 115 nm, while 125LP is sensitive to wave lengths greater than 125 nm up to approximately 170 nm. These two filters require different factors for converting count/sec to brightness in kilo-Rayleighs (1 kR = $10^9/4$ p photons cm^{-2} sr^{-1} s^{-1}). The conversion factors were originally generated by a synthetic UV spectrum of auroral emission from H_2 and Lya emission [19]. These different conversion factors for two filters were calculated to compensate for the different wavelength sensitivities of different filters. In our calculation, we consider the newly calculated variation of the conversion factor corresponding to the atmospheric absorption measured by the color ratio [2, 18]. In the data reduction process, the image size was scaled corresponding to Jupiter's distance at 4.2 AU from Earth with the pixel size of 0.025 arc second. The brightness variation of each MAW spot was analyzed for its Full Width at Half Maximum (FWHM) to obtain the angular size, as seen in Figure 1. In addition to the previous study of the connection between the angular size of Io's magnetic footprint and the satellite's longitude, the peak emission of the footprint is taken into consideration. From all data observed in 2007, the footprints were chosen based on their distances to the limb, corresponding to Serio and Clarke (2008) and Wannawichian et al. (2010) [14, 16]. This limit provides footprints that are far from the limb, more than 2100 km, with no significant geometric distortions.

3. RESULTS AND DISCUSSION

Angular extensions of the Io magnetic footprint from several observations by the Hubble Space Telescope in 2007 show a temporal variation as a function of observing time. From the results in Figure 3, there are strong variations in the angular size of Io's magnetic footprint. Several peaks appear to be noticeable; for example, when Io was near 80 and 295 degrees longitude. It must be noted that there is another peak near 0 degrees as well, which is not completely related to the magnetic footprint brightness, as shown in Figure 4. The variation of angular size appears to be under the influence of Io's system III longitude.

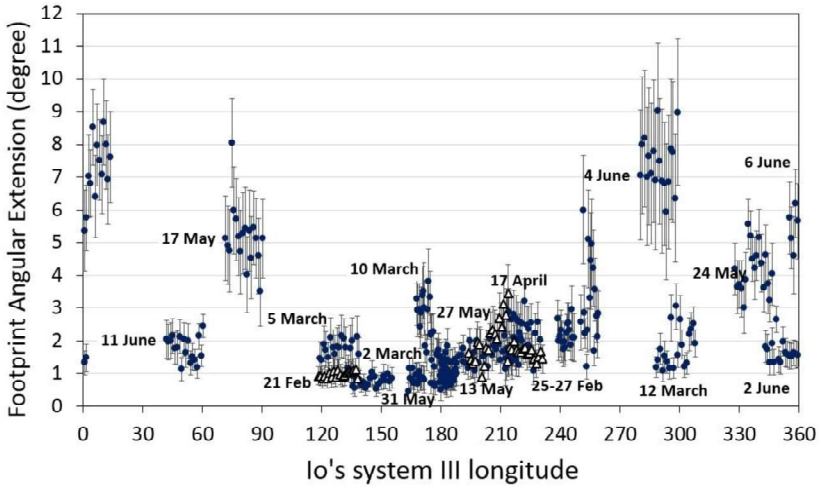


Figure 3. The angular sizes of Io's magnetic footprint from several observations by HST during 2007 campaign. The angular size was obtained by an analysis of Full Width at Half Maximum (FWHM) of each MAW spot, as seen in Figure 1. For clarification, the data on February 21, 23, and 26 were plotted with triangular symbols.

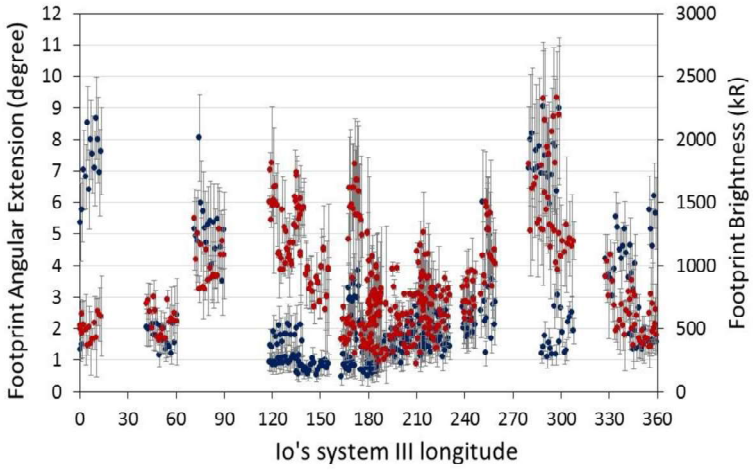


Figure 4. The angular sizes of Io's magnetic footprint (blue dots) from several observations by HST during the 2007 campaign, as shown in Figure 3, are compared with the magnetic footprint brightness (red dots). The unit of brightness is in kilorayleighs (1 kR = 10^9 photon $cm^{-2}s^{-1}$ into 4π steradians [25]).

There are several possibilities for the controlling factors of Io's angular size. The first factor could be the volcanic eruptions on Io. In February and March 2007, during the New Horizon's spacecraft Jupiter flyby, several eruptions of volcanoes on Io were detected [20]. The next factor could be variation in the plasma torus. Temporal and longitudinal variation of the plasma torus was observed in Cassini UVIS observations by Steffl et al. (2008) [21]. Another explanation for the variation could be Io's locations. The location of Io in Jupiter's magnetosphere appears to be strongly correlated with the brightness of the satellite's magnetic footprint [14].

Previously, Wannawichian et al. (2010) [14] showed that the footprint brightness varies in the form of a general sinusoidal trend, which corresponds to the location of Io in Jupiter's magnetosphere. Accordingly, the comparison of brightness and angular size as a function of Io's system III longitude is shown in Figure 4. Overall, the Pearson correlation between the brightness and the angular size of Io's magnetic footprint was found to be 0.730. This correlation implies a positive relationship between the magnetic footprint brightness and its angular size. It is noticeable that the relationships between these two properties of the magnetic footprint vary in different months during HST's 2007 campaign. We conclude, therefore, that the correlations between the brightness and angular size of Io's magnetic footprint varies between the different observations, as shown in Table 1. The correlations between footprint brightness and angular size appear to be strongest during the observations in March and June 2007. This result implies some connection with the volcanic eruptions on Io, which were reported to be strong during February and May 2007 [20, 22]. It has been suggested that a strong mass loading from

Table 1. Correlation between the brightness and angular size of Io's magnetic footprint based on different observations.

Observation Months in 2007	Correlation between the brightness and angular size	Ranges of Io's System III longitude (°)	Correlation between the brightness and angular size
February	0.816	0-30	0.930
March	0.893	31-100	0.949
April	0.838	101-160	0.918
May	0.723	161-270	0.883
June	0.878	271-360	0.845

Io's volcanoes can weaken the field aligned-current, which is connected to the auroral emission in Jupiter's ionosphere [22]. As a result, after the strong eruptive events, throughout February and at the end of May 2007, the relaxation of mass loading led to the increase of precipitating particles into Jupiter's auroral region. Consequently, the better correlations between the auroral magnetic footprint brightness and angular size was detected. It is significant to note that, from previous studies by Bonfond et al. (2009; 2010) [4, 12], the inter-spot distances vary strongly with Io's system III longitude.

The spot brightness and size should be carefully accounted for when the inter-spot distances are very small, since the merging between MAW and TEP spots is possible. During our analysis of the MAW emission, occasionally the TEP spots appeared near the main emission. Therefore the detail analysis of spot-by-spot evolution to clarify the general trend in this work should be further studied. In addition, the similar feature of spot multiplicity was also found for the case of Ganymede auroral footprint [18]. Moreover the influence of Io's volcanism over Jupiter's radio emission, corresponding to expansion of the main auroral oval, as well as the Ganymede footprint, appears to vary with system III longitude [22, 23]. Therefore longitudinal and time variations, based on volcanic activities on Io, should be taken into account. Taking into account the complex configuration of Jupiter's magnetic field, Io's northern and southern magnetic footprints were found to vary differently [4, 12]. As shown in Figure 5, the angular extensions of northern and southern magnetic footprints clearly show different trends. The variation of surface magnetic field as well as the magnetic anomaly in northern hemisphere could play a major role in the brightness and the angular extension of the footprint. Previous numerical studies, using magnetohydrodynamics (MHD) model proposed that the Alfven wave and corotational lag relate to conditions in Io's plasma wake [24]. The match between the calculated downstream current distribution, corresponding to corrotational lag of up to 500 seconds, and Io's brightest footprint spot, MAW, suggested the inter-spot angle between MAW and TEP to be 7° or smaller. This is the same range as our analyzed extension angle. The corotational motion of downstream flux tube could play an important role in controlling the inter-spot distance and correspondingly interfering with the MAW extension angle.

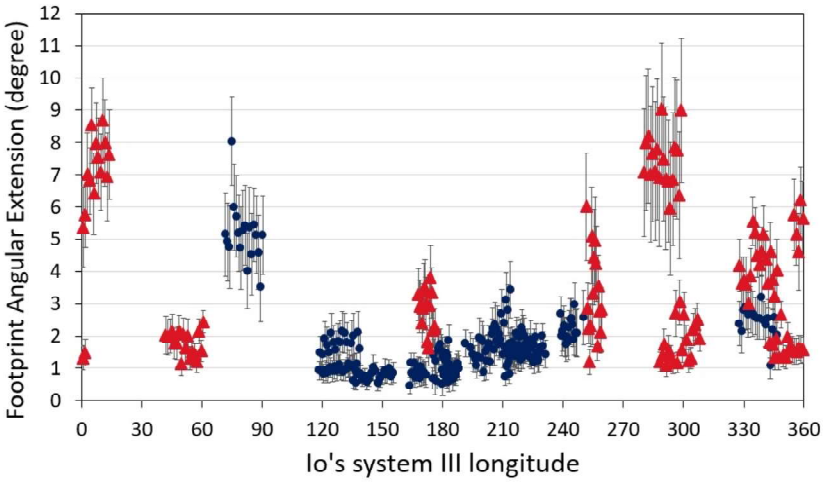


Figure 5. The angular sizes of Io's northern magnetic footprint (blue dots) from several observations by HST during the 2007 campaign, as shown in Figure 4, are compared with the angular size of southern magnetic footprint (triangular symbols).

4. CONCLUSIONS

During several HST observations, Io's auroral magnetic footprint emissions appeared to be highly variable in terms of brightness and angular size. Two clear peaks near 80 and 295 degrees longitude are as expected and related to Io's locations in the plasma torus as shown in Figure 2. A strong correlation (> 0.7) was found between the brightness and angular size, with the best correlations found for the observations performed in March and June 2007. The results suggest a connection between the morphology of Io's magnetic footprint and the volcanic activities on Io. Previous works [4, 12, 22, 23] showed possible interferences due to the TEP and tail emission in the MAW emission, along with longitudinal variation of the influence of Io's volcanic activity. These effects should be carefully taken into consideration in future studies. The detail analysis of temporal variations should be further investigated.

ACKNOWLEDGEMENTS

This work is based on observations by the NASA/ESA Hubble Space Telescope, obtained at the Space Telescope Science Institute, which is operated by AURA Inc. for NASA, which is under a close collaboration with John T. Clarke and Jonathan D. Nichols. This research was supported by NASA grants HST-GO-10506.01-A and HST-GO-10862.01-A from the Space Telescope Science Institute to Boston University. Additional support was from Thailand Research Fund grants TRG5880091 and RTA5980003.

REFERENCES

[1] Kivelson M.G., Bagenal F., Kurth W.S., Neubauer F.M., Paranicas C. and Saur J., Magnetospheric Interactions with Satellites, in Bagenal F., Dowling T. and McKinnon W., eds., *Jupiter The Planet, Satellites and Magnetosphere*, Cambridge Univ. Press, Cambridge, UK, 2004: 513-536.

[2] Gustin J., Bonfond B., Grodent D. and Gerard J.C., *J. Geophys. Res.*, 2012; **117**: A07316, DOI 10.1029/2012JA017607.

[3] Clarke J.T., Grodent D., Cowley S.W.H., Bunce E.J., Zarka P., Connerney J.E.P. and Satoh T., Jupiter's Aurora, in Bagenal F., Dowling T. and McKinnon W., eds., *Jupiter The Planet, Satellites and Magnetosphere*, Cambridge Univ. Press, Cambridge, UK, 2004: 639-670.

[4] Bonfond B., Grodent D., Gerard J.C., Radioti A., Dols V., Delamere P.A. and Clarke J.T., *J. Geophys. Res.*, 2009; **114**: A07224, DOI 10.1029/2009JA014312.

[5] Bonfond B., Grodent D., Gerard J.C., Radioti A., Saur J. and Jacobsen S., *Geophys. Res. Lett.*, 2008; **35**: L05107, DOI 10.1029/2007GL032418.

[6] Gerard J.C., Saglam A., Grodent D. and Clarke J.T., *J. Geophys. Res.*, 2006; **111**: A04202, DOI 10.1029/2005JA011327.

[7] Smyth W.H. and Marconi M.L., *Icarus*, 2005; **176**: 138-154.

[8] Grodent D., *Space Sci. Rev.*, 2015; **187**: 23-50.

[9] Hill T.W. and Pontius D.H., *J. Geophys. Res.*, 1998; **103**: 19879-19886.

[10] Prange R., Rego D., Southwood D., Zarka P., Miller S. and Ip W., *Nature*, 1996; **379**: 323-325.

[11] Clarke J.T., Ballester G.E., Trauger J., Evans R., Connerney J.E.P., Stapelfeldt K., Crisp D., Feldman P.D., Burrows J., Casertano S., Gallagher III J.S., Griffiths R.E., Hester J., Hoessesl J.G., Holtzman J.A., Krist J.E., Meadows V., Mould J.R., Scowen P.A., Watson A.M. and Westphal J.A., *Science*, 1996; **274**: 404-409.

[12] Bonfond B., *J. Geophys. Res.*, 2010; **115**: A09217, DOI 10.1029/2010JA015475.

[13] Wannawichian S., Clarke J.T. and Nichols J.D., *Chiang Mai J. Sci.*, 2016; **43**: 870-875.

[14] Wannawichian S., Clarke J.T. and Nichols J.D., *J. Geophys. Res.*, 2010; **115**: A02206, DOI 10.1029/2009JA014456.

[15] Clarke J.T., Ballester G., Trauger J., Ajello J., Pryor W., Tobiska K., Connerney J.E.P., Gladstone G.R., Waite Jr.J.H., Jaffel L.B. and Gerard J.C., *J. Geophys. Res.*, 1998; **103**: 20217-20236.

[16] Serio A.W. and Clarke J.T., *Icarus*, 2008; **197**: 368-374.

[17] Wannawichian S., Clarke J.T., Bagenal F., Smyth W.H., Peterson C.A. and Nichols J.D., *J. Geophys. Res.*, 2013; **118**: 3336-3345.

[18] Bonfond B., Hess S., Gerard J.C., Grodent D., Radioti A., Chantry V., Saur J., Jacobsen S. and Clarke J.T., *Planet. Space Sci.*, 2013; **88**: 64-75.

[19] Gerard J.C., Gustin J., Grodent D., Delamere P. and Clarke J.T., *J. Geophys. Res.*, 2002; **107**: 1-30.

[20] Spencer J.R., Stern S.A., Cheng A.F., Weaver H.A., Reuter D.C., Retherford K., Lunsford A., Moore J.M., Abramov O., Lopes R.M.C., Perry J.E., Kamp L., Showalter M., Jessup K.L., Marchis F., Schenk P.M. and Dumas C., *Science*, 2007; **318**: 240-243.

[21] Steffl A.J., Delamere P.A. and Bagenal F., *Icarus*, 2008; **194**: 153-165.

[22] Clarke J.T., Ajello J., Ballester G., Jaffel L.B., Connerney J., Gerard G.C., Gladstone G.R., Grodent D., Pryor W., Trauger J. and Waite J.H., *Nature*, 2002; **415**: 997-1000.

[23] Yoneda M., Tsuchiya F., Misawa H., Bonfond B., Tao C., Kagitani M. and Okano S., *Geophys. Res. Lett.*, 2013; **40**: 671-675.

[24] Bonfond B.S., Hess F., Bagenal J.C., Gerard D., Grodent A., Radioti J., Gustin and Clarke J.T., *Geophys. Res. Lett.*, 2013; **40**: 4977-4981.

[25] Chen C.X., *J. Geophys. Res.*, 2007; **112**: A03204, DOI 10.1029/2006JA011599.

Monthly Notices
of the
ROYAL ASTRONOMICAL SOCIETY

MNRAS **487,** 975–980 (2019)
Advance Access publication 2019 May 16

doi:10.1093/mnras/stz1354

Fickian and non-Fickian diffusion of cosmic rays

Luiz F. S. Rodrigues [1]★ Andrew P. Snodin,[2] Graeme R. Sarson[1] and Anvar Shukurov[1]

[1]*School of Mathematics, Statistics and Physics, University of Newcastle, Newcastle upon Tyne NE1 7RU, UK*
[2]*Department of Mathematics, Faculty of Applied Science, King Mongkut's University of Technology North Bangkok, Bangkok 10800, Thailand*

Accepted 2019 May 13. Received 2019 May 8; in original form 2018 September 20

ABSTRACT

Fluid approximations to cosmic ray (CR) transport are often preferred to kinetic descriptions in studies of the dynamics of the interstellar medium (ISM) of galaxies, because they allow simpler analytical and numerical treatments. Magnetohydrodynamic simulations of the ISM usually incorporate CR dynamics as an advection–diffusion equation for CR energy density, with anisotropic, magnetic-field-aligned diffusion with the diffusive flux assumed to obey Fick's law. We compare test particle and fluid simulations of CRs in a random magnetic field. We demonstrate that a non-Fickian prescription of CR diffusion, which corresponds to the telegraph equation for the CR energy density, can be easily calibrated to match the test particle simulations with great accuracy. In particular, we consider a random magnetic field in the fluid simulation that has a lower spatial resolution than that used in the particle simulation to demonstrate that an appropriate choice of the diffusion tensor can account effectively for the unresolved (subgrid) scales of the magnetic field. We show that the characteristic time that appears in the telegraph equation can be physically interpreted as the time required for the particles to reach a diffusive regime and we stress that the Fickian description of the CR fluid is unable to describe complex boundary or initial conditions for the CR energy flux.

Key words: diffusion – magnetic fields – turbulence.

1 INTRODUCTION

Cosmic rays (CRs) are an important ingredient of the interstellar medium (ISM) of galaxies, with a typical energy density comparable to the magnetic energy density and the turbulent gas kinetic energy density, and they contribute significantly to the support of the galactic gaseous discs against gravity and drive galactic outflows (Kulsrud 2005). Significant efforts have been made to include CRs in magnetohydrodynamic (MHD) simulations of the ISM and assess their importance in the outflows (e.g. Girichidis et al. 2016; Simpson et al. 2016; Farber et al. 2018; Holguin et al. 2018) and galactic dynamos (e.g. Hanasz, Wóltański & Kowalik 2009). The transport of CRs is usually quite simplified in these works, where the CR population is modelled as a single fluid under the advection–diffusion approximation, with the diffusive flux taken to follow Fick's law. CR diffusion is assumed to be either isotropic, anisotropic but with negligible diffusion perpendicular to the magnetic field, or to have both parallel and perpendicular diffusivities (Strong, Moskalenko & Ptuskin 2007; Zweibel 2013, 2017; Grenier, Black & Strong 2015). In all of these cases, constant values are taken for the diffusivities, with a parallel (or isotropic) component typically of order $\kappa_\parallel = 10^{28}$ cm^2 s^{-1} and a perpendicular diffusivity, $\kappa_\perp$, 10–1000 times smaller.

Meanwhile, a coherent theory of CR propagation and confinement has been sought, mostly using quasi-linear theory (see Strong et al. 2007, and references therein) verified and extended using simulations of test particles (e.g. Snodin et al. 2016, and references therein).

One of the dynamical roles of CRs in the ISM is to provide an additional force due to their pressure gradient that acts on the background gas. The CR particles responsible for this effect gyrate about magnetic field lines with a Larmor radius that is much smaller than scales resolved in modern ISM simulations. The CR fluid description should then account for the effective CR dynamics at the scale resolved in the simulations. Here we consider CR diffusion in random magnetic fields that can be examined via test particle simulations where the relevant small scales are reasonably well resolved. We devise simple numerical experiments to examine whether anisotropic diffusion prescriptions with constant, $\kappa_\parallel/\kappa_\perp$, applied to fluid simulations at a relatively low spatial resolution can capture the properties of test particle propagation in simulations at higher resolution. In particular, we compare the standard anisotropic Fickian diffusion of CRs with a non-Fickian one that leads, instead of the diffusion equation, to the telegraph equation for the number (or energy) density of the particles. The telegraph equation contains an additional time-scale τ that accounts for the finite propagation speed of the CR distribution (e.g. Bakunin 2008) and allows for the differentiation between the early ballistic behaviour of the particles and the subsequent diffusive CR spread. The telegraph equation

★ E-mail: luiz.rodrigues@newcastle.ac.uk

© 2019 The Author(s)
Published by Oxford University Press on behalf of the Royal Astronomical Society

Downloaded from https://academic.oup.com/mnras/article-abstract/487/1/975/5490402 by Mahidol University user on 16 July 2019

is also a convenient way to avoid numerical problems close to singular magnetic X-points, and may also allow for larger time steps in an explicit numerical scheme than that with the Fickian approach (Snodin et al. 2006). Litvinenko & Noble (2016) compare numerical solutions of fluid equations for CR propagation that result from various approximations to the Fokker–Planck equation, including the telegraph equation, and confirm the relevance of this approximation. Our goal is to compare test particle simulations of CR propagation with the telegraph equation approximation to derive optimal parameters of the latter that can inform subgrid models of CR propagation in a comprehensive MHD simulation of the multiphase ISM. We discuss the dependence of the CR diffusion parameters on the CR properties, on the test particle magnetic field power spectrum, and on the resolution of the fluid simulation. We describe our numerical experiments with test particle and fluid descriptions in Sections 2.1 and 2.2, respectively. The general results and a proposed calibration procedure for the diffusion parameters are presented in Sections 3.1 and 3.2. In Section 4, we discuss the results further and summarize our conclusions.

2 NUMERICAL EXPERIMENTS

2.1 Test particle simulations

We use test particle simulations of CR propagation in a random magnetic field as a reference to which fluid simulations can be compared and calibrated. These simulations are very similar to those performed by Snodin et al. (2016). For a direct comparison with fluid simulations, we construct a random, time-independent, periodic, magnetic field $\boldsymbol{B}(\boldsymbol{x})$on a uniform Cartesian mesh of side length L and resolution 1280 points in each direction (the *discrete model* described by Snodin et al. 2016). We use an isotropic magnetic field with a power spectrum $M(k) \propto k^s$, over the range $k_{\rm min} \leq k \leq k_{\rm max}^{\rm particle}$, with $k_{\rm min} = 2\pi/L$ and $k_{\rm max}^{\rm particle} = 640\pi/L = 320k_{\rm min}$, and consider the cases $s = -5/3$ and $s = -2$. Within the simulation volume L^3, we placed 2.1×10^7 test particles of a given energy, initially distributed in space so that their number density follows

$$n(x, y, z) \propto \exp\left[-\frac{x^2}{2\sigma_0^2}\right], \quad (x, y, z) \in [-L/2, L/2]^3\,, \tag{1}$$

being non-uniform in the x-direction but homogeneous in the other directions. The half-width σ_0 was chosen to correspond to approximately 71 mesh points ($0.0552L$). The initial velocities of the particles were distributed isotropically. For each particle, we then solved the equation of motion

$$\ddot{\boldsymbol{x}} = \alpha\dot{\boldsymbol{x}} \times \boldsymbol{B}[\boldsymbol{x}(t)]\,, \tag{2}$$

where $\boldsymbol{x}(t)$ is the particle position, $\alpha = qLB_{\rm rms}/(\gamma mcv_0)$, with q the particle charge, m the particle mass, γ the particle Lorentz factor, c the speed of light, v_0 a reference speed, and $B_{\rm rms}$ the root-mean-square magnetic field strength. Here we neglect electric fields, so that the particle energy is conserved. We take $\alpha = 320$ and $v/v_0 = 1$ for each particle, so that the dimensionless Larmor radius, $R_{\rm L}/L = 1/320$, is somewhat smaller than the scales resolved in the fluid simulations discussed below, but also a few times larger than the test particle grid resolution. Typically, each particle trajectory was integrated up to a maximum dimensionless time of $t = 2.8$, corresponding to approximately $142t_{\rm L}$, where $t_{\rm L} = 2\pi R_{\rm L}/v_0$ is the Larmor time-scale.

2.2 Fluid description of CR propagation

We compare the test particle results with simulations where the CRs are approximated as a fluid governed by the equations (Snodin et al. 2006)

$$\frac{\partial\varepsilon}{\partial t} = -\nabla\cdot\boldsymbol{F}\,, \qquad \tau\frac{\partial F_i}{\partial t} = -\kappa_{ij}\nabla_j\varepsilon - F_i, \tag{3}$$

where ε is the CR energy density, $\boldsymbol{F}$ is the associated energy flux, and κ_{ij} is a diffusion tensor given by

$$\kappa_{ij} = \kappa_\perp\delta_{ij} + (\kappa_\parallel - \kappa_\perp)\hat{B}_i\hat{B}_j\,, \tag{4}$$

where $\hat{\boldsymbol{B}} = \boldsymbol{B}/|\boldsymbol{B}|$ is the unit vector along the magnetic field. Here the diffusivity along magnetic field lines is usually taken to be much larger than the diffusivity perpendicular to field lines, $\kappa_\parallel \gg \kappa_\perp$. The case $\tau = 0$ corresponds to anisotropic Fickian diffusion, which we refer to as the *Fickian* prescription. The case $\tau = 0$ leads to the CR distribution spreading at an infinite speed, so that an initially spatially localized CR energy distribution will be redistributed over all space available after any finite time. This is a well-known artefact of the diffusion approximation. When $\tau \neq 0$, these equations correspond to a generalized form of the telegraph equation for ε, which we shall refer to as the *Telegraph* prescription.

2.2.1 CR propagation and the telegraph equation

The telegraph equation for the CR distribution function has been studied in several previous works (e.g. Gombosi et al. 1993; Litvinenko & Schlickeiser 2013; Tautz & Lerche 2016), including its connection to a hyperdiffusive equation that arises more naturally in higher order expansions of the energy flux (Malkov & Sagdeev 2015). The main reason for using this prescription has been to capture the non-diffusive behaviour at short times, corresponding to (superdiffusive) ballistic particle motion, followed by a transition to the diffusive regime. For the CR distribution function, the time-scale τ can be connected with the pitch angle diffusivity (Litvinenko & Schlickeiser 2013). One difference from the Fickian case is that the maximum signal propagation speed (parallel to magnetic field lines) is reduced to $(\kappa_\parallel/\tau)^{1/2}$.

It has been claimed that the telegraph equation is not suitable for modelling CR propagation as it does not conserve the total number of particles or, equivalently, their total energy (Malkov & Sagdeev 2015; see also Tautz & Lerche 2016). However, this assertion seems to be based on misunderstanding. Indeed, consider the one-dimensional telegraph equation for the energy density of particles $\varepsilon(x, t)$ in $|x| < \infty$:

$$\tau\frac{\partial^2\varepsilon}{\partial t^2} + \frac{\partial\varepsilon}{\partial t} + V\frac{\partial\varepsilon}{\partial x} = \kappa\frac{\partial^2\varepsilon}{\partial x^2}\,, \tag{5}$$

where V is the advection speed, assumed to be constant for simplicity, and κ is the diffusivity. Adopting natural boundary conditions $\varepsilon = 0$ and $\partial\varepsilon/\partial x = 0$ at $x = \pm\infty$, the total energy of the particles $E(t) = \int_{-\infty}^{\infty}\varepsilon(x, t)\,{\rm d}x$ can easily be shown to satisfy

$$\frac{{\rm d}E}{{\rm d}t} + \tau\frac{{\rm d}^2E}{{\rm d}t^2} = 0\,, \tag{6}$$

which solves to yield

$$E = C + K{\rm e}^{-t/\tau}\,, \tag{7}$$

where C and K are constants. Since the telegraph equation is of second order in t, two initial conditions for $E(t)$ have to be specified:

Downloaded from https://academic.oup.com/mnras/article-abstract/487/1/975/5490402 by Mahidol University user on 16 July 2019

$E(0) = E_0$ at $t = 0$ for the initial energy and $\partial E/\partial t = 0$ at $t = 0$. Then the only admissible solution is $E = E_0 = \text{const}$, expressing the conservation of the total energy (and similarly for the total number of particles). Other authors disregard the second initial condition, which seems to be the cause of confusion regarding the conservation of E, as they then analyse an incomplete solution $E = E_0 + K(\mathrm{e}^{-t/\tau} - 1)$.

2.2.2 *Fluid simulations*

We solve equations (3) and (4) using the PENCIL CODE[1] (Brandenburg & Dobler 2010), a code for non-ideal MHD using sixth-order spatial finite differences. The simulation domain comprises a box of 80^3 grid points, with periodic boundary conditions.[2] The magnetic field is the same as that used in the test particle simulation, but with the smallest scales removed by truncating the spectrum $M(k)$ at $k_{\rm max}^{\rm fluid} = 40\pi/L = k_{\rm max}^{\rm particle}/16$, resulting in a magnetic field specified on a coarser grid. As in the test particle simulations, the magnetic field does not evolve during the simulation.

The choice of a much coarser resolution for the magnetic field in the fluid simulation reflects the fact that it is usually not feasible to simultaneously resolve the scales of interest of a particular astrophysical problem and the Larmor radius of the relevant CR population. For example, the typical resolution in simulations of multiphase supernova-driven ISM is of order of a few pc, while the Larmor radius is of order 10^{-6}–10^{-5} pc for CR energies of 1–10 GeV in a 5 μG magnetic field. Thus, any effects arising from the unresolved small scales, $k > k_{\rm max}^{\rm fluid}$, need to be accounted for through an adequate choice of the parameters that control CR diffusion, i.e. the diffusivities $\kappa_{\shortparallel}$, $\kappa_\perp$, and, in the Telegraph case, the characteristic time-scale τ.

We chose an initial condition for the CR energy density consistent with the particle distribution in equation (1) by assuming a single population of CRs, i.e. $\varepsilon(x, y, z) = n(x, y, z)E_{\rm cr}$, where n is the particle number density and $E_{\rm cr}$ is the energy of an individual particle. In the fluid simulation, the initial half-width of the CR distribution, σ_0, corresponds to approximately 4.4 mesh points, consistent with the particle simulations.

While in the Fickian prescription the initial condition for $\boldsymbol{F}$ is fully determined by the initial condition for ε, the Telegraph prescription requires a separate initial condition for $\boldsymbol{F}$. In agreement with the initial condition used for the particles, whose initial velocities have random, isotropic directions, we impose the zero flux initial condition, $\boldsymbol{F} = \boldsymbol{0}$.

3 RESULTS

3.1 Test particle simulations

Results of the test particle simulations are shown as dashed curves in Fig. 1, where the magnetic field has spectral index $s = -5/3$ (left-hand column) and $s = -2$ (right-hand column). In the upper panels, we show the variance σ^2 of the CR number density distribution along the x-axis as a function of time. The *global effective diffusivity* $\kappa_{\rm eff} \equiv \frac{1}{2}\,\mathrm{d}\sigma^2/\mathrm{d}t$ is shown in the middle panels. The variance σ^2 of the test particle distribution deviates strongly from the simple linear dependence on time that would be expected in the case of an isotropic Fickian diffusion. This is also visible in the variation of $\kappa_{\rm eff}$ with time, which first increases sharply, reaches a peak, and then decays to an asymptotic value. This behaviour reflects the transition from ballistic to diffusive behaviour and is characterized by the time interval $t_{\rm peak}$ after which $\kappa_{\rm eff}$ reaches a maximum $\kappa_{\rm peak}$. The transition is sensitive to the spectral index of the random field, with $t_{\rm peak} \approx 0.31L/v_0$ for $s = -5/3$ and $t_{\rm peak} \approx 0.43L/v_0$ for $s = -2$.

3.2 Fluid simulations

We found that it is possible to reproduce the behaviour of the test particle simulation with the Telegraph fluid simulation. For a fixed value of $r = \kappa_{\shortparallel}/\kappa_\perp$, we found that $t_{\rm peak}$ and $\kappa_{\rm peak}$ are controlled by τ and $\kappa_{\shortparallel}$, respectively. Therefore, the fluid simulation can be calibrated using the following simple iterative procedure, where the iteration steps are labelled with index i:

$$\kappa_\parallel^{(i+1)} = \kappa_\parallel^{(i)}\,\frac{\kappa_{\rm peak}^{\rm particle}}{\kappa_{\rm peak}^{(i)}}\,, \quad \tau^{(i+1)} = \tau^{(i)}\,\frac{t_{\rm peak}^{\rm particle}}{t_{\rm peak}^{(i)}}\,. \tag{8}$$

Thus, one runs a fluid simulation for given $\kappa_\parallel^{(i)}$ and $\tau^{(i)}$, and from this run $\kappa_{\rm peak}^{(i)}$ and $t_{\rm peak}^{(i)}$ are computed. Then, in the next iteration, the fluid simulation is re-run using $\kappa_\parallel^{(i+1)}$ and $\tau^{(i+1)}$; note that for this particular simulation set-up the computational cost of each run is very low. The iteration is performed until both $\kappa_{\rm peak}$ and $t_{\rm peak}$ differ from $\kappa_{\rm peak}^{\rm particle}$ and $t_{\rm peak}^{\rm particle}$, respectively, by less than 0.5 per cent. The iterations typically converge to this accuracy in 2–4 steps.

In Fig. 2, each of the curves is obtained with a different choice of r, calibrated using equation (8). This ratio controls the slope of $\kappa_{\rm eff}(t)$ at late times, therefore controlling the asymptotic value of $\kappa_{\rm eff}$. The relative difference between $\kappa_{\rm eff}$ obtained from the fluid and particle simulations, $\delta = (\kappa_{\rm eff}^{\rm fluid} - \kappa_{\rm eff}^{\rm particle})/\kappa_{\rm eff}^{\rm particle}$, is shown in the bottom panel. We use the time averaged value $\langle\delta\rangle$ as a goodness-of-fit measure, which is shown in Fig. 3. We find that the ratio $r = \kappa_{\shortparallel}/\kappa_\perp$ giving the best fit to the test particle results depends on the spectrum of the magnetic field, with $r \approx 325$ for $s = -5/3$, and $r \approx 525$ for $s = -2$.

The best-fitting parameters are summarized in Table 1 and correspond to the solid green curves in Fig. 1. The dashed orange curves in those figures show the Fickian prescription for the same choice of $\kappa_{\shortparallel}$ and $\kappa_\perp$. The lower panels of those figures show δ for both fluid prescriptions compared with the test particle simulation. For $s = -5/3$, the effective diffusivity, $\kappa_{\rm eff}$, of the CR distribution resulting from the calibrated Telegraph simulation differs from that in the test particle simulation by at most 2 per cent at any time. For $s = -2$ we find similarly small differences in $\kappa_{\rm eff}$ for $t \lesssim 0.8L/v_0$ and $t \gtrsim 1.7L/v_0$, but δ increases up to ∼30 per cent for $t \approx 1.1L/v_0$. This leaves an imprint in the variance at later times (top right-hand panel of Fig. 1). Albeit small, such a feature occurs independent of the specific parameter choice (see right-hand panel of Fig. 2). The Fickian solution does not capture the ballistic phase of particle propagation. However, at sufficiently large times, the effective diffusivity in the Fickian case is in good agreement with both the Telegraph and test particle results. In considering these differences, it is perhaps worth noting that the diffusion coefficient is typically unknown by almost a factor of 2.

The calibrated Telegraph model is able to reproduce local features, as shown in Fig. 4, where slices through the test particle

[1] http://pencil-code.nordita.org/

[2] We examined the effect of other choices of boundary conditions, and the effect proved negligible for this particular set-up, since the width of the CR distribution (initially set to $2\sigma_0$) is much smaller than L throughout the simulation.

Downloaded from https://academic.oup.com/mnras/article-abstract/487/1/975/5490402 by Mahidol University user on 16 July 2019

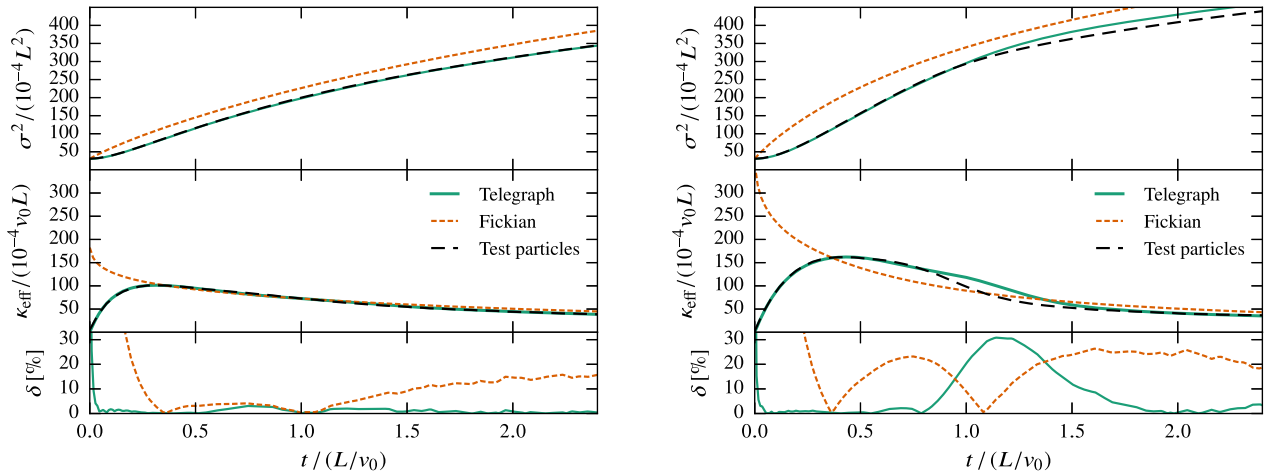


Figure 1. Comparison between the results of test particle simulations and fluid simulations using the Telegraph and Fickian prescriptions (with the same choice of calibrated diffusivities $\kappa_{\parallel}$ and $\kappa_{\perp}$) for a magnetic field with $s = -5/3$, in the left-hand side column, and $s = -2$, in the right-hand side column. The top panels show time evolution of the variance σ^2 of the CR distribution along the x-axis, the middle panels show the time evolution of the effective diffusivity, $\kappa_{\rm eff} = \frac{1}{2}\partial\sigma^2/\partial t$, and bottom panels show the relative difference in $\kappa_{\rm eff}$, $\delta = (\kappa_{\rm eff,\,f} - \kappa_{\rm eff,\,p})/\kappa_{\rm eff,\,p}$, with indices 'f' and 'p' referring to the fluid and test particle descriptions.

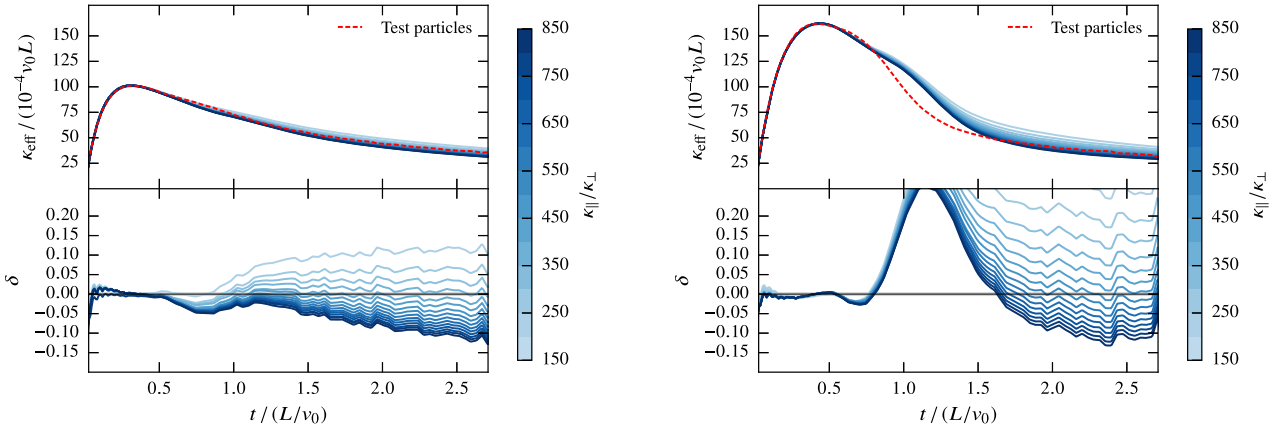


Figure 2. Impact of the choice of the ratio $r = \kappa_{\parallel}/\kappa_{\perp}$ for a magnetic field with $s = -5/3$ (left-hand column) and $s = -2$ (right-hand column). The top panels show the time evolution of the effective global diffusivity $\kappa_{\rm eff}$ for properly calibrated Telegraph models with different choices of r (colour coded, with the colour bar shown on the right of each column). The bottom panels show the fractional error in $\kappa_{\rm eff}$.

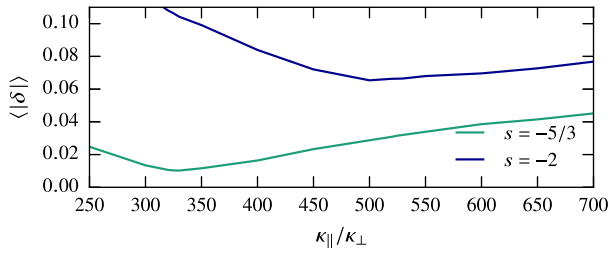


Figure 3. The time-averaged fractional error in $\kappa_{\rm eff}$ as a function of the ratio of CR diffusivities for two choices of the spectral index of the magnetic spectrum as specified in the legend.

simulation box are compared with the corresponding slices of the fluid simulations at various times and locations. Both the asymmetry in the distribution and small-scale variations are reproduced better by the Telegraph model.

Table 1. The best-fitting parameters used in the fluid simulations shown in Fig. 1, values of $t_{\rm peak}$ and $\kappa_{\rm peak}$, and their relation to the model parameters.

	$s = -5/3$	$s = -2$
$\kappa_{\rm peak}/(v_0L)$	0.010	0.016
$\kappa_{\parallel}/(v_0L)$	0.054	0.109
$\kappa_{\perp}/(v_0L)$	0.00017	0.00021
$\kappa_{\parallel}/\kappa_{\perp}$	325	525
$t_{\rm peak}/(L/v_0)$	0.31	0.43
$\tau/(L/v_0)$	0.17	0.33
$\kappa_{\parallel}/\kappa_{\rm peak}$	5.35	6.70
$\tau/t_{\rm peak}$	0.55	0.77
$(\kappa_{\parallel}/\tau)^{1/2}/v_0$	0.56	0.57

3.3 Variability of $t_{\rm peak}$ in test particle simulations

In the above, we have selected $R_{\rm L}$ for test particles that allows for reasonable comparison with fluid simulations. However, the dynamically important CRs in the ISM have much smaller $R_{\rm L}$.

Downloaded from https://academic.oup.com/mnras/article-abstract/487/1/975/5490402 by Mahidol University user on 16 July 2019

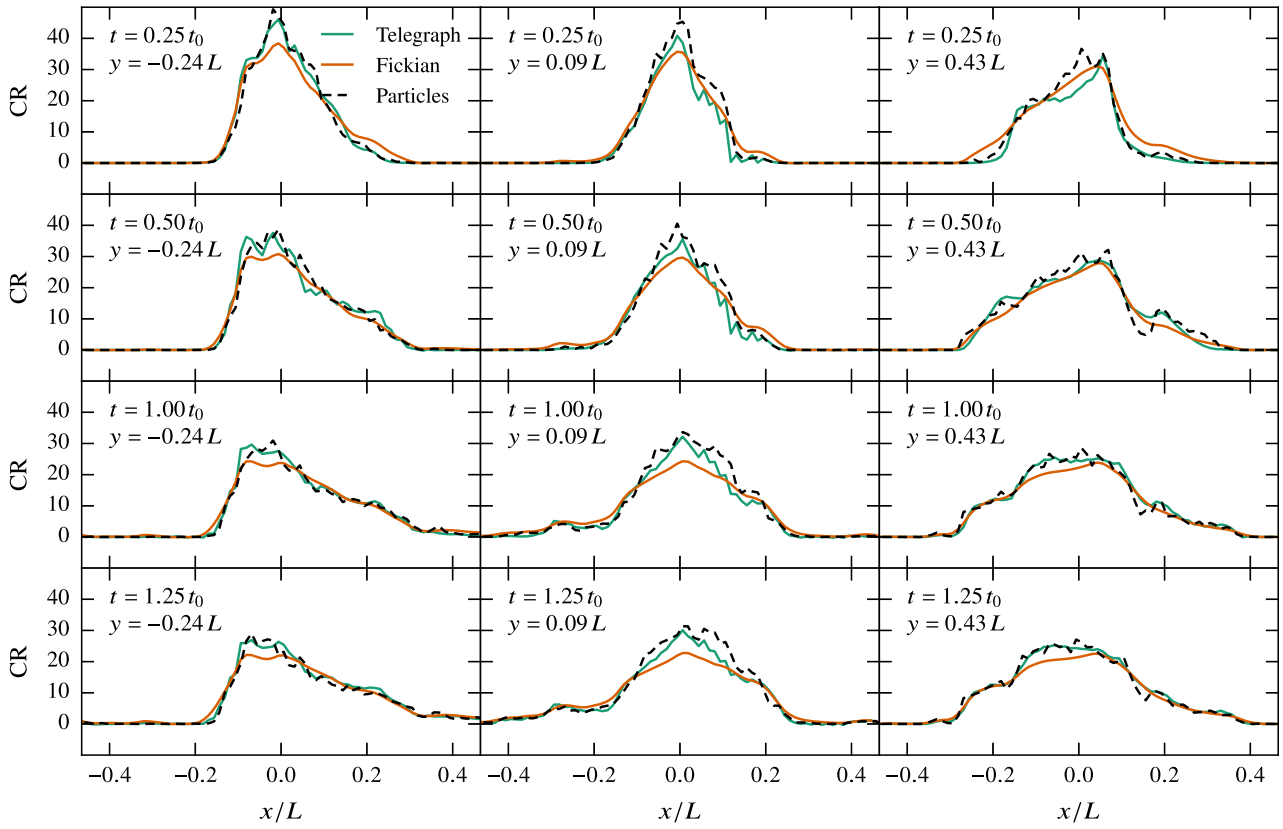


Figure 4. Time evolution (top to bottom) of the CR distribution along the x-axis obtained by integrating the results over parallelepipeds extended along the x-axis and $0.05L$ in width along y and z passing through arbitrarily chosen positions in y and z (left to right). The vertical axis shows, in arbitrary units, the total number of particles and their energy in the integration domain. The higher accuracy of the Telegraph model is apparent.

Since it appears that the time of the peak, $t_{\rm peak}$, and τ are connected, an investigation of how $t_{\rm peak}$ varies with particle energy (or $R_{\rm L}$) may suggest a suitable range of τ to use in more realistic fluid simulations. In this section, we perform test particle simulations, but now utilizing the *continuum model* for the magnetic field described by Snodin et al. (2016), where the magnetic field is constructed in the form of Fourier series with random phases. This implementation allows one to probe much lower particle energies than the discrete mesh model used above, where the mesh spacing controls the smallest value of $R_{\rm L}$ accessible. However, it still remains impractical to faithfully explore energies much below $R_{\rm L} \lesssim 10^{-4}L$, and so one can at best extrapolate to infer the behaviour at the smallest relevant scales. This model magnetic field has fluctuations at a wide range of geometrically spaced wavenumbers to ensure sufficient resonant scattering of the particles at small scales. We take $k_{\rm max}^{\rm particle}/k_{\rm min} = 1024$, and $N = 1024$ distinct wave vectors.

In Fig. 5 (data shown in Table 2), we show the dependence of $t_{\rm peak}$ on $R_{\rm L}$ and on the spectral index, s, using a set of test particle simulations. The scaling with $R_{\rm L}$ is approximately linear in all cases. At sufficiently large $R_{\rm L}$ ($R_{\rm L} \gtrsim 0.03L$ for the values of s considered here), the peaks vanish (i.e. the peak and asymptotic values coincide), so $t_{\rm peak}$ cannot be determined. Apparently, there is a non-zero intercept at low $R_{\rm L}$, which appears to depend linearly on s.

At such small scales, it is expected that particles will be scattered by self-generated waves (e.g. Kulsrud & Pearce 1969; Wentzel

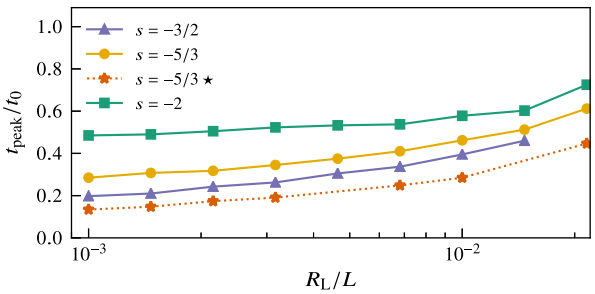


Figure 5. Dependence of $t_{\rm peak}$ on the Larmor radius $R_{\rm L}$ (expressed in units of L) in the test particle simulations, for different choices of the magnetic spectral index s. The data points shown with stars are obtained with a CR self-scattering model discussed in the text. These results show that an adequate choice of the parameter τ needs to correctly account for the energy of the modelled CR population and the form of the (subgrid) magnetic spectrum. (Data shown in Table 2.)

1974), which may have some effect on $t_{\rm peak}$. In an attempt to account for this we adopt the simple scattering model used by Seta et al. (2018), which introduces an isotropic random change to the particle pitch angle with respect to the local magnetic field once per Larmor time $t_{\rm L}$. In this model, the average change in the angle is proportional to $(R_{\rm L}/L)^{1/4}$. Applying this to the $s = -5/3$ case, we find a reduction in the intercept, but not a significant difference in the slope, as shown in Fig. 5.

Downloaded from https://academic.oup.com/mnras/article-abstract/487/1/975/5490402 by Mahidol University user on 16 July 2019

Table 2. Larmorradius and $t_{\rm peak}$ for different choices of magnetic spectral index, s. The star indicates the run with CR self-scattering model (see text).

	$t_{\rm peak}/t_0$			
$10^3 R_{\rm L}/L$	$s=-3/2$	$s=-5/3$	$s=-5/3\star$	$s=-2$
1.00	0.20	0.28	0.13	0.48
1.47	0.21	0.31	0.15	0.49
2.15	0.24	0.32	0.17	0.51
3.16	0.26	0.34	0.19	0.52
4.64	0.30	0.38		0.53
6.81	0.34	0.41	0.25	0.54
10.0	0.40	0.46	0.28	0.58
14.7	0.46	0.51		0.60
21.5	0.55	0.61	0.45	0.72
31.6		0.78	0.67	0.76

4 DISCUSSION AND CONCLUSIONS

Inspection of Fig. 1 shows that the Fickian prescription for the diffusion of CRs is unable to capture the transition from a ballistic to a diffusive regime, which is manifest at earlier times in test particle simulations. Nevertheless, the effective diffusivity asymptotically converges to that of the test particles using $\kappa_{\shortparallel}$ and $\kappa_{\perp}$ as calibrated for the Telegraph prescription.

The detailed agreement between the test particle results and solutions of the telegraph equation in Fig. 4 is remarkable, given that the diffusion coefficients adopted are global constants that have no direct dependence on the local magnetic field properties. This suggests strongly that the telegraph equation is a viable model for simulations of CR propagation using a fluid description, with a subgrid model for their diffusion. The higher is the spatial resolution of such simulations and the larger is the particle energy, the more important can be initial deviations of the particle propagation from a diffusive behaviour at the numerically resolved scales, and the properly calibrated telegraph equation proves to be able to capture such behaviours.

Our results lead to an estimate of the time-scale τ, a parameter in the telegraph equation. Taking the outer scale of the turbulence $L \approx 100\,{\rm pc}$ and assuming that the dynamically important CRs (mainly protons) have energy of order 1 GeV (i.e. $R_{\rm L} \simeq 10^{12}\,{\rm cm}$), the presence of a non-zero intercept in Fig. 5 indicates that $\tau \simeq 20\,{\rm yr}$ – under the assumption of $\tau \approx 0.5 t_{\rm peak}$ and taking $t_{\rm peak} \approx 0.12 \times (100\,{\rm pc})/c$, extrapolated from the self-scattering $s=-5/3$ case. The maximum propagation speed for disturbances in the CR fluid is related to τ and follows as $v_{\rm max} = (\kappa_{\shortparallel}/\tau)^{1/2} \simeq 10^9\,{\rm cm\,s^{-1}}$.

It is worth noticing that the asymptotic value of the global diffusivity, $\kappa_{\rm eff}$, is about *an order of magnitude smaller* than the local diffusivity, $\kappa_{\shortparallel}$, which is applied at the mesh scale in the fluid simulation. This must be taken into account when choosing simulation parameters: to achieve a global effective diffusivity of order $10^{28}\,{\rm cm^2\,s^{-1}}$ – consistent with best fits to CR observational data (Strong et al. 2007) – our results suggest that a local diffusivity of at least $\kappa_{\shortparallel} \sim 10^{29}\,{\rm cm^2\,s^{-1}}$ needs to be adopted.

We have assumed CRs are scattered primarily by extrinsic turbulence, rather than self-generated waves that would lead to self-confinement (see e.g. Zweibel 2017, for a discussion of these two regimes). (For self-confined CRs, one might employ modified fluid equations, such as those of Thomas & Pfrommer 2019.) We have also neglected dynamical effects of CRs on the gas density and velocity and, thereby, on the magnetic field. It is, however, unlikely that such effects can change the nature of the CR diffusion process.

ACKNOWLEDGEMENTS

We thank the referee for their suggestions. We thank Amit Seta and Sergei Fedotov for useful discussions. LFSR, GRS, and AS acknowledge financial support of STFC (ST/N000900/1, Project 2) and the Leverhulme Trust (RPG-2014-427). APS was supported by the Thailand Research Fund (RTA5980003). This research has made use of NASA's Astrophysics Data System.

REFERENCES

Bakunin O. G., 2008, Turbulence and Diffusion: Scaling Versus Equations. Springer-Verlag, Berlin
Brandenburg A., Dobler W., 2010, Astrophysics Source Code Library, record ascl:1010.060
Farber R., Ruszkowski M., Yang H. Y. K., Zweibel E. G., 2018, ApJ, 856, 112
Girichidis P. et al., 2016, ApJ, 816, L19
Gombosi T. I., Jokipii J. R., Kota J., Lorencz K., Williams L. L., 1993, ApJ, 403, 377
Grenier I. A., Black J. H., Strong A. W., 2015, ARA&A, 53, 199
Hanasz M., Wóltański D., Kowalik K., 2009, ApJ, 706, L155
Holguin F., Ruszkowski M., Lazarian A., Farber R., Yang H. Y. K., 2018, preprint (arXiv:1807.05494)
Kulsrud R. M., 2005, Plasma Physics for Astrophysics. Princeton Univ. Press, Princeton, NJ
Kulsrud R., Pearce W. P., 1969, ApJ, 156, 445
Litvinenko Y. E., Noble P. L., 2016, Phys. Plasmas, 23, 062901
Litvinenko Y. E., Schlickeiser R., 2013, A&A, 554, A59
Malkov M. A., Sagdeev R. Z., 2015, ApJ, 808, 157
Seta A., Shukurov A., Wood T. S., Bushby P. J., Snodin A. P., 2018, MNRAS, 473, 4544
Simpson C. M., Pakmor R., Marinacci F., Pfrommer C., Springel V., Glover S. C. O., Clark P. C., Smith R. J., 2016, ApJ, 827, L29
Snodin A. P., Brandenburg A., Mee A. J., Shukurov A., 2006, MNRAS, 373, 643
Snodin A. P., Shukurov A., Sarson G. R., Bushby P. J., Rodrigues L. F. S., 2016, MNRAS, 457, 3975
Strong A. W., Moskalenko I. V., Ptuskin V. S., 2007, Annu. Rev. Nucl. Part. Sci., 57, 285
Tautz R. C., Lerche I., 2016, Res. Astron. Astrophys., 16, 162
Thomas T., Pfrommer C., 2019, MNRAS, 485, 2977
Wentzel D. G., 1974, ARA&A, 12, 71
Zweibel E. G., 2013, Phys. Plasmas, 20, 055501
Zweibel E. G., 2017, Phys. Plasmas, 24, 055402

This paper has been typeset from a TEX/LATEX file prepared by the author.

Downloaded from https://academic.oup.com/mnras/article-abstract/487/1/975/5490402 by Mahidol University user on 16 July 2019

The Astrophysical Journal, 880:124 (5pp), 2019 August 1 https://doi.org/10.3847/1538-4357/ab288f
© 2019. The American Astronomical Society. All rights reserved.

X-Rays from $e^{\pm}$ Pair Halos

A. Eungwanichayapant[1], W. Luangtip[2], W. Maithong[3], and D. Ruffolo[4]
[1] School of Science, Mae Fah Luang University, Chiang Rai 57100, Thailand; anant@mfu.ac.th
[2] Department of Physics, Faculty of Science, Srinakharinwirot University, Bangkok 10110, Thailand
[3] Faculty of Science, Chiang Mai Rajabhat University, Chiang Mai 50300, Thailand
[4] Department of Physics, Faculty of Science, Mahidol University, Bangkok 10400, Thailand
Received 2018 November 14; revised 2019 May 22; accepted 2019 June 9; published 2019 August 1

Abstract

It was previously suggested that $e^{\pm}$ pair halos could be observed in γ-rays. Searching for pair halos is a challenging topic in γ-ray astronomy that has not yet yielded a convincing detection for an individual object. Here we propose that X-ray observations could reveal the existence of $e^{\pm}$ pair halos. To support our suggestion, we computed the observed energy and spatial distribution of X-ray photons from the pair halos and check the feasibility of pair halo detection by current and future X-ray observatories. The results show that current X-ray missions could register a positive signal for the pair halos created under some conditions. For a magnetic field (B) of $\sim$1 μG, the X-ray could be observable for a seed gamma-ray energy of $E_{\gamma_0} \gtrsim 50$ TeV. If $E_{\gamma_0} \sim 100$ TeV, the observable range of B would be $B \gtrsim 300$ nG.

Key words: galaxies: active – galaxies: halos – gamma rays: galaxies – X-rays: galaxies

1. Introduction

Very high energy (VHE) γ-rays ($E > 10$ TeV) from extragalactic sources such as active galactic nuclei (AGNs) are absorbed during propagation (Costamante et al. 2003; H.E.S.S. Collaboration et al. 2017). The absorption of γ-rays by $\gamma\gamma$ pair production with cosmic infrared background (CIB) photons produces $e^{\pm}$ pairs, which can scatter cosmic microwave background (CMB) photons to produce more γ-rays. The combination of these two processes leads to an electromagnetic cascade, which will continue until the upscattered γ-rays have insufficient energy to be absorbed by the CIB.

The ambient magnetic field strength B plays an important role in the electromagnetic cascade, and different ranges of B can lead to different phenomena in observations. As a result, $e^{\pm}$ halos were proposed as new tools for probing the ambient magnetic fields over various scales. A very weak magnetic field, $10^{-20} < B < 10^{-15}$, leads to very little deflection of the cascading $e^{\pm}$ trajectories, which could cause "pair echoes," i.e., delayed observations of IC γ-rays from the cascades after the intrinsic γ-rays from sources (Takahashi et al. 2008). For a somewhat stronger magnetic field, $10^{-16} < B < 10^{-12}$, the deflection of the $e^{\pm}$ can extend the secondary γ-rays around the initial direction of the γ-ray sources (Elyiv et al. 2009). If the magnetic field is strong enough ($\gtrsim$1 nG), the gyroradius of the $e^{\pm}$ with $E \ll 1$ PeV will be smaller than the inverse Compton (IC) scattering mean free path (Figure 1) and the $e^{\pm}$ will gyrate before scattering the CMB photons. As the result, the electromagnetic cascades that develop around the central source produce a spherical cloud of $e^{\pm}$ pairs called "$e^{\pm}$ pair halos."

In 1994, a model of $e^{\pm}$ pair halos was first proposed by Aharonian et al. (1994). Only the spectral energy distributions (SEDs) of the γ-rays from pair halos were computed in that work. Later on, the angular distribution of the γ-rays from the pair halos was calculated by Eungwanichayapant & Aharonian (2009). Most work on the $e^{\pm}$ pair halos has focused on radiation in the gamma band. Observational searches for pair halos have also been performed only with γ-rays. The first attempt was by the HEGRA group (Aharonian et al. 1999b), and other searches were by Ando & Kusenko (2010) and Neronov et al. (2011). A very exciting result was the hint of a positive signal from stacked *Fermi*-LAT data of 24 BL Lac objects by Chen et al. (2015). Their work concludes that the ambient intergalactic magnetic field was around 10^{-17}–10^{-15} G. Here we consider the possibility of stronger ambient magnetic fields around some AGNs.

In certain conditions, pair halos do radiate X-rays via the synchrotron process, providing another window for observing the pair halos. In this work, we computed the energy and surface brightness of synchrotron radiation from the pair halos that develop relatively close to the AGNs, within several hundred kiloparsecs, on the assumption that the ambient magnetic fields of that size scale are in the range of nG to μG. We used the simulation results to study characteristics of the X-ray pair halos and determine the feasibility of observing them using current X-ray observatories such as *Chandra, XMM-Newton*, and *NuSTAR* and a future observatory like *Athena*.

2. X-Rays from Pair Halos

To compute the energy distribution of the X-ray photons from a pair halo, we applied a Monte Carlo simulation to follow electromagnetic cascades generated by intrinsic VHE γ-rays. All $e^{\pm}$s created by cascades in an ambient magnetic field $B > 1$ nG have curved trajectories. It is reasonable to assume for simulation purposes that the $e^{\pm}$ pairs stay at the production sites because their gyroradii ($\sim 10^{-2}$–10^{2} kpc) are much smaller than the size of the pair halo, which scales with the pair production (PP) mean free path length ($\gtrsim$1 Mpc). On the other hand, the travel time needs to be computed in order to determine the synchrotron energy distributions. The emission time, t, and the energy, E, of the cascading $e^{\pm}$ were used to compute the synchrotron emission time distribution, $\tau(E) = dt/dE$. The synchrotron differential power spectrum from an electron with a pitch angle α is (see, e.g., Blumenthal & Gould 1970; Rybicki & Lightman 2004)

$$\frac{dW_\nu}{dt} = \frac{\sqrt{3}\, e^3 B \sin\alpha}{mc^2} G\left(\frac{\nu}{\nu_c}\right), \quad (1)$$

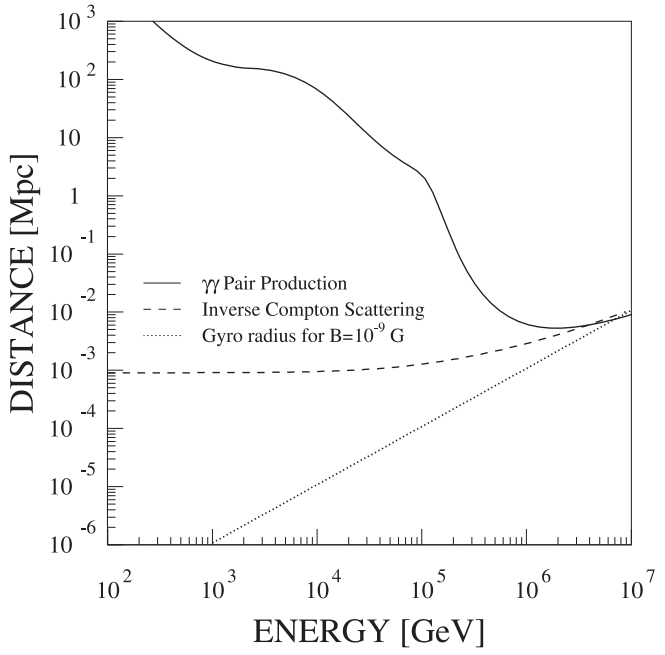


Figure 1. Comparison of important mean free path lengths in the model, assuming $B = 1$ nG.

where $G(x)$ is expressed in terms of a modified Bessel function $K(\xi)$ as

$$G(x) \equiv x \int_x^\infty K_{\frac{5}{3}}(\xi) d\xi, \tag{2}$$

and ν_c is the critical frequency

$$\nu_c(E, \alpha) = \frac{3}{2} \frac{E^2 eB \sin\alpha}{m^3 c^5}. \tag{3}$$

We calculated the differential energy spectrum of the radiation of the cascading $e^\pm$ pairs by integrating the product of the differential power spectrum with the pitch angle distribution and the emission time distribution:

$$W_\nu = \int \frac{\sqrt{3}\, e^3 B}{mc^2} \left[\int_0^\pi G\left(\frac{\nu}{\nu_c}\right) \frac{1}{2} \sin^2\alpha \; d\alpha \right] \tau(E) dE, \tag{4}$$

noting that ν_c depends on E and α. Assuming an isotropic pitch angle distribution, we converted the synchrotron differential energy, W_ν, to be the pair halo synchrotron differential flux, F_ν, with this normalization:

$$F_\nu = \frac{L_{\gamma_0}}{E_{\gamma_0} 4\pi d_s^2} W_\nu, \tag{5}$$

where L_{γ_0} is the intrinsic gamma luminosity of an AGN, E_{γ_0} is the total energy of the intrinsic gamma photons emitted by the AGN in our simulation, and d_s is the distance from the AGN. The angular distance θ from the central source is another important observable quantity from the pair halos. To compute the distribution of the angular distance with high statistical accuracy and limited numerical expense, the utilization of spherical symmetry of pair halos in Eungwanichayapant & Aharonian (2009), in which the pair halos look the same in all directions, is still a good strategy. Then we created an observer sphere with radius d_s covering the AGN in our simulation. Every time the photons were generated and hit the sphere, we calculated the angular distances by determining the angle between the normal vector of the sphere and the direction of a photon emitted in a random direction.

3. Results

The SED within 0.°1 and surface brightness of the synchrotron photons from $e^\pm$ pair halos are shown in Figure 2 for a pair halo initiated by a monoenergetic source located at $z = 0.129$ with[5] γ-luminosity of 10^{45} erg s^{-1} and an ambient magnetic field of 1 μG. The synchrotron SEDs from pair halos triggered by various intrinsic γ-ray energies, E_{γ_0}, in the left panel of Figure 2(a) show that most of the synchrotron energy is contained in the X-ray band. When E_{γ_0} increases, the maximum energy is higher and more energy flux is contained in the higher-energy bands. The SEDs are very sensitive to the primary γ-ray energy when 10 TeV $< E_{\gamma_0} <$ 100 TeV. For the observing region within 0.°1 ($\approx$460 kpc) and the relatively large PP mean free path, the $e^\pm$s that radiate the X-rays were the first generation created only by the primary γ-rays. As a result, the X-ray SED depends on E_{γ_0}. This fact can explain the surface brightnesses of the X-rays from the pair halos in the right panel of Figure 2(b), which have the same structure when $E_{\gamma_0} = 10$, 50 and 100 TeV. On the other hand, at $\gtrsim$500 TeV, the SEDs do not depend on E_{γ_0} because with the very small PP mean free path (2–10 kpc) of the primary γ-rays, several generations of the cascades have been developed and created $e^\pm$ of various energies within 0.°1 already. The surface brightness in this case is more centrally peaked.

The pair halo SEDs for different ambient magnetic field strengths, B, are shown in Figure 3(a). The range of the SEDs extended to higher energy and the energy flux increased at all energies when the magnetic field increased. The magnitudes of the surface brightnesses in Figure 3(b) are also sensitive to the considered magnetic fields (1 nG–1 μG), so that a higher magnetic field leads to a higher surface brightness. It is interesting to note that both the SED and brightness increase with a higher rate when $B > 1$ μG. On the other hand, we found that the profiles of all surface brightnesses are exactly the same within simulation uncertainties, which implies that the magnetic field in this range does not affect the images of X-ray pair halos.

In the model of pair halo emission, even though IC is responsible for γ-ray emission, this process can also generate photons in other bands including X-rays. Our computational results in Figure 4 show that the X-ray flux from synchrotron radiation of higher-energy $e^\pm$ pairs significantly exceeds that from IC of lower-energy pairs when $B \gtrsim 3$ nG. This implies that we cannot discriminate between synchrotron and IC emission of X-rays if the magnetic field is below 3 nG.

4. Observational Feasibility

We also examine whether the pair halo X-ray emission theoretically proposed in this work would be detected by the current generation as well as the future X-ray observatories: *Chandra*, *XMM-Newton*, *NuSTAR*, and *Athena*. The observed count rate for each X-ray instrument was simulated by an

[5] The redshift of 1ES1426+428, one of the promising candidates for detecting a pair halo.

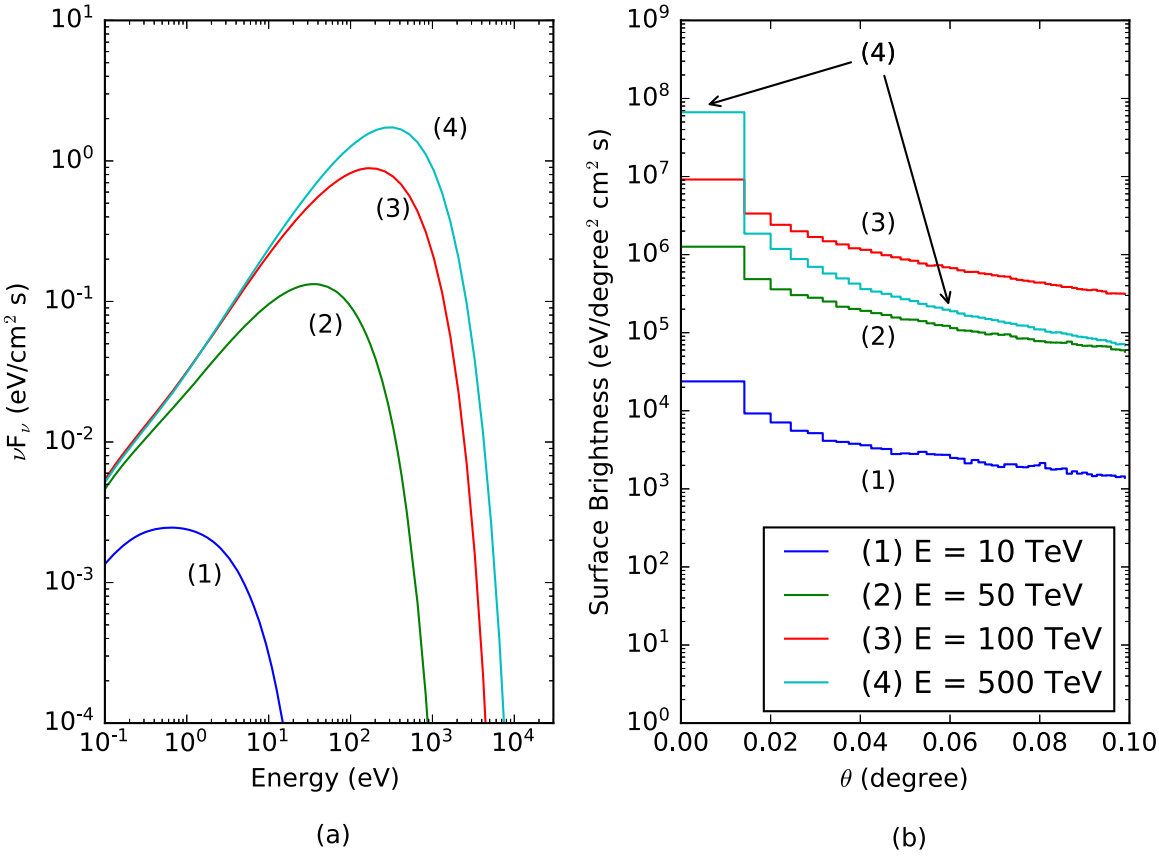


Figure 2. Pair halos for different monoenergetic primary γ-ray energies. (a) Pair halo SEDs for X-ray emission within $0.^\circ1$ of the AGN. (b) Pair halo surface brightness distributions.

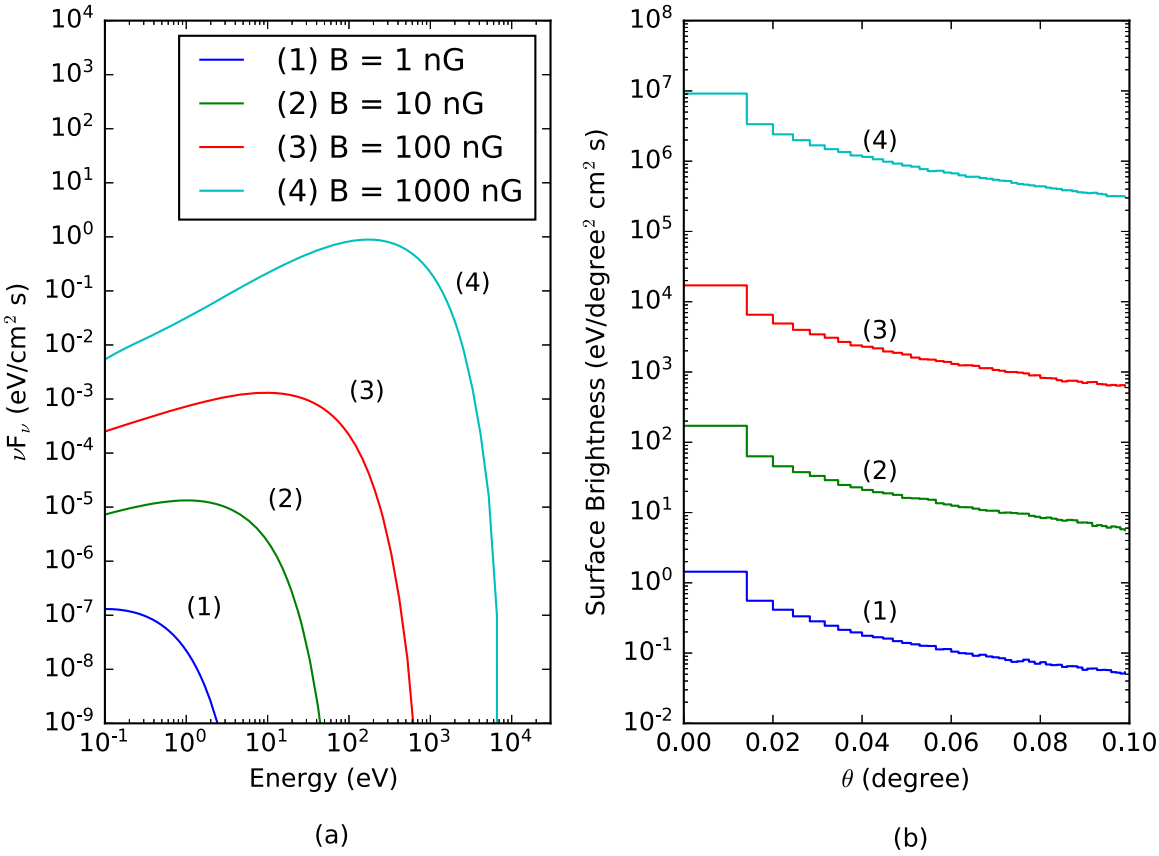


Figure 3. Pair halos in different magnetic fields. (a) The SEDs and (b) the surface brightnesses.

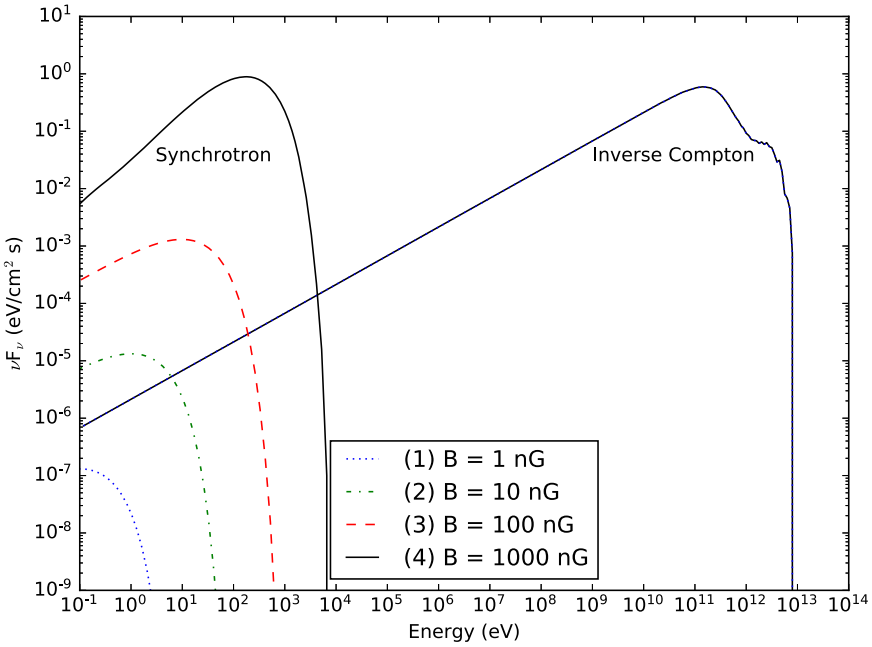


Figure 4. Pair halo SED from inverse Compton scattering (Eungwanichayapant & Aharonian 2009) and synchrotron radiation with different magnetic fields.

X-Ray Spectral Fitting Package (XSPEC)[6] using the current response matrix files (RMFs) and ancillary response files (ARFs) of the instruments available in the official web pages of the observatories. In this section, we consider the halo emission as an extended source with the angular radius of 0.°1 during the simulation. Note that although the halo emission might extend beyond 0.°1, in fact the flux might be reduced by more than an order of magnitude (see the right panels of Figures 2 and 3) compared with the flux obtained from the central region. Moreover, the effective area of the X-ray telescope is normally lower as a function of angular distance from the focal point; for example, the effective area of *XMM-Newton* decreases by ∼30% at 0.°1.[7] Given that, observing the halo emission at the region beyond the angular radius of 0.°1 would be ineffective. Here, we calculated the halo flux obtained from different physical conditions: intrinsic γ-ray energy varied from 10 to 100 TeV for constant B of 1000 nG and B ranged from 10 to 700 nG for constant γ-ray of 100 TeV. In addition, we also accounted for foreground Galactic extinction by adding absorption ($N_{\rm H}$) of 1.7×10^{20} cm^{-2} along the line of sight into the models to make the models more realistic in the observations.

Table 1 (top section) shows the X-ray photon count rate of each X-ray instrument that could be obtained from the pair halos at different halo parameters. We note that the count rate of the *NuSTAR* X-ray telescope is not reported here because our simulating results show that the telescope capability is not suitable to detect the halo. In fact, since the telescope was designed to detect X-ray photons in a hard energy band (3–79 keV), a large fraction of the halo flux is out of the *NuSTAR* energy bandpass (see left panels of Figures 2 and 3). In addition, the instrument count rates listed in Table 1 might not be highly accurate due to the limitation of available ready-made ARFs. In fact, using ARFs that are averaged over an area larger or smaller than the halo could result in underestimation or overestimation of the count rates, respectively, by some fraction. We regard our calculation as a first-order approximation to estimate the possibility of detecting the halo.

From Table 1, it is clear that the X-ray emission obtained from the halo at $E_{\gamma_0} \leqslant 10$ TeV and $B \leqslant 1000$ or at $E_{\gamma_0} \leqslant 100$ TeV and $B \leqslant 10$ nG could not be detected by either current generation instruments or the future mission *Athena*, since pair halo flux is substantially lower than the sensitivity limit of the instruments. In addition, it is also impossible to detect the halo emission in which E_{γ_0} and B are below 100 TeV and 100 nG, respectively, using *Chandra*/ACIS-S. This implies that not all halo X-ray emission would be detected by the current or near-future X-ray observatories, and might be one reason why the halo emission has not been detected yet.

To get more information, we proceeded to calculate the exposure time required to detect a halo by the X-ray instruments. Here, we consider the instrument and central AGN photons as the background contamination in the calculation. In fact, the instrument background count rate information can be obtained from the official web pages of the observatories. In the case of the central AGN, the count rate was estimated for each instrument using the tool WEBPIMM[8]; the model assumes an AGN luminosity of 10^{45} erg s^{-1} located at a distance of 529 Mpc in which the AGN spectrum can be described by an absorbed power-law spectrum with a photon index of 2 and $N_{\rm H}$ of 1.7×10^{20} cm^{-2}. In the case of *Athena*, for which the AGN count rate cannot be estimated by WEBPIMM, we calculated it using the XSPEC in which the same AGN spectral model, the RMF, and the ARF were applied. We take these AGN count rates as well as those of the instruments as the background count rate and calculate the signal-to-noise ratio for marginal detection of the halo at the confidence level of 3σ. The results are shown in Table 1 (bottom section). Interestingly, it is found that the exposure time required in many cases is less than 100 ks, implying that the halos at these conditions should have already been detected by current instruments if they exist; these

[6] https://heasarc.gsfc.nasa.gov/xanadu/xspec/

[7] https://xmm-tools.cosmos.esa.int/external/xmm_user_support/documentation/uhb/effareaoffaxis.html

[8] https://heasarc.gsfc.nasa.gov/cgi-bin/Tools/w3pimms/w3pimms.pl

Table 1
The Calculated Halo Photon Count Rate and Required Exposure Time to Detect the Halo for Each X-Ray Instrument

Pair Halo Parameter[a]		X-Ray Instrument		
E_{γ_0} (TeV)	B (nG)	*XMM-Newton* EPIC pn	*Chandra* ACIS-S	*Athena* WFI
		Predicted Count Rate (count s^{-1})		
10	1000	n/a[b]	n/a[b]	n/a[b]
30	1000	7×10^{-4}	6×10^{-6}	4.1×10^{-3}
50	1000	2.4×10^{-2}	3.8×10^{-4}	2.3×10^{-1}
70	1000	2.2×10^{-1}	4.6×10^{-3}	2.7
100	1000	1.4	5.1×10^{-2}	2×10^{1}
100	10	n/a[b]	n/a[b]	n/a[b]
100	100	6×10^{-6}	n/a[b]	5.8×10^{-5}
100	300	2.9×10^{-3}	5.8×10^{-5}	3.1×10^{-2}
100	500	4.8×10^{-2}	1.1×10^{-3}	6.1×10^{-1}
100	700	2.7×10^{-1}	6.8×10^{-3}	3.6
		Required Exposure Time (ks)[c]		
30	1000	4.5×10^{5}	n/a[b]	1.2×10^{5}
50	1000	3.9×10^{2}	1.6×10^{5}	3.9×10^{1}
70	1000	4.6	1.1×10^{3}	2.9×10^{-1}
100	1000	1.1×10^{-1}	9.2	5.7×10^{-3}
100	100	6.1×10^{9}	n/a[b]	6.1×10^{8}
100	300	2.7×10^{4}	6.9×10^{6}	2.2×10^{3}
100	500	9.5×10^{1}	2×10^{4}	5.5
100	700	3.1	5.1×10^{2}	1.7×10^{-1}

Notes.
[a] The pair halo parameters, i.e., seed gamma-ray energy (E_{γ_0}) and magnetic field (B), used to simulate the instrument count rate.
[b] The count rate obtained from the halo emission is substantially below the sensitivity limit of the instrument so that the halo cannot be detected by the instrument.
[c] The required exposure time for each detector to detect the halo at the confidence level of 3σ.

are the cases where $E_{\gamma_0} \geqslant 70$ TeV and $B \geqslant 1000$ nG, or $E_{\gamma_0} \geqslant 100$ TeV and $B \geqslant 500$ nG. However, since there has been no observational evidence reporting the detection of the halo emission in any blazars in the X-ray waveband, these could result in an observational constraint that halos in the real universe might have $E_{\gamma_0} \leqslant 70$ TeV if $B = 1000$ nG or $B \leqslant 500$ nG if $E_{\gamma_0} = 100$ TeV.

There should be a range of physical parameters for which pair halo could be detectable by the current and near-future X-ray telescopes. If B is ∼1000 nG, the observable E_{γ_0} range would be $E_{\gamma_0} \gtrsim 50$ TeV in which the exposure time needed for the detection is $\lesssim$4000 ks for *XMM-Newton* or just ∼400 ks for *Athena*. On the other hand, if E_{γ_0} is ∼100 TeV, the observable range of B would be $B \gtrsim 300$ nG in which the exposure time of $\lesssim$30,000 ks and $\lesssim$2000 ks is required for *XMM-Newton* and *Athena*, respectively. Note that in some cases the required exposure time can be up to ∼30,000 ks, and normally this cannot be done with a single observation. However, we regard that this exposure interval is feasible by combining the data from multiple observations together, assuming that the level of halo flux variability is very low (Aharonian et al. 1994, 1999a). In fact, this technique has been applied with gamma-ray data to search for halos, and could be applied with the X-ray data. In brief, the spatial distribution of the observed central AGN flux was compared statistically with that of the instrument point-spread function. If they are not consistent (i.e., excess photons are observed in the AGN surface brightness radial profile), this could be evidence of the halo emission (see, e.g., Ando & Kusenko 2010; Neronov et al. 2011; Ackermann et al. 2013; Chen et al. 2015). In future work we will undertake the analysis of X-ray data for candidate halos.

5. Conclusions

Before this work, almost all research on $e^{\pm}$ pair halos focused on γ-rays. However, X-rays provide another window in which pair halos should emit synchrotron radiation. We propose a new approach to search for pair halos by computing the SED and surface brightness of X-rays from the pair halos. Our results show that we can gain information on the magnetic field surrounding the central source from the SEDs and surface brightness of the X-ray pair halos. Our calculations also show that 1 μG is the maximum strength of the ambient magnetic field in which the pair halos can be formed. This corresponds to the fact that when the $e^{\pm}$ gyrate in a 1 μG field surrounded by the CMB photon field, the synchrotron and Compton scattering energy-loss rate would be about the same. If the magnetic field is stronger than this, the $e^{\pm}$ lose most of their energy by synchrotron radiation and cannot efficiently generate next-generation cascade $e^{\pm}$.

While this is an exciting possibility, observing the pair halos can be challenging. Nevertheless, our simulation results show that the pair halo flux level for some conditions could lie within the capability of current and near-future missions of X-ray telescopes to detect, i.e., $E_{\gamma_0} \gtrsim 50$ TeV for $B \approx 1000$ nG, and $B \gtrsim 300$ nG for $E_{\gamma_0} \approx 100$ TeV.

This work was supported by grants from the Coordinating Center for Thai Government Science and Technology Scholarship Students, National Science and Technology Development Agency (grant No. FDA-CO-2561-5837-TH), and the Thailand Research Fund (grant Nos. MRG5080345 and RTA5980003). The authors would like to thank the National Astronomical Research Institute of Thailand (NARIT) for supporting computing facilities.

ORCID iDs

A. Eungwanichayapant https://orcid.org/0000-0002-0692-1914
W. Luangtip https://orcid.org/0000-0002-4516-6042
D. Ruffolo https://orcid.org/0000-0003-3414-9666

References

Ackermann, M., Ajello, M., Allafort, A., et al. 2013, ApJ, 765, 54
Aharonian, F., Akhperjanian, A. G., Barrio, J. A., et al. 1999a, A&A, 349, 29
Aharonian, F. A., Akhperjanian, A. G., Barrio, J. A., et al. 1999b, A&A, 349, 11
Aharonian, F. A., Coppi, P. S., & Völk, H. J. 1994, ApJL, 423, L5
Ando, S., & Kusenko, A. 2010, ApJL, 722, L39
Blumenthal, G. R., & Gould, R. J. 1970, RvMP, 42, 237
Chen, W., Buckley, J. H., & Ferrer, F. 2015, PhRvL, 115, 211103
Costamante, L., Aharonian, F., Ghisellini, G., & Horns, D. 2003, NewAR, 47, 677
Elyiv, A., Neronov, A., & Semikoz, D. 2009, PhRvD, 80, 023010
Eungwanichayapant, A., & Aharonian, F. 2009, IJMPD, 18, 911
H.E.S.S. Collaboration, Abdalla, H., Abramowski, A., et al. 2017, A&A, 606, A59
Neronov, A., Semikoz, D. V., Tinyakov, P. G., & Tkachev, I. I. 2011, A&A, 526, A90
Rybicki, G. B., & Lightman, A. P. 2004, Radiative Processes in Astrophysics (2nd ed.; Berlin: Wiley)
Takahashi, K., Murase, K., Ichiki, K., Inoue, S., & Nagataki, S. 2008, ApJL, 687, L5

Direct Determination of a Bare Neutron Counter Yield Function

J. W. Bieber[1], J. Clem[1], P. Evenson[1], A. Hallgren[2], J. Madsen[3], P.-S. Mangeard[1], W. Nuntiyakul[4,5], R. Pyle[6], D. Ruffolo[7], A. Sáiz[7], S. Tilav[1]

[1]Bartol Research Institute, Department of Physics and Astronomy, University of Delaware, Newark, DE 19716, USA
[2]Department of Physics and Astronomy, Uppsala University, Box 516, S-75120 Uppsala, Sweden
[3]Department of Physics, University of Wisconsin-River Falls, River Falls, WI 54022, USA
[4]Department of Physics and Materials Science, Faculty of Science, Chiang Mai University, Chiang Mai 50200, Thailand
[5]Research Center in Physics and Astronomy, Faculty of Science, Chiang Mai University, Chiang Mai 50200, Thailand
[6]Pyle Consulting Group, Inc., St. Charles, IL 60174, USA.
[7]Department of Physics, Faculty of Science, Mahidol University, Bangkok 10400, Thailand

Key Points:

- Bare neutron counters measured secondary cosmic rays from a ship over a wide range of magnetic latitudes.
- Simultaneous measurements of the primary cosmic ray spectrum by spacecraft allow a direct determination of the bare neutron counter yield function.
- Together with a neutron monitor, which has a different yield function, bare neutron counters can determine the cosmic ray spectral index.

Corresponding author: W. Nuntiyakul, waraporn.n@cmu.ac.th

Abstract

Ground based neutron counters are a standard tool for detecting atmospheric showers from GeV-range primary cosmic rays of either solar or galactic origin. Bare neutron counters, a type of lead-free neutron monitor, function much like standard neutron monitors but have different yield functions primarily because they are more sensitive to neutrons of low energy. When operated together with standard monitors the different yield functions allow estimates to be made of the energy spectrum of galactic or solar particles. In 2010 a new array of twelve bare neutron detectors was installed at the South Pole to operate together with the neutron monitor there. Prior to installation, two of the detectors were operated on a ship that traveled from Sweden to Antarctica and back from November 2009 to April 2010. The purpose of this latitude survey was to use Earth's magnetic field as a spectrometer, blocking cosmic rays below the local cutoff rigidity (momentum per unit charge), from which we determined the response function vs. rigidity of these bare counters. By comparing that measured response function to direct measurements of the cosmic ray spectrum taken by the PAMELA spacecraft, we were able to make a direct determination of the yield function for these detectors.

1 Introduction

Like a standard neutron monitor (NM64) [*Hatton & Carmichael*, 1964], a bare neutron detector provides a ground based measurement of the flux of cosmic ray particles in space by counting neutrons present in the atmospheric cascade of secondary particles produced by the primary cosmic rays. These neutrons are detected by induced nuclear fission of a gas, either ^{3}He or ^{10}B in boron-trifluoride ($^{10}BF_3$), inside a cylindrical proportional counter. Electrons released when the fission energy ionizes the gas inside the detector are accelerated by the high potential difference maintained between a central wire and the outer conducting surface of the detector. The resulting cascade produces a measurable pulse that is electronically counted. These counts are related to the flux of cosmic rays interacting with the Earth's atmosphere, but the relation is complex and depends on the spectrum and composition of the primary particles. Bare neutron detectors are sensitive to lower energy primary particles than an NM64 but are more sensitive to environmental effects. As there is no standard design for a bare neutron detector each installation must be analyzed and calibrated individually since the performance may vary with construction technique.

The relation between the primary flux and the detected particles is most fundamentally expressed by the yield function (YF), which is an energy dependent effective geometric factor. The differential response function (DRF) is the product of the yield function and the primary particle spectrum. The counting rate of the detector is the integral over rigidity of the DRF.

The DRF of a ground based detector can be measured by using the Earth's magnetic field as a magnet spectrometer. At any given location the magnetic field blocks cosmic rays below a certain cutoff rigidity (P_C), where rigidity is particle momentum per unit charge ($P = pc/q$). In a latitude survey the detector is transported through a range of magnetic latitude [*Nuntiyakul et al.*, 2014] so that the counting rate can be measured as a function of geomagnetic cutoff rigidity. At each location of the survey the cutoff can be calculated from geomagnetic field models. The cutoff is also a function of time because the geomagnetic field is variable, both intrinsically and in response to the influence of the sun on the magnetosphere. Comparing two points with closely spaced cutoffs, the difference in counting rate divided by the difference in cutoff rigidity is exactly the DRF.

The present work reports data from a ship-borne latitude survey using two bare neutron counters during 2009 – 2010. During the survey there were no GeV-range solar particle events so the bare counters detected showers exclusively from galactic cosmic rays. Previous latitude surveys with bare counters were conducted with a single bare counter

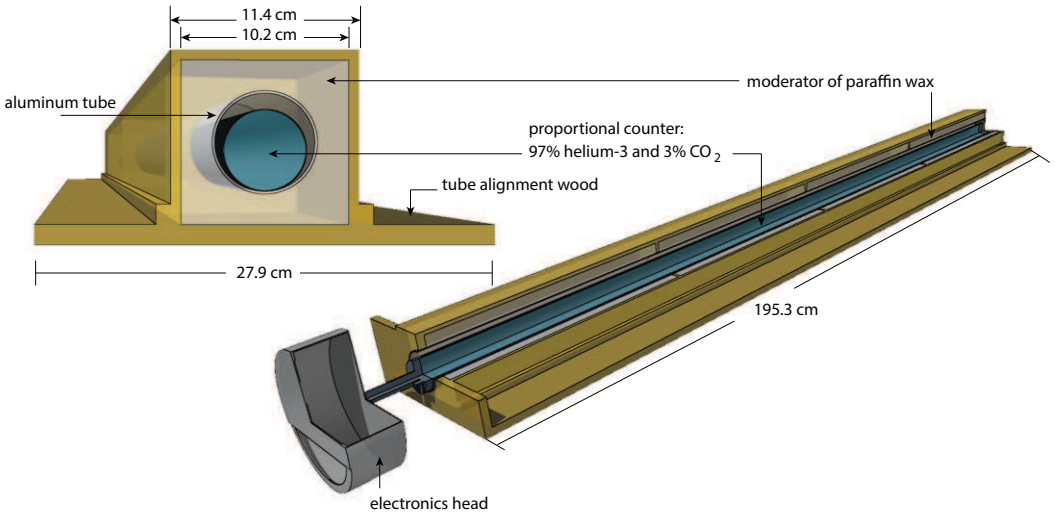


Figure 1. Rendering of an end view and cutaway oblique view of a bare neutron counter to detect cosmic ray showers. The present work analyzes data from two such bare neutron counters operated on a ship for a latitude survey in 2009 – 2010. Since 2010 the two counters have taken data at the South Pole.

in 1976 [*Potgeiter et al.*, 1980], three bare counters in 1995-6 [*Nuntiyakul et al.*, 2018], and two bare counters in 1996 [*Dorman et al.*, 2000]. Each survey used a different bare counter design. The resulting DRF were compared by *Nuntiyakul et al.* [2018].

At the United States Amundsen-Scott South Pole Station a standard three unit neutron monitor (3NM64)[*Hatton & Carmichael*, 1964], located on a platform outside the station, uses lead to convert relatively high energy neutrons (primarily 10 MeV to 1 GeV) to lower energy neutrons for detection by ^{3}He proportional counters. In past years BP-28 (BF_3) detectors were operated nearby as bare neutron counters. The YF of the bare neutron detectors and NM64 have a different energy dependence so the counting rate ratio changes in response to changes in the primary spectrum. In particular we have made extensive use of this to estimate the spectral index and intensity of solar energetic particles [*Bieber and Evenson*, 1991; *Bieber et al.*, 2002; *Ruffolo et al.*, 2006; *Bieber et al.*, 2013a]. In 2010 the BP28 counters were replaced by an array of twelve bare ^{3}He detectors of two different designs. Ten of the detectors have no moderator, whereas two of them have paraffin moderators. The two with moderators are the exact units carried on the icebreaker Oden from Sweden to Antarctica and back in 2009 – 2010. By comparing the DRF measured in this latitude survey with simultaneous measurements of the cosmic ray spectra outside the atmosphere we were able to produce a direct measurement of the YF of these detectors. To our knowledge this is the first report of a latitude survey of bare neutron counters that were also installed at a fixed station for long term measurements of cosmic rays, and also the first direct determination of a bare neutron counter yield function.

2 Observation

2.1 Instrumentation

The bare neutron detector design used in the latitude survey is shown in Figure 1. It consists of an LND25373 ^{3}He neutron counter [*Pyle et al.*, 1999] surrounded by a paraffin wax moderator inside a wooden box. The survey itself had the primary goal of calibrating an "IceTop Tank" [*Abbasi et al.*, 2013], i.e. an ice Cherenkov detector of cosmic ray showers for the IceTop surface component of the IceCube Neutrino Observatory at



Figure 2. Insulated shipping container containing two bare neutron counters on board the Swedish ice-breaker Oden.

the South Pole. In essence this is a 2000 kg block of clear ice. The results for the IceTop tank are still being analyzed and will be reported separately. The ice block was housed in a temperature-controlled freezer container with the two neutron detectors strapped on top. The container was then loaded onto the Oden as shown in Figure 2.

2.2 The 2009 – 2010 Latitude Survey

The geographic route of this survey is plotted in Figure 3 where we also show contours of effective vertical geomagnetic cutoff rigidity, the minimum rigidity that a particle needs to reach the top of the atmosphere from interplanetary space, calculated for April 8, 2010 at 12:00 UT. The survey began on 11 November of 2009 from Helsingborg, Sweden at a cutoff rigidity of 1.88 GV. There was an extensive port call in Uruguay at approximately 8.2 GV, after which the survey continued to McMurdo Station, Antarctica. Note that in Earth's polar regions the geomagnetic cutoff rigidity can be quite low, but the primary cosmic ray rigidity must exceed an atmospheric cutoff of approximately 1 GV for the atmospheric shower to generate counts in a ground level neutron detector. The return trip was via Punta Arenas at 5 GV, and Uruguay at 8.2 GV, and finally back to Sweden on 26 April 2010.

3 Data

Data were obtained with our standard acquisition system as used in previous surveys [*Nuntiyakul et al.*, 2014]. The counting rate of each detector was recorded once per second together with the attitude of the ship (pitch and roll). Once per minute the barometric pressure was recorded, as was the position of the ship derived from GPS data, which also provided absolute timing. Apparent geomagnetic cutoffs [*Lin et al.*, 1995; *Bieber et al.*, 1997; *Clem et al.*, 1997] were calculated at half hour intervals.

The overall data quality was quite good apart from one time period where the GPS system was unreliable. As noted below, some additional intervals were also excluded from the analysis. Systematic corrections were only applied for barometric pressure and short term solar modulation of the galactic cosmic ray flux. A summary of the data is presented in Figure 4, while the exclusions and corrections are discussed below.

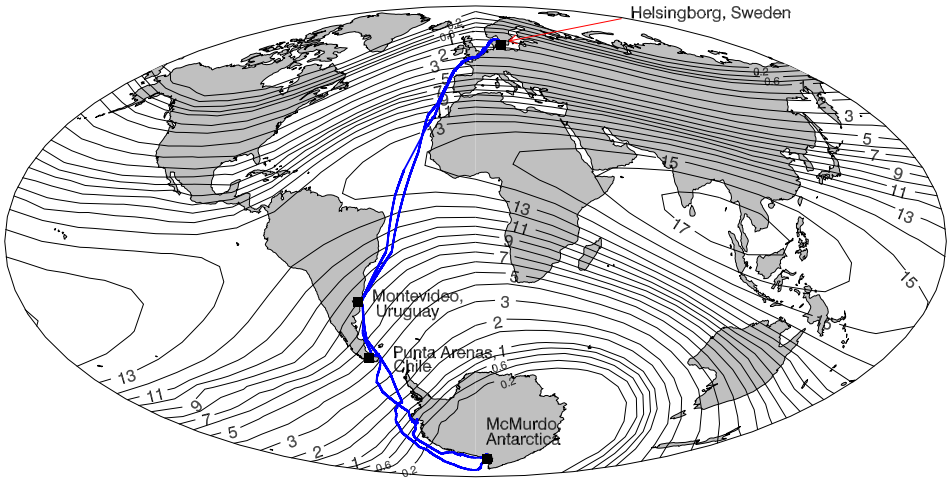


Figure 3. Route of the Oden for the 2009 – 2010 latitude survey, superimposed on contours of the 2010 effective vertical cutoff rigidity, calculated for April 08, 2010 at 12:00 UT. Numbers at each contour indicate the effective vertical cutoff rigidity in GV. This survey carried two bare neutron counters, permitting a direct determination of their yield function vs. rigidity.

3.1 Data Exclusions

As in our previous bare neutron detector survey [*Nuntiyakul et al.*, 2018] the detectors showed major increases in counting rate during port calls. We removed those time periods from our analysis and also removed time periods with a clear effect of proximity to land near Göteborg Sweden, in the estuary of the river Plate in Uruguay, and in the Magellan Strait. We also excluded all of the data in the vicinity of McMurdo Station. Exclusions for these geographic reasons are indicated in blue in Figure 4. Although we could detect no overall dependence of the counting rate on the attitude of the ship, there were indications of excess fluctuations related to high seas during some storm periods. We therefore excluded data when the standard deviation of the roll and/or pitch angles exceeded some (rather arbitrary) limits, shown in red in Figure 4. Also shown in red are a few points excluded due to obviously wrong counting rates or bad pressure measurements.

A major Forbush decrease due to a solar storm occurred during the northbound period. In terms of the fractional day of the year 2009 (DOY), we removed the data from DOY = 460.433 to DOY = 465.641 from our analysis to exclude the time period when the spectrum of cosmic rays at the top of the atmosphere was affected by this solar storm, including the recovery period. Data excluded for this reason are shown in orange in Figure 4(b).

3.2 Barometric Pressure Correction

A neutron monitor is extremely sensitive to barometric pressure. In fact it might be said that it is primarily a barometer that is somewhat influenced by cosmic ray variations. In any event, to study cosmic rays major corrections for barometric pressure are necessary. For a stationary installation a simple phenomenological solution is to make a long term scatter plot of changes in count rate vs local barometric pressure. Since these processes are fundamentally uncorrelated, a long enough time series yields a rather accurate correction that can be applied to that installation. It is a feature of the neutron monitor that the simple air mass, measured by barometric pressure, determines nearly all of the variation in response. There are some clear exceptions, one of which is the noticeable dependence

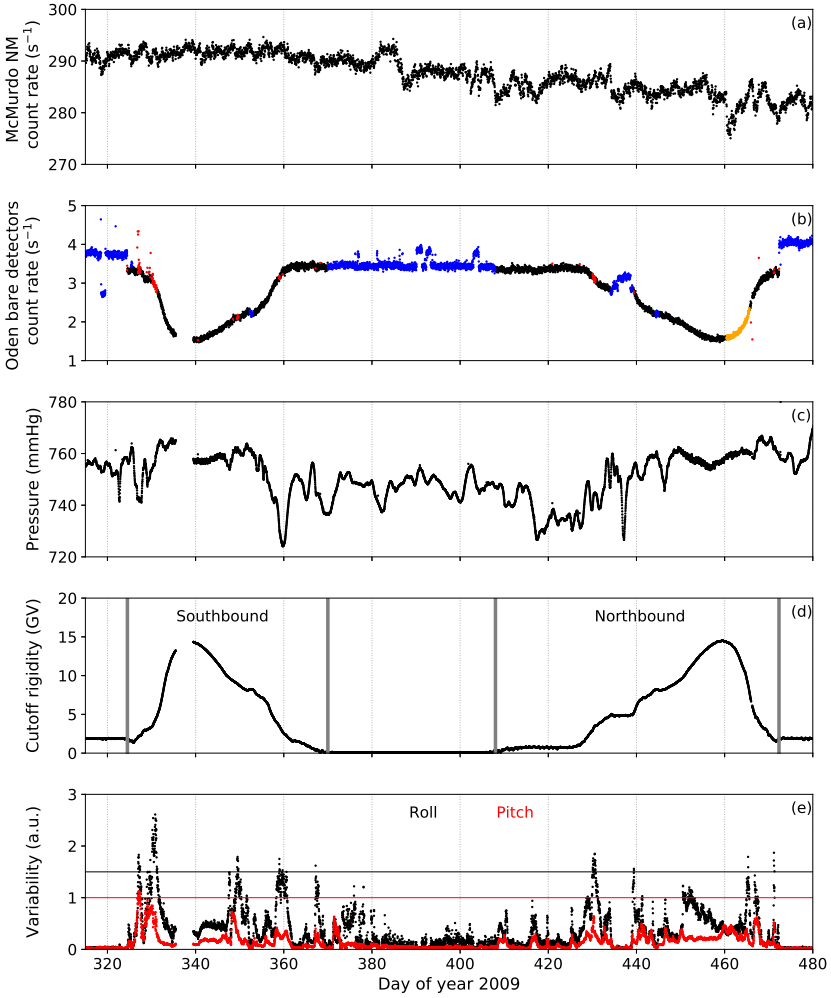


Figure 4. Data set used in this analysis. (a) Pressure corrected count rate of the 18NM64 McMurdo neutron monitor. (b) Pressure corrected count rate of the two bare neutron counters on board the Oden. Black points were accepted as valid data while points of other colors were excluded as discussed in the text. (c) Atmospheric pressure at the Oden in mmHg. (d) Apparent cutoff rigidity at the Oden in GV; vertical lines define the Southbound and Northbound intervals. (e) Standard deviation of Oden roll (black) and pitch(red) angles (arbitrary units). Horizontal lines show the applied cuts for rejecting time periods of strong pitch or roll.

on atmospheric water vapor exhibited by the Princess Sirindhorn Neutron Monitor at Doi Inthanon, Thailand [*Ruffolo et al.*, 2016; *Mangeard et al.*, 2018]. Dependence on overall atmospheric structure has also been demonstrated in simulations [*Mangeard et al.*, 2016].

Along with purely local effects due to the surroundings and station construction there is a systematic variation of the barometer correction with geomagnetic cutoff since the spectrum of particles hitting the atmosphere varies systematically with cutoff. For a fixed station this is automatically included in the empirically derived coefficient, while the implicit time dependence due to modulation differences in the spectrum is generally ignored.

For a latitude survey there is an additional problem of principle with the barometer correction because there is a general correlation of atmospheric properties with geomagnetic cutoff. The average atmospheric pressure is approximately 20 mmHg lower in Arctic and Antarctic regions than it is at the equator, and there are structural differences in the atmosphere as well. A basic assumption that we adopt in our analysis is that the same coefficient that removes fluctuations in the data also serves to correct the observed counting rate to "sea level", i.e. an atmospheric pressure of 760 mmHg.

For a typical latitude survey the detector does not spend long enough at each value of the cutoff (even when grouped into, for example, 2 GV bins) to determine a pressure coefficient by the phenomenological method. By using 14 surveys with substantially equivalent instruments *Nuntiyakul et al.* [2014] were able to establish (for an NM64) the pressure coefficient, β

$$\beta = 1.006 \times 10^{-2} - 1.53 \times 10^{-4} P_c \tag{1}$$

such that

$$C_p = C e^{\beta(p - p_{\rm ref})} \tag{2}$$

where C_p is the pressure corrected counting rate, C is the uncorrected counting rate, and p is the barometric pressure in units of mmHg, and $p_{\rm ref}$ = 760 mmHg.

Nuntiyakul et al. [2018] showed that for fixed stations the coefficient for bare neutron detectors and neutron monitors is typically slightly different but did not find a consistent pattern as a function of cutoff. Attempts to derive a bare neutron detector coefficient for the single survey produced results that, within large statistical errors, were indistinguishable from the NM64 result. That was also the case for for our analysis of the current survey. Therefore we again simply applied the NM64 barometer correction, Eq. (1), to the bare neutron detector count rate.

3.3 Short Term Modulation

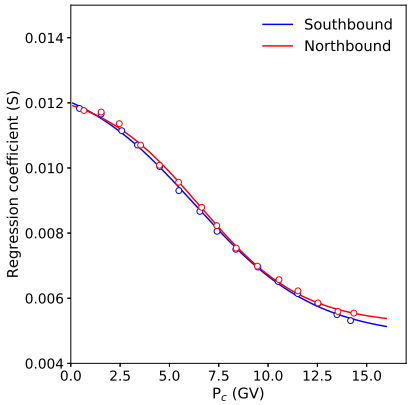
The McMurdo monitor count rate in Figure 4(a) indicates time variations in the galactic cosmic ray flux due to solar activity, known as solar modulation. Even a cursory examination reveals that the overall level of solar modulation is quite different near the early "southbound" and the late"northbound" portions of the survey. We consider this difference quite an important one to preserve in the analysis, and indeed think that a self consistent handling of this difference strengthens our determination of the yield function.

However there is also considerable variation within each interval. Since our ultimate comparison is with long term (monthly) averages of spacecraft data we developed a correction for this variation. Although the method of correction is the same for the two intervals, the parameters are determined independently for each because the cosmic ray spectrum changed. Our correction for short-term variations in modulation level is based on variations in the McMurdo counting rate. There are two steps to this analysis.

First, following the methods of *Nuntiyakul et al.* [2014], we determined regression coefficients (S) between the bare neutron detector counting rate corrected for pressure for each rigidity bin, i.e., 0–1 GV, 1–2 GV, ..., and 13–14 GV and the McMurdo count rate

228 **Table 1.** Derived Parameters for Survey Intervals

Parameter	Southbound	Northbound
S_0	0.0130(2)	0.0125(1)
S_1	0.0048(1)	0.0005(10)
S_2	7(1)	12(2)
S_3	0.33(2)	0.38(2)
$\overline{m}$ (s^{-1})	291.4	284.8
N_0 (s^{-1})	3.416 (3)	3.348(2)
α	8.39(9)	8.51(6)
κ	0.991(4)	0.987(3)



229 **Figure 5.** Regression coefficients for short term modulation as a function of cutoff rigidity.

217 corrected for pressure, C_P. The relationship between S and P_c is plotted in Figure 5. Sec-
218 ond, we found that the following function, with the parameters S_i given in Table 1, pro-
219 vides a reasonably good fit to the data:

220 $$S(P_c) = S_0 + \frac{S_1 - S_0}{1 + S_2 e^{-S_3 P_c}} \tag{3}$$

221 We then used S calculated by equation 3 as a function of P_c to correct the counting rate
222 to the average McMurdo value for each part of the survey separately:

223 $$C_{ps} = C_p - S(P_c)(m - \overline{m}) \tag{4}$$

224 where C_{ps} is the normalized Oden neutron monitor counting rate corrected for pressure
225 and short-term GCR variation, m is the McMurdo counting rate, and $\overline{m}$ is the average Mc-
226 Murdo counting rate for the specific interval of the survey. C_{ps} was used to determine the
227 response function.

230 4 Bare Neutron Detector Yield Function

231 4.1 Latitude Survey Response Functions

232 Solar modulation conditions were quite different for the southbound and northbound
233 intervals of the latitude survey. The southbound interval was largely during the record cos-
234 mic ray maximum of late 2009. Indeed, this time period witnessed the highest GCR flux
235 in the over 60 years since continuous NM measurements have been available [*McDonald*

et al., 2010; *Mewaldt et al.*, 2010; *Oh et al.*, 2013]. The northbound interval followed a very fast decrease of the count rate in early 2010. Therefore we continue to separate the analysis of these two intervals and use the standard technique of fitting C_{ps} (the pressure and short term variation corrected count rate) as a function of rigidity cutoff using the Dorman function [*Dorman et al.*, 1969]

$$N(P_c) = N_0(1 - e^{-\alpha P_c^{-\kappa}}). \tag{5}$$

The DRF is defined as

$$N(P_c) = \int_{P_c}^{\infty} DRF(P)dP, \tag{6}$$

which can be analytically obtained as the derivative of the Dorman function with respect to cutoff rigidity:

$$DRF(P) = N_0\alpha\kappa P^{-\kappa-1}e^{-\alpha P^{-\kappa}}. \tag{7}$$

Figure 6 shows the Dorman function fit to each interval separately along with the corresponding DRF. Parameters of the fit are included in Table 1. In performing these fits we excluded all data from geomagnetic cutoffs below 0.5 GV. This is because the actual cutoff there is entirely atmospheric. Hence the data below 0.5 GV do not provide additional useful information and the distinct polar atmospheric conditions may affect the fitting. Eliminating these data is in and of itself not a problem since the Dormmn function has zero slope as the cutoff approaches zero. When the Dorman functions and DRF for southbound and northbound intervals are plotted together in Figure 7 the modulation difference is clearly apparent.

4.2 Direct Determination of Yield Functions

Conceptually the yield function of the neutron detectors is simply the ratio of the DRF to the particle spectrum at the top of the atmosphere. A complication is that each particle species has its own yield function and spectra of different elements have different rigidity dependence. We approximate the multiple ion species actually present by assuming that there are only protons and helium-4 nuclei (alpha particles), since the spectra of the heavier elements tend to resemble the alpha spectrum but at significantly lower intensity, and multiply the alpha spectrum by a scale factor F_{hn} to account for heavier elements.

To evaluate the yield function several assumptions are made. First, we use the Local Interstellar Spectrum (LIS) derived from spacecraft and balloon data [*Ghelfi et al.*, 2016, 2017a]. A force-field approximation [*Gleeson and Axford*, 1968] of the solar modulation was applied to the LIS using the solar modulation parameter Φ determined by *Ghelfi et al.* [2017b] for the time of interest. Then, we assume a ratio between the yield functions of protons and alphas, $F_Y(R)$, similar to that for a standard NM64 as proposed by *Caballero-Lopez & Moraal* [2012]. Finally, we include the contribution of heavy nuclei by a multiplicative scale factor, F_{hn}, to the alpha particle yield function. We consider two published estimates of this scale factor. One is $F_{hn,C} = 1.584$ from *Caballero-Lopez & Moraal* [2012], to be consistent with their calculation of F_Y, and the second is $F_{hn,G} = 1.445$ from *Ghelfi et al.* [2017b] to be consistent with their calculation of Φ. The yield function of the bare counters to protons is calculated as:

$$Y_p(P) = \frac{DRF(P)}{J_p(P,\Phi) + F_{hn}F_Y(P)J_\alpha(P,\Phi)}, \tag{8}$$

where $J_p(P,\Phi)$ and $J_\alpha(P,\Phi)$ are the spectra of protons and alphas at the top of the atmosphere, respectively. The yield function to the alphas is then determined as:

$$Y_\alpha(P) = F_Y(P)Y_p(P) \tag{9}$$

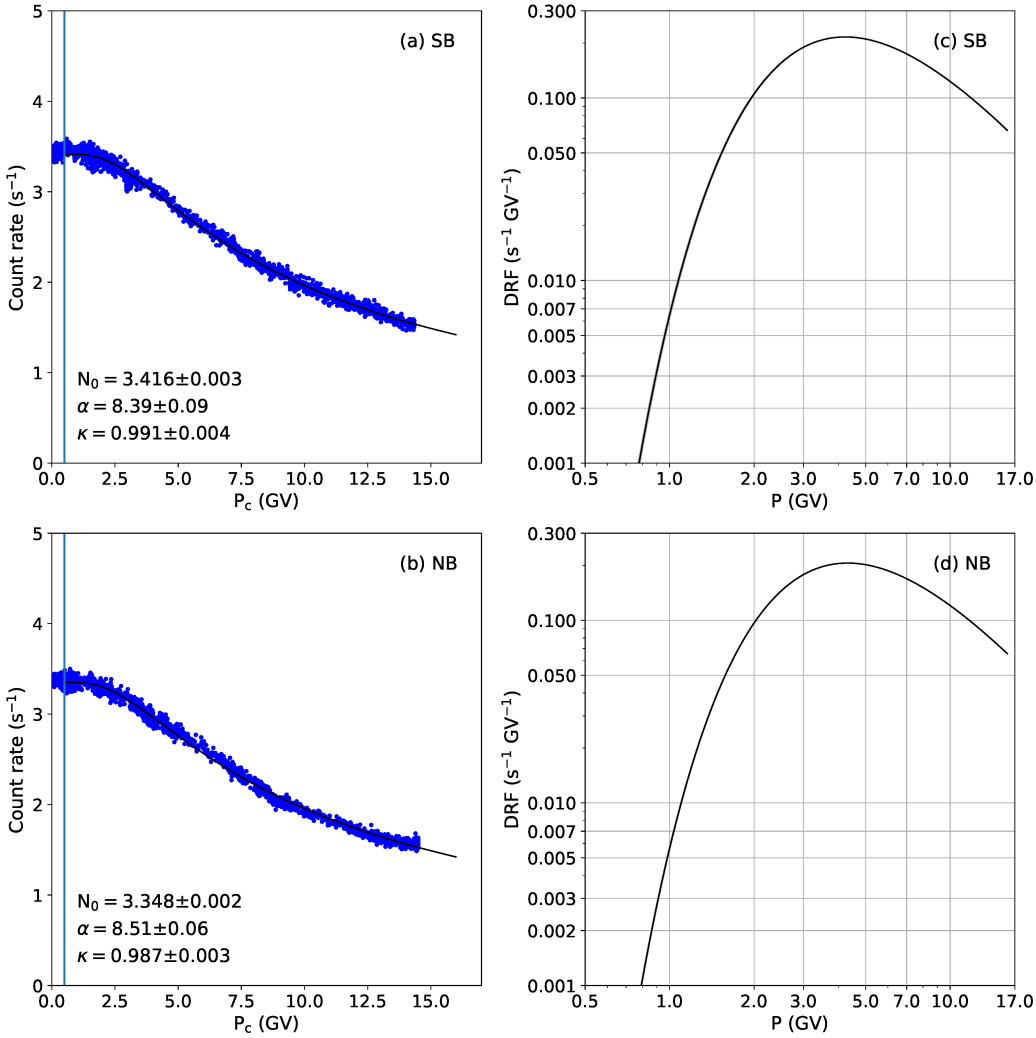


Figure 6. Separate Dorman function fits to (a) southbound (SB) and (b) northbound (NB) bare neutron detector count rates. (c) and (d) show the resulting differential response functions (DRF). The vertical line shows the lower cutoff limit used during the fitting procedure.

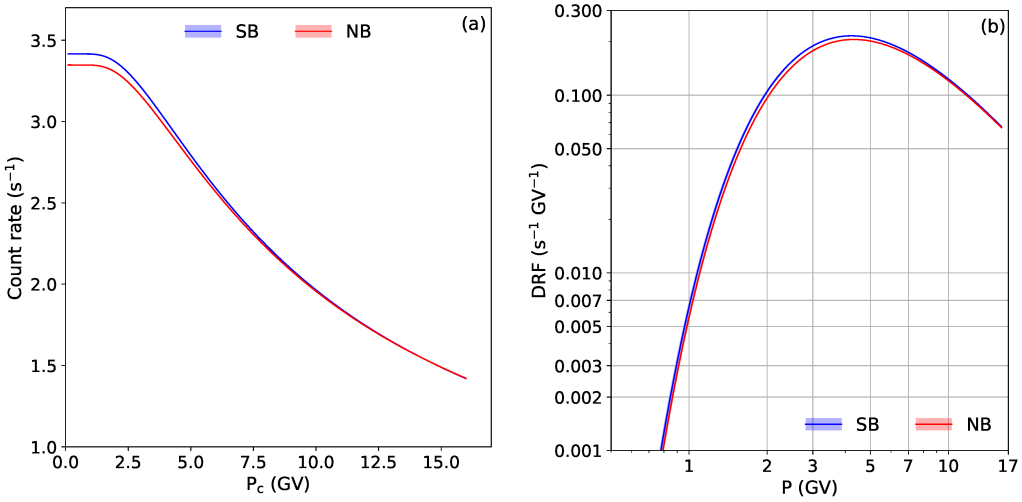


Figure 7. Comparison of (a) the Dorman functions and (b) the differential response functions for Southbound and Northbound survey intervals.

The two legs of the latitude survey of 2009 present distinguishable solar modulation conditions and provide two estimates of the yield functions. For the southbound interval, we use the solar modulation parameter determined using the time dependent PAMELA spectrum [*Ghelfi et al.*, 2017b] [and references therein]. The average modulation parameter estimated from the PAMELA monthly spectra from November and December 2009 is $\Phi_{PAM,SB} = 414 \pm 30$ MV (private communication with authors of *Ghelfi et al.* [2017b]). To the best of the authors' knowledge, time dependent spectra from PAMELA have not been published for the northbound interval. Therefore we use the time dependent solar modulation parameter calculated from the McMurdo neutron monitor counting rate [*Ghelfi et al.*, 2017b; *Maurin et al.*, 2014]. During the northbound interval the average value was $\Phi_{McM,NB} = 484$ MV with a standard deviation of 19 MV. (Data were extracted from the database located at `http://lpsc.in2p3.fr/crdb/`). As a consistency check, during the Southbound interval, the average hourly solar modulation parameter was $\Phi_{McM,SB} = 422$ MV with a standard deviation of 8 MV, in agreement with $\Phi_{PAM,SB} = 414 \pm 30$. The standard deviations of the solar modulation parameters are used to estimate the uncertainties of the average fluxes for each interval, which are plotted in Figure 8.

With this set of assumptions, and using $F_{hn,G}$, the yield functions were calculated numerically and are presented in Figure 9(a). There is a very good agreement between the yield functions calculated for the two periods, with a ratio compatible with 1 within the uncertainty (bands in Figure 9(b) represent 1σ statistical uncertainty). Changing F_{hn} to $F_{hn,C}$ would induce a systematic change of about 3% to the yield functions. Figure 10 compares the yield function derived in this work to the yield function that was derived by *Bieber and Evenson* [1991] for the bare neutron detectors with standard NM64 moderators that were used at the South Pole from 1987 to 2005. The ratio of percent increases of the bare counters to the neutron monitor was used to determine the spectral index of relativistic solar ions [*Bieber et al.*, 2002; *Ruffolo et al.*, 2006; *Bieber et al.*, 2013a]. *Bieber and Evenson* [1991] derived yield functions from a fit to the proton spectrum and the response functions proposed by *Stoker* [1985]. Use of the "Stoker B" yield function produced better consistency with particle spectra determined using observations of the same event from different geomagnetic cutoffs. To be consistent in the comparison we have constructed the yield function displayed in the figure from only the proton spectrum in our analysis. It is therefore somewhat different from the proton yield function displayed in Figure 9(a). The

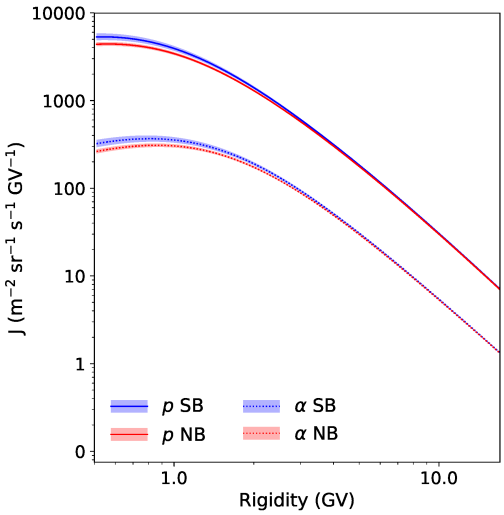


Figure 8. Average fluxes for protons and alpha particles at the top of the atmosphere during the two intervals of the latitude survey as inferred from PAMELA data.

Bieber and Evenson [1991] yield functions are normalized to our determination at 17 GV. There is a general similarity of the new determination to the previous ones, but they are clearly different. At the present we cannot draw any conclusions as to the cause of the difference, since the detectors, moderators, modulation level and assumptions about the primary cosmic ray spectrum are all different.

4.3 Bare Neutron Detectors at South Pole

In order to better use that technique to measure the spectral index of relativistic solar ions it was our original intent to upgrade the array of bare neutron detectors at the South Pole to achieve a statistical precision approximately equal to that of the 3NM64 (which typically records $\approx$ 300 counts per second). Based on our prior experience with BP-28 detectors this would require installing approximately twelve units, mounted outside the station. To minimize the problems of shipping hazardous materials we decided to use LND25373 ^{3}He detectors similar to those in the 3NM64 operated at the station. We also chose to use compact moderators to minimize the size of an insulated enclosure required to operate outside the station. We took the opportunity to carry two detectors with compact monitors on the Oden voyage to determine their yield functions as described in this paper. To our surprise, tests revealed that the compact moderators increased the counting rates only slightly, and there was little difference operating inside or outside the station. As a result we decided not to proceed with an outside insulated enclosure and to instead operate with the array of ten unmoderated and two moderated detectors indoors as shown in Figure 11.

At present we are working on simulations to try to understand why the moderator increased the count rate only slightly. We include a discussion of the tests we conducted of various options. The test results are summarized in Table 2. In all cases the counting rates are expressed as counts per second per detector. The high rate at South Pole is mostly due to the high altitude. The rates presented are not corrected for barometric pressure or modulation level; the dates when the data were taken are recorded for possible interpretation in that context.

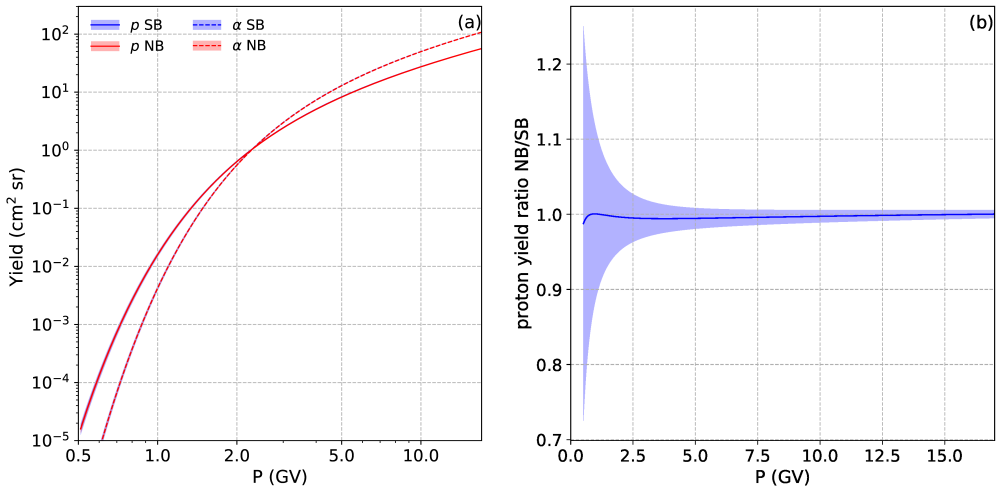


Figure 9. (a) Yield functions of the two bare neutron counters for protons and alphas derived from the 2009 – 2010 latitude survey and particle spectra at the top of the atmosphere as described in the text. (b) Ratio of the southbound to the northbound proton yield functions. We use $F_{hn,G}$ as the scaling factor from *Ghelfi et al.* [2017b].

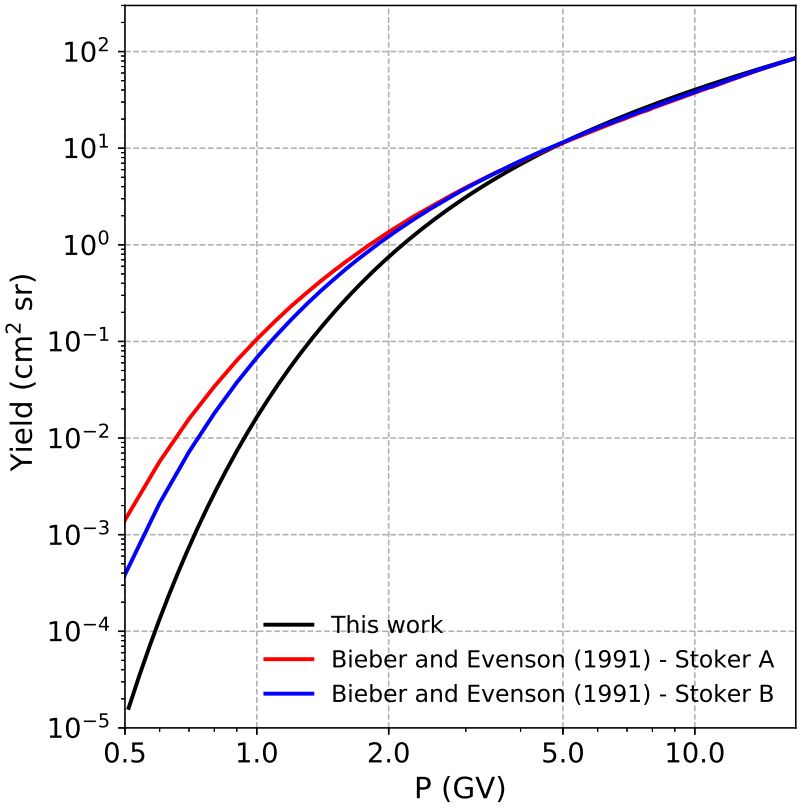


Figure 10. Yield functions from this work compared to the determination of *Bieber and Evenson* [1991], with arbitrary normalization.

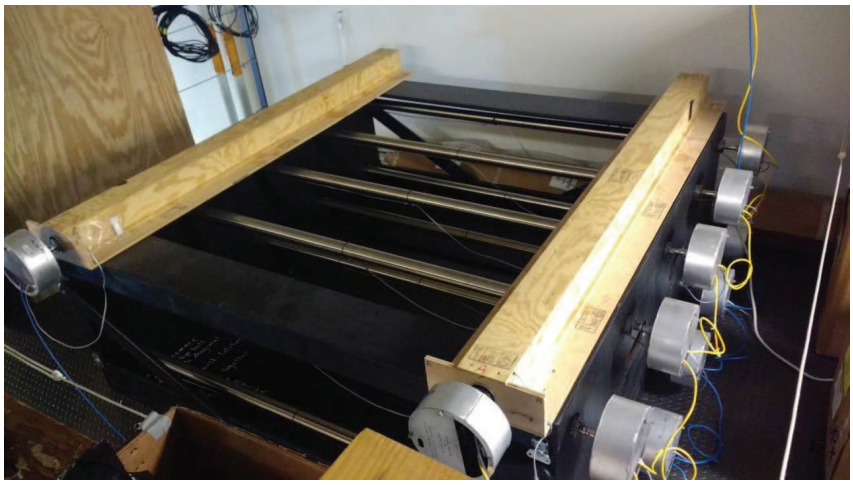


Figure 11. Bare neutron detector array at South Pole. Ten unmoderated detectors are mounted in a stacked array with the two moderated detectors on top.

Table 2. Bare ^{3}He Neutron Detector Tests

Location	Moderator	Rate	Date
	South Pole, Antarctica		
B2	None	13.492(4)	2012
B2	Paraffin	14.862(5)	2012
B2	Donut	13.82(2)	2010-01-23
Snow	Donut	12.88(9)	2010-01-26
	University of Delaware, USA		
Patio	None	1.487(4)	2010-08-26
Patio	Paraffin	1.727(5)	2010-08-27
Patio	Donut	1.448(4)	2010-08-27
Patio	Standard	2.585(5)	2010-08-30
Shop	None	0.844(1)	2010-08-31
Shop	Paraffin	0.889(1)	2010-08-27
Shop	Donut	1.111(1)	2010-08-27
Shop	Standard	1.257(1)	2010-08-31

These tests were conducted in different locations and configurations. Location "B2" is the primary science staging area inside the Amundsen-Scott station at the South Pole. "Snow" refers to a location outside the station approximately 100 meters from the nearest structure with the detectors resting on the snow surface. "Patio" is a paved outdoor area adjacent to Sharp Laboratory on the University of Delaware Campus, while "Shop" is inside the electronics shop in Sharp Laboratory – located in the basement, largely under the "Patio".

The "B2" and "Snow" tests were conducted using the detectors that are now installed in the South Pole NM64 [*Evenson et al.*, 2011; *Bieber et al.*, 2013b]. The tests in Delaware used the detectors carried on the Oden. Tests were made exchanging detectors and moderators, but differences were minimal so only representative results are included in the table.

In Table 2 "Paraffin" refers to containment in the moderators carried on the Oden. No significant difference was seen between the two moderators. "None" refers to no moderator at all. "Standard" refers to the moderator used in a standard NM64 neutron monitor. It is a polyethylene cylinder with an inner diameter of 20.5 cm, an outer diameter of 24.5 cm, and a length of 2.27 m. "Donuts" are annular polyethylene supports used to mount LND25373 detectors, which have an outer diameter of only 6cm, in NM64 moderators. Tests were also made with the detector supported by the donuts but otherwise bare. The "None" and "Paraffin" values for B2 are long term averages over the year 2012 when mounted in the array as shown in Figure 11.

In addition to having similar counting rates, the moderated and unmoderated detectors at South Pole demonstrably have similar yield functions. Only one relativistic solar particle event, or Ground Level Enhancement (GLE) of significant size has been observed since the installation of the current bare neutron detector array, that of May 17, 2012. The responses of the 3NM64, bare detectors and IceTop tanks at the South Pole were clearly different and allowed a determination of the spectrum of the solar energetic particles responsible for the enhancement [*IceCube Collaboration*, 2013]. However no significant difference in the response of the moderated and unmoderated bare detectors was noted. This is illustrated in Figure 12. The regression of variations in panel (a) (caused by modulation and barometric pressure variations) is nearly identical to that in panel (b) (caused by the solar particle enhancement) even though those variations involve very different primary particle spectra. Therefore the yield function derived in the present work can be applied (with at most a multiplicative factor) to all the bare counters presently at South Pole. In further work we plan to use the measured yield function to "calibrate" the bare counter to NM count rate ratio in terms of the spectral index for relativistic solar particles.

5 Conclusions

We performed a latitude survey of two bare neutron counters with compact paraffin moderators that detected atmospheric showers from galactic cosmic rays on board the Swedish icebreaker Oden during 2009 – 2010. By taking such measurements as the ship traversed a wide range of magnetic latitudes, we were able to measure the response function of the bare detectors for the distinct conditions of solar modulation (i.e., effects of solar activity on the galactic cosmic ray flux) during the southbound interval (mostly late 2009) and the northbound interval (early 2010). Combining these measurements with cosmic ray spectra inferred from the PAMELA spacecraft, we derived two estimates of the yield function that are in very good agreement, marking the first direct determination of the yield function of bare neutron detectors. Those two detectors were later installed as part of an array of 12 bare detectors at the South Pole, where a NM (with a distinct yield function) is also operated, so this determination of the bare detector yield function will improve the quality of future determinations of the spectral index of relativistic solar par-

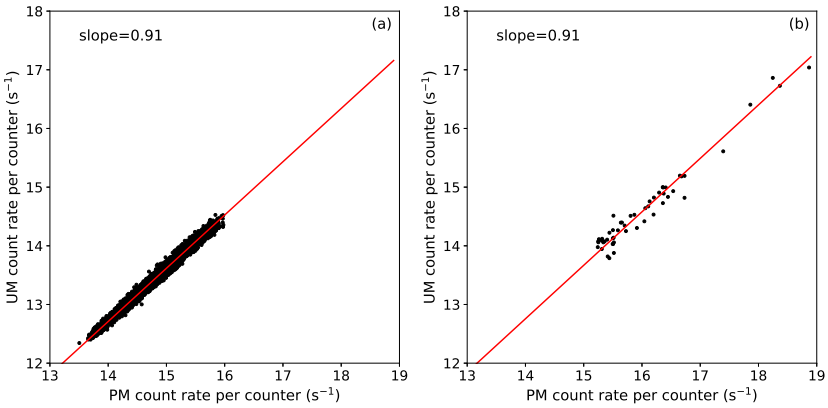


Figure 12. Count rates of the 10 unmoderated (UM) neutron detectors at South Pole as a function of the count rate of the two paraffin moderated (PM) neutron detectors for (a) Galactic cosmic rays throughout the year 2012, and (b) Ground Level Enhancement 71 due to solar particles on May 17, 2012.

ticles based on measurements of the bare detector to NM count rate ratio during ground level enhancements detected at the South Pole.

Acknowledgments

Support from the Swedish Polar Research Secretariat for the opportunity to use the ice-breaker Oden and special funding from the Swedish Research Council for associated costs (Project Oden Southern Ocean 2009 – 2011) is gratefully acknowledged. The research was also supported in part by Thailand Research Fund Grant RTA5980003 and Research Grant for New Scholar MRG6280155 and United States National Science Foundation Award OPP0838838. We also thank Leonard Shulman, James Roth and Jessica Sun for their technical assistance in preparing the equipment and David Maurin for providing monthly solar modulation derived from monthly measurements of PAMELA. Several U.S. and Swedish students worked on the project. The first students aboard the Oden were Matthias Danninger, a PhD student from Stockholm University, and University of Wisconsin River Falls (UWRF) physics major Drew Anderson, who traveled from Sweden to Uruguay. In Uruguay, Samantha Jakel, University of Wisconsin Rock County, and Henric Taavola, Uppsala University, boarded the Oden to complete the trip to Antarctica. Kyle Jero, a UWRF Physics major, took the last leg from Antarctica to Chile along with Matthias Danninger who continued on board through the return to Sweden.

References

Abbasi, R., Y. Abdou, M. Ackermann et al. (2013). IceTop: The surface component of IceCube, *Nuclear Instruments and Methodsin Physics Research A*, vol. 700, pp. 188–220.

Bieber, J. W., J. Clem, & P. Evenson (1997). Efficient computation of apparent cutoffs,in *Proceedings of the 12th International Cosmic Ray Conference*, vol. 2, pp. 389–392.

Bieber, J. W., & P. Evenson (1991), Determination of energy spectra for the large solar particle events of 1989, in *Proceedings of the 22nd International Cosmic Ray Conference*, vol. 3, pp. 129–132.

Bieber, J. W., Dröge, W., Evenson, P., Pyle, R., Ruffolo, D., Pinsook, U., et al. (2002). Energetic particle observations during the 2000 July 14 solar event. *Astrophysical Journal*, 567, 622–634. https://doi.org/10.1086/338246

Bieber, J.W., J.Clem, P.Evenson, R.Pyle, A.Sáiz, & D.Ruffolo (2013), Giant ground level enhancement of relativistic solar protons on 2005 January 20. I. Spaceship Earth observations, *The Astrophysical Journal*, 771, 92 (13pp). https://doi.org/10.1088/0004-637X/771/2/92

Bieber, J., J. Clem, P. Evenson, S. Oh, & R. Pyle (2013), Continued decline of South Pole neutron monitor counting rate, *Journal of Geophysical Research: Space Physics*, 118. https://doi.org/10.1002/2013JA018915

Caballero-Lopez, R. A., & H. Moraal (2012), Cosmic-ray yield and response functions in the atmosphere, *Journal of Geophysical Research*, 117, A12103. https://doi.org/10.1029/2012JA011794

Clem, J. M., Bieber, J. W., Evenson, P., Hall, D., Humble, J. E., & Duldig, M. (1997), Contribution of obliquely incident particles to neutron monitor counting rate. *Journal of Geophysical Research*, 102, 26, 919–26, 926. https://doi.org/10.1029/97JA02366)

Dorman, L. I., Fedchenko, S. G., Granitsky, L. V., & Rishe, G. A. (1969). Coupling and barometer coefficients for measurements of cosmic ray variations at altitudes of 260 – 400 mb. In *Proceedings of the 11th International Conference on Cosmic Rays*, Vol. 2, pp. 233 – 236. Budapest.

Dorman, L. I., Villoresi, G., Iucci, N., Parisi, M., Tyasto, M. I., Danilova, O. A., & Ptitsyna, N. G. (2000). Cosmic ray survey to Antarctica and coupling functions for neutron component near solar minimum (1996 – 1997): 3. Geomagnetic effects and coupling functions. *Journal of Geophysical Research: Space Physics*, 105, 21,047 – 21,056. https://doi.org/10.1029/2000JA900051

Evenson P., J. Bieber, J. Clem & R.Pyle (2011), South Pole Neutron Monitor Lives Again, *Proceedings of the 32nd International Conference on Cosmic Rays*, 11, 459 – 462. https://doi.org/10.7529/ICRC2011/V11/0622

Ghelfi, A., Barao, F., Derome, L., & Maurin, D. (2016), Non-parametric determination of H and He interstellar fluxes from cosmic-ray data, *Astron. Astrophys.*, 591, A94. https://doi.org/10.1051/0004-6361/201527852.

Ghelfi, A., Barao, F., Derome, L., & Maurin, D. (2017a), Erratum: Non-parametric determination of H and He interstellar fluxes from cosmic-ray data, *Astron. Astrophys.*, 605, C2. https://doi.org/10.1051/0004-6361/201527852e

Ghelfi, A., Maurin, D., Cheminet, A., Derome, L., Hubert, G., & Melot, F. (2017b), Neutron monitors and muon detectors for solar modulation studies: 2. ϕ time series, *Advances in Space Research*, 60, 833-847. https://doi.org/10.1016/j.asr.2016.06.027

Gleeson, L. J., & W. I. Axford (1968), solar modulation of galactic cosmic rays, *Astrophysical Journal*, 154, 1011-1026.

Hatton, C.J. & H. Carmichael (1964), Experimental investigation of the NM-64 Neutron Monitor, *Canadian Journal of Physics*, 42, 2443-2472.

IceCube Collaboration, M.G. Aartsen, R. Abbasi, Y. Abdou, M. Ackermann, J. Adams, et al. (2013), Ground level enhancement of May 17, 2012 observed at South Pole, *Proceedings of the 33rd International Conference on Cosmic Rays*, paper 0368, [arXiv:1309.7006v2, astro-ph.HE].

Lin, Z., Bieber, J. W., & Evenson, P. (1995), Electron trajectories in a model magnetosphere: Simulation and observation under active conditions. *Journal of Geophysical Research*, 100, 23543–23550. https://doi.org/10.1029/95JA02696

Mangeard, P.-S., D. Ruffolo, A. Sáiz, W. Nuntiyakul, J. W. Bieber, J. Clem, P. Evenson, R. Pyle, M. L. Duldig, & J. E. Humble (2016), Dependence of the neutron monitor count rate and time delay distribution on the rigidity spectrum of primary cosmic rays, *Journal of Geophysical Research: Space Physics*, 121, 11, 620–11, 636. https://doi.org/10.1002/2016JA023515

Mangeard, P.-S., J. Clem, P. Evenson, R. Pyle, W. Mitthumsiri, D. Ruffolo, A. Sáiz, & T. Nutaro (2018), Distinct Pattern of Solar Modulation of galactic Cosmic Rays above a High Geomagnetic Cutoff Rigidity *Astrophysical Journal*, 858:43 (12pp). https://doi.org/10.3847/1538-4357/aabd3c

Maurin, D. , F. Melot, & R. Taillet (2014) A database of charged cosmic rays, *Astronomy & Astrophysics*, 569, A32. https://doi.org/10.1051/0004-6361/201321344

McDonald, Frank B., William R. Webber, & Donald V. Reames (2010), Unusual time histories of galactic and anomalous cosmic rays at 1 AU over the deep solar minimum of cycle 23/24, *Geophysical Research Letters*, 37, L18101. https://doi.org/10.1029/2010GL044218

Mewaldt, R.A., A.J. Davis, K.A. Lave, R.A. Leske, E.C. Stone, M.E. Wiedenbeck, W.R. Binns, E.R. Christian, A.C. Cummings, G.A. de Nolfo, M.H. Israel, A.W. Labrador, & T.T. von Rosenvinge (2010),Record-setting cosmic-ray intensities in 2009 and 2010, *Astrophysical Journal Letters*, 723:L1-L6. https://doi.org/10.1088/2041-8205/723/1/L1

Nuntiyakul, W., P. Evenson, D. Ruffolo, A. Sáiz, J. W. Bieber, J. Clem, et al. (2014), Latitude survey investigation of galactic cosmic ray solar modulation during 1994–2007, *Astrophysical Journal*, *795*, 11. https://doi.org/10.1088/0004-637X/795/1/11

Nuntiyakul, W., Sáiz, A., Ruffolo, D., Mangeard, P.-S., Evenson, P., Bieber, J. W., et al. (2018), Bare neutron counter and neutron monitor response to cosmic rays during a 1995 latitude survey, *Journal of Geophysical Research: Space Physics*, 123, 7181–7195. https://doi.org/10.1029/2017JA025135

Oh, S., J. W. Bieber, P. Evenson, J. Clem, Y. Yi, & Y. Kim (2013), Record neutron monitor counting ratesfrom galactic cosmic rays, *Journal of Geophysical Research: Space Physics*, 118, 5431-5436. https://doi.org/10.1002/jgra.50544

Potgieter, M. S., Raubenheimer, B. C., Stoker, P. H., & van der Walt, A. J. (1980). Modulation of cosmic rays during solar minimum. Part 2. Cosmic ray latitude distribution at sea-level during 1976. *South African Journal of Physics*, 3(3–4), 77–89.

Pyle, R., P. Evenson, J.W. Bieber, J.M. Clem, J.E. Humble, & M.L. Duldig (1999), The use of ^{3}He Tubes in a Neutron Monitor Latitude Survey, in *Proc. 26th Int. Cosmic Ray Conf.*, SH 3.6.26, ADS: 1999ICRC....7..386P

Ruffolo, D., Tooprakai, P., Rujiwarodom, M., Khumlumlert, T., Wechakama, M., Bieber, J. W., et al. (2006). Relativistic solar protons on 1989 October 22: Injection and transport along both legs of a closed interplanetary magnetic loop. *Astrophys. J.*, 639, 1186–1205. https://doi.org/10.1086/499419

Ruffolo, D., et al. (2016), Monitoring short-term cosmic ray spectral variations using neutron monitor time delay measurements, *Astrophys. J.*, 817, 38. https://doi.org/10.3847/0004-637X/817/1/38

Stoker, P. H. (1985), Spectra of solar proton ground level events using neutron monitor and neutron moderated detector recordings, in *Proc. 19th Int. Cosmic Ray Conf.*, vol. 4, pp. 114–117.

Stoker, P. H., & B. C. Raubenheimer (1985), The neutron moderated detector and ground-based cosmic ray modulation studies, in *Proceedings of the 19th International Conference on Cosmic Rays*, vol. 5, pp. 502–505.

Stoker, P. H., A. J. van der Walt, & M. S. Potgieter (1980), Modulation of cosmic rays during solar minimum. Part 1. Cosmic ray intensity survey at sea-level during 1976: Experimental details, *South African Journal of Physics*, *3*, 73–76.

AGU FALL MEETING
San Francisco | 12–16 December 2016

SH43B-2567: Simulations of Lateral Transport and Dropout Structure of Energetic Particles from Impulsive Solar Flares

Thursday, 15 December 2016
13:40 - 18:00
Moscone South - Poster Hall

We simulate trajectories of energetic particles from impulsive solar flares for 2D+slab models of magnetic turbulence in spherical geometry to study dropout features, i.e., sharp, repeated changes in the particle density, and the particles' lateral transport. Among random-phase realizations of 2D turbulence, a spherical harmonic expansion can generate homogeneous turbulence over a sphere, but a 2D fast Fourier transform (FFT) locally mapped onto the lateral coordinates in the region of interest is much faster computationally, and we show that the results are qualitatively similar. We then use the 2D FFT field as input to a 2D MHD simulation, which dynamically generates realistic features of turbulence such as coherent structures. The magnetic field lines and particles spread non-diffusively (ballistically) to a patchy distribution reaching up to 25° from the injection longitude and latitude at r~1 AU. This dropout pattern in field line trajectories has sharper features in the case of the more realistic 2D MHD model, in better qualitative agreement with observations. The initial dropout pattern in particle trajectories is relatively insensitive to particle energy, though the energy affects the pattern's evolution with time. We make predictions for future observations of solar particles near the Sun (e.g., at 0.25 AU), for which we expect a sharp pulse of outgoing particles along the dropout pattern, followed by backscattering that first remains close to the dropout pattern and later exhibits cross-field transport to a distribution that is more diffusive, yet mostly contained within the dropout pattern found at greater distances. Partially supported by the Thailand Research Fund (Grants BRG5880009 and RTA5980003), the U.S. NSF (AGS-1063439), NASA (NNX14AI63G & NNX15AB88G), and the Solar Probe Plus/ISIS project.

Authors

David J Ruffolo
Thailand Center of Excellence in Physics
Mahidol Univ

Paisan Tooprakai
Thailand Center of Excellence in Physics
Chulalongkorn University

Achara Seripienlert
Rajamangala University of Technology Thanyaburi
Thailand Center of Excellence in Physics

Piyanate Chuychai
Thailand Center of Excellence in Physics
Burapha University

William H Matthaeus *
University of Delaware

Find Similar

View Related Events

Day: Thursday, 15 December 2016

AGU FALL MEETING
San Francisco | 12–16 December 2016

SA43A-2388: Gamma-ray Emission of the Earth's Upper Atmosphere in Geographical Coordinates with *Fermi*-LAT

Thursday, 15 December 2016
13:40 - 18:00
Moscone South - Poster Hall

The Earth is extremely bright in gamma rays as viewed by the *Fermi* Large Area Telescope (LAT). This gamma-ray emission of the Earth is produced by the interactions of cosmic rays (CRs), high-energy particles in space, with the Earth's upper atmosphere. Here we analyze the Earth's photons in the geographical coordinate system (latitude and longitude) from 58 months of data, using the latest version of the LAT event selection (Pass 8). Preliminary results of our analysis, which are the gamma-ray intensity maps of the Earth at energies from ~1 to 10 GeV, will be presented. This study provides a better understanding of the geomagnetic field, the Earth's upper atmosphere, and CRs. This project is partially supported by the Thailand Research Fund (Grant TRG5880173 and RTA5980003).

Authors

Suttiwat Madlee *
Mahidol University

Warit Mitthumsiri
Mahidol University

Seth Digel
Kavli Institute for Particle Astrophysics and Cosmology, SLAC National Accelerator Laboratory, Stanford University

David J Ruffolo
Mahidol University

Find Similar

View Related Events

Day: Thursday, 15 December 2016

AGU FALL MEETING
San Francisco | 12–16 December 2016

SH41D-04: GeV Solar Energetic Particle Observation and Search by IceTop from 2011 to 2016

Thursday, 15 December 2016
09:00 - 09:15
Moscone West - 2011

Only three Ground Level Enhancements (GLEs) produced by GeV solar energetic particles have been confirmed in the present solar cycle, and those have been quite small by historical standards. At the same time direct observations of high energy solar particles from spacecraft have become available. This has resulted in some discussion as to whether the definition of a GLE as an event detectable on the ground (as opposed to a statement about the spectral form of the event) is an appropriate scientific classification. The combination of instruments at the Amundsen – Scott Station at the geographic South Pole offers an opportunity to span the two worlds. Operating at high altitude and low geomagnetic cutoff the neutron monitor at Pole has nevertheless traditionally been accepted as making a “ground level” observation. An enhanced array of bare neutron detectors and IceTop (the surface component of the IceCube Neutrino Observatory) now allow spectral information to be extracted from events that are too small to use geomagnetic techniques to obtain spectra. We report our spectral measurements for the three confirmed GLEs and compare them to other available data on these events. We also present preliminary results of an ongoing study of 34 particle events selected to have significant enhancements in the > 100 MeV channel in GOES data in terms of possible detections and sensitivity limits. Supported in part by Thailand Research Fund grant RTA5980003 and US National Science Foundation awards PLR-1341562 and PHY-1505990.

Authors

Paul Arthur Evenson *
University of Delaware

David J Ruffolo
Mahidol University

Pradiphat Muangha
Mahidol University

Scientific Team: IceCube Collaboration

Find Similar

View Related Events

Day: Thursday, 15 December 2016

AGU FALL MEETING
San Francisco | 12–16 December 2016

SH31B-2598: Cosmic Ray Modulation Observed by the Princess Sirindhorn Neutron Monitor at High Rigidity Cutoff

Wednesday, 14 December 2016
08:00 - 12:20
Moscone South - Poster Hall

Neutron monitors (NMs) are the premier instruments for precisely tracking time variations in the Galactic cosmic ray (GCR) flux at the GV-range. For more than 60 years, the worldwide NM network has provided continuous measurements of the solar induced variations of the GCR flux impinging Earth and the data cover about six 11-year solar cycles. The recent rise of space exploration, with PAMELA and AMS-02 spacecraft, brings new energy sensitive measurements of GCR fluxes. Moreover since late 2007, the range of sensitivity of the worldwide NM network has been increased wih the installation of the Princess Sirindhorn Neutron Monitor (PSNM), at the summit of Doi Inthanon, Thailand's highest mountain (2565m altitude). PSNM records the GCR flux with the world's highest vertical rigidity cutoff for a fixed station, 16.8 GV. PSNM data now cover the period from the last solar minimum to the recent solar maximum and give us the opportunity to study the effect of the solar modulation at such high rigidity for the first time. We present here the observations of PSNM since 2007. The observed solar modulation is much weaker than predicted by the force field model with Φ inferred from NM data at low cutoff. We compare measurements with those from NMs located at low rigidity cutoff and with spacecraft data, and discuss the solar modulation at high rigidity. Partially supported by the Thailand Research Fund (RTA5980003) and US National Science Foundation awards PLR-1341562, PLR-1245939, and their predecessors.

Authors

Pierre-Simon Mangeard *
University of Delaware

John M Clem
University of Delaware

Paul Arthur Evenson
University of Delaware

Roger Pyle
University of Delaware

David J Ruffolo
Mahidol University

Alejandro Saiz
Mahidol University

Tanin Nutaro
Ubon Ratchathani University

Find Similar

View Related Events

Day: Wednesday, 14 December 2016

AGU FALL MEETING
San Francisco | 12–16 December 2016

SH21C-2542: CHARGED PARTICLE DIFFUSION IN ISOTROPIC RANDOM MAGNETIC FIELDS

Tuesday, 13 December 2016
08:00 - 12:20
Moscone South - Poster Hall

Study of the transport and diffusion of charged particles in a turbulent magnetic field remains a subject of considerable interest. Research has most frequently concentrated on determining the diffusion coefficient in the presence of a mean magnetic field. Here we consider diffusion of charged particles in fully three-dimensional isotropic turbulent magnetic fields with no mean field, which is pertinent to many astrophysical situations. The nature of particle transport in turbulent fields is highly dependent on their energy. The higher energy particles can sample many field lines within one gyration since the gyro-radius of the higher energy particles is larger than the correlation. The lower energy particles whose gyro-radius is much smaller than the correlation length of the magnetic field, on the other hand, are tied to a field line for a much longer period of time. We therefore classify different ranges of particle energy depending upon the ratio of the Larmor radius of the charged particle to the characteristic outer length scale of turbulence and propose three different theoretical models each applicable to distinct range of particle energies. The theoretical results are compared with those from computer simulations, showing good agreement.

Authors

Prachanda Subedi *
University of Delaware

William H Matthaeus
University of Delaware

Wirin Sonsrettee
Organization Not Listed

David J Ruffolo
Mahidol University

Tulasi N Parashar
University of Delaware

Pasquale Blasi
GRAN SASSO SCIENCE INSTITUTE

Rohit Chhiber
University of Delaware

Piyanate Chuychai
Mahidol University

Pablo Dmitruk
Consejo Nacional de Investigaciones Científicas y Técnicas - Phys. Dept. UBA

Minping Wan
Organization Not Listed

David Montgomery
Dartmouth College

Find Similar

View Related Events

Day: Tuesday, 13 December 2016

PROCEEDINGS OF SCIENCE

Simulations of Lateral Transport and Dropout Structure of Energetic Particles from Impulsive Solar Flares

P. Tooprakai[a,b], **A. Seripienlert**[b,c,d,e], **D. Ruffolo**[*b,c], **P. Chuychai**[b,f], **W. H. Matthaeus**[g]

[a] *Department of Physics, Faculty of Science, Chulalongkorn University, Bangkok 10330, Thailand.*
[b] *Thailand Center of Excellence in Physics, CHE, Ministry of Education, Bangkok 10400, Thailand.*
[c] *Department of Physics, Faculty of Science, Mahidol University, Bangkok 10400, Thailand.*
[d] *Division of Physics, Faculty of Science and Technology, Rajamangala University of Technology Thanyaburi, Pathum Thani 12110, Thailand.*
[e] *Now at Dacon Inspection Services Co., Ltd., Rayong 21130, Thailand.*
[f] *Department of Physics, Faculty of Science, Burapha University, Chonburi 20131, Thailand.*
[g] *Bartol Research Institute and Department of Physics and Astronomy, University of Delaware, Newark, DE 19716, USA.*
E-mail: paisan.to@chula.ac.th, tikim7@gmail.com, david.ruf@mahidol.ac.th, piyanate@gmail.com, whm@udel.edu.

We simulate trajectories of energetic particles from impulsive solar flares for 2D+slab models of magnetic turbulence in spherical geometry to study dropout features, i.e., sharp, repeated changes in the particle density. Among random-phase realizations of two-dimensional (2D) turbulence, a spherical harmonic expansion can generate homogeneous turbulence over a sphere, but a 2D fast Fourier transform (FFT) locally mapped onto the lateral coordinates in the region of interest is much faster computationally, and we show that the results are qualitatively similar. We then use the 2D FFT field as input to a 2D MHD simulation, which dynamically generates realistic features of turbulence such as coherent structures. The magnetic field lines and particles spread nondiffusively (ballistically) to a patchy distribution reaching up to 25 degrees from the injection longitude and latitude at $r \sim 1$ AU. This dropout pattern in field line trajectories has sharper features in the case of the more realistic 2D MHD model, in better qualitative agreement with observations. The initial dropout pattern in particle trajectories is relatively insensitive to particle energy, though the energy affects the pattern's evolution with time. We make predictions for future observations of solar particles near the Sun (e.g., at 0.25 AU), for which we expect a sharp pulse of outgoing particles along the dropout pattern, followed by backscattering that first remains close to the dropout pattern and later exhibits cross-field transport to a distribution that is more diffusive, yet mostly contained within the dropout pattern found at greater distances.

35th International Cosmic Ray Conference
12-20 July, 2017
Bexco, Busan, Korea

[*] Speaker.

© Copyright owned by the author(s) under the terms of the Creative Commons Attribution-NonCommercial-NoDerivatives 4.0 International License (CC BY-NC-ND 4.0).

PoS(ICRC2017)135

1. Introduction

Observations of energetic particles from impulsive solar flares, which have narrow source regions of particle injection at the Sun [19], can exhibit "dropouts" in which the particle flux at a spacecraft disappears and reappears repeatedly [10, 15]. This has been interpreted in terms of a filamentary distribution of magnetic field lines connected to the source region, which convects past the spacecraft along with the solar wind. The filamentation has been attributed to photospheric motions [9] or in situ interplanetary turbulence [21, 28].

In our work (see also [26]), we model the transport of SEPs from impulsive solar flares using the 2D+slab model of magnetic turbulence, which has been shown to provide a useful model of observed solar wind fluctuations [3, 13] and parallel scattering of energetic particles [2], and has shown to be equivalent to a model of fluctuations generated by photospheric motions [8]. Previous simulations in Cartesian geometry have demonstrated that dropout patterns naturally result from magnetic field line trajectories in 2D+slab turbulence [21], due to temporary topological trapping of some trajectories near O-points of the 2D turbulence with suppressed diffusive escape [6], a mechanism that also applies to particle trajectories [25]. The combination of these mechanisms can lead to local trapping boundaries [5, 23], which may have been found by in situ observations in the solar wind (e.g., [24, 27]). Here we use a spherical geometry, for different types of 2D turbulence models together with slab fluctuations, and trace trajectories of magnetic field lines and protons of varying energy as a function of distance from the Sun.

2. Modeling

2.1 2D+Slab Magnetic Turbulence Models in Spherical Geometry

In spherical geometry, we express the total magnetic field as [22]

$$\mathbf{B} = \mathbf{B}_0(r) + \mathbf{b}(\mathbf{r}) = \frac{r_1^2}{r^2}\left[B_1\hat{\mathbf{r}} + \mathbf{b}^{slab}(r) + \mathbf{b}^{2D}(\varphi,\Lambda)\right]. \tag{2.1}$$

Here $\mathbf{B}_0$ is a radial mean magnetic field of magnitude B_1 at r_1, which we take to be 1 AU. The two fluctuation components, the slab turbulence $\mathbf{b}^{slab}$ and 2D turbulence $\mathbf{b}^{2D}$, are perpendicular to the mean field, which is consistent with observations that magnetic turbulence in the solar wind is $\approx$ 90% transverse to the mean field [1, 12]. The 2D field can be written as $\mathbf{b}^{2D}(\varphi,\Lambda) = \nabla\times[a(\varphi,\Lambda)\hat{\mathbf{r}}]$, where $a(\varphi,\Lambda)$ is the magnetic potential function. We use the radial mean field as a rough approximation to the Parker spiral field [17] because it is difficult to formulate a global, homogeneous 2D fluctuating field for the latter. The fraction of fluctuation energy in slab fluctuations is taken to be 20%, according to [2, 3]. The slab fluctuations are first generated in Cartesian coordinates [26]. For a spherical geometry, we identify the parallel z-coordinate with the radius r and use $b_\varphi^{slab}(r) = b_x^{slab}(z)$ and $b_\Lambda^{slab}(r) = b_y^{slab}(z)\sec\Lambda$, so that $\nabla\cdot\mathbf{b}^{slab} = 0$. To some degree this violates the condition of homogeneity, but because we limit our simulations to an angular region of $-25^\circ < \varphi < 25^\circ$ and $-25^\circ < \Lambda < 25^\circ$, centered around the solar equator, the factor of $\sec\Lambda$ has only a minor effect.

For the 2D fluctuation component, we employed three different computational models; for details see [26]. The first model is a spherical harmonic expansion (SHE) of the potential function, evaluated up to $l_{max} = 2200$ using the numerical method of [11]. The second is a 2D FFT

PoS(ICRC2017)135

model, following [22], where we generate a potential function a in terms of the Cartesian coordinates (x,y) and then map it onto the angular coordinates (φ,Λ) at the reference radius $r_1 = 1$ AU. After generating $a(k_x,k_y)$, we use an inverse fast Fourier transform to efficiently calculate $a(x,y)$ at 1024×1024 grid points, and then map the Cartesian potential $a(x,y)$ onto the heliolongitude using $\varphi = x/r_1$ and the heliolatitude using $\Lambda = y/r_1$.

For an improved representation of 2D magnetic turbulence in the solar wind, our third method used the 2D FFT potential function in Cartesian coordinates as an initial condition and evolved the field for one nonlinear time according to the 2D MHD equations [23]. This leads to smoother equipotential contours and also tends to produce current sheets and other coherent structures that are not expected in random-phase representations such as the 2D SHE and 2D FFT models.

2.2 Trajectories of Magnetic Field Lines and Particles

We find the trajectories of magnetic field lines by using the streamline equation:

$$\frac{dr}{B_r} = \frac{rd\Lambda}{B_\Lambda} = \frac{r\cos\Lambda d\varphi}{B_\varphi}, \tag{2.2}$$

which can be written in terms of components as

$$\frac{d\Lambda}{dr} = \frac{1}{r}\frac{B_\Lambda}{B_r}, \tag{2.3}$$

$$\frac{d\varphi}{dr} = \frac{1}{r\cos\Lambda}\frac{B_\varphi}{B_r}. \tag{2.4}$$

For particle trajectories, we solve the Newton-Lorentz equation:

$$\gamma m\dot{\mathbf{v}} = q(\mathbf{v}\times\mathbf{B}), \tag{2.5}$$

where $\gamma = 1/\sqrt{1-v^2/c^2}$ is the Lorentz factor, m is the particle mass, $\mathbf{v}$ is the particle velocity, $\mathbf{B}$ is the interplanetary magnetic field, c is the speed of light, and q is the particle charge.

The field line equations or Newton-Lorentz equation was solved by the Cash-Karp method [4, 18], a fifth-order Runge-Kutta method with an adaptive step size, using a version of the *Streamline* code [7]. In each case, 50,000 magnetic field line or particle trajectories were traced from random initial locations within a circle of angular radius 2.5° at $r = 0.1$ AU. This serves to model the narrow injection region expected for an impulsive solar flare. The initial direction of each particle (at $t = 0$ and $r = 0.1$ AU) was parallel to the local magnetic field line, due to the expected effect of strong adiabatic focusing at $r < 0.1$ AU [20].

3. Magnetic Connectivity to a Narrow Injection Region

Figure 1 shows the angular coordinates of simulated magnetic field lines at varying radius r from the Sun for MHD. After an initial concentration in a narrow injection region at $r = 0.1$ AU, the field line distribution distorts into a complex pattern at higher r, i.e., the initial flux tube "shreds" [14]. In all cases, we find that SEP trajectories closely follow these magnetic field line trajectories at early times. Then as an observer (spacecraft) moves relative to this pattern, the complex filamentation of magnetic connectivity leads to a "dropout" pattern of repeated disappearance and

PoS(ICRC2017)135

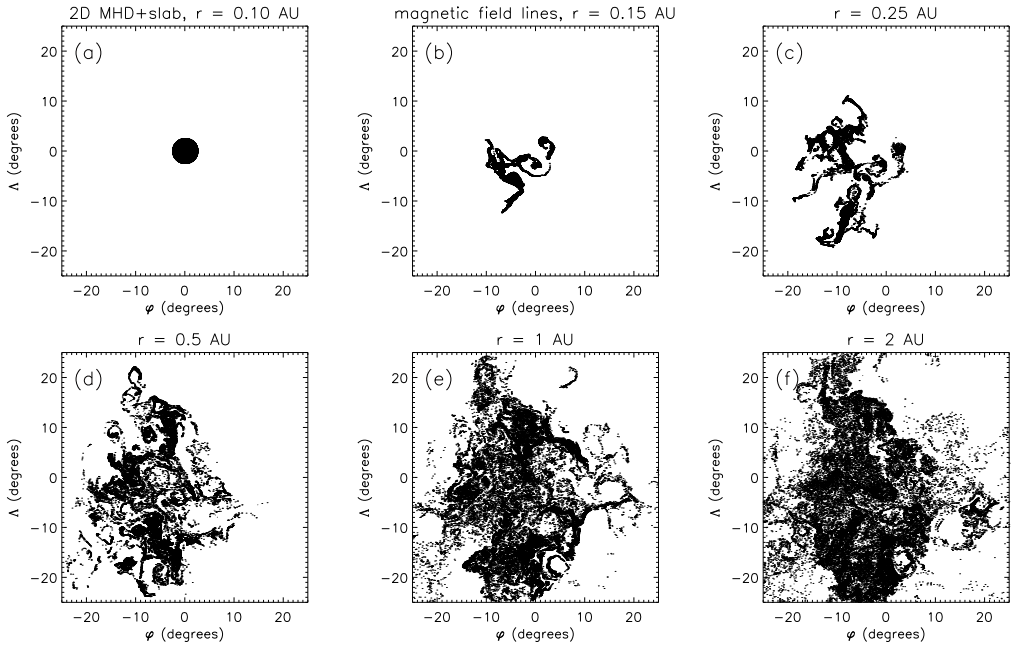


Figure 1: Trajectories of 50,000 magnetic field lines in heliolongitude and heliolatitude as a function of radius r from the Sun, starting at random initial locations at $r = 0.1$ AU within a circle of radius 2.5°, for the 2D MHD + slab magnetic fluctuation model. This model is a refinement of the random-phase 2D FFT model, which is used as the initial condition for solving the 2D MHD equations. The resulting 2D MHD magnetic field includes coherent structures, and the field line trajectories displayed here exhibit finer filamentation than for the random-phase field models.

reappearance of energetic particle flux. Therefore, we first discuss the fundamental issue of magnetic connectivity, which determines whether or not particles will have access to a given location at early times.

Comparing results for the two random-phase 2D magnetic fields, the dropout patterns are qualitatively similar for 2D SHE and 2D FFT [26]. This justifies the use of the computationally cheaper 2D FFT model for dropout modeling, and also its use as an initial condition for the 2D MHD procedure. While the dropout patterns for 2D MHD (Figure 1) are similar to those for 2D FFT on the largest scales, on smaller scales the 2D MHD model yields much finer (narrower) dropout features. This highlights the important role played by the coherent structures generated by the MHD equations, which are not present in the random-phase models.

4. Dropout Patterns at $r = 1$ AU

We examine the dropout patterns at $r = 1$ AU from the Sun in terms of particle trajectories over different time ranges. For greater clarity and generality, we express the time ranges in terms of the pathlength, $s = vt + 0.1$ AU, where v is the particle speed (which is constant in a static magnetic field, as used in our simulations). Since we inject particles at $t = 0$ and $r = 0.1$ AU, vt expresses

PoS(ICRC2017)135

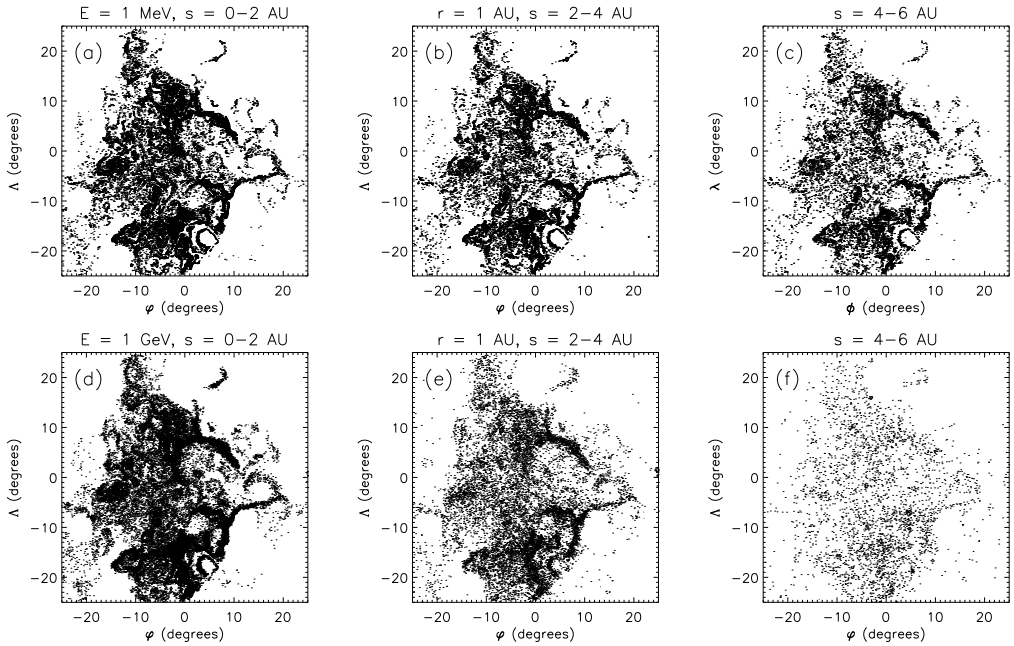


Figure 2: Heliolongitude and heliolatitude when crossing $r = 1$ AU of 50,000 solar energetic protons that started at random initial locations at $r = 0.1$ AU within a circle of radius 2.5°, for the 2D MHD + slab magnetic fluctuation model. We show proton arrival locations at $r = 1$ AU for various ranges of time, expressed in terms of pathlength from the Sun, $s = vt + 0.1$ AU, for kinetic energy $E = 1$ MeV (a-c) and $E = 1$ GeV (d-f).

the pathlength along the actual particle orbit beyond $r = 0.1$ AU, and we add 0.1 AU to account for the pathlength before injection (assuming radial propagation there).

For low-energy protons of 1 MeV, Figure 2(a) shows that the initial dropout pattern of arrival locations during $s = 0$ to 2 AU almost exactly matches the pattern of field line locations at $r = 1$ AU (Figure 1(e)). In other simulations, we have found that this holds up to a proton energy of 100 MeV. Thus for early times we confirm that we can learn about dropouts in particle trajectories by examining the distribution of magnetic connectivity in terms of field line trajectories. At this low energy, Figures 2(b) and (c) show quite similar distributions at later times, corresponding to s ranges from 2 to 4 AU and 4 to 6 AU, respectively. The protons arriving at these later times have typically traveled beyond $r = 1$ AU and scattered back, so our results indicate that during outward transport and backscattering the low energy protons remain quite close to their initial field lines.

Figure 2(d) shows that at $E = 1$ GeV, the proton arrival locations at early times (during $s = 0$ to 2 AU) have spread slightly compared with the field line locations. The distribution for $s = 2$ to 4 AU (Figure 2(e)) has spread noticeably over small scales. Then for $s = 4$ to 6 AU (Figure 2(f)), the whole dropout pattern is mostly washed out, indicating substantial cross-field transport during transport forward and backward along the interplanetary magnetic field. Nevertheless, there is still a clear outer boundary to the distribution of arrival locations, which remains rather sharp.

PoS(ICRC2017)135

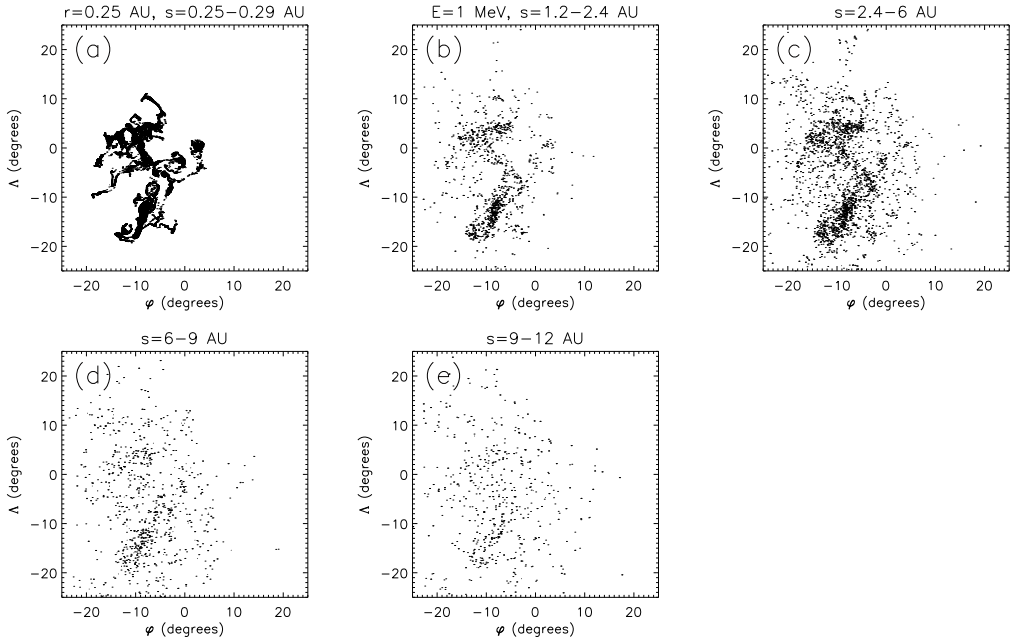


Figure 3: Heliolongitude and heliolatitude when crossing $r = 0.25$ AU of 50,000 solar energetic protons at $E = 1$ MeV that started at random initial locations at $r = 0.1$ AU within a circle of radius 2.5°, for the 2D MHD + slab magnetic fluctuation model, for various ranges of time, expressed in terms of the pathlength s. As in Figure 2, the broader distribution at late times has a rather sharp edge and is still not fully diffusive. This Figure indicates the type of SEP distributions that could be observed by the Solar Probe Plus and Solar Orbiter missions when they approach close to the Sun; time intensity profiles could be very different from event to event, depending on the spacecraft location relative to the dropout structure.

5. Implications for Solar Probe Plus and Solar Orbiter Observations

In this Section we explore some interesting properties of the lateral distribution of SEPs from impulsive solar events when observed close to the Sun, and the prospects for observing such features with the upcoming Solar Orbiter and Solar Probe Plus missions. As seen in Figure 3(a), protons in the initial pulse had an angular distribution exactly like the magnetic field line distribution (Figure 1(c)), indicating transport along the turbulent field lines. After backscattering from larger r, the angular distribution of protons arriving at $r = 0.25$ AU during $s = 1.2$ to 2.4 AU (Figure 3(b)) is similar to the field line distribution but now somewhat spread out, indicating some cross-field transport. Later, during $s = 2.4$ to 9 AU (Figure 3(c-d)), there is a superposition of that distribution, with minor spreading from the field line distribution, together with a broader distribution. Then from $s = 9$ to 12 AU (Figure 3(e)) only the broader distribution is apparent. Note, however, that the broader distribution is still confined to a specific angular region, with a rather sharp edge. This region corresponds well with the envelope of the field line distribution at $r = 0.5$ AU (Figure 1(d)), which in this representation is predominantly at $\varphi < 0$. Thus the effect of cross-field is limited by trapping boundaries, and the spread of the particle distribution at fixed radius at these times is not well described as a diffusive process over the entire sphere.

PoS(ICRC2017)135

In general, a moving spacecraft may measure a combination of effects of parallel transport (governing the time-intensity profile along a field line) and the lateral distribution (manifest as dropout features). For a spacecraft near Earth, the time scales are well separated, with parallel transport effects taking place over longer time scales than dropouts, so both processes can be studied. However, as seen in Figure 3, at $r = 0.25$ AU the particle intensity along a given field line varies rapidly during the initial pulse, which is also the time period when the dropout pattern is clearest. This may make it challenging to distinguish between changes due to parallel transport or due to dropouts, unless repeated dropouts are observed. A further issue is that solar events may involve multiple bursts of particle acceleration and release. These are often indistinguishable after transport to 1 AU, but may represent an additional source of time structure in observations close to the Sun.

The Solar Orbiter mission aims to reach an orbit with perihelion at about $r = 0.28$ AU, where it may have an angular speed close to the Sun's rotational speed. This is useful for extended observations of specific regions on the solar surface. For dropouts, the implication is that Solar Orbiter may be nearly co-rotating with the filamentary field line distribution. This will minimize the effect of the dropout pattern and make the SEP time profiles sensitive mainly to injection and parallel transport effects.

When a spacecraft nearly co-rotates with the Sun, or if the time required to traverse dropout features is longer than their duration, the time intensity profile will be very different from event to event, depending on the spacecraft location relative to the dropout structure. At $r = 0.25$ AU, Figure 3 shows that even if the angular distance from the mean field connection is small, a spacecraft that remains in a region devoid of connected field lines may see no initial pulse of SEPs, only those backscattering with cross-field transport from greater r. They should then detect a Sunward anisotropy of SEPs. On the other hand, a spacecraft in a well-connected region should see a sharp coherent pulse of nearly scatter-free SEPs followed (possibly after a gap) by the wake of backscattered SEPs.

The Solar Probe Plus mission aims to reach an orbit with a much closer perihelion at $r = 0.04$ AU, where the orbital speed will approach 200 km s^{-1}, which would correspond to an angular speed of 3.4×10^{-5} s^{-1}. This will be faster than the solar rotation frequency by 3.1×10^{-5} s^{-1}, and Solar Probe Plus would traverse the field line structures at 6.4° h^{-1}. This close to the Sun, the SEPs observed by the EPI-Hi and EPI-Lo instruments [16] should be essentially scatter-free, so the time profile of SEPs along connected field lines should reflect the time dependence of injection by the flare, which could last for tens of minutes. Dropout features should be very sharp (see, e.g., Figure 1(b), for a distance of 0.05 AU from the source) and could quite possibly be observed during the course of SEP emission. Simultaneous information about the time profile and location of particle injection (e.g., from γ-ray imaging) would provide valuable data concerning magnetic connectivity near the Sun.

Considering observations when Solar Probe Plus is farther from the Sun, the spacecraft orbit as described above would co-rotate with the Sun at $r = 0.13$ AU, and at $r = 0.25$ AU its orbital angular frequency will be about 4 times lower than the Sun's rotation. With a relative angular speed of 2.1×10^{-6} s^{-1} or about 0.4° h^{-1}, it will be more difficult to measure dropouts during the initial pulse of SEPs. At larger distances, the duration of the dropout pattern will increase and dropouts should again be readily detectable.

PoS(ICRC2017)135

Acknowledgments

This work was supported by grants BRG5880009 and RTA5980003 from the Thailand Research Fund, the US National Science Foundation Solar Terrestrial program grant AGS-1063439, and NASA grants NNX14AI63G (Heliospheric Grand Challenge Research) and NNX15AB88G (Living with a Star Program). WHM is a co-investigator on the ISIS instrument suite (EPI-Hi and EPI-Lo) and is partially supported by the Solar Probe Plus project.

References

[1] Belcher, J. W., & Davis, L., Jr. 1971, JGR, 76, 3534

[2] Bieber, J. W., Matthaeus, W. H., Smith, C. W., et al. 1994, ApJ, 420, 294

[3] Bieber, J. W., Wanner, W., & Matthaeus, W. H. 1996, JGR, 101, 2511

[4] Cash, J. R., & Karp, A. H. 1990, ACM Trans. Math. Softw., 16, 201

[5] Chuychai, P., Ruffolo, D., Matthaeus, W. H., & Meechai, J. 2007, ApJ, 659, 1761

[6] Chuychai, P., Ruffolo, D., Matthaeus, W. H., & Rowlands, G. 2005, ApJL, 633, L49

[7] Dalena, S., Chuychai, P., Mace, R. L., et al. 2012, CoPhC, 183, 9

[8] Giacalone, J., Jokipii, J. R., & Matthaeus, W. H. 2006, ApJL, 641, L61

[9] Giacalone, J., Jokipii, J. R., & Mazur, J. E. 2000, ApJL, 532, L75

[10] Gosling, J. T., Skoug, R. M., McComas, D. J., & Mazur, J. E. 2004, ApJ, 614, 412

[11] Holmes, S. A., & Featherstone, W. E. 2002, JGeod, 76, 279

[12] Isaacs, J. J., Tessein, J. A., & Matthaeus, W. H. 2015, JGRA, 120, doi:10.1002/2014JA020661

[13] Matthaeus, W. H., Goldstein, M. L., & Roberts, D. A. 1990, JGR, 95, 20673

[14] Matthaeus, W. H., Gray, P. C., Pontius, D. H., Jr., & Bieber, J. W. 1995, PhRvL, 75, 2136

[15] Mazur, J. E., Mason, G. M., Dwyer, J. R., et al. 2000, ApJL, 532, L79

[16] McComas, D. J., Alexander, N., Angold, N., et al. 2014, SSRv, doi:10.1007/s11214-014-0059-1

[17] Parker, E. N. 1958, ApJ, 128, 664

[18] Press, W. H., Teukolsky, S. A., Vetterling, W. T., & Flannery, B. P. 1992, Numerical recipes in FORTRAN: The art of scientific computing, 2nd ed. (Cambridge: Cambridge Univ. Press), 713

[19] Reames, D. V. 1999, SSRv, 90, 413

[20] Ruffolo, D., & Khumlumlert, T. 1995, GeoRL, 22, 2073

[21] Ruffolo, D., Matthaeus, W. H., & Chuychai, P. 2003, ApJL, 597, L169

[22] Ruffolo, D., Seripienlert, A., Tooprakai, P., Chuychai, P., & Matthaeus, W. H. 2013, ApJ, 779, 74

[23] Seripienlert, A., Ruffolo, D., Matthaeus, W. H., & Chuychai, P. 2010, ApJ, 711, 980

[24] Tessein, J. A., Ruffolo, D., Matthaeus, W. H., & Wan, M. 2016, GeoRL, 43, 3620

[25] Tooprakai, P., Chuychai, P., Minnie, J., et al. 2007, GeoRL, 34, L17105

[26] Tooprakai, P., Seripienlert, A., Ruffolo, D., Chuychai, P., and Matthaeus, W. H. 2016, ApJ, 831, 195

[27] Trenchi, L., Bruno, R., Telloni, D., et al. 2013, ApJ, 770, 11

[28] Zimbardo, G., Pommois, P., & Veltri, P. 2004, JGR, 109, A02113

PoS(ICRC2017)135

PROCEEDINGS OF SCIENCE

Tracking cosmic-ray spectral variations with neutron monitor time-delay measurements at high cutoff rigidity during 2007-2017

C. Banglieng[a,b], **D. Ruffolo**[*a], **A. Sáiz**[a], **P. Evenson**[c], **T. Nutaro**[d]

[a] *Department of Physics, Faculty of Science, Mahidol University, Bangkok 10400, Thailand.*
[b] *National Astronomical Research Institute of Thailand (NARIT), Chiang Mai 50180, Thailand.*
[c] *Bartol Research Institute, Department of Physics and Astronomy, University of Delaware, Newark, DE 19716, USA.*
[d] *Department of Physics, Faculty of Science, Ubon Ratchathani University, Ubon Ratchathani 34190, Thailand.*
E-mail: bchanoknan@gmail.com, david.ruf@mahidol.ac.th, alejandro.sai@mahidol.ac.th, evenson@udel.edu, tnutaro@yahoo.com.

We present measurements of the leader fraction of neutron monitor counts that did not follow other counts in the same counter tube from the same cosmic ray shower. We use time-delay histograms collected at the Princess Sirindhorn Neutron Monitor at Doi Inthanon, Thailand, which has the world's highest vertical cutoff rigidity for a fixed station (16.8 GV). Changes in the leader fraction are a precise indicator of cosmic ray spectral variations above the cutoff. Our data set from 2007 to 2017 spans a full cycle of solar modulation, including the all-time cosmic ray maximum of 2009 and minimum near the end of 2014, the count rate now having returned to its initial value. The electronics to collect time-delay histograms have been upgraded twice, and we have corrected for such changes to develop a long-term leader fraction dataset. We examine the spectral variation of Galactic cosmic rays above ∼17 GV resulting from solar modulation and its solar magnetic polarity dependence.

35th International Cosmic Ray Conference
12-20 July, 2017
Bexco, Busan, Korea

[*] Speaker.

© Copyright owned by the author(s) under the terms of the Creative Commons Attribution-NonCommercial-NoDerivatives 4.0 International License (CC BY-NC-ND 4.0).

PoS(ICRC2017)025

1. Introduction

Neutron monitors (NMs) are ground-based detectors of secondary neutrons from interactions of primary cosmic rays in Earth's atmosphere. With high count rates and stable operation, NMs have precisely tracked variations in the flux of Galactic cosmic rays (GCRs) for decades and perform key measurements of solar modulation, i.e., variations with the roughly 11-year sunspot cycle [4] and 22-year solar magnetic cycle [5]. Solar modulation is scientifically interesting because the GCRs traverse the heliosphere on their way to Earth and provide remote sensing of heliospheric propagation conditions relating to the turbulent solar wind and interplanetary magnetic field.

Solar modulation is strongly energy-dependent [9], and a disadvantage of ground-based measurements is that the primary cosmic ray energy is not directly measured. The energy response of an NM can be controlled to some extent by its location on Earth's surface, using Earth itself as a magnetic spectrometer. For a given location and particle arrival direction there is a rather sharp geomagnetic cutoff in rigidity (momentum per charge) below which particles cannot reach Earth's atmosphere. The effective geomagnetic cutoff for vertically arriving particles varies from $\sim$17 GV in and near Thailand to <0.01 GV in some polar regions; for low geomagnetic cutoff, there is also an atmospheric cutoff at $\sim$1 GV, which is the threshold for primary cosmic rays to produce atmospheric secondaries detected by the NM at ground level. Therefore, while NM count rates track the GCR flux, the worldwide NM network also provides some information on GCR spectral variations in an intermediate rigidity range when comparing count rates at different cutoff rigidities. However, although individual NM count rate measurements can have high statistical precision, there are various uncertainties involved with comparing long-term data from different locations. These include the strong dependence of the NM yield function on the altitude of the station and also effects of different NM configurations, electronic dead time, structures surrounding the stations, seasonal effects, and atmospheric structure [1, 7, 8], as well as long-term drifts [12].

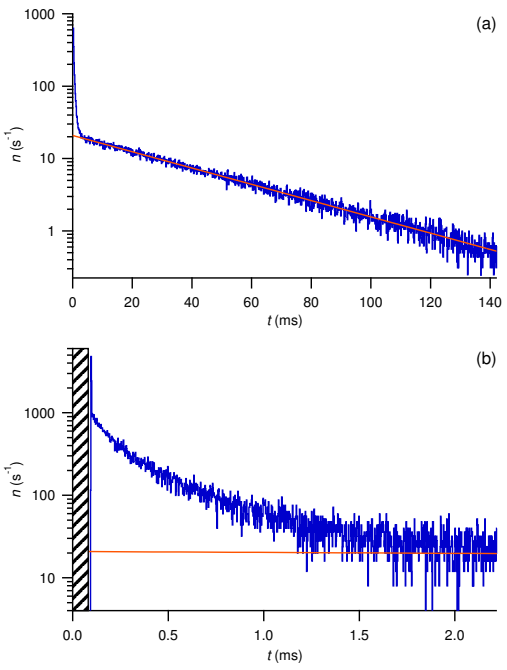


Figure 1: Example of time delay histograms collected for one neutron counter tube in the PSNM at Doi Inthanon during one hour. (a) Long time delays follow an exponential distribution (red) as expected for unrelated neutron detection events. (b) At short time delays ($<$ 2 ms), the distribution deviates substantially from that exponential because many counts are associated other counts due to the same primary cosmic ray. The hashed region indicates the dead time of the time delay histogram, t_d. From histograms such as these, we extract the leader fraction L of neutrons that did not follow a previous neutron detected in the same tube from the same cosmic ray, and L serves as an indicator of the spectral index of primary cosmic rays.

PoS(ICRC2017)025

For these reasons, we have developed a capability to precisely track spectral variations using data from a single NM station. We built specialized electronics to record neutron time-delay histograms [3], and an example of the resulting time-delay histograms is shown in Figure 1. We also developed analysis techniques to remove the effect of chance coincidences and extract the "leader fraction" L of neutron monitor counts that did not follow other counts in the same counter tube from the same cosmic ray shower [13]. Data from latitude surveys with a ship-borne NM during 2001-2007 show that L varies with cutoff rigidity in the manner expected from Monte Carlo simulations [8], confirming that variations in L indicate variations in the primary cosmic ray spectrum. The first fixed NM station where these electronics were used is the Princess Sirindhorn Neutron Monitor (PSNM) at Doi Inthanon, Thailand, which has the world's highest cutoff rigidity for a fixed station (vertical cutoff $\approx$ 16.8 GV). Here we present a long-term dataset of the leader fraction at Doi Inthanon from 2007 December to 2017 June, which spans a full cycle of solar modulation, including the all-time cosmic ray maximum of 2009 and minimum near the end of 2014, the count rate now having returned to its initial value. While comparisons of NM count rates provide spectral information over rigidities within the worldwide range of cutoff rigidities, the leader fraction at Doi Inthanon indicates spectral variations at a rigidity beyond the Earth's maximum cutoff.

2. Analysis of Neutron Time-Delay Histograms

2.1 Observations at Doi Inthanon, Thailand

PSNM is located at the summit of Doi Inthanon, Thailand's highest mountain, at longitude 18.59°N, longitude 98.49°E, and altitude 2560 m. It employs 18 neutron detectors ($^{10}BF_3$ proportional counter tubes) in the standard NM64 design (i.e., an 18NM64 configuration) with all tubes individually surrounded lead producer and arranged in a continuous single row inside the polyethylene reflector. Over the solar modulation cycle, the total count rate ranges from about 605 to 625 Hz, corresponding to 2.18 to 2.25 million counts per hour. Details about the detector can be found in [13].

Our specialized electronics that output histograms of the time delays between successive neutron detections in the same counter tube [3] were first implemented on a series of latitude surveys from 2000 to 2007 [8]. Similar systems have been developed by other groups (e.g., [2, 6]). The first use of our electronics at a fixed station was at PSNM since the start of operations in 2007 August. Here we analyze data taken since 2007 December 9, the start of operations with the complete set of 18 counter tubes.

Table 1 details the evolution of the firmware in the electronics and the software in the data acquisition system used to collect time delay histograms at PSNM. We refer to the firmware originally implemented as the 600 series. We originally collected daily time-delay histograms, and then changed to hourly histograms on 2009 June 29. The 600 series collected only 16 time delays per s per tube, resulting in the "first-pulse bias" described by [13]. Then we upgraded to the 700 series on 2011 Jan 15, allowing almost all time delays (at $\approx$34 Hz per tube) to be collected for improved statistics. We upgraded to the 800 series on 2014 Jun 11 in order to record absolute times and calculate cross-tube time delays (see [14]), which are not used in the present analysis. The 800 series firmware also reduced the time-delay dead time for improved collection of time-delay

PoS(ICRC2017)025

Table 1: Time periods of leader fraction data collection from the 18NM64 at Doi Inthanon, Thailand.

Time period	Start date	End date	Cadence	Firmware series (Number of tubes)	Software version[a]
1	2007 Dec 9	2009 Jun 28	Daily	600 (18)	—
1	2009 Jun 29	2011 Jan 15	Hourly	600 (18)	—
2	2011 Jan 15	2014 Feb 8	Hourly	700 (18)	—
3	2014 Feb 8	2014 Jun 11	Hourly	700 (17)	—
4	2014 Oct 17	2015 Mar 3	Hourly	800 (18)	8.46-8.47
5	2015 Mar 3	2015 May 31	Hourly	800 (18)	8.50
6	2015 May 31	2016 Jun 30	Hourly	600 (6), 800 (12)	8.50-8.82
7	2016 Jun 30	2017 Jun 7	Hourly	800 (18)	8.82

[a] Only relevant for 800 series firmware.

data (note that the dead time related to the count rate was never changed). Starting with the 800 series, time delays are calculated by the data acquisition software. The software version changes that affected the time-delay histograms are indicated in Table 1. The 800 series data did not yield a useful estimate of the leader fraction from 2014 June to 2014 October while the software was under development. Note that there were no changes to the circuitry used for count rate data, which were collected continuously from the 18NM64 since 2007 December.

Note that our electronics to record time-delay histograms have more recently been implemented at other fixed NM stations: at the South Pole (on 1 NM tube since 2014 January, then later on all 3 NM tubes), at McMurdo, Antarctica (on 6 tubes from 2015 January until the station closed on 2017 January 7), at Newark, USA (on 3 tubes since 2015), and at Jang Bogo, Antarctica (on all 5 tubes since 2015 December). Those data will be analyzed in further work.

2.2 Extraction of the Leader Fraction

As shown in Figure 1, at long time delays the histograms are dominated by chance coincidences, which strongly affect traditional measures of multiplicity in a fixed time window. Therefore, [13] developed methods to statistically remove the effect of chance coincidences to extract the leader fraction L. This is defined as the fraction of neutron counts that did not follow another count in the same tube due to the same primary cosmic ray, i.e., did not follow another count in the same tube with a short time delay that is not consistent with chance coincidence. Statistically, more energetic primary cosmic rays lead to more energetic secondary particles that produce more neutrons when interacting inside the neutron monitor (typically in the lead producer), which can then be detected as sequences of more counts in the same tube with shorter time delays. Thus a harder cosmic ray spectrum with a lower spectral index leads to a lower leader fraction. Ref. [13] showed that the leader fraction at Doi Inthanon can indicate short-term spectral variations; the present work extends that to determine a long-term time series of L for the study of solar modulation.

PoS(ICRC2017)025

Ref. [13] described three methods for determining L, and implemented the first (Method 1). However, in the present work, when comparing data from different software versions, we find that Method 2 is more robust under such changes, perhaps because it uses short time delays more than long time delays, and we now use Method 2.

2.3 Normalization and Correction of the Leader Fraction

To interpret long-term variation of the leader fraction, we have normalized for version changes in the electronics and data acquisition, and developed corrections of L (for Method 2) for variations of pressure and water vapor.

Note that NM count rates are essentially always corrected for pressure variation, and at the tropical location of Doi Inthanon, correction for water vapor is necessary when studying bare counter rates and the leader fraction [13]. [It even affects the count rate, with a peak-to-peak seasonal variation of 0.3% [9], but we do not correct the count rate for water vapor in the present work.] Those works described corrections based on the surface water vapor pressure E_w at Doi Inthanon as calculated from the Global Atmospheric Data Assimilation (GDAS) database (see http://ready.arl.noaa.gov/gdas1.php). In particular, [13] found a nonlinear relationship between pressure-corrected L and E_w, which they modeled using power-law relationships. Here we have integrated over the atmospheric model to estimate the integrated water vapor I as a function of time. When examining data from each individual tube using the 700 series electronics, we find a nearly linear relationship between pressure-corrected L and I. Our interpretation is that the leader fraction, which mainly responds to sub-GeV secondary neutrons from the atmospheric cascades of cosmic rays [8], has a small effect from water vapor throughout the atmosphere that is nearly linear in I. The surface water vapor E_w can serve as a proxy for I but often saturates during the rainy season (with nearly 100% relative humidity), so that L has a nonlinear relationship with E_w. In that case, I should provide a more accurate measure of water vapor content for correcting L at Doi Inthanon.

Each counter tube has a different value of L, mainly due to its position and electronic dead time [13]. We first normalized L from each tube to a standard set of tubes based on statistics of measured L ratios. These ratios were independent of the firmware and software version, though on 2014 Dec 7 we swapped the end tubes 1 and 18, requiring separate normalizations of the end tubes before and after that time. After that normalization, L was averaged over all tubes that provided good data. An overall normalization for each normalization period in Table 1 was directly determined from calibration periods when we simultaneously operated different firmware versions on different sets of tubes for a statistical comparison, or by matching the time series before and after a transition.

3. Long-Term Variation of the Leader Fraction

Figure 2 shows preliminary results for the corrected and normalized leader fraction L from the 18NM64 at Doi Inthanon, Thailand from 2007 December to 2017 June, as well as the count rate C over that time. The count rate shows solar modulation over a complete cycle, having increased to the time of the highest GCR flux of the Space Age in 2009 [11, 10, 12], decreased to a cosmic ray minimum in 2014, and now increased back above its starting value. Figure 3 shows trimester (three-month) averaged data for L vs. C over the same time period. Numerical labels indicate the

PoS(ICRC2017)025

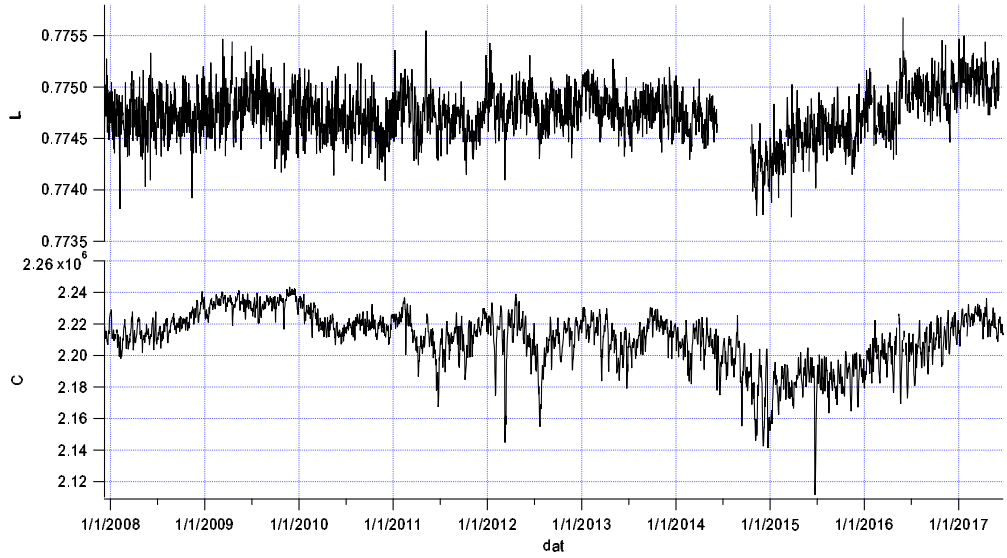


Figure 2: Preliminary results for the leader fraction L (upper panel) and count rate C (lower panel, in counts per hour) vs. time in the 18NM64 at Doi Inthanon, Thailand at vertical cutoff rigidity ≈ 16.8 GV during 2007-2017. The near constancy of L, an indicator of spectral variation well above the cutoff, indicates that during the period surrounding the record-high cosmic ray peak of 2009, the solar modulation extended up to much higher rigidity than the cutoff. After the cosmic ray minimum in 2014, L varied in tandem with C, indicating that solar modulation did not extend far above the cutoff.

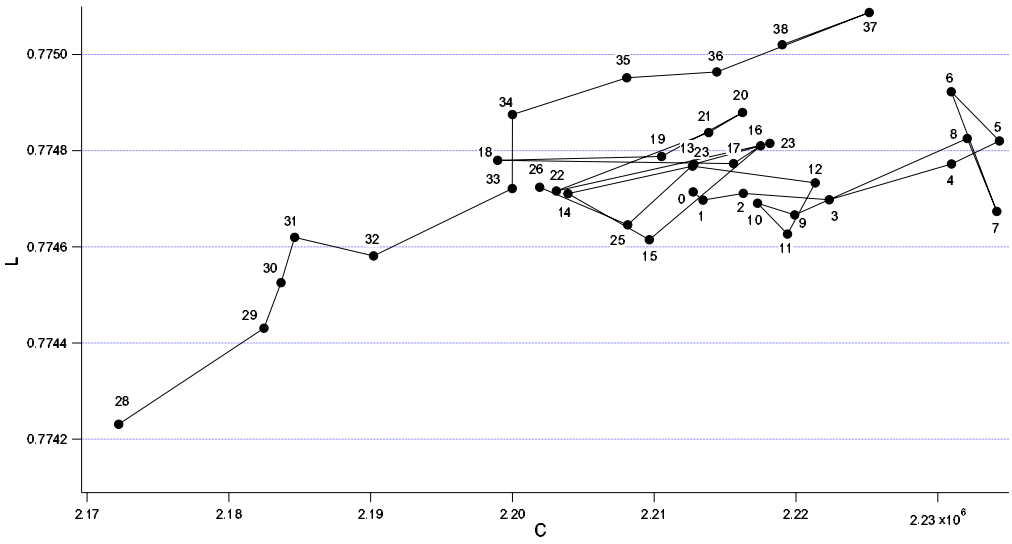


Figure 3: Preliminary results for trimester (three-month) averages of the leader fraction L vs. count rate C (in counts per hour) in the 18NM64 at Doi Inthanon during 2007-2017. Labels indicate the time period, starting at 0 for the last trimester of 2007 and ending at 38 for the second trimester of 2017. The hysteresis indicates that for solar modulation over this period, the spectrum did not "roll" down and "unroll" back up in the same way.

PoS(ICRC2017)025

time period, starting at 0 for the last trimester of 2007 and ending at 38 for the second trimester of 2017.

Note that L serves as a measure of the GCR spectral index at rigidities substantially above the cutoff rigidity of ≈17 GV (i.e., increasing L implies a lower multiplicity and a softer spectrum), while C measures the GCR flux just above the cutoff [8]. How might we expect L to vary with solar modulation? A basic concept of solar modulation is that the cosmic ray spectrum "rolls" downward from the local interstellar spectrum (LIS) and then "unrolls" back up again. The change in the spectrum is much greater at low rigidity, while at sufficiently high rigidity there is almost no solar modulation. Thus we expect that L should increase with increasing C, as the GCR spectrum unrolls to the softer LIS. The widely used range of models with a single modulation parameter assume that the spectrum always rolls and unrolls with the same spectral shape. From such models, we would expect L vs. C to move along a constant track. Any substantial hysteresis (deviation from a prior track) cannot be explained by a model with a single modulation parameter.

From Figures 2 and 3, we can roughly divide the dataset into three modulation periods. From 2007 December to 2010 December (trimesters 0 to 12), C varied significantly but L was roughly constant with minor variations. This corresponds to a horizontal band in Figure 3. Physically, if the flux varies without significant spectral variation, that implies that the GCR spectrum was rising and falling without much change in spectral index. In other words, the solar modulation extended to rigidities much higher than the cutoff.

During the second modulation period, from 2011 January to 2014 June (trimesters 13 to 26), both L and C stayed in the same range with some fluctuations, including Forbush decreases, which have not been removed in the present analysis. ([13] showed that some but not all Forbush decreases in C are also accompanied by decreases in L.) This corresponds to a special 4-year plateau in C at Doi Inthanon, corresponding to the time when the heliospheric current sheet tilt angle $\gtrsim 50^\circ$, a plateau was not observed in NM at low cutoff rigidity [9]. The weak variation of L confirms that there was little systematic change in modulation conditions during this time period above the Doi Inthanon cutoff rigidity of about 17 GV. During this time there was a change in solar magnetic polarity.

After trimester 27 when the time delay histograms were not usable, we observed a third modulation period from 2014 October to 2017 June (trimesters 28 to 38), i.e., to the end of our analysis period, in which C and L increased in tandem from their solar-cycle minimum values. Interestingly, L reached a higher value in 2017 than during the record-high GCR maximum of 2009, indicating an even softer spectrum in 2017. When L changes strongly together with C, this indicates a strong change in the spectrum over rigidities above the cutoff, implying that the spectral change due to modulation in this period was concentrated at rigidities slightly above the cutoff, with much less change at rigidities well above the cutoff. In other words, the solar modulation did not extend far above the cutoff, in contrast with the first modulation period.

This third period has a nearly linear track in L vs. C that is not consistent with the horizontal track during 2007 December to 2010 September. The intermediate second modulation period, in which neither L or C varied systematically over about 4 years, is at a region of the C-L plane that could be assigned to either track. The existence of two distinct tracks in this plane cannot be explained by models with a single modulation parameter. These results serve as yet another example of a difference in solar modulation after a change in solar magnetic polarity. We see that the leader

PoS(ICRC2017)025

fraction inferred from time-delay histograms at Doi Inthanon provides new information on solar modulation above ~ 20 GV, extending the rigidity range of information from the worldwide NM network.

Acknowledgments

We thank Warit Mitthumsiri and Pierre-Simon Mangeard for useful discussions. This work was supported by grant RTA5980003 from the Thailand Research Fund and by US National Science Foundation awards PLR-1245939 and PLR-1341562 and their predecessors.

References

[1] Aiemsa-ad, N., Ruffolo, D., Sáiz, A., et al. 2015, JGRA, 120, 5253

[2] Balabin, Yu. V., Gvozdevsky, B. B., Vashenyuk, E. V., & Schur, L. I. 2008, Proc. 30th ICRC (Mérida), 1, 257

[3] Bieber, J. W., Clem, J. M., Duldig, M. L., et al. 2004, ApJ, 601, L103

[4] Forbush, S. E. 1954, JGR, 59, 525

[5] Jokipii, J. R., & Thomas, B. 1981, ApJ, 243, 1115

[6] Kollár, V., Kudela, K., & Minarovjech, M. 2011, Contrib. Astron. Obs. Skalnaté Pleso, 41, 5

[7] Mangeard, P.-S., Ruffolo, D., Sáiz, A., Madlee, S., & Nutaro, T. 2016a, JGRA, 121, 743

[8] Mangeard, P.-S., Ruffolo, D., Sáiz, A., et al. 2016b, JGRA, 121, 11620

[9] Mangeard, P.-S., Clem, J., Evenson, P., et al., these proceedings

[10] McDonald, F. B., Webber, W. R., & Reames, D. V. 2010, GRL, 37, L18101

[11] Mewaldt, R. A., Davis, A. J., Lave, K. A., et al. 2010, ApJL, 723, L1

[12] Oh, S., Bieber, J. W., Evenson, P., et al. 2013, JGRA, 118, 5431

[13] Ruffolo, D., Sáiz, A., Mangeard, P.-S., et al. 2016, ApJ, 817, 38

[14] Sáiz, A., Mitthumsiri, W., Ruffolo, D., Evenson, P., & Nutaro., T, these proceedings

PoS(ICRC2017)025

PROCEEDINGS OF SCIENCE

Measurement of cross-counter leader fractions in an 18NM64: Detecting single and multiple atmospheric secondaries

Alejandro Sáiz*, **Warit Mitthumsiri, David Ruffolo**
Department of Physics, Faculty of Science, Mahidol University, Bangkok 10400, Thailand
E-mail: alejandro.sai@mahidol.ac.th, warit.mit@mahidol.ac.th, david.ruf@mahidol.ac.th

Paul Evenson
Bartol Research Institute, University of Delaware, Newark, DE 19716, USA
E-mail: evenson@udel.edu

Tanin Nutaro
Department of Physics, Faculty of Science, Ubon Ratchathani University, Ubon Ratchathani 34190, Thailand
E-mail: tnutaro@yahoo.com

The Princess Sirindhorn Neutron Monitor (PSNM) is an 18NM64 (with 18 counter tubes in a continuous row) at 2560 m altitude in Doi Inthanon, Thailand. In late 2015, the electronics in the PSNM were upgraded so as to return an absolute time, referenced to the GPS time, for each neutron count recorded. The timing accuracy is approximately ± 3 μs. This permits extending the well-known concept of multiplicity (multiple correlated counts in one detector) to what we refer to as 'cross multiplicity' or correlation of counts in one detector with those in another. At present, the data are recorded as cross-counter time-delay histograms with 5-μs bins. A cross-counter relative leader fraction L_{ij} can be defined as the fraction of pulses measured in counter number i that are uncorrelated in time with the next pulse in counter j. For simplicity, we derive average cross-counter leader fractions L_Δ with $\Delta = |i-j|$ as a function of counter tube separation, from a tube separation $\Delta = 0$ (i.e., using the same tube) to $\Delta = 17$. For low tube separation, L_Δ rapidly increases with increasing Δ, as expected from the spatial spreading of neutrons produced by the same atmospheric secondary particle inside the neutron monitor. At high tube separation, L_Δ increases slowly with increasing Δ and remains different from unity, which we interpret as due to multiple atmospheric secondaries arriving in rapid succession after originating from the same primary cosmic ray.

35th International Cosmic Ray Conference
10–20 July, 2017
Bexco, Busan, Korea

*Speaker.

© Copyright owned by the author(s) under the terms of the Creative Commons Attribution-NonCommercial-NoDerivatives 4.0 International License (CC BY-NC-ND 4.0).

PoS(ICRC2017)047

1. Introduction

Neutron monitors (NMs) are ground-based detectors of 'secondary' cosmic rays (mostly neutrons) that are produced in Earth's atmosphere by interactions of ('primary') cosmic rays with energies $\sim$1 GeV and above. In an NM, a number of gas-filled proportional counters operate inside several tons of Pb (the producer) to detect individual 'tertiary' neutrons produced from the collisions of atmospheric secondary cosmic rays with Pb nuclei. The rate of detection, and its variations, can then be related to the flux of primary cosmic rays arriving to Earth.

The Princess Sirindhorn Neutron Monitor (PSNM) is located on the top of Doi Inthanon, Thailand's highest mountain, at longitude 18.59° N, longitude 98.49° E, and 2560 m above sea level. The geomagnetic cosmic ray cutoff there is higher than at any other NM location around the world. The main detector contains 18 neutron counters in a continuous row following the NM64 design [1]; 3 other counters operate outside the Pb producer (bare counters).

Aiming to have a measurement of cosmic ray energies as well as flux, the data acquisition system at the PSNM records also the time of each neutron detection. The distributions of time delays, or times between consecutive neutron detections, can be analyzed to extract a leader fraction L that quantifies the number of detections that are statistically uncorrelated with the previous detection, relative to the total [2]. Typically, two neutron detections that originate from two different cosmic rays are uncorrelated in time as in a Poisson process; on the other hand, tertiary neutrons produced by the same atmospheric secondary in the Pb are detected within a few ms and statistically correlated. Thus L can be shown to be related to the energy spectrum of cosmic rays, since production in the Pb increases for higher cosmic ray energy.

In our previous work [2, 3], time delay distributions were studied for consecutive detections in the same neutron counter, and L was calculated for each of the 18 counters independently. Here we note that neutrons produced together in the Pb (from the same secondary) often get detected by different counters. Also, some time correlation may arise from the detection of different atmospheric secondaries that were produced together in the atmosphere (i.e., from the same primary). For the sake of understanding these processes, in late 2015 the electronics in the PSNM acquisition system were upgraded to allow for cross-counter time delay analysis. In this work, we introduce the technique that allows us to study time correlations between neutrons detected in different counters, we define the appropriate cross-counter leader fractions, and we present some preliminary results of their measurement at the PSNM.

2. Absolute times in an NM

To allow for time calculations, the electronics on each neutron counter tube runs an oscillator at 3686.40 kHz to define a sequence timer. When a new detection pulse is registered, its time is recorded based on the sequence timer. A time delay between consecutive pulses recorded in the same counter tube can be easily computed from the difference between values of the sequencer; this technique has been used in the PSNM since it started operating in 2007 [2]. However, since the oscillators on different counters are not synchronized, and the main data acquisition system needs to 'read' the data from each counter sequentially, the values of the sequencer for two different counters are not enough to compute a cross-counter time delay.

PoS(ICRC2017)047

To circumvent this difficulty, the new system deployed in late 2015 uses a once-per-second signal, based on GPS time, sent simultaneously from the main system to all the counters; each counter then records the value of its sequencer corresponding to that synchronization signal. When the data acquisition software receives the data, it can then convert the value of the sequencer of each counter into a GPS time; for stability, this is done once per minute by a fit to the once-per-second values received during the last minute. The achieved timing accuracy is estimated to be approximately ± 3 μs.

3. Distributions of cross-counter time delays

Once every neutron detection is assigned a GPS time, any desired time delay can be computed simply as a difference. In this work, we define a cross-counter time delay t from counter i to counter j, for each detection in counter i, as the time until the earliest detection in counter j. Let $R_{ij}(t)$ be the 'survival' probability that no event on counter j has arrived within time delay t after the event of interest on counter i. In analogy with [2], we have

$$R_{ij}(t) = \exp(-\alpha_j t) \exp\left[-\int_0^t \beta_{ij}(t')\mathrm{d}t'\right], \tag{3.1}$$

where α_j is the probability per time of a chance coincidence in counter j, and $\beta_{ij}(t')$ is the probability of a temporally related count on j after time delay t'. (While there is no direct electronic dead time to prevent registration of a count on a different tube j after a count on i, $\beta_{ij}(t')$ does include indirect effects of the dead time. For example, if a count on i immediately followed a count on j, then j would be unable to register a new count for ~ 80 μs.) At a time t, after a few ms, $\beta_{ij}(t')$ is very close to zero (i.e., the neutron counts associated with the same primary CR have all been collected) and the second exponential tends to a constant value that we call the leader fraction L_{ij}, i.e., the probability that a count on i is not temporally associated with any later count on j. Then the normalized distribution of time delays n_{ij} is given by

$$n_{ij}(t) = -\frac{\mathrm{d}R_{ij}}{\mathrm{d}t}. \tag{3.2}$$

At long times, the exponential tail of the normalized distribution can then be expressed as

$$n_{ij}(t) \to \alpha_j L_{ij} \exp(-\alpha_j t) \qquad t > t_{\mathrm{trans}} \tag{3.3}$$

for a transition time t_{trans} of a few ms.

To reduce the number of recorded distributions and increase the statistics, in this work we analyze the combined distributions of cross-counter time delays at a given counter separation Δ, or $n_\Delta(t)$, with $\Delta = |i-j|$, for $\Delta = 0, \ldots, 17$. The case $\Delta = 0$ of zero separation is the same-tube time delay distribution studied in our previous work, combined for the 18 counters. Some examples of (unnormalized) distributions are shown in Figure 1. These distributions are recorded both as short-time histograms (with bin size of about 4.9 μs for $t < 5$ ms) and long-time histograms (with bin size of about 0.98 ms up to $t = 1$ s). In Figure 1 the transition from short-time to long-time histogram is visible at $t = 5$ ms. The dashed lines indicate each of the exponential functions that best fit the long-time histogram tail up to 200 ms. Although most prominent at the smaller values of Δ, the peak

PoS(ICRC2017)047

at small t is evident at every separation, indicating that there are some counts that are temporally associated even at the maximum separation of 17, from counter 1 to counter 18. Our interpretation is that the large cross-counter multiplicity seen at small separation is due to interactions inside the NM that produce multiple neutrons and counts on nearby counters. However, for counters at large separation, there is a nearly constant residual cross-counter multiplicity that we attribute to multiple atmospheric secondaries from the same cosmic ray that lead to counts on different random counters.

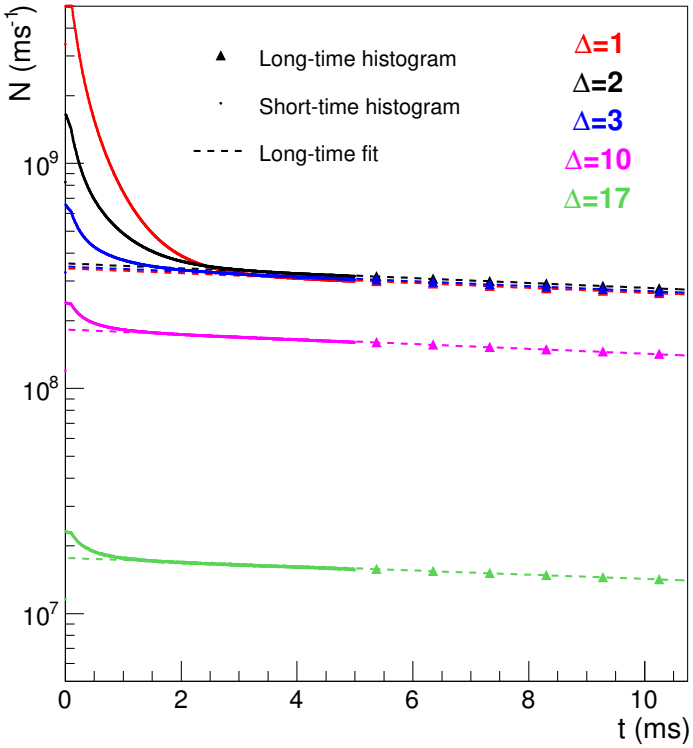


Figure 1: Unnormalized distributions of cross-counter time delays t at counter separation Δ of 1, 2, 3, 10, and 17. Each distribution comes from histograms of t accumulated for $\sim$ 4800 h. Dashed lines are exponential fit functions to the data between 10 and 200 ms.

4. Calculation of cross-counter leader fraction

We define the cross-counter leader fraction at separation Δ, L_Δ, by combining all combinations ij of counters with $|i-j| = \Delta$. Assuming the values of α_j are similar for all j, the equation for the exponential tail then becomes

$$n_\Delta(t) \to \alpha L_\Delta \exp(-\alpha t) \qquad t > t_{\text{trans}}. \tag{4.1}$$

We can use this expression to estimate L_Δ from hourly histograms of t by fitting an exponential function to some interval where $t > t_{\text{trans}}$.

To study the overall properties of L_Δ with good accuracy, in this work we add together several months of hourly data before estimating L_Δ. To improve the fit, we remove the hours when the value

PoS(ICRC2017)047

of α deviated from the mean (α varies due to changes in atmospheric pressure), so the resulting accumulated histograms contain ~ 4800 h of data. For each of the 18 histograms ($\Delta = 0, \ldots, 17$), an exponential function is fit to the t interval 10–200 ms. The two parameters from the fit give α and L_Δ after proper normalization.

5. Results

Figure 2 shows the cross-counter leader fraction L_Δ as a function of counter separation Δ. The values start at less than 0.8 for separation zero (same counter) and quickly increase when considering cross-counter time delays between distant counters, approaching a constant value close to 1. A value of $L_\Delta = 1$ would correspond to totally uncorrelated neutron detections between counters (a Poisson process). However, the value of L_Δ that is observed, which seems to vary little for separations 6–17, is never consistent with 1. We can also see that it cannot be 1 from Figure 1, where the peak at short t is visible above the exponential tail for all separations. A fit to the combined histogram including all separations larger than 5 gives a value $L_{\Delta>5} = 0.9973$.

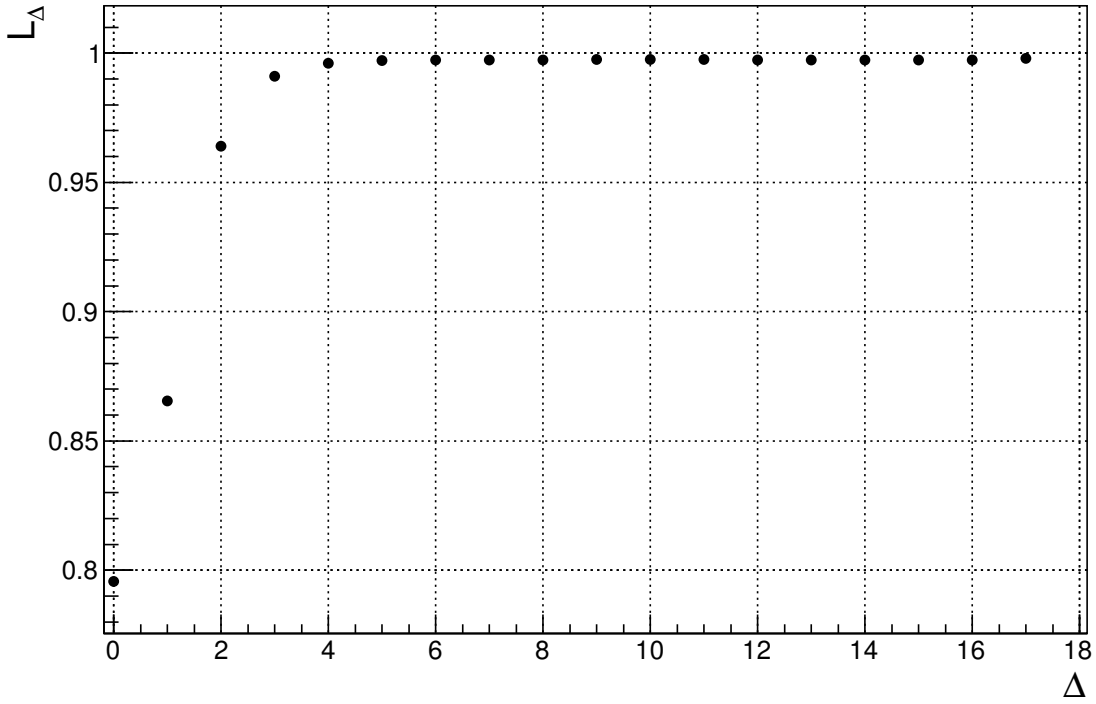


Figure 2: Cross-counter leader fraction L_Δ as a function of counter separation Δ.

For small separation Δ, we can understand the leader fraction (inverse of the multiplicity) as coming from the production of multiple tertiary neutrons in the Pb producer, which subsequently travel inside the NM before being detected by two different counters. The variation of L_Δ with Δ is also consistent with that idea, since there is a smaller probability for a neutron to travel a longer distance inside the NM between the point of production and the point of detection. However, for large separations, propagation of tertiary neutrons inside the NM is not a satisfactory explanation because of the constancy of the value of L_Δ. The most plausible mechanism that could produce

PoS(ICRC2017)047

values of L_Δ different from 1 and independent of Δ is the arrival of two different atmospheric secondary particles that are correlated in time. Secondary cosmic rays are always part of a particle cascade that originates from a single primary cosmic ray and that can extend tens or hundreds of km when it reaches the ground. Thus we would expect the spatial correlation between secondaries to depend on distance negligibly at these scales (counter to counter separation is 0.5 m) and two of these secondaries could arrive to the NM with probability that is independent of Δ.

We therefore interpret the value ~ 0.997 of the cross-counter leader fraction at large counter separation as an atmospheric secondary leader fraction between two counters, which quantifies a correlation between particles of the same atmospheric cascade and that should be present at any distance, and even when no tertiary neutrons are involved. One example, but difficult to test, would be two NMs separated by several km. Another case that could possibly present this atmospheric leader fraction less than 1 is a bare counter. At PSNM, there are three 'bare' counters that are not surrounded by Pb producer (or polyethylene reflector), and the neutrons they detect may include both secondary (atmospheric) neutrons and tertiary neutrons produced from materials in the environment. To test this idea we also calculated the (same-counter) leader fraction L for the 3 bare counters in PSNM, and we find values between 0.996 and 0.998. This suggests that multiple atmospheric secondaries may play a major role in the multiplicity of bare counters.

Considering the entire NM, with 18 counters, the secondary leader fraction can be estimated as $L^{18}_{\Delta>5} = 0.953$. In other words, considering the entire NM, 95.3% of the counts did not follow another count from the same primary cosmic ray and a different atmospheric secondary particle, while 4.7% of the counts did. If we make the additional assumption that energy of the atmospheric secondary is independent of the probability that another secondary produced a count somewhere in the NM, i.e., that probability is independent of the multiplicity due to a given secondary, then we can estimate that 4.7% of the atmospheric secondaries that produced counts in the NM were accompanied by another secondary that also produced counts in the NM. The secondary leader fraction, estimated as 0.953, represents the inverse of the secondary multiplicity, estimated as 1.049.

In previous work, we have shown that the same-counter leader fraction serves as a measure of the Galactic cosmic ray spectral index, and used it to identify short-term spectral variations during Forbush decreases due to solar storms as well as long-term spectral variations due to modulation with the solar activity cycle [2, 3, 4]. The atmospheric secondary leader fraction should be used to correct this same-counter leader fraction when comparing with Monte Carlo results for individual atmospheric secondaries. In further work, we will study whether the cross-counter leader fraction can also serve as an estimate of the cosmic ray spectral index, and whether it provides distinct information from the same-counter leader fraction in order to further constrain the cosmic ray spectrum.

Acknowledgments

Partially supported by the Thailand Research Fund award RTA5980003, TRG5880173, and US National Science Foundation awards PLR-1245939 and PLR-1341562 and their predecessors.

PoS(ICRC2017)047

References

[1] C. J. Hatton and H. Carmichael, *Experimental investigation of the NM-64 neutron monitor*, *CaJPh* **42**, 2443 (1964).

[2] D. Ruffolo, A. Sáiz, P.-S. Mangeard, N. Kamyan, P. Muangha, T. Nutaro, S. Sumran, C. Chaiwattana, N. Gasiprong, C. Channok, C. Wuttiya, M. Rujiwarodom, P. Tooprakai, B. Asavapibhop, J. W. Bieber, J. Clem, P. Evenson and K. Munakata, *Monitoring short-term cosmic-ray spectral variations using neutron monitor time-delay measurements*, *ApJ* **817**, 38 (2016).

[3] P.-S. Mangeard, D. Ruffolo, A. Sáiz, W. Nuntiyakul, J. W. Bieber, J. Clem, P. Evenson, R. Pyle, M. L. Duldig and J. E. Humble, *Dependence of the neutron monitor count rate and time delay distribution on the rigidity spectrum of primary cosmic rays*, *JGRA* **121**, 11620 (2016).

[4] C. Banglieng, D. Ruffolo, A. Sáiz, P. Evenson and T. Nutaro, *Tracking cosmic-ray spectral variations with neutron monitor time-delay measurements at high cutoff rigidity during 2007–2017*, these proceedings.

PoS(ICRC2017)047

PROCEEDINGS OF SCIENCE

Cosmic Ray Modulation Observed by the Princess Sirindhorn Neutron Monitor at High Rigidity Cutoff

P.-S. Mangeard*[a], J. Clem[a], P. Evenson[a], R. Pyle[b], W. Mitthumsiri[c], D. Ruffolo[c], A. Sáiz[c], T. Nutaro[d]

[a] *Bartol Research Institute, University of Delaware, Newark, DE 19716, USA.*
[b] *Pyle Consulting Group, Inc., St. Charles, IL 60174, USA.*
[c] *Department of Physics, Faculty of Science, Mahidol University, Bangkok 10400, Thailand.*
[d] *Department of Physics, Faculty of Science, Ubon Ratchathani University, Ubon Ratchathani 34190, Thailand.*
E-mail: psmangeard@gmail.com, clem@bartol.udel.edu, evenson@udel.edu, rogerpyle@gmail.com, warit.mit@mahidol.ac.th, david.ruf@mahidol.ac.th, alejandro.sai@mahidol.ac.th, tnutaro@yahoo.com.

Solar modulation refers to Galactic cosmic ray (GCR) variations with the ∼11-year sunspot cycle and ∼22-year solar magnetic cycle, and is relevant to the space radiation environment and effects on Earth's atmosphere. Its complicated dependence on solar and heliospheric conditions is only roughly understood but has been empirically modeled in terms of a single modulation parameter. Most analyses of solar modulation used neutron monitor (NM) data from locations with relatively low geomagnetic cutoff rigidity, i.e., the threshold for cosmic rays to penetrate Earth's magnetic field. The Princess Sirindhorn Neutron Monitor (PSNM) at Doi Inthanon, Thailand has the highest cutoff rigidity (≈17 GV) where observations span a complete solar modulation cycle (since late 2007). The pattern of solar modulation at Doi Inthanon during 2011-2014 was qualitatively very different from that at low geomagnetic cutoff, and is not well described by the same modulation parameter. At other times, NM count rates from Doi Inthanon and McMurdo, Antarctica (cutoff <0.01 GV) are linearly correlated and confirm the observation from latitude surveys in the previous solar cycle that the slope of the correlation changes with solar magnetic polarity. Low solar magnetic tilt angles (<40°, at negative polarity) were well correlated with variations at both NM stations as expected from drift models. At higher tilt angle, the Doi Inthanon count rate is well correlated with the interplanetary magnetic field, which is consistent with an expected increase in diffusion at high rigidity short-circuiting effects of drifts and the heliospheric current sheet.

35th International Cosmic Ray Conference
10-20 July, 2017
Bexco, Busan, Korea

*Speaker.

© Copyright owned by the author(s) under the terms of the Creative Commons Attribution-NonCommercial-NoDerivatives 4.0 International License (CC BY-NC-ND 4.0).

PoS(ICRC2017)036

1. Introduction

Galactic cosmic rays (GCRs) are sensitive to solar and heliospheric effects while they propagate from outside the heliosphere to Earth. The GCR flux near Earth is modulated throughout the sunspot (11-year [8]) and solar magnetic (22-year [15]) cycles. As a result, observations of this solar modulation provide important information about global properties of the heliosphere because the GCR transport is affected by the interplanetary magnetic field (IMF), magnetic turbulence, and solar wind speed. High-precision measurements of solar modulation of GCRs are available from fixed NM stations, and these are the subject of the present work. Each NM count rate is an integral measurement above a rather sharp cutoff rigidity. At low cutoff rigidity, there have been continuous measurements of solar modulation for six solar cycles [20, 23].

These detailed time series have defied a simple explanation. One popular model is the spherically symmetric force field model, in which cosmic ray spectra at Earth are characterized by a single modulation parameter, ϕ [5, 13]. Based on NM observations at low cutoff rigidity, empirical modulation parameters have been tabulated as a function of time [12, 24]. Furthermore, there are observed effects of the solar magnetic polarity, A. Guiding center drifts of the charged cosmic rays in the IMF [14, 16] were proposed as a mechanism to explain changes in the time profiles of NM count rates upon a solar magnetic polarity reversal [15]. Another proposed mechanism involves the effect of magnetic helicity on GCR diffusion [3]. Both effects should depend on the product qA. Such charge sign-dependent modulation has been observed [1, 2, 9], but charge sign and energy dependences are not yet fully resolved.

So far, most reported analyses of solar modulation based on NM time series were for relatively low cutoff rigidity; there are not many long-term time series of NM data at $P_c > 12$ GV, as shown in Figure 1. Here we express P_c using the apparent cutoff rigidity [4, 7] determined using the

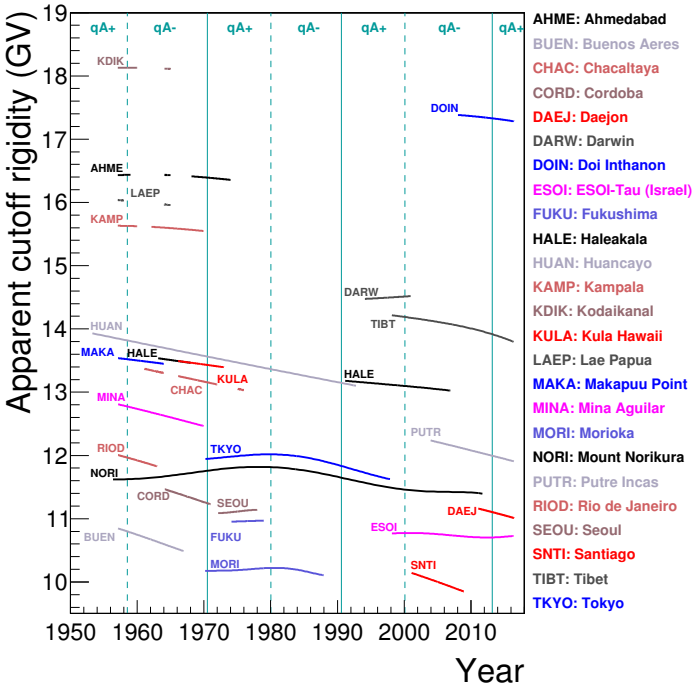


Figure 1: Time periods and apparent cutoff rigidities above 9.5 GV for which NM data are available. Reversals in solar magnetic polarity, near sunspot maxima, are indicated by vertical lines. Since NMs are sensitive to relativistic (positively charged) GCR ions, positive magnetic polarity $A > 0$ results in qA-positive solar modulation, and $A < 0$ results in qA-negative solar modulation. Among the few time series spanning a solar cycle, the NM data from Doi Inthanon, Thailand have the highest apparent cutoff rigidity (over 17 GV) and are the focus of this study.

PoS(ICRC2017)036

International Geomagnetic Reference Field (IGRF-12) and the methods of [17]. For NM stations worldwide with $P_c > 9.5$ GV, Figure 1 shows the time of operation and P_c. We see that there were few NM stations at high P_c with data that spanned a solar cycle and a magnetic polarity reversal. Among these, only the Princess Sirindhorn Neutron Monitor at the summit of Doi Inthanon (DI), Thailand (18.59°N, 98.49°E, altitude 2560 m) had $P_c > 17$ GV, which is the highest cutoff of any NM currently in operation.

In this paper we show that the solar modulation of GCRs as observed at DI from 2007 December to 2017 January exhibited a qualitatively distinct pattern from that observed at low cutoff rigidity. We also demonstrate that a force-field model using an empirical modulation parameter $\phi(t)$ as determined from low-cutoff NM data provides a poor description of the time profile measured at DI. In other words, the spectral effects of solar modulation over roughly 1 to 17 GV are too complex to be well described by a single modulation parameter. We compare the DI NM count rate profile with low-P_c data from McMurdo, as well as the sunspot number, tilt angle of the heliospheric current sheet (HCS), and IMF, and we identify different patterns of solar modulation during periods of low and high tilt angle.

2. Solar Modulation at High Cutoff Rigidity

Neutron Monitor data preparation. PSNM is operated at DI with a complete set of 18 BP-28 ($^{10}BF_3$) neutron counter tubes with the standard NM64 configuration (18NM64). Further details are available from [22]. The present study considers monthly or Carrington (solar) Rotation (CR) averages. The count rate has been corrected for variations in atmospheric pressure. Because of important differences in meteorological conditions at this tropical location between the rainy and the dry seasons, the pressure-corrected count rates have been further corrected using the water-vapor pressure at the surface. The peak-to-peak annual wave in the pressure corrected count rate is not negligible and is estimated at $\sim 0.3\%$ ($\sim 10\%$ of the peak-to-peak solar modulation). More details about this correction will be presented in an article in preparation.

Neutron monitor count rates. Figure 2(a) and 2(b) present the NM count rates averaged over CRs for DI and McMurdo, respectively. From late 2007, the two NM count rates increased until a maximum in late 2009. This GCR maximum followed a very low minimum in the mean total sunspot number (Figure 2(c)) as reported by WDC-SILSO, Royal Observatory of Belgium, Brussels[1], with some delay as expected for solar effects to propagate throughout the heliosphere. After the GCR maximum, both NM count rates mostly decreased throughout 2010. Then two distinct patterns developed: the McMurdo count rate (at low cutoff rigidity) generally decreased from mid-2010 until early 2015, whereas the DI count rate (at high cutoff rigidity) remained relatively stable up to mid-2014. This 4-year plateau started about 2 years before the polarity reversal at the sun observed by WSO (Figure 2(d)) and more than a year before the first polarity reversal in the north hemisphere of the Sun. We can safely assume that this plateau is not directly related to the solar polarity reversal. After removing the main Forbush decreases, some relatively large variations of the count rates at DI with a time scale of several CRs can still be observed. Those variations are also seen in the count rate at McMurdo. This period is followed by a very fast decrease of the

[1] See http://sidc.be/silso/home

PoS(ICRC2017)036

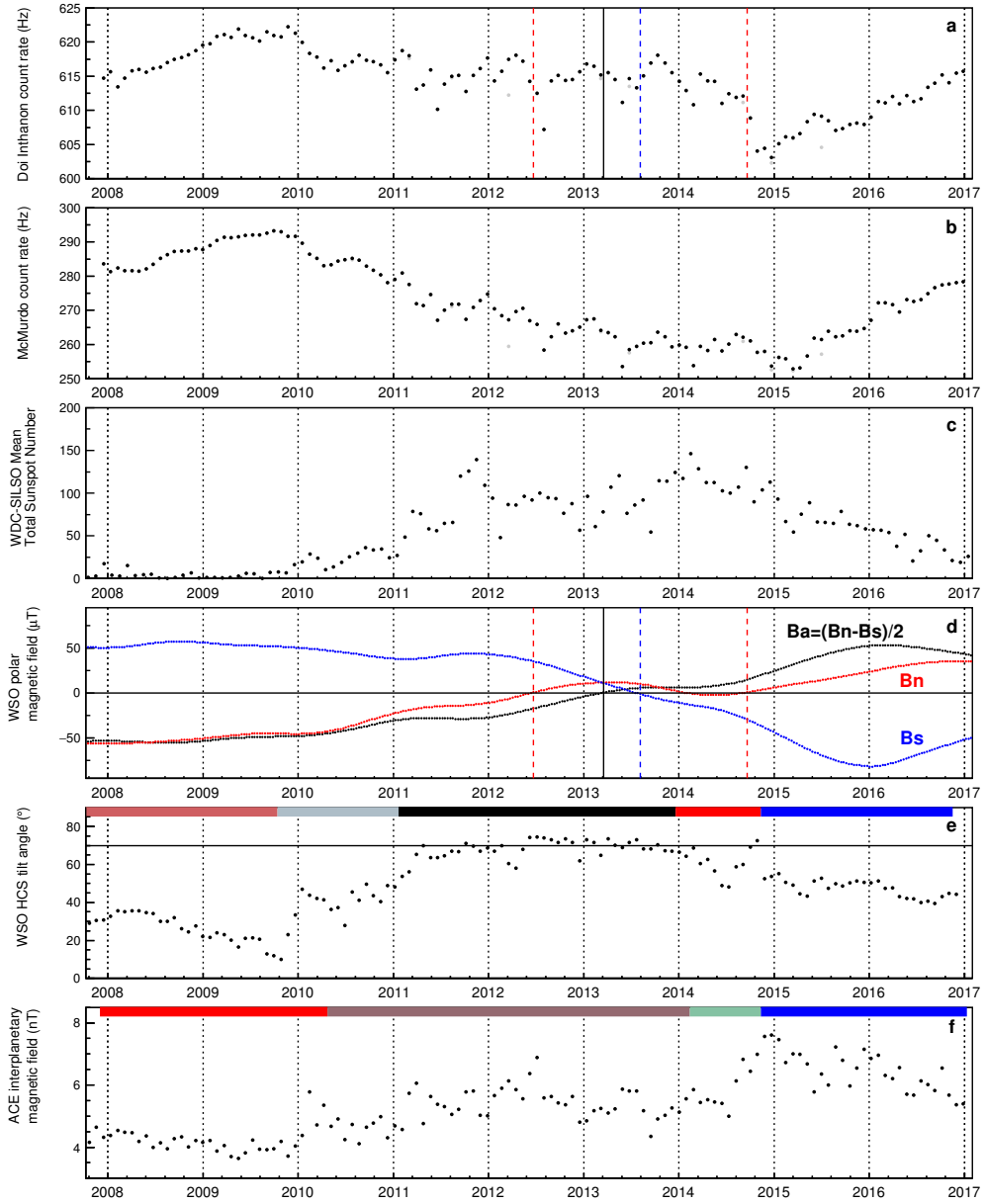


Figure 2: Time series from late 2007 to early 2017 of (a) the pressure- and water vapor-corrected NM count rate at Doi Inthanon, averaged over Carrington rotations (CRs), (b) the pressure-corrected NM count rate at McMurdo, Antarctica, averaged over CRs, (c) WDC-SILSO monthly mean total sunspot number, (d) WSO solar polar magnetic fields (traces explained in the text), (e) WSO heliospheric current sheet tilt angle, averaged over CRs, and (f) *ACE*-MAG interplanetary magnetic field, averaged over CRs. In (a) and (b), fluxes before and after removing periods of strong Forbush decreases are shown by gray and black points, respectively. Vertical lines in panels (a) and (d) indicate the first and last zero crossings of Bn (red, dashed lines) and the zero crossings of Bs (blue, dashed line) and Ba (black, solid line). The horizontal line in panel (e) indicates a tilt angle of 70°; values above this line should be considered as lower limits. The color code over panel (e) indicates time periods of distinct tilt angle levels or trends, as used in Figure 5, while another color code over panel (f) indicates time periods of distinct trends in the count rate at DI, as used in Figures 3 and 6.

PoS(ICRC2017)036

DI count rate that led to the count rate minimum at the end of 2014. The time of the decrease matched with the increase of the ratio e^+/e^- observed by PAMELA [1] and the end of the polarity reversal propagation through the whole heliosphere. From early 2015, the two NM count rates increased until 2017. The last large Forbush decrease was observed in June 2015 and marked the end of the sunspot maximum. The CR-averaged NM count rates at Doi Inthanon and McMurdo are also compared in Figure 3. We note that from December, 2007 (the start of our analysis period) to April, 2010 and from July, 2015 to January, 2017 (the end of our analysis period), there is a very good linear relationship between the two count rates. Note that these time periods correspond to relatively lower tilt angles, roughly speaking when the tilt angle was below about 50°. Such a linear relationship was also found for a ship-borne NM and the McMurdo NM during 1994-2007 [19], with the exception of the year 2000, which again was when the tilt angle was high. Note that the period of high tilt angle during the previous solar cycle (during 2000) was much shorter than during the present solar cycle (during 2010-2014). We also confirm the results of [19, 21] that the slope of the linear relationship between NMs at different cutoffs was higher during the time of negative solar magnetic polarity (Figure 3(b)). This Figure also shows that the slopes were very similar during the periods of rising and falling GCR flux at Doi Inthanon during the $qA < 0$ period.

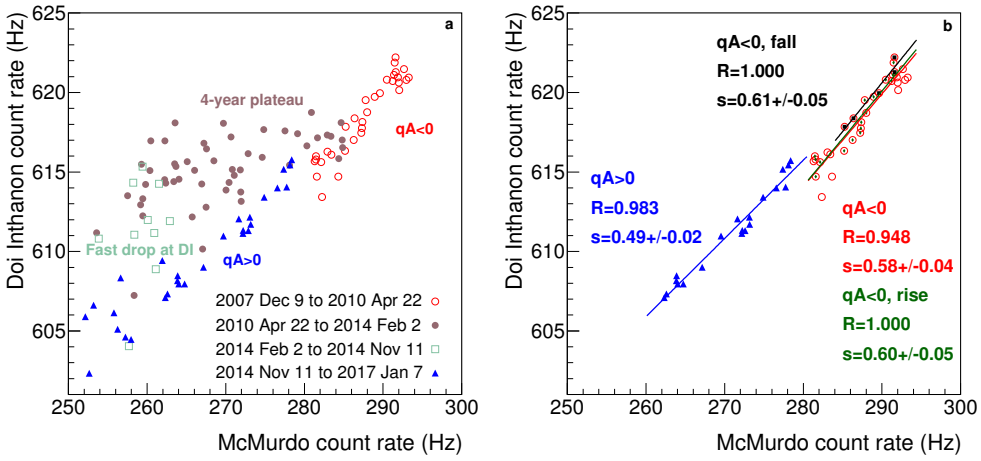


Figure 3: (a) Scatter plot of neutron monitor count rates at Doi Inthanon, Thailand (high cutoff rigidity) and McMurdo, Antarctica (low cutoff rigidity) from December, 2007 to January, 2017. (b) Same plot restricted to the earliest and latest time periods, for a low solar activity and a heliospheric current sheet tilt angle $\lesssim$50°; at such times the two stations' count rates have a linear relationship, and the slope depends on solar magnetic polarity as found by [19, 21]. For higher tilt angle, from mid-2010 to late 2014, there is no longer a linear relationship, as DI has a distinct pattern of solar modulation from that observed at low cutoff.

Comparison with force-field model using modulation parameter determined from monitors at lower cutoff rigidity. For three NM stations, we derived the time series of the spectra of proton and helium at the top of the atmosphere from time series of the solar modulation parameter as seen by a single NM[2] [10, 11, 12], Φ_{NM}. We then applied the simulated yield functions from [18] to determine the count rates expected at DI. The comparison of the simulated count rates with the

[2]Data are available at http://lpsc.in2p3.fr/crdb

PoS(ICRC2017)036

observations at DI are presented in Figure 4. During times of high tilt angle, the solar modulation parameter time series based on NMs at low cutoff provide a poor description of solar modulation at Doi Inthanon, at high cutoff, indicating that solar modulation over a wide rigidity range is not well described by a single empirical modulation parameter. These results are compatible with a spectral crossover at 5-6 GV.

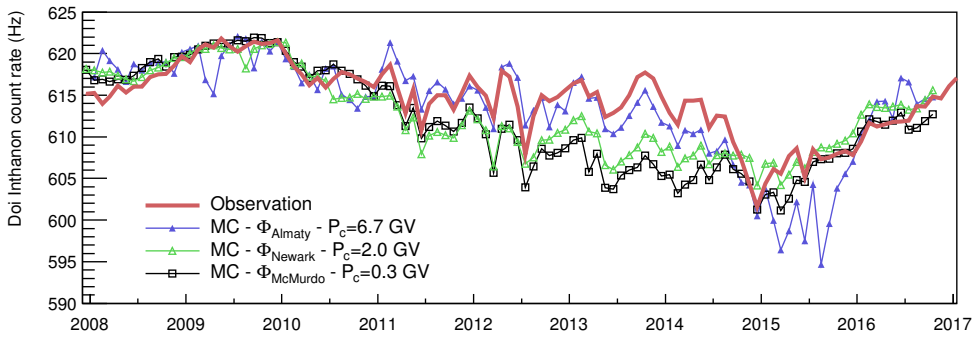


Figure 4: Comparison of the count rate at Doi Inthanon with simulated count rates estimated using the Local Interstellar Spectrum from [10, 11] with the force-field approximation. The solar modulation parameters were estimated from NMs with different rigidity cutoffs, i.e., Almaty, McMurdo, and Newark with the method presented in [12]. The Monte Carlo count rates were normalized to that of PSNM at the cosmic ray maximum (December 2009).

Comparison with tilt angle of heliospheric current sheet. During $qA < 0$, the excess count rate during the solar minimum coincides with a very low value of the tilt angle, 10-20°. This is in agreement with the calculation of [25]. Their model, which includes drift and a wavy neutral sheet, shows a dependence on the tilt angle of the solar modulation during the negative solar polarity. Small tilt angle implies a low modulation effect and thus a high count rate in comparison to that at large tilt angle. From their calculation, we can also expect a much larger dependence on the tilt angle below 30° and a plateau in the modulation for $\alpha \gtrsim 50°$. This behaviour is observed at both DI and McMurdo, respectively, in Figures 5(a) and 5(b). During $qA > 0$, the count rates are less correlated with the tilt angle as expected from solar modulation models that include drifts [25].

Comparison with interplanetary magnetic field. Figure 2(f) presents the time series of the IMF during the period of interest of this work. Inverse correlation between the IMF and the count rate of a NM at low cutoff (Mount Wellington) was already observed and described in [6]. They also reported a loss of correlation in 1969, 1980 and 1990 near the periods of solar polarity reversal. In Figures 6(a) and 6(b) we compared, respectively, the count rates at DI and at McMurdo with the IMF. The loss of correlation, at low rigidity cutoff, between the count rate at McMurdo and the IMF is observed during not only the polarity reversal but during the full period of high tilt angle, i.e., the 4-year plateau (filled circles). However, at DI the correlation at high rigidity cutoff between the count rate at DI and the IMF remained during times at high tilt angle. We observed here a distinct pattern between the modulations at high and low cutoff during the period of high tilt angle and strong solar activity. This could also explain the loss of correlation between the data of the latitude surveys and McMurdo near 2000. This is consistent with an expected increase in diffusion at high

PoS(ICRC2017)036

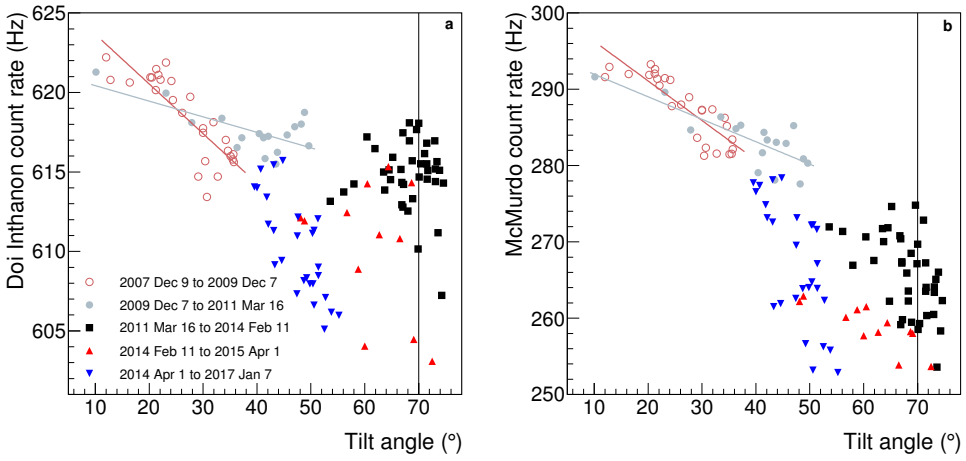


Figure 5: Correlations between the count rates (average per CR) at DI (a) and McMurdo (b) with the WSO heliospheric current sheet tilt angle, averaged over CRs. A delay of two CRs was applied to the count rates to maximize the correlation factors.

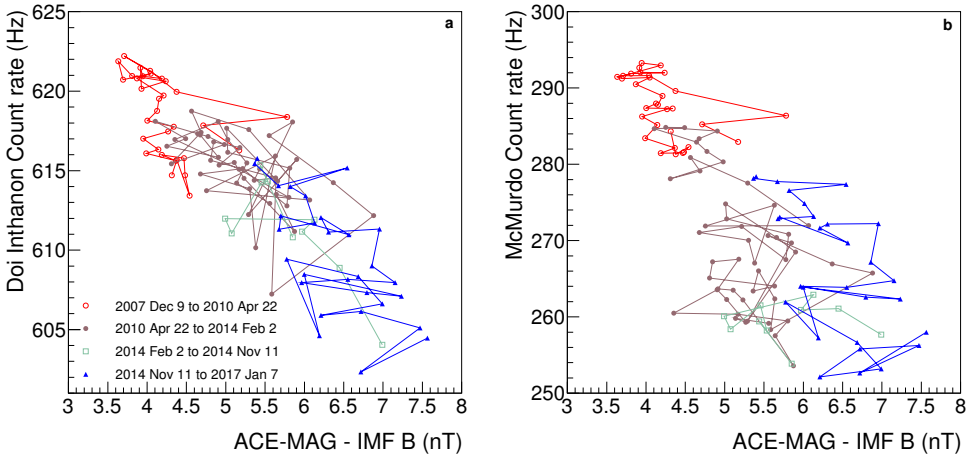


Figure 6: Correlations between the count rates (average per CR) at DI (a) and McMurdo (b) with *ACE*-MAG interplanetary magnetic field, averaged over CRs.

rigidity short-circuiting effects of drifts and the heliospheric current sheet for high tilt angle.

3. Conclusions

During the period of low solar activity, the modulation at high and low cutoffs are linearly related as found by [19]. The slope of the linear relationship depends mainly on the solar polarity. However, during the period of high solar activity, there is a distinct pattern of solar modulation at high cutoff rigidity. A plateau in the count rate at DI is observed while the count rate at McMurdo keeps decreasing. Thus a simple single modulated parameter derived from low cutoff NM data is inadequate to reproduce the modulation at high rigidity.

PoS(ICRC2017)036

Physically, at low tilt angle during the $qA < 0$ polarity (2007 December - 2011 March), the tilt angle is well correlated with NM count rates at low or high rigidity, as expected by drift models. However, at high tilt angle, the DI count rate is better explained by the IMF, which is related to diffusion coefficients. Indeed the overall correlation for the entire solar modulation cycle between the DI count rate and the IMF is quite strong.

Acknowledgments

Partially supported by the Thailand Research Fund awards RTA5980003 and TRG5880173, the United States National Science Foundation awards PLR-1245939, PLR-1341562 and their predecessors.

References

[1] Adriani, O., Barbarino, G. C., Bazilevskaya, G. A., et al. 2016, PhRvL, 116, 241105

[2] Asaoka, Y., Shikaze, Y., Abe, K., et al. 2002, PhRvL, 88, 051101

[3] Bieber, J. W., & Burger, R. A. 1990, ApJ, 348, 597

[4] Bieber, J. W., Clem, J., & Evenson, P. 1997, in Proc. 25th ICRC (Durban), 2, 389

[5] Caballero-Lopez, R. A., & Moraal H. 2004, JGR, 109, A01101

[6] Cane, H. V., Wibberenz, G., Richardson, I. G. & Von Rosenvinge, T. T., 1999, GRL, 26, 5, 565–568

[7] Clem, J. M., Bieber, J. W., Evenson, P., et al. 1997, JGR, 102, 26919

[8] Forbush, S. E. 1954, JGR, 59, 525

[9] Garcia-Munoz, M., Meyer, P., Pyle, K. R., Simpson, J. A., & Evenson, P. 1986, JGR, 91, 2858

[10] Ghelfi, A., Barao, F., Derome, L., & Maurin, D. 2016, A&A, 591, A94

[11] Ghelfi, A., Barao, F., Derome, L., & Maurin, D. 2016, erratum: arXiv:1511.08650v3

[12] Ghelfi, A., Maurin, D., Cheminet, A., et al. 2017, AdSpR, in press

[13] Gleeson, L. J., & Axford, W. I. 1968, ApJ, 154, 1011

[14] Jokipii, J. R., Levy, E. H., & Hubbard, W. B. 1977, ApJ, 213, 861

[15] Jokipii, J. R., & Thomas, B. 1981, ApJ, 243, 1115

[16] Levy, E. H. 1976, JGR, 81, 2082

[17] Lin, Z., Bieber, J. W., & Evenson, P. 1995, JGR, 100, 23543

[18] Mangeard, P.-S., Ruffolo, D., Sáiz, A., Madlee, S., & Nutaro, T. 2016a, JGRA, 121, 743

[19] Nuntiyakul, W., Evenson, P., Ruffolo, D., et al. 2014, ApJ, 795, 11

[20] Oh, S., Bieber, J. W., Evenson, P., et al. 2013, JGRA, 118, 5431

[21] Popielawska, B. 1992, P&SS, 40, 811

[22] Ruffolo, D., Sáiz, A., Mangeard, P.-S., et al. 2016, ApJ, 817, 38

[23] Simpson, J. A. 2000, SSRv, 93, 11

[24] Usoskin, I. G., Bazilevskaya, A., & Kovaltsov, G. A. 2011, JGR, 116, A02104

[25] Webber, W. R., Potgieter, M. S., & Burger, R. A. 1990, ApJ, 349, 634

PoS(ICRC2017)036

PROCEEDINGS OF SCIENCE

Observation of cosmogenic nuclide Be-7 concentrations in the air at Bangkok and trajectory analysis of global air-mass motion

Soichiro Suzuki*[a], Hirohisa Sakurai[a], Fuyuki Tokanai[a], Emiko Inui[b], Hirofumi Shimizu[c], Kimiaki Masuda[d], Warit Mitthumsiri[e], David Ruffolo[e], Ronald Macatangay[f], Satoshi Kikuchi[a], Yutaka Kurebayashi[a]

[a] *Department of Physics, Yamagata University*
[b] *Radioisotope Laboratory, Yamagata University*
[c] *Department of Earth and Environmental Sciences, Yamagata University*
[d] *ISEE. Nagoya University*
[e] *Department of Physics Faculty of Science, Mahidol University, Bangkok, Thailand*
[f] *National Astronomical Research Institute of Thailand, Chiang Mai, Thailand*
E-mail: yamagata.tokanaiekn@gmail.com, sakurai@sci.kj.yamagata-u.ac.jp, tokanai@sci.kj.yamagata-u.ac.jp, Inui@sci.kj.yamagata-u.ac.jp, s12e014@st.yamagata-u.ac.jp, kmasuda@stelab.nagoya-u.ac.jp, warit.mit@mahidol.ac.th, david.ruf@mahidol.ac.th, ronmcdo@gmail.com

We have been continuously observing the daily Be-7 concentrations at Bangkok in Thailand (13.765° N, 100.526° E) since June 2014 to investigate the relationship between solar activities and the variation of cosmogenic nuclides in low latitude. The Be-7 concentrations show a clear seasonal variation with the high and low concentrations during January to May and June to December, respectively, for each year. In order to understand the seasonal variations, we calculated back trajectories of air mass by HYSPLIT. The calculation indicates that the back trajectories are distinguished three patterns in a year, which are "Indian Ocean trajectories", "Continental trajectories", and "Pacific Ocean trajectories". Moreover, we estimated monthly amount of Be-7 coming to Bangkok for each trajectories by EXPACS. From these findings, the amount of Be-7 is high during Continental and Pacific Ocean trajectories. On the other hand, one is low during Indian Ocean trajectories. This phase of calculated Be-7 can explain the seasonal variation. Comparing this phase and the phase of observed Be-7 concentrations, there is a time lag of one or two months.

35th International Cosmic Ray Conference ICRC217-
10-20 July, 2017
Bexco, Busan, Korea

*Speaker.

© Copyright owned by the author(s) under the terms of the Creative Commons Attribution-NonCommercial-NoDerivatives 4.0 International License (CC BY-NC-ND 4.0).

1. Introduction

Cosmogenic radioactive nuclide Be-7 of the half-life of 53 days is produced by spallation interactions between cosmic rays and nitrogen or oxygen in the atmosphere. Once produced, they are immediately oxidized and then attach to aerosols. The aerosols with Be-7 fall down to the ground surface by dry deposition and/or wet deposition.

The nuclide Be-7 is a useful tool to investigate time variations in cosmic rays coming to the whole Earth, because the Be-7 is globally produced in the atmosphere and are fallen down to the surface through global scale air-mass transport. Thus, we have been observing daily Be-7 concentrations sampling aerosols in surface air at Bangkok located at a high cut-off rigidity of the geomagnetic field. There are few observations for the area compared with those for the mid-latitudes[1].

The Be-7 concentrations in surface air are disturbed by a global scale air-mass transport after the Be-7 is produced in the atmosphere. The transport includes the air-mass exchange between the stratosphere and the troposphere, the vertical transport in the troposphere, and the horizontal transport such as from the polar to the tropical region. Therefore, when investigating the time variations in cosmic rays such as solar modulation from those of Be-7 concentrations, it is important to clarify which region that the Be-7 at a sampling site are coming from which region and through which the three-dimensional paths through the atmosphere.

So, we calculated the Be-7 coming to Bangkok employing two kinds of simulators of the Hybrid Single-Particle Lagrangian Integrated Trajectory model (HYSPLIT) and Excel-based Program for calculating Atmospheric Cosmic-ray Spectrum (EXPACS)[2][3].The air-mass trajectories to the sampling site are simulated using the backward function of HYSPLIT and the production rates of Be-7 are simulated for an arbitrary point in the earth atmosphere using EXPACS. In this report, we describe the time profiles of observed Be-7 concentrations at the Bangkok sampling site for three years, the simulated air-mass trajectories, and the amount of Be-7 coming to Bangkok by the simulation, discussing the relationships between them.

2. Experiment and Method

2.1 Sampling and Measurement

Daily Be-7 concentrations in the atmosphere have been continuously observed at the Faculty of Science, Mahidol University in Bangkok since June, 2014. The sampling location is at 13.765° N, 100.526° E, and the altitude is 15 m. A high-volume air sampler (HV-500R) manufactured by SIBATA Company is set for collection of aerosols from the air. The air was collected at 500L per minute. The aerosols with Be-7 is trapped in a sheet of the glass fiber filter with the diameter of 110mm (ADVENTEC GB-100R). The radioactivity of Be-7 in the filter, which emits γ-ray of 477.6keV, was measured using the high-purity germanium γ-rays detector GCW3023 (CANBERRA) at the 20m underground laboratory of the Institute for Cosmic Ray Research (ICRR), Tokyo University. The background level of the detector system is 6.0×10^{-3} cpm on the equivalent channel to the γ-rays energy of the Be-7.

2.2 HYSPLIT and EXPACS

We analyzed the trajectories of air mass motion using HYSPLIT. In this simulation, the meteorological data set GDAS1 (Global Data Assimilation System) was provided by the NOAA's (National Oceanic and Atmospheric Administration) Air Resources Laboratory (ARL). The back trajectories were calculated for all on one dates from June in 2014 to December in 2016 as follows: The end point of trajectories, at which the sampling site, was set at 13.765° N, 100.526° E, with the altitude of 3 m. The trajectory was backward traced up to 30 days with the time interval of 1 hour. The number of calculated trajectories on one date is 24 paths with the time interval of 1 hour. To calculate the production of Be-7 on the trajectory air-mass boxes with 1 km cubic cells are put on the trajectory at 1 hour interval. So the number of air-mass boxes reaching the end point is 720 boxes for the trace duration of 30 days

To calculate amount of Be-7 on each of air mass trajectories flown in Bangkok, we investigated using EXPACS simulation program. EXPACS can calculate the energy spectrum of neutrons and protons at an arbitrary altitude, latitude, longitude, and date considering the vertical cut-off rigidity and the solar modulation of the primary galactic cosmic rays spectra. Using EXPACS, Be-7 production rate $P(x,y,z,t)$ [atoms/g/s] in a time t and three-dimensional coordinates (x,y,z) is calculated as follows:

$$P(x,y,z,t) = \int_{E_1}^{E_2} F_{n,p}(E,x,y,z,t) N_{N,O}(x,y,z) \sigma_{Be-7}(E) dE, \tag{2.1}$$

,where $F_{n,p}(E,x,y,z,t)$ [particles/cm^2/s] is the energy spectrum of neutrons or protons, $N_{N,O}(x,y,z)$ [atoms/g_{air}] is a number of nitrogen or oxygen in air mass, and σ_{Be-7} [cm^2] is the cross-section of Be-7 production. E_1 and E_2 are 10 [MeV] and 100 [GeV], respectively.

The Be-7 in the troposphere, in general, are shown by a differential equation in the box model as follows:

$$\frac{dN_t}{dt} = P - \lambda N_t + k_s N_s - k_t N_t,$$

,where N_t, N_s, and $P(x,y,z,t)$ are Be-7 at the troposphere and stratosphere, and production rate of Be-7, respectively, and k_t, k_s[4][5], and λ are removal rates from boxes in the troposphere and the stratosphere, and disintegration constant of Be-7, respectively.

Since we focused on the air mass trajectories in the troposphere as the first attempt, in the calculation the exchange between the troposphere and the stratosphere was neglected and hence k_s=0. Also, assuming equilibrium between the production rate and the remove rate of Be-7 in the cell, the amount of Be-7 in each cell on the trajectory was calculated. Moreover, as the Be-7 disintegrated in and was removed out of the cell until the cell reaching the end point, the effect was taken account for the amount of Be-7 as follows:

$$N(\tau) = \frac{P(x,y,z,t)}{\lambda + k_t} e^{-(\lambda + k_t)\tau}, \tag{2.2}$$

, where τ is the trace back time. Finally, for a trajectory traced back with the maximum trace back time τ_{max}[6], the total amount of Be-7 reaching the end point was shown as follows:

$$N(\tau_{max}) = \int_{\tau=0}^{\tau=\tau_{max}} N(\tau) d\tau, \tag{2.3}$$

To compare with the monthly profile of observed Be-7 concentrations, the total amount of Be-7 was calculated for the trajectories with the time resolution of 1 hour for one month and then they were averaged.

3. Results and Discussion

3.1 Time profiles of the Be-7 concentrations and trajectories by HYSPLIT analysis

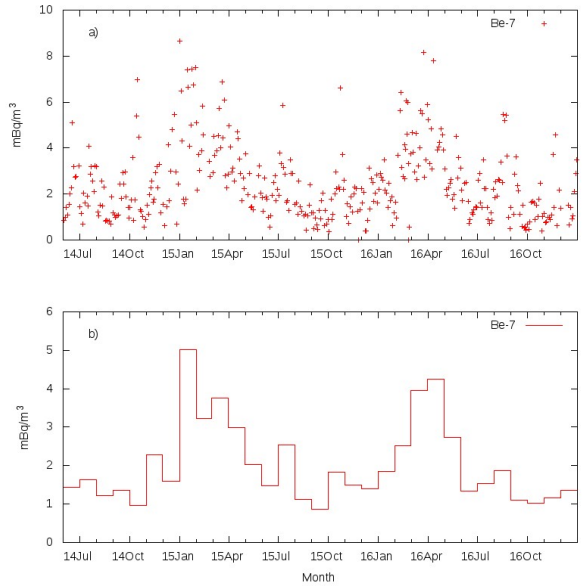


Figure 1: Time profiles of daily and monthly Be-7 concentrations in Bangkok

Fig.1a) and b) show the time profiles of the daily and monthly of observed Be-7 concentration from June in 2014 to December in 2016. The Be-7 concentration shows a clear seasonal variation with the high and low concentrations of 3.4 mBq/m^3 and 1.5 mBq/m^3 during January to May and June to December, respectively, for both years. The peak of high Be-7 concentration is 2.3 times as large as that of the low Be-7 concentration. Fig.2 shows the time profile of Be-7 concentration

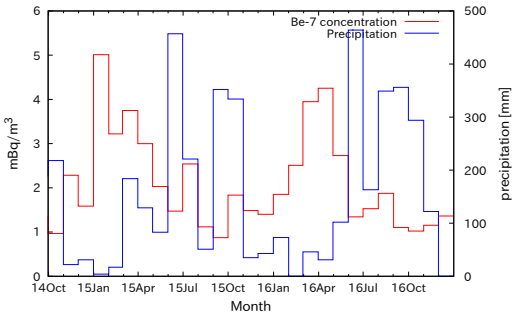


Figure 2: Time profiles of monthly Be-7 concentration and precipitation at Bangkok

compared with that of the monthly precipitation[7] in Bangkok from June in 2014 to December

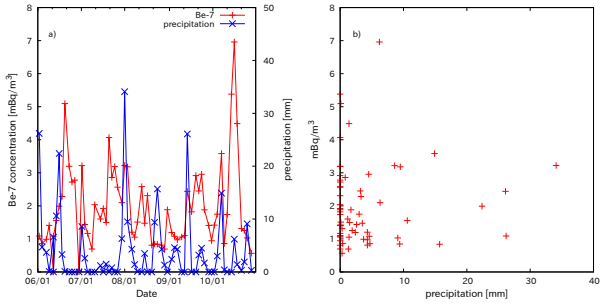


Figure 3: a) Time profiles of daily Be-7 concentration and precipitation during the rain season in2014 at Bangkok. b) scatter plot between them

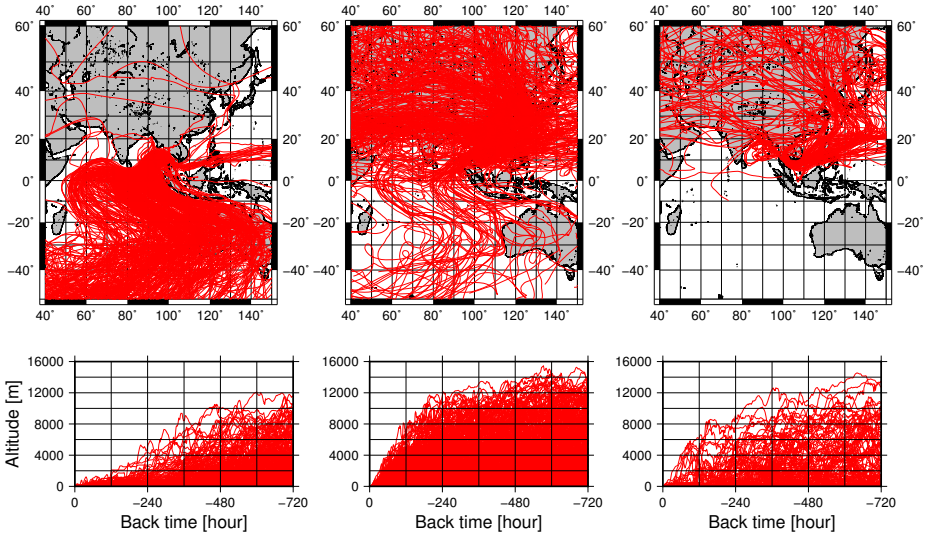


Figure 4: Back trajectories and altitudes of those trajectories. The left panels are from May to September. The center panels are from October to February. The right panels are from March to April.

in 2016. At Bangkok, the rain season is during May to September and the period of small precipitation is during October and April in a year. The seasons correspond to the Indian trajectory, the Continental and Pacific Ocean trajectories of air-mass motion, respectively, as shown in next section. In general, as aerosols are scavenged by rain, it is considered that the Be-7 concentrations are in low level at rainy season. However, as shown in Fig.3a) and b), the relationship between the Be-7 concentration and the precipitation is not so simple from the time profile of daily Be-7 concentration compared with that of the daily precipitation, and the scatter diagram between them for the rain season from June to October in 2014. Therefore, in addition to the local meteorological effects it is necessary to investigate transport processes of Be-7 with global scale.

Fig.4 shows the back trajectories coming to Bangkok and the altitudes of trajectories simulated by HYSPLIT. Their trajectories have three patterns, which we call "Indian Ocean trajectory", "Continental trajectory", and "Pacific Ocean trajectory", corresponding to three durations in the year. The Indian Ocean trajectories, the Continental trajectories, and the Pacific Ocean trajectories are coming to Bangkok through the Indian Ocean, the Eurasian Continents, and the Pacific Ocean. Fig.5 shows the average trajectories for each month. It is clear that the air masses are

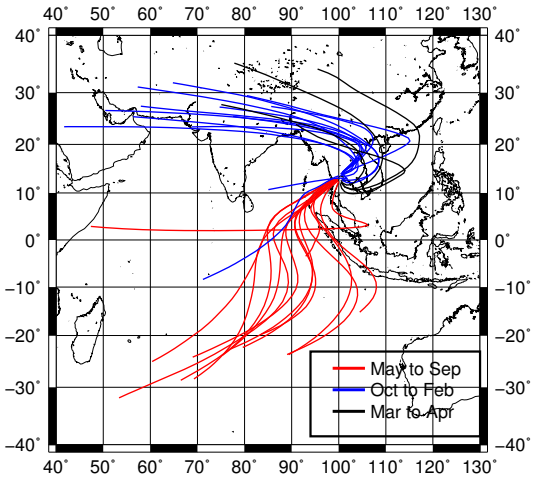


Figure 5: Monthly average latitude and longitude

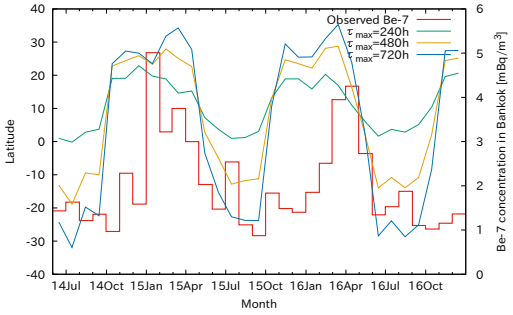


Figure 6: Time profiles of monthly latitudes and the observed Be-7 concentrations

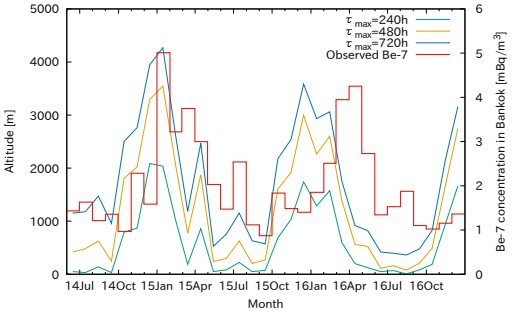


Figure 7: Time profiles of monthly altitudes and the observed Be-7 concentrations

passing through the Indian Ocean, the Eurasian Continent, and the Pacific Ocean, respectively, corresponding to the three seasons.

Fig.6 shows the time profiles of average latitudes for the calculated trajectories for three values τ_{max} (240, 480 and 720 hours), compared with the time profile of the observed Be-7 concentration. The trajectories during October to April, which are the Continental trajectory and the Pacific Ocean trajectory, are passing through relatively high latitudes of approximately 30 degrees. Also, the trajectories during the May to the September, which are the Indian Ocean trajectory, are passing through roughly tropical latitudes. The periods of the enhanced Be-7 concentrations are included in the duration of higher latitudes.

Fig.7 shows the time profiles of average altitudes for the calculated trajectories for τ_{max} (240, 480 and 720 hours), compared with the time profile of the observed Be-7 concentration. The trajectories during October to February, which are corresponding to the Continental trajectory, are passing through relatively higher altitudes. Also, the trajectories during the May to the September, which are corresponding to the Indian Ocean trajectory, are passing through low altitudes. The period of the enhanced Be-7 concentration is shifted from the peak month of the altitudes. Thus, although there are some connection between the seasonal variation of the observed Be-7 concentrations and the air-mass trajectories, the relationship between them is not so clear. Hence, it is

important to simulate the amount of Be-7 transported to Bangkok by each trajectory.

3.2 Simulated Be-7 by EXPACS for trajectories by HYSPLIT

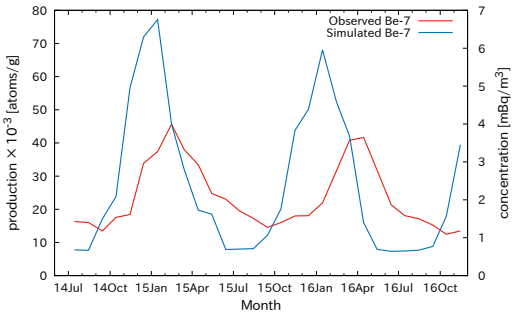


Figure 8: Time profiles of the simulated Be-7 τ_{max}=240 hours and the observed Be-7 concentrations by moving averages

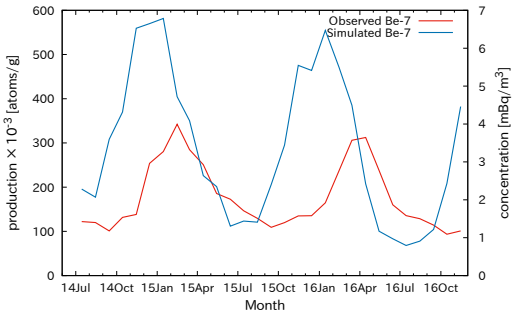


Figure 9: Time profiles of the simulated Be-7 τ_{max}=720 hours and the observed Be-7 concentrations by moving averages

Fig.8 shows the monthly time profile of the simulated amount of Be-7 coming to Bangkok and that of the observed Be-7 concentration with the blue and red lines, respectively. Both lines are moving averages over three months. The simulated Be-7 has an enhanced portion during October to April with a peak in January. Also, the period between the two peaks in 2014 and 2015 is just 1 year, indicating an exactly seasonal variation. Although the observed Be-7 concentration has a time profile similar to the simulated Be-7, the peaks are in February with a time lag of approximately one month from the simulated Be-7. Fig.9 is the same as Fig.8 excepting for the τ_{max}=720 hours. Although the enhancement of the simulated Be-7 shows a broader shape for the larger τ_{max}, the relationship of the time profiles between the observed Be-7 concentrations and the simulated Be-7 is as good as that for τ_{max}=240 hours. The time lag might imply a contribution of the stratosphere component of Be-7 because air mass for the Continental and the Pacific Ocean trajectories passes through high altitudes in the troposphere as shown in Fig.4.

Table 1: Yearly Be-7 concentration at Bangkok, Yamagata, Sun spots Number(SSN), neutron intensity in Thule, N(720) simulated Be-7 for τ_{max}=720 hours in 2014 (from June 2014 to May 2015) and 2015 (from June 2015 to May 2016)

Period	Be-7 at Bangkok (mBq/m^3)	Be-7 at Yamagata (mBq/m^3)	SSN	Thule NM (cnts/hr)	N(720)
2014	2.29	4.9	94.4	4222	247.1
2015	2.11	5.1	57.4	4298	212.5
Rate of variability to 2014(%)	-7.9	4.1	-39.1	1.8	-14.0

Tab.1 shows the Be-7 concentration. The neutron intensity in Thule, and the Sunspot number (SSN) for each year from June 2014 and 2015. The neutron at Thule neutron monitor showing modulation of cosmic rays is increasing with 1.8%, corresponding to the SSN of 39.2% which

indicates a decrease phase of solar activity. Although the Be-7 concentration at Yamagata, Japan which locates in mid-latitude (38.25° N, 140.25° E) is increasing with 4.1% as well as the neutron, the Be-7 concentration at Bangkok is decreasing with 7.9%. Since the simulated Be-7 is decreasing with 14.0% as well as the observed Be-7 concentration at Bangkok, the decrease against to the increase of neutron at polar region might imply a time lag of produced Be-7 coming to the low latitudes.

4. Conclusion

To investigate the relationship between cosmogenic nuclides at low latitude and solar activity, we have been observing the daily Be-7 concentrations at Bangkok, Thailand. The Be-7 concentration was high (3.4 mBq/m^3) during January to May and low (1.5 mBq/m^3) during June to December. From the HYSPLIT analysis, the air mass trajectories for three seasons are characterized by three patterns, "Indian Ocean trajectory", "Continental trajectory", and "Pacific Ocean trajectory". So, we calculated the amount of Be-7 for each trajectory using EXPACS simulations. The time profile of the simulated Be-7 is similar to the observed Be-7 concentration excepting for time lag of one month for the peaks between the simulation and observation. We note that scavenging of aerosols by precipitation may also play a role.

Acknowledgment

The authors also are deeply grateful to the ICRR, which provided the use of the low-background facility for measuring low-level radioactivity. Part of this work was supported by JSPS KAKENHI Grant number 25287051 and JP15K05097. Also, this work is supported partially supported by grant RTA5980003 from the Thailand Research Fund. And this research project is partially supported by Thailand Research Fund awards RTA5980003 and TRG5880173.

References

[1] S. Kikuchi, H. Sakurai, S. Gunji, F. Tokanai. *Temporal Variation of Be-7 concentrations in atmosphere for 8 y from 2000 at Yamagata, Japan: solar influence on the Be-7 time series* J. of Environmental Radioactivity, 100,pp.515-521,2009.

[2] T.Sato and K.Niita. *Analytical functions to predict cosmic-ray neutron spectra in the atmosphere*. Radiat.Res., Vol.166,pp.544-555,2006.

[3] T.Sato, H.Yasuda, K.Nitta, A.Endo, and L.Sihver. *Development of parma: Phits based analytical radiation model in the atmosphere* Radiat. Res., Vol.170,pp.244-259,2008.

[4] H. Nagai, W. Tada, and T. Kobayashi. *Production rates of ^{7}Be and ^{10}Be in the atmosphere*. Nuclear Instruments and Methods in Physics Research B, Vol. 172, pp. 796-801, 2000.

[5] J.F.Bleichrodt. *Mean tropospheric residence time of cosmic-ray-produced beryllium7 at north temperate latitudes*. J.Geophys.Res, Vol. 83, pp.3058-3062, 1978.

[6] K.Hirose,M.Aoyama,Y.Katsuragi, and Y.Sugimura. *Annual deposition of Sr-90, Cs-137 and Pu-239,240 from the 1961-1980 nuclear explosions: a simple model*. Journal of the Meteorological Society of Japan, Vol.65,No.2,pp. 259-277,1987.

[7] *http://www.data.jma.go.jp/gmd/cpd/monitor/index.html*. Meteorological Agency, Japan.

PROCEEDINGS OF SCIENCE

GeV Solar Energetic Particle Observation and Search by IceTop from 2011 to 2016

The IceCube Collaboration[†], **Pierre-Simon Mangeard**[‡], **Pradiphat Muangha**[♯], **Roger Pyle**[♮], **David Ruffolo**[♯], **and Alejandro Sáiz**[♯]

[†] *http://icecube.wisc.edu/collaboration/authors/icrc17_icecube*
[‡] *University of Delaware, Newark Delaware USA*
[♯] *Mahidol University, Bangkok Thailand*
[♮] *Pyle Consulting Group, St. Charles Illinois USA*
E-mail: evenson@udel.edu

Only three Ground Level Enhancements (GLEs) produced by GeV-range solar energetic particles have been confirmed in the present solar cycle, and those have been quite small by historical standards. At the same time direct observations of high energy solar particles from spacecraft have become available. The combination of instruments at the Amundsen - Scott Station at the geographic South Pole offers an opportunity to span the two disparate sets of measurements. Operating at high altitude and low geomagnetic cutoff the neutron monitor at Pole has nevertheless traditionally been accepted as making a "ground level" observation. An enhanced array of bare neutron detectors and IceTop (surface ice Cherenkov detectors in the IceCube Neutrino Observatory) in principle allow spectral information to be extracted from events that previously were too small to use geomagnetic techniques to obtain spectra. We report our spectral measurements for the three confirmed GLE and compare them to other available data on these events. We also present preliminary results of an ongoing study of 34 particle events selected to have significant enhancements in the > 100 MeV channel in GOES data in terms of possible detections and sensitivity limits.

Corresponding author: Paul Evenson*
University of Delaware, Newark Delaware USA

35th International Cosmic Ray Conference - ICRC2017
10-20 July, 2017
Bexco, Busan, Korea

*Speaker.

© Copyright owned by the author(s) under the terms of the Creative Commons Attribution-NonCommercial-NoDerivatives 4.0 International License (CC BY-NC-ND 4.0).

1. Introduction

The only Solar Energetic Particle (SEP) events of relevance to radiation hazards at aircraft altitude are so called Ground Level Enhancements (GLE). GLE can also provide advance warning of lower energy SEP that are primarily responsible for damage to spacecraft [8]. With precision transport modeling [10] it is possible to infer the time profile of acceleration to GeV energies and investigate mean free paths and unusual transport conditions (such as magnetic bottlenecks and loops) in the interplanetary medium [2].

Spaceborne detectors [3, 1] now approach the energy range of ground based detectors. In fact AMS-02 has approximately the same collecting power as the South Pole neutron monitor. It has much better energy and composition sensitivity, but only "looks" in one constantly changing direction at a time. The duration of one orbit is much longer than the timescale of the evolution of anisotropy in a typical solar event. Therefore the network of ground based detectors will remain a vital partner for the life of AMS-02, and will continue observations beyond the planned end of the AMS-02 mission. It is important that systematic investigation of GeV solar particle events remain firmly rooted in this ground based network. Detectors such as IceTop, enhanced neutron detectors at the South Pole [4], and the new neutron monitor at Dome C [9] are important recent additions to this network.

Unfortunately just as these new tools have become available, the number of GLEs during the past solar maximum has been extremely low compared to that in previous solar cycles. Only three GLE have been reported; two are commonly accepted [7, 12] and one is considered problematic [9] because it was not detected by sea level instruments. A question of fundamental importance is whether the paucity of GLEs in the present solar cycle is due to the overall SEP flux of the events, or instead is a spectral effect. To investigate this question we have undertaken to use data from IceTop and from the neutron detectors at the South Pole to understand event systematics. In this paper we discuss our initial event selection and preliminary results. Characterization of the energy spectra and quantitative detection limits are a work in progress.

1.1 IceTop Tanks

IceCube is a cubic-kilometer scale neutrino detector completed in 2010 installed at the geographic South Pole [6]. Reconstruction of the direction, energy and flavor of the neutrinos relies on the optical detection of Cherenkov radiation emitted by charged particles produced in the interactions of neutrinos in the surrounding ice or the nearby bedrock. The Cherenkov light is measured by Digital Optical Modules (DOMs) containing photomultipliers deployed in the ice between depths of 1450 m and 2450 m. IceTop, the surface component of IceCube, is an air shower array with 81 stations. Each station consists of two Cherenkov detector "tanks" which are 2600 kg blocks of clear ice containg standard IceCube DOMs. One DOM in each tank is operated at high gain and the other at low gain in order to extend the dynamic range of the tank. To measure GeV cosmic ray fluxes we use count rates from two discriminators in each high gain DOM, termed SPE (Single Photo Electron) and MPE (Multi Photo Electron). The SPEs are set at selected thresholds ranging between 1 and 20 photoelectrons, while the MPEs are all set near 20 photoelectrons. Changing the discriminator level on a DOM "tunes" the response function of the DOM as illustrated in Figure

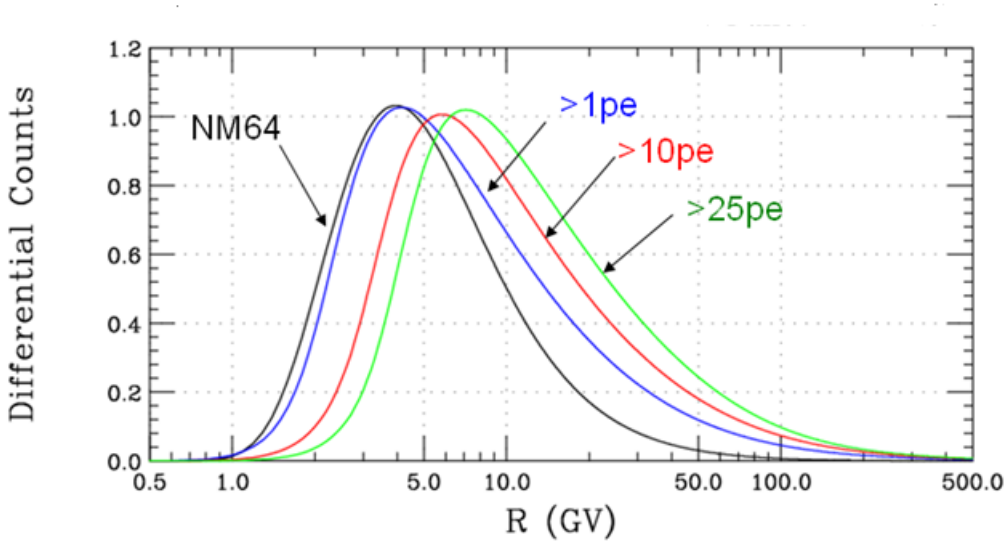


Figure 1: Illustration of response functions of neutron monitor and IceTop tanks for zero GV geomagnetic cutoff and the typical pressure altitude at the South Pole. Calculations were done using FLUKA and GEANT for galactic cosmic ray spectra and composition appropriate to solar minimum modulation conditions.

1. Comparing the counting rates of the various discriminators allows determination of the energy spectrum of the incident particles [7].

1.2 South Pole Neutron Monitor and Polar Bare

There is also a 3NM64 neutron monitor [5] at the South Pole with response (also shown in Figure 1) peaking at lower energy than any of the IceTop thresholds. Lead free neutron detectors at Pole, that we refer to as the “Polar Bares” although a more common name is “Moderated Neutron Detectors" respond to still lower energy [11]. The Bare to Monitor Ratio and the increase in the count rate of either have traditionally been used to identify small GLE [8].

2. Methodology

2.1 GOES Event Selection

In this analysis, we search for GLEs using five years of IceTop and South Pole neutron monitor data. High energy (above 1 GeV) particles responsible for GLEs are almost always part of a steeply falling but continuous spectrum extending to much lower energy. We therefore base our event selection on observations of lower energy protons by the GOES geostationary satellites. We use 5-minute averaged integral proton fluxes for energy thresholds of 10 MeV, 50 MeV, and 100 MeV. We chose events where the peak of GOES >100 MeV proton flux was 0.14 pfu (particle flux unit; 1 particle cm^{-2} $\mathrm{sr}^{-1}\mathrm{s}^{-1}$) because this selection produced cleanly defined onset times. A total of 34 events were found during 2011 to 2016, as listed in Table 2.1. The three known GLE are highlighted in the table. After the events were chosen based on the peak flux, the onset time was

taken as the first measurement clearly above the background. These onset times, as listed in Table 2.1, were used to search for further GLEs that may have escaped independent detection.

YYYY/MM/DD	HH:MM	YYYY/MM/DD	HH:MM	YYYY/MM/DD	HH:MM	YYYY/MM/DD	HH:MM
2011/03/21	03:45	2012/01/27	18:30	2012/09/28	01:15	2014/01/07	19:20
2011/06/07	06:50	2012/03/07	01:30	2013/04/11	07:55	2014/02/20	08:00
2011/08/04	04:20	2012/03/13	17:35	2013/04/24	23:45	2014/02/25	03:30
2011/08/09	08:10	** 2012/05/17 **	01:50	2013/05/22	13:20	2014/04/18	13:20
2011/09/06	03:00	2012/07/07	00:00	2013/09/30	02:30	2014/09/01	21:55
2011/09/06	23:05	2012/07/08	18:00	2013/10/28	18:30	2014/09/10	21:25
2011/09/23	03:20	2012/07/12	17:05	2013/11/02	08:35	** 2015/10/29 **	02:55
2011/11/04	00:05	2012/07/19	06:40	2013/12/28	18:50		
2012/01/23	04:10	2012/07/23	08:30	** 2014/01/06 **	08:00		

Table 1: List of events where greater than 100 MeV protons were clearly detected by the GOES spacecraft. Events previously identified as GLE are indicated with yellow shading and "**". The times given are the onset times used in the analysis.

2.2 IceTop Analysis

Figure 2 shows GLE 71, which occurred on 2012 May 17, as observed by IceTop and the neutron detectors. In the left panel the top traces shows the summed counting rate of the 12 bare neutron detectors and the 3NM64 (kHz). Then there are traces the IceTop DOMs grouped in order of increasing threshold (i.e. decreasing count rate): SPEa, SPEb, SPEc, SPEd, and MPE. These are expressed as the average counting rate per DOM in kHz. The lower panel shows the GOES proton fluxes above three energy thresholds. The steep energy spectrum of the GLE is evident from the pattern of the increases which are quite pronounced at the low thresholds and nearly invisible at the high thresholds.

We use counting rate as a proxy for discriminator setting and also as a simple correction for snow accumulation on the tank. In other words we assume that the reduction in counting rate due to snow accumulation changes the response in the same way as a similar reduction in count rate due to increasing the threshold. This approximation is discussed in more detail by [7] where we also present a preliminary energy spectrum for this event.

In order to conduct a systematic and quantitative search for high energy particles we compare an interval where they might be expected with an immediately preceding interval assumed to contain only background. The dividing line between the two intervals and the length of the intervals were chosen to maximize the visibility of the three established GLE, and then were applied uniformly to the remaining 31 events to conduct the search. The dividing line is always 10 minutes prior to the GOES onset.

Figure 2 shows "base" and "pulse" intervals as well as the GOES onset indicated by the dashed line. We define two statistics, the first is the fractional change of a count rate ratio. For this, both the pulse and base intervals are taken to be 60 minutes. The rate ratio itself, defined by $R_S = (SPEa + SPEb)/(SPEc + SPEd)$, is computed for each minute as shown in the top right panel of Figure 2. For the survey, R_S is averaged over both pulse (R_{SP}) and base (R_{SB}) intervals. The fractional change in the ratio is then $(R_{SP} - R_{SB})/R_{SB}$.

The second statistic is formed from a plot of the fractional change in counting rate of each DOM as a function of the average counting rate of the DOM. This is illustrated in the lower right panel of Figure 2. In this case the averages were taken over 50 minutes. The statistic is the slope of a straight line fit to the distribution, also shown in the figure. (The linear fit appears as a curve on the linear vs. log axes of the figure) Although seemingly closely related, these two statistics are not tightly correlated for background events, as discussed below.

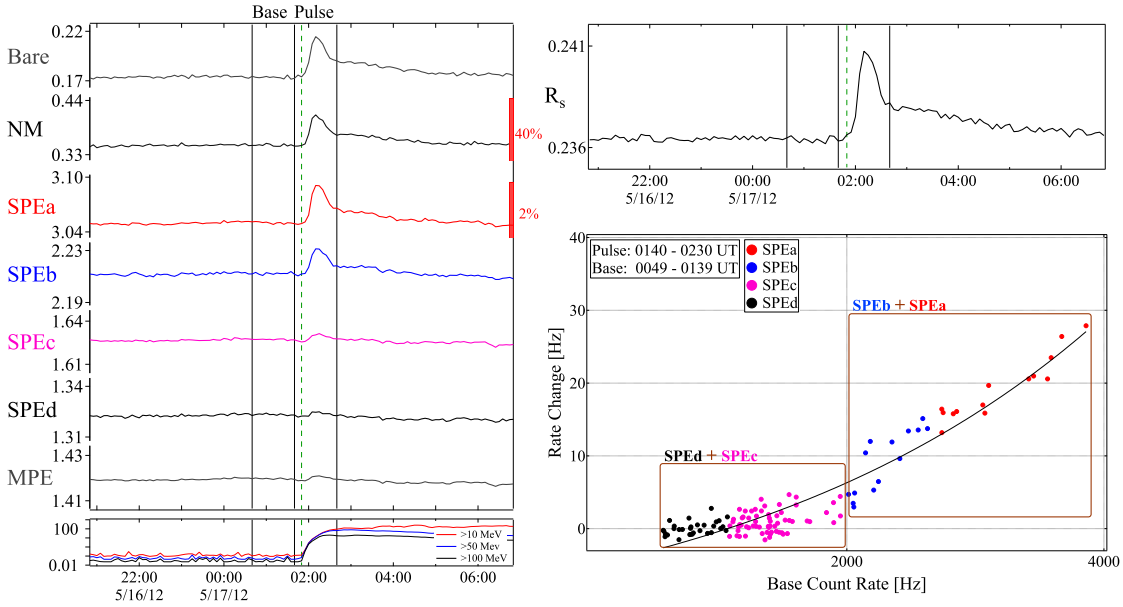


Figure 2: The ground level enhancement (GLE71) on 2012 May 17. Left: Observations at South Pole and GOES Spacecraft. Right Top: Analysis to produce ratio parameter. Right Bottom: Analysis to produce ratio parameter. (Horizontal axis on log scale and vertical axis on linear scale.) See text for details.

2.3 South Pole Neutron Monitor and Polar Bare Analysis

The Polar Bares respond to lower energy particles on average than the NM64. The fractional Bare to Monitor ratio and the fractional increase in the count rate of the monitors form a pair of parameters that have traditionally been used to search for small GLE. We use these two parameters, constructed for the same 60 minute intervals as the IceTop ratio statistic, as an alternate method of searching for small GLE, representative of the traditional approach.

3. Results

Figure 3 compares the IceTop analysis with the neutron monitor analysis as scatter plots of the two parameters defined for each. The May 2012 (GLE71) event stands out clearly. Both the January 2014 (GLE72) and October 2015 (GLE73) events lie outside the cluster near the origin if one considers the joint distribution of both parameters, although there are larger fluctuations in either parameter separately. As noted above, the two parameters are not tightly correlated in cases where there is no clear observation of energetic particles.

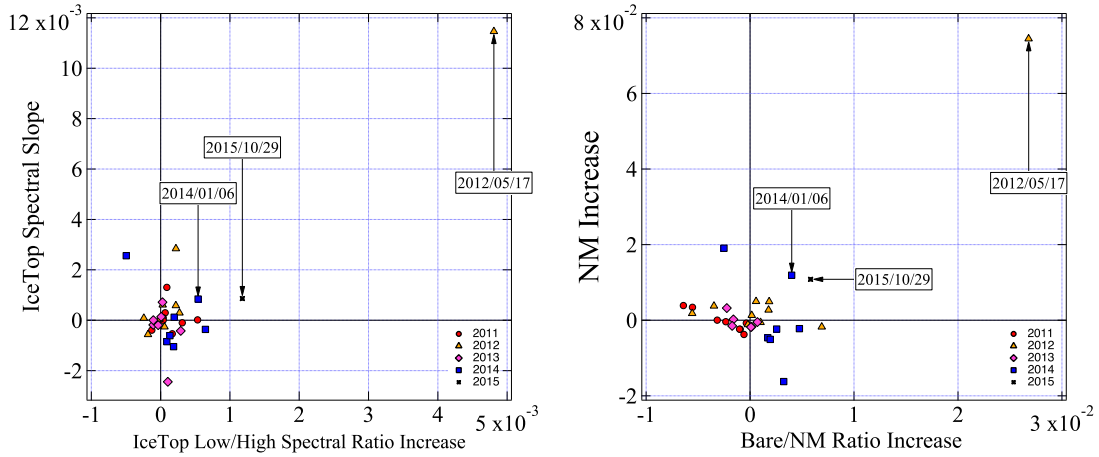


Figure 3: Left: IceTop spectral slope against IceTop spectral ratio. See text for details. Right: Neutron Monitor increase against Bare to Monitor Ratio.

The October 2015 event is barely detected, as the full analysis presented in Figure 4 shows. The identification of this event as GLE73 is supported by the simultaneous detection by the neutron monitor at Dome C in Antarctica [9]. Recognition as GLE73 is in fact debated within the community since it was not detected by any sea level neutron monitors. This therefore probably represents the smallest event that can be detected as a GLE.

Although the two search parameters for IceTop are mostly uncorrelated in the "background" region it is curious that the IceTop spectral ratio parameter clearly has more positive values than negative. It is tempting to speculate that this might indicate the presence of low fluxes of high energy particles as a general feature but we rather think that it is due to some kind of structure in the background.

An example of such a structured background would be the well known Forbush decreases, which have the property that they produce rapid decreases in the counting rate followed by slow increases. The net result is that for intervals chosen at random the count rate is more likely to be increasing rather than decreasing. We would have to investigate whether such an effect might be present in the IceTop ratio before drawing any conclusions. Unfortunately such an investigation is itself not well defined since solar particle events are seldom isolated events. Large events in particular often come in clusters accompanied by major, correlated perturbations of the solar wind.

In this search the monitor data are essentially statistics limited, with the South Pole monitor counting at roughly 300 Hz. In contrast, an IceTop DOM at MPE threshold counts at approximately 1.2 kHz, giving the entire array of 162 tanks at least a factor of ten better statistical accuracy. Unfortunately for this work the increased statistical precision has revealed true fluctuations in the background approximately the same size as the statistical fluctuations in the neutron monitors. Figure 4 shows this clearly, particularly for the higher thresholds where the rates during the pulse interval are clearly *lower* than during the baseline interval. In this case, however, the change in the spectral ratio is still giving a rather clear indication that solar particles are present.

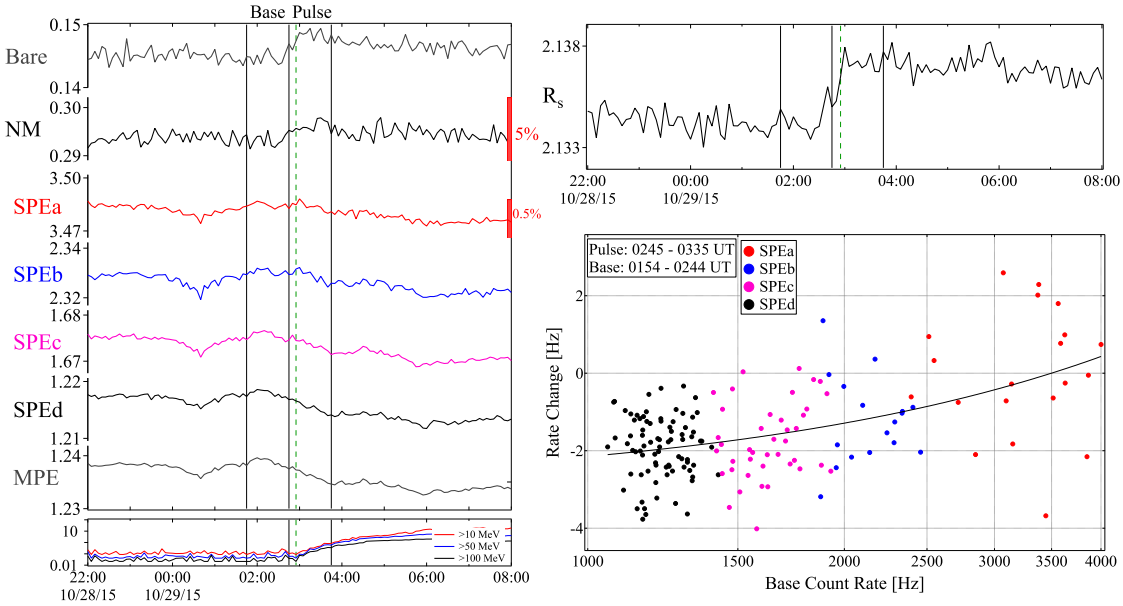


Figure 4: The small ground level enhancement (GLE73) on 2015 October 29.

4. Summary and Conclusions

Our analysis of 34 solar particle events selected for the presence of greater than 100 MeV protons at a GOES spacecraft revealed no definitive GLE other than the ones already known. GLE73, on 2015 October 29 is probably the smallest GLE that could be detected with any degree of certainty. A truly quantitative statement in terms of absolute particle fluxes is not possible because the visibility of the increase depends on the time structure of the event and the asymptotic direction of the detector. IceTop and the Antarctic neutron monitors have similar sensitivity limits for GLE detection although for different reasons. The monitors are statistics limited, but the greater statistical precision of IceTop has revealed true fluctuations in the background approximately the same size as the statistical fluctuations in the neutron monitors. The silver lining to this is that the better statistical accuracy of IceTop will allow a more detailed study of cosmic ray fluctuations, sometimes called "scintillations", than has previously been possible.

5. Acknowledgements

Supported in part by US National Science Foundation awards PLR-1245939 and PLR-1341562 and their predecessors, as well as grant RTA5980003 from the Thailand Research Fund.

References

[1] Adriani, O., G.C. Barbarino, G.A. Bazilevskaya *et al.*, Observations of the 2006 December 13 and 14 solar particle events in the 80 MeV/N Ű 3 GeV/N range from space with the PAMELA detector, *Astrophysical Journal* **742** (2011) 102-112, doi:10.1088/0004-637X/742/2/102.

[2] Bieber, John W., Wolfgang Droege, Paul A. Evenson, Roger Pyle, David Ruffolo, Udomsilp Pinsook, Paisan Tooprakai, Manit Rujiwarodom and Thiranee Khumlumlert, Energetic particle observations during the 2000 July 14 solar event, *Astrophysical Journal* **567** (2002) 622-634.

[3] Bindi, V., Solar energetic particles measured by AMS-02, *International Cosmic Ray Conference 34*, The Hague, Netherlands, (2015) PoS(ICRC2015)108.

[4] Evenson, Paul, John Bieber, John Clem and Roger Pyle, South pole neutron monitor lives again, *International Cosmic Ray Conference 32*, Beijing, (2011).

[5] Hatton, C. J., The Neutron Monitor, *Progress in Elementary Particle and Cosmic Ray Physics* **X** (1971), American Elsevier Publishing Company, New York.

[6] **IceCube** Collaboration, M. G. Aartsen et al., The IceCube Neutrino Observatory: Instrumentation and Online Systems, *JINST* **12** (2017) P03012.

[7] **IceCube** Collaboration, Ground level enhancement of May 17, 2012, observed at South Pole, Paper 0368, *International Cosmic Ray Conference 33*, Rio De Janeiro, (2013).

[8] Oh, S.Y., J.W. Bieber, J. Clem, P. Evenson, R. Pyle, Y. Yi, and Y.K. Kim, South Pole neutron monitor forecasting of solar proton radiation intensity, *Space Weather* **10** (2012), S05004, doi:10.1029/2012SW000795.

[9] Poluianov, Stepan, Ilya Usoskin, Alexander Mishev, Harm Moraal, Helena Krüger, Giampietro Casasanta, Rita Traversi, Roberto Udisti, Mini neutron monitors at concordia research station, Central Antarctica, *J. Astron. Space Sci.* **32(4)** (2015), 281-287 http://dx.doi.org/10.5140/JASS.2015.32.4.281.

[10] Sáiz, Alejandro, Paul Evenson, David Ruffolo, and John W. Bieber, On the estimation of solar energetic particle injection timing from onset times near earth, *Astrophysical Journal* **626** (2005) 1131-1137.

[11] Stoker, P.H., Spectra of solar proton ground level events using neutron monitor and neutron moderated detector recordings, *International Cosmic Ray Conference 19*, La Jolla **4** (1985) 114-117.

[12] Thakur, N., N. Gopalswamy, H. Xie, P. Makela, S. Yashiro1, S. Akiyama, and J. M. Davila, Ground level enhancement in the 2014 january 6 solar energetic particle event, *Astrophysical Journal Letters* **790** (2014) L13-17.

PROCEEDINGS OF SCIENCE

Impulsive Increase of Galactic Cosmic Ray Flux Observed by IceTop

The IceCube Collaboration[†], **Pierre-Simon Mangeard**[‡], **Pradiphat Muangha**[♯], **Roger Pyle**[♮], **David Ruffolo**[♯], **and Alejandro Sáiz**[♯]

[†] *http://icecube.wisc.edu/collaboration/authors/icrc17_icecube*
[‡] *University of Delaware, Newark, DE 19716, USA*
[♯] *Mahidol University, Bangkok 10400, Thailand*
[♮] *Pyle Consulting Group, St. Charles, IL 60174, USA*
E-mail: evenson@udel.edu

On 2017 January 18 scaler rates in the IceTop detectors at the South Pole revealed an impulsive increase in the galactic cosmic ray flux lasting a few hours. In addition to the neutron monitor at Pole the event was detected clearly by the Mawson neutron monitor and faintly at Jang Bogo. No other neutron monitors appear to have seen the increase. The event was in many ways reminiscent of the 2015 June 22 event observed by the GRAPES muon detectors. Both events occurred during the declining phase of a Forbush decrease, at a time of increasing geomagnetic activity, and were observed by a limited number of neutron monitors with similar asymptotic directions. The magnitude of the impulse was in both cases such that the flux returned briefly to approximately the pre-decrease level. Distinctly unlike the 2015 June 22 event, a changing geomagnetic cutoff cannot explain the 2017 January 18 event because the cutoff at South Pole is nearly zero and the detector response is atmosphere limited. We therefore interpret the 2017 January 18 event in terms of the structure of the Forbush decrease and (possibly changing) asymptotic directions. With our interpretation of the January event in mind we also comment on possible alternative interpretations of the GRAPES event.

Corresponding author: Paul Evenson*
University of Delaware, Newark, DE 19716, USA

35th International Cosmic Ray Conference
10-20 July, 2017
Bexco, Busan, Korea

*Speaker.

© Copyright owned by the author(s) under the terms of the Creative Commons Attribution-NonCommercial-NoDerivatives 4.0 International License (CC BY-NC-ND 4.0).

1. Introduction

IceCube is a cubic-kilometer scale neutrino detector completed in 2010 installed at the geographic South Pole [3]. Reconstruction of the direction, energy and flavor of the neutrinos relies on the optical detection of Cherenkov radiation emitted by charged particles produced in the interactions of neutrinos in the surrounding ice or the nearby bedrock. The Cherenkov light is measured by Digital Optical Modules (DOMs) containing photomultipliers deployed in the ice between depths of 1450 m and 2450 m. IceTop is an air shower array with 81 stations located above the in ice installation. A station consists of two Cherenkov "tanks" which are 2000 kg blocks of clear ice using standard DOMs to measure Cherenkov radiation emitted by secondary charged particles. One DOM in each tank is operated at high gain and the other at low gain in order to extend the dynamic range of the tank.

To measure GeV cosmic ray fluxes we use count rates from two discriminators in each high gain DOM, termed SPE (Single Photo Electron) and MPE (Multi Photo Electron). The SPE are set at selected thresholds ranging between 1 and 20 photoelectrons while the MPE are all set near 20 photoelectrons. Setting the discriminator level on a DOM "tunes" the response function of the DOM. The array of different thresholds allows determination of the energy spectrum and time structure of variations in the interplanetary cosmic ray flux. See [4] for a more extensive discussion of the energy response of IceTop. There is also a 3NM64 neutron monitor [2] at the South Pole with response peaking at lower energy than any of the IceTop thresholds. Lead free neutron detectors with yet lower energy response that we refer to as the "Polar Bares" (although a more common name is "Moderated Neutron Detectors") [9] are installed in the main station. For details of the neutron detectors at the South Pole see [1].

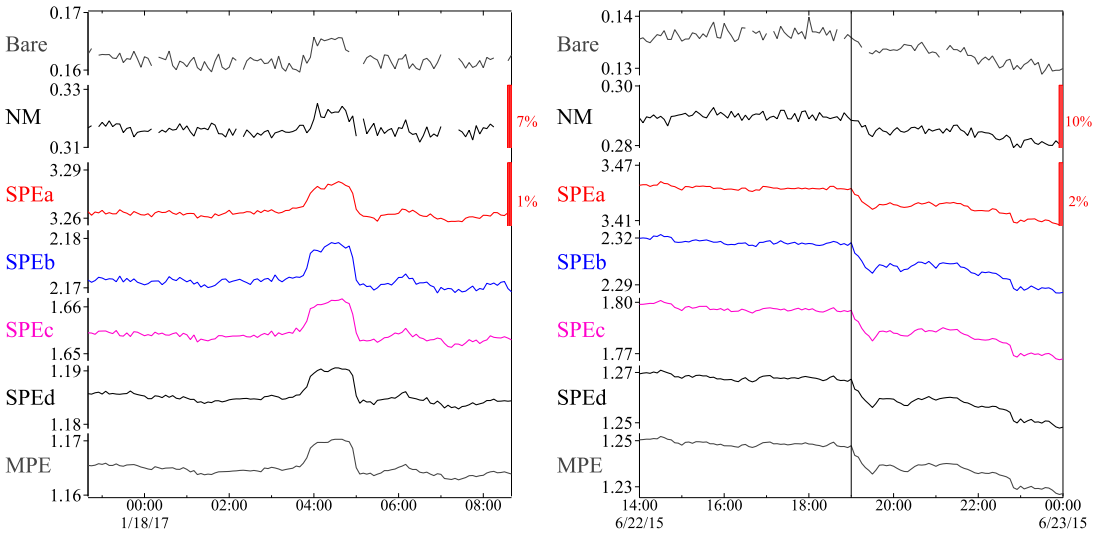


Figure 1: Left: Impulsive increase in cosmic ray flux seen by IceTop and the South Pole neutron detectors on 2017 January 18. Right: IceTop response at the time of the impulsive increase reported by GRAPES on 2015 June 22. All plots are logarithmic with rates expressed in kHz.

On 2017 January 18 IceTop observed the impulsive increase in the cosmic ray flux illustrated at the left in Figure 1. In this figure the top two traces show the total count rate of the moderated

neutron detectors and 3NM64 neutron monitor respectively, while the next five traces give the average counting rate of IceTop DOMs grouped in order of increasing threshold. The similar-sized increase at all thresholds in IceTop and neutron detectors indicate that the impulsive increase has a hard spectrum, very close to that of the galactic cosmic rays. A small enhancement was also seen at the nearby neutron monitors at Mawson and Jang Bogo, but no others. Thus it is evidently a highly anisotropic fluctuation in the galactic cosmic rays – as opposed to a Ground Level Enhancement (GLE) resulting from solar energetic particles (SEP).

The event seen by IceTop was in many ways reminiscent of the 2015 June 22 pulse event observed by the GRAPES-3 tracking muon telescope in Ooty, India [7]. Both the IceTop and GRAPES events occurred during the declining phase of a Forbush decrease, at a time of increasing geomagnetic activity, and were observed by a limited number of neutron monitors with at similar geographic locations. The magnitude of the impulse was in both cases such that the flux returned briefly to approximately the pre-decrease level. An explanation proposed for the GRAPES event [7] is a temporary reduction in the geomagnetic cutoff amounting to 0.5 GV to 0.7 GV depending on the incident direction of the particles.

On the right in Figure 1 we show data from the South Pole detectors at the time the pulse event was observed by GRAPES. Since any SEP event gives a much stronger increase at low cutoff rigidity the absence of an increase at South Pole definitively confirms that the event is not a classic GLE. The clear depression in count rates at the South Pole at the time of the start of the GRAPES pulse (vertical line) was presumably produced by the same magnetic disturbance. Since the cutoff is zero at the South Pole, and therefore cannot decrease, the lack of a pulse in and of itself does not contradict the explanation proposed [7] for the GRAPES event.

However, by the same logic, a changing geomagnetic cutoff cannot explain an increase such as seen on 2017 January 18. The only explanation for the 2017 January 18 event is a significant anisotropy in the interplanetary cosmic ray flux. Whether the anisotropy was transient in time or was a result of changing asymptotic directions due to the active geomagnetic conditions at that time cannot be decided. With this picture of the 2017 January 18 event in mind we propose that the GRAPES event also was a manifestation of interplanetary anisotropy rather than a cutoff variation. Primarily we argue that a cutoff variation would make predictions for the world network of neutron monitors that are not in accord with observations.

2. Geomagnetic Cutoff Variations

The Princess Sirindhorn Neutron Monitor (PSNM) on Doi Inthanon in Thailand is close to GRAPES, both geographically and in cutoff rigidity. At PSNM the vertical cutoff, in geomagnetic quiet conditions, is 16.7 GV, whereas the directionally averaged cutoff is 17.3 GV. The counting rate at PSNM at the time of the GRAPES event is shown at the top of the left panel in Figure 2. The timing and structure of the pulse at PSNM is similar to that of the GRAPES pulse. Using our calculated yield functions for PSNM [6] we also find that the magnitude of the increase at PSNM is quite consistent with a cutoff reduction of approximately 0.6 GV. As Figure 2 shows, all neutron monitors show the onset of a large Forbush decrease near this time. Because of the Forbush decrease the identification of a pulse is somewhat subjective but it is clear that only a other few neutron monitors show a pulse as well defined as that at PSNM. For the monitors where the pulse

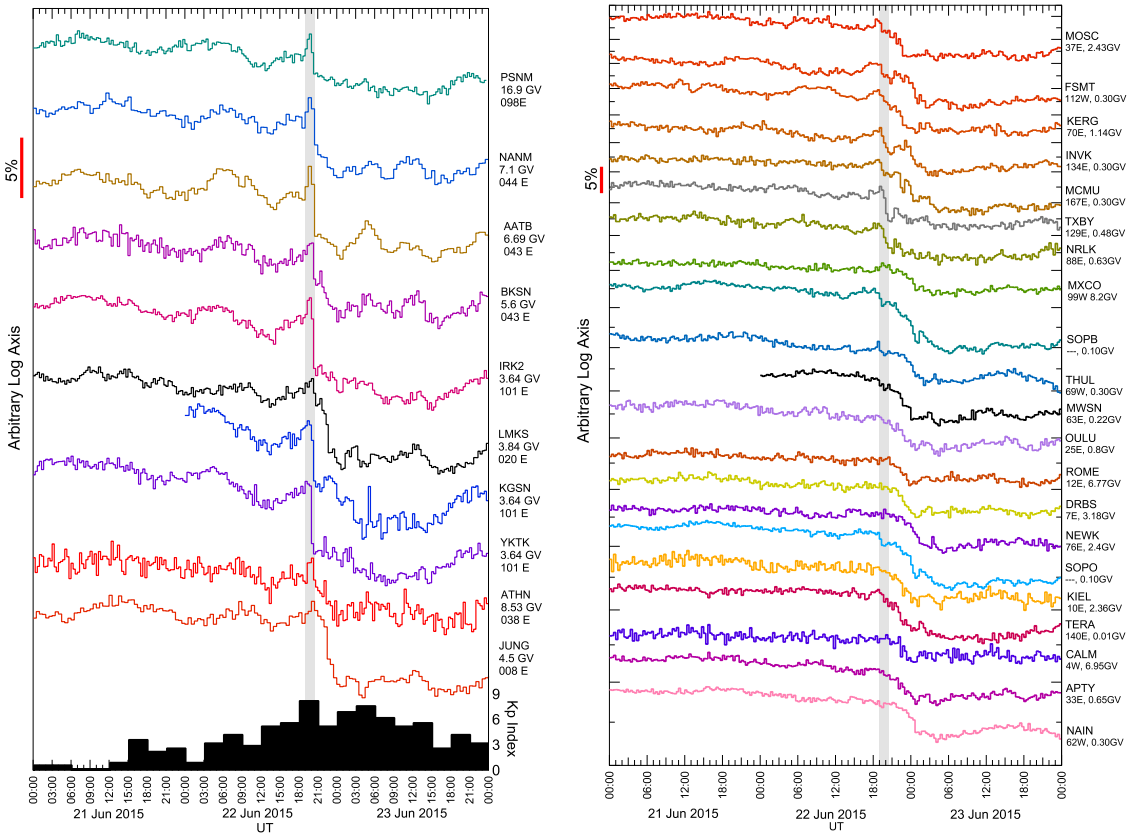


Figure 2: Left: Response of several neutron monitors having the largest increase at the same time as that observed by GRAPES on 2015 June 22. The Kp index of geomagnetic activity is shown in the lower panel. Right: Multiple neutron monitor observations ranked approximately by the intensity of the observed pulse. The approximate duration of the GRAPES pulse is indicated by the gray shading.

is clear (shown in the left panel of Figure 2) the Forbush decrease generally begins immediately and steeply following the pulse. For the other monitors the onset is not as sharp and is delayed by varying amounts. This behavior is characteristic of commonly observed Forbush decrease *precursors*. For a discussion and classification approach to such precursors, see[8].

We also find that a cutoff variation localized to the vicinity of the GRAPES detector is unlikely. In the commonly used Tsyganenko [11] model of the response of the magnetosphere to perturbation by interplanetary disturbances any variation in the geomagnetic cutoff is a fully global process. In this model the geomagnetic field cannot be described as a simple superposition of the interplanetary field and the internal (IGRF) field. Rather, the disturbance of the solar wind perturbs global current systems, and it is these current systems that affect the cutoff. Since these current systems are global, any change in the cutoff must also be global. The left panel of Figure 3 shows our calculation of cutoff changes predicted by the Tsyganenko model, performed by the method described in [5], as a function of Kp, the geomagnetic parameter that is the input to the Tsyganenko model.

Kp is an index computed from the range of fluctuations in the horizontal component of the magnetic field measured at ground level at a specifically defined array of locations. For an excellent discussion of why the single parameter Kp provides a good description of the state of the

magnetosphere see [10]. Note that it is an inescapable prediction of the Tsyganenko model that all locations on Earth have correlated changes in the geomagnetic cutoff, and indeed that cutoff changes are systematically larger for lower cutoffs.

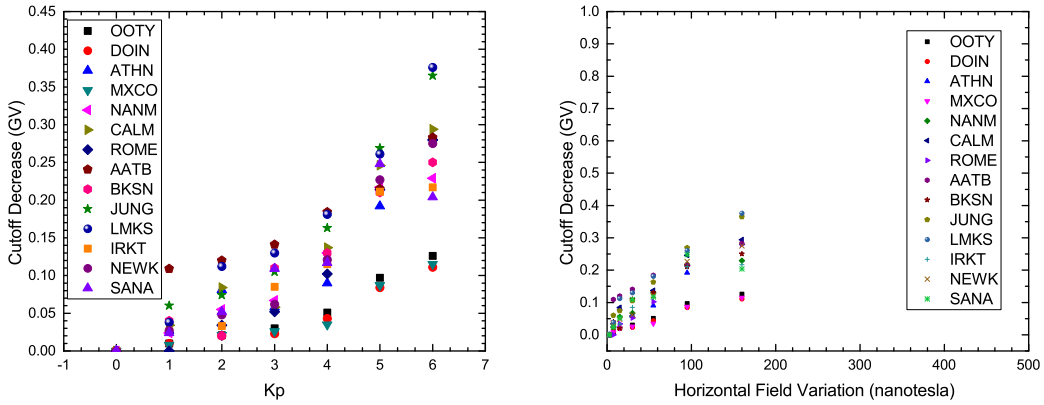


Figure 3: Cutoff reduction at various neutron monitors in the Tsyganenko model. Left: Plotted as a function of the single parameter in the model, integral values of the quasi logarithmic Kp. Right: Plotted as a function of the underlying linear magnetospheric parameter. The horizontal axis extends to 500 nT, which corresponds to Kp=8, the approximate value needed for extrapolation in the 2015 June 18 event. The cluster of points are the same as those in the left panel and thus indicate the values of Kp on this scale.

Unfortunately for the present analysis the Tsyganenko model relies on a fit to data to derive coefficients that describe all of the current systems that are assumed to follow Kp. Data above Kp=6 are too sparse to allow such a fit at these values. Consequently we cannot directly do the calculation for the Kp=8 level at the time of the GRAPES pulse. However the model employs physically meaningful parameters that describe specific magnetospheric current systems so there is no reason to assume that the model itself fails at that time.

The right panel of Figure 3 shows the calculated cutoff decrease plotted as a function of the range of variation of the horizontal surface field, which is the underlying linear parameter of the quasi-logarithmic Kp. The extent of the horizontal axis has been chosen to approximate the degree of extrapolation necessary to reach Kp=8. Linear extrapolation of the cutoff change at Ooty and Doi Inthanon (the lowest sequence of points on the figure) yields a somewhat smaller value than the 0.6 GV that would produce the effect seen at these stations, particularly considering that Kp changes from 6 to 8 at that time, not from 0 to 8. Exact agreement of the extrapolation with observation is not important to our argument. The key point is that the amount of extrapolation required is not so large that the model itself would fail in such a way as to modify the conclusion that cutoff changes are a global, not local, phenomenon.

3. Geographic Distribution

Figure 4 shows the distribution of neutron monitors at the time of the GRAPES event with symbols indicating our somewhat subjective classification of the appearance of a pulse at the monitor. Using the data in Figure 2 we have assigned (basically by eye) one of three categories to each

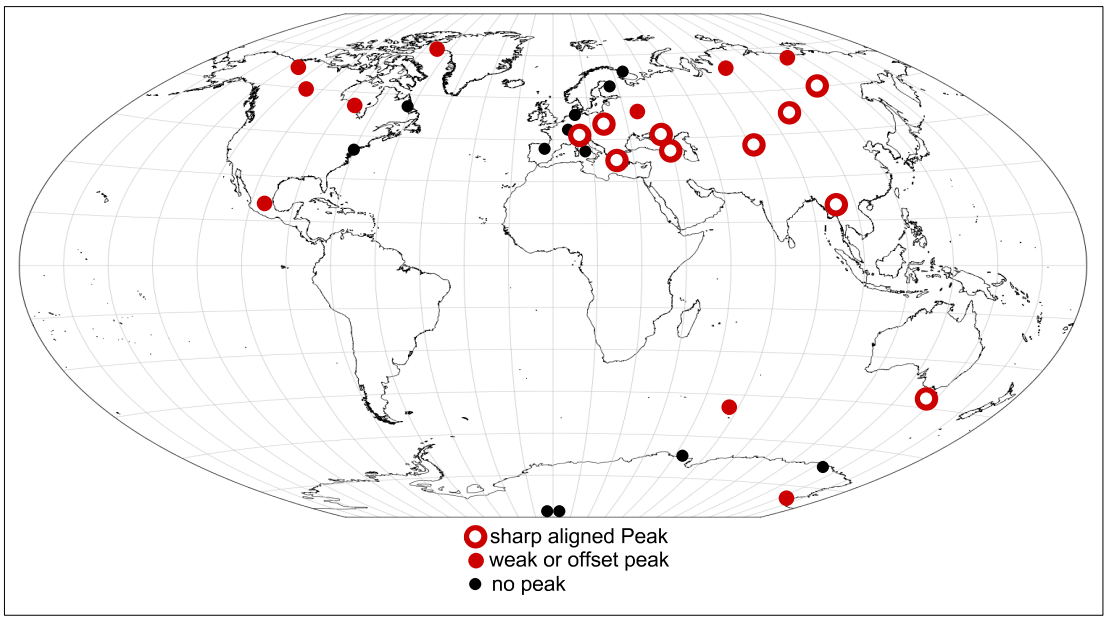


Figure 4: Geographic distribution of pulse visibility on 22 June 2015. Symbols indicate the location of neutron monitors classified as observing sharp aligned peaks, offset or weak peak, or no peak.

monitor: "sharp aligned peak", "offset or weak peak", or "no peak". The geographic distribution of these categories is well organized by location, as expected for an anisotropy effect. According to Figure 3 changes in cutoff rigidity are not restricted to Asian longitudes. European stations have the strongest predicted cutoff changes yet most of them show no peak. This strongly argues against the interpretation of the GRAPES event in terms of a cutoff change.

4. Discussion and Conclusions

There is a general similarity in the morphology of the 2015 June 22 event observed by GRAPES and the 2017 January 18 event observed by IceTop. Both have a small, well defined but geographically localized increase in counting rate at the time of a magnetospheric disturbance. At the South Pole a lowering of the cutoff is impossible, so the only explanation for the 2017 January 18 event is anisotropy in the cosmic ray flux.

For the GRAPES peak on 2015 June 22 a cutoff change is possible, and the required magnitude of the cutoff change is consistent with an extrapolation of the Tsyganenko model. However the peak is not global as would be predicted by that model. The peak is also visible at several polar locations where the cutoff is so low that a change could not produce a visible pulse. Thus we favor anisotropy, rather than cutoff change as the preferred explanation. This anisotropy could either be temporary or could be a feature that is long lasting but only briefly observed because the asymptotic directions of the detector are changed by the geomagnetic disturbance. We also note that Kp is only defined in three hour intervals, and is clearly elevated over an interval more extensive than the GRAPES pulse. A more detailed look at the event, using a more fine-grained magnetospheric parameter, is

clearly required to isolate changes in the cutoff predicted by conventional models from those that might lie outside these models.

5. Acknowledgements

We acknowledge the NMDB database, founded under the European Union's FP7 programme (contract no. 213007) for providing neutron monitor data, and acknowledge individual monitors following the information given on the respective station information sub-page under www.nmdb.eu. Supported in part by US National Science Foundation awards PLR-1245939 and PLR-1341562 and grant RTA5980003 from the Thailand Research Fund.

References

[1] Evenson, Paul, John Bieber, John Clem and Roger Pyle, South Pole neutron monitor lives again, *International Cosmic Ray Conference 32*, Beijing, (2011).

[2] Hatton, C. J., The Neutron Monitor, *Progress in Elementary Particle and Cosmic Ray Physics* **X** (1971), American Elsevier Publishing Company, New York.

[3] **IceCube** Collaboration, M. G. Aartsen et al., The IceCube Neutrino Observatory: Instrumentation and Online Systems, *JINST* **12** (2017) P03012.

[4] **IceCube-Gen2** Collaboration, GeV solar energetic particle observation and search by IceTop from 2011 to 2016, PoS(ICRC2017)132 (these proceedings).

[5] Lin, Zhongmin, John W. Bieber, and Paul Evenson, Electron trajectories in a model magnetosphere: simulation and observation under active conditions, *Journal Of Geophysical Research* **100** (1995) 23,543 - 23,549.

[6] Mangeard, P.-S., D. Ruffolo, A. Sáiz, S. Madlee, and T. Nutaro, Monte Carlo simulation of the neutron monitor yield function, *J. Geophys. Res. Space Physics* **121** (2016) doi:10.1002/2016JA022638.

[7] Mohanty, P.K., K.P. Arunbabu, T. Aziz *et. al.*, Transient weakening of earth's magnetic shield probed by a cosmic ray burst, *PRL* **117** (2016) 171101.

[8] Papailiou, M., H. Mavromichalaki, A. Belov, E. Eroshenko and V. Yanke, Precursor effects in different cases of forbush decreases, *Solar Phys.* **276** (2012) 337-350 DOI 10.1007/s11207-011-9888-1.

[9] Stoker, P.H., Spectra of solar proton ground level events using neutron monitor and neutron moderated detector recordings, *International Cosmic Ray Conference 19*, La Jolla **4** (1985) 114-117.

[10] Thomsen, M.F., Why Kp is such a good measure of magnetospheric convection, *Space Weather* **2** (2004) S11004, doi:10.1029/2004SW000089.

[11] Tsyganenko, N.A., Global quantitative models of the geomagnetic field in the cislunar magnetosphere for different disturbance levels, *Planet. Space Sci.* **35** (1987) 1347-1358.

Ground Level Enhancements in Solar Energetic Particles Observed by IceTop during 2011 to 2016

Pradiphat Muangha[1,2], Paul Evenson[1], Pierre-Simon Mangeard[1], and the IceCube Collaboration
[1]University of Delaware, Newark, DE, USA
[2]Now at Mahidol University, Bangkok, Thailand

Ground level enhancements (GLEs) are sudden increases in cosmic ray intensity, due to relativistic (GeV-range) ions from solar storms, with such a strong flux that their atmospheric showers can be detected by ground-based detectors above the Galactic cosmic ray background. They are of practical interest because the strong relativistic ion flux can pose a space weather hazard to astronauts, air crews, and aircraft electronics, and provide the earliest direct indication of a space radiation storm. Here we survey GLEs during the present solar cycle, in particular during 2011-2016, as observed by the IceTop surface detectors in the IceCube Neutrino Observatory. Our search focused on 34 particle events selected to have significant enhancements in the >100 MeV proton channel of the GOES spacecraft. We find 3 GLEs that exhibit clear signals in IceTop of GeV-range solar ions. We discuss sensitivity limits, and provide a broader context in which these 3 GLEs are found to be much weaker than some GLEs in previous solar cycles. Partially supported by Thailand Research Fund grant RTA5980003 and US National Science Foundation awards PLR-1341562 and PHY-1505990.

Studies of cosmic rays using neutron monitors in Antarctica

David Ruffolo

Mahidol University ***Thailand***

The flux of cosmic rays, i.e., energetic particles from space, can be tracked with great precision using ground-based detectors of atmospheric secondary particles, especially by neutron monitors that detect secondary neutrons. What do Thailand and Antarctica have in common for cosmic ray detection? The geomagnetic cutoff (threshold) energy for cosmic rays to reach Earth is highest in and near Thailand and lowest in the polar regions. Here we report on cosmic ray studies using neutron monitors in Antarctica and Thailand, which cover the extreme cosmic ray energies for these detectors. We have performed precision modeling of relativistic ions from several major solar storms as detected by the Spaceship Earth network of polar neutron monitors, including some in Antarctica. We also analyzed data from a series of "latitude surveys" by a ship-borne neutron monitor that crossed a wide range of geomagnetic cutoffs, as normalized using the neutron monitor at McMurdo, Antarctica, to infer changes in the cosmic ray spectrum due to "solar modulation" over the 11-year sunspot cycle and 22-year solar magnetic cycle. Finally we report on a comparison between solar modulation observed by the neutron monitors at Doi Inthanon, Thailand and at McMurdo that reveals a distinct pattern of solar modulation at high cutoff. Partially supported by NARIT and by the Thailand Research Fund (grant RTA5980003).

Analysis of Data from the 2009-10 Ship-Borne Bare Neutron Counter Latitude Survey

Waraporn Nuntiyakul

Chandrakasem Rajabhat University ***Thailand***

Within our solar system, space weather is influenced by the solar wind and the interplanetary magnetic field (IMF) carried by the solar wind plasma. Severe space weather storms can expose people to increased radiation levels, shut down electrical systems, and interfere with radio signals. Space weather probably effects the weather and climate on our planet but we do not yet have a precise understanding of the influence. Space weather can be monitored at ground level by indirectly observing changes in the interplanetary magnetic field with detectors that measure cosmic rays from the Sun and galactic sources. The specific objective of this research is to refine understanding of the detectors termed “bare neutron counters” which are now installed at the United States National Science Foundation station at the geographic South Pole. The main goal is to determine the response function of detectors using data collected on a latitude survey on the Swedish icebreaker Oden from Helsingborg, Sweden to McMurdo, Antarctica and back from November of 2009 to April of 2010. Initial results on the data due to pressure variations and short-term variations in modulation level over the course of survey based on variations in the McMurdo count rate are reported. Supported in part by the Thailand Research Fund via Research Grant for New Scholar MRG6080086 and Research Team Promotion Grant RTA5980003.

Modeling polar-region atmospheric ionization induced by the giant solar storm on 20 January 2005

Warit Mitthumsiri

Mahidol University ***Thailand***

Ionization in Earth's troposphere is mainly due to Galactic cosmic rays. Occasionally, solar storms produce intense relativistic ion beams that significantly increase such ionization. One of the largest recorded solar radiation storms, on 20 January 2005, resulted in up to 55-fold increases in the count rates of ground-based particle detectors in Antarctica. We use McMurdo and Inuvik neutron monitor data to reconstruct accurate time profiles of ion energy spectra above the atmosphere at each location. Using data-driven atmospheric models, we perform Monte Carlo simulations of particle-air interactions and calculate atmospheric ionization and potential biological dosage versus altitude and time for each location. These techniques can help evaluate possible influences of solar activity on atmospheric chemistry and cloud formation. This research project is partially supported by the Thailand Research Fund (Grants No. TRG5880173 and No. RTA5980003).

Contribution ID : **2** Type : **not specified**

Gamma-Ray and Neutron Monitor Observations of the 2017 September 10 Solar Eruptive Event

Tuesday, 24 April 2018 11:15 (20)

In early September 2017, during solar minimum, Active Region 12673 produced 26 M-class and four X-class flares. Gamma-ray emission >100 MeV was observed by the Fermi Large Area Telescope (LAT) for several hours following the X8.2 flare that began at 15:35 UT on September 10 when the active region was at or beyond the solar limb. It was associated with an ~1700 km/s coronal mass ejection (CME) and a high-energy solar energetic particle event observed in space and by neutron monitors. There appear to be three distinct phases of >100 MeV gamma-ray emission, each with energy spectra consistent with the decay of neutral and charged pions produced by protons above a few hundred MeV. The early part of the first >100 MeV phase began at about 15:56 UT, about one minute after the onset of the CME, and followed the time history of the impulsive flare phase as observed in hard X-rays and nuclear de-excitation line gamma rays that lasted until about 16:05 UT.mThe second phase of the >100 MeV gamma-ray emission began at 15:58 UT and peaked two minutes later at the highest solar flux level ever recorded by LAT. This emission was observed until about 16:08UT when the slow onset of the third >100 MeV phase, lasting about 10 hours, became dominant. This is the same time when Type II radio emission, indicating the presence of a shock, was observed. These latter two phases of >100 MeV emission were not detected in hard X-rays and nuclear deexcitation line gamma-rays observed by RHESSI and GBM. We discuss our spectral and temporal analyses of these three phases of >100 MeV gamma-ray emission and their possible origins. We also compare these observations with the Fort Smith neutron monitor measurements early in the Ground Level Event to determine whether protons producing the first two phases of gamma-ray emission (GLE) were also released into interplanetary space. This work was in part supported by Thailand Research Fundgrant RTA5980003.

Primary author(s) : SHARE, Gerald; MURPHY, Ronald (Naval Research Laboratory); EVENSON, Paul (University of Delaware); RUFFOLO, David (Mahidol University); Dr PATTARAKIJWANICH, Petchara (Department of Physics, Faculty of Science, Mahidol University, Bangkok 10400, Thailand); Dr PYLE, Roger (Pyle Consulting Group)

Presenter(s) : SHARE, Gerald

Session Classification : Late Tuesday Morning

Your abstract submission has been received

Click HERE to print this page now.

You have submitted the following abstract to Triennial Earth Sun-Summit . Receipt of this notice does not guarantee that your submission was free of errors.

Gamma-Ray and Neutron Monitor Observations of the 2017 September 10 Solar Eruptive Event

Gerald H Share, University of Maryland College Park, Astronomy, College Park, MD, United States, Ronald J Murphy, US Naval Research Laboratory, Washington, DC, United States, Anne K Tolbert, Catholic University of America, Washington, DC, United States, Petchara Pattarakijwanich, Mahidol University, Department of Physics, Faculty of Science, Bangkok, Thailand, David J Ruffolo, Mahidol Univ, Department of Physics, Faculty of Science, Bangkok, Thailand, Paul Arthur Evenson, University of Delaware, Newark, DE, United States and Roger Pyle, Pyle Consulting Group, St. Charles, IL, United States

Abstract Text:

In early September 2017, during solar minimum, Active Region 12673 produced 26 M-class and four X-class flares. Gamma-ray emission >100 MeV was observed by the Fermi Large Area Telescope (LAT) for several hours following the X8.2 flare that began at 15:35 UT on September 10 when the active region was at or beyond the solar limb. It was associated with an ~1700 km/s coronal mass ejection (CME) and a high-energy solar energetic particle event observed in space and by neutron monitors at ground level. There appear to be three distinct phases of >100 MeV gamma-ray emission, each with energy spectra consistent with the decay of neutral and charged pions produced by protons above a few hundred MeV. The early part of the first >100 MeV phase began at about 15:56 UT, about one minute after the onset of the CME, and followed the time history of the impulsive flare phase as observed in hard X-rays and nuclear de-excitation line gamma rays that lasted until about 16:05 UT. The second phase of the >100 MeV gamma-ray emission began at 15:58 UT and peaked two minutes later at the highest solar flux level ever recorded by LAT. This emission was observed until about 16:08 UT when the slow onset of the third >100 MeV phase, lasting about 10 hours, became dominant. This is the same time when Type II radio emission, indicating the presence of a shock, was observed. These latter two phases of >100 MeV emission were not detected in hard X-rays and nuclear de-excitation line gamma-rays observed by RHESSI and GBM. We discuss our spectral and temporal analyses of these three phases of >100 MeV gamma-ray emission and their possible origins. We also compare these observations with Fort Smith neutron monitor measurements early in the Ground Level Enhancement to determine whether relativistic ions producing the first two phases of gamma-ray emission made a significant contribution to the interplanetary population. This work was in part supported by Thailand Research Fund grant RTA5980003.

Session Selection:
Late-phase solar activity in September 2017

Submitter's E-mail Address:
share@astro.umd.edu

Abstract Title:
Gamma-Ray and Neutron Monitor Observations of the 2017 September 10 Solar Eruptive Event

Requested Presentation Type:

Oral presentation

Previously Published?:
No

Abstract Payment:
Paid (agu-2018tess-334713-2002-4581-3426-7573)

For non-students only: I do not want to be a judge in the SPD Student Poster Competition.

First Presenting Author

Presenting Author

Gerald H Share

Primary Email: share@astro.umd.edu
Phone: ARRAY(0xf3eddd0)

Affiliation(s):

University of Maryland College Park
Astronomy
College Park MD 20910-0000 (United States)

Second Author

Ronald J Murphy

Primary Email: ronald.murphy@nrl.navy.mil

Affiliation(s):

US Naval Research Laboratory
Washington DC (United States)

Third Author

Anne K Tolbert

Primary Email: kim.tolber@nasa.gov

Affiliation(s):

Catholic University of America
Washington DC (United States)

Fourth Author

Petchara Pattarakijwanich

Primary Email: petchara_p@hotmail.com

Affiliation(s):

Mahidol University
Department of Physics, Faculty of Science
Bangkok (Thailand)

Fifth Author

David J Ruffolo

Primary Email: ruffolo.physics@gmail.com
Phone: 6622015756

Affiliation(s):

Mahidol Univ
Department of Physics, Faculty of Science
Bangkok 10400 (Thailand)

Sixth Author

Paul Arthur Evenson

Primary Email: evenson@udel.edu
Phone: 3028312988

Affiliation(s):

University of Delaware
Newark DE (United States)

Seventh Author

Roger Pyle

Primary Email: pyle@udel.edu
Phone: ARRAY(0xe3077ec)

Affiliation(s):

Pyle Consulting Group

St. Charles IL 19716-0350 (United States)

If necessary, you can make changes to your abstract submission

- To access your submission in the future, point your browser to: User Portal
- Your Abstract ID# is: 334713.
- Any changes that you make will be reflected instantly in what is seen by the reviewers.
- After the abstract proposal is submitted, you are not required to go through all submission steps to make edits. For example, click the "Authors" step in the Abstract Submission Control Panel to edit the Authors and then click save or submit.
  When you have completed your submission, you may close this browser window or submit another abstract proposal: Call for Abstracts.

Tell us what you think of the abstract submission process

Journal of Physics: Conference Series

PAPER • **OPEN ACCESS**

The comparative study of the radiation shielding of $PbO–Li_2O–B_2O_3$ glass system by using FLUKA to XCOM and experimental data

To cite this article: C Sriwunkum *et al* 2018 *J. Phys.: Conf. Ser.* **1144** 012135

View the article online for updates and enhancements.



IOP ebooks™

Bringing you innovative digital publishing with leading voices to create your essential collection of books in STEM research.

Start exploring the collection - download the first chapter of every title for free.

This content was downloaded from IP address 202.28.179.6 on 07/08/2019 at 05:42

IOP Conf. Series: Journal of Physics: Conf. Series **1144** (2018) 012135 doi:10.1088/1742-6596/1144/1/012135

The comparative study of the radiation shielding of $PbO-Li_2O-B_2O_3$ glass system by using FLUKA to XCOM and experimental data

C Sriwunkum[1], T Nutaro[1] and A Saiz[2]

[1] Department of Physics, Faculty of Science, Ubon Ratchathani University, Ubon Ratchathani, 34190, Thailand

[2] Department of Physics, Faculty of Science, Mahidol University, Bangkok, 10400, Thailand

E-mail: chahkrit.sr.60@ubu.ac.th

Abstract. We had investigated the efficacy of FLUKA Monte Carlo code for the gamma radiation shielding parameter calculation of $(60-x)\,PbO-x\,Li_2O-40\,B_2O_3$ glasses (where $0 \leq x \leq 25$ mol%) at photon energies, 356, 662, 1173, and 1332 keV. Then we compared the mass attenuation coefficients, mean free path, effective atomic number, and electron density to standard XCOM data and experimental results from recently published work. We found that simulated and calculated results agreed well with those published results, for which the maximum relative deviation is less than 1.5 % for all the glass samples.

1. Introduction

During the past decade, there has been growing interest in the area of radiation shielding materials due to their applications in various fields such as radiation protection, hadron therapy, and nuclear power plants, etc. [1, 2]. Concretes are among the most commonly used radiation shielding materials against ionizing radiations because of their high density and easy to shape for any construction [3]. However, there are many disadvantages of concrete material, for example, it is not transparent to visible light, aggregates expansion, and forms crack, etc. [4–6]. One alternative shielding material is glass, due to its radiation protection compared to concretes of the same width and high optical transparency. Also, their properties can be to modified by changing other compounds [7–9].

Previously, different types of glasses have been studied by many researchers [8–13]. In the present article, $PbO-Li_2O-B_2O_3$ glass has been considered since lead-oxide (PbO) is known for their excellent infrared transmission, large density, and high refractive index [14]. In the process of glass formation, lead-oxide does not form oxide a network by itself, so the other glass such as silicate, phosphate, and borate are required. Borate (B_2O_3) is one of the most commonly used as an oxide network former because of its high glass forming ability, low thermal expansion, and high stability when added with alkali metal oxide (i.e., Li_2O, Na_2O, K_2O) [15]. Recently, the radiation shielding properties of the present glasses have been theoretically studied by using Monte Carlo (MC) simulation, provided in FLUKA program [16–18]. MC in FLUKA is coded in FORTRAN language for simulations of transport and interaction of electrons, neutrons, photons, all the corresponding antiparticles and heavy ions in matter [19]. Furthermore, theoretical

Content from this work may be used under the terms of the Creative Commons Attribution 3.0 licence. Any further distribution of this work must maintain attribution to the author(s) and the title of the work, journal citation and DOI.
Published under licence by IOP Publishing Ltd

values of attenuation coefficients of the different elements and compounds were also studied by applying mixture rule using XCOM program [20]. Thus, this has encouraged us to be interested in radiation shielding properties of the selected glass studied by both techniques.

The goal of this work is to study the efficacy of FLUKA to investigate the $\gamma-$ray shielding parameter of $PbO-Li_2O-B_2O_3$ glass system by calculating mass attenuation coefficients, mean free path, effective atomic number, and electron density at energies, 356, 662, 1173, and 1332 keV. The obtained results are compared with the values calculated by using XCOM program and previous experiments. Mean free path values for the selected glasses also have been compared with standard shielding concretes.

2. Materials and methods

2.1. Material specification of glass samples

The chemical composition, chemical formula, mass density, and thickness of the (60−x) PbO−x Li_2O−40 B_2O_3; where x = 0, 5, 10, 15, 20 and 25 mol% glass system were taken from Kumar [21] (see table 1).

Table 1. Chemical composition, chemical formula, mass density, and thickness of glass samples.

Glass Sample	Composition (mol%) PbO	Li_2O	B_2O_3	Chemical Formula	Density (g/cm^3)	Thickness (cm)
G1	60	0	40	$Pb_3B_4O_9$	6.306	0.741
G2	55	5	40	$Pb_{11}B_{16}Li_2O_{36}$	6.144	0.712
G3	50	10	40	$Pb_5B_8Li_2O_{18}$	5.786	0.648
G4	45	15	40	$Pb_9B_{16}Li_6O_{36}$	5.553	0.659
G5	40	20	40	$Pb_2B_4Li_2O_9$	5.378	0.756
G6	35	25	40	$Pb_7B_{16}Li_{10}O_{36}$	5.138	0.684

2.2. Theoretical calculation

In this section, we conclude the theoretical relations used in the present article. The mass attenuation coefficients (μ_m) of the glass samples were determined by the transmission method according to Lambert-Beer's law [8, 21]:

$$\mu_m = \frac{\ln\left(\frac{I_0}{I}\right)}{\rho d} \tag{1}$$

where I_0 and I are incident and attenuated intensities of γ radiation, respectively, d is the thickness, and ρ is a density of the material. Moreover, theoretical values of μ_m obtained using the XCOM program for the selected glasses, based on mixture rule [20]:

$$\mu_m = \sum\nolimits_i w_i(\mu_m)_i \tag{2}$$

where w_i and $(\mu_m)_i$ (obtained directly from XCOM database) are the percentages by weight and μ_m of the ith constituent in the mixture material sample, respectively. Values of μ_m were then used to calculate the mean free path (λ), effective atomic number (Z_{eff}) and electron density (N_{el}). Details on theoretical calculation of these parameters can be found in various literature [17, 21].

2.3. FLUKA Simulation process

In this study, cylindrical geometries were employed in FLUKA code for modeling of glass samples. To measure the attenuation coefficients of the glass samples, the narrow beam transmission geometry depicted in figure 1 was simulated using radiation source as isotropic with collimated and monoenergetic $\gamma-$ray at energies, 356, 662, 1173 and 1332 keV for each calculation. In simulation setup, a radiation source, lead collimator, detector, and glass sample were located by considering the location points according to the narrow beam transmission geometry from experimental setup [21]. The isotropic source and detector were enclosed in a lead container with face aperture 2 cm. A cylindrical NaI detector [22], 7.62 cm in diameter and 7.62 cm in length, was 66 cm far from the radiation source. Three lead collimators with apertures 0.4, 0.6, and 0.2 cm, respectively, are shown in the figure 1. One collimator located in front of the radiation source and another one was in front of the detector. To get absorbed dose amounts in the detection region, USRTRACK estimator has been utilized. This type of estimator gives the average flux in a cell (detector volume) for each $\gamma-$ray emitted from the radiation source.

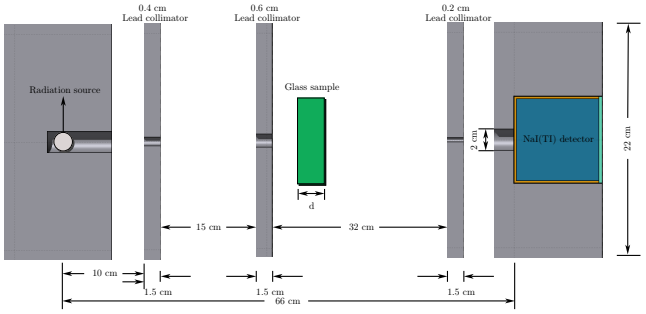


Figure 1. Total simulation geometry (sizes are not on scale).

3. Result and discussion

We found that the results agree very well with the experimental data and 10 million primary particles were used for the simulation with the statistical errors less than 0.3 %. In figure 2, the relative deviation (RD) values, the differences between simulated and calculated values of mass attenuation coefficients from both methods are in good agreement with experimental data, taken from Ref. [21]. The value of RD {(Theo.−Exp.)×100/Exp.} [4] ranges from 0.02% to

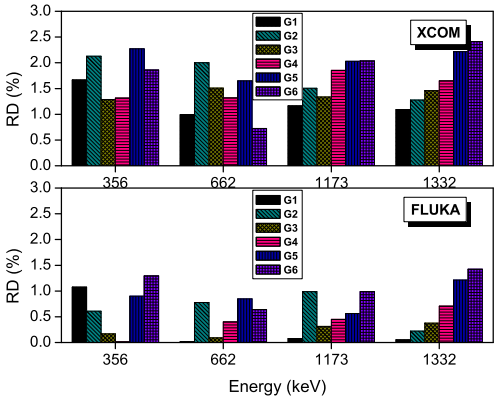


Figure 2. RD values between theoretical results with experimental data.

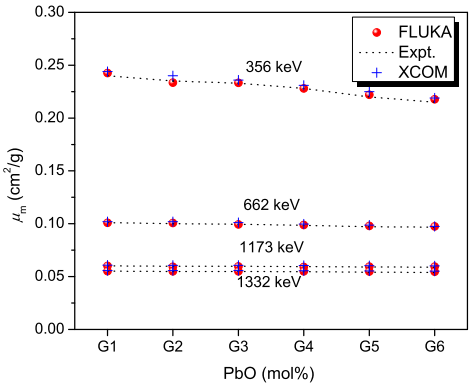


Figure 3. Variation of mass attenuation coefficients against PbO concentration.

1.43% and from 0.72% to 2.41% obtained from FLUKA and XCOM, respectively. The results from FLUKA obtained better agree with the experimental data compared to XCOM. However, the different values from both techniques could be due to nuclear data uncertainties, differences in the employed methods and databases, the geometry of the system for simulation, experimental conditions, and error in physical quantities (i.e., densities, thickness, and intensities of radiation source). The simulation and calculation values of the mass attenuation coefficients of the studied glasses are given in figure 3. It is clear that the decrease in mass attenuation coefficients with PbO contents may be due to the decrease in weight fraction of higher atomic number constituent (Pb) compared to other elements [10].

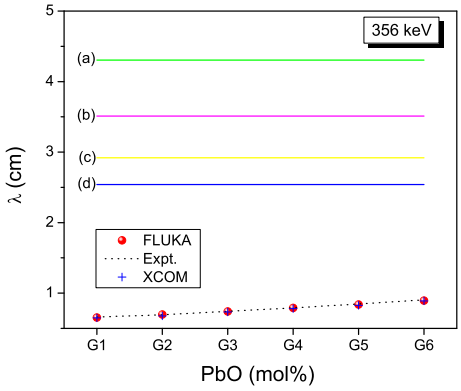


Figure 4. Comparison of mean free path in photon energy 356 keV.

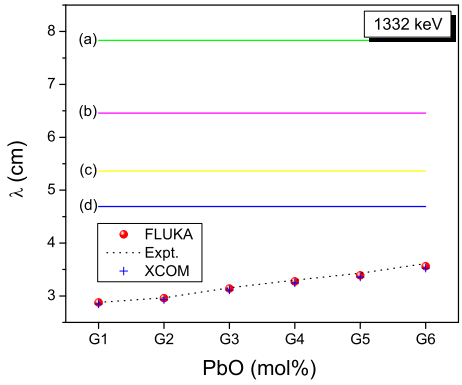


Figure 5. Comparison of mean free path in photon energy 1332 keV.

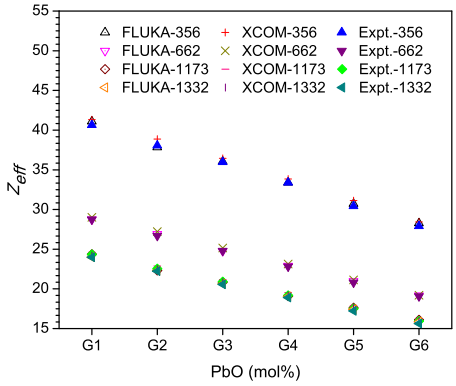


Figure 6. Variation of effective atomic numbers of glass samples.

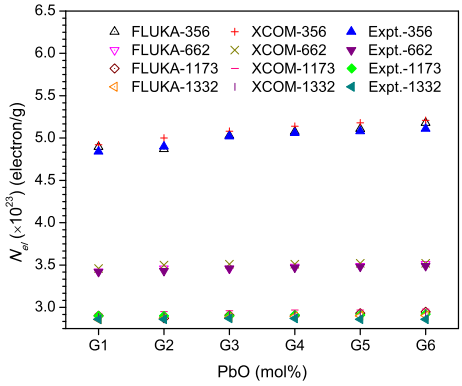


Figure 7. Variation of effective electron density of glass samples.

For shielding ability, lower values of the mean free path are desired. In this work, the mean free path values of $PbO-Li_2O-B_2O_3$ glasses have been compared to that of other standard shielding concretes (ordinary (a), ilmenite-limonite (b), ilmenite (c) and steel-scrap (d)) in photon energy 356 and 1332 keV [23]. It is clear from figure 4 and figure 5 that, the values of the mean free path for all selected glasses are lower than that of the common shielding concretes. Therefore,

it indicates that the shielding effectiveness of the studies glasses is better than the conventional concretes. Variation in effective atomic number and electron density of glass samples with different PbO contents at various photon energies are plotted and shown in figure 6 and figure 7, respectively. It is evident from figure 6 and figure 7 that the effective atomic number increases with a decrease in electron density and an increase in the concentration. It also found that effective atomic number and electron density decrease with an increase in incident photon energy. These values from two theoretical methods are in good agreement with experimental data.

4. Conclusion

In the present work, γ radiation shielding parameters of $PbO-Li_2O-B_2O_3$ glasses were investigated at different energies (356, 662, 1173, and 1332 keV) by using FLUKA and XCOM program. Mass attenuation coefficient values obtained from both methods are in good agreement with experimental data. The mean free path values of all glassy systems are lower than that of the standard shielding concretes. It was also found that the mass attenuation coefficient, effective atomic number, and electron density decrease with an increase of photon energy. Moreover, FLUKA MC code may be useful as an alternative method to the calculated γ shielding parameter for other glass systems which experiment cannot be set up.

Acknowledgments

We would like to thank the Research Professional Development Project Under the Science Achievement Scholarship of Thailand (SAST) for financial support. This research was partially supported by grant RTA5980003 from the Thailand Research Fund.

References

[1] Fugaru V *et al* 2015 *Acta Phys. Pol.* A **127** 1427–29
[2] Manohara S R, Hanagodimath S M and Gerward L 2009 *J. Nucl. Mater.* **479** 465–72
[3] Bootjomchai C *et al* 2012 *Radiat. Phys. Chem.* **81** 785–90
[4] Bagheri R, Moghaddam A K and Yousefnia H 2017 *J. Nucl. Sci. Technol.* **49** 216–23
[5] Mostafa A M A, Issa S A M, and Sayyed M I 2017 *J. Alloys Compd.* **708** 294–300
[6] Kaur S and Singh K J 2014 *Ann. Nucl. Energy* **63** 350–4
[7] Kirdsiri K *et al* 2011 *Ann. Nucl. Energy* **38** 1438–41
[8] Singh K *et al* 2002 *Nucl. Instrum. Methods Phys. Res.* B **194** 1–6
[9] Singh S *et al* 2008 *Nucl. Instrum. Methods Phys. Res.* B **226** 140–6
[10] Kirdsiri K *et al* 2009 *Ann. Nucl. Energy* **36** 1360–5
[11] Kaewkhao J and Limsuwan P 2010 *Nucl. Instrum. Methods Phys. Res.* A **619** 295–7
[12] Chanthima N and Kaewkhao J 2013 *Ann. Nucl. Energy* **55** 23–8
[13] Issa S A M 2016 *Radiat. Phys. Chem.* **120** 33–7
[14] Kaundal R S *et al* 2010 *J. Phys. Chem. Solids* **71** 1191–5.
[15] Limkitjaroenporn P *et al* 2011 *J. Phys. Chem. Solids* **72** 245–51
[16] Lakshminarayana G *et al* 2018 *J. Non-Cryst. Solids* **481** 65–73
[17] Kumar A *et al* 2018 *J. Non-Cryst. Solids* **481** 604–7
[18] Bagheri R *et al* 2018 *J. Non-Cryst. Solids* **479** 62–71
[19] Saito K and Moriuchi S 1981 *Nucl. Instrum. Methods* **185** 299–308
[20] Gerward L *et al* 2004 *Radiat. Phys. Chem.* **136** 653–4
[21] Kumar A 2017 *Radiat. Phys. Chem.* **136** 50–3
[22] Mouhti I, Elanique A and Messous M Y 2017 *J. Mater. Environ. Sci.* **8** 4560–5
[23] Bashter I I 1997 *Ann. Nucl. Energy* **24** 1389–401

Journal of Physics: Conference Series

PAPER • **OPEN ACCESS**

The comparative studies of gamma-ray shielding properties of the PbO–BaO–B_2O_3 glass system by using FLUKA code to XCOM program and accessible experimental data

To cite this article: C Mutuwong *et al* 2018 *J. Phys.: Conf. Ser.* **1144** 012130

View the article online for updates and enhancements.



IOP ebooks™

Bringing you innovative digital publishing with leading voices to create your essential collection of books in STEM research.

Start exploring the collection - download the first chapter of every title for free.

This content was downloaded from IP address 202.28.179.6 on 07/08/2019 at 05:40

IOP Conf. Series: Journal of Physics: Conf. Series **1144** (2018) 012130 doi:10.1088/1742-6596/1144/1/012130

The comparative studies of gamma-ray shielding properties of the PbO–BaO–B_2O_3 glass system by using FLUKA code to XCOM program and accessible experimental data

C Mutuwong[1,*], T Nutaro[1] and A Saiz[2]

[1]Department of Physics, Faculty of Science, Ubon Ratchathani University, WarinChamrap, Ubon Ratchathani, Thailand

[2]Department of Physics, Faculty of Science, Mahidol University, Bangkok, Thailand

E-mail: chalermpon.mu.60@ubu.ac.th

Abstract. We had performed computer simulations by using FLUKA for investigating the gamma-ray shielding properties of the xPbO–(50-x)BaO–50B_2O_3 glass systems for the 356, 662, 1173, and 1330 keV photons (gamma-rays) energies. Then we compared the results to XCOM and the previous experimental published data. We found that the results agree very well with the XCOM and the real data. Furthermore, we also found that the results from FLUKA are closer to the experimental data than the XCOM.

1. Introduction

There have been trying to develop the radiation shielding materials protecting people from various kinds of radiation such as the nuclear research reactors, nuclear power plants, cosmic rays from the outer space and also from the medical radioactive substances or sources and etc. In order to control and decrease the intensity of radiation to acceptable safety level to human, we need the appropriate shielding materials. The studying of different fundamental parameters which are related to shielding against harmful and dangerous radiations is very important [1–3].

Glasses changed properties by adding heavy metal oxide such as PbO are interesting for this study because they are high density and high refractive index. These qualities make them an essential material for the development of advanced optical communication and gamma radiation shielding materials [4].

Previously, experimental studies on the gamma-ray shielding properties of the xPbO–(50-x)BaO–50B_2O_3 glass systems (where $5 \leq x \leq 45$ mol%) at 356, 662, 1173, 1330 keV photons energies have been conducted [5]. The aim of this study is to apply FLUKA for investigating the gamma-ray shielding properties of this glass systems. Thus, the shielding parameters of them were measured by means of FLUKA code, which is a fully integrated Monte Carlo simulation package for the interaction and transport of particles and nuclei in matters. The simulated results were compared with the reported experimental and XCOM results [5], which is a program or dataset for calculating X-ray and γ-ray attenuation coefficients of the different elements, compounds, and mixtures [6]. In addition, the gamma-ray shielding effectiveness has also been compared with the standard concretes in terms of their half value layer.


Content from this work may be used under the terms of the Creative Commons Attribution 3.0 licence. Any further distribution of this work must maintain attribution to the author(s) and the title of the work, journal citation and DOI.
Published under licence by IOP Publishing Ltd

2. Methodologies

2.1. FLUKA simulation

Figure 1 is a visual representation of what the computer needs to model in order to agree with the earlier experimental setup [5] such as positions, dimensions, geometries, and materials.

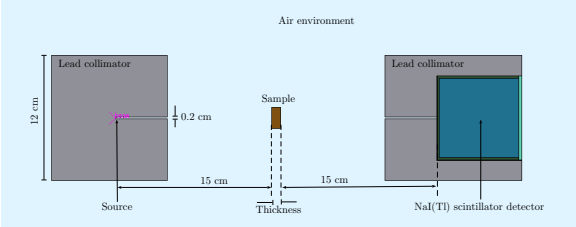


Figure 1. Cross-sectional geometry of total simulation model.

The simulation details consist of three main parts. Firstly, a beam source used for this model is a mono-energetic photon beam (aperture 0.2 cm dimension). The second is glass samples. The material specification of each glass samples listed in table 1 was added to be compound materials by COMPOUND card. In addition, the cylindrical geometries, 2.0 cm diameter and different thickness, were used for modeling all of the glass samples. Finally, a NaI scintillation detector (3 × 3 in) was enclosed by lead collimator made of a 13-cm-length lead cylinder, with 12 cm and 0.2 cm outer and inner diameter respectively. The materials and inner structure of the NaI detector were obtained from Mouhti *et al.* [7]. The computer simulations were run with 5 million number of primary histories.

The mass attenuation coefficients (μ_m) of the glass samples were determined by the transmission method ($\mu_m = \frac{1}{\rho t}\ln\left(\frac{I_0}{I}\right)$). In the simulation, I_0 and I represents the average particles flux values passed through the detector without shielding material and with shielding material, respectively, ρ and t are density and thickness of glass samples, respectively.

Table 1. Chemical composition, density, thickness, and weight fraction of atomic composition of the xPbO–(50-x)BaO–50B_2O_3 (where $5 \leq x \leq 45$ mol%) glass systems obtained from Issa [5].

Sample	Composition (mol%)			Density	Thickness	Element			
	PbO	BaO	B_2O_3	g/cm^3	cm	B	O	Ba	Pb
S1	5	45	50	4.318	0.523	0.15529	0.39526	0.40304	0.04642
S2	10	40	50	4.460	0.633	0.15529	0.39362	0.35826	0.09283
S3	15	35	50	4.602	0.752	0.15529	0.39199	0.31348	0.13925
S4	20	30	50	4.744	0.834	0.15529	0.39036	0.26870	0.18566
S5	25	25	50	4.886	0.912	0.15529	0.38872	0.22391	0.23208
S6	30	20	50	5.028	1.254	0.15529	0.38709	0.17913	0.27850
S7	35	15	50	5.170	1.321	0.15529	0.38546	0.13435	0.32491
S8	40	10	50	5.312	1.435	0.15529	0.38382	0.08957	0.37133
S9	45	5	50	5.454	1.511	0.15529	0.38219	0.04478	0.41774

2.2. XCOM program

XCOM is a software or dataset based on mixture rule ($(\mu_m)_{glass} = \sum_i^n w_i(\mu_m)_i$), where w_i and $(\mu_m)_i$ are the weight fraction and mass attenuation coefficient of ith element in energy from 1 keV to 100 GeV. It requires input the weight fractions of the constituent elements listed in table 1 to calculate the μ_m values of the present glasses by using mixture rule. It does not need the experimental setup.

3. Result and discussion

Mass attenuation coefficients (μ_m), mean free path (MFP), and half value layer (HVL) of the glass samples computed by FLUKA and XCOM for each photons energies are presented in table 2, as well as accessible experimental data [5]. Moreover, these μ_m values are compared with the experimental data by using RD = |theoretical − experimental| × 100/experimental.

Table 2. Comparison between the simulated (Fluka), calculated (Xcom), and experimental (Exp) results of mass attenuation coefficients, mean free path, and half value layer of the glass samples with different photons energies.

samples	E (keV)	μ_m (cm^2/g)			MFP (cm)			HVL (cm)		
		Fluka	Xcom	Exp	Fluka	Xcom	Exp	Fluka	Xcom	Exp
S1	356	0.1260	0.1265	0.1260	1.84	1.83	1.84	1.27	1.27	1.27
	662	0.0775	0.0780	0.0777	2.99	2.97	2.98	2.07	2.06	2.07
	1173	0.0555	0.0558	0.0552	4.17	4.15	4.20	2.89	2.88	2.91
	1330	0.0516	0.0520	0.0512	4.48	4.45	4.52	3.11	3.09	3.14
S2	356	0.1323	0.1331	0.1327	1.69	1.68	1.69	1.17	1.17	1.17
	662	0.0791	0.0795	0.0793	2.83	2.82	2.83	1.96	1.95	1.96
	1173	0.0558	0.0562	0.0557	4.02	3.99	4.03	2.78	2.77	2.79
	1330	0.0520	0.0524	0.0517	4.32	4.28	4.34	2.99	2.97	3.01
S3	356	0.1392	0.1397	0.1378	1.56	1.56	1.58	1.08	1.08	1.09
	662	0.0806	0.0810	0.0799	2.70	2.68	2.72	1.87	1.86	1.89
	1173	0.0561	0.0566	0.0559	3.87	3.84	3.89	2.68	2.66	2.69
	1330	0.0523	0.0527	0.0520	4.16	4.12	4.18	2.88	2.86	2.90
S4	356	0.1457	0.1463	0.1462	1.45	1.44	1.44	1.00	1.00	1.00
	662	0.0823	0.0826	0.0825	2.56	2.55	2.56	1.78	1.77	1.77
	1173	0.0565	0.0571	0.0565	3.73	3.69	3.73	2.58	2.56	2.59
	1330	0.0526	0.0530	0.0524	4.01	3.98	4.02	2.78	2.76	2.79
S5	356	0.1521	0.1529	0.1524	1.35	1.34	1.34	0.93	0.93	0.93
	662	0.0836	0.0841	0.0838	2.45	2.43	2.44	1.70	1.69	1.69
	1173	0.0570	0.0575	0.0568	3.59	3.56	3.60	2.49	2.47	2.50
	1330	0.0529	0.0534	0.0526	3.87	3.83	3.89	2.68	2.66	2.70
S6	356	0.1587	0.1595	0.1572	1.25	1.25	1.27	0.87	0.86	0.88
	662	0.0850	0.0856	0.0844	2.34	2.32	2.36	1.62	1.61	1.63
	1173	0.0574	0.0579	0.0571	3.46	3.43	3.48	2.40	2.38	2.41
	1330	0.0531	0.0537	0.0529	3.74	3.70	3.76	2.59	2.57	2.61
S7	356	0.1651	0.1661	0.1640	1.17	1.16	1.18	0.81	0.81	0.82
	662	0.0865	0.0871	0.0860	2.24	2.22	2.25	1.55	1.54	1.56
	1173	0.0578	0.0583	0.0576	3.35	3.32	3.36	2.32	2.30	2.33
	1330	0.0536	0.0540	0.0534	3.61	3.58	3.62	2.50	2.48	2.51
S8	356	0.1716	0.1727	0.1711	1.10	1.09	1.10	0.76	0.76	0.76
	662	0.0881	0.0886	0.0878	2.14	2.12	2.14	1.48	1.47	1.49
	1173	0.0582	0.0588	0.0582	3.24	3.20	3.23	2.24	2.22	2.24
	1330	0.0539	0.0544	0.0539	3.49	3.46	3.49	2.42	2.40	2.42
S9	356	0.1783	0.1793	0.1778	1.03	1.02	1.03	0.71	0.71	0.71
	662	0.0895	0.0901	0.0894	2.05	2.03	2.05	1.42	1.41	1.42
	1173	0.0586	0.0592	0.0587	3.13	3.10	3.12	2.17	2.15	2.17
	1330	0.0542	0.0547	0.0542	3.38	3.35	3.38	2.34	2.32	2.34

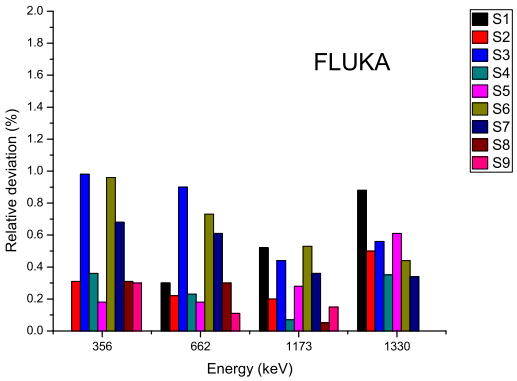


Figure 2. Relative different between FLUKA results and experimental data.

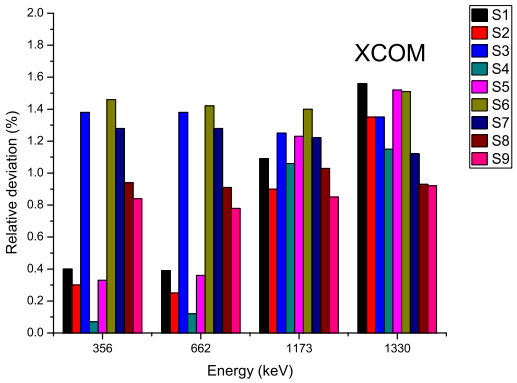


Figure 3. Relative different between XCOM results and experimental data.

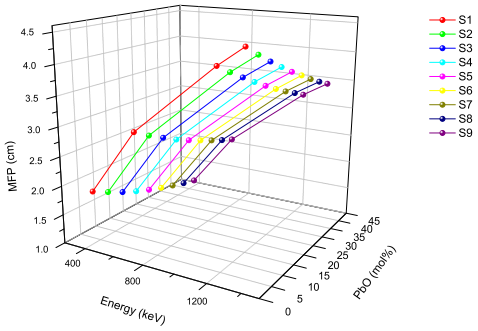


Figure 4. Variation of MFP with photons energies of glass systems.

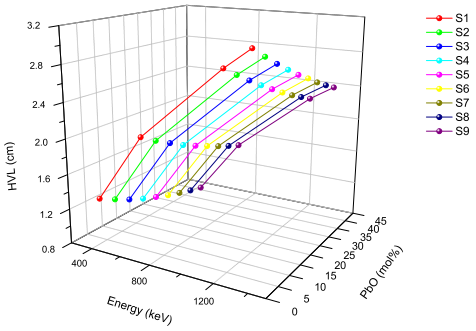


Figure 5. Variation of HVL with photons energies of glass systems.

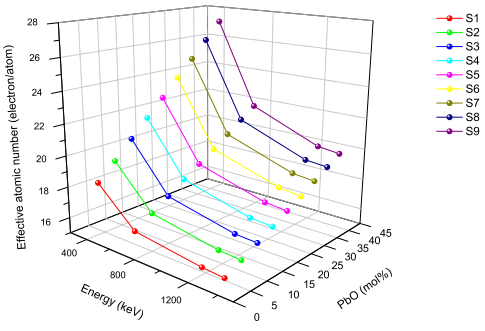


Figure 6. Variation of Z_{eff} with photons energies of glass systems.

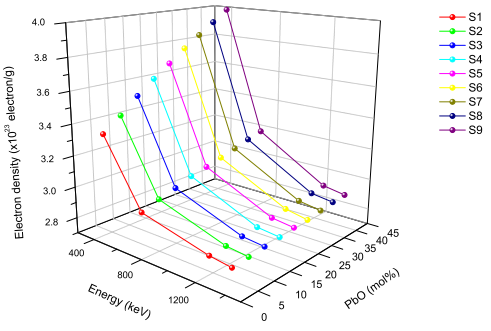


Figure 7. Variation of N_{eff} with photons energies of glass systems.

The relative different (RD) between FLUKA and XCOM results with experimental data of μ_m are shown in figure 2 and 3. There are values less than 0.98% for FLUKA and 1.56% for XCOM. It is clear that these results are good agreement with experimental data but the results from FLUKA are slightly closer to the experimental data than the XCOM. All simulation data

obtained by FLUKA were reported with less than 0.1% statistical error. However, the end of the simulation process spends time so long about 14 hours, which are longer than XCOM.

The values of the mean free path (MFP) and half value layer (HVL) of samples are illustrated in figure 4 and 5, respectively. Both MFP and HVL decrease as lead oxide increase and increase as gamma-ray energies increase. The effective atomic number (Z_{eff}) and electron density (N_{eff}) of glass systems are shown in figure 6 and 7. It was found that the values of Z_{eff} and N_{eff} increase as mole percent of lead oxide increase and decrease as gamma-ray energies increase.

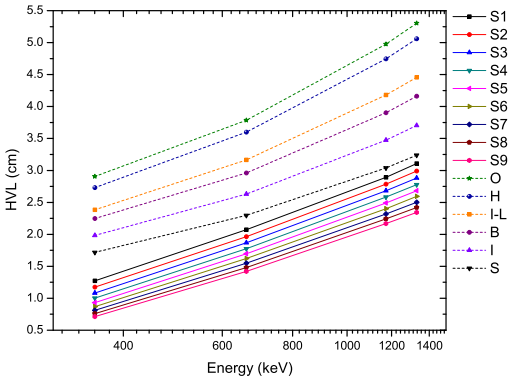


Figure 8. Comparison of the half value layer of glass samples with standard shielding concretes; Ordinary (O), Hematite-serpentine (H), Ilmenite-limonite (I-L), Basalt-magnetite (B), Ilmenite (I), and Stell-scarp (S).

The HVL values have been compared with HVL of the standard radiation shielding concretes obtained by Bashter [8] and shown in figure 8. We found that all glass samples are having the lower values of the HVL as compared to standard concretes. Therefore, the PbO-BaO-B_2O_3 glass is better radiation shielding materials than these standard concretes in the same thickness.

4. Conclusion

We have succeeded in investigating gamma-ray shielding properties of the PbO–BaO–B_2O_3 glass systems at the 356, 662, 1173, and 1330 keV photons energies by using FLUKA simulation. We found that the results from FLUKA are slightly closer to the experimental data than the XCOM but the finish simulation procedure spends time longer than XCOM. In addition, FLUKA may be used as a better alternative in the experiment to evaluate the gamma-ray shielding properties for other glass systems.

Acknowledgments

The authors are grateful to the Science Achievement Scholarship of Thailand (SAST) for financial support. This research is partially supported by grant RTA5980003 from the Thailand Research Fund.

References

[1] Singh N, Singh K J, Singh K and Singh H 2006 *Radiat. Meas.* **41** 84–8
[2] Bagheri R, Moghaddam A K and Yousefnia H 2017 *Nucl. Eng. Technol.* **49** 216–23
[3] Sharifi S, Bagheri R and Shirmardi S 2013 *Ann. Nucl. Energy* **53** 529–34
[4] Singh V P, Badiger N and Kaewkhao J 2014 *J. Non-Cryst. Solids* **404** 167–73
[5] Issa S A 2016 *Radiat. Phys. Chem.* **120** 33–7
[6] Gerward L, Guilbert N, Jensen K B and Levring H 2004 *Radiat. Phys. Chem.* **71** 653–4
[7] Mouhti H I, Elanique A and Messous M Y 2017 *J. Mater. Environ. Sci.* **8** 4560–5
[8] Bashter I 1997 *Ann. Nucl. Energy* **24** 1389–401

[2] *2National Astronomical Research Institute of Thailand (NARIT), Chiang Mai, Thailandd*

[3] *Department of Physics and Materials Science, Faculty of Science, Chiang Mai University, Chiang Mai, Thailand*

[4] *Department of Physics and Astronomy, University of North Carolina at Chapel Hill, Chapel Hill, NC 27599, USA*

Corresponding Author(s): chaiyaphorn_nilarat@cmu.ac.th

PSR J10203+0038 is a transitional millisecond pulsar (tMSP) in an eclipsing binary system, which has been observed to switch between the radio loud millisecond pulsar (MSP) and low-mass-X-ray binary (LMXB) states. This behavior offers a great opportunity to study the origin of MSPs and confirming the 'recycling' scenario, a theoretical model of MSP's origin. We develop an automated pipeline to monitor the system using Python programming language and Source-Extractor software for detecting the objects and measuring its magnitude. We obtain a series of observations with the 0.6m PROMPT-8 telescope at Cerro Tololo in Chile. The magnitude threshold for alert has been set 16.884 mag in R filter. When the magnitude of the system increases over the limit, 16.884 mag in filter R, the pipeline will alert us about the next possible switching of this system. The pipeline has been running on server at National Astronomical Research of Thailand (NARIT) since January 2018. We have found that, during January and February 2018, the system still remains in LMXB state.

A7: Astronomy I / 735

Point Source Classification on Astronomical Photometric Images Using Artificial Neural Network

Author(s): Rattanapong Yoyponsan[1]

Co-author(s): Utane Sawangwit [2] ; Siramas Komonjinda [3]

[1] *Chiang Mai University*

[2] *National Astronomical Research Institute of Thailand (NARIT)*

[3] *Chiang Mai University*

Corresponding Author(s): toey.yoyponsan@gmail.com

Gravitational Optical Transient Observer (GOTO) is a set of telescopes primarily for optical follow-up observation of gravitational wave from projects such as LIGO and VIRGO. It can cover at least18 square degree of sky, and at most 36 square degree per pointing. The secondary objective of GOTO is to perform an all-sky survey. Each night, it could cover as much as 20,000 square degree of sky. Such large area of coverage produces as large number of objects. It was estimated to be able to collect 20 million sources per night. Processing such quantity of data manually is extremely difficult. One of the most challenging task is to perform object classification. A solution to this problem is to have machine perform classification, which is possible via machine learning algorithm. In this work, we use supervise machine learning performed on simulated data to create a point source classifier. We will focus on application and performance of artificial neural network in peforming classification of point sources.

A7: Astronomy I / 704

Tracking cosmic-ray spectral variations during 2007-2018 using neutron monitor time-delay measurements

Author(s): Chanoknan Banglieng[1]

Co-author(s): Alejandro Saiz [2] ; David Ruffolo [2] ; Hannarong Janthaloet [2] ; Paul Evenson [3] ; Tanin Nutaro [4] ; Roger Pyle [3] ; Surujhdeo Seunarine [5] ; Jim Madsen [6]

[1] *National Astronomical Research Institute of Thailand (NARIT), Mahidol University*

[2] *Mahidol University*

[3] *University of Delaware*

[4] *Ubon Ratchathani University*

[5] *University of Wisconsin-River Falls*

[6] *UW-River Falls*

Corresponding Author(s): bchanoknan@gmail.com

Neutron monitors usually measure the flux of cosmic rays above a geomagnetic cutoff rigidity (momentum per charge). Recently, we have developed a new capability to also study the momentum (or energy) distribution of cosmic rays. Here we use time-delay histograms collected at the Princess Sirindhorn Neutron Monitor (PSNM), Thailand, which has the world's highest vertical cutoff rigidity for a fixed station (16.8 GV), and the South Pole neutron monitor with a low geomagnetic cutoff rigidity (near 0 GV). We present measurements of the leader fraction L of neutron monitor counts that did not follow other counts in the same counter tube from the same cosmic ray shower. Variations in the cosmic-ray spectrum can be precisely indicated by changes in L. PSNM started to collect time-delay histograms in Dec 2007 and the South Pole station started in Nov 2013. The electronics have been upgraded during our measurement period, and we have corrected for such changes to develop a long-term leader fraction dataset. In addition, environmental effects from the atmosphere including pressure and water vapor have been corrected. Our procedure extends precise tracking of solar modulation of the galactic cosmic ray flux to higher energies, above 17 GeV. We find that L varied with the sunspot cycle, and a hysteresis between L and the count rate implies a change in the shape of the cosmic ray spectrum due to solar modulation from before to after the solar magnetic polarity reversals of 2012-2014. Up until early 2014, solar modulation extended to energies well above the Doi Inthanon cutoff, but afterwards it extended only shortly above the cutoff. Measurements of L from the South Pole are particularly precise and will allow detailed studies of spectral variation of cosmic rays during Forbush decreases due to solar storms and over 27-day variations due to the Sun's rotation. Partially supported by Grant RTA5980003 from the Thailand Research Fund.

A7: Astronomy I / 663

A Study of the Orbital Period of WASP-43b

Author(s): Ekburus Boonsoy[1]

Co-author(s): Nuanwan Sanguansak [2] ; Supachai Awiphan [3]

[1] *SUT*

[2] *SUT, NARIT*

[3] *NARIT, Thailand*

Corresponding Author(s): ekburus.dd@gmail.com

WASP-43b is a hot Jupiter exoplanet with an ultrashort orbital period, 0.81347 days. From previous studies, there is a possibility that the orbital period of WASP-43b is decreasing. However, from the recent studies, the results show that there is no change in the orbital period of the system. Therefore, in this work, the orbital period change of WASP-43b is investigated. Nine transit light curves obtained from three telescopes, 0.7m ROP-NM at Regional Observatory for the public Nakhon Ratchasima, 0.5m TRT-TNO at Thai National Observatory and, 0.7m TRT-GAO at Gao Mei Gu Observatory in 2017-2018 are presented. We combine the mid transit time from our data with published mid transit time of WASP-43b. The result shows that WASP-43b has an orbital period change with the rate dP⁄dt=+8.576 milliseconds per years. Therefore, there is no evidence from tidal effect in the system.

A7: Astronomy I / 669

A07: Astronomy I (Poster) / 583

Comparison of lunar calendar with lunar phase that calculate from photos of the moon

Author(s): Anutida Makmee[None]

Co-author(s): Sathon Vijarnwannaluck

Corresponding Author(s): a.nut.i@hotmail.com

The Thai lunar calendar was made from the phase of moon to defined Buddhist days and Thai traditions. The waning moon is caused by a mutual orbit of the earth, the sun and the moon. Lunar phase is ratio of bright area to the total area. The different phase each day makes a cause in the lunar calendar. The moon's synodic period is 29.53059 days but number of days in each month must be integer. Therefore there are two type of Lunar month, the 29 day month (odd number month) and the 30 day month (even number month). We have been using lunar calendar for long time so it has error. This project wants to compare lunar phase calculated from photos of the moon with Thai calendar and that from Stellarium Program. The photos were taken on 7th - 9th , 14th - 15th day before new moon and 1st , 7th – 9th day before full moon in 5th – 7th month of lunar calendar in the year 2017. And more information was collected in 1st - 4th month of the lunar calendar in year 2018. From this, we enlarged the image, made a concentric circle and print the pictures on A4 paper. Next we measured radius and the longest of dark edge for each photo. Then we calculate the lunar phase from data and compared with calendar. The calendars determined that the increase and decrease of lunar phase for each day are constant, reference point is at 6 a.m. on 1st day before new moon at the starting of the month. The result shows this method can find the lunar phase from the photos at 3 decimal places. The lunar phase from the photos and the program are similar and error is linearly independent. When compared lunar phase from photos with the calendar, 9th day before new moon and 7th day before full moon are the most error. While 7th day before new moon, full moon day, 9th before full moon give the error close to zero. The graph error of time is similar the sine function. The error of lunar phase is positive; the lunar phase from photos more than theory. If elongation error is 6 degree, 57% of information isn't in the error range.

A07: Astronomy I (Poster) / 602

Environmental Correction of Neutron Monitor Leader Fractions

Author(s): Hannarong Janthaloet[1]

Co-author(s): Alejandro Saiz Rivera [1] ; Chanoknan Banglieng [2] ; David Ruffolo [1] ; Pradiphat Muangha [2]

[1] *Mahidol University*

[2] *National Astronomical Research Institute of Thailand (NARIT)*

Corresponding Author(s): hannarong.jan@student.mahidol.ac.th

Cosmic rays are high energy particles from space that we can measure by ground-based detectors, including neutron monitors. The leader fraction represents the fraction of the neutron count rate that is not associated with a previous neutron count in the same tube from the same nuclear interaction. The leader fraction includes new and exciting information about the cosmic ray energy distribution. However, environmental factors including atmospheric pressure and water vapor also affect the leader fraction. We have developed methods to correct the leader fraction to remove these environmental effects. Partially supported by Grant RTA5980003 from the Thailand Research Fund.

A07: Astronomy I (Poster) / 610

Abstract Preview - Step 3/4

- print version -

Session: Astrophysics and Astronomy in the Polar Regions

Polar program: None

Title: Solar Energetic Particle Spectra using Neutron Detectors at South Pole

Author(s): Waraporn Nuntiyakul[1] (w.nuntiyakul@gmail.com), John Bieber[2], John Clem[2], Paul Evenson[2], Tom Gaisser[2], Allan Hallgren[3], James Madsen[4], Pierre-Simon Mangeard[2], Roger Pyle[5], David Ruffolo[6], Alejandro Sáiz[6], Surujhdeo Seunarine[4], Serap Tilav[2]

Institute(s): *[1]Chiang Mai University, Department of Physics and Materials Science, Chiangmai, Thailand, [2]University of Delaware, Department of Physics and Astronomy, Bartol Research Institute, Newark, United States, [3]Uppsala University, Department of Physics and Astronomy, Box 516, Uppsala, Sweden, [4]University of Wisconsin-River Falls, Physics Department, River Falls, United States, [5]Pyle Consulting Group, Inc., St. Charles, United States, [6]Mahidol University, Department of Physics, Faculty of Science, Ratchathewi, Thailand*

Text: Neutron monitors are ground-level detectors of cosmic ray induced atmospheric secondary particles (mostly neutrons) that are employed worldwide to study variations in the flux of galactic cosmic rays and solar energetic particles (SEPs) in the GeV regime. The neutron monitor standard design (NM64) minimizes detector response to neutrons below ~10 MeV produced by cosmic ray interactions in the ambient medium. Bare detectors or simply “bares”, which lack the lead and polyethylene of NM64 detect such neutrons and therefore respond on average to cosmic rays of lower energy. The array of NM64 and bares at the South Pole has been used for many years to measure SEP spectra relying primarily on relative response functions derived from a single latitude survey in 1976. We have recently completed analysis of a second survey from Nov, 1995 to Feb, 1996 from three bares operated together with a 3NM64. The solar modulation conditions in 1995 and 1976 were remarkably similar but the results from the 1995-6 survey differ significantly from the interpretation of the 1976 survey most commonly used for the determination of SEP spectra. We present results from a third survey from Nov, 2009 to Apr, 2010 with two bares that are now installed at the South Pole. A significant correction to the 2009-10 data due to highly different modulation conditions, and implications for interpretation of SEP spectra will be discussed.

Supported in part by Thailand Research Fund grants MRG6080086 and RTA5980003.

Preferred Presentation Type: Oral Presentation

Conference: POLAR 2018 · Abstract: A-938-0002-01377 · **Status: Submitted (checked)**

Print Back

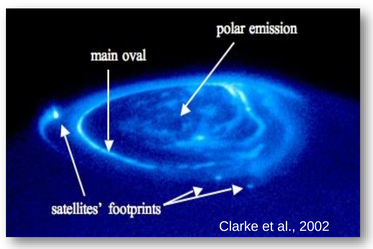
Angular Size of Io Magnetic Footprint's Main Alfvèn Wing Spot: In Corresponding to Satellite's Locations

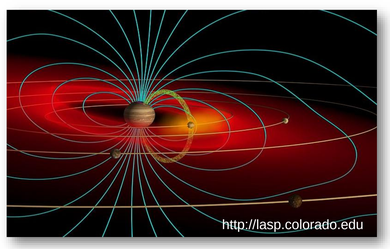
Wannawichian S., Clarke J. T., and Nichols J. D.

Abstract Satellites in planetary magnetosphere are often affected by the interaction between magnetospheric plasma and satellites' atmospheres. Due to the interaction, picked up currents travel along the magnetic field line from interaction region toward the planet's ionosphere. These currents clearly connect the vicinity of Io to Jupiter' ionosphere via magnetic field lines. In ionosphere, spot emissions can be detected at the end magnetic field line, which is known as 'Auroral Magnetic Footprint'. Io's magnetic footprint is a prominent auroral feature, which locates few degrees latitude lower from Jupiter's main auroral emission. Corresponding to interaction region at Io approximately 1.5 Io radii, the size of Io's magnetic footprint is expected to be approximately ~100 km. In this study, the size of the footprints, especially the Main Alfvèn wing spot (MAW), will be analyzed based on FUV imaging by Advanced Camera for Surveys (ACS) instrument on Hubble Space Telescope (HST). The images of Jupiter's auroral region were taken in 1998, 2000, 2001, and 2007 during HST's campaigns. For different epochs of observations, the angular sizes of Io's magnetic footprint varied with general trend, in which several emission peaks were detected. This result could be interpreted to have some correlation with the footprint brightness. According to in situ observations of plasma environment near Io, temporal and special variations of Jupiter magnetospheric plasma could be one of the factors that affect the brightness and angular size of Io's magnetic footprint.

Aurora: Satellite's Magnetic Footprint

Corresponding to difference between plasma corotating velocity and satellite's orbital velocity, the electrodynamic interaction between Jupiter's magnetospheric plasma and Io's atmospheric particles takes place in the vicinity of Io. The interaction causes Alfvènic disturbance and results in picked up charge particles along the magnetic field line from interaction region toward Jupiter Ionosphere [Kivelson et al., 2004]. Precipitating electrons cause the auroral emission at the foot of magnetic flux tube, as Satellite's magnetic footprint. Io's magnetic footprint is the most prominent emission.





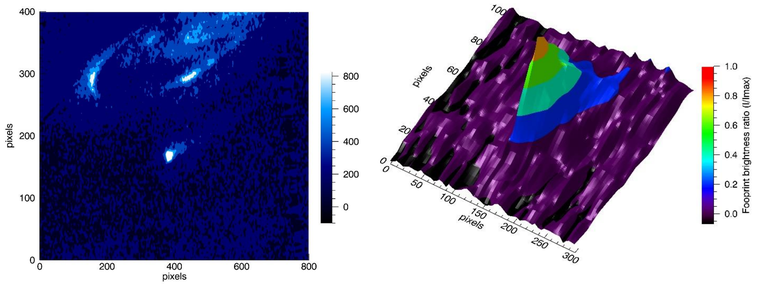
HST Observations: Data Analysis

Far-ultraviolet (FUV) imaging of auroral emissions



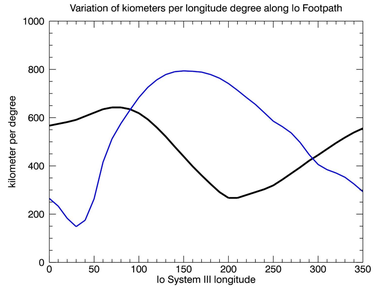
Hubble Space Telescope (HST)

Variation of brightness and size of Io's magnetic footprint is studied based on FUV images of Jupiter's auroral region, taken by ACS instrument onboard Hubble Space Telescope in 2007. Pipeline routine was developed at Boston University [Nichols et al., 2009]. Specifically, the brightness and size of Main Alfvèn Wing spot was investigated. The size of magnetic footprint corresponds to the angular size of Full Width at Half Maximum (FWHM) of the main emission spot. The brightness of the footprint is in in kilo-Rayleighs (1 kR = $10^9/4\ \pi$ photons $cm^{-2}\ sr^{-1}\ s^{-1}$).

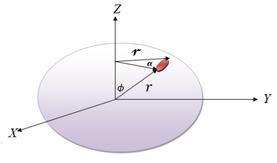


Along with the peak emission of Io's magnetic footprint (left image taken on March 2, 2007), angular extension of the footprint was analyzed as equivalent scale to the full width at half maximum (FWHM) of the emission.

Io's Angular Size: mapping on Jupiter surface



The ratio of kilometers per degree for angular size projected on Jupiter's surface as a function of the System III longitude, corresponding to the Io's footpath summarized by Bonfond et al. [2009]. The blue line is for northern footprint and the black line for southern footprint.



Where $r = \sqrt{x^2 + y^2}$, ellpsoid equation for coordinate is

$$\frac{x^2}{a^2} + \frac{y^2}{b^2} + \frac{z^2}{c^2} = 1.$$

In case of Jupiter, we can write

$$\frac{x^2}{a^2} + \frac{y^2}{a^2} + \frac{z^2}{c^2} = 1$$

Where $a = 71{,}492$ km and $c = 66{,}854$ km. Above equation can be written as

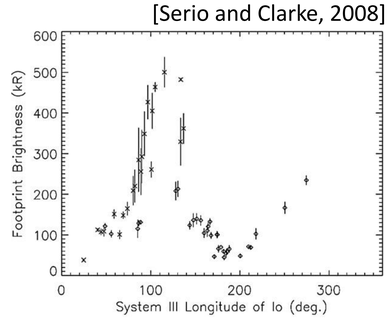
$$r^2 = \frac{a^2c^2}{c^2\sin\phi^2 + a^2\cos\phi^2}$$

Where θ is longitude and ϕ is co-latitude. From angular extension α, physical extension is $\alpha \cdot r\sin\phi$ km.

Io's Magnetic Footprint Brightness

Based on STIS/HST observations during 1997-2001, the systematic variation of Io's magnetic footprint brightness was found to strongly connect with Io's location in System III longitude, which is an indication of Io's position in the plasma torus [Serio and Clarke, 2008] and confirmed by Wannawichian et al. (2013). Along with the location of Io in plasma torus, the study of Io's magnetic footprint from 1997 to 2009 showed that the magnetic field asymmetry also influences the variation of Io's magnetic footprint brightness [Bonfond et al., 2013].

[Serio and Clarke, 2008]



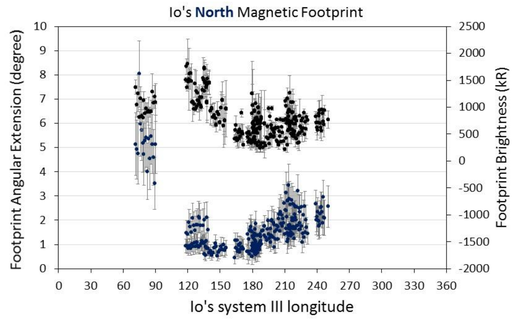
Io's Magnetic Footprint Size

With FUV auroral imaging by HST Wild Planetary Camera 2 (WFPC2), Clarke et al. (1996) found that, while the magnetic flux mapped to Io's diameter projecting to distance of 200 km at Jupiter's ionosphere, the full width at half maximum of the footprint should be between 1000-2000 km. The more detail study of the main spot's size, by Telescope Imaging Spectrograph (STIS) and Advanced Camera for Surveys (ACS) instruments on HST, revealed that the footprint's size varies between approximately 400 – 8000 km, or 1°-14° on the planet, which is suggested to depend on the size of interaction region at Io [Bonfond, 2010].

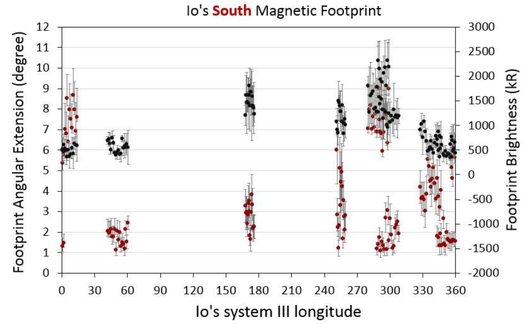
Current Work

In this study, the variation of angular extension from another observation era by the HST in 2007 is presented. In addition, a direct comparison between the angular size and the brightness of Io's magnetic footprint will reveal the influence of satellite location in the plasma torus on electrodynamic interaction at Io.

- Angular extensions of the Io magnetic footprint from several observations by the Hubble Space Telescope in 2007 show a temporal variation as a function of observing time.
- There is a strong variation trend in the angular size of Io's magnetic footprint. Several peaks appear to be noticeable; for example, when Io was near 80 and 295 degrees longitude. It must be noted that there is another peak near 0 degrees as well, which is not completely related to the magnetic footprint brightness.
- The variation of angular size appears to be under the influence of Io's system III longitude. Another explanation for the variation was due to Io's locations. The location of Io in Jupiter's magnetosphere appears to be strongly correlated with the brightness, and correspondingly the size of the satellite's magnetic footprint



The angular sizes of Io's magnetic footprint (blue dots) in Jupiter's northern auoroal region from HST observations during the 2007 campaign in comparison with the magnetic footprint brightness (black dots).



The angular sizes of Io's magnetic footprint (red dots) in Jupiter's southern auoroal region from HST observations during the 2007 campaign in comparison with the magnetic footprint brightness (black dots).

ACKNOWLEDGEMENTS This work is based on observations by the NASA/ESA Hubble Space Telescope, obtained at the Space Telescope Science Institute, which is operated by AURA Inc. for NASA. This research was supported by NASA grants HST-GO-10506.01-A and HST-GO-10862.01-A from the Space Telescope Science Institute to Boston University. Additional support was from Thailand Research Fund grants TRG5880091 and RTA5980003.

REFERENCES

Bonfond B., et al., *Geophys. Res. Lett.,* 2008; **35**: L05107, DOI 10.1029/2007GL032418.
Bonfond B., et al., *J. Geophys. Res.*, 2009; **114**: A07224, DOI 10.1029/2009JA014312.
Bonfond B., *J. Geophys. Res.*, 2010; **115**: A09217, doi:10.1029/2010JA015475.
Bonfond B., et al., *Planet. Space Sci.*, 2013; **88**: 64–75.
Clarke J. T., et al., *Science*, 1996; 274: 404-409
Clarke J. T., et a.., *J. Geophys. Res.*, 1998; **103**: 20217-20236
Clarke J. T., et al., Cambridge Univ. Press, Cambridge, UK, 2004: 639-670.
Gérard J-C., et al., *J. Geophys. Res.*, 2006; **111**: A04202, DOI 10.1029/2005JA011327.
Kivelson M. G., et al., Cambridge Univ. Press, Cambridge, UK, 2004: 513-536.
Nichols, J. D., et a., *J. Geophys. Res.*, 2009; **114**: doi:10.1029/2009JA014051
Prangé R., et al., *Nature*, 1996; **379**: 323-325
Serio A. W., and Clarke J. T., *Icarus*, 2008; **197**: 368-374
Wannawichian S., Clarke J. T., and Nichols J. D., *J. Geophys. Res.*, 2010; **115**: A02206, DOI 10.1029/2009JA014456.
Wannawichian, S., et al., *Geophys. Res.*, 2013; **118**: 3336–3345

AGU 100 FALL MEETING
Washington, D.C. | 10–14 Dec 2018

SH32A-06: Field Line Trapping, Transport, and Random Walk in an Expanding Medium with Implications for SEP Transport

Wednesday, 12 December 2018
11:35 - 11:50
Walter E Washington Convention Center - 204A-C

The random walk of magnetic field lines is an important ingredient in understanding the spatial transport of both field lines and charged particles. As solar energetic particles (SEPs) propagate away from solar sources, their interaction with both the smooth and unresolved (or random) components of the magnetic field influences where they may be observed. In an inhomogeneous medium such as the solar wind, field line transport must respond also to expansion, as well as large-scale shears. By perturbatively considering the effects of large-scale expansion, we develop a formalism in which the differential equation describing the field line random walk contains a contribution from the large-scale expansion, i.e., a non-stochastic contribution, and an additional contribution due to random magnetic displacements. The formalism is heuristically developed based on standard assumptions made in nonlinear diffusion theory. We then employ this formalism within a global magnetohydrodynamic (MHD) simulation of the solar wind, coupled with a turbulence transport model, to estimate the diffusive spreading of magnetic field lines that originate at different regions on the solar surface. We also provide an estimation of the heliocentric distance up to which field lines originating in magnetic islands can remain trapped in filamentary structures, which could explain the so-called “dropout” pattern seen in SEP observations. The statistical results obtained from the global solar wind simulations are compared with simulations of particle and field line trajectories for the case of a simple spherical expansion superposed on explicit realizations of MHD turbulence. Partially supported by grant RTA5980003 from the Thailand Research Fund, by the NASA Parker Solar Probe mission through the ISOIS project and subcontract SUB0000165 from Princeton Univ. to Univ. Delaware, by the NASA HGC program grant NNX14AI63G, and by the NASA LWS program under grant NNX15AB88G.

Authors

David J Ruffolo
Mahidol University

Rohit Chhiber
University of Delaware

William H Matthaeus
University of Delaware

Arcadi V. Usmanov
NASA Goddard SFC

University of Delaware

Paisan Tooprakai
Chulalongkorn University

Piyanate Chuychai
33/5 Moo 16, Tambon Bandu, Muang District

Melvyn L Goldstein
NASA Goddard SFC

Find Similar

View Related Events

Day: Wednesday, 12 December 2018

AGU 100 FALL MEETING
Washington, D.C. | 10–14 Dec 2018

SH31A-04: Magnetic Field Line Random Walk in Arbitrarily Stretched Isotropic Turbulence

Wednesday, 12 December 2018
08:36 - 08:48
Walter E Washington Convention Center - 207B

Many astrophysical and laboratory plasmas involve turbulent magnetic fluctuations,

and the resulting magnetic field line random walk (FLRW) plays an

important role in guiding particle and heat transport. We use a non-perturbative

analytic framework based on Corrsin's hypothesis to study diffusive field line random

walks in isotropic turbulence stretched by an arbitrary factor α, including

isotropic (α=1), quasi-2D (α << 1), and quasi-1D (α >> 1) turbulence. Analytic closed-form solutions are obtained for extreme cases of α and B_0,

and are verified by numerical solutions of the equations. We use Padé approximants to interpolate all versions of theory for extreme cases of α to any B_0. With the stretched isotropic turbulence, the FLRW behavior scaled by the Kubo number R can be qualitatively understood. Additional

confirmation is provided by computer simulations to trace turbulent magnetic

field lines, which do not employ Corrsin's hypothesis. This work was partially supported by the Thailand

Research Fund award RTA5980003.

Authors

Wirin Sonsrettee
Panyapiwat Institute of Management

David J Ruffolo
Mahidol University

William H Matthaeus
University of Delaware

Andrew P Snodin
King Mongkut's University of Technology North Bangkok

Pat Wongpan
Now at: University of Otago

Mahidol University

Piyanate Chuychai
33/5 Moo 16, Tambon Bandu, Muang District

Paisan Tooprakai
Chulalongkorn University

Satwik Vyas
Indian Institute of Technology Roorkee

Jatumet Thueanmuenwai
Chulalongkorn University

Samagorn Boonnum
Chulalongkorn University

Find Similar

View Related Events

Day: Wednesday, 12 December 2018

AGU 100 FALL MEETING
Washington, D.C. | 10–14 Dec 2018

SH51C-2840: Drift and Diffusion of Energetic Charged Particles in Nonaxisymmetric Two-Component Magnetic Turbulence with Nonuniform Large Scale Field

Friday, 14 December 2018
08:00 - 12:20
Walter E Washington Convention Center - Hall A-C (Poster Hall)

The guiding center drift in a nonuniform magnetic field is an important process in energetic particle transport and solar modulation of cosmic rays. A turbulent magnetic field is known to reduce the particle drift, but studies to date have mainly focused on axisymmetric turbulence, whereas solar wind expansion is expected to stretch turbulent structures preferentially in certain directions. In this study, we discuss both theory and numerical simulations about the perpendicular transport of energetic charged particles in nonaxisymmetric two-component (2D+slab) turbulence with a nonuniform background field in terms of the Fokker-Planck coefficients of drift and diffusion in each direction. We numerically trace trajectories of charged particles in this model magnetic field, where the large scale field, in the *z*-direction, is a function of *x* and we vary an ellipticity parameter ξ that controls the nonaxisymmetry of the 2D+slab turbulence. The 2D turbulence is made nonaxisymmetric by stretching the 2D structures along *x* or *y*. Then we compute the ensemble average drift and diffusion coefficients to explore the particle transport in various cases, in comparison with theoretical results. This work was partially supported by the Thailand Research Fund award RTA5980003.

Authors

Piyanate Chuychai
33/5 Moo 16, Tambon Bandu, Muang District

Eugene Engelbrecht
National Institute for Theoretical Physics (NITheP)

Center for Space Research, North-West University

David J Ruffolo
Mahidol University

Find Similar

View Related Events

Day: Friday, 14 December 2018

A simplified phase coherence index to characterize intermittent fluctuations

D. Ruffolo[1,*] and A. P. Snodin[2]

[1]Department of Physics, Faculty of Science, Mahidol University, Bangkok, 10400, Thailand
[2]Department of Mathematics, Faculty of Applied Science, King Mongkut's University of Technology North Bangkok, Bangkok 10800, Thailand
* Corresponding author. E-mail address: david.ruf@mahidol.ac.th

Abstract

Intermittency refers to fluctuations with a non-Gaussian distribution of increments. For example, turbulent fluctuations in a fluid or plasma typically have a finite spatial correlation scale λ, and increments (differences) in the fluctuating quantity at locations separated by d have a Gaussian distribution for $d >> \lambda$ but a leptokurtic distribution (with enhanced tails) for $d << \lambda$. Physically, this implies that in turbulence, relatively large jumps in physical quantities over small scales are unusually frequent, indicating coherent structures with enhanced vorticity or electric current where energy dissipation is enhanced. Among other measures, a phase coherence index (PCI) has been widely used to characterize intermittency. The original definition of the PCI requires transforming an original data set into surrogate data sets, the phase coherent surrogate and phase randomized surrogate, usually by means of a Fourier transform, manipulation of the Fourier phases, and an inverse Fourier transform. We point out that this definition can depend on the sample size. In the limit of a large sample, the phase coherent surrogate plays no role, and the phase randomized surrogate simply has a Gaussian distribution for the same variance. We therefore propose a simplified phase coherence index (SPCI) in which these properties are assumed without requiring preparation of the surrogate data sets, greatly decreasing the computation time. We also point out that this SPCI is directly related to the mean increment magnitude of the original data set in comparison with a Gaussian distribution of the same variance. This implies that it is a direct measure of leptokurticity and not an independent measure as some previous work has implied. We discuss generalization of this SPCI to multidimensions and higher-order moments. Supported by grant RTA5980003 from the Thailand Research Fund.

Keywords: phase coherence index, intermittency, turbulence, distributions

Track 01 **O01-ID094**

Empirical Model of Magnetic Field Line Spreading in Isotropic Turbulence with Zero Mean Field

Wirin Sonsrettee*

Faculty of Engineering and Technology, Panyapiwat Institute of Management, Nonthaburi 11120, Thailand
*Corresponding author.E-mail address: bturbulence@gmail.com

Abstract

In many cases, the random walk of magnetic field line in isotropic turbulence with zero mean field is appropriate to describe the transport of energetic particles in the interstellar medium of our Galaxy. To understand the transport, our previous work determined the asymptotic field line diffusion coefficient by using Corrsin's hypothesis and presumed models of field line spreading. Two of those models of field line spreading are the diffusive decorrelation (DD) model and the random ballistic decorrelation (RBD) model. The variances of the field line displacement in, say, the x direction for the DD and RBD models are assumed as $\sigma_x^2 = 2D|\Delta\tau| = 2(\tilde{\lambda}/\sqrt{3})b|\Delta\tau|$ and $\sigma_x^2 = (1/3)b^2|\Delta\tau|^2$, respectively. τ is the field line displacement parameter defined as $d\tau = ds/B$, where s is the arc length along the field line and B is the magnitude of the total magnetic field. D is the asymptotic diffusion coefficient, b is the rms magnetic fluctuation and $\tilde{\lambda}$ is the ultrascale. Comparing with simulation results, the DD and RBD models predict the D values with $\leq 15\%$ error and $\leq 21\%$ error, respectively. To improve the theoretical model empirically, in this work, we assume that the proper model of the variance is $\sigma_x^2 = \beta(b|\Delta\tau|)^{\alpha}$, where β is a proportional constant and α is an exponent. We extrapolate β with the proportional constants of DD and RBD models. Comparing with the simulation result of Kolmogorov turbulence, we obtain $\alpha = 0.8694$. To test the validity, we compare the theoretical results of $\sigma_x^2 = \beta(b|\Delta\tau|)^{0.8694}$ model, which is formulated from Kolmogorov turbulence, with simulation results of two other turbulences: Iroshnikov–Kraichnan turbulence and weak turbulence. The theoretical results of the empirical model match the computer simulation results very well (with $\leq 0.9\%$ error). This research is supported by grant RTA5980003 from the Thailand Research Fund.

Keywords: diffusion, interstellar medium, magnetic fields, turbulence

Track 01 **O01-ID106**

A Data-Driven Simulation Study of Magnetic Reconnection at the Leading Edge of an Interplanetary Coronal Mass Ejection on 2005 January 21

P Prapan, K Malakit and D Ruffolo

Department of Physics, Faculty of Science, Mahidol University, Bangkok, 10400, Thailand
* Corresponding author. E-mail address: pakkapawn.prp@student.mahidol.ac.th

Abstract

Magnetic Reconnection is a magnetic field rearrangement that causes the system to achieve the lower energy state through transferring the energy retained in the magnetic field into kinetic and thermal energy of the plasma. There is some interesting observational evidence of magnetic reconnection that was observed in the interplanetary region between the Sun and the Earth's magnetosphere by *Chian* and *Muñoz* (2011). On 2005 January 21, four *Cluster* spacecraft detected asymmetric reconnection at the leading edge of an interplanetary coronal mass ejection (ICME). In this work we model asymmetric reconnection in that event. We perform a data-driven simulation using a Particle-In-Cell (PIC) model, which treats both ions and electrons as non-interacting particles. Finally, we compared our results with observational data. This research is supported by grant RTA5980003 and grant MRG6180176 from the Thailand Research Fund.

Keywords: magnetic reconnection, asymmetric reconnection, particle-in-cell

Track 01 **P01-ID030**

Finding the response function of neutron monitors through FLUKA simulations: A case study of the Changvan neutron monitor

Audcharaporn Pagwhan[1,2], Waraporn Nuntiyakul[1*], Alejandro Saiz[3]

1 Department of Physics and Materials Science, Faculty of Science, Chiang Mai University, Chiang Mai, 50200, THAILAND
2 National Astronomical Research Institute of Thailand (NARIT), Chiang Mai, 50180, THAILAND
3 Department of Physics, Faculty of Science, Mahidol University, Bangkok, 10400, THAILAND
* Corresponding author. E-mail address: waraporn.n@cmu.ac.th

Abstract

Neutron monitors are the arch instruments for measuring the neutron debris left after primary cosmic rays enter the Earth's atmosphere, and tracking time variations in the cosmic rays at GeV-range energies. The neutron monitor standard design (NM64) contains lead, termed the producer that, when hit by a high-energy neutron, emits low energy neutrons. These are slowed further by the polyethylene moderator and are detected by induced nuclear fission of ^{10}B in a $^{10}BF_3$ gas-filled proportional counter. An outer layer of polyethylene, termed the reflector, contains the low energy neutrons produced in the lead and excludes low energy environmental neutrons. A bare neutron counter or simply "bare", which lacks the lead of the NM64 monitor, detects such neutrons and therefore responds on average to cosmic rays of lower energy. We develop and build, in Thailand, well-behaved portable neutron monitors housed in a standard insulated shipping container, called "Changvan", in order to conduct long-term research in polar regions. At any given location, the magnetic field of the Earth blocks cosmic rays below a well-defined geomagnetic cutoff. Due to limited time and budget, we were unable to install three units of the NM64, technically known as a 3NM64, as intended, and instead a 2NM64 (two tubes flanking left and right) with a center bare were installed in the Changvan. Monte Carlo simulations to study the detection efficiency of the Changvan neutron monitors can be used. FLUKA is one of the well-known Monte Carlo codes to simulate cosmic ray cascades. In this work, we have modified the geometry model of the Changvan in FLUKA to look more realistic. We study the thickness of the container's walls that affects the response function. Besides that, we also simulate the Changvan neutron monitors with different surrounding conditions developed to determine the differences in the response functions. The simulation results will be discussed in the presentation. Supported by grants MRG6280155 and RTA5980003 from the Thailand Research Fund.

Keywords: neutron monitor, Changvan, FLUKA simulation

Track 01 **P01-ID046**

Water Vapor Correction to Cosmic Ray Flux Measurements with Neutron Counters at Doi Inthanon

Yanee Tangjai[1,2], Waraporn Nuntiyakul[1*], David Ruffolo[3], Chanoknan Banglieng[3]

[1] Department of Physics and Materials Science, Faculty of Science, Chiang Mai University, Chiang Mai, 50200, Thailand
[2] National Astronomical Research Institute of Thailand (NARIT), Chiang Mai, 50180, THAILAND
[3] Department of Physics, Faculty of Science, Mahidol University, Bangkok, 10400, THAILAND
[*]Corresponding author. E-mail address: waraporn.n@cmu.ac.th

Abstract

High-energy cosmic rays interact in the upper atmosphere, leading to a shower of subatomic particles, some of which reach Earth's surface. Large ground-level detectors use these secondary particles to provide accurate measurements of variations in the cosmic ray flux from space. One widely used type of detector is the "neutron monitor (NM64)" that is mostly sensitive to the neutron component of the atmospheric shower with high precision (~0.1%) over such time scales. A bare neutron counter, which lacks the lead and polyethylene of the NM64, detects neutrons of lower energy and therefore responds on average to cosmic rays of lower energy. To avoid data contamination by variations in pressure and precipitable water vapor (PWV) here we show the results of the count rate and the bare/NM64 count rate ratio as corrected for pressure and PWV dependences. We corrected the data from the Princess Sirindhorn Neutron Monitor at Doi Inthanon, Chiang Mai, Thailand, with the world's highest vertical geomagnetic cutoff rigidity, 16.8 GV, from December 2007 to December 2017 and searched for evidence of cosmic ray spectral variations from systematic changes in the bare/NM64 count rate ratio. Supported by grants MRG6280155 and RTA5980003 from the Thailand Research Fund.

Keywords: precipitable water vapor, cosmic rays, neutron monitor

Track 01 **O01-ID240**

Atmospheric water vapor correction to cosmic ray spectrum measurements from Princess Sirindhorn Neutron Monitor

C. Banglieng[1,2], P. Muangha[1,2], D. Ruffolo[1,*], A. Sáiz[1], H. Janthaloet[1], P. Evenson[3], T. Nutaro[4], P. Supnithi[5] and J. Budtho[5]

[1]Department of Physics, Faculty of Science, Mahidol University, Bangkok, Thailand
[2]National Astronomical Research Institute of Thailand (NARIT), Chiang Mai, Thailand
[3]Bartol Research Institute, Department of Physics and Astronomy, University of Delaware, Newark, DE, USA.
[4]Department of Physics, Faculty of Science, Ubon Ratchathani University, Ubon Ratchathani, Thailand.
[5]Telecommunications Engineering Department, Faculty of Engineering, King Mongkut's Institute of Technology Ladkrabang
*Corresponding author. E-mail address: david.ruf@mahidol.ac.th

Abstract

Since 2007, the count rate of the Princess Sirindhorn Neutron Monitor (PSNM) at the summit of Doi Inthanon, Thailand has been used for measuring the flux of galactic cosmic rays above the geomagnetic cutoff rigidity (~17 GV). PSNM has also collected time-delay histograms for estimating the leader fraction L of neutron monitor counts that did not follow other counts, which can be used to track variation of cosmic ray spectrum by using data from a single neutron monitor station. The neutron monitor count rates from all stations have been corrected for the variation of atmospheric pressure. In previous work, we also found a very strong variation of L due to variations in water vapor pressure, especially at the tropical location of Doi Inthanon. The atmospheric pressure at PSNM has been measured directly by two Digiquartz barometers but water vapor pressure has been inferred indirectly from the Global Atmospheric Data Assimilation (GDAS) database. In this work, we developed a new correction by using a smoothed time series of the precipitable water vapor (PWV) to provide a model for the water vapor effect on L. We will compare the results from smoothed PWV evaluated from GDAS and the Modern-Era Retrospective analysis for Research and Applications, Version 2 (MERRA-2), as well as PWV inferred from direct GPS measurement at Doi Inthanon. Partially supported by Grant RTA5980003 from the Thailand Research Fund.

Keywords: cosmic rays, neutron monitors, water vapor pressure

Track 01 **O01-ID241**

Can single secondary particles from cosmic rays explain the high counter multiplicity rate at the Princess Sirindhorn Neutron Monitor?

H. Janthaloet[*,1],D. Ruffolo[1], P.-S. Mangeard[2] and A.Sáiz[1]

[1]Department of Physics, Faculty of Science, Mahidol University, Bangkok, 10400, Thailand.
[2]Department of Physics and Astronomy, University of Delaware, Newark, DE, 19716, USA.
* Corresponding author. E-mail address: hannarong.jan@student.mahidol.ac.th

Abstract

Primary cosmic rays (PPs) are high energy particles including protons and heavier nuclei, many of which originated outside our solar system. When PPs interact with Earth's atmosphere, they can generate more particles, for example, electrons, neutrons, pions, etc. We call these secondary cosmic ray particles (SPs). A neutron monitor (NM) is a ground based detector that mostly detects secondary neutrons from PPs. We can study time variation of the PP flux or spectrum by using NMs. When SPs hit the lead inside the detector, they can produce more neutrons that can be detected by proportional counters (containing $^{10}BF_3$ gas). In Thailand, the Princess Sirindhorn Neutron Monitor station (PSNM) is located at Doi Inthanon, Thailand's highest mountain, which has the highest geomagnetic cutoff of any NM station in the world. In this work, we want to explain results from a recent experiment regarding high counter multiplicity, in which most of the counter tubes registered counts within a short time window. We simulate SP detection at PSNM and address this question: Can single secondary particles from cosmic rays explain the high counter multiplicity rate measured at the Princess Siridhorn Neutron Monitor? To answer this, we performed state of the art Monte Carlo simulations with the FLUKA program, extending NM modeling capabilities. Supported by grant RTA5980003 from the Thailand Research Fund.

Keywords: cosmic rays, neutron, multiplicity, computer simulation

Track 06 **P06-ID253**

Motion of charged particles around the region of magnetic reconnection : a test charge approach

Suthipong Ngamkhum* and Kittipat Malakit

Department of Physics , Faculty of Science and Technology, Thammasat University, Pathumthani , 12121 , Thailand
*Corresponding author. E-mail address: suthipong.ngamkhum@gmail.com

Abstract

This study focuses on the motion of charged particles that are under the influence of electric and magnetic fields around the region of magnetic reconnection by using a test-charge approach. In order to simulate the motion of particle, we use and compare two methods to step particle forward in time: Euler's method and Boris algorithm. We found that stepping particle forward using Boris algorithm conserves energy and retains circular motion of particle under a magnetic field better than stepping forward with Euler's method. After studying the methods for stepping forward particle, we used the Boris algorithm to step forward particle under the magnetic and electric fields of magnetic reconnection obtained from a particle-in-cell simulation, which is expected to produce the most realistic electric and magnetic fields out of all types of reconnection simulation available. Finally, the motions of charged particles around the reconnection region are then analyzed. This research is supported by grant RTA5980003 and grant MRG6180176 from the Thailand Research Fund.

Keywords: magnetic reconnection, motion of charged particles, test charge approach

Track 01 **O01-ID251**

Observations of the Earth's Gamma-ray Emission in Geographical Coordinates by *Fermi* LAT

S. Madlee,[1*] W. Mitthumsiri,[1] D. Ruffolo,[1] S. Digel,[2] and W. Nuntiyakul[3]

[1]Department of Physics, Faculty of Science, Mahidol University, Bangkok 10400, Thailand
[2]Kavli Institute for Particle Astrophysics and Cosmology, SLAC National Accelerator Laboratory, Stanford University, Stanford, California 94305, USA
[3]Department of Physics and Materials Science, Faculty of Science, Chiang Mai University, Chiang Mai 50200, Thailand
* Corresponding author. E-mail address: suttiwat.mad@student.mahidol.ac.th

Abstract

Interactions between cosmic rays (CRs), high-energy particles in space, and the Earth's atmosphere produce showers of secondary particles including gamma rays, which dominate Earth's gamma-ray emission. In this study, we analyze Earth's gamma-ray photons between 0.2 and 20 GeV as detected by the Large Area Telescope (LAT) onboard the *Fermi* Gamma-ray Space Telescope, which was launched in 2008 to orbit the Earth at roughly 550-km altitude. We present preliminary results of an analysis of the Earth's gamma-ray emission in the geographical coordinates (latitude and longitude) using 9 years of the latest version of the LAT event selection (Pass 8). We show that the gamma-ray intensity from a given geographic location is inversely related to the geomagnetic cutoff rigidity (where rigidity is the particle momentum per charge, and the geomagnetic cutoff rigidity is the threshold rigidity needed to for a CR to penetrate Earth's magnetic field and enter the atmosphere), taking into account the direction from which the CR arrived. We also measure the yield function of gamma rays over 0.2 GeV produced per CR proton as a function of the CR rigidity. This work will enhance our understanding about the geomagnetic field and CRs. This research project is supported by Grant RTA5980003 from the Thailand Research Fund.

Keywords: Earth's gamma-ray emission, cosmic rays

Track 01 **O01-ID312**

Galactic Cosmic-Ray Anisotropy During Forbush Decreases: A Case Study of Six Forbush Decrease Events

G. Ihongo [1,2], D. Ruffolo [1], A. Sáiz [1], U. Tortermpun [1], J. W. Bieber [3], and A. C.-L. Chian [4,5,6]

[1]Department of Physics, Faculty of Science, Mahidol University, Bangkok 10400, Thailand
[2]Department of Physics, Faculty of Science, Benue State University Makurdi 102119, Nigeria.
[3]Bartol Research Institute, Department of Physics and Astronomy, University of Delaware, Newark, DE 19716, USA
[4]School of Mathematical Sciences, University of Adelaide, Adelaide, SA 5005, Australia
[5]Institute of Aeronautical Technology, São José dos Campos, SP, 12228-900, Brazil
[6]National Institute for Space Research, São José dos Campos, SP, 12227-010, Brazil

Abstract

Galactic cosmic ray anisotropy inferred from ground observations of galactic cosmic rays during Forbush decrease events can provide very useful information on local plasma and magnetic field structures such as the magnetic field structures of an interplanetary coronal mass ejection (ICME), because the galactic cosmic ray distribution allows remote sensing of distant conditions. Here, we employed an improved technique initially developed by Tortempun et al. (2018), to study galactic cosmic ray anisotropy during 6 Forbush decrease events and found that the anisotropy parallel to the magnetic field vector (B) anticorrelates with the anisotropy perpendicular to the magnetic field vector (B). For example, our results showed spikes of high perpendicular anisotropy and weak parallel anisotropy during period of interplanetary shock-sheath interactions, while a high parallel anisotropy is seen during the period of magnetic cloud passage.
The authors acknowledge support from Grant RTA5980003 from the Thailand Research fund.

Keywords: cosmic rays, anisotropy, distributions

Track 01 **O01-ID294**

Pitch Angle Diffusion Coefficients in Test Particle Simulations and the Estimation of the Particle Parallel Mean Free Path

Chanidaporn Pleumpreedaporn and Andrew Snodin

Department of Mathematics, Faculty of Applied Science, King Mongkut's University of Technology North Bangkok, Bangkok 10800, Thailand
E-mail address: pim4599@hotmail.com

Abstract

The transport of energetic charged particles in turbulent magnetic fields is a topic of interest in various astrophysical contexts. In order to estimate the mean free path of a particle in the direction parallel to the mean magnetic field, one can use theoretical expressions that employ pitch angle diffusion coefficients. In this work we review some of the methods used in estimating pitch angle diffusion coefficients from test particle computer simulations. We examine if these methods and theoretical approaches are able to provide consistent estimates of the parallel mean free path, that can also be obtained directly from computer simulations. We perform test particle simulations for synthetic turbulence models over a range of turbulence parameters and particle energies. From the trajectories of test particles, pitch angle distribution functions and statistics of pitch angle displacements are obtained, which are then used to estimate the pitch angle diffusion coefficients. We find that a method using the pitch angle flux and derivative of the pitch angle distribution is able to provide accurate values for the parallel mean free path over the range of parameters considered. Other methods considered are accurate only for a limited range of the turbulent fluctuation strength, or must be evaluated at a specific time to provide a reasonable estimate.
Supported by grant RTA5980003 from the Thailand Research Fund.

Keywords: diffusion, magnetic fields, turbulence

PROCEEDINGS OF SCIENCE

Neutron monitor time-delay measurements to track cosmic ray spectral variation due to solar modulation at high and low cutoff rigidity

C. Banglieng[*1,2], H. Janthaloet[1], D. Ruffolo[1], A. Sáiz[1], W. Mitthumsiri[1], P. Evenson[3], T. Nutaro[4], R. Pyle[5], S. Seunarine[6], and J. Madsen[6],

[1] *Department of Physics, Faculty of Science, Mahidol University, Bangkok 10400, Thailand.*
[2] *National Astronomical Research Institute of Thailand (NARIT), Chiang Mai 50180, Thailand.*
[3] *Bartol Research Institute and Department of Physics and Astronomy, University of Delaware, Newark, DE 19716, USA.*
[4] *Department of Physics, Faculty of Science, Ubon Ratchathani University, Ubon Ratchathani 34190, Thailand.*
[5] *Pyle Consulting Group, Inc., St. Charles, IL 60174, USA.*
[6] *Department of Physics, University of Wisconsin, River Falls, WI 54022, USA.*
E-mail: bchanoknan@gmail.com, hannarong.jan@student.mahidol.ac.th, david.ruf@mahidol.ac.th, alejandro.sai@mahidol.ac.th, warit.mit@mahidol.ac.th, evenson@udel.edu, tnutaro@yahoo.com, rogerpyle@gmail.com, surujhdeo.seunarine@uwrf.edu, james.madsen@uwrf.edu

The solar modulation of Galactic cosmic rays (GCRs) provides remote sensing of heliospheric conditions throughout the ∼11-yr sunspot cycle and ∼22-yr solar magnetic cycle. Neutron monitors (NMs) can measure cosmic ray rates above a cutoff rigidity with high precision (∼0.1%) over such time scales. To avoid systematic uncertainties in comparing NM count rates from different stations, here we study solar modulation of the GCR spectrum by independently using neutron time-delay histograms to determine the leader fraction L, i.e., the inverse neutron multiplicity, as a proxy of the GCR spectral index above the cutoff. Data were collected using specialized electronics at two high-altitude NM stations: 1) the Princess Sirindhorn Neutron Monitor (PSNM) at Doi Inthanon, Thailand, with the world's highest vertical geomagnetic cutoff rigidity, 16.8 GV, from 2007 December to 2018 September, and 2) the South Pole Neutron Monitor with an atmosphere-limited cutoff of ∼1 GV, from 2013 December to 2018 September. After correcting for pressure and (in Thailand) precipitable water vapor, we find that L is roughly correlated with the count rate, but also exhibits hysteresis that indicates a change in spectral shape after the change in solar magnetic polarity. These methods enhance the high-precision GCR spectral information from the worldwide NM network and extend it to higher rigidity.

36th International Cosmic Ray Conference -ICRC2019-
July 24th - August 1st, 2019
Madison, WI, U.S.A.

*Speaker.

© Copyright owned by the author(s) under the terms of the Creative Commons Attribution-NonCommercial-NoDerivatives 4.0 International License (CC BY-NC-ND 4.0).

1. Introduction

Neutron monitors (NMs) are ground-based detectors of secondary neutrons from nuclear cascade in the Earth's atmosphere. NMs have high precisely measured the variation of Galactic cosmic rays due to the solar modulation, i.e., variations with the roughly 11-year sunspot cycle and 22-year solar magnetic cycle. Solar modulation is strongly energy-dependent and a disadvantage of NMs is that the primary cosmic ray energy cannot be measured directly. The magnetic latitude on the Earth's surface can be used to provide the cutoff rigidity (momentum per charge), the lowest of cosmic rays that can arrive at the atmosphere above the monitor. The effective geomagnetic cutoff for vertically arriving particles varies from $\sim$17 GV in and near Thailand to $<$ 0.01 GV in some polar regions. Therefore, the worldwide NM network can provide some information on GCR spectral variations in an intermediate rigidity range when comparing count rates at different cutoff rigidities. Although individual NM can measure cosmic ray flux with high statistical precision, comparison of long-term data from different stations are many effects to concern such as different NM configurations, electronic dead time, structures surrounding the stations, seasonal effects, and atmospheric structure as well as long-term drifts.

Therefore, we have developed a capability to precisely track spectral variations using data from an individual NM station. By using the specialized electronics were designed to record neutron time-delay histograms. The techniques to remove the effect of chance coincidences and extract the "leader fraction" L of neutron monitor count that did not follow other counts in the same counter tube from the same cosmic ray shower were also developed in the previous work as shown in Ref. [11]. Princess Sirindhorn Neutron Monitor (PSNM) at Doi Inthanon, Thailand, which has the world's highest vertical cutoff rigidity ($\approx$ 16.8 GV) is the first fixed station using these electronics. In addition, South Pole Neutron Monitor at Antarctica, which the lowest vertical cutoff rigidity started using these electronics in 2013 Dec. Here we present a long-term dataset of the leader fraction at Doi Inthanon from 2007 December to 2018 April, which spans a full cycle of solar modulation, including the all-time cosmic ray maximum of 2009 and minimum near the end of 2014 and also at South Pole from 2013 December to 2018 April which started near solar minimum.

2. Neutron monitor time-delay observations

In our analysis, we used time-delay measurement from Princess Sirindhorn Neutron Monitor (PSNM) which located at the summit of Doi Inthanon, Thailand's highest mountain, at latitude 18.59°N, longitude 98.49°E and altitude 2560 m, has taken count rate and recorded the time delay between successive count in the same neutron counter tube using the specialized electronics with a complete set of the standard 18NM64 configuration since 2007 December 9 and South Pole NM, the neutron monitor station at an altitude of 2828 m with three 1NM64 detectors, has taken time delays since 2013 Dec 9 on the only one tube with 600 series.

Table 1 and 2 describes the development of the firmware in the electronics and the software in the data acquisition system used to collect time delay histograms at PSNM and South Pole NM recently. PSNM has used our electronics since the start of operations in 2007 August. In our analysis, we started to analyze data when the complete set of 18 counter tubes were operated. The normalization periods at Doi Inthanon (DI-1 to DI-9) are characterized depending on the significant

changes in firmware and/or software. Note that the changes these do not affect the separate circuitry used to record count rate. The original firmware 600 series used to collect time-delay histograms at Doi Inthanon and South Pole during the earlier periods as in DI-1 and SP-1 are limited to collect only 16 Hz per tube resulting in the "fist-pulse bias" described by [11]. Then during DI-2 starting on 2011 January 15, we upgraded to the 700 series to collect time delays at up to 48 Hz per tube for improved statistics but South Pole NM had never used the 700 series.

On 2014 February 8, we started the process of upgrading to the 800 series firmware on Tube 1 but this initial version of firmware did not provide usable histograms then during DI-3 we use only 700 series firmware on the remaining 17 tubes. The complete development of the 800 series firmware was first used for 18 counter tubes on 2014 June 11 in order to calculate absolute times and cross-tube time delays, which are not used in the present analysis [12]. Because of the absolute time delays are calculated by the data acquisition software, therefore can depend on changes in the software version or computer. Starting with the 800 series during DI-4a, there were problems of software that can be corrected with a daily cadence, after that hourly histograms are usable again. On 2014 December 7, we swapped the counter tube number 1 and 18 in order to study the effect of tube position. During DI-5, we changed the software version to record time delays and the normalization L was lower than L during DI-4. We did not observe any differences in L associate with further changes in the software version. At the same time, South Pole NM has used the 800 series for the complete set of 3 counter tubes, but the time-delay histograms recorded during 2014 Nov 28 - 2015 Mar 2, were not useful. After 2015 Mar 3, South Pole NM had been used the 800-series firmware to collect time delay histograms from all 3 counter tubes.

To normalize L from the 600-series firmware, we did the experiment to calibrate L of 600 series to 800 series in DI-6 periods as details in Table 1. We also performed calibration for South Pole between 2017 Dec 18 and 2018 Jan 30 after that we used 800 series for all tubes. On 2016 May 18, we upgraded the data acquisition computer for PSNM to be the newer computer and we found L of 800 series from the newer computer slightly higher than L from older computer. Therefore, we performed an experiment again during DI-8 as detail in Table 1. Afterward, PSNM has used the 800-series to collect time-delay histograms. Our analysis ended on 2018 April 19.

3. Leader fraction analysis

3.1 Extraction of the leader fraction

The definition of leader fraction L is the fraction of neutron counts that did not follow another count in the same tube due to the same primary cosmic rays. Therefore, These leader neutrons did not follow another count in the same tube with a short time delay that is not consistent with chance coincidence. Ref.[11] developed method to statistically remove the effect of chance coincidence to extract the leader fraction. More energetic primary cosmic rays lead to more energetic secondary particles that produce more neutrons when interacting inside the neutron monitor (typically in the lead producer), which can then be detected as sequences of more counts in the same tube with shorter time delays. Thus a harder cosmic ray spectrum with a lower spectral index leads to a lower leader fraction. There were three methods described in Ref.[11] and this work used the first method to calculate the leader fraction L.

Table 1: Time periods of neutron time-delay data collection from the 18NM64 at Doi Inthanon, Thailand

Normalization period	Start date	End date	Cadence	Firmware series (Number of tubes)	Software version[a]
DI-1a	2007 Dec 9	2009 Jun 28	Daily	600 (18)	-
DI-1b	2009 Jun 29	2011 Jan 15	Hourly	600 (18)	-
DI-2	2011 Jan 15	2014 Feb 8	Hourly	700 (18)	-
DI-3	2014 Feb 8	2014 Jun 11	Hourly	700 (17)	-
DI-4a	2014 Jun 11	2014 Dec 6	Daily	800 (18)	8.34-8.46
DI-4b	2014 Dec 7	2015 Mar 3	Hourly	800 (18)	8.47
DI-5	2015 Mar 3	2015 May 29	Hourly	800 (18)	8.50
DI-6a	2015 May 31	2016 May 17	Hourly	600 (6), 800 (12)	8.50-8.82
DI-6b	2016 May 18	2016 Jun 30	Hourly	600 (6), 800 (12)	8.82
DI-7	2016 Jun 30	2017 Jun 12	Hourly	800 (18)	8.82
DI-8	2017 Jun 12	2017 Aug 3	Hourly	600(6), 700(6), 800(6)	8.91-8.93
DI-9	2017 Aug 4	2018 Apr 19	Hourly	800 (18)	8.93-8.124

[a]Only relevant for 800 firmware.

Table 2: Time periods of neutron time-delay data collection from the 3×1NM64 at South Pole, Antarctica

Normalization period	Start date	End date	Cadence	Firmware series (Number of tubes)	Software version[a]
SP-1	2013 Dec 9	2014 Nov 27	Hourly	600 (1)	-
SP-2a	2015 Mar 3	2015 Mar 5	Hourly	800 (3)	8.47
SP-2b	2015 Mar 6	2017 Dec 9	Hourly	800 (3)	8.50-8.80
SP-3	2017 Dec 18	2018 Jan 30	Hourly	600 (1), 800 (2)	8.80
SP-4	2018 Jan 31	2018 Apr 19	Hourly	800 (3)	8.80

[a]Only relevant for 800 firmware.

3.2 Correction and Normalization of the Leader Fraction

NM count rates are always corrected for pressure variation so for the leader fraction L has been found to vary with P as well. Moreover, at the tropical location of Doi Inthanon, water vapor variation is affected to both L and C. Even though the effect of water vapor on count rate has small, with a peak-to-peak seasonal variation of 0.3% but significant for study solar modulation at Doi Inthanon because the peak-to-peak variation due to solar modulation is 3% [10]. In this work, we did the correction for L and C based on Precipitable Water Vapor (PWV),i.e., the height of liquid water (in mm) that would result if all the water vapor in the atmosphere were to condense at the surface, at Doi Inthanon as determined from the Global Atmospheric Data Assimilation (GDAS) database (see http://ready.arl.noaa.gov/gdas1.php). However, South Pole is extremely dry location,

the effect of atmospheric water vapor are negligible.

The pressure and water vapor corrected L for each counter tube are different mainly due to its position and electronics dead time. We first normalized L from each tube to a standard set of tubes based on statistics of measured L ratios. These ratios were slightly dependent on the firmware, so we used the mean ratios for each firmware. The systematic effect from histograms of the software version before version 8.50 that provides a higher L. Therefore, we performed an experiment on 2018 Mar 20 to simultaneously collect time-delay histograms using software version 8.47 and 8.11. The mean ratio of L as determined from these two software versions was used to normalize L from normalization period DI-4. We used the mean ratio of L in the normalization period DI-8 to normalize L from 600- and 700- series firmware to 800 series firmware. After that normalization, L was averaged over all tubes that provided good data.

4. Spectral variations of galactic cosmic rays

Figure 1 and 2 show the results for the correction and normalization leader fraction L from the 18NM64 at Doi Inthanon, Thailand from 2007 December to 2018 April and 3-NM64 South Pole from 2013 December to 2018 April recently same as the count rate C over time. The count rate at Doi Inthanon, Thailand indicates solar modulation over a complete cycle, having increased to the time of the highest GCR flux of the Space Age in 2009, decreased to a cosmic ray minimum in 2014, and now increase back above its starting value while South Pole actually has measured the count rate since 1964 March but we show only the time period when the specialized electronics installed to measure time delay then the count rate indicated the minimum in 2014 at the starting time and now increase. Figure 3 shows trimester (three-month) averaged data for L vs. C over the same time period from Doi Inthanon, Thailand and Figure 4 shows monthly average data for L vs. C from South Pole.

The leader fraction L inform a GCR spectral index while C measures the GCR flux above the cutoff rigidities then at Doi Inthanon with $\sim$ 17 GV and $\lesssim$1 GV at South Pole. A basic concept of solar modulation is that the cosmic ray spectrum "rolls" downward from the local interstellar spectrum (LIS) and then "unrolls" back up again and the change in the spectrum is much greater at low rigidity, while at sufficiently high rigidity there is almost no solar modulation. Thus we expect to see L should increase with C for the softer, as the GCR spectrum unrolls to the softer LIS.

At Doi Inthanon, from 2007 December to 2010, C measured the increasing of the cosmic ray flux to the maximum value in 2009 but L was roughly constant with minor variations. As well as Figure 3 associates the horizontal band of L versus C in trimester 1 to 12 then in this time period, the variation of flux changed without significant in spectral variation, that means the GCR spectrum was rising and falling without changing in spectral index. In other words, the solar modulation extended to rigidities much higher than the cutoff at Doi Inthanon.

After that, from 2011 January to 2014 June, C and L at Doi Inthanon was nearly constant with some fluctuation, including Forbush decreases which have not been removed in this analysis. This also corresponds to trimester 13 to 26 that changing of L versus C varies at the same level. At South Pole, the leader fraction L started on 2013 December 9 as shown in Figure 2 and 4. Unfortunately, for South Pole at this time period, the leader fraction analysis started near the GCR minimum and using the 600 series on only one tube collected time-delay histograms that provided L with higher

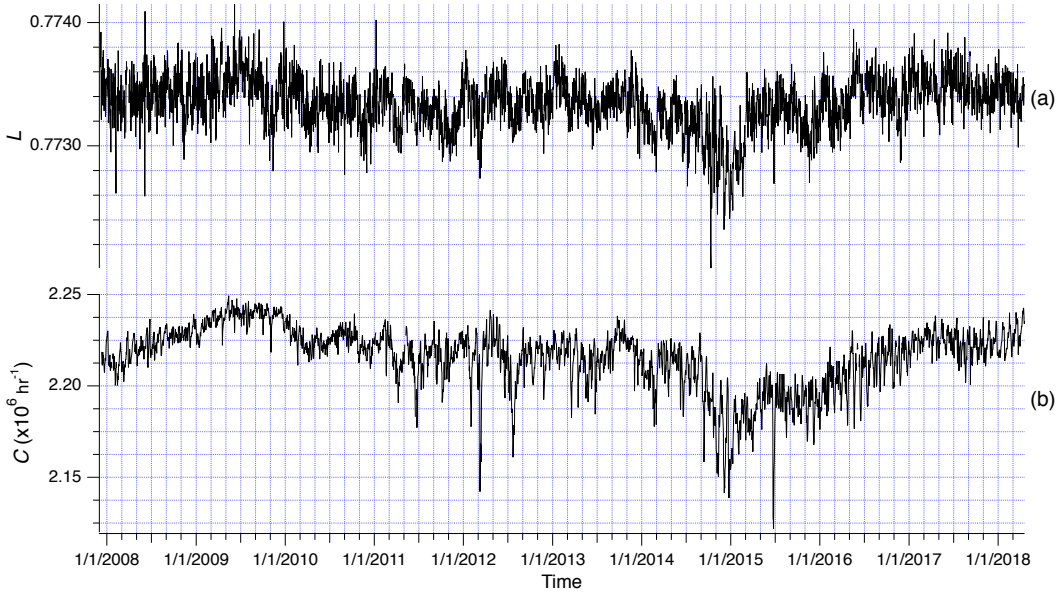


Figure 1: Preliminary results for the daily average data of (a) the leader fraction L and (b) count rate C vs. time in the 18NM64 at Doi Inthanon, Thailand at vertical cutoff rigidity $\approx$ 16.8 GV during 2007 Dec 9 to 2018 Apr 19. The near constancy of L, an indicator of spectral variation well above the cutoff, indicates that during the period surrounding the record-high cosmic ray peak of 2009, the solar modulation extended up to much higher rigidity than the cutoff. After the cosmic ray minimum in 2014, L varies in tandem with C, indicating that solar modulation did not extend far above the cutoff.

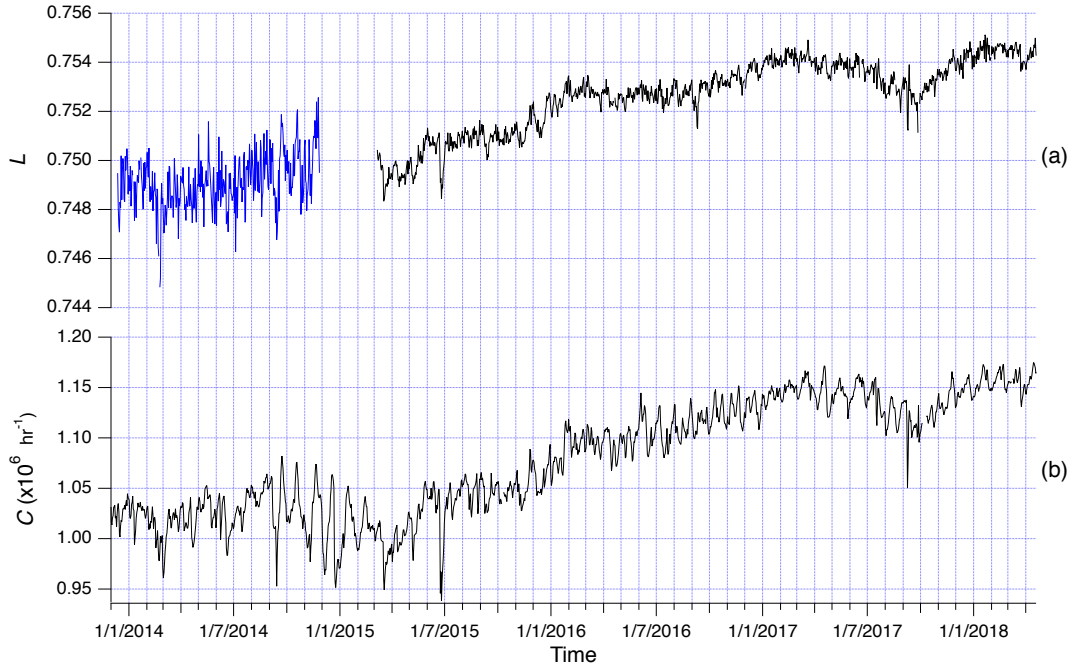


Figure 2: Preliminary results for the daily average data of (a) the leader fraction L and (b) count rate C vs. time in the 3$\times$1NM64 at South Pole, Antarctica at vertical cutoff rigidity $\lesssim$ 0.1 GV during 2013 Dec 9 to 2018 Apr 19.

statically uncertainty than L from three tubes with the 800 series as shown in Figure 2. However, the variation of L and C at South Pole show in Figure 2 we found a strong variation due to the 27-day synodic period in both L and C data. In addition, Forbush decreases observed in C data also are accompanied by decreases in L. Therefore, in Figure 4 during month 1 to 7 when L and C varies together with some uncertainty, we cannot confirm that spectrum change over cutoff at South Pole due to solar modulation.

After 2014 June, C from both Doi Inthanon and South Pole NMs downward to a minimum value near the end of 2014 and after 2015 January, both stations C increased tile the end of our analysis. The decrease and increase of L and C strongly together (trimester 27 to 42 in Figure 3 at Doi Inthanon and month 13 to 49 in Figure 4 at South Pole) indicate a strong change in the spectrum over rigidities above the cutoff. Especially for Doi Inthanon, the spectral change due to modulation in this period was concentrated at rigidities slightly above the cutoff, with much less change at rigidities well above the cutoff. Unlike the trimester 1 to 26, in this time period, the solar modulation did not extend far above the cutoff. In addition, the hysteresis in Figure 3 indicates that for solar modulation over this period, the spectrum did not “roll" down and “unroll" back up in the same way. Because of the statistical uncertainty of time delay measurement at the earlier time period of our analysis, we cannot found the hysteresis at this low cutoff rigidities. However, at Doi Inthanon after trimester 36, L was roughly constant near as the starting time of our analysis while C still increase implying that the solar modulation extended far above the cutoff again. In contrast with South Pole L change with C in the same linear trend.

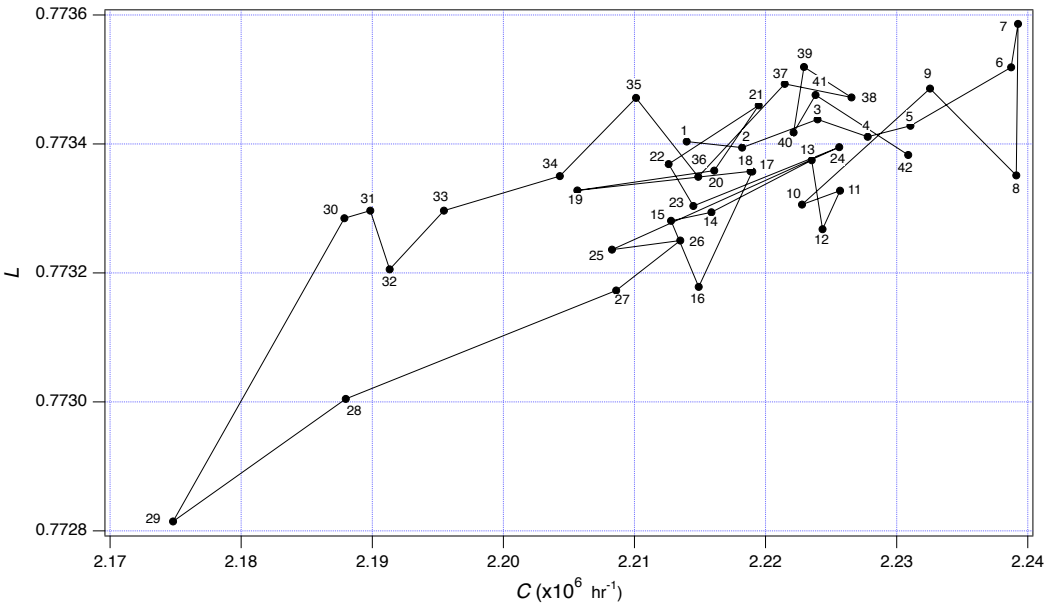


Figure 3: Preliminary results for trimester (three-month) averages of the leader fraction L vs. count rate C (in counts per hour) in the 18NM64 at Doi Inthanon during 2007 Dec 9 to 2018 Apr 19. The hysteresis indicates that for solar modulation over this period, the spectrum did not “roll" down and “unroll" back up in the same way.

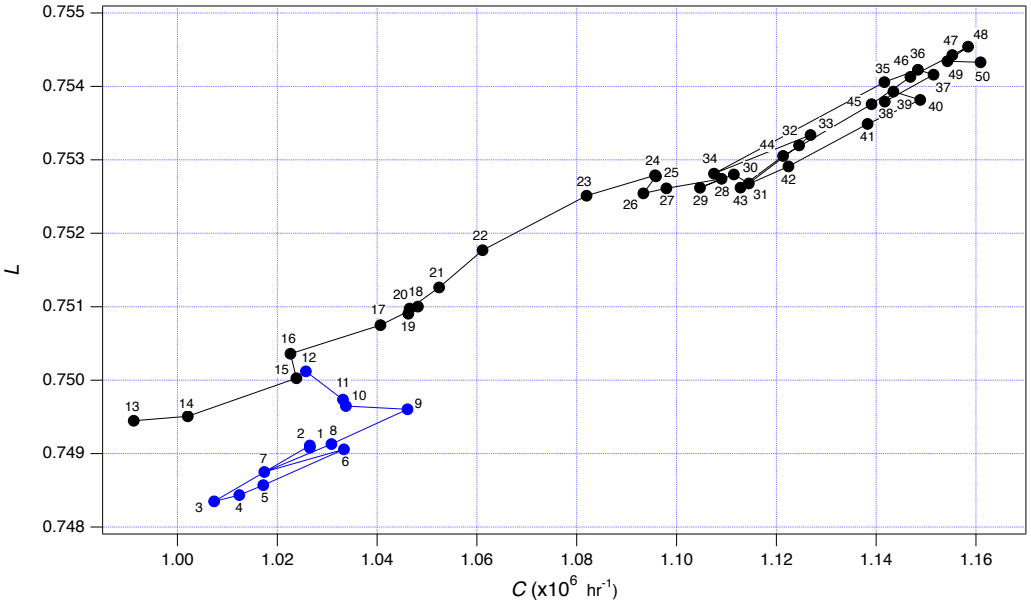


Figure 4: Preliminary results for monthly averages of the leader fraction L vs. count rate C (in counts per hour) in the 3×1NM64 at South Pole during 2013 Dec 9 to 2018 Apr 19.

5. Acknowledgments

This work was partially supported by the Thailand Research Fund award RTA590003 and the US National Science Foundation awards PLR-1245939 and PLR1341562, and their predecessors. We thank Pradiphat Muangha and Ronald Macatangay for useful discussions.

References

[1] Aiemsa-ad, N., Ruffolo, D., Sáiz, A., et al., 2015, JGRA, 120, 5253

[2] Balabin, Yu. V., Gvozdevsky, B. B., Vashenyuk, E. V., & Schur, L. I. 2008, Proc. 30th ICRC (Mérida), 1, 257

[3] Bevis, M., Businger, S., Herring, T. A., et al. 1992, JGR, 97, 15787

[4] Bieber, J., Clem, J., Evenson, P., Oh, S., & Pyle, R. 2013, JGRA, 118, 1

[5] Forbush, S. E. 1954, JGR, 59, 525

[6] Jokipii, J. R., & Thomas, B. 1981, ApJ, 243, 1115

[7] Kollár, V., Kudela, K., & Minarovjech, M. 2011, Contrib. Astron. Obs. Skalnaté Pleso, 41, 5

[8] Mangeard, P.-S., Ruffolo, D., Sáiz, A., Madlee, S., & Nutaro, T. 2016a, JGRA, 121, 743

[9] Mangeard, P.-S., Ruffolo, D., Sáiz, A., et al. 2016b, JGRA, 121, 11620

[10] Mangeard, P.-S., Clem, J., Evenson, P., et al. 2018, ApJ, 858, 43

[11] Ruffolo, D., Sáiz, A., Mangeard, P.-S., et al. 2016, ApJ, 817, 38

[12] Sáiz, A., Mitthumsiri, W., Ruffolo, D., Evenson, P., & Nutaro, T. 2017, Proc. 35th ICRC (Busan), 47

PROCEEDINGS OF SCIENCE

Bare Neutron Counter and Neutron Monitor Response to Cosmic Rays during a 1995 Latitude Survey

W. Nuntiyakul[*a,b], **A. Sáiz**[c], **D. Ruffolo**[c], **P.-S. Mangeard**[d,e], **P. Evenson**[e], **J. W. Bieber**[e], **J. Clem**[e], **R. Pyle**[f], **M. L. Duldig**[g], **J. E. Humble**[g]

[a] *Department of Physics and Materials Science, Faculty of Science, Chiang Mai University, Chiang Mai 50200, Thailand*

[b] *Research Center in Physics and Astronomy, Faculty of Science, Chiang Mai University, Chiang Mai 50200, Thailand*

[c] *Department of Physics, Faculty of Science, Mahidol University, Bangkok 10400, Thailand*

[d] *National Astronomical Research Institute of Thailand (NARIT), Chiang Mai 50180, Thailand*

[e] *Department of Physics and Astronomy, University of Delaware, Newark, DE 19716, USA*

[f] *Pyle Consulting Group, Inc., St. Charles, IL 60174, USA*

[g] *School of Natural Sciences, University of Tasmania, Hobart, Tasmania 7001, Australia*

E-mail: waraporn.n@cmu.ac.th, alejandro.sai@mahidol.ac.th, david.ruf@mahidol.ac.th, psmangeard@gmail.com, evenson@udel.edu, jwbieber@bartol.udel.edu, clem@bartol.udel.edu, RogerPyle@gmail.com, Marc.Duldig@utas.edu.au, John.Humble@utas.edu.au

Neutron monitors of standard design (IGY or NM64) are employed world-wide to study variations in the flux of galactic cosmic rays and solar energetic particles in the GeV range. The design minimizes detector response to neutrons below ∼10 MeV produced by cosmic ray interactions in the ambient medium. Increasingly, however, such neutrons are of interest as a means of obtaining spectral information on cosmic rays, for studies of soil moisture, and for nuclear threat detection. Bare neutron counters, a type of lead-free neutron monitor, can detect such neutrons, but comparatively little work has been done to characterize the dependence of their count rate on cutoff rigidity. We analyze data from three bare neutron counters operated on a ship together with a 3-tube NM64 monitor from November, 1995 to February, 1996 over a wide range of magnetic latitude, i.e., a latitude survey. The bare counter design used foamed-in-place polyurethane insulation to keep the temperature uniform and to some extent moderate high-energy neutrons. When the ship was near land, the bare/NM64 count rate ratio was dramatically higher. Considering only data from open sea, the bare and NM64 pressure coefficients are not significantly different. We determine the response function of these bare counters, which is weighted to Galactic cosmic rays of lower energy than the NM64. This measurement of the response function may improve determination of the spectral index of solar energetic particles and Galactic cosmic rays from a comparison of bare and NM64 count rates.

36th International Cosmic Ray Conference -ICRC2019-
July 24th - August 1st, 2019
Madison, WI, U.S.A.

*Speaker.

© Copyright owned by the author(s) under the terms of the Creative Commons Attribution-NonCommercial-NoDerivatives 4.0 International License (CC BY-NC-ND 4.0).

PoS(ICRC2019)114

1. Introduction

Neutron monitors are ground-level detectors of cosmic-ray-induced atmospheric secondary particles that respond mostly to secondary neutrons [12]. Neutron monitors of the standard IGY and NM64 designs are optimized so that their count rates provide a precise and reliable measurement of the GeV-range cosmic-ray flux [8]. In particular, a neutron monitor at a given location is most sensitive to cosmic rays within a range in rigidity (momentum per charge, expressed in GV) somewhat above the local geomagnetic cutoff, which varies from near 0 GV at Earth's polar regions to ∼17 GV at some parts of the geomagnetic equator, and above the atmospheric cutoff of $\gtrsim$1 GV needed to generate atmospheric secondary particles that can be recorded at ground level (see the response functions determined by [9]). A standard neutron monitor includes a lead *producer* to increase the response to high energy primary cosmic rays. Standard neutron monitors are operated at more than 40 locations worldwide, taking advantage of the varying geomagnetic cutoff, and are widely used to monitor Earth's radiation environment due to relativistic solar energetic particles and galactic cosmic rays and their variations associated with solar activity, and for applications concerning space weather and space radiation.

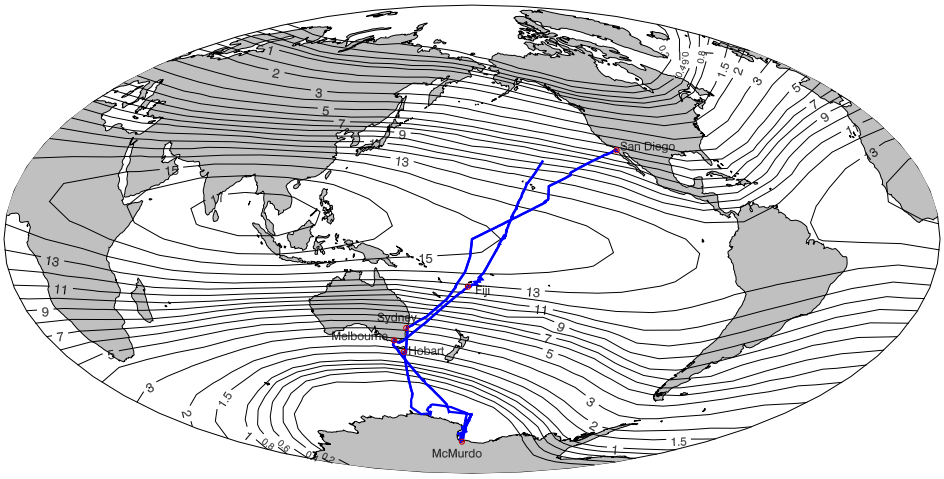


Figure 1: Track of the USCGC Polar Star for the 1995–1996 survey, superimposed on contours of vertical cutoff rigidity. Numbers give vertical cutoff rigidity in GV. This survey carried a standard neutron monitor (3NM64) and three bare neutron detectors, permitting a direct comparison of their response to primary cosmic rays.

Such observations can be complemented by measurements using bare neutron counters that lack the reflector and lead producer of standard neutron monitors, making them also sensitive to atmospheric neutrons of $\leq$ 10 MeV. Such detectors are widely used to detect soil moisture [15], for nuclear threat detection [7], and to obtain spectral information on solar energetic particles.

From a fixed location, a standard neutron monitor (NM64) count rate alone cannot be used to measure the energy spectrum of cosmic rays. However, since a bare counter has a different energy response from an NM64, operating them together provides some knowledge of the spectrum [e.g., [1, 3]] while avoiding the systematic errors of comparing count rates from different locations [figure 2 of [11]]. The accuracy of this method requires knowing how the energy responses of the different types of detector are related.

PoS(ICRC2019)114

In this work we focus on developing optimal methods for extracting the response function of three bare counters that were operated aboard the U.S. Coast Guard icebreaker *Polar Star* along the route illustrated in Figure 1. This voyage was one of a series of latitude surveys in which the magnetic field of the Earth was used as a spectrometer to explore the time dependence of the spectrum of cosmic rays striking the atmosphere [9]. All of these surveys carried a NM64 neutron monitor with 3 counter tubes, i.e., a 3NM64, and in addition the survey from San Diego, USA to McMurdo, Antarctica and back during a voyage of ∼4 months from 6 November 1995 to 20 March 1996 carried three bare detectors. The key results have also been presented by [10].

2. Methodology

2.1 Latitude Surveys and Response Functions

The count rate $N(t)$ of a ground based detector resulting from the impact of cosmic rays at the top of the atmosphere is described by

$$N(\Theta,\Phi,h,t) = \int_0^\infty \left[\sum_i J_i(P,t)\, Y_i(P,h)\right] T(P,\Theta,\Phi,t)\, \mathrm{d}P, \tag{2.1}$$

where J_i is the Galactic cosmic ray spectrum for primary cosmic rays of particle type i near Earth expressed as a function of rigidity (P) and time (t). The yield function Y_i for primary particles of type i, a function of rigidity (P) and atmospheric depth (h), is the actual relationship between the cosmic ray flux at the top of atmosphere and the observed count rate from the detectors. The transmission function T_i describes the transmission through the magnetosphere of the Earth. It is a function of rigidity (P), latitude (Θ) and longitude (Φ) of the detector location, and time (t).

At a given latitude and longitude, the effective cutoff rigidity for transmission through Earth's magnetic field depends on the arrival direction of each primary cosmic ray described by the local zenith and azimuthal angles. However T_i can be approximated by a step function at a single cutoff rigidity P_c, that we call the *apparent cutoff rigidity*. With the assumption that the transmission is a step function, the count rate relation becomes

$$N(P_\mathrm{c},h,t) = \int_{P_\mathrm{c}}^\infty \sum_i J_i(P,t)\, Y_i(P,h)\, \mathrm{d}P. \tag{2.2}$$

The apparent cutoff used in this work considers both vertically incident particles and obliquely incident particles [5]; this is calculated individually at one-hour intervals at the actual position of the ship with a time-dependent model of the magnetic field according to an *efficient* method [2].

The differential response function (DRF) is defined as the negative of the derivative of the count rate as a function of cutoff rigidity. The most common type of analysis for measuring a response function is called the Dorman analysis [6], in which corrections are first applied to the data points, then a parameterized function of P_c, termed a *Dorman function*, is fitted to the data:

$$N(P_\mathrm{c}) = N_0 \left(1 - \mathrm{e}^{-\alpha P_\mathrm{c}^{-\kappa}}\right), \tag{2.3}$$

where N_0, α, and κ are unphysical parameters that provide a good representation of the integral response function N, which can be analytically differentiated to determine the DRF:

$$N(P_\mathrm{c}) = \int_{P_\mathrm{c}}^\infty \mathrm{DRF}(P)\, \mathrm{d}P, \tag{2.4}$$

PoS(ICRC2019)114

$$\mathrm{DRF}(P) = N_0 \alpha P^{-\kappa-1} \kappa \mathrm{e}^{-\alpha P^{-\kappa}}. \tag{2.5}$$

From Eq. (2.2) and (2.4), we can obtain the DRF as the summed product of $J_i(P,t)$ and $Y_i(P,h)$:

$$\mathrm{DRF}(P) = -\left[\frac{\mathrm{d}N}{\mathrm{d}P_\mathrm{c}}\right]_P = \sum_i J_i(P,t)\, Y_i(P,h). \tag{2.6}$$

2.2 Instrumentation

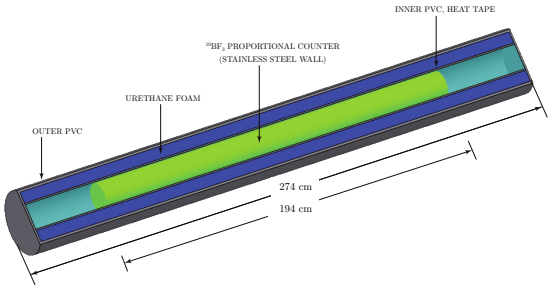


Figure 2: Rendered sketch of the "bare" neutron counter configuration used in this work. Each BP-28 neutron-sensitive proportional counter was operated inside a 20 cm diameter PVC pipe covered with heat tape and thermally insulated by foamed-in-place polyurethane inside a larger, 30 cm diameter PVC pipe.

The 1995 latitude survey employed two types of neutron detectors, three bare neutron detectors and a 3NM64 neutron monitor. The three bare counters (BCs) were installed exposed on an upper deck of the ship, whereas the 3NM64 was installed in an insulated shipping container (called the "TasVan"). The detectors are Chalk River BP-28 proportional counter cylinders filled with boron trifluoride gas (enriched in the isotope ^{10}B). The boron nuclei react with neutrons and undergo nuclear fission. Unlike for an NM64, there is no standard design for bare neutron counters. A rendered drawing of the detector is shown in Figure 2.

3. Data Reduction

3.1 Overview

Throughout this work all the dates during the survey will be referred to as "day of the year of 1995" (DOY1995). The 12th generation International Geomagnetic Reference Field (IGRF12) and the 1989 revision of the [13] model were used for calculating the cutoff rigidity. Numerical results for the 3NM64 in the present work differ slightly from those presented by [9] for three main reasons: (1) data intervals were selected such that they had good data in both the BCs and the 3NM64 whereas the earlier study only considered the 3NM64; (2) no corrections for short term modulation based on the McMurdo count rate were applied in this work; and (3) no normalization of the data to the McMurdo count rate was performed in this work.

3.2 Initial Processing

Our data were recorded with one second time resolution together with clinometer readings to allow for possible corrections due to the varying orientation of the ship in rough seas. We made histograms of the one second readings for each tube for each hour of the survey, and only used seconds with 0 to 4 counts. We eliminated the noise with one hour resolution from this stage. We deferred rejecting bad hours to a later stage of analysis. Only data with BC/NM count rate ratios within $\pm 3\sigma$ of a reference value are selected for further analysis, as specified in [10].

PoS(ICRC2019)114

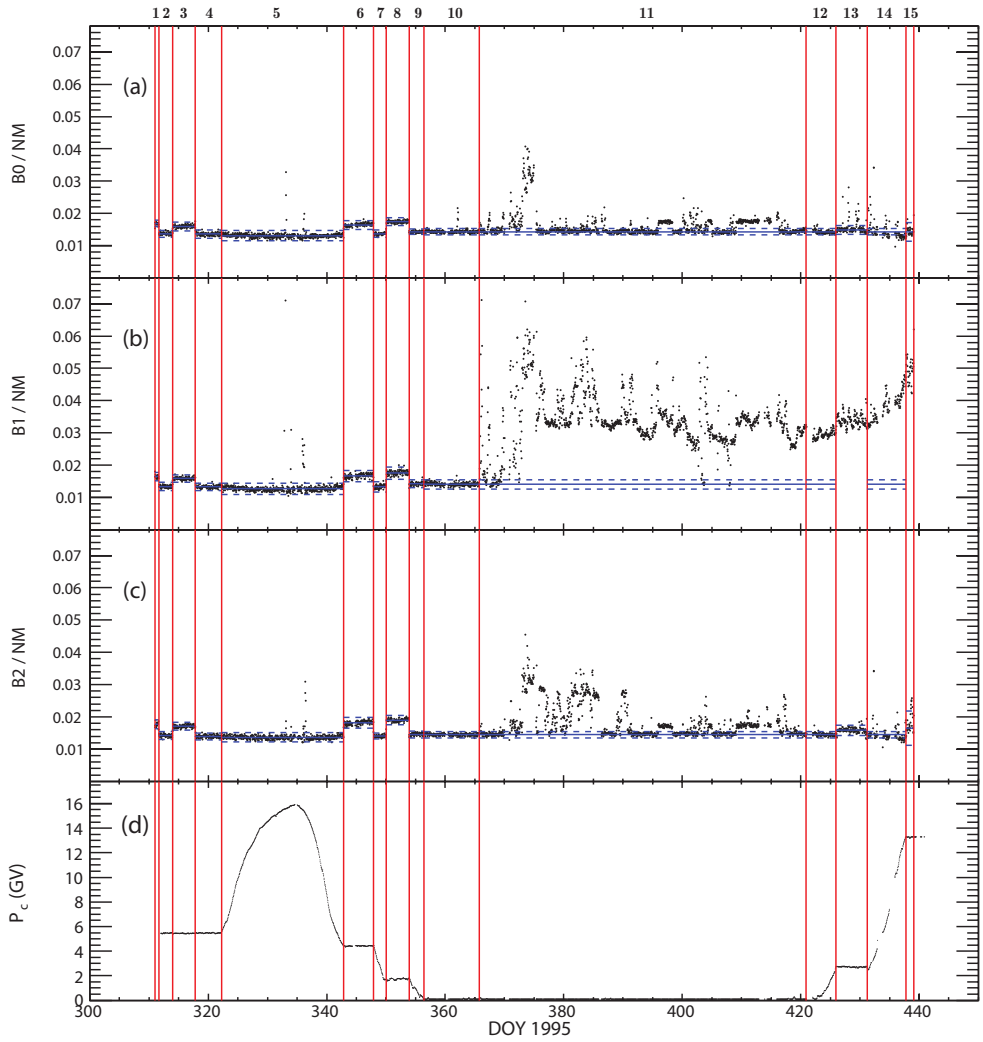


Figure 3: Summary of hourly averaged data as a function of time. (a)–(c) Ratios of individual bare detector count rates to 3NM64 count rate. Red vertical lines define 15 time periods used in the analysis. In each time period, the horizontal blue solid line shows the reference value $\langle B_i/\mathrm{NM}\rangle$ and blue dashed lines illustrate the $\pm 3\sigma$ interval around the reference. (d) Apparent geomagnetic cutoff rigidity P_c.

3.3 Data Cleaning Based on Neutron Monitor Count Rate

The selection of usable data (data *cleaning*) and the adjustment of bad or missing individual counter data (data *correction*) is performed based on BC-to-NM ratios (B_i/NM) and BC-to-BC ratios (B_i/B_j). We start by choosing appropriate time periods during the 1995 survey year for which data were taken in a relative stable environment. The 15 time periods used (TP1 to TP15) are shown in Figure 3. Data cleaning is then applied separately for each time period. This division into time intervals is based on the locations near which the ship passed, i.e., San Diego, Sydney, Hobart, McMurdo, Melbourne, and Fiji, as well as on apparent step-like changes in the ratio values elsewhere. For each time period we generated histograms of the hourly B_i/NM values to characterize and remove outliers. Figure 3(a)–(c) illustrates the individual B_i/NM ratios as a function of time. The red vertical lines show the division in time periods. The blue solid horizontal

PoS(ICRC2019)114

lines illustrate the B_i/NM *reference values* $\langle B_0/\mathrm{NM}\rangle$, $\langle B_1/\mathrm{NM}\rangle$, and $\langle B_2/\mathrm{NM}\rangle$. In most cases, these were defined as the mean of a Gaussian fit to the ratio histogram for each time period. For three time periods, namely TP11, TP12, and TP14, we used the reference calculated during TP10 because it was noticed that the noise was too high for the center BC (B_1). Using the TP10 ratio reference for those three problematic time periods, we avoided bias in the data that could induce further analysis errors. For the $\langle B_1/\mathrm{NM}\rangle$ ratio reference, during TP13 and TP15 data were also noisy but no appropriate reference based on another time period with similar environment could be identified, so those intervals have no reference available. The blue horizontal dashed lines illustrate plus and minus three standard deviations from the reference for each time period, also based on the Gaussian fit. B_i/NM data points lying outside the range defined by three standard deviations (i.e., $\pm 3\sigma$) from the reference were considered to indicate bad data and the count rate B_i was then corrected (if possible) as explained in the next section or removed before subsequent analysis.

3.4 Data Correction Based on BC Ratios

The rough and changing conditions on board the ships caused the response of individual BCs to occasionally change, become noisy, or even stop completely. In order to correct for these effects during the surveys, we used the inherent redundancy of the three bare detectors. The histograms of individual BC ratio values (B_0/B_1, B_1/B_2, and B_2/B_0) were plotted for each time period (except for periods with no appropriate reference for the B_i/NM ratio, as mentioned above). For TP1–TP10, reference values were calculated for these BC ratios based on a fit to a Gaussian, but for TP11, TP12, and TP14 we used the BC ratio reference of TP10 instead. For TP13 and TP15, the BC ratios were not used because the center tube had bad counts during the whole time period and there was no other appropriate reference. We defined the range of three standard deviations ($\pm 3\sigma$) from the reference values $\langle B_i/B_j\rangle$ to identify count rates that needed to be corrected. The reference values for the BC ratios were then used to correct those count rates, using the same method as explained in [9]. The count rates of the three bare tubes for each hour (B_1, B_2, and B_3) were corrected if the BC ratio data were outside the 3σ range and there was a valid BC ratio reference for calculating the missing data.

3.5 Barometric Pressure Correction

We carefully investigated the correction for variation in barometric pressure with the data from the 1995 survey. We also calculated pressure coefficients for the ratios of the summed count rate of the three BCs (3BC) to that of the 3NM64. Since there is no evidence for a major difference in coefficients from the survey data alone, in the present analysis we have corrected both 3BC and 3NM64 with the well-determined coefficient from the 13-year data set for the 3NM64 [9].

We also extracted coefficients from historical data for two different land-based BC configurations and the 3 $\times$ 1NM64 neutron monitor at South Pole and for BCs and an 18NM64 at Doi Inthanon, Thailand. In addition, we set up BCs at Newark, Delaware (three spare BP-28 counters) and McMurdo (one BP-28 removed from the NM64) to investigate this issue. In general, there is no specific pattern with altitude or cutoff; rather the data provide an additional caution regarding the environmental sensitivity of bare detectors. In other words, the observed pressure coefficient of the shipborne BC to NM64 count rate ratio is consistent with zero, given the uncertainties.

PoS(ICRC2019)114

3.6 Port Effects

The extreme sensitivity of bare detectors to the environment is clearly illustrated in Figure 4, which shows the ratio of the BC to NM count rate after all of the corrections discussed above have been applied. Substantial increases in the ratio occur whenever the ship is in port, as was also found by [14]. This can be explained by a higher density of albedo neutrons near solid ground compared with open water, and the fact that neutron detectors lacking a reflector (such as the BCs) are much more sensitive to these environmental neutrons than the standard NM64. We therefore classified the data carefully so as to be certain that the results we report are representative of the open ocean.

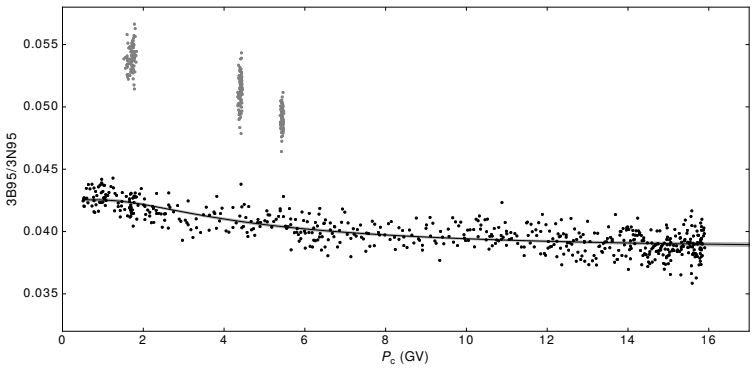


Figure 4: BC/NM ratio in 1995 as a function of apparent geomagnetic cutoff rigidity P_c. Black dots: ship in open sea. Gray dots: port calls at Hobart ($P_c = 1.71$ GV), Sydney ($P_c = 4.41$ GV), and San Diego ($P_c = 5.45$ GV). Line: ratio of Dorman functions shown in Figure 5(a),(b). Each dot represents a 1-hr data point.

4. Response Functions

To quantify the dependence shown in Figure 4 we performed a fit to a Dorman function [6] to the data for 3BC and 3NM64 separately. To do the fit we minimize the least squares function using the Levenburg-Marquardt algorithm, and provide estimates for the statistical errors in the determination of the parameters from the scatter of the data points about the resulting fit. The results of the fits are shown in Figure 5. In this case, as in subsequent ones, we show the best fit as a solid line and the (two sigma) range of possible fits as a shaded area.

5. Conclusions

We report an analysis of data taken using three bare neutron counters with a novel design and a standard three-counter neutron monitor (3NM64) on board the U.S. Coast Guard icebreaker *Polar Star* from 6 November 1995 to 20 March 1996, over a route from San Diego, USA to McMurdo Base, Antarctica and back to the northern Pacific Ocean. This latitude survey sampled geomagnetic cutoffs over $0 < P_c < 15$ GV, allowing a determination of the BC and 3NM64 response functions over that range. Various techniques were used to clean and correct the data. The pressure correction coefficient as a function of P_c was previously determined for this ship-borne 3NM64 (using data from 13 latitude surveys over 1994–2007 [9], and here we investigated whether the BC count rate

PoS(ICRC2019)114

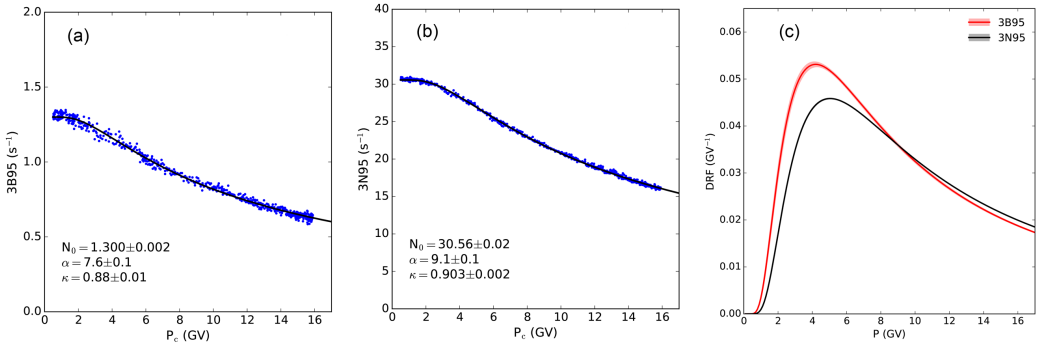


Figure 5: Dorman function fits to (a) bare and (b) neutron monitor data separately. (c) Comparison of the normalized differential response functions (bare neutron detectors and standard 3NM64) for the 1995 latitude survey. (Modified from [10].)

requires a different pressure coefficient. We concluded that the statistics available for these BCs are insufficient to determine whether the pressure coefficients are different, and therefore we used the same coefficient. The BC response was strongly affected by proximity to any port along the route, and such time periods were excluded when determining the response functions.

6. Acknowledgments

This study is supported in part by the Thailand Research Fund via grant RTA5980003 and Research Grant for New Scholar MRG6280155; by the U.S.National Science Foundation via awards PLR-1341562, PLR-1245939, and their predecessors; and by the Australian Antarctic Division.

References

[1] Bieber, J. W., & Evenson, P. 1991, in Proc. 22nd ICRC (Dublin), 3, 129–132

[2] Bieber, J. W., Clem, J., & Evenson, P. 1997, in Proc. 25th ICRC (Durban), 2, 389–392

[3] Bieber, J. W., Clem, J., Evenson, P., et al. 2013, ApJ, 771, 92

[4] Caballero-Lopez, R. A., & Moraal, H. 2012, JGR, 117, A12, 103

[5] Clem, J. M., Bieber, J. W., Evenson, P., et al. 1997, JGR, 102, 26, 919–26

[6] Dorman, L. I., Fedchenko, S. G., et al. 1969, in Proc. 11th ICRC (Budapest), 2, 233–236

[7] Kouzes, R. T., E. R. Siciliano, J. H. Ely, et al. 2008, *Nucl. Instrum. Meth. Phys. Res. A*, 584, 383–400

[8] Hatton, C. J., & Carmichael, H. 1964, Can. J. Phys., 42, 2443–2472

[9] Nuntiyakul, W., Evenson, P., Ruffolo D., et al. 2014, ApJ, 795, 11

[10] Nuntiyakul, W., Sáiz, A., Ruffolo, D., et al. 2018, JGR, 123, 7181

[11] Ruffolo, D., Sáiz, A., Mangeard, P.-S., et al. 2016, ApJ, 817, 38

[12] Simpson, J. A. Jr. 1948, PhRvL, 73, 1389–1391

[13] Tsyganenko, N. A. 1987, Planet. Space Sci., 35, 1347–1358

[14] Villoresi, G., Dorman, L. I., Iucci, N., et al. 2000, JGR, 105, 21, 025–21, 034

[15] Zreda, M., D. Desilets, T. P. A. Ferré, and R. L. Scott 2008, *Geophys. Res. Lett.*, 35, L21,402

PoS(ICRC2019)114

PROCEEDINGS OF SCIENCE

Galactic Cosmic-Ray Anisotropy During Forbush Decreases: Evidence for Diffusive Barriers and Large-Scale Flow

G.D. Ihongo[*a,b], **D. Ruffolo**[a], **A. Sáiz**[a], **U. Tortermpun**[a], **J. W. Bieber**[c], **A. C.-L. Chian**[d,e,f]

[a] *Department of Physics, Faculty of Science, Mahidol University, Bangkok 10400, Thailand.*
[b] *Department of Physics, Faculty of Science, Benue State University, Makurdi PMB 102119, Nigeria.*
[c] *Bartol Research Institute, University of Delaware, Newark, DE 19716, USA.*
[d] *School of Mathematical Sciences, University of Adelaide, Adelaide, SA 5005, Australia.*
[e] *Institute of Aeronautical Technology (ITA), São José dos Campos, SP, 12228-900, Brazil.*
[e] *National Institute for Space Research (INPE), P.O. Box 515, São José dos Campos, SP, 12227-010, Brazil.*
E-mail: domgrace1@gmail.com, david.ruf@mahidol.ac.th.

The flux of Galactic cosmic rays (GCRs) can undergo a Forbush decrease (FD) during the passage of a shock, sheath region, or magnetic flux rope associated with a coronal mass ejection (CME). Cosmic-ray observations during FDs can provide information complementary to in situ observations of the local plasma and magnetic field, because cosmic-ray distributions allow remote sensing of distant conditions. Here we develop techniques to determine the GCR anisotropy before and during an FD using data from neutron monitors worldwide. For example, for the FD starting on 2013 April 13, we find that at times with strong magnetic fluctuations and strong cosmic-ray scattering, there were spikes of high perpendicular anisotropy and weak parallel anisotropy. These results, along with the near constancy of parallel anisotropy across magnetic field reversals, are consistent with diffusive barriers causing the decrease in GCR flux before the arrival of the flux rope. In contrast, within the CME flux rope there was a strong parallel anisotropy in the direction predicted from a theory of drift motions into one leg of the magnetic flux rope and out the other, confirming that the anisotropy can remotely sense a large-scale flow of GCRs through a magnetic flux rope.

36th International Cosmic Ray Conference -ICRC2019-
July 24th - August 1st, 2019
Madison, WI, U.S.A.

*Speaker.

© Copyright owned by the author(s) under the terms of the Creative Commons Attribution-NonCommercial-NoDerivatives 4.0 International License (CC BY-NC-ND 4.0).

1. Introduction

The flux of GCRs can undergo a FD during the passage of a shock, sheath region or magnetic flux rope associated with a CME [1, 2], which can also cause variations in the distribution of GCR.

Consequently, the significance of GCR anisotropy and FD cannot be overemphasized. For instance, it can provide very important and useful information on the properties of solar wind plasma [1, 2, 3, 4, 5, 6]. In addition to the above, a good knowledge of GCR anisotropy can provide remote information about the structure of CME flux ropes, and this could be related to various space weather effects and space weather forecasting. GCR anisotropy can also shed light on understanding the propagation of GCR [7].

With the aforementioned motivation, there have been comprehensive articles about the characteristics of Forbush decreases and their causes, where the arrival of a CME shock has been identified as the major cause of Forbush decrease [1, 8, 9, 10, 11].

The anisotropy of GCRs has also been investigated by several authors. For example, CMEs can cause depressions in the cosmic ray intensity both locally, when an observer is inside the interplanetary structure (ejecta) and remotely, if the ejecta is energetic enough to create an interplanetary shock to which the observer is magnetically connected. After the shock and ejecta have passed, the intensity gradually recovers as particles diffuse in around the shock.

Following the previous studies, we have modeled GCR anisotropy using a technique initially developed by [2], alongside normalized count rates from NM stations. In this analysis, we improve the technique by using only polar stations to make the process cleaner and we have also calculated the actual asymptotic directions for each hour so the actual asymptotic directions calculated using the approximate K_p indices are used for each hour in the analysis. This is in contrast to the previous procedure where the asymptotic directions calculated for all hours of one day were used across all days throughout the analysis. Another important improvement of the technique is that we have redefined the daily average.

For the FD starting on 2013 April 13, we find that at times with strong magnetic fluctuations and strong cosmic-ray scattering, there were spikes of high perpendicular anisotropy and weak parallel anisotropy. These results, along with the near constancy of parallel anisotropy across magnetic field reversals, are consistent with diffusive barriers causing the decrease in GCR flux before the arrival of the flux rope. Within the CME flux rope there was a strong parallel anisotropy in the direction predicted from a theory of drift motions into one leg of the magnetic flux rope and out the other [22], confirming that the anisotropy can remotely sense a large-scale flow of GCRs through a magnetic flux rope.

2. Data Information and Procedure

2.1 Data Information

We used data from polar NM stations with good statistics and no major data gaps during the period of FD. These stations and their geographic locations along with their geomagnetic cutoff rigidity are presented in table 1.

The neutron monitor data were obtained from the Neutron Monitor Database [1]. We used data from all available polar stations in this database of the worldwide network of neutron monitors with good data for the time period considered. We also used level 2 data from the ACE spacecraft[2] for the solar wind speed, magnitude (B) and geocentric solar-ecliptic (GSE) components of the interplanetary magnetic field.

Table 1: Sources of Neutron Monitor Data

NM Location	Station Code	Geographic Latitude (deg)	Geographic Longitude P_c (GV)	Cutoff Rigidity P_m (GV)
Thule, Greenland	TH	76.50	-68.70	0.00
Fort Smith, Canada	FS	60.02	-111.93	0.00
Peawanuck, Canada	PE	54.98	-85.44	0.00
Barentsburg, Russia	BA	78.06	14.21	0.00
McMurdo, Antarctica	MC	-77.90	166.60	0.00
Terre Adélie, Antarctica	TA	-66.55	140.00	0.00
Nain, Canada	NA	56.55	-61.68	0.01
South Pole, Antarctica	SP	-90.00	0.00	0.09
Inuvik, Canada	IN	68.36	-133.72	0.18
Mawson, Antarctica	MA	-67.60	62.87	0.22
Jang Bogo, Antarctica	JB	-74.62	164.23	0.30
Tixie Bay, Russia	TB	71.36	128.54	0.48
Norilsk, Russia	NO	69.26	88.05	0.58
Apatity, Russia	AP	67.57	33.40	0.65
Oulu, Finland	OU	65.05	25.47	0.81
SANAE, Antarctica	SA	-70.32	-2.35	1.06
Kerguelen, near Antarctica	KE	-49.35	70.25	1.14

2.2 Procedure

The first order anisotropy $\boldsymbol{\delta}$ of galactic cosmic rays can be related to the count rate of NM station n at a given time t, using the following general equation [2]:

$$\begin{aligned} A_n(t) = \sum_{l=0}^{8} w_l \int_{P_{min,n,l}}^{P_{max}} \left(\frac{-dN(P_c)}{dP_c}\Big|_P \right) T_{n,l}(P) \frac{P}{D(t)+P} \\ \times \{1 + [\delta_x(t) + \chi_x(t,P)]\, n_{n,l,x}(t,P) + [\delta_y(t) + \chi_y(t,P)]\, n_{n,l,y}(t,P) \\ + [\delta_z(t) + \chi_z(t,P)]\, n_{n,l,z}(t,P)\}\, dP. \end{aligned} \tag{2.1}$$

[1] http://www.nmdb.eu

[2] http://http://www.srl.caltech.edu/ACE/ASC

In equation 2.1, l is one of 9 directions with weights w_l set to $1/2$ for the vertical direction and $1/16$ for the other 8 directions at zenith angle 30° and azimuthal angles equally spaced over $22^\circ.5 - 337^\circ.5$ [2, 13]. $N(P_c)$ is the NM response function, and the Dorman fit from a latitude survey during $2004-2005$ was used for this [2, 14]. This survey year was selected because it is the survey year for which the modulation of galactic cosmic rays was similar to that during 2013. The transmission function $T_{nl}(P)$ is set to 1 in this analysis because only polar stations were used. δ_x, δ_y and δ_z represent the first order anisotropy in GEO_x, GEO_y, and GEO_z-components respectively, and $\boldsymbol{\chi}$ is the Compton-Getting anisotropy. Finally, the unit vector $\boldsymbol{n}(t,P)$ accounts for the asymptotic directions of GCR at NM stations; to find the asymptotic directions we used a particle trajectory code from the Bartol Research Institute [15, 16] together with an accurate model of the terrestrial magnetic field including any field disturbance present as indicated by the K_p index value at each hour.

To avoid a mis-representation of the fixed North-South anisotropy $(\delta_z(t))$ and equatorial anisotropy $(\delta_x(t)$ and $\delta_y(t))$, we first evaluate $\delta_z(t)$ in GEO coordinates using the following equation [2]:

$$\frac{T(t)-M(t)}{2P_t(t)} = \frac{\sum_{l=0}^{8} w_l \int_{P_{min,n,l}}^{P_{max}} \left(\frac{-dN(P_c)}{dP_c}\Big|_P\right) T_{n,l}(P) \frac{P}{D(t)+P} \left[\delta_z(t)+\chi_z(t,P)\right] \left[n_{T,l,z}(t,P)-n_{M,l,z}(t,P)\right] dP}{2\sum_{l=0}^{8} w_l \int_{P_{min}}^{P_{max}} \left(\frac{-dN(P_c)}{dP_c}\Big|_P\right) dP}. \tag{2.2}$$

where $T(t)$ and $M(t)$ are the normalized count rates of Thule and McMurdo, respectively. $P_t(t)$ is the average count rate of all polar stations. Here, we have used only polar stations with atmospheric cutoff rigidity approximately 1 GV and as such the transmission $T = 1$.

Then we determine the equatorial anisotropy $(\delta_x(t)$ and $\delta_y(t))$ by performing a least squares fit to equation (2.3) for all NM stations simultaneously:

$$\frac{C_n(t)}{C_{n,d}(t)} = \frac{A_n(t)}{B_n(t)}, \tag{2.3}$$

From (2.3), $C_n(t)$ is the count rate of individual stations at a given time t, $A_n(t)$ represents the modeled count rate, $B_n(t)$ models the daily average over equatorial directions and is equal to $A_n(t)$ but with $n_{n,l,x} = n_{n,l,y} = 0$, and $C_{n,d}(t)$ is the daily running average defined by equation (2.4). We calculate this by defining $C_n^{'}(t)$ as the NM count rate $C_n(t)$ divided by the average count rate $(P_t(t))$. Then we use equation (2.4) and multiply the result by $P_t(t)$:

$$C_{n,d}^{'}(t) = \frac{1}{2}\left[C_n^{'}(t) + \left(\frac{C_n^{'-}(t)+C_n^{'+}(t)}{2}\right) - \frac{1}{4}\left(\frac{C_n^{'--}(t)+C_n^{'++}(t)}{2} - C_n^{'}(t)\right)\right], \tag{2.4}$$

where $C_n^{'-}(t), C_n^{'--}(t), C_n^{'+}(t)$ and $C_n^{'++}(t)$ are the count rate ratios of same NM station at times $t-12$ hours, $t-24$ hours, $t+12$ hours and $t+24$ hours respectively. Then we use $C_{n,d}(t) = C_{n,d}^{'}(t)P_t(t)$. The daily running average as defined in equation (2.4) is designed to average over

any daily wave in the normalized count rates. Then $C_{n,d}(t)$ is modeled using $B_n(t)$. Examples of $C_n(t)/C_{n,d}(t)$ are given in Figure 1

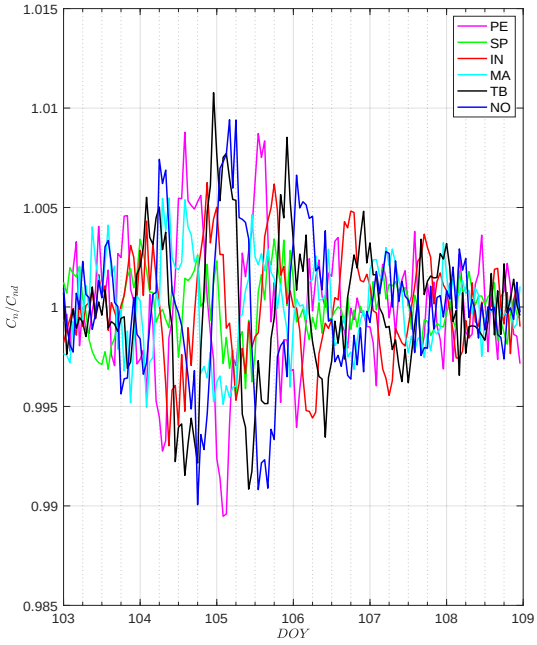


Figure 1: Count rates divided by daily running average for the FD starting 2013 April 13 for selected NM stations. Such ratios for each station are considered to deviate from 1 due to equatorial anisotropy as expressed by Eq. 2.3

.

The anisotropies obtained from the procedure described in section 2 are first converted from GEO coordinates to GSE coordinates and then further decomposed into components parallel and perpendicular to the interplanetary magnetic field $\boldsymbol{B}$. This is to enable us interpret the anisotropy results in the solar wind frame.

3. Results and Discussion

In order to accurately interpret our results, we first analyze plasma and magnetic field data to identify the distinct structures in the interplanetary coronal mass ejections (ICMEs), as well as shock arrival times and possible flux ropes, alongside hourly count rates from NM stations. Figure 2a shows plasma data and magnetic field parameters from the Wind spacecraft. Figure 2b shows hourly count rates from selected NM stations before and during a FD. Figure 2c shows our results for first order cosmic-ray anisotropy [3] . Figure 2d shows the cosmic-ray anisotropy magnitude in the solar wind frame perpendicular and parallel to the interplanetary magnetic field from the

[3]Note that δ_x was misplotted in [2]

ACE spacecraft. Here B, B_z, ΔB_{rms}, T_p, V_p, θ,ϕ, sym-H, and $|V_{sw}|$ are magnetic field magnitude, $z-$component of magnetic field, root mean square fluctuation of magnetic field magnitude, proton temperature, proton flow speed, latitude of magnetic field vector, longitude of magnetic field vector, longitudinally symmetric disturbance index for the horizontal (dipole) direction and the modulus of solar wind speed respectively. Then S, $B1$, $B2$, and MC stand for the shock arrival time, times of intense magnetic fluctuations and magnetic cloud respectively. δ_x, δ_y, δ_z, $\delta_\perp$ and $\delta_\parallel$ represent cosmic-ray first order anisotropy in GSE X, Y and Z coordinates. All times from ACE and Wind, which are located at the L_1 Lagrangian point, are shifted one hour later when comparing with data at Earth to roughly account for the solar wind travel time.

Grouping of stations in Figure 2b is according to similar viewing directions. For example, dark red is for stations in Europe, dark blue is for Russian stations and light blue is for stations in Antarctica. Notations at the right of the plot indicate the station code (first letters of two words in a station name or first two letters of one-word name) and geomagnetic cut-off rigidity in GV. Note that for polar stations, the response to cosmic rays is determined by an atmospheric cutoff of ≈ 1 GV. Arrows at the right are to show Northward and Southward asymptotic directions at Thule (TH) and McMurdo (MC) respectively.

Our results revealed an anti-correlation between $\delta_\parallel$ and $\delta_\perp$. For example, there is often an increase in $\delta_\perp$ at times with stronger rms fluctuation ΔB_{rms}. This is consistent with diffusive anisotropy and theories of perpendicular diffusion [2, 23, 24], that perpendicular diffusion increases with increasing $(\Delta B_{rms}/B)$.

In contrast, $\delta_\parallel$ was generally lower during times with stronger magnetic fluctuations and higher during times of weak fluctuations, for instance, within a CME flux rope where magnetic fluctuations are very weak. This is in good agreement with theoretical expectations that strong fluctuations can cause strong cosmic ray scattering leading to low parallel diffusion coefficient [2]. This is also consistent with the idea that a parallel diffusive barrier is responsible for the decrease of cosmic ray flux in the sheath region [19]. Note that in Figure 2d, we indicate the sign of $\delta_\parallel$ in terms of higher GCR flux when viewing along $+\boldsymbol{B}$ (blue) or $-\boldsymbol{B}$ (red)[4]. The color often changes with a reversal of $\boldsymbol{B}$, which is consistent with the idea that parallel scattering and flow processes do not necessarily depend on the sign of $\boldsymbol{B}$.

Within the CME flux rope there was a strong parallel anisotropy in the direction predicted from a theory of drift motions into one leg of the magnetic flux rope and out the other [22], confirming that the anisotropy can remotely sense a large-scale flow of GCRs through a magnetic flux rope. These methods have also been applied to other FD events, as will be addressed in further work.

[4]Colors were also incorrectly applied to $\delta_\parallel$ in [2]

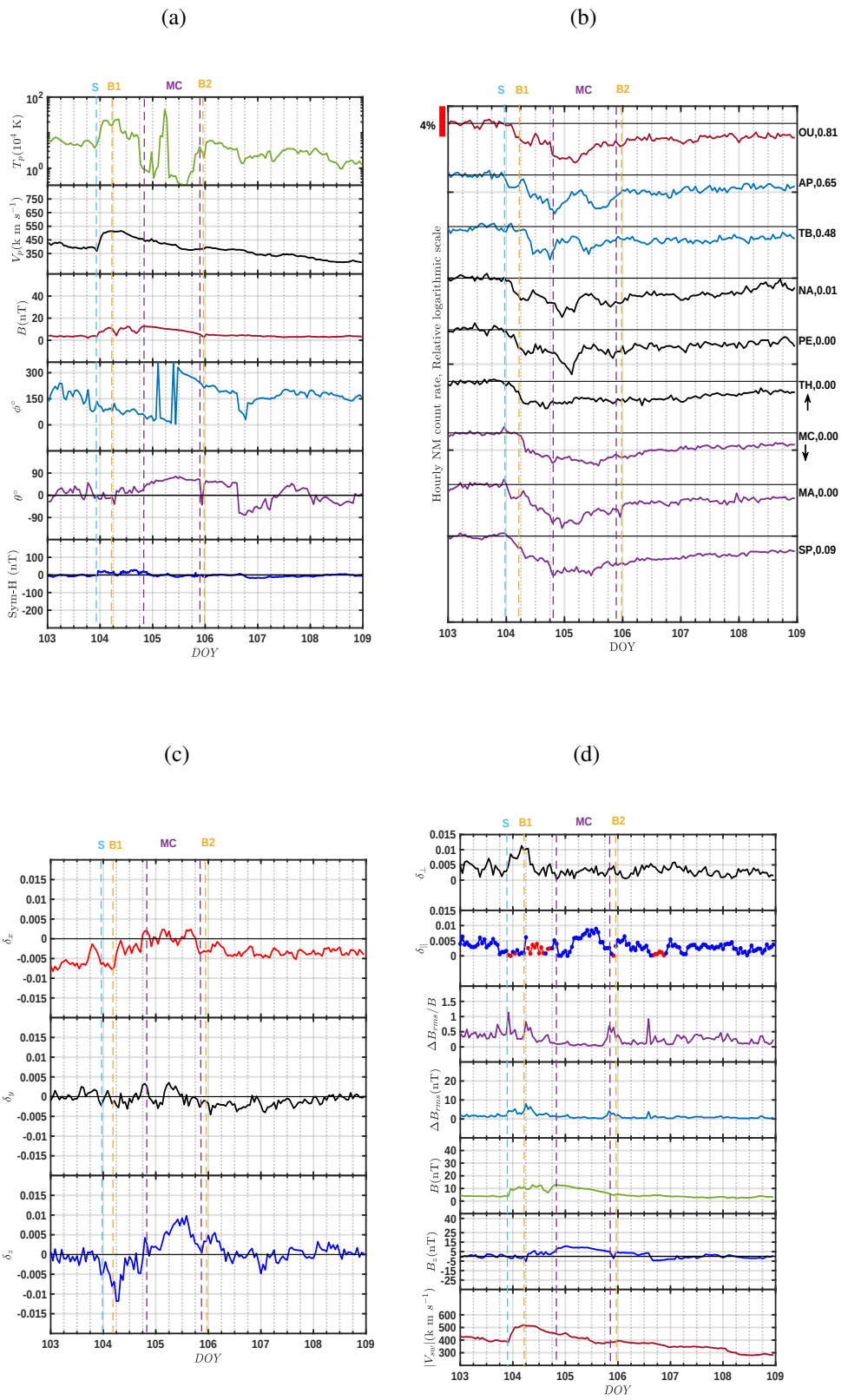


Figure 2: Results of our analysis for the FD starting 13 April 2013. See text for details.

References

[1] Forbush, S. E. 1937, Phys. Rev, 51, 1108.

[2] Tortermpun, U., Ruffolo, D. and Bieber J. W. 2018, The Astrophysical Journal Letters, 852: L26.

[3] Belov, A. V., Bieber, J.W., Eroshenko, E.A., Evenson, P., Pyle, R., and Yanke, G.V. 2003, Adv. Space Res. Vol. 31, No 4, pp. 919 – 924.

[4] Yurchyshyn V. B., Wang H., Goode, P. R. and Deng, Y. 2001, The Astrophysical Journal 563, 381 – 388.

[5] Liu, Y., Manchester, W. B., IV., Kasper, J.C., Richardson, D.J. and Belcher, W.J. 2007, The Astrophysical Journal 665: 1439 – 1447.

[6] Tsurutani, B.T. and Gonzalez, W.D., 1997, in Magnetic Storms, Geophys. Monogr. Ser., Vol. 98, pp. 77 – 89.

[7] Amenomori M., et al. 2017,The Astrophysical Journal 836 : 153.

[8] Cane H. V., 2000, Space Science Reviews 93:55- 77.

[9] Lockwood, J. A.: 1971, Space Sci. Revs. 12, 658–715.

[10] Iucci, N., Pinter, S., Parisi, M., Storini, M., and Villoresi, G., 1986, Nuovo Cimento 9C, 39–50.

[11] Barnden, L. R.: 1973, "Forbush Decreases 1966–1972; Their Solar and Interplanetary Associations and Their Anisotropies", Proc. 13th Int. Cosmic Ray Conf. 2, 1271–1276.

[12] Aguilar, M., Aisa, D., Alpat, B., et al. 2015, PhRvL, 114, 171103.

[13] Bieber, J. W., Clem, J., and Evenson, P. 1997, Proc. ICRC (Durban), 2, 389

[14] Nuntiyakul W., Evenson P., Ruffolo D., Sáiz, A., Bieber, J. W., Clem, J., Pyle, R., Duldig, M. L., and Humble, J. E., 2014, ApJ, 795, 11

[15] Lin Zhongmin, Bieber, J. W., Evenson P. 1995, Journal of Geophysical Research, 100, NO. A12.

[16] Nuntiyakul, W., Evenson, P., Ruffolo, D., Sáiz, A., Bieber, J. W., Clem, J., Pyle R., Duldig, M. L., and Humble, J. E., 2018, Journal of Geophysical Research: Space Physics, 123, 7181.

[17] Hapgood, M.A. 1992, Planet. Space Sci., Vol 40, $No5.pp.711 - 717$

[18] Russell, T.C. 1971, Cosmic Electrodynamics, 2, 184 – 196.

[19] Wibberenz, G., le Roux, J. A., Potgieter, M. S., and Bieber, J. W. 1998, SSRv,83, 309

[20] Nagashima, K., Fujimoto, K., Sakakibara, S., Morishita, I., and Tatsuoka, R.1992, P & SS, 40, 1109.

[21] Fushishita, A., Kuwabara, T., Kato, C., et al. 2010, ApJ, 715, 1239.

[22] Krittinatham, W., and Ruffolo, D. 2009, ApJ, 704, 831.

[23] Shalchi, A. 2010, ApJL, 720, $L127$.

[24] Ruffolo, D., Pianpanit, T., Matthaeus, W. H., & Chuychai, P. 2012, ApJ, 747, L34

[25] Cane, H. V., Richardson, I. G., and Wibberenz, G. 1995, Proc. ICRC (Rome), 4, 377.

[26] Kadokura, A., and Nishida, A. 1986, JGR, 91, 13.

[27] Kuwabara, T., Bieber, J. W., Evenson, P., et al. 2009, JGR, 114$A05109$

PROCEEDINGS OF SCIENCE

Detecting single and multiple atmospheric secondaries in an 18NM64

Alejandro Sáiz*, **Warit Mitthumsiri**, **David Ruffolo**
Department of Physics, Faculty of Science, Mahidol University, Bangkok 10400, Thailand
E-mail: alejandro.sai@mahidol.ac.th, warit.mit@mahidol.ac.th, david.ruf@mahidol.ac.th

Paul Evenson
Bartol Research Institute, University of Delaware, Newark, DE 19716, USA
E-mail: evenson@udel.edu

Tanin Nutaro
Department of Physics, Faculty of Science, Ubon Ratchathani University, Ubon Ratchathani 34190, Thailand
E-mail: tnutaro@yahoo.com

We present an update on the analysis of cross-counter time-delay histograms with 5 μs bins as recorded since late 2015 in the Princess Sirindhorn Neutron Monitor, an 18NM64 (with 18 counter tubes in a continuous row) at 2560 m altitude in Doi Inthanon, Thailand. A cross-counter relative leader fraction L_{ij} can be defined as the fraction of pulses measured in counter number i that are uncorrelated in time with the most recent pulse in counter j. For low tube separation, L_{ij} rapidly increases with increasing tube separation $|i-j|$, as expected from the spatial spreading of neutrons produced by the same atmospheric secondary particle inside the neutron monitor. At high tube separation, L_{ij} increases slowly with increasing tube separation and remains different from unity, which we interpret as due to multiple atmospheric secondaries arriving in rapid succession after originating from the same primary cosmic ray. We study temporal variations of the cross-counter relative leader fraction at large tube separation ($|i-j|>6$, or roughly more than 3 m) and analyze the possible contribution of atmospheric effects to the data.

36th International Cosmic Ray Conference -ICRC2019-
July 24th - August 1st, 2019
Madison, WI, U.S.A.

*Speaker.

© Copyright owned by the author(s) under the terms of the Creative Commons Attribution-NonCommercial-NoDerivatives 4.0 International License (CC BY-NC-ND 4.0).

1. Introduction

Neutron monitors (NMs) are ground-based detectors of 'secondary' cosmic rays (mostly neutrons) that are produced in Earth's atmosphere by interactions of ('primary') cosmic rays with energies $\sim$1 GeV and above. In an NM, a number of cylindrical, gas-filled proportional counters operate inside several tons of Pb (the producer) to detect individual 'tertiary' neutrons produced from the collisions of atmospheric secondary cosmic rays with Pb nuclei. The rate of detection, and its variations, can then be related to the flux of primary cosmic rays arriving to Earth.

The Princess Sirindhorn Neutron Monitor (PSNM) is located on the top of Doi Inthanon, Thailand's highest mountain, at latitude 18.59° N, longitude 98.49° E, and 2560 m above sea level. The geomagnetic cosmic ray cutoff there is higher than at any other NM location around the world. The main detector contains 18 neutron counters in a continuous row following the NM64 design [1]; 3 other counters operate outside the Pb producer (bare counters).

As explained previously [2], the data acquisition system at the PSNM records also the absolute time of each neutron detection, with a few μs accuracy. The goal of this extra, non-standard measurement is to have an estimation of cosmic ray energies as well as flux. The distributions of time delays, or times between consecutive neutron detections, can be analyzed to extract a leader fraction L that quantifies the number of detections that are statistically uncorrelated with the previous detection, relative to the total [3]. Typically, two neutron detections that originate from two different cosmic rays are uncorrelated in time as in a Poisson process; on the other hand, tertiary neutrons produced by the same atmospheric secondary in the Pb are detected within a few ms and are statistically correlated. Thus L can be shown to be related to the energy spectrum of cosmic rays, since production in the Pb increases for higher cosmic ray energy.

In our previous work [3, 4, 5, 6], time delay distributions were studied for consecutive detections in the same neutron counter, and L was calculated for each of the 18 counters independently. As noted above, this measurement is dominated by neutrons produced together in the Pb (from the same secondary), which most of the times are detected in the same counter but often get detected by different counters. Also, some time correlation may arise from the detection of different atmospheric secondaries that were produced together in the atmosphere (i.e., from the same primary). For the sake of understanding these processes, in late 2015 the electronics in the PSNM acquisition system were upgraded to allow for cross-counter time delay analysis. In this work, we present an update on the study of time correlations between neutrons detected in different counters, using cross-counter leader fractions, and analyze the effects of atmospheric pressure and humidity in our measurements, with the aim of studying time variations that could be associated to changes in cosmic ray spectrum.

2. Definition of cross-counter leader fractions

As in our previous report [2], we define a cross-counter time delay t from counter i to counter j, for each detection in counter i, as the time until the earliest detection in counter j. The distribution of time delays typically shows an excess of events at short times that arises from correlated neutron detections, on top of an exponential distribution that corresponds to the chance coincidence of uncorrelated secondary neutrons (produced by different primary cosmic rays). For a normalized

distribution of time delays n_{ij}, said exponential tail can be expressed as

$$n_{ij}(t) \to \alpha_j L_{ij} \exp(-\alpha_j t) \qquad t > t_{\text{trans}} \tag{2.1}$$

for a transition time t_{trans} of a few ms, where α_j is the probability per unit time of a chance coincidence in counter j, and the cross-counter leader fraction L_{ij} represents the probability that a count on counter i is not temporally associated with any later count on counter j [2].

To reduce the number of recorded distributions and increase the statistics, we initially analyzed the 18 combined distributions of cross-counter time delays at a given counter separation Δ, or $n_\Delta(t)$, with $\Delta = |i-j|$, for $\Delta = 0,\ldots,17$. There is, however, an intrinsic difference in the values of the chance coincidence probability α_j from counter to counter that suggests that these combined distributions $n_\Delta(t)$ may deviate from the simple exponential form described above. The most important discrepancy in the values of α_j appears between counters at the 'end' positions of the continuous row of counters (first and last counter) and the other 'middle' counters. The value of α_j is typically $\sim 15\%$ lower at end counters, mainly due to the smaller amount of Pb surrounding these counters. Thus, since August, 2017, the number of recorded distributions was increased to the 50 different combinations for which the counters detecting the early and late neutrons were either a 'middle' (m) or 'end' (e) counter: $n_\Delta^{\text{mm}}(t)$, $n_\Delta^{\text{me}}(t)$, $n_\Delta^{\text{em}}(t)$, and $n_\Delta^{\text{ee}}(t)$.

The corresponding 50 values of cross-counter leader fraction can be labelled L_Δ^{mm} with $\Delta = 0,\ldots,15$, L_Δ^{me} and L_Δ^{em} with $\Delta = 1,\ldots,16$, and L_Δ^{ee} with $\Delta = 0$ and 17. The two cases with $\Delta = 0$ (zero separation) are similar to the same-counter leader fractions studied in our previous work, but combined for the 16 middle counters or the 2 end counters. As in previous work, a fit of each time delay distribution to an exponential function for a specific range of t (50–200 ms in this case) is used to estimate the corresponding cross-counter leader fraction after proper normalization.

3. Results for accumulated distributions

Total distributions of cross-counter time delays were accumulated between August 5th, 2017 and August 31st, 2018 for a total of ~ 9000 h. Figure 1 shows the cross-counter leader fraction L_Δ as a function of counter separation Δ for that period, for the different 'middle'-'end' combinations. The values start at less than 0.8 for separation zero (same counter) and quickly increase when considering cross-counter time delays between distant counters, approaching a constant value close to 1. A value of $L_\Delta = 1$ would correspond to totally uncorrelated neutron detections between counters (a Poisson process). However, the value of L_Δ that is observed, which seems to vary little for separations 6–17, is never consistent with 1.

Among the four 'middle'-'end' combinations, values of L_Δ at small counter separation ($\Delta < 3$) are higher when the counter on which the early neutron was detected is of the 'middle' type than when it is an 'end' type. Assuming these L_Δ are related to groups of same-secondary events, the mechanism to explain this can be the same that is at play in the same-counter L reported previously [3], for which values of L are lowest at the two end counters and even slightly lower at the second-from-end positions than for middle counters. The smaller amount of Pb surrounding end counters may account for a smaller fraction of 'leaders', or the proximity of the lateral polyethylene reflector slabs reflecting tertiary neutrons back may generate an increase in the number of 'followers', or both.

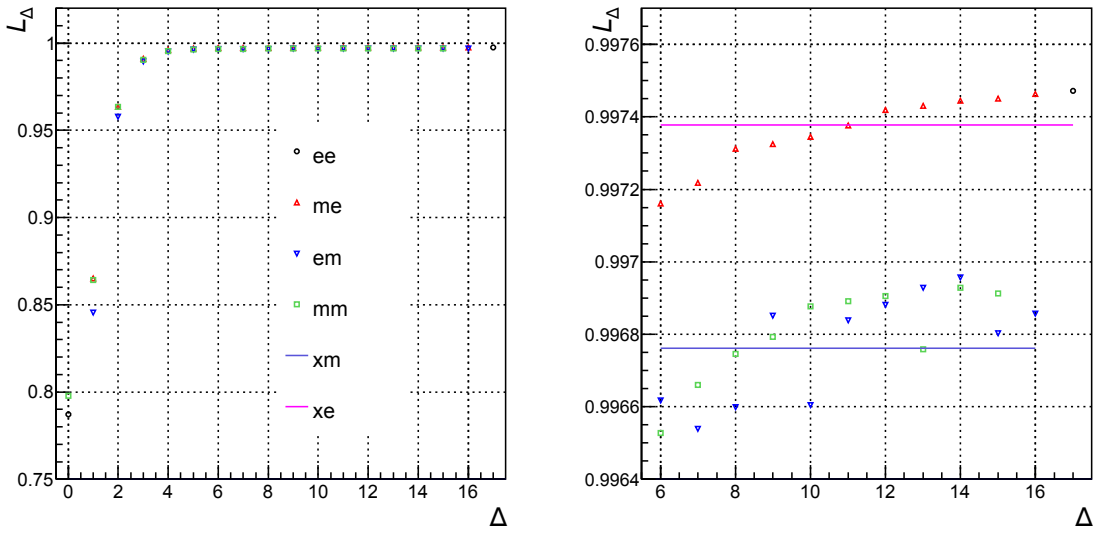


Figure 1: Cross-counter leader fraction L_Δ as a function of counter separation Δ.

On the other hand, the large separation values of L_Δ are mostly determined by the type of counter on which the late neutron is detected. Based on this, we also analyze combined distributions for all separations of 6 positions or more for cases 'mm'+'em' and 'me'+'ee', giving two values of large-separation leader fraction $L^{\rm xm}_{\Delta>5}$ and $L^{\rm xe}_{\Delta>5}$, respectively, shown as horizontal lines on the right panel of Figure 1. Both values are consistent with the $L_{\Delta>5}$ value of 0.997 reported previously for an earlier time period and all counter combinations with separation 6 or larger [2].

For these large separation cases, L_Δ is related to multiple secondaries and its higher value when the later counter is of 'end' type is related to these counters being less efficient at registering counts (by $\sim 15\%$, see above), which makes the multiplicity lower in this case compared to the case when the later counter is of 'middle' type (note that the average multiplicity is $1/L$). These two values ($L^{\rm xm}_{\Delta>5}$ and $L^{\rm xe}_{\Delta>5}$) are very similar but also close to 1, so the corresponding 'follower fractions' $1-L_\Delta$ actually differ by about 20% between the two cases.

4. Results for hourly distributions

Values of the different cross-counter leader fractions were also calculated for each hour in the period between August 5th, 2017 and August 31st, 2018. As is usual with the same-counter leader fraction [3], changes in atmospheric pressure produce a very small change in the measured value of L, but variations in atmospheric water vapor (quite pronounced between the rainy and dry seasons) have a larger effect. Figure 2 shows three examples of correlations between hourly values of L_Δ and the atmospheric pressure and humidity. Variations with pressure (top panels) are more easily identified by subtracting the daily average on both P and $\log L_\Delta$. The correlation (fit line) can be used to remove pressure effects. Subsequently, a correlation between pressure-corrected L_Δ and humidity can be identified and a further correction applied to L_Δ. As explained elsewhere [6], we characterize atmospheric humidity using the precipitable water vapor (PWV) determined from the GDAS (Global Atmospheric Data Assimilation) database (see http://ready.arl.noaa.gov/gdas1.php).

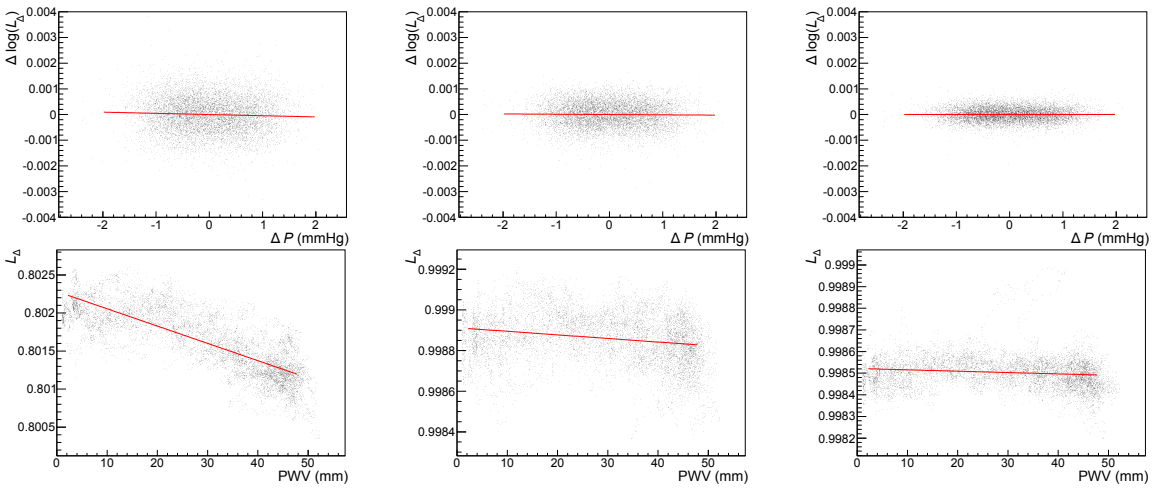


Figure 2: Dependence of L_Δ on (top panels) atmospheric pressure and (bottom panels) atmospheric humidity for the cases (left to right) $L^{\rm mm}_{\Delta=0}$, $L^{\rm xe}_{\Delta>5}$, and $L^{\rm xm}_{\Delta>5}$.

In Figure 2, one of the same-counter leader fractions is presented, for comparison purposes, together with the two combined large-separation leader fractions. For the latter, the effects of atmospheric humidity appear to be less important; however, considering the follower fraction $1-L_\Delta$ instead of the leader fraction L_Δ gives similar order-of-magnitude variations with PWV for large and small counter separation.

The values of $L^{\rm xe}_{\Delta>5}$ and $L^{\rm xm}_{\Delta>5}$, already corrected for atmospheric pressure and humidity effects, are presented in Figure 3 as follower fractions $1-L_\Delta$ relative to the average of this period. The apparent time fluctuations of $\sim 20\%$ or larger can only be attributed to current uncertainties of the method. No clear time dependence was found for this time interval.

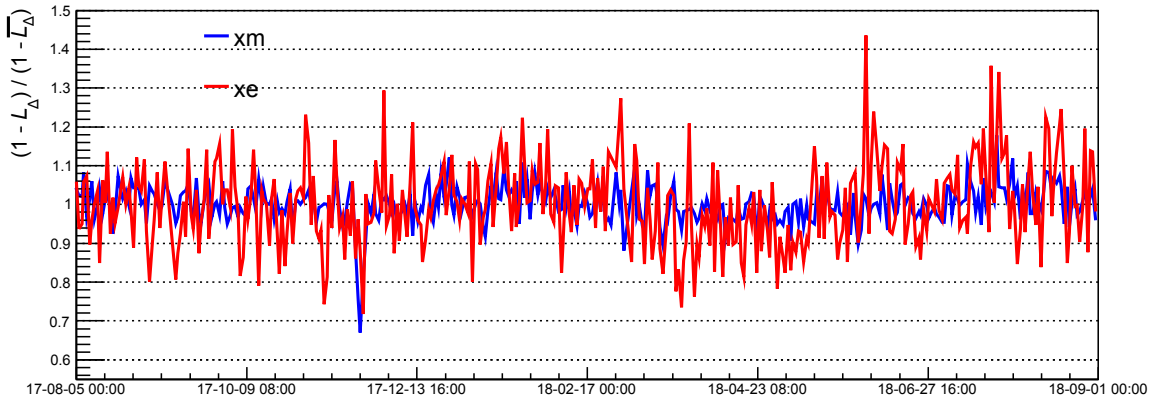


Figure 3: Relative variations of the follower fractions $1-L^{\rm xe}_{\Delta>5}$ and $1-L^{\rm xm}_{\Delta>5}$ for the time interval studied.

5. Conclusions

We present results from a new data-acquisition electronics system that measures cross-counter time delay histograms at the Princess Sirindhorn Neutron Monitor at the summit of Doi Inthanon,

Thailand. For these, we have extracted cross-counter leader fractions, which are related to cross-counter neutron multiplicity. An analysis of the cross-counter leader fraction as a function of counter separation distance reveals a nearly constant cross-counter multiplicity at large counter separation, not consistent with 1. We attribute this to multiple atmospheric secondary particles from the same primary cosmic ray. We have measured the effects of atmospheric pressure and water vapor on the cross-counter leader fraction, and corrected for these effects during August, 2017–August, 2018. After correction, no clear time dependence was found for this time period.

In future work, we will analyze Monte Carlo simulations of atmospheric particle showers to estimate the expected time delay distributions of secondary neutrons and justify that distant cross-counter multiplicity is indeed due to multiple secondaries. We will also report on data taken for individual events for which 15 or more counters present simultaneous detections (within 1 ms) and explore their possible origin associated to same-primary atmospheric showers.

Acknowledgments

Partially supported by the Thailand Research Fund award RTA5980003, TRG5880173, and US National Science Foundation awards PLR-1245939 and PLR-1341562 and their predecessors.

References

[1] C. J. Hatton and H. Carmichael, *Experimental investigation of the NM-64 neutron monitor*, *CaJPh* **42**, 2443 (1964).

[2] A. Sáiz, W. Mitthumsiri, D. Ruffolo, P. Evenson and T. Nutaro, *Measurement of cross-counter leader fractions in an 18NM64: Detecting single and multiple atmospheric secondaries*, in proceedings of *35th International Cosmic Ray Conference*, PoS(ICRC2017)047 (2017).

[3] D. Ruffolo, A. Sáiz, P.-S. Mangeard, N. Kamyan, P. Muangha, T. Nutaro, S. Sumran, C. Chaiwattana, N. Gasiprong, C. Channok, C. Wuttiya, M. Rujiwarodom, P. Tooprakai, B. Asavapibhop, J. W. Bieber, J. Clem, P. Evenson and K. Munakata, *Monitoring short-term cosmic-ray spectral variations using neutron monitor time-delay measurements*, *ApJ* **817**, 38 (2016).

[4] P.-S. Mangeard, D. Ruffolo, A. Sáiz, W. Nuntiyakul, J. W. Bieber, J. Clem, P. Evenson, R. Pyle, M. L. Duldig and J. E. Humble, *Dependence of the neutron monitor count rate and time delay distribution on the rigidity spectrum of primary cosmic rays*, *JGRA* **121**, 11620 (2016).

[5] C. Banglieng, D. Ruffolo, A. Sáiz, P. Evenson and T. Nutaro, *Tracking cosmic-ray spectral variations with neutron monitor time-delay measurements at high cutoff rigidity during 2007–2017*, in proceedings of *35th International Cosmic Ray Conference*, PoS(ICRC2017)025 (2017).

[6] C. Banglieng, H. Janthaloet, D. Ruffolo, A. Sáiz, W. Mitthumsiri, P. Evenson, T. Nutaro, R. Pyle, S. Seunarine and J. Madsen, *Neutron monitor time-delay measurements to track cosmic ray spectral variation due to solar modulation at high and low cutoff rigidity*, these proceedings.

Your Abstract Has Been Submitted For The AGU Fall Meeting 2019. You Will Receive An Email Confirmation.

Click HERE to print this page now.

- This page indicates that you have completed your abstract submission and an email confirmation will be sent to you.
- **If you do not receive an email confirmation**, please contact agu@confex.com to ensure your abstract was submitted and to have a confirmation email sent to you.
- This confirmation does not guarantee that your abstract was accepted and only confirms that your abstract will be submitted for consideration by the Program Committee.
- In this system, there is no '**Draft**' option. Once the abstract is submitted, you may review, edit or withdraw your abstract until the deadline of **31 July 2019 23:59 EDT/03:59 +1 GMT**.
- **Do not withdraw a paid abstract submission if edits are needed or to begin a new submission. You may make any edits to your abstract until the submission deadline.**
- **Abstract fees are nonrefundable.**
- Once submitted, your abstract will need to be withdrawn if you no longer wish to have it considered by the Program Committee.
- Consider making your submission citable and more discoverable by adding it to the Earth and Space Science Open Archive (ESSOAr). ESSOAr is free to post and view content. Please read our submission guide and FAQ for more information.

Flocculation, switchbacks, and loss of Alfvenicity: Indicators of shear-driven turbulence in the young solar wind?

David J Ruffolo[1], **William H Matthaeus**[2], Craig DeForest[3], Tulasi Parashar[2], Melvyn L Goldstein[4,5], D Aaron Roberts[6], Rohit Chhiber[2], Arcadi V. Usmanov[2,4], Thierry Dudok de Wit[7], Riddhi Bandyopadhyay[8], Alexandros Chasapis[9], Bennett Maruca[10], Marco C M Velli[11] and Justin Christophe Kasper[12],
(1)Mahidol University, Department of Physics, Faculty of Science, Bangkok, Thailand, (2)University of Delaware, Newark, DE, United States, (3)Southwest Research Institute, Boulder, CO, United States, (4)NASA Goddard SFC, Greenbelt, MD, United States, (5)University of Maryland Baltimore County, Baltimore, MD, United States, (6)NASA Goddard SFC, Code 672, Greenbelt, MD, United States, (7)LPC2E, CNRS and University of Orléans, Orléans, France, (8)University of Delaware, Department of Physics and Astronomy, Newark, DE, United States, (9)Laboratory for Atmospheric and Space Physics, Boulder, United States, (10)Center for Astrophysics, Berkeley, CA, United States, (11)University of California Los Angeles, Earth Planetary and Space Sciences, Los Angeles, CA, United States, (12)University of Michigan, Ann Arbor, MI, United States

Abstract Text:

Since the first preliminary announcements of Parker Solar Probe results [1], there has been increased discussion of “switchbacks” and speed enhancements such as those observed in Helios data [2]. A familiar explanation relies on outward propagation of large amplitude remnants of magnetic reconnection at lower altitudes. Such a mechanism is plausible and difficult to rule out. However, another possibility exists, namely that the onset of strong shear-driven turbulence, beginning just outside the Alfvén critical region, may induce the switchbacks through large-scale perturbation of the flow. This scenario is consistent with a suite of observable effects already apparent in imaging [3] and in situ datasets [2]. DeForest et al. interpreted the transition from elongated striae to relatively isotropic flocculae as a signature of the onset of shear-driven

turbulent activity some 20-80 Rs from the photosphere, where the magnetic field ceases to be a dominant constraint on transverse motions; this interpretation has received support from turbulence-driven global simulations of the solar wind [4]. The presence of velocity shears is also strongly suggested by coronal imaging at lower altitudes [5]. Somewhere above the conventional Alfvén point such shears can begin supplying turbulence energy [6] while also destroying Alfvénicity by injection of kinetic energy but not cross helicity [7]. If indeed the flocculation signifies large fluctuations or even turnover associated with vortices, then specific features of shear driven turbulence may be anticipated in imaging data from the upcoming PUNCH mission and in ongoing analysis of in situ Parker Solar Probe observations. Details of these signatures will be given here. Research supported in part by grant RTA5980003 from the Thailand Research Fund, by NASA under NNX17AB79G, 80NSSC18K1210, 80NSSC18K1648, and by the PSP ISOIS project as subcontract under NNN06AA01C.

[1] S. Bale, invited talk, 2018 Fall AGU Meeting

[2] T. Horbury, L. Matteini & D. Stansby, MNRAS 478, 1980 (2018)

[3] C. DeForest et al., Astrophys. J. 828, 66 (2016)

[4] R. Chhiber et al., Astophys. J. Lett. 856, L39 (2018)

[5] C. DeForest et al., Astrophys. J. 862, 18 (2018)

[6] G. Zank et al., JGR 101, 17093 (1996); B. Breech et al., JGR 113, A08105 (2008)

[7] D. A. Roberts et al., JGR 97, 17115 (1992); see also Fig. 3 of D. A. Roberts, Astrophys. J. 711, 1044 (2010)

Session Selection:
Fundamental Physics of the Solar Corona and Inner Heliosphere

Submitter's E-mail Address:
ruffolo.physics@gmail.com

Abstract Title:
Flocculation, switchbacks, and loss of Alfvenicity: Indicators of shear-driven turbulence in the young solar wind?

Requested Presentation Type:
Assigned by Program Committee (oral or Poster)

Previously Published?:
No

AGU On-Demand:
Yes

Abstract Payment:
Paid (agu-fm19-571914-0762-1580-8979-5568)

For non-students only: I do not want to be involved in OSPA or the mentoring program.

First Author

David J Ruffolo
Primary Email: ruffolo.physics@gmail.com

Affiliation(s):

Mahidol University
Department of Physics, Faculty of Science
Bangkok (Thailand)

Second Presenting Author
Presenting Author

William H Matthaeus
Primary Email: whm@udel.edu

Affiliation(s):

University of Delaware Department of Physics and Astronomy
Newark DE (United States)

Third Author

Craig DeForest
Primary Email: deforest@boulder.swri.edu

Affiliation(s):

Southwest Research Institute
Boulder CO 80305 (United States)

Fourth Author

Tulasi Parashar
Primary Email: tulasi@udel.edu

Affiliation(s):

University of Delaware
Newark DE (United States)

Fifth Author

Melvyn L Goldstein
Primary Email: u2mlg1@gmail.com

Affiliation(s):

University of Maryland Baltimore County
Baltimore MD 2150 (United States)

NASA Goddard SFC
Greenbelt MD 20771-0001 (United States)

Sixth Author

D Aaron Roberts
Primary Email: aaron.roberts@nasa.gov

Affiliation(s):

NASA Goddard SFC
Code 672
Greenbelt MD 20771-0000 (United States)

Seventh Author

Rohit Chhiber
Primary Email: rohitc@udel.edu

Affiliation(s):

University of Delaware
Newark DE (United States)

Eighth Author

Arcadi V. Usmanov
Primary Email: avusmanov@gmail.com

Affiliation(s):

NASA Goddard SFC
Greenbelt MD 20771-0001 (United States)

University of Delaware
Newark DE (United States)

Ninth Author

Thierry Dudok de Wit
Primary Email: ddwit@cnrs-orleans.fr

Affiliation(s):

LPC2E, CNRS and University of Orléans
Orléans (France)

Tenth Author

Riddhi Bandyopadhyay
Primary Email: riddhib@udel.edu

Affiliation(s):

University of Delaware
Department of Physics and Astronomy
Newark DE (United States)

Eleventh Author

Alexandros Chasapis
Primary Email: Alexandros.chasapis@lasp.colorado.edu

Affiliation(s):

Laboratory for Atmospheric and Space Physics
Boulder (United States)

Twelfth Author

Bennett Maruca
Primary Email: bmaruca@udel.edu

Affiliation(s):

Center for Astrophysics
Berkeley CA 94720 (United States)

Thirteenth Author

Marco C M Velli
Primary Email: mvelli@jpl.nasa.gov

Affiliation(s):

University of California Los Angeles
Earth Planetary and Space Sciences
Los Angeles CA 90095 (United States)

Fourteenth Author

Justin Christophe Kasper
Primary Email: jckasper@umich.edu

Affiliation(s):

University of Michigan
Ann Arbor MI 48109 (United States)

If necessary, you can make changes to your abstract submission

- You may access your submission to make any edits or submit another abstract by clicking here.
- Your Abstract ID# is: 571914.

- Any changes that you make will be reflected instantly in what is seen by the reviewers.
- After the abstract proposal is submitted, you are not required to go through all submission steps to make edits. For example, click the "Authors" step in the Abstract Submission Control Panel to edit the Authors and then click save or submit.
- When you have completed your submission, you may close this browser window or submit another abstract Abstract Viewer.

Tell us what you think of the abstract submission process